

International
Journal of



quantum chemistry

QUANTUM CHEMISTRY

SYMPOSIUM NO. 28, 1994

Proceedings of the
International Symposium on

Atomic, Molecular, and
Condensed Matter
Theory and
Computational
Methods

Held at the Marriott at Sawgrass Resort
Ponte Vedra Beach, Florida, February 12-19, 1994

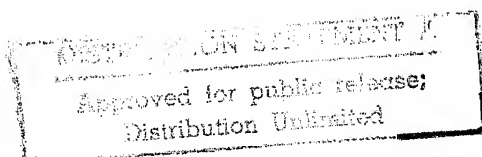
Editor in Chief: Per-Olov Löwdin

Special Editors: N. Yngve Öhrn
John R. Sabin
Michael C. Zerner

An Interscience* Publication
published by JOHN WILEY & SONS

New York • Chichester • Brisbane • Toronto •
Singapore

UQSAF
ISSN 0360-8832



19950206 088

International Journal of QUANTUM CHEMISTRY

Quantum Chemistry Symposium No. 28

*Proceedings of the
International Symposium on
Atomic, Molecular, and Condensed Matter
Theory and Computational Methods*

N00014-93-1-0343

DTIC
ELECTE
FEB 14 1995
S G D

DTIC QUALITY INSPECTED

Held at Ponte Vedra Beach, Florida,
February 12-19, 1994

Editor-in-Chief: Per-Olov Löwdin

Special Editors: N. Yngve Öhrn, John R. Sabin, and
Michael C. Zerner

an Interscience® Publication
published by JOHN WILEY & SONS

ion For	
CRA&I	<input checked="" type="checkbox"/>
TAB	<input type="checkbox"/>
ounced	<input type="checkbox"/>
cation	

Distribution /	
Availability Codes	
Dist	Avail and / or Special
A-1	

International Journal of QUANTUM CHEMISTRY

Quantum Chemistry Symposia

Honorary Editorial Board:

Gerhard Herzberg Kenichi Fukui

Editor-in-Chief: Per Olov Löwdin

Editors: Jean-Louis Calais N. Yngve Öhrn

Associate Editors: Erkki Brändas Osvaldo Goscinski John R. Sabin Michael Zerner

Editorial Board:

Tang Au-Chin	Laurens Jansen	Kimio Ohno	Alberte Pullman
Enrico Clementi	Norman H. March	Robert G. Parr	Bernard Pullman
Raymond Daudel	Roy McWeeny	Ruben Pauncz	Harrison Shull
Ernest Davidson	Saburo Nagakura	John A. Pople	Paul von Ragué Schleyer
George G. Hall			Rudolf Zahradnik

Advisory Editorial Board:

M. V. Basilevsky	M. García-Sucre	U. Kaldor	C. Leforestier	W. Reinhardt
M. Bénard	J. Gerratt	M. Karelson	S. Lunell	S. Rettrup
F. Bernardi	O. Gropen	H. Kashiwagi	J. P. Malrieu	W. G. Richards
J. Bertran	N. C. Handy	J. Katriel	P. Mezey	D. Salahub
G. Biczó	A. E. Hansen	D. Klein	H. Monkhorst	N. F. Stepanov
D. Bishop	J. T. Hynes	M. Klessinger	V. Ortiz	C. Thomson
P. Carsky	B. Jeziorski	P. A. Kollman	P. Pulay	F. Weinhold
L. Cederbaum	M. S. Jhon	L. Lathouwers	M. A. Ratner	H. Weinstein
G. Corongiu	P. Jorgensen			
P. Fulde				

This volume constitutes a part of the annual subscription to the *International Journal of Quantum Chemistry*, vols. 49–52, and as such is supplied without additional charge to subscribers. Single copies can be purchased from the Subscription Department, John Wiley & Sons, Inc.

The *International Journal of Quantum Chemistry* (ISSN 0360-8832) is published semi-monthly with two extra issues in November, by John Wiley & Sons, Inc. Copyright © 1994 John Wiley & Sons, Inc. All rights reserved. No part of this publication may be reproduced in any form or by any means, except as permitted under section 107 or 108 of the 1976 United States Copyright Act, without either the prior written permission of the publisher, or authorization through the Copyright Clearance Center, 27 Congress Street, Salem, MA 01970, (508) 744-3350, fax (508) 745-9379. Second-class postage paid at New York, NY, and at additional mailing offices.

The code and the copyright notice appearing at the bottom of the first page of an article in this journal indicate the copyright owner's consent that copies of the article may be made for personal or internal use, or for the personal or internal use of specific clients, on the condition that the copier pay for copying beyond that permitted by Sections 107 or 108 of the U.S. Copyright Law. This consent does not extend to other kinds of copying, such as copying for general distribution, for advertising or promotional purposes, for creating new collective works, or for resale. Such permission requests and other permission inquiries should be addressed to the Permissions Dept. Subscription price (1994): \$2,465.00 in the US, \$2,725.00 in Canada and Mexico, \$2,822.50 outside North America. All subscriptions outside US will be sent by air. Personal rate (available only if there is an institutional subscription): \$125.00 in North America, \$255.00 outside North America. Subscriptions at the personal rate are available only to individuals. Payment must be made in US dollars drawn on a US bank. Claims for undelivered copies will be accepted only after the following issue has been received. Please enclose a copy of the mailing label. Missing copies will be supplied when losses have been sustained in transit and where reserve stock permits. Please allow four weeks for processing a change of address. For subscription inquiries, please call (212) 850-6645.

Postmaster: Send address changes to Subscription Department, John Wiley & Sons, Inc., 605 Third Avenue, New York, New York 10158.

Printed in the United States of America.

This journal is printed on acid-free paper.

Contents

Introduction	
<i>N. Y. Öhrn, J. R. Sabin, and M. C. Zerner</i>	1
On the Occasion of Yngve Öhrn's 60th Birthday	
<i>R. J. Bartlett, E. Deumens, P.-O. Löwdin, D. A. Micha, H. J. Monkhorst, J. R. Sabin, S. B. Trickey, and M. C. Zerner</i>	3
Correlation and Propagation in Time	
<i>J. Linderberg</i>	7
Electron-Nuclear Dynamics of Molecular Systems	
<i>A. Diz and Y. Öhrn</i>	11
Semidirect Algorithms in Electron Propagator Calculations	
<i>V. G. Zakrzewski and J. V. Ortiz</i>	23
Treatment of Molecular Resonances Using the Bi-Orthogonal Dilated Electron Propagator with Application to the $^2\Pi_g$ Shape Resonance in e - N_2 Scattering	
<i>M. N. Medikeri and M. K. Mishra</i>	29
Evaluation of Integrals Appearing in the Hylleraas CI Method by Expanding $1/r_{ij}$ in Terms of a Complete Basis Set	
<i>J. E. Pérez, H. H. Cuenya, R. H. Contreras, F. S. Ortiz, H. Grinberg, C. G. Giribet, and M. C. Ruiz de Azúa</i>	39
Self-Consistent Coupling of Atomic Orbitals to a Moving Charge	
<i>H. F. M. da Costa and D. A. Micha</i>	49
Aspects Related to Quantum Studies of Multiphoton Excitation and Dissociation of Diatomic Molecules	
<i>T.-F. Jiang and J.-M. Yuan</i>	65
Electron Scattering Mechanisms in Giant Magnetoresistance Computed by the LACO Full-Potential Method	
<i>R. K. Nesbet</i>	77
From Parallel to Distributed Computing for Reactive Scattering Calculations	
<i>A. Laganà, O. Gervasi, R. Baraglia, and D. Laforenza</i>	85
The Calculation of Feshbach Resonances Using Coupled Propagator Equations	
<i>H. Zhan, Y. Zhang, and P. Winkler</i>	103
Isotope Effects in Laser-Induced Multiphoton Molecular Dynamics	
<i>O. Atabek</i>	113

Contents Continued on Next Page

Chemistry and Phase Transitions from Hypervelocity Impacts <i>C. T. White, S. B. Sinnott, J. W. Mintmire, D. W. Brenner, and D. H. Robertson</i>	129
Evaluation of Group Theoretical Characteristics Using the Symbolic Manipulation Language MAPLE <i>U. Taneri and J. Paldus</i>	139
The Coupled Cluster Theory of Quantum Lattice Systems <i>R. F. Bishop and Y. Xian</i>	155
Influence of Rotation on Multiphoton Processes in HF <i>J. Broeckhove, B. Feyen, and P. van Leuven</i>	173
Effective Core Potential Study of Multiply Bonded Transition Metal Complexes of the Heavier Main Group Elements <i>M. T. Benson, T. R. Cundari, Y. Li, and L. A. Strohecker</i>	181
Coupled-Cluster Singles, Doubles, and Triples Calculations with Hartree-Fock and Brueckner Orbital Reference Determinants: A Comparative Study <i>J. D. Watts and R. J. Bartlett</i>	195
Relativistic Coupled Cluster Theory Based on the No-Pair Dirac- Coulomb-Breit Hamiltonian: Relativistic Pair Correlation Energies of the Xe Atom <i>E. Eliav, U. Kaldor, and Y. Ishikawa</i>	205
Topological Analysis of Valence Electron Charge Distributions from Semiempirical and <i>Ab Initio</i> Methods <i>M. Hô, H. Schmider, K. E. Edgecombe, and V. H. Smith, Jr.</i>	215
Convergence of a Sequence of Lower Bounds for $\langle 1/r \rangle$ for the Noble Gas, Alkali, and Alkaline Earth Atoms <i>P. Csavinsky</i>	227
A New Representation for Ground States and Its Legendre Transforms <i>A. Cedillo</i>	231
New Approximation to the Bound States of Schrödinger Operators with Coulomb Interaction <i>M. A. Núñez and G. Izquierdo B.</i>	241
On a Form of Nonlinear Dissipative Wave Mechanics Valid in Position- and Momentum-Space <i>D. Schuch</i>	251
Franck-Condon Factors and Squeezed States <i>A. Palma, L. Sandoval, and M. Martín</i>	261

Extreme Electron Correlation Effects on the Electric Properties of Atomic Anions <i>S. Canuto</i>	265
Effects of the Finite Duration of Quantum Tunneling in Laser-Assisted Scanning Tunneling Microscopy <i>M. J. Hagmann</i>	271
Theoretical Ion Implantation Profiles for Low Energy Protons under Channeling Conditions <i>J. A. Nobel, J. R. Sabin, and S. B. Trickey</i>	283
Energy Depositions of Protons in Allotropic Carbon Ultrathin Films <i>J. Z. Wu, S. B. Trickey, J. R. Sabin, and J. Nobel</i>	299
Examination of the Limits of Accuracy of the Extended Koopmans' Theorem Ionization Potentials into Excited States of Ions of LiH, He ₂ , and Li ₂ <i>R. C. Morrison, C. M. Dixon, and J. R. Mizell, Jr.</i>	309
Chiroptical Techniques and Their Relationship to Biological Molecules, Big or Small <i>A. Rauk and T. B. Freedman</i>	315
Multicavity SCRF Calculation of Ion Hydration Energies <i>G. H. F. Diercksen, M. Karelson, T. Tamm, and M. C. Zerner</i>	339
Quantum-Mechanical Investigation of Large Water Clusters <i>K. N. Kirschner and G. C. Shields</i>	349
Solvent Effects on the Electronic Spectrum of Reichardt's Dye <i>R. Bicca de Alencastro, J. D. da Motta Neto, and M. C. Zerner</i>	361
Determination of Higher Electric Polarizability Tensors from Unrelaxed Coupled Cluster Density Matrix Calculations of Electric Multipole Moments <i>T. Pluta, J. Noga, and R. J. Bartlett</i>	379
Nonlinear Optical Effects in Molecules and Polymers: Issues and Opportunities <i>P. N. Prasad and S. P. Karna</i>	395
Calculation of Optical Second-Harmonic Susceptibilities and Optical Activity for Crystals <i>Z. H. Levine</i>	411
The Relation between Magnetism and Electronic Transport Properties in Strongly Correlated Electron Liquids, Including High <i>T_c</i> Materials <i>N. H. March</i>	421

Complexity of Entanglements and Degree of Folding in Branched Polymers with Excluded-Volume Interaction <i>G. A. Arteca</i>	433
<i>Ab Initio</i> Investigation of the Static Polarizability of Planar and Twisted Infinite Polythiophene Chains <i>D. H. Mosley, J. G. Fripiat, B. Champagne, and J.-M. André</i>	451
Dependence of the Electronic Structure on the Chain Geometry in Stereoregular Polypropylene: An Exploratory Theoretical Study <i>I. Flamant, D. H. Mosley, M. Deleuze, J. M. Andre, and J. Delhalle</i>	469
Semiempirical Studies of the Interaction between Metals and π -Conjugated Polymers: Sodium on Diphenylpolyenes and Aluminum on Poly(<i>p</i> -phenylenevinylene) and Derivatives <i>M. Lögdhund and J. L. Brédas</i>	481
Elemental Carbon Isomerism <i>D. J. Klein and X. Liu</i>	501
A Note on the Number of Spanning Trees in Buckminsterfullerene <i>N. Trinajstić, Z. Mihalić, and F. E. Harris</i>	525
Theoretical Study on the Non-Adiabatic Photodissociation Process of Argon Cluster Ions Ar_7^+ <i>T. Ikegami and S. Iwata</i>	529
First-Principles Monte Carlo Simulated Annealing Study of the Structures and Properties of Hydrogenated Lithium Clusters <i>V. Keshari and Y. Ishikawa</i>	541
On the Interaction of Cyanate and Thiocyanate Anions with Li^+ and Mg^{2+} <i>M. Probst</i>	553
SC-MEH-MO Calculations on Lanthanide Systems. I. $\text{Sm}(\text{Cp}^*)_2$, <i>bis</i> (Pentamethyl-Cyclopentadienyl) $\text{Sm}(\text{II})$ <i>E. A. Boudreaux and E. Baxter</i>	565
Structural and Electronic Studies of Ga_3As_3 , Ga_4As_3 , and Ga_3As_4 <i>P. Piquini, S. Canuto, and A. Fazzio</i>	571
Diborane, Dialane, and Digallane: Accurate Geometries and Vibrational Frequencies <i>D. H. Magers, R. B. Hood, and J. Leszczyński</i>	579
Relativistic Density-Functional Studies of Naked and Ligated Gold Clusters <i>O. D. Häberlen, S.-C. Chung, and N. Rösch</i>	595

Dynamics of Metallic and Molecular Hydrogen through Density-Functional Simulations <i>J. Theilhaber</i>	611
Thermochemical Tests of a Kinetic-Energy Dependent Exchange-Correlation Approximation <i>A. D. Becke</i>	625
Density-Functional LCAO Calculations for Solids: Comparison between Hartree-Fock and Kohn-Sham Structural Properties <i>M. Causá and A. Zupan</i>	633
A Density Functional Study of the Interaction of CO ₂ with a Pd Atom <i>S. Sirois, M. Castro, and D. R. Salahub</i>	645
A Study of Small Systems Containing H and O Atoms Using Nonlocal Functionals: Comparisons with <i>Ab Initio</i> and Experiment <i>J. M. Seminario</i>	655
Electronic Properties of Multiple Delta-Doped Layers in Silicon and GaAs <i>L. M. R. Scolfaro, D. Beliaev, J. R. Leite, A. T. Lino, and E. K. Takahashi</i>	667
Quantum Size Effects in Hexagonal Aluminum Films <i>J. C. Boettger, U. Birkenheuer, N. Rösch, and S. B. Trickey</i>	675
On the Role of Doping in High-T _c Superconductors <i>C. Mei and V. H. Smith, Jr.</i>	687
List of Participants	695
Author Index	711

Introduction

The 34th annual Sanibel Symposium, organized by the faculty and staff of the Quantum Theory Project of the University of Florida, was held on February 12–19, 1994 at the Marriott at Sawgrass Resort, Ponte Vedra Beach, Florida. More than 300 participants gathered for 8 days of lectures and informal discussions.

The format of the symposium adopted for the past few years was followed again this year with a compact 8-day schedule with an integrated program of quantum biology, quantum chemistry, and condensed matter physics. The topics of the sessions covered by these proceedings include Propagator and Resolvent Theory, Perturbation Theory, Density Functional Theory for Molecules, High Performance Parallel Computing Algorithms, Weakly Bound Molecular Systems, Theoretical Inorganic Chemistry, Temporal Phenomena, Quantum Dynamics at Interphases, Energy Depositions, Non-Linear Optical Phenomena, and Novel Condensed Systems.

The articles have been subjected to the ordinary refereeing procedures of the *International Journal of Quantum Chemistry*. The articles presented in the sessions on quantum biology and associated poster sessions are published in a separate volume of the *International Journal of Quantum Chemistry*.

The organizers acknowledge the following sponsors for their support of the 1994 Sanibel Symposium:

- The Office of Naval Research through Grant NO0014-93-1-0343. "This work relates to Department of Navy Grant NO0014-93-1-0343 issued by the Office of Naval Research. The United States Government has a royalty-free license throughout the world in all copyrightable material contained herein."
- U.S. Army Research Office (Physics)/CRDEC and U.S. Army Edgewood RD&E Center through Grant DAAH04-94-G-0015. "The views, opinions, and/or findings contained in this report are those of the author(s) and should not be construed as an official Department of the Army position, policy, or decision, unless so designated by other documentation."
- U.S. Department of Energy through Grant DE-FG05-94ER61785.
- International Science Foundation.
- CAChe.
- IBM.
- Silicon Graphics.
- Sun Microsystems.
- The University of Florida.

Very special thanks go to the staff of the Quantum Theory Project of the University of Florida for handling the numerous administrative, clerical, and practical details. The organizers are proud to recognize the contributions of Mrs. Judy Parker, Ms. Leann Golemo, Mrs. Karen Yanke, Ms. Sandra Weakland, Mr. Sullivan Beck, Dr. Agustín Diz, and Dr. Erik Deumens. All the graduate students of the Quantum Theory Project, who served as “gofers” are gratefully recognized for their contributions to the 1994 Sanibel Symposium.

N. Y. ÖHRN
J. R. SABIN
M. C. ZERNER

On the Occasion of Yngve Öhrn's 60th Birthday

The 34th Sanibel Meeting was distinguished by recognizing the 60th birthday of one of its principal, long-time (33 years) organizers, Yngve Öhrn. Two sessions at the meeting entitled "Ode on a Swedish Öhrn" and "Ode on a Swedish Öhrn: Second Stanza" emphasized some of the research advances whose roots lie in Yngve's group. (See the representative selection of papers below.) You might have expected these sessions to deal with "Proper-gators," as Yngve and Jan Linderberg were primarily responsible for establishing these methods as one of the three principal approaches to the correlation problem (along with MBPT/CC and CI), and they did to some extent; but reflecting Yngve's group's continuing, original contributions, they also featured their new combined electron-nuclear dynamics approach that uses coherent states, but no Born-Oppenheimer approximation or potential energy surfaces, i.e., the "END" method! In these sessions, in many poster presentations, and now, in these Proceedings, we have heard from Yngve's students and postdocs, and as a credit to him as a teacher, they were inspired to establish their *original* research paths. Yet their contributions are characterized by the same rigor and attention to detail that they initially learned in the Öhrn group. (A list of his students and postdoctoral associates is appended.)

No doubt building upon administrative skills learned as a chief organizer of the Sanibel Meeting, Yngve spent five years distinguishing himself as an unusually successful department chairman. One of his accomplishments was turning one senior position in QTP into two, for which two of us are especially grateful! A short list of other accomplishments include marrying Ann, a tremendous asset; memberships in the Swedish, Finnish, and Danish academies; editing the *International Journal of Quantum Chemistry*; being the director of QTP for more than 10 years; and, while in high school, being regional champion in the 100 meter dash, high jump, and discus, while finishing third in Sweden as a member of the 4×100 relay team! He also played left field for the QTP softball team that retired *undefeated!*

Yngve, many happy returns from your many friends.

Rodney J. Bartlett
Erik Deumens
Per-Olov Löwdin
David A. Micha
Hendrik J. Monkhorst
John R. Sabin
Samuel B. Trickey
Michael C. Zerner

Selected Publications

- [1] E. W. Thulstrup and Y. Öhrn, "Configuration Interaction Studies of NO and NO⁺ with Comparisons to Photoelectron Spectra," *J. Chem. Phys.* **37**, 3716 (1972).
- [2] "Propagators in Quantum Chemistry" (Academic Press, 1973, with J. Linderberg).
- [3] G. D. Purvis and Y. Öhrn, "Electron Propagator Calculations for the Photoelectron Spectrum for Open Shell Molecules with Application to the Oxygen Molecule," *J. Chem. Phys.* **62**, 2045 (1975).
- [4] Y. Öhrn and J. Linderberg, "The Consistent RPA Ground State," *Int. J. Quant. Chem.* **15**, 343 (1979).
- [5] Y. Öhrn and G. Born "Molecular Electron Propagator Theory and Calculations," *Adv. Quantum Chem.* (ed. Löwdin) **13**, 1 (1981).
- [6] J. V. Ortiz and Y. Öhrn, "Electron Propagator Calculations of Molecular Electron Affinities," *Chem. Phys. Lett.* **77**, 548 (1981).
- [7] H. J. Jensen, B. Weiner, J. V. Ortiz, and Y. Öhrn, "Powerful Procedure for Optimizing AGP States," *Int. J. Quant. Chem.* **S16**, 615 (1982).
- [8] M. Mishra, O. Goscinski, and Y. Öhrn, "Treatment of Resonances with the Dilated Electron Propagator: Auger and Shape Resonances of Be with a Second Order Self Energy," *J. Chem. Phys.* **79**, 5505 (1983).
- [9] M. Mishra, H. A. Kurtz, O. Goscinski, and Y. Öhrn, "Treatment of Resonances with the Dilated Electron Propagator: The P Shape Resonance in the e-Mg Scattering," *J. Chem. Phys.* **79**, 1896 (1983).
- [10] E. Deumens, B. Weiner, and Y. Öhrn, "Time Dependent Antisymmetric Geminal Power Theory Using a Coherent State Formulation," *Nuclear Physics* **A466**, 85 (1987).
- [11] J. Linderberg, Y. Öhrn, B. Vessal, and S. B. Padkjaer, "Numerical Implementation of Reactive Scattering Theory," *J. Chem. Phys.* **90**, 6254 (1989).
- [12] E. Deumens, A. Diz, H. Taylor, and Y. Öhrn, "Time Dependent Dynamics of Electrons and Nuclei," *J. Chem. Phys.* **96**, 6820 (1992).
- [13] E. Deumens and Y. Öhrn, "Manual for the Electron Nuclear Dynamics Software ENDyne," University of Florida Report, November 24, 1992.
- [14] E. Deumens, A. Diz, R. Longo, and Y. Öhrn, "Time Dependent Theoretical Treatments of the Dynamics of Electrons and Nuclei in Molecular Systems," *Rev. Mod. Phys.* (1994).
- [15] R. Longo, A. Diz, E. Deumens, and Y. Öhrn, "Influence of Electronic-Nuclear Coupling on Dynamics," *Chem. Phys. Lett.* **220**, 305 (1994).

Graduate Students

- | | |
|---|--|
| 1. Josef Kouba (Ph.D., 1970) | 9. Gregory Born (Ph.D., 1979) |
| 2. Rodney J. Bartlett (Ph.D., 1971)
(jointly with Per-Olov Löwdin) | 10. Manoj K. Mishra
(Ph.D., 1981) |
| 3. Jess L. Thompson (M.Sc., 1971) | 11. Vincent Ortiz (Ph.D., 1981) |
| 4. Nelson H. F. Beebe (Ph.D., 1972)
(jointly with Per-Olov Löwdin) | 12. Rina Basu Roy Chowdhury
(Ph.D., 1985) |
| 5. Jack A. Smith (Ph.D., 1973) | 13. Agustín C. Diz (Ph.D., 1992) |
| 6. George D. Purvis III (Ph.D., 1973) | 14. Ricardo L. Longo
(Ph.D., 1993) |
| 7. R. Lynn Tyner (Redmon)
(Ph.D., 1975) | 15. Juan Oreiro (current) |
| 8. Henry A. Kurtz (Ph.D., 1977) | 16. Jorge Morales (current) |

Postdoctoral Associates

- | | |
|----------------------------------|-------------------------------------|
| 1. Maurice Cohen (1968) | 12. Eeva-Kaarina Viinikka (1975) |
| 2. John Gruninger (1969) | 13. Poul Thulstrup (1975) |
| 3. Michael R. M. Hayns (1970) | 14. Nils Elander (1976) |
| 4. Suheil Abdulnur (1970) | 15. Richard Lozes (1979–81) |
| 5. James Howell (1970) | 16. Brian Weiner (1983–85) |
| 6. Erik Thulstrup (1970, 1972) | 17. Hans-Jørgen Jensen (1985, 1986) |
| 7. Poul Jørgensen (1971) | 18. Erik Deumens (1986, 1988) |
| 8. Milos Vucelic (1972) | 19. Hugh Taylor (1990–93) |
| 9. Andreas Andersen (1972) | 20. Benoît Champagne (1993) |
| 10. Michael Hehenberger (1975) | 21. Benny Mogensen (1993) |
| 11. Christoph Nehrkorn (1974–75) | |

Correlation and Propagation in Time

JAN LINDERBERG

Department of Chemistry, Aarhus University, DK-8000 Aarhus C, Denmark

Abstract

Developments, through some 35 years, in the theory of electronic structure and reaction dynamics are reviewed from the perspective available to a close collaborator to Yngve Öhrn. © 1994 John Wiley & Sons, Inc.

Ode

*A scholar by name Yngve Öhrn
approaches a rather sharp turn
going full pace,
he's really an ace,
it seems he'll never adjourn.*

Three dozen years ago, when I was working quietly at my desk at the Quantum Chemistry Group at Uppsala University, Yngve Öhrn presented himself at my door as having been hired by Per-Olov Löwdin as a new assistant at the group. He came with an excellent academic record, a soon to be completed officer's training in the Signal Corps of the Swedish army, and he was a sharp athlete. It turned out, with time, that the two of us had a similar background from steel mill towns of less than urban settings. I have been most fortunate to become a personal friend and associate of Yngve Öhrn and I will attempt to give a sketch of his contributions to the field of quantum chemistry.

Electronic correlation was at the top of the agenda at Uppsala in the late fifties, Löwdin had published his comprehensive review [1] and Lajos Rédei had completed his study on the mixed use of superposition of configurations and correlation factors [2]. Second quantization methods were gaining prominence in many-particle problems and I was assigned to present the classical papers of Born, Jordan, and Fock [3] to the Quantum Chemistry Group. Yngve was directed towards the use of interparticle coordinates for three electron systems, an arduous task with many mathematical and numerical ramifications. The paper [4], which came out of this, demonstrates the analytical clarity and algorithmic proficiency that has been a hallmark of Öhrn's writings ever since. It paved the way for some of the

most accurate calculations on the states of the Lithium-like ions that have been performed [5].

Part of the work on the multidimensional integrals required for the use of interparticle coordinates was completed during Yngve Öhrn's and Jan Nordling's tenure as resident Swedes at the Quantum Theory Project in 1961–63. Yngve produced, while at Florida, another piece of work, together with Reid, that was indicative of his talent and interests in correlation phenomena. A direct method for the computation of the natural orbitals was designed and implemented with good results [6].

Öhrn returned to Uppsala in the spring of 1963, after having ended his stay in the United States with a period at Wisconsin, in Hirschfelder's group, where he befriended, and, I am sure, impressed a number of people, among them Egil Hyleraas from Oslo. Yngve's presence gave me the opportunity to be part of a collaborative effort with him. Our first joint project was spawned by Anders Fröman and concerned excited states of the Cesium atom [7]. The spectroscopist Kjell Bockasten could not describe the levels of the 2F -series with conventional fitting procedures and Fröman identified the problem as arising from the penetration of the excited orbital into the core region where the effective potential just about supports a bound f -state. Yngve and I did the numerical work and confirmed this analysis.

The Cesium problem made us aware that we worked well together and we embarked on another project which was to influence our lives strongly. John Hubbard, who made significant contributions towards an understanding of the correlation problem in the free electron gas in the middle of the fifties, came out with his first papers on the correlation phenomena in narrow energy bands and magnetic materials in 1963. His set-up was quite similar to the Pariser–Parr–Pople model for conjugated systems and we took upon ourselves to explore Hubbard's notions in this field. We connected our efforts to the most elegant work of Coulson and Longuet–Higgins from the forties [8] and had early gratification with regard to the descriptions of excitation features of conjugated hydrocarbons [9]. These papers were part of the dissertation that Yngve Öhrn defended for the degree Doctor of Philosophy at the University of Uppsala in May 1966. Our esteemed teacher, Per-Olov Löwdin, used the occasion to plant a seed of further inspiration by questioning the N -representability of the Green function decoupling methods.

I will not dwell further on the development of propagator theory, a special section of this symposium is dedicated to this, but I ensure you that our work on the monograph *Propagators in Quantum Chemistry* [10] was a most satisfying experience. A good deal of it took place at Aarhus where Öhrn was a visiting professor in 1970–71. I sometimes refer to him as my contraauthor for his kind and insistent efforts to straighten out my algebra and syntax.

Yngve Öhrn resumed his career at Florida in 1966. He initiated a series of detailed and accurate investigations of diatomic systems using the methods of superposition of configurations. The use of natural orbitals rather than conventional Hartree–Fock based orbitals proved economical and led to results that have lasting value for the interpretation of spectral features. Uniformly accurate potential curves were obtained for neutral, as well as for positive and negative, species [11].

Aarhus University has derived great benefits from the work of Yngve Öhrn, he has been a frequent visitor and has spent extended periods with us. He has extended generous hospitality to a large number of Danes at Gainesville and taught them the stern lessons of hard work and accuracy. In addition he has entrusted us to care for several of his graduates. His influence has been felt also at Copenhagen and Odense, and he was elected as a foreign member of the Royal Danish Academy of Sciences and Letters in recognition of his scientific standing.

Yngve Öhrn served as chairman of the Department of Chemistry at the University of Florida in the late seventies and early eighties. He led the department with integrity and scholarly leadership to increased strength, most notably for our community, by bringing Rodney Bartlett and Michael Zerner to the faculty. I was particularly impressed with the creation of an advisory panel for the department to which distinguished alumni were invited. It should also be pointed out that his efforts on the fiscal scene were successful.

My review of Yngve Öhrn's academic career is about to be concluded, not for lack of material, but rather a sense of inadequacy on my part. The surge of scientific effort that emanates from him has assumed a new dimension in recent years. Time-dependent ways of addressing the vexing problems of chemical processes have been introduced by Yngve and his collaborators [12] through novel and challenging techniques. By means of coherent states and Lie group analysis he propagates his systems in a manifestly N-representable fashion. We will learn more about this from his own mouth shortly.

Acknowledgments

The organisers of the thirty-fourth Sanibel Symposium gave me the opportunity to present this address and I am grateful for generous support. Support for the collaborative efforts between the University of Florida and Aarhus University has been provided by these institutions: The National Science Foundation, The Danish Natural Research Council, and The Danish Research Academy.

Bibliography

- [1] P. O. Löwdin, *Adv. Chem. Phys.* **2**, 245 (1959).
- [2] L. Rédei and P. O. Löwdin, *Phys. Rev.* **114**, 752 (1959).
- [3] P. Jordan and E. P. Wigner, *Z. Phys.* **47**, 631 (1928); V. Fock, *Z. Phys.* **75**, 622 (1932).
- [4] Yngve Öhrn and Jan Nordling, *J. Chem. Phys.* **39**, 1864 (1963).
- [5] Yngve Öhrn and Jan Nordling, *Ark. Fys.* **31**, 471 (1966); S. Larsson, *Phys. Rev.* **169**, 49 (1968).
- [6] C. Reid and Y. Öhrn, *Rev. Mod. Phys.* **35**, 445 (1963).
- [7] A. Fröman, J. Linderberg, and Y. Öhrn, *J. Opt. Soc. Am.* **54**, 1064 (1964).
- [8] C. A. Coulson and H. C. Longuet-Higgins, *Proc. R. Soc. London, Ser. A* **191**, 39 (1947); **192**, 16 (1947); **193**, 447 (1948); **193**, 456 (1948); **195**, 188 (1948).
- [9] J. Linderberg and Y. Öhrn, *Proc. R. Soc. London, Ser. A* **285**, 445 (1965); Y. Öhrn and J. Linderberg, *Phys. Rev.* **139**, A1063 (1965). Reprinted in the "Series of Selected Papers in Physics," by the Physical Society of Japan, *Theory of Molecular Structure II*, 131 (1966).
- [10] J. Linderberg and Y. Öhrn, *Propagators in Quantum Chemistry* (Academic Press, London, England, 1973).

- [11] J. Kouba and Y. Öhrn, *J. Chem. Phys.* **52**, 5387 (1970); *ibid* **53**, 3923 (1970); *Int. J. Quantum Chem.* **5**, 539 (1971); E. W. Thulstrup and Y. Öhrn, *J. Chem. Phys.* **57**, 3716 (1972); A. Andersen and Y. Öhrn, *J. Mol. Spectrosc.* **45**, 358 (1973); M. Vucelic, Y. Öhrn, and J. R. Sabin, *J. Chem. Phys.* **59**, 3003 (1973); P. W. Thulstrup, E. W. Thulstrup, A. Andersen, and Y. Öhrn, *J. Chem. Phys.* **60**, 3975 (1974).
- [12] Y. Öhrn, E. Deumens, A. Diz, R. Longo, J. Oreiro, and H. Taylor, in *Time-Dependent Molecular Dynamics*, J. Broeckhove and L. Lathouwers, Eds. (Plenum Press, New York, 1992), p. 279.

Received March 3, 1994

Electron–Nuclear Dynamics of Molecular Systems

AGUSTÍN DIZ and YNGVE ÖHRN

Quantum Theory Project, University of Florida, Gainesville, Florida 32611-8435

Abstract

The content of an *ab initio* time-dependent theory of quantum molecular dynamics of electrons and atomic nuclei is presented. Employing the time-dependent variational principle and a family of approximate state vectors yields a set of dynamical equations approximating the time-dependent Schrödinger equation. These equations govern the time evolution of the relevant state vector parameters as molecular orbital coefficients, nuclear positions, and momenta. This approach does not impose the Born–Oppenheimer approximation, does not use potential energy surfaces, and takes into account electron–nuclear coupling. Basic conservation laws are fully obeyed. The simplest model of the theory employs a single determinantal state for the electrons and classical nuclei and is implemented in the computer code ENDyne. Results from this *ab-initio* theory are reported for ion–atom and ion–molecule collisions.

© 1994 John Wiley & Sons, Inc.

Introduction

Physical measurements on molecular systems involve the use of a probe and study the change of the system or the probe. Such change implies an evolving molecular state, which at least in principle can be obtained as a solution to the time-dependent Schrödinger equation. This is the fundamental equation that governs the dynamics of electrons and atomic nuclei, the building blocks of molecular systems. Quantum chemistry and molecular dynamics often focus on the stationary states, which are solutions to the time-independent Schrödinger equation. Furthermore, the coupling of electronic and nuclear dynamics is forced to obey the adiabatic approximation thereby leading to the theoretical constructs of electronic adiabatic states, corresponding potential energy surfaces, and nonadiabatic coupling terms.

The stationary states form a basis in which the evolving states can be expressed and interpreted. However, their calculation could be an unnecessary and costly detour in order to obtain the evolving states that describe molecular events. Stationary electronic states and their associated potential energy surfaces have occupied quantum chemistry and molecular dynamics since the beginning of quantitative theory. Yet, one knows of no fundamental reason why a molecular event, other than in exceptional cases, should take place on a potential energy surface. Possibly, a few potential energy surfaces with associated coupling terms would give a reasonable description. However, their pointwise determination is an extremely costly process, the fitting of them and the coupling terms to suitable analytical forms

frought with uncertainties, and the dynamics on even two or three such surfaces only possible for the simplest of systems.

Therefore, a method that can generate accurate evolving states without resorting to the expensive generation of potential energy surfaces would be important. In this article we review some of the accomplishments of the END (Electron Nuclear Dynamics) [1] theory, which is such an approach that treats the full electronic-nuclear dynamics with all coupling terms. This method generates equations of motion that approximate the time-dependent Schrödinger equation. Their solution involves time integration with often small steps because of the mixture of fast (electronic) and slow (nuclear) time scales and might be considered computationally demanding. However, when the cost of generating accurate potential energy surfaces and their coupling terms is included in the overall accounting of dynamical methods employing them, their advantage over END in computational effort disappears.

Time-dependent theoretical methods are emerging important tools for the study of molecular processes. Explicit consideration of the time parameter makes it possible to follow, say, the detailed evolution of a reactive event from reactants to products and leads naturally to the theoretical determination of transition probabilities and rates. Since the generation of a quality surface is such a daunting task for a many-atom system, one often resorts to the construction of empirical and semi-empirical surfaces as the diatomics in molecule (DIM) surfaces. Although inexpensive to generate, such surfaces are not accurate for the study of detailed dynamics. If only a single such surface is used, as is often the case, then the dynamics of the electrons is neglected. Only by incorporating two or more surfaces and their couplings is the effect of electronic dynamics included [2].

In spite of these difficulties electronic-nuclear dynamics are being studied with the use of potential energy surfaces. The surface hopping model [3] has seen some success, but needs additional nondynamical assumptions about the electronic-nuclear coupling. Dynamics on potential energy surfaces with conical intersection [4], and wave-packet dynamics on vibrationally coupled dissociative potential energy surfaces [5,6] have been carried out with interesting results. Multiconfiguration time-dependent self-consistent field approximations for dynamics with curve crossings [7] have been developed and applied with promising results. Direct integration methods for the time-dependent Schrödinger equation [8] have been developed and applied also for dynamics with two surfaces. However, the direct methods using numerical grid techniques are so far limited to dynamical problems in three or fewer dimensions.

There are approaches, such as the Close-Coupling method [9,10] used in study of atomic and molecular collisions, where electronic dynamics is considered. However, these methods employ nondynamical straight line or Coulomb nuclear trajectories and ignore the details of the nuclear dynamics. While fixed trajectories work well for collisional phenomena at energies above 1 keV/amu, they lead to spurious dynamics at lower collision energies.

Another body of work has its origin in the approach to simulating annealing by Car and Parrinello [11]. This approach has been generalized to study dynamics of molecular systems or clusters [12,13,14] and uses a fictitious mass associated to

the molecular orbital coefficients to generate newtonian-like equations for them in time. The method attempts to follow the lowest potential energy surface of the system, without having to perform an electronic optimization at each new nuclear geometry. Thus it is very much like dynamics on a single potential energy surface, but without the cost of generating the full surface.

The END (Electron Nuclear Dynamics) theory of Öhrn, Deumens, et al. [1,15–17] uses the time-dependent variational principle (TDVP) to generate equations that approximate the time-dependent Schrödinger equation and govern the time evolution of electronic and nuclear dynamical variables on a generalized phase space. The choice of trial wave function for the electrons and the nuclei determines the level of approximation. Both electrons and nuclei are treated fully dynamically including coupling terms. The dynamics of participating nuclei and electrons is subject to the instantaneous forces due to the full Coulomb interactions and there is no need to generate potential energy surfaces and associated stationary states.

A related method by Runge and Micha [18,19] uses the Frenkel variational principle to derive equations for the electronic degrees of freedom and then use the eikonal approximation for the nuclei moving in the potential given by the electrons and the nuclear Coulomb repulsion. This method has been applied to proton–hydrogen and hydrogen–hydrogen collisions.

The simplest level of the END theory employs a single determinant for the electrons and the classical limit for the nuclei. This level of approximation has been implemented in a computer code ENDyne [20]. In spite of its simplicity this level of theory yields accurate results for transition probabilities, differential and total cross sections for a great variety of ion–atom and ion–molecule reactive collisions. The END theory for a multiconfigurational and for an antisymmetrized geminal power (AGP) electronic wave function has also been published [21,22].

The next section gives an overview of the END theory and the conservation theorems; the third discusses the effect of the nonadiabatic coupling terms. If these couplings are neglected, the calculation tends to follow a potential energy surface, in a Car–Parinello-like fashion. An example shows that dynamics without these terms are in disagreement with experiment. When the couplings are included agreement is excellent.

END Theory

The details of the END theory [16] and the associated ENDyne code [17] for the simplest level of theory are published, so it suffices here to give a summary survey to show the fundamental generality and pleasing structure of the dynamical equations.

The TDVP [23] for a full quantum approach requires stationarity of the action with the Lagrangian

$$L = \frac{\left\langle \Psi \left| \frac{i}{2} \left(\frac{d}{dt} - \frac{\tilde{d}}{dt} \right) - H \right| \Psi \right\rangle}{\langle \Psi | \Psi \rangle}, \quad (1)$$

where H is the full molecular Hamiltonian and Ψ the electronic-nuclear many-body wave function. The derivative \tilde{d}/dt acts on the bra. The choice of trial wave function determines the details of the dynamical equations. Representing the nuclei by Gaussian wave packets in the limit of zero widths results in a classical description with nuclear masses M , positions R , and momenta P equivalent to employing the Lagrangian

$$L = \frac{1}{2} \sum_k (\tilde{P}_k \cdot \dot{R}_k - \dot{P}_k \cdot R_k) + \sum_k \frac{\tilde{P}_k^2}{2M_k} + \frac{\left\langle \Psi_{el} \left| \frac{i}{2} \left(\frac{d}{dt} - \frac{\tilde{d}}{dt} \right) - H_{el} \right| \Psi_{el} \right\rangle}{\langle \Psi_{el} | \Psi_{el} \rangle}, \quad (2)$$

where the electronic Hamiltonian H_{el} includes the nuclear-nuclear repulsion. The END theory even admits a mixed approach with some of the nuclei treated by classical and others by quantum mechanics.

The full quantum TDVP approach with a completely general form of trial function yields the time-dependent Schrödinger equation. Restricting the trial wave function to a particular form leads to a set of coupled first-order differential equations [23,16] governing the time evolution of the, in general, complex wave-function parameters. The parameters assume the role of dynamical variables and form a generalized phase space. This phase space is not flat but has a nonunit metric and results in a Hamiltonian form of dynamical equations. The choice of wave-function parameters becomes critical to ensure nonredundancy and continuous trajectories.

For the case of a single determinantal N -electron state vector Thouless [24] has provided the suitable parametrization. A Thouless determinant $|z\rangle$ is an antisymmetric product of nonorthogonal spin orbitals

$$\chi h = \phi_h + \sum_{p=N+1}^K z_{ph} \phi_p, \quad (3)$$

which in END are expressed in terms of an atomic orbital basis set, $\{\phi_i; i = 1, K\}$, centered on the nuclei. The molecular orbital coefficients $\{z_{ph}\}$ and their complex conjugates are the electronic dynamical variables. This form of wave function has the capacity to become any determinantal N -electron wave function in the basis as the coefficients assume different values. The dynamical equations describing particles with widely different time scales are stiff and as they are integrated in rather short discrete time steps the z -coefficients change producing at each instant a different determinantal function. This turns out to be a surprisingly accurate description of the electronic degrees of freedom.

A Thouless determinant is an example of a coherent states in the theory of Lie groups [25]. The z -coefficients constitute a complex, continuous, nonredundant parametrization and this parameter space also has a positive measure $d\mu(z)$ such that the resolution of the identity

$$I = \int |z\rangle \langle z| d\mu(z) \quad (4)$$

exists.

The dynamical equations can be given the matrix form

$$\begin{pmatrix} iC & 0 & iC_R & 0 \\ 0 & -iC^* & -iC_R^* & 0 \\ iC_R^\dagger & -iC^T & C_{RR} & -I \\ 0 & 0 & I & 0 \end{pmatrix} \begin{pmatrix} \dot{z} \\ \dot{z}^* \\ \dot{\vec{R}} \\ \dot{\vec{P}} \end{pmatrix} = \begin{pmatrix} \partial E / \partial z^* \\ \partial E / \partial z \\ \partial E / \partial \vec{R} \\ \partial E / \partial \vec{P} \end{pmatrix}, \quad (5)$$

where the total energy is

$$E = \sum_k \left(\frac{P_k^2}{2M_k} \right) + \frac{\langle z | H_{el} | z \rangle}{\langle z | z \rangle}. \quad (6)$$

The matrix on the left of Eq. (5) is the metric matrix. Should the basis set not depend on the nuclear coordinates the cross terms mixing nuclear and electronic degrees of freedom disappear. The basis could also be made dependent on nuclear momenta. This would include further coupling terms in the bottom row and right-most column. The couplings in Eq. (5) are

$$\begin{aligned} C &= \frac{\partial^2 \ln S(z^*, \vec{R}', z, \vec{R})}{\partial z^* \partial z} \Big|_{\vec{R}=\vec{R}'} \\ C_R &= \frac{\partial^2 \ln S(z^*, \vec{R}', z, \vec{R})}{\partial z^* \partial R} \Big|_{\vec{R}=\vec{R}'} \\ C_{RR} &= -2 \operatorname{Im} \frac{\partial^2 \ln S(z^*, \vec{R}', z, \vec{R})}{\partial R' \partial R} \Big|_{\vec{R}=\vec{R}'} \end{aligned} \quad (7)$$

They are derived from the overlap

$$S(z^*, \vec{R}', z, \vec{R}) = \langle z; R' | z; R \rangle \quad (8)$$

of determinants at geometries R and R' .

The END theory yields a dynamics that satisfies the conservation laws of important physical quantities, as total energy, total momentum, and total angular momentum [16,17]. The important conservation of total linear and angular momentum only holds when the electron-nuclear coupling terms are included.

Electron-Nuclear Coupling

The dynamical metric of Eq. (5) couples the electronic and nuclear degrees of freedom. The third row of the metric matrix has coupling terms that ensure the conservation of total momentum [16]. The theory must satisfy such conservation laws to be able to produce accurate detailed information about nuclear and electronic quantities. One might think that at higher energies the momentum of the nuclei overwhelms the contribution from the electrons when properties are computed, but that this is not the case is shown by our results.

The first row of the metric matrix couples the electronic degrees of freedom to the nuclear velocities. These coupling terms make up the matrix representation of

the translation operator and provide the transformation of the z -coefficients as the centers of the basis functions move from one instant to the next. One could, alternatively, use a basis with explicit *electron translation factors* [26] $\exp(-i\vec{v}_A \cdot \vec{r})$, where \vec{v}_A is the velocity of center A , but in its full implementation this would require extension of current integral codes.

Time-independent approaches introduce nonadiabatic coupling by expanding the full wave function in terms of adiabatic states with each term being a product of an eigenstate of the electronic Hamiltonian and a nuclear wave function. The coupling terms arise from the nuclear kinetic energy operator acting on the electronic adiabatic states, which are parametrically dependent on the nuclear positions. Such coupling terms are absent when the full wave function is expanded in terms of diabatic states with each term being a product of an electronic state independent of nuclear coordinates and a nuclear wave function. Similarly, in time-dependent treatments coupling terms emerge from using electronic basis functions that depend on nuclear coordinates, and possibly also on nuclear velocities. These coupling terms are absent when the electronic basis is fixed in space, as is the case for numerical grids fixed in the lab frame. The dynamical metric matrix in Eq. (5) would in such a case have no coupling terms.

The influence of the nonadiabatic coupling terms in Eq. (5) is in many cases essential in order to describe even a qualitatively correct dynamics [27]. Neglecting the coupling terms in END generates dynamical equations identical to those used by others [28]. Other approaches that neglect electron-nuclear coupling include dynamics on a single potential energy surface and dynamics using fictitious kinetic energy terms to force the dynamics close to a surface as does the method of Car and Parrinello [11,13,14]. Part of the coupling effects can be handled via electron translation factors, as is done by Micha and Runge [19], but that still accounts for only part of the coupling. A dynamic treatment such as the Close-Coupling method [29,9] uses electron translation factors, but limits the dynamics to fixed trajectories, which also neglects full electron-nuclear coupling terms.

Total cross sections may not be too sensitive to the neglect of electron-nuclear coupling terms, but differential cross sections and details such as the presence or absence of rainbow scattering, state-to-state transition probabilities, branching of reaction channels, etc. cannot be predicted without accounting for the full coupling.

In Figure 1 the electron transfer probability at 250 eV for the $H^+ + H$ system as a function of scattering angle is depicted. Results from two experiments [30,31] are compared to the END using a pVDZ basis. Experiments have a finite angular resolution. In Ref. [30] the resolution is reported to be $\Delta\theta = 0.4^\circ$ while Ref. [31] reports $\Delta\theta = 0.6^\circ$. END calculations were averaged to reflect the finite angular resolutions of the two experiments. This was done by calculating probabilities sufficiently close together (at some points every 0.02° apart) and then averaging the probabilities inside $\pm\Delta\theta/2$ of a given angle θ . It is interesting to note that the experimental values reported in Ref. [30] are actually more consistent with an angular resolution of 1° rather than 0.4° . The results by Helbig and Everhart are in excellent agreement with END for the maxima, but the minimum value is too high. This is most likely due to some experimental problem since the oscillations

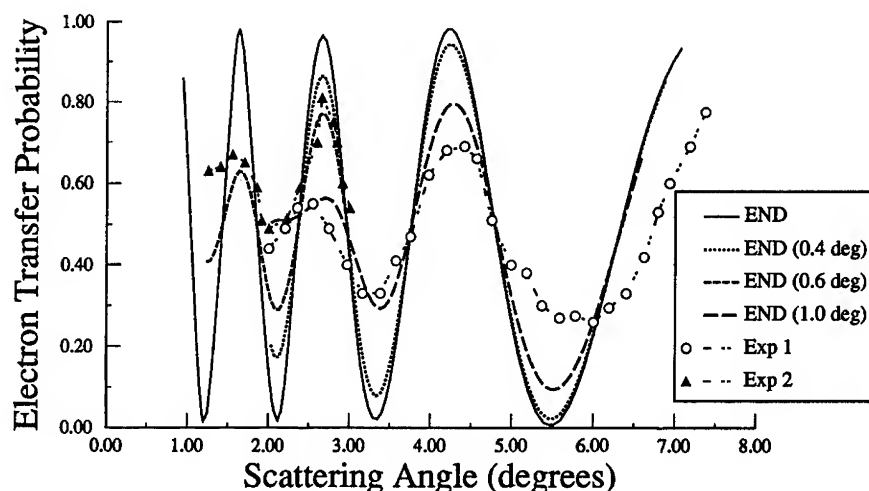


Figure 1. Transfer probability versus scattering angle for $p + H$ collision at 250 eV. END using pVDZ basis and three averaged results using an angular resolution $\pm\Delta\theta$ given in parenthesis. Experiments: Exp 1: Ref. [30], Exp 2: Ref [31].

should be symmetric about a probability of 0.5 [30]. Other sources of error in the experimental results are the determination of the dissociation fraction (H/H_2 in the collision region) and the calibration necessary between the different processes (elastic, charge transfer). Another problem is that as the scattering angle grows, the number of scattered particles falls very steeply. This actually shifts the minima and maxima towards larger angles, as seen in the results for Houver et al. at angles larger than 4° . This is because more particles are measured coming from the $-\Delta\theta$ than $+\Delta\theta$ range about a given angle θ . With these considerations, one can conclude that the agreement between theory and experiment is excellent.

In Figure 2 the END results for the same transfer probability (using perfect resolution) is compared to the results that completely neglect the electron-nuclear coupling and one for which the couplings in the electronic part only (i.e., the first row of the metric of Eq. (5) is retained). The latter means that there is no conservation of total momentum. It is clear that the neglect of the coupling terms leads to wrong behavior with increasing scattering angle; either incorrect number of oscillations or shifted positions of the peaks.

Reactive Collisions

ENDyne calculations of total and differential cross sections of ion-atom collisions such as proton/hydrogen, proton/helium, proton/lithium, alpha/helium [16,32–34] with rather modest Gaussian basis sets have shown excellent agreements with an abundance of experimental data.

For instance, proton/helium collisions have been studied [32] in great detail for a variety of collision energies from 500 to 5,000 eV. The classical differential cross

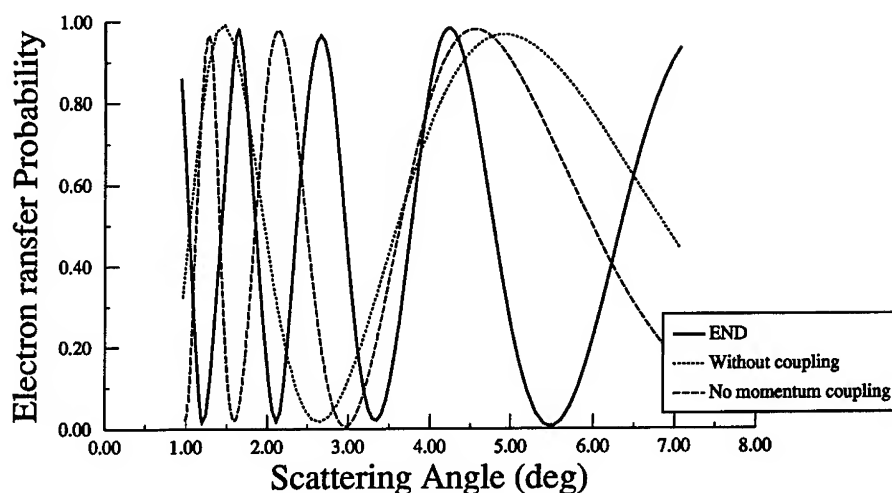


Figure 2. Transfer probability versus scattering angle for $p + H$ collision at 250 eV, using pVDZ basis. Solid line same as in Figure 1. Dotted line: without any electron-nuclear coupling. Dashed line: neglecting momentum conserving couplings.

sections for electron transfer and elastic processes are calculated using a pVDZ basis set with excellent agreement with experiment for rainbow angles. The differential elastic cross sections with a simple semiclassical correction are indistinguishable from the experimental results.

Ongoing work for small collisional systems at energies from a few to a fraction of an eV yields similarly encouraging results. Since END imposes no restrictions on the dynamics, beyond that of basis sets and wave-function form, basically all channels accessible from given initial conditions can be studied. The analysis of processes involving ionization with one or more electron departing are just being started. Processes involving ion-molecule collisions with bond breaking and bond formation are readily accessible with END.

Proton-hydrogen molecule collisions at 30 eV have been the subject of detailed experimental investigation [35]. There have been several attempts to explain the experiments using semi-classical [35,36] and quantum descriptions of the nuclei [37,38]. In all these approaches DIM surfaces were used. Florescu et al. modified the surfaces to achieve quantitative agreement with experiment [36]. Preliminary results from END show that the rainbow angle is calculated more accurately than by using DIM surfaces and the approximations inherent in the Trajectory Surface Hopping (TSH) [35] and infinite order sudden approximation (IOSA) [37,38] approaches.

Experiment puts the primary rainbow angle for charge transfer in the $H^+ + H_2$ collision at 30 eV between 6° and 7° . The TSH and quantal IOSA approach methods place it at 10° [35,37,38]. Preliminary END results place the primary rainbow to be near 8.5° , with new calculations lowering this result. The primary rainbow angle for elastic and vibrationally excited collisions is also observed to be between 6° and

7°. The other approaches show a shift of approximately 2.5° to larger angles, while preliminary END results show a value of 7.5° for the rainbow angle.

Table I shows the different channels for the proton on H₂ collision as identified by ENDyne (no differentiation among different vibrational states is made here). It is clear from these results that the assumptions made in the IOSA and the use of a DIM surface for this system are somewhat questionable. The orientation of the system is important in defining the outcome of a collision. It is more important for small impact parameters than for large ones. Furthermore, dissociation is not accounted for in the IOSA approach.

The total breakup channels are, of course, not accessible by the close-coupling theory or any other approach using the so-called impulse approximation that does not permit the nuclear arrangement of the molecule to adjust during the collision. Some channels for the smallest impact parameters correspond to nuclear transfer and should, strictly speaking not be included in the electron transfer cross section. It is almost impossible, however, to separate experimentally these processes from the transfer, since the outgoing proton or hydrogen atom have almost the same energy as the incoming proton.

Therefore it is essential to have a fully dynamical theory accounting for electron nuclear coupling as the END in order to get all accessible product channels and to interpret the experiment properly. Artificial restrictions on the electron-nuclear dynamics by prescribed trajectories, by frozen nuclear configurations, by forcing the dynamics to take place on a potential energy surface, or on several surfaces with ad hoc hopping introduce nonphysical dynamics and errors that are hard to control.

Another system under study is the low energy collisions of H₂⁺ with H₂. This system exhibits much of the complexity of a general molecular collisional system and there are no accurate potential energy surfaces available. For the few theoretical dynamics studies that have been performed on this system [39,40] approximate potential energy surfaces are used, and the agreement with experiment is wanting. Preliminary results for END using a 1s, 2s basis for collinear initial conditions with a single impact parameter (i.e., assuming spherically symmetric molecular species)

TABLE I. Product channels for various orientations and their impact parameter ranges for H⁺ + H₂ collisions at 30eV. Θ is the angle formed between the initial velocity vector of the proton (defined as the z axis) and the H₂ axis. The initial orientation of the H₂ molecule with respect to the x-z plane is ϕ . The impact parameter b is zero at the CM of H₂ and increases along the x axis. A range of probabilities is shown for the charge transfer channel.

(Θ, ϕ)	Dissociation	Proton exchange	Charge transfer (probability)
(0, 0)	—	$0.0 < b < 0.3$	$0.3 < b$ (0.4–0.0)
(45, 0)	$0.65 < b < 1.2$	$0.0 < b < 0.65$	$1.2 < b$ (0.24–0.0)
(90, 0)	$0.0 < b < 0.6$ $1.1 < b < 1.35$	$0.6 < b < 1.1$	$1.4 < b$ (0.26–0.0)
(90, 45)	$0.0 < b < 0.4$	—	$0.4 < b$ (0.2–0.0)

show good agreement with experimental total cross section for the formation of $\text{H}_3^+ + \text{H}$. Further studies are being carried out beyond these simple assumptions for the initial conditions including all channels.

Acknowledgments

The authors acknowledge the stimulating collaboration with Erik Deumens, Ricardo Longo, Benny Mogensen, Jorge Morales, Juan Oreiro, and their permission to quote some of the results obtained by them. This work is supported by a grant from the Office of Naval Research. One of us (YÖ) would like to thank the faculty and staff of the QTP for making the Sanibel Symposium 1994 so special for him.

Bibliography

- [1] Y. Öhrn et al., "Time evolution of electrons and nuclei in molecular systems," in *Time-Dependent Quantum Molecular Dynamics*, J. Broeckhove and L. Lathouwers, Eds. (Plenum, New York, 1992), pp. 279–292.
- [2] B. H. Lengsfeld and D. R. Yarkony, *Adv. Chem. Phys.* **82**, 1 (1992).
- [3] J. C. Tully and R. K. Preston, *J. Chem. Phys.* **55**, 562 (1971).
- [4] U. Manthe and H. Köppel, *J. Chem. Phys.* **93**, 1658 (1990).
- [5] U. Manthe and H. Köppel, *J. Chem. Phys.* **93**, 345 (1990).
- [6] U. Manthe, H. Köppel, and L. S. Cederbaum, *J. Chem. Phys.* **95**, 1708 (1991).
- [7] Z. Kotler, A. Nitzan, and R. Kosloff, *Chem. Phys. Lett.* **153**, 483 (1988).
- [8] R. Kosloff, *J. Phys. Chem.* **92**, 2087 (1988).
- [9] M. Kimura and N. F. Lane, "The low-energy, heavy-particle collisions—A close-coupling treatment," in *Advances in Atomic, Molecular and Optical Physics*, D. Bates and B. Bederson, Eds. (Academic, New York, 1990), p. 79.
- [10] W. Fritsch and C. D. Lin, *Phys. Rep.* **202**, 1 (1991).
- [11] R. Car and M. Parrinello, *Phys. Rev. Lett.* **55**, 2471 (1985).
- [12] D. K. Remler and P. A. Madden, *Mol. Phys.* **70**, 921 (1990).
- [13] B. Hartke and E. A. Carter, *Chem. Phys. Lett.* **189**, 358 (1992).
- [14] B. Hartke and E. A. Carter, *J. Chem. Phys.* **97**, 6569 (1992).
- [15] E. Deumens and Y. Öhrn, *J. Mol. Struct. (THEOCHEM)* **199**, 23 (1989).
- [16] E. Deumens, A. Diz, H. Taylor, and Y. Öhrn, *J. Chem. Phys.* **96**, 6820 (1992).
- [17] E. Deumens, A. Diz, R. Longo, and Y. Öhrn, *Rev. Mod. Phys.* **66** (1994).
- [18] K. Runge, D. A. Micha, and E. Q. Feng, *Int. J. Quantum Chem.: Quantum Chem. Symp.* **24**, 781 (1990).
- [19] D. A. Micha and K. Runge, "Electronic energy and charge transfer in slow atomic collisions: A time-dependent molecular orbital approach," in *Time-Dependent Quantum Molecular Dynamics*, J. Broeckhove and L. Lathouwers, Eds. (Plenum, New York, 1992), pp. 247–266.
- [20] E. Deumens, A. Diz, and H. Taylor, *Manual for the Electron Nuclear Dynamics Software ENDyne*, QTP, U. of Florida, 1992.
- [21] E. Deumens, Y. Öhrn, and B. Weiner, *J. Math. Phys.* **32**, 1166 (1991).
- [22] B. Weiner, E. Deumens, and Y. Öhrn, *J. Math. Phys.* **35**, 1139 (1994).
- [23] P. Kramer and M. Saraceno, *Geometry of the Time-Dependent Variational Principle in Quantum Mechanics* (Springer, New York, 1981).
- [24] D. J. Thouless, *Nucl. Phys.* **21**, 225 (1960).
- [25] J. R. Klauder and B.-S. Skagerstam, *Coherent States, Applications in Physics and Mathematical Physics* (World Scientific, Singapore, 1985).
- [26] J. B. Delos, *Rev. Mod. Phys.* **58**, 287 (1981).
- [27] R. Longo, A. Diz, E. Deumens, and Y. Öhrn, *Chem. Phys. Lett.* **220**, 305 (1994).
- [28] M. J. Field, *J. Chem. Phys.* **96**, 4583 (1992).

- [29] W. Fritsch and C. D. Lin, Phys. Rev. A **26**, 762 (1982).
- [30] J. C. Houver, J. Fayeton, and M. Barat, J. Phys. B: At. Mol. Phys. **7**, 1358 (1974).
- [31] H. F. Helbig and E. Everhart, Phys. Rev. **140**, A715 (1965).
- [32] R. Longo, E. Deumens, and Y. Öhrn, J. Chem. Phys. **99**, 4554 (1993).
- [33] A. Diz, *Electron Nuclear Dynamics: A Theoretical Treatment Using Coherent States and the Time-Dependent Variational Principle*, Ph.D. Thesis, University of Florida, Gainesville, FL, 1992.
- [34] R. Longo, *Exploring a New Time-Dependent Method for Molecular Quantum Dynamics*, Ph.D. Thesis, University of Florida, Gainesville, FL, 1993.
- [35] G. Niedner, M. Noll, J. Toennies, and Schlier, J. Chem. Phys. **87**, 2686 (1987).
- [36] A. Florescu, M. Sizun, and V. Sidis, J. Chem. Phys. **99**, 7277 (1993).
- [37] M. Baer, G. Niedner, and J. P. Toennies, J. Chem. Phys. **88**, 1461 (1988).
- [38] M. Baer, G. Niedner-Schatteburg, and J. P. Toennies, J. Chem. Phys. **91**, 4169 (1989).
- [39] M. Baer and C. Y. Ng, J. Chem. Phys. **93**, 7787 (1990).
- [40] C. W. Eaker and G. C. Schatz, Chem. Phys. Lett. **127**, 343 (1986).

Received June 2, 1994

Semidirect Algorithms in Electron Propagator Calculations

V. G. ZAKRZEWSKI and J. V. ORTIZ

Department of Chemistry, University of New Mexico, Albuquerque, New Mexico 87131

Abstract

Electron propagator calculations have been executed with a semi-direct algorithm that generates only a subset of transformed electron repulsion integrals and that takes advantage of Abelian point group symmetry. Diagonal self-energy expressions that are advantageous for large molecules are employed. Illustrative calculations with basis sets in excess of 200 functions include evaluations of the ionization energies of C_7^{2-} and $Zn(C_5H_5)_2$. In the former application, a bound dianion obtains for a D_{3h} structure. In the latter, many final states of the same symmetry are calculated without difficulty. © 1994 John Wiley & Sons, Inc.

Introduction

The scope of applications for electron propagator techniques [1–7] continues to expand in several directions. Open shell species can be examined with multiconfigurational, self-consistent field reference states [8] and with renormalized correlation corrections to unrestricted Hartree–Fock reference states [9,10]. Evaluation of final state properties and total energies has been facilitated by calculation of electron binding energy gradients and by reference state energy gradients corresponding to contour integral expressions for total energies [11,12]. The interpretative advantages of the one-electron picture provided by electron propagator theory have provided insights into the structure and bonding of a variety of molecules [13]. Direct and semi-direct methods for Hartree–Fock and correlated calculations have enabled applications to increasingly larger systems [14] and can be adapted to propagator methods. In this contribution, semi-direct algorithms for calculating self-energy corrections to uncorrelated results are employed for the evaluation of ionization energies of C_7^{2-} and $Zn(C_5H_5)_2$. This offering, in honor of Professor Yngve Öhrn's 60th birthday, owes a debt to his pioneering work in propagator methods of quantum chemistry.

Methods

Nondiagonal self-energy calculations at the second order and 3+ levels [15] are carried out for certain test calculations on C_7^{2-} . These methods are integrated into the Gaussian program suite [16] in a modified version of EPT90 [17].

Extensive program revisions have been applied to diagonal self-energy calculations in third order and in the OVGf [18] approximation. Abelian point group symmetry is used in the calculation of second and third order self-energy diagrams. A semi-direct procedure, where transformed electron repulsion integrals are retained only if they contain at least one occupied orbital index, has been employed. The most difficult portion of the calculation pertains to the evaluation of the third order self-energy diagram with a four-particle ladder vertex. For the p th diagonal element of the self-energy matrix, this diagram is

$$-\frac{1}{4} \sum_{iabcd} \frac{\langle pi||ab \rangle \langle ab||cd \rangle \langle cd||pi \rangle}{(E + \epsilon_i - \epsilon_a - \epsilon_b)(E + \epsilon_i - \epsilon_c - \epsilon_d)}$$

where i is an occupied index and a, b, c, d are virtual indices. It is calculated without storage of the block of transformed integrals with four virtual indices [19]. Electron repulsion integrals in the atomic basis are needed at a certain intermediate point in this calculation, which is similar to the evaluation of the four-particle ladder term in third order many-body perturbation theory (MBPT) [20]. While previous versions of our programs have assumed the availability of electron repulsion integrals in the atomic basis, the present version instead generates these integrals as they are needed. The number of arithmetic operations in this step is proportional to the number of occupied orbitals times the fourth power of the number of virtual orbitals. This scaling factor is the same as that required for partial integral transformations that have been implemented in the Gaussian suite for post-SCF calculations. Use of this semi-direct algorithm allows execution of the applications discussed below on an IBM RISC 6000, model 550 workstation with 64 Mb main memory and 2 Gb external disk. Diagonal self-energy calculations now can be performed routinely for basis sets with 200–300 basis functions.

Ionization Energies of C_7^{2-}

A recent experimental report on carbon cluster dianions has indicated that the smallest bound species has seven carbon atoms [21]. Geometry optimizations on linear species have been performed for C_7 , C_7^- , and C_7^{2-} at the restricted Hartree-Fock level with a double ζ plus polarization basis [22]. At the latter geometry, electron propagator theory (EPT) ionization energy calculations are executed with a UHF reference state for the ${}^3\Sigma_g^-$ dianion. The 3s2p1d, 3s3p1d, and 3s2p2d basis sets of another work [23] are employed. Nondiagonal second order and nondiagonal EPT(3+) [15] self-energies generate the dianion ionization energies in Table I. Correlation effects decrease the ionization energies to the ${}^2\Sigma_g$ final state of the anion. Discrepancies between second order and EPT(3+) results are small; it is likely that the correlation treatment is not qualitatively incorrect. The second basis differs from the first by the addition of diffuse p functions, but the EPT(3+) ionization energy is still far from being bound. Use of a double polarization set in the third basis has but a minor effect on the propagator results. Even with the addition of more diffuse and polarization functions, it is likely that the dianion is not bound in this linear structure at the second order or 3+ levels.

TABLE I. $D_{\infty h} C_7^{2-}$ Ionization energy (eV).

Basis	Koopmans	EPT (2)	EPT (3+)
3s2p1d	-0.459	-1.790	-1.789
3s3p1d	-0.005	-1.432	-1.265
3s2p2d	-0.378	-1.656	-1.603

A more promising species exhibits D_{3h} symmetry and has been examined with Hartree-Fock and configuration interaction techniques [24]. Three spokes of two carbons each radiate from a central carbon in this planar structure. Geometry optimizations at the second order MBPT level with the 3s2p1d basis produce a distance of 1.422 Å between the central carbon and its neighbors, while the distance between the latter carbons and their outer neighbors is 1.284 Å. Examination of molecular orbitals indicates that the dianion can be considered isoelectronic with a $D_{3h} C(CN)_3^+$ structure, where the cationic, three-coordinate carbon at the center is covalently bound to three cyanide groups. Diagonal self-energy calculations are performed at a geometry optimized with second order MBPT and the 3s2p1d basis. These calculations have been performed on three final states with the 3s3p1d basis. At the Koopmans level, the dianion is bound with respect to the anion at this geometry. Correlation effects destabilize the dianion with respect to the anion, but the former species is still bound by 0.4 eV. The quality of the basis is improved by replacing the double ζ , correlation-consistent [25] component of the 3s3p1d basis with its triple ζ counterpart. The results are summarized in Table II. The dianion is clearly bound with respect to the anion. Pole strengths (P) are close to 0.9, indicative of the validity of the perturbative and diagonal self-energy arguments underlying these calculations. Additional correlation effects would probably diminish the predicted ionization energy of the dianion, but augmented basis sets are likely to have the opposite effect. An estimate of 0.6 eV for the vertical ionization energy of the dianion strongly suggests that the D_{3h} structure is responsible for the stability of the heptatomic species.

TABLE II. $D_{3h} C_7^{2-}$ Ionization energies (eV).

Final state	Koopmans	3rd order	OVGF	P
[3s3p1d] Basis Set: 119 AOs				
$^2A_2'$	0.97	0.76	0.40	.88
$^2E''$	1.07	0.87	0.62	.88
$^2E'$	1.93	1.57	1.12	.87
[4s4p2d1f] Basis Set: 231 AOs				
$^2A_2'$	1.03	0.92	0.55	.87
$^2E''$	1.11	1.04	0.79	.87
$^2E'$	1.98	1.74	1.28	.87

Ionization Energies of $\text{Zn}(\text{C}_5\text{H}_5)_2$

Metallocenes are among the most important structural motifs in organometallic chemistry. Their photoelectron spectra have been extensively studied [26]. As a test of the semidirect algorithms, a preliminary study was undertaken for $\text{Zn}(\text{C}_5\text{H}_5)_2$, a closed-shell species with a d^{10} electron configuration on the metal center. Basis sets were taken from a previous study on $\text{Zn}(\text{CH}_3)_2$ [27]. Geometry optimizations at the second order MBPT level were performed without f functions on Zn. These functions are included in the propagator calculations; a total of 220 contracted functions is generated in this manner. At the optimized geometry, the Zn-ring centroid distance is 1.951 Å, the C-ring centroid distance is 1.222 Å, the C—H distance is 1.092 Å, and the ring centroid-C—H angle is 90.7°. Table III displays results for various states. The order of states from the uncorrelated calculations is preserved in the propagator calculations. Pole strengths are 0.8 or 0.9 and indicate the qualitative validity of the Koopmans picture of the final states. Newton's method for finding the zeroes of a function is used in the pole searches. Each of these searches converges within three iterations; there are no difficulties in obtaining excited final states of a given symmetry type.

Conclusions

Electron propagator calculations on large molecules have been facilitated through semi-direct algorithms where only transformed electron repulsion integrals with at least one occupied index are explicitly calculated. Diagonal approximations to the self-energy matrix have been employed. For C_2^{2-} , the D_{3h} structure is bound with respect to the corresponding monoanion. In $\text{Zn}(\text{C}_5\text{H}_5)_2$, it is easy to obtain many cationic, final states of a given symmetry through application of ordinary pole search methods.

TABLE III. D_{3h} $\text{Zn}(\text{C}_5\text{H}_5)_2$ Ionization energies (eV).

Final state	Koopmans	3rd order	OVGF	P
$^2E'_1$	7.66	7.59	7.34	.90
$^2E'_1$	9.30	9.14	8.88	.90
$^2A''_2$	14.08	12.82	12.42	.82
$^2E''_2$	14.11	13.10	12.54	.90
$^2E'_2$	14.13	13.10	12.56	.90
$^2E'_1$	14.77	13.59	13.12	.90
$^2E'_1$	14.90	13.72	13.26	.90
$^2A'_1$	15.39	14.01	13.63	.78
$^2A'_1$	18.80	17.32	16.70	.86
$^2A''_2$	18.96	17.47	16.92	.85
$^2E'_2$	19.90	18.09	17.49	.84
$^2E''_2$	19.94	18.12	17.56	.84

Acknowledgments

This work was partially supported by the National Science Foundation under Grants CHE-9101777 and CHE-9321434 and by the Petroleum Research Fund under Grant 24512-AC6.

Bibliography

- [1] J. Linderberg and Y. Öhrn, *Propagators in Quantum Chemistry* (Academic Press, New York, 1973).
- [2] B. T. Pickup and O. Goscinski, *Mol. Phys.* **26**, 1013 (1973).
- [3] L. S. Cederbaum and W. Domcke, *Adv. Chem. Phys.* **26**, 206 (1977).
- [4] J. Simons, *Theor. Chem. Adv. Persp.* **3**, 1 (1978).
- [5] M. F. Herman, K. F. Freed, and D. Yeager, *Adv. Chem. Phys.* **48**, 1 (1981).
- [6] Y. Öhrn and G. Born, *Adv. Quantum Chem.* **13**, 1 (1981).
- [7] W. von Niessen, J. Schirmer, and L. S. Cederbaum, *Comput. Phys. Rep.* **1**, 57 (1984).
- [8] J. A. Nichols, D. L. Yeager, and P. Jorgensen, *J. Chem. Phys.* **80**, 293 (1984); J. T. Golab and D. L. Yeager, *J. Chem. Phys.* **87**, 2925 (1987).
- [9] J. V. Ortiz, *Int. J. Quantum Chem., Quantum Chem. Symp.* **25**, 35 (1991).
- [10] J. V. Ortiz, *Chem. Phys. Lett.* **199**, 530 (1992).
- [11] J. Cioslowski and J. V. Ortiz, *J. Chem. Phys.* **96**, 8379 (1992).
- [12] J. V. Ortiz, *Int. J. Quantum Chem., Quantum Chem. Symp.* **26**, 1 (1992).
- [13] See, for example, the following references: J. V. Ortiz, *J. Chem. Phys.* **92**, 6728 (1990); J. V. Ortiz, *Chem. Phys. Lett.* **169**, 116 (1990); J. V. Ortiz, *J. Am. Chem. Soc.* **113**, 1102 (1991); J. V. Ortiz, *J. Chem. Phys.* **94**, 6064 (1991); J. V. Ortiz, *Polyhedron* **10**, 1285 (1991); J. V. Ortiz, *J. Am. Chem. Soc.* **113**, 3593 (1991); J. V. Ortiz and J. W. Mintmire, *J. Phys. Chem.* **95**, 8609 (1991); J. V. Ortiz, *Macromolecules* **26**, 2989 (1993); J. V. Ortiz and C. M. Rohlfing, *Macromolecules* **26**, 7282 (1993).
- [14] P. R. Taylor, *Int. J. Quantum Chem.* **31**, 521 (1987); S. Saebo and J. Almlöf, *Chem. Phys. Lett.* **154**, 83 (1989); M. Head-Gordon, J. A. Pople and M. J. Frisch, *Chem. Phys. Lett.* **153**, 503 (1988); J. Almlöf, K. Faegri, and K. Korsell, *J. Comp. Chem.* **3**, 385 (1982); R. Ahlrichs, M. Bär, M. Häser, H. Horn, and C. Kölmel, *Chem. Phys. Lett.* **162**, 165 (1989); S. Saebo and J. Almlöf, *Chem. Phys. Lett.* **154**, 83 (1989); M. Feyereisen, J. Nichols, J. Oddershede, and J. Simons, *J. Chem. Phys.* **96**, 2978 (1992).
- [15] J. V. Ortiz, *J. Chem. Phys.* **99**, 6716 (1993).
- [16] Gaussian 90, Revision F, M. J. Frisch, M. Head-Gordon, G. W. Trucks, J. B. Foresman, H. B. Schlegel, K. Ragavachari, M. Robb, J. S. Binkley, C. Gonzalez, D. J. Defrees, D. J. Fox, R. A. Whiteside, R. Seeger, C. F. Melius, J. Baker, R. L. Martin, L. R. Kahn, J. J. P. Stewart, S. Topiol, and J. A. Pople, Gaussian, Inc., Pittsburgh, PA, 1990.
- [17] J. V. Ortiz, EPT90, an *ab initio* electron propagator program; J. V. Ortiz, *Int. J. Quantum Chem., Quantum Chem. Symp.* **23**, 321 (1989).
- [18] L. S. Cederbaum, W. Domcke, and W. von Niessen, *J. Phys. B* **10**, 2963 (1977).
- [19] J. A. Pople, J. S. Binkley, and R. Seeger, *Int. J. Quantum Chem., Quantum Chem. Symp.* **10**, 1 (1976).
- [20] R. J. Bartlett, *Ann. Rev. Phys. Chem.* **32**, 359 (1981), and references therein.
- [21] S. N. Schauer, P. Williams, and R. N. Compton, *Phys. Rev. Lett.* **65**, 625 (1990).
- [22] J. Watts and R. J. Bartlett, *J. Chem. Phys.* **97**, 3445 (1992).
- [23] V. G. Zakrzewski and J. V. Ortiz, *J. Chem. Phys.* **100**, 6614 (1994).
- [24] T. Sommerfeld, M. K. Scheller, and L. S. Cederbaum, *Chem. Phys. Lett.* **209**, 216 (1993).
- [25] T. H. Dunning, *J. Chem. Phys.* **90**, 1007 (1989).
- [26] J. C. Green, *Struct. Bonding (Berlin)* **43**, 37 (1981).
- [27] V. G. Zakrzewski and J. V. Ortiz, *J. Chem. Phys.* **100**, 6508 (1994).

Treatment of Molecular Resonances Using the Bi-Orthogonal Dilated Electron Propagator with Application to the $^2\Pi_g$ Shape Resonance in $e\text{-N}_2$ Scattering

MILAN N. MEDIKERI* and MANOJ K. MISHRA

Department of Chemistry, Indian Institute of Technology, Powai, Bombay 400 076, India

Abstract

Preliminary results from the first application of the bi-orthogonal dilated electron propagator to the treatment of molecular resonances are presented for the energy and the width of the $^2\Pi_g$ shape resonance in $e\text{-N}_2$ scattering. The corresponding resonant Feynman–Dyson amplitudes (FDAs) are plotted to get a quantitative affirmation of the topology of the lowest unoccupied molecular orbital (LUMO) for N_2 . It is shown that a plot of the resonant FDAs offer new insights into the role of correlation in the formation and decay of molecular shape resonances. © 1994 John Wiley & Sons, Inc.

Introduction

It is a great pleasure to be able to contribute to the special session on Propagator and Resolvent theory honoring Professor Yngve Öhrn. One of us (M. K. M.) did his Ph.D. under him and fondly recollects his gentle guidance, meticulous teaching, and indulgent support. Yngve Öhrn has been instrumental in establishing the electron propagator method as a popular and potent tool for molecular structure calculations [1,2] and references to his work are bound to be strewn throughout this volume. The present work is an outgrowth of the work M. K. M. did for his dissertation, and we are pleased to dedicate the results from this first application of the bi-orthogonal dilated electron propagator to the treatment of molecular resonances to Yngve.

The biorthogonal dilated electron propagator technique [3–5] has been employed extensively for direct calculation of atomic Auger and shape resonance energies and widths [3–11]. A review of the different approaches to the construction of the complex scaled electron propagator is offered by Mishra [3]. More recently, the Feynman–Dyson amplitudes (FDAs) of the bi-orthogonal dilated electron propagator have been used to investigate the orbital picture of shape resonance formation and decay [11]. It has been argued [11] that since the resonances are believed to result from a temporary trapping of the impinging electron in one of the unoccupied

* CSIR Senior Research Fellow.

orbitals of the target and unoccupied (virtual) orbital, energies of the Fock operator can be completely altered even with a minor modification of the primitive basis; the conventional SCF procedures cannot be used for identifying *the* resonant orbital. However, the FDA(s) associated with the resonant pole(s) of the biorthogonal dilated electron propagator based on an underlying bi-variational SCF [12–15] may be *rigorously* and *unequivocally* associated with *the resonant* orbital and have been successfully utilized for a quantitative affirmation of the orbital picture of metastable anion formation in atoms [11].

The lowest unoccupied molecular orbitals (LUMOs) are central to phenomenological theories of chemical reactivity. Although qualitative correlation of LUMOs with metastable anionic resonances is available in abundance [16,17], a quantitative affirmation once again would require an unequivocal mechanism for the identification of the unoccupied resonant orbital of the molecular target in which the impinging electron will get trapped. Such a characterization can be made by identifying the resonant pole(s) of the dilated electron propagator with the resonance resulting from the temporary trapping of the impinging electron in the LUMO and associating the corresponding FDA(s) with the resonant orbital/LUMO [11]. All the applications of the bi-orthogonal dilated electron propagator, however, have been limited to the treatment of atomic resonances so far.

The $^2\Pi_g$ shape resonance in $e\text{-N}_2$ scattering has been the favorite test case for the study of molecular resonances [18–26] and the topology of the $1\pi_g$ LUMO of N_2 is a well-established textbook example. For these reasons we have also chosen the $^2\Pi_g$ shape resonance in $e\text{-N}_2$ scattering for the first application of the bi-orthogonal dilated electron propagator to the treatment of molecular resonances.

In the next (second) section we outline our method. In the first part of the third section, we discuss the results for energy and width obtained from our second- and zeroth-order decouplings. The FDAs corresponding to the zeroth- and second-order resonant poles correlate well with the textbook portrayal of the $1\pi_g$ N_2 LUMO, and the differences between the amplitudes from the two decouplings as also between the resonant FDA on the real line and in the complex plane (for the optimal value of the dilation parameter) are used to elicit mechanistic insights about the formation and decay of molecular shape resonances in the second part of the third section. A brief survey of the main results concludes this article.

Method

The Dyson equation for the bi-orthogonal matrix electron propagator $\mathbf{G}(\eta, E)$ may be expressed as [4,5]

$$\mathbf{G}^{-1}(\eta, E) = \mathbf{G}_0^{-1}(\eta, E) - \mathbf{\Sigma}(\eta, E), \quad (1)$$

where $\mathbf{G}_0(\eta, E)$ is the zeroth-order propagator for the uncorrelated electron motion here chosen as given by the bivariational SCF approximation [12–15] and $\eta = \alpha e^{-i\theta}$ is the complex scaling (dilation) parameter (the method of complex scaling has been reviewed in the literature [27a]; there are also some recent applications of complex scaling [27b]). The self-energy matrix $\mathbf{\Sigma}(\eta, E)$ contains the relaxation and

correlation effects and may be determined through perturbative or renormalized decouplings [4,5].

Solution of the bivariational SCF equations for the N -electron ground state yields a set of occupied and unoccupied orbitals $\{\psi_i\}$. In terms of these orbitals the matrix elements of $G_0^{-1}(\eta, E)$ are

$$(G_0^{-1}(\eta, E))_{ij} = (E - \epsilon_i)\delta_{ij}, \quad (2)$$

where ϵ_i , the orbital energy of the i th orbital, is obviously the zeroth-order pole of the dilated electron propagator. The corresponding orbital ψ_i is the zeroth-order FDA. The propagator Eq. (1) may be recast as

$$G^{-1}(\eta, E) = E\mathbf{1} - \mathbf{L}(\eta, E), \quad \mathbf{L} = \boldsymbol{\epsilon} + \boldsymbol{\Sigma}, \quad (3)$$

and the poles of the dilated electron propagator are the energy-dependent eigenvalues of $\mathbf{L}(\eta, E)$ given by

$$\mathbf{L}(\eta, E)\chi_n(\eta, E) = \mathcal{E}_n(\eta, E)\chi_n(\eta, E), \quad (4)$$

which satisfy the relation

$$\mathcal{E}_n(\eta, E) = E \quad (5)$$

and may be obtained by iterative diagonalization [28] of \mathbf{L} .

The Feynman-Dyson amplitude χ_n corresponding to the n th $(N+1)$ -electron state is given by

$$\chi_n = \int \Psi_n^{N+1*}(1, 2, 3, \dots, N, N+1, n) \\ \times \Psi_0^N(1, 2, 3, \dots, N)d(1)d(2)d(3)\cdots d(N), \quad (6)$$

where Ψ_0^N is the optimal single determinantal description of the N -electron target based on the bi-variationally determined SCF orbitals $\{\psi_i\}$ and Ψ_n^{N+1} is the n th $(N+1)$ state generated by the creation operator manifold $\{a_i \wedge, a_i \wedge a_j \wedge a_k \wedge; j > i\}$ [4,5]. In the bivariationally obtained biorthogonal orbital basis $\{\psi_i\}$, χ_n is a linear combination [29]

$$\chi_n(\vec{r}) = \sum_i C_{ni}\psi_i(\vec{r}), \quad (7)$$

where the mixing of the canonical orbitals allows for the incorporation of correlation and relaxation effects. In the zeroth ($\boldsymbol{\Sigma} = 0$) and quasiparticle approximations (diagonal $\boldsymbol{\Sigma}$), there is no mixing. The difference between perturbative second order ($\boldsymbol{\Sigma}^2$) or renormalized diagonal $2ph$ -TDA ($\boldsymbol{\Sigma}^{2ph-TDA}$) decouplings manifests itself through differences between the mixing coefficients C_{ni} from these approximations [2,5]. Our recent experience with different decouplings [5,10,11] is that the more demanding diagonal $2ph$ -TDA decoupling does not necessarily lead to an improved characterization, and our treatment here is limited to the zeroth- and second-order decouplings of the dilated electron propagator.

The basic computational difference between the atomic and the molecular dilated electron propagator stems from the non-dilatation-analyticity of the Born-Oppen-

heimer Hamiltonian [30–33]. A computationally tractable solution is offered by Moiseyev–Corcoran method of treating the nuclear attraction integrals for the dilated Hamiltonian [32]. This is the method adopted in an alternative approach to the construction of the molecular dilated electron propagator [26,34] based on real SCF as the zeroth-order approximation [28], and we follow the same modified procedure for the calculation of the complex three center nuclear attraction integrals in the construction of our molecular biorthogonal dilated electron propagator.

Results and Discussion

Energetics

The basis functions employed in our calculation are the 4s,9p atom centered CGTOs employed in a previous characterization of this resonance [26]. The resonant trajectories from both the zeroth-order and the second-order decouplings are plotted in Figure 1. No attempt at basis set optimization or optimization of the radial scale factor α has been attempted in this demonstrative first application. However, the fact that the resonance is uncovered without any radial scaling and with very small amount of rotation ($\theta_{\text{opt}} = 0.02$ radians) speaks well for the effectiveness of our technique. The results for the energy and the width of the $^2\Pi_g e\text{-N}_2$ resonance are collected in Table I. Our results compare reasonably with those from experiment and other related techniques [24–26]. Surprisingly, the zeroth-order results offer

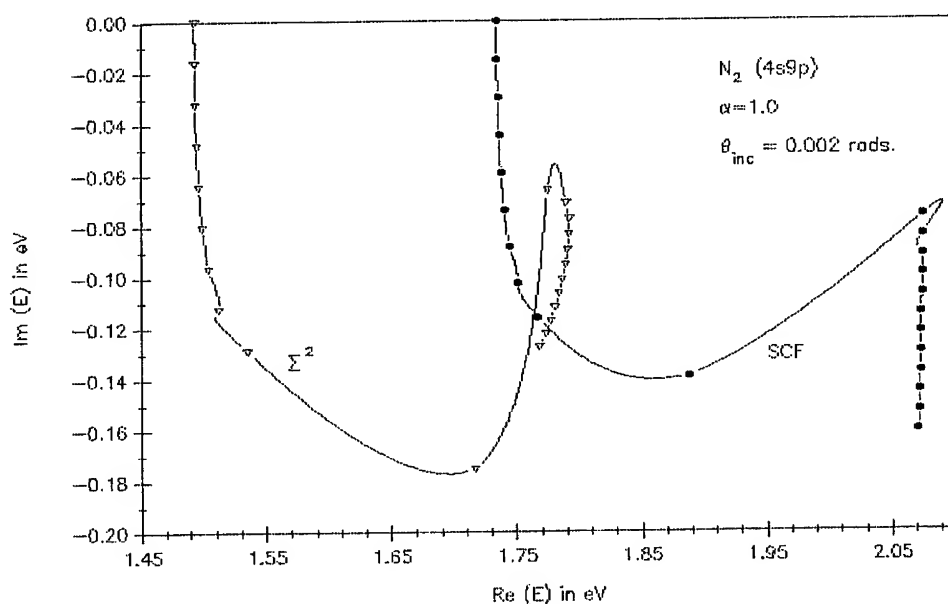


Figure 1. Theta trajectory for the resonant root from zeroth-order and second-order decouplings of the dilated electron propagator.

TABLE I. Energy and width of the $^2\Pi_g N_2^-$.

Method/reference	Energy (eV)	Width (eV)
Experiment [35, 36]	2.20	0.57
Static exchange [18]	3.70	1.16
Static exchange <i>R</i> -matrix [19]	2.15	0.34
Stabilization method [20]	2.44	0.32
<i>R</i> -matrix [21]	3.26	0.80
Complex SCF [22]	3.19	0.44
Stieltjes imaging technique [23]	2.23 ^a	0.40
Many-body optical potential [24]	2.20	—
Many-body optical potential [25]	2.61 ^b	0.58
	2.26 ^c	0.42
	2.54 ^d	0.54
Second-order dilated electron propagator with real SCF [26]	2.14	0.26
Zeroth-order dilated electron propagator (this work)	2.07	0.14
Second-order dilated electron propagator (this work)	1.77	0.13

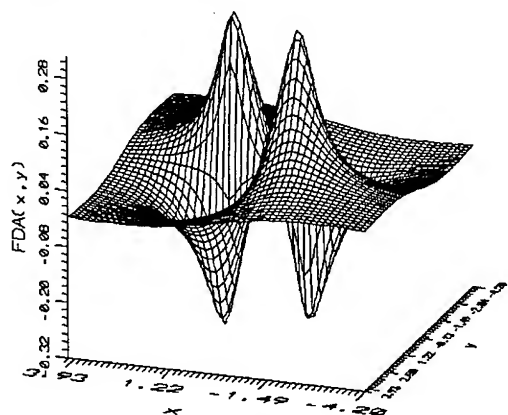
^a Configuration interaction.^b Second order.^c 2p-h TDA.^d ADC (3).

better agreement with the experimental data both for the energy and the width than those from the second order. The results presented here are, however, without any basis-set or radial scale optimization, and any definitive conclusion other than the effectiveness and promise of this technique is unwarranted. In any case, since these molecular resonances have a rich vibrational structure [16], further calculations with internuclear distances spanning the stretchings involved in at least the first few vibrations are essential for a comprehensive characterization of the energy and the width.

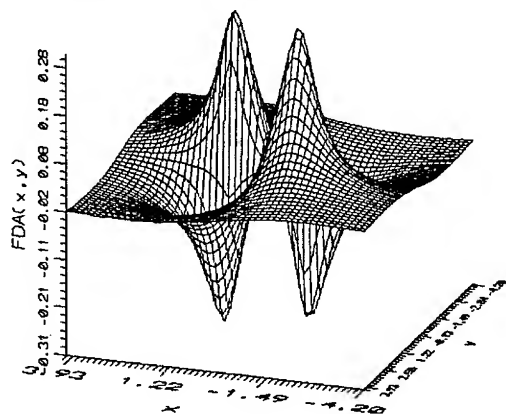
Mechanism

It is easily seen from Figure 1 that the correlation and relaxation effects incorporated by the second-order decoupling stabilize the resonance by lowering both its energy and the width. Mechanistic insights emerge from an analysis of the corresponding FDAs on the real line (Fig. 2) which clearly resemble the familiar $1\pi_g$ orbital of the general chemistry textbooks. The difference between the second-order and the zeroth-order FDA on the real line (Fig. 2) makes obvious the mechanism for stabilization by showing that the lobes of the second-order FDA are both less positive and less negative compared to those of the zeroth order, i.e., the correlation/relaxation decreases the antibonding nature of the $1\pi_g$ orbital and thereby prepares it for metastable anion formation.

Zeroth order (SCF) Feynman Dyson Amplitude



Second order Feynman Dyson Amplitude



Difference between Second order and Zeroth order

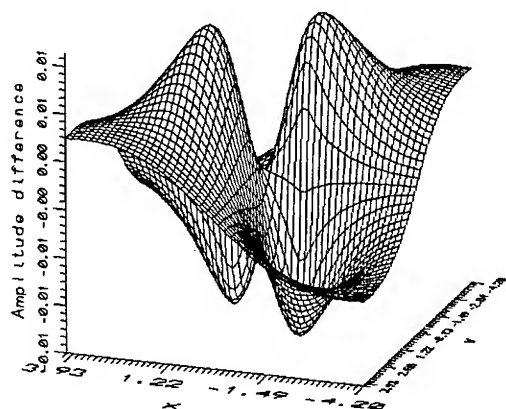
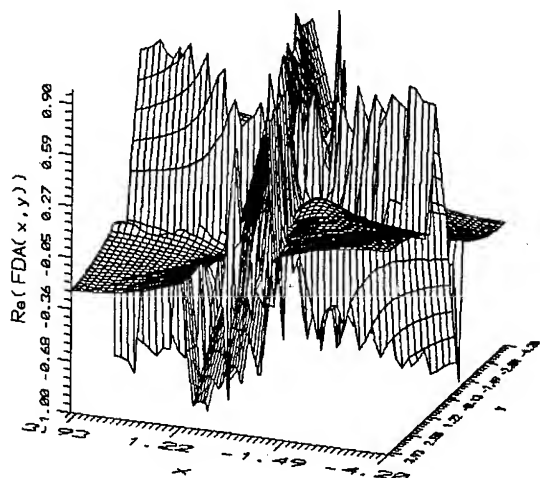


Figure 2. Feynman-Dyson amplitudes from the zeroth- and second-order dilated electron propagator corresponding to the resonant roots of Figure 1 on the real line. The plot of the difference between the second- and zeroth-order amplitude reveals that correlation stabilizes the $1\pi_g$ orbital by reducing its antibonding character.

The metastability is facilitated by the accumulation of the amplitude for the optimal complex scaling parameter as shown in Figure 3. Where there was no amplitude in the internuclear region on the real line (Fig. 2), in Figure 3 we see amplitude accumulation in the internuclear region for the optimal value of the

Real part of Second order Feynman Dyson Amplitude



Imaginary part of Second order Feynman Dyson Amplitude

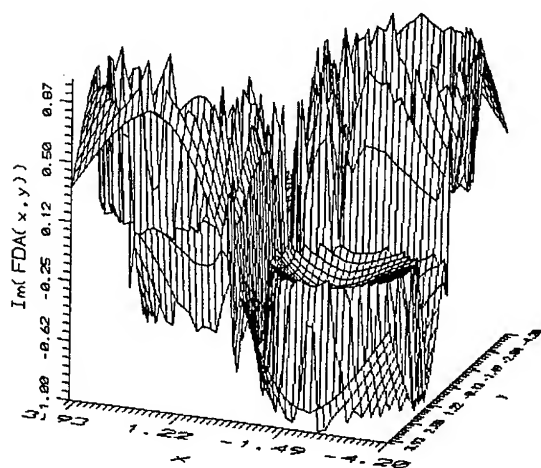


Figure 3. Feynman-Dyson amplitude corresponding to the resonant second-order pole for optimal theta. The resonant metastable anion formation is clearly indicated by the amplitude accumulation in the internuclear region absent on the real line.

complex scaling parameter. As argued earlier for atomic resonances [11] the resonant FDAs once again offer a quantitative and rigorous affirmation of the orbital picture of resonances, and the complex scaling parameter is seen to have a critical role in their unmasking.

Concluding Remarks

The preliminary results from the first application of the biorthogonal dilated electron propagator to a well-characterized molecular resonance provide sufficient promise about its effectiveness in dealing with the energetics of the molecular resonance formation and decay. An examination of the resonant FDAs offers mechanistic insights which bring out the chemistry of the resonance formation in some detail. Such a quantitative affirmation of the resonance formation, to the best of our knowledge, has not been available earlier, and we conclude with the sense of excitement we feel about the new insights that may emerge from a more comprehensive application to many more systems like the $^2\Pi$ resonance in e -CO scattering or the resonance resulting from the trapping of electron in the π^* orbital of C_2H_4 . As mentioned earlier, even the present results need to be revisited with more exhaustive basis sets, optimized radial scale factors, internuclear relaxation, and other decouplings. An effort along these lines is underway in our group.

Acknowledgments

This investigation has been sponsored by the Department of Science and Technology, India, through their Grant No. SP/S1/F60/88. Their support is gratefully acknowledged. M. N. M. is grateful to the CSIR, India for a predoctoral fellowship (No. 9/87(160)/93 EMR-I).

Bibliography

- [1] J. Linderberg and Y. Öhrn, *Propagators in Quantum Chemistry* (Academic, New York, 1973).
- [2] Y. Öhrn and G. Born, *Adv. Quantum Chem.* **13**, 1 (1981).
- [3] M. Mishra, in *Lecture Notes in Quantum Chemistry*, Vol. 50, D. Mukherjee, Ed. (Springer-Verlag, Berlin, 1989), pp. 223ff.
- [4] M. Mishra, P. Froelich, and Y. Öhrn, *Chem. Phys. Lett.* **81**, 339 (1981).
- [5] M. N. Medikeri, J. Nair, and M. K. Mishra, *J. Chem. Phys.* **99**, 1869 (1993).
- [6] M. Mishra, H. A. Kurtz, O. Goscinski, and Y. Öhrn, *J. Chem. Phys.* **79**, 1896 (1983).
- [7] M. Mishra, O. Goscinski, and Y. Öhrn, *J. Chem. Phys.* **79**, 5494 (1983).
- [8] M. Mishra, O. Goscinski, and Y. Öhrn, *J. Chem. Phys.* **79**, 5505 (1983).
- [9] M. N. Medikeri and M. K. Mishra, *Chem. Phys. Lett.* **211**, 607 (1993).
- [10] M. N. Medikeri and M. K. Mishra, *Proc. Ind. Acad. Sci. Chem. Sci.*, to appear.
- [11] M. N. Medikeri and M. K. Mishra, *J. Chem. Phys.* **100**, 2044 (1994).
- [12] M. Mishra, Y. Öhrn, and P. Froelich, *Phys. Lett.* **A81**, 4 (1981).
- [13] P. Froelich and P. O. Löwdin, *J. Math. Phys.* **24**, 89 (1983).
- [14] P. O. Löwdin, P. Froelich, and M. Mishra, *Int. J. Quant. Chem.* **36**, 867 (1989).
- [15] P. O. Löwdin, P. Froelich, and M. Mishra, *Adv. Quant. Chem.* **20**, 185 (1989).
- [16] K. D. Jordan and P. D. Burrow, *Acc. Chem. Res.* **11**, 341 (1978).
- [17] J. Simons and K. D. Jordan, *Chem. Rev.* **87**, 535 (1987); K. D. Jordan and P. D. Burrow, *ibid.* **87**, 557 (1987).

- [18] B. L. Schneider, Phys. Rev. A24, 1 (1981).
- [19] B. L. Schneider, M. Le Courneuf, and V. K. Lan, Phys. Rev. Lett. 43, 1927 (1979).
- [20] J. S.-Y. Chao, M. F. Falcetta, and K. D. Jordan, J. Chem. Phys. 93, 1125 (1990).
- [21] M. Krauss and F. H. Mies, Phys. Rev. A1, 1592 (1974).
- [22] T. N. Rescigno, A. E. Orel, and C. W. McCurdy, J. Chem. Phys. 73, 6347 (1980).
- [23] A. U. Hazi, T. N. Rescigno, and M. Kurilla, Phys. Rev. A23, 1089 (1981).
- [24] M. Berman, O. Walter, and L. S. Cederbaum, Phys. Rev. Lett. 50, 1979 (1983).
- [25] H. D. Meyer, Phys. Rev. A40, 5605 (1989).
- [26] R. Donnelly, Int. J. Quant. Chem. Quant. Chem. Symp. 16, 653 (1982).
- [27] (a) W. P. Reinhardt, Ann. Rev. Phys. Chem. 33, 223 (1982); B. R. Junker, Adv. At. Mol. Phys. 18, 207 (1982); Y. K. Ho, Phys. Rep. 99, 2 (1983); (b) U. Peskin and N. Moiseyev, J. Chem. Phys. 97, 6443 (1992); O. E. Alon and N. Moiseyev, Phys. Rev. A46, 3807 (1992); W. Sun, C. W. McCurdy, and B. H. Lengsfeld, J. Chem. Phys. 97, 5480 (1992).
- [28] R. A. Donnelly and J. Simons, J. Chem. Phys. 73, 2858 (1980).
- [29] J. V. Ortiz, J. Chem. Phys. 92, 6728 (1990); J. V. Ortiz and J. W. Mintmire in *Silicon-Based Polymer Science: A Comprehensive Resource*, John M. Zeigler and F. W. Gordon Fearon, Eds., Advances in Chemistry Series No. 224, (American Chemical Society, Washington, DC, 1990); J. V. Ortiz and Jyh-Shing Lin, Chem. Phys. Lett. 171, 197 (1990); J. V. Ortiz, Chem. Phys. Lett. 169, 116 (1990).
- [30] C. W. McCurdy and T. N. Rescigno, Phys. Rev. Lett. 41, 1364 (1978).
- [31] B. Simon, Phys. Lett. A71, 211 (1979).
- [32] N. Moiseyev and C. Corcoran, Phys. Rev. A20, 814 (1979).
- [33] J. D. Morgan and B. Simon, J. Phys. B14, 1167 (1981).
- [34] R. A. Donnelly, Int. J. Quant. Chem. S19, 337 (1985); J. Chem. Phys. 84, 6200 (1986).
- [35] G. J. Schulz, Rev. Mod. Phys. 45, 423 (1973).
- [36] A. Herzenberg, J. Phys. B1, 548 (1968); D. T. Birtwhistle and A. Herzenberg, J. Phys. B4, 53 (1971).

Received March 8, 1994

Evaluation of Integrals Appearing in the Hylleraas CI Method by Expanding $1/r_{ij}$ in Terms of a Complete Basis Set

J. E. PÉREZ,* H. H. CUENYA,* R. H. CONTRERAS,† F. S. ORTIZ,*
H. GRINBERG,† C. G. GIRIBET,† and M. C. RUIZ DE AZÚA†

**Dptos. de Química y Física y de Matemática, Fac. de Cs. Exs. Fco-Qcas y Nat., Universidad Nacional de Río Cuarto, Estafeta Postal No. 9, (5800) Río Cuarto, Argentina, †Dpto. de Física, Fac. de Cs. Exs. y Nat., Universidad de Buenos Aires, Cdad. Univ., Pab. 1, (1428) Buenos Aires, Argentina*

Abstract

A new approach for solving multielectronic integrals in quantum chemistry is presented. The Coulomb potential r_{12}^{-1} is expanded in a complete function set within a finite spherical domain of radius R . This expansion yields a series where the \tilde{r}_1 and \tilde{r}_2 variables are symmetrically separated. The generalization to other potentials is briefly discussed. The Yukawa potential $\exp(-\zeta r_{12})/r_{12}$, and the functions $\exp(-\zeta r_{12}^2)$ and $\exp(-\zeta r_{12})$ are considered as particular cases. As an example of the potentialities of this approach, a certain type of four-electron integrals that appear in the Hylleraas CI method are evaluated. Results thus obtained are discussed in terms of the approximations made and compared with values obtained using other procedures available in the literature. © 1994 John Wiley & Sons, Inc.

Introduction

In a previous article [1] a novel approach to calculate the electronic integrals that appear in an SCF-LCAO calculation using any type of sufficiently fast decaying atomic orbitals in the basis set was presented. It was based on the expansion of the binary products of atomic orbitals entering in those integrals in terms of an adequate complete function basis set. This complete function set was built up in a finite domain defined by a sphere of radius R whose value can be chosen according to the problem dealt with. The functions defining this complete set are solutions of the Helmholtz equation with boundary conditions devised as to make the Coulomb integral particularly simple [1].

Bielelectronic integrals of an SCF-LCAO calculation, multielectronic integrals that appear in the realization of Hylleraas Configuration Interaction, HCl [2–4] as well as others which appear in different models that intend to take into account electronic correlation [5], contain in their integrands atomic orbital products and functions of the interelectronic distances. These functions are called, hereafter, *potential functions*.

In this article a different approach to study similar problems is presented. Instead of expanding binary atomic orbital products in terms of the mentioned complete

function set as in the previous article [1], the potential function is expanded in terms of the same complete function set. Such expansions allow one to “decouple” the potential functions $f(r_{12})$ in symmetrically separated integration variables \vec{r}_1 and \vec{r}_2 [6,7], permitting the concrete realization of the corresponding multielectronic integrals. It is also shown that this expansion can be performed along two different lines.

Finally, how to apply these ideas to implement the practical calculation of four-electron integrals over gaussian-type orbitals that appear in the HCI method [4] is shown and some numerical values are presented which are compared with those obtained using other methods available in the literature [3]. The promising potentialities of this approach are briefly discussed.

Symmetrical Separation of the \vec{r}_1 and \vec{r}_2 Variables in Potential Functions of the Form $f(r_{12})$

Basis Set Functions Employed in the Present Work

In a previous work [1], it has been shown that a complete set of functions $\{U_{lmn}(\vec{r})\}$, with $l = 0, 1, \dots, m = -l, -(l-1), \dots, l$ and $n = 1, 2, \dots$, can be defined such that each $U_{lmn}(\vec{r})$ is a solution of the Helmholtz equation inside a sphere of radius R , and satisfies the following integral equation:

$$\int_{r' \leq R} dV' \frac{U_{lmn}(\vec{r}')}{|\vec{r} - \vec{r}'|} = \left(\frac{4\pi}{k_{ln}^2} \right) U_{lmn}(\vec{r}) \quad (1)$$

where, in spherical coordinates,

$$U_{lmn}(\vec{r}) = B_{ln} \frac{J_{l+1/2}(k_{ln}r)}{r^{1/2}} Y_{lm}(\theta, \phi) \quad (2)$$

with $r \leq R$, $J_{l+1/2}(x)$ is the Bessel function of the first kind of half integer order [8], B_{ln} are the corresponding radial normalization constants which are equal to $2^{1/2}/[RJ_{l+1/2}(k_{ln}R)]$, $Y_{lm}(\theta, \phi)$ are the normalized spherical harmonics [9], and k_{ln} satisfy an appropriate radial boundary condition, i.e., Eq. (1) evaluated at $|\vec{r}| = a$. Essentially, this condition is:

$$J_{l-1/2}(k_{ln}R) = 0 \quad (3)$$

i.e., for each $l = 0, 1, \dots$ the $n = 1, 2, \dots$ index stands for the n th zero of $J_{l-1/2}(x)$.

The functions given in Eq. (2) are suitable for the purposes of this work.

Symmetrical Separation of Variables for the Coulomb Potential

The complete basis set $\{U_{lmn}(\vec{r})\}$, can be used for expanding any function that belongs to the $L^2(r < R)$ Hilbert Space. In particular, $f(\vec{r}_{12}) = |\vec{r}_1 - \vec{r}_2|^{-1} \equiv r_{12}^{-1}$ for each \vec{r}_2 satisfying $\vec{r}_1 \neq \vec{r}_2$ and $0 \leq r_1, r_2 \leq R$, assumes the following expression:

$$r_{12}^{-1} = \sum_{lmn} C_{lmn} U_{lmn}(\vec{r}_1) \quad (4)$$

with

$$C_{lmn} = \int_{r_1 \leq R} dV_1 \frac{U_{lmn}^*(\vec{r}_1)}{|\vec{r}_1 - \vec{r}_2|} = \left(\frac{4\pi}{k_{ln}^2}\right) U_{lmn}^*(\vec{r}_2) \quad (5)$$

where the last expression results from Eq. (1).

Equations (4) and (5) yield the symmetric separation of r_{12}^{-1} in \vec{r}_1 and \vec{r}_2 ,

$$|\vec{r}_1 - \vec{r}_2|^{-1} = 4\pi \sum_{lmn} \frac{U_{lmn}^*(\vec{r}_2) U_{lmn}(\vec{r}_1)}{k_{ln}^2} \quad (6)$$

It is worthy of mention that the Laplace expansion [10] of r_{12}^{-1} :

$$r_{12}^{-1} = \frac{4\pi}{r_>} \sum_{lm} \left(\frac{r_<}{r_>}\right)^l (2l+1)^{-1} Y_{lm}^*(\theta_2, \phi_2) Y_{lm}(\theta_1, \phi_1) \quad (7)$$

allows one to relate $(r_<^l/r_>^{l+1})$ with the sum over n in Eq. (6), as a direct consequence of the linear independence of spherical harmonics. That is:

$$\left(\frac{1}{2l+1}\right) \frac{r_<^l}{r_>^{l+1}} = \sum_{n=1}^{\infty} \frac{R_{ln}(r_<) R_{ln}(r_>)}{k_{ln}^2} \quad (8)$$

where

$$R_{ln}(r) = B_{ln} J_{l+1/2}(k_{ln} r) / r^{1/2}$$

The series in Eq. (8) is the discrete analogous of the well known (see p. 274 of Ref. [11]) relation:

$$\frac{1}{l+1/2} \left(\frac{r_<}{r_>}\right)^{l+1/2} = \int_0^{\infty} \frac{dk}{k} J_{l+1/2}(kr_>) J_{l+1/2}(kr_<) \quad (9)$$

This analogy is a direct consequence of the close connection existing between the present discrete approach and the Fourier Transform Method (see Sec. 2.4 of Ref. [1]).

A Brief Outline to Generalize the Results for Arbitrary Potentials

Given a function $f(r)$, with $0 \leq r \leq R$, its expansion in terms of the complete set defined in this section, is:

$$f(r) = \sum_{n=1}^{\infty} Z_n \frac{\sin(k_{0n} r)}{r} \quad (10)$$

where

$$Z_n \equiv B_{0n} \left(\frac{2}{\pi k_{0n}}\right)^{1/2} C_{00n} = B_{0n} \left(\frac{2}{\pi k_{0n}}\right)^{1/2} \int_{r \leq R} dV U_{00n}^*(\vec{r}) f(r) \quad (11)$$

It is important to note that if $f(r)$ is continuous in $[0, R]$ then the series of Eq. (10) uniformly converges in the interval $[\delta, R - \delta]$ with δ arbitrarily small, [12, p. 602].

The next step is to put $r = r_{12}$ in Eq. (10), under the assumption that $r_{12} \leq R$. Making use of the following relation [11, p. 221],

$$\frac{\sin(k_{0n}r_{12})}{r_{12}} = 2\pi^2 \sum_{l=0}^{\infty} \sum_{m=-l}^l F_{lmn}^*(\vec{r}_1) F_{lmn}(\vec{r}_2) \quad (12)$$

where

$$F_{lmn}(\vec{r}_i) = Y_{lm}(\theta_i, \phi_i) J_{l+1/2}(k_{0n}r_i) / r_i^{1/2}$$

Eq. (10) transforms into:

$$f(r_{12}) = 2\pi^2 \sum_{lmn} Z_n F_{lmn}^*(\vec{r}_1) F_{lmn}(\vec{r}_2) \quad (13)$$

The procedure depicted above generates a separated expansion for the potential $f(r_{12})$ in a "complicated" region defined by the condition $r_{12} \leq R$. In particular it is appropriate to be used in the evaluation of integrals of the potential functions if the domain of integration is restricted to $r_1, r_2 \leq R/2$. The parameter R is selected in the way discussed in Appendix I of Ref. [1], i.e., assuring that the error due to the truncation of the space is negligible as a consequence of the exponentially decaying property of atomic orbitals.

From Eq. (11) and Eq. (13) it is clear that the C_{00n} coefficients provide the sufficient information to separate the variables \vec{r}_1 and \vec{r}_2 . To illustrate this point, the C_{00n} coefficients for the Yukawa potential and for the functions $\exp(-\alpha r_{12})$ and $\exp(-\alpha r_{12}^2)$ are explicitly given in what follows.

The C_{00n} coefficient which corresponds to $\exp(-\zeta r)/r$ is:

$$\begin{aligned} C_{00n} &= \int d\omega \int_0^R dr r^2 R_{0n}(r) Y_{00}^*(\omega) \exp(-\zeta r)/r \\ &= (4\pi)^{1/2} B_{0n} \left(\frac{2}{\pi k_{0n}} \right)^{1/2} \frac{k_{0n} - \exp(-\zeta R) \zeta \sin(k_{0n}R)}{\zeta^2 + k_{0n}^2} \\ &\equiv 4\pi \frac{U_{00n}^*(\vec{0})}{\zeta^2 + k_{0n}^2} + \exp(-\zeta R) Q_n \end{aligned} \quad (14)$$

where

$$U_{00n}^*(\vec{0}) = (-1)^{n+1} k_{0n} / [2\pi R]^{1/2}$$

and

$$Q_n = -B_{0n} \left(\frac{8}{k_{0n}} \right)^{1/2} \zeta \frac{\sin(k_{0n}R)}{\zeta^2 + k_{0n}^2} \quad (15)$$

The C_{00n} coefficient which corresponds to $\exp(-\zeta r)$ is:

$$\begin{aligned}
 C_{00n} &= (4\pi)^{1/2} B_{0n} \left(\frac{2}{\pi k_{0n}} \right)^{1/2} \int_0^R dr r \exp(-\zeta r) \sin(k_{0n} r) \\
 &= (4\pi)^{1/2} B_{0n} \left(\frac{2}{\pi k_{0n}} \right)^{1/2} \left\{ \frac{2\zeta k_{0n}}{(\zeta^2 + k_{0n}^2)^2} + \exp(-\zeta R) \right. \\
 &\quad \cdot (-1)^n \cdot \left(\frac{R\zeta}{\zeta^2 + k_{0n}^2} + \frac{\zeta^2 - k_{0n}^2}{(\zeta^2 + k_{0n}^2)^2} \right) \Big\} \\
 &\equiv 8\pi\zeta \frac{U_{00n}^*(\vec{0})}{(\zeta^2 + k_{0n}^2)^2} + \exp(-\zeta R) M_n
 \end{aligned} \tag{16}$$

where

$$M_n = B_{0n} \left(\frac{8}{k_{0n}} \right)^{1/2} (-1)^n \left\{ \frac{\zeta R}{\zeta^2 + k_{0n}^2} + \frac{\zeta^2 - k_{0n}^2}{(\zeta^2 + k_{0n}^2)^2} \right\} \tag{17}$$

Analogously, the $\exp(-\zeta r^2)$ function gives:

$$\begin{aligned}
 C_{00n} &= \int d\omega \int_0^R dr r^2 B_{0n} \frac{J_{1/2}(k_{0n} r)}{r^{1/2}} Y_{00}^*(\omega) \exp(-\zeta r^2) \\
 &= (4\pi)^{1/2} B_{0n} \left(\frac{2}{\pi k_{0n}^2} \right)^{1/2} \left\{ \int_0^\infty dr r \exp(-\zeta r^2) \sin(k_{0n} r) \right. \\
 &\quad \left. - \int_R^\infty dr r \exp(-\zeta r^2) \sin(k_{0n} r) \right\} \\
 &\equiv \left(\frac{\pi}{\zeta} \right)^{3/2} \exp(-k_{0n}^2/4\zeta) U_{00n}^*(\vec{0}) + e_n
 \end{aligned} \tag{18}$$

where

$$e_n = -B_{0n} \left(\frac{8}{k_{0n}^2} \right)^{1/2} \int_R^\infty dr r \exp(-\zeta r^2) \sin(k_{0n} r) \tag{19}$$

it can be shown that $|e_n|$ is a quantity of order $\exp(-\zeta R^2)$.

The three examples shown above have a common structure. The second terms in Eqs. (14), (16), and (18) are negligible with respect to the corresponding first ones (provided a large R value is selected). Moreover, these first terms can be expressed as the product of the basis function evaluated at $\vec{r} = \vec{0}$ and the Fourier Transform of the corresponding potential specialized in the k_{0n} eigenvalues. Consequently, eq. (13) can be considered as the discrete analogous of the relation [13]:

$$f(r_{12}) = (32\pi)^{1/2} \sum_{lm} Y_{lm}^*(\omega_1) Y_{lm}(\omega_2) H(r_1, r_2) \tag{20}$$

where

$$H_l(r_1, r_2) = \int_0^\infty dk k^2 j_l(kr_1) j_l(kr_2) \mathcal{F}(k)$$

with $j_l(x)$ representing the spherical Bessel functions of order l ; $\mathcal{F}(k)$ is the Fourier transform of $f(r)$. Comparison of Eqs. (13) and (20) gives:

$$2\pi^2 \sum_{n=1}^{\infty} Z_n \frac{J_{l+1/2}(k_{0n}r_1) J_{l+1/2}(k_{0n}r_2)}{(r_1 r_2)^{1/2}} = (32\pi)^{1/2} H_l(r_1, r_2) \quad (21)$$

Alternatively, the direct expansion referred to in the last subsection, for an arbitrary function $f(r_{12})$ ultimately is:

$$f(r_{12}) = \sum_{lm} \sum_{n,n'=1}^{\infty} A_{lm,nn'} U_{lmn}(\vec{r}_2) U_{lmn'}(\vec{r}_1) \quad (22)$$

where $A_{lm,nn'}$ comes from the scalar product:

$$(U_{l'm'n'}(1) U_{lmn}(2), f(r_{12})) = \delta_{ll'} \delta_{mm'} A_{lm,nn'} \quad (23)$$

The expansion obtained in Eq. (13) differs from the one given in Eq. (22) in the following points: in the former only the $\{k_{0n}\}$ and the $\{C_{00n}\}$ subsets are needed in contrast to the information required to obtain Eqs. (22) and (23). Moreover, for an arbitrary potential Eq. (22) contains one extra summation compared to Eq. (13). However, it must be emphasized that the expansion Eq. (13) is restricted to the smaller domain $r_1, r_2 \leq R/2$, as discussed above.

In particular, for the Coulomb case, the summation over n' in Eq. (22) is eliminated as a consequence of the property of the $\{U_{lmn}(\vec{r})\}$ functions shown in Eq. (1), thus obtaining the expansion Eq. (6). At present, the convergence properties of the expansions for r_{12}^{-1} following each one of the two approaches discussed above are being analyzed.

Evaluation of a Class of Integrals Appearing in the Hylleraas CI Method

It is well known [3,4] that four-electron integrals of the type:

$$E_{abcdefgh} = \int dV_1 dV_2 dV_3 dV_4 \rho_{ab}(\vec{r}_1) \rho_{cd}(\vec{r}_2) \rho_{ef}(\vec{r}_3) \rho_{gh}(\vec{r}_4) \cdot r_{12} r_{23}^{-1} r_{34} \quad (24)$$

are needed in the HCI method. Here, $abcdefgh$ are indices for the bicentric $\rho_{xy}(\vec{r})$ atomic orbital product densities.

The standard approach to evaluate this eight-center quantity is to replace r_{ij}^{-1} (and analogously r_{ij}) by the following representation [3,4]:

$$r_{ij}^{-1} = \pi^{-1/2} \int_0^\infty dx x^{-1/2} \exp(-x r_{ij}^2) \quad (25)$$

and then to interchange the integration variables, permitting the spatial integrals to be performed analytically, provided that gaussian atomic orbitals are used. The remaining integrals (three dimensional in general) are evaluated numerically.

A new method to perform the evaluation of $E_{a \dots h}$ can be obtained using the expansion of Eq. (6). To this end both integrals over \vec{r}_1 and \vec{r}_2 must be carried out partitioning the space into two regions, one is a sphere of radius R and the other is the rest of the space. Therefore, Eq. (24) transforms into:

$$E_{a \dots h} = \int_{\substack{r_1, r_4 < \infty \\ r_2, r_3 < R}} dV_1 dV_2 dV_3 dV_4 \rho_{ab}(\vec{r}_1) \rho_{cd}(\vec{r}_2) \rho_{ef}(\vec{r}_3) \rho_{gh}(\vec{r}_4) \\ \cdot r_{12} r_{23}^{-1} r_{34} + e_{a \dots h}(R) = 4\pi \sum_{lmn} \frac{C_{lmn}^{abcd} C_{lmn}^{efgh}}{k_{ln}^2} + e_{a \dots h}(R) \quad (26)$$

where

$$C_{lmn}^{abcd} = \int_{\substack{r_1 < \infty \\ r_2 < R}} dV_1 dV_2 \rho_{ab}(\vec{r}_1) \rho_{cd}(\vec{r}_2) r_{12} U_{lmn}^*(\vec{r}_2) \quad (27)$$

and $e_{a \dots h}(R)$ is the error of truncation of space. It can be shown (for analogies see Appendix I of ref. [1] that it is a quantity of order $\exp(-\text{const. } R^2)$ for gaussian-type orbitals, provided the ρ_{cd} and ρ_{ef} densities correspond to atomic orbitals centered inside the mentioned sphere.

In practice, it is convenient to extend the integration over \vec{r}_2 in Eq. (31) to the whole space. The new coefficients thus obtained will be denoted by T_{lmn}^{abcd} . Although this introduces a new source of error, it greatly simplifies their computation [1]. In what follows, this source of error together with $e_{a \dots h}(R)$ and the truncation of the series in Eq. (26), will be tested in a simple but important example.

The case to be explicitly considered is such that:

$$\rho_{ab}(\vec{r}) = \exp\left(-\frac{\alpha\beta}{\alpha+\beta} |\vec{A} - \vec{B}|^2\right) \exp\left(-(\alpha+\beta) \left|\vec{r} - \frac{\alpha\vec{A} + \beta\vec{B}}{\alpha+\beta}\right|^2\right) \quad (28)$$

where \vec{A} and \vec{B} are fix vectors that localize two 1S gaussian orbitals with orbital exponents α and β , respectively. In this example, $\alpha\vec{A} + \beta\vec{B} = \gamma\vec{C} + \delta\vec{D} = \dots = \vec{0}$ with $\alpha = \beta = \gamma = \dots = 0.5$ a.u. and $|\vec{A} - \vec{B}| = |\vec{C} - \vec{D}| = 3.0349$ a.u.

The standard approach yields the following bidimensional integral:

$$E_{a \dots h} = K_{ab} K_{cd} K_{ef} K_{gh} 2\pi^{9/2} \int_0^\infty dx \int_0^\infty dy (x-y)^{-1/2} \\ \cdot \frac{\partial^2}{\partial x \partial y} ([f(x)f(y)]^{-1} [f(x)g(y) + f(y)g(x)]^{-1/2}) \quad (29)$$

where $f(x) = 1 + 2x$, $g(x) = 1 + x$ and K_{ij} is the constant factor in Eq. (28). The numerical integration of Eq. (29) was carried out using Gauss-Tchebicheff quadrature [11, p. 42], after the change of variable $x = (1+t)/(1-t)$ (analogously for y). The result, with the same number of integration points in x and y , is displayed in Table I. It is worthy of mention its monotonic behavior and the 10^{-7} a.u. reached precision with only 20 points.

TABLE I. Comparison of the values obtained for the integral Eq. (24) as obtained using the numerical integration Eq. (29) and the expansion Eq. (26) performed using the approximate coefficients defined in Eq. (30). See text for the description of the atomic orbitals involved.

Method Eq. (29)	Integration points	Result (a.u.)	
	20×20	0.179555632	
	40×40	0.179555674	
	60×60	0.179555676	
	100×100	0.179555676	
Method Eq. (26) (Int. points: 40)	Radius of sphere (a.u.)	Number of terms	Result (a.u.)
	4	5	0.179555500
		10	0.179555679
		15	0.179555679
	7	5	0.177401483
		10	0.179555459
		15	0.179555680
		20	0.179555680
	10	5	0.164561488
		10	0.179499393
		15	0.179555521
		20	0.179555680
		25	0.179555680

The new method requires the evaluation of the T_{lmn}^{abcd} coefficients, given by:

$$\begin{aligned}
 T_{lmn}^{abcd} &= \int_{r_1, r_2 < \infty} dV_1 dV_2 \rho_{ab}(\vec{r}_1) \rho_{cd}(\vec{r}_2) r_{12} U_{lmn}^*(\vec{r}_2) \\
 &= -\pi^{-1/2} \int_0^\infty \frac{dx}{x^{1/2}} \frac{\partial}{\partial x} \int dV_1 dV_2 \rho_{ab}(\vec{r}_1) \rho_{cd}(\vec{r}_2) \exp(-xr_{12}^2) U_{lmn}^*(\vec{r}_2) \\
 &= \delta_{l0} \delta_{m0} K_{ab} K_{cd} U_{00n}(\vec{0}) \int_0^\infty dx \frac{F(x) \exp\left(-\frac{k_{0n}^2}{4W(x)}\right)}{(1+x^2)(1+2x^2)^{5/2}}
 \end{aligned} \tag{30}$$

where $W(x) = (1 + 2x^2)/(1 + x^2)$, $F(x) = 6(1 + x^2) - [k_{0n}^2/2W(x)]$, and $k_{0n} = (n - 0.5)(\pi/R)$ with $n = 1, 2, \dots$. After the change of variable $x = (1 + t)/(1 - t)$, the integral in Eq. (30) was evaluated numerically by means of Gauss-Tchebicheff quadrature, with a fixed number of integration points which was set equal to 40.

Table I also shows the results for $E_{a \dots h}$ obtained by the systematic variation of R and the number of terms for the partial sums of the series in Eq. (26). The following comments are pertinent.

The best partial sums, for each R , are very close to the values obtained with the standard method (which is the reference value in this work). This is an indicator that all sources of error would generate controllable quantities. It occurs also that the greater the R value the more number of terms are needed to achieve a given precision. Due to the rapidly decaying property of gaussian orbitals, it seems that $R = 4$ a.u. is a sufficient value. The last point to stress is that the $\exp(-k_{0n}^2/4W)$ factor in Eq. (30) ensures an optimum rate of convergence for the series; this can be demonstrated by obtaining an upper bound to the integral, which has the factor $\exp(-k_{0n}^2/4W_{\max})$.

Concluding Remarks

Expansions of potential functions in a complete function set presented in this article are found to be an interesting alternative for solving several types of electronic integrals that appear in quantum chemistry. It is interesting to note that two approaches were followed to obtain expansions within a finite domain of potential functions of type $f(r_{12})$ where the variables \vec{r}_1 and \vec{r}_2 are symmetrically separated. In one of these approaches all eigenvalues $\{k_{ln}\}$ are used and only for the Coulomb potential a three indices summation is obtained (compare Eq. (22) with Eq. (6)). Within the other approach, use is made of the spherical symmetry of $f(r_{12})$ to obtain a three-indices expansion in which the variables are symmetrically separated term by term [see Eq. (13)]. In this case, only a subset of eigenvalues $\{k_{0n}\}$ is required. However, the validity of these expansions is restricted to regions smaller than the sphere of radius R , and, therefore, the advantage of using only a subset of eigenvalues and not all of them, in some cases can be superseded by the need of including a larger number of terms to obtain an adequate accuracy in the final values. For this reason an adequate comparison between these two approaches would require a more detailed study for different particular cases. However, it is important to recall that for the numerical values shown above for some Hylleraas CI integrals using gaussian orbitals a sphere of radius $R = 4$ a.u. seems to yield an adequate accuracy when the expansion Eq. (6) is used.

Acknowledgments

Grants from CONICET, UBA, CONICOR, and SECYT-UNRC are gratefully acknowledged.

Bibliography

- [1] J. E. Pérez, H. H. Cuenya, R. H. Contreras, F. S. Ortiz, H. Grinberg, M. C. Ruiz de Azúa, and C. G. Giribet, *Theor. Chim. Acta*, in press.
- [2] N. C. Handy, in *Computational Techniques in Quantum Chemistry and Molecular Physics*, G. H. F. Diercksen, B. T. Sutcliffe, and A. Veillard, Eds. (Reidel, Dordrecht, 1975).
- [3] W. Kutzelnigg, *Theor. Chim. Acta* **68**, 445 (1985).
- [4] E. Clementi, G. Corongiu, and S. J. Chakravorty, *ESCOM Leiden*, E. Clementi, Ed. (Kingston, New York, 1990), Chap. 5, p. 235.
- [5] S. J. Chakravorty and E. Clementi, *Phys. Rev. A* **39**, 2290 (1989).

- [6] N. Cressy and K. Ruedenberg, *Int. J. Quantum Chem.* **3**, 493 (1969).
- [7] O. Steinborn, *ETO Multicenter Molecular Integrals*, C. A. Weatherford and H. W. Jones, Eds. (Reidel Publishing Co., Dordrecht, Boston, London, 1982), p. 7.
- [8] M. Abramowitz and I. E. Stegun, *Handbook of Mathematical Functions and Tables* (National Bureau of Standards, App. Math. Series, Dover, NY, 1972), Chap. 10.
- [9] D. M. Brink and G. R. Satchler, *Angular Momentum*, 2nd. ed. (Clarendon, Oxford, 1968), p. 18.
- [10] O. Steinborn, *Chem. Phys. Lett.* **3**, 671 (1969).
- [11] H. Hochstadt, *Functions of Mathematical Physics* (Dover, NY, 1986).
- [12] G. N. Watson, *A Treatise on the Theory of Bessel Functions* (University Press, London, 1966), Chap. 18.
- [13] O. Steinborn, *NATO Advanced Study Institute on Methods in Computational Molecular Physics, Lectures Notes* (Plenum, New York, 1982), Chap. 5.

Received May 3, 1994

Self-Consistent Coupling of Atomic Orbitals to a Moving Charge

HERBERT F. M. DA COSTA and DAVID A. MICHA

*Quantum Theory Project, Departments of Chemistry and of Physics,
University of Florida, Gainesville, Florida 32611*

Abstract

We describe the time evolution of hydrogenic orbitals perturbed by a moving charge. Starting with the equation for an atom interacting with a charge, we use an eikonal representation of the total wavefunction, followed by an eikonal approximation, to derive coupled differential equations for the temporal change of the orbitals and the charge's trajectory. The orbitals are represented by functions with complex exponents changing with time, describing electronic density and flux changes. For each orbital, we solve a set of six coupled differential equations; two of them are derived with a time-dependent variational procedure for the real and imaginary parts of the exponents, and the other four are the Hamilton equations of the positions and momenta of the moving charge. The molecular potentials are derived from the exact expressions for the electronic energies. Results of calculations for 1s and 2s orbitals show large variation of the real exponent parts over time, with respect to asymptotic values, and that imaginary parts remain small. © 1994 John Wiley & Sons, Inc.

Introduction

Time-dependent molecular phenomena can be described in terms of time-dependent molecular orbitals written as linear combinations of atomic orbitals with time-dependent coefficients. Recent work on ion-atom collisions at low collision velocities (small compared with electronic velocities) show that accurate results for probabilities of electron transfer can be obtained provided suitable atomic basis sets are used [1-7]. It is well known that improved results can be obtained in the calculation of potential energies, for example, in H_2^+ and H_2 , by allowing for variable atomic orbital exponents as nuclear distances decrease [8]. A similar situation may be expected for dynamical phenomena, but there is no information about temporal changes of orbital exponents as functions of the velocities of slow moving charges.

The present study addresses this case. It starts with the equation for the interaction of an atom with a charge, at a given total energy. It then introduces an eikonal representation of the total wavefunction for electrons and nuclei [9-11] and takes the eikonal limit of short de Broglie wavelengths for the nuclear motions to derive coupled equations for the atomic orbitals and the nuclear trajectories. The atomic orbitals satisfy a time-dependent Schrödinger equation which can be solved by

using a time-dependent variational principle (TDVP) [12,13] with a suitable trial form for the orbitals.

Some of the early applications of variational principles in atomic collisions made use of real exponential parameters [14–16]. In the late '70s Kleber and co-workers [17,18] started using complex parameters because they describe some physical features, like the flux of the electron charge, that are not present in treatments with real parameters only.

In this work we describe the effect of a charge moving in the plane of two nuclei, on hydrogenic atomic orbitals with complex exponents which change in time. The eikonal approximation leads to coupling of the Hamiltonian equations for the trajectories to the differential equations for the atomic orbital parameters that are derived from the time-dependent variational principle. The six coupled differential equations for each orbital (two for the exponential parameters and four for the positions and momenta) are solved numerically using a Runge–Kutta fourth-order algorithm [19].

We use a simple model consisting of an electron moving in the field of two nuclear charges of number Z_T , for the target atom, and Z_P , for the projectile. The electronic orbitals are kept centered at the target atom, which does not move, so that its orbitals change in time during the interaction with the moving projectile due to the variation with time of the target's effective nuclear charge. Electron transfer is not allowed. This model describes the interaction of a low energy projectile with oriented valence orbitals in a molecule or at a solid surface. By restricting the orbital variation to its exponent, it is possible to evaluate the importance of varying nuclear charges in dynamical phenomena, and to develop a computational procedure to parametrize the orbitals as linear combinations of Gaussian orbitals. This has recently been done by introducing a scaling of the electron radial variable with the effective nuclear charge, to isolate the atomic orbitals from their time dependence and to find Gaussian combinations valid for all times [20].

Coupling of Trajectories with Orbitals

In this section we use the eikonal representation for the wavefunction of electrons and nuclei [10] to derive the Hamilton equations of motion that couple the trajectory of the projectile to the electronic motions in a target atom.

We are interested in the interaction between a projectile with a positive charge $Z_P e$ and a target atom with an electron around a charge $Z_T e$. The time-dependent Hamiltonian of a single electron, of mass m , at position \mathbf{r} moving around the target is

$$H_{el}(\mathbf{R}) = -\frac{\hbar^2}{2m} \nabla^2 - \frac{Z_T e^2}{r} - \frac{Z_P e^2}{|\mathbf{r} - \mathbf{R}|}. \quad (1)$$

The vector \mathbf{R} gives the position of the projectile nucleus relative to the target nucleus.

The Hamilton Equations of Motion for the Projectile Trajectory

We assume that the nuclear motion is almost classical. For the sake of convenience in the introduction of the eikonal (or short de Broglie wavelength) approximation, we represent the total wave function Ψ , for all electrons and nuclei, as [10,21]

$$\Psi(\mathbf{r}, \mathbf{R}) = \chi(\mathbf{r}, \mathbf{R}) \exp[iS(\mathbf{R})/\hbar], \quad (2)$$

where by choice the function S is real and χ is complex-valued. The phase of χ can compensate in principle for deviations from the correct phase. The function χ satisfies the equation

$$\left[\frac{1}{2M} \left(\frac{\hbar}{i} \frac{\partial}{\partial \mathbf{R}} + \frac{\partial S}{\partial \mathbf{R}} \right)^2 + H_{\mathbf{R}} - E \right] |\chi(\mathbf{R})\rangle = 0, \quad (3)$$

where M is the reduced mass of the colliding pair, $H_{\mathbf{R}}$ is the Hamiltonian for fixed nuclear positions,

$$H_{\mathbf{R}} = H_{\text{el}} + Z_P Z_T / R, \quad (4)$$

with H_{el} being the electronic Hamiltonian, and E is the total energy, for all electrons and nuclei. Here we have used the Dirac bracket notation to omit the electron variables. Projecting the above equation on $\langle \chi |$, and taking the real part of the result, we obtain the following equation for the function S :

$$\begin{aligned} \frac{1}{2M} \left(\frac{\partial S}{\partial \mathbf{R}} \right)^2 + V_{\text{qu}} \left(\frac{\partial S}{\partial \mathbf{R}}, \mathbf{R} \right) &= E, \\ V_{\text{qu}} &= V + V' + V'', \\ V &= \langle \chi | H_{\mathbf{R}} | \chi \rangle / \langle \chi | \chi \rangle, \\ V' &= \frac{i\hbar}{2M} \frac{\partial S}{\partial \mathbf{R}} \left[\left\langle \frac{\partial \chi}{\partial \mathbf{R}} \middle| \chi \right\rangle - \left\langle \chi \middle| \frac{\partial \chi}{\partial \mathbf{R}} \right\rangle \right] / \langle \chi | \chi \rangle, \\ V'' &= -\frac{\hbar^2}{2M} \frac{1}{2} \left[\left\langle \frac{\partial^2 \chi}{\partial \mathbf{R}^2} \middle| \chi \right\rangle + \left\langle \chi \middle| \frac{\partial^2 \chi}{\partial \mathbf{R}^2} \right\rangle \right] / \langle \chi | \chi \rangle. \end{aligned} \quad (5)$$

Therefore, the function S satisfies a time-independent Hamilton–Jacobi equation with a quantum potential that depends on the electronic state, which can be solved introducing trajectories [22]. Defining the momentum

$$\mathbf{P} = \frac{\partial S}{\partial \mathbf{R}}, \quad (6)$$

it follows that trajectories can be obtained for a fixed energy E introducing position and momentum functions of the time t .

We use the eikonal approximation for short wavelengths $\lambda = \hbar/|\mathbf{P}|$ imposing that

$$\left| \left\langle \chi \left| \frac{\partial \chi}{\partial \mathbf{R}} \right| \right\rangle / \langle \chi | \chi \rangle \right| \ll \lambda^{-1},$$

$$\left| \left\langle \chi \left| \frac{\partial^2 \chi}{\partial \mathbf{R}^2} \right| \right\rangle / \left\langle \chi \left| \frac{\partial \chi}{\partial \mathbf{R}} \right| \right\rangle \right| \ll \lambda^{-1}. \quad (7)$$

The eikonal approximation allows us to neglect V' and V'' so that S is the mechanical action given by

$$S(\mathbf{R}) = S(\mathbf{R}_1) + \int_{\mathbf{R}_1}^{\mathbf{R}} d\mathbf{R}' \cdot \mathbf{P}(\mathbf{R}') \quad (8)$$

along the trajectories of the nuclear variables determined by the effective (momentum independent) potential

$$V(\mathbf{R}) = E_{\text{el}}(\mathbf{R}) + \frac{Z_P Z_T}{R},$$

$$E_{\text{el}}(\mathbf{R}) = \langle \chi | H_{\text{el}} | \chi \rangle / \langle \chi | \chi \rangle, \quad (9)$$

where E_{el} is the electronic energy. Therefore, we can rewrite the Hamilton–Jacobi equation as Hamiltonian equations

$$\frac{d\mathbf{P}}{dt} = - \frac{dV}{d\mathbf{R}}, \quad (10)$$

and

$$\frac{d\mathbf{R}}{dt} = \frac{\mathbf{P}}{M}. \quad (11)$$

The eikonal approximation also simplifies the differential equation for the preexponential function so that

$$\left[\frac{\mathbf{P}}{M} \cdot \frac{\hbar}{i} \frac{\partial}{\partial \mathbf{R}} + H_{\text{R}} - V(\mathbf{R}) \right] |\chi(\mathbf{R})\rangle = 0. \quad (12)$$

Since the nuclear motions are now described by time-dependent position vectors, it is convenient to introduce time-dependent electronic states by means of

$$|\chi[\mathbf{R}(t)]\rangle = |\phi(t)\rangle \exp[i\alpha(t)], \quad (13)$$

where the phase can be chosen to eliminate a term in t in the differential equation for χ to obtain

$$\left[\frac{\hbar}{i} \frac{\partial}{\partial t} + H_{\text{el}}(t) \right] |\phi(t)\rangle = 0. \quad (14)$$

The trajectories and these orbitals evolve in time in a self-consistent way, and their coupled differential equations must be solved simultaneously. The choice of

atomic orbital parametrization replaces the equation for ϕ by equations for its time-dependent parameters. These equations can be derived from a variational procedure as follows.

Time Evolution of Atomic Orbitals

The Time-Dependent Variational Principle

We use a time-dependent variational principle for an atomic orbital ϕ in terms of an action functional given by [13]

$$\mathcal{A}[\phi, \phi^*] = \int_{t_1}^{t_2} dt \mathcal{L}[\phi, \phi^*], \quad (15)$$

with the Lagrangian functional \mathcal{L} being expressed as

$$\mathcal{L}[\phi, \phi^*] = \left[\frac{i\hbar}{2} \left(\left\langle \phi \left| \frac{\partial \phi}{\partial t} \right\rangle - \left\langle \frac{\partial \phi}{\partial t} \left| \phi \right\rangle \right) - \langle \phi | H_{el} | \phi \rangle \right] / \langle \phi | \phi \rangle, \quad (16)$$

where we show the dependence on the complex valued state ϕ , whose complex conjugate ϕ^* appears in the “bra”s. It is convenient to separate from $|\phi\rangle$ a time-dependent normalization factor $N(t)$,

$$\phi(\mathbf{r}, t) = N(t) \psi(\mathbf{r}, t), \quad (17)$$

so that $\langle \phi | \phi \rangle = 1$. Variation of the action \mathcal{A} with respect to $N(t)$ gives [23]

$$N(t) = N(t_1) \exp \left[-\frac{i}{\hbar} \int_{t_1}^t dt' \frac{\left\langle \psi \left| \left(H_{el} - i \frac{\partial}{\partial t'} \right) \right| \psi \right\rangle}{\langle \psi | \psi \rangle} \right] \quad (18)$$

In the limit of large internuclear distances we have that $H_{el} \simeq H_T$, the electronic Hamiltonian for the target atom. We choose ψ so that asymptotically $H_T \psi = E_{el}(\infty) \psi$, which gives

$$N(t) \simeq \exp[-(i/\hbar) E_{el}(\infty)(t - t_1)]. \quad (19)$$

We express each one of the orbitals $\psi(\mathbf{r}, t)$, in terms of a complex time-dependent exponential parameter

$$\zeta(t) = \lambda(t) + i\kappa(t). \quad (20)$$

We therefore have two real variational parameters per orbital. The function $\psi[\mathbf{r}; \zeta(t)]$ is normalized to unity before the collision and will stay normalized during the collision because the Hamiltonian H_{el} is real.

Since $\psi[\mathbf{r}; \zeta(t)]$ depends on time only through the parameters λ and κ , we can write

$$\frac{\partial}{\partial t} = \dot{\lambda} \frac{\partial}{\partial \lambda} + \dot{\kappa} \frac{\partial}{\partial \kappa}, \quad (21)$$

with a dot indicating a derivative with respect to time.

Now we can express the Lagrangian as

$$\mathcal{L}[\phi, \phi^*] = L(\lambda, \kappa, \dot{\lambda}, \dot{\kappa}), \quad (22)$$

with

$$L(\lambda, \kappa, \dot{\lambda}, \dot{\kappa}) = \frac{i\hbar}{2} \left[\left\langle \psi(\zeta) \left| \left(\dot{\lambda} \frac{\partial}{\partial \lambda} + \dot{\kappa} \frac{\partial}{\partial \kappa} \right) \psi(\zeta) \right\rangle - \left\langle \left(\dot{\lambda} \frac{\partial}{\partial \lambda} + \dot{\kappa} \frac{\partial}{\partial \kappa} \right) \psi(\zeta) \right| \psi(\zeta) \right\rangle \right] - \langle \psi(\zeta) | H_{\text{el}} | \psi(\zeta) \rangle. \quad (23)$$

The application of the variational principle $\delta \mathcal{A} = 0$ to the Lagrangian in Eq. (22) leads to the Euler-Lagrange equations

$$\frac{d}{dt} \left(\frac{\partial L}{\partial \dot{\lambda}} \right) - \frac{\partial L}{\partial \lambda} = 0 \quad (24)$$

and

$$\frac{d}{dt} \left(\frac{\partial L}{\partial \dot{\kappa}} \right) - \frac{\partial L}{\partial \kappa} = 0. \quad (25)$$

Time Dependence of Exponents in Hydrogenic Orbitals

Atomic Orbitals and Energies

We use normalized complex time-dependent hydrogenic orbitals, written in terms of both ζ and its complex conjugate ζ^* for 1s, 2s, and 2p orbitals,

$$\psi_{1s}(\mathbf{r}; \zeta_{1s}) = \frac{1}{\sqrt{\pi}} \left(\frac{\zeta_{1s} + \zeta_{1s}^*}{2} \right)^{3/2} e^{-\zeta_{1s} r}, \quad (26)$$

$$\psi_{2s}(\mathbf{r}; \zeta_{2s}) = \frac{1}{2\sqrt{2\pi}} \left(\frac{\zeta_{2s} + \zeta_{2s}^*}{2} \right)^{3/2} \left[1 - \left(\frac{\zeta_{2s} + \zeta_{2s}^*}{2} \right) \frac{r}{2} \right] e^{-\zeta_{2s} r/2} \quad (27)$$

$$\psi_{2p_z}(\mathbf{r}; \zeta_{2p}) = \frac{1}{4\sqrt{2\pi}} \left(\frac{\zeta_{2p} + \zeta_{2p}^*}{2} \right)^{5/2} r e^{-\zeta_{2p} r/2} \cos(\theta), \quad (28)$$

$$\psi_{2p_y}(\mathbf{r}; \zeta_{2p}) = \frac{1}{4\sqrt{2\pi}} \left(\frac{\zeta_{2p} + \zeta_{2p}^*}{2} \right)^{5/2} r e^{-\zeta_{2p} r/2} \sin(\theta) \sin(\phi), \quad (29)$$

and

$$\psi_{2p_x}(\mathbf{r}; \zeta_{2p}) = \frac{1}{4\sqrt{2\pi}} \left(\frac{\zeta_{2p} + \zeta_{2p}^*}{2} \right)^{5/2} r e^{-\zeta_{2p} r/2} \sin(\theta) \cos(\phi). \quad (30)$$

The electronic energies for the electron in the orbitals ψ depend on \mathbf{R} in two ways: through the dependence of the electronic Hamiltonian and also through the variation of the exponent parameters with \mathbf{R} . These dependencies can be obtained from

$$E_{el}(\mathbf{R}) = \frac{\langle \psi(\mathbf{R}) | H_{el}(\mathbf{R}) | \psi(\mathbf{R}) \rangle}{\langle \psi(\mathbf{R}) | \psi(\mathbf{R}) \rangle}. \quad (31)$$

These energies are given for the 1s orbital by

$$E_{1s}(\mathbf{R}) = W_{1s} - (Z_P e^2 / R) f_{1s}(\lambda_{1s} R), \quad (32)$$

with

$$f_{1s}(x) = 1 - (1 + x) \exp(-2x); \quad (33)$$

for the 2s orbital by

$$E_{2s}(\mathbf{R}) = W_{2s} - (Z_P e^2 / R) f_{2s}(\lambda_{2s} R), \quad (34)$$

with

$$f_{2s}(x) = 1 - \left(1 + \frac{3}{4}x + \frac{x^2}{4} + \frac{x^3}{8} \right) \exp(-x); \quad (35)$$

and for the 2p orbitals by

$$E_{2p_z}(\mathbf{R}) = E_{2p_z'}(R) \cos^2(\Theta) + E_{2p_x'}(R) \sin^2(\Theta), \quad (36)$$

$$E_{2p_y}(\mathbf{R}) = E_{2p_y'}(R), \quad (37)$$

$$E_{2p_x}(\mathbf{R}) = E_{2p_x'}(R) \cos^2(\Theta) + E_{2p_z'}(R) \sin^2(\Theta), \quad (38)$$

where Θ is the angle between \mathbf{R} and the z-axis, and

$$E_{2p_{x'(y')}}(R) = W_{2p} + \frac{Z_P e^2}{R} f_{2p_{x'(y')}}(\lambda_{2p} R), \quad (39)$$

$$f_{2p_{x'}}(x) = 1 - \frac{6}{x^2} + \left(\frac{6}{x^2} + \frac{6}{x} + 2 + \frac{x}{4} \right) \exp(-x), \quad (40)$$

$$E_{2p_z'}(R) = W_{2p} - \frac{Z_P e^2}{R} f_{2p_z'}(\lambda_{2p} R), \quad (41)$$

$$f_{2p_z'}(x) = 1 + \frac{12}{x^2} - \left(\frac{12}{x^2} + \frac{12}{x} + 7 + \frac{11}{4}x + \frac{3}{4}x^2 + \frac{x^3}{8} \right) \exp(-x), \quad (42)$$

and

$$W_{nl} = \frac{\hbar^2}{2m} \left(\frac{\lambda_{nl}^2 + \kappa_{nl}^2}{n^2} \right) - \frac{Z_T e^2}{n^2} \lambda_{nl}. \quad (43)$$

We have used the (x,z) -plane as the collision plane, with the initial projectile velocity parallel to the $+z$ -axis, and $x_P(t)$ and $z_P(t)$ the projectile coordinates, so that

$$R(t) = \sqrt{z_P(t)^2 + x_P(t)^2}, \quad \cos[\Theta(t)] = z_P(t)/R(t). \quad (44)$$

To simplify calculations, we have evaluated the matrix elements for p orbitals in the body-fixed frame, the (x',z') coordinate system with the z' -axis going from the target to the projectile location, and rotated them to the space fixed frame, the (x,z) coordinate system, in which the time propagations have been performed.

Physical Meaning of the Exponential Parameters

The real components of the complex parameters, λ_{nl} , are related to the expectation value of the radius

$$\langle \psi_{nlk}(t) | r | \psi_{nlk}(t) \rangle = \frac{1}{2\lambda_{nl}} [3n^2 - l(l+1)]. \quad (45)$$

This shows that when λ_{nl} grows during the interaction, then the orbital shrinks as expected.

The imaginary components of the complex parameters, κ_{nl} , can be understood in connection with the radial flux of the probability

$$\langle n_r \cdot \mathbf{J}_{nlk} \rangle = \frac{\hbar}{2mi} \left(\left\langle \psi_{nlk} \left| \frac{\partial \psi_{nlk}}{\partial r} \right. \right\rangle - \left\langle \frac{\partial \psi_{nlk}}{\partial r} \left| \psi_{nlk} \right. \right\rangle \right) = -\frac{1}{n} \frac{\hbar}{m} \kappa_{nl} \quad (46)$$

At large distances the flux must be zero, so that κ must be chosen to begin with equal to zero. As time increases, a positive κ indicates a negative radial electron flux, moving toward the nucleus, while a negative κ indicates outward flux.

Equations of Motion for the Orbital Exponents

For the 1s orbital the equations of motion are

$$m\dot{\lambda}_{1s} = \frac{2}{3} \hbar \lambda_{1s}^2 \kappa_{1s}, \quad (47)$$

and

$$m\dot{\kappa}_{1s} = \frac{2}{3} \hbar \lambda_{1s}^2 \left[\frac{Z_{1s}(t)}{a_0} - \lambda_{1s} \right], \quad (48)$$

where a_0 is the hydrogen Bohr radius and the effective charge $Z_{1s}(t)$ is given by

$$Z_{1s}(t) = Z_T + Z_P F_{1s}(\lambda_{1s} R), \quad (49)$$

where

$$F_{1s}(x) = (1 + 2x) \exp(-2x). \quad (50)$$

One should keep in mind that what we mean by effective charge $Z_{nlk}(t)$ is not the same as the effective nuclear charge in, for instance, Slater-type orbitals.

In a similar way we find for the 2s orbital the following equations of motion:

$$m\dot{\lambda}_{2s} = \frac{1}{12} \hbar \lambda_{2s}^2 \kappa_{2s}, \quad (51)$$

and

$$m\dot{\kappa}_{2s} = \frac{1}{12} \hbar \lambda_{2s}^2 \left[\frac{Z_{2s}(t)}{a_0} - \lambda_{2s} \right], \quad (52)$$

with the effective charge being

$$Z_{2s}(t) = Z_T + Z_P F_{2s}(\lambda_{2s} R), \quad (53)$$

where

$$F_{2s}(x) = \left(1 + x - \frac{x^2}{2} + \frac{x^3}{2} \right) \exp(-x). \quad (54)$$

For the $2p_k$ orbitals we derive the equations of motion from the average Lagrangian $\bar{L} = (L_x + L_y + L_z)/3$, where L_k is obtained from ϕ_{2pk} , to obtain

$$m\dot{\lambda}_{2p} = \frac{1}{10} \hbar \lambda_{2p}^2 \kappa_{2p}, \quad (55)$$

and

$$m\dot{\kappa}_{2p} = \frac{1}{10} \hbar \lambda_{2p}^2 \left[\frac{\bar{Z}_{2p}(t)}{a_0} - \lambda_{2p} \right], \quad (56)$$

where the effective charge $\bar{Z}_{2p} = (Z_{2p_x} + Z_{2p_y} + Z_{2p_z})/3$ is obtained in the space-fixed axes from

$$Z_{2p_z}(t) = Z_T + Z_P \frac{z_P(t)^2}{R(t)^2} A(\lambda_{2p} R) + Z_P \frac{x_P(t)^2}{R(t)^2} B(\lambda_{2p} R), \quad (57)$$

$$Z_{2p_y}(t) = Z_T + Z_P B(\lambda_{2p} R), \quad (58)$$

and

$$Z_{2p_x}(t) = Z_T + Z_P \frac{x_P(t)^2}{R(t)^2} A(\lambda_{2p} R) + Z_P \frac{z_P(t)^2}{R(t)^2} B(\lambda_{2p} R). \quad (59)$$

Here $A(x)$ and $B(x)$ are defined by

$$A(x) = -\frac{96}{x^3} + \left(\frac{96}{x^3} + \frac{96}{x^2} + \frac{48}{x} + 17 + 5x + \frac{3}{2}x^2 + \frac{1}{2}x^3 \right) \exp(-x), \quad (60)$$

and

$$B(x) = \frac{48}{x^3} - \left(\frac{48}{x^3} + \frac{48}{x^2} + \frac{24}{x} + 7 + x \right) \exp(-x), \quad (61)$$

from which $\bar{Z}_{2p} = Z_T + Z_P F_{2p}(\lambda_{2p} R)$ with $F_{2p} = (A + 2B)/3$.

Equations of Motion for the Trajectories

The potential gradients to be used in the Hamilton equations can be obtained by differentiation of the electronic energies written as functions of x_P , z_P , κ , and λ . We show here the results for the 1s and 2s orbitals. For these orbitals V depends only on R and the gradients are given by

$$\frac{dV}{dR} = \left(\frac{\partial V}{\partial R} \right)_{\kappa, \lambda} + \left(\frac{\partial V}{\partial \kappa} \dot{\kappa} + \frac{\partial V}{\partial \lambda} \dot{\lambda} \right) / \dot{R} \quad (62)$$

with the time derivatives of the exponent parameters obtained from the previous equations, and the time derivative of the radius R obtained from the Hamilton equations. Keeping the exponent parameters fixed, the gradients give the forces when changes in the effective charges are ignored.

Letting Q be either x_P or z_P , we obtain

$$\left(\frac{\partial V_{1s}}{\partial Q} \right)_{\kappa, \lambda} = Z_P e^2 \frac{Q}{R^3} \left[1 - (1 + 2\lambda_{1s} R + 2\lambda_{1s}^2 R^2) \times \exp(-2\lambda_{1s} R) \right] - Z_P Z_T \frac{Q}{R^3}, \quad (63)$$

$$\left(\frac{\partial V_{2s}}{\partial Q} \right)_{\kappa, \lambda} = Z_P e^2 \frac{Q}{R^3} \left[1 - \left(1 + \lambda_{2s} R + \frac{1}{2} \lambda_{2s}^2 R^2 + \frac{1}{8} \lambda_{2s}^4 R^4 \right) \times \exp(-\lambda_{2s} R) \right] - Z_P Z_T \frac{Q}{R^3}. \quad (64)$$

The above gradients are used in the Hamilton equations to give the trajectories.

Numerical Results

Numerical results were obtained for a proton colliding with a hydrogen atom at rest, at a range of projectile velocities and impact parameters typical of slow collisions between ions and atoms. Therefore, $Z_P = Z_T = 1$, and $M = 1836$ a.u. A selection of results is presented in what follows. In these examples, the velocities of the projectile were $v_P = 0.01$ and 0.02 a.u., corresponding to collision energies of nearly 2.5 and 10.0 eV.

For each orbital the four Hamiltonian equations for a trajectory [Eqs. (10) and (11)], coupled to the two equations of motion for the orbital exponents [Eqs. (47)

and (48) for the 1s orbital, and Eqs. (51) and (52) for the 2s orbital] were solved numerically using a Runge-Kutta fourth-order algorithm [19], with the forces from Eqs. (63) and (64). We tested the algorithm with different input values of time steps and starting distances, and the numerical results are consistent. We also obtained the same results using a predictor-corrector algorithm to solve the equations of motion.

Figures 1 and 2 show the time evolution of λ and κ , respectively, for the 1s orbital, at the two velocities $v_p = 0.01$ and 0.02 a.u. and impact parameters of 1.0, 2.0, 3.0, and 4.0 a.u. Figures 3 and 4 show the projectile trajectories for the above velocities and impact parameters and the V_{1s} potential. Figures 5 and 6 show λ and κ results for the 2s orbital at $v_p = 0.02$ a.u., and impact parameters of 4.0, 5.0, 6.0, and 7.0 a.u. Finally Figure 7 gives the trajectories for a target 2s orbital at $v_p = 0.02$ au and the mentioned impact parameters.

The two sets of peaks in Figure 1 correspond to the two velocities; starting at the same distance along the z-axis, the interaction occurs sooner at the larger projectile velocity, so that the peaks to the left are for the larger velocity, $v_p = 0.02$ a.u., and the ones to the right for the smaller value of 0.01 a.u. The real parts of the exponents are found to increase over time, reflecting the larger charge seen by the electron as the projectile approaches. The effect is quite large, with higher peaks for the larger velocity and smaller impact parameters, and wider peaks for the lower velocity. This reflects the longer interval during which the orbital is distorted at the smaller

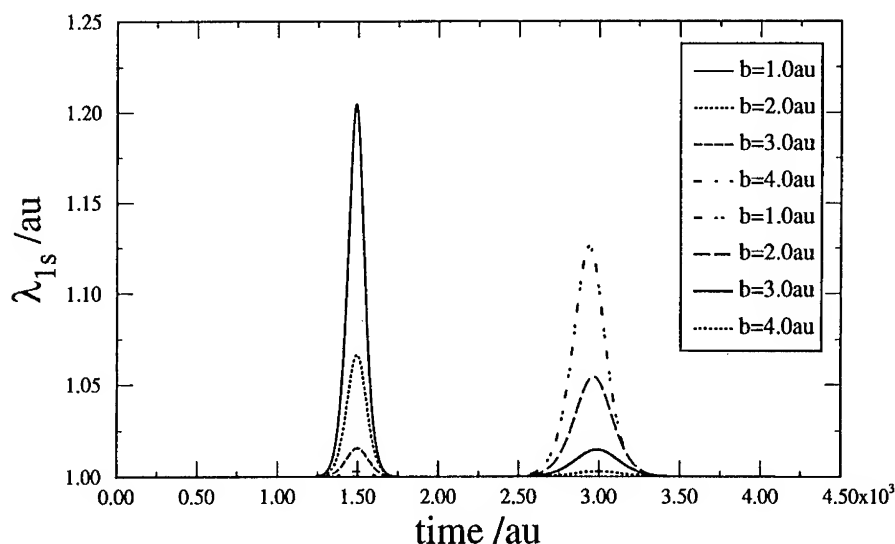


Figure 1. Real part λ of the orbital exponent for a proton colliding with a hydrogen atom, for the 1s orbital, vs. time, in atomic units, at projectile velocities $v_p = 0.01$ a.u. (peaks at right) and 0.02 a.u. (peaks at left) and impact parameters of 1.0, 2.0, 3.0, and 4.0 a.u., with the V_{1s} potential.

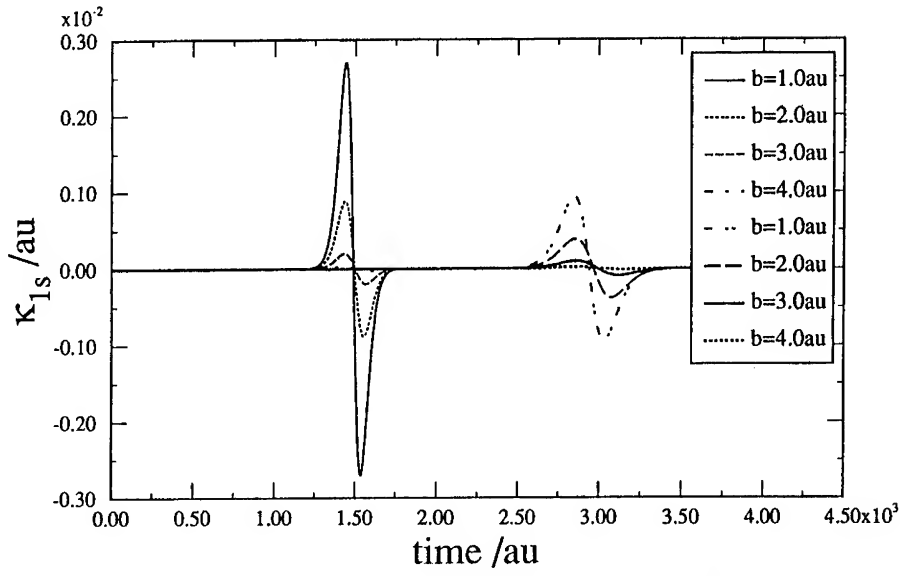


Figure 2. Imaginary part κ , for the same conditions as Figure 1.

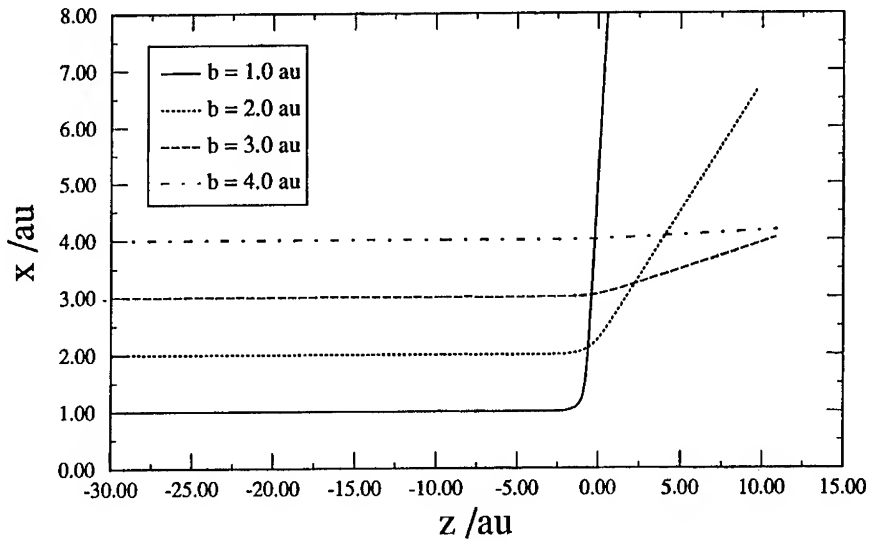


Figure 3. Projectile trajectories for the conditions of Figure 1 with the projectile velocity $v_p = 0.01$ a.u., in the (x, z) plane.

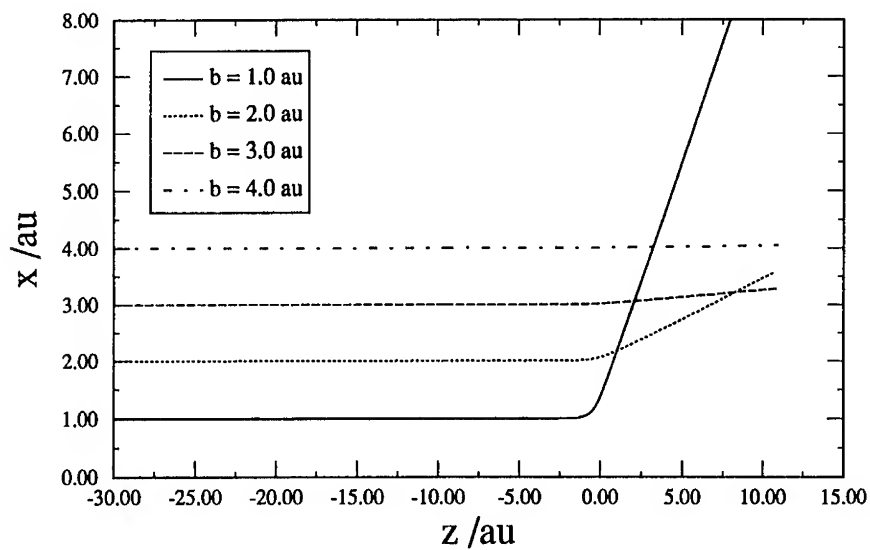


Figure 4. Projectile trajectories for the conditions of Figure 1 with the projectile velocity $v_p = 0.02 \text{ a.u.}$, in the (x, z) plane.

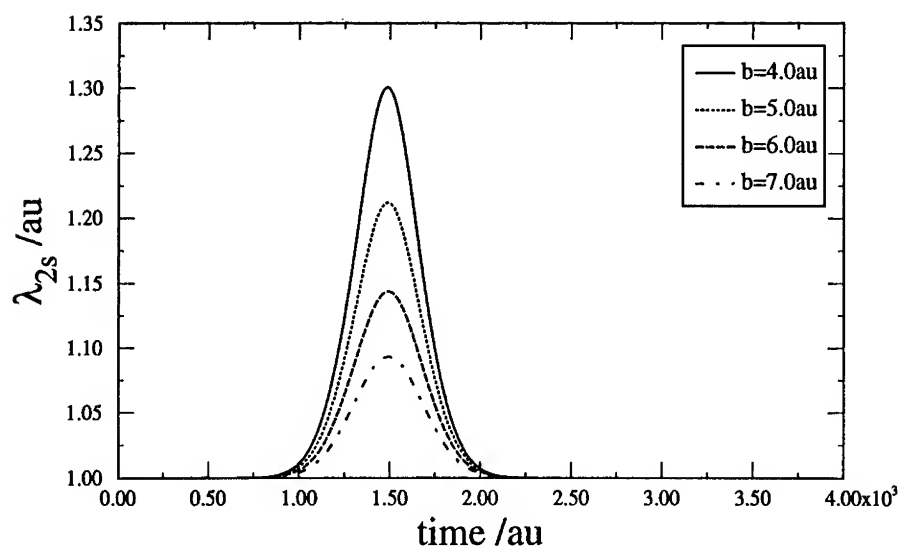


Figure 5. Results for the real part λ of the $2s$ orbital at $v_p = 0.02 \text{ a.u.}$ and impact parameters of 4.0, 5.0, 6.0, and 7.0 a.u.

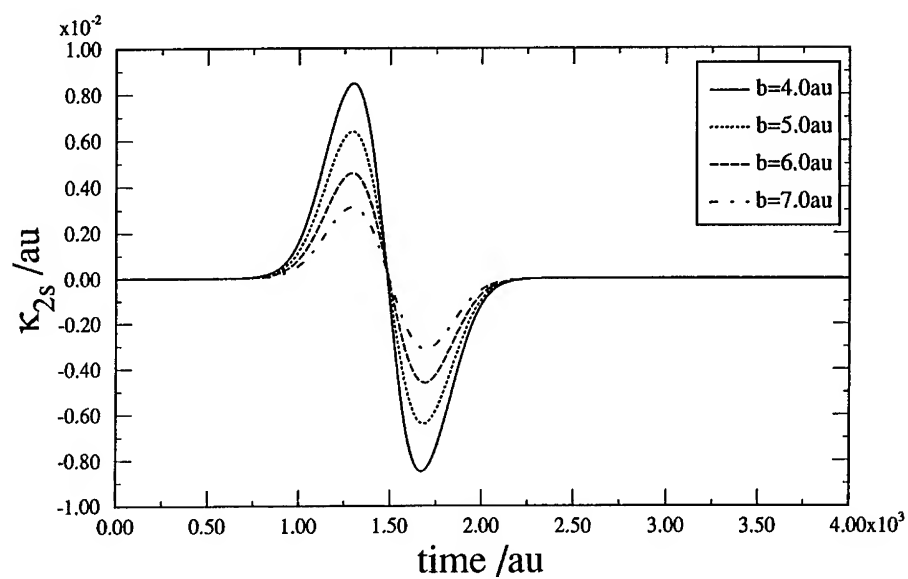


Figure 6. Results for the imaginary part κ of the 2s orbital at $v_p = 0.02$ a.u. and impact parameters of 4.0, 5.0, 6.0, and 7.0 a.u.

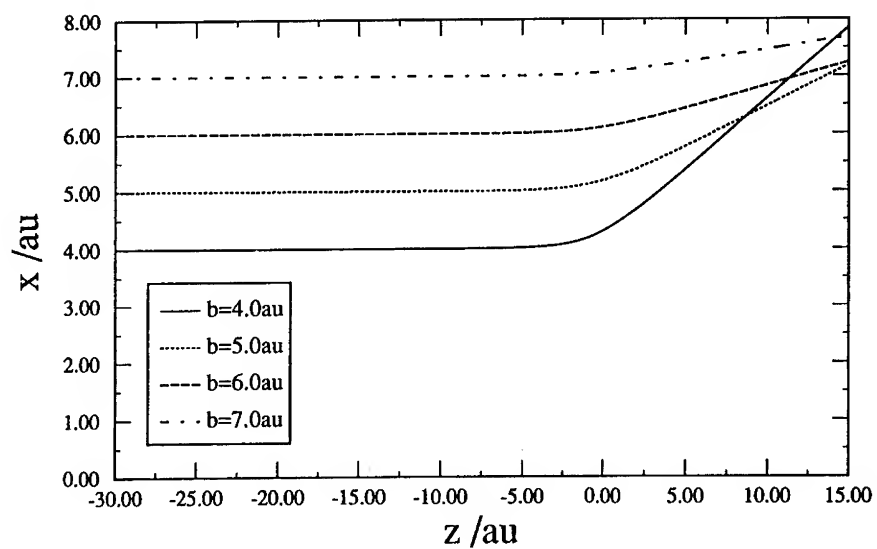


Figure 7. Projectile trajectories for the conditions of Figure 5, in the (x, z) plane.

velocity. The imaginary parts of the exponents, in Figure 2, change sign, first increasing to positive values and then taking negative values. This shows that the electron flux is inwards as the charge approaches, and outwards as it departs. Again peaks are higher for the larger velocity and wider for the smaller velocity. The numerical change is much smaller than for the real part, but is clearly present.

The trajectories are quite different for the several impact parameters at a given velocity, and show large deflections at small impact parameters. The ones with large scattering angles involve the more pronounced changes in the effective charge and the electron flux. The changes are much smaller when the deflection is small, and scattering is nearly forward.

The situation is similar for the 2s orbital. Here the deflection angles are smaller because the impact parameters are larger. However, the changes in effective charge and flux are even larger than for the 1s orbital, because the 2s orbital is more spread out and therefore more sensitive to the presence of the projectile charge. The conclusion is that effective charges are important even at low scattering angles for higher excited orbitals.

Conclusion

Combining the eikonal approximation with a time-dependent variational derivation of the differential equations for the parameters of the electronic wavefunctions, it has been possible to describe the time evolution of an atomic orbital distorted by a moving charge. This depends not only on the distance between nuclei, which is a conformational effect, but also depends on impact parameters and velocities. Therefore, our treatment provides insight which goes beyond what we know from electronic structure calculations for molecules.

Generally, we have found it necessary to work with complex electronic wavefunctions, to properly describe electronic flux effects. The presence of an imaginary part in orbital exponents means that orbitals acquire an oscillatory nature in time when a projectile charge is present at short distances. Expectation values of properties show also a time dependence; in the case of the electronic flux, this turns out to change sign with time as the projectile approaches and then departs: flux goes in the incoming part of the trajectory, and out in the outgoing part.

Results for the evolution of the real and imaginary components of the complex parameters of 1s and 2s orbitals show large variations of the real parts over time with respect to asymptotic values, and that imaginary parts remain small.

The real part of the atomic orbitals change extensively with time, with the change being larger for higher velocities and low impact parameters. Variations are more pronounced for the excited atomic orbital.

Acknowledgments

We acknowledge financial support from the National Science Foundation and the Office of Naval Research. One of us (H. F. M. D. C.) acknowledges financial support from CNPq (the Brazilian agency for scientific research).

Bibliography

- [1] R. McCarroll, in *Atomic and Molecular Collision Theory*, F. A. Gianturco, Ed. (Plenum, New York, 1980), Chap. 2.
- [2] J. B. Delos, *Rev. Mod. Phys.* **53**, 87 (1981).
- [3] M. Kimura and N. F. Lane, *Adv. At. Molec. and Opt. Phys.* **26**, 79 (1990).
- [4] W. Fritsch and C. D. Lin, *Phys. Rep.* **202**, 1 (1991).
- [5] B. Gazdy and D. A. Micha, *Phys. Rev. A* **36**, 546 (1987).
- [6] K. Runge, D. A. Micha and E. Q. Feng, *Int. J. Quantum. Chem. Quantum Chem. Symp.* **24**, 781 (1990).
- [7] E. Deumens, A. Diz, H. Taylor, and N. Y. Ohrn, *J. Chem. Phys.* **96**, 6820 (1992).
- [8] I. Levine, *Quantum Chemistry*, 4th edition (Prentice-Hall, Englewood Cliffs, NJ, 1991), Chap. 13, and references therein.
- [9] D. A. Micha, *J. Chem. Phys.* **78**, 7135 (1983).
- [10] D. A. Micha and K. Runge, in *Time-Dependent Quantum Molecular Dynamics*, J. Broeckhove and L. Lathouwers, Eds. (Plenum, New York, 1992), p. 247.
- [11] D. A. Micha, *Int. J. Quantum Chem.*, (1994), to appear.
- [12] J. Frenkel, *Wave Mechanics. Advanced General Theory* (Oxford University Press, Oxford, 1934), p. 436.
- [13] P. Kramer and M. Saraceno, *Geometry of the Time-Dependent Variational Principle in Quantum Mechanics*, Lecture Notes in Physics, Vol 140 (Springer-Verlag, Berlin, 1981).
- [14] Y. N. Demkov, *Sov. Phys. JETP* **11**, 1351 (1960).
- [15] N. C. Sil, *Proc. Phys. Soc.* **75**, 194 (1960).
- [16] R. McCarroll, R. D. Piacentini, and A. Salin, *J. Phys.* **B3**, 137 (1970).
- [17] M. Kleber and J. Zwiegel, *Z. Phys.* **A280**, 137 (1977).
- [18] M. Kleber, *J. Phys.* **B11**, 1069 (1978).
- [19] W. H. Press, B. P. Flannery, S. A. Teukolsky, and W. T. Vetterling, *Numerical Recipes*, 2nd. ed. (Cambridge University Press, New York, 1992), Chap. 15.
- [20] H. F. M. da Costa and D. A. Micha, *J. Comput. Chem.* **15**, 653 (1994).
- [21] J. M. Cohen and D. A. Micha, *J. Chem. Phys.* **97**, 1038 (1992).
- [22] H. Goldstein, *Classical Mechanics* (Addison-Wesley, Reading, MA, 1959), Chap. 9.
- [23] M. L. Riley and T. A. Green, *Phys. Rev. A* **4**, 619 (1971).

Received May 19, 1994

Aspects Related to Quantum Studies of Multiphoton Excitation and Dissociation of Diatomic Molecules

TSIN-FU JIANG

Institute of Physics, National Chiao Tung University, Hsinchu, Taiwan 30050, Republic of China

JIAN-MIN YUAN

Department of Physics and Atmospheric Science, Drexel University, Philadelphia, Pennsylvania 19104

Abstract

We have carried out quantum-mechanical studies of infrared multiphoton excitation and dissociation of diatomic molecules modeled by Morse oscillators. Two different aspects of such processes are investigated: one concerns quantum dynamics near a nonlinear resonance induced by an external field and calculations of the associated quasienergies and quasi-eigen functions; and the other addresses the effects of dipole moment functions on the above-threshold dissociation spectra, obtained by solving the time-dependent Schrödinger equation directly using the momentum-space Fourier-Grid method. © 1994 John Wiley & Sons, Inc.

Introduction

Morse oscillators have often been studied as a model of molecular photodissociation, for its simplicity and availability of exact quantum solutions [1]. In this article we investigate two quite different aspects of its quantum solutions: In the first part we apply a recent approach of Holthaus [2] to analyze the quantum dynamics near a nonlinear resonance of a driven molecule, a subject related to quantum Kolmogorov–Arnold–Moser (KAM) theorem [3]. For a driven system, Holthaus procedure involves a local quantization of the unperturbed Hamiltonian in action space near a resonant level and arriving at a Schrödinger equation, which is shown to be equivalent to a Mathieu equation. Applying the Floquet theorem to the Mathieu equation, Holthaus shows that for 1:1 and 1:2 resonances quasienergies and wave functions are easily calculable, being related to the well-known characteristic values and Mathieu functions. The results indicate that the effect of a sinusoidal field is to rearrange the energy levels, similar to the reordering of levels caused by a DC field, that is, the Stark or Zeeman effects. His theory has been applied to the driven systems of a particle in a box and a particle in a triangular well, yielding very interesting results. For instance, tunneling between invariant manifolds and scarring of Floquet states by classical periodic orbits can be studied analytically.

In this article we present some preliminary results of applying Holthaus theory to the photo-excitation of an NO molecule, modeled by a driven Morse oscillator.

This system, being noncompact, is more complicated than the above two systems. Details of the theory, applied to a Morse system, will be given in the next section and results presented in the third section.

In the second part of the article we continue the investigation of the molecular photodissociation process by solving the Schrödinger equation in the momentum space [4] and probe the roles of the dipole moment function in the above-threshold-dissociation (ATD) spectra of molecules. The numerical method that we use will be described and results presented.

Quantum Theory of Nonlinear Resonance

The Hamiltonian of a Morse oscillator with an effective dipole moment function $q_{\text{eff}}\mu(r)$ in the presence of an electromagnetic field can be written as

$$H = \frac{p^2}{2m} + D(1 - e^{-\alpha(r-r_0)})^2 - q_{\text{eff}}E(t)\mu(r). \quad (1)$$

Using the dimensionless variables defined in Ref. [5], we can rewrite the Hamiltonian in the following form

$$\mathcal{H} = H_0 - \frac{A(t)\Omega}{2} \mu(x) \cos \Omega t \quad (2)$$

$$H_0 = \frac{p_x^2}{2} + \frac{(1 - e^{-x})^2}{2} = I - \frac{I^2}{2} \quad (3)$$

where $x = \alpha(r - r_0)$, p_x is the momentum conjugate to x , I is the action variable of the Morse oscillator, and Ω is the optical frequency. The effective field amplitude function, $A(t) = (q_{\text{eff}}E(t)/\alpha\Omega D)$, will be assumed constant in the first part of our studies and be given a sine-squared pulse shape in the second part.

Both the coordinate and momentum variables can be expressed in terms of the action-angle variables, (I, θ) . In particular, the coordinate expression is given by

$$x(I, \theta) = \ln \left(\frac{1 + \sqrt{2E} \cos \theta}{1 - 2E} \right), \quad (4)$$

which is periodic in θ and can thus be expanded into a Fourier cosine series given below:

$$x(I, \theta) = \sum_{n=0}^{\infty} f_n(I) \cos n\theta, \quad (5)$$

where $f_n(I)$ is given by

$$f_0(I) = \ln \frac{1 + \sqrt{1 - 2E}}{2(1 - 2E)} \quad (6)$$

and

$$f_n(I) = -\frac{2}{n} \left(\frac{-\sqrt{2E}}{1 + \sqrt{1 - 2E}} \right)^n, \quad n = 1, 2, 3, \dots \quad (7)$$

In the above equations, $E = H_0(I)$ is the oscillator energy. We then expand the dipole moment function about the equilibrium interatomic distance and keep only the linear term for the nonlinear resonance analysis. By substituting the Fourier series of x in the total Hamiltonian we obtain

$$\mathcal{H}(I, \theta, t) = E - \frac{A(t)\Omega}{4} \sum_{n=0}^{\infty} f_n(I) [\cos(n\theta - \Omega t) + \cos(n\theta + \Omega t)] . \quad (8)$$

Chirikov's resonant approximation consists of keeping the N th term which satisfies the condition: $N\theta \simeq \Omega t$ and dropping all fast varying terms in the above series. The Hamiltonian around a 1: N resonance then becomes

$$\mathcal{H}(I, \theta, t) = E(I_N) + \omega(I_N)\Delta I - \frac{\Delta I^2}{2} - \frac{A(t)\Omega}{4} f_N(I_N) \cos(N\theta - \Omega t) . \quad (9)$$

where we have also expanded E about the resonant action, I_N , and the oscillator frequency at resonance, $\omega(I_N)$, is defined by

$$\omega(I_N) = \frac{\Omega}{N} . \quad (10)$$

We note that the expansion of E to the second order in ΔI is exact for a Morse oscillator.

Following Holthaus we quantize the system at this stage by replacing ΔI by $-i\hbar_{\text{eff}}(\partial/\partial\theta)$ and obtain a time-dependent Schrödinger equation, which can be reduced into a Mathieu equation:

$$u''(z) + [a - 2q \cos(2z)]u(z) = 0 \quad (11)$$

under the transformation $2z = N\theta - \Omega t$ and

$$\psi(\theta, t) = \tilde{\psi}(z, t) = u(z)e^{-iWt/\hbar_{\text{eff}}} . \quad (12)$$

In the Mathieu equation, a and q are defined by

$$a = \frac{8}{N^2 \hbar_{\text{eff}}^2} [E(I_N) - W] \quad (13)$$

and

$$q = \frac{A\Omega}{N^2 \hbar_{\text{eff}}^2} f_N(I_N) , \quad (14)$$

where \hbar_{eff} is the effective Planck constant associated with the dimensionless variables. In the case of a 1:1 resonance, on which we shall focus in the next section, solutions of the Mathieu eigenvalue equation are given by the π -periodic Mathieu functions and the allowed eigenvalues a correspond to the characteristic values $a_{2n}(q)$, $b_{2n}(q)$ [2,6].

Nonlinear Resonance in NO

In this section we apply the theory of the last section to the analysis of a 1:1 resonance in an NO molecule and assume that the photon energy is such that the 11th ($n = 10$) vibrational level is in resonance with the field. NO has 55 vibrational states in the ground electronic state such that \hbar_{eff} is about $\frac{1}{55}$, or more precisely, the inverse of 55.04. I_1 is then equal to $(n + \frac{1}{2})\hbar_{\text{eff}} = 0.1908$, thus $\omega(I_1) = \Omega = 1 - I_1 = 0.8092$ or 1540.9 cm^{-1} . For this photon field we present in Figure 1 the phase portrait on the Poincaré surface of section at $A = 0.020$, where we see a large 1:1 primary resonance zone centered close to I_1 in the figure. We estimate from the area in phase space that this resonance zone can support about 7 bound states. The 1:2 and 1:3 primary resonance zones are also clearly visible in Figure 1.

We have calculated the quasienergy spectrum of the Floquet states which are quantized around the 1:1 resonance region. The quasienergies of the lowest 13 states are plotted in Figure 2 as a function of the field amplitude A . It is interesting to see that degeneracy at low fields (presumably brought about by the resonant photon energy) is lifted up as the perturbed field strength increases and at higher fields the quasienergy levels become almost regularly spaced. On the other hand, the results seem to indicate that for a strongly bound molecule like NO ($D = 0.239 \text{ a.u.}$) one needs a much more intense field than $A = 0.05$ to perturb effectively the 10th states of the NO molecule.

We plot in Figure 3 the probability density, $|\psi(x, t)|^2$, of the $a_0(q)$ and $b_2(q)$ Floquet states at $A = 0.02$ in xt -space. These two states correspond to the two

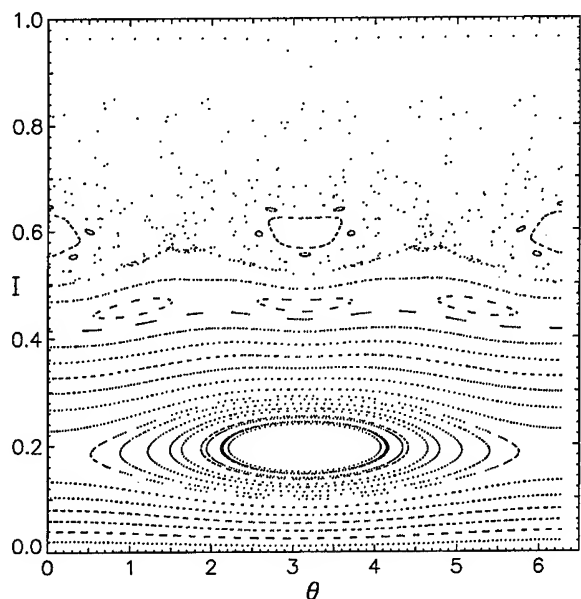


Figure 1. Poincaré section plot of 30 classical trajectories for the driven Morse oscillator at $A = 0.02$ and $\Omega = 0.8092$ in action-angle space.

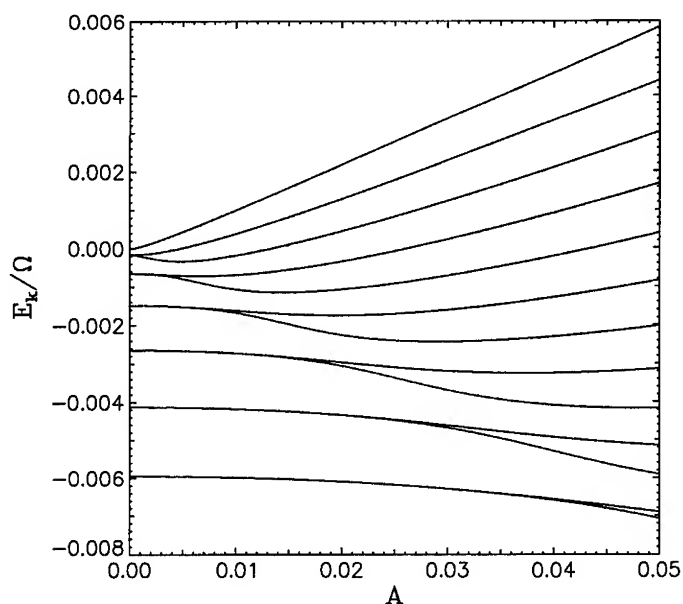


Figure 2. Quasienergy spectrum of the lowest 13 Floquet states around the 1:1 resonance zone of NO at $A = 0.02$ and $\Omega = 0.8092$. $E_k = W_k - E(I_N)$, scaled by the photon energy $\hbar\Omega$, is plotted versus the scaled field strength, A .

topmost levels in Figure 2. Figure 3 shows that the quantum wave functions are clearly influenced by the vortex tubes [7] surrounding the classical periodic orbits. Calculations aiming at comparing the above results with the exact quantum solutions using the method described in later sections are in progress. Related to the comparison, we note that since the system is noncompact, the quasienergies are complex numbers. The quasienergy spectrum shown in Figure 2 represents only the real parts of the quasienergies and is meaningful when the imaginary parts are negligibly small.

Staggered Time Discretization Algorithm

In the second part of the article—that is, the rest of the sections—we concentrate on the ATD spectra of the HF molecule and see how they are influenced by two different types of dipole moment functions. This has been done by solving directly the time-dependent Schrödinger equation

$$i\hbar \frac{\partial \psi}{\partial t} = H(t)\psi. \quad (15)$$

First, let us decompose the state into real and imaginary parts, namely, $\psi = \psi_r + i\psi_i$. Considering the staggered time discretization $t_n = n\Delta t$ up to the second order, we obtain

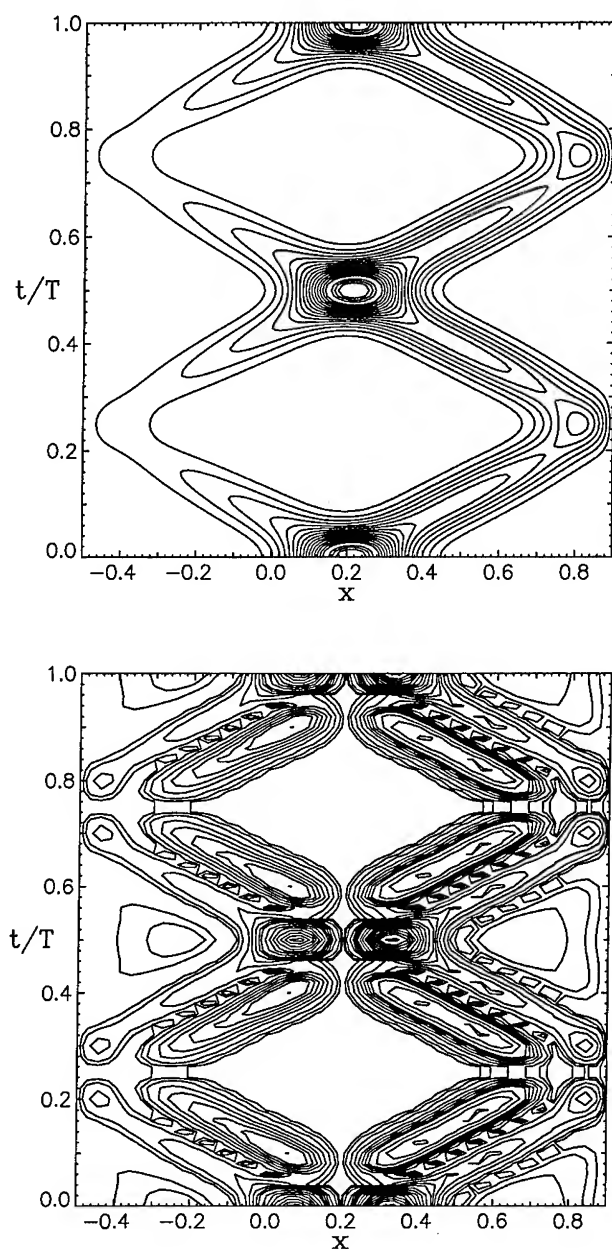


Figure 3. Contour plots of probability density distributions of Floquet states around the 1:1 resonance zone of NO at $A = 0.02$ and $\Omega = 0.8092$. (a) The a_0 state (b) The b_2 state. Time t is scaled by the optical period, T .

$$\begin{aligned}\psi_r(t_{n+1/2}) &= \psi_r(t_{n-1/2}) + H\Delta t\psi_i(t_n) \\ \psi_i(t_{n+1}) &= \psi_i(t_n) - H\Delta t\psi_r(t_{n+1/2}).\end{aligned}\quad (16)$$

For a real Hamiltonian, we rewrite by setting $h \equiv H\Delta t$ the above equations in matrix form

$$u_{n+1} = \begin{pmatrix} 1 & h \\ -h & 1 - h^2 \end{pmatrix} u_n \equiv A u_n \quad (17)$$

$$u_n = A^n u_0 \quad (18)$$

where $u_n = (\psi_r(t_{n-1/2}), \psi_i(t_n))$. The stability criterion is provided by the eigenvalues of A , given by

$$\lambda = \frac{-(h^2 - 2) \pm \sqrt{(h^2 - 2)^2 - 4}}{2}, \quad (19)$$

from which we obtain $|\lambda| = 1$ when $\Delta t < 2/H$. The step size is determined by the energy eigenvalue of largest absolute value. For a time-dependent Hamiltonian, we need to find $\max_i[\text{eigval}(H)]$ [8]. Once the stability condition has been satisfied, the staggered leap-frog time discretization is much faster than the Burlisch-Stoer algorithm used in a previous study [4].

For practical applications of the staggered leap-frog algorithm, we often have to modify the physical Hamiltonian as done in the driven HF molecule, described below.

Modified Morse Hamiltonian

We investigate in the following sections the multiphoton dissociation dynamics of an HF molecule driven by a laser pulse with the shape function $E(t)$ [in the Hamiltonian (1)] given by

$$E(t) = E_m \sin(\omega t) \cdot \sin^2\left(\frac{\pi t}{T}\right). \quad (20)$$

The molecular constants of HF are: $D = 0.225$, $r_0 = 1.7329$, $\alpha = 1.1741$, $q_{\text{eff}} = 0.31$ and $m = 1744.7$ (given in atomic units). In this article we compare the difference in dynamics of two different types of dipole moment functions; in one case the dipole function is approximated by

$$\mu(r) = (x + a) \exp \frac{-(x + a)}{b}, \quad (21)$$

where $a = 2$, $b = 2$ will be used later. This form, introduced by Heather and Metiu [9] and used by Lu et al. [10], mimics qualitatively the *ab initio* and observed dipole function of HF. In the second case, we use the simplest possible form in momentum space, that is,

$$\mu(p) = A \cdot p, \quad (22)$$

where A is the vector potential of the field.

An efficient and accurate way to treat the continuum in a photodissociation problem is to solve the time-dependent Schrödinger equation directly in momentum space as illustrated in Ref. [4]. To employ the staggered algorithm in momentum space, we artificially add a symmetric part of the potential and $\mu(r)$ in the negative r region. Without external field, the Hamiltonian becomes parity symmetric. For each eigenvalue, we now have doubly degenerate eigenfunctions with even- and odd-parity. We note that the added negative r part of the potential will not affect the physics of the problem, because the potential barrier at $r = 0$ is very high relative to the dissociation energy, the set of odd-parity eigenfunctions corresponds to the pseudo-complete set of the physical Morse potential. We verify this point by noting that the odd-parity eigenfunctions obtained here are in exact agreement with our previous results [4], where no extension of the potential was made.

Momentum-Space Fourier-Grid Hamiltonian Method

We solve the time-dependent Schrödinger Eq. (16) using the momentum-space Fourier-Grid Hamiltonian (p -FGH) formalism as introduced in Ref. [4]. With the present extension of symmetric Hamiltonian, the Schrödinger equation reads as:

$$i\hbar \frac{\partial}{\partial t} \psi(k) = \frac{k^2 \hbar^2}{2m} + \int V(k - k') \psi(k') dk' - q_{\text{eff}} E(t) \int \mu(k - k') \psi(k') dk', \quad (23)$$

where

$$V(k - k') = \frac{1}{2\pi} \int_{-\infty}^{+\infty} V(r) e^{-i(k-k')r} dr, \quad (24)$$

and

$$\mu(k - k') = \frac{1}{2\pi} \int_{-\infty}^{+\infty} \mu(r) e^{-i(k-k')r} dr. \quad (25)$$

With symmetrized $V(r)$ and $\mu(r)$, their Fourier transforms are all real. In our calculation, 480 grid points are used in an evenly spaced grid and the range of x is 16 a.u. and of momentum k is -94.2 to $+94.2$ a.u. Diagonalization of the unperturbed Schrödinger equation gives 24 bound levels and 216 discretized pseudocontinuum levels. Each level is doubly degenerate and the physical basis is the set of 240 odd-parity eigenfunctions. The reliability of the time-dependent p -FGH calculation has been established in [4] on the transition probabilities from the ground state to excited states $|n\rangle$ of a harmonic oscillator and will not be repeated here. We integrate Eq. (24) by p -FGH with the staggered time discretization algorithm already discussed.

Results on ATD

We study the ATD spectrum of an HF molecule initially prepared in the 14th vibrational state driven by a laser field of frequency $\Omega = 0.0425$ (1074 nm). The

photon frequency is such that absorption of a single photon will reach beyond the dissociation limit and the range of momentum grid used permits a maximal absorption of nearly 60 photons. In our calculations we use a pulse duration of 100 optical cycles and a time step of 0.1 a.u. which fulfills the stability criterion. Furthermore, to prevent alias errors from the grid boundaries, a filter function $f(k) = (1 + \exp(-a_1|k - b_1|))^{-1}$ with $a_1 = 1.25$, $b_1 = 85$ is multiplied to the wave function at each time step.

We calculate the multiphoton dissociation spectra of $\alpha_0 = 0.025$ (about 100 terawatt/cm²), where

$$\alpha_0 = E_m/m\Omega^2. \quad (26)$$

Figure 4 shows an example of such a calculation in which we plot the projection of the wave function at the end of a laser pulse onto unperturbed eigenstates, that is, we plot the population of each level versus the eigenenergy. The peak at $4.3 \hbar\Omega$ corresponds to the initial 14th vibrational state. The higher-energy peaks evenly spaced in $\hbar\Omega$ represent the contributions from the above-threshold-dissociation process. We have superposed results from the two different dipole moment functions [Eqs. (21) and (22)] in Figure 4. It makes clear that while dominant features are essentially the same between contributions of these two types of dipole functions,

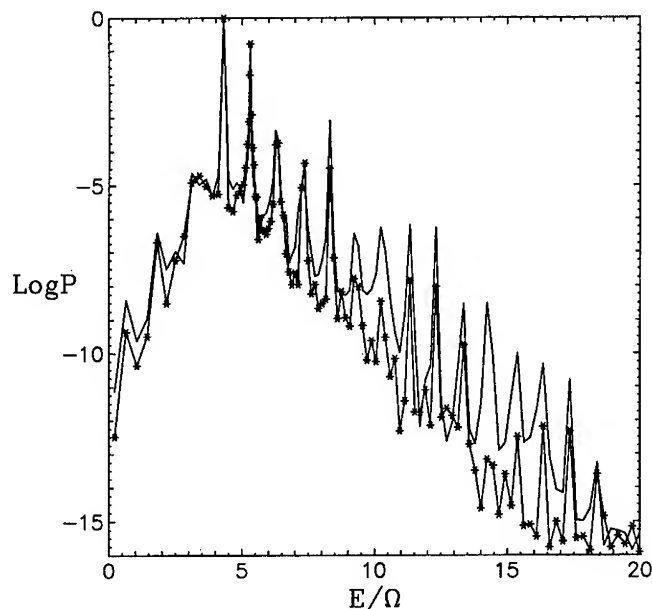


Figure 4. Projection of the final wave function on the unperturbed HF eigenstates for $\alpha_0 = 0.025$. HF is initially prepared in the 14th state with eigenenergy $4.3 \hbar\Omega$. The stars mark results at eigenenergies, which are connected by straight lines to guide the eyes. Starred curve corresponds to the results of the exponential dipole moment function, and the unstarred curve denotes results of $A \cdot p$ function.

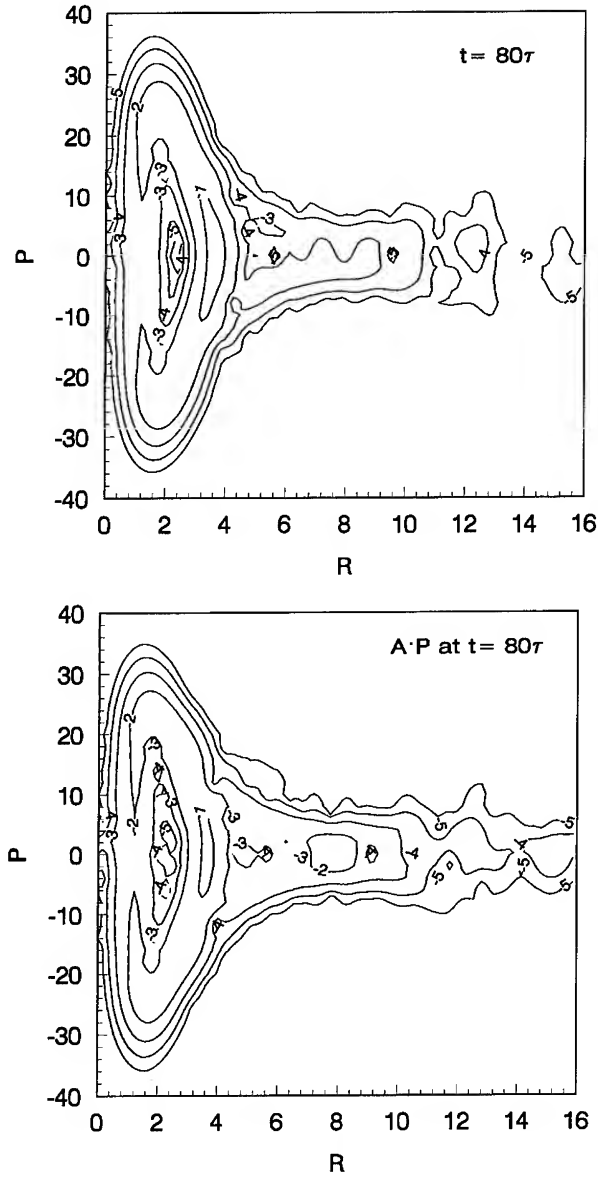


Figure 5. Husimi distribution of the HF wave function at $80T$ for $\alpha_0 = 0.025$. HF is initially prepared in the 14th state with eigenenergy $4.3 \hbar\Omega$. The pulse duration is $100T$.

(a) Results for the exponential dipole function and (b) for the $A \cdot p$ function.

there are distinct differences. Clearly the $A \cdot p$ function causes more rapid transitions between eigenstates than the xe^{-x} function (called the exponential function below), thus higher-order ATD peaks are more pronounced for the $A \cdot p$ function. We can examine the situation from another point of view.

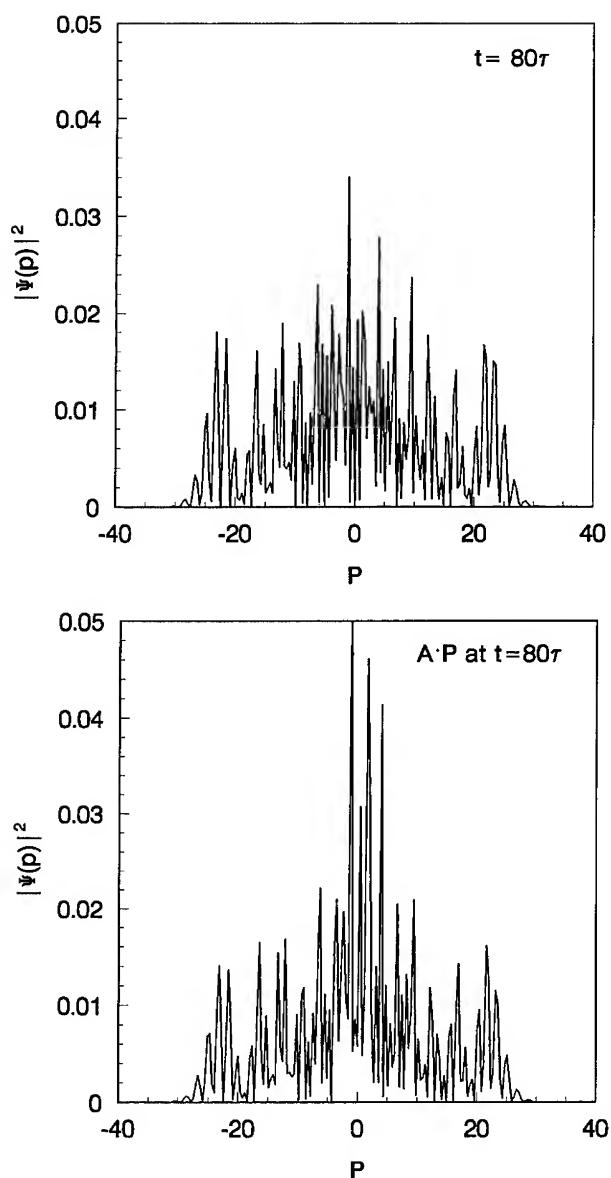


Figure 6. Momentum-space density distribution of HF at $80T$ for $\alpha_0 = 0.025$. HF is initially prepared in the 14th state with eigenenergy $4.3 \hbar\Omega$. The pulse duration is $100T$.

(a) Results for the exponential dipole function and (b) for the $A \cdot p$ function.

In Figure 5 we plot the Husimi distributions of the momentum wave functions at $t = 80$ optical periods for these two cases. Besides other details, they show again that the $A \cdot p$ function seems to spread out the probability density more quickly

towards dissociation. This, however, does not correspond to wider momentum distributions, just some more pronounced peaks at low momenta, as revealed in Figure 6.

These figures also illustrate the power of the momentum-space method in solving problems involving a continuum. Our calculation reveals that the dissociation channel mainly corresponds to the low momentum part of the wave packet and the momentum distribution is usually confined throughout the entire dissociation process. In contrast, a wave packet in the coordinate space will quickly spread out when it reaches continuum to cause difficulties in the wave propagation method. Finally, we note that the Husimi and momentum distributions for these two cases appear to eyes to be very similar for the short-time evolution of the pulse. It is only when it is close to the end of the pulse that the differences become more apparent.

Our results also show that the higher-order ATD peaks grow with laser intensity, which is characteristic of atomic above-threshold-ionization (ATI) as well. But the ATD structure is basically different from ATI, because the dissociation fragments are neutral atoms, which can not be driven to oscillations by the laser field as easily as atomic electrons. The important ponderomotive shift which causes the suppression of lower ATI peaks is therefore absent in the ATD spectra.

As mentioned at the end of the third section that work is in progress in applying the p-FGH method to the NO molecule so that we can compare results with those from the Mathieu equation approach.

Acknowledgments

JMY expresses his gratitude to Dr. Martin Holthaus for the suggestion of the Mathieu-equation approach to the driven Morse oscillator problem. We are also grateful to Mr. Ue-Li Pen for the development of staggered leap frog algorithm and the stimulating discussions related to it. The work is supported by the Donors of the Petroleum Research Fund, administered by the American Chemical Society and the National Science Council of Taiwan under Contract No. NSC-83-0208-M009-002.

Bibliography

- [1] J. F. Heagy, Z. M. Lu, J. M. Yuan, and M. Vallieres in *Quantum Non-Integrability, Directions in Chaos*, Vol. 4, D. F. Feng and J. M. Yuan, Eds. (World Scientific, Singapore, 1992), p. 322.
- [2] M. Holthaus in *Chaos, Solitons, and Fractals*, Special issue on Quantum Chaos (1994).
- [3] L. E. Reichl and W. A. Lin, *Phys. Rev.* **A33**, 3598 (1986).
- [4] T. F. Jiang, *Phys. Rev.* **A48**, 3995 (1993).
- [5] J. F. Heagy and J. M. Yuan, *Phys. Rev.* **A41**, 571 (1990).
- [6] G. Blanch in *Handbook of Mathematical Functions*, M. Abramowitz and I. A. Stegun, Eds. (Dover, New York, 1972), p. 721.
- [7] H. P. Breuer and M. Hothaus, *Ann. Phys. (N.Y.)* **211**, 249 (1991).
- [8] B. Visscher, *Comp. in Phys. Nov./Dec.* 596 (1991).
- [9] R. Heather and H. Metiu, *J. Chem. Phys.* **86**, 5496 (1987).
- [10] Z. M. Lu, M. Vallières, J. M. Yuan, and J. Heagy, *Phys. Rev. A*, **45**, 5512 (1992).

Electron Scattering Mechanisms in Giant Magnetoresistance Computed by the LACO Full-Potential Method

R. K. NESBET

IBM Research Division, Almaden Research Center, 650 Harry Road, San Jose, California 95120-6099

Abstract

The linearized atomic-cell orbital (LACO) method for local density functional calculations has been implemented in a program package for energy bands and valence shell energies of regular periodic solids. This method has been used to compute spin-dependent electrical resistivity due to scattering by displaced interface atoms in a layered CuCo superlattice. The magnetoresistance ratio $\Delta R/R(\uparrow\uparrow)$ obtained for this scattering mechanism is 25.03. When the computed interface resistivity is weighted by estimated interpenetration concentration and combined with bulk resistivity, $\Delta R/R$ reduces to the expected experimental magnitude for adjacent CuCoCu layers. © 1994 John Wiley & Sons, Inc.

Introduction

Multiple scattering theory (MST) is used in the energy-band formalism of Korringa, Kohn, and Rostoker (KKR) [1,2] to construct an exact solution of the Schrödinger equation for a spatially periodic muffin-tin potential, which is constant in the interstitial region between nonoverlapping spheres. The great advantage of this KKR formalism is that the wave function is constructed from functions computed separately within each atomic sphere, allowing the use of exact local solutions of the Schrödinger equation at a given energy as basis functions for the full many-atom problem. This localization has been exploited most fully in the linearized muffin-tin orbital (LMTO) method of Andersen and collaborators [3]. The LMTO method uses multiple scattering theory to fit periodic boundary conditions by forming linear combinations of basis functions on all atoms. The MTO basis functions are evaluated at a set of specified energy values. Interpolation in this energy grid is achieved by using these basis functions in the variational principle for the Schrödinger or Dirac equation. One-electron energies are obtained as eigenvalues of an effective Hamiltonian matrix for each point of different translational symmetry in the Brillouin zone of a periodic solid.

Generalization of multiple-scattering formalism to space-filling local potentials, not restricted to muffin-tin form, is important, because such potentials are needed in solids and molecules to describe covalent bonding, partial charge transfer, and locally nonspherical fields. Several different, and to some extent conflicting, derivations of generalized KKR equations have been published, all based on the integral-

equation formalism used originally by KKR. The derivation of Williams and Morgan [4] can be taken as a point of reference. The LACO method is a form of full-potential multiple scattering theory in which the standard Green-function formalism is converted to expressions involving Wronskian surface integrals over the interfaces between adjacent space-filling atomic cells. Since the LACO formalism is derived as an extension of classical potential theory to the Schrödinger equation, certain formal results required for the validity of MST can be proven in a more direct way than is possible in the integral-equation approach [5].

Model calculations [6] have shown that the suspected formal failure of MST for space-filling cells in fact reduces to the very practical issue of convergence of computational methods in which a variational trial function cannot be made exactly continuous with continuous normal derivative across an interface between adjacent cells. The LACO method replaces the usual Rayleigh–Schrödinger variational principle by that of Schlosser and Marcus [7], which explicitly includes a correction term for mismatch across an interface. LACO differs from the variational cellular method (VCM) of Leite and collaborators [8], based on this Schlosser–Marcus (SM) variational principle, by organizing the computations in analogy to the LMTO method. If atomic-cell orbitals (ACOs) are defined as the extension of local basis functions across cell boundaries by fitting to energy-derivative functions in other cells, the correct linear combinations of these functions to form periodic Bloch waves are determined by structure constants of standard LMTO form. At each point in the reduced Brillouin zone, these ACO basis functions are used in the SM variational principle. The usual Hamiltonian matrix elements are modified by surface-integral terms due to mismatch of the trial wave function. These Schlosser–Marcus or VCM terms provide a closure correction for internal sums that occur in the usual formulation of MST [9]. Inclusion of these terms extends the accuracy of earlier LACO calculations, reported in self-consistent energy-band calculations on fcc Cu [10].

Giant Magnetoresistance

Giant magnetoresistance (GMR) is observed in layered Fe/Cr [11], and in other materials in which magnetic layers are separated by a nonmagnetic spacer metal [12,13]. If the magnetization of successive magnetic layers is originally not parallel, electrical resistivity is greatly reduced when parallel alignment is forced by an applied magnetic field. Application of GMR to magnetic recording devices may greatly increase data densities compared with existing technology. The present work is intended to clarify the underlying mechanism of GMR.

GMR has been studied [14] by a spin-dependent generalization of the Fuchs–Sondheimer theory of thin film conductivity [15]. Hood and Falicov [14] have recently extended the theory to include potential wells that depend on spin alignment, with a more complete description of spin-dependent interface scattering. This parameterized theory is in reasonable accord with experiment, except that use of experimental mean free paths for bulk scattering tends to underestimate the magnetoresistance. The Fuchs–Sondheimer theory treats interface scattering differently from bulk scattering. Several authors [16–18] have used quantum theory

based on the Kubo formalism. GMR occurs when the mean free path in a magnetized material is strongly spin-dependent, primarily due to spin-dependent interface scattering, but also from spin-dependent bulk scattering. All of these prior theoretical studies depend on parameterization and on simplified models of the electronic energy band structure.

The present work reports first-principles calculations of the electronic structure and electrical conductivity of a superlattice model of spin-polarized CuCo. The translational unit cell is (CuCoCu)(CuCoCu) on a 001 tetragonal lattice whose atoms have the geometry of fcc Cu. Transport theory is simplified here in several ways in order to make calculations tractable, but consequences of the spin-dependent energy band structure are worked out in detail. The essential approximations are that the interface penetration scattering mechanism is treated in the weak-scattering limit of isolated impurities, and scattering-in terms (vertex corrections in Kubo theory) are neglected in the Boltzmann equation. This latter approximation was used by Butler and Stocks in calculations on substitutional alloys, later extended using Kubo theory by Butler [19]. The approximation appears to be justified for transition elements when s,d-to-s,d transitions are important, and has recently been used for GMR calculations [20]. The formalism developed by these authors can be applied to extend the present calculations to fully quantitative results, but this was not considered essential for the present exploration of basic scattering mechanisms. Calculation of interface scattering beyond the present weak-scattering limit requires treating interpenetrating atomic layers as a binary alloy.

If there is no thermal gradient, and if mean free paths are larger than the translational unit cell, the Boltzmann equation for a regular periodic solid requires only Fermi surface data and state-to-state transition probabilities for dissipative scattering mechanisms. All required quantities relevant to the Fermi surface are obtained here from first-principles calculations, as are transition probabilities for scattering due to random interpenetration of adjacent Co and Cu layers. Bulk scattering is treated much less specifically by using empirical values of the mean free path for residual resistivity in pure Co and Cu.

In multiple-scattering theory, as used here in the LACO (linearized atomic-cell orbital) method [9], energy bands $\epsilon(\mathbf{k},s)$ are determined by the secular equation $\det(I - tg) = 0$. Here $t(\epsilon)$ is a site-diagonal atomic-cell scattering matrix and $g(\mathbf{k})$ is an energy-independent matrix of structure constants. The energy-band structures of magnetic and spacer species in typical GMR materials match closely at the Fermi energy for one spin direction, while there is substantial mismatch for the opposite spin [21]. The t -matrices of the two species must have a similar relationship, since energy bands in a fixed space lattice are determined entirely by the t -matrices. If atoms are interchanged due to interpenetration at a spacer interface, the difference of t -matrices must be small for one spin direction and large for the other, implying strong dependence of scattering on spin. The transition amplitude for this scattering mechanism is determined in the weak-scattering limit by the impurity scattering matrix Δt , the difference between the t -matrices of the interchanged species, evaluated at the Fermi energy.

Comparison of Co and Cu densities of states indicates that matrix elements Δt should be small for majority-spin electrons and large for minority-spin electrons, in layered CuCo with parallel Co spins. This expectation is confirmed by the present computations. Matrix elements Δt are of intermediate size for antiparallel Co spins. Spin dependence of the computed transition probabilities implies spin dependence of the resistivity. The present computations indicate that for parallel alignment of magnetization in the Co layers the minority-spin resistivity is much greater than the majority-spin resistivity. Since the resistivity for antiparallel alignment is of intermediate magnitude, the magnetoresistance is very large.

This spin-dependent scattering mechanism differs from the well-known Mott effect, which provides an explanation of the increased resistivity of transition metals compared with noble metals. Because transitions into final d-states reduce the relaxation time of a wave packet at the Fermi energy, resistivity due to any dissipative scattering mechanism depends on spin if the density of states does so. When the transition probability itself depends on spin, stronger spin dependence is possible than that due to the Mott effect alone. Scattering due to the atomic-cell t -matrices by themselves is phase-coherent, described by transmission and reflection coefficients that depend on spin and direction, but does not contribute to electrical resistivity. In contrast, scattering due to Δt is dissipative, in the sense that each Bloch wave acquires an energy width or inverse lifetime, characteristic of impurity scattering by a displaced atom at a random site.

A relaxation time τ is defined if collisions cause a perturbed distribution function to relax locally in its parameter space and exponentially in time to the equilibrium distribution f_0 . If τ is defined, the classical steady-state Boltzmann equation for a homogeneous material with no thermal gradient implies the electrical conductivity tensor

$$\sigma_{ij} = -e^2 \int \tau v_i (\partial f_0 / m \partial v_j) d^3v. \quad (1)$$

The semiclassical Boltzmann equation for electrons replaces $f(\mathbf{x}; \mathbf{v})$ by the Fermi-Dirac distribution function $f(\mathbf{k}, b, s)$, indexed by distinct eigenstates, specified by \mathbf{k} in the reduced Brillouin zone, by a band index b , and by a spin index s . Classical electron velocity is replaced by wave-packet group velocity, $\mathbf{v} = (1/2\hbar) \nabla_{\mathbf{k}} \epsilon$, in atomic units if the energy ϵ is in Rydberg units. In the reduced Brillouin zone for a translational cell of volume Ω , the number-of-states element is $[2] (\Omega/8\pi^3) (1/2\hbar v) d\epsilon dS$, where dS is an element of the constant- ϵ surface. In a spin-polarized system, the factor indicated here by $[2]$ is replaced by a sum over the spin index. On the Fermi surface, $v_j = v_F l_j$, where \mathbf{l} is a unit normal vector, and at $T = 0$ K, $\partial f_0 / \hbar \partial k_j = -2v_F l_j \delta(\epsilon - \epsilon_F)$.

If scattering-in terms in the Boltzmann equation are neglected, the relaxation time τ is the reciprocal of the transition probability at the Fermi surface,

$$\tau^{-1}(\mathbf{k}, b, s) = \frac{\Omega}{8\pi^3} \sum_{b'} \int dS' (\hbar v_F')^{-1} \frac{2\pi}{\hbar} |(\mathbf{k}', b', s | \Delta t_s | \mathbf{k}, b, s)|^2. \quad (2)$$

In Eq. (2) the final density of states is proportional to the reciprocal Fermi velocity. An increased final density of states for either spin implies a relative decrease of the relaxation time. This is the Mott effect, giving spin-dependent conductivities even for spin-independent transition probabilities.

The implied semiclassical electric current density is $j_i = \sum_j \sigma_{ij} E_j$, where the conductivity tensor is

$$\sigma_{ij} = \frac{e^2}{8\pi^3 \hbar} \sum_S \int_{\epsilon=\epsilon_F} \tau v_{Fi} l_j dS. \quad (3)$$

A sum over distinct energy bands, assumed in Eq. (3), is not indicated explicitly. Equation (3) implies that electrical conductivity can depend on spin only through spin dependence of the Fermi surface or of the mean free path $\lambda(\mathbf{k}, b, s) = \tau v_F$. In general, σ is dominated by the largest values of λ , and spin dependence of λ implies magnetoresistance.

Calculations

The LACO system of programs for electronic structure calculations has recently been extended to ferromagnetic metals. Preliminary calculations on fcc Cu and on both paramagnetic and ferromagnetic fcc Co provided initial radial density functions for 001-tetragonal (CuCoCu)(CuCoCu), on the Cu lattice, for which self-consistent calculations were carried to convergence for both parallel $\uparrow\uparrow$ and antiparallel $\uparrow\downarrow$ alignments of the Co spin axes. A local basis designated by $\text{spd}\{\text{fg}\}$ was used. The orbital basis sets on each atom included (spd) orbital basis functions at each electronic band energy, with intermediate boundary sums carried through (fg) solid harmonics.

The matrix Δt for the interface scattering mechanism considered here is the difference of spin-dependent self-consistent atomic-cell t -matrices computed, as described recently [22], from rectangular matrices characteristic of full-potential theory. Matrix elements of Δt were computed using Bloch wave eigenvectors of the secular matrix. Incoherent scattering by each displaced atom was assumed. Equations (2) and (3) were used to compute the state-dependent relaxation time and spin-dependent electrical conductivity tensor, respectively. Integrals over the Fermi surface required in these expressions were carried out by a tetrahedral interpolation scheme. These calculations have not been carried to convergence with respect to the number of points in the Brillouin zone, but test calculations indicate that the interpolation method used is relatively stable, and that the preliminary results given here are not subject to large error. A subsequent publication will give details of the computations.

Relaxation times due to the interpenetration effect were computed in the form $c\tau$, where c is the (unknown) concentration of Co atoms exchanged with Cu in adjacent planes. The spin dependence of $c\tau$ and dependence on spin polarization is very large, characterized in atomic units by the orders of magnitude

$$\begin{aligned} \uparrow\uparrow(f) \quad c\tau(\uparrow) &\simeq 10^4 & c\tau(\downarrow) &\simeq 10^1; \\ \uparrow\downarrow(a) \quad c\tau(\uparrow) &\simeq 10^2 & c\tau(\downarrow) &\simeq 10^2. \end{aligned}$$

The resulting conductivity tensor is strongly spin-dependent. Computed in-plane conductivities, again multiplied by the concentration c , are (in atomic units)

$$\begin{array}{lll} \uparrow\uparrow(f) & c\sigma(\uparrow) = 2.0378, & c\sigma(\downarrow) = 0.0032, & c\sigma(f) = 2.0410, \\ \uparrow\downarrow(a) & c\sigma(\uparrow) = 0.0392, & c\sigma(\downarrow) = 0.0392, & c\sigma(a) = 0.0784. \end{array}$$

The implied magnetoresistance ratio, defined here by $[\rho(f) - \rho(a)]/\rho(f) = [\sigma(f) - \sigma(a)]/\sigma(a)$, is 25.03 from this mechanism alone. Results of similar large magnitude have recently been reported from layered KKR/CPA calculations [20].

Recent first-principles calculations by Sticht [23] are similar to the present work, but do not evaluate a specific scattering mechanism and take the relaxation time to be constant and independent of spin. This is inconsistent with Eq. (2) here, since spin-dependent Fermi surface and Fermi velocity imply spin-dependent τ . The present results include this Mott effect, together with the direct effect of spin-dependent interface scattering. In order to separate these two aspects of the physical mechanism, the calculations were repeated with the state-dependent transition probability replaced in Eq. (2) by its average over initial state and spin. The modified values of $c\sigma$ computed in this way are

$$\begin{array}{lll} \uparrow\uparrow(f) & c\sigma(\uparrow) = 0.0419, & c\sigma(\downarrow) = 0.0027, & c\sigma(f) = 0.0446, \\ \uparrow\downarrow(a) & c\sigma(\uparrow) = 0.0038, & c\sigma(\downarrow) = 0.0038, & c\sigma(a) = 0.0076. \end{array}$$

The implied magnetoresistance ratio is 4.87. Hence, in the present example, the Mott effect by itself leads to significantly smaller GMR than does the combination of Mott effect and spin-dependent interface scattering.

A model of bulk scattering is provided by using spin and state independent values of the mean free path λ in Eq. (3). Empirical low-temperature values for typical experimental materials are [24] $\lambda(\text{Cu}) = 200 \text{ \AA}$, $\lambda(\text{Co}) = 70 \text{ \AA}$. $1/\lambda$ for each species is weighted by the relative number of atoms in the unit cell. The implied values of σ for pure bulk scattering are

$$\begin{array}{lll} \uparrow\uparrow(f) & \sigma(\uparrow) = 1.2288, & \sigma(\downarrow) = 1.1610, & \sigma(f) = 2.3898, \\ \uparrow\downarrow(a) & \sigma(\uparrow) = 1.4350, & \sigma(\downarrow) = 1.4350, & \sigma(a) = 2.8700. \end{array}$$

The implied magnetoresistance ratio for spin-independent bulk scattering is -0.17 , opposite in sign to the observed GMR. This result indicates that, despite the spin dependence of the Fermi surface, purely spin-independent scattering cannot account for GMR.

For comparison with observed GMR, resistivities due to bulk scattering and to interface scattering must be combined. In the weak-scattering limit, scattering probabilities due to bulk and interface mechanisms are additive, and the implied spin-dependent resistivities must be added separately for the spin-up and spin-down electrons in the two-fluid model postulated here. The resulting spin-indexed current densities are independent, and are of greatly different magnitude in the spin-aligned material. Adding the spin-indexed conductivities gives a rational formula that interpolates $\Delta R/R$ between pure bulk and interface scattering limits as a function of

c. If the interpenetration concentration is $c \simeq 0.10$, which is not unreasonable for atomic species closely spaced in the periodic table, and other quantities are taken from the data given above, this formula implies $\Delta R/R \simeq 1.0$, comparable to an estimate of $\simeq 2.0$ [24] for the empirical limit in Cu/Co at low temperature, with adjacent magnetic and spacer atomic layers, but no true bulk spacer material.

Conclusions

The present first-principles calculations show that interface scattering due to interpenetration of adjacent magnetic and spacer atomic layers can produce large magnetoresistance, if the difference between atomic scattering t -matrices at the Fermi energy depends strongly on spin orientation. Hence spin-dependent energy band structure can be correlated with the occurrence of GMR. Comparing published densities of states [25], Co/Cu bands agree for majority-spin electrons and disagree for minority-spin electrons at the Fermi energy, while the opposite is true for Fe/Cr and Fe/Rh. The present study predicts that electric current is spontaneously polarized in spin-aligned magnetized GMR materials. Opposite polarization is expected in Co/Cu and Fe/Cr (or Fe/Rh), respectively.

Acknowledgments

The author is indebted for helpful discussions and comments to W. H. Butler, B. A. Gurney, F. Herman, B. A. Jones, V. Kalmyer, S. S. P. Parkin, V. S. Speriosu, and W. A. Harrison.

Bibliography

- [1] J. Korringa, *Physica* **13**, 392 (1947).
- [2] W. Kohn and N. Rostoker, *Phys. Rev.* **94**, 1111 (1954).
- [3] O. K. Andersen, *Phys. Rev.* **B12**, 3060 (1975); H. L. Skriver, *The LMTO Method* (Springer-Verlag, New York, 1984).
- [4] A. R. Williams and J. van W. Morgan, *J. Phys.* **C7**, 1085 (1974).
- [5] R. K. Nesbet, *Phys. Rev. B* **41**, 4948 (1990).
- [6] W. H. Butler and R. K. Nesbet, *Phys. Rev.* **B42**, 1518 (1990).
- [7] H. Schlosser and P. M. Marcus, *Phys. Rev.* **131**, 2529 (1963).
- [8] L. G. Ferreira and J. R. Leite, *Phys. Rev.* **A18**, 335 (1978); A. C. Ferraz, M. I. T. Chagas, E. K. Takahashi, and J. R. Leite, *Phys. Rev.* **B29**, 7003 (1983).
- [9] R. K. Nesbet, *Phys. Rev.* **B45**, 11491 (1992).
- [10] R. K. Nesbet and Tjet Sun, *Phys. Rev.* **B36**, 6351 (1987).
- [11] M. N. Baibich, J. M. Broto, A. Fert, F. Nguyen Van Dau, F. Petroff, P. Etienne, G. Creuzet, A. Friederich, and J. Chazelas, *Phys. Rev. Lett.* **61**, 2472 (1988); G. Binash, P. Grünberg, F. Saurenbach, and W. Zinn, *Phys. Rev.* **B39**, 4828 (1989).
- [12] S. S. P. Parkin, N. More, and K. P. Roche, *Phys. Rev. Lett.* **64**, 2304 (1990); S. S. P. Parkin, R. Bhadra, and K. P. Roche, *Phys. Rev. Lett.* **66**, 2152 (1991); D. H. Mosca, F. Petroff, A. Fert, P. A. Schroeder, W. P. Pratt, Jr., and R. Laloe, *J. Magn. Magn. Mater.* **94**, L1 (1991); S. S. P. Parkin, Z. G. Li, and D. J. Smith, *Appl. Phys. Lett.* **58**, 2710 (1991); S. S. P. Parkin, *Phys. Rev. Lett.* **71**, 1641 (1993).
- [13] B. Dieny, V. S. Speriosu, S. S. P. Parkin, B. A. Gurney, D. R. Wilhoit, and D. Mauri, *Phys. Rev.* **B43**, 1297 (1991); V. S. Speriosu, B. Dieny, P. Humbert, B. A. Gurney, and H. Lefakis, *Phys. Rev. B* **44**, 5358 (1991).

- [14] R. E. Camley and J. Barnaś, Phys. Rev. Lett. **63**, 664 (1989); J. Barnaś, A. Fuss, R. E. Camley, P. Grünberg, and W. Zinn, Phys. Rev. **B42**, 8110 (1990); A. Barthélémy and A. Fert, Phys. Rev. **B43**, 13124 (1991); B. L. Johnson and R. E. Camley, Phys. Rev. **B44**, 9997 (1991); R. Q. Hood and L. M. Falicov, Phys. Rev. **B46**, 8287 (1992).
- [15] K. Fuchs, Proc. Camb. Phil. Soc. **34**, 100 (1938); E. H. Sondheimer, Adv. Phys. **1**, 1 (1952).
- [16] P. M. Levy, S. Zhang, and A. Fert, Phys. Rev. Lett. **65**, 1643 (1990); S. Zhang, P. M. Levy, and A. Fert, Phys. Rev. **B45**, 8689 (1992).
- [17] A. Vedyayev, B. Dieny, and N. Ryzhanova, Europhys. Lett. **19**, 329 (1992).
- [18] A. Okiji, H. Nakanishi, K. Sakata, and H. Kasai, Jpn. J. Appl. Phys. **31**, L706 (1992).
- [19] W. H. Butler and G. M. Stocks, Phys. Rev. **B29**, 4217 (1984); W. H. Butler, Phys. Rev. **B31**, 3260 (1985).
- [20] W. H. Butler, J. M. MacLaren, and X.-G. Zhang, Proc. Mater. Res. Soc. **313**, 59 (1993).
- [21] W. H. Butler, lecture notes (unpublished, 1992).
- [22] R. K. Nesbet, Phys. Rev. **B45**, 13234 (1992).
- [23] J. Sticht, lecture notes (unpublished, 1992).
- [24] S. S. P. Parkin, private communication.
- [25] V. L. Moruzzi, J. F. Janak, and A. R. Williams, *Calculated Electronic Properties of Metals* (Pergamon, New York, 1978).

Received May 13, 1994

From Parallel to Distributed Computing for Reactive Scattering Calculations

ANTONIO LAGANÀ

Dipartimento di Chimica, Università di Perugia, Perugia, Italy

OSVALDO GERVASI

Centro di Calcolo, Università di Perugia, Perugia, Italy

RANIERI BARAGLIA and DOMENICO LAFORENZA

CNUCE, Pisa, Italy

Abstract

Some reactive scattering codes have been ported on different innovative computer architectures ranging from massively parallel machines to clustered workstations. The porting has required a drastic restructuring of the codes to single out computationally decoupled cpu intensive subsections. The suitability of different theoretical approaches for parallel and distributed computing restructuring is discussed and the efficiency of related algorithms evaluated. © 1994 John Wiley & Sons, Inc.

Introduction

The possibility of carrying out extended reactive scattering calculations strongly relies on the availability of highly performing computers and on the ability of constructing computational procedures capable of taking advantage of the innovative architectural features of these machines. Due to the intrinsic limitations of single processor architectures in reaching high computing speed, the only way of performing extended reactive scattering calculations using commercially available technology is to split computer codes into weakly coupled sections and make them run concurrently on several processors.

A way of designing an efficient concurrent architecture is to connect several processors through a dedicated network. The processors execute independently some processes and receive through the network the necessary information to start, continue, and terminate the calculations. Through the network they also return the results and eventually receive instructions on how to start new processes. The design of the dedicated network is most often the key feature of a parallel machine. In designing the network of a parallel computer much care has to be put in ensuring an efficient handling of communications between distant (in terms of network connections) processors. On the contrary, the role played by individual processors is mainly to provide (possibly fast and cheap) computing power and some I/O functionalities. Therefore, the computing nodes are quite often sufficiently well-

performing commercial (or custom) processor chips. More complex (mainly front-end) operations are usually handled by a (sometimes assembled in the same cabinet) workstation.

An alternative practical way of distributing the calculations over concurrent processors is to make use of clustered workstations. In this case, the computing element is a real computer that can provide a richer working environment. In this case, however, communications are dealt by either a local or a geographical network. Obviously, such a network is less efficient than that of parallel computers making it vital that applications are partitioned into truly loosely coupled processes.

To take advantage of concurrent processing, one needs software tools providing easy means to maximize the efficiency of the different processors and minimize the data traffic on the network. To this end use can be made of a language suitable for the exploitation of the parallelism of the problem. The language to use may be a sequential one enriched with parallel extensions (e.g., HPF, PVM, etc.) or a native parallel language (e.g., Occam, etc.). Use can also be made of semiautomatic parallelization tools, like Mimdizer, which can detect parallel features of the source code.

There is, however, no surrogate for an efficient design of the application. This can only result from a combination of a deep understanding of the physics of the investigated problem, a detailed knowledge of the properties of the adopted algorithms and an appropriate exploitation of the peculiar architectural features of the used machine. What is more, there is not a unique parallelization golden recipe even for established applications. The efficiency of parallel algorithms, models and architectures may drastically vary (even for the same application) when the value of the parameters changes. For these reasons, in our approach to concurrent computing, we adapted our choices both to the nature of the problem and to the characteristics of the adopted computational procedure.

Since our interests focus on reactive scattering calculations, we have first restructured a classical trajectory code to run on a distributed memory MIMD parallel machine of the hypercube type. The parallel implementation of the atom-diatom classical trajectory code on an nCUBE 2 machine is discussed in the next section. Due to the difficulty of fitting the parallel tasks of a reduced dimensionality method into the limited local memory of the nCUBE available to us, we have used for its implementation on a multiprocessor architecture a fewer processor machine with larger node memory. Details of this parallel implementation are given in the third section. Higher memory and cpu demands of alternative or more rigorous approaches to chemical reactivity have prompted the use of more complex computational nodes. To gain experience on the use of parallel architectures based on more complex computing elements, we chose to implement the reduced dimensionality code on clustered workstations. To this end, we made also use of some parallelization software tools. A description of these efforts is given in the fourth section.

The Trajectory Code

The simplest computational approach to the calculation of the reactive properties of molecular systems are those inspired by classical mechanics. In these approaches

the nuclei of the atoms are considered as mass-points moving on a potential energy surface and obeying Newtonian mechanics. Obviously, any formulation of the motion equations equivalent to the Newtonian one can be adopted to describe the motion of the reactive system. Our trajectory code, originally inspired by Ref. [1], integrates Hamilton's equations.

Though extensively described in the literature [2], the main features of the quasiclassical approach to atom-diatom reactivity are outlined here to facilitate the understanding of the parallel restructuring.

The Quasiclassical Method

For an atom-diatom system $A + BC$ at a given value of the translational energy E_{tr} , the detailed quasiclassical cross section from the reactant vibrotational vj to the product (AB , BC or AC) vibrotational $v'j'$ state is defined as

$$\sigma_{vj,v'j'}(E_{tr}) = K \int_0^1 d\xi_1 \int_0^1 d\xi_2 \cdots \int_0^1 d\xi_k f_{vj,v'j'}(\xi_1, \xi_2, \dots, \xi_k; E_{tr}) \quad (1)$$

In Eq. (1) K is a normalization constant and k is 5 when a proper choice of the initial reference frame is made. In this case, the ξ variables are defined as $\xi_1 = (1 - \cos \vartheta^0)/2$, $\xi_2 = \eta^0/(2\pi)$, $\xi_3 = (b/b_{\max})^2$, $\xi_4 = \beta^0/\pi$, $\xi_5 = \phi^0/(2\pi)$ where the angle ϑ (the superscript "0" means initial value) gives the orientation of the diatom BC with respect to the atom-diatom A , BC vector, the phase angle η determines the BC oscillator elongation, b and β are the distance of the relative collision velocity vector from the BC center of mass and the angle it forms with the plane of the triatom, respectively, and ϕ is the angle formed by the rotational angular momentum of BC with the same plane. The function $f_{vj,v'j'}(\xi_1, \xi_2, \xi_3, \xi_4, \xi_5; E_{tr})$ is a Boolean function. Its value is one only when after integrating the Hamilton equations of the system starting from the given set of initial conditions and the vibrotational vj state, the products can be assigned to the final $v'j'$ vibrotational quantum state. In a quasiclassical approach the continuum classical state $v_c'j_c'$ is usually discretized by assigning it to the closest (discrete) quantum state $v'j'$.

In general, the integral of Eq. (1) is evaluated using a Monte Carlo method. As a result, the detailed reactive cross section can be written as

$$\sigma_{vj,v'j'}(E_{tr}) = \frac{\pi b_{\max}^2}{N} \sum_{i=1}^N f_{vj,v'j'}(\xi_1^i, \xi_2^i, \xi_3^i, \xi_4^i, \xi_5^i; E_{tr}) \quad (2)$$

where N is the number of integrated trajectories. More frequently, however, experimental quantities are less detailed than the state-to-state cross section. As an example, in many gas kinetics studies, what is actually needed is the rate coefficient $k_{v,v'}(T)$ defined as

$$k_{v,v'}(T) = \left(\frac{8}{k^3 T^3 \pi \mu} \right)^{1/2} \sum_{j=0}^{\infty} \frac{(2j+1) e^{-\epsilon_j/kT}}{Q_R(T)} \int_0^{\infty} dE_{tr} E_{tr} e^{-E_{tr}/kT} \sigma_{vj,v'}(E_{tr}) \quad (3)$$

where ϵ_j is the energy of the rotational state j , $Q_R(T)$ is the BC rotational partition function, k is the Boltzmann's constant, μ is the A, BC reduced mass and $\sigma_{vj,v'}(E_{tr})$ is the degeneracy averaged detailed reactive cross section summed over product rotational states. In the case of rate coefficient calculations, a further integration over the energy is needed and, altogether, a six-dimensional integral has to be evaluated. However, when using a Monte Carlo approach, the same algorithm described for the calculation of the cross section can be used and, as a consequence, the same parallelization recipes can be applied.

The Structure of the Computer Code

As sketched in the scheme of Figure 1, on a conventional computer, the trajectory code can be divided into three sections.

The first section of the code is dedicated to input the data and calculate the variables of common use throughout the code. This section sets the different options for selecting the initial conditions (e.g., single energy or thermal distributions, fixed or random orientation, etc.), the type of the potential used, the mode and frequency of printing out information on the individual trajectory evolution and on collective indicators. This section does also work out the mass factors, convergence, and accuracy check variables, debugging flags and limits of the integration domain.

The second section iterates over the number of trajectories to be integrated the necessary operations. The first of these operations is the generation of a string of pseudo-random numbers and its conversion into validated initial values of the integration variables. This has to be strictly sequential to be deterministic (i.e., to generate the same sequence of events when changing working conditions like when distributing the trajectories on a different number and type of processors). To this end, the pseudo-random sequence is generated using a routine that, given a seed, generates a new seed and a random number in the interval 0–1. The second operation of this section consists of integrating the 12 Hamilton first-order differential equations using a numerical integrator. The integration is carried out from a sufficiently

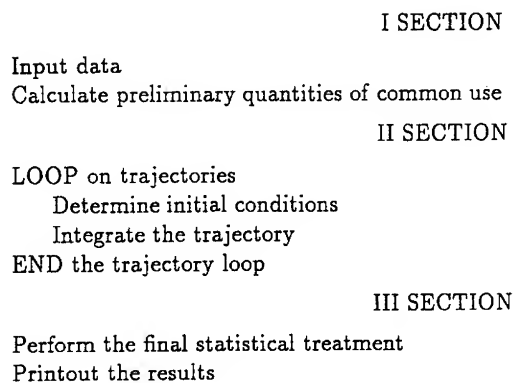


Figure 1. Scheme of the quasiclassical trajectory code.

large atom-diatom distance to a point where one of the three internuclear distances is again large enough to consider the process ended (the check of the internuclear distances is performed at each integration step). The third operation consists of working out the product characteristics from the final value of the integrated variables (i.e., vibrational, rotational, and translational energy of the products as well as their vector properties). This allows an update of the statistical indicators related to distributions of scalar and vector properties of the products.

The final section of the code carries out a statistical analysis of the final outcome of the integrated trajectories to print out cross sections and product distributions for the different reaction channels.

The Parallel Restructuring of the Trajectory Program

A parallel version of the trajectory code was implemented on the nCUBE 2 computer [3]. The nCUBE machine is a multiprocessor computer made of 2^d (d is the dimension of the cube. The machine used for trajectory calculations has $d = 7$) computing elements connected on a hypercube network. On this network each processor is assigned a d -bit code having the property of differing by one bit only for adjacent nodes. Each computing element (or node) is provided with a custom processor having a peak performance of 2.5 Mflops (double precision) and a node local memory of 4 Mbytes. Only neighboring nodes are directly connected. All other nodes communicate through intermediate nodes (though communication does not interfere with current execution). Routing functions allow a dynamical allocation of the communication paths. Once communication paths have been set, they remain active till an "end-of-transmission" packet is forwarded. A SUN workstation acts as a front-end computer and provides a user-friendly environment for development and production.

Message receiving and sending occurs through *nread* and *nwrite* functions [4]. The issuing of an *nread* instruction blocks the execution while when using *nwrite* the current process continues executing. The parallelism can be implemented using the following library functions: *n_frun*, *n_fork*, *n_sleep*, *n_npwait* and *n_wake*. The *n_frun* function activates a new process on one of the allocated nodes of the hypercube. Once a process has been successfully activated, it returns its identification number. To duplicate the calling process on the same node use has to be made of the *n_fork* function. To suspend a process either for a given interval of time or until a given condition applies the *n_sleep* and *n_npwait* instructions have to be issued. The resumption of a process is obtained by means of the function *n_wake*. To handle I/O, functions like *n_screate*, *n_fopen*, *n_fclose*, *n_fread*, and *n_fwrite* can be used to create, open, close, read, and write a file in a parallel fashion.

A simplistic way of implementing on the nCUBE a parallel version of the trajectory code is to distribute among several processors the section of the program devoted to the integration of the motion equations. In fact, once the sequential determination of the five initial conditions is performed each integration of the motion equations (i.e., each trajectory calculation) is a fully independent process. Therefore, when adopting a farm parallel model [5], the *farmer* can distribute the integration of

the different trajectories to the several *worker* nodes once the related initial conditions have been determined. Unfortunately, such an approach, though appropriate for a few processor machine, fails to give high speedups (the speedup S_p is defined as the ratio T_S/T_p i.e., the ratio between the times necessary to run the application on a single node and that on N_p nodes) when a large number N of trajectories needs to be integrated in a many processor machine.

Both T_S and T_p can be partitioned into a time needed to run the strictly sequential part (s and s' , respectively) and the time needed to run the part that can be executed in parallel (p and p' , respectively). In the limit of $s = s' = 0$ and $p = N_p p'$, the speedup is exactly N_p . Deviations from this limiting value are due to overheads associated with the introduction of parallelization functions as well as to waiting times caused by communication synchronization or by the non-negligibility of s . All these elements become important when the number of trajectories to be integrated is large as is quite often the case of reactions relevant to practical applications.

For this reason, we performed a more appropriate restructuring of the code by minimizing the communications and placing the generation and validation of initial conditions inside the *worker* process. Only the generation of the first seed of each trajectory was kept at the *master* level to ensure determinism. Once the seed vector (of dimension N) has been constructed, it is distributed to the *worker* processors. From this vector, following a message of the *master*, the *worker* takes the element corresponding to the trajectory to be run. Starting from this seed, a pseudo-random substring and related initial conditions are generated and validated as a part of the in-node work. This allows a dramatic reduction of both the workload of the *master* and the amount of transmitted data.

A similar modification was introduced to improve the return of the results. More in detail, communications were drastically reduced by performing an in-node update of the statistical indexes. Statistical indexes are collected by the *farmer* at the end of the *worker* activity to assemble a global statistical analysis.

In this way, it has been possible to obtain a speedup of 119 when running 4096 trajectories on 128 nodes. Presently, the parallelized version of the code is used for production runs to integrate batches of 100 000 trajectories per job in an average time of 7 hr. This has allowed a highly detailed analysis of isotope and threshold properties of the Li + FH reaction [6].

The Reduced Dimensionality Quantum Approach

Accurate treatments of atom-diatom reactive scattering are quantum-mechanical. Unfortunately, up to date, some theoretical and computational difficulties prevent a straightforward extension of these methods to the calculation of cross sections and rate constants of generic atom-diatom reactions. Therefore, the most popular approach to the calculation of these quantities are based on the reduction of the dimensionality of the problem by introducing some dynamical constraints. The reduced dimensionality method we considered for a parallel implementation is the Reactive Infinite Order Sudden (RIOS) one.

The Reactive Infinite Order Sudden Method

A detailed description of the RIOS method is given in the literature [7]. In the present article we discuss only those details that help the understanding of the restructuring. The RIOS state (v) to state (v') integral reactive cross section $\sigma_{v,v'}(E_{tr})$ is defined as:

$$\sigma_{v,v'}(E_{tr}) = \frac{\pi}{k_v^2} \sum_l (2l+1) \int_{-1}^1 |S_{vl,v'}(\Theta; E_{tr})|^2 d \cos \Theta \quad (4)$$

where $k_v^2 = 2\mu(E - \epsilon_v)$, E is the total energy, ϵ_v is the energy of the vibrational state v , l is the (decoupled) orbital quantum number, and $S_{vl,v'}(\Theta; E_{tr})$ is the detailed fixed OS matrix element. To evaluate rate coefficients from RIOS cross sections one can use a j shifting model to approximate the dependence of the cross section from the initial rotational quantum number j . According to this model

$$\sigma_{vj,v'}(E_{tr}) = \sigma_{v,v'}(E_{tr} - \epsilon_{vj} + \epsilon_v) \quad (5)$$

where ϵ_{vj} is the vibrotational energy of the vj state. To calculate the $S_{vl,v'}(\Theta; E_{tr})$ elements the following set of coupled differential equations

$$\left[\frac{d^2}{dR^2} - D \right] \psi(R; \Theta) = 0 \quad (6)$$

have to be integrated. The elements of the matrix D of Eq. (6) are defined as

$$D_{vv'} = \left\langle \zeta_v \left| \frac{l(l+1)}{R^2} + \frac{j(j+1)}{r^2} \right| \zeta_{v'} \right\rangle + \frac{2\mu}{\hbar^2} (\epsilon_v - E) \delta_{vv'}$$

or

$$D_{vv'} = \left\langle \zeta_v \left| \eta^2 \left[\frac{l(l+1)}{R^2} + \frac{j(j+1)}{r^2} \right] \right| \zeta_{v'} \right\rangle + \frac{2\mu}{\hbar^2} \left[\frac{\epsilon_v + \epsilon_{v'}}{2} - E \right] \cdot \langle \zeta_v | \eta^2 | \zeta_{v'} \rangle + \frac{3\delta_{vv'}}{4\sigma}$$

depending on whether we are dealing with the cartesian or the polar region. In fact, though Eq. (6) is formulated in mass scaled Jacobi coordinates R and r (the integration coordinate in this region is R) in the strong interaction region the related circular coordinates σ and u are used (in this case the reaction coordinate is the arc u which is linked to η by the relationship $\eta = 1 + u/\sigma$). Equations (6) were obtained by expanding the RIOS scattering wavefunction $\Xi^{\text{IOS}}(R, r; \Theta)$ in the partial differential equation

$$\left[-\frac{\hbar^2}{2\mu} \left(\frac{1}{R} \frac{\partial^2}{\partial R^2} R + \frac{1}{r} \frac{\partial^2}{\partial r^2} r - \frac{A_l}{R^2} - \frac{B_j}{r^2} \right) + V(R, r; \Theta) - E \right] \Xi^{\text{IOS}}(R, r; \Theta) = 0 \quad (7)$$

in terms of the eigenfunctions $\zeta_v(r; R, \Theta)$ of the equation of the bound coordinate r

$$\left[-\frac{\hbar^2}{2\mu} \frac{d^2}{dr^2} + V(r; R, \Theta) - \epsilon_v \right] \zeta_v(r; R, \Theta) = 0 \quad (8)$$

Equation (7) is obtained from the exact (electronically adiabatic) nuclear Schrödinger equation by applying at the same time both the centrifugal sudden and the energy sudden approximations. In Eq. (7) $A_l = \hbar^{-2}l(l+1)$ and $B_j = \hbar^{-2}j(j+1)$ are the coefficients of the decoupled orbital and rotational terms of the Hamiltonian with l and j being the related quantum numbers.

To integrate Eqs. (6) for each value of Θ , the (R, r) plane is divided into two regions by a straight line originating at $R = r = 0$ and following the ridge separating the entrance from the exit channel. By connecting the reactant and product half planes onto a single one, one can uniquely match entrance and exit channel solutions. Then, the two channels are segmented into several small sectors and for each sector the eigenvalues ϵ_v and eigenfunctions $\zeta_v(r; R, \Theta)$ are calculated. The asymptotic solution is constructed using an initial value propagation method. The method propagates sector by sector the **R** matrix. From its asymptotic value, the detailed fixed Θ scattering reactive matrix elements $S_{v'l,v'}(\Theta; E)$ are derived by imposing the appropriate boundary conditions.

The Structure of the Computer Code

The schematic structure of the RIOS code is illustrated in the scheme of Figure 2. As illustrated in the figure, the program consists of three sections.

In the first section input data are read-in and variables of general interest are evaluated.

Scattering calculations are performed in the second section II in which a DO loop (the outermost loop) runs over the collision angle values (as will be discussed below, this DO loop was at first not activated in the parallel versions of the code and each job was performing single angle calculations). In the first subsection, during the first run, all the energy-independent quantities necessary for the integration of Eqs. (6) are calculated and stored on disk for use in next energy calculations (even from different runs). The three calculation blocks of this subsection, devoted to take cuts of the potential energy channel, calculate related vibrational eigenvalues and eigenfunctions and, finally, assemble overlap and coupling matrices, are to be executed in a strict sequential order. In the second subsection, after reading the information from disk, the integration of fixed angle, fixed energy, and fixed l values scattering equations is performed by propagating the ratio between the function and its derivative (**R** matrix method). The sector-by-sector propagation is a strictly recursive process. At the end of the propagation, the **S** matrix is derived from the **R** matrix and stored on disk for further use by programs devoted to the calculation of differential and integral cross sections.

The third section is devoted to final calculations and results printout.

SECTION I

Input data
Calculate quantities of common use

SECTION II

LOOP on collision angles

subsection a

IF first run THEN
 Search the turning center
 LOOP on sectors
 Calculate the sector potential cut
 Store the sector potential cut
 END the sector loop
 LOOP on sectors
 Calculate sector eigenvalues and eigenfunctions
 Store sector eigenvalues and eigenfunctions
 END the sector loop
 LOOP on sectors
 Calculate the intersector overlap matrix
 Store the intersector overlap matrix
 Calculate the sector coupling matrix
 Store the sector coupling matrix
 END the sector loop
 ENDIF

subsection b

LOOP on energies
 Read the intersector overlap matrix
 Read the sector coupling matrix
 Embed the energy dependence into the coupling matrix
 LOOP on l quantum number
 Integrate fixed angle, fixed l scattering equations
 Storage of detailed S matrix elements on disk
 Check for convergency on l
 END the l loop
 Calculate the fixed angle contribution to the cross section
 Printout the fixed angle contribution to the cross section
 END the energy loop
 Integration over the collision angle
 END the angle loop

SECTION III

Perform final calculations
Printout the reactive cross section

Figure 2. Scheme of the RIOS code.

The Parallel Restructuring of the RIOS Code

A first parallel version of the RIOS code was implemented on a multiprocessor IBM 3090 [8]. As already mentioned, to this end, use was made of a single angle version of the program and the single energy, single l propagation (the more cpu demanding part of the second section) was distributed among concurrent processors

for parallel execution. The choice of exploiting the parallelism at such an inner level was motivated by the queueing policy usually adopted by computer centers for time-sharing computers. The need for handling the large files containing fixed angle quantities necessary to carry out the propagation as well as the heavy cpu time request make the RIOS jobs be assigned low priorities when running on centralized computers. Therefore, by keeping memory occupation at the lowest (single angle) level possible, we had the possibility of exploiting the parallelism on l . Such a choice is able to ensure a satisfactory load balancing even at moderately high energies.

In practice, the restructuring of the Fortran code consisted in incorporating into a single routine the whole body of the l DO loop (the propagation) with the exception of the convergence check. Such a restructuring led to fairly high speedups [8].

A limitation of the implementation of the code on a shared memory machine was that, due to the little number of processors available, the batch of (single angle) energies dealt by individual jobs had to be kept small to the end of keeping turnaround times in the limit of a few hours.

A parallel distributed machine that, while offering a sufficient node computing speed and memory size, gave us the possibility of distributing the calculation over a number of processors larger than that of shared memory architectures was the Meiko Computing Surface [9]. This machine is made of a set of modules each containing several boards. Each board is based on transputers used as processors dedicated to communication and scalar calculations. Vector boards integrate the transputers with Intel i860 chips. Specialized boards for parallel I/O, display elements, etc. can also be added. The Computing Surface has an adjustable node interconnection topology. An additional feature of this machine is the System Supervisor bus. This provides a separate global way of communication allowing a direct control over individual processing elements. The Computing Surface we used was operated by a SUN Sparcstation using CStools [10] as a parallelization tool. CStools (Communication Sequential Tools) supports the programming of multiprocessor applications by structuring the parallel application as a set of sequential programs exchanging data and synchronizing the operations by means of message passing routines. To this end, CStools provides the user with the following types of functionalities: (a) communication services (CSN) which take care of interprocess communications (retransmissions, multiplexing, buffering, etc.) transparently with respect to the actual physical connections of the system which is seen as fully connected and homogeneous; (b) system services (RTE) which provide standard local and remote operating system support to the nodes and processes; (c) configuration tools which make it easier to describe the layout of the parallel application and how the application will be mapped on the hardware; (d) runtime development tools which assist the user in the implementation of parallel applications.

The machine used for implementing the parallel version of RIOS was made of INTEL i860 nodes having a peak speed of 80 Mflops and a 8 Mbyte memory. On this machine, we have been able to run RIOS using 400 sectors and a vibrational basis set of dimension 15 (a dimension more than sufficient in the investigated

energy range). Following a processor farm model, the main process was copied into a computing element (node zero) acting as a *farmer* while the propagation section was copied inside all remaining computing elements acting as *worker* nodes. After feeding at the beginning all the *worker* processors with one l value of the first energy, the *farmer* waits for the first result to return. As soon as a *worker* sends back the result of its calculation, the *farmer* checks for convergency of the cross section with l . In case of convergency, it stops the *workers* and starts a new energy (if there is any left). If convergency has not yet been reached, the *farmer* supplies the *worker* with a new l value to be processed. Speedups measured using the parallel version of the code amount to 1.86, 3.52, 6.02, and 12.5 when using 2, 4, 7, and 16 *worker* processors. Such a high performance allowed us to carry out extensive calculations of the RIOS cross sections of the Li + FH reaction using a fine energy grid (0.001 eV) to compare with time-dependent treatments [11].

Towards Three-Dimensional Approaches

Presently, we are working at building parallel computational procedures able to cope with the problem of determining three-dimensional (3D) quantum cross sections for atom-diatom reactions. To this end, we are proceeding along two different lines. The main line is to extend to higher dimensionality the approach followed here, i.e., single out a reaction coordinate on which carry out an initial value integration of the coupled differential equations obtained after averaging over the remaining coordinates. Details of this type of parallel approaches are given below. The second line consists of exploiting radically different parallel approaches.

As far as the exploitation of potential parallelism of alternative approaches is concerned, in collaboration with G. G. Balint-Kurti two of us compared the performance of parallel implementations of time-independent and time-dependent reduced dimensionality numerical procedures [11]. Presently, reduced dimensionality time-independent approaches, such as that on which the RIOS code is based, seem to be better suited for parallel implementation than time-dependent ones. To find an alternative theoretical approach more naturally leading to strongly decoupled computational procedures, we are following the guidelines given by Fox and collaborators in Ref. [12] for solving wave-function problems. To this end, we have reformulated the Hamiltonian in a way that confines the problem into a finite space and provides a more natural scheme for using regular grids [13].

Progress along the main stream of our research lines seems to be more rewarding in the short term. To this end, we have started to design the restructuring of a three-dimensional quantum reactive scattering program based on the Adiabatically adjusting Principal axes of inertia Hyperspherical (APH) coordinates. This approach [14] takes as a reaction coordinate the hyperradius ρ defined as $\rho^2 = R^2 + r^2$. Remaining APH coordinates are the hyperangles θ and χ defined as

$$\begin{aligned}
\tan \theta &= \frac{[(R^2 - r^2)^2 + 4R^2 \cdot r^2 \cos^2 \Theta]^{1/2}}{2R \cdot r \sin \Theta} \\
\sin(2\chi) &= \frac{2R \cdot r \cos \Theta}{[(R^2 - r^2)^2 + 4R^2 \cdot r^2 \cos^2 \Theta]^{1/2}} \\
\cos(2\chi) &= \frac{R^2 - r^2}{[(R^2 - r^2)^2 + 4R^2 \cdot r^2 \cos^2 \Theta]^{1/2}} \quad (9)
\end{aligned}$$

In the APH approach the scattering matrix elements are obtained by integrating, for all values of the total angular momentum J leading to non-negligible reactivity, the following set of coupled differential equations in ρ .

$$\left[\frac{\partial^2}{\partial \rho^2} + \frac{2\mu E}{\hbar^2} \right] \psi_{i\Lambda}^{Jpn}(\rho) = \frac{2\mu}{\hbar^2} \sum_{i'\Lambda'} \langle \Phi_{i\Lambda}^{Jp} \hat{D}_{\Lambda M}^{Jp} | H_i | \Phi_{i'\Lambda'}^{Jp} \hat{D}_{\Lambda' M'}^{Jp} \rangle \psi_{i'\Lambda'}^{Jpn}(\rho) \quad (10)$$

Equations (10) are the 3D hyperspherical analogous of the RIOS Eqs. (6). In them

$$H_i = T_h + T_r + T_c + V_\rho + V(\rho, \theta, \chi) \quad (11)$$

and

$$T_h = -\frac{\hbar^2}{2\mu\rho^2} \left(\frac{4}{\sin 2\theta} \frac{\partial}{\partial \theta} \sin 2\theta \frac{\partial}{\partial \theta} + \frac{1}{\sin^2 \theta} \frac{\partial^2}{\partial \chi^2} \right) \quad (12)$$

$$T_r = A(\rho, \theta) J_x^2 + B(\rho, \theta) J_y^2 + C(\rho, \theta) J_z^2 \quad (13)$$

$$T_c = -\frac{i\hbar \cos \theta}{\mu\rho^2 \sin 2\theta} J_y \frac{\partial}{\partial \chi} \quad (14)$$

$$V_\rho = \frac{15\hbar^2}{8\mu\rho^2} \quad (15)$$

with $A(\rho, \theta)$, $B(\rho, \theta)$, and $C(\rho, \theta)$ being defined as

$$A(\rho, \theta) = \frac{1}{\mu\rho^2(1 + \sin \theta)} \quad (16)$$

$$B(\rho, \theta) = \frac{1}{2\mu\rho^2 \sin^2 \theta} \quad (17)$$

$$C(\rho, \theta) = \frac{1}{\mu\rho^2(1 - \sin \theta)} \quad (18)$$

The integration of Eqs. (10) is carried out from near zero to a large value of the hyperradius. At large ρ values, the equations are usually reformulated in Jacobi coordinates (at large distance, Jacobi coordinates separate the different reaction channels). As for the RIOS code, the integration along the reaction coordinate is performed by segmenting the ρ interval into several small sectors. What makes the APH approach really differ from the RIOS one is the fact that, within each sector i ,

the fixed total angular momentum J and related projection M global wave function Ψ^{JMpn} is expanded as

$$\Psi^{JMpn} = \sum_{iA} \rho^{-5/2} \psi_{iA}^{Jpn}(\rho) \Phi_{iA}^J(\theta, \chi; \rho_i) \hat{D}_{iA}^{Jp}(\alpha, \beta, \gamma) \quad (19)$$

where $\hat{D}_{iA}^{Jp}(\alpha, \beta, \gamma)$ is the normalized Wigner function in the three Euler angles, ψ is a function of the reaction coordinate ρ while Φ is a function of the two hyperangles chosen to satisfy at a fixed value of the hyperradius, ρ_i , the two-dimensional differential equation

$$[T_h + G\hbar^2 J(J+1) + V_{\rho_i} + (C - G)\hbar^2 \Lambda^2 + V(\theta, \chi; \rho_i) + \varepsilon_{iA}^J(\rho_i)] \Phi_{iA}^J(\theta, \chi; \rho_i) = 0 \quad (20)$$

with $G = (A + B)/2$. The higher dimensionality of Eq. (20) with respect to Eq. (8), makes the memory demand of the 3D method approach much larger than that of RIOS. As a result, to go beyond the memory limits of the previously used machines, we decided to distribute the APH 3D calculations on a cluster of workstations.

To gain experience on how to distribute quantum reactive scattering numerical procedures on clustered workstations, we started by implementing the RIOS program on this type of architectures. In fact, the structure of the RIOS computational procedure is similar to that of APH when an analogy between the DO loop over the collision angle of the former and the DO loop over the total angular momentum of the latter is established.

Software Tools for Parallel Distributed Computing

To pursue our goals, we used two different parallelization software tools aimed at making easier the restructuring and the implementation of computer codes on distributed systems. Some of these tools are of public domain and, therefore, they can be easily obtained in the proper version for a variety of machines. Other tools are commercial products and therefore need to be bought. The tools we used are: PVM [15] (Parallel Virtual Machine) version 2.4.1 and Network Linda 2.5 [16].

PVM is a product developed jointly at the Oak Ridge National Laboratory and at the Emory University. It is available as a source via an anonymous ftp. PVM is based upon a message passing philosophy and is made of a library of primitives. To run PVM a *daemon* must be made active on all the clustered machines. The *daemon* is the execution time support of PVM. The primitives are user interfaces that need to be inserted into the Fortran code to make explicit the parallelism according to the message passing model. A PVM parallel application is based on executable versions of cooperating programs (components) loaded on one or more machines considered as parts of a large virtual machine. The *master daemon* (the first started *daemon*) generates local *daemons* on the machines of the cluster as specified by the configuration file. Local *daemons* take care of creating and managing PVM processes running on the same machine as well as of communicating with the other *daemons*.

With the PVM release we used (more recently PVM has been modified to cope with the problem) the application has to be written in a way that takes care of possible faults. That PVM version, in fact, while providing functions for detecting malfunctioning of the individual components of the virtual machine is unable to restart on a different computer of the cluster an abnormally ended process on a different computer of the cluster. As far as the communication between the different processes is concerned, PVM adopts the one-to-one (point-to-point) and the one-to-many (broadcast) communication procedures without limitations for the size and the number of exchanged messages. When sending a message, the control is returned to the calling process as soon as the buffer can memorize the next message regardless of the state of the receiver. When receiving a message, if the message is nonblocking, the control immediately returns to the calling process with specifications about whether or not the message has been received. On the contrary, for blocking messages, the control is returned to the calling process only after completion of the process.

Linda has been originally designed at the Yale University and is presently commercialized by a private company [17]. Contrary to PVM, Linda has a shared memory approach to the parallelism (even when dealing with distributed memory architectures such as clustered workstations). Linda is based on four simple operations which need to be inserted in the high level language source code to create and execute parallel processes. Linda acts through a common space (*tuple space*) consisting of a series of objects (*tuples*) which are handled by a pattern recognition procedure and accessed through a template. A template and a tuple match only when having: (a) the same number of fields (value and formal fields); (b) the same type of homologous formal fields; (c) the same content for the homologous value fields. A tuple may be passive (data) or active (process). When a process comes to an end, it becomes a passive tuple containing in one field the results generated by the process. There are two ways of generating tuples: one in which the tuple passed as a parameter is evaluated inside the calling process and added to the tuple space, the other in which the evaluation is carried out by a new *ad hoc* generated process while the calling process goes on executing without waiting for the evaluation of the tuple. There are also two operations to read-and-eliminate tuples (each with its nonblocking variant). One of these verifies the correspondence between the template and the tuple. If the tuple satisfies such a correspondence it is eliminated (a random one if there are several). The other read-and-eliminate tuple verifies the correspondence without elimination. The process is stopped if no tuple satisfies the correspondence.

The Code Restructuring for Distributed Computing

Critical features of loosely coupled architectures (such as clustered workstations) are the high latency and the small bandwidth of the communication network. For this reason, only computational tasks needing little (or no) communication can be efficiently distributed on a cluster of workstations. Therefore, whenever possible, several computational tasks should be collected together in the same distributed

process and related communications grouped together. On the contrary, a great advantage of using distributed architectures is, as already mentioned, the possibility of having shorter turnaround times than on centralized time sharing supercomputers thanks to the power of the processor and to the more friendly-to-use environment. For the RIOS code this has led to the choice of including the outermost DO loop in single job calculations.

A first restructuring was inspired to the distribution scheme adopted on shared memory machines, i.e., by adopting a distribution at an inner level. In this case, however, since memory occupation is not a great problem, the distribution was moved from the l to the energy loop. This means that one or more single energy entire DO loop over l is assigned for execution to each individual *worker*. Obviously, such a strategy is successful only when the number of energies to be calculated is large enough (with respect to the number of used processors) to allow a true dynamical assignment of the work by the *farmer* and that enough l values are needed at each energy before reaching convergence. Only in this way can, in fact, a good load balance be achieved. Such a situation was rather infrequent in the past. In fact, as already mentioned, in calculations on centralized supercomputers we could deal, in general, only with a limited number of energies per job. The enhanced processor speed and the possibility of distributing the calculations among different machines without being delayed by a penalizing queue policy, have made it feasible to extend the calculations to many more energies than before while leading to a lower turnaround time. This has made it possible to investigate in detail the energy dependence of several reactions of interest for practical applications.

When implementing the PVM version of the code based on this restructuring strategy, we kept the same processor farm organization adopted for the Meiko Computing Surface. Accordingly, the RIOS code was divided into a *farmer* program MSIOS running on the *master* machine and a *worker* program (SLIOS) running on *slave* machines. The *farmer* program takes care of reading input data and distributing the work among the *workers* which carry out one or more cycles of the energy DO loop. Using PVM, data to be distributed to the *worker* processes can be properly packed and handled as a single message. In PVM language this means that, after the processes have been *enrolled* as PVM *farmer* or *worker* processes, an *fpout* instruction is issued by the MSIOS PVM *master*. This converts the data to be sent to the *worker* SLIOS PVM process into the proper XDR transfer format. Then MSIOS executes also the *fsend* instruction to perform the transfer to SLIOS. On the *worker* side the corresponding operations are *frcv* to collect the data sent by the *farmer* process and *fget* to back-convert them from the XDR format. Similarly, when closing the DO loop after reaching convergence on l , the *worker* transfers the results to the *farmer* process using an *fpout* and an *fsend* instruction which, respectively, convert and return the results. These operations are matched by an *frcv* and an *fget* instruction of the *farmer* to back-transform and collect the results. Since a sending does not inhibit the continuation of the process execution, when *worker* processes deal with more than one energy, single energy results can be returned while next energy is being processed. When the calculations concerning the batch of the assigned

energies is completed, the PVM processes enrolled by *farmer* and *worker* processors are released by executing a *fleave* instruction.

The same processor farm structure was retained also when using Linda. The main difference between PVM and Linda is that the set of instructions used for data transfer in Linda are presented as shared memory operations. As typical of shared memory approaches, the code was organized as a main (MSIOSL) calling, among others, the subroutine SLIOSL embodying the process to be distributed. In analogy with the PVM version, SLIOSL contains DO cycles of the iteration over energy. The main program MSIOSL reads-in the data from the input file and activates the primitive *worker* processes through *eval*. Then the execution of SLIOS and related data are dealt as tuples of a common memory space. The content of the tuple space is shared between the *farmer* and *worker* processes. Communications are implemented by creating, consuming, and reading tuples. More in detail, the *farmer* writes tuples containing data for the calculations in the related space. These are read-in without being consumed by the *worker* processes. The tuples related to fixed energy calculations completed by the *workers* are consumed by the *farmer* at the returning of the results. When a *worker* reads a tuple containing the information about the calculations to be carried out, it consumes that tuple. If more calculations need to be performed it then creates a new tuple containing updated information. When a *worker* finds that there is no more work to be carried out (i.e., when all energies are completed for all angles) it does not create a new tuple. As a result, the *master* finds that the work to be done has been completed and writes a tuple containing the message "ended-job" for all the *workers*. The flexibility of both hardware and software working environments offered us the possibility of experimenting different parallel implementations of the code. Though the work is still in a preliminary stage, speedups of 3.6 and 4.7 were reached when using PVM and Linda, respectively.

Conclusions

In an attempt to produce fast and accurate means of calculating reactive properties of simple molecular systems, we ended up by facing a basic (and, under some aspects, also old) question: how does the evolution of computer technology impact the way chemists design new theoretical approaches and build related computational procedures? Under this respect, in fact, the present evolution of the computer technology is a real challenge for theoretical chemists. In about ten years we have seen the birth and the death of single highly powered processor supercomputers while concurrent processor architectures have grown so fast to make available peak speeds of giga and teraflops. Using resources available at our institutions we followed an itinerary that provides a tentative partial answer to the mentioned question by considering as a case study theoretical approaches to reactive scattering.

We started by implementing the quasiclassical procedure for calculating reactive cross sections of atom-diatom systems since this is the most parallel-oriented computational approach to reactive scattering. For this approach the use of a small memory parallel multicomputer (an nCUBE 2) was found to be appropriate since the application was cpu-intensive. It was not difficult, however, to realize that even

“embarrassingly parallel” problems may lead to poor speedups. We learned that to make full profit from a highly parallel machine the distribution of the work among concurrent nodes has to be carefully designed to avoid conflicts and bottlenecks associated both with the sequential parts of the code and the way of distributing the workload between the *farmer* and the *workers*.

Then we started the implementation of the more accurate quantum codes. This prompted us another question on how far the technology may go without facing the problem of confronting itself with user needs. In fact, while working on finding alternatives to present theoretical approaches (which were developed using single processor technology, i.e., sequential architectures), to carry out present and near-future dynamical investigations we had to implement parallel versions of some of the existing quantum numerical procedures. In general, quantum techniques are based on numerical approaches making use of large matrices whose operations can be parallelized at the price of a significant loss of efficiency. To minimize the loss of efficiency, the node memory has to be large enough to accommodate all the matrices needed by the parallelized section of the code while the considered section has to be self-containing to the extent of requiring little data transfer. For this reason, we moved to a computer architecture having a more modular (less integrated) structure but larger node memories (after all, other conceptually appealing features of innovative architectures had to be dropped in the past when moving from prototypes to commercial machines).

By switching to parallel machines with bigger memories, we have been able to efficiently run parallel versions of the RIOS program without sacrificing the size of the expansion basis set and the number of sectors to be used for the propagation. This was still insufficient for dealing with the accurate 3D quantum approach which needs much larger memories. To this end we have considered the use of a cluster of workstations. For this large (virtual) machine, memory is less a problem since each computing element is a complete computer. This makes it possible to handle the very large matrices usually associated with 3D quantum methods. Obviously, other problems arise when using clustered workstations (faults handling, software and hardware alignment, the slowness of the network, etc.). This makes clustered workstations an unsatisfactory solution for handling reactive scattering calculations. Fortunately, commercially available machines are evolving towards massively parallel architectures having local memories of several hundreds or thousands megabytes. Then, the problem becomes the choice of the right mix of memory size, network bandwidth, and cpu speed which makes a parallel architecture suitable for a particular reactive scattering calculation.

Acknowledgments

Calculations have been performed at the IBM ECSEC (Roma, Italy), at CNUCE (Pisa, Italy), and at the ACS (Milano, Italy). Financial support from CNR (Italy) and NATO (Grant CRG920051) is acknowledged.

References

- [1] QCPE No. 273, Bloomington, IN.
- [2] M. L. Raff and D. L. Thompson, in *Theory of Chemical Reaction Dynamics*, M. Baer, Ed., (CRC Press, Boca Raton, 1985), Vol. III, p. 1.
- [3] nCUBE 2 6400 Series Supercomputers; Technical Overview, NCUBE Corporation, 1989.
- [4] User Handbook, Version P2.1, NCUBE Corporation, 1987.
- [5] R. J. Helliot and C. A. R. Hoare, *Scientific Applications on Multiprocessors*, (Prentice-Hall, New York, 1989); D. J. Pritchard and C. R. Askew, D. B. Carpenter, I. Glendinning, A. J. G. Hey, and D. A. Nicole, "Practical Parallelism Using Transputer Arrays" in *Lecture Notes in Computer Science*, (Springer-Verlag, Berlin, 1987), p. 258.
- [6] A. Laganà, G. Ochoa de Aspuru Berriozabal, X. Gimenez, J. M. Lucas, and A. Aguilar, *Quasiclassical versus quantum isotope effects in Li + FH*, VII European workshop on Molecular Spectroscopy and Photon-induced Dynamics, Maratea, Italy, 1993; A. Laganà, G. Ochoa de Aspuru Berriozabal, X. Gimenez, J. M. Lucas, and A. Aguilar, *Threshold effects and reaction barrier in the Li + FH reaction and its isotopic variants*, J. Chem. Phys., submitted.
- [7] E. Garcia, L. Ciccarelli, and A. Laganà, *Theor. Chim. Acta*, **72**, 253 (1987); A. Laganà, E. Garcia, and O. Gervasi, J. Chem. Phys. **89**, 7238 (1988); E. Garcia, O. Gervasi, and A. Laganà, in "Approximate Quantum Techniques for Atom Diatom Reactions" in *Supercomputer Algorithms for Reactivity, Dynamics and Kinetics of Small Molecules*, A. Laganà, Ed. (Reidel, Dordrecht, 1989).
- [8] A. Laganà, O. Gervasi, R. Baraglia, and D. Laforenza, "Vector and Parallel Restructuring for Approximate Quantum Reactive Scattering Computer Codes" in *High Performance Computing*, J. L. Delahyes and E. Gelenbe, Eds. (North Holland, Amsterdam, 1989).
- [9] Hardware Reference Manual, Meiko, 1989.
- [10] CStools Reference Manual, Meiko, 1989.
- [11] G. G. Balint-Kurti, F. Gögtas, S. P. Mort, A. R. Offer, A. Laganà, and O. Gervasi, J. Chem. Phys. **99**, 9567 (1993).
- [12] G. C. Fox, M. A. Johnson, G. A. Lyzenga, S. W. Otto, J. K. Salmon, and D. W. Walker, *Solving Problems on Concurrent Processors* (Prentice-Hall International Inc., London, 1988).
- [13] E. Garcia and A. Laganà, *Mol. Phys.* **56**, 621 (1985); (b) *ibid.*, **56**, 629 (1985); A. Laganà, G. Ferraro, E. Garcia, O. Gervasi, and A. Ottavi, *Chem. Phys.* **168**, 341 (1992); A. Laganà, R. Cambi, P. Spatola, and G. Ferraro, *Bond Order Approaches to Some Spectroscopy and Scattering Problems* (Molec X, Salamanca, Spain, 1994).
- [14] R. T. Pack and G. A. Parker, J. Chem. Phys. **87**, 3888 (1987).
- [15] V. S. Sunderam, *Concurrency: Practice and experience* **2**(4), 315 (1990); G. A. Geist and V. S. Sunderam, *Concurrency: Practice and experience* **4**(4), 293 (1992); A. Beguelin, J. Dongarra, G. A. Geist, R. Manchek, and V. S. Sunderam, *A user's guide to PVM Parallel Virtual Machine* (Oak Ridge National Laboratory, TN, 1992).
- [16] N. Carriero and D. Gelenter, *How to Write a Parallel Program: A Guide to the Perplexed* in *ACM Computer Surveys* **21**(3), 323 (1989).
- [17] Scientific Computing Associated.

Received March 23, 1994

The Calculation of Feshbach Resonances Using Coupled Propagator Equations

HONGBIN ZHAN, YINCHUN ZHANG, and PETER WINKLER

Department of Physics, University of Nevada, Reno, Nevada 89557

Abstract

A coupled channel theory of resonances has been formulated within the propagator approach of many-body theory and applied to the $1s3s^2$ resonance of e -helium scattering. This system has previously been studied both experimentally and theoretically. Our results for the width of the resonance agree well with these earlier findings. © 1994 John Wiley & Sons, Inc.

Introduction

The interest in propagator approaches to the calculation of atomic and molecular properties has increased in recent years due to highly sophisticated approaches for the computation of the fundamental operators of the theory. Among them, the construction of the self-energy operator through fourth order of many-body perturbation theory [1] and of superoperators partially through fourth order [2,3], and the numerical implementation of self-energy operators complete in third order [4] deserve particular mention. Another strong motivation for renewed interest in propagator approaches may be attributed to the ease using the propagator concept of developing physical intuition when the theory is represented in terms of Feynman diagrams. While most existing propagator calculations evaluate bound-state properties of atomic systems, the application of the Green function concept to scattering problems—after isolated early work [5,6] and noteworthy progress in electron-molecule scattering [7,8]—is relatively unexplored. The present work is the extension of a theoretical approach formulated in an earlier publication [9] and contains the first numerical application of the coupled propagator method to Feshbach resonances.

Although this study focusses on width calculations for electron scattering resonances when more than one decay channel is open, the approach evaluates also resonance energies as the discussion of our results in the fourth section will show. In the framework of Green function theory, the presence of several decay channels requires the introduction of nondiagonal self-energy operators and has to our knowledge not been addressed before in a numerical study.

Until recently the major method of solving for poles of the resolvent operator $(\epsilon - H)^{-1}$ which correspond to resonances was the Feshbach method [10,11]. Following the work of Balslev, Aguilar, and Combes [12,13], however, there has

been considerable activity in using the alternative method of dilatation transformations [14–24]. At the same time it has been shown [25,26] that Siegert's resonance theory [27] can be set up directly as a well-behaved, complex matrix eigenvalue problem. In the framework of both the dilatation transformation approach and the direct Siegert method, the problem of solving for the complex energy can be reduced to a problem of diagonalizing matrices the structure of which is similar to those encountered in configuration interaction solutions for normal bound-state eigenvalues. The complex nature of the approach, however, requires computationally more demanding variational criteria which have been addressed in a recent paper [28].

Review of the Siegert Method

The central equation of the propagator approach with or without resonance boundary conditions is Dyson's nonrelativistic pseudo-eigenvalue equation

$$[\mathcal{E}_n(\varepsilon) - \mathcal{L}(\varepsilon)]\Phi_n(r, \varepsilon) = 0 \quad (1)$$

with Layzer's operator [29]

$$\mathcal{L}(\varepsilon) = -\frac{1}{2}\nabla^2 + V + \Sigma(\varepsilon) \quad (2)$$

which contains an energy independent one-electron part V including the Hartree-Fock contribution (for Feshbach resonances preferably in a V^{N-1} representation) and an integral operator

$$\Sigma(\varepsilon)\Phi(r, \varepsilon) = \int d^3r' \Sigma(r, r'; \varepsilon)\Phi(r', \varepsilon) \quad (3)$$

which describes the effects of the many-electron background in principle accurately. The eigenvalues $\mathcal{E}_n(\varepsilon = \mathcal{E}_n)$, i.e., taken at values of the energy input parameter ε which coincide with one of the calculated eigenvalues, correspond to energy differences $\mp\{\mathcal{E}_0(N) - \mathcal{E}_n(N \pm 1)\}$ and may be identified with electron affinities and ionization potentials, respectively, if real valued, and with the energies of electron scattering and Auger resonances, respectively, if complex valued. In simple cases with not more than one decay channel open, the imaginary parts of the energy are related to resonance widths Γ_n by the usual relation

$$\text{Im } \mathcal{E}_n = -\frac{1}{2}i\Gamma_n \quad (4)$$

This equivalence holds also above the first excitation threshold of the remaining atom: The $1s3s^2$ state of the negative helium ion, as an example, can decay into continua associated with the $1s^2$ and the $1s2s$ and $1s2p$ states of the helium atom. Since the excited states of the target occur either as spin singlets or triplets, there are five open continua to be considered. In such cases, the imaginary part of the energy is then related to the total width of the compound state.

In the single-channel direct Siegert approach the complex eigenmatrix $(\mathcal{E} - \mathcal{L})$ to be diagonalized is set up in a basis of self-consistently obtained orbitals in the V^{N-1} representation plus one Siegert orbital of the form

$$k(r) = f(r)r^{-1}\exp[i(Kr + \frac{1}{2}\pi l)]Y_{lm}(\Omega) \times \text{spin function} \quad (5)$$

with $\mathcal{I}mK < 0$. Here $f(r)$ is a cutoff function, e.g., $[1 - \exp(-\beta r)]^{l+1}$, required for potentials which are singular at the origin. During the iterative calculation the complex exponent K of the Siegert orbital has to be determined such that $\mathcal{E}_n = \epsilon = \frac{1}{2}K^2$ for the resonance to be evaluated. This is the self-consistency condition.

The form of the matrix to be diagonalized in the Siegert method with just one channel open is given by

$$\begin{pmatrix} \langle k | \mathcal{A}(\epsilon) | k \rangle & \cdots & \langle k | \mathcal{B}(\epsilon) | \beta \rangle & \cdots \\ \cdots & \cdots & \cdots & \cdots \\ \langle \alpha | \mathcal{B}(\epsilon) | k \rangle & \cdots & \langle \alpha | \mathcal{B}(\epsilon) | \beta \rangle & \cdots \end{pmatrix} \quad (6)$$

with

$$\mathcal{B}(\epsilon) = \frac{1}{2}K^2 - \mathcal{L}(\epsilon) \quad (7)$$

and

$$\langle k | \mathcal{A}(\epsilon) | k \rangle = -\frac{1}{2} \langle k | \{ d[\ln f(r)]/dr \}^2 | k \rangle - \langle k | V_f(\epsilon) | k \rangle. \quad (8)$$

The latter matrix element derives originally also from the operator $\mathcal{B}(\epsilon)$ given in Eq. (7) but has all potentially divergent contributions cancelled out from the start. Here V_f stands for the finite range parts of all the potentials. All divergent terms in the matrix solution of Dyson's equation cancel exactly once self-consistency has been achieved. The explicit cancellation above does neither affect the final solution nor the iterative process to obtain the final solution.

The Case of Two Open Channels

The formalism described so far yields the complex energy of a two-particle-one-hole (2p1h) state in the case of a Feshbach resonance and a 2h1p state in the case of an Auger type resonance. In both cases, it has been assumed that the metastable state undergoes autoionization to the ground state as the only possible decay mode and that radiative decay can be ignored. Above the first excitation threshold of the target system, however, there are other decay channels available and we face the complexity of a multichannel problem. As we focus here primarily on width calculations, we use an approximate version of the self-energy operator introduced by other groups [30], which is of sufficiently simple structure to present the method without unwieldy formalism. To compare our calculated widths to previous experimental and theoretical results, we apply the method to the helium atom, although larger atoms are feasible and even better candidates for applications of many-body theory.

For illustration purposes we restrict our presentation here to a fictitious case of two interacting decay channels. This is adequate for the present example if we disregard temporarily the existence of the 1s2p excited target state as well as triplet configurations of the 1s2s and 1s2p of the target. In reality, the 1s3s² state of helium has five distinct decay channels which are all coupled together. For the excited

states 1s2s and 1s2p of the target, we have included both singlet and triplet symmetries. This has been done, however, in an energetically degenerate approximation, so that the problem can be set up as one of two interacting s-wave channels and one p-wave channel. The calculated widths are little affected by small variances in the energy.

With only two open decay channels (distinguished by superscripts 0 and 1) the coupled equations which replace Eq. (1) take on the following form:

$$\begin{aligned} \{\mathcal{E}_0(\epsilon) - [-\frac{1}{2}\nabla^2 + V]\} \Phi_0(r, \epsilon) - \int \Sigma^{[0,0]}(r, r'; \epsilon) \Phi_0(r', \epsilon) d^3r' \\ = \int \Sigma^{[0,1]}(r, r'; \epsilon) \Phi_1(r', \epsilon) d^3r' \quad (9) \end{aligned}$$

and

$$\begin{aligned} \{\mathcal{E}_0(\epsilon) - [-\frac{1}{2}\nabla^2 + V + \lambda]\} \Phi_1(r, \epsilon) - \int \Sigma^{[1,1]}(r, r'; \epsilon) \Phi_1(r', \epsilon) d^3r' \\ = \int \Sigma^{[1,0]}(r, r'; \epsilon) \Phi_0(r', \epsilon) d^3r' \quad (10) \end{aligned}$$

In the second equation we have added and subtracted the first excitation energy λ of the target realizing that $\mathcal{E}_0(\epsilon) = \frac{1}{2}k_1^2 + \lambda$. The potential V , which is part of both equations, contains the Hartree-Fock potential *corresponding to the ground state of the target*. While this is appropriate for the first equation, it is not so for the second. The first two terms of $\Sigma^{[1,1]}$ —explicitly given in Eq. (12)—contain the necessary modification for *an excited reference state*. The remaining terms of $\Sigma^{[1,1]}$ describe correlation and polarization of the compound system in the intermediate state. In the following it is assumed that the excited configuration is specified by a hole v in the valence shell with the corresponding electron promoted to the orbital t .

If the functions Φ are represented as a linear superposition of basis orbitals, the problem can be solved as a complex matrix eigenvalue problem. This is the approach taken here in solving the coupled propagator equations. In particular, the matrix elements of the self-energy operators $\Sigma^{[\sigma, \sigma']}$ (here with σ, σ' either 0 or 1) are given below. We use the abbreviated form $\langle ab | cd \rangle$ for the antisymmetrized two-electron matrix elements of the Coulomb interaction.

$$\Sigma_{\alpha\alpha'}^{[0,0]} = \frac{1}{2} \sum_{hh'p} \frac{\langle \alpha p | hh' \rangle \langle hh' | \alpha' p \rangle}{\epsilon + \epsilon_p - \epsilon_h - \epsilon_{h'}} + \frac{1}{2} \sum_{pp'} \frac{\langle \alpha v | pp' \rangle \langle pp' | \alpha' v \rangle}{\epsilon + \epsilon_v - \epsilon_p - \epsilon_{p'} - S_{pp'}}, \quad (11)$$

$$\begin{aligned} \Sigma_{\alpha\alpha'}^{[1,1]} = \Delta_{\alpha\alpha'}^{[1]} + \sum_{h \neq v; p \neq t} \frac{\langle h\alpha | \alpha' p \rangle}{\epsilon_h - \epsilon_p} \Delta_{ph}^{[1]} + \frac{1}{2} \sum_{p \neq t; h, h' \neq v} \frac{\langle \alpha p | hh' \rangle \langle hh' | \alpha' p \rangle}{(\epsilon - \lambda) + \epsilon_p - \epsilon_h - \epsilon_{h'}} \\ + \frac{1}{2} \sum_{p, p' \neq t; h \neq v}^{+t} \frac{\langle \alpha t | pp' \rangle \langle pp' | \alpha' t \rangle}{(\epsilon - \lambda) + \epsilon_t - \epsilon_p - \epsilon_{p'} - S_{pp'}} \quad (12) \end{aligned}$$

and

$$\Sigma_{\alpha\alpha'}^{[0,1]} = \Sigma_{\alpha'\alpha}^{[1,0]} = \frac{1}{2} \sum_{p'p} \frac{\langle \alpha t | | pp' \rangle \langle pp' | | \alpha' v \rangle}{(\epsilon - \lambda) + \epsilon_t - \epsilon_p - \epsilon_{p'} - S_{pp'}} + \sum_{p \neq t} \frac{\langle \alpha t | | \alpha' p \rangle}{\epsilon_p - \epsilon_v} \Delta_{pv}^{[1]}. \quad (13)$$

In these equations the operator $\Delta^{[1]}$ expresses the difference between the self-energy operator for the excited target state and that for the ground state as a reference configuration. It is defined as

$$\Delta^{[1]} \equiv \sum_{l \neq v}^{+t} \langle l | | l \rangle - \sum_l^{\text{occ}} \langle l | | l \rangle = \langle t | | t \rangle - \langle v | | v \rangle \quad (14)$$

with *nonvanishing* matrix elements $\Delta_{ab}^{[1]}$. The first of these sums runs over all orbitals occupied in the HF ground state *minus the v th one plus the initially unoccupied orbital t* . The term $S_{pp'}$ indicates a shift of the energy denominators corresponding to repeated interactions of the two excited (active) electrons. In the V^{N-1} representation the particle-hole ladders have been included *in zeroth order*, and we are left with the summation of just the particle-particle ladders

$$S_{pp'} = \frac{1}{2} \langle pp' | | pp' \rangle. \quad (15)$$

The factor $\frac{1}{2}$ has been introduced to simulate the effect of nondiagonal ladder terms according to a procedure suggested by Born and Öhrn [30]. The exact inclusion of nondiagonal ladder sums in a multichannel approach requires substantially more computational effort. It turns out that the ladder correction affects the energy substantially only when the active electrons are both in the same n l -orbital.

Calculation and Results

The first step in our calculation is a Hartree-Fock-Roothaan calculation with respect to the ground state of the helium atom. We have in the past studied various forms of analytic basis sets which in the present problem have both to represent bound electron states and to approximate the continuum orbitals within a reasonably extended region about the origin. The Slater type basis used in the present study is the one used by Doll and Reinhardt [31] in their landmark study of Green function theory applied to atoms. This basis has been augmented by two s and p orbitals each to better represent the outer region.

The prominent role of the continuum orbitals in resonance calculations warrants the computation of initially unoccupied orbitals in the V^{N-1} representation. While in general we have to distinguish between different such choices, for two electron systems the only possibility corresponds to the removal of one $1s$ electron. The present approach assumes a single hole in the valence shell also for heavier atoms or ions. The corresponding Fock operator is then given by

$$\mathcal{F} = -\frac{1}{2} \nabla^2 - Z/r + 2\mathcal{J}_v - \mathcal{K}_v \quad (16)$$

with the familiar definition of the direct and exchange operators \mathcal{J} and \mathcal{K} .

The effect of this particular V^{N-1} representation is to calculate the virtual electron orbitals in the field of only $N - 1$ electrons as opposed to the rather unphysical mean field provided by the N electrons of Hartree-Fock theory. Although the resulting orbital energies ϵ_{nl} in zeroth order are not expected to be really close to experimental values, the corresponding orbitals are at least bound and require therefore less correction from higher-order terms of many-body perturbation theory. With a basis of seven s-, five p-, and two d-orbitals, we obtain three bound orbitals of s-symmetry and one each of p- and d-symmetry.

With this real basis we routinely evaluate an approximate real value of the resonance energy by evaluating the diagrams given in Figure 1. The analytic continuation to the complex energy plane is then being performed by adding two complex-valued Siegert orbitals to the real basis of Slater type orbitals. As in our previous work, we choose the form of the complex orbitals as

$$\Phi_{K_j}(r) = [1 - \exp(-\beta_j r)]^{l+1} \exp(iK_j - i\pi l/2) \quad (17)$$

where the subscripts $j = 0, 1$ now distinguish between the two interacting s-continua associated with the decays $1s[(3s)^2 {}^1S] \rightarrow 1s[(1sK_0s) {}^1S]$ and $1s[(3s)^2 {}^1S] \rightarrow 1s[(2sK_1s) {}^1S]$, respectively. The decay $1s[(3s)^2 {}^1S] \rightarrow 1s[(2pKp) {}^1S]$ contributes to the width of the resonance as well. In fact, it is by far the biggest contribution as will be discussed below.

The first factor on the right-hand side of Eq. (17) is a cutoff function to regularize the Siegert orbital at the origin. Its form is arbitrary except that experience has shown that the chosen form is simple enough to allow for analytic evaluation of integrals containing the Siegert orbital and that its use leads to very reasonable results. A complete basis set for the expansion of the interior region would not be affected by the choice of the cutoff factor. In connection with a less than complete basis set, however, one expects some dependence of the results on the particular choice. We have studied this dependence by varying the exponent β and found that there is always a reasonably wide range for β within which the calculated width remains almost constant. This interval ranges from $\beta = 10$ to 200. The results for the real part of the energy are even less affected by the cutoff function.

For the transition $1s[(3s)^2 {}^1S] \rightarrow 1s[(2pKp) {}^1S]$ a similar stability with respect to the cut-off exponent has been found. The cutoff procedure seems to be an un-critical one.

The structure of the matrix operator to be diagonalized when two interacting continua are present is given as

$$\begin{pmatrix} \mathcal{E}_0(\epsilon) - [-\frac{1}{2}\nabla^2 + V] - \hat{\Sigma}^{[0,0]} & -\hat{\Sigma}^{[0,1]} \\ -\hat{\Sigma}^{[1,0]} & \mathcal{E}_0(\epsilon) - [-\frac{1}{2}\nabla^2 + V - \lambda_1] - \hat{\Sigma}^{[1,1]} \end{pmatrix} \quad (18)$$

Here each entry indicates a matrix of the type given in Eq. (6).

The final result for the total width of the $1s(3s)^2$ resonance has been determined to be $\Gamma = 25.33$ meV. This compares reasonably well to the experimental values of $\Gamma = 36$ meV of Brunt et al. [32] and $\Gamma = 32.5$ meV of Andrick [33], as well as to Nesbet's early calculation [34] of $\Gamma = 25.2$ meV. We have to remember that the

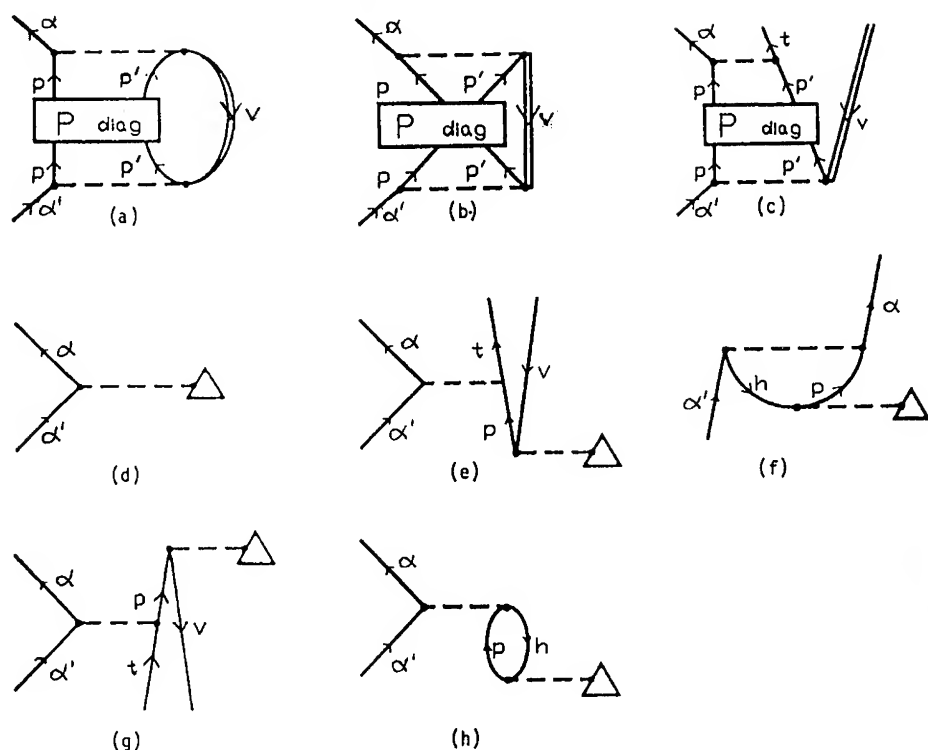


Figure 1. The diagrams included in the present work and corresponding to terms in Eqs. (11)–(13). Diagrams (a) and (b) correspond to the direct and exchange contributions of the elastic channel in V^{N-1} representation. In the case that the system is initially in the excited state the sums over the intermediate states are restricted as explicitly given in the formulae of Eqs. (12) and (13). The boxes symbolize the contribution from the diagonal ladder sum [Eq. (15)] and the double-stroke fermion lines indicate renormalized hole energies: In V^{N-1} representation the infinite sums of particle–hole interactions are taken into account in zeroth order which decouples the hole lines from the rest of the diagrams. In order to improve the energy denominators, it is justified to replace the Hartree–Fock orbital energy by a higher order approximation, e.g., the hole energy of the present Green function calculation. Because in the present work the energy is of small concern, we do not emphasize this particular point and use Hartree–Fock values for all occupied orbital energies. Diagram (c) is the direct diagram corresponding to an inelastic scattering event. The corresponding exchange diagram has the same topology with the upper labels p and p' interchanged. The terms (e) and (g) have to be included to obtain consistency through second order. Diagrams (d)–(h) affect the change in reference state which is roughly equivalent to the familiar Δ SCF method. The corresponding potential is symbolized by $\Delta^{(1)}$ and is defined by Eq. (14).

basis employed in this study is minimal. But given the small size of the basis set and the approximations, the results of this study are encouraging because the numerical results exhibit a high degree of computational stability. In particular, the long-standing problem of finding zero eigenvalues of the Dyson equation close to

the zeroes of the denominators of the self-energy operator seems to have disappeared since we use the Simplex algorithm AMOEBA [35] instead of the more conventional Newton–Raphson approach.

Our result for the total width consists of the combined contributions of the decays leading to the interacting s-continua $\Gamma_{1s+2s} = 7.13$ meV and with the contribution from the p-channel included $\Gamma_{1s+2s+2p} = 25.33$ meV. It is interesting to turn off the channel interaction between the s-channels in Eqs. (9) and (10). The partial widths of the individual contributions then are $\Gamma_{1s} = 2.8$ meV for the transition to $1s[(1sk_0s) {}^1S]$ and $\Gamma_{2s} = 1.5$ meV for the transition to $1s[(2sk_1s) {}^1S]$. The sum of these contributions is noticeably different from the value for Γ_{1s+2s} given above. This result demonstrates the increased accuracy of the solution functions Φ_{K_0} and Φ_{K_1} in the coupled approach as opposed to the solutions in the uncoupled case.

The calculated real part of the energy is 22.53 eV which compares reasonably well to the experimental result [32] of (22.45 ± 0.02) eV.

Discussion

The aim of the direct Siegert method is to calculate a decaying state as if it were stationary. In order to achieve this goal, an analytic continuation onto the complex energy plane has to be performed. This has been done here by augmenting a localized basis set of exponentially decreasing functions with functions that satisfy the asymptotic resonance boundary condition [27]. As this boundary condition depends on the complex eigenenergy of the decaying state, an iterative computation is required. This iterative procedure is an integral part of the Green function method even in calculations of real-valued ionization potentials. The main additional complication in resonance calculations is the need to search the complex plane for poles of the propagator. In practice, this is being done by varying the complex wave number K of the Siegert orbital until self-consistency has been achieved.

Acknowledgments

The authors would like to dedicate this contribution to Professor Yngve Öhrn on the occasion of his sixtieth birthday and in appreciation of his pioneering work in the field of propagator methods in physics and chemistry. Work supported by the Division of Chemical Sciences, Office of Basic Energy Sciences, Office of Energy Research, U.S. Department of Energy.

Note Added in Proof

After submission of the manuscript we extended the present calculation to fully include the coupling of intermediate states in which two p-electrons are coupled to zero orbital angular momentum. This extension yields an improved width of $\Gamma = 33.01$ meV, which is in almost perfect agreement with the experimental data referred to in the manuscript.

Bibliography

- [1] J. Schirmer, L. S. Cederbaum, and O. Walter, Phys. Rev. A **28**, 1237 (1983).
- [2] J. V. Ortiz, J. Chem. Phys. **89**, 6348 (1988).

- [3] J. V. Ortiz, Int. J. Quantum Chem. Quantum Chem. Symp. **S23**, 321 (1989).
- [4] O. Walther and J. Schirmer, J. Phys. B: Atom. Molec. Phys. **14**, 3805 (1981).
- [5] B. Schneider, H. S. Taylor, and R. Yaris, Phys. Rev. **A1**, 855 (1970).
- [6] G. Csanak, H. S. Taylor, and R. Yaris, Phys. Rev. **A3**, 1322 (1971).
- [7] M. Berman, O. Walter, and L. S. Cederbaum, Phys. Rev. Lett. **50**, 1979 (1983).
- [8] H.-D. Meyer, J. Phys. B: Atom. Molec. Phys. **21**, 3777 (1988).
- [9] P. Winkler, Int. J. Quantum Chem. Quantum Chem. Symp. **S19**, 201 (1986).
- [10] H. Feshbach, Ann. Phys. **5**, 357 (1958).
- [11] H. Feshbach, Ann. Phys. **19**, 287 (1962).
- [12] E. Balslev and J. M. Combes, Commun. Math. Phys. **22**, 280 (1971).
- [13] J. Aguilar and J. M. Combes, Commun. Math. Phys. **22**, 269 (1979).
- [14] B. Simon, Ann. Math. **97**, 247 (1973).
- [15] G. D. Doolen, J. Phys. B: Atom. Molec. Phys. **8**, 525 (1975).
- [16] R. Yaris and P. Winkler, J. Phys. B: Atom. Molec. Phys. **11**, 1475 (1978).
- [17] P. Winkler and R. Yaris, J. Phys. B: Atom. Molec. Phys. **11**, 1481 (1978).
- [18] P. Winkler and R. Yaris, J. Phys. B: Atom. Molec. Phys. **11**, 4257 (1978).
- [19] N. Moiseyev, P. R. Certain, and F. Weinhold, Mol. Phys. **36**, 1613 (1978).
- [20] C. W. McCurdy and T. N. Rescigno, Phys. Rev. **A20**, 234 (1979).
- [21] C. W. McCurdy, in *Electron-Molecule and Photon-Molecule Collisions*, T. N. Rescigno, V. McKoy, and B. Schneider, Eds. (Plenum, New York, 1979).
- [22] W. P. Reinhardt, Ann. Rev. Phys. Chem. **33**, 223 (1982).
- [23] M. Mishra, O. Goscinsky, and Y. Öhrn, J. Chem. **79**, 5494 (1983).
- [24] M. Mishra, O. Goscinsky, and Y. Öhrn, J. Chem. **79**, 5505 (1983).
- [25] A. D. Isaacson, C. W. McCurdy, and W. H. Miller, Chem. Phys. **34**, 311 (1978).
- [26] R. Yaris, R. Lovett, and P. Winkler, Chem. Phys. **43**, 29 (1979).
- [27] A. J. F. Siegert, Phys. Rev. **56**, 750-52 (1939).
- [28] A. J. Layzer, Phys. Rev. **129**, 897 (1963).
- [29] P. Winkler, in *AIP Conference Proceedings No. 260* (American Institute of Physics, College Park, MD, 1992), p. 72.
- [30] G. Born and Y. Öhrn, Chem. Phys. Lett. **61**, 307 (1979).
- [31] J. D. Doll and W. P. Reinhardt, J. Chem. Phys. **57**, 1169 (1972).
- [32] J. N. H. Brunt, G. C. King, and F. H. Read, J. Phys. B: Atom. Molec. Phys. **10**, 433 (1977).
- [33] D. Andrick, J. Phys. B: Atom. Molec. Phys. **12**, L175 (1979).
- [34] R. K. Nesbet, J. Phys. B: Atom. Molec. Phys. **11**, L21 (1978).
- [35] W. H. Press, B. P. Flannery, S. A. Teukolsky, and W. T. Vetterling, *Numerical Recipes* (Cambridge University Press, Cambridge 1989).

Received April 7, 1994

Isotope Effects in Laser-Induced Multiphoton Molecular Dynamics

OSMAN ATABEK

Laboratoire de Photophysique Moléculaire, Bât. 213, Université Paris-Sud, 91405 Orsay, France

Abstract

Optical nonlinearities affecting absorption spectra, above threshold dissociation, bond softening, and vibrational trapping are among the most important processes that have so far been examined when describing the dynamics of multiphoton excitation and fragmentation of molecular systems subject to intense laser fields. The relative merits of time-dependent and independent approaches are overviewed and discussed within the framework of H_2^+ photodissociation for which recent experimental data are available. Isotopes $\text{H}_2^+ - \text{D}_2^+$ behave in a markedly different manner with respect to the radiative coupling. Some of these differences are exploited for the detailed understanding of the underlying mechanism of the bond softening process. It is shown that this is not merely a single photon potential barrier lowering mechanism as has previously been invoked, but a competition between this mechanism and another five photon exchange mechanism, namely the simultaneous absorption of three photons followed by the subsequent emission of two photons. As for the vibrational trapping process, the relative sensitivity of the isotopes to the laser characteristics is such that, by adequately adjusting the wavelength and the intensity, one can suppress the fragmentation of one of the isotopes by locally confining it, whereas the other dissociates very fast. This is used as a possible scheme for isotope separation using intense lasers.

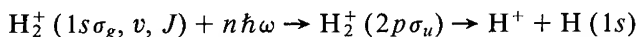
© 1994 John Wiley & Sons, Inc.

Introduction

The technological possibility to reach large radiation field strengths and recent advances in high-intensity experiments and above-threshold ionization of atoms [1] have oriented renewed interest in the strong laser induced multiphoton dissociation dynamics (MPD) of small polyatomics [2,3]. Optical nonlinearities and important distortions in absorption lineshapes have experimentally been observed, for field intensities exceeding 10^{10} W/cm^2 [2]. At higher intensities even more intriguing is the rise of equally spaced multiple peaks in the fragments kinetic-energy distribution spectra, corresponding to the absorption of several photons [4]. Situations where more than one photon are simultaneously absorbed, although the energy carried by one of them may be enough for the fragmentation to occur, are depicted and termed above-threshold dissociation (ATD) [3,5]. Following the excitation process, subsequent stimulated absorption and emission mechanisms may take place during the fragmentation itself, leading to product distributions carrying information on the cumulative history of the overall dynamics. Photofragments

with low kinetic energy may be very abundant in strong fields due to the breaking of their velocity by a kind of bremsstrahlung effect resulting from a photon emission [3]. The interplay between the multiphoton excitation step and radiative processes taking place in MPD reveals two notable intense-field phenomena: (i) the chemical bond can be "softened" (bond softening BS) by the laser-induced lowering of some potential energy barriers leading to efficient photodissociation of low-lying vibrational levels [4,6]; (ii) in contrast to the low-lying states which become less and less stable, for some specific frequencies and intensities the lifetimes of high-lying resonances may increase and consequently the molecular bond may be harder to break. The laser is confining the molecule in a finite region of the phase space inducing thus a stabilization and a population trapping which have been termed vibrational trapping VT [7,8] or bond hardening [9b].

Molecular hydrogen ion represents the model system for these studies mainly because of its simple and known structure, involving within the Born–Oppenheimer approximation, two electronic states well separated from the higher excited electronic manifold. The ground and dissociative states which describe the molecular dissociation process:



correspond to $(1s\sigma_g)^2\Sigma_g^+$ and $(2p\sigma_u)^2\Sigma_u^+$, respectively [10].

Isotopes (H_2^+ , D_2^+) show quite different behaviors with respect to strong radiative couplings, leading to barrier lowerings or trappings which monitor the aforementioned multiphoton bond softening or hardening mechanisms. They have experimentally been addressed by Yang et al. [11] who measured different ATD branching ratios for H_2^+ and D_2^+ over a wide range of laser parameters ($8 \cdot 10^{11}$ to $4 \cdot 10^{13}$ W/cm² for 532 and 527 nm wavelengths and 50 ps to 10 ns pulses). Their results showing, in particular, a higher two-versus one-photon dissociation ratio for the heavier isotope, are in qualitative agreement with the BS model.

The present article is devoted to a detailed understanding of the bond softening and vibrational trapping mechanisms taking place during the dissociation of H_2^+ and its isotope D_2^+ when subjected to intense continuous-wave cw lasers (10^8 – 10^{14} W/cm²). More precisely, concerning BS studied at the resonant three-photon absorption at 329.7 nm wavelength, it is shown how the different behaviors of the isotopes may enlighten the discussion concerning the competition between two possible fragmentation pathways, i.e., a single photon tunneling process through a potential barrier lowering mechanism, or a five-photon process resulting from an excitation by three-photon absorption followed by two subsequent photon emissions [12–14]. As for the VT mechanism, an application aiming to isotope separation in the $\text{H}_2^+ - \text{D}_2^+$ system is proposed. This is actually based on laser-induced quasi-bound states that can suppress the photodissociation of one of the isotopes whereas the other has still a large dissociation rate. Such states, the existence of which has previously been evidenced [15], can be reached by appropriately adjusting laser parameters (wavelength within the range 95 to 120 nm corresponding to a leading single-photon absorption and intensities of the order of 10^{13} W/cm²). The next

section gives a general overview of the theoretical models commonly used in this context. BS and VT processes with their underlying mechanisms referring to isotope effects are discussed in the third and fourth sections, respectively.

Theoretical Models

A considerable amount of theoretical effort has recently been devoted to H_2^+ dissociation in strong laser fields, which can conceptually be viewed within two different frames. The first is a time-dependent approach [16]. It offers a thorough physical picture of a time-resolved MPD basically driven by an intense electromagnetic field which, practically, can only be achieved using short laser pulses. One has to calculate the time evolution of a wave packet, under the action of a time-dependent Hamiltonian $H(t)$. The Schrödinger equation governing this evolution is:

$$i\hbar \frac{d}{dt} \begin{bmatrix} \psi_g(R,t) \\ \psi_u(R,t) \end{bmatrix} = H(t) \begin{bmatrix} \psi_g(R,t) \\ \psi_u(R,t) \end{bmatrix} \quad (1)$$

where R designates the dissociative nuclear coordinate. ψ_g and ψ_u are the wave-packet components on the ground g and excited u states which are radiatively coupled. The Hamiltonian, in the Born–Oppenheimer approximation, is written as:

$$H(t) = \begin{bmatrix} -1/2 \frac{d^2}{dR^2} + V_g(R) & -\mu(R)\mathcal{E}(t) \\ -\mu(R)\mathcal{E}(t) & -1/2 \frac{d^2}{dR^2} + V_u(R) \end{bmatrix} \quad (2)$$

$V_g(R)$ and $V_u(R)$ are the corresponding potential energies and $\mu(R)$ the electronic transition dipole moment. In the absence of any field, the ion is supposed to be at the $v = 0$ vibrational level of its ground state g . The electromagnetic field amplitude $\mathcal{E}(t)$ is given as a product of a time-dependent shape function $\varepsilon(t)$ by a real cosine form, with peak frequency ω :

$$\mathcal{E}(t) = \varepsilon(t) \cos \omega t \quad (3)$$

A variety of techniques have been used to solve [Eq. (1)] among which wave-packet propagations by repeated application of short time propagators in the split operator form [16,17]; wave operator theory within Bloch formalism [6,13] or adiabatic time evolution [18]. The sensitivity of the results with respect to the pulse shape has extensively been studied [13,18] in particular for an accurate determination of the total number n of photons taking part in an ATD or BS mechanism ending up with a net absorption of p photons [13]. An additional advantage of the finite duration of the radiative interaction is that difficulties related with the use of the length or velocity gauges [3] can simply be relaxed. We have however to point out that the possible presence of long-lived resonances inducing the local trapping

of the wave packet (as in VT for instance) or merely its spreading, render time-dependent calculations unefficient and prohibitively long.

A Floquet expansion of the molecule-plus-field Hamiltonian, valid for pulses long enough to lead to near periodic laser fields, results into a time-independent approach. The main advantage of this approach is the interpretative tool it provides, in terms of the stationary field-dressed adiabatic molecular states which have so far been the basis for the understanding of the underlying molecular bond models [3,9]. We have to emphasize that the Floquet analysis we are referring to, becomes exact, only within the assumption of a cw laser, for which:

$$\mathcal{E}(t) = \varepsilon_o \cos \omega t \quad (4)$$

The Hamiltonian [Eq. (2)] being time-periodic, Floquet's theory states that the solution for a given energy E can be expanded as:

$$\Psi_\ell(R, t) = e^{-iEt/\hbar} \sum_m e^{im\omega t} \phi_{\ell, m}(R) \quad (5)$$

with $\ell = g$ or u . ϕ 's are the unknown nuclear functions. By substitution of [Eq. (5)] into [Eq. (1)], one gets:

$$\sum_m e^{im\omega t} \left\{ \left[-\frac{1}{2} \frac{d^2}{dR^2} + V_\ell(R) + m\hbar\omega - E \right] \phi_{\ell, m}(R) - \frac{1}{2} \mu(R) \varepsilon_o [e^{i\omega t} + e^{-i\omega t}] \phi_{\ell' \neq \ell, m}(R) \right\} = 0 \quad (6)$$

After multiplication by $e^{-in\omega t}$, followed by a time integration over a finite interval T , and making use of the identity:

$$\frac{1}{T} \int_0^T e^{-in\omega t} e^{im\omega t} dt = \delta_{nm} \quad (7)$$

a system of time-independent close coupled equations results:

$$\left[-\frac{1}{2} \frac{d^2}{dR^2} + V_\ell(R) + n\hbar\omega - E \right] \phi_{\ell, n}(R) = \frac{1}{2} \mu(R) \varepsilon_o [\phi_{\ell' \neq \ell, n-1}(R) + \phi_{\ell' \neq \ell, n+1}(R)] \quad (8)$$

The network of diabatic potentials of the dressed molecule is indicated in Figure 1, where each electron-field channel is labeled by a pair of indices (g or u for the electronic part together with the specification of the photon number n). It is precisely this curve-crossing model or its adiabatic representation, where the interchannel coupling is diagonalized (see Fig. 1), which supports the understanding of potential barrier lowerings or adiabatic channel closings, at the origin of the BS and VT mechanisms.

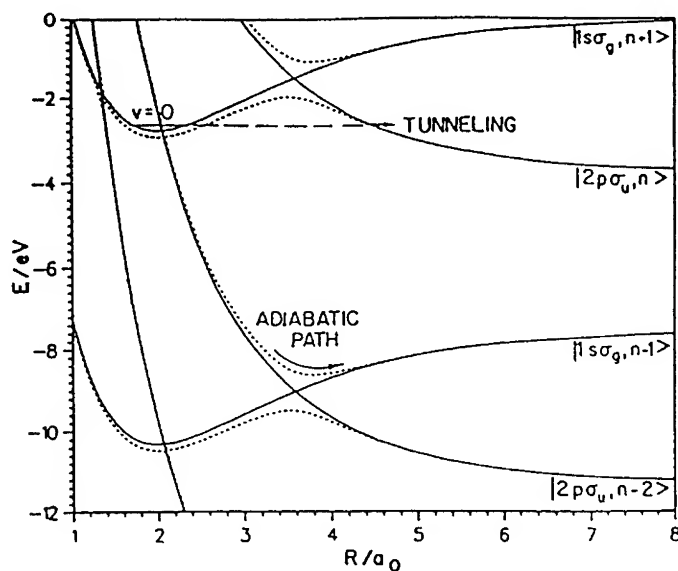


Figure 1. Potential energy curves of H_2^+ dressed by a cw-laser of 329.7 nm wavelength and of intensity $1.4 \times 10^{13} \text{ W/cm}^2$. The solid lines correspond to the diabatic channels. The dotted lines represent the adiabatic curves resulting from the diagonalization of the radiative interaction.

For moderate field intensities and in cases where radiative couplings are localized at curve crossing regions a semiclassical approximation* may be assumed as a simple interpretative tool for the relative probabilities of photon absorption or emission processes. More precisely the Landau-Zener probability W_{ij}^{LZ} for a transition between *diabatic* channels *i* and *j* is given by [19]:

$$W_{ij}^{LZ} = 1 - \exp(-\pi v_{ij}^{LZ}) \quad (9)$$

with the Landau-Zener parameter [7a]:

$$v_{ij}^{LZ} = \frac{2V_{ij}^2}{\hbar v |\Delta F_{ij}|} = 1.662 \cdot 10^{-11} \frac{\mathcal{M}^{1/2} \mu^2 I}{\Delta E^{1/2} |\Delta F_{ij}|} \quad (10)$$

where V_{ij} and v are the coupling (radiative in the present case) and the classical velocity at the crossing point R_c . \mathcal{M} is the reduced mass in a.m.u., μ in a.u., I the field intensity in W/cm^2 , ΔE the scattering energy in cm^{-1} measured from the energy at the crossing point position, and ΔF_{ij} the difference of slopes in $\text{cm}^{-1}/\text{\AA}$ of the diabatic potentials at their crossing. This formula shows in particular that the diabatic transition probability from *g* to *u* at their crossing position (see Fig. 1

* Throughout this article "quantal" or "semiclassical" apply only to the molecule, the field being always introduced classically.

at $R_c \sim 3.5$ a.u.) is increasing with the laser intensity. In other words, the adiabatic path (leading to a photon emission when going from channel $|2p\sigma_u, n-2\rangle$ to channel $|1s\sigma_g, n-1\rangle$) is favored for higher intensities or, at a given intensity, for the heaviest isotope.

The semiclassical theory has also been invoked for supporting the interpretation of the VT mechanism [20] by the presence of a field-induced upper closed adiabatic potential (as in Fig. 2) where the wave packet can be trapped [8]. The existence of quasi-bond levels (or infinitely long-lived resonances) in curve crossing situations has first been pointed out by Bandrauk and Child in semiclassical electronic predissociation models, where, *accidentally*, a bound level supported by the attractive upper adiabatic potential coincides with a vibrational level supported by the closed diabatic potential [15]. When the curve crossing problem results from radiatively coupled field-dressed molecular states, coincidences may be obtained at will by just properly adjusting the laser wavelength (i.e., the relative energy positioning of the potentials) and intensity (i.e., the strength of the coupling). More precisely, a resonance of zero width results from the semiclassical evaluation of the poles of the scattering matrix when a diabatic level of turning points a_- and b_+ is close to an adiabatic level of turning points a_+ and b_+ (all turning points being associated with adiabatic potentials V_- and V_+) [15,21]. The destructive interference which results can be interpreted [22] using Child's diagrammatic method [23] given as an inset of Figure 2. The lines with the arrows indicate the adiabatic channel JWKB wave functions and the rectangular boxes designate the splitting and mixing operations

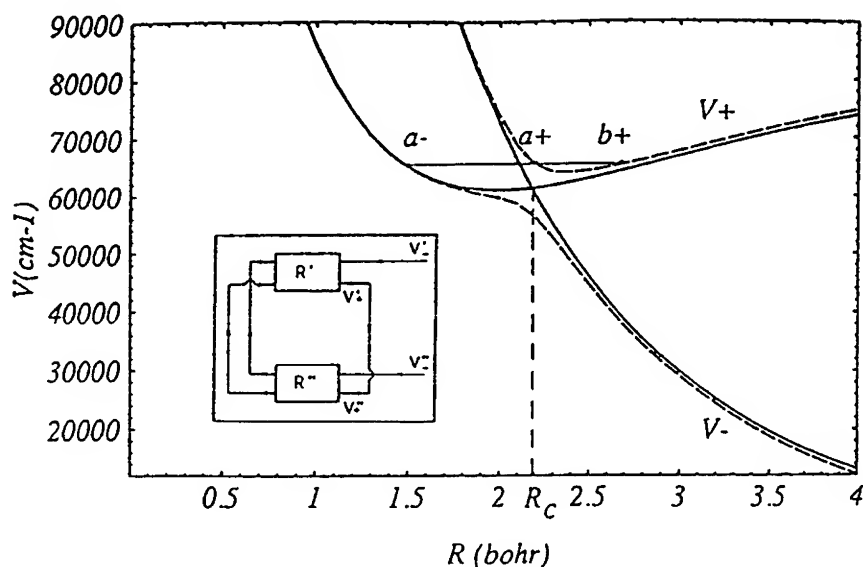


Figure 2. Same as for Figure 1 for a cw laser of 120 nm wavelength and of intensity 1.25×10^{13} W/cm². The corresponding Child's diagram is shown as an inset.

undergone by the wavelets at the crossing position R_c . The Gamow-Siegert resonance criterion imposes a zero incoming amplitude in the open channel V_- , i.e. $V_-'' = 0$. The corresponding outgoing amplitude V_-' results from an infinite summation of elementary steps each representing reflections of the wavelets at the left (a_+ and a_-) and right (b_+) turning points and their mixing around R_c . For such an elementary step, an amplitude \tilde{V}'_+ deposited in channel V_+ at R_c , undergoes a unique reflection at b_+ , followed by reflections at a_{\pm} after a channel mixing at R_c , and results into an outgoing amplitude \tilde{V}'_- [19b,21]:

$$\tilde{V}'_- = -\lambda(1 - \lambda^2)^{1/2} e^{-i\chi} [e^{2i(\alpha_+ + \beta_+ + \chi)} - e^{2i(\alpha_- + \beta_+)}] \tilde{V}'_+ \quad (11)$$

where λ and the phase correction factor χ are given in terms of a real valued parameter ν [19b,21]:

$$\lambda = \exp(-\pi\nu) \quad (12)$$

and

$$\chi = \arg \Gamma(i\nu) - \nu \ln \nu + \pi/4 \quad (13)$$

For weak field situations or constant (i.e., R -independent) radiative couplings, ν is merely the Landau-Zener parameter given by [Eq. (10)]. It is also to be noticed that χ varies from $-\pi/4$ in the weak field limit, to 0 in the strong field limit [22]. Other energy-dependent phase factors building up [Eq. (11)] are:

$$\alpha_{\pm}(E) = \int_{a_{\pm}}^{R_c} k_{\pm}(R) dR; \quad \beta_+(E) = \int_{R_c}^{b_+} k_+(R) dR \quad (14)$$

where

$$k_{\pm}(R) = \frac{\sqrt{2\mathcal{M}}}{\hbar} [E - V_{\pm}(R)]^{1/2} \quad (15)$$

Actually, the width of the resonance being given by [22,24]:

$$\Gamma = \frac{\hbar^2}{2\mathcal{M}} k_- |V'_-|^2 \quad (16)$$

a quasi-bound state of infinite lifetime corresponds to a vanishing outgoing amplitude V'_- in the open channel. This can be obtained if all elementary steps contribute a null amplitude \tilde{V}'_- , by cancellation of the sum of exponentials in [Eq. (11)] or by fulfilling the following conditions:

$$\alpha_+(E) + \beta_+(E) + \chi = (v_+ + 1/2)\pi \quad (17a)$$

$$\alpha_-(E) + \beta_+(E) = (v_- + 1/2)\pi \quad (17b)$$

with integer values for v_+ and v_- . These conditions are close to state that the energy E is that of a vibrational bound state of the adiabatic potential $V_+(R)$ [Eq. 17(a)]

of the ground diabatic potential [Eq. 17(b)]. The position E_r and the width of the resonance as resulting from the semiclassical analysis are [19b,21]:

$$E_r = (E_{v_2} + ux E_{v_+}) / (1 + ux) \quad (18)$$

$$\Gamma = \pi ux(1 + ux^2)(E_{v_2} - E_{v_+})^2 / [\hbar \omega_2(1 + ux)^3] \quad (19)$$

where

$$u = \lambda^{-2} - 1 \quad (20)$$

and

$$x = \omega_2 / \omega_+ \quad (21)$$

ω_2 and ω_+ being the local energy spacings. Equations (18) and (19) give the lowest order formula in terms of the energy differences involved, indicating that a coincidence between the v_+ adiabatic level (of energy E_{v_+}) and the v_2 diabatic level (of energy E_{v_2}) leads to a laser-induced quasi-bound state monitoring the suppression of dissociation by a VT mechanism in the $V_+(R)$ closed diabatic channel.

The time-independent quantum version of the theory presents, however, some difficulties in relation with the so-called persistent effects arising in the case of a homonuclear ion characterized by a spatially diverging dipole moment. The diabatic channels remain coupled at infinite R , in the electric-field gauge $\mu \mathcal{E}$ producing thus a nonstandard scattering situation: observables related to asymptotically well-behaved noninteracting free fragments cannot be defined. The adiabatic representation transfers the persistent effects into nonadiabatic couplings which remain local, allowing thus a proper description of the free fragments, but introduces additional kinetic terms in Eq. (8) [25]. It has very recently been shown how the complex rotation of the coordinate R circumvent these difficulties leading to an accurate treatment of the close-coupled equations [Eq. (8)] even with diverging interchannel couplings [26]. Another limitation is the proper description of the preparation step. In very strong field situations, leading to resonance overlappings, the correspondence between the field-free initial molecular state and laser-induced resonances is hazardous. An elegant technique is the so-called artificial channel [12]. The treatment is a generalization of Shapiro's work [27] and refers to two artificial channels: the first open artificial channel aiming to transform the otherwise half-collision situation into a full collision and the second closed artificial channel being the true initial unperturbed (field-free) molecular state. A summation over field induced resonances (including cases of overlapping) is carried out in an indirect way, from the scattering amplitude between the artificial entrance channel and the final physical continuum.

The outcome of these calculations are the total and partial dissociation rates or reaction probabilities (i.e., branching ratios) to reach fragmentation channels describing the net absorption of a given number of photons. They are obtained either by an asymptotic flow analysis of the wave-packet components on the different electronic states in the time-dependent version, or by solving the close-coupled system of the time-independent version. In the stationary approach the total rate

results from the quantized complex energy eigenvalue of the resonance as its imaginary part [9a] and the obtention of the partial widths is based on a complex-energy probability-flux analysis [26] or on the evaluation of appropriate matrix elements of the scattering operator of the artificial full collisional model [12].

Although rotational effects have already been discussed by McCann and Bandrauk [28], in calculations to be presented hereafter we are using a J-conserving approximation, as has often been done in previous works [8]. Such an approximation may be relaxed by including an expansion in a reasonably complete set of rotational states in the time-independent version or by an appropriate angle-dependent propagator in the time-dependent approach [29].

Isotope Effects in Bond Softening

Calculations are done for the $\text{H}_2^+ - \text{D}_2^+$ system, for several field values covering the range from weak ($I = 10^8 \text{ W/cm}^2$) up to very strong ($I = 10^{14} \text{ W/cm}^2$) intensities for the laser wavelength of $\lambda = 329.7 \text{ nm}$ which corresponds to an energetically favorable vertical three-photon transition from the bound ($1s\sigma_g, v = 0, j = 1$) to the continuum ($2p\sigma_u$) state. Time-independent models referring either to complex quantization of the complex scaled Hamiltonian [26] or artificial channel technique [12] give results which are in close agreement, when convergence is reached with respect to the number of Floquet blocks. In addition, time-dependent wave-packet calculations with a pulsed laser, also lead to qualitatively comparable informations [6]. The results obtained for a cw laser acting on H_2^+ are displayed in Figure 3. Four regimes are depicted with respect to the intensity:

(i) For low intensities ($I < 10^{10} \text{ W/cm}^2$) a single photon absorption mechanism prevails, as is expected from Fermi golden rule. Although the total dissociation rate Γ remains very low ($< 10^{-9} \text{ cm}^{-1}$) due to very weak radiative couplings or inefficient tunneling between $|1s\sigma_g, n+1\rangle$ and $|2p\sigma_u, n\rangle$ a local intensity power law ($\Gamma \propto I^{n^*}$), as displayed in the inset of Figure 3, gives, in conformity with a linear regime, a plateau value at $n^* = 1$.

(ii) For intermediate intensities ($I = 10^{10} \text{ W/cm}^2 - 10^{12} \text{ W/cm}^2$) the dissociation basically proceeds through the absorption of three photons, i.e., through channel $|2p\sigma_u, n-2\rangle$ with a dissociation rate Γ reaching ca. 10^{-5} cm^{-1} . The three-photon partial width is dominating over the single-photon width, with only a moderate contribution from the two-photon one. This corresponds to an ATD regime with the appearance of another plateau value for the power law at $n^* = 3$.

(iii) For high intensities ($I = 10^{12} \text{ W/cm}^2 - 10^{13} \text{ W/cm}^2$) there is a competition between the three- and two-photon partial widths. This can be envisioned in terms of partial fluxes along the adiabatic path of Figure 1. Following the simultaneous absorption of three photons ($|1s\sigma_g, n+1\rangle \rightarrow |2p\sigma_u, n-2\rangle$) one photon is subsequently emitted during the dissociation process itself and the system ends up in channel $|1s\sigma_g, n-1\rangle$ with a net amount of two absorbed photons. The power law remains with a plateau at $n^* = 3$ and the total rate approaches $\Gamma \simeq 10^{-2} \text{ cm}^{-1}$.

(iv) For very high intensities ($I > 10^{13} \text{ W/cm}^2$) surprisingly the one-photon partial width is increasing very fast with rather high total dissociation rates (Γ of

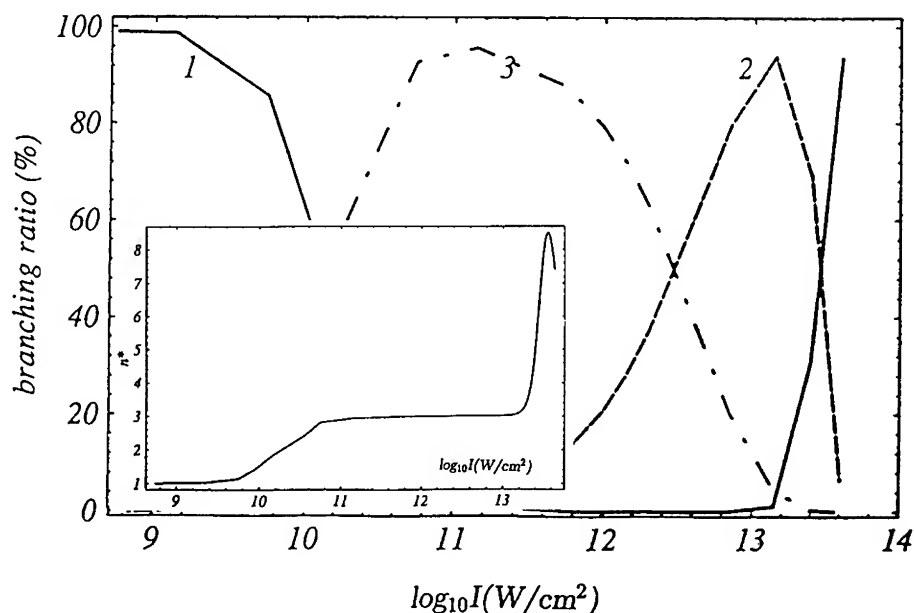


Figure 3. Branching ratios (%) accounting for the net absorption process of one (solid line), two (dashed line), or three (dotted-dashed line) photons as a function of intensity.

The corresponding power law n^* as a function of intensity is given as an inset.

the order of several cm^{-1}). The laser-induced deformation of the molecular force field is so large that the system fragments efficiently through the BS mechanism. There is no integer n^* which satisfies the power law. This means that, if the power law is to be related to the Born expansion of the transition operator: $T = V + VG_oV + VG_oVG_oV + \dots$ (G_o being the resolvent) in terms of powers of the radiative coupling V , there is no leading term ensuring the convergence of the series. The understanding of the underlying mechanism is still an open question.

An early interpretation emphasizes the net single-photon mechanism by very important lowering and flattening of the adiabatic potential barrier at the avoided curve crossing occurring between $|1s\sigma_g, n+1\rangle$ and $|2p\sigma_u, n\rangle$ channels, leading to fragmentation by tunneling (cf. Fig. 1) [5,6,12]. More recently, it has also been noted that another five-photon mechanism, namely the initial absorption of three photons followed by the emission of two photons, may compete with the previous mechanism. Although, due to this possible competition, there is no plateau at $n^* = 1$ or $n^* = 5$ for the total dissociation rate, the interpretation of spectral widths obtained from time-dependent calculations support the five-photon mechanism [13]. It is worthwhile to point out that a closer inspection of the way in which the isotope substitution affects the dissociation branching ratios may give additional information concerning the inherent mechanisms [14].

A measure of the efficiency of the dissociation via three-photon versus two-photon channels (or two-photon versus one-photon) is the ratio $R_{32} = P_3/P_2$ (or $R_{21} = P_2/P_1$) of the partial widths corresponding to dissociation with a net absorption of one (P_1), two (P_2) or three photons (P_3). Figure 4 displays their values as a function of the field intensity and for the two isotopes. As has previously been stated, it is clear from [Eq. (9)] that the heavier isotope D_2^+ with less velocity behaves more adiabatically, i.e., realizes in a more efficient way the diabatic jump, than the lighter H_2^+ . For intermediate and high intensity regimes, where the fragmentation process is monitored by the three- and two-photon crossing channels, the $|2p\sigma_u, n-2\rangle \rightarrow |1s\sigma_g, n-1\rangle$ diabatic transition is favored for the heavier isotope. The results are in conformity with the LZ model, i.e.: $R_{32}(H_2^+) > R_{32}(D_2^+)$. For very high intensities, the branching ratio P_3 toward the three-photon dissociation channel remains negligible and it is the ratio R_{21} of the two- to the one-photon channel which is significant for the discussion. The results displayed in Figure 4, namely $R_{21}(H_2^+) > R_{21}(D_2^+)$, cannot be interpreted in terms of a net single photon absorption process by a tunneling through an adiabatic potential barrier. This mechanism would favor the light H_2^+ , which in addition experiences a lower barrier (smaller mass, higher vibrational frequency), leading to $R_{21}(H_2^+) < R_{21}(D_2^+)$.

Conversely, a coherent five-photon interpretation within the LZ model can be retained, referring to three steps: (i) an initial three-photon absorption between indirectly coupled diabatic channels $|1s\sigma_g, n+1\rangle$ and $|2p\sigma_u, n-2\rangle$ at the avoided crossing position $R \simeq 2$ a.u. (cf. Fig. 1); (ii) a first photon emission at $R \simeq 3.5$ a.u. at the position of the second curve crossing between radiatively coupled channels

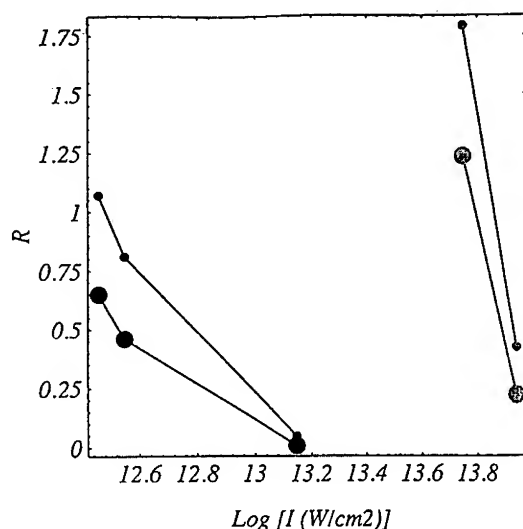


Figure 4. Ratio of the partial widths ($R_{ij} = P_i/P_j$) as a function of the field intensity. Small dark circles for $R_{32}(H_2^+)$; large dark circles for $R_{32}(D_2^+)$, small light circles for $R_{21}(H_2^+)$, and large light circles for $R_{21}(D_2^+)$.

$|2p\sigma_u, n-2\rangle$ and $|1s\sigma_g, n-1\rangle$; (iii) a subsequent second photon emission leading to a transition from the diabatic channel $|1s\sigma_g, n-1\rangle$ to $|2p\sigma_u, n\rangle$ (but without curve crossing). For the first two steps the transition probability is larger for the heavier isotope D_2^+ . Although the LZ formula cannot directly be transposed for the last step, one can presumably argue that the heavier isotope is again favored for this transition, namely because of its lower velocity, such that actually D_2^+ is exposed to the radiative field for a longer time than H_2^+ , resulting, finally, into $R_{21}(H_2^+) > R_{21}(D_2^+)$. We have thus given an additional proof to the fact that the BS mechanism cannot merely be interpreted as a field-dressed barrier lowering described by a single photon exchange. One has rather to consider a competition between this single and the aforementioned five-photon mechanisms.

Isotope Separation Using Vibrational Trapping

An important and interesting feature concerning the diabatic-adiabatic level coincidences, which are at the origin of the vibrational trapping mechanism, as depicted by [Eq. (19)], is their great sensitivity with respect to the laser and molecular characteristics. In particular, a coincidence obtained for a given molecule-plus-field system does not hold when one proceeds to an isotopic substitution. A very efficient D_2^+ versus H_2^+ isotope separation technique results, using an intense laser field ($I \approx 10^{13}$ W/cm²) to stabilize D_2^+ while dissociating H_2^+ .

The semiclassical theory [Eqs. (11)–(21)], apart from providing an interpretative approach for the VT mechanism, can also be invoked to adjust, at least approximately, the laser parameters (wavelength and intensity) so as to guide exact quantum calculations. These are done by solving the close-coupled equations of the time-independent Floquet Hamiltonian [Eq. (8)] and by imposing the Gamow–Siegert end-point conditions within the frame of the complex rotation of the coordinate [30]. The two laser wavelengths we are considering, namely $\lambda = 120$ nm and $\lambda = 95$ nm, illustrate two distinct curve-crossing situations: c^+ (i.e., crossing at the right of the equilibrium position) and c^- (i.e., crossing at the left of the equilibrium position) type of dissociation, respectively. In addition, both wavelengths, being close to the maximum of the absorption lineshape of H_2^+ ($\lambda \approx 115$ nm), even for the relatively strong fields which are used, validate the rotating wave approximation (RWA) in its time-independent quantal and semiclassical versions. The results are displayed in Figure 5.

Using a semiclassical approach the first occurrence, for D_2^+ , of a diabatic-adiabatic level coincidence is $v_2 = 2$, $v_+ = 0$ for $\lambda = 120$ nm, at $I = 1.25 \cdot 10^{13}$ W/cm², or $v_2 = 1$, $v_+ = 0$ for $\lambda = 95$ nm but with a stronger field of I ca. $2.81 \cdot 10^{13}$ W/cm². The semiclassically estimated critical field intensities leading to coincidences do not differ by more than 15% when calculated by using either $\chi = 0$ or χ given by the LZ approximation [Eq. (10) implemented in Eq. (13)]. The upper panels [(a) and (c)] of Figure 5, display, on an enlarged scale, the variations of the resonance width in the vicinity of the critical intensities for D_2^+ as resulting from semiclassical [Eq. (19)], quantal within RWA (one Floquet block) and multi-Floquet blocks

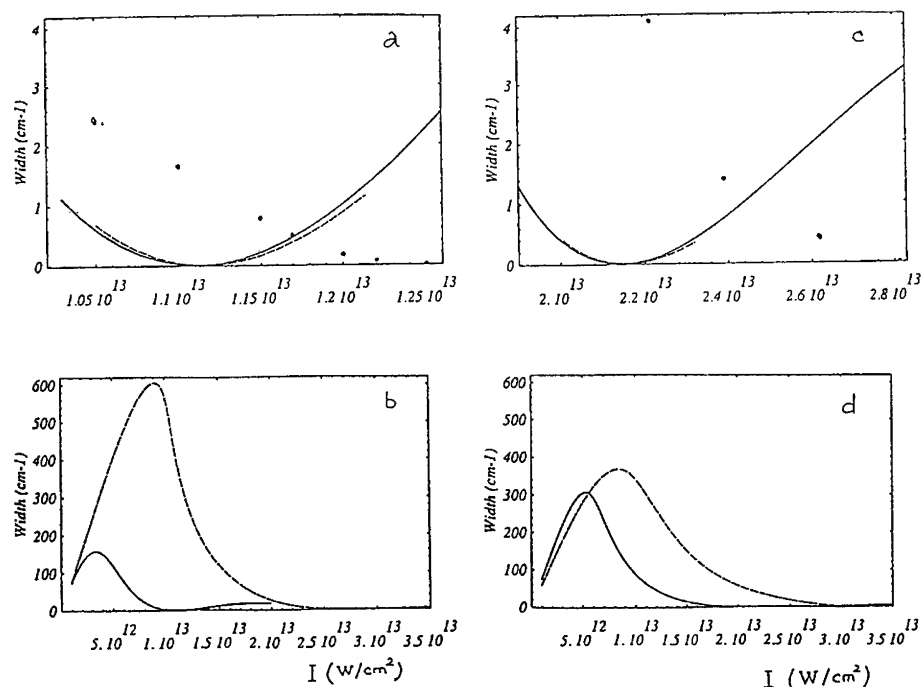


Figure 5. The resonance width (in cm^{-1}) as a function of the laser intensity (in W/cm^2). Panels (a) and (b) correspond to $v_2 = 2$ and $\lambda = 120$ nm. D_2^+ dissociation in the vicinity of the critical intensity is depicted in panel (a) where dots are for the semiclassical approximation; solid line for the single Floquet block approximation and the dashed line for converged quantal calculations. In panel (b) the solid line is for the D_2^+ dissociation rate; the dashed line for the H_2^+ dissociation rate. Panels (c) and (d) are the same as (a) and (b), respectively, but referred to the $v_2 = 1$ resonance for $\lambda = 95$ nm.

converged quantal [Eq. (8)] calculations [20]. The semiclassical approach systematically leads to vanishing widths for larger intensities as compared with the quantal approaches, the differences remain, however, reasonably small. RWA turns out to be valid, when compared with the exact converged quantal calculation, for both wavelengths, clearly supporting that for these wavelengths (close to the top of the one-photon absorption lineshape), the reference Floquet block is the one responsible for the suppression of the dissociation. The lower pannels [(b) and (d)] of Figure 5 compare the intensity dependence of the widths of D_2^+ and H_2^+ on a wider scale. The following points can be raised:

(i) A linear regime for the behavior of the widths with respect to the intensity is observed in the weak field regime ($I < 10^{12} \text{ W}/\text{cm}^2$). For $\lambda = 120$ nm, the dissociation rate of H_2^+ dominates over that of D_2^+ , while a reverse situation is depicted for $\lambda = 95$ nm.

(ii) Optical nonlinearities appear for stronger fields as has been discussed previously [9a]. The dissociation rate reaches a maximum value at $I \simeq 4 \times 10^{12}$ W/cm² for D₂⁺ and $I \simeq 10^{13}$ W/cm² for H₂⁺, at $\lambda = 120$ nm. The corresponding values at $\lambda = 95$ nm are slightly higher, i.e., $I \simeq 6 \times 10^{12}$ W/cm² for D₂⁺ and $I \simeq 1.1 \times 10^{13}$ W/cm² for H₂⁺.

(iii) An overall decrease towards zero for both D₂⁺ and H₂⁺ and for both wavelengths dominates the strong field regime. The most important information is that the zero minima of D₂⁺ correspond, for both wavelengths, to a rather large width of H₂⁺, namely $\Gamma \simeq 600$ cm⁻¹ (for $\lambda = 120$ nm) and $\Gamma \simeq 100$ cm⁻¹ (for $\lambda = 95$ nm). This clearly shows that one can proceed to a specific choice for a laser wavelength and intensity such that D₂⁺ dissociation may completely be suppressed, whereas for the same field H₂⁺ is still dissociating fast. We have thus evidenced the possibility of an isotope separation based on a VT mechanism. Great efficiency is expected for properly prepared initial vibrational states of a rotation-free isotope interacting with a cw laser.

Recent calculations [31,32] show, however, that multiple rotational excitation dominates at three-photon avoided crossings and even partly destroys the stabilization [33]. Isotope effects are thus basically sensitive for single photon VT mechanism (i.e., the frame of the present work). For the wavelengths under consideration and for moderately strong fields, the relative importance of rotational excitation seems to contribute to the *yield* but not to the *efficiency* of the isotope separation scheme [20].

Bibliography

- [1] R. R. Freeman and P. H. Bucksbaum, J. Phys. **B24**, 325 (1991); A. D. Bandrauk and S. C. Wallace, Eds., Coherence Phenomena in Atoms and Molecules in Laser Fields, NATO ASI, vol. B287 (Plenum Press, 1992).
- [2] C. Cornaggia, D. Normand, J. Morellec, G. Mainfray, and C. Manus, Phys. Rev. **A34**, 207 (1986).
- [3] A. Giusti-Suzor, X. He, O. Atabek, and F. H. Mies, Phys. Rev. Lett. **64**, 515 (1990).
- [4] P. H. Bucksbaum, A. Zavriyev, H. G. Muller, and D. W. Schumacher, Phys. Rev. Lett. **64**, 1883 (1990).
- [5] A. D. Bandrauk, E. Constant, and J. M. Gauthier, J. Phys. II, France **1**, 1033 (1991); A. D. Bandrauk, E. Aubanel, and J. M. Gauthier, Laser Physics **3**, 381 (1993).
- [6] G. Jolicard and O. Atabek, Phys. Rev. **A46**, 5845 (1992).
- [7] (a) A. D. Bandrauk and M. L. Sink, J. Chem. Phys. **74**, 1110 (1981); (b) A. D. Bandrauk and G. Turcotte, J. Chem. Phys. **77**, 3867 (1982).
- [8] A. Giusti-Suzor and F. H. Mies, Phys. Rev. Lett. **68**, 3869 (1992).
- [9] (a) X. He, O. Atabek, and A. Giusti-Suzor, Phys. Rev. **A38**, 5586 (1988); *ibid*, Phys. Rev. **A42**, 1585 (1990); S. I. Chu, J. Chem. Phys. **94**, 7901 (1991); (b) G. Yao and S. I. Chu, Chem. Phys. Lett. **197**, 413 (1992); *ibid*, Phys. Rev. **A48**, 485 (1993).
- [10] F. V. Bunkin and I. I. Tugov, Phys. Rev. **A8**, 601 (1973).
- [11] B. Yang, M. Saeed, L. F. DiMauro, A. Zavriyev, and P. H. Bucksbaum, Phys. Rev. **A44**, R1458 (1991).
- [12] S. Miret-Artes, O. Atabek, and A. D. Bandrauk, Phys. Rev. **A45**, 8056 (1992).
- [13] O. Atabek and G. Jolicard, Phys. Rev. **A49**, 1186 (1994).
- [14] S. Miret-Artes and O. Atabek, Phys. Rev. **A49**, 1502 (1994).
- [15] A. D. Bandrauk and M. S. Child, Mol. Phys. **19**, 95 (1970).

- [16] D. Kosloff and R. Kosloff, *J. Comput. Phys.* **52**, 35 (1983); R. Kosloff, *J. Phys. Chem.* **92**, 2087 (1988); R. W. Heather, *Comput. Phys. Commun.* **63**, 446 (1991); R. W. Heather and F. H. Mies, *Phys. Rev.* **A44**, 7560 (1991).
- [17] A. D. Bandrauk and H. Shien, *Chem. Phys. Lett.* **176**, 428 (1991).
- [18] T. T. Nguyen Dang, *J. Chem. Phys.* **90**, 2657 (1989); H. Abou-Rachid, T. T. Nguyen Dang, R. K. Chaudhury, and X. He, *J. Chem. Phys.* **97**, 5497 (1992).
- [19] (a) L. D. Landau and E. M. Lifshitz, *Quantum Mechanics* (Pergamon, New York, 1965); (b) M. S. Child, *Semiclassical Mechanics with Molecular Applications* (Oxford University Press, New York, 1991), pp. 62–63.
- [20] O. Atabek, M. Chrysos, and R. Lefebvre, *Phys. Rev.* **A49**, R8 (1994).
- [21] A. D. Bandrauk and O. Atabek, *J. Phys. Chem.* **91**, 6469 (1987).
- [22] R. Lefebvre, in *Half Collision Resonance Phenomena in Molecules AIP Conference Proceedings* 225, Eds. M. Garcia-Sucre, G. Raseev, and S. C. Ross, Eds. (Caracas, 1990), pp. 175–193.
- [23] M. S. Child, *J. Mol. Spectrosc.* **53**, 280 (1974).
- [24] M. Chrysos and R. Lefebvre, *J. Phys.* **B26**, 2627 (1993).
- [25] T. T. Nguyen Dang, S. Durocher, and O. Atabek, *Chem. Phys.* **129**, 451 (1989).
- [26] M. Chrysos, O. Atabek, and R. Lefebvre, *Phys. Rev.* **A48**, 3845 (1993); *ibid*, 2855 (1993).
- [27] M. Shapiro, *J. Chem. Phys.* **56**, 2582 (1972).
- [28] J. F. McCann and A. D. Bandrauk, *Phys. Rev.* **A42**, 2806 (1990); *ibid*, *J. Chem. Phys.* **96**, 903 (1992).
- [29] C. E. Dateo and H. Metiu, *J. Chem. Phys.* **95**, 7392 (1991); A. Keller, R. Numico, and O. Atabek (to be published).
- [30] O. Atabek and R. Lefebvre, *Phys. Rev.* **A22**, 1817 (1980); N. Moiseyev, S. Friedland, and P. R. Certain, *J. Chem. Phys.* **74**, 4739 (1981).
- [31] E. E. Aubanel, J. M. Gauthier, and A. D. Bandrauk, *Phys. Rev.* **A48**, 2145 (1993).
- [32] E. Charron, A. Giusti-Suzor, and F. H. Mies, *Phys. Rev.* **A49**, R641 (1994).
- [33] E. E. Aubanel, A. Conjusteau, and A. D. Bandrauk, *Phys. Rev.* **A48**, R4011 (1993).

Received June 2, 1994

Chemistry and Phase Transitions from Hypervelocity Impacts

C. T. WHITE, S. B. SINNOTT, J. W. MINTMIRE, and D. W. BRENNER

Naval Research Laboratory, Washington, DC 20375-5000

D. H. ROBERTSON

Indiana University-Purdue University at Indianapolis, Indianapolis, Indiana 46202

Abstract

Molecular dynamics simulations are used to study hypervelocity impacts of an ultrathin flyer plate with a semi-infinite two-dimensional model diatomic molecular solid. We show that these hypervelocity impacts can produce a dissociative phase transition from a molecular to a close-packed solid in the target material. We also show that hypervelocity impacts of ultrathin plates can produce extensive chemical reactions leading to a detonation accompanied by a phase transition in an energetic version of the model.

© 1994 John Wiley & Sons, Inc.

Introduction

Advances in technology have led to the development of a variety of methods to launch flyer plates, microprojectiles, and pellets at velocities in excess of several kilometers per second [1]. The shock wave that results when these hypervelocity projectiles strike stationary targets typically separates the unperturbed material by only a few lattice spacings from the shocked solid which experiences pressures of several hundred kilobars, temperatures of several thousand degrees kelvin, while flowing at velocities of several kilometers per second [2]. These extreme but ephemeral conditions have been used to uncover new high pressure phases of solids [3] as well as explore synthetic routes to novel materials such as "hexagonal" diamond [4] (lonsdaleite) originally discovered in granular form in meteorites. Indeed, as early as 1956 Bancroft, Peterson, and Minshall reported data from shock loading experiments that proved the existence of a previously undetected high pressure phase of iron [5]. The signature of this transition was the presence of a split shock wave. Since Bancroft, Peterson, and Minshall's initial observations, shock wave splitting caused by polymorphic phase transitions has been observed in many other systems [3].

A better atomic-scale understanding of the physical and chemical events that occur during shock-wave loading should not only aid in the design of more resilient materials but also in the production of safer and more reliable explosives. However, the shock processes induced by hypervelocity impacts or sustained by detonations

occur at such short time (subpicosecond) and length scales (subnanometer scales) that they are difficult to probe experimentally. The short time and length scale of these processes, however, make them ideal for classical molecular dynamics simulations [6]. In addition, although starting from an atomic-scale description, molecular dynamics simulations have proven able to treat sufficiently many atoms for long enough times to reproduce the continuum behavior of planar shock waves described by hydrodynamic theory [7,8]. Hence, molecular dynamics simulations are ideal for modeling atomic-scale processes associated with shock waves and for relating this atomic-scale behavior to the continuum properties of condensed phase shock waves.

Shock loading resulting from hypervelocity impacts can induce chemical as well as physical changes in materials. An extreme example is that of a solid explosive which when struck can undergo catastrophic exothermic chemical reactions. A less spectacular but no less important example is the short-time corrosive chemistry that can occur when nanometer scale clusters strike surfaces at hypervelocities.

We have developed a series of related many-body reactive potentials that allow processes such as adhesion and friction [9,10], and shock-induced phase changes and chemistry [8,11] to be studied at atomic-scale resolution. Herein, we summarize and relate some of the results we have obtained in using a subset of these potentials to simulate the processes that can occur during the hypervelocity impact of an ultra-thin flyer plate with a model diatomic molecular solid. Specifically, we discuss results of a series of molecular dynamics simulations of the hypervelocity impact of a nanometer thick flyer plate with several model 2-D diatomic molecular solids. We find that even this ultrathin flyer plate—if accelerated to hypervelocities—can have sufficient momentum to induce a polymorphic (dissociative) transition from a molecular to close-packed solid in the target material. In addition, we show how such impacts can lead to extensive chemical reactions—even to the point of producing a detonation in an energetic version of the model. In the next section we briefly review the model used in these simulations. Then a series of our results are discussed. The final section provides a summary.

Model

The model potentials used in our studies are based on empirical bond order potentials such as those used by Tersoff to describe silicon [12] but tailored by us to treat reactive diatomic molecular solids [8]. Within this approach the total potential energy, E_B , of a collection of N atoms is represented by,

$$E_B = \sum_i^N \sum_{j>i}^N \{ f_c(r_{ij}) [V_R(r_{ij}) - \bar{B}_{ij} V_A(r_{ij})] + V_{vdW}(r_{ij}) \}, \quad (1)$$

where the molecular bonding portion of the potential consists of a repulsive term, $V_R(r)$, and an attractive term, $V_A(r)$, both modeled by exponentials. A Lennard-Jones potential, V_{vdW} , is used to describe the weak long-ranged van der Waals interaction. This Lennard-Jones potential is truncated not only at large distances but also at close-range bonding separations to allow for covalent bonding. The bond

order function, $\bar{B}_{ij} \equiv (B_{ij} + B_{ji})/2$, introduces many-body effects into the potential by modifying $V_A(r)$ according to the local bonding environment. These many-body effects arise from the hidden electronic degrees of freedom that are not treated explicitly in the model. For an isolated diatomic molecule \bar{B}_{ij} is unity and the potential reduces to a generalized Morse function familiar in the description of diatomic bonding [13]. For more highly coordinated structures \bar{B}_{ij} is no longer unity, but rather decreases with the increasing number and strength of competing bonds the atoms i and j form. This decrease in \bar{B}_{ij} reflects the finite number of valence electrons these atoms have available for bonding. Hence \bar{B}_{ij} represents an effective valence which can be tailored through its dependence on environment to describe either highly coordinated metals [14], tetrahedrally bonded semiconductors [15] and insulators or low coordination molecular solids with a few strong bonds [8].

In what follows the functions and associated parameters entering Eq. (1) have been chosen to describe a diatomic molecular solid at ambient conditions as described in detail elsewhere [8]. The diatomic molecules that make up this model solid can be composed of either like (A_2 or B_2) or unlike (AB) molecules. These diatomic molecules all have reasonable physical and chemical characteristics including binding energies, bond lengths, vibrational frequencies, and barriers to chemical reaction [8]. In addition, the diatomic molecular solids formed from these diatomic molecules have reasonable physical characteristics including densities, solid-state sound speeds, and high pressure phase transitions [8].

The A_2 and B_2 molecules entering this model are taken to have identical binding energies of 5 eV while the binding energy of each AB molecule is set to 2 eV. Hence simulations starting from an AB molecular solid allow for the possibility of exothermic chemical reactions from the higher energy AB molecules to the more stable A_2 and B_2 molecular products. In contrast, simulations starting from either A_2 or B_2 molecular solids do not have the possibility of any net release of energy. This model then allows simulations of hypervelocity impacts with target materials composed of either energetic or nonenergetic diatomic molecules.

Results and Discussion

Hypervelocity impact simulations are initiated by slamming an ultrathin thin flyer plate composed of 20 layers or less of the target material into the edge of the semi-infinite model diatomic molecular crystal initially at rest. Both the flyer plate and the molecular crystal are initially taken to have near-zero temperature and pressure. The dynamics of the system resulting from this hypervelocity impact is then studied by integrating Hamiltonian's equations of motion using a Nordsieck predictor-corrector method [15]. During these simulations periodic boundary conditions are imposed perpendicular to the direction of shock propagation.

A series of studies were first carried out assuming an all A_2 or equivalently an all B_2 diatomic molecular solid. A sequence of snapshots for a simulation beginning with the 15 km/sec velocity plate is shown in Figure 1. At 0.8 ps [Fig. 1(a)] only a single compressional shock wave is visible. Across this shock front the diatomic

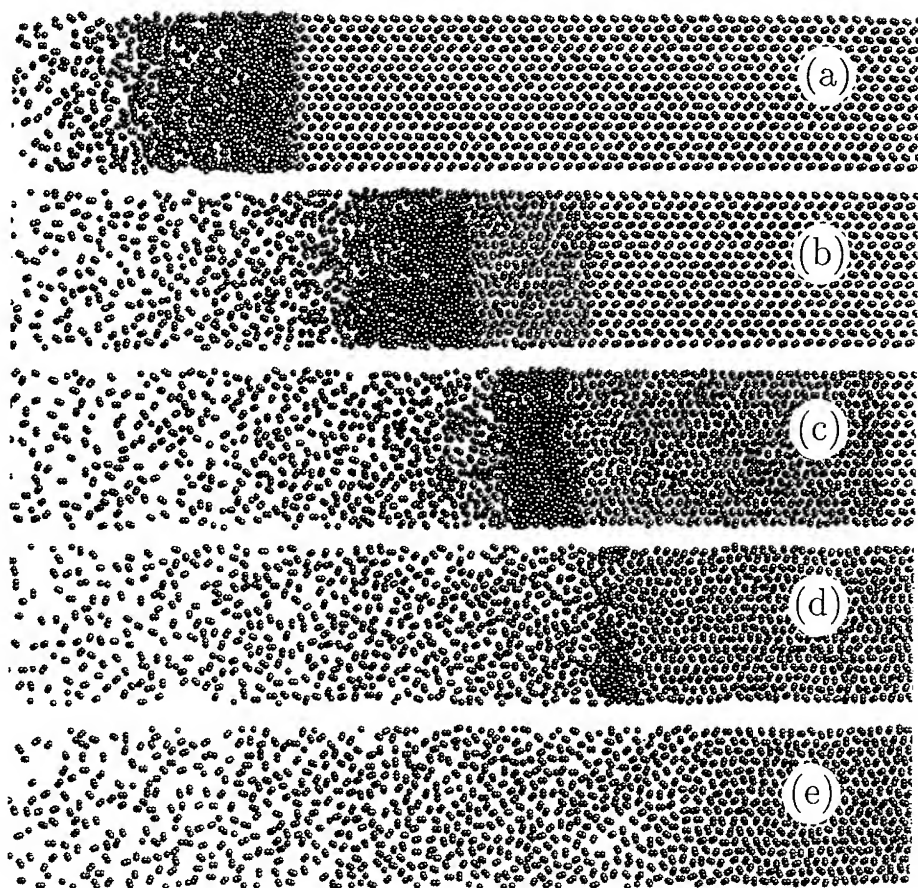


Figure 1. Snapshots of the simulation begun with the 15 km/sec flyer plate at: (a) 0.8; (b) 1.6; (c) 2.4; (d) 3.2; and, (e) 4.0 ps after the impact with the all A_2 diatomic molecular solid. The shock waves are propagating from left to right.

molecular solid (DMS) transforms directly to a close-packed solid (CPS). Although the density of this CPS, ρ_{CPS} , is approximately 2.4 times larger than the density of the DMS, ρ_{DMS} , the average nearest-neighbor interatomic separation in this phase, d_{NN} , is actually 20% larger due to an increase in the interatomic coordination. These properties of the CPS make this DMS to CPS transition similar to the dissociative transition reported in diatomic molecular solids of iodine [16] and bromine [17]. This transition occurs at 21 GPa in I_2 and 81 GPa in Br_2 leading to an increase in the overall relative density, ρ_{CPS}/ρ_{DMS} , of 1.7 for I_2 and 2.3 for Br_2 , and an increase in d_{NN} of around 15% for both materials.

At 1.6 ps [Fig. 1(b)] a second leading compressional shock wave has appeared in the 15 km/sec simulation. Across this new front the diatomic molecules are compressed and rotated from their initial positions in the undisturbed crystal but

retain their molecular identity. Once the second shock front is clearly visible it rapidly separates from the dissociative front, as can be seen by comparing Figure 1(b) to Figure 1(c). Although both the compressional and dissociative shock fronts propagate at velocities in excess of the speed of sound in the undisturbed crystal, the velocity of the dissociative front rapidly decreases from more than 12 km/sec at 0.5 ps to about 3 km/sec at 2.4 ps. In contrast, the velocity of the leading compressional shock remains pinned around 12 km/sec while the dissociative front exists, only gradually beginning to slow after the CPS disappears. As the dissociative front slows the accompanying dissociative zone also narrows as this region is consumed from behind by the rarefaction wave [Fig. 1(a)–Fig. 1(d)]. Figures 1 and 2 show that (Fig. 2) this front also begins to smear with the material behind entering a mixed phase region by 2.4 ps [Fig. 1(c)] as the velocity of the dissociative front approaches 3 km/sec. This mixed phase is clearly present at 3.2 ps [Fig. 1(d)] just prior to the complete disappearance of the dissociative zone.

A dissociative phase together with an accompanying split shock wave such as shown in Figure 1(b) is also present in all the other simulations begun with flyer plate velocities between 10 to 20 km/sec. Although the appearance of the leading compressional wave is delayed for higher impact plate velocities, once formed this front always exhibits a velocity near but slightly less than 12 km/sec, provided the dissociative region remains well-defined. In all simulations exhibiting a split shock wave, the dissociative zone begins to lose its identity only after the particle flow velocity behind the dissociative front slows to near 3 km/sec.

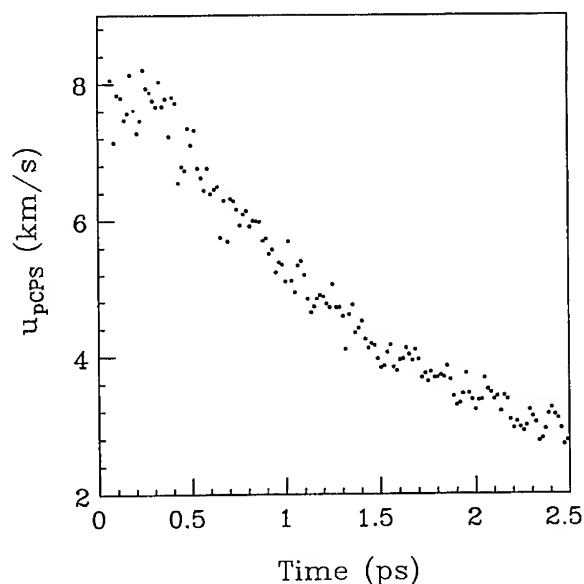


Figure 2. Scatter plot of u_{pCPS} 3.0 Å behind the dissociative front for the hypervelocity impact simulation depicted in Figure 1.

The general properties of these hypervelocity impact simulations as well as the explicit behavior shown in Figure 1 are all consistent with continuum predictions of a shock induced phase transition. An important property of these phase transitions is the compressional shock wave splitting that might occur. If split compressional shock waves are present, then continuum theory predicts [18] that the leading shock front starts material flow bringing it to the point of transition while the transition occurs across the second compressional shock front. A split shock wave with the transition occurring across the second front is just what is observed in Figure 1(b) and 1(c).

The continuum theory of planar shock waves also predicts [18] that a shock wave propagates into a medium (assumed at rest and characterized by a pressure P_0 and a specific volume V_0) with a velocity D given by:

$$D = (1 - V/V_0)^{-1}u_p, \quad (2)$$

where the particle flow velocity behind this shock front, u_p , is given by:

$$u_p = \sqrt{(V_0 - V)(P - P_0)}, \quad (3)$$

with V the specific volume and P the pressure of the shocked material. Therefore, because the leading shock front carries the pressure, P_T , and specific volume, V_T , of the phase transition, its velocity from Eqs. (2) and (3) is given by $D_1 = \sqrt{(P_T - P_0)/(V_0 - V_T)}$, and hence is predicted as pinned at a constant value determined by the properties of the phase transition and the undisturbed molecular crystal. In addition, the second front can only exist as a shock front so long as the particle flow velocity behind this front exceeds the particle flow velocity in the leading compressional zone, $u_{p1} = \sqrt{(V_0 - V_T)(P_T - P_0)}$. Hence u_{p1} is also a constant determined by the properties of the phase transition and the initial state. Continuum theory therefore explains why when two shock waves are present in the system—regardless of the impact plate velocity—the first shock propagates at a near constant velocity D_1 , while the second always fragments as the particle velocity behind this front, u_{pCFS} , approaches a fixed value, u_{p1} . Elsewhere we have shown [8] that for the present model: $V_T \approx 4.5 \text{ \AA}^2/\text{atom}$; $P_T \approx 0.813 \text{ eV/\AA}^2$; $V_0 \approx 6.14 \text{ \AA}^2/\text{atom}$; and $P_0 \approx 0.00 \text{ eV/\AA}^2$; results which imply that $D_1 \approx 11.5 \text{ km/sec}$ and $u_{p1} \approx 3.0 \text{ km/sec}$. These predictions differ no more than 5% from the corresponding near-constant values of D_1 and u_{p1} observed in all of these flyer plate simulations confirming the consistency of the continuum interpretation.

The snapshots shown in Figure 1 also suggest that hypervelocity impacts sufficient to induce a local dissociative transition should also be capable of causing substantial chemical rearrangement of the atoms in the dissociative zone. To explore the possibility of chemistry induced by hypervelocity impacts we have used the energetic AB version of our model diatomic molecular solid. Hence, rather than starting with an all A_2 molecular solid we now start with an all AB molecular solid which when shocked might undergo exothermic chemical reactions to yield the more stable A_2 and B_2 molecules. As noted in the "Model" section the exothermic gas-phase half reactions, $AB + B \rightarrow B_2 + A$ and $BA + A \rightarrow A_2 + B$ —taken as identical

in the model—are each assumed to liberate 3.0 eV. This 3.0 eV is similar to the 3.3 eV of energy liberated in the exothermic reaction $\text{N} + \text{NO} \rightarrow \text{N}_2 + \text{O}$ thought important in the detonation of NO. Also, the transition states for these two identical reactions occur in a collinear geometry with an early barrier to reaction which is typical of atom–diatom exothermic reactions. In addition, the barrier for these two model reactions is 0.11 eV. This barrier is greater than but similar to the barrier reported for the exothermic reaction $\text{F} + \text{H}_2 \rightarrow \text{FH} + \text{F}$ [19].

Figure 3 depicts a snapshot of a simulation begun by the impact of a four-layer, 6.0 km/sec flyer plate with the AB model molecular solid. As in Figure 1(b), four distinct regions are present: the unreacted molecular solid, a leading compressional region, a close packed solid (CPS) phase, and a product region. Hence, the AB molecular solid also exhibits a split shock wave structure and associated polymorphic phase transition similar to that found in the A_2 simulations. However, in contrast to the all- A_2 model, the CPS phase does not shrink but rather grows at a constant rate as the simulation progresses. The work necessary to maintain and increase this CSP is supplied by the exothermic chemical reactions induced by the shock wave. These exothermic reactions almost completely convert the AB molecular solid to the lower energy A_2 and B_2 molecular products clearly visible to the far left of Figure 3. In this way, the simulation depicted in Figure 3 has become a chemically sustained shock wave with the velocities of the three interfaces separating the four distinct regions soon reaching constant but different values as shown in Figure 4. As we will discuss in detail elsewhere, many properties of this chemically sustained shock wave such as peak pressure, particle flow velocity, and power generation are all consistent with a detonation. Hence, Figure 3 demonstrates that hypervelocity impacts are not only capable of causing chemical reactions but also catastrophic chemical reactions leading to a detonation.

Whether or not a chemically sustained shock wave occurs depends on the mass and impact velocity of the flyer plate. Specifically, as the number of layers in the flyer plate is increased the minimum impact velocity for initiation decreases approaching an asymptotic value of about 4.5 km/sec. Thus, even macroscopically thick flyer plates must impact at hypervelocities to cause a chemically sustained shock wave in the model material. This result agrees with the observed insensitivity of crystalline explosives to initiation.

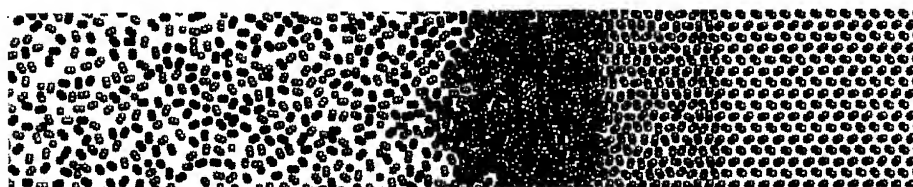


Figure 3. Snapshot at 5.1 ps of a simulation begun with the impact of a four-layer, 6.0 km/sec flyer plate with the AB model energetic diatomic molecular solid. The two types of atoms are depicted as light and dark. The shock front is propagating from left to right.

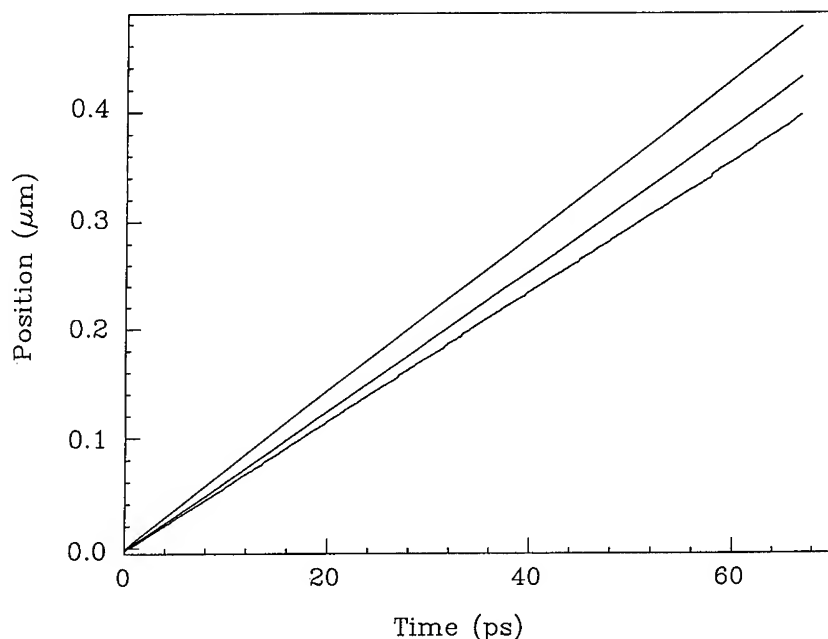


Figure 4. The positions of the three interfaces between the four distinct regions as a function of time for a simulation begun with an impact velocity of 6 km/sec.

Summary

In summary, we have reported the results of a series of molecular dynamics simulations of hypervelocity impacts of an ultra-thin plate with a model diatomic molecular solid. At these high impact velocities even this ultra-thin plate is found able to induce a dissociative phase transition to a close-packed solid with accompanying complex behavior such as shock wave splitting. Although this close-packed phase persists for less than 10 ps and is confined to a domain less than 10 nm wide it still behaves in a manner consistent with continuum theory. Additional simulations of hypervelocity impacts of an ultrathin flyer plate with a model diatomic energetic material not only produce a dissociative phase transition but also extensive chemical reactions leading to a chemically sustained shock wave.

Acknowledgments

This work was supported in part by the Office of Naval Research both at NRL and at IUPUI. One of us (SBS) acknowledges a NRC/NRL Postdoctoral Research Associateship.

Bibliography

- [1] See, e.g., *Shock Compression in Condensed Matter—1989*, S. C. Schmidt, J. N. Johnson, and L. W. Davison, Eds. (North-Holland, Amsterdam, 1990), and references therein.

- [2] See e.g., W. C. Davis, *Sci. Am.* **256**, 106 (1987).
- [3] G. E. Duvall and R. A. Graham, *Rev. Mod. Phys.* **49**, 523 (1977).
- [4] D. J. Erskine and W. J. Nellis, *Nature* **349**, 317 (1991).
- [5] D. Bancroft, E. L. Peterson, and S. Minshall, *J. Appl. Phys.* **27**, 291 (1956).
- [6] M. L. Elert, D. M. Deaven, D. W. Brenner, and C. T. White, *Phys. Rev.* **B39**, 1453 (1989).
- [7] B. L. Holian, *Phys. Rev.* **A36**, 3943 (1987).
- [8] D. H. Robertson, D. W. Brenner, and C. T. White, *Phys. Rev. Lett.* **67**, 3132 (1991).
- [9] J. A. Harrison, C. T. White, R. J. Colton, and D. W. Brenner, *Phys. Rev.* **B46**, 9700 (1992).
- [10] J. A. Harrison, C. T. White, R. J. Colton, and D. W. Brenner, *MRS Bullentin* **18**, 50 (1993).
- [11] D. W. Brenner, D. H. Robertson, M. L. Elert, and C. T. White, *Phys. Rev. Lett.* **70**, 2174 (1993).
- [12] J. Tersoff, *Phys. Rev. Lett.* **56**, 632 (1986); *Phys. Rev.* **B37**, 6991 (1988).
- [13] See e.g., J. N. Murrell, S. Carter, S. C. Farantos, P. Huxley, and A. J. C. Varandas, *Molecular Potential Energy Functions* (Wiley, Chichester, 1984), p. 4.
- [14] G. C. Abell, *Phys. Rev.* **B31**, 6184 (1985).
- [15] C. W. Gear, *Numerical Initial Value Problems in Ordinary Differential Equations* (Prentice-Hall, Englewood Cliffs, NJ, 1971), p. 148.
- [16] K. Takemura, S. Minomura, O. Shimomura, Y. Fujii, and J. D. Axe, *Phys. Rev.* **B26**, 998 (1982).
- [17] Y. Fujii, K. Hase, Y. Ohishi, H. Fujihisa, N. Hamaya, K. Takemura, O. Shimomura, T. Kikegawa, Y. Amemiya, and T. Matsushita, *Phys. Rev. Lett.* **63**, 536 (1989).
- [18] Ya. B. Zel'dovich and Yu. P. Raizer, *Physics of Shockwaves and High Temperature Hydrodynamic Phenomena*, Vols. 1 and 2, (Academic Press, New York, 1967), Vol. 1, §13; Vol. 2, §19.
- [19] G. C. Fettis, J. H. Knox, and A. F. Trotman-Dickenson, *J. Chem. Soc. London*, 1064 (1960).

Received June 15, 1994

Evaluation of Group Theoretical Characteristics Using the Symbolic Manipulation Language MAPLE

U. TANERI* and J. PALDUS†

*Quantum Theory Group, Department of Applied Mathematics, University of Waterloo, Waterloo,
Ontario N2L 3G1 Canada*

Abstract

Relying on theoretical developments exploiting quasispin and the pseudo-orthogonal group in the Hubbard model of cyclic polyenes, the general expressions for generating polynomials, providing the dimensional information for relevant irreducible representations, were derived (M. D. Gould, J. Paldus, and J. Čížek, *Int. J. Quantum Chem.*, in press). These generating polynomials result from q -dimensional formulas through rather tedious algebraic manipulations involving ratios of polynomials with fractional powers. It is shown that these expressions may be efficiently handled using the symbolic manipulation language MAPLE and the dimensional information for an arbitrary spin, isospin, and quasimomentum obtained. Exploitation of symbolic computation for other group theoretical problems that are relevant in quantum chemical calculations and their relationship with Gaussian polynomial based combinatorial approaches is also briefly addressed and various possible applications outlined. © 1994 John Wiley & Sons, Inc.

Introduction

In order to arrive at various attributes of symmetry groups or their chains that are needed for their exploitation in quantum mechanics, particularly in deriving or calculating the characters of their irreducible representation (irreps), one often relies on suitable generating polynomials. Perhaps the best known example of such a procedure is represented by Frobenius' theorem of the symmetric group representation theory (see, e.g., Eq. (7–24) of [1]) yielding directly all the simple characters $\chi_{(\lambda)}^{(\lambda)}$ of the irrep $(\lambda) \equiv (\lambda_1, \lambda_2, \dots, \lambda_N)$ of S_N as the coefficients of the Schur polynomial $S_{(\lambda)}(x)$ in the product $s_{(l)}(x) \equiv \prod_r s_r(x)^{\alpha_r}$ of power sum or Newton polynomials s_r ,

$$s_r(x) = \sum_i x_i^r, \quad (1)$$

* Permanent address: Quantum Theory Group, Department of Chemistry, Eastern Mediterranean University, Gazi Magosa, T.R.N.C., Mersin 10 Turkey. Also at Department of Systems Design, Faculty of Engineering, University of Waterloo, Waterloo, Ontario N2L 3G1 Canada.

† Also at Department of Chemistry and Guelph-Waterloo Center for Graduate Work in Chemistry, Waterloo Campus, University of Waterloo, Waterloo, Ontario N2L 3G1 Canada.

that are associated with the partition $(l) \equiv (1^{\alpha_1} 2^{\alpha_2} 3^{\alpha_3} \cdots)$ labelling the S_N classes, namely

$$s_{(l)}(x) = \sum_{(\lambda)} x_{(l)}^{(\lambda)} S_{(\lambda)}(x). \quad (2)$$

Since any finite group G is isomorphic with a suitable subgroup of the symmetric or permutation group S_N of an appropriate order (Cayley's theorem), the usefulness of the representation theory of S_N in the general case is self-evident. Moreover, there exists an intimate relationship between the representation theory of S_N and that of compact Lie groups thanks to Weyl's global approach that relies on the tensor powers of the fundamental representation, which is provided by the group itself or, rather, by its Lie algebra. Recall also that unitary groups $U(n)$ play the same role for the compact Lie groups as do permutation groups for finite groups. This intimate relationship is also reflected in various group theoretical approaches to the N -electron correlation problem employing n -orbital models, where the interplay between the S_N , $U(n)$ and $SU(2)$ based approaches is well known [2-5].

As a special case of the general character theory, one often requires only the characters of the identity, providing the appropriate dimensions. Let us recall here, for example, the special case of Weyl's dimension formula (often referred to nowadays as Weyl-Paldus dimension formula [3,6,7]) giving the number of spin-adapted configurations, characterized by the total spin quantum number S , for the n -orbital model of an N -electron system that is described by a spin-independent Hamiltonian [8,9],

$$D_n(a, b, c) = \frac{b+1}{n+1} \binom{n+1}{a} \binom{n+1}{c}, \quad (3)$$

where (a, b, c) designates Paldus label of the two-column $U(n)$ irrep $\langle 2^a 1^b 0^c \rangle$ given by $a = \frac{1}{2}N - S$, $b = 2S$ and $c = n - \frac{1}{2}N - S$ and $\binom{n}{m} = n!/(n-m)!m!$ is the usual binomial coefficient. An equivalent form of this and related dimension formulas may be often derived using simple combinatorial means, independently of group theory [10].

Nonetheless, even when relying on a combinatorial approach, it is often useful to employ the technique of generating polynomials. In this way, for example, Pauncz [11] derived generating polynomials yielding a number of configurations associated with a given level in the harmonic level excitation diagram (HLED) [12,13]. This result was later generalized by Katriel et al. [14] for both fermions and bosons, giving the number of configurations involving any number of particles with an arbitrary elementary spin, as well as for the number of configurations specified by the total orbital weight [13] and by the degree of excitation.

More recently, these results were further generalized for atomic and nuclear systems involving both fermionic and bosonic levels with a fixed number of particles per level, giving the number of states with conserved total angular momentum and spin [15-17]. These results are useful for the calculation of nuclear level densities [18] as well as for the spectroscopy of partly-filled shell ions in crystalline environ-

ments [19]. For this latter purpose, a new generating polynomial was introduced by Kibler and Katriel [20]. Another application exploiting generalization of the dimension formula (3) for the determination of spectroscopic terms was recently put forward by Torre et al. [21].

Another extensive exploitation of the dimension formulas, such as Eq. (3), giving the number of symmetry adapted configurations, is found in the many-electron theory based on spin-adapted reduced Hamiltonians (SRH) of Valdemoro [22] and in the so-called spectral distribution method (SDM) of nuclear physics [23–25]. In both cases one evaluates fixed-symmetry traces over finite N -body spaces, although various distinct formalisms may be employed. The relationship between both approaches [25,26] was pointed out by Nomura [27], which in turn inspired Karwowski and Valdemoro [28] to derive a set of recurrent relations expressing traces of products of the occupation number operators, which are essential for the construction of the effective two-body SRH, solely in terms of the dimensions given by Eq. (3).

The direct exploitation of generating polynomials, such as given by Eq. (2), may prove to be rather demanding. We quote in this regard Hamermesh [1, p. 197] who states that Frobenius' formula (2) "looks (and is!) formidable, and we shall therefore deal with it to devise methods which are tractable." Such developments are invariably based on the theory of polynomial rings in an arbitrary number of variables and in particular on the theory of symmetric functions [29]. This type of approach was, for example, exploited by Sunko and Svrtan [15,16]. However, in view of recent developments in symbolic computation, it is of interest to explore the possibilities offered by these powerful tools in handling directly the generating polynomials and extracting the desired information.

In this article we shall thus employ MAPLE [30] in order to extract the dimensional information from recently obtained generating polynomials [31] for the number of symmetry-adapted configurations of the Hubbard cyclic polyene model with conserved spin, quasispin, and quasimomentum. These generating polynomials were obtained [31] with the help of $U(n)$ q -dimension formula [32] that originates from the recently developed theory of quantum groups [33,34]. We briefly overview the resulting expressions in the next section and subsequently explore their computational implementation using MAPLE [30]. We also point out the close relationship between the generating polynomials originating from the q -character or q -dimension formalism [31,32] and those resulting from combinatorial considerations that are usually formulated in terms of Gaussian polynomials.

q -Dimension Formulas for the Cyclic Polyene Hubbard Model

The Hubbard Hamiltonian for the linear chain with n equidistant and equivalent sites, satisfying the Born–von Kármán cyclic boundary conditions, has the form

$$H^{(H)} = \beta \sum_{i=1}^n \sum_{\sigma=\pm 1} (X_{i,\sigma}^\dagger X_{i+1,\sigma} + X_{i+1,\sigma}^\dagger X_{i,\sigma}) + U \sum_{i=1}^n n_{i,-1} n_{i,1}, \quad (4)$$

where β designates the resonance (hopping) integral, U the one-center on-site Coulomb integral, $X_{i,\sigma}^\dagger$ ($X_{i,\sigma}$) the creation (annihilation) operator associated with the i th

site spin orbital with azimuthal spin σ , $\sigma = \pm 1$, and $n_{i,\sigma}$ the corresponding spin orbital occupation number operator

$$n_{i,\sigma} = X_{i,\sigma}^\dagger X_{i,\sigma} . \quad (5)$$

All the indices are taken modulo n , $n + 1 \equiv 1 \pmod{n}$, reflecting the cyclic boundary conditions mentioned above. Expressing U in the units of β , we can set $\beta = -1$, and characterize the Hamiltonian (4) by a single parameter representing the coupling constant. Moreover, choosing a convenient energy zero by shifting the number operators by their mean values, we obtain the following often used form of the Hubbard Hamiltonian [31,35,36]

$$\tilde{H} = U \sum_{i=1}^n (n_{i,1} - \frac{1}{2})(n_{i,-1} - \frac{1}{2}) - \sum_{i=1}^n (E_{i,i+1} + E_{i+1,i}) , \quad (6)$$

where we employed the $U(n)$ generators

$$E_{ij} \equiv E_{i,j} = \sum_{\sigma=\pm 1} X_{i,\sigma}^\dagger X_{j,\sigma} \quad (7)$$

of the unitary group approach [6-9]. Clearly,

$$\tilde{H} = H^{(H)} + \frac{1}{2} U(\frac{1}{2}n - \hat{N}) , \quad (8)$$

where

$$\hat{N} = \sum_{i=1}^n n_i, \quad n_i = n_{i,1} + n_{i,-1} \quad (9)$$

is the total electron number operator, so that for a given system with a fixed number of sites n , occupied by a fixed number of electrons N , the last term in Eq. (8) represents a constant shift. We shall only consider lattices with an even number of sites and designate

$$n = 2m . \quad (10)$$

In view of the apparent spin independence of \tilde{H} , we can express it entirely in terms of $U(n)$ generators (7) as follows

$$\tilde{H} = \frac{1}{2} U \sum_{i=1}^n (E_{i,i})^2 - \sum_{i=1}^n (E_{i,i+1} + E_{i+1,i}) + \frac{1}{2} U(\frac{1}{2}n - 2\hat{N}) , \quad (6')$$

and we can restrict ourselves to a fixed irrep of $U(n)$ with Paldus labels (a, b, c) of dimension given by Eq. (3), since \tilde{H} commutes with the $SU(2)$ operators

$$S_z = \frac{1}{2}(\mathcal{E}_{1,1} - \mathcal{E}_{-1,-1}), \quad S_+ = \mathcal{E}_{1,-1}, \quad S_- = \mathcal{E}_{-1,1}, \quad (11)$$

where

$$\mathcal{E}_{\sigma,\tau} = \sum_{i=1}^n X_{i,\sigma}^\dagger X_{i,\tau}, \quad (\sigma, \tau = \pm 1) \quad (12)$$

designate the SU(2) generators. The electron number operator (9) represents clearly the first order invariant of both U(n) and U(2),

$$\hat{N} = \sum_{i=1}^n E_{i,i} = \sum_{\sigma=\pm 1} \mathcal{E}_{\sigma,\sigma}. \quad (13)$$

In addition to this obvious SU(2) spin invariance of the Hamiltonian \tilde{H} , Eqs. (6) and (6'), it also possesses a quasi-spin SU(2) invariance [37,38], with the quasi-spin operator \mathbf{Q} defined by its components

$$Q_z = \frac{1}{2}(\hat{N} - n), \quad Q_+ = \sum_{i=1}^n (-1)^i X_{i,-1}^\dagger X_{i,1}^\dagger, \quad Q_- = Q_+^\dagger. \quad (14)$$

To account for this quasi-spin invariance, it is useful to introduce the pseudo-orthogonal group O(m, m) with infinitesimal generators [31]

$$\alpha_{ij} = (-1)^i E_{ij} - (-1)^j E_{ji} = -\alpha_{ji}, \quad (15)$$

satisfying the commutation relations

$$[\alpha_{ij}, \alpha_{kl}] = g_{jk}\alpha_{il} + g_{il}\alpha_{jk} - g_{ik}\alpha_{jl} - g_{jl}\alpha_{ik},$$

with the orthogonal group metric

$$g_{ij} = (-1)^i \delta_{ij}. \quad (16)$$

The Hermiticity condition now reads

$$\alpha_{ij}^\dagger = (-1)^{i+j} \alpha_{ji} = (-1)^{i+j+1} \alpha_{ij}. \quad (17)$$

It can then be shown [31] that the square of the quasi-spin $Q^2 \equiv \mathbf{Q} \cdot \mathbf{Q}$, with eigenvalues $Q(Q+1)$ where Q designates the quasi-spin quantum number, is determined by the second order U(n) and O(m, m) Casimir invariants (summation convention over repeated indices is implied here)

$$I_2 = E_{ij}E_{ji} \quad (18)$$

and

$$I_2^0 = \frac{1}{2}(-1)^{i+j} \alpha_{ij} \alpha_{ji}, \quad (19)$$

respectively, namely

$$Q^2 = \frac{1}{2}(I_2 - I_2^0) + \frac{1}{4}(n - \hat{N})(n - \hat{N} + 2) - \frac{1}{2}\hat{N}. \quad (20)$$

Similarly as in the U(n) case, one labels the weights by the eigenvalues of the Cartan subalgebra commuting self-adjoint operators

$$h_j = \alpha_{2j,2j-1}, \quad (1 \leq j \leq m), \quad (21)$$

and the irreps of O(m, m) by the highest weights (under the lexicographic labeling). Again, at most two column irreps of O(m, m) can occur [31], so that we employ Paldus-type labels (a_0, b_0, c_0), $a_0 + b_0 + c_0 = m$, to designate the relevant O(m, m) irrep, whose dimension is now

$$D_m^0(a_0, b_0, c_0) = \frac{(b_0 + 1)(n - 2a_0 - b_0 + 1)}{(n + 1)(n + 2)} \binom{n + 2}{a_0} \binom{n + 1}{a_0 + b_0 + 1}. \quad (22)$$

Considering the $U(n) \downarrow O(m, m)$ branching rules, one then finds [31] that the $U(n)$ irrep $\Gamma(a, b, c)$ decomposes as follows

$$\Gamma(a, b, c) = \bigoplus_{a_0=0}^{a \wedge c} \Gamma^0(a_0, b_0, c_0), \quad (23)$$

with

$$b_0 = b \wedge (n - 2a_0 - b), \quad (24)$$

where $\Gamma^0(a_0, b_0, c_0)$ designate the $O(m, m)$ irrep with the highest weight (a_0, b_0, c_0) and

$$x \wedge y := \min\{x, y\}. \quad (25)$$

All the states in $\Gamma(a, b, c)$ have the azimuthal quasi-spin quantum number $Q_z = \frac{1}{2}(N - n)$, $N = 2a + b$ and the $O(m, m)$ irrep $\Gamma^0(a_0, b_0, c_0)$ is characterized by the quasi-spin

$$Q = \frac{1}{2}|n - N| + c \wedge a - a_0 = \frac{1}{2}(n - b) - a_0. \quad (26)$$

Thus, the allowed values of quasi-spin are [31]

$$\frac{1}{2}|n - N| \leq Q \leq \frac{1}{2}(n - b). \quad (27)$$

To account, finally, for the spatial symmetry invariance characterized by the cyclic group C_n , one has to consider the $O(m, m) \downarrow C_n$ branching rules. Labelling the C_n irreps by the quasi-momentum quantum number k and exploiting the q -character formalism [32], we find [31] generating polynomials yielding the desired dimensional information or multiplicities of the states characterized by quantum numbers N, S, Q and k . Thus, for a given $n = 2m$ and N , the total spin quantum number S determines the relevant $U(n)$ irrep (a, b, c) , $a = \frac{1}{2}N - S$, $b = 2S$, $c = n - a - b$; the quasi-spin quantum number Q specifies the $O(m, m)$ irrep (a_0, b_0, c_0) ,

$$\begin{aligned} a_0 &= \frac{1}{2}|n - N| + c \wedge a - Q, \\ b_0 &= b \wedge [n - 2(c \wedge a) - b], \\ c_0 &= m - a_0 - b_0, \end{aligned} \quad (28)$$

and, finally, the quasi-momentum k labels the relevant C_n irrep, $0 \leq k < n$. The desired generating polynomial $F_{(a_0, b_0, c_0)}(q)$ is given by [31]

$$F_{(a_0, b_0, c_0)}(q) = q^\rho D_q^0[a_0, b_0], \quad (29)$$

where

$$\rho = \frac{1}{2}(n + 1)N - (m + 1)(a - a_0), \quad (30)$$

and $D_q^0[a_0, b_0]$ is the $O(m, m)$ q -dimension given by

$$D_q^0[a_0, b_0] = \frac{[b_0 + 1]}{[n + 1]} \begin{bmatrix} n + 2 \\ a_0 \end{bmatrix} \begin{bmatrix} n + 2 \\ a_0 + b_0 + 1 \end{bmatrix} \times \left(\frac{[n + 2 - a_0][n + 1 - a_0 - b_0] - q^{-m-1}[a_0 + b_0 + 1][a_0]}{[n + 2]^2} \right). \quad (31)$$

The square brackets on the right-hand side of Eq. (31) designate the polynomials in q defined as follows

$$[r] = q^{(1/2)r} - q^{-(1/2)r}, \quad (32)$$

and the "binomial coefficients" are defined in analogy to their standard meaning by

$$\begin{bmatrix} r \\ s \end{bmatrix} = \frac{[r]!}{[r - s]![s]}, \quad 0 \leq s \leq r \quad (33)$$

where now

$$[r]! = \begin{cases} [r] \cdot [r - 1] \cdot \dots \cdot [1], & r \geq 1 \\ 1, & r = 0. \end{cases} \quad (34)$$

In the limit $q \rightarrow 1$ the q -dimension formula (31) reduces to the $O(m, m)$ dimension formula (22).

Once the generating polynomial (29) is obtained, it is sufficient to transform it to the standard form

$$F_{(a_0, b_0, c_0)}(q) = \sum_{k=1}^{n-1} m_k^0(a_0, b_0) q^k, \quad (35)$$

by reducing its exponents modulo n to the numbers in the set $\{0, 1, \dots, n - 1\}$. The coefficients $m_k^0(a_0, b_0)$ then represent the desired dimensions or C_n -multiplicities.

MAPLE Implementation and Results

In order to get the idea of algebraic manipulations that are involved in the construction of generating polynomials (35), yielding the desired C_n -multiplicities, we briefly consider the simplest cyclic polyene with the nondegenerate ground state, representing the π -electron model of benzene. In this case $n = N = 6$, $m = 3$ so that all states have a vanishing azimuthal quasi-spin $Q_z = 0$. The possible spin quantum numbers are clearly $S = 0, 1, 2$, and 3 , so that the following $U(6)$ irreps are involved:

$$(a, b, c) = (3, 0, 3), (2, 2, 2), (1, 4, 1) \text{ and } (0, 6, 0). \quad (36)$$

Considering only the most important case of singlet and triplet configurations ($b = 0$ and 2 , respectively), we easily find the following decompositions using Eq. (23),

$$\Gamma(3, 0, 3) = \Gamma_0^0(3, 0, 0) \oplus \Gamma_1^0(2, 0, 1) \oplus \Gamma_2^0(1, 0, 2) \oplus \Gamma_3^0(0, 0, 3), \quad (37a)$$

and

$$\Gamma(2, 2, 2) = \Gamma_0^0(2, 0, 1) \oplus \Gamma_1^0(1, 2, 0) \oplus \Gamma_2^0(0, 2, 1), \quad (37b)$$

with the quasispin Q , Eq. (26), indicated by the subscript on the $O(3, 3)$ irrep symbol Γ_Q^0 .

The required generating polynomial for, e.g., the irrep $\Gamma_1^0(2, 0, 1)$ is thus [see Eq. (29)]

$$F_{(2,0,1)}(q) = q^{17} D_q^0[2, 0], \quad (38)$$

where

$$\begin{aligned} D_q^0[2, 0] &= \frac{[1]}{[7]} \frac{[8]}{[2]} \frac{[8]}{[3]} \frac{[6][5] - q^{-4}[3][2]}{[8]^2} \\ &= \frac{[7][6]([6][5] - q^{-4}[3][2])}{[3][2]^2[1]}, \end{aligned} \quad (39)$$

with $[r]$ defined by Eq. (32). Employing, next, the decompositions

$$\begin{aligned} [r] = [2\rho + 1] &= q^{r/2} - q^{-r/2} \\ &= [1](q^\rho + q^{\rho+1} + \cdots + q + 1 + q^{-1} + \cdots + q^{-\rho}) \end{aligned} \quad (40)$$

for $\rho = 1, 2$, and 3 and using the fact that

$$\begin{aligned} (q^2 + 1 + q^{-2})(q^2 + q + 1 + q^{-1} + q^{-2}) \\ = (q + 1 + q^{-1})(q^3 + q + 1 + q^{-1} + q^{-3}), \end{aligned} \quad (41)$$

we find that

$$\begin{aligned} D_q^0[2, 0] &= (q^3 + q^2 + q + 1 + q^{-1} + q^{-2} + q^{-3})(q^2 + 1 + q^{-2}) \\ &\quad \times (q^3 + q + 1 + q^{-1} + q^{-3} - q^{-4}), \end{aligned} \quad (42)$$

which, after the reduction mod 6 gives

$$D_q^0[2, 0] = 16 + 12q + 16q^2 + 12q^3 + 16q^4 + 12q^5,$$

yielding the required dimensions $m_k^0(2, 0)$, $k = 0, 1, \dots, 5$. Note that in view of the additional symmetry (D_{nh}) of the model, as well as the particle-hole symmetry for the half-filled shell case, we have that $m_k^0(a_0, b_0) = m_{n-k}^0(a_0, b_0)$.

The key step in this algorithm is clearly the factorization of the q -dimension (31) and the expansion and normalization of the resulting generating polynomial. This is achieved using the following code

```

#
Dq2 := factor(Dq);
Dq3 := q^qhat*DQ2;
Dq4 := expand(Dq3);
#
reducer := proc (t, x, mm) local d;
              d := degree(t, x);
              subs (x^d = x^(d mod mm), t);
end;
#
res := map(reducer, DQ4, q, n);
resfct := sort(res);
Fq[ic, jc] := resfct;
#

```

(43)

where Dq designates the $O(m, m)$ q -dimension produced by another subroutine, $qhat = R$ as given by Eq. (30) and $Dq3$ is the $O(m, m)$ generating polynomial (29). Following the factorization, the generating polynomial $Dq3$ is expanded and reduced to the standard form (35) with the help of a procedure called "reducer." Note that except for this latter procedure, all the other operations (factor, expand, map, and sort) represent the standard functions in MAPLE. The resulting dimensionalities are then suitably tabulated or may be used by other programs.

We illustrate the results in Tables I, II, and III giving the C_n -multiplicities for all the singlet and triplet states of cyclic polyenes with 6, 10, and 18 sites (for the singlets of benzene see also Table II of [31], which was obtained manually). Other spin multiplicities or polyenes with an even number of sites ($n = 2m$), or their various ions ($n \neq N$) can be obtained using the same code. To illustrate the efficiency of MAPLE we present some typical timings in Table IV.

Discussion

The results presented in the preceding section indicate the usefulness of the symbolic manipulation languages, such as MAPLE, for an efficient handling of rather complex algebraic expressions, even though the required computational time increases appreciably with the increasing polyenic size. Nonetheless, a good deal of useful information can be extracted in this way by directly exploiting various generating functions mentioned in the Introduction.

We also wish to mention that although the Pariser-Parr-Pople (PPP) Hamiltonian [9,39] is not invariant with respect to quasi-spin, it exhibits the so-called alternancy symmetry [40,41], which is intimately related with the parity of quasi-spin [31,38]: even (odd) quasi-spin species correspond to minus (plus) states in Pariser's classification [40]. Moreover, even the PPP Hamiltonian spectral properties may be better understood when quasi-spin is employed as an approximate symmetry [42]. Further, we note that in Ref. [31] we also presented the generating polynomials for the direct $U(n) \downarrow C_n$ subduction in which q -dimension analogue of Weyl-Paldus formula (3)

TABLE I. Dimensions of various subproblems labeled by the quasispin Q or by the corresponding $O(3, 3)$ irrep label (a_0, b_0, c_0) , $c_0 = 3 - a_0 - b_0$ and quasi-momentum $k(k = 0, 1, \dots, 5)$ for both singlets (a) and triplets (b) of the cyclic polyene with $n = N = 6$.

(a) Singlets

k	(a_0, b_0)			
	(3, 0)	(2, 0)	(1, 0)	(0, 0)
0	16	12	4	0
1, 5	8	16	3	0
2, 4	14	12	4	0
3	10	16	2	1
Dim $\Gamma(a_0, b_0)$	70	84	20	1
Q	0	1	2	3

(b) Triplets

k	(a_0, b_0)		
	(2, 0)	(1, 2)	(0, 2)
0	12	16	2
1, 5	16	14	3
2, 4	12	16	2
3	16	14	3
Dim $\Gamma(a_0, b_0)$	84	90	15
Q	0	1	2

replaces the $O(m, m)$ formula (22) or (31). Clearly, this formalism can be employed in the absence of quasi-spin symmetry.

Let us, finally, briefly indicate a general relationship between the q -dimension generating functions and those usually encountered in combinatorial type approaches that often employ Gaussian polynomials (see Appendix of [31] for a brief outline of q -characters and q -dimensions). The basic quantity in the q -character formalism is the q -Weyl denominator function P_q ,

$$P_q = \prod_{\alpha \in \Phi^+} (q^{\alpha/2} - q^{-\alpha/2}), \quad (44)$$

where Φ^+ designates the set of positive roots of the simple Lie algebra L . For the q -dimensions, the relevant denominator function becomes

$$P_q(\mu) = \prod_{\alpha \in \Phi^+} (q^{\frac{1}{2}(\mu, \alpha)} - q^{-\frac{1}{2}(\mu, \alpha)}), \quad (45)$$

TABLE II. Dimensions of various subproblems labeled by the quasispin Q or by the corresponding $O(5, 5)$ irrep label (a_0, b_0, c_0) , $c_0 = 5 - a_0 - b_0$ and quasi-momentum $k(k = 0, 1, \dots, 9)$ for both singlets (a) and triplets (b) of the cyclic polyene with $n = N = 10$.

(a) Singlets

k	(a_0, b_0)					
	(5, 0)	(4, 0)	(3, 0)	(2, 0)	(1, 0)	(0, 0)
0	576	876	420	74	6	0
1, 9	534	906	405	80	5	0
2, 8	574	876	420	74	6	0
3, 7	534	906	405	80	5	0
4, 6	574	876	420	74	6	0
5	536	906	405	80	4	1
Dim $\Gamma(a_0, b_0)$	5544	8910	4125	770	54	1
Q	0	1	2	3	4	5

(b) Triplets

k	(a_0, b_0)				
	(4, 0)	(3, 2)	(2, 2)	(1, 2)	(0, 2)
0	876	1396	588	96	4
1, 9	906	1376	600	93	5
2, 8	876	1396	588	96	4
3, 7	906	1376	600	93	5
4, 6	876	1396	588	96	4
5	906	1376	600	93	5
Dim $\Gamma(a_0, b_0)$	8910	13860	5940	945	45
Q	0	1	2	3	4

where (\cdot) designates Weyl group invariant bilinear form induced on the weights by the Killing form [43]. Clearly, the factors appearing on the right-hand side of Eq. (45) give rise to the basic factors $[r]$, Eq. (32), in the generating polynomials employed.

It is straightforward to realize that the q -binomial coefficients, Eq. (33), appearing in the q -dimension formulas, are in fact very closely related to Gaussian polynomials, which are defined as follows

$$\begin{bmatrix} r \\ s \end{bmatrix}_G = \frac{[r]_G!}{[r-s]_G! [s]_G!}, \quad 0 \leq s \leq r \quad (46)$$

TABLE III. Dimensions of various subproblems labeled by the quasispin Q or by the corresponding $O(9, 9)$ irrep label (a_0, b_0, c_0) , $c_0 = 9 - a_0 - b_0$ and quasi-momentum $k(k = 0, 1, \dots, 17)$ for both singlets (a) and triplets (b) of the cyclic polyene with $n = N = 18$.

k	(a_0, b_0)									
	(9, 0)	(8, 0)	(7, 0)	(6, 0)	(5, 0)	(4, 0)	(3, 0)	(2, 0)	(1, 0)	(0, 0)
0	4538596	9278320	7139256	3074424	790944	120708	10524	470	10	0
1, 17	4535000	9281260	7137333	3075507	790464	120894	10473	480	9	0
2, 16	4538528	9278320	7139292	3074388	790944	120714	10518	470	10	0
3, 15	4535066	9281260	7137294	3075546	790464	120888	10479	480	9	0
4, 14	4538528	9278320	7139292	3074388	790944	120714	10518	470	10	0
5, 13	4535000	9281260	7137333	3075507	790464	120894	10473	480	9	0
6, 12	4538594	9278320	7139256	3074424	790944	120708	10524	470	10	0
7, 11	4535000	9281260	7137333	3075507	790464	120894	10473	480	9	0
8, 10	4538528	9278320	7139292	3074388	790944	120714	10518	470	10	0
9	4535068	9281260	7137294	3075546	790464	120888	10479	480	8	1
Dim $\Gamma(a_0, b_0)$	81662152	167036220	128489400	55349280	14232672	2174436	188955	8550	170	1
Q	0	1	2	3	4	5	6	7	8	9

(b) Triplets

k	(a_0, b_0)								
	(8, 0)	(7, 2)	(6, 2)	(5, 2)	(4, 2)	(3, 2)	(2, 2)	(1, 2)	(0, 2)
0	9278320	18846288	14275760	5996592	1482360	213240	16776	640	8
1, 17	9281260	18843936	14277440	5995752	1482780	213120	16816	635	9
2, 16	9278320	18846288	14275760	5996592	1482360	213240	16776	640	8
3, 15	9281260	18843936	14277440	5995752	1482780	213120	16816	635	9
4, 14	9278320	18846288	14275760	5996592	1482360	213240	16776	640	8
5, 13	9281260	18843936	14277440	5995752	1482780	213120	16816	635	9
6, 12	9278320	18846288	14275760	5996592	1482360	213240	16776	640	8
7, 11	9281260	18843936	14277440	5995752	1482780	213120	16816	635	9
8, 10	9278320	18846288	14275760	5996592	1482360	213240	16776	640	8
9	9281260	18843936	14277440	5995752	1482780	213120	16816	635	9
Dim $\Gamma(a_0, b_0)$	167036220	339212016	256978800	107931096	26686260	3837240	302328	11475	153
Q	0	1	2	3	4	5	6	7	8

TABLE IV. Timing data of some quasi-spin MAPLE implementations^a (in seconds on four processor silicon graphics, challenge L).

$n = N$	4	6	10	14	18	22	26	30
S & T	2.55 (0.95)	5.32 (2.40)	12.08 (7.55)	28.26 (20.62)	51.53 (40.15)	110.62 (93.65)	199.26 (175.17)	338.48 (306.30)
FULL ^b	2.92 (1.17)	5.84 (3.07)	20.98 (12.25)	65.91 (42.48)	160.14 (114.13)			

^a Figures in parenthesis indicate the timings of factorization scheme only.^b All possible multiplicities.

where again

$$[r]_G! = \begin{cases} [r]_G[r-1]_G \cdots [1]_G, & r \geq 1, \\ 1, & r = 0, \end{cases} \quad (47)$$

but where now

$$[r]_G = 1 - q^r. \quad (48)$$

Since, obviously

$$[r] = -q^{-r/2}[r]_G, \quad (49)$$

we have that

$$\begin{bmatrix} r \\ s \end{bmatrix} = q^{-\frac{1}{2}s(r-s)} \begin{bmatrix} r \\ s \end{bmatrix}_G, \quad (50)$$

so that we can easily express our generating polynomials in terms of Gaussian-type quantities, involving integral powers. Thus, for the $U(n)$ q -dimension (cf. Eq. (39) of [31])

$$D_q[a, b] = \frac{[b+1]_G}{[n+1]_G} \begin{bmatrix} n+1 \\ a \end{bmatrix}_G \begin{bmatrix} n+1 \\ c \end{bmatrix}_G, \quad (51)$$

which in the limit $q \rightarrow 1$ reduces to Eq. (3), we find that

$$D_q[a, b] = q^{\rho_G} D_q[a, b]_G \quad (52)$$

where now

$$D_q[a, b]_G = \frac{[b+1]_G}{[n+1]_G} \begin{bmatrix} n+1 \\ a \end{bmatrix}_G \begin{bmatrix} n+1 \\ c \end{bmatrix}_G, \quad (53)$$

and

$$\rho_G = \frac{1}{2}b(n-c) - \frac{1}{2}N(n-a). \quad (54)$$

Similarly, defining the Gaussian analog of the $O(m, m)$ q -dimension, as follows

$$\begin{aligned} D_q^0[a_0, b_0]_G &= \frac{[b_0+1]_G}{[n+1]_G} \begin{bmatrix} n+2 \\ a_0 \end{bmatrix}_G \begin{bmatrix} n+2 \\ a_0+b_0+1 \end{bmatrix}_G \\ &\times \frac{[n+2-a_0]_G[n+1-a_0-b_0]_G - q^{m-2a_0-b_0}[a_0+b_0+1]_G[a_0]_G}{[n+2]_G^2}, \end{aligned} \quad (55)$$

we get for the generating polynomial $F_{(a_0, b_0, c_0)}(q)$ the expression

$$F_{(a_0, b_0, c_0)}(q) = q^{\eta_G} D_G^0[a_0, b_0]_G \quad (56)$$

where

$$\eta_G = \frac{1}{2}N(n+1) - (m+1)(a-a_0) + a_0(a_0+b_0) - \frac{1}{2}b_0(n-b_0). \quad (57)$$

It would be worthwhile to explore this form of generating functions using both computational as well as analytical approaches. In the latter case, one can exploit the fact that the logarithm of a Gaussian polynomial together with the multiplicative Gaussian factors (48) results in a simple sum of terms of the type $\log(1-x)$ which when expanded can provide a rather simple recursive scheme for the calculation of the desired polynomial coefficients [15]. Concerning the computational advantages of the Gaussian polynomial form, our preliminary tests indicate that it speeds up the execution by about 20%.

Acknowledgments

The authors are grateful to Professor Keith Geddes and Dr. Greg Fee of the Waterloo MAPLE Group for their kind help and useful advice. One of us (U.T.) also wishes to express her thanks to the Departments of Applied Mathematics and Systems Design Engineering of the University of Waterloo for making her stay at Waterloo possible. The continued support by NSERC is also gratefully acknowledged (J.P.).

Bibliography

- [1] M. Hamermesh, *Group Theory and Its Application to Physical Problems* (Addison-Wesley, Reading, MA, 1962).
- [2] J. Paldus, in *The Unitary Group for the Evaluation of Electronic Energy Matrix Elements*, Lecture Notes in Chemistry, Vol. 22 (Springer-Verlag, Berlin, Germany, 1981), pp. 1-50; in *Mathematical Frontiers in Computational Chemical Physics*, IMA Series, Vol. 15, D. G. Truhlar, Ed. (Springer-Verlag, Berlin, Germany, 1988), pp. 262-299; and references therein.
- [3] J. Karwowski, in *Methods in Computational Molecular Physics*, NATO ASI Series, Series B: Physics, Vol. 293, S. Wilson and G. H. F. Dierksen, Eds. (Plenum, New York, 1992), pp. 65-98.
- [4] M. A. Robb and U. Niazi, in *Reports in Molecular Theory* (CRC Press, Boca Raton, FL, 1990), Vol. 1, pp. 23-55.
- [5] X. Li and J. Paldus, *J. Math. Phys.* **31**, 1589 (1990).
- [6] F. A. Matsen and R. Pauncz, *The Unitary Group in Quantum Chemistry* (Elsevier, Amsterdam, The Netherlands, 1986).
- [7] M. D. Gould and G. S. Chandler, *Int. J. Quantum Chem.* **25**, 553, 603 (1984); **27**, 787 (E) (1985).
- [8] J. Paldus, *J. Chem. Phys.* **61**, 5321 (1974).
- [9] J. Paldus, in *Theoretical Chemistry: Advances and Perspectives*, H. Eyring and D. Henderson, Eds. (Academic, New York, 1976), Vol. 2, pp. 131-290.
- [10] J. C. Mulder, *Mol. Phys.* **10**, 479 (1966).
- [11] R. Pauncz, *Int. J. Quantum Chem., Quantum Chem. Symp.* **15**, 101 (1981).
- [12] J. Paldus, in *Electrons in Finite and Infinite Structures*, Proceedings of NATO ASI, P. Phariseau and L. Scheire, Eds. (Plenum, New York, 1977), pp. 411-429.
- [13] M. J. Downward and M. A. Robb, *Theor. Chim. Acta* **46**, 129 (1977).
- [14] J. Katriel, R. Pauncz, and J. C. Mulder, *Int. J. Quantum Chem.* **23**, 1855 (1983).
- [15] D. K. Sunko and D. Svrtan, *Phys. Rev. C* **31**, 1929 (1985).
- [16] D. K. Sunko, *Phys. Rev. C* **33**, 1811 (1986).
- [17] J. Katriel and A. Novoselsky, *J. Phys. A: Math. Gen.* **22**, 1245 (1989).
- [18] J. R. Huizenga and L. G. Moretto, *Annu. Rev. Nucl. Sci.* **22**, 427 (1972).

- [19] M. Kibler and G. Grenet, Phys. Rev. B23, 967 (1981), Int. J. Quantum Chem. 29, 485 (1986).
- [20] M. Kibler and J. Katriel, Phys. Lett. A147, 417 (1990).
- [21] A. Torre, L. Lain, and J. Millan, J. Mol. Structure (Theochem) 287, 63 (1993).
- [22] C. Valdemoro, Phys. Rev. A31, 2114 (1985).
- [23] J. B. French, in *Nuclear Structure*, A. Hossain, Harum-ar-Raschid, and M. Islam, Eds. (North-Holland, Amsterdam, The Netherlands, 1967), p. 85.
- [24] B. J. Dalton, S. M. Grimes, J. P. Vary, and S. A. Williams (Eds.), *Theory and Application of Moment Methods in Many-Fermion Systems* (Plenum, New York, 1980).
- [25] M. Nomura, Progr. Theor. Phys. 51, 489 (1974); J. Math. Phys. 26, 738, 965 (1985); 27, 536 (1986); 31, 351 (1990).
- [26] J. Karwowski, W. Duch, and C. Valdemoro, Phys. Rev. A33, 2254 (1986).
- [27] M. Nomura, Phys. Rev. A37, 2709 (1988).
- [28] J. Karwowski and C. Valdemoro, Phys. Rev. A37, 2712 (1988).
- [29] I. G. Macdonald, *Symmetric Functions and Hall Polynomials* (Clarendon, Oxford, England, 1979).
- [30] B. W. Char, K. O. Geddes, G. H. Gonnet, and S. M. Watt, *MAPLE Users Guide, First Leaves and MAPLE Reference Manual*, 4th ed. (WATCOM Publications Ltd., Waterloo, Ont., Canada, 1985).
- [31] M. D. Gould, J. Paldus, and J. Čížek, Int. J. Quantum Chem., in press.
- [32] R. B. Zhang, M. D. Gould, and A. J. Bracken, Commun. Math. Phys. 137, 13 (1991).
- [33] M. Jimbo, Commun. Math. Phys. 102, 247 (1986); Lett. Math. Phys. 10, 63 (1985); 11, 247 (1986); V. G. Drinfeld, Proc. ICM Berkeley 1, 798 (1986).
- [34] V. G. Kac, *Infinite Dimensional Lie Algebras* (Cambridge University Press, Cambridge, England, 1985).
- [35] C. N. Yang, Phys. Rev. Lett. 63, 2144 (1989); C. N. Yang and S. C. Zhang, Mod. Phys. Lett. B4, 759 (1990); M. Pernici, Europhys. Lett. 12, 75 (1990).
- [36] F. H. L. Essler, V. E. Korepin, and K. Schoutens, Phys. Rev. Lett. 67, 3848 (1991); Nucl. Phys. B372, 559 (1991); *ibid.* B 384, 431 (1992).
- [37] O. J. Heilmann and E. H. Lieb, Trans. N.Y. Acad. Sci. 33, 116 (1971).
- [38] J. Čížek, R. Pauncz and E. R. Vrscaj, J. Chem. Phys. 78, 2468 (1983).
- [39] R. G. Parr, *The Quantum Theory of Molecular Electronic Structure* (Benjamin, New York, 1963).
- [40] R. Pariser, J. Chem. Phys. 24, 250 (1956).
- [41] J. Koutecký, J. Paldus, and J. Čížek, J. Chem. Phys. 83, 1722 (1985) and references therein.
- [42] J. Čížek and J. Paldus, unpublished results.
- [43] J. E. Humphreys, *Introduction to Lie Algebras and Representation Theory* (Springer, New York, 1972).

Received February 17, 1994

The Coupled Cluster Theory of Quantum Lattice Systems

RAYMOND F. BISHOP and YANG XIAN

*Department of Mathematics, University of Manchester Institute of Science and Technology (UMIST),
P.O. Box 88, Manchester M60 1QD, United Kingdom*

Abstract

The coupled cluster method is widely recognized nowadays as providing an *ab initio* method of great versatility, power, and accuracy for handling in a fully microscopic and systematic way the correlations between particles in quantum many-body systems. The number of successful applications made to date within both chemistry and physics is impressive. In this article we review our recent extensions of the method which now provide a unifying framework for also dealing with strongly interacting infinite quantum lattice systems described by a Hamiltonian. Such systems include both spin-lattice models (such as the anisotropic Heisenberg or XXZ model) exhibiting interesting magnetic properties, and electron lattice models (such as the tJ and Hubbard models), where the spins or fermions are localized on the sites of a regular lattice; as well as lattice gauge theories [such as the Abelian $U(1)$ model of quantum electrodynamics and non-Abelian $SU(n)$ models]. Illustrative results are given for both the XXZ spin lattice model and $U(1)$ lattice gauge theory. © 1994 John Wiley & Sons, Inc.

Introduction

The power of the coupled cluster method (CCM) as an *ab initio* technique in microscopic quantum many-body theory is widely known and well documented in quantum chemistry [1,2], particularly where results of extremely high accuracy are required, such as for the calculation of molecular energy differences of chemical significance or for the calculation of parity violation in atoms. However, the CCM has also been used much more widely in quantum many-body theory and quantum field theory, where it has now become what is probably the most powerful, most universally applicable, and numerically most accurate of all available fully microscopic frameworks for describing in a fully rigorous fashion the quantum correlations between systems of interacting particles. The number of successful applications to date within both chemistry and physics is truly impressive. In most cases the numerical results achieved are either the best or among the best available. A recent review for a quantum chemistry audience of the applications of the CCM outside chemistry has been given by one of the present authors [3]. Bartlett has given a comparable review [1] within chemistry. In addition, there have been many recent reviews of the method itself, including those given in Refs. [3–12].

This widespread success of the CCM applications to both finite and extended systems in continuous space has naturally led to the method being applied in the

last few years [13–24] to quantum-mechanical systems defined on an extended regular spatial lattice. Examples of such applications include: (i) spin-lattice systems, such as the solid phases of ^3He [13] and various models of interest in magnetism, e.g., the spin- $\frac{1}{2}$ anisotropic Heisenberg (or XXZ) model [14] and its extension to higher spins [15], and the spin-1 Heisenberg-biquadratic model [16]; (ii) models of strongly interacting electrons on lattices, such as the Hubbard model [19–21]; and (iii) lattice gauge field theories [22–24].

The recent discovery of high-temperature superconductors has played a large part in the resurgence of interest in spin and electron lattice models. For example, among the various models proposed, the Hubbard model of electrons on a two-dimensional (2D) square lattice is widely believed to describe the essential correlations of the active electrons in these ceramic cuprate materials. Furthermore, the antiferromagnetic Heisenberg model of spins on a lattice can be derived from the Hubbard model at half-filling, and is itself believed to describe the electronic properties of the undoped insulating precursors to the high- T_c materials.

We also note that even quantum-mechanical spin-lattice systems with very simple Hamiltonians are often endowed with very complicated physical properties and intricate phase diagrams. Their behavior is often quite unlike that of their classical counterparts. An obvious example is the one-dimensional (1D) Heisenberg model, which is fully integrable by the Bethe ansatz technique [25] in the spin- $\frac{1}{2}$ case, from which it is known to have a gapless excitation spectrum, but which is conjectured [26] to have a nonzero gap in the nonintegrable spin-1 case. More generally, such quantal spin systems often exhibit a rich variety of orderings and phases as functions of the combinations of interactions (e.g., nearest-neighbor plus next-nearest-neighbor), the lattice structure, the spin of the particles, the number of spatial dimensions, and such other external variables as the applied magnetic field. A single system can thus display one or more of: phases with Ising-like long-range order, dimerized or trimerized phases, valence-bond solid structure, and much other exotic and often only poorly understood structure. In the light of both this richness of behavior and the existence of various exact solutions for several models with certain values of their parameters, spin-lattice models provide a particular challenge for quantum many-body theory to provide an accurate and detailed microscopic description of their manifold properties.

A comparable challenge is provided by lattice gauge field theory, which was originally introduced to provide a cure for the chronic divergences inherent in comparable field theories in a spatial continuum. Lately, lattice gauge models have become of interest in their own right, partly because they provide an especially severe test for theoretical techniques due to their intrinsically nonperturbative character and the limitations imposed by the requirement to impose manifest gauge-invariance at all stages. However, lattice gauge models share many of the features and attributes of spin-lattice models. It has been our intention to exploit this similarity and to develop the CCM as a unifying framework for treating all infinite-lattice Hamiltonians. In particular, we have shown how various CCM lattice approximation schemes developed for the spin models can be simply modified for use with both Abelian and non-Abelian lattice gauge theories.

The remainder of this article is organized as follows. In the next section we describe the basic elements of the CCM which are needed for the analysis of a general many-body system. In the third section we consider in some detail the XXZ model Hamiltonian as an archetypal spin-lattice problem to which the CCM can be applied. Particular attention is paid to the development of suitable approximation schemes. We also show that these lead to results of very high accuracy at relatively low orders of implementation. In the subsequent section we demonstrate how analogues of these schemes may be applied with comparable success to lattice gauge theories, where we choose the $U(1)$ model as a concrete example. Our findings are summarized in the final section, where we also indicate possible further extensions of the CCM and consider its potential for even wider applications.

Basic Elements of the CCM Formalism

In order to describe quantitatively the multiparticle correlations in a quantum many-body system one always needs a model (or reference) state $|\Phi\rangle$ against which to compare them. In the CCM the only requirement on $|\Phi\rangle$ is that it forms a *cyclic vector* with respect to which we may define two subalgebras, namely that of the multiconfigurational creation operators $\{C_J^\dagger\}$ and that of their Hermitian-conjugate destruction counterparts $\{C_J\}$. Very importantly, both subalgebras are required to be Abelian, i.e., $[C_J^\dagger, C_{J'}^\dagger] = 0 = [C_J, C_{J'}]$, where each set-index J labels a general multiparticle cluster configuration with respect to $|\Phi\rangle$, which itself thus plays the role of vacuum (or reference) state. We thus require that the operators $\{C_J^\dagger\}$ and $\{C_J\}$ are complete, in the sense that arbitrary ket and bra states within the appropriate many-body Hilbert space \mathcal{H} may be decomposed as the respective linear combinations,

$$|\Psi\rangle = \sum_J f_J C_J^\dagger |\Phi\rangle; \langle\tilde{\Psi}| = \sum_J \tilde{f}_J \langle\Phi| C_J. \quad (1)$$

This is clearly achievable if the identity operator I within \mathcal{H} has the resolution,

$$I = \sum_J C_J^\dagger |\Phi\rangle \langle\Phi| C_J. \quad (2)$$

For practical purposes it is also convenient, but not essential, if the operators form an orthonormal set, in the following sense,

$$\langle\Phi| C_J C_{J'}^\dagger |\Phi\rangle = \delta(J, J'), \quad (3)$$

where $\delta(J, J')$ is some (suitably defined) delta function between the set indices $\{J\}$.

As an example we consider the familiar application of the CCM to an N -electron molecule. Here $|\Phi\rangle$ is chosen as an N -electron Slater determinant formed from the lowest N levels of an (orthonormal) set of suitably defined molecular (spin-) orbitals. The set-indices in the fixed- N Hilbert space, $J \rightarrow \{p_1, \dots, p_m; \alpha_1, \dots, \alpha_m\}$, now represent an m -particle/ m -hole cluster configuration, where the single-particle indices $\{\alpha_i\}$ label the single-hole states that can be created by removing

an electron from $|\Phi\rangle$, and the single-particle indices $\{p_i\}$ label the remaining unoccupied or particle states.

The CCM is now characterized by writing the exact ground ket state $|\Psi_0\rangle$ of the many-body Hamiltonian H in terms of an *exponentiated* cluster correlation operator S ,

$$|\Psi_0\rangle = e^S |\Phi\rangle; \quad H|\Psi_0\rangle = E_0 |\Psi_0\rangle, \quad (4)$$

which may be decomposed wholly and exactly in terms of creation operators,

$$S = \sum_J' \mathcal{S}_J C_J^\dagger, \quad (5)$$

where, by definition, the prime on the sum over configurations $\{J\}$ excludes the $J = 0$ term corresponding to the identity operator, $C_0^\dagger \equiv I$. We thus have the *intermediate normalization condition*, $\langle \Phi | \Psi_0 \rangle = \langle \Phi | \Phi \rangle = 1$, in the usual scheme where $\langle \Phi | C_J^\dagger | \Phi \rangle = 0$, $\forall J \neq 0$. The correlation operator of an N -body system may itself also be decomposed as a linear superposition of n -body partitions, $S = \sum_{n=1}^N S_n$, where S_n describes the configurations formed by exciting n particles from their single-particle states occupied in $|\Phi\rangle$.

The reason for writing the correlation operator in the exponential form of Eqs. (4) and (5), rather than in the linear form of Eq. (1) which is typical of the configuration-interaction (CI) method, lies at the heart of the CCM [3,5,7]. Particularly important features of the exponential form are: (i) its proper counting of *independent* excitations (e.g., n independent pairs of particles excited from $|\Phi\rangle$ are properly described by the wave function $(1/n!) S_n^2 |\Phi\rangle$); (ii) its automatic incorporation of the important linked-cluster theorem of Goldstone; and (iii) its incorporation of *size-extensivity*, so that such extensive variables as the ground-state energy E_0 scale properly with particle number in the infinite limit $N \rightarrow \infty$, even when S is truncated.

In practice the CCM is implemented by restricting the cluster amplitudes $\{\mathcal{S}_J\}$ to some (finite or infinite) subset of the entire set, within a well-defined hierarchy of such approximations. Solutions for the amplitudes retained are then found by first rewriting the ground-state Schrödinger Eq. (4) in the similarity-transformed form,

$$(e^{-S} H e^S - E_0) |\Phi\rangle = 0, \quad (6)$$

which underpins the CCM. By taking the inner products of Eq. (6) with the complete set of states comprising $|\Phi\rangle$ itself and $\{C_J^\dagger |\Phi\rangle; J \neq 0\}$, we find, respectively,

$$\langle \Phi | e^{-S} H e^S | \Phi \rangle = E_0, \quad (7)$$

$$\langle \Phi | C_J e^{-S} H e^S | \Phi \rangle = 0; \quad J \neq 0. \quad (8)$$

The set of Eqs. (8) represents a coupled set of nonlinear equations for the c -number coefficients $\{\mathcal{S}_J\}$, equal in number to the number of retained configurations $\{J\}$. In terms of their solutions, Eq. (7) then gives the corresponding approximant for the ground-state energy, $E_0 = E_0[\mathcal{S}_J]$.

The well-known expansion in terms of nested commutators,

$$e^{-S}He^S = H + [H, S] + \frac{1}{2!} [[H, S], S] + \dots, \quad (9)$$

together with the fact that each of the individual terms in the expansion of Eq. (5) for the operator S commutes with all others, ensures that every element of S in Eq. (5) is linked directly to the Hamiltonian in each of the terms in Eq. (9). No unlinked (or, equivalently, disconnected) terms or diagrams can arise, and each of the coupled equations (8) is of linked-cluster type. Furthermore, when each term in the Hamiltonian H in second-quantized form contains only a finite number of single-particle destruction operators defined with respect to $|\Phi\rangle$, as is usually the case, the otherwise infinite series of Eq. (9) will always terminate after a finite number of terms. As a consequence, the left-hand sides of Eqs. (7) and (8) are expressions of finite order in the retained coefficients $\{\mathcal{S}_J\}$, and no further (artificial or approximate) truncation is required for their evaluation. The CCM thus fundamentally differs from its unitarity-transformation counterpart that would arise in a standard variational formulation, in which the bra state $\langle\Psi_0|$ is simply taken as the manifest Hermitian conjugate, $\langle\Phi|e^{S^\dagger}$, of $|\Psi_0\rangle$.

The above feature is very important, and leads naturally to the biorthogonal description of states within the CCM (rather than the more usual orthogonal description), in which the manifest Hermitian conjugacy of corresponding bra and ket states is lost. While the bra states are not needed to calculate the ground-state energy, they are needed to calculate such other ground-state expectation values as order parameters. In what has become known [5] as the normal version of the CCM, the bra ground-state is parametrized in the form,

$$\langle\tilde{\Psi}_0| = \langle\Phi|\tilde{S}e^{-S}; \quad \langle\tilde{\Psi}_0|H = E_0\langle\tilde{\Psi}_0|, \quad (10)$$

$$\tilde{S} = 1 + \sum_J' \tilde{\mathcal{S}}_J C_J, \quad (11)$$

with explicit normalization,

$$\langle\tilde{\Psi}_0|\Psi_0\rangle = \langle\Phi|\Psi_0\rangle = \langle\Phi|\Phi\rangle = 1. \quad (12)$$

Equation (10) readily leads to the equations,

$$\langle\Phi|\tilde{S}(e^{-S}He^S - E_0)C_J^\dagger|\Phi\rangle = 0, \quad \forall J, \quad (13)$$

which, by making use of Eq. (7) and the fact that $[S, C_J^\dagger] = 0$ for all set-indices J , may easily be rewritten as,

$$\langle\Phi|\tilde{S}e^{-S}[H, C_J^\dagger]e^S|\Phi\rangle = 0, \quad \forall J. \quad (14)$$

Equations (13) and (14) have the form of coupled but *linear* equations for the bra-state coefficients $\{\tilde{\mathcal{S}}_J\}$ once the ket-state coefficients $\{\mathcal{S}_J\}$ are used as known input. Once again, the resulting equations contain only finite powers of S since the nested commutator expansions again terminate as before. It is not difficult to show that Eq. (13) has the formal solution

$$\langle \Phi | \tilde{S} = \langle \Phi | - \langle \Phi | e^{-S} H e^S Q (Q e^{-S} H e^S Q - E_0)^{-1} Q, \quad (15)$$

$$Q \equiv I - |\Phi\rangle\langle\Phi|, \quad (16)$$

in terms of which the ground-state expectation value of an arbitrary operator A can be written as

$$\begin{aligned} \bar{A} &= \bar{A}[\mathcal{S}] \equiv \langle \tilde{\Psi}_0 | A | \Psi_0 \rangle \\ &= \langle \Phi | e^{-S} A e^S | \Phi \rangle - \langle \Phi | e^{-S} H e^S Q (Q e^{-S} H e^S Q - E_0)^{-1} Q e^{-S} A e^S | \Phi \rangle. \end{aligned} \quad (17)$$

We note that Eq. (8) guarantees that $\tilde{H} = E_0$, as given by Eq. (7).

Excited states $\{|\Psi_\lambda\rangle\}$ are described within the CCM [27] by linear excitation operators $\{X^\lambda\}$ which act on the corresponding exact ground-state wave function $|\Psi_0\rangle$,

$$|\Psi_\lambda\rangle = X^\lambda |\Psi_0\rangle = X^\lambda e^S |\Phi\rangle; \quad H |\Psi_\lambda\rangle = E_\lambda |\Psi_\lambda\rangle \equiv (E_0 + \varepsilon_\lambda) |\Psi_\lambda\rangle, \quad (18)$$

where X^λ is again decomposed wholly in terms of creation pieces with respect to $|\Phi\rangle$,

$$X^\lambda = \sum_J X_J^\lambda C_J^\dagger. \quad (19)$$

Hence the operators S and X^λ commute. The excited-state Schrödinger Eq. (18) may be combined with its ground-state counterpart of Eq. (4) to give the CCM eigenvalue equation,

$$e^{-S} [H, X^\lambda] e^S |\Phi\rangle = \varepsilon_\lambda X^\lambda |\Phi\rangle, \quad (20)$$

for the excitation energy, $\varepsilon_\lambda \equiv E_\lambda - E_0$, directly. Equation (20) may be equivalently written as,

$$(Q e^{-S} H e^S Q - E_0) Q X^\lambda |\Phi\rangle = \varepsilon_\lambda Q X^\lambda |\Phi\rangle, \quad (21)$$

from which we see that the excitation energies are given by diagonalizing in the space spanned by the states $\{C_J^\dagger |\Phi\rangle; J \neq 0\}$ the same matrix $(Q e^{-S} H e^S - E_0)$ as needs to be formally inverted in Eq. (15) to find \tilde{S} . In all practical implementations of the CCM, this space is truncated to some (finite or infinite) subspace spanned by a subset of the states. The operators S , \tilde{S} , and X^λ given by Eqs. (5), (11), and (19) are thus approximated by restricting the sum over configurations $\{J\}$ to the appropriate subset.

In the following two sections we show how the above general CCM scheme can be applied to both spin-lattice Hamiltonian systems and Hamiltonian lattice gauge theories.

Applications to Spin Lattices

We illustrate the application of the CCM to spin-lattice problems by considering the archetypal XXZ or anisotropic Heisenberg model as a specific example. This model comprises N spins, with spin quantum number s , on the sites $\{l\}$ of a d -

dimensional regular lattice, which interact via nearest-neighbor couplings described by the Hamiltonian

$$H = \frac{1}{2} \sum_{l=1}^N \sum_{\rho=1}^z \left[\Delta s_l^z s_{l+\rho}^z + \frac{1}{2} (s_l^+ s_{l+\rho}^- + s_l^- s_{l+\rho}^+) \right], \quad (22)$$

where the index l runs over all $N (\rightarrow \infty)$ lattice sites with the usual periodic boundary condition imposed; the index ρ runs over all z nearest-neighbor sites (i.e., z is the coordination number of the lattice); the operators s_l^z and $s_l^\pm \equiv s_l^x \pm i s_l^y$ are spin- s operators which obey the usual $SU(2)$ angular momentum commutation relations; and Δ is the anisotropy parameter, which in the special case $\Delta = 1$ gives the isotropic Heisenberg model. For present purposes we consider only bipartite lattices, where the lattice is composed of two equivalent alternating sublattices, denoted as A and B . Bipartite lattices thus include the important 1D chain and the 2D square lattice. The restriction to bipartite lattices excludes such lattices as the triangular lattice and such associated effects as frustration. We also restrict attention here to the case $\Delta > 0$, where for the 1D chain, for example, the system is known to be antiferromagnetic in its ground state.

In order to perform a CCM analysis of this model we must now first choose a model state $|\Phi\rangle$. Although there are many alternative choices [16], we illustrate the approach here with what is possibly the simplest and most obvious choice, namely where $|\Phi\rangle$ is chosen to be the (classical) Néel state $|N\rangle$ in which all spins on the A -sublattice have z -component $s^z = -s$, say, and all those on the B -sublattice have $s^z = +s$. This state thus has perfect antiferromagnetic long-range order, but is an eigenstate of the quantum Hamiltonian of Eq. (22) only in the Ising model ($\Delta \rightarrow \infty$) limit. The single-spin creation operators with respect to $|N\rangle$ are clearly the spin-raising operators $\{s_i^+\}$ for sites i on the "spin-down" A -sublattice and the spin-lowering operators $\{s_j^-\}$ for sites j on the "spin-up" B -sublattice. Each of these operators can act a maximum of $2s$ times on a single site before the state $|N\rangle$ is annihilated.

The XXZ Hamiltonian of Eq. (22) is easily seen to commute with the operator $s_{\text{total}}^z \equiv \sum_{l=1}^N s_l^z$. Hence, the antiferromagnetic ground-state $|\Psi_0\rangle$ may, by definition, be sought in the subspace where $s_{\text{total}}^z = 0$. Equations (4) and (5) thus become, in this case,

$$|\Psi_0\rangle = e^S |N\rangle; \quad S = \sum_{m=1}^{N/2} S_{2m}, \quad (23)$$

with cluster correlation operators S_{2m} expressed with a somewhat arbitrary choice of normalization constant as,

$$S_{2m} = \frac{(-1)^m}{(m!)^2} \sum_{i_1, i_2, \dots, i_m} \sum_{j_1, j_2, \dots, j_m} \mathcal{S}_{i_1 i_2 \dots i_m j_1 j_2 \dots j_m} s_{i_1}^+ s_{i_2}^+ \dots s_{i_m}^+ s_{j_1}^- s_{j_2}^- \dots s_{j_m}^-, \quad (24)$$

where indices $\{i_l\}$ and $\{j_m\}$ refer to sites on the A - and B -sublattices, respectively. The equivalent analogues of Eqs. (10) and (11) are,

$$\langle \tilde{\Psi}_0 | = \langle N | \tilde{S} e^{-S}; \quad \tilde{S} = 1 + \sum_{m=1}^{N/2} \tilde{S}_{2m}, \quad (25)$$

$$\tilde{S}_{2m} = \frac{(-1)^m}{(m!)^2} \sum_{i_1, i_2, \dots, i_m} \sum_{j_1, j_2, \dots, j_m} \tilde{\mathcal{S}}_{i_1 i_2 \dots i_m j_1 j_2 \dots j_m} s_{i_1}^- s_{i_2}^- \dots s_{i_m}^- s_{j_1}^+ s_{j_2}^+ \dots s_{j_m}^+, \quad (26)$$

Clearly, for spin- s particles the coefficients $\mathcal{S}_{i_1 \dots i_m j_1 \dots j_m}$ and $\tilde{\mathcal{S}}_{i_1 \dots i_m j_1 \dots j_m}$ vanish if any one of the lattice indices appears more than $2s$ times.

The ground-state energy per particle may simply be calculated from Eq. (7). We find,

$$\frac{E_0}{N} = -\frac{zs^2}{2} (\Delta + 2b_1), \quad (27)$$

where, as before, z is the lattice coordination number, and $b_1 \equiv \mathcal{S}_{i, i+\rho}$ is the nearest-neighbor pair correlation coefficient. We note that b_1 is independent of both the index i (by lattice translational invariance) and the index ρ (by the lattice symmetries under rotations and reflections). We also note that Eq. (27) is exact. The coefficient b_1 is itself calculated from the coupled sets of equations for the coefficients $\{\mathcal{S}_{i_1 \dots i_m j_1 \dots j_n}\}$, which are determined as in Eq. (8), with $C_J \rightarrow s_{i_1}^- \dots s_{i_n}^- s_{j_1}^+ \dots s_{j_n}^+$. As usual the number of such equations must be truncated in practice by restricting the configurations retained in Eqs. (24) and (26), and then solving Eqs. (8) and (14) without further approximations, keeping in each case the same configurations for these coupled sets of equations, so that we have one equation in each set for each retained ket- or bra-state coefficient. The algebraic form of the sets of Eqs. (8), for example, is that of a coupled set of multinomial equations, each term of which is easily seen from Eq. (9) to be of degree no higher than fourth, by noting the bilinear form of the Hamiltonian of Eq. (22) and the specific $SU(2)$ commutation relations. Their explicit evaluation is straightforward, although very tedious and time-consuming if done by hand if more than a few configuration coefficients are retained. Nevertheless, the algebraic reduction is very amenable to automation using computer-algebraic techniques, and many of the actual results given below have been found this way.

All that remains at this point, in order to perform a CCM calculation, is to consider appropriate truncation hierarchies. These cannot ever be uniquely specified, and must always be motivated on physical grounds for the problem at hand. We discuss here two such schemes. From previous applications of the CCM to systems defined in a spatial continuum, the most well-known truncation hierarchy is the so-called SUB n scheme defined by truncating the summations in Eqs. (23) and (25) so that one retains only up to n -body correlation coefficients,

$$S \rightarrow S_{\text{SUB}n} \equiv \sum_{k=1}^n S_k; \quad \tilde{S} \rightarrow \tilde{S}_{\text{SUB}n} \equiv 1 + \sum_{k=1}^n \tilde{S}_k. \quad (28)$$

For example, the CCM coupled equations for the two-spin-flip ket-state coefficients $\mathcal{S}_{i,j}$ are now found from the relation,

$$\langle N | s_i^- s_j^+ e^{-S_2} H e^{S_2} | N \rangle = 0. \quad (29)$$

Straightforward evaluation of Eq. (29) yields the coupled equations,

$$\sum_{\rho} \left[(1 + 2\Delta b_1 + 2b_1^2) \delta_{\rho, r} - 4s(\Delta + 2b_1)b_r + 4s^2 \sum_{r'} b_{r'} b_{r-r'+\rho} \right] = 0, \quad (30)$$

where $b_r \equiv \mathcal{S}_{i,j}$ with $r \equiv j - i$, and we have taken advantage of the translational invariance of the lattice. We note that in 1D r is simply a (positive or negative) odd integer, whereas in 2D r is a lattice vector connecting sites on opposite sublattices. Rotational and reflectional symmetry imposes extra relations among the coefficients $\{b_r\}$: for example, in 1D, $b_{-r} = b_r$. The bra-state coefficients $\tilde{b}_r \equiv \tilde{\mathcal{S}}_{i,j}$ are defined, and equivalent relations derived, similarly.

The full set of nonlinear SUB2 Eqs. (30) can be solved analytically by a sublattice Fourier transform method [14]. For the 1D chain, for example, the solution is

$$b_r = K \int_0^\pi \frac{dq \cos rq}{\pi \cos q} (1 - \sqrt{1 - k^2 \cos^2 q}),$$

$$K \equiv \frac{1}{2s} (\Delta + 2b_1), \quad k^2 \equiv \frac{1 + 2\Delta b_1 + 2b_1^2}{(\Delta + 2b_1)^2}. \quad (31)$$

The coefficient b_1 is thus determined self-consistently by putting $r = 1$ in Eq. (31), from which the ground-state energy may be immediately found from Eq. (27). Results for the 1D spin- $\frac{1}{2}$ chain and the 2D spin- $\frac{1}{2}$ square lattice are given in Tables I and II, respectively. Very interestingly, the exact SUB2 solution of Eq. (31) predicts a phase transition at the terminating point in Eq. (31) for which $k \rightarrow k_c = 1$, and beyond which the equation has no real solution. This terminating condition determines a critical anisotropy Δ_c , such that no real SUB2 solution exists for $\Delta < \Delta_c$. Numerical solutions yield the values $\Delta_c \approx 0.3728, 0.7985$, and 0.8872 for the spin- $\frac{1}{2}$ models on the 1D chain, 2D square lattice, and 3D cubic lattice, respectively.

TABLE I. Ground-state energy per spin as a function of Δ for the 1D spin- $\frac{1}{2}$ XXZ model. Shown are the results of the full SUB2 and various LSUB n schemes, defined in the text, together with the exact results for comparison.

Method	Δ					
	0.0	0.5	1.0	1.5	2.0	5.0
SUB2	—	-0.3506	-0.4186	-0.5075	-0.6079	-1.2986
LSUB2	-0.2887	-0.3412	-0.4167	-0.5069	-0.6076	-1.2986
LSUB4	-0.3193	-0.3692	-0.4363	-0.5195	-0.6155	-1.2995
LSUB6	-0.3198	-0.3730	-0.4400	-0.5218	-0.6167	-1.2995
LSUB8	-0.3196	-0.3741	-0.4414	-0.5226	-0.6170	-1.2995
LSUB10	-0.3194	-0.3745	-0.4420	-0.5230	-0.6171	-1.2995
Exact	-0.3183	-0.3750	-0.4432	-0.5234	-0.6172	-1.2995

TABLE II. Ground-state energy per spin for the 2D spin- $\frac{1}{2}$ Heisenberg model ($\Delta = 1$) on a square lattice. Shown are the results of the full SUB2 and various LSUB(w, d) schemes, defined in the text, together with the results of spin-wave theory (SWT) of Ref. [29], and from the Green's function Monte Carlo (GFMC) calculations of Ref. [28] for comparison.

SUB2	LSUB(6,6)	LSUB(8,8)	LSUB(10,10)	SWT	GFMC
-0.6508	-0.6483	-0.6531	-0.6644	-0.6580	-0.6692

We have shown elsewhere [14,15], by the further calculation of the spin-spin correlation functions, the staggered magnetization, and the low-lying excitations, that the above critical point really corresponds to the known Ising-Heisenberg phase transition, which is known to occur at $\Delta = 1$ in the 1D spin- $\frac{1}{2}$ chain. (We also note that when more of the higher-order multi-spin correlations neglected in SUB2 approximation are included, the value of Δ_c moves closer to this exact value [14], as expected.) For example, we have shown by calculating from Eqs. (18) and (19) the spin-wave-like excitations on top of the SUB2 ground state, that the low-lying excitation spectrum has a finite gap for $\Delta > \Delta_c$ and that this gap exactly vanishes as $\Delta \rightarrow \Delta_c$ for lattices of all dimensions. Furthermore, the staggered magnetization M^z , defined for a spin on the site j on the ("up") B -sublattice as,

$$M^z \equiv \frac{1}{s} \langle s_j^z \rangle = \frac{1}{s} \langle \Phi | \tilde{S} e^{-S} s_j^z e^S | \Phi \rangle, \quad (32)$$

can easily be evaluated in the SUB2 approximation as,

$$M_{\text{SUB2}}^z = 1 - 4s \sum_r \tilde{b}_r b_r. \quad (33)$$

The exact solution of Eq. (31) for $\{b_r\}$ and its counterpart for $\{\tilde{b}_r\}$ yield that $M_{\text{SUB2}}^z \rightarrow 0$ as $\Delta \rightarrow \Delta_c$ in the 1D case, in agreement with the exact result [25] at $\Delta = 1$, but that M_{SUB2}^z remains nonzero as $\Delta \rightarrow \Delta_c$ in 2D and 3D. For example, for the important 2D spin- $\frac{1}{2}$ model on the square lattice, $M_{\text{SUB2}}^z \approx 0.682$ at $\Delta = \Delta_c$. This value is in good agreement with the results of recent large-scale Monte Carlo simulations and the other best available calculations cited in Ref. [14].

We now turn our attention to an alternative approximation scheme which is specifically and closely tailored to lattice systems. The capability of predicting phase transitions in the SUB2 and higher SUB n schemes is clearly related to their inclusion of at least some correlations of arbitrarily long range. However, if we wish to calculate only the energy or other properties of the ground state which are not sensitive to possibly nearby phase transitions, we can employ a very efficient alternative scheme which in practice is capable of very high accuracy. This scheme, denoted as the LSUB n scheme, takes advantage of the localized nature of the interactions, so that one retains at a given order of the approximation only those local configurations in the cluster correlation operators S and \tilde{S} specified by the index n . Very specifically, for the problem at hand the LSUB n approximation retains only those configurations

which contain any number of flipped spins with respect to the Néel model state over a localized region of at most n contiguous sites on the lattice, and which are compatible with the condition that $s_{\text{total}}^z = 0$.

As a simple example we consider the spin- $\frac{1}{2}$ 1D chain. The LSUB2 scheme retains for the operator S only the single coefficient $b_1 \equiv \mathcal{S}_{i,i+1}$, whose determining equation from Eq. (30) is given by,

$$1 - 2\Delta b_1 - 3b_1^2 = 0, \quad (34)$$

with (physical) solution $b_1 = (\sqrt{\Delta^2 + 3} - \Delta)/3$, and corresponding estimate for the ground-state energy given from Eq. (27) as $E_0/N = -5/12 \approx -0.4167$ for the isotropic ($\Delta = 1$) Heisenberg case. This is surprisingly close to the full SUB2 result of -0.4186 for this case. For the higher-order LSUB n approximations, the number of independent configurations retained in the correlation operator S or \hat{S} grows rapidly with n (e.g., for $n = 4, 6, 8$, and 10 , the corresponding numbers of independent configurations are $3, 9, 26$, and 81 , respectively). These are illustrated in Figure 1 for the LSUB6 case. As can be seen from Table I, we obtain ground-state energies with very high accuracy in this LSUB n scheme, even for relatively low values of the truncation index n , and even for values of $\Delta < 1$ for which the exact ground state has no vestige at all of the perfect long-range order present in the Néel model state.

Turning to the 2D lattice, it is clear that the number of configurations at a given LSUB n level is considerably higher than in 1D. For example, in LSUB4 approximation for the square lattice there are seven independent spin-flip configurations. However, we can introduce two further parameters in an attempt to categorize the relative importance of the configurations more finely. The first of these is the number w of "wrong" bonds produced by flipping spins with respect to the Néel state. Classically, the breaking of each Néel "up-down" bond in the antiferromagnetic regime costs energy, and hence configurations with the smallest values of w are, *a priori*, likely to be the most important. Secondly, an extension of the seemingly important concept in 1D of locale size leads us to consider the length d of the "domain boundary" of a given configuration, defined as the number of lattice bonds crossed by a minimal-area circuit (as indicated by the dashed lines in Fig. 2) enclosing all of the flipped spins.

We may thus introduce an LSUB(w, d) approximation for the 2D lattice in which only those spin-flip configurations with values of these parameters not exceeding

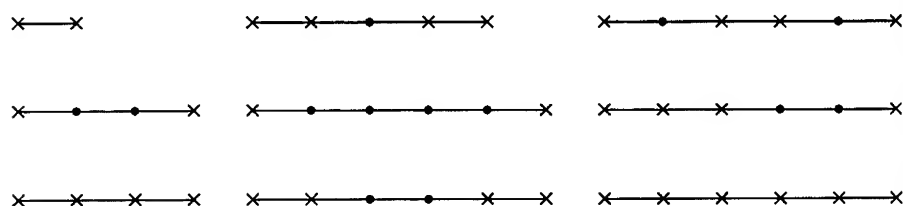


Figure 1. The nine independent configurations of the LSUB6 scheme for the 1D spin- $\frac{1}{2}$ XXZ model. The crosses indicate the flipped spins with respect to the Néel model state.

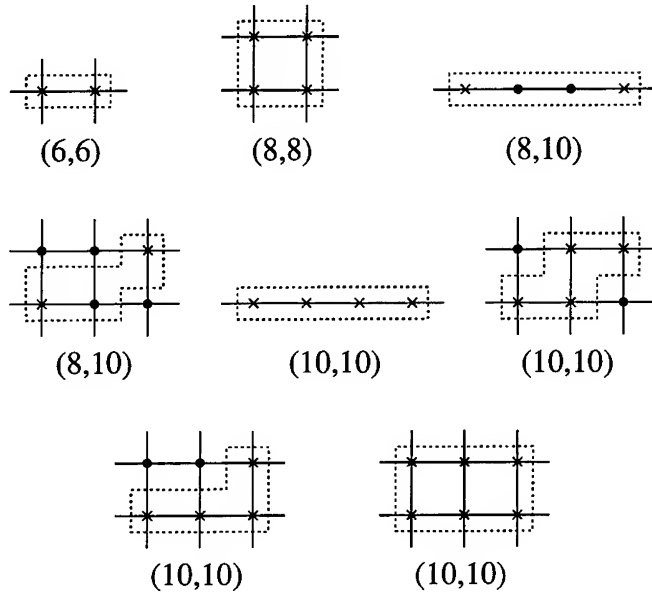


Figure 2. The eight independent configurations of the LSUB(10, 10) scheme for the 2D spin- $\frac{1}{2}$ XXZ model on a square lattice. The weights (w , d) defined in the text are shown below each configuration.

w and d , respectively, are retained. For example, the LSUB(10, 10) approximation retains the 8 configurations shown in Figure 2. These include all 7 of the 2D LSUB4 configurations, plus the most compact 6-spin-flip LSUB6 cluster. Results for the ground-state energy of the 2D spin- $\frac{1}{2}$ Heisenberg ($\Delta = 1$) square lattice are shown in Table II. We observe again the excellent convergence properties of our approximation scheme, by comparing with the available Green's function Monte Carlo (GFMC) results [28], and note the marked improvement over the spin-wave theory (SWT) results [29]. It is interesting to note that just as in the LSUB n scheme for the 1D model, our LSUB(w , d) scheme consistently gives good results for the ground-state energy, for all values of $\Delta \gtrsim 0$. We also point out that our local CCM approximation schemes, such as the LSUB n and LSUB(w , d) schemes, systematically reproduce the various terms in the perturbation theory series in the $\Delta \rightarrow \infty$ limit [14], at the same time as they provide an effective continuation of the perturbative results far into the nonperturbative regime. This same characteristic of the CCM schemes will be emphasized again in the following applications to lattice gauge theory. Finally, at a rather more pragmatic level, it is also gratifying to note that the LSUB(w , d) scheme provides a rather effective practical selection of the clusters of greatest significance, to the extent that at any given order the numerical magnitudes of the coefficients of the neglected clusters are, by and large, small in comparison to those retained, for all values of $\Delta \gtrsim 0$. We have verified this observation both by comparison with the $\Delta = 1$ results of Ref. [17] and by several calculations of our own carried out to higher orders.

Applications to Lattice Gauge Field Theory

We turn now to analogous applications of CCM techniques to lattice gauge theory, where as a specific example we shall consider the Abelian $U(1)$ model of quantum electrodynamics in two discretized spatial plus one continuous time $(2 + 1)$ dimensions. The $U(1)$ group element on a link l originating at a lattice site with position vector \mathbf{n} in (positive) direction k is $U_k(\mathbf{n}) \equiv \exp[iA_k(\mathbf{n})]$, and the lattice Hamiltonian is

$$H = \frac{1}{2} \sum_{k,\mathbf{n}} E_k^2(\mathbf{n}) + \lambda \sum_{k,\mathbf{n}} [1 - \cos B_k(\mathbf{n})], \quad (35)$$

where $E_k(\mathbf{n})$ is the electric field on the links of the lattice and $B_k(\mathbf{n})$ is the magnetic field defined as the lattice curl, $B_i(\mathbf{n}) = \epsilon_{ijk}[A_k(\mathbf{n} + \mathbf{e}_j) - A_k(\mathbf{n})]$ around the elementary square plaquettes defined by the unit lattice vectors \mathbf{e}_i . Quantum mechanics is imposed in the temporal gauge through the basic commutation relation, $[A_k(\mathbf{n}), E_k(\mathbf{n}')] = i\delta_{kk'}\delta_{\mathbf{n}\mathbf{n}'}$, which is realizable via the representation $E_k(\mathbf{n}) \rightarrow -i\partial/\partial A_k(\mathbf{n})$. The Hamiltonian may then be represented wholly in terms of the plaquette variables, $B_p (\equiv B_k(\mathbf{n}))$, in the gauge-invariant sector. For example, in $2 + 1$ dimensions, we find

$$H = \sum_p \left[-2 \frac{\partial^2}{\partial B_p^2} + \lambda(1 - \cos B_p) \right] + \sum_{\langle p,p' \rangle} \frac{\partial^2}{\partial B_p \partial B_{p'}}, \quad (36)$$

where the second sum over $\langle p, p' \rangle$ indicates all nearest neighbor pairs of plaquettes. Equation (36) thus defines an infinite many-body problem with compact variables, $-\pi < B_p \leq \pi$.

In the non-Abelian $SU(N)$ case the basic variables are the $SU(N)$ matrices defined on each link l in terms of the $N^2 - 1$ group generators, and the conjugate "chromoelectric" fields E_l^α have $N^2 - 1$ components. Thus, for $SU(2)$ the group element on each link has the general form $U = d_0 \mathbf{1} + i\mathbf{d} \cdot \boldsymbol{\sigma}$, where the σ_k are the usual Pauli matrices, and the real coefficients d_α lie on a sphere in four-dimensional Euclidean space, $d_0^2 + \sum_{k=1}^3 d_k^2 = 1$. The potential term in Eq. (36) generalizes to $\lambda \sum_p (N - \text{ReTr} U_p)$, where $U_p \equiv U_1 U_2 U_3^\dagger U_4^\dagger$ for the plaquette formed from the four links $l = 1, 2, 3, 4$ in cyclic order.

Our main goal is now to provide a CCM parametrization of the physical (i.e., gauge-invariant) ground state and excited ("glueball") states of the above Hamiltonian in the vacuum sector [22,24]. We thus need firstly to choose a model state $|\Phi\rangle$. A convenient choice is the so-called electric ($\lambda \rightarrow 0$) vacuum $|0\rangle$, for which $E_l|0\rangle = 0$ for all l . The CCM now parametrizes the exact ground state in terms of $|\Phi\rangle \rightarrow |0\rangle$ as in Eq. (4), with a cluster correlation operator S given by a sum over all possible linearly independent linked clusters of Wilson loops,

$$S = \sum_{\Gamma} \sum_p \mathcal{S}_{\Gamma} A_{\Gamma}(p), \quad (37)$$

with $\Gamma (\equiv \{\gamma_i; i = 1, 2, \dots, n\}; n = 1, 2, \dots)$ and p denoting the geometry and position of the oriented loop clusters respectively, and $A_{\Gamma} = A_{\gamma_1} \cdots A_{\gamma_n}$, with

$A_\gamma \equiv \text{Tr}[U \cdots U]_\gamma$ for each closed loop γ . The ground-state energy E_0 and correlation coefficients $\{\mathcal{S}_\Gamma\}$ are determined as in Eqs. (7) and (8), respectively, with $C_J \rightarrow A_\Gamma^\dagger(p)$, and where the inner products incorporate the appropriate group measure. Furthermore, for the Hamiltonian of Eq. (36) and the correlation operator of Eq. (37), the expansion of Eq. (9) terminates at the term of second order in S .

Henceforth we focus on the specific $U(1)$ model of Eq. (36) in $2 + 1$ dimensions. (In earlier work [24] we have studied the same $U(1)$ model in $1 + 1$ dimensions, which has similar qualitative behavior. By contrast, the same model in $3 + 1$ dimensions is expected to show marked differences.) The electric vacuum state is thus simply a constant. Furthermore, the operator S can be partitioned into k -plaquette pieces, $S = \sum_{k \in 1}^{N_p} S_k$, where $N_p \rightarrow \infty$ is the total number of elementary square plaquettes in the lattice. We have, for example,

$$S_1 = \sum_{n=1}^{\infty} \sum_{p=1}^{N_p} \mathcal{S}_p(n) \cos nB_p; \quad (38)$$

$$S_2 = \sum_{n,n'=1}^{\infty} \sum_{p,p'=1}^{N_p} [\mathcal{S}_{p,p'}^{(1)}(n, n') \cos nB_p \cos n'B_{p'} + \mathcal{S}_{p,p'}^{(2)}(n, n') \sin nB_p \sin n'B_{p'}], \quad (39)$$

where the prime on the sum in Eq. (39) excludes the term with $p = p'$. For this case we have $S^\dagger = S$, and the inner products in the coupled equations of Eqs. (7) and (8) are simply the multiple integrals over all plaquette variables $\{B_p\}$ within the range $-\pi < B_p < \pi$. We also note that the multi-plaquette correlation operators $\{S_k\}$ have a close relation to the usual Wilson loops A_Γ mentioned above. For example, the simple trigonometric relation, $2 \cos B_1 \cos B_2 = \cos(B_1 + B_2) + \cos(B_1 - B_2)$ corresponds to the relationship between Wilson loops illustrated in Figure 3. Our particular parametrization exemplified by Eqs. (38) and (39) is not only complete but is also especially useful in view of the orthonormality of the basis.

It should now be immediately clear that the multi-plaquette correlations in the exact ground state $|\Psi_0\rangle$ can be approximated by truncating the operator S using the analogues of the schemes described previously for the spin-lattice systems. Further subtruncations are also possible here, in terms of the numbers of modes $\{n_i\}$ kept in the summations in Eqs. (38) and (39) and their higher-order counterparts. For example, the $\text{LSUB}(m)$ scheme ignores, firstly, all terms in S between $k > n$ plaquettes and between $k < n$ plaquettes if these k plaquettes occupy a region which cannot be delimited by at most n contiguous plaquettes on the lattice; and, secondly, all terms in the resulting $\text{LSUB}(n)$ correlation operator with $\sum_i n_i > m$. The mode

Figure 3. Graphical illustration of a relationship between the $U(1)$ Wilson loops.

numbers $\{n_i\}$ clearly bear a direct relationship with the winding numbers of the equivalent Wilson loops retained in the sum for S . Thus, it should also be clear how to generalize our approach to the non-Abelian $SU(N)$ lattice gauge theories.

The ground-state energy for our $U(1)$ model in $2 + 1$ dimensions is shown in Figure 4 and Table III as a function of λ , as obtained in the SUB1 and LSUB2(m) schemes. The full SUB1 calculation is completely equivalent to the one-body Mathieu problem, and the SUB1(m) subtruncations are found to converge extremely rapidly with increasing m even for large values of λ . We also include for comparison some results of n th-order strong-coupling ($\lambda \rightarrow 0$) perturbation theory (denoted as $PTn(S)$); lowest-order weak-coupling ($\lambda \rightarrow \infty$) perturbation theory ($PT(W)$); the results from an analytic continuation of the strong-coupling perturbation series due to Hamer, Oitmaa, and Zheng (HOZ) [30]; and those from the t -expansion calculation of Morningstar [31]. One sees that our LSUB2(m) results also converge quickly as m increases; and that the LSUB2(10) results are in very good agreement with those from the careful analysis of Morningstar, even for large values of λ well into the weak-coupling regime.

Discussion

It is interesting to note that for the XXZ spin-lattice model discussed, the LSUB n approximation exactly reproduces the results of n th-order perturbation theory in

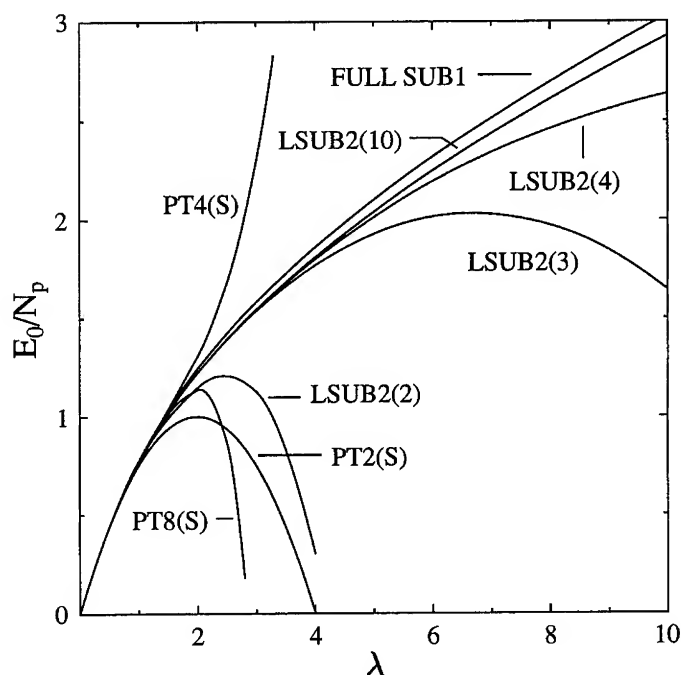


Figure 4. Ground-state energy per plaquette of the $U(1)$ model on the square lattice.

TABLE III. Ground-state energy per plaquette at several values of λ for the $U(1)$ model in $2 + 1$ dimensions. Shown are the results of various LSUB2(n) schemes, together with the full SUB1 results and the results of both strong ($\lambda \rightarrow 0$) and weak ($\lambda \rightarrow \infty$) coupling limits in perturbation theory. We show the results of 4th- and 8th-order strong-coupling perturbation theory, PT4(S) and PT8(S) respectively, and of lowest-order weak-coupling perturbation theory, PT(W). The results from an analytic continuation of the strong-coupling perturbation series by Hamer, Oitmaa, and Zheng [30] (denoted as HOZ), and from the t -expansion calculations of Morningstar [31], are also included for comparison purposes.

Method	λ								
	0.5	1	2	3	4	5	6	8	9
SUB1	0.4391	0.7724	1.2430	1.5828	1.8597	2.1000	2.3156	2.6966	2.8688
LSUB2(2)	0.4386	0.7652	1.1468	1.1280	0.3019	-2.8326	-15.108	—	—
LSUB2(3)	0.4387	0.7681	1.2216	1.5371	1.7691	1.9282	2.0153	1.9720	1.8424
LSUB2(4)	0.4387	0.7681	1.2214	1.5428	1.7994	2.0123	2.1921	2.4585	2.5568
LSUB2(6)	0.4387	0.7681	1.2217	1.5453	1.8099	2.0404	2.2482	2.6188	2.7886
LSUB2(8)	0.4387	0.7681	1.2217	1.5454	1.8100	2.0404	2.2477	2.6142	2.7797
LSUB2(10)	0.4387	0.7681	1.2216	1.5452	1.8095	2.0393	2.2456	2.6096	2.7734
HOZ	—	—	1.215	—	1.785	—	2.2	—	—
PT4(S)	0.4387	0.7690	1.3042	2.2898	4.8667	10.632	21.638	—	—
PT8(S)	0.4387	0.7673	1.1358	-0.7375	-20.873	—	—	—	—
PT(W)	0.5627	0.8434	1.2402	1.5447	1.8015	2.0276	2.2321	2.5917	2.7596
Morningstar	—	0.7675	—	—	1.796	—	—	—	2.763

the limit $\Delta \rightarrow \infty$ [14]. The strong-coupling ($\lambda \rightarrow 0$) perturbation series is similarly reproduced from our LSUB n equations for the $U(1)$ lattice gauge theory [22,24]. Thus, our LSUB n approximations effectively comprise a well-defined analytic continuation or resummation of such perturbation series within the context of a rather natural and consistent hierarchical scheme. From the numerical results obtained, the CCM approach is seen to be far superior in this sense to the alternative rather *ad hoc* approaches for extending the range of validity or the accuracy of similar perturbative sequences, which are usually based on generalized Padé approximants or similar techniques.

From the results obtained to date we hope to have convinced the reader that the CCM approach indeed provides a unified many-body theory of quantal Hamiltonian lattice systems. Obvious extensions then present themselves as worthy of study. For the spin-lattice systems it is of interest to investigate other models, such as the spin-1 Heisenberg-biquadratic chain [16], or spin- $\frac{1}{2}$ chains with both nearest-neighbor and next-nearest-neighbor couplings. In this context the use of alternative model states $|\Phi\rangle$ is of particular interest. For the lattice gauge models we are also interested in extending our very preliminary work done so far in the vacuum sector on the $U(1)$ excitation gap (or glueball mass) [24] and on the non-Abelian $SU(2)$ model. In principle, the work described above for the vacuum sector can also be extended to the charged (or “colored”) sector by the further inclusion in the correlation operator S of sums over open paths on the lattice, representing tubes of electric flux between staggered fermions, as well as the sums over closed paths (i.e., the Wilson loops) already considered.

Finally, the quality of our results obtained so far convinces us that the extension of the current CCM approach to additional Hamiltonian lattice systems is well justified. An obvious example is the class of strongly interacting electronic lattice systems, including such topical models as the Hubbard and tJ models which, despite intensive recent study by various theoretical techniques, are still only partially understood. Preliminary work in this direction has been reported [19–21], and we hope to present results of our own soon.

Acknowledgments

We thank our collaborators J. B. Parkinson and R. G. Hale in the case of the spin-lattice models, and A. S. Kendall and L. Y. Wong in the case of lattice gauge theory, for their assistance. One of us (RFB) also gratefully acknowledges the support of a research grant from the Science and Engineering Research Council (SERC) of Great Britain.

Bibliography

- [1] R. J. Bartlett, *J. Phys. Chem.* **93**, 1697 (1989).
- [2] R. J. Bartlett, *Theor. Chim. Acta* **80**, 71 (1991)—and note also that issues 2–6 of this volume are entirely devoted to articles on the coupled cluster theory of electron correlations in many-electron systems.
- [3] R. F. Bishop, *Theor. Chim. Acta* **80**, 95 (1991).
- [4] R. F. Bishop and K. H. Lührmann, *Phys. Rev. B* **17**, 3757 (1978).
- [5] J. Arponen, *Ann. Phys. (NY)* **151**, 311 (1983).
- [6] H. Kümmel, in *Nucleon–Nucleon Interaction and Nuclear Many-Body Problems*, S. S. Wu and T. T. S. Kuo, Eds. (World Scientific, Singapore, 1984), p. 46.
- [7] R. F. Bishop and H. G. Kümmel, *Phys. Today* **40**(3), 52 (1987).
- [8] J. S. Arponen, R. F. Bishop, and E. Pajanne, *Phys. Rev. A* **36**, 2519 (1987); **36**, 2539 (1987).
- [9] R. F. Bishop, *Int. J. Quantum Chem., Quantum Chem. Symp.* **24**, 197 (1990).
- [10] J. S. Arponen and R. F. Bishop, *Ann. Phys. (NY)* **207**, 171 (1991).
- [11] R. F. Bishop, in *Dirkfest '92: A Symposium in Honor of J. Dirk Walecka's Sixtieth Birthday*, W. W. Buck, K. M. Maung, and B. D. Serot, Eds. (World Scientific, Singapore, 1992), p. 21.
- [12] J. S. Arponen and R. F. Bishop, *Ann. Phys. (NY)* **227**, 275 (1993); **227**, 334 (1993).
- [13] M. Roger and J. H. Hetherington, *Phys. Rev. B* **41**, 200 (1990).
- [14] R. F. Bishop, J. B. Parkinson, and Yang Xian, *Phys. Rev. B* **43**, 13782 (1991); **44**, 9425 (1991); *Theor. Chim. Acta* **80**, 181 (1991); in *Condensed Matter Theories*, Vol. 6, S. Fantoni and S. Rosati, Eds. (Plenum, New York, 1991), p. 37; *J. Phys.: Condens. Matter* **4**, 5783 (1992); in *Recent Progress in Many-Body Theories*, Vol. 3, T. L. Ainsworth, C. E. Campbell, B. E. Clements, and E. Krotscheck, Eds. (Plenum, New York, 1992), p. 117.
- [15] R. F. Bishop, J. B. Parkinson, and Yang Xian, *Phys. Rev. B* **46**, 880 (1992).
- [16] R. F. Bishop, J. B. Parkinson, and Yang Xian, *J. Phys.: Condens. Matter* **5**, 9169 (1993).
- [17] F. E. Harris, *Phys. Rev. B* **47**, 7903 (1993).
- [18] F. Cornu, Th. Jolicouer, and J. C. Le Guillou, CEA-Saclay preprint T93/120 (1993).
- [19] M. Roger and J. H. Hetherington, *Europhys. Lett.* **11**, 255 (1990).
- [20] C. F. Lo, E. Manousakis, and Y. L. Wang, *Phys. Lett. A* **156**, 42 (1991).
- [21] F. Petit and M. Roger, *Phys. Rev. B* (1994), in press.
- [22] R. F. Bishop and Yang Xian, *Acta Phys. Polonica B* **24**, 541 (1993).
- [23] C. H. Llewellyn Smith and N. J. Watson, *Phys. Lett. B* **302**, 463 (1993).
- [24] R. F. Bishop, A. S. Kendall, L. Y. Wong, and Yang Xian, *Phys. Rev. D* **48**, 887 (1993); in *Condensed Matter Theories*, Vol. 8, L. Blum and F. B. Malik, Eds. (Plenum, New York, 1993), p. 269.

- [25] H. A. Bethe, *Z. Phys.* **71**, 205 (1931); L. Hulthén, *Ark. Mat. Astron. Fys.* **A26**, No. 11 (1938); J. des Cloiseaux and J. J. Pearson, *Phys. Rev.* **128**, 2131 (1962); L. D. Faddeev and L. A. Takhtajan, *Phys. Lett.* **A85**, 375 (1981).
- [26] F. D. M. Haldane, *Phys. Lett.* **A93**, 464 (1983); *Phys. Rev. Lett.* **50**, 1153 (1983).
- [27] K. Emrich, *Nucl. Phys.* **A351**, 379 (1981); **A351**, 397 (1981).
- [28] N. Trivedi and D. M. Ceperley, *Phys. Rev. B* **41**, 4552 (1990).
- [29] P. W. Anderson, *Phys. Rev.* **86**, 694 (1952); T. Oguchi, *Phys. Rev.* **117**, 117 (1960).
- [30] C. J. Hamer, J. Oitmaa, and W. H. Zheng, *Phys. Rev. D* **45**, 4652 (1991).
- [31] C. J. Morningstar, *Phys. Rev. D* **46**, 824 (1992).

Received March 28, 1994

Influence of Rotation on Multiphoton Processes in HF

J. BROECKHOVE, B. FEYEN,* and P. VAN LEUVEN

*Rijksuniversitair Centrum Antwerpen (RUCA), Department of Mathematics and Computer Sciences,
Groenenborgerlaan 171, B2020 Antwerpen, Belgium*

Abstract

In this contribution we are concerned with the role of rotational motion in multiphoton processes induced by a laser field of high intensity. We use the pseudospectral split operator method for the propagation of the quantum wavefunction. The rotation is treated by decomposition of the HF wavefunction in its angular momentum components. © 1994 John Wiley & Sons, Inc.

Introduction

The phenomenon of infrared multiphoton excitation (MPE) and dissociation (MPD) is one of the many interesting spectroscopic discoveries of the previous decades. Irradiation of the molecule with an intense laser field generates excitation through discrete levels, and then on into the quasicontinuum and continuum. In the latter regime the transitions are resonant, but in the former much depends on the level spacing in the system. The spacing of the individual discrete levels determines the fraction of molecules to be excited up to the quasicontinuum, and it is therefore key to the efficiency of the overall process.

The above does not apply directly to diatomics [1], where one is taken directly from discrete levels to the continuum. And, indeed, calculations have shown that, even with extremely intense monochromatic lasers, dissociation probability is generally low in diatomics. This is due to the field frequency becoming completely off-resonance as one ladders through the anharmonically spaced higher levels. Several calculations have shown that the application of two fields [2–4] or the use of chirped fields [5] alleviates the off-resonance condition and is capable of producing significant excitation and dissociation rates.

The present contribution is motivated by the observation that many of the studies of infrared MPE in diatomics are based on a description of the molecule, containing only the internuclear vibrational coordinate. In a full description, which includes the angles specifying the orientation of the molecular axis with respect to the field, the transitions can be vibration-rotational with $\Delta j = 0, \pm 1$. Thus the anharmonic shift in the vibrational levels can be compensated by the addition or removal of rotational energy, in order to sustain near-resonance in a sequence of transitions.

* Research associate IIKW, Belgium.

The reduced, purely vibrational, description eliminates the rotational splitting from the level scheme and in that way conceivably impacts significantly on the MPE process. Our objective is to find out whether this is indeed the case.

We investigate, in both descriptions, the MPE of HF irradiated by an intense infrared (IR) laser, using a pseudospectral method to compute the time evolution of the quantum wavefunctions. In the next section we give an outline of the method, focusing on the features related to the treatment of the angular coordinates. The results of our calculations and their interpretation are presented in the third section.

Theoretical Background

The pseudospectral approach to the calculation of the vibrational motion of a diatomic is by now well established. Several methods are available, i.e., second order differencing [6], split operator [7], and Lanczos [8]. We will use the split operator method.

The time evolution associated with the vibrational nuclear motion in an external field is obtained from the time-dependent Schrödinger equation

$$i \frac{\partial \Psi}{\partial t}(R, t) = \hat{H}(t)\Psi(R, t) = [\hat{T} + \hat{V}(t)]\Psi(R, t) \quad (1)$$

with kinetic energy and potential operators

$$\hat{T} = -\frac{1}{2m} \frac{\partial^2}{\partial R^2}, \quad (2)$$

$$\hat{V} = \hat{V}_0 - \mu(R)E \cos(\Omega t). \quad (3)$$

This equation is formally solved by applying the time evolution operator to the initial condition

$$\Psi(t) = U(t, t_0)\Psi(t_0), \quad (4)$$

where U is to be constructed using the Dyson time-ordering operator

$$U(t, t_0) = \mathcal{T} \exp\left(-i \int_{t_0}^t ds \hat{H}(s)\right). \quad (5)$$

The time ordering is required because of the presence of a time-dependent term in the Hamiltonian.

The key concept in the split-operator method is to split the total time interval into short time slices and to approximate the evolution operator over each time slice

$$U(t, t + \varepsilon) = \exp\left(-i \frac{\varepsilon}{2} \hat{T}\right) \exp\left(-i \int_t^{t+\varepsilon} ds \hat{V}(s)\right) \exp\left(-i \frac{\varepsilon}{2} \hat{T}\right) \quad (6)$$

This decomposition is correct up to second order in ε . The power of this algorithm lies in the splitting of the potential and kinetic terms. The action of the first is evaluated while the wavefunction is in a coordinate representation, i.e., defined

by its values on a grid in coordinate space. For the second, one transforms the wavefunction to the momentum representation, using the discrete Fourier transform associated with the grid. The kinetic energy operator is multiplicative in that representation, so that its action is easily evaluated. Afterwards one transforms the wavefunction back to the coordinate representation with an inverse Fourier transform. This is a viable approach because of the availability of fast Fourier transform (FFT) software that performs these transformations very efficiently. The decomposition outlined above, including the elimination of the time-ordering operator, is correct up to second order in epsilon provided that the potential has a well-behaved time dependence [9]. Higher-order approximations to the propagator are also possible (see, for example, [10]). Their use allows one to extend the time slice epsilon based on the higher-order precision, but on the other hand involves more operations per time step due to the presence of more than three factors [as in formula (6)] in the approximate propagator. This is a trade-off issue, involving cpu-time consumption, accuracy, and programming effort, in which we have chosen to use the second-order scheme.

When all degrees of freedom are included in the description, i.e., $\Psi = \Psi(R, \theta, \phi, t)$ with (θ, ϕ) defining the molecular orientation with respect to the axis of the linearly polarized field, the Hamiltonian modifies to

$$\hat{V}(t) = \hat{V}_0(R) - \mu(R)E \cos \theta \cos(\Omega t) \quad (7)$$

because of the angular dependence on the external field. One now has to make a choice concerning the computational approach to these angular coordinates. One possibility is to extend the grid representation of the wavefunction to the angular domain [11] and to use the corresponding transform when evaluating the angular kinetic terms. Another possibility is to use a basis set expansion for the angular variables, i.e.,

$$\Psi = \sum_{lm} \psi_{lm}(R, t) Y_{lm}(\theta, \phi) \quad (8)$$

Each ψ_{lm} represents the vibrational motion in the (l, m) angular momentum channel. We will pursue the latter approach because it has some distinct advantages in the particular case of a molecule in an external dipolar field.

In the basis set representation the time-dependent Schrödinger equation couples the various angular momentum components:

$$i \frac{\partial \psi_{lm}}{\partial t} = \sum_l \hat{H}_{ll'}^{(m)} \psi_{l'm}, \quad (9)$$

where

$$\hat{H}_{ll'}^{(m)} = \left[-\frac{1}{2m} \frac{\partial^2}{\partial R^2} + \frac{l(l+1)}{R^2} + V_0(R) \right],$$

$$\hat{H}_{ll'}^{(m)} = E\mu(R) < Y_{lm} | \cos \theta | Y_{l'm} > \cos(\Omega t).$$

Thus the wavefunction is now a vector with various l -components and \hat{H} a matrix

operator coupling the components. It is diagonal in m and couples only nearest neighbor l -components (i.e., $|l - l'| = 1$). The strength of the coupling does depend on m and is given by the following expression using 3j-symbols [12]:

$$\langle Y_{lm} | \cos \theta | Y_{l'm} \rangle = (-1)^m \sqrt{\frac{3(2l+1)(2l'+1)}{4\pi}} \times \begin{pmatrix} l & 1 & l' \\ 0 & 0 & 0 \end{pmatrix} \begin{pmatrix} l & 1 & l' \\ -m & 0 & m \end{pmatrix}. \quad (10)$$

The matrix structure of the Hamiltonian requires only minimal modifications of the split operator method. Again one has

$$\Psi(t + \varepsilon) = U(t, t + \varepsilon)\Psi(t) \quad (11)$$

or, componentwise,

$$\psi_l(t + \varepsilon) = \sum_{l'} U_{ll'}(t, t + \varepsilon)\psi_{l'}(t) \quad (12)$$

with

$$U_{ll'}(t, t + \varepsilon) = \left[\exp\left(-i \frac{\varepsilon}{2} \hat{T}\right) \exp\left(-i \int_t^{t+\varepsilon} ds \hat{V}(s)\right) \exp\left(-i \frac{\varepsilon}{2} \hat{T}\right) \right]_{ll'}. \quad (13)$$

The kinetic energy is represented by a diagonal matrix in the l -vector space and as a consequence the above simplifies to

$$U_{ll'}(t, t + \varepsilon) = \exp\left(-i \frac{\varepsilon}{2} \hat{T}\right) \left[\exp\left(-i \int_t^{t+\varepsilon} ds \hat{V}(s)\right) \right]_{ll'} \exp\left(-i \frac{\varepsilon}{2} \hat{T}\right). \quad (14)$$

Thus we continue to use transformations to momentum space to evaluate the kinetic energy factors in the propagation formula. The only new feature is that for the potential term one now has to exponentiate a matrix. A similar technique is used in the pseudospectral calculations involving two or more electronic states with nonadiabatic coupling [13–15].

Results and Discussion

In our calculations we have used the HF potential V_0 given by Coxon and Hageorgiou [16]. It is defined by analytical expressions in the regions of small and large R and by tensioned cubic spline fits to experimental data for the intermediate region. The dipole function μ was taken from Zemke et al. [17]. It is linear at small distances, zero for $R > 20$ a.u., and in between it is defined by a tensioned cubic spline fit to ab initio data. The electric field strength E and the field frequency Ω are the two variable parameters in our calculation. We consider a value of E corresponding to a field intensity of 43.7 TW/cm² as in [18]. The values of Ω are taken in the range relevant for multiphoton resonances in the vibrational spectrum, i.e., from 0.015 to 0.021 a.u.

Throughout the calculations, we have used the same initial condition Ψ_0 , viz., the HF ground state calculated with the renormalized Numerov method [19]. In the full description, i.e., angular variables included, the rotational quantum numbers for Ψ_0 are $l = 0$, $m = 0$. As explained in the previous section, only the latter is good quantum number.

For detailed results of the purely vibrational calculations we refer to [20,21]. Here we will focus on the angular momentum features of the rovibrational calculation. In view of the strength of the external field, a significant occupation probability for a number of l -channels can be expected *a priori*. As a first step, we need to determine which l -channels are to be included in the calculation. To this end, we have performed a calculation with channels up to $l = 7$ and found that starting with $l = 4$ the maximum probability per channel is less than 5% at any point in time and lower than 2% on the average. At $l = 7$, those numbers have dropped by an order of magnitude. Thus we have used $l = 3$ as a cutoff in all subsequent calculations. The predominance of the lower angular momentum components is illustrated in Figure 1. It displays the time-averaged expectation value of the l^2 operator. This quantity tends towards a numerical value of approximately 3.0 indicating a limited presence at $l = 2$ [where $l(l+1) = 6$] and higher.

The relevant field frequencies for transitions from the ground state are the multiphoton frequencies $\Omega_n = (E_{v=n,l=0} - E_{v=0,l=0})/n$, i.e., the frequencies at which the n -photon process is in resonance with the transition from $v = 0$ to $v = n$ vibrational states. Figure 2 shows the vibrational occupation probabilities $P_v = \sum_l P_{vl} = \sum_l |\langle \Psi(t) | \Phi_{vl} \rangle|^2$ at the four-photon frequency $\Omega_4 = 0.01695$ a.u. Again the rovibrational stationary states are determined using the renormalized Numerov method. One clearly notices a significant amount of probability at $v = 4$ during the time intervals that $v = 0$ is depleted. The presence of nonnegligible probability in other vibrational channels is consistent with the picture of a higher-order transition process that proceeds in a sequential manner [22]. In order to ascertain the strength of

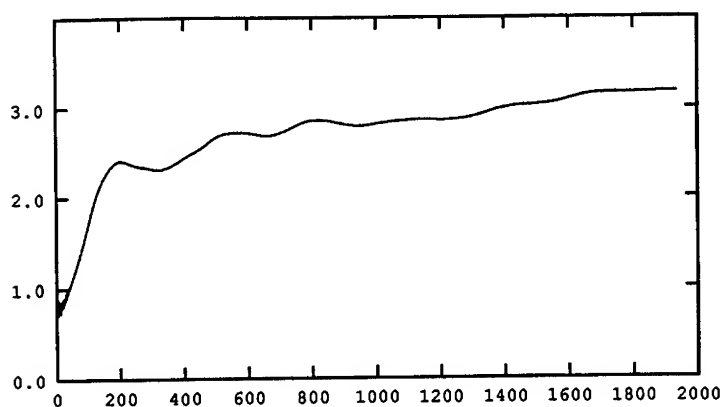


Figure 1. Time averaged $\langle l^2 \rangle$ versus averaging interval. $\Omega = 0.01695$ a.u. Intensity = 43.7 TW/cm^2 . Time in fs.

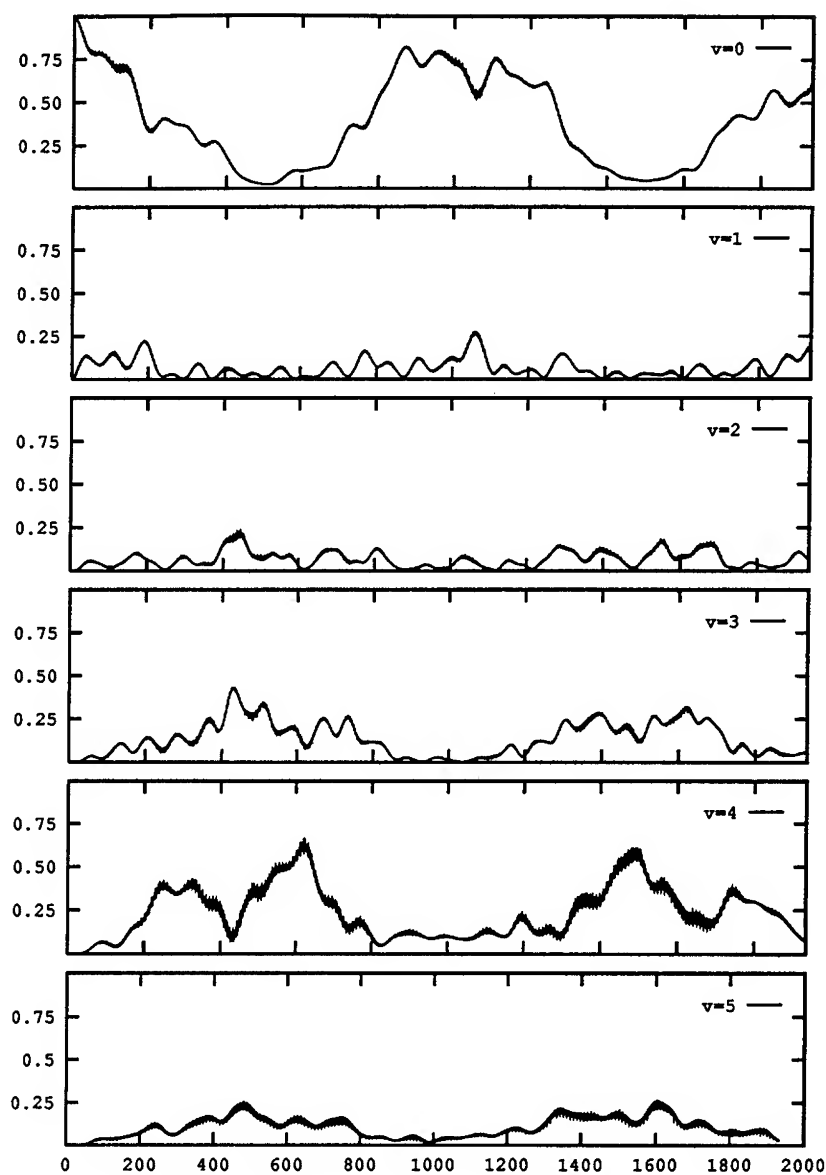


Figure 2. Vibrational occupation probabilities. $\Omega = 0.01695$ a.u. Intensity = 43.7 TW/cm^2 . Time in fs.

multiphoton effects over a broader range of field frequencies, we have calculated the time-averaged absorbed energy as a function of the frequency Ω of the external field. The result is shown in Figure 3 and should be compared to Figure 4 with the same quantity calculated in a purely vibrational approach. In the latter one can

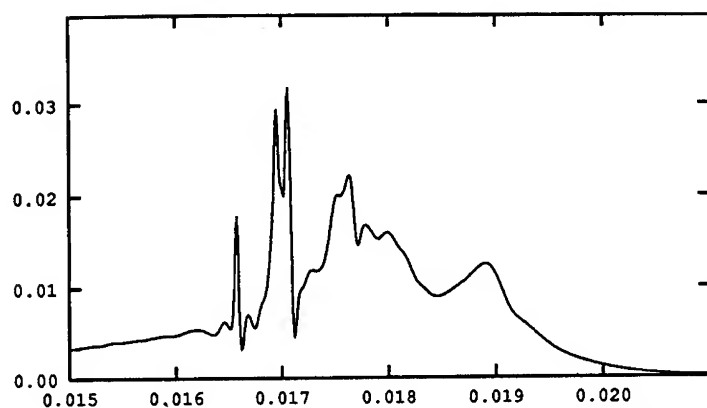


Figure 3. Time averaged energy versus frequency of the driving field at intensity of 43.7 TW/cm² for the full description. Energy and frequency in a.u.

distinguish the multiphoton transitions from $v = 3$ to $v = 8$ at frequencies $\Omega_3 = 0.01735$, $\Omega_4 = 0.01695$, $\Omega_5 = 0.01620$, $\Omega_7 = 0.01583$, and $\Omega_8 = 0.01546$ a.u. In the comparison of Figures 3 and 4 two things stand out. There is an overall decrease in the absorbed energy and a more pronounced structure of the dominant peaks. We attribute the first effect to a stronger effective field strength in the purely vibrational calculation. Indeed, in the rovibrational calculation, the molecule will experience different orientations with respect to the field, at which there is lower effective interaction strength than in case it is aligned with the field. Thus a lowering of the absorbed energy is to be expected. It is not clear how to define field strengths that are comparable in this situation. The center of gravity of the groups of transition frequencies defined by $\Omega_{vl} = (E_{vl} - E_{v=0,l=0})/v$ correspond to the four- and five-

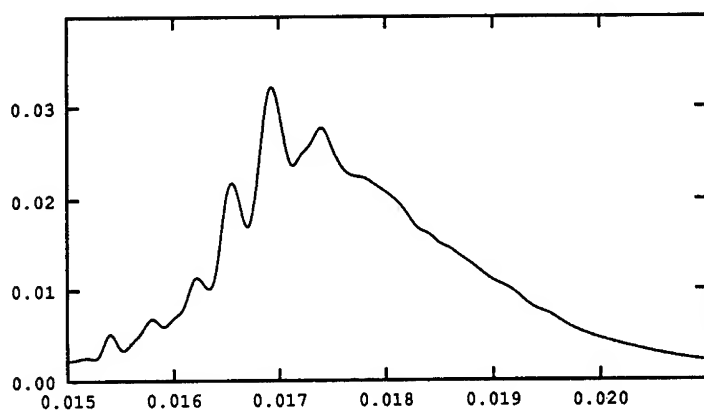


Figure 4. Time averaged energy versus frequency of the driving field at intensity of 43.7 TW/cm² for the vibrational description. Energy and frequency in a.u.

photon peaks in Figure 4. A deeper understanding of these peaks requires an l -resolved analysis of the data, which is currently under way.

Conclusion

In this contribution we have investigated the use of a hybrid method for computing the time evolution of HF in an external dipole field. The method combines discretisation on a grid for the vibrational coordinate and a basis set expansion for the angular coordinate. The resulting multi- l -component wavefunction is propagated with the split-operator method, where the interaction is now an (l, l') matrix. This straightforward approach is possible because the external dipole field is an $l = 1$ rotation tensor. As a consequence, its matrix elements in the basis set are known analytically. The viability of this approach is due also to the fact that a low cutoff value can be used in the l -expansion. This is demonstrated in our calculations. Because of this, the extension of the vibrational description to include the rotational motion does not introduce an excessive computational burden.

Bibliography

- [1] S. Chelkowski and A. D. Bandrauk, *Phys. Rev. A* **41**, 6480 (1990).
- [2] G. Jolicard and E. Austin, *J. Chem. Phys.* **95**, 5056 (1991).
- [3] G. Jolicard and G. D. Billing, *J. Chem. Phys.* **90**, 346 (1989).
- [4] B. G. Dibble and R. B. Shirts, *J. Chem. Phys.* **94**, 3451 (1991).
- [5] S. Chelkowski, A. D. Bandrauk, and P. B. Corkum, *Phys. Rev. Lett.* **65**, 2355 (1990).
- [6] D. Kosloff and R. Kosloff, *J. Comput. Phys.* **52**, 35 (1983).
- [7] M. D. Feit, J. A. Fleck, and A. Steiger, *J. Comput. Phys.* **47**, 412 (1982).
- [8] F. Le Quéré and C. Leforestier, *J. Chem. Phys.* **92**, 247 (1990).
- [9] J. A. Fleck, J. R. Morris, and M. D. Feit, *Appl. Phys.* **10**, 129 (1976).
- [10] K. Takahashi and K. Ikeda, *J. Chem. Phys.* **99**, 8680 (1993).
- [11] M. R. Hermann and J. A. Fleck, *Phys. Rev. A* **38**, 6000 (1988).
- [12] D. M. Brink and G. R. Satchler, *Angular Momentum* (Clarendon Press, Oxford, England, 1968).
- [13] J. Alvarellos and H. Metiu, *J. Chem. Phys.* **88**, 4957 (1988).
- [14] F. M. Fernandez and D. A. Micha, *J. Chem. Phys.* **97**, 8173 (1992).
- [15] B. Feyen, J. Broeckhove, and P. Van Leuven, *J. Phys. B: At. Mol. Phys.* **26**, 4471 (1993).
- [16] J. A. Coxon and P. G. Hajigeorgiou, *J. Mol. Spectrosc.* **142**, 254 (1990).
- [17] W. T. Zemke, et al., *J. Chem. Phys.* **95**, 7846 (1991).
- [18] R. B. Walker and R. K. Preston, *J. Chem. Phys.* **67**, 2017 (1977).
- [19] B. R. Johnson, *J. Chem. Phys.* **67**, 4086 (1977).
- [20] J. Broeckhove, B. Feyen, and P. Van Leuven, *Int. J. Quantum Chem.* **26**, 435 (1992).
- [21] J. Broeckhove, B. Feyen, and P. Van Leuven, *J. Mol. Struct. (Theochem)* **261**, 265 (1992).
- [22] S. Nakai and W. J. Meath, *J. Chem. Phys.* **96**, 4991 (1992).

Received May 3, 1994

Effective Core Potential Study of Multiply Bonded Transition Metal Complexes of the Heavier Main Group Elements

MICHAEL T. BENSON, THOMAS R. CUNDARI,*
YUEPING LI, and LYNN A. STROHECKER

Department of Chemistry, Memphis State University, Memphis, Tennessee 38152

Abstract

A computational study, using relativistic effective core potentials, is presented of transition metal-main group multiply bonded complexes, of interest in the context of catalysis and chemical vapor deposition of TM/MG materials. Model d^0 transition metal complexes chosen are of the general form Cl_nME where $M = \text{Zr}$ ($n = 2$), Ta ($n = 3$), and W ($n = 4$). Main group elements of interest are the tetrrels ($E = \text{C}, \text{Si}, \text{Ge}, \text{Sn}$), pnictogens ($E = \text{N}, \text{P}, \text{As}, \text{Sb}$), and chalcogens ($E = \text{O}, \text{S}, \text{Se}, \text{Te}$). A comparison between calculated metric data and available experimental data for a wide range of $\text{TM}=\text{MG}$ complexes will help in further assessing efficient computational approaches to TM complexes, particularly of the heavier MG elements, as a function of metal, ligand and level of theory. In the present work restricted Hartree Fock (RHF) and Møller–Plesset second order perturbation theory (MP2) wavefunctions were employed. In most cases there are small differences between RHF and MP2 calculated geometries, with both methods showing good agreement with experimental data, suggesting these approaches will be suitable for the study of larger, more experimentally relevant models. Changes in ZrE bond lengths for $E = \text{chalcogen}$ (upon going from RHF to MP2) suggest a fundamentally different description between the Zr-oxo bond and heavier chalcogens, a result supported by recent experimental data for a series of Zr-chalcogenides. To date no examples have been reported of arsinidene and stibinidene complexes. Computational results show similar behavior among the heavier pnictogen complexes, i.e., $L_nM=EH$ ($E = \text{P}, \text{As}, \text{Sb}$), suggesting that strategies used to synthesize phosphinidenes may be suitable in the search for the first $L_nM=\text{AsR}$ and $L_nM=\text{SbR}$ complexes. Additionally, calculations suggest that design of ligand sets which yield linearly coordinated phosphinidenes (and presumably As and Sb analogues) will lead to phosphinidenes with stronger metal–pnictogen bonds and increased thermodynamic stability versus nonlinearly coordinated examples. © 1994 John Wiley & Sons, Inc.

Introduction

Complexes with a multiple bond between a transition metal (TM) and main group (MG) element ($\text{TM}=\text{MG}$) are of considerable importance [1]. These complexes participate in a variety of catalytically important reactions such as oxo ($L_nM=\text{O}$) mediated alkane oxidations [2] and methane activation by imidos ($L_nM=\text{NR}$) [3]. Multiply bonded complexes are also important in advanced materials research, e.g., as intermediates in chemical vapor deposition (CVD) of solid state nitrides, oxides, and carbides [4]. The majority of $\text{TM}=\text{MG}$ complexes contain MG elements

* To whom all correspondence should be addressed. e-mail: cundari@memstvx1.memst.edu

from the first main group row (i.e., C, N, and O), although a growing number of examples involving heavier MG elements have been recently reported [5–7]. Multiply bonded complexes of the heavier tetrrels (Group IVA) are extremely rare, with few known examples for all TMs and no structurally characterized examples for early, high-valent TMs [5]. Silylidenes ($L_nM=Si(R)R'$) have been proposed as intermediates in silane polymerization [5b]. Stephan et al. have recently developed synthetic routes into phosphinidenes ($L_nM=PR$) of Zr and demonstrated their ability to activate C–H bonds [6b]. Sulfidos ($L_nM=S$) have been envisaged as intermediates in xanthine oxidase [7d] and catalytic hydrodesulfurization of petroleum feedstocks [7e]. Thus, in addition to fundamental interest in multiple bonding of the heavier MG elements, $TM=MG_{heavy}$ complexes represent a nearly untapped resource for the inorganic chemist searching for novel reactivity [5–7].

The growing importance of $TM=MG_{heavy}$ complexes provides strong motivation for computational studies of their bonding. Computational chemistry methods have become almost routine for the lighter MG elements [8], but numerous opportunities remain in the development of efficient approaches to the chemistry of the d-, f-, and heavier sp-block elements. A variety of methods, ranging from Extended Hückel, to other semiempirical methods, to density functional theory, have been implemented to meet the challenges of computational d- and f-block chemistry [9]. Effective core potentials (ECPs) represent another promising technique for studying interesting chemical problems across the entire Periodic Table [9,10]. Combined with the use of modern techniques for treating electron correlation and emerging technologies such as parallel computing [11], ECPs appear to be a very powerful method for dealing with inorganic systems.

The present work is a continuation of computational studies of $TM=MG$ bonding and reactivity [12]. Model d^0 complexes are of the general form Cl_nME where $M = Zr$ ($n = 2$), Ta ($n = 3$), and W ($n = 4$). Main group elements are the tetrrels ($E = C, Si, Ge, Sn$), pnictogens ($E = N, P, As, Sb$), and chalcogens ($E = O, S, Se, Te$). A comparison between calculated metric data and available experimental data for a wide range of $TM=MG$ complexes will help in further assessing efficient computational approaches to more experimentally relevant $TM=MG_{heavy}$ complexes.

Computational Methods

Three main challenges arise in computational d- and f-block chemistry: large numbers of electrons (many of them core), importance of electron correlation, and increased relativistic effects for heavier elements [9]. The effects of electron correlation, particularly on the calculation of geometries, is mitigated to a large degree by the empty d shell in the complexes studied here. Our main approach to the challenges of computational d- and f-block chemistry is the design, testing, and use of effective core potentials [12]. Great savings in time, memory, and disk space are effected by replacing the many core electrons, and the basis functions describing them, with a small number of potentials [10]. ECPs indirectly address the correlation problem by reducing resources needed for other parts of the computational exercise so that more can be directed towards electron correlation. Transition metal ECPs

are generated from all-electron, Dirac-Fock calculations, and thus incorporate Darwin and mass velocity relativistic effects, while spin-orbit coupling is averaged out in potential generation [10a]. From a chemical standpoint, ECP methods afford great leeway in the choice of interesting problems, particularly with respect to assessing the role of the central metal, since calculations on congeners within a triad are carried out with near equal facility. In our experience [12] with the Stevens relativistic ECP scheme [10a] we have found no degradation in accuracy as one descends a TM triad towards the heavier metals (for which relativistic effects will be most important).

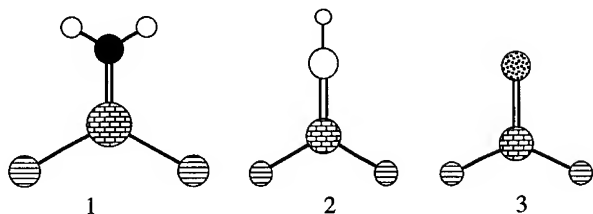
Calculations employ the GAMESS program [11]. Effective core potentials (ECPs) and valence basis sets are used for all heavy atoms and the -31G basis set for H [10a]. ECPs replace the innermost core orbitals for the TMs and all core orbitals for main-group (MG) elements. Thus, the ns, np, nd, (n + 1)s, and (n + 1)p are treated explicitly for the d-block; for the main-group ns and np are treated explicitly [10a]. Transition metal valence basis sets are quadruple and triple zeta for the sp and d shells, respectively, while main-group elements have a double-zeta valence basis. Basis sets for heavy, main-group elements are augmented with a d polarization function [8]. Geometries are optimized using restricted Hartree Fock (RHF) and Møller-Plesset second order perturbation theory (MP2) wavefunctions [13] for closed-shell singlets. Core electrons are not included in the MP2 expansion since most (other than the ns and np for the TMs) are replaced with an ECP. Bond lengths and angles for TM=MG complexes are typically predicted to within 1-3% of experimental models using the present computational scheme [12] involving complexes in a variety of geometries, formal oxidation states, and metals from the entire transition series. It will be seen below that in the majority of cases very good agreement is obtained between calculated and experimental metric data (even for Ta and W complexes) using these relativistic ECPs.

Results

Zirconium Complexes

Until recently, few TM=MG complexes of the Ti-triad (Group IVB) metals could be found which were stable enough to be structurally characterized [1]. Parkin and Howard have reported a series of terminally-bonded Zr and Hf chalcogenidos [7a], while Arnold and Christou [7b] have reported Zr- and Hf-telluridos. Some work has been done on pnictogens (Group VA), primarily for nitrogen [1]. A series of ECP studies of Zr-imido chemistry have been reported [14]. Stephan et al. have recently characterized the first Zr-phosphinidene [6b]. To date, no $L_nM=AsR$ or $L_nM=SbR$ complexes have been synthesized. An X-ray analysis of a terminally bound tetrelide has, to our knowledge, not been reported other than the Zr-alkylidene of Fryzuk et al. [15]. An ECP study of Group IVB alkylidenes and silylidenes has been reported [16].

The Zr complexes, 1-3, are of the form Cl_2ZrEH_n ($n = 0, 1, 2$). Geometry optimizations for Cl_2ZrE are done under C_{2v} symmetry to facilitate comparison among the various complexes. The tetrelide (1), imido (2, $E = N$), and chalcogenido (3) complexes are C_{2v} minima. The Zr-Cl bond lengths range from 2.40 to 2.45 Å



(RHF) and 2.37 to 2.43 Å (MP2), and are consistent with a mean literature value of $\text{Zr}-\text{Cl} = 2.47 \pm 0.06$ Å (coordination numbers from six to nine) [17]. The $\text{Zr}-\text{Cl}$ bond lengths shorten only slightly (≤ 0.05 Å) upon the addition of correlation, suggesting that ZrCl bonds are well described at the Hartree-Fock level.

Tetrelide Complexes, 1. Metric data for Zr tetrelides (**1**) are collected in Table I. The calculated ZrC bond length (1.99 Å, RHF; 1.98 Å, MP2) is in excellent agreement

TABLE I. Cl_2ZrE complexes.

M/E/level ^a	ZrE (Å)	ZrCl (Å)	EZrCl (°)	Exp. ZrE ^b
Zr/CH ₂ /RHF	1.99	2.43	113	2.024(4) Å
Zr/CH ₂ /MP2	1.98	2.40	112	
Zr/SiH ₂ /RHF	2.54	2.42	112	2.815(1) Å
Zr/SiH ₂ /MP2	2.52	2.37	112	
Zr/GeH ₂ /RHF	2.57	2.42	112	
Zr/GeH ₂ /MP2	2.54	2.37	113	
Zr/SnH ₂ /RHF	2.77	2.42	111	
Zr/SnH ₂ /MP2	2.73	2.37	113	
Zr/NH/RHF	1.79	2.45	117	aver. = 1.85 Å
Zr/NH/MP2	1.83	2.43	114	
Zr/PH/RHF	2.25	2.41	120	2.505(4) Å
Zr/PH/MP2	2.28	2.40	117	
Zr/AsH/RHF	2.33	2.41	121	
Zr/AsH/MP2	2.37	2.40	118	
Zr/SbH/RHF	2.53	2.41	121	
Zr/SbH/MP2	2.55	2.38	119	
Zr/O/RHF	1.66	2.44	119	1.804(4) Å
Zr/O/MP2	1.78	2.42	113	
Zr/S/RHF	2.20	2.41	118	aver. = 2.32 Å
Zr/S/MP2	2.23	2.40	114	
Zr/Se/RHF	2.32	2.40	118	2.480(1) Å
Zr/Se/MP2	2.37	2.39	115	
Zr/Te/RHF	2.55	2.41	119	aver. = 2.69 Å
Zr/Te/MP2	2.61	2.39	115	

^a All complexes are C_{2v} , see **1**–**3**; M/E/level notation denotes the transition metal, ligand, and level of theory (RHF or MP2), respectively.

^b Experimental ME bond lengths, where available, are reported. Where more than one bond length is available the average is reported. Note the ZrSi value corresponds to a single bond. See text for further details.

with the value of $\text{ZrC} = 2.024(4) \text{ \AA}$ for a structurally characterized Zr-alkylidene [15]. The ZrSi bond in $\text{Cl}_2\text{ZrSiH}_2$ (2.54 \AA , RHF; 2.52 \AA , MP2) and the ZrGe bond in $\text{Cl}_2\text{ZrGeH}_2$ (2.57 \AA , RHF; 2.54 \AA , MP2) are considerably shorter, as expected, than the ZrSi and HfGe single bonds reported for $\text{Cp}_2\text{Zr}(\text{Si}(\text{TMS})_3)\text{Me}$ ($2.815(1) \text{ \AA}$, [18]) and $\text{Cp}^*\text{Cl}_2\text{HfGe}(\text{TMS})_3$, ($\text{Cp}^* = \eta^5 - \text{C}_5\text{Me}_5$; $\text{TMS} = \text{SiMe}_3$), ($2.740(1) \text{ \AA}$, [19]), respectively. The ZrSn bond length in $\text{Cl}_2\text{ZrSnH}_2$ is 2.77 \AA at the RHF level, contracting slightly at the MP2 level (2.73 \AA). The relative bond lengths for heavier tetrelides mirror the differences in covalent radii ($r_{\text{cov}}(\text{Si}) = 1.17 \text{ \AA}$; $r_{\text{cov}}(\text{Ge}) = 1.22 \text{ \AA}$; $r_{\text{cov}}(\text{Sn}) = 1.40 \text{ \AA}$ [20]). However, the covalent radius of C is 0.77 \AA , and so the ZrC bond in the alkylidene is expected to be $\approx 0.40 \text{ \AA}$ shorter than the silylidene; however, the difference is closer to 0.5 \AA (Table I). Similar comparisons can be made between Cl_2ZrCH_2 and its germilydene and stannylidene analogues. The differences in ME bond lengths for the heavier tetrels mirror differences in covalent radii. These data suggest that Zr $d\pi\text{--C } p\pi$ bonding is considerably stronger than in the heavier congeners, but that the strength of metal–ligand π -bonding is similar among the heavier tetrelides.

Pnictogen Complexes, 2. Geometric data for the C_{2v} structures of Cl_2ZrEH ($\text{E} = \text{N, P, As, Sb}$), are listed in Table I. The MP2 values calculated for ME bond lengths are slightly larger than the RHF values, but by no more than 0.04 \AA . The lengthening in ME upon going from RHF to MP2 contrasts to the contraction seen for the Zr-tetrelides (*vide supra*), but the differences are small in both cases. As with the tetrelides, the small changes in ME bond lengths upon going from RHF to MP2 wavefunctions suggest that modeling of the heavier pnictogen complexes of the form $\text{L}_n\text{M}=\text{ER}$ with RHF and MP2 wavefunctions is appropriate. The calculated Zr-imido bond lengths, 1.79 \AA (RHF) and 1.83 \AA (MP2), are in good agreement with reported data: Zr-imido = $1.826(4) \text{ \AA}$ ($\text{Cp}_2\text{Zr}(\text{THF})(=\text{N}-t\text{--Bu})$ [3d] and $1.868(3) \text{ \AA}$ ($\text{Zr}(\text{NHAr})_2(\text{py})_2(=\text{NAr})$) [3e]. The calculated ZrP bond length in Cl_2ZrPH (2.25 \AA , RHF; 2.28 \AA , MP2) is much shorter than the Zr-phosphinidene bond length ($2.505(4) \text{ \AA}$) in $\text{Cp}_2\text{Zr}(\text{PMes}')(\text{PMe}_3)$, $\text{Mes}' = 2,4,6\text{-tri-}t\text{-butyl-phenyl}$ [6b]. The phosphinidene in $\text{Cp}_2\text{Zr}(\text{PMes}')(\text{PMe}_3)$ is coordinated in a bent fashion ($\text{Zr}=\text{P}-\text{C} \approx 116.1(4)^\circ$) despite the bulk of the Mes' , suggesting a strong driving force for a ZrP bonding description which is closer to a double bond (with a stereochemically active lone pair on P). The C_{2v} symmetry constraint was relaxed for an MP2 optimization of Cl_2ZrPH . A C_s structure ($5.0 \text{ kcal mol}^{-1}$ lower in energy than $\text{C}_{2v}\text{--Cl}_2\text{ZrPH}$) is found with a ZrP bond length of 2.38 \AA , or 0.1 \AA longer than $\text{C}_{2v}\text{--Cl}_2\text{ZrPH}$, thus much closer to experiment [6b].

Chalcogenido Complexes, 3. The geometrical characteristics of the chalcogenidos Cl_2ZrE ($\text{E} = \text{O, S, Se, Te}$) were computed (Table I); in all cases, the C_{2v} structure is a minimum. The predicted ZrE bond lengths compare reasonably well with experimental values [7a]. The oxo provides the best agreement with experiment [7a]: $\text{ZrO} = 1.804(4) \text{ \AA}$ ($\text{ZrO} = 1.66 \text{ \AA}$ (RHF), 1.78 \AA (MP2)). The Zr sulfido, selenido, and tellurido experimental bond lengths in $(\text{Cp}')_2\text{Zr}(\text{E})(\text{py})$, ($\text{Cp}' = \eta^5\text{--C}_5\text{Me}_4\text{Et}$), are $2.334(2) \text{ \AA}$, $2.480(1) \text{ \AA}$, and $2.729(1) \text{ \AA}$, respectively, all approximately 7% longer than the RHF values (Table I) [7a]. A related zirconocene sulfido, $\text{Cp}_2^*\text{Zr}(4\text{--}t\text{--Bu--py})(\text{S})$ [21], has a similar Zr-sulfido bond length, $2.316(1) \text{ \AA}$, to that found in $(\text{Cp}')_2\text{Zr}(\text{S})(\text{py})$ [7a]. However, a Zr-tellurido without Cp ligands,

$\text{Zr}(\text{Te}(\text{sitel})_2(\text{dmpe})_2)$, has been reported [7b] and shows a ZrTe bond length to the terminal tellurido of 2.650(1) Å, or ≈ 0.08 Å shorter than that in $(\text{Cp}')_2\text{Zr}(\text{Te})(\text{py})$ [7a]. Replacement of the Cl with Cp to yield Cp_2ZrE has been shown to lengthen Zr-chalcogenido bond lengths by 5% [22], in much better agreement with experiment [7a]. Thus, it must be noted that multiple bonds between transition metals and main group elements are quite sensitive to the nature of the TM's coordination environment.

Tantalum Complexes

Multiply-bonded complexes of Ta occupy a special place in the history of TM=MG chemistry. The synthesis and characterization of a Ta-alkylidene by Schrock is the first example of a d^0 carbene complex [1]. To date, no heavier tetrelide analogues have been reported. A large number of Ta-imidos have been studied, in part due to their intermediacy in CVD of TaN from organometallic precursors [4c,23]. Schrock et al. have reported the crystal structure of a Ta-phosphinidene [6c], $\text{Ta}(\text{PCy})[\text{N}(\text{TMS})\text{—CH}_2\text{CH}_2\text{—}]_3\text{N}$ (Cy = cyclohexyl, TMS = SiMe_3), one of only five structurally characterized phosphinidenes [6b–f] and only one of two examples with linear PR coordination [6c,d]. Ta-oxos are extremely rare; the complex $\text{Ta}(\text{O})(\text{N—i—Pr})_3$ is the only Ta-oxo whose structure is reported in the compendium by Nugent and Mayer [1]. A few examples of mono-sulfido complexes of Ta^V have been structurally characterized, e.g., $\text{STa}(\text{S}_2\text{CNEt}_2)_3$ [24]. Arnold and Christou have reported $\text{Ta}(\text{E})[\text{N}(\text{TMS})\text{—CH}_2\text{CH}_2\text{—}]_3\text{N}$, E = Se, Te [25].

The Ta complexes studied are of the form Cl_3TaEH_n ($n = 0, 1, 2$), **4–6**. The geometry optimizations for Cl_3TaE (**6**) and Cl_3TaEH (**5**) complexes are done under C_{3v} symmetry, while Cl_3TaEH_2 (**4**) complexes are C_s symmetry (Table II). The Ta-chalcogenidos and Cl_3TaNH are C_{3v} minima, while the Ta-tetrelides are C_s minima. For the tetrelides, **4**, Ta- Cl_a bond lengths range from 2.35 to 2.38 Å (RHF) and 2.30 to 2.32 Å (MP2). The Ta- Cl_b bond lengths range from 2.31 to 2.33 Å (RHF) and 2.27 to 2.29 Å (MP2). The Ta-Cl bond lengths for the pnictogen (**5**) and chalcogenido (**6**) complexes range from 2.30 to 2.33 Å (RHF and MP2). The mean Ta-Cl bond length for 83 reported crystal structures of six-coordinate Ta complexes (the smallest coordination number reported) is 2.383 ± 0.055 Å [17].

Tetrelide Complexes, 4. The metric data for Ta-tetrelides, **4**, are listed in Table II. The calculated TaC bond length in Cl_3TaCH_2 (1.90 Å (RHF) and 1.92 Å (MP2)) is in excellent agreement with the only published Ta-alkylidene bond length for a four-coordinate Ta-alkylidene, i.e., 1.888(29) Å for

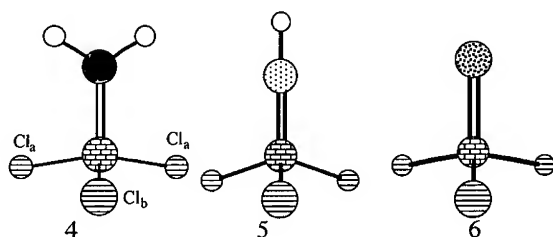


TABLE II. Cl_3TaE complexes.

M/E/level ^a	TaE	TaCl _a (Å)	TaCl _b (Å)	ETaCl _a (°)	ETaCl _b (°)	Exp. TaE ^b
Ta/CH ₂ /RHF	1.90	2.35	2.31	106	105	1.888(29) Å
Ta/CH ₂ /MP2	1.92	2.32	2.29	105	106	
Ta/SiH ₂ /RHF	2.41	2.37	2.32	108	103	
Ta/SiH ₂ /MP2	2.40	2.31	2.27	109	103	
Ta/GeH ₂ /RHF	2.46	2.37	2.32	108	102	
Ta/GeH ₂ /MP2	2.43	2.30	2.27	110	104	
Ta/SnH ₂ /RHF	2.67	2.38	2.33	109	101	
Ta/SnH ₂ /MP2	2.63	2.30	2.27	112	103	
Ta/NH/RHF	1.72	2.33		108		aver. = 1.77 Å
Ta/NH/MP2	1.78	2.32		106		
Ta/PH/RHF	2.15	2.32		111		2.145(7) Å
Ta/PH/MP2	2.21	2.31		108		
Ta/AsH/RHF	2.23	2.32		111		
Ta/AsH/MP2	2.31	2.31		108		
Ta/SbH/RHF	2.43	2.32		112		
Ta/SbH/MP2	2.53	2.33		108		
Ta/O/RHF	1.67	2.31		108		1.725(7)
Ta/O/MP2	1.74	2.31		106		
Ta/S/RHF	2.12	2.30		109		aver. = 2.18 Å
Ta/S/MP2	2.17	2.30		107		
Ta/Se/RHF	2.24	2.30		110		2.330(1) Å
Ta/Se/MP2	2.31	2.30		107		
Ta/Te/RHF	2.47	2.30		110		2.568(1) Å
Ta/Te/MP2	2.54	2.31		107		

^a The pnictogen (5) and chalcogen (6) complexes are C_{3v} ; the tetrelides are C_s (4). The M/E/level notation denotes the transition metal, ligand, and level of theory (RHF or MP2), respectively. See 4 for definitions of Cl_a and Cl_b .

^b Experimental ME bond lengths, where available, are reported. Where more than one bond length is available, the average is denoted. See text for further details.

$\text{Ta}(=\text{C}(\text{H})\text{TMS})(\text{CH}_2\text{TMS})(\text{O}-2,6\text{-di-}t\text{-Butyl-phenyl})$ [1]. The Ta-tetrelide bond lengths for the heavier members are $\text{TaSi} = 2.41$ (RHF), 2.40 (MP2); $\text{TaGe} = 2.46$ Å (RHF), 2.43 Å (MP2); $\text{TaSn} = 2.67$ Å (RHF), 2.63 Å (MP2). A Ta-silyl has recently been characterized [26]; the TaSi bond length in the formally single bonded complex is 2.680(15) Å, providing an upper limit for the Ta-silylidene bond length. To our knowledge, no $\text{Ta}=\text{Ge}$ or $\text{Ta}=\text{Sn}$ complexes have been reported. The MP2 calculated TaE bond lengths are slightly less than the RHF values, except for the alkylidene. Similar behavior (except for the alkylidene) is observed for the Zr complexes. However, the variance between calculated $\text{TM}=\text{MG}$ bond lengths at the two levels of theory (Table II), going from the alkylidene ($\Delta\text{RHF/MP2} = 0.02$ Å) to the stannylidene ($\Delta\text{RHF/MP2} = 0.04$ Å) is very small, suggesting that electron correlation is not as important for the Ta-tetrelides.

Pnictogen Complexes, 5. Metric data for Cl_3TaEH (5), are collected in Table II. Differences between RHF and MP2 bond lengths increases as the pnictogen becomes

heavier, a difference much greater than for Ta-tetrelides. The Ta-imido shows the least variance ($\Delta\text{RHF/MP2} = 0.06 \text{ \AA}$) and the Ta-stibinidene changes the most upon the inclusion of correlation ($\Delta\text{RHF/MP2} = 0.10 \text{ \AA}$) (Table II). The results demonstrate the growing importance of electron correlation for heavier MG elements when describing a series of related bonds, although the magnitude of the lengthening is 4% or less. The calculated Ta-imido bond lengths (1.72 \AA (RHF) and 1.78 \AA (MP2)) are consistent with literature values for four-coordinate Ta-imidos: $1.77(2) \text{ \AA}$ ($\text{Ta}(\text{N}-t\text{-Bu})(\text{NMe}_2)_3$), $1.763(6) \text{ \AA}$ ($\text{Ta}(\text{N}-t\text{-Bu})(\text{NTMS}_2)_2\text{Cl}$), and $1.776(8) \text{ \AA}$ ($\text{Ta}(\text{NAr})(\text{NArC}_2\text{H}_4\text{Ph})(\text{OAr})_2$, Ar = 2,6- $\text{C}_6\text{H}_3\text{Me}_2$) [1]. The TaP bond length in Cl_3TaPH (2.15 \AA (RHF) and 2.21 \AA (MP2)) is in agreement with the value of $2.145(7) \text{ \AA}$ for $\text{Ta}(\text{PCy})[\text{N}(\text{TMS})\text{—CH}_2\text{CH}_2\text{—}]_3\text{N}$ [6c], which is linearly coordinated, Ta-P-C $\approx 170(1)^\circ$, and thus closer to a TaP triple bond description. The calculated TaAs bond length is 2.23 \AA (RHF) (2.31 \AA , MP2), and the TaSb bond length in Cl_3TaSbH is 2.43 \AA (RHF) (2.53 \AA , MP2). The differences in covalent radii [20] for the heavier pnictogens ($r_{\text{cov}}(\text{As}) - r_{\text{cov}}(\text{P}) = 0.11 \text{ \AA}$; $r_{\text{cov}}(\text{Sb}) - r_{\text{cov}}(\text{As}) = 0.31 \text{ \AA}$; $r_{\text{cov}}(\text{Sb}) - r_{\text{cov}}(\text{P}) = 0.20 \text{ \AA}$) mirror the calculated Ta-pnictogen bond lengths at both the RHF and MP2 levels (Table II). As before, this suggests that the description of the TM-pnictogen bond is similar among the heavier pnictogen complexes, so that potential strategies for stabilizing phosphinidenes should be applicable to AsR and SbR analogues.

Chalcogenido Complexes. 6. Calculated metric data for the Ta-chalcogenides, 6, are collected in Table II. The Ta-oxo complex Cl_3TaO has a bond length of 1.67 \AA (RHF) ($\text{TaO} = 1.74 \text{ \AA}$, MP2) in agreement with the value of $1.725(7) \text{ \AA}$ for $\text{Ta}(\text{O})(\text{N}-i\text{-Pr})_3$ [2]. The TaS bond lengths (2.12 \AA (RHF) and 2.17 \AA (MP2)) correspond well with the average of the eight reported terminal Ta^{VS} bond lengths, 2.18 \AA [24]. The Ta-chalcogenido bond lengths for Cl_3TaSe (2.24 \AA , RHF; 2.31 \AA , MP2) and Cl_3TaTe (2.47 \AA , RHF; 2.54 \AA , MP2) are in agreement with those for $\text{Ta}(\text{E})[\text{N}(\text{TMS})\text{—CH}_2\text{CH}_2\text{—}]_3\text{N}$, TaSe = $2.330(1) \text{ \AA}$ and TaTe = $2.568(1) \text{ \AA}$ [25]. Experimental Ta-chalcogenido bond lengths are closer to MP2 calculated values (aver. error $\approx 1\%$) than the RHF values (aver. error $\approx 4\%$), suggesting that electron correlation at the MP2 level may be more appropriate for these chalcogenidos. However, other than $\text{Ta}(\text{O})(\text{N}-i\text{-Pr})_3$, all experimental Ta-chalcogenidos have coordination numbers greater than our four-coordinate models. Lengthening of the Ta-chalcogenido bond upon going from an RHF to MP2 wavefunction is approximately the same for all chalcogens ($\Delta\text{RHF/MP2} \approx 0.07 \text{ \AA}$).

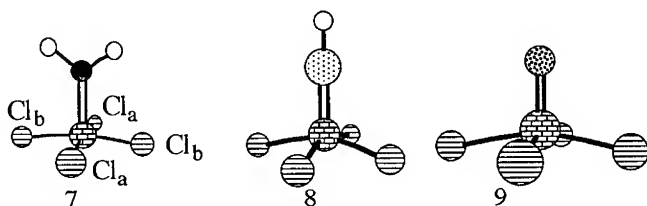
Tungsten Complexes

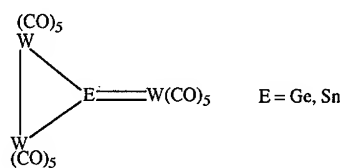
Multiply-bonded complexes of the Group IVB metals are well known [1]. High-valent (d^0) TM=MG complexes are somewhat rarer than lower valent examples and are primarily limited to the first row main group elements [1]. Trans- $\text{W}(\text{Te})_2(\text{PMe}_3)_4$ represents the first terminal tellurido [27]; Parkin and Rabinovich have subsequently characterized a series of related bis(chalcogenido) complexes [27b]. An interesting series of d^0 chalcogenidos, Cl_4WE (E = O, S, Se), have been studied by Page et al. [28] using gas-phase electron diffraction. Mononuclear, terminal W complexes of the heavier pnictogens and tetrels are very rare [6d–f].

The geometry optimizations of Cl_4WE (7–9), Table III, for the pnictogens (8) and chalcogens (9) are done under the constraints of C_{4v} symmetry. The chalcogenidos (9) and Cl_4WNH are C_{4v} minima. The tetrelides (7) possess C_s minima. Calculated W—Cl bond lengths range from 2.28 Å to 2.45 Å (RHF), and from 2.28 Å to 2.50 Å (MP2) (Table III). The average value for all W—Cl bonds (RHF and MP2 values) is 2.34 ± 0.05 Å, consistent with the mean experimental value of 2.39 ± 0.03 Å for W—Cl (CN = 5) [17].

Tetrelide Complexes, 7. The geometries of the tetrelides Cl_4WEH_2 (E = C, Si, Ge, Sn), 7, were computed (Table III). The calculated carbon-metal bond of 1.87 Å (RHF) is in quite good agreement with the W-alkylidene bond lengths of 1.882(14) Å and 1.942(9) Å reported for five-coordinate d^0 complexes [1]. The WC bond in Cl_4WCH_2 shortens by 0.01 Å upon going from the RHF to MP2 level, thus remaining in good agreement with the experimental models. To our knowledge, no structural analysis of a W-silylidene has been reported. The complexes $[\text{W}(\text{CO})_5]_3\text{E}$, 10, (E = Ge, Sn) have been structurally characterized [5a]. The shorter of the W-tetrel bonds (denoted with a double bond in 10) are 2.511(1) Å and 2.702(2) Å for the Ge and Sn complexes, respectively [5a]. Calculated values for Cl_4WEH_2 are $\text{WGe} = 2.45$ Å (RHF) and 2.40 Å (MP2), and $\text{WSn} = 2.70$ Å (RHF) and 2.56 Å (MP2), in agreement with those found in complexes 10. In both cases the RHF values are closer to experiment [5a], although any designation of bond character in these complexes is tenuous. The differences in the WE bond lengths in 10 is 0.19 Å, a value which is intermediate between the difference between the RHF (Sn – Ge = 0.25 Å) and MP2 (Sn – Ge = 0.16 Å) WE bond lengths for Cl_4WEH_2 (Table III). Note that the MP2 difference in W-tetrelide bond length is closer to the difference in the covalent radii of Ge and Sn (diff. = 0.18 Å, [20]).

Pnictogen Complexes. The calculated WN bond length in C_{4v} Cl_4WNH (1.66 Å, RHF; 1.75 Å, MP2) is in agreement with the range of bond lengths (WN = 1.736(5)–1.757(5) Å, [1]) for square pyramidal W-imidos. Cowley et al. [6d] have characterized a linearly coordinated (W—P—C = $168.2(2)^\circ$) W(IV)-phosphinidene with WP = 2.169(1) Å, in between the RHF value of WP = 2.08 Å and the MP2 value of WP = 2.20 Å for C_{4v} - Cl_4WPH . It is interesting to note that a nonlinearly coordinated W(IV)-phosphinidene, $\text{Cp}_2\text{W}(\text{PMes})$, has a substantially longer WP bond length, WP = 2.349(5) Å [6f]. The WE bond lengths in Cl_4WAsH and Cl_4WSbH differ by ≈ 0.20 Å at the RHF and MP2 levels (Table III). As with the other C_{4v} - Cl_4WEH complexes the WE bond lengthens by ≈ 0.12 Å upon the inclusion of correlation at the MP2 level. Complexes of WAs and WSb with any bond order are rare; Huttner et al. [29] have reported $[\text{W}(\text{CO})_5]_3\text{E}_2$ (E = As, Sb), 11. Average WE bond lengths in 11 are 2.83 Å (E = As) and 3.02 Å (E = Sb). The assignment of a





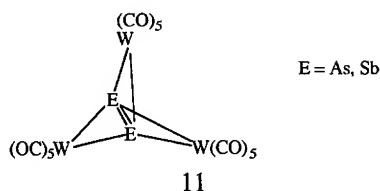
WE bond order of one to **11** is not clear, but the bond lengths should be an upper limit to the W-pnictogen bond lengths in Cl_4WAsH and Cl_4WSbH . Additionally, the difference in W-pnictogen bond lengths in **11** ($\text{WSb} - \text{WAs} = 0.19 \text{ \AA}$) is consistent with that calculated for Cl_4WAsH and Cl_4WSbH , further proof that bonding descriptions among the heavier pnictogens are similar.

TABLE III. Cl_4WE complexes.

M/E/level ^a	WE	WCl_a (\AA)	WCl_b (\AA)	EWCl_a ($^\circ$)	EWCl_b ($^\circ$)	Exp. WE ^b
W/CH ₂ /RHF	1.87	2.40	2.28	98	106	aver. = 1.91 \AA
W/CH ₂ /MP2	1.86	2.35	2.28	101	105	
W/SiH ₂ /RHF	2.37	2.40	2.30	102	87	
W/SiH ₂ /MP2	2.44	2.50	2.29	124	59	2.511(1) \AA
W/GeH ₂ /RHF	2.45	2.43	2.29	96	94	
W/GeH ₂ /MP2	2.40	2.35	2.36	102	72	
W/SnH ₂ /RHF	2.70	2.45	2.28	89	106	2.702(2) \AA
W/SnH ₂ /MP2	2.56	2.28	2.31	83	112	
W/NH/RHF	1.66	2.34		104		aver. = 1.75 \AA
W/NH/MP2	1.75	2.34		102		
W/PH/RHF	2.08	2.35		105		
W/PH/MP2	2.20	2.34		103		2.169(1) \AA
W/AsH/RHF	2.17	2.35		105		
W/AsH/MP2	2.29	2.34		103		
W/SbH/RHF	2.37	2.36		105		2.203(4) \AA
W/SbH/MP2	2.50	2.33		103		
W/O/RHF	1.63	2.32		104		
W/O/MP2	1.73	2.33		102		2.086(6) \AA
W/S/RHF	2.07	2.32		105		
W/S/MP2	2.16	2.34		102		
W/Se/RHF	2.17	2.33		105		2.203(4) \AA
W/Se/MP2	2.30	2.34		102		
W/Te/RHF	2.40	2.33		105		
W/Te/MP2	2.53	2.36		102		

^a The pnictogen (**8**) and chalcogen (**9**) complexes are C_{4v} ; the tetrelides are C_s (**7**). The M/E/level notation denotes the transition metal, ligand, and level of theory (RHF or MP2), respectively. See **7** for definitions of Cl_a and Cl_b .

^b Experimental ME bond lengths, where available, are reported. Where more than one bond length is available, the average is given. See text for further details.



The Chalcogen Complexes. The Cl_4WE complexes ($\text{E} = \text{O}, \text{S}, \text{Se}, \text{Te}$) provide an exciting opportunity to compare ECP calculated geometries (RHF and MP2 wavefunctions) with experimental gas-phase data [28]. The Cl_4WE complexes are calculated to be C_{4v} minima which supports the conclusions of Page et al. based on electron diffraction (ED) [28]. The WCl bonds lengthen by 0.01 Å (oxo) to 0.03 Å (tellurido) upon going from an RHF to MP2 wavefunction, and thus remain in excellent agreement with experimental values, $\text{WCl} = 2.28$ Å [28]. The angle between the WE and WCl bonds contract by 2° ($\text{E} = \text{O}$) or 3° ($\text{E} = \text{S}, \text{Se}, \text{Te}$). Experimental EWCl bond angles are 102° ($\text{E} = \text{O}$), 104° ($\text{E} = \text{S}$), and 104° ($\text{E} = \text{Se}$) in good agreement with the RHF and MP2 values. The reported experimental values of WE in Cl_4WE are 1.685(15) Å ($\text{E} = \text{O}$), 2.086(6) Å ($\text{E} = \text{S}$), and 2.203(4) Å ($\text{E} = \text{Se}$) [28]. The WE bond length, as expected, shows the greatest change upon the inclusion of electron correlation, RHF values are shorter than experimental values by ≈ 0.05 Å. On average the MP2 calculated WE bond lengths (Table III), are 0.11 Å longer than the RHF calculated WE bond lengths, so that experimental W-chalcogen bond lengths in Cl_4WE fall in between the RHF and MP2 calculated values. Thus, the MP2 wavefunction tends to slightly overcorrect for WE bond lengthening. However, the differences in the RHF and MP2 optimized geometries are small and thus both levels of theory yield good agreement with the ED data of Page et al. [28].

Summary and Conclusions

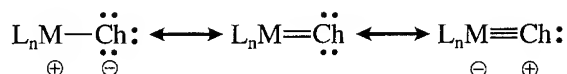
Several points of interest were noted in this research which are of interest in the context of studying $\text{TM}=\text{MG}$ complexes, both in terms of future directions for experimental and computational research. The most important points are summarized below.

As expected [12], the change in $\text{TM}=\text{MG}$ bond lengths upon going from RHF to MP2 (for a given metal) are of similar magnitude and tend to increase as one goes toward the heavier MG elements. An obvious exception is the Zr-chalcogenidos, Cl_2ZrE ($\text{E} = \text{O}, \text{S}, \text{Se}, \text{Te}$) (Table I): $\Delta_{\text{RHF/MP2}} = 0.12$ Å (O), 0.03 Å (S), 0.05 Å (Se), and 0.06 Å (Te); ZrE bonds are longer at the MP2 level than RHF. It is of interest that inclusion of correlation causes the greatest change in the Zr-oxo bond length, since strong metal $d\pi$ -ligand $p\pi$ bonding for first row MG elements typically yields the best RHF description in a series of related $\text{TM}=\text{MG}$ complexes. Based on an analysis of X-ray crystallographic data for $\text{Cp}_2\text{ZrE}(\text{py})$ [7a] and ECP studies of Cp_2ZrE models [22] it was concluded that the description of the Zr-oxo linkage is more like that of a single bond, while the heavier chalcogenido complexes were more weighted towards a double bond description of the Zr-chalcogenido bond. A

triple bond description of the Zr-chalcogenido linkage is inconsistent with the observed reactivity of $\text{Cp}_2\text{Zr}(\text{E})(\text{py})$ [7a]. A doubly bonded structure, with a greater number of covalent bonds, is expected to be better described at the Hartree-Fock level than a singly bonded structure in which $\text{TM}=\text{MG}$ bonding is more dative in nature. Taken together, experimental and computational results suggest a fundamental difference in the bonding description between oxo complexes and heavier chalcogenidos for Group IVB complexes.

Small differences are found between RHF and MP2 geometries in the overwhelming majority of cases. The Cl_4WE ($\text{E} = \text{O}, \text{S}, \text{Se}$) complexes, for which there are exact experimental models [28], yield RHF determined WE bond lengths which are shorter than experimental values by $\approx 0.05 \text{ \AA}$; whereas the MP2 calculated WE bond lengths (Table III) are longer by a nearly equivalent amount. When compared to experiment [28], the MP2 wavefunction tends to slightly overcorrect for WE bond lengthening. Other geometric parameters for Cl_4WE show minimal changes upon the inclusion of electron correlation. Thus, the differences in the RHF and MP2 optimized geometries are small and both levels of theory yield reasonable agreement with the ED data of Page et al. [28] for even the heaviest member of the series, i.e., Cl_4WSe . The W-tetrelide complexes (Table III) show some of the largest changes in geometry upon the inclusion of electron correlation, suggesting that future studies of W-tetrelide complexes may need to be carried out using more sophisticated and computationally intensive, multiconfiguration methods. The close agreement between RHF and MP2 calculated geometries for the remaining models supports the contention that these computationally efficient methods can provide a route to the theoretical study of $\text{TM}=\text{MG}$ complexes which are more realistic models of synthetic targets.

The ZrP linkage in Cl_2ZrPH lengthens by 0.1 \AA upon going from linear (i.e., triple bond) to bent (i.e., double bond) PH coordination. Experimental data exists to support the calculational results. The TaP bond length in a linearly coordinated Ta-phosphinidene [6c] is 0.36 \AA shorter than the ZrP bond length in a bent Zr-phosphinidene [6b]; this difference in TM-phosphinidene bond lengths is much greater than the difference in the metallic radii of Zr and Ta ($R_{\text{Zr}} = 1.454 \text{ \AA}$, $R_{\text{Ta}} = 1.343 \text{ \AA}$, diff. = 0.111 \AA). Also, a linearly coordinated W(IV)-phosphinidene has $\text{WP} = 2.169(1) \text{ \AA}$ [6d], while a nonlinearly coordinated W(IV)-phosphinidene [6f], $\text{Cp}_2\text{W}(\text{PMe}_3)_2$, has a WP bond which is 0.18 \AA longer, $\text{WP} = 2.349(5) \text{ \AA}$. Letting the WPH angle in $\text{C}_{4v}\text{-Cl}_4\text{WPH}$ relax from 180° leads to a C_s minimum ($15.8 \text{ kcal mol}^{-1}$ lower in energy at the RHF level) with $\text{WP} = 2.22 \text{ \AA}$, or 0.14 \AA longer than in $\text{C}_{4v}\text{-Cl}_4\text{WPH}$ (Table III). The changes in M-P bond length as a function of M-P-H angle are exciting in the context of trying to make stable phosphinidenes since a linearly coordinated phosphinidene should be of greater kinetic (by tying up the P lone pair) and thermodynamic (by strengthening the TM-phosphinidene linkage) stability. The metric data suggest similar descriptions of the $\text{TM}=\text{MG}$ linkage among the heavier pnictogens so that similar proposals for



$L_nM=AsR$ and $L_nM=SbR$ complexes, which are currently not known, can be made. A joint theory-experiment study is underway to test these hypotheses and identify synthetic targets (through modification of R and L_n) which favor linearly coordinated PR , AsR , and SbR [30].

Acknowledgments

Effective core potential studies of transition metal-main group multiple bonding at Memphis State are supported by the Air Force Office of Scientific Research (93-10105), Petroleum Research Fund (administered by the American Chemical Society), the Joint Institute for Computational Science (a coalition between Memphis State, University of Tennessee-Knoxville, Oak Ridge, and Vanderbilt to encourage the use of parallel computing in Tennessee), IBM, and the National Science Foundation (through grant CHE-9314732 and their support of the National Center for Supercomputing Applications and the Cornell National Supercomputing Facility). The communication of experimental results prior to publication by Profs. Ged Parkin (Columbia), Doug Stephan (Windsor), and Ben Xue (Tennessee) is also gratefully acknowledged.

Bibliography

- [1] W. A. Nugent and J. M. Mayer, *Metal-Ligand Multiple Bonds* (Wiley, New York, 1988).
- [2] (a) P. R. Ortiz de Montellano, Ed., *Cytochrome P-450* (Plenum: New York, 1986); (b) P. C. H. Mitchell and F. Trifiro, *J. Chem. Soc., A*, 3183 (1970).
- [3] (a) C. C. Cummins, S. M. Baxter, and P. T. Wolczanski, *J. Am. Chem. Soc.* **110**, 8731 (1988); (b) C. P. Schaller and P. T. Wolczanski, *Inorg. Chem.* **32**, 131 (1993); (c) J. de With and A. D. Horton, *Angew. Chem. Int. Ed. Engl.* **32**, 903 (1993); (d) P. J. Walsh, F. J. Hollander, and R. G. Bergman, *J. Am. Chem. Soc.* **110**, 8729 (1988); (e) R. D. Profflet, C. H. Zambrano, P. E. Fanwick, J. J. Nash, and I. P. Rothwell, *Inorg. Chem.* **29**, 4364 (1990).
- [4] (a) D. C. Bradley, *Chem. Rev.* **89**, 1317 (1989); K. G. Caulton and L. G. Hubert-Pfaltzgraf, *Chem. Rev.* **90**, 969 (1990); (b) M. Nandi, D. Rhubright, and A. Sen, *Inorg. Chem.* **29**, 3066 (1990); (c) M. M. Banaszak Holl, P. T. Wolczanski, and G. D. Van Duyne, *J. Am. Chem. Soc.* **112**, 7989 (1990); (d) M. H. Chisholm, K. G. Caulton, and Z. Xue, *Chem. Mater.* **3**, 384 (1991).
- [5] (a) W. Petz, *Chem. Rev.* **86**, 1019 (1986); (b) J. F. Harrod, T. Ziegler, and V. Tschinke, *Organometallics* **9**, 897 (1990).
- [6] (a) A. H. Cowley and A. R. Barron, *Acc. Chem. Res.* **21**, 81 (1988); (b) D. W. Stephan, Z. Hou, and T. C. Breen, *Organometallics* **12**, 3145, 3158 (1993); (c) R. R. Schrock, C. C. Cummins, and W. M. Davis, *Angew. Chem., Int. Ed. Engl.* **32**, 756 (1993); (d) A. H. Cowley, B. Pellerin, J. L. Atwood, and S. G. Bott, *J. Am. Chem. Soc.* **112**, 6734 (1990); (e) P. B. Hitchcock, M. F. Lappert, and W. P. Leung, *J. Chem. Soc., Chem. Commun.* 1282 (1987); (f) R. Bohra, P. B. Hitchcock, M. F. Lappert, and W. P. Leung, *Polyhedron* **8**, 1884 (1989).
- [7] (a) G. Parkin and W. A. Howard, *J. Am. Chem. Soc.* **116**, 606 (1993); (b) V. Christou and J. Arnold, *J. Am. Chem. Soc.* **114**, 6240 (1992); (c) E. Diemann and A. Müller, *Coord. Chem. Rev.* **10**, 79 (1973); (d) A. A. Eagle, L. J. Laughlin, C. G. Young, and E. R. T. Tiekint, *J. Am. Chem. Soc.* **114**, 9195 (1992); (e) D. Rabinovich and G. Parkin, *J. Am. Chem. Soc.* **113**, 5904 (1991).
- [8] W. J. Hehre, L. Radom, P. v. R. Schleyer, and J. A. Pople, *Ab-Initio Molecular Orbital Theory* (Wiley, New York, 1986).
- [9] (a) M. C. Zerner and D. Salahub, *The Challenge of d- and f-Electrons* (ACS, Washington, DC, 1989); *Quantum Chemistry: The Challenge of Transition Metals and Coordination Chemistry*, A. Veillard, Ed. (Reidel, Dordrecht, The Netherlands, 1985).
- [10] The derivation of the effective core potentials used in this research are described in (a) M. Krauss, W. J. Stevens, H. Basch, and P. G. Jasien, *Can. J. Chem.* **70**, 612 (1992); (b) W. J. Stevens, H.

- Basch, M. Krauss, *J. Chem. Phys.* **81**, 6026 (1984); (c) T. R. Cundari and W. J. Stevens, *J. Chem. Phys.* **98**, 5555 (1993).
- [11] M. W. Schmidt, K. K. Baldridge, J. A. Boatz, J. H. Jensen, S. Koseki, N. Matsunaga, M. S. Gordon, K. A. Nguyen, S. Su, T. L. Windus, S. T. Elbert, J. Montgomery, and M. Dupuis, *J. Comput. Chem.* **14**, 1347 (1993).
- [12] T. R. Cundari and M. S. Gordon, *Coord. Chem. Rev.* (submitted).
- [13] P. Carsky, B. A. Hess, and L. J. Schaad, *J. Comput. Chem.* **5**, 280 (1984).
- [14] (a) T. R. Cundari, *Int. J. Quantum Chem., Quantum Chem. Symp.* **26**, 793 (1992); (b) T. R. Cundari, *J. Am. Chem. Soc.* **114**, 7879 (1992); (c) T. R. Cundari, *J. Am. Chem. Soc.* **114**, 10557 (1992); (d) T. R. Cundari, *Organometallics* **12**, 1998 (1993).
- [15] M. D. Fryzuk, S. S. H. Mao, M. J. Zaworotko, and L. R. MacGillivray, *J. Am. Chem. Soc.* **115**, 5336 (1993).
- [16] (a) T. R. Cundari and M. S. Gordon, *Organometallics* **11**, 55 (1992); (b) T. R. Cundari and M. S. Gordon, *J. Am. Chem. Soc.* **113**, 5231 (1991); (c) T. R. Cundari and M. S. Gordon, *J. Phys. Chem.* **96**, 631 (1992); (d) T. R. Cundari and M. S. Gordon, *Organometallics* **11**, 3122 (1992); (e) T. R. Cundari and M. S. Gordon, *J. Am. Chem. Soc.* **114**, 539 (1992).
- [17] A. G. Orpen, L. Brammer, F. H. Allen, O. Kennard, D. G. Watson, and R. Taylor, *J. Chem. Soc., Dalton Trans.* **S1**, (1989).
- [18] B. K. Campion and T. D. Tilley, *J. Am. Chem. Soc.* **109**, 2049 (1987).
- [19] (a) Due to the lanthanide contraction Hf and Zr are roughly the same size; thus, one usually observes that Hf-element and Zr-element bonds are nearly equal [16a-d, 14b-d]; (b) H. G. Woo, W. P. Freeman, and T. D. Tilley, *Organometallics* **11**, 2198 (1992).
- [20] L. Pauling, *The Nature of the Chemical Bond*, 3rd ed. (Cornell University Press, Ithaca, NY, 1960).
- [21] M. J. Carney, P. J. Walsh, and R. G. Bergman, *J. Am. Chem. Soc.* **112**, 6426 (1990).
- [22] M. T. Benson, T. R. Cundari, S. J. Lim, H. D. Nguyen, and K. Pierce-Beaver, *J. Am. Chem. Soc.* **116**, 3955 (1994).
- [23] See, for example, the following abstracts from the Inorganic Section of the 1991 National ACS Meeting, New York, August 1991: Nos. 55, 74, 103, 104, 174, 176, 230, 278, and 309.
- [24] (a) M. G. B. Drew, D. A. Rice, and D. M. Williams, *J. Chem. Soc., Dalton Trans.* 845 (1984); (b) E. J. Petersen, R. B. von Dreele, and T. M. Brown, *Inorg. Chem.* **17**, 1410 (1978); (c) J. Sola, Y. Do, J. M. Berg, and R. H. Holm, *Inorg. Chem.* **24**, 1706 (1985).
- [25] V. Christou and J. Arnold, *Angew. Chem., Int. Ed. Engl.* **32**, 1450 (1993).
- [26] Z. Xue, Dept. of Chemistry, University of Tennessee, personal communication.
- [27] (a) D. Rabinovich and G. Parkin, *J. Am. Chem. Soc.* **113**, 5904 (1991); (b) G. Parkin, Dept. of Chemistry, Columbia University, personal communication.
- [28] E. M. Page, D. A. Rice, K. Hagen, L. Hedberg, and K. Hedberg, *Inorg. Chem.* **30**, 4758 (1991).
- [29] G. Huttner, B. Sigwarth, H. Zsolnai, and G. Berke, *J. Organomet. Chem.* **226**, C5 (1982); G. Huttner, U. Weber, B. Sigwarth, and O. Scheidsteger, *Angew. Chem., Int. Ed. Engl.* **21**, 215 (1982).
- [30] T. R. Cundari and D. W. Stephan, work in progress.

Received March 8, 1994

Coupled-Cluster Singles, Doubles, and Triples Calculations with Hartree-Fock and Brueckner Orbital Reference Determinants: A Comparative Study

JOHN D. WATTS and RODNEY J. BARTLETT

*Quantum Theory Project, Departments of Chemistry and Physics,
University of Florida, Gainesville, Florida 32611-2085*

Abstract

A series of complete coupled-cluster singles, doubles, and triples (CCSDT) calculations have been performed with Hartree-Fock (HF) and Brueckner (B) orbitals. Calculations have been performed with a double-zeta plus polarization basis set on the H_2O , SiH_2 , NH_2 , BeO , C_2 , CN^+ , and BN molecules. Calculations on H_2O and SiH_2 at equilibrium and stretched geometries show negligible difference between HF- and B-CCSDT energies. This is also true for NH_2 , except when the bonds have been stretched to twice their equilibrium values, at which point there is about a 2.5 milli-Hartree (mE_h) difference. Calculations on the isoelectronic systems BeO , C_2 , CN^+ , and BN were performed at equilibrium geometries. Even though these systems have large T_1 amplitudes, the difference between HF- and B-CCSDT energies is only about 1 mE_h . For the CCSD method and the CCSD(T) method, which includes triple excitations in an approximate, noniterative manner, however, somewhat larger differences are observed between HF- and B-CC results. Finally, some properties of BN were computed using HF- and B-CC methods. There are quite small differences between the HF- and B-CCSDT results, but significantly larger ones for the more approximate CCSD and CCSD(T) methods. For this difficult system, where the CCSD(T) approximation seems to be inadequate for HF orbitals, the use of Brueckner orbitals improves the agreement of CCSD(T) with CCSD(T) substantially for r_e and ω_e , although the difference for μ is unaffected. © 1994 John Wiley & Sons, Inc.

Introduction

The subject of Brueckner orbitals has a long history [1–7]. These orbitals derive from Brueckner's work in the theory of nuclear matter [1]. Brueckner orbitals are eigenfunctions of an effective one-particle operator, and thus are sometimes referred to as the orbitals of an "exact SCF" theory [3]. They also provide the single determinant with the maximum overlap with the exact wave function.

Brueckner orbitals are defined to be those orbitals which make the single excitation amplitudes C_i^a vanish in the full configuration interaction (FCI) wave function. In practice, of course, Brueckner orbitals are obtained for some approximate method, such as truncated CI or truncated coupled-cluster (CC) methods. For example, Chiles and Dykstra [6] obtained Brueckner orbitals with respect to the CC singles-and-doubles (CCSD) method, and they termed this method CCD ($T_1 = 0$).

In the last few years there has been a revival of interest in the use of Brueckner orbitals in CC methods. Handy et al. [8] implemented a scheme which they termed "Brueckner doubles" (BD). This is identical to the CCD ($T_1 = 0$) scheme of Chiles and Dykstra [6] and has been denoted B-CCD by Stanton et al. [9]. This notation emphasizes that the method is just a CCD calculation with Brueckner orbitals, the latter being those which make the CCSD T_1 amplitudes vanish. Triple excitations have been included noniteratively in these Brueckner orbital methods, in the same manner as in the CCSD + T(CCSD) [10] and CCSD(T) [11,12] methods. Handy et al. defined and implemented a method which they termed BD(T), while Stanton et al. used a slight extension of this which they called B-CCD(T) [9,12]. Raghavachari et al. [13] have added noniterative triple and quadruple excitation corrections to the BD model to give the BD(TQ) method, which is the Brueckner orbital analogue of the CCSD + TQ*(CCSD) [14] and CCSD(TQ) [13] methods. The Brueckner orbital variant of the iterative CCSDT method [15–18] has also been considered [19]. As well as energies, analytical derivatives have been implemented for the BD and BD(T) methods [20,21]. A straightforward determination of Brueckner orbitals requires a series of CC calculations, with orbitals being modified after each CC calculation [6]. However, with an atomic orbital formulation of CC theory, it is possible to perform a B-CC calculation with about the same computational cost as a single CC calculation [22].

Along with these methodological developments, there have now been a number of B-CC calculations, particularly comparisons with HF-CC results [23,24]. Some of the most significant recent results relate to symmetry breaking questions, as anticipated by earlier studies [5]. For example: (1) it has been shown that with a Brueckner reference determinant, the distance at which the spin-restricted solution becomes unstable is greater than if an RHF reference determinant is used [8]; (2) it has been shown that in some cases when the Hartree–Fock orbitals suffer from symmetry breaking, the Brueckner orbitals are not symmetry broken [9].

While there have now been quite a number of B-CC calculations incorporating a *noniterative* treatment of triple excitations, there are rather few in which triple excitations are incorporated *iteratively*. To the best of our knowledge, there is only one study in of this type [19]. However, this work does not present any HF-CCSDT results for comparison, and it uses only a minimal basis set. In this article, we provide a comparison of Brueckner and Hartree–Fock CCSDT results for several difficult examples, using double-zeta plus polarization (DZP) basis sets. We also include some CCSD and CCSD(T) results for comparison.

Computational Details

All of the calculations have been performed with the ACES II program system [25,26]. Brueckner orbitals were determined in the manner described by Chiles and Dykstra [6]. Thus, one begins with a set of orthonormal orbitals. These are in principle arbitrary, but in this work are Hartree–Fock orbitals. With these orbitals, a CC calculation is performed. From the T_1 amplitudes and the initial orbitals, one generates a new set of orbitals, according to the equations

$$C_{\mu i} = C_{\mu i}^{(0)} + \sum_a t_i^a C_{\mu a}^{(0)} \quad (1)$$

$$C_{\mu a} = C_{\mu a}^{(0)} - \sum_i t_i^a C_{\mu i}^{(0)}. \quad (2)$$

Here i and a denote occupied and virtual molecular orbitals, respectively, and μ labels the atomic orbitals. The new orbitals are then orthonormalized and used in another CC calculation. This generates a new set of T_1 amplitudes, from which a new set of orbitals is generated. This process is repeated until convergence, at which time the orbitals are Brueckner orbitals. Of course, this procedure requires several CC calculations, and is not recommended as an efficient method for generating Brueckner orbitals (cf. Ref. [22]), but is adequate for testing purposes.

Several systems have been studied. In the first group of calculations, the H_2O , NH_2 , and SiH_2 molecules were studied with a double-zeta plus polarization (DZP) basis set at equilibrium geometries and at geometries with stretched bonds. The geometries are the same as those used in FCI calculations [27–29]. The O and N basis sets are the $4s2p$ contractions of Dunning [30] augmented with the d polarization functions of Redmon et al. [31]. The H basis set in the H_2O and NH_2 calculations is Dunning's $2s$ set [30], augmented with the p exponent of Redmon et al. (0.7). In the SiH_2 calculations the H basis set is the same, except that the p function has an exponent of 1.0. The Si basis set is the $6s4p$ set of Dunning and Hay [32] with a d function of 0.3 [29]. In the second group, single point energy calculations were performed at geometries close to experimental equilibrium geometries [33] of the lowest closed-shell states of the isoelectronic series BeO, C_2 , CN^+ , and BN with a DZP basis set. For B, C, and N, the basis set comprised the $4s2p$ set of Dunning [30] and the polarization functions of Redmon et al. (0.386 (B), 0.654 (C), and 0.902 (N)). The Be basis set was the $3s2p$ set of Dunning and Hay [32] with a polarization exponent of 0.6 [34], and the O basis set was Dunning's $4s2p$ set [30] with a polarization exponent of 0.85 [32]. The bond lengths used in the calculations are 1.331 Å (BeO), 1.243 Å (C_2), 1.173 Å (CN^+), and 1.28 Å (BN). The final group of calculations involved determination of some properties of the $a^1\Sigma^+$ state of BN using the same DZP basis set as described above. Throughout this work, all electrons were correlated and spherical harmonic d functions were used, except in the calculations on H_2O which used Cartesian d functions.

In order to give a quantitative indication of the size of the T_1 CC amplitudes, we have computed the “ \mathcal{T}_1 diagnostic” of Lee and Taylor [35], which is defined by

$$\mathcal{T}_1 = \sqrt{\frac{1}{2N} \sum_{ai} [t_i^a(\alpha)^2 + t_i^a(\beta)^2]} \quad (3)$$

for SCF orbitals where N is the number of correlated electrons. As \mathcal{T}_1 is a measure of the difference of a set of orbitals from Brueckner orbitals, it is expected to correlate with the difference between CC results computed with Brueckner and another set of orbitals [23]. Contrary to the opinion of some, this diagnostic should not be used as a measure of multi-reference character, as it ignores the amplitudes of

double excitations which have a dominant role in expressing that aspect. As any set of orbitals may be obtained from another from e^{T_1} , the size of T_1 is an orbital measure.

We also report the total CC energy and the CC correlation energy. The former is the sum of the energy of the reference determinant and the CC correlation energy for that determinant:

$$E_{\text{tot}} = \langle \Phi_0 | e^{-T} H e^T | \Phi_0 \rangle = E_{\text{ref}} + E_{\text{corr}} \quad (4)$$

$$E_{\text{ref}} = \langle \Phi_0 | H | \Phi_0 \rangle \quad (5)$$

$$E_{\text{corr}} = \langle \Phi_0 | e^{-T} (H - E_{\text{ref}}) e^T | \Phi_0 \rangle \quad (6)$$

where Φ_0 is the reference determinant and T is the cluster operator.

Results

H_2O

Symmetrical bond stretching in H_2O has many times [15] been used as a test of approximate methods. As the bonds are stretched, the single determinant reference function provides a progressively less satisfactory description, which is reflected by large amplitudes in the CC wave function. Studies have shown that CC methods which include triple excitations provide excellent agreement with FCI at the equilibrium geometry (r_e) and also when the bonds have been stretched to one-and-a-half times their equilibrium lengths ($1.5r_e$). At $2r_e$, the performance is reasonable, but not so good, with the CC energies a few millihartrees (mE_h) below the FCI energy.

In Table I, we compare the CC energies obtained using both restricted Hartree-Fock (RHF) and Brueckner reference determinants. It is seen that the HF-CCSDT and B-CCSDT energies are essentially identical, although as the bond length is increased, the B-CCSDT "correlation energy," as it is measured relative to the B reference, becomes significantly larger than the HF-CCSDT correlation energy (as the T_1 amplitudes become larger, the Brueckner orbitals deviate more from Hartree-Fock ones). The small difference in the CCSDT energies seen here is another example of the well-known (approximate) invariance of the results of CC methods (particularly those having the full e^{T_1} operator in the wave operator) to choice of reference determinant [36].

TABLE I. Comparison of HF- and B-CCSDT energies of H_2O at equilibrium and stretched geometries. DZP basis set, atomic units.

Method	Property	r_e	$1.5r_e$	$2r_e$
HF-CCSDT	E_{tot}	-76.27360	-76.08727	-75.97141
	E_{corr}	-0.23289	-0.28605	-0.38850
	T_1	0.006	0.022	0.049
B-CCSDT	E_{tot}	-76.27359	-76.08716	-75.97144
	E_{corr}	-0.23395	-0.29287	-0.41332

TABLE II. Comparison of HF- and B-CCSDT energies of SiH₂ at equilibrium and stretched geometries. DZP basis set, atomic units.

Method	Property	r_e	$1.5r_e$	$2r_e$
HF-CCSDT	E_{tot}	-290.19614	-290.08138	-289.99867
	E_{corr}	-0.17920	-0.20704	-0.29152
	T_1	0.009	0.020	0.045
B-CCSDT	E_{tot}	-290.19613	-290.08129	-289.99834
	E_{corr}	-0.18098	-0.21400	-0.31509

SiH₂

This example is similar to H₂O, but in fact is a more severe test, since even at equilibrium more than one determinant contributes significantly to the wave function. The B-CCSDT and HF-CCSDT results are shown in Table II. The results are basically the same as for H₂O, again the B-CCSDT and HF-CCSDT energies being essentially identical.

²A₁ NH₂

A number of FCI comparisons have been performed for this system [8,12,37]. They have demonstrated that whether one starts from a UHF or an ROHF reference determinant, it is extremely difficult to reproduce the FCI energy well at $2r_e$. We have found that the complete CCSDT method, with both UHF- and ROHF reference determinants, is able to provide a good description, but this is not true of the CCSD(T) method or iterative approximations to CCSDT [12].

In Table III we show the B-CCSDT and HF-CCSDT results. We see that at r_e and $1.5r_e$ the energies are virtually identical, but that at $2r_e$ there is a $2.5 mE_h$ difference. Considering that the B-CCSDT results have less spin contamination, one might imagine that they would be closer to FCI. However, our previous comparison with FCI

TABLE III. Comparison of HF- and B-CCSDT energies of NH₂. ²A₁ at equilibrium and stretched geometries. DZP basis set, atomic units.

Method	Property	r_e	$1.5r_e$	$2r_e$
HF-CCSDT	E_{tot}	-55.70288	-55.53192	-55.42792
	E_{corr}	-0.17693	-0.20638	-0.16713
	T_1	0.005	0.023	0.087
	$2S + 1$	2.0000	2.0001	2.0156
B-CCSDT	E_{tot}	-55.70287	-55.53188	-55.42556
	E_{corr}	-0.17753	-0.21003	-0.23152
	$2S + 1$	2.0000	2.0000	2.0074

[12] showed that the UHF-CCSDT energy was about $1.5 \text{ m}E_h$ above the FCI energy, so the B-CCSDT energy is apparently in poorer agreement with FCI.

Four Difficult 12-Electron Systems: The Lowest Singlet States of BeO, C₂, CN⁺, and BN

We now consider four closed-shell, isoelectronic systems which have significant contributions from excited determinants at their equilibrium geometries. BeO has quite large T_1 amplitudes, but small T_2 amplitudes. C₂ has smaller T_1 amplitudes, but large T_2 amplitudes, while CN⁺ and BN have large T_1 and large T_2 amplitudes. In Table IV we show \mathcal{T}_1 along with the largest T_1 and T_2 amplitudes. We note that these data illustrate our earlier statement about \mathcal{T}_1 not being an adequate measure of multi-reference character. Thus, from the largest amplitudes, it seems unreasonable to say that BeO has more multi-reference character than C₂, even though \mathcal{T}_1 is larger for BeO than for C₂. \mathcal{T}_1 completely follows the size of the largest t_i^a . When an important double excitation is present, we expect potential errors in single reference CC methods due to an inadequate description of the multi-reference character.

We have performed HF-CC and B-CC calculations on these systems with a DZP basis set at geometries close to observed equilibrium geometries. The results are shown in Table V. In all cases, Brueckner orbitals increase the CCSD energy by 2–3 $\text{m}E_h$. The behavior of CCSD(T) is mixed, but correlates with the value of \mathcal{T}_1 . Thus, for the systems with smaller \mathcal{T}_1 , BeO and C₂, the Hartree–Fock and Brueckner results are very close, while for CN⁺ and BN there is a significant difference. For CCSDT, the differences between the Brueckner and Hartree–Fock references are somewhat smaller than for CCSD.

a¹ Σ⁺ BN: Molecular Properties

The lowest singlet state of the BN molecule provides a considerable challenge to theoretical calculations since, even at equilibrium, there are significant contributions from singly and doubly excited determinants. A recent study by Martin et al. [38] compared the results of a variety of CC and multi-reference CI methods. It was

TABLE IV. Comparison of largest T_1 and T_2 amplitudes and \mathcal{T}_1 for BeO, C₂, CN⁺, BN. DZP basis set, geometries close to experiment (see text).

Method	Property	BeO	C ₂	CN ⁺	BN
CCSD	Largest t_i^a	−0.124	0.085	−0.179	0.211
	Largest t_{ij}^{ab}	−0.048	−0.309	−0.309	−0.243
	\mathcal{T}_1	0.042	0.031	0.059	0.065
CCSDT	Largest t_i^a	−0.139	0.085	0.187	0.230
	Largest t_{ij}^{ab}	−0.056	−0.386	−0.403	−0.341
	\mathcal{T}_1	0.045	0.031	0.062	0.071

TABLE V. Comparison of HF- and B-CC energies of the lowest singlet states of BeO, C₂, CN⁺, BN. DZP basis set, atomic units, and geometries close to experiment (see text).

Method	Property	BeO	C ₂	CN ⁺	BN
HF-CCSD	E_{tot}	-89.66581	-75.72907	-91.99553	-79.20780
	E_{corr}	-0.24459	-0.33994	-0.37145	-0.31561
	T_1	0.042	0.031	0.059	0.065
B-CCSD	E_{tot}	-89.66273	-75.72602	-91.99274	-79.20469
	E_{corr}	-0.25202	-0.35646	-0.40461	-0.34366
HF-CCSD(T)	E_{tot}	-89.67455	-75.75555	-92.02868	-79.23585
	E_{corr}	-0.25333	-0.36642	-0.39634	-0.33377
	T_1	0.042	0.031	0.059	0.065
B-CCSD(T)	E_{tot}	-89.67506	-75.75581	-92.02604	-79.23319
	E_{corr}	-0.26435	-0.38625	-0.42964	-0.36228
HF-CCSDT	E_{tot}	-89.67591	-75.75454	-92.02447	-79.23339
	E_{corr}	-0.25470	-0.36541	-0.40039	-0.34120
	T_1	0.045	0.031	0.062	0.071
B-CCSDT	E_{tot}	-89.67464	-75.75391	-92.02354	-79.23203
	E_{corr}	-0.26532	-0.38325	-0.42647	-0.36226

suggested that for this system the considerable multi-reference character made a noniterative treatment of triple excitations, as in CCSD(T), insufficiently accurate. In particular, significant differences between CCSD(T) and CCSDT results were obtained, and CCSD(T) gave a smaller bond length and a larger frequency than CCSD, which is most unusual.

We have now performed a series of CCSD, CCSD(T), and CCSDT calculations of equilibrium properties using Brueckner and RHF reference determinants and a DZP basis set. The results are shown in Table VI. The Hartree-Fock results are in line with those of Martin et al. The CCSD and CCSDT r_e and ω_e are similar, while the CCSD(T) r_e is smaller and the ω_e is larger. When one uses instead Brueckner orbitals, several changes take place. The CCSD bond length decreases by about 0.005 Å, with

TABLE VI. Calculated properties of $a^1 \Sigma^+$ BN from HF- and B-CC calculations. DZP basis set.

Method	Energy/ E_h	$r_e/\text{\AA}$	ω_e/cm^{-1}	μ/D	T_1
HF-CCSD	-79.20819	1.2983	1650	1.922	0.059
HF-CCSD(T)	-79.23595	1.2892	1686	1.625	0.062
HF-CCSDT	-79.23389	1.3006	1656	1.702	0.063
B-CCSD	-79.20492	1.2937	1712	1.873	
B-CCSD(T)	-79.23384	1.3034	1655	1.584	
B-CCSDT	-79.23252	1.3001	1668	1.662	

a corresponding increase in ω_e . The CCSD(T) changes are in the opposite direction, with a particularly large bond length change. For CCSDT, the changes are somewhat smaller, but again there is a significant bond length decrease. With Brueckner orbitals, the CCSD(T) results are much closer to the CCSDT results than is the case with Hartree-Fock orbitals. Judging by a comparison with MRCI data [38], CCSDT seems to provide a reasonable description of this system, although it is likely that connected quadruple excitations [39] will be necessary for really accurate work, particularly for calculating the energy difference between this singlet state and the ground state [38].

It follows that, for this system, one can further improve the performance of CCSD(T) by using Brueckner orbitals, which is indicative of important higher order T_1 corrections.

Conclusions

The present calculations are the first comparisons between HF- and B-CCSDT results. The differences between the two sets of results are of little chemical significance. For the bond stretching examples considered, the use of Brueckner orbitals does not lead to energetic improvements, although the spin contamination of the UHF results is reduced slightly. The B-CCSDT energies of BeO, C₂, CN⁺, and BN are all no more than about 1 kcal mol⁻¹ higher than the HF-CCSDT energies. For the BN properties, the differences between the HF-CCSDT and B-CCSDT results may be significant. At present, it is not clear which results are better, and the answer will have to await larger basis set studies. On the whole, our recommendation is that if one can afford a full CCSDT calculation, little is to be gained by obtaining Brueckner orbitals. A possible exception, which needs to be studied further, would be symmetry breaking problems, for which there are some clear advantages to using a set of orbitals which are not symmetry broken [9].

Perhaps the most interesting aspect of this study is the observation of how Brueckner orbitals improved the CCSD(T) results for BN. If this is a general pattern of behavior, it will be of some value, and this should be further investigated.

Acknowledgments

This work has been supported by the United States Air Force Office of Scientific Research under Grant No. AFOSR-F49620-93-1-0127. The Ohio Supercomputer Center is thanked for provision of computer facilities for development of the ACES II program system.

Bibliography

- [1] K. A. Brueckner, Phys. Rev. **96**, 508 (1954).
- [2] R. K. Nesbet, Phys. Rev. **109**, 1632 (1958); Adv. Chem. Phys. **9**, 321 (1969).
- [3] P. O. Lowdin, J. Math. Phys. **3**, 1171 (1962); Adv. Chem. Phys. **14**, 283 (1969).
- [4] W. Kutzelnigg and V. H. Smith, J. Chem. Phys. **41**, 896 (1964); S. Larsson and V. H. Smith, Phys. Rev. **178**, 137 (1969).
- [5] J. Paldus, J. Cizek, and B. A. Keating, Phys. Rev. **A8**, 640 (1973).

- [6] R. A. Chiles and C. E. Dykstra, *J. Chem. Phys.* **74**, 4544 (1981).
- [7] L. Stolarczyk and H. J. Monkhorst, *Int. J. Quantum Chem. Symp.* **18**, 267 (1984).
- [8] N. C. Handy, J. A. Pople, M. Head-Gordon, K. Raghavachari, and G. W. Trucks, *Chem. Phys. Lett.* **164**, 185 (1989).
- [9] J. F. Stanton, J. Gauss, and R. J. Bartlett, *J. Chem. Phys.* **97**, 5554 (1992).
- [10] M. Urban, J. Noga, S. J. Cole, and R. J. Bartlett, *J. Chem. Phys.* **83**, 4041 (1985).
- [11] K. Raghavachari, G. W. Trucks, J. A. Pople, and M. Head-Gordon, *Chem. Phys. Lett.* **157**, 479 (1989).
- [12] J. D. Watts, J. Gauss, and R. J. Bartlett, *J. Chem. Phys.* **98**, 8718 (1993).
- [13] K. Raghavachari, J. A. Pople, E. S. Replogle, and M. Head-Gordon, *J. Phys. Chem.* **94**, 5579 (1990).
- [14] R. J. Bartlett, J. D. Watts, S. A. Kucharski, and J. Noga, *Chem. Phys. Lett.* **165**, 513 (1990).
- [15] J. Noga and R. J. Bartlett, *J. Chem. Phys.* **86**, 7041 (1987).
- [16] G. E. Scuseria and H. F. Schaefer III, *Chem. Phys. Lett.* **152**, 382 (1988).
- [17] J. D. Watts and R. J. Bartlett, *J. Chem. Phys.* **93**, 6104 (1990).
- [18] J. D. Watts and R. J. Bartlett, *Int. J. Quantum Chem. Symp.* **27**, 51 (1993).
- [19] K. Raghavachari, J. A. Pople, E. S. Replogle, M. Head-Gordon, and N. C. Handy, *Chem. Phys. Lett.* **167**, 115 (1990).
- [20] R. Kobayashi, N. C. Handy, R. D. Amos, G. W. Trucks, M. J. Frisch, and J. A. Pople, *J. Chem. Phys.* **95**, 6723 (1991).
- [21] R. Kobayashi, R. D. Amos, and N. C. Handy, *Chem. Phys. Lett.* **184**, 195 (1991).
- [22] C. Hampel, K. A. Peterson, and H.-J. Werner, *Chem. Phys. Lett.* **190**, 1 (1992).
- [23] T. J. Lee, R. Kobayashi, N. C. Handy, and R. D. Amos, *J. Chem. Phys.* **96**, 8931 (1992).
- [24] R. Kobayashi, H. Koch, P. Jørgensen, and T. J. Lee, *Chem. Phys. Lett.* **211**, 94 (1993).
- [25] ACES II is a quantum chemical program package especially designed for CC and MBPT energy and gradient calculations. Elements of this package are: the SCF, integral transformation, correlation energy, and gradient programs written by J. F. Stanton, J. Gauss, J. D. Watts, W. J. Lauderdale, and R. J. Bartlett; the VMOL integral and VPROPS property integral programs written by P. R. Taylor and J. Almlöf; a modified version of the integral derivative program ABACUS written by T. Helgaker, H. J. Aa. Jensen, P. Jørgensen, J. Olsen, and P. R. Taylor.
- [26] J. F. Stanton, J. Gauss, J. D. Watts, W. J. Lauderdale, and R. J. Bartlett, *Int. J. Quantum Chem. Symp.* **26**, 879 (1992), and references therein.
- [27] C. W. Bauschlicher, Jr. and P. R. Taylor, *J. Chem. Phys.* **85**, 2779 (1986).
- [28] C. W. Bauschlicher, Jr., S. R. Langhoff, P. R. Taylor, N. C. Handy, and P. J. Knowles, *J. Chem. Phys.* **85**, 1469 (1986).
- [29] C. W. Bauschlicher, Jr. and P. R. Taylor, *J. Chem. Phys.* **86**, 1420 (1987).
- [30] T. H. Dunning, Jr., *J. Chem. Phys.* **53**, 2823 (1970).
- [31] L. T. Redmon, G. D. Purvis III, and R. J. Bartlett, *J. Am. Chem. Soc.* **101**, 2856 (1979).
- [32] T. H. Dunning, Jr. and P. J. Hay, in *Methods of Electronic Structure Theory*, H. F. Schaefer III, Ed. (Plenum, New York, 1977).
- [33] K. P. Huber and G. Herzberg, *Constants of Diatomic Molecules* (Van Nostrand Reinhold, New York, 1979).
- [34] G. E. Scuseria, T. P. Hamilton, and H. F. Schaefer III, *J. Chem. Phys.* **92**, 568 (1990).
- [35] T. J. Lee and P. R. Taylor, *Int. J. Quantum Chem. Symp.* **23**, 199 (1989).
- [36] R. J. Bartlett, *J. Phys. Chem.* **93**, 1697 (1989), and references therein.
- [37] S. J. Cole and R. J. Bartlett, *J. Chem. Phys.* **86**, 873 (1987).
- [38] J. M. L. Martin, T. J. Lee, G. E. Scuseria, and P. R. Taylor, *J. Chem. Phys.* **97**, 6549 (1992).
- [39] S. A. Kacharski and R. J. Bartlett, *J. Chem. Phys.* **97**, 4282 (1992).

Relativistic Coupled Cluster Theory Based on the No-Pair Dirac–Coulomb–Breit Hamiltonian: Relativistic Pair Correlation Energies of the Xe Atom

EPHRAIM ELIAV* and UZI KALDOR

School of Chemistry, Tel Aviv University, 69978 Tel Aviv, Israel

YASUYUKI ISHIKAWA

Department of Chemistry and the Chemical Physics Program, University of Puerto Rico, P.O. Box 23346, San Juan, Puerto Rico 00931-3346

Abstract

Relativistic pair correlation energies of Xe were computed by employing a recently developed relativistic coupled cluster theory based on the no-pair Dirac–Coulomb–Breit Hamiltonian. The matrix Dirac–Fock–Breit SCF and relativistic coupled cluster calculations were performed by means of expansion in basis sets of well-tempered Gaussian spinors. A detailed study of the pair correlation energies in Xe is performed, in order to investigate the effects of the low-frequency Breit interaction on the correlation energies of Xe. Nonadditivity of correlation and relativistic (particularly Breit) effects is discussed. © 1994 John Wiley & Sons, Inc.

Introduction

The majority of contemporary *ab initio* calculations have been performed on light atoms and molecules containing them, with which a large part of chemical research is concerned. However, important physical and chemical processes involve heavy atoms, where relativistic effects cannot be ignored. Because relativistic and correlation effects play an essential role in the electronic structure of heavy-atom systems, relativistic many-body theories have become the subject of active research interest in recent years [1]. Since relativistic effects can be large and may not always be treated as a small perturbation, it is often necessary to forfeit the Schrödinger equation in favor of the Dirac equation in order to describe the electronic structure of heavy-atom systems.

In the last few years, relativistic many-body perturbation theory (MBPT) [2–5] and relativistic coupled cluster (CC) theory [6–9], which account for both relativistic and electron correlation effects, were developed by several groups using basis sets of local and global functions. The relativistic MBPT and CC algorithms, based on an expansion in analytic basis functions [2–9], have the advantage of providing a

* Formerly Ilyabaev.

compact and discrete representation of the complete Dirac spectrum, and greatly facilitate the evaluation of the many-body diagrams using finite summations [3]. Furthermore, by invoking the finite basis set expansion in terms of Gaussian spinors (G-spinors), these relativistic many-body theories can be applied to molecular electronic structure problems in a straightforward way.

In a previous study [10], a relativistic MBPT based on the no-pair Dirac-Coulomb (DC) Hamiltonian was used to compute the pair Coulomb correlation energies of Xe and their nonadditive contributions [10] due to the interference between the relativistic and Coulomb correlation effects. The valence, core-valence, and core contributions of the relativistic pair correlations were analyzed in detail. The results strongly indicated that the relativistic and Coulomb correlation effects are additive in the valence shell of Xe. However, in a subsequent study on relativistic MBPT based on the Dirac-Coulomb-Breit (DCB) Hamiltonian [4], the low-frequency Breit interaction was found to significantly affect the electron correlation in He and He-like ions. In that study, the instantaneous Coulomb and low-frequency Breit interactions were treated using a unified formalism in both the construction of the Dirac-Fock-Breit (DFB) self-consistent field (SCF) potential and in the evaluation of MBPT diagrams. The results on the He-like ions indicate that relativity and electron correlation become strongly nonadditive when the Breit interaction is included as an integral part of the two-electron interaction.

Recently, we have developed a relativistic version of the multireference valence-universal Fock-space CC theory based on the no-pair DCB Hamiltonian, and implemented it by employing analytic basis expansion in terms of G-spinors [11-13]. The relativistic coupled cluster algorithm also treats the instantaneous Coulomb and the low-frequency Breit interactions as an integral part of the two-electron interaction in both the SCF and relativistic CC procedures. The method was also applied to many-electron systems, and yielded accurate ionization potentials, excitation energies, and fine-structure splittings for Au [11], for highly ionized ions with 2-5 electrons [12], and for alkali metal atoms [13]. In the present study we employ this relativistic coupled cluster theory based on the no-pair DCB Hamiltonian [11] to compute the pair correlation energies of Xe. The main objective of the present study is to perform a detailed analysis of the pair correlation energies in order to investigate the effects of the low-frequency Breit interaction on the valence correlation energies of Xe. The pair energies are partitioned into core, core-valence, and valence shell contributions, to investigate where the correlation energy and nonadditive contributions originate. The Xe atom has 54 electrons, and is to our knowledge the heaviest atom to which all-electron CC calculations with analytic basis functions have been applied. The next section outlines our relativistic CC method based on the no-pair DCB Hamiltonian. The analysis of the relativistic pair correlation energies in Xe is presented in the third section.

Method

The relativistic many-body Hamiltonian cannot be expressed in closed potential form. An approximate relativistic Hamiltonian most commonly used is the time-honored "no-pair" DC Hamiltonian [14,15]

$$H_+ = \sum_i h_D(i) + \mathcal{L}_+ \sum_{i < j} V_{ij} \mathcal{L}_+, \quad (1)$$

where (in a.u.) h_D is the one-electron Dirac Hamiltonian with the nuclear potential V_{nuc}

$$h_D = c\vec{\alpha} \cdot \vec{p} + \beta c^2 + V_{\text{nuc}}, \quad (2)$$

and the instantaneous Coulomb interactions between electrons are

$$V_{ij} = r_{ij}^{-1}. \quad (3)$$

$\vec{\alpha}$ and β are the Dirac matrices. The operator \mathcal{L}_+ is defined as the product $L_+(1) \cdot L_+(2) \cdots L_+(n)$, with $L_+(i)$ the projection operator onto the space spanned by the positive-energy eigenfunctions of the Dirac-Fock-Coulomb (DFC) operator [16]. In this form, the no-pair Hamiltonian is restricted to contributions from the positive-energy branch of the DFC spectrum. The no-pair DC Hamiltonian, however, is deficient in that it is both noncovariant and not accurate enough for high-precision calculation of fine structure separations and binding energies of the inner-shell electrons. Adding the low-frequency Breit interaction,

$$B_{ij} = -\frac{1}{2r_{ij}} [\vec{\alpha}_i \cdot \vec{\alpha}_j + (\vec{\alpha}_i \cdot \vec{r}_{ij})(\vec{\alpha}_j \cdot \vec{r}_{ij})/r_{ij}^2], \quad (4)$$

to the instantaneous Coulomb operator introduces the leading effects of the transverse photon exchange and remedies the lack of covariance of the no-pair DC Hamiltonian [14,15]. Inclusion of the Breit interaction results in a Hamiltonian which contains all effects through second order in α , the fine-structure constant [15]. The no-pair DCB Hamiltonian [15]

$$H_+ = \sum_i h_D(i) + \mathcal{L}_+ \sum_{i > j} (r_{ij}^{-1} + B_{ij}) \mathcal{L}_+ \quad (5)$$

provides a satisfactory starting point for calculations on many-electron systems in the sense that it treats the electrons relativistically, treats the most important part of the electron-electron interaction nonperturbatively, and puts the Coulomb and Breit interactions on the same footing in DFB SCF and relativistic CC calculations. In order to study the electron correlation induced by the Breit interaction, the instantaneous Coulomb and frequency-independent Breit interactions are treated as an integral part of the two-electron interaction in the DFB SCF and relativistic CC calculations [11].

In q -number theory the Dirac-Coulomb-Breit Hamiltonian H_+ is rewritten in terms of normal-ordered products of the spinor operators, $\{r^+s\}$ and $\{r^+s^+ut\}$ [14,15,4],

$$H = H_+ - \langle 0|H_+|0 \rangle = \sum_{rs} f_{rs} \{r^+s\} + \frac{1}{4} \sum_{rstu} \langle rs||tu \rangle \{r^+s^+ut\}, \quad (6)$$

where

$$\langle rs||tu \rangle = \langle rs|tu \rangle - \langle rs|ut \rangle \quad (7)$$

and

$$\langle rs|tu\rangle = \int dx_1 dx_2 \Psi_r^*(x_1) \Psi_s^*(x_2) (r_{12}^{-1} + B_{12}) \Psi_t(x_1) \Psi_u(x_2). \quad (8)$$

Here, f_{rs} and $\langle rs|tu\rangle$ are, respectively, elements of the one-electron Dirac–Fock and antisymmetrized two-electron Coulomb–Breit interaction matrices over Dirac four-component spinors. The effect of the projection operators \mathcal{L}_+ is now taken over by normal ordering, denoted by the curly braces in the equations above, which requires annihilation operators to be moved to the right of creation operators as if all anticommutation relations vanish. The Fermi level is set at the top of the highest occupied positive-energy state, and the negative-energy states are ignored.

By adopting the no-pair approximation, a natural and straightforward extension of the nonrelativistic CC theory emerges. The correlated wave function is obtained from the uncorrelated Ψ_0 by an exponential wave operator,

$$\Psi = \Omega \Psi_0, \quad \Omega = \exp\{S\}, \quad (9)$$

where S is the normal-ordered excitation operator [17]

$$S = S_1 + S_2 + \cdots = \sum_{rs} s_s^r \{r^+ s\} + \frac{1}{4} \sum_{rstu} s_{tu}^{rs} \{r^+ s^+ t u\} + \cdots, \quad (10)$$

with excitation amplitudes s_s^r , s_{tu}^{rs} , etc. The expansion of S is truncated here after S_2 , to yield the CCSD (coupled cluster with single and double excitations) scheme.

Once the iterative coupled cluster equations converge and give the excitation amplitudes, the correlation energy is obtained by

$$E = \sum_{rs} s_s^r f_{rs} + \frac{1}{4} \sum_{rstu} s_{tu}^{rs} \langle rs||tu\rangle. \quad (11)$$

Only the second sum appears if HF (or DF) orbitals are used, which is the case in the present work. The correlation energy of the ij pair is obtained by limiting the hole indices tu in that sum to ij , and summing over all particle indices rs .

Detailed account of the matrix DFB SCF formalism and its applications to many-electron systems has been given in previous publications [4] and is not repeated here. The speed of light was taken to be 137.037 a.u. throughout this work. The nonrelativistic limit was simulated by setting the speed of light to $c = 10^4$. Another set of SCF calculations was done without the Breit term. This is the conventional DFC SCF scheme based on the no-pair DC Hamiltonian [2–4].

A basis set of well-tempered Gaussian-type functions reported by Huzinaga and Klobukowski [18] was used in contracted and uncontracted form [19]. The nonrelativistic, DFC and DFB SCF calculations were done with the uncontracted (21s19p13d) basis set. In a previous study, the (21s19p13d) primitives set was contracted to generate a [14s13p10d] contracted set for MBPT calculations on Xe [19]. This was done by grouping the functions of highest exponents (see Table II of Ref. [19]). The relativistic correlation energy of the contracted set reproduces over 99% of that of the uncontracted basis [19]. We have employed the same set

of contracted functions in the present CC calculations, and added uncontracted Gaussians up to $L_{\max} = 5$ to yield a $[14s13p10d7f6g5h]$ basis set. The exponents for the high- l functions were taken from the same well-tempered series [18]. The highest exponent for the f and g sectors was 110.24499, and for the h sector—52.022218. The finite-nucleus model discussed in Ref. [4] was employed for V_{nuc} of Eq. (2). The atomic mass used in the calculations was 131.30 amu. Calculations were done on the IBM RS6000/320 and 360 workstations at Tel Aviv University.

Results and Discussion

Table I displays the SCF and correlation (CCSD) energies computed with the nonrelativistic, DFC and DFB wave functions. The DFC SCF energy obtained with the uncontracted G-spinor basis set is higher by 0.017 a.u. than the DFC energy of -7446.9010 a.u. computed by numerical finite difference DF [20]. We have computed the nonrelativistic limit E_{HF} by taking $c = 10^4$ in the DFC SCF calculations. This gave -7232.0717 a.u. The relativistic energy lowering, which is the difference between the total DFC SCF energy E_{DFC} and the nonrelativistic limit E_{HF} , is 214.83 a.u.

The inclusion of the Breit term in the two-electron interaction raises the DFB SCF energy above the DFC SCF energy. The variational Breit energy, computed as the difference $E_{\text{DFB}} - E_{\text{DFC}}$, is the level shift in the total SCF energy due to the inclusion of the Breit interaction in the SCF process. This is 5.77 a.u. for Xe. The energy shift is primarily due to a large upward shift in the inner-shell spinor energies [4].

The nonrelativistic (NR), DC and DCB correlation energies are those computed by applying the CCSD method to the nonrelativistic, DC and DCB Hamiltonians, respectively. The difference between the relativistic (DC and DCB) correlation energies and the NR correlation energy is the relativistic correction to the correlation energy. This correction is given in the last column of Table I. Comparing the results of the relativistic calculations yielded by the DC and DCB Hamiltonians with the nonrelativistic results, the DC Hamiltonian is seen to account for only a small fraction of the relativistic correction to the correlation energy, 0.027 a.u. This non-additive contribution is due to the interference between relativity and electron

TABLE I. SCF and correlation energies of Xe (in a.u.). The SCF energies are given for the uncontracted $(21s19p13d)$ and contracted $[14s13p10d]$ bases, the CCSD correlation energies for the contracted basis augmented by $7f6g5h$.

	SCF		Correlation	Nonadditive energy ^a
	Uncontracted	Contracted		
NR	-7232.0717	-7232.0467	-2.5926	
DC	-7446.8836	-7443.3180	-2.6199	0.027
DCB	-7441.1138	-7437.5270	-2.6956	0.103

^a Relativistic correction to correlation energy.

TABLE II. Pair correlation energies of Xe (in millihartree). [14s13p10d7f6g5h] basis set.

Pair	Pair energy		
	NR	DC	DCB
Valence			
5p5p	-71.39	-71.10	-71.08
5p5s	-26.29	-27.25	-27.23
5s5s	-6.02	-6.05	-6.05
Core-Valence			
5p4d	-114.20	-117.53	-117.46
5p3d	-11.06	-11.63	-11.64
5p4p	-17.60	-17.95	-17.97
5p3p	-3.42	-3.45	-3.48
5p2p	-1.16	-1.22	-1.29
5p4s	-3.37	-3.22	-3.22
5p3s	-0.84	-0.79	-0.79
5p2s	-0.28	-0.28	-0.29
5p1s	-0.11	-0.11	-0.14
5s4d	-39.46	-44.62	-44.61
5s3d	-4.80	-5.68	-5.68
5s4p	-9.93	-10.80	-10.82
5s3p	-1.55	-1.75	-1.76
5s2p	-0.42	-0.50	-0.50
5s4s	-1.63	-1.69	-1.70
5s3s	-0.34	-0.35	-0.36
5s2s	-0.10	-0.11	-0.11
5s1s	-0.03	-0.04	-0.06
Core			
4d4d	-369.14	-367.98	-368.58
4d3d	-156.79	-155.67	-157.17
4d4p	-184.05	-185.92	-186.17
4d3p	-48.56	-46.10	-46.46
4d2p	-16.89	-16.47	-17.19
4d4s	-46.87	-46.73	-46.82
4d3s	-12.02	-10.72	-10.78
4d2s	-4.14	-3.80	-3.98
4d1s	-0.19	-0.16	-0.19
3d3d	-367.74	-368.86	-375.35
3d4p	-73.50	-77.78	-77.83
3d3p	-197.60	-197.65	-200.61
3d2p	-121.33	-118.59	-123.27
3d4s	-22.81	-26.24	-26.23
3d3s	-49.23	-50.24	-50.84
3d2s	-30.97	-28.20	-29.37
3d1s	-1.23	-1.06	-1.23
4p4p	-53.24	-53.84	-53.96
4p3p	-30.69	-31.21	-31.53
4p2p	-11.48	-12.09	-12.77

(Continued)

TABLE II. (Continued)

Pair	Pair energy		
	NR	DC	DCB
Core			
4p4s	-26.40	-27.30	-27.36
4p3s	-7.77	-7.42	-7.46
4p2s	-2.74	-2.79	-2.90
4p1s	-1.09	-1.14	-1.43
3p3p	-55.53	-56.11	-57.31
3p2p	-55.66	-58.15	-62.03
3p4s	-9.35	-10.37	-10.43
3p3s	-27.21	-27.39	-27.83
3p2s	-12.95	-13.14	-13.75
3p1s	-5.71	-5.96	-7.46
2p2p	-131.34	-135.07	-146.66
2p4s	-2.99	-3.46	-3.50
2p3s	-11.53	-13.06	-13.41
2p2s	-44.12	-45.94	-49.63
2p1s	-31.09	-31.67	-38.54
4s4s	-4.64	-4.77	-4.79
4s3s	-2.47	-2.49	-2.53
4s2s	-0.73	-0.78	-0.84
4s1s	-0.24	-0.28	-0.42
3s3s	-4.57	-4.59	-4.71
3s2s	-3.28	-3.46	-3.80
3s1s	-1.11	-1.30	-2.00
2s2s	-7.45	-7.73	-8.77
2s1s	-5.31	-6.08	-9.75
1s1s	-24.89	-24.06	-41.69

correlation, which arises from the use of relativistic single-particle states but the same two-body interaction, i.e., the instantaneous Coulomb interaction. The bulk of the relativistic correction to the correlation energy comes from the inclusion of the Breit interaction in the two-body interaction, i.e., from the use of the DCB Hamiltonian. This relativistic correction is 0.103 a.u., which represents 4% of the total correlation energy, -2.6956 a.u.

In recent years, quasi-relativistic effective core potential calculations have been performed on diatomic Xe₂ and XeCl [21,22]. In these calculations, the 5s and 5p orbitals of Xe were taken to be the valence orbitals. All the remaining orbitals were treated as core, and were replaced by a set of effective core potentials for valence-only calculations. The present study correlates *all* electrons. If the 5s and 5p are called valence spinors and the rest are core spinors, the total of 66 pair correlation energies for ground-state Xe may be partitioned into valence, core-valence, and core contributions. Table II gives the pair correlation energies partitioned in this manner. The NR, DC, and DCB pair energies were computed from the corresponding wave functions. The results indicate clearly that the largest cor-

relation contributions, both relativistic and nonrelativistic, come from the $4d4d$ and $3d3d$ pairs, followed by other pairs which involve $4d$ and $3d$ spinors (e.g., $4d4p$, $4d3d$, $3d4p$, $3d3p$). This may easily be understood, because the $4d$ and $3d$ shells each include ten electrons, and the dynamical correlation among these electrons is not accounted for in the SCF step. The relativistic corrections to the pair correlation energies, i.e., the difference between the relativistic and the nonrelativistic pair correlation energies, are primarily associated with the inner-shell pairs.

The valence, core-valence, and core contributions of the NR, DC, and DCB pair correlation energies, as well as the nonadditive relativistic corrections, are tabulated in Table III. The valence and core-valence contributions of the DCB pair energies are 4% and 8%, respectively, of the overall DCB correlation energy of Xe, -2.6956 a.u. The valence contribution of the nonadditive relativistic correction, 0.7 millihartree, accounts for only 0.7% of the overall nonadditive energy, 0.103 a.u.; it is also 0.7% of the valence pair correlation energy, -0.1044 a.u. This shows that relativity and correlation effects are additive in the valence shell of Xe. The nonadditive contribution comes primarily from the pair correlations in the inner-shell

TABLE III. Core, core-valence, and valence contributions of pair and nonadditive energies (in a.u.). $[14s13p10d7f6g5h]$ basis set.

	Pair energy	Nonadditive energy ^a
Core		
NR	-2.2786	
DC	-2.2938	0.0152
DCB	-2.3694	0.0908
Core-Valence		
NR	-0.2103	
DC	-0.2217	0.0114
DCB	-0.2218	0.0115
Valence		
NR	-0.1037	
DC	-0.1044	0.0007
DCB	-0.1044	0.0007
Total		
NR	-2.5926	
DC	-2.6199	0.027
DCB	-2.6956	0.103

^a Relativistic correction to pair correlation energy.

core. The core contribution of the nonadditive relativistic correction accounts for 88% of the total nonadditive energy. Although the relativistic correction of the valence pair correlation is negligible, the inclusion of the Breit interaction may be important in accounting for fine-structure splittings of open-shell systems [11–13].

Table II shows that the nonadditive relativistic corrections in a number of DC pair energies in the core shell are of comparable magnitude but with opposite sign. Because of the large cancellation of the nonadditive relativistic corrections in the core shell, the overall nonadditive energy of the DC correlation energy remains small. Because of the absence of such cancellation, the overall nonadditive relativistic correction of the DCB correlation energy is an order of magnitude larger than that of the DC correlation energy.

Acknowledgments

This work was supported by the Israel Science Foundation and by the U.S.-Israel Binational Science Foundation. Y. Ishikawa has been supported by the National Science Foundation through Grant No. PHY-9008627. All grants are gratefully acknowledged.

Bibliography

- [1] See, e.g., *The Effects of Relativity in Atoms, Molecules, and the Solid State*, S. Wilson, I. P. Grant, and B. L. Gyorffy, Eds. (Plenum Press, New York, 1991).
- [2] W. R. Johnson and J. Sapirstein, *Phys. Rev. Lett.* **57**, 1126 (1986); W. R. Johnson, S. A. Blundell, and J. Sapirstein, *Phys. Rev. A* **37**, 307 (1988); **41**, 1689 (1990).
- [3] H. M. Quiney, I. P. Grant, and S. Wilson, *Phys. Scripta* **36**, 460 (1987); H. M. Quiney, I. P. Grant, and S. Wilson, in *Lecture notes in Chemistry*, Vol. 52, *Many-Body Methods in Quantum Chemistry*, U. Kaldor, Ed. (Springer, Berlin, 1989); *J. Phys. B* **23**, L271 (1990).
- [4] Y. Ishikawa, *Phys. Rev. A* **42**, 1142 (1990); Y. Ishikawa and H. M. Quiney, *Phys. Rev. A* **47**, 1732 (1993).
- [5] A. Rutkowski, *J. Phys. B* **19**, 3443 (1986); A. Rutkowski and W. H. E. Schwarz, *Theor. Chim. Acta* **76**, 391 (1990).
- [6] S. A. Blundell, W. R. Johnson, Z. W. Liu, and J. Sapirstein, *Phys. Rev. A* **39**, 3768 (1989); S. A. Blundell, W. R. Johnson, and J. Sapirstein, *Phys. Rev. A* **43**, 3407 (1991).
- [7] E. Ilyabaev and U. Kaldor, *Chem. Phys. Lett.* **194**, 95 (1992); E. Ilyabaev and U. Kaldor, *J. Chem. Phys.* **97**, 8455 (1992); E. Ilyabaev and U. Kaldor, *Phys. Rev. A* **47**, 137 (1993).
- [8] H. Sekino and R. J. Bartlett, *Int. J. Quantum Chem., Quantum Chem., Symp.* **24**, 241 (1990).
- [9] E. Lindroth and S. Salomonson, *Phys. Rev. A* **41**, 4659 (1990); E. Lindroth and J. Hvarfner, *Phys. Rev. A* **45**, 2771 (1992); E. Lindroth and A. Ynnerman, *Phys. Rev. A* **47**, 961 (1993).
- [10] Y. Ishikawa, *Int. J. Quantum Chem., Quantum Chem. Symp.* **26**, 127 (1992).
- [11] E. Eliav, U. Kaldor, and Y. Ishikawa, *Phys. Rev. A* **49**, 1724 (1994).
- [12] E. Eliav, U. Kaldor, and Y. Ishikawa, *Chem. Phys. Lett.* **222**, 82 (1994).
- [13] E. Eliav, U. Kaldor, and Y. Ishikawa, *Phys. Rev. A* (in press).
- [14] J. Sucher, *Phys. Rev. A* **22**, 348 (1980).
- [15] J. Sucher, *Phys. Scripta* **36**, 271 (1987); *J. Phys. B* **21**, L585 (1988).
- [16] M. Mittleman, *Phys. Rev. A* **4**, 893 (1971); *ibid.* **A 5**, 2395 (1972).
- [17] I. Lindgren, *Int. J. Quantum Chem., Quantum Chem. Symp.* **12**, 33 (1978); S. Salomonson, I. Lindgren, and A.-M. Mårtensson, *Phys. Ser.* **21**, 351 (1980); I. Lindgren and J. Morrison, *Atomic Many-Body Theory*, 2nd ed. (Springer-Verlag, Berlin, 1986).

- [18] S. Huzinaga and M. Klobukowski, *J. Mol. Struct. (Theochem)* **167**, 1 (1988); S. Huzinaga, M. Klobukowski, and H. Tatewaki, *Can. J. Chem.* **63**, 1812 (1985).
- [19] Y. Ishikawa, *Can. J. Chem.* **70**, 399 (1992).
- [20] I. P. Grant, B. J. McKenzie, P. H. Norrington, D. F. Mayers, and N. C. Pyper, *Comp. Phys. Commun.* **21**, 207 (1980).
- [21] W. R. Wadt, P. J. Hay, and L. R. Kahn, *J. Chem. Phys.* **68**, 1752 (1978).
- [22] J. Andzelm, S. Huzinaga, M. Klobukowski, and E. Radzio, *Mol. Phys.* **52**, 1495 (1984).

Received April 1, 1994

Topological Analysis of Valence Electron Charge Distributions from Semiempirical and *Ab Initio* Methods

MINHHUY HÔ, HARTMUT SCHMIDER, KENNETH E. EDGECOMBE,
and VEDENE H. SMITH, JR.

Department of Chemistry, Queen's University, Kingston K7L 3N6, Ontario, Canada

Abstract

Topological properties of the charge density $\rho(\vec{r})$ of a series of diatomic molecules, as well as ethane, ethene, and acetylene are calculated at the Hartree-Fock level employing various basis sets, and by the AM1 method. The effect of the core orbitals on the bonding regions in these molecules is examined. The results help to evaluate the utility of AM1 wavefunctions for analyzing the topological properties of the charge density. © 1994 John Wiley & Sons, Inc.

The Theory of Atoms in Molecules

The theory of atoms in molecules, proposed by Bader and co-workers [1], has been proven useful for predicting and explaining many chemical properties. The theory is based on the topology of the electronic charge density $\rho(\vec{r})$, stated in terms of paths traced by its gradient vectors $\vec{\nabla}\rho(\vec{r})$. These vectors point in the directions of the *steepest* ascent of $\rho(\vec{r})$, and the collection of gradient paths associated with a charge distribution is called the *gradient vector field*. The gradient vectors partition the molecule into subsystems bounded by the so-called *zero-flux surfaces* $S(\vec{r})$, which satisfy the equation

$$\vec{\nabla}\rho(\vec{r}) \cdot \vec{n}(\vec{r}) = 0 \quad \forall \vec{r} \in S(\vec{r}), \quad (1)$$

where $\vec{n}(\vec{r})$ denotes the unit vector normal to the surface $S(\vec{r})$.

Smith et al. [2] and Collard and Hall [3] have shown that main characteristics of a molecular structure are exhibited at maxima (peaks), minima (pits), or saddle points (passes or pales) of the charge distribution. At these points, known as the *critical points*, the gradient vector field $\vec{\nabla}\rho(\vec{r})$ vanishes. Critical points may be classified according to their *rank* and *signature*. The rank of a critical point equals the number of nonzero eigenvalues λ_i of the Hessian matrix of $\rho(\vec{r})$ at that point. The signature is the difference between the number of positive and negative eigenvalues. For critical points of rank three, designated as (*rank, signature*), (3, +3) called pits, (3, +1) pales, (3, -1) passes, and (3, -3) peaks. The total number of each type of

critical point for a system of a finite number of nuclei is described topologically by the so-called *Poincaré–Hopf* relation;

$$n - b + r - c = 1, \quad (2)$$

where n , b , r , and c denote the numbers of peaks, passes, pales, and pits, respectively.

If, in a molecule, $\rho(\vec{r})$ shows a saddle point when viewed in every plane containing the internuclear axis, then there is a critical point at which $\rho(\vec{r})$ is a minimum with respect to the direction along the line of the nuclei, and a maximum with respect to *all* directions perpendicular to this line (i.e., a pass). Such a critical point is called a *bond critical point*.

The occurrence of a bond-critical point in the region between two centers is a *necessary* condition for the existence of a bond [4,5]. There are *two and only two* gradient paths that originate at the bond critical point and terminate at the neighboring peaks.¹ The value of $\rho(\vec{r})$ along this path is maximal with respect to two independent perpendicular directions. This is a definition of a *bond path*. The existence of a bond path is a *necessary and sufficient* condition for the existence of a bond.

The bond ellipticity ε shows the extent to which the electronic charge is preferentially accumulated in a given plane [6]. It is calculated as

$$\varepsilon = \lambda_1/\lambda_2 - 1, \quad (3)$$

where λ_1 and λ_2 are the magnitudes of the negative curvatures along the axis perpendicular to the bond path, which indicate the rates of decrease of $\rho(\vec{r})$.

Associated with the charge density is its Laplacian $\nabla^2\rho(\vec{r})$. The Laplacian of a function is a measure of its *lumpiness* [7]. It is the sum of the curvatures in the electron density along any three orthogonal coordinate axes at the point \vec{r} :

$$\nabla^2\rho(\vec{r}) = \frac{\partial^2\rho(\vec{r})}{\partial x^2} + \frac{\partial^2\rho(\vec{r})}{\partial y^2} + \frac{\partial^2\rho(\vec{r})}{\partial z^2}. \quad (4)$$

The sign of $\nabla^2\rho(\vec{r})$ indicates whether the charge density is locally depleted [$\nabla^2\rho(\vec{r}) > 0$] or locally concentrated [$\nabla^2\rho(\vec{r}) < 0$].

The location of the bond critical point, and the value of the Laplacian of the charge density at this point have been shown to be useful in the study of molecular electronic structure [1,8–11].

Valence-Orbital Wavefunctions in AMI

Topological analysis usually uses electron densities calculated from quantum mechanical methods, such as the Hartree-Fock method (SCF). Thus it naturally inherits any problems associated with these methods. One of the commonly known drawbacks of *ab initio* methods is the computational time and memory requirements and hence their cost. As a result, despite their accurate description of one electron

¹ With the exception of structures containing bifurcation or conflict catastrophe points, which vanish upon infinitesimal geometrical changes.

properties, there have been few *ab initio* calculations performed on large molecules. On the other hand, although there are many calculations at the semiempirical level on large systems, hitherto no one has used wavefunctions obtained from semiempirical calculations to study topological properties. We shall consider one such method, namely, the AM1 method [12].

In this method, energy contributions arising from core electrons and their interactions with valence electrons are represented only in a parameterized form. As a consequence, no explicit charge distribution associated with these electrons can be given. The resulting AM1 wavefunctions, therefore, contain only valence orbitals. In Figure 1, the charge density of a substituted oxirane, computed by the AM1 method, clearly exhibits local minima (i.e., pits) at the positions of the nuclei. This replacement of a peak by a pit at the site of every heavy atom also alters the number of passes and pales present in the molecular density. For example, if in a given density one peak becomes a pit, and the number of $(3, -1)$ critical points is to remain constant, the Poincaré–Hopf relation [Eq. (2)] forces the occurrence of two additional pales. If more atoms without core are present, and the condition of constant number of passes is relaxed, the picture becomes rapidly very complex. A detailed topological analysis of such a charge distribution is not warranted.

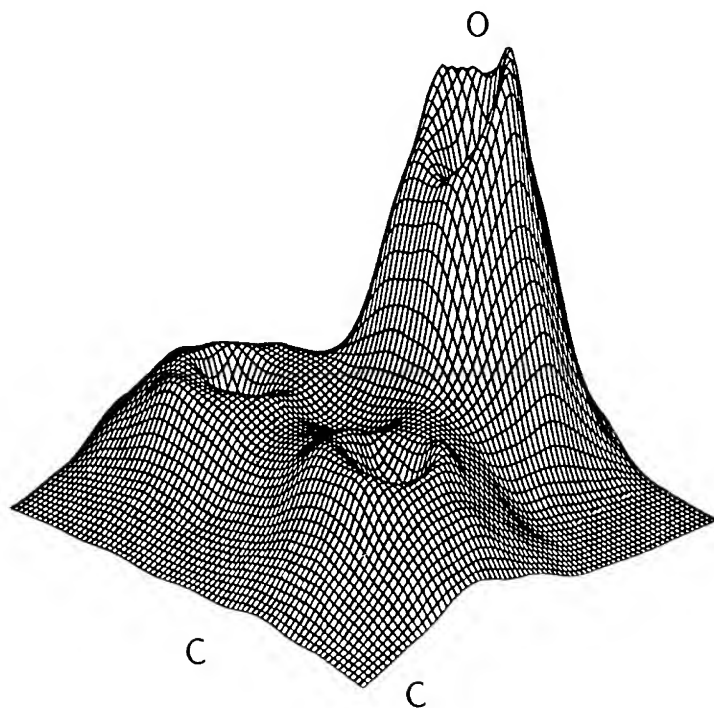


Figure 1. Charge density of a substituted oxirane computed by the AM1 method. Note the local minima at the positions of the nuclei.

An example for such a rather complicated pattern of peaks and pales is given in Figure 1.

This exclusion of the inner-shell orbitals raises the obvious question of how the topological properties of the molecule are affected. To our knowledge, there have been no investigations of this and the related problem of wavefunctions using pseudopotentials. The impact of such a study would nevertheless be important, since it could extend the molecular size for the topological analysis. The average bioorganic molecule is in general out of reach of *ab initio* calculations. Unless one can use AM1 or other semiempirical wavefunctions to study topological properties, the theory of atoms in molecules seems to be of little practical use for organic chemistry at the present time.

In this paper, we study the electronic behavior of a series of diatomic molecules, as well as ethane, ethene, and acetylene at the HF level with the STO-3G, 3-21G, 6-31G basis sets, and employing the AM1 method. The calculations were performed using the GAUSSIAN86 package [13], and the topological analysis was done with the PROAIM program [14]. Both programs were implemented on an IBM 3081 computer.

The wavefunctions of the ground states of the diatomics H_2 , NH, OH, HF, HCl, CH, CN, CO, CF, CS, CCl and the polyatomics C_2H_6 , C_2H_4 , and C_2H_2 were calculated. The bond distances and ground state configurations of the diatomic molecules and the polyatomic molecules shown in Table I were taken from Hubert and Herzberg [15] and Herzberg [16], respectively.

To examine fully the contribution of the inner-shell orbitals to the bonding region and especially to the bond critical point, these orbitals were removed from the *ab initio* wavefunctions (by deleting the MO coefficients of the "core orbitals" from

TABLE I. Input data for the molecules treated in this paper.

	MO ground state configuration	Bond distance (α_0)
1H_2	$^1\Sigma_g^+$	1.4010
$^{14}N^1H$	$^3\Sigma^-$	1.9581
$^{16}O^1H$	$^2\Pi_i$	1.8325
$^1H^{19}F$	$^1\Sigma^+$	1.7325
$^1H^{35}Cl$	$^1\Sigma^+$	2.4086
$^{12}C^1H$	$^2\Pi_r$	2.1163
$^{12}C^{14}N$	$^2\Sigma^+$	2.2144
$^{12}C^{16}O$	$^1\Sigma^+$	2.1322
$^{12}C^{19}F$	$^2\Pi_r$	2.4034
$^{12}C^{32}S$	$^1\Sigma^+$	2.9005
$^{12}C^{35}Cl$	$^2\Pi_{1/2}$	3.1086
C_2H_6	$^1A_{1g}$	2.9026 (C—C)
C_2H_4	1A_g	2.5303 (C—C)
C_2H_2	$^1\Sigma_g^+$	2.2828 (C—C)

the total wavefunctions). The topological properties of the remaining wavefunctions were then compared with the original and the AM1 wavefunctions.

Results and Discussion

The numerical results of the topological analysis of the considered molecules are summarized in Tables II–V. The tables list for all basis sets employed in the HF framework, as well as for the AM1 description, locations of bond critical points, charge densities, Laplacians of ρ , and the eigenvalues of the Hessian. *Ab initio* calculations, from which the core contributions have been removed, are denoted by the letter C added to the basis set specification.

In general, one may say that the AM1 description of the topological properties in the bonding region is quite similar to those of the *ab initio* calculations (see, e.g., Fig. 2). For the region behind the nuclei, in particular, the AM1 results show excellent agreement with the 6-31G results. This region behind the nuclei is responsible for nonbonded interactions, which are of essential importance for conformational analysis.

For heterodiatomic systems, the bond critical point locations found from the AM1 results deviate on average by $0.08 a_0$ from those found by 6-31G calculations (see Tables II–IV). The STO-3G and 3-21G results agree only marginally better with

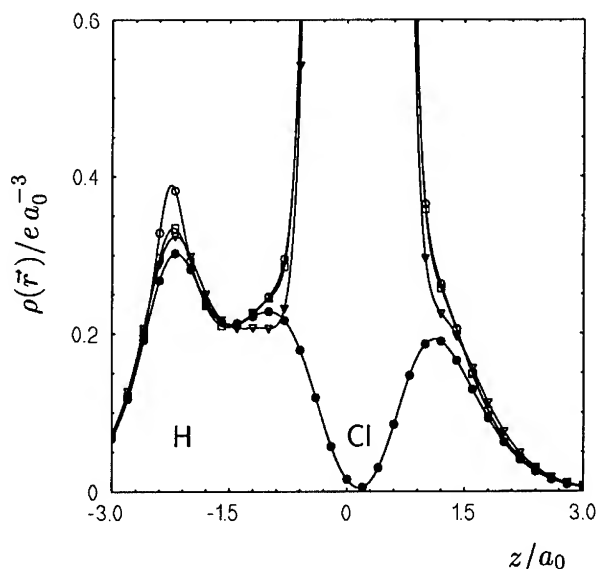


Figure 2. Charge densities along the H—Cl bond at the Hartree–Fock level with various basis sets, and employing the AM1 method. The z axis is the bond coordinate and the origin is arbitrarily set at the center of mass. Empty circles: HF/6-31G; empty squares: HF/3-21G; triangles: HF/STO-3G; full circles: AM1.

TABLE II. Topological properties of various diatomic hydrides.^a

	Location of $\rho_b(a_0)$	ρ_b (ea_0^{-3})	$\nabla^2\rho$ (ea_0^{-5})	λ_1 (ea_0^{-5})	λ_2 (ea_0^{-5})	λ_3 (ea_0^{-5})
Hydrogen						
AM1	0.7006	0.25253	-0.82702	-0.96985	-0.96985	1.11268
STO-3G	0.7006	0.25560	-0.83708	-0.98165	-0.98165	1.12622
3-21G	0.7006	0.23854	-0.67781	-0.78780	-0.78780	0.89778
6-31G	0.7006	0.24339	-1.05082	-0.86507	-0.86507	0.67931
Nitrogen hydride						
AM1	1.2968	0.32606	-1.02751	-0.97632	-0.97632	0.92512
STO-3G	1.2805	0.31351	-0.99884	-0.91211	-0.91211	0.82539
STO-3GC	1.2803	0.31348	-0.99958	-0.91162	-0.91162	0.82365
3-21G	1.3755	0.29789	-0.87221	-1.01904	-1.01904	1.16588
3-21GC	1.3749	0.29782	-0.87498	-1.01741	-1.01741	1.15984
6-31G	1.3703	0.30694	-1.23066	-1.01650	-1.01650	0.80235
6-31GC	1.3701	0.30692	-1.23085	-1.01624	-1.01624	0.80163
Hydrogen oxide						
AM1	1.4654	0.37380	-3.09293	-1.78480	-1.73510	0.42761
STO-3G	1.3636	0.36608	-2.18105	-1.55627	-1.47450	0.84975
STO-3GC	1.3635	0.36608	-2.18085	-1.55608	-1.47430	0.84953
3-21G	1.3697	0.33559	-1.35684	-1.46282	-1.39111	1.49708
3-21GC	1.4637	0.32551	-1.35784	-1.46237	-1.39063	1.49576
6-31G	1.4108	0.34164	-1.62624	-1.53484	-1.47405	1.38266
6-31GC	1.4108	0.34163	-1.62639	-1.53470	-1.47390	1.38221
Hydrogen fluoride						
AM1	^b					
STO-3G	^b					
3-21G	1.3649	0.35189	-2.24320	-1.76069	-1.76069	1.27818
6-31G	1.3979	0.35177	-1.85908	-2.00307	-2.00307	2.14706
Hydrogen chloride						
AM1	1.6018	0.21156	-0.34857	-0.38588	-0.38588	0.43201
STO-3G	1.4755	0.20647	-0.37336	-0.13998	-0.13998	0.00886
STO-3GC	1.4290	0.20573	-0.44237	-0.22915	-0.22915	0.01593
3-21G	1.6510	0.20772	-0.36109	-0.44593	-0.44593	0.53078
3-21GC	1.6578	0.20714	-0.36943	-0.44051	-0.44051	0.51160
6-31G	1.6032	0.20999	-0.39463	-0.43980	-0.43980	0.48497
6-31GC	1.5990	0.20976	-0.40702	-0.43547	-0.43547	0.46393

^a The location of the bond critical point is the distance from the heavier atom.^b No bond critical point.

the 6-31G results. For the symmetric bonds, the locations of the bond critical points are of course identical for AM1 and the *ab initio* ones. The AM1 values of $\rho(\vec{r})$ at the bond critical point vary by an average of $0.03\ ea_0^{-3}$ from the corresponding 6-31G calculations. The worst case is acetylene where the difference is $0.07\ ea_0^{-3}$ (see Table V). AM1 correctly predicts the sign of the Laplacian of the charge density at the bond critical points. The magnitudes, however, deviate from 6-31G results by a large average of $0.4\ ea_0^{-5}$, where the worst case (OH, Table II) shows a difference of $1.5\ ea_0^{-5}$. The topological shape of the charge density in the bonding region

TABLE III. Topological properties of heteronuclear diatomics containing carbon and a first-row atom and carbon hydride.^a

	Location of ρ_b (a_0)	ρ_b (ea_0^{-3})	$\nabla^2\rho$ (ea_0^{-5})	λ_1 (ea_0^{-5})	λ_2 (ea_0^{-5})	λ_3 (ea_0^{-5})
Carbon hydride						
AM1	1.1977	0.23955	-0.52311	-0.60319	-0.45026	0.53034
STO-3G	1.1861	0.24256	-0.62518	-0.60831	-0.44947	0.43259
STO-3GC	1.1801	0.24233	-0.65427	-0.60529	-0.44329	0.39431
3-21G	1.3391	0.24516	-0.74125	-0.65273	-0.57224	0.48372
3-21GC	1.3359	0.24488	-0.74780	-0.65013	-0.56886	0.47119
6-31G	1.3118	0.24641	-0.70185	-0.67555	-0.59111	0.56848
6-31GC	1.3106	0.24633	-0.70782	-0.67455	-0.58977	0.55650
Carbon nitride						
AM1	^b					
STO-3G	1.4662	0.36712	1.17349	-0.45775	-0.45775	2.08897
STO-3GC	^b					
3-21G	1.4392	0.43301	-0.22856	-0.95677	-0.95677	1.68498
3-21GC	^b					
6-31G	1.4473	0.43131	-0.07886	-0.87077	-0.87077	1.66269
6-31GC	^b					
Carbon monoxide						
AM1	^b					
STO-3G	1.4323	0.37405	2.46638	-1.14616	-1.14616	4.75872
STO-3GC	^b					
3-21G	1.3983	0.44397	1.03454	-1.53316	-1.53316	4.10086
3-21GC	^b					
6-31G	1.4124	0.45084	0.87288	-1.54174	-1.54174	3.95635
6-31GC	^b					
Carbon fluoride						
AM1	^b					
STO-3G	1.6298	0.23707	1.45720	-0.71725	-0.18512	0.23596
STO-3GC	^b					
3-21G	1.6054	0.26082	0.50262	-0.75863	-0.35414	1.61539
3-21GC	^b					
6-31G	1.6153	0.25738	0.74929	-0.81262	-0.36168	1.29235
6-31GC	^b					

^a The location of the bond critical point is the distance from the heavier atom.^b No bond critical point.

expressed by the ellipticity ϵ is in general also correctly calculated by AM1. Note that for Σ states, ϵ is zero, and for Π states, it has a finite value.

As one may easily see from Figure 3, the removal of the core orbitals does not significantly affect the electronic description at the bond critical point. The topological properties of CH, OH, HCl, CCl, and C₂H₆ from the valence *ab initio* wavefunctions are very similar to their full counterparts (also compare Tables II and IV). For the case of CN, CO, CF, and CS, the absence of the core orbitals makes the bond critical points disappear for both the AM1 wavefunctions and the valence *ab initio* ones. This problem is, however, not due to the inability of AM1 to calculate

TABLE IV. Topological properties of heteronuclear diatomics containing carbon and a second-row atom.^a

	Location of ρ_b (a_0)	ρ_b (ea_0^{-3})	$\nabla^2\rho$ (ea_0^{-5})	λ_1 (ea_0^{-5})	λ_2 (ea_0^{-5})	λ_3 (ea_0^{-5})
Carbon sulfide						
AM1	^b					
STO-3G	1.6503	0.26185	-0.61940	-0.31901	-0.31901	0.01863
STO-3GC	^b					
3-21G	1.4503	0.25840	-0.68574	-0.36361	-0.36361	0.04148
3-21GC	^b					
6-31G	1.1553	0.24066	0.20843	-0.25107	-0.25107	0.71057
6-31GC	^b					
Carbon chloride						
AM1	1.9048	0.20166	-0.23800	-0.30518	-0.20420	0.27137
STO-3G	1.9609	0.19964	-0.31141	-0.31928	-0.18731	0.19518
STO-3GC	1.9871	0.19920	-0.36976	-0.32120	-0.17376	0.12520
3-21G	1.8186	0.19761	-0.28159	-0.33790	-0.28013	0.33643
3-21GC	1.8201	0.19692	-0.29187	-0.33589	-0.27771	0.32172
6-31G	1.7854	0.20379	-0.48777	-0.34185	-0.29363	0.38671
6-31GC	1.7861	0.20365	-0.57724	-0.34128	-0.29288	0.37643

^a The location of the bond critical point is the distance from the heavier atom.^b No bond critical point.

the charge density in the bonding region of these molecules, or to the direct contribution of the core orbitals to the charge density in this region. The bond critical point is the minimum in the charge density along the internuclear path. The short bond lengths plus the high atomic charges of the N, O, F, and S atoms suppress these minima in CN, CO, CF, and CS and thus pose a systematic problem for the AM1 (Fig. 4), as well as for the valence *ab initio* wavefunctions.

Fortunately, the problem does usually not occur in *all* heterodiatom systems with short bond lengths and large differences in atomic charges. For instance, in various cases of hydrides such as OH, HCl, CH, and the CCl molecule, the AM1 results are in excellent agreement with the 6-31G Hartree-Fock calculations (see Tables III and V). To further assess the problem, we have also computed the topological properties of various polyatomic molecules. The problem seems to persist in the CO fragment in methanol, the CO double bond in formic acid, and the CN triple bond in hydrogen cyanide. On the other hand, systems containing COC fragments, such as oxirane or diethyl ether, and the CN single bonds, such as in methyl amine, show perfectly normal behavior at their AM1 bond critical points.

A possible solution to the problem of the absence of some bond critical points for the AM1 wavefunctions is, of course, to add the missing core orbitals. As an example, we have augmented the AM1 density of carbon monoxide with the C and O core contributions from atomic wavefunctions provided by Clementi and Roetti [17]. The result in Figure 4 shows that the augmented AM1 charge density is much closer to that of the 6-31G than the STO-3G density. Again, core orbitals show

TABLE V. Topological properties of C—C in ethane, ethene and acetylene.^a

	Location of ρ_b (a_0)	ρ_b (ea_0^{-3})	$\nabla^2\rho$ (ea_0^{-5})	λ_1 (ea_0^{-5})	λ_2 (ea_0^{-5})	λ_3 (ea_0^{-5})
Ethane						
AM1	1.4513	0.23644	-0.58653	-0.39990	-0.39990	0.21327
STO-3G	1.4513	0.24177	-0.65504	-0.40540	-0.40540	0.15576
STO-3GC	1.4513	0.24172	-0.65744	-0.40524	-0.40524	0.15304
3-21G	1.4513	0.22065	-0.54146	-0.37476	-0.37476	0.20806
3-21GC	1.4513	0.22035	-0.54775	-0.37346	-0.37346	0.19917
6-31G	1.4513	0.22274	-0.40251	-0.37221	-0.37221	0.34190
6-31GC	1.4513	0.22269	-0.40513	-0.37196	-0.37196	0.33879
Ethene						
AM1	1.2652	0.29948	-0.65734	-0.52093	-0.28900	0.15257
STO-3G	1.2652	0.31372	-0.83554	-0.54561	-0.31807	0.02813
3-21G	1.2652	0.32302	-0.99444	-0.64214	-0.51912	0.16682
6-31G	1.2652	0.32295	-0.85465	-0.64049	-0.52448	0.31031
Acetylene						
AM1	1.1414	0.31549	-0.34113	-0.20498	-0.20498	0.06883
STO-3G ^b	0.8668	0.34422	-0.15532	-0.25744	-0.25744	0.35956
3-21G	1.1414	0.39123	-0.16063	-0.63775	-0.63775	0.11486
6-31G	1.1414	0.38807	-1.18456	-0.60201	-0.60201	0.05586

^a The location of the bond critical point is the distance from either of the C atoms.

^b A (3, -3) critical point is found at the bond midpoint, 1.1414 a_0 away from each carbon atom. The (3, -1) critical point is reported here.

insignificant effects on the charge density in the bonding region as well as in the regions behind the nuclei, but reintroduce a bond critical point, and thus make the AM1 density accessible to a more complete topological analysis. Similar behaviors are found with the augmented AM1 densities in the cases of the CO bond in methanol and formic acid, the CN bond in CN molecule and in hydrogen cyanide, and in the CS and CF molecules.

The exception is the HF molecule, in which even the augmented AM1 density does not exhibit a bond critical point. In this case, core orbitals were only added to the fluorine atom, since hydrogen does not have a core. The problem is rather due to the inappropriate description of the charge density in the vicinity of the hydrogen nucleus. For other hydrides, this insufficiency, expressed in a too "flat" hydrogenic density, is not very relevant for the internuclear region. For HF, however, the electronegative fluorine atom contracts the charge to such an extent that the hydrogen peak almost degenerates to a shoulder. The resulting bond critical point is therefore quite faint, and vanishes altogether if the basis set is not flexible enough. This phenomenon occurs as well in the HF/STO-3G description, although the latter includes the core by default. The fact that AM1 and HF/STO-3G hydrogen densities show great similarities is very well demonstrated by the case of the hydrogen molecule. One can see from Table II that the topological properties at the bond critical

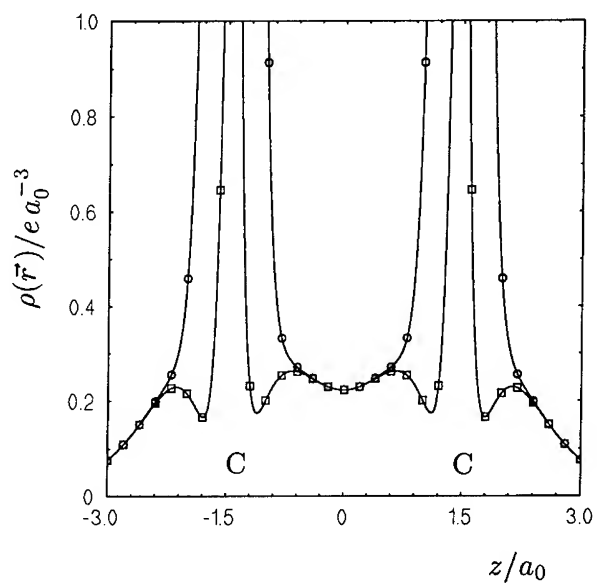


Figure 3. Total (circles) and valence (squares) charge density along the C—C bond of ethane at the HF/6-31G level. The z axis is the bond coordinate and the origin is arbitrarily set at the bond midpoint.

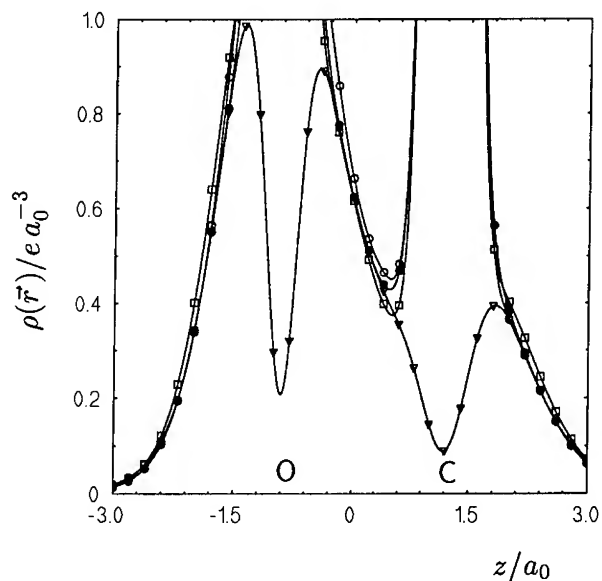


Figure 4. Charge density of carbon monoxide along the bond axis at the HF/6-31G (empty circles), HF/STO-3G (empty squares), AM1 (triangles) levels, and at the AM1 level augmented with atomic core contributions (full circles). The z axis is the bond coordinate and the origin is arbitrarily set at the center of mass.

point from the AM1 density are only marginally closer to the 6-31G results than those of the STO-3G.

In the case of C_2H_2 , Wiberg and co-workers [18] reported a (3, -3) critical point (i.e., a local maximum in the charge density) at the center of the CC bond for the 6-31G* and 6-31G** basis sets on a Hartree-Fock level. Both Wiberg and Gatti et al. [19] showed that these nonnuclear peaks disappeared with more flexible basis sets and/or electron correlation. We found that the maximum also occurs with the STO-3G basis set, but *not* for the (medium-quality) 6-31G or 3-21G bases. Again, the AM1 wavefunction exhibits similar behavior to those of the 3-21G and 6-31G split-valence basis sets. According to the Poincaré-Hopf relation, the peak at the bond midpoint causes two additional passes on the molecular axis. The latter are reported in Table V. For a more recent discussion of these "pseudo-atoms" in other chemical systems, see, e.g., [20] and references therein.

Conclusion

In summary, results from various systems indicate that the absence of the core orbitals results in relatively small discrepancies in some, and negligible discrepancies in others with respect to the description of the electronic properties in the bonding region, as well as the region behind the nuclei. However, the systematic problem in the topological analysis of the AM1 wavefunctions for several mostly π -bonded systems with short bond lengths and large differences in atomic charges is the absence of bond critical points. This problem may, however, be resolved by adding the missing core orbitals from atomic wave functions, which are cheaply and readily available.

The topological properties resulting from the AM1 functions are quite similar to those from *ab initio* calculations with various basis sets. In fact, the AM1 results seem to be more consistent with Hartree-Fock calculations in a split-valence (6-31G) basis than the corresponding SCF functions employing a minimal (STO-3G) basis.

These results give rise to some optimism concerning the applicability of topological analysis to large molecules, for which calculations on an *ab initio* level are beyond the limits of present-day computing. It may be speculated that semi-empirical methods, which represent the valence regions of molecules with acceptable accuracy, may be used in combination with atomic core contributions to give a description, even of extended systems, that allows the analysis of the molecules in terms of the charge density, its critical points, and its Laplacian. This would open a wide field of possibilities including, under favorable conditions, solid-state systems, where the replacement of core contributions by "pseudo-potentials" is very common.

Bibliography

- [1] R. F. W. Bader, *Atoms in Molecules: A Quantum Theory* (Oxford University Press, New York, 1990), and references therein.
- [2] V. H. Smith, Jr., P. F. Price, and I. Absar, *Isr. J. Chem.* **16**, 187 (1977).
- [3] K. Collard and G. G. Hall, *Int. J. Quantum Chem.* **12**, 623 (1977).

- [4] R. F. W. Bader and A. K. Chandra, *Can. J. Chem.* **46**, 953 (1968).
- [5] R. F. W. Bader, in B. M. Deb, editor, *The Force Concept in Chemistry* (Wiley, New York, 1980).
- [6] R. F. W. Bader, T. S. Slec, D. Cremmer, and E. Kraka, *J. Am. Chem. Soc.* **105**, 5061 (1983).
- [7] P. M. Morse and H. Feshbach, *Methods of Theoretical Physics, Part I* (McGraw-Hill, New York, 1953).
- [8] K. B. Wiberg, R. F. W. Bader, and C. D. H. Lau, *J. Am. Chem. Soc.* **109**, 985 (1987).
- [9] K. B. Wiberg, R. F. W. Bader, and C. D. H. Lau, *J. Am. Chem. Soc.* **109**, 1001 (1987).
- [10] K. E. Edgecombe and R. J. Boyd, *Int. J. Quantum Chem.* **29**, 959 (1986).
- [11] R. J. Boyd and K. E. Edgecombe, *J. Comput. Chem.* **8**, 489 (1987).
- [12] M. J. S. Dewar, E. Zoebisch, E. F. Healy, and J. J. P. Stewart, *J. Am. Chem. Soc.* **107**, 3902 (1985).
- [13] M. J. Frisch, J. S. Binkley, H. B. Schelgel, K. Raghavachari, C. F. Melius, R. L. Martin, J. J. P. Stewart, F. W. Bobrowicz, C. M. Rohlfing, L. R. Kahn, D. J. Defrees, R. Seeger, R. A. Whiteside, D. J. Fox, E. M. Fleuder, and J. A. Pople, *GAUSSIAN86* (Carnegie-Mellon Quantum Chemistry Publishing Unit, Pittsburgh, PA, 1984).
- [14] R. F. W. Bader, personal communication, McMaster University, Hamilton, ON, Canada.
- [15] K. Huber and G. Herzberg, *Molecular Spectra and Molecular Structure, Volume IV. Constants of Diatomic Molecules* (Van Nostrand Reinhold, New York, 1979).
- [16] G. Herzberg, *Molecular Spectra and Molecular Structure, Volume III. Electronic Spectra and Electronic Structure of Polyatomic Molecules* (D. Van Nostrand, Toronto, 1967).
- [17] E. Clementi and C. Roetti, *At. Data Nucl. Data Tables* **14**, 177 (1974).
- [18] K. B. Wiberg, C. H. Hadad, T. J. LePage, C. M. Breneman, and M. J. Frisch, *J. Phys. Chem.* **96**, 671 (1992).
- [19] C. Gatti, P. MacDougall, and R. F. W. Bader, *J. Chem. Phys.* **88**, 3792 (1988).
- [20] K. E. Edgecombe, R. O. Esquivel, V. H. Smith, Jr., and F. J. Müller-Plathe, *J. Chem. Phys.* **97**, 2595 (1992).

Received March 22, 1994

Convergence of a Sequence of Lower Bounds for $\langle 1/r \rangle$ for the Noble Gas, Alkali, and Alkaline Earth Atoms

P. CSAVINSZKY

Department of Physics and Astronomy, Orono, Maine 04469-5709

Abstract

This article considers 2×2 , 3×3 , 4×4 , and 5×5 Gram determinantal inequalities among $\langle r^n \rangle$, where r is the distance from the atomic nucleus. The elements of these determinants involve $n = -1, 0, 1$; $n = -1, 0, 1, 2, 3$; $n = -1, 0, 1, 2, 3, 4, 5$; and $n = -1, 0, 1, 2, 3, 4, 5, 6, 7$. The 2×2 , 3×3 , 4×4 , and 5×5 determinantal inequalities are used to obtain lower bound estimates of $\langle 1/r \rangle$ for atoms of spherically symmetric charge distributions. The 2×2 , 3×3 , and 4×4 inequalities have been applied to He, Ne, Ar, Kr, Xe; Li, Na, K, Rb; and Be, Mg, Ca, Sr. The 5×5 inequality has been applied only to He, Li, and Be. It is found that the lower bound values of $\langle 1/r \rangle$, for all atoms considered, appear to converge to the quantum mechanical values of Boyd, who calculated them with the Roothaan–Hartree–Fock wavefunctions of Clementi and Roetti. © 1994 John Wiley & Sons, Inc.

Introduction

The possibility of deriving a bound on one expectation value of a quantity in terms of other expectation values of the same quantity via an inequality is an intriguing one. The establishment of inequalities involving $\langle r^n \rangle$, where r is the distance from the atomic nucleus, permits one to pose the question: To what accuracy can one calculate an expectation value of r raised to a certain power in terms of other expectation values of r raised to other powers?

In the present work Gram determinantal inequalities are used to obtain lower bounds for $\langle 1/r \rangle$ from 2×2 , 3×3 , 4×4 , and 5×5 determinants, whose elements are $\langle r^n \rangle$. The 2×2 inequality involves $\langle r^n \rangle$ with $n = -1, 0, 1$. The 3×3 inequality contains $\langle r^n \rangle$ with $n = -1, 0, 1, 2, 3$. The 4×4 inequality has elements $\langle r^n \rangle$ with $n = -1, 0, 1, 2, 3, 4, 5$, while the 5×5 inequality involves $\langle r^n \rangle$ with $n = -1, 0, 1, 2, 3, 4, 5, 6, 7$.

The above description shows that $\langle 1/r \rangle$, a quantity whose value is mainly determined by distances close to the atomic nucleus, is “synthesized” by a number of $\langle r^n \rangle$ values which involve distances far from the atomic nucleus. The question that arises is the following: do the $\langle 1/r \rangle$ values obtained for a particular atom from 2×2 , 3×3 , 4×4 , and 5×5 Gram determinantal inequalities converge to the quantum mechanical values of $\langle 1/r \rangle$ calculated by Boyd [1] with the Roothaan–Hartree–Fock wavefunctions of Clementi and Roetti [2]? The answer seems to be

in the affirmative for the spherically symmetrical atoms He, Ne, Ar, Kr, Xe; Li, Na, K, Rb; and Be, Mg, Ca, Sr.

Determinantal Inequalities

The 2×2 and 3×3 determinantal inequalities with elements $\langle r^{-1} \rangle$, $\langle r^0 \rangle$, $\langle r \rangle$ and $\langle r^{-1} \rangle$, $\langle r^0 \rangle$, $\langle r \rangle$, $\langle r^2 \rangle$, $\langle r^3 \rangle$ were obtained by Gadre and Matcha [3], while the 4×4 inequality, with elements $\langle r^{-1} \rangle$, $\langle r^0 \rangle$, $\langle r \rangle$, $\langle r^2 \rangle$, $\langle r^3 \rangle$, $\langle r^4 \rangle$, and $\langle r^5 \rangle$, was obtained by Csavinszky [4]. The 5×5 inequality, with elements $\langle r^{-1} \rangle$, $\langle r^0 \rangle$, $\langle r \rangle$, $\langle r^2 \rangle$, $\langle r^3 \rangle$, $\langle r^4 \rangle$, $\langle r^5 \rangle$, $\langle r^6 \rangle$, and $\langle r^7 \rangle$, is given in the present article. It is mentioned here that the expectation values $\langle r^6 \rangle$ and $\langle r^7 \rangle$ have been calculated by the author by making use of the analytical approximations for $D(r)$, given by Boyd [1]. The derivation of the determinantal inequalities is based on the Gram inequality [5],

$$\left| \int f_\lambda(x) f_\mu(x) dx \right| \geq 0 \quad \lambda, \mu = 1, 2, 3, \dots \quad (1)$$

In Ref. [3], $f_n(x)$ was defined by*

$$f_n(x) = 4\pi r^{2n-1} \rho(r)^{1/2} \quad n = 1, 2, 3, \dots, N, \quad (2)$$

where $\rho(r)$ is the (position) electron density.

It is noted that

$$\rho(r) = (1/4\pi) r^{-2} D(r), \quad (3)$$

where $D(r)$ is the (position) radial electron density, normalized to unity.

The expectation values of powers of r are obtained [1] from

$$\langle r^n \rangle = \int_0^\infty r^n D(r) dr \quad (4)$$

The 2×2 , 3×3 , 4×4 , and 5×5 determinantal inequalities are given below

$$\begin{vmatrix} \langle r^{-1} \rangle & 1 \\ 1 & \langle r \rangle \end{vmatrix} \geq 0 \quad (5)$$

$$\begin{vmatrix} \langle r^{-1} \rangle & 1 & \langle r \rangle \\ 1 & \langle r \rangle & \langle r^2 \rangle \\ \langle r \rangle & \langle r^2 \rangle & \langle r^3 \rangle \end{vmatrix} \geq 0 \quad (6)$$

$$\begin{vmatrix} \langle r^{-1} \rangle & 1 & \langle r \rangle & \langle r^2 \rangle \\ 1 & \langle r \rangle & \langle r^2 \rangle & \langle r^3 \rangle \\ \langle r \rangle & \langle r^2 \rangle & \langle r^3 \rangle & \langle r^4 \rangle \\ \langle r^2 \rangle & \langle r^3 \rangle & \langle r^4 \rangle & \langle r^5 \rangle \end{vmatrix} \geq 0 \quad (7)$$

$$\begin{vmatrix} \langle r^{-1} \rangle & 1 & \langle r \rangle & \langle r^2 \rangle & \langle r^3 \rangle \\ 1 & \langle r \rangle & \langle r^2 \rangle & \langle r^3 \rangle & \langle r^4 \rangle \\ \langle r \rangle & \langle r^2 \rangle & \langle r^3 \rangle & \langle r^4 \rangle & \langle r^5 \rangle \\ \langle r^2 \rangle & \langle r^3 \rangle & \langle r^4 \rangle & \langle r^5 \rangle & \langle r^6 \rangle \\ \langle r^3 \rangle & \langle r^4 \rangle & \langle r^5 \rangle & \langle r^6 \rangle & \langle r^7 \rangle \end{vmatrix} \geq 0. \quad (8)$$

* There is a misprint in Ref. [3]. The function f_n is given in Ref. [3] as $f_n = [4\pi\rho(r)^{2n-1}]^{1/2}$ ($n = 1, 2, 3, \dots$). The correct expression is displayed in Eq. (2) of the present article, and in Eq. (2) of Ref. [4].

TABLE I. Lower bound and quantum mechanical (QM) values (in a.u.) of $\langle r^{-1} \rangle$ for the noble gas atoms.

Atom	$\langle r^{-1} \rangle$				QM
	2×2	3×3	4×4	5×5	
He	1.078	1.366	1.487	1.548	1.687
Ne	1.267	1.754	2.064	—	3.111
Ar	1.120	1.808	2.204	—	3.874
Kr	1.372	2.138	2.552	—	5.079
Xe	1.382	2.189	2.680	—	5.886

Putting the 2×2 , 3×3 , 4×4 , and 5×5 determinants in Eqs. (5)–(8) equal to zero, one can calculate lower bounds to $\langle 1/r \rangle$ arising from these determinants. The $\langle 1/r \rangle$ values for the noble gas atoms, the alkali atoms, and the alkaline earth atoms are displayed in Tables I, II, and III.

Discussion

A look at Table I reveals that, for the noble gas atom He, the lower bound values of $\langle 1/r \rangle$, calculated from the 2×2 , 3×3 , 4×4 , and 5×5 Gram determinants, show an increase as one goes in succession from the 2×2 to the 5×5 case. Table I shows that, for the noble gas atoms Ne, Ar, Kr, and Xe, the lower bound values of $\langle 1/r \rangle$, calculated from the 2×2 , 3×3 , and 4×4 Gram determinants, also show an increase as one moves from the 2×2 to the 3×3 , and then to the 4×4 case. For all atoms in Table I, the calculated lower bound values of $\langle 1/r \rangle$ appear to converge toward the quantum mechanical (QM) values of $\langle 1/r \rangle$, calculated by Boyd [1].

Table II shows that, for the Li atom, the lower bound values of $\langle 1/r \rangle$ increase, as one proceeds in succession from the 2×2 to the 5×5 case. The same is true for Na, K, and Rb, since the lower bound values of $\langle 1/r \rangle$ increase as one goes from the 2×2 , 3×3 , and then to the 4×4 case. The converging trend of the lower bound values of $\langle 1/r \rangle$, for all atoms in Table II, to the QM values of $\langle 1/r \rangle$, calculated by Boyd [1], is again clearly seen.

TABLE II. Lower bound and quantum mechanical (QM) values (in a.u.) of $\langle r^{-1} \rangle$ for the alkali atoms.

Atom	$\langle r^{-1} \rangle$				QM
	2×2	3×3	4×4	5×5	
Li	0.598	1.084	1.334	1.456	1.905
Na	1.014	1.461	1.679	—	3.221
K	0.977	1.407	1.740	—	3.942
Rb	1.242	1.732	2.122	—	5.126

TABLE III. Lower bound and quantum mechanical (QM) values (in a.u.) of $\langle r^{-1} \rangle$ for the alkaline earth atoms.

Atom	$\langle r^{-1} \rangle$				QM
	2×2	3×3	4×4	5×5	
Be	0.653	1.124	1.429	1.593	2.102
Mg	0.979	1.526	1.679	—	3.327
Ca	0.941	1.459	1.791	—	4.008
Sr	1.195	1.784	2.170	—	5.173

Table III shows the same converging trend for the lower bound value of $\langle 1/r \rangle$ for Be, as one goes in succession from the 2×2 to the 5×5 case. For Mg, Ca, and Sr the lower bound values of $\langle 1/r \rangle$ seem to converge also to the QM values of Boyd [1], as one proceeds from the 2×2 to the 4×4 case.

Conclusion

On the basis of the behavior of the lower bound values of $\langle 1/r \rangle$, displayed in Tables I, II, and III, the author expects further manifestation of convergence to the QM values of $\langle 1/r \rangle$, should one extend the calculations by consideration of 6×6 , 7×7 , . . . etc. Gram determinantal inequalities.

In closing, it should also be mentioned that Weinhold [6] dealt with the application of Gram determinants to some physical quantities.

Yet another comment should be made about two recent articles: one by Angulo and Dehesa [7], and the other one by Gálvez and Porras [8]. The first-article contains inequalities for $\langle r^n \rangle \langle r^{n-2} \rangle$, while the second contains the more complicated inequality $\langle r^{k-3} \rangle \leq (2Z/k) \langle r^{k-2} \rangle$, where Z is the atomic number and $k = 1, 2, 3$. (For even more complicated inequalities among $\langle r^k \rangle$, Ref. [8] should be consulted.)

Bibliography

- [1] R. J. Boyd, *Can. J. Phys.* **55**, 452 (1977).
- [2] E. Clementi and C. Roetti, *At. Data Nucl. Data Tables* **14**, 177 (1974).
- [3] S. R. Gadre and R. L. Matcha, *J. Chem. Phys.* **74**, 589 (1981).
- [4] P. Csavinsky, *Int. J. Quantum Chem., Quantum Chem. Symp.* **27**, 377 (1993).
- [5] R. Courant and D. Hilbert, *Methods of Mathematical Physics* (Interscience, New York, 1955), Vol. I, p. 62.
- [6] F. Weinhold, *Adv. Quantum Chem.* **6**, 299 (1972).
- [7] J. C. Angulo and J. S. Dehesa, *Phys. Rev. A* **44**, 1516 (1991).
- [8] F. J. Gálvez and I. Porras, *Phys. Rev. A* **44**, 144 (1991).

A New Representation for Ground States and its Legendre Transforms

ANDRÉS CEDILLO

*Departamento de Química, Universidad Autónoma Metropolitana-Iztapalapa,
Ap. Postal 86-219; Villa Coapa, DF 14391; México*

Abstract

The ground-state energy of an electronic system is a functional of the number of electrons (N) and the external potential (v): $E = E[N, v]$, this is the energy representation for ground states. In 1982, Nalewajski defined the Legendre transforms of this representation, taking advantage of the strict concavity of E with respect to their variables (concave respect v and convex respect N), and he also constructed a scheme for the reduction of derivatives of his representations. Unfortunately, N and the electronic density (ρ) were the independent variables of one of these representations, but ρ depends explicitly on N . In this work, this problem is avoided using the energy per particle (ϵ) as the basic variable. In this case ϵ is a strict concave functional respect to both of his variables, and the Legendre transformations can be defined. A procedure for the reduction of derivatives is generated for the new four representations and, in contrast to the Nalewajski's procedure, it only includes derivatives of the four representations. Finally, the reduction of derivatives is used to test some relationships between the hardness and softness kernels. © 1994 John Wiley & Sons, Inc.

Introduction

Consider an N -electron system, under the influence of an external potential, $v(\mathbf{r})$. For this system the Hamiltonian has this form:

$$\hat{H}_{N,v} = \hat{H}_N^{(0)} + \sum_{i=1}^N v(\mathbf{r}_i), \quad (1)$$

where

$$\hat{H}_N^{(0)} = \sum_{i=1}^N -\frac{1}{2} \nabla^2 + \sum_{i=1}^{N-1} \sum_{j=i+1}^N \frac{1}{|\mathbf{r}_i - \mathbf{r}_j|}. \quad (2)$$

If the operator $\hat{H}_{N,v}$ has a nondegenerated ground state, then the ground-state energy is

$$E[N, v] \equiv \min_k \{ E_k | \hat{H}_{N,v} \Psi_k = E_k \Psi_k \}, \quad (3)$$

where $\{\Psi_k\}$ are the N -particle antisymmetric eigenfunctions of $\hat{H}_{N,v}$, and the ground-state density is given by:

$$\rho(\mathbf{r}) \equiv N \int \Psi^*(\mathbf{x}_1, \dots, \mathbf{x}_N) \Psi(\mathbf{x}_1, \dots, \mathbf{x}_N) d\sigma_1 d\mathbf{x}_2 \cdots d\mathbf{x}_N, \quad (4)$$

where Ψ is the ground-state wave function, and $\mathbf{x} \equiv \{\mathbf{r}, \sigma\}$ contains the spatial and spin coordinates. If one assumes that E is differentiable with respect to N , then the differential form of eq. (3) is [1]:

$$dE = \mu dN + \int \rho(\mathbf{r}) \delta v(\mathbf{r}) d\mathbf{r}, \quad (5)$$

where

$$\mu = \left(\frac{\partial E}{\partial N} \right)_v, \quad \rho(\mathbf{r}) = \left(\frac{\delta E}{\delta v(\mathbf{r})} \right). \quad (6)$$

In addition, E has a strict concavity respect to N and v . From the experimental ionization potentials of atoms and molecules [2] one can see that E is a convex function of N , while E is a concave functional of $v(\mathbf{r})$ [3]. This fact allows one to use Legendre transformations to find alternative representations for ground states [4]:

$$\begin{aligned} F[N, \rho] &\equiv E - \int \rho(\mathbf{r}) v(\mathbf{r}) d\mathbf{r} \\ \Omega[\mu, v] &\equiv E - \mu N \\ R[\mu, \rho] &\equiv E - \mu N - \int \rho(\mathbf{r}) v(\mathbf{r}) d\mathbf{r}. \end{aligned} \quad (7)$$

Unfortunately N and ρ are not independent variables:

$$N = \int \rho(\mathbf{r}) d\mathbf{r}, \quad (8)$$

and the functional $F[N, \rho]$ is not a functional of two independent variables.

In this work, this problem is avoided by constructing a new representation for ground states. This new representation turns out to be a concave functional of both of its variables and its Legendre transformations do not present the former problem.

A systematic method for the reduction of derivatives is also developed for this kind of functionals and this method is used to test some relationships between chemical reactivity parameters.

The Energy per Particle

The main problem with the functional $F[N, \rho]$ comes from the Legendre transformation:

$$F[N, \rho] \equiv E[N, v] - \int v(\mathbf{r}) \left(\frac{\delta E}{\delta v(\mathbf{r})} \right)_N d\mathbf{r}, \quad (9)$$

which replaces the dependence in v with the derivative of E with respect to v (in this case, ρ), leaving the other variable (N) unchanged.

Taking into account that the density depends explicitly on N , Eq. (4), then one can extract N from the density:

$$\rho(\mathbf{r}) = NP(\mathbf{r}), \quad (10)$$

where $P(\mathbf{r})$ is the one-particle probability:

$$P(\mathbf{r}) \equiv \int \Psi^*(\mathbf{x}_1, \dots, \mathbf{x}_N) \Psi(\mathbf{x}_1, \dots, \mathbf{x}_N) d\sigma_1 d\mathbf{x}_2 \cdots d\mathbf{x}_N, \quad (11)$$

and it must integrate to one.

From eq. (5), one can find the differential form of the energy per particle, $\varepsilon \equiv E/N$,

$$d\varepsilon = Mdv + \int P(\mathbf{r})\delta v(\mathbf{r}) d\mathbf{r}, \quad (12)$$

where

$$\nu \equiv \ln N, \quad (13)$$

and

$$M \equiv \left(\frac{\partial \varepsilon}{\partial \nu} \right)_v = \mu - \varepsilon = -\frac{E - \mu N}{N}$$

$$P(\mathbf{r}) = \left(\frac{\delta \varepsilon}{\delta v(\mathbf{r})} \right)_\nu. \quad (14)$$

Then the energy per particle is a functional of ν and v ,

$$\varepsilon = \varepsilon[\nu, v]. \quad (15)$$

Since N and ν have a one-to-one correspondence, ν and v determine the ground-state energy and, therefore, the energy per particle. Then Eq. (15) is also a representation for ground states.

This new functional also has strict concavity. In Figure 1, experimental values of ε , for helium to argon, are plotted versus ν , and one can see that ε is a concave function of ν , for a fixed potential and $\nu \geq \ln 2$. And for a given value of ν (and therefore a fixed value of N), ε is a concave functional of v [3]:

$$\varepsilon[\nu, (1 - \alpha)v_1 + \alpha v_2] \geq (1 - \alpha)\varepsilon[\nu, v_1] + \alpha\varepsilon[\nu, v_2]. \quad (16)$$

Then $\varepsilon[\nu, v]$ has the same concavity with respect to its independent variables. In this case [5], the Legendre transformations of ε can be defined:

$$\phi[\nu, P] \equiv \varepsilon[\nu, v] - \int P(\mathbf{r})v(\mathbf{r}) d\mathbf{r}$$

$$\omega[M, v] \equiv \varepsilon[\nu, v] - M\nu$$

$$\pi[M, P] \equiv \varepsilon[\nu, v] - M\nu - \int P(\mathbf{r})v(\mathbf{r}) d\mathbf{r}, \quad (17)$$

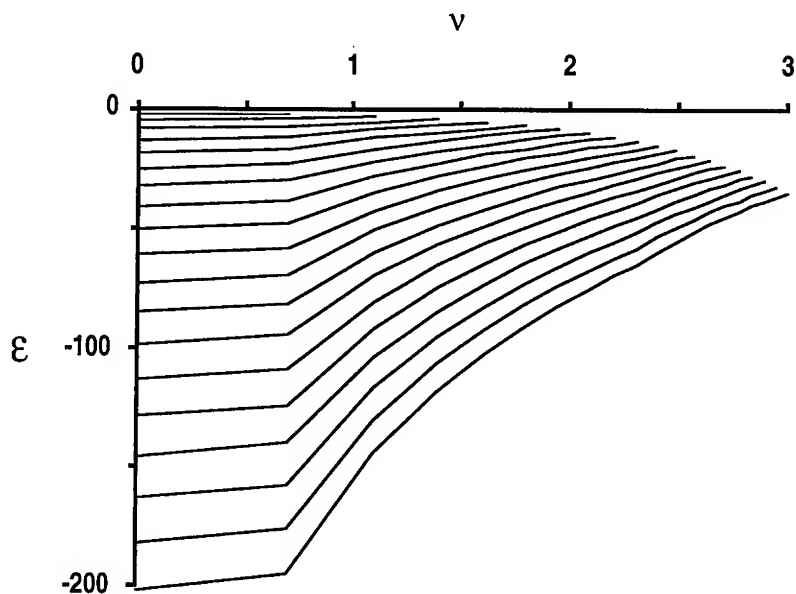


Figure 1. Experimental energies per particle for helium to argon.

and these representations can be related with those from Eq. (7). As a special case,

$$\phi[\nu, P] \equiv \frac{1}{N} \left[E - \int \rho(\mathbf{r}) v(\mathbf{r}) d\mathbf{r} \right] = \frac{F[N, \rho]}{N}, \quad (18)$$

where one can see that the independent variables of ϕ do not have an explicit dependence.

These new functionals are also ground-state representations, since the strict concavity assures a one-to-one mapping for its independent variables [5]. From Eq. (12) one can find the differential form of the new representations:

$$\begin{aligned} d\phi &= M d\nu - \int v(\mathbf{r}) \delta P(\mathbf{r}) d\mathbf{r} \\ d\omega &= -\nu dM + \int P(\mathbf{r}) \delta v(\mathbf{r}) d\mathbf{r} \\ d\pi &= -\nu dM - \int v(\mathbf{r}) \delta P(\mathbf{r}) d\mathbf{r}, \end{aligned} \quad (19)$$

and each of the four new representations yield a Maxwell's relation, see Table I.

Reduction of Derivatives

All the functionals used in this work depend on a scalar variable and on a function. Let x be the scalar variable and $y(\mathbf{r})$, the function. To obtain general relationships among quantities from any two representations, it is convenient to work with an

TABLE I. Maxwell's relations for the new representations.

Representation	Maxwell's relation
$[\nu, v]$	$\left(\frac{\delta M}{\delta v(\mathbf{r})}\right)_v = \left(\frac{\partial P(\mathbf{r})}{\partial \nu}\right)_v$
$[M, v]$	$\left(\frac{\delta \nu}{\delta v(\mathbf{r})}\right)_M = -\left(\frac{\partial P(\mathbf{r})}{\partial M}\right)_v$
$[\nu, P]$	$\left(\frac{\delta M}{\delta P(\mathbf{r})}\right)_v = -\left(\frac{\partial v(\mathbf{r})}{\partial \nu}\right)_P$
$[M, P]$	$\left(\frac{\delta \nu}{\delta P(\mathbf{r})}\right)_M = \left(\frac{\partial v(\mathbf{r})}{\partial M}\right)_P$

arbitrary quantity A . The differential form of A can be written in both representations:

$$dA = \left(\frac{\partial A}{\partial x_1}\right)_{y_1} dx_1 + \int \left(\frac{\delta A}{\delta y_1(\mathbf{r})}\right)_{x_1} \delta y_1(\mathbf{r}) d\mathbf{r}$$

$$dA = \left(\frac{\partial A}{\partial x_2}\right)_{y_2} dx_2 + \int \left(\frac{\delta A}{\delta y_2(\mathbf{r})}\right)_{x_2} \delta y_2(\mathbf{r}) d\mathbf{r}, \quad (20)$$

where $\{x_i\} = \{\nu, M\}$ and $\{y_i\} = \{v, P\}$. Also dx_2 and dy_2 can be expressed in terms of dx_1 and dy_1 , and then both equations become identical. By equating the coefficients of the independent variables, the following relations are obtained:

$$\left(\frac{\partial A}{\partial x_1}\right)_{y_1} = \left(\frac{\partial A}{\partial x_2}\right)_{y_2} \left(\frac{\partial x_2}{\partial x_1}\right)_{y_1} + \int \left(\frac{\delta A}{\delta y_2(\mathbf{r})}\right)_{x_2} \left(\frac{\partial y_2(\mathbf{r})}{\partial x_1}\right)_{y_1} d\mathbf{r}$$

$$\left(\frac{\delta A}{\delta y_1(\mathbf{r})}\right)_{x_1} = \left(\frac{\partial A}{\partial x_2}\right)_{y_2} \left(\frac{\delta x_2}{\delta y_1(\mathbf{r})}\right)_{x_1} + \int \left(\frac{\delta A}{\delta y_2(\mathbf{r}')}\right)_{x_2} \left(\frac{\delta y_2(\mathbf{r}')}{\delta y_1(\mathbf{r})}\right)_{x_1} d\mathbf{r}', \quad (21)$$

where the transformation coefficients are second derivatives in the representation of $[x_1, y_1]$ and they must be expressed in terms of the second derivatives of the representation of $[x_2, y_2]$. These reductions can be made by replacing x_1 and $y_1(\mathbf{r})$ in Eq. (21). The rearrangement of the resulting equation leads to the following implicit relations for the second derivatives of the representation of $[x_1, y_1]$:

$$\delta(\mathbf{r} - \mathbf{r}') = \int \left(\frac{\delta y_2(\mathbf{r}')}{\delta y_1(\mathbf{r})}\right)_{x_1} \left[\left(\frac{\delta y_1(\mathbf{r}')}{\delta y_2(\mathbf{r}')}\right)_{x_2} - \left\{ \left(\frac{\partial x_1}{\partial x_2}\right)_{y_2} \right\}^{-1} \left(\frac{\partial y_1(\mathbf{r}')}{\partial x_2}\right)_{y_2} \left(\frac{\delta x_1}{\delta y_2(\mathbf{r}')}\right)_{x_2} \right] d\mathbf{r}'$$

$$\left(\frac{\delta x_2}{\delta y_1(\mathbf{r})}\right)_{x_1} = - \left\{ \left(\frac{\partial x_1}{\partial x_2}\right)_{y_2} \right\}^{-1} \int \left(\frac{\delta y_2(\mathbf{r}')}{\delta y_1(\mathbf{r})}\right)_{x_1} \left(\frac{\delta x_1}{\delta y_2(\mathbf{r}')}\right)_{x_2} d\mathbf{r}'$$

$$\left(\frac{\partial x_2}{\partial x_1}\right)_{y_1} \left(\frac{\partial y_1(\mathbf{r})}{\partial x_2}\right)_{y_2} = - \int \left(\frac{\delta y_1(\mathbf{r})}{\delta y_2(\mathbf{r}')}\right)_{x_2} \left(\frac{\partial y_2(\mathbf{r}')}{\partial x_1}\right)_{y_1} d\mathbf{r}'. \quad (22)$$

From the first equation one must find $[\delta y_2/\delta y_1]_{x_1}$ by solving the integral equation. Using this solution, the other two derivatives can be obtained directly if one takes into account that $[\delta x_2/\delta y_1]_{x_1}$ and $[\partial y_2/\partial x_1]_{y_1}$ are related by a Maxwell's relation. With these derivatives, the reduction of derivatives can be done with Eq. (21).

If one independent variable is common to both representations, then the reduction equations become simpler. There are two different cases—one generates algebraic relationships, whereas the other gives functional equations. Both cases are described below.

When the second variable is the same in both representations, $y_2 = y_1 = y$, the reduction equations take their simplest form. These representations differ in their real variable, $[x_1, y]$ and $[x_2, y]$, and the reduction equations can be written in the following form:

$$\begin{aligned} \left(\frac{\partial A}{\partial x_1}\right)_y &= \left(\frac{\partial A}{\partial x_2}\right)_y \left(\frac{\partial x_2}{\partial x_1}\right)_y \\ \left(\frac{\delta A}{\delta y(\mathbf{r})}\right)_{x_1} &= \left(\frac{\partial A}{\partial x_2}\right)_y \left(\frac{\delta x_2}{\delta y(\mathbf{r})}\right)_{x_1} + \left(\frac{\delta A}{\delta y(\mathbf{r})}\right)_{x_2}, \end{aligned} \quad (23)$$

where the second derivatives of $[x_1, y]$ are given by

$$\begin{aligned} \left(\frac{\partial x_2}{\partial x_1}\right)_y &= \left\{ \left(\frac{\partial x_1}{\partial x_2}\right)_y \right\}^{-1} \\ \left(\frac{\delta x_2}{\delta y(\mathbf{r})}\right)_{x_1} &= - \left\{ \left(\frac{\partial x_1}{\partial x_2}\right)_y \right\}^{-1} \left(\frac{\delta x_1}{\delta y(\mathbf{r})}\right)_{x_2}. \end{aligned} \quad (24)$$

The relations given in the last equations correspond to the well-known chain-rule, inverse-derivative, and cyclic-rule of differential calculus.

The other case occurs when $x_2 = x_1 = x$, in which the derivatives from the representation of $[x, y_1]$ are reduced in terms of those from $[x, y_2]$:

$$\begin{aligned} \left(\frac{\partial A}{\partial x}\right)_{y_1} &= \left(\frac{\partial A}{\partial x}\right)_{y_2} + \int \left(\frac{\delta A}{\delta y_2(\mathbf{r})}\right)_x \left(\frac{\partial y_2(\mathbf{r})}{\partial x}\right)_{y_1} d\mathbf{r} \\ \left(\frac{\delta A}{\delta y_1(\mathbf{r})}\right)_x &= \int \left(\frac{\delta A}{\delta y_2(\mathbf{r}')}\right)_x \left(\frac{\partial y_2(\mathbf{r}')}{\partial y_1(\mathbf{r})}\right)_x d\mathbf{r}', \end{aligned} \quad (25)$$

with

$$\begin{aligned} \delta(\mathbf{r} - \mathbf{r}') &= \int \left(\frac{\delta y_2(\mathbf{r}')}{\delta y_1(\mathbf{r})}\right)_x \left(\frac{\delta y_1(\mathbf{r}')}{\delta y_2(\mathbf{r})}\right)_x d\mathbf{r}' \\ \left(\frac{\partial y_2(\mathbf{r})}{\partial x}\right)_{y_1} &= - \int \left(\frac{\delta y_2(\mathbf{r})}{\delta y_1(\mathbf{r}')}\right)_x \left(\frac{\partial y_1(\mathbf{r}')}{\partial x}\right)_{y_2} d\mathbf{r}'. \end{aligned} \quad (26)$$

In this case $[\delta y_2/\delta y_1]_x$ must be solved from the functional inverse-equation, and Eq. (25, 26) corresponds to the functional generalizations of the algebraic relations given by Eqs. (23, 24).

These three cases can be found in the derivative reduction problems and in the following section they will be applied to test some relationships between some reactivity parameters.

Relationships between Reactivity Parameters

Density Functional Theory (DFT) has been widely used to study the chemical reactivity, and most of the reactivity parameters provided by this theory are derivatives. Then the methodology from the last section will be used with these quantities.

DFT is based in the Hohenberg-Kohn theorems [6]. The first theorem states that the ground-state energy is a functional of the ground-state density:

$$E = E^{\text{HK}}[\rho] \equiv F^{\text{HK}}[\rho] + \int \rho(\mathbf{r})v(\mathbf{r}) d\mathbf{r}. \quad (27)$$

The second is a variational principle for the energy, it establishes that the functional $E^{\text{HK}}[\rho]$ takes its minimum value for the exact ground-state density. In the variational procedure, one restriction must be included, namely that the density must be normalized to the number of electrons:

$$N[\rho] = \int \rho(\mathbf{r}) d\mathbf{r} = N. \quad (28)$$

This restriction is incorporated through a Lagrange's multiplier, μ , and the resulting Euler-Lagrange equation takes the following form:

$$\frac{\delta F^{\text{HK}}}{\delta \rho(\mathbf{r})} + v(\mathbf{r}) = \mu, \quad (29)$$

where μ can be identified with the chemical potential of the system [1].

Since most of the chemical reactivity parameters are derivatives involving μ , N , v , and ρ , at first, one can relate the representations of $\varepsilon[\nu, v]$ and $\omega[M, v]$. The relationships for the second derivatives of both representations are

$$\begin{aligned} \left(\frac{\partial M}{\partial \nu} \right)_v &= \left\{ \left(\frac{\partial \nu}{\partial M} \right)_v \right\}^{-1} \\ \left(\frac{\delta M}{\delta v(\mathbf{r})} \right)_v &= - \left\{ \left(\frac{\partial \nu}{\partial M} \right)_v \right\}^{-1} \left(\frac{\delta \nu}{\delta v(\mathbf{r})} \right)_M \\ \left(\frac{\delta P(\mathbf{r})}{\delta v(\mathbf{r}')} \right)_v &= \left\{ \left(\frac{\partial \nu}{\partial M} \right)_v \right\}^{-1} \left(\frac{\partial P(\mathbf{r})}{\partial M} \right)_v \left(\frac{\partial P(\mathbf{r}')}{\partial M} \right)_v + \left(\frac{\delta P(\mathbf{r})}{\delta v(\mathbf{r}')} \right)_M, \end{aligned} \quad (30)$$

and they can be related with the derivatives of the original representations, Eqs. (3,7):

$$\begin{aligned} \left(\frac{\partial \mu}{\partial N} \right)_v &= \left\{ \left(\frac{\partial N}{\partial \mu} \right)_v \right\}^{-1} \\ \left(\frac{\delta \mu}{\delta v(\mathbf{r})} \right)_N &= \left\{ \left(\frac{\partial N}{\partial \mu} \right)_v \right\}^{-1} \left(\frac{\delta \rho(\mathbf{r})}{\delta \mu} \right)_v \\ \left(\frac{\delta \rho(\mathbf{r})}{\delta v(\mathbf{r}')} \right)_N &= \left\{ \left(\frac{\partial N}{\partial \mu} \right)_v \right\}^{-1} \left(\frac{\partial \rho(\mathbf{r})}{\partial \mu} \right)_v \left(\frac{\partial \rho(\mathbf{r}')}{\partial \mu} \right)_v + \left(\frac{\delta \rho(\mathbf{r})}{\delta v(\mathbf{r}')} \right)_\mu. \end{aligned} \quad (31)$$

These derivatives have been previously defined. The hardness [7],

$$\eta = \left(\frac{\partial \mu}{\partial N} \right)_v, \quad (32)$$

the softness [8],

$$S = \left(\frac{\partial N}{\partial \mu} \right)_v, \quad (33)$$

the Fukui function [9],

$$f(\mathbf{r}) \equiv \left(\frac{\partial \rho(\mathbf{r})}{\partial N} \right)_v = \left(\frac{\delta \mu}{\delta v(\mathbf{r})} \right)_N, \quad (34)$$

the local softness [8],

$$s(\mathbf{r}) \equiv \left(\frac{\partial \rho(\mathbf{r})}{\partial \mu} \right)_v = - \left(\frac{\delta N}{\delta v(\mathbf{r})} \right)_\mu, \quad (35)$$

and the linear response coefficient for the density,

$$\chi(\mathbf{r}, \mathbf{r}') \equiv \left(\frac{\delta \rho(\mathbf{r})}{\delta v(\mathbf{r}')} \right)_N, \quad (36)$$

are then related by Eq. (30). This equation becomes:

$$\begin{aligned} \eta &= 1/S \\ f(\mathbf{r}) &= s(\mathbf{r})/S \\ \chi(\mathbf{r}, \mathbf{r}') &= \frac{s(\mathbf{r})s(\mathbf{r}')}{S} + \left(\frac{\delta \rho(\mathbf{r})}{\delta v(\mathbf{r}')} \right)_\mu, \end{aligned} \quad (37)$$

and these relations are found in Refs. [8,10].

Another quantity of interest is the hardness kernel [10],

$$\tilde{\eta}(\mathbf{r}, \mathbf{r}') \equiv \frac{\delta F^{\text{HK}}[\rho]}{\delta \rho(\mathbf{r}) \delta \rho(\mathbf{r}')} . \quad (38)$$

It can be written in terms of the derivatives of the representation of $\phi[\nu, P]$, since ϕ determines ε , $E^{\text{HK}}[\rho[\nu, P]]$, and therefore F^{HK} . Some of its properties [10–12] can be also obtained with the same procedure:

$$\begin{aligned} \int \left[\int \tilde{\eta}(\mathbf{r}, \mathbf{r}') \alpha(\mathbf{r}') d\mathbf{r}' \right] f(\mathbf{r}) d\mathbf{r} &= \eta \int \alpha(\mathbf{r}) d\mathbf{r} \\ \int \tilde{\eta}(\mathbf{r}, \mathbf{r}') f(\mathbf{r}') d\mathbf{r}' &= \eta, \end{aligned} \quad (39)$$

where $\alpha(\mathbf{r})$ is an arbitrary function and the property $\int f(\mathbf{r}) d\mathbf{r} = 1$ was used. The softness kernel [10] was defined as the functional inverse of the hardness kernel:

$$\int \tilde{\eta}(\mathbf{r}, \mathbf{r}') s(\mathbf{r}', \mathbf{r}'') d\mathbf{r}' = \delta(\mathbf{r}, \mathbf{r}'') . \quad (40)$$

This equation can be solved, in terms of derivatives:

$$s(\mathbf{r}, \mathbf{r}') = \sigma f(\mathbf{r}) f(\mathbf{r}') - \chi(\mathbf{r}, \mathbf{r}') , \quad (41)$$

where

$$\sigma \equiv \int s(\mathbf{r}, \mathbf{r}') d\mathbf{r}' d\mathbf{r} , \quad (42)$$

and its value can be determined by substitution in the inverse equation, Eq. (40):

$$\sigma = \frac{1}{\eta} = S , \quad (43)$$

then

$$s(\mathbf{r}, \mathbf{r}') = S f(\mathbf{r}) f(\mathbf{r}') - \chi(\mathbf{r}, \mathbf{r}') , \quad (44)$$

and the softness kernel can be identified with $[\delta\rho(\mathbf{r})/\delta v(\mathbf{r}')]_{\mu}$ by comparison with Eq. (37).

Discussion

The energy per particle, as a functional of v and $v(\mathbf{r})$, is an alternative representation for ground states. This functional has a strict concavity with respect to its independent variables and its Legendre transformations can be defined. These functionals are also ground-state representations.

The independent variables of one of the original representations, $F[N, \rho]$, have an explicit dependence. The corresponding new functional do not present this problem.

A systematic method for the reduction of derivatives, for this kind of functionals, was described. This procedure was proved by testing some relationships between the reactivity parameters provided by Density Functional Theory.

The methodology for the reduction of derivatives presented here only involves derivatives from the four new representations, in contrast with Nalewajski's procedure [13], which involves some derivatives that do not belong to any representation.

Bibliography

- [1] R. G. Parr, R. A. Donnelly, M. Levy, and W. E. Palke, J. Chem. Phys. **68**, [8] 3801-3806 (1978).
- [2] C. E. Moore, NSRDS-NBS **34**, (1970).

- [3] E. H. Lieb, *Int. J. Quantum Chem.* **24**, 243–277 (1983).
- [4] R. F. Nalewajski and R. G. Parr, *J. Chem. Phys.* **77**, [1] 399–407 (1982).
- [5] V. I. Arnold, *Mathematical Methods of Classical Mechanics*, (Springer, New York, 1978), p. 61.
- [6] P. Hohenberg and W. Kohn, *Phys. Rev.* **B136**, [3] 864–871 (1964).
- [7] R. G. Parr and R. G. Pearson, *J. Am. Chem. Soc.* **105**, 7512–7516 (1983).
- [8] W. Yang and R. G. Parr, *Proc. Natl. Acad. Sci. USA* **82**, 6723–6726 (1985).
- [9] R. G. Parr and W. Yang, *J. Am. Chem. Soc.* **106**, 4049–4050 (1984).
- [10] M. Berkowitz and R. G. Parr, *J. Chem. Phys.* **88**, 2554–2557 (1988).
- [11] S. K. Gosh, *Chem. Phys. Lett.* **172**, [1] 77–82 (1990).
- [12] M. Berkowitz, S. K. Gosh, and R. G. Parr, *J. Am. Chem. Soc.* **107**, 6811–6814 (1985).
- [13] R. F. Nalewajski, *J. Chem. Phys.* **78**, [10] 6112–6120 (1983).

Received June 6, 1994

New Approximation to the Bound States of Schrödinger Operators with Coulomb Interaction

MARCO A. NÚÑEZ

*Departamento de Física, Universidad Autónoma Metropolitana, Iztapalapa,
A.P. 55-534, C.P. 09340 México, D.F., Mexico*

GUSTAVO IZQUIERDO B.

*Departamento de Matemáticas, Universidad Autónoma Metropolitana, Iztapalapa,
A.P. 55-534, C.P. 09340 México, D.F., Mexico*

Abstract

In this work we present a mathematical formulation of the physical fact that *the bound states of a quantum system confined into a box Ω (with impenetrable walls) are similar to those of the unconfined system, if the box Ω is sufficiently large*, and it is shown how the bound states of atomic and molecular Hamiltonians can be approximated by those of the system confined for a box Ω large enough (Dirichlet eigenproblem in Ω). Thus, a method for computing bound states is obtained which has the advantage of reducing the problem to the case of compact operators. This implies that a broad class of numerical and analytic techniques used for solving the Dirichlet problem, may be applied in full strength to obtain accurate computations of energy levels, wave functions, and other physical properties of interest. © 1994 John Wiley & Sons, Inc.

Introduction

In the past several authors have computed the bound states of Schrödinger operators imposing Dirichlet boundary conditions [1–8]. By this we mean solving by some method the time-independent Schrödinger equation corresponding to the quantum system within a box Ω with impenetrable walls (Dirichlet eigenproblem), and it has been observed that the eigenvalues and other expectation values of the confined system converge to the values of the free system as the size of the box Ω grows.

The aim of the present work is (1) to give the mathematical results that support this procedure (Theorems 3 and 4), (2) to show how these results explain some results found by other authors in particular cases, (3) discuss how to solve the Dirichlet problem by standard numerical methods (third section) and (4) to discuss some theoretical advantages of this procedure to compute bound states of atomic and molecular hamiltonians.

The mathematical results (Theorems 3 and 4) that support the convergence of the method proposed here have a simple physical interpretation, namely: *Taking a sufficiently large box Ω , the bound states of the free quantum system are slightly*

perturbed by the boundary $\partial\Omega$. Therefore, both the free and confined systems have similar bound states for large enough Ω .

The Method

Consider the eigenproblem associated with a free atom or molecule in the Bohr–Oppenheimer approximation,

$$H\psi^{(i)} = -\Delta\psi^{(i)} + q(x)\psi^{(i)} = E^{(i)}\psi^{(i)}, \quad (1)$$

with Δ the $3N$ -dimensional Laplacian, $q(x)$ the potential associated with N particles interacting with each other by Coulomb forces and $\psi^{(i)}$ one of the eigenfunctions associated to the *energy level* $E^{(i)}$.

We will show how the bound states of the free system (1) can be approximated by those of the Dirichlet eigenproblem associated with the system inside a box Ω_n with impenetrable walls $\partial\Omega_n$, or

$$H_{\Omega_n}\psi_{\Omega_n}^{(i)} = -\Delta\psi_{\Omega_n}^{(i)} + q(x)\psi_{\Omega_n}^{(i)} = E_{\Omega_n}^{(i)}\psi_{\Omega_n}^{(i)}, \quad \psi_{\Omega_n}^{(i)}(\partial\Omega_n) = 0, \quad (2)$$

as Ω_n grows in the following manner; Namely, Ω_n will be a sequence of boxes such that $\Omega_n \subset \Omega_{n+1}$ and grow to cover the whole space R^3 as $n \rightarrow \infty$.

Every box Ω_n defines an open region in the $3N$ -dimensional configuration space R^{3N} , which we denote by Ω_n with boundary $\partial\Omega_n$, abusing the notation. The operators H and H_{Ω_n} denote the self-adjoint Schrödinger operators associated with Eqs. (1) and (2) in $L_2(R^{3N})$ and $L_2(\Omega_n)$, respectively, and whose energy functionals are given by [9]

$$h(u, v) = \langle \nabla u, \nabla v \rangle + \langle qu, v \rangle \quad \text{for } u, v \in W^{1,2}(R^{3N}), \quad (3)$$

$$h_{\Omega_n}(u, v) = \langle \nabla u, \nabla v \rangle_{\Omega_n} + \langle qu, v \rangle_{\Omega_n} \quad \text{for } u, v \in W_0^{1,2}(\Omega_n), \quad (4)$$

with $\langle, \rangle, \langle, \rangle_{\Omega_n}$ the usual inner products of $L_2(R^{3N})$ and $L_2(\Omega_n)$ and the following notation is used $\langle \nabla u, \nabla v \rangle = \sum_{k=1}^{3N} \langle \partial u / \partial x_k, \partial v / \partial x_k \rangle$.

Convergence to the Energy Levels of H

Let α be the bottom of the *essential or continuous spectrum* of H . Then any element in the spectrum $\sigma(H)$ of H and below α is an isolated eigenvalue with finite multiplicity. These eigenvalues as well as those of H_{Ω_n} can be characterized with aid of the min–max principle [9].

Proposition 1. The number $\mu^{(k)}$ given by

$$\mu^{(k)} = \sup_{B_{k-1}} \inf_{B_{k-1}^\perp} \{ (h(f, f) : f \in W^{1,2}(R^{3N}), \langle f, f \rangle = 1) \} < \alpha$$

is the k th eigenvalue of H , *counting multiplicity*. In similar way, the number

$$\mu_{\Omega_n}^{(k)} = \sup_{B_{0,k-1}} \inf_{B_{\Omega_n,k-1}^\perp} \{ h_{\Omega_n}(f, f) : f \in W_0^{1,2}(\Omega_n), \langle f, f \rangle_{\Omega_n} = 1 \}$$

is the k th eigenvalue of H_{Ω_n} , *counting multiplicity*.

Remark 2. If the energy level $E^{(j)}$ of the free system has multiplicity m_j and is ordered according to $E^{(1)} < E^{(2)} < \dots < \alpha$, then the relation with the eigenvalues $\mu^{(k)}$ given by the min-max principle is

$$\mu^{(k_i)} < E^{(i)} = \mu^{(k_i+1)} = \dots = \mu^{(k_i+m_i)} < \mu^{(k_i+m_i+1)} \quad \text{with } k_i = \sum_{j=1}^{i-1} m_j,$$

and a similar result holds between the energy levels $E_{\Omega_n}^{(i)}$ and eigenvalues $\mu_n^{(k)}$ of H_{Ω_n} .

The convergence result to the eigenvalues of H is the following one.

Theorem 3 [7,8]. Let $\mu^{(k)}, \mu_{\Omega_n}^{(k)}$ be the eigenvalues of H, H_{Ω_n} given by the min-max principle. Then

$$\mu^{(k)} \leq \mu_{\Omega_{n+1}}^{(k)} \leq \mu_{\Omega_n}^{(k)} \quad \text{and} \quad \lim_{n \rightarrow \infty} \mu_{\Omega_n}^{(k)} = \mu^{(k)} \quad \text{for } k \geq 1. \quad (5)$$

If $E^{(i)} (= \mu^{(k_i+1)})$ has multiplicity m_i , $k_i = \sum_{j=1}^{i-1} m_j$, then

$$\lim_{n \rightarrow \infty} \mu_{\Omega_n}^{(k_i+j)} = E^{(i)} \quad \text{holds for } j = 1, \dots, m_i. \quad (6)$$

In particular, if $E^{(i)}$ is nondegenerate then $\{\mu_{\Omega_n}^{(k_i+1)}\}_{n=1}^{\infty}$ is the unique sequence converging to it.

Convergence to the Wave Functions of H

The quantity to verify the convergence of wave functions is the norm $\| \cdot \|$ of $L_2(R^{3N})$: $\|f\| = \langle f, f \rangle^{1/2}$.

Theorem 4 [7,8]. Let $E^{(i)}$ be an energy level of H with multiplicity m_i , and let $A_n^{(i)} = \{\mu_{\Omega_n}^{k_i+1}, \dots, \mu_{\Omega_n}^{k_i+m_i}\}$ be the set of eigenvalues of H_{Ω_n} converging to $E^{(i)}$ according Eq. (26). Then the following statements are true:

- (i) If $Q^{(i)}$ and $Q_{\Omega_n}^{(i)}$ are the orthogonal projections on the eigenspaces associated to $E^{(i)}$ and $A_n^{(i)}$, then $Q_{\Omega_n}^{(i)}$ converges in the operator's norm to $Q^{(i)}$ as $n \rightarrow \infty$.
- (ii) If $\psi^{(i)}$ and $\psi_{\Omega_n}^{(i)}$ are wave functions of the above eigenspaces, then

$$\lim_{n \rightarrow \infty} \|\psi^{(i)} - Q_{\Omega_n}^{(i)} \psi^{(i)}\| = 0 \quad \text{and} \quad \lim_{n \rightarrow \infty} \|\psi_{\Omega_n}^{(i)} - Q^{(i)} \psi_{\Omega_n}^{(i)}\| = 0, \quad (7)$$

where $\psi_{\Omega_n}^{(i)}(x) = 0$ for $x \notin \Omega_n$.

- (iii) In particular, if $E^{(i)}$ is nondegenerate and $\psi^{(i)}$ and $\psi_{\Omega_n}^{(i)}$ are normalized and have the same phase, then

$$\lim_{n \rightarrow \infty} \|\psi_{\Omega_n}^{(i)} - \psi^{(i)}\| = 0 \quad \text{and} \quad \lim_{n \rightarrow \infty} \|\nabla \psi_{\Omega_n}^{(i)} - \nabla \psi^{(i)}\| = 0. \quad (8)$$

Remark 5. By Theorems 3 and 4 the convergence of the set $A_n^{(i)}$ to $E^{(i)}$ implies the convergence of the corresponding eigenspaces. But the orthogonal projection associated to each individual eigenvalue $\mu_n^{(i)}$ of H_{Ω_n} need not be convergent [7,8].

Example: Hydrogen atom in boxes. As particular cases of above results, we have the work of Ley-Koo and coworkers [2,3], who computed the exact solutions in an increasing sequence of boxes Ω_n with different shapes for hydrogen and molecular ion H_2^+ , showing in an explicit way that *the convergence to the properties of the free system does not depend on the shape of Ω_n* , as Theorems 3 and 4 establish. We now discuss briefly the hydrogen results.

Ley-Koo and Rubinstein [2] considered the hydrogen atom inside boxes defined by pairs of confocal, coaxial and mutually intersecting paraboloidal surfaces which are open in opposite directions. Introducing the parabolic coordinates (ξ, η, φ) for the electron in terms of its usual spherical coordinates

$$\xi = r(1 - \cos \theta), \quad \eta = r(1 + \cos \theta), \quad \varphi = \varphi,$$

the shape and position of the boxes is defined by the surfaces

$$(\xi_n^0 = \text{const}, \eta, \varphi), \quad (\xi, \eta_n^0 = \text{const}, \varphi),$$

where the center of mass at the origin is the focus and ξ_n^0 and η_n^0 are the respective focal distances. By simplicity we consider symmetrical boxes $\xi_n^0 = \eta_n^0$. Therefore, *the box Ω_n limited by the paraboloidal surfaces grows as $\xi_n^0 \rightarrow \infty$* . The Dirichlet boundary conditions are given by

$$\psi_{\Omega_n}^{(1)}(\xi_n^0, \eta, \varphi) = 0, \quad \psi_{\Omega_n}^{(1)}(\xi, \eta_n^0, \varphi) = 0.$$

The wave function $\psi_{\Omega_n}^{(1)}$ was computed using functional series.

In agreement with Theorem 3, Table I shows that the energy ground state $\mu_n^{(1)}$ tends asymptotically from above to $\mu^{(1)}$ as Ω_n grows ($\xi_n^0 \rightarrow \infty$). The convergence of wave functions was verified with the calculation of the isotropic and anisotropic components of hyperfine splitting given by

$$A_{\text{iso}} = b_0 |\psi_{\Omega_n}^{(1)}(0)|^2, \quad A_{33} = b_0 \langle \psi_{\Omega_n}^{(1)} | (3z^2 - r^2) r^{-5} | \psi_{\Omega_n}^{(1)} \rangle.$$

Table I shows the convergence of these values to its values of the free system as $\xi_n^0 \rightarrow \infty$.

Ley-Koo and Cruz [3] considered the hydrogen atom inside ellipsoidal boxes. The nucleus is localized at one of the focii. Introducing prolate spheroidal coordinates for the electron in terms of its usual spherical coordinates, we have

TABLE I. Convergence of the ground state energy $\mu_n^{(1)}$, isotropic and anisotropic components of hyperfine splitting for the hydrogen atom inside symmetrical boxes with paraboloidal walls.

ξ_n^0	$\mu_n^{(1)}$	A_{iso}/b_0	A_{33}/b_0
1.4177	6.250 00	555.9673	-38.4120
3.1599	-0.250 00	115.1934	-2.6441
6.3707	-0.961 17	56.8796	-0.1307
11.5577	-0.999 60	50.8870	-0.0014

Distance ξ_n^0 are given in bohrs and energies in Ryd.

$$\xi = (r_1 + r_2)/R, \quad \eta = (r_1 - r_2)/R, \quad \varphi = \varphi,$$

with R the distance of foci and r_1, r_2 the distance of the electron from the foci. The ellipsoidal boxes are defined by $(\xi_n^0 = \text{const}, \eta, \varphi)$, and hence the box Ω_n limited by the ellipsoidal surface grows as $\xi_n^0 \rightarrow \infty$. Clearly, the boundary condition is given by $\psi_{\Omega_n}^{(i)}(\xi_n^0, \eta, \varphi) = 0$. In agreement with Theorems 3 and 4, Table II shows the convergence of the energy ground state and A_0 and A_{33}^0 of the confined system to their values of the free system.

Numerical Implementation

Apparently the approximation by confined systems replaces the original problem (1) by another one (2) whose numerical solution is as complicated as that of the original one (1). However, the Dirichlet problem in boxes has a set of properties that are crucial for the convergence and stability of standard numerical methods such as projections methods (which include the Ritz method) as well as the finite-element and finite-difference methods. These properties are due to Sobolev space $W_0^{1,2}(\Omega)$ [the domain of h_Ω , Eq. (4)] and do not occur with the domain $W^{1,2}(R^{3N})$ of h [Eq. (3)].

As is known [9,10], $W_0^{1,2}(\Omega)$ and $W^{1,2}(R^{3N})$ endowed with the inner products

$$\langle f, g \rangle_1 = \langle \nabla f, \nabla g \rangle + \langle f, g \rangle \quad \text{for } f, g \in W^{1,2}(R^{3N}),$$

$$\langle f, g \rangle_{1,\Omega} = \langle \nabla f, \nabla g \rangle_\Omega + \langle f, g \rangle_\Omega \quad \text{for } f, g \in W_0^{1,2}(\Omega),$$

are themselves Hilbert spaces. The canonical injection between the Hilbert spaces $W^{1,2}(R^{3N})$ and $L_2(R^{3N})$ is the operator i defined by

$$i: W^{1,2}(R^{3N}) \rightarrow L_2(R^{3N}): f \rightarrow if = f,$$

and, clearly, by $\|if\| \leq \|f\|_1$, i is a bounded operator. In similar way the following operator is also bounded:

$$i_\Omega: W^{1,2}(\Omega) \rightarrow L_2(\Omega): f \rightarrow i_\Omega f = f.$$

TABLE II. Convergence of the ground state energy $\mu_n^{(1)}$, isotropic and anisotropic components of hyperfine splitting for the hydrogen atom inside boxes with ellipsoidal walls.

ξ_n^0	$\mu_n^{(1)}$	A_{iso}/b_0	A_{33}^0/b_0^0
2.2298	0.05	111.2170	2.2163
3.0697	-0.75	75.2017	0.0419
5.1423	-0.99	52.8402	0.0015
7.9309	-0.999	50.7999	0.0073

Distances ξ_n^0 in bohrs and energies in Ryd.

The fundamental difference between i and i_Ω is that i_Ω is a *compact* operator, result due to the properties of $W_0^{1,2}(\Omega)$ and the *boundedness* of Ω [9,10]. This simple fact is responsible of the salient numerical properties of the Dirichlet eigenproblem (2), which we discuss briefly below.

- (1) The resolvent $R_\Omega(z) = (H_\Omega - z)^{-1}$ is a self-adjoint *compact* operator in $L_2(\Omega)$ [8,9]. Therefore, if $\{\phi_n\}_1^\infty$ is an orthonormal basis of $L_2(\Omega)$ and P_m denotes the orthogonal projection on the m -dimensional space with basis $\{\phi_n\}_1^m$, then the $m \times m$ matrix $R_\Omega(m, z) = P_m R_\Omega(z) P_m$ converges in the *operator's norm* to $R_\Omega(z)$. Hence may be proved the following result [11].

Theorem 6. Let $\mu_\Omega^{(k)}(m)$ be an eigenvalue of the $m \times m$ matrix $H_\Omega(m) = P_m H_\Omega P_m$ given by the min-max principle. Then

- (i) $\mu_\Omega^{(k)}(m)$ converges to the eigenvalue $\mu_\Omega^{(k)}$ of H_Ω as $m \rightarrow \infty$.
- (ii) If the energy level $E_\Omega^{(i)}$ of H_Ω has multiplicity m_i , then the set $A_\Omega^{(i)}(m) = \{\mu_\Omega^{(k_i+1)}(m), \dots, \mu_\Omega^{(k_i+m_i)}(m)\}$ ($m > m_i$) converge to it.
- (iii) If $Q_\Omega^{(i)}$ and $Q_\Omega^{(i)}(m)$ are the orthogonal projections on the eigenspaces of $E_\Omega^{(i)}$, $A_\Omega^{(i)}(m)$, then $Q_\Omega^{(i)}(m)$ converges to $Q_\Omega^{(i)}$ in the *operator's norm*. Furthermore, if $\psi_\Omega^{(i)}$ and $\psi_\Omega^{(i)}(m)$ are wave functions in these spaces, then

$$\lim_{m \rightarrow \infty} \|\psi_\Omega^{(i)} - Q_\Omega^{(i)}(m)\psi_\Omega^{(i)}\| = 0 \quad \text{and} \quad \lim_{m \rightarrow \infty} \|\psi_\Omega^{(i)}(m) - Q_\Omega^{(i)}\psi_\Omega^{(i)}(m)\| = 0.$$

- (2) A similar result to the above theorem can be obtained working in the space $W_0^{1,2}(\Omega)$ endowed with the inner product $\langle \cdot, \cdot \rangle_{W_\Omega}$ given by

$$\langle f, g \rangle_{W_\Omega} = h_\Omega(f, g) - \zeta \langle f, g \rangle_\Omega \quad (\zeta < E^{(1)}). \quad (9)$$

In this case the first derivatives of the wave functions also converge since they are contained in the inner product $\langle \cdot, \cdot \rangle_{W_\Omega}$ [8].

- (3) The approach by confined systems appears in a *natural* way when the schemes of finite element and finite difference are applied to the free system, since these can be only applied in bounded regions. In these methods, *compactness* arguments together with the *coerciveness* of h_Ω [Eq. (4)]

$$h_\Omega(f, f) \geq C_1 \|f\|_{1,\Omega}^2 - C_2 \|f\|_\Omega^2$$

play a crucial role in the convergence analysis [10–12].

Remark 7. Compactness properties allows us to give error estimates of approximate eigenvalues and eigenfunctions obtained from the methods mentioned above as well as to prove their numerical *stability* [10–12].

We now discuss two simple numerical examples.

Helium atom solved variationally in boxes. A simple example of computation of energy ground state for the helium was given by Marin and Cruz [4], who used the functions

$$\psi_{\Omega}^{(1)}(ar_1, ar_2) = f_{1s}(ar_1)f_{1s}(ar_2)(R - r_1)(R - r_2) \quad (10)$$

to approximate the Dirichlet wave function $\psi_{\Omega}^{(1)}$ within a sphere Ω with radius R . The function $f_{1s}(ar)$ is the 1s hydrogenic wave function of the free system and the parameter a was used to minimize the energy of the confined system. Table III shows the convergence of the energy ground state (1S) as a function of R as well as the values computed by Ludeña [1]. The slow convergence is explained by using a single base function. Now, by *compactness*, one can expect a more rapid convergence if the number of basis functions is increased. This is illustrated below.

Hydrogen atom solved by Ritz method in spheres. In Ref. [5] the Ritz method was used to compute accurate Dirichlet wave functions of the hydrogen atom within a sphere of radius R . The basis functions used in every box are given by

$$\varphi_{Rk}(a, r) = e^{-ar}(R - r)r^k, \quad k = 1, 2, 3, \dots \quad (11)$$

with a an arbitrary parameter. Table IV shows the fast convergence of energy, wave function and $\langle r^2 \rangle$ of confined hydrogen to those of the 1s state of the free system as $R \rightarrow \infty$. By *compactness*, the convergence of the Ritz method in boxes does *not* depend on a . This fact was used in Ref. [5] to optimize a in a such way that it gives the asymptotic behavior of the free system wave functions of a particular state. In Table IV we have the computation of the 2p and 3p states using this procedure. The convergence of eigenfunctions was verified using the Cauchy criterion.

Comparison with the Standard Ritz Method in $L_2(R^{3N})$

In this section some theoretical advantages of the approximation by confined systems respect to the Ritz method in $L_2(R^{3N})$ are discussed. To this end, we give a summary of the latter one.

TABLE III. Convergence of the ground state energy $\mu_n^{(1)}$ for the helium atom within a sphere of radius R_n .

R_n	a^a	$\mu_n^{(1)b}$	$\mu_n^{(1)c}$
0.5	0.7465	22.9229	22.79095
1.5	0.9339	-1.8456	-1.86422
2.5	1.1510	-2.7273	-2.76644
4.0	1.3701	-2.8302	-2.85852
6.0	1.4924	-2.8426	-2.86151

^a Parameter of functions (3.2).

Energies in Ryd and distnces in a_0 .

^b Variational calculations with a single function (10), Ref. [4].

^c SCF calculations of Ludeña [1].

TABLE IV. Convergence of energies, wave functions and the moment $\langle r^2 \rangle$ of the hydrogen atom within a sphere with radius R , toward those of the free system.

$[R, m]$	$\mu_{Rm}^{(k)}$	$\ \psi_{Rm} - \psi_{\text{exac}}\ $	$\langle r^2 \rangle$
	1s state $a = 1.0$		
[4, 4]	-0.483	0.165[0]	2.27
[11, 7]	-0.499 999 845	0.482[-3]	2.999 85
[18, 10]	-0.499 999 999 999 46	0.982[-6]	2.999 999 998 8
[25, 13]	-0.500 000 000 000 00	0.500[-7]	3.000 000 000 000
[32, 16]	Same	0.500[-8]	Same
$[R', m']$	$[R, m]$	$\ \psi_{R'm'} - \psi_{Rm}\ $	
	2p state $a = 0.5$		
[64, 13]	[84, 16]	0.635[-7]	30.000 000 000
	3d state $a = 0.333$		
[64, 12]	[84, 15]	0.378[-5]	126.000 000 000

m denotes the number of base functions (3.3) of the Ritz expansion with exponent a , and $\|, \|$ denotes the norm of $L_2(\infty)$. Atomic units are used.

According to the Ritz method, the bound states of H are approximated by those of the m -dimensional matrix $H_m = P_m H P_m$, where P_m is the orthogonal projection on an m -dimensional space with basis $\{\phi_k\}_1^m$ and $\{\phi_k\}_1^\infty$ is a complete basis of $W^{1,2}(R^{3N})$. As is known [13], with such a basis, the *nondegenerate energy levels* $E_m^{(i)}$ of H_m converge to those $E^{(i)}$ of H for $i < l$, provided that $E^{(l)}$ is the *first degenerate energy level*.

Let $\psi^{(i)}$ and $\psi_m^{(i)}$ eigenfunctions of the above *nondegenerate energy levels* $E^{(i)}$ and $E_m^{(i)}$, with their phase properly chosen. Then, the convergence of eigenvalues together with the Eckart's inequality and its generalizations,

$$\|\psi_m^{(i)} - \psi^{(i)}\| \leq \frac{E_m^{(i)} - E^{(i)}}{E^{(i+1)} - E^{(i)}}, \quad (12)$$

implies the convergence in the norm of $\psi_m^{(i)}$ to the exact one. Furthermore, from the inequality $h(f, f) + C_1 \|f\|^2 \geq C_2 \|\nabla f\|^2$ one obtains, as in Theorem 4 [Eq. (8)], that

$$\lim_{m \rightarrow \infty} \|\nabla \psi_m^{(i)} - \nabla \psi^{(i)}\| = 0.$$

In a previous section we discussed the role of the *compactness* arguments in the convergence analysis of numerical methods for solving eigenproblems. Now, a necessary condition in order to have operators with *compact* resolvent, is that their spectrum consists entirely of isolated eigenvalues with finite multiplicity [9]. Therefore, the Hamiltonian H associated with the free system does *not* has a compact resolvent $R(z) = (H - z)^{-1}$. This implies the following facts:

(1) The $m \times m$ matrices $R_m(z) = P_m R(z) P_m$ cannot converge in the operators norm to $R(z)$ [if this were the case, then $R(z)$ would be compact]. At this

point the approximation by confined systems is salient (see the paragraph above Theorem 6).

(2) Compactness arguments permits us to analyze the convergence and stability of methods for solving numerically the Dirichlet problem (2.2) (Remark 7), while the noncompactness of $R(z)$ imposes the necessity of developing new alternatives to make such analysis.

(3) The convergence of the Ritz method in $L_2(R^{3N})$ has been proved for simple states [13]. But even when the convergence to degenerate energy levels holds true, Eckart's inequality and its generalizations cannot be used to analyze the convergence of the corresponding eigenspaces, since such analysis requires a relationship between the orthogonal projections associated to the exact and approximate eigenspaces. Newly, at this point the approximation by confined systems is salient (Theorems 4 and 6). Furthermore, by working in $W_0^{1,2}(\Omega)$ endowed with the inner product (9), we can obtain information about the first derivatives of the eigenfunctions associated to degenerate states.

(4) Respect to the calculation of expectation and transition values different from the energy levels, there is an important difference between the approach by confined systems and the usual Ritz method in $L_2(R^{3N})$. Klahn and Morgan [14] showed in detail how the Ritz expansion with a Gaussian basis set for the hydrogen atom wave functions gives approximate moments which diverge or converge to a wrong limit, even when the Ritz wave functions converge correctly in the norm of $L_2(R^3)$, pointing out that the correct calculations depend on the ability of finite linear combinations to duplicate the nonanalyticities (cusps) in the exact wave function.

In boxes the calculation of expectation and transition values of a symmetric operator is quit simple. Consider, for example, the operator $S = r^k$ (with $k \geq 0$) associated with the moment $\langle r^k \rangle_\Omega$ of the one-electron density of confined system. Since S is a bounded operator in $L_2(\Omega)$, then any numerical sequence $\psi_\Omega^{(i)}(m)$ converging to $\psi_\Omega^{(i)}$ in the norm $\| \cdot \|_\Omega$ of $L_2(\Omega)$ satisfies

$$\lim_{m \rightarrow \infty} \langle \psi_\Omega^{(i)}(m), r^k \psi_\Omega^{(i)}(m) \rangle_\Omega = \langle \psi_\Omega^{(i)}, r^k \psi_\Omega^{(i)} \rangle_\Omega$$

independently on the local peculiarities of $\psi_\Omega^{(i)}$. It remains to prove that the expectation value $\langle \psi_\Omega^{(i)}, r^k \psi_\Omega^{(i)} \rangle_\Omega$ converges to that of the free system when $\psi_\Omega^{(i)}$ converges toward $\psi^{(i)}$ as Ω grows [Eq. (8)]. This result was rigorously proven in Ref. [15] for a wide class symmetric operators, including r^k with $k \geq -2$, in the 1-dimensional case, and it is intuitively obvious in several dimensions since the free and confined systems have bounded states with similar properties when Ω is large enough.

The above discussion points out the relevance that the approach through confined systems may have to compute with accuracy and certainty, the most significant quantities in quantum chemistry, avoiding technical difficulties that accompany the Ritz method in $L_2(R^{3N})$. Furthermore, it shows that numerical methods (such as the finite-element and finite-difference schemes) that have been scarcely used may be applied with positive results.

Acknowledgments

We gratefully thank Professors Eduardo Pina G. and L. S. Garcia Colin of the Universidad Autónoma Metropolitana Iztapalapa for their invaluable help and support.

Bibliography

- [1] E. V. Ludeña, J. Chem. Phys. **66**, 468 (1977). R. N. Chaudhuri and B. Mukherjee, J. Phys. **A17**, 277 (1984). J. Gorecki and B. Byers, J. Chem. Phys. **89**, 2138 (1988).
- [2] E. Ley-Koo and S. Rubinstein, J. Chem. Phys. **73**, 887 (1980).
- [3] E. Ley-Koo and S. A. Cruz, J. Chem. Phys. **74**, 4603 (1981).
- [4] J. L. Marin and S. A. Cruz, J. Phys. **B24**, 2899 (1991) and references therein.
- [5] M. A. Nuñez, Phys. Rev. **A47**, 3620 (1993).
- [6] M. A. Nuñez and G. Izquierdo, Int. J. Quantum Chem. **47**, 405 (1993).
- [7] M. A. Nuñez and G. Izquierdo, Approximation to the bound states for Schrödinger operators with Coulomb interaction, submitted.
- [8] M. A. Nuñez, Int. J. Quantum Chem. **50**, 113 (1994).
- [9] M. Reed and B. Simon, *Methods of Modern Mathematical Physics* (Academic, New York, 1978), Vol. IV.
- [10] O. A. Ladyzhenskaya, *The Boundary Value Problems of Mathematical Physics* (Springer-Verlag, New York, 1985).
- [11] M. A. Krasnosel'skii, G. M. Vainiko, et al., *Approximate Solution of Operators Equations* (Wolters-Noordhoff, Groningen, 1972), pp. 269-292.
- [12] H.-J. Reinhardt, *Analysis of Approximation Methods for Differential and Integral Equations* (Springer-Verlag, New York, 1985), Chaps. 1, 2, 8, and 9, and references therein.
- [13] B. Klahn and W. A. Bingel, Theoret. Chim. Acta (Ber.) **44**, 9 (1977).
- [14] B. Klahn and J. D. Morgan III, J. Chem. Phys. **81**, 410 (1984).
- [15] M. A. Nunez, Computation of expectation values with Dirichlet one-dimensional wave functions, Int. J. Quantum Chem., to appear.

Received May 17, 1994

On a Form of Nonlinear Dissipative Wave Mechanics Valid in Position- and Momentum-Space

DIETER SCHUCH

*Institut für Theoretische Physik, J.W. Goethe-Universität, Robert-Mayer-Str. 8-10,
60054 Frankfurt am Main, Germany*

Abstract

In wave mechanics an appropriate description of a system under the influence of a linearly velocity dependent frictional force can be given by a nonlinear Schrödinger equation (NLSE) with logarithmic nonlinearity. However, the particular logarithmic form of the dissipative nonlinear frictional term in the NLSE is connected with the definition of the momentum- or velocity-operator in position-space. Therefore, in momentum-space, this form of the NLSE is no longer correct to describe the same physical situation. This can be seen, e.g., from the fact that, in contrast to the linear case, the Fourier transform of the solution of the NLSE in position-space does not fulfill anymore the logarithmic NLSE in momentum-space. It will be shown, using results obtained from the theory in position-space, that it is possible to find a form of the nonlinear dissipative frictional term which is valid in position- as well as in momentum-space. Using this form, the NLSE looks like a diffusion equation with complex diffusion coefficient, i.e., a combination of a diffusion and a Schrödinger equation. The solution of this NLSE in momentum-space will be discussed. © 1994 John Wiley & Sons, Inc.

Introduction

Over the last few decades many approaches were introduced to describe open quantum systems, i.e., systems which dissipate mechanical energy and show an irreversible evolution in time. The variety of attempts can be divided into two main categories: they either use the system-plus-reservoir approach or modify the quantum mechanical equations of motion. Among the second category, Hamiltonians which are explicitly time-dependent [1,2] and nonlinear Schrödinger equations (NLSE) [3–7] have been proposed. Most of these approaches were criticized because they yield some dubious or even unphysical results such as stationary damped states [3,4], wrong frequencies for the damped harmonic oscillator [3–5,7] or even violation of the uncertainty principle [1,2]. However, it has been shown [8,9], that all the above-mentioned shortcomings can be overcome if time-symmetry is broken on all levels of the equations of motion. These equations are the ones determining the time-evolution of the mean-values of position and momentum (corresponding to the classical equations of motion), the wave mechanical Schrödinger equation (SE), and the equation for the related density function, thus turning a continuity equation into a Fokker–Planck-type equation. This results in a NLSE

$$i\hbar \frac{\partial}{\partial t} \Psi(\mathbf{r}, t) = \left\{ -\frac{\hbar^2}{2m} \Delta + V(\mathbf{r}) + \tilde{W}_s \right\} \Psi(\mathbf{r}, t) \quad (1)$$

with logarithmic nonlinearity in position-space. The dissipative nonlinear term

$$\tilde{W}_s = \frac{\hbar\gamma}{i} (\ln \Psi - \langle \ln \Psi \rangle) \quad (2)$$

in this equation corresponds to a linear velocity dependent frictional force.

However, the particular logarithmic form of the frictional term \tilde{W}_s is connected with the definition of the momentum- or velocity-operator in position-space. (This definition can also be used to "rederive" the NLSE [10].) This can be seen, e.g., from Schrödinger's original papers [11,12], where he used, for the canonical momentum, the definition

$$\mathbf{p}_s = \frac{\hbar}{i} \frac{\nabla \Psi}{\Psi} = \frac{\hbar}{i} \nabla \ln \Psi = m\mathbf{v}_s. \quad (3)$$

Obviously, the mean value of \mathbf{p}_s

$$\langle \mathbf{p}_s \rangle = \int \Psi^* \frac{\hbar}{i} \frac{\nabla \Psi}{\Psi} \Psi d\mathbf{r} = \int \Psi^* \frac{\hbar}{i} \nabla \Psi d\mathbf{r} = \left\langle \frac{\hbar}{i} \nabla \right\rangle = \langle \mathbf{p}_{\text{op}} \rangle, \quad (4)$$

is equivalent to the mean value of the quantum mechanical momentum-operator $\mathbf{p}_{\text{op}} = (\hbar/i)\nabla$ in position-space. In this representation the negative gradient of \tilde{W}_s has the form of a frictional force linearly proportional to the velocity \mathbf{v}_s , $-\nabla \tilde{W}_s = -\gamma m\mathbf{v}_s$.

However, in momentum-space, the momentum-operator is simply a c -number, $\mathbf{p}_{\text{op}} = \mathbf{p}$, whereas now, the position-operator is connected with the Nabla-operator in momentum-space, ∇_p , via $\mathbf{r}_{\text{op}} = -(\hbar/i)\nabla_p$. Therefore, if \tilde{W}_s is used in the same logarithmic form as in position-space, the negative momentum-space gradient of \tilde{W}_s , $-\nabla_p \tilde{W}_s$, no longer yields a frictional force which is linearly proportional to velocity (with a negative sign), as $\nabla_p \ln \Psi$ is linearly proportional to position (with a positive sign).

So, in momentum-space, this form of the NLSE is no longer correct to describe the same physical situation. This can also be seen from the fact that the Fourier-transform (FT) of the wave packet (WP) solutions in position-space are (in contrast to the linear theory) no longer solutions of the NLSE in momentum-space, if the form of \tilde{W}_s remains unchanged.

In order to find a form of the nonlinear frictional term which is valid in position- as well as in momentum-space, results obtained from the NL-theory in position-space can be used.

This new form shows similarities with another nonlinear equation which was essentially based on mathematical arguments. It can also, at least formally, be transformed into a linear differential equation.

Exact analytic Gaussian-shaped WP solutions of the NLSE in momentum-space will be given and their properties will be compared with those of the corresponding WPs in position-space.

To an Alternative Form of the Dissipative Term

Using results from the dissipative theory in position-space [10,13], new variables which contain the same information on the wave- and particle-aspects as the wave-function of the time-dependent SE can be defined. With the help of these variables it is possible to express the nonlinear dissipative term in a form which is applicable in position- and momentum-space.

Analyzing the exact analytic Gaussian WP solutions of the NLSE (discussed here for the damped harmonic oscillator (HO) in one dimension) in position-space

$$\Psi_{WP}(x,t) = N(t) \exp \left\{ i \left[y(t) \tilde{x}^2 + \frac{1}{\hbar} \langle p \rangle \tilde{x} + K(t) \right] \right\}, \quad (5)$$

where $\tilde{x} = x - \langle x \rangle = x - \eta(t)$ [the explicit form of the $N(t)$ and $K(t)$ is not relevant to the following discussion], it is found that the maximum of the WP at $x = \langle x \rangle$ (= mean value of position x) follows the classical trajectory $\langle x \rangle = \eta(t)$, which obeys the Newtonian equation

$$\ddot{\eta} + \gamma \dot{\eta} + \omega^2 \eta = 0, \quad (6)$$

thus expressing the particle aspect.

The wave aspect, connected with the finite WP-width which is proportional to the position uncertainty, $\langle \tilde{x}^2 \rangle^{1/2} = (\langle x^2 \rangle - \langle x \rangle^2)^{1/2}$, can be obtained from the imaginary part of the complex coefficient $y(t)$ via

$$y_I = \frac{1}{4\langle \tilde{x}^2 \rangle} = \frac{m}{2\hbar\alpha^2}. \quad (7)$$

The time-evolution of the WP-width is governed by the nonlinear Riccati equation for the *complex* quantity $2\hbar y(t)/m$:

$$\left(\frac{2\hbar}{m} \dot{y} \right) + \gamma \left(\frac{2\hbar}{m} y \right) + \left(\frac{2\hbar}{m} y \right)^2 + \omega^2 = 0. \quad (8)$$

Additional insight into the dynamics of the investigated system can be obtained by linearizing Eq. (8) with the help of the substitution

$$\frac{2\hbar}{m} y = \frac{\tilde{\lambda}}{\bar{\lambda}}, \quad (9)$$

introducing the new *complex* variable $\tilde{\lambda} = \tilde{u} + i\tilde{z} = \alpha \exp(i\varphi - \gamma t/2)$, to transform the nonlinear Riccati equation (8) into the linear Newtonian equation of motion

$$\ddot{\tilde{\lambda}} + \gamma \dot{\tilde{\lambda}} + \omega^2 \tilde{\lambda} = 0. \quad (10)$$

It can be shown [10,13] that in cartesian coordinates, \tilde{z} is directly proportional to the classical trajectory, $(\alpha_0 p_0/m)\tilde{z} = \langle x \rangle = \eta(t)$, thus reflecting the particle aspect, whereas in polar coordinates, the absolute value of $\tilde{\lambda}$ is proportional to $\alpha(t) = (2m\langle \tilde{x}^2 \rangle/\hbar)^{1/2}$, as defined in Eq. (7), thus reflecting the wave aspect or position-uncertainty.

The desired form of the frictional term should not explicitly depend on the potential of the problem, but somehow be connected with the velocity and/or kinetic energy of the system, as it describes a velocity dependent frictional force.

Requiring that the condition

$$\tilde{W}_s \Psi_{WP} = \tilde{W}_D \Psi_{WP} \quad (11)$$

has to be fulfilled, it is possible to express \tilde{W}_s , with the help of $\tilde{\lambda}$, in terms of the operator of kinetic energy (and its mean value):

$$\tilde{W}_D = \gamma \left(\frac{\tilde{\lambda}}{\tilde{\lambda}} \right) \frac{1}{2m} (p_{op}^2 - \langle p_{op}^2 \rangle). \quad (12)$$

This form of the frictional term is valid in position- and momentum-space. It has obviously the same property as the logarithmic nonlinearity \tilde{W}_s , namely a disappearing mean value, $\langle \tilde{W}_D \rangle = 0$. Therefore, \tilde{W}_D influences the dynamics of the observable system by altering the wavefunction, as the solution of the NLSE is different from the solution of the linear SE, although \tilde{W}_D itself is not observable. This is similar to the situation where the motion of a Brownian particle is affected by the interaction with the environment, although the motion of the surrounding molecules cannot be directly observed.

Comparison with Similar Equations

The form (12) of our dissipative nonlinearity shows similarity to an attempt by Gisin [14–19] to describe open quantum systems. This approach is based on the “assumption that quantum systems are always in a pure state, whether exchanging energy with their surrounding or not” [18]. The time-evolution of the system is supposed to be compatible with the Hilbert space structure of quantum kinematics and to preserve superpositions in a certain sense (for mathematical details see, e.g., [17,19]). It can be shown that under these conditions there exists a contractive semigroup of linear operators $W_t = e^{Zt}$ with a generator Z which can be written as

$$Z = -\frac{i}{\hbar} H - B. \quad (13)$$

However, a corresponding time-dependent SE of the form

$$\frac{\partial}{\partial t} \Psi(t) = \left\{ -\frac{i}{\hbar} H - B \right\} \Psi(t) \quad (14)$$

would have the “unpleasant feature that it does not preserve the norm of a vector, which is the usual demand for the evolution equation in quantum theory” [20]. This problem can be solved by adding the mean value of the operator B , $\langle B \rangle = \int \Psi^*(t) B \Psi(t) d\mathbf{r} / \int \Psi^*(t) \Psi(t) d\mathbf{r}$, to the rhs of Eq. (14). Then the normalized solutions $\Psi(t)$ satisfy the equation

$$i\hbar \frac{\partial}{\partial t} \Psi(t) = \left\{ H + \frac{\hbar}{i} (B - \langle B \rangle) \right\} \Psi(t), \quad (15)$$

which is, due to the introduction of the mean value $\langle B \rangle$, a *nonlinear* differential equation.

The *physical* meaning of the operator B is not specified in Eq. (15); only its mathematical properties are used. The occurrence of $\langle B \rangle$ also guarantees the property mentioned in connection with our dissipative term \tilde{W}_s (which is also valid for \tilde{W}_D), namely that the mean value of the term additional to the usual Hamiltonian H on the rhs of the NLSE disappears.

According to Sz-Nagy's theorem the contraction semigroup W_t can be dilated to a unitary evolution on a larger Hilbert space [17–19].

It was also shown that Eq. (15) may be derived using the general formalism of master equations [16]. Due to the formal similarities, the same should also apply to our NLSE.

The properties of Eq. (15) are discussed in detail in [14]; here, only the following will be mentioned:

- a) Eq. (15) conserves the norm of $\Psi(t)$;
- b) if Ψ is an eigenstate of B , then Eq. (15) reduces to the usual SE;
- c) the evolution of the mean value of the (time-independent) operator B reads:
 $(d/dt)\langle B \rangle = -2(\langle B^2 \rangle - \langle B \rangle^2) = -2(B - \langle B \rangle)^2 \leq 0$ and $(d/dt)\langle B \rangle = 0$ iff Ψ is an eigenfunction of B .

Especially for $B = kH$ this leads to

$$\frac{d}{dt}\langle H \rangle = -2k(\langle H^2 \rangle - \langle H \rangle^2) = -2k(H - \langle H \rangle)^2 \leq 0. \quad (16)$$

Of note is that up to this point k can be any function with positive valued real part in order to guarantee the decrease of energy.

Properties a) and b) are also valid for our nonlinear dissipative terms \tilde{W}_s and \tilde{W}_D . However, in our case, the *physical* meaning of the occurring operators is specified and related to some frictional force. A property similar to c) has been shown [9] to be valid also for the logarithmic dissipative term \tilde{W}_s .

For the choice $B = kH$, as shown in Gisin's case, the decrease of the mean value of energy [see Eq. (16)] would be proportional to (the square of) $H = T + V$, i.e., it would depend explicitly on the potential V . In classical mechanics, however, even for $V \neq 0$ (e.g., as for the damped HO), the energy dissipation is only proportional to the kinetic energy T according to $\dot{E}_{\text{class}} = -2\gamma T_{\text{class}}$. Therefore, a form of B which is independent of V , but related to the kinetic energy $T = p^2/2m$, seems to be reasonable. This condition, however, is fulfilled by the new form \tilde{W}_D of our NL frictional term. So, \tilde{W}_D can be considered as a kind of physically-motivated specification of Gisin's formal, mathematically-motivated approach.

Similarities with other equations can be found, if the new form \tilde{W}_D in our NLSE is considered in position-space (in the following in one dimension),

$$\tilde{W}_D = \gamma \left(\frac{\tilde{\lambda}}{\tilde{\lambda}} \right) \left(-\frac{\hbar^2}{2m} \frac{\partial^2}{\partial x^2} - \left(-\frac{\hbar^2}{2m} \frac{\partial^2}{\partial x^2} \right) \right). \quad (17)$$

The second derivative with complex coefficient can be combined with the operator of kinetic energy allowing one to write the NLSE in position-space in the form

$$\frac{\partial}{\partial t} \Psi(x,t) = \left\{ f(t) \frac{\partial^2}{\partial x^2} + \frac{1}{i\hbar} V(x) - g(t) \right\} \Psi(x,t) \quad (18)$$

with

$$f(t) = \left(1 + \gamma \frac{\tilde{\lambda}}{\lambda} \right) i \frac{\hbar}{2m} : \text{complex "diffusion coefficient"}$$

$$g(t) = \frac{\gamma}{i\hbar} \frac{\tilde{\lambda}}{\lambda} \left\langle \frac{p_{op}^2}{2m} \right\rangle : \text{nonlinearity.}$$

Formally, $g(t)$ is just a (complex) time-dependent function. However, in order to actually calculate the mean value, the solution Ψ of the NLSE has to be known.*

Considering the case $V = 0$, i.e., free motion with damping, and treating $g(t)$ formally as a mere time-dependent function, $g(t)$ can be removed from the equation via the transformation

$$\Psi(x,t) = \hat{\Psi}(x,t) \exp \left\{ - \int_0^t g(t') dt' \right\}. \quad (19)$$

The equation for $\hat{\Psi}(x,t)$,

$$\frac{\partial}{\partial t} \hat{\Psi}(x,t) - f(t) \frac{\partial^2}{\partial x^2} \hat{\Psi}(x,t) = 0 \quad (20)$$

has the form of a diffusion equation with a *complex* time-dependent diffusion coefficient $f(t)$. Keeping in mind that the SE for the free motion has the form of a diffusion equation with a purely imaginary diffusion coefficient, $i\hbar/2m$, Eq. (20) is a combination of a reversible linear SE and an irreversible diffusion equation. For both of these equations the superposition principle holds. This might explain why, for the damped free motion in position-space, our NLSE shows a kind of superposition property, as there exist plane-wave type solutions which can be superimposed to form a Gaussian WP-type solution of the NLSE [21].

Solutions in Momentum-Space

In the following, the new form (12) of our dissipative frictional term shall be considered in momentum-space and the solutions of the corresponding NLSE (here for the HO in one dimension) shall be analyzed.

Now also in our nonlinear theory, in analogy to the linear theory, the solution in momentum-space can simply be obtained by FT of the solution in position-space. So, the FT of the WP-solution (5),

* It might be possible to apply iterative techniques, e.g., as in the Hartree-Fock method.

$$\Psi_{WP}(p,t) = \left(\frac{1}{2\pi\hbar}\right)^{1/2} \int_{-\infty}^{+\infty} \Psi_{WP}(x,t) e^{-ipx/\hbar} dx, \quad (21)$$

leads to the Gaussian WP-solution in momentum-space,

$$\Psi_{WP}(p,t) = \left(\frac{a}{\hbar}\right)^{1/2} N(t) \exp\left\{i\left[\frac{ia(t)}{2\hbar^2} \tilde{p}^2 - \frac{\langle x \rangle}{\hbar} \tilde{p} + K(t) - \frac{\langle x \rangle \langle p \rangle}{\hbar}\right]\right\} \quad (22)$$

with $\tilde{p} = p - \langle p \rangle$ and $(am/i\hbar) = \tilde{\lambda}/\lambda$.

The particle aspect is again expressed by the fact that the maximum of the WP coincides with the classical momentum $\langle p \rangle = m\dot{\eta}$, where the classical trajectory $\eta = \langle x \rangle$ is determined by the Newtonian equation of motion (6).

The wave aspect, i.e., the momentum-uncertainty $\langle \tilde{p}^2 \rangle^{1/2} = (\langle p^2 \rangle - \langle p \rangle^2)^{1/2}$ or the WP-width in momentum-space, is connected with the real part of the complex coefficient $a(t)$ via

$$\frac{a_R m}{\hbar} = \frac{\hbar m}{2\langle \tilde{p}^2 \rangle}. \quad (23)$$

The time-evolution of the WP-width in momentum-space is also governed by a Riccati equation, now for the complex quantity $(am/i\hbar)$:

$$\left(\frac{\dot{am}}{i\hbar}\right) - \gamma\left(\frac{am}{i\hbar}\right) - \omega^2\left(\frac{am}{i\hbar}\right)^2 - 1 = 0. \quad (24)$$

As can be seen from the respective definitions (using the complex variables $\tilde{\lambda}$ and λ), the transition from position- to momentum-space (in order to obtain the information on the dynamics of the wave aspect) does not actually need the FT, but simply the inverse of the corresponding quantity has to be calculated, as

$$\left(\frac{am}{i\hbar}\right) = \left(\frac{2\hbar}{m} y\right)^{-1} = \frac{\tilde{\lambda}}{\lambda} \quad (25)$$

is valid.

The nonlinear complex Riccati Eq. (24) can, as well as the Riccati Eq. (8) in position-space, be linearized to the complex Newtonian Eq. (10). The connections among these equations are shown in Figure 1. Therefore, with the results obtained in this work, analytical expressions for the time-dependence of position- and momentum-uncertainty, and thus of the uncertainty product for dissipative systems, can be determined explicitly simply by solving the complex Newtonian Eq. (10) for given initial conditions.

Conclusions and Perspectives

It has been shown that it is possible to obtain a dissipative wave mechanical equation with a nonlinear dissipative term which is valid in position- and momentum-space. This form of our NLSE shows similarities to an approach by Gisin and,

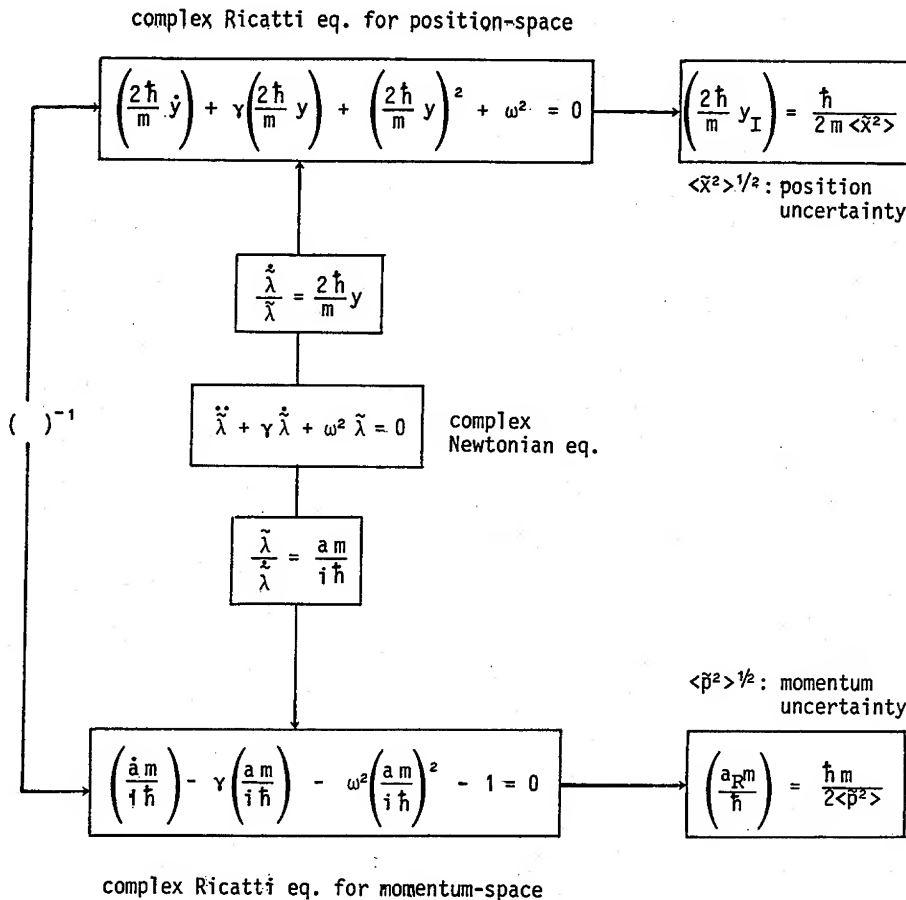


Figure 1. Connections among the equations determining the time-dependence of position- and momentum-uncertainties: The complex variable entering the nonlinear Riccati equation for the momentum uncertainty is the inverse of the corresponding variable in the Riccati equation for the position uncertainty and both are linked via the variable λ in the complex linear Newtonian equation.

for the damped free motion in position-space, it is formally a combination of a reversible SE and an irreversible diffusion equation.

The NLSE in *momentum*-space possesses exact analytic Gaussian WP solutions. The maximum of the WP obeys the classical equation of motion; the time-dependence of the WP-width is determined by a complex Riccati equation and provides the time-dependence of the momentum-uncertainty. This Riccati equation can be obtained from the corresponding Riccati equation for the position-uncertainty simply by considering the inverse variable, not needing any FT.

In a continuation of this work it shall be investigated how the equations of motion describing the wave- and particle-aspects in momentum-space are connected and

if there also exists a dynamical invariant of Ermakov–Lewis type similar to the dissipative case in position-space [10,13]. Furthermore, the question of the superposition properties of our NLSE allowing the establishment of a Green's function formalism to describe the propagation of a dissipative system in time is of interest and will be discussed in forthcoming work.

Acknowledgments

The author would like to thank R. J. Jelitto for his support of, and interest in, this work.

Bibliography

- [1] P. Caldirola, *Nuovo Cimento* **18**, 393 (1941).
- [2] E. Kanai, *Progr. Theoret. Phys.* **3**, 440 (1948).
- [3] M. D. Kostin, *J. Chem. Phys.* **57**, 3589 (1972).
- [4] M. D. Kostin, *J. Stat. Phys.* **12**, 145 (1975).
- [5] K. Albrecht, *Phys. Lett.* **B56**, 127 (1975).
- [6] R. W. Hasse, *J. Math. Phys.* **16**, 2005 (1975).
- [7] B. R. Cho, Suhak Gwa Mulri (Korean) (*Math. and Phys.*) **3**, 37 (1980).
- [8] D. Schuch, K.-M. Chung, and H. Hartmann, *J. Math. Phys.* **24**, 1652 (1983).
- [9] D. Schuch and K.-M. Chung, *Int. J. Quantum Chem.* **29**, 1561 (1986).
- [10] D. Schuch, *Int. J. Quantum Chem.* **42**, 663 (1992).
- [11] E. Schrödinger, *Ann. Phys.* **79**, 361 (1926).
- [12] E. Schrödinger, *Ann. Phys.* **79**, 734 (1926).
- [13] D. Schuch, *Int. J. Quantum Chem., Quantum Chem. Symp.* **23**, 59 (1989).
- [14] N. Gisin, *J. Phys. A: Math. Gen.* **14**, 2259 (1981).
- [15] N. Gisin, *Helv. Phys. Acta* **54**, 457 (1981).
- [16] N. Gisin, *Physica* **111A**, 364 (1982).
- [17] N. Gisin, *J. Math. Phys.* **24**, 1779 (1983).
- [18] N. Gisin, in *Quantum Probability and Applications to the Quantum Theory of Irreversible Processes*, Lecture Notes in Mathematics 1055, L. Accardi, A. Frigerio, and V. Gorini Eds. (Springer-Verlag, Berlin, Germany, 1984), p. 126.
- [19] N. Gisin, *J. Phys. A: Math. Gen.* **19**, 205 (1986).
- [20] W. Daniel, *Helv. Phys. Acta* **55**, 330 (1982).
- [21] D. Schuch, K.-M. Chung, and H. Hartmann, *J. Math. Phys.* **25**, 3086 (1984).

Received February 17, 1994

Franck–Condon Factors and Squeezed States

A. PALMA*

*Instituto Nacional de Astrofísica, Óptica y Electrónica (INAOE), Apartado Postal 51 y 216,
Tonanzintla, Puebla, Pue. 72000, Mexico*

L. SANDOVAL and M. MARTÍN

*Benemérita Universidad Autónoma de Puebla (BUAP), Instituto de Física "L.R.T.",
Apartado Postal J-48, Puebla, Pue. 72570, Mexico*

Abstract

Similarities between the Franck–Condon effect and the concept of Squeezed States have been advanced as a conjecture in the past, or noticed as a marginal fact, without giving a full explanation of how these two important concepts are connected. In this work we outline a unifying formulation that contains as special cases both phenomena. The power of the new approach is shown in a general formula from which all particular cases can be derived. © 1994 John Wiley & Sons, Inc.

Several years ago we started working the derivation of recurrence and closed formula for Franck–Condon factors through the formalism of second quantization [1]. Some authors had tried to realize this goal before us. The pioneering work of S. Koide [2] is especially worthy of mention, because he reaches a closed formulae first derived by Ansbacher [3] by means of analytic methods.

Other authors [4–8] have tried in some way to give a complete algebraic formulation for this problem. Especially important is the work of Fernández [7] and Ma and Rhodes [9], who consider the problem of time-dependent transition probabilities and obtain recurrence relations by an algebraic formulation which is in somehow similar to the one we worked some years ago [1,10,11].

In light of these efforts a unique algebraic formulation for Franck–Condon, Squeezed States, and the Young's Double Slit experiment seems to be possible. This will reveal the mathematical structure and clarify the physics which is behind these phenomena.

In this article we are going to give a common algebraic formulation for the Franck–Condon and the Squeezed States based on the approach we had worked in the past.

The essence of the Franck–Condon Effect, the Squeezed States, and perhaps the Double Slit experiment can be seen as distortions and translations from one potential well to another. This fact can be described quite well by a mapping operator

* On sabbatical leave of absence from Instituto de Física (BUAP).

$$|n\rangle_G = \hat{O}|n\rangle_E \quad (1)$$

between the states of the two wells.

The operator \hat{O} can assume different forms depending which particular case we are interested in, but the most general form which covers all particular cases is

$$\hat{O} = e^{Aa^{\dagger 2}} e^{Ba^{\dagger}} : e^{Ca^{\dagger}a} : e^{Da} e^{Ea^2} e^F \quad (2)$$

where a^{\dagger} and a are the well-known creation and annihilation boson operators. The notation $: :$ means normal order for boson operators. A particular realization of this operator for the case of the Franck-Condon Effect is given in Eq. (8) of Ref. [10].

It is possible to derive a closed formula for intensities; this can be done by means of the Cauchy relations for complex variable

$$\langle m|\hat{O}|n\rangle = \frac{(m!n!)^{1/2}}{(2\pi i)^2} \oint \oint \frac{ds}{s^{m+1}} \frac{dt}{t^{n+1}} \langle 0|\exp(sa)\hat{O}\exp(ta^{\dagger})|0\rangle \quad (3)$$

and by using the well-known creation and annihilation properties of boson operators and the integral representation of Hermite polynomials we obtain:

$$\langle m|\hat{O}|n\rangle = \mathcal{H}(m!n!)^{1/2} \sum_{k=0}^{[m,n]} M_{mnk} H_{m-k}\left(\frac{B}{2iA^{1/2}}\right) H_{n-k}\left(\frac{D}{2iE^{1/2}}\right) \quad (4)$$

where

$$M_{mnk} = \frac{e^{kC}}{k!} \frac{(iA^{1/2})^{m-k}}{(m-k)!} \frac{(iE^{1/2})^{n-k}}{(n-k)!}$$

and H_n is a Hermite polynomial of degree n and \mathcal{H} is a normalization constant. This expression is a generalization of that obtained for the first time by Ansbacher [3] for the case of Franck-Condon factors, afterwards it has been rederived by several authors [1,6]. The important thing we want to point out here is that this formula can be used in the calculation of intensities for Franck-Condon factors, Squeezed States, and perhaps the Double Slit Experiment. In other words the algebraic formulation in the present work unifies both phenomena and gives the mathematical support to the idea advanced some years ago by Wheeler, about the parallelism between these three phenomena [12].

In order to derive special cases from Eq. (4) we need to give the values of the constants appearing in it (A, B, C, D, E, F).

The squeezed states are obtained if we make the next identification

$$\begin{aligned} A &= \frac{z}{2|z|} \tanh|z|, \\ B &= \alpha - \frac{\alpha^* z}{|z|} \tanh|z|, \\ C &= \operatorname{sech}|z| - 1, \\ D &= -\alpha^* \operatorname{sech}|z|, \\ E &= -\frac{z^*}{2|z|} \tanh|z| \\ F &= \ln(\mathcal{H}) \end{aligned}$$

where the normalization constant is given by

$$\mathcal{H} = (\operatorname{sech}|z|)^{1/2} \exp\left(\frac{-|\alpha|^2}{2} - z\alpha^* \frac{\tanh|z|}{2|z|}\right)$$

where α and z are the well-known parameters appearing in the definition of the squeezed operator [13]. The case of Franck-Condon can be obtained by identifying directly Eq. (2) with Eq. (8) of Ref. [10].

In order to show the power of the present formulation we expose here the exact evaluation of the coefficients $c_n(\lambda)$ which appear in Ref. [14] in a sudden approximation description of squeezed states. For that purpose we consider the expression

$$\langle 0 | H_n(-i\gamma^* a) H_m(i\gamma a^+) | 0 \rangle = \frac{n!}{2\pi i} \frac{m!}{2\pi i} \oint \oint \frac{dt}{t^{n+1}} \frac{ds}{s^{m+1}} \langle 0 | \mathcal{F} | 0 \rangle \quad (5)$$

where

$$\mathcal{F} = f(s, t, a, a^+, \gamma) = \exp(-t^2 - 2i\gamma^* t a) \exp(-s^2 + 2i\gamma s a^+)$$

it can be easily seen that Eq. (5) is a particular case of Eq. (3). After some algebraic manipulations, this expression can be evaluated exactly, giving

$$\langle 0 | H_n(-i\gamma^* a) H_m(i\gamma a^+) | 0 \rangle = n!m! \sum_{k=0}^{[m,n]} \frac{4|\gamma|^{2k}}{k!} \frac{H_{n-k}(0)}{(n-k)!} \frac{H_{m-k}(0)}{(m-k)!}$$

where $[m, n]$ denotes the smaller of n and m , in fact this is the formula which gives the Franck-Condon overlap [15] for squeezed states with zero displacement ($\alpha = 0$).

Another particular case of our formulation is the case treated in Ref. [16], we obtain their basic Eq. (4) making the following identifications

$$n = 0, \mathcal{H} = \left[\frac{2\sqrt{s}}{s+1} \right]^{1/2} \exp\left(\frac{s\alpha^2}{s+1}\right), \quad A = \frac{1-s}{2(1+s)}, \quad B = -\frac{2s\alpha}{1+s}$$

from our Eq. (4).

In summary we have shown here that there exist a unifying algebraic formulation for the Franck-Condon Effect, the Squeezed States, and perhaps the Double Slit experiment. The parallelism between these phenomena was advanced some years ago by Wheeler [12]. We have shown here that they, at least for the FCF and SS, can be obtained as particular cases of a more general algebraic formulation. Although we have shown results only for FCF and SS, work for the case of Young's Double Slit experiment is in progress.

Acknowledgment

We acknowledge SNI-CONACYT (México) for the received fellowships.

Bibliography

- [1] A. Palma and J. Morales, *Int. J. Quantum Chem.* **S17**, 393 (1983).
- [2] S. Koide, *Z. Naturforsch. Teil A15*, 123 (1960).

- [3] F. Ansbacher, Z. Naturforsch. Teil A **14**, 889 (1959).
- [4] J. Katriel, J. Phys. B **3**, 1315, (1970).
- [5] W. Witschel, Int. J. Quantum Chem. **10**, 951 (1976).
- [6] K. Nishikawa, Int. J. Quantum Chem. **12**, 859 (1977).
- [7] F. M. Fernández, Z. Phys. **D9**, 187 (1988).
- [8] I. Ozkän, Int. J. Quantum Chem. **XXVI**, 339 (1984).
- [9] X. Ma and W. Rhodes, Phys. Rev. A **39**, 1941 (1989).
- [10] A. Palma and L. Sandoval, Int. J. Quantum Chem. **S22**, 503 (1988).
- [11] L. Sandoval, A. Palma, and J. F. Rivas, Int. J. Quantum Chem. **S23**, 183 (1989).
- [12] J. A. Wheeler, Lett. Math. Phys. **10**, 201 (1985).
- [13] D. F. Walls, Nature **306**, 141 (1983).
- [14] J. A. Bergou, M. Hillery, and D. Yu, Phys. Rev. A **43**, 515 (1991).
- [15] L. Sandoval, M. Martín, J. F. Rivas, and A. Palma, Phys. Rev. A **46**, 6095 (1992).
- [16] W. Schleich, R. J. Horowicz, and S. Varro, Phys. Rev. A **40**(12), 7405 (1989).

Received May 13, 1994

Extreme Electron Correlation Effects on the Electric Properties of Atomic Anions*

SYLVIO CANUTO

Instituto de Física, Universidade de São Paulo, CxP 20516, 01452-990 São Paulo, SP, Brazil

Abstract

The contribution of the electron correlation effects to the calculated dipole polarizability and hyperpolarizability of the first-row atomic anions is calculated and analyzed. It is shown that the total correlation contribution to the dipole hyperpolarizability is extremely large with the Hartree-Fock model accounting for only a small fraction of the accurate result. The linear and, more pronounced, the nonlinear response of atomic anions to the application of an electric field emphatically shows the effects of the correlated motion of the electrons. © 1994 John Wiley & Sons, Inc.

The static dipole polarizability is the primary response of an atomic or molecular system to the application of a weak static electric field [1]. As such it relates to a great variety of physical properties and phenomena [1,2]. In recent years with the increasing accuracy of *ab initio* many-electron calculations there has been a growing interest in calculating atomic static [3,4] and dynamic [5] dipole polarizabilities. Since the last 10 years or so one has accumulated accurate theoretical predictions of the static dipole polarizabilities of neutral ground [3–5] and excited [6] states of atoms. Generally, for neutral ground state atoms 10% of the polarizability value is due to the electron correlation effects [3,4]. It is only in more recent years, that negative ions started to receive more systematic attention [7–19]. In the large majority [7–17] these have been limited to closed-shell H^- [11,15,16], Li^- [12–14,17], and F^- [7–10] systems. The dipole polarizabilities of B^- , C^- , and O^- have recently been calculated [18]. The electron correlation effect is large and very important for these anionic systems. For the dipole hyperpolarizability of anions, very few theoretical investigations have been made [14,16,17,20]. One may add to this that experimental values for the dipole polarizabilities and hyperpolarizabilities of anions are generally not available. In fact, there is only little chance for direct measurements on the free atomic anion. It is even possible that the free atomic anion is unstable towards electron detachment as Be^- , N^- , and Ne^- , for instance [21–23]. These prompt the necessity of well-defined theoretical procedures to provide accurate numerical results and for understanding the contributing terms to the dipole polarizabilities and hyperpolarizabilities of stable atomic anions.

* This work was supported by CNPq and FAPESP (Brazil).

In this work we shall report that for some atomic anions the electron correlation contribution to the hyperpolarizability may gross to 80 or 90%. That is, the true correlated value is several times larger than the Hartree-Fock SCF value. This extreme effect is demonstrated for the stable first-row atomic anions, in special H^- , C^- , and F^- , using many-body perturbation theory (MBPT), coupled-cluster (CC), and configuration interaction (CI) models [3], within the finite-field approach [3,4] using a five-point quartic fit of the energy. All calculations were made using the Gaussian-90 program [24].

There has been some very recent interest on the electron correlation effects of H^- [11,16,22]. H^- is a particularly interesting system to analyze in more detail the role of the electron correlation effects to the dipole polarizability and hyperpolarizability. First, it is the only negative ion where the exact nonrelativistic limits, both for the energy and polarizability (but not for the hyperpolarizability) are known [25]. Second, there are no systematic analysis of the low-order correlation contributions. Third, as H^- is a two-electron system, it is amenable to a full CI (FCI) calculation thus allowing, by comparison with the exact result, to minimize basis set deficiencies and to get a clear picture of the correlation effects and the accuracy of low-order theoretical methods. Also, the dipole hyperpolarizability of H^- is still subjected to large uncertainties [16] and the precise role of the electron correlation effects are not known. We have thus first calculated the dipole polarizability and dipole hyperpolarizability of H^- . The basis set was optimized for obtaining the FCI dipole polarizability of H^- within the exact nonrelativistic limit. The final basis consists of $12s8p5d2f$ totally uncontracted gaussian-type functions. The FCI energy is only 0.22 mhartree above the exact result [25,26] and 0.39 mhartree below the previously best FCI result [22]. Another measure of the accuracy of the present results for H^- can be obtained from the calculated electron affinity value of 0.749 eV. This is better than the best basis-set-based result available (0.740 eV) [22] and comparable with the near-exact 135-term Hylleraas [25] value of 0.755 eV or the recommended exact value of 0.754 eV [27]. The calculated polarizability and hyperpolarizability of H^- are given in Table I. The SCF result for the polarizability is in sharp agreement with the exact coupled-Hartree-Fock result and it is only 44% of the FCI result. Of course, only single (S) and double (D) excitations contribute to the correlation effects in H^- . It is seen in Table I that single excitations are crucial. The indirect contribution of single excitations (obtained from the difference of FCI and CID) is higher than the direct contribution of double excitations (obtained from the difference of CID and SCF). This is perhaps the first example where the contribution of single excitations to the dipole polarizability is higher than the double excitations contribution. As a consequence, the partial inclusion of single excitations contribution gives only poor results compared to the FCI limit.

The situation is more dramatic for the dipole hyperpolarizability. Previous calculations for the dipole hyperpolarizability of H^- include an early uncoupled Hartree-Fock value of 8.0×10^6 a.u. [28] which is nearly twice our SCF (with coupled Hartree-Fock quality) value of 4.37×10^6 a.u. Previous correlated calculations were performed by using variation-perturbation theory with Hylleraas-type functions, but were considered unreliable by the authors [20]. Indeed their

TABLE I. The calculated dipole polarizability and hyperpolarizability of H^- with different electron correlation contributions. Basis set is $12s\ 8p\ 5d\ 2f$.

Method	Polarizability (a.u)	Hyperpolarizability (10^6 a.u)
SCF	91.39	4.37
MBPT (2)	124.48	11.25
MBPT (3)	136.46	12.04
D-MBPT (4)	143.50	13.18
SD-MBPT (4)	147.73	14.84
CID	146.20	12.79
CCD	146.20	12.79
CCD + S (4)	150.43	14.45
CCD + S (CCD)	160.21	16.59
FCI	208.30	54.29
MCSCF-LR ^a	217.0	
MEMPT ^b	201.8	76.0
Exact ^c	206.39 ± 2.45	

^a Multiconfigurational self-consistent-field linear response value of Fowler, Jorgensen, and Olsen [11].

^b Many-electron many-photon theory results of Nicolaides, Mercouris, and Piangos [16].

^c 135-term Hylleraas-type result of Glover and Weinhold [25].

value of 17.0×10^6 a.u. is too small. A recent calculation [16] has given the more acceptable value of 76.0×10^6 a.u. Our best calculated value is 54.3×10^6 a.u. It is remarkable to see that the SCF model accounts for less than 10% of the exact result. It is also striking to see that the indirect contribution of single excitations is responsible for about 76% of the total dipole hyperpolarizability of H^- . A complete double-excitation calculation obtained either from CCD or CID will give only about 24% of the exact value—an extremely poor performance.

The situation for the other stable atomic anions is also interesting. Li^- shows an unusual near-degeneracy [12,13] in the ground state, which is even more acute than the classical Be case. Correlation effects are found to be very large for the dipole polarizability and hyperpolarizability of Li^- [12–14]. The other stable anions of the first-row present similar extreme correlation contribution. The polarizability of F^- was studied by several investigators [7–10] with results limited to the MBPT(4) level or to very limited inclusion of triple excitations. It is clear that high order single and triple excitations are necessary for an accurate description of the dipole polarizability of F^- . As this seems to have not been considered before we have first calculated the dipole polarizability of F^- using highly correlated methods, including QCISD(T) [29] which is known to be very accurate even for difficult systems. The results obtained with a large uncontracted basis set ($14s9p6d2f$) are displayed in Table II and clearly show that MBPT(4) is not enough to give accurate estimates of the dipole polarizability and hyperpolarizability of F^- . The result of 18.0 a.u. for the dipole polarizability of F^- should be the best result now available. Table II

TABLE II. The calculated dipole polarizability and hyperpolarizability of F^- with different electron correlation contributions. Basis set is $14s9p6d2f$. Correlated finite field energies are accurate within nine decimal figures to give an estimated numerical error of 0.005×10^6 a.u. for the hyperpolarizabilities. SCF energies are correct within 10 decimal figures.

Method	Polarizability (a.u)	Hyperpolarizability (10^6 a.u)
SCF	10.91	0.009
MBPT (2)	17.19	0.022
MBPT (3)	12.86	0.010
DQ-MBPT (4)	14.36	0.014
SDQ-MBPT (4)	17.47	0.026
MBPT (4)	21.05	0.044
CCD	14.03	0.012
CCD + ST (4)	20.72	0.041
QCISD	18.01	0.048
QCISD (T)	17.96	0.058

also shows the calculated hyperpolarizability of F^- . No previous high-order calculations were found in the literature. Our results indicate that the SCF value is only 15% of the best calculated result. Thus the correlation contribution to the hyperpolarizability of F^- is about 85%. The actual correlated result is thus nearly seven times larger than the Hartree-Fock model implies.

The extreme correlation contribution to the hyperpolarizability of atomic anions may be exemplified again in $C^-(^4S)$. The dipole polarizability of C^- has been reported recently [18], but there is no previous studies of its hyperpolarizability. Again a large uncontracted basis set, $14s9p6d2f$, was used to compute its polarizability and hyperpolarizability using the high-order QCISD(T) correlated scheme [29]. The results of our calculation (with all electrons included) for the dipole polarizability and hyperpolarizability of C^- are given in Table III. For the dipole polarizability, the SCF value is about 60% of the best correlated result and the inclusion of high-order single and triple excitations are very important. For the hyperpolarizability, the Hartree-Fock model accounts for only about 23% of the QCISD(T) value with an extreme contribution of the electron correlation effects of about 77%. In other words, the true correlated value for the dipole hyperpolarizability of C^- is about four times larger than that obtained at the uncorrelated SCF level. The inclusion of all electrons (core and valence) in the correlated calculations is important to obtain absolute values for the polarizability and hyperpolarizability, but the qualitative aspects regarding the extreme correlation contributions are obtained already at the frozen core level.

Summarizing, high-order single and triple excitations give important contributions to the dipole polarizability and hyperpolarizability of the stable first-row atomic anions. For H^- we show that the indirect contribution of single excitations is larger than the direct contribution of double excitations to the dipole polarizability. For the dipole hyperpolarizability, electron correlation effects are extreme and account

TABLE III. The calculated dipole polarizability and hyperpolarizability of C^- with different electron correlation contributions. Basis set is $14s9p6d2f$.

Method	Polarizability (a.u)	Hyperpolarizability (10^6 a.u)
SCF	50.13	0.61
MBPT (2)	65.89	1.28
MBPT (3)	65.04	1.22
DQ-MBPT (4)	63.31	1.14
SDQ-MBPT (4)	66.06	1.30
MBPT (4)	71.02	1.53
CCD	63.26	1.14
CCD + ST (4)	70.98	1.53
CCD + ST (CCD)	69.94	1.48
QCISD	74.92	2.22
QCISD (T)	81.55	2.63

for more than 90% of the full CI result, more than 75% coming from the interaction of single and double excitations. The full CI value for the dipole polarizability is 208.3 a.u as compared to the exact nonrelativistic limit of 206.4 ± 2.5 a.u. For the dipole hyperpolarizability this limit is not known and our full CI result is 54.3×10^6 a.u. For C^- and F^- , the Hartree-Fock treatment gives only about 25 and 15%, respectively, of the best correlated values for the dipole hyperpolarizabilities, with about 75 and 85% being due to the detailed correlated motion of the electrons. Our best value for the dipole hyperpolarizability of C^- is 2.63×10^6 a.u and for F^- it is 0.06×10^6 a.u obtained using the highly correlated QCISD(T) theoretical scheme. These extreme correlation effects should be considered in any theoretical treatment of the electric properties of atomic anions. To the application of an electric field, atomic anions respond linearly, and more markedly nonlinearly, with a highly correlated motion of the electrons.

Bibliography

- [1] A. Dalgarno, Adv. Phys. **11**, 281 (1962); A. D. Buckingham, Adv. Chem. Phys. **12**, 107 (1967); T. M. Miller and B. Bederson, Adv. Mol. Phys. **13**, 1 (1977).
- [2] N. F. Lane, Rev. Mod. Phys. **52**, 29 (1980); F. A. Gianturco and A. Jain, Phys. Rep **143**, 347 (1986); Y. R. Shen, *Principles of Nonlinear Optics* (Wiley, New York, 1984); H. A. Szymanski, *Raman Spectroscopy* (Plenum Press, New York, 1967); M. A. Castro and S. Canuto, J. Phys. B (in press) (1993).
- [3] M. Urban, I. Cernusak, V. Kellö, and J. Noga, *Methods in Computational Chemistry*, S. Wilson, Ed. (Plenum Press, New York, 1987), Vol. 1, p. 117; C. E. Dykstra, *Ab Initio Calculation of the Structures and Properties of Molecules* (Elsevier, Amsterdam, 1988); R. J. Bartlett, J. Phys. Chem. **93**, 1697 (1989).
- [4] I. Cernusak, G. H. F. Dierksen, and A. J. Sadlej, Phys. Rev. A **33**, 814 (1986); H. J. Werner and W. Meyer, Phys. Rev. A **13**, 13 (1976); V. Kellö, A. J. Sadlej, and K. Faegri Jr, Phys. Rev. A **47**, 1715 (1993); E. F. Archibong and A. J. Thakkar, Phys. Rev. A **44**, 5478 (1991); M. A. Castro and S. Canuto, Phys. Lett. A **176**, 105 (1993).
- [5] T. K. Ghosh, A. K. Das, M. A. Castro, S. Canuto, and P. K. Mukherjee, Phys. Rev. A **48**, 2826 (1993); H. P. Saha, Phys. Rev. A **47**, 2865 (1993).

- [6] K. Anderson and A. Sadlej, *Phys. Rev. A* **46**, 2356 (1992); C. A. Nicolaides and Th. Mercouris, *Phys. Rev. A* **44**, 7827 (1991).
- [7] C. Nelín, B. O. Roos, A. Sadlej, and P. E. M. Siegbahn, *J. Chem. Phys.* **77**, 3607 (1982); G. H. F. Diercksen and A. J. Sadlej, *Mol. Phys.* **47**, 33 (1982); A. Sadlej, *J. Phys. Chem.* **83**, 1653 (1979).
- [8] S. A. Kucharski, Y. S. Lee, G. D. Purvis III, and R. J. Bartlett, *Phys. Rev. A* **29**, 1619 (1984).
- [9] G. H. F. Diercksen and A. J. Sadlej, *Mol. Phys.* **59**, 889 (1986).
- [10] L. Adamowicz, R. J. Bartlett, and A. J. Sadlej, *J. Chem. Phys.* **88**, 5749 (1988).
- [11] P. W. Fowler, P. Jorgensen, and J. Olsen, *J. Chem. Phys.* **93**, 7256 (1990).
- [12] S. Canuto, W. Duch, J. Geertsen, F. Müller-Plathe, J. Oddershede, and G. E. Scuseria, *Chem. Phys. Lett.* **147**, 435 (1988).
- [13] H. Ågren, J. Olsen, H. J. A. Jensen, and P. Jorgensen, *Phys. Rev. A* **40**, 2265 (1989).
- [14] E. F. Archibong and A. J. Thakkar, *Chem. Phys. Lett.* **173**, 579 (1990).
- [15] P. W. Fowler and P. A. Madden, *Phys. Rev. B* **29**, 1035 (1984).
- [16] C. A. Nicolaides, Th. Mercouris, and N. A. Piangos, *J. Phys. B* **23**, L669 (1990).
- [17] C. A. Nicolaides, Th. Mercouris, and G. Aspromallis, *J. Opt. Soc. Am. B* **7**, 494 (1990).
- [18] S. Canuto, M. A. Castro, and P. K. Mukherjee, *Phys. Rev. A* (in press).
- [19] A. K. Das, D. Ray, and P. K. Mukherjee, *Theoret. Chim. Acta* **82**, 223 (1992).
- [20] M. N. Grasso, K. T. Chung, and R. P. Hurst, *Phys. Rev.* **167**, 1 (1968).
- [21] K. Raghavachari, *J. Chem. Phys.* **82**, 4142 (1985).
- [22] R. A. Kendall, T. H. Dunning, Jr., and R. J. Harrison, *J. Chem. Phys.* **96**, 6796 (1992).
- [23] C. Y. Tang, J. R. Wood, D. J. Pegg, J. Dellwo, and G. D. Alton, *Phys. Rev. A* **48**, 1983 (1993).
- [24] GAUSSIAN 90, Revision F, M. J. Frisch, M. Head-Gordon, G. W. Trucks, J. B. Foresman, H. B. Schlegel, K. Raghavachari, M. Robb, J. S. Binkley, C. Gonzalez, D. J. Defrees, D. J. Fox, R. A. Whiteside, R. Seeger, C. F. Melius, J. Baker, R. L. Martin, L. R. Kahn, J. J. P. Stewart, S. Topiol, and J. A. Pople, Gaussian, Inc., Pittsburgh PA, 1990.
- [25] R. M. Glover and F. Weinhold, *J. Chem. Phys.* **65**, 4913 (1976).
- [26] K. Frankowski and C. L. Pekeris, *Phys. Rev.* **146**, 46 (1966).
- [27] H. Hotop and W. C. Lineberger, *J. Phys. Chem. Ref. Data* **14**, 731 (1985).
- [28] P. W. Langhoff, J. D. Lyons, and R. P. Hurst, *Phys. Rev.* **148**, 18 (1966).
- [29] K. Raghavachari, G. W. Trucks, J. A. Pople, and M. Head-Gordon, *Chem. Phys. Lett.* **157**, 479 (1989); K. Raghavachari, *Ann. Rev. Phys. Chem.* **42**, 615 (1991).

Received March 2, 1994

Effects of the Finite Duration of Quantum Tunneling in Laser-Assisted Scanning Tunneling Microscopy

MARK J. HAGMANN

*Department of Electrical and Computer Engineering, Florida International University,
Miami, Florida 33199*

Abstract

Previous measurements of tunnel conductance in heterostructures and experiments with Josephson junctions suggest quantum tunneling has a definite duration. We use semiclassical methods to determine the effects of this delay on the tunneling current in a laser-assisted STM. A planar-planar STM model is used with the exact multiple image potential, and the energy distribution for a free-electron metal. It is necessary to average over the phase at barrier entry, and iteration with back propagated solutions is required to obtain the transmission coefficients for evenly spaced phases and specified energies at barrier entry. The simulations suggest that the dependence of the tunneling current on the wavelength of illumination can serve as a basis for determining the duration of barrier traversal. A power flux density of 10^{11} W/m² would be required at several wavelengths from 1 to 10 μ m. It is possible that thermal effects could be separated from the modeled phenomena by determining the time dependence of the tunneling current with a pulsed laser. © 1994 John Wiley & Sons, Inc.

Introduction

The duration of quantum tunneling is a topic that has generated much interest and controversy (for reviews, see [1]). Experiments with heterostructures [2] and Josephson junctions [3] suggest that a specific time is associated with barrier traversal. A variety of methods have been considered for calculating the duration of quantum tunneling, but their results do not agree [1].

The duration of quantum tunneling has practical significance. For example, measurements of tunnel conductance in heterostructures differ from theory by as much as 2 orders of magnitude unless the image corrections are adjusted to allow for the traversal time [2]. Tunneling also occurs in the ohmic contacts of most solid state devices [4], but the traversal time is probably on the order of 10 fs so that it may generally be ignored. However, we anticipate that delays from quantum tunneling will have to be considered as progress continues in picosecond switching, terahertz technology, and femtosecond optical pulses [5]. At high energies it is necessary to include tunneling through the reaction barrier in transition state theory in order to obtain accurate quantal microcanonical rate constants [6]. Thus, it appears that the accuracy of models of chemical reactivity would be increased by

correcting for delays from barrier penetration in addition to the well-known delays associated with passage over the barrier [7].

Laser-assisted scanning tunneling microscopy, utilizing the effects of laser radiation impinging on the gap between the tip and the sample in a scanning tunneling microscope (STM), has shown promise for obtaining improved resolution, and has been considered for use in imaging insulators [8]. The STM is extremely sensitive to radiation, and has been used as a detector to record absorption or fluorescence in laser spectroscopy [9].

An experimental value of operational tunneling time has been reported that is based on measurements of current rectification in a laser-illuminated STM [10]. However, the observed decrease in current with increasing barrier length is similar to the dependence of transmission on the barrier length, so that it appears that the data may be explained without reference to tunneling times. It is the objective of the present paper to examine the effects of the finite duration of quantum tunneling in laser-assisted scanning tunneling microscopy in order to determine if there are phenomena that could be used as a basis for experimentally determining the duration of quantum tunneling.

Method of Analysis

We model tunneling [11] as a "climb over the barrier" during energy fluctuations consistent with the uncertainty principle. Cohen postulated [12] that the probability of such fluctuations decreases exponentially with the product of their magnitude and duration, which product we refer to as the action of a fluctuation, and showed that this assumption leads to the WKB solution for an opaque barrier. Cohen did not consider the duration of tunneling, but we have shown [11] that his postulate results in the semiclassical traversal time which is given by

$$T_{sc} = \int_0^d \sqrt{\frac{m}{2[V(z) - E]}} dz, \quad (1)$$

where m and E are the mass and energy of the particle and the barrier has height $V(z)$ over the interval $0 < z < d$. We follow the convention of calling this time "semiclassical" because it is the classical time for traversing the inverted barrier [13].

While the result is not unanimous, 11 other methods of analysis, in addition to considerations of energy fluctuations, also result in the semiclassical expression for the traversal time. These procedures include (1) barrier modulation [13,14], (2) modulating the incident wave [15], (3) solutions for a sharp wave packet [16], (4) flux-flux correlation [17], (5) dissipation by a string [18], (6) dynamics of image potentials [19], (7) temperature effects in macroscopic tunneling [20], (8) "bounce" time for macroscopic tunneling [21], (9) distributions of momentum [22], (10) duality with ray optics [23], and (11) calculations with path integrals [24]. Analyses based on measurements of the tunnel conductance in heterostructures [2] are also consistent with the semiclassical expression for the traversal time.

Various approximations have been used in modeling the potential barrier of an STM. For example, Miskovsky et al. [25,26] used numerical methods to solve the one-dimensional Schrödinger equation for hyperboloidal-planar and planar-planar models of the metal electrodes with exact multiple image corrections for the transiting electrons. They also tested an approximation used earlier by Simmons [27] for the image corrections with planar-planar models. Garcia [28] made calculations for planar-planar and hemispherical-planar models, as well as for the approximation of a square potential barrier. To avoid being restricted to electrode shapes for which analytical solutions for the potential are known, Bar'yudin et al. [29] used numerical methods to calculate the potential when the tip electrode was represented by a cone with a smoothed vertex. However, it appears that they did not make image corrections for the transiting electrons. Previous to the work in the present paper, as a first approximation we [30] used a square potential barrier and neglected image corrections for the transiting electrons.

Miskovsky et al. [25,26] found little difference between the values of the potential with hyperboloidal-planar and planar-planar models of the metal electrodes in an STM when using exact multiple image corrections for the transiting electrons. There is a slight asymmetry in the hyperboloidal-planar barrier which is only significant when calculating current rectification, a phenomenon which would not occur without asymmetry. Since none of the models correspond to the actual shapes of the electrodes in an STM, for simplicity we have chosen to use the planar-planar model in the present work.

The exact multiple image correction to the potential barrier for a planar-planar model [25,27,31] is given by

$$V_I(z) = -\frac{e^2}{8\pi\epsilon_0} \left[\frac{1}{2z} + \sum_{n=1}^{\infty} \left(\frac{ns}{(ns)^2 - z^2} - \frac{1}{ns} \right) \right], \quad (2)$$

where e is the magnitude of the electron charge, z is the coordinate of the transiting electron, and the two image planes are located at $z = 0$ and $z = s$, respectively. Miskovsky et al. [25] found that the values of potential for planar-planar models of an STM are typically within 2% of those for hyperboloidal-planar models when exact multiple image corrections are used. However, when only the first few terms of the infinite series in Eq. (2) are used there are errors of 40–50%, and errors of 10–15% occur using the Simmons approximation for the series. Other approximations to the infinite series have also been suggested [32]. In computations we use the following expression in which the part of the summation for $n > N - 1$ is approximated by an integral:

$$V_I(z) = -\frac{e^2}{8\pi\epsilon_0} \left[\frac{1}{2z} + \sum_{n=1}^{N-1} \left(\frac{ns}{(ns)^2 - z^2} - \frac{1}{ns} \right) - \frac{1}{2S} \ln \left(1 - \frac{z^2}{N^2 S^2} \right) \right]. \quad (3)$$

Six-place accuracy is obtained using Eq. (3) with $N = 7$, whereas 79 terms are required in order to obtain the same accuracy with Eq. (2).

We use a free electron model for the tip and sample electrodes, and define the potential as zero for $z < z_T$ which corresponds to the tip. For $z > z_s$, which corresponds to the sample electrode, the potential is given by $\epsilon_{FT} - \epsilon_{FS} - eV_0$ where ϵ_{FT} and ϵ_{FS} are the Fermi energy of the tip and the sample, respectively, and V_0 is the applied potential difference. In the gap between the two electrodes, for which $z_T < z < z_s$, the potential is given by

$$V(z) = \epsilon_{FT} + \phi_T + (z/s)[\epsilon_{FS} + \phi_S - \epsilon_{FT} - \phi_T - eV_0] + V_I(z), \quad (4)$$

where ϕ_T and ϕ_S are the work functions of the tip and the sample, respectively, and $V_I(z)$ is the image correction specified in Eq. (2). The trapezoidal portion of the barrier, which is added to the image potential in Eq. (4), is probably appropriate for distances greater than 0.3 nm from flat metal surfaces [33]. The detailed shape of the barrier at smaller distances, which depends on the particular metal surface, is not considered in the present analysis. The values of z_T and z_s are determined algebraically by setting $V(z)$ in Eq. (4) equal to the specified values of the potential within the two electrodes. The value of z_T is slightly greater than zero, and the value of z_s is slightly less than s , so that the two image planes are just below the surfaces of the metal electrodes.

The transmission coefficient is calculated by approximating the potential from Eq. (4) with a sequence of segments that are flat barriers and/or wells [34]. We begin by assuming that there is a transmitted wave with unit amplitude, but no incident wave, at $z = z_s$. Then the wave is backpropagated, by sequentially determining the incident and reflected waves at the near side of each barrier segment, until the amplitudes of the incident and reflected waves are found at $z = z_T$. Since the transmitted wave is required to have unit amplitude, the transmission coefficient is the reciprocal of the square of the magnitude of the incident wave at $z = z_T$. After thus calculating the forward current, this procedure is repeated to determine the transmission coefficient for the return current due to electrons flowing from the sample to the tip.

In modeling the effects of a laser, we assume that each barrier segment is traversed in the semiclassical time (or the classical time where the energy exceeds the potential). The energy of the electron is updated at each step of back propagation in calculating the transmission coefficient in order to allow for interaction with the electric field of light. Both the change in energy during transit of the barrier and the traversal time depend on the phase on entering the barrier. It is necessary to average the values of the transmission coefficient for a large number of evenly spaced phases at barrier entry for each specified value of energy in order to determine the mean values of the forward and reverse current. Iteration with the back propagated solutions is required in order to obtain each of the averaged values of the transmission coefficient since each must correspond to a specified value of particle energy and phase on entering the barrier.

The magnitude of the forward or return current density is given by the product of the electronic charge and the number of electrons per unit area per unit time,

$$J(F, T) = e \int_0^\infty D(F, E) N(E, T) dE, \quad (5)$$

where $D(F, E)$ is the transmission coefficient and $N(E, T) dE$ is the number of electrons with normal energy between E and $E + dE$ impinging on the surface from within the metal. Following the free-electron theory of metals [33], and assuming that $N(E, T)$ is given by the equilibrium value, we set

$$N(E, T) = \frac{mk_B T}{2\pi^2 \hbar^3} \ln \left[1 + \exp \left(- \frac{E - \epsilon_F}{k_B T} \right) \right], \quad (6)$$

where m is the electron mass, k_B is Boltzmann's constant, T is the temperature, and \hbar is Planck's constant. The Fermi energy ϵ_F is set equal to ϵ_T for the forward current and ϵ_S when determining the return current.

We use Eq. (5) to determine the forward and return current density at specified values of the applied potential, temperature, and the wavelength and power flux density of the laser. The integral in Eq. (5) is approximated by a sum over a series of evenly spaced energies that are chosen so that the values of current density at the ends of the interval are less than 0.1% of the maximum. The increment of energy is typically 0.05 eV. A total of 1500 barrier intervals is typically required in the calculations. Time-averaged values of the current density are determined using the results for a minimum of 100 evenly spaced phases at barrier entry. The results of simulations are presented in the following section of this paper.

Results of Analysis

Figures 1 and 2 illustrate some of the phenomena which occur in an STM without illumination by a laser. These two figures show the ratio of the return current to the forward current, and the net tunneling current, as a function of the applied bias potential V_0 . Since a planar-planar model was used, and both electrodes were assumed to have the same characteristics (tungsten with $\phi = 4.5$ eV at 20°C), there is no asymmetry so that the return current equals the forward current for a net tunneling current of zero when there is no applied bias.

The length of the gap between the tip and the sample is 10 Å in Figure 1 and 15 Å in Figure 2. In Figure 1 it may be seen that the tunneling current increases linearly with the applied bias when the gap length is 10 Å. The tunneling junction has an electrical resistance of approximately 3 MΩ with this relatively short gap length. In Figure 2 it may be seen that, except for very low values of the applied bias, the tunneling current increases exponentially with the bias when the gap length has the relatively large value of 15 Å. These observations may be understood by considering the behavior of the WKB approximation for the transmission coefficients. The net tunneling current, which is the difference between the forward and reverse currents, may be approximated by an integral of the difference between two exponentials. For small values of the gap length, or for sufficiently small values of the applied bias with a gap having arbitrary length, the difference between the two

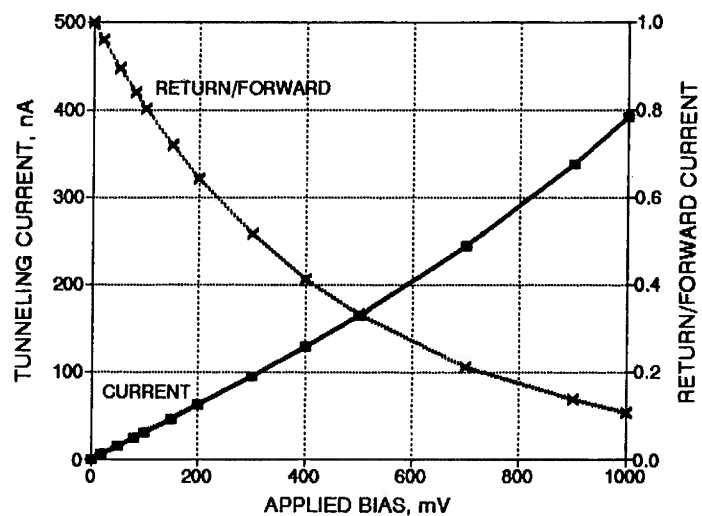


Figure 1. Ratio of the return current to the forward current, and the net tunneling current, as a function of the applied bias for an STM with a tungsten tip and sample at 20°C and a gap length of 10 Å.

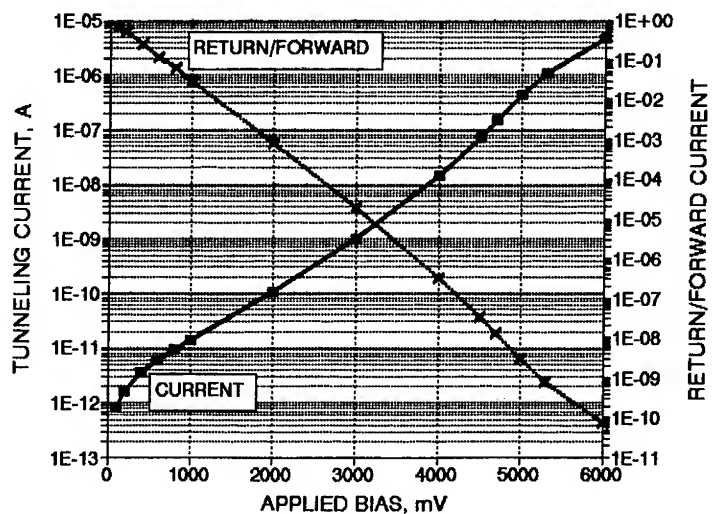


Figure 2. Ratio of the return current to the forward current, and the net tunneling current, as a function of the applied bias for an STM with a tungsten tip and sample at 20°C and a gap length of 15 Å.

exponential terms is small. Thus, by expanding the difference between the two terms, it may be seen that the tunneling current is approximately proportional to the applied bias. However, for relatively large values of the gap length, the exponential term representing the return current may be neglected, so that the tunneling current varies exponentially with the applied bias. There is a significant difference in the energy distributions of the tunneling electrons for the two gap lengths used in Figures 1 and 2. Lower energy electrons may cross the barrier in the forward and return currents with 10 Å than with the longer gap length of 15 Å.

Figure 3 shows the tunneling current as a function of the applied bias and the length of the gap in a planar-planar model of an STM. As in the two previous figures, the calculations were made for a tungsten tip and sample at 20°C, assuming there is no illumination by a laser. It may be seen in Figure 3 that, for small values of the applied bias, the tunneling current decreases by approximately a factor of 10 for each increase in the gap length by 1 Å, which agrees with experiments [35]. However, the slope is decreased for larger values of the applied bias. This change in slope is consistent with the observation that the tunneling current varies more rapidly with the applied bias as the gap length is increased, noted previously when comparing Figures 1 and 2.

The simulations described in the remainder of this section include illumination by a laser. As the electrons interact with the electric field of light, the periodic nature of that field serves as a clock for the motion of the particles. Thus, unlike the simulations described earlier, specific effects will be seen that are caused by the finite duration of quantum tunneling.

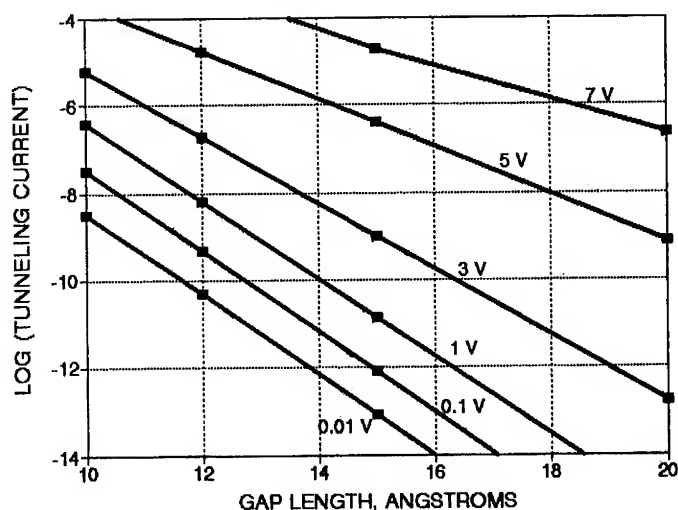


Figure 3. Tunneling current as a function of the applied bias and the length of the gap for an STM with a tungsten tip and sample at 20°C.

Figure 4 shows the effect of the applied bias and the length of the gap on the ratio of the tunneling current with illumination by a laser to the current without the laser. The calculations were made for a tungsten tip and sample at 20°C, assuming a power flux density of 10^{11} W/m² at a wavelength of 10 μ m. Analyses suggest [36] that illumination with such a large value of power flux density would cause significant heating of the tip in an STM, thus increasing emission from the tip. This conclusion is supported by analyses and experiments [37,38] made previously for laser-illuminated field emission. Nevertheless, it was necessary to use a power flux density of 10^{11} W/m² in the simulations in order to obtain significant effects. For a power flux density of 10^{11} W/m² the electric field intensity has a magnitude of 8.68 MV/m rms, so that the change in energy of the transiting electrons over the short distance between the tip and the sample is on the order of milli-electron volts.

It may be seen in Figure 4 that, for constant applied bias, the effect of the laser on the tunneling current increases with the length of the gap. This may be understood because increasing the gap length increases the total distance for interaction of the electrons with the electric field of light. For a constant gap length and small values of the applied bias, the increase in the tunneling current due to the laser increases with the bias. This may be understood because increasing the bias decreases the contribution to the current by electrons with energies well below the Fermi level, and we have found that the effect of the laser is less pronounced at the lower energies. However, the increase in tunneling current is less pronounced for large values of the bias, which we attribute to increased dominance by the static field

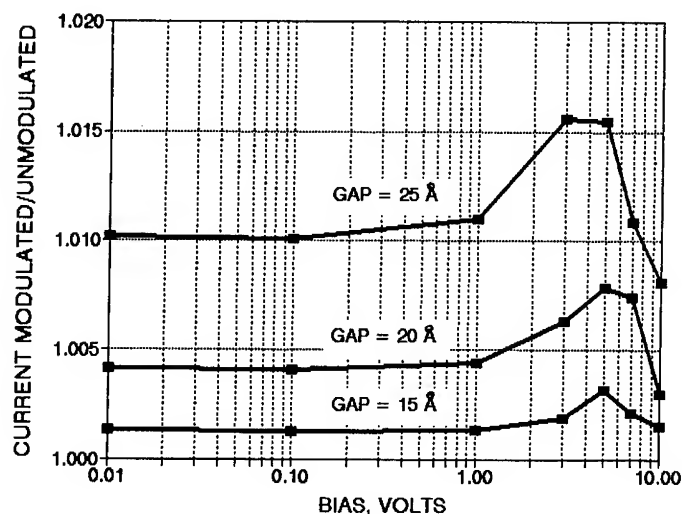


Figure 4. Increase in tunneling current due to illumination as a function of the applied bias and the length of the gap for an STM with a tungsten tip and sample at 20°C with a power flux density of 10^{11} W/m² at a wavelength of 10 μ m.

rather than the electric field of light. Thus, for a constant gap length there is a value of the applied bias for which the effect of the laser is maximum.

Figure 5 shows the effect of the wavelength of illumination on the ratio of the tunneling current with the laser to the current without illumination. The calculations were made for an STM with a tungsten tip and sample at 20°C, with a gap length of 25 Å, an applied bias of 5 V, and a power flux density of 10^{11} W/m². The values of gap length and bias were chosen to correspond to the values for which the effect of illumination appears to be maximum in Figure 4.

It may be seen in Figure 5 that the increase in tunneling current due to illumination vanishes for short wavelengths, and approaches a constant in the long wavelength limit. These two characteristics are in agreement with the results of earlier calculations in which, as a first approximation, we [30] used a square potential barrier and neglected image corrections for the transiting electrons. These two effects may be understood as follows: For modulation at long wavelengths for which the period is much greater than the traversal time, the tunneling electron sees a static electric field added to the barrier. Thus, the height of the barrier is either increased or decreased depending on the phase at the time at which the particle enters the barrier. Due to the nonlinear dependence of current on barrier height these changes do not cancel, but rather the mean value of the tunneling current is increased. For example, by averaging values calculated using the transmission coefficient for a rectangular barrier it may be shown that when 2.5 eV electrons are incident on a barrier with a height of 3.0 V and a length of 2.0 nm the current is increased by 4.2% by adding 1% modulation to the height of the barrier. On the other hand, for

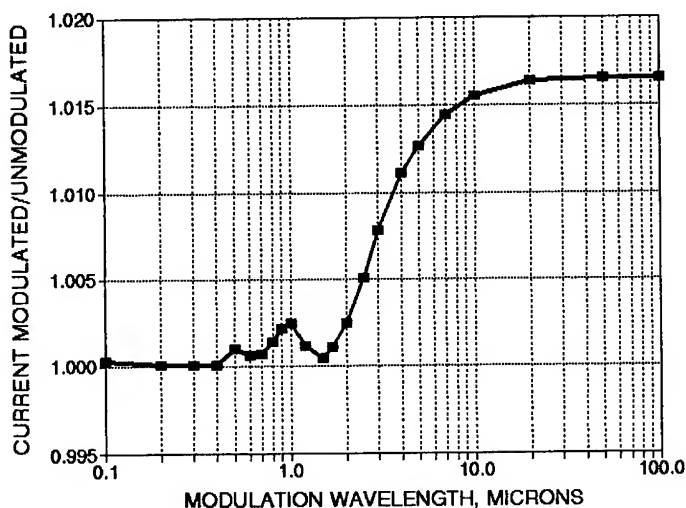


Figure 5. Increase in tunneling current due to illumination as a function of the wavelength for an STM with a tungsten tip and sample at 20°C with a gap length of 25 Å, an applied bias of 5 V, and a power flux density of 10^{11} W/m².

illumination at short wavelengths for which the period is less than the traversal time, the energy of the tunneling electron is alternately increased and decreased due to interaction with the electric field of light, and the effects due to these changes tend to cancel.

Discussion and Conclusions

Pimpale, Holloway, and Smith [14] described numerical solutions for a Gaussian wavepacket incident on a Gaussian barrier with oscillating height. Their method differs from that used in this paper, but they also observed that (1) transmission is maximum in the low frequency limit, (2) transmission decreases to that for the unmodulated barrier in the high frequency limit, and (3) averaging is required because the transmission depends on the phase at the time at which the particle enters the barrier. The numerical procedure used in the present paper has the advantage that the tunneling current may be determined for a specific value of energy, or for the distribution of energies in a free-electron metal, rather than for the distribution in a Gaussian wavepacket.

The results of the analysis presented in this paper suggest that it may be possible to determine the duration of barrier traversal from measurements of the tunneling current in a laser-assisted STM. However, there are many phenomena [39] such as current rectification, photoassisted tunneling, thermal-assisted tunneling, and thermal expansion, which have not been included in the present simulations. For example, the calculations for Figures 4 and 5 were made assuming illumination with a power flux density of 10^{11} W/m², and analyses and experiments [36–38] have shown that a substantial increase in the tunneling current may be caused by heating of the tip with the focused beam of a laser. It is possible that thermal effects could be separated from the nonthermal phenomena which are modeled in this paper by measuring the time dependence of the tunneling current. This is because the thermal relaxation time is on the order of μ s to ms, as compared with times of a few picoseconds for the nonthermal effects of laser illumination [38].

Since a planar-planar model was used for the barrier in an STM, we have not included the asymmetry which others [25,26] have previously considered as the cause for optical rectification. An experimental value of operational tunneling time has already been determined from measurements of rectification in a laser-illuminated STM [10]. However, it appears that the experimental phenomena that have been referred to as "current rectification" may be attributed to other effects instead of the interaction of the electric field of light with tunneling electrons [36,40]. Thus, it is possible that the experimental phenomena are not directly related to the duration of quantum tunneling.

Even with a power flux density of 10^{11} W/m², for which the electric field is 8.68 MV/m rms, the effects of a laser on the tunneling current in an STM are quite small. This is because the change in energy of the transiting electrons over the short distance between the tip and the sample is only on the order of milli-electron volts. In Figure 4 it is seen that the effect of a laser on the tunneling current increases

with the length of the gap, which may be understood because this increases the total distance for interaction of the electrons with the electric field of light. Thus, it may be more appropriate to use a field emission tube than an STM for the determination of tunneling times because of the increased length of the barrier [41].

Acknowledgments

We are grateful to James Mantovani, George Flynn, John Breen, Henry Gray, and Judith Krasnow for helpful discussions. This work was supported by NSF Grant ECS-9303397.

Bibliography

- [1] A. P. Jauho, in *Hot Carriers in Semiconductor Nanostructures*, J. Shah, Ed. (Academic, New York, 1992), pp. 121–151; R. Landauer and Th. Martin, *Rev. Mod. Phys.* **66**, 217 (1994).
- [2] P. Gueret, E. Marclay, and H. Meier, *Appl. Phys. Lett.* **53**, 1617 (1988).
- [3] D. Esteve, J. M. Martinis, C. Urbina, E. Turlot, M. H. Devoret, H. Grabert, and S. Linkwitz, *Physica Scr.* **T29**, 121 (1989).
- [4] J. Crofton, P. A. Barnes, and M. J. Bozack, *Am. J. Phys.* **60**, 499 (1992).
- [5] E. Golovchenko, E. M. Dianov, and P. V. Mamyshev, *J. Opt. Soc. Am.* **B7**, 172 (1990).
- [6] D. C. Chatfield, R. S. Friedman, D. W. Schwenke, and D. G. Truhlar, *J. Phys. Chem.* **96**, 2414 (1992).
- [7] N. Abusalbi, D. J. Kouri, M. Baer, and E. Pollak, *J. Chem. Phys.* **82**, 4500 (1985).
- [8] M. Volcker, W. Krieger, T. Suzuki, and H. Walther, *J. Vac. Sci. Technol.* **B9**, 541 (1991).
- [9] Z. Hasan, D. Andsager, D. Saltz, K. Cartwright, and M. H. Nayfeh, *Rev. Sci. Instrum.* **63**, 2099 (1992).
- [10] H. Q. Nguyen, P. H. Cutler, T. E. Feuchtwang, Z.-H. Huang, Y. Kuk, P. J. Silverman, A. A. Lucas, and T. E. Sullivan, *IEEE Trans. Electron Devices* **36**, 2671 (1989); A. A. Lucas, P. H. Cutler, T. E. Feuchtwang, T. T. Tsong, T. E. Sullivan, Y. Kuk, H. Nguyen, and P. J. Silverman, *J. Vac. Sci. Technol.* **A6**, 461 (1988).
- [11] M. J. Hagnmann, *Solid State Commun.* **82**, 867 (1992).
- [12] B. L. Cohen, *Am. J. Phys.* **33**, 97 (1965).
- [13] M. Büttiker and R. Landauer, *Phys. Scr.* **32**, 429 (1985).
- [14] A. Pimpale, S. Holloway, and R. J. Smith, *J. Phys.* **A24**, 3533 (1991).
- [15] M. Büttiker and R. Landauer, *IBM J. Res. Dev.* **30**, 451 (1986).
- [16] K. W. H. Stevens, *J. Phys. C* **16**, 3649 (1983); P. Moretti, *Phys. Scr.* **45**, 18 (1992).
- [17] E. Pollak and W. H. Miller, *Phys. Rev. Lett.* **53**, 115 (1984).
- [18] A. Schmid, *Ann. Phys. (NY)* **170**, 333 (1986).
- [19] M. Jonson, *Solid St. Commun.* **33**, 743 (1980).
- [20] R. Bruinsma and P. Bak, *Phys. Rev. Lett.* **56**, 420 (1986).
- [21] A. J. Legett, *Prog. Theor. Phys. Suppl.* **69**, 80 (1980).
- [22] A. A. Sokolov, Y. M. Loskutov, and I. M. Ternov, *Quantum Mechanics*, Scripta Technica trans. (Holt, Rinehart and Winston, New York, 1966), pp. 102–103; P. Schnupp, *Thin Solid Films* **2**, 177 (1968).
- [23] L. S. Schulman, in *Le Dualisme Onde-Corpuscle*, S. Diner et al., Ed. (Reidel, Dordrecht, 1984), pp. 270–271.
- [24] L. S. Schulman and R. W. Ziolkowski, in *Path Integrals from meV to MeV*, V. Sa-yakanit, W. Sritrakool, J. Berananda, M. C. Gutzwiller, A. Inomata, S. Lundquist, J. R. Klauder, and L. S. Schulman, Eds. (World Scientific, Singapore, 1989), p. 25.
- [25] N. M. Miskovsky, P. H. Cutler, T. E. Feuchtwang, and A. A. Lucas, *Int. J. Infrared mm Waves (USA)* **2**, 739 (1981).

- [26] H. Q. Nguyen, P. H. Cutler, T. E. Feuchtwang, and N. Miskovsky, *Surf. Sci.* **160**, 331 (1985).
- [27] J. G. Simmons, *J. Appl. Phys.* **35**, 2472 (1964).
- [28] N. Garcia, *IBM J. Res. Dev.* **30**, 533 (1986).
- [29] L. E. Bar'yudin, V. L. Butalov, and D. A. Telnov, *J. Appl. Phys.* **71**, 946 (1992).
- [30] M. J. Hagmann and L. Zhao, *Int. J. Quantum Chem. Quantum Symp.* **27**, 807 (1993).
- [31] W. R. Smythe, *Static and Dynamic Electricity* (McGraw-Hill, New York, 1950).
- [32] G. Binnig, N. Garcia, H. Rohrer, J. M. Soler, and F. Flores, *Phys. Rev. D* **20**, 4816 (1984).
- [33] A. Modinos, *Field, Thermionic, and Secondary Electron Emission Spectroscopy* (Plenum, New York, 1984).
- [34] T. M. Kalotas and A. R. Lee, *Am. J. Phys.* **59**, 48 (1991).
- [35] G. Binnig, H. Rohrer, C. Gerber, and E. Weibel, *Physica* **109 & 110 B**, 2075 (1982).
- [36] N. M. Miskovsky, S. H. Park, J. He, and P. H. Cutler, *J. Vac. Sci. Technol.* **B11**, 366 (1993).
- [37] M. J. G. Lee, R. Reifenberger, E. S. Robins, and H. G. Lindenmayr, *J. Appl. Phys.* **51**, 4996 (1980).
- [38] M. J. G. Lee and E. S. Robins, *J. Appl. Phys.* **65**, 1699 (1989).
- [39] Z. Hassan, D. Andsager, D. Saltz, K. Cartwright, and M. H. Nayfeh, *Rev. Sci. Instrum.* **63**, 2099 (1992).
- [40] R. J. Hamers and D. G. Cahill, *J. Vac. Sci. Technol.* **B9**, 514 (1991).
- [41] M. J. Hagmann, *J. Vac. Sci. Technol.* (1993), to appear.

Received April 22, 1994

Theoretical Ion Implantation Profiles for Low Energy Protons under Channeling Conditions

J. A. NOBEL, JOHN R. SABIN, and S. B. TRICKEY

Quantum Theory Project, University of Florida, Gainesville, Florida 32611

Abstract

We present early results from the CHANNEL code, which simulates the passage of ionized projectiles through bulk solids. CHANNEL solves the classical equations of motion for the projectile using a force obtained from the gradient of the quantum mechanically derived coulombic potential of the solid [determined via a full potential augmented plane wave (FLAPW) calculation on the bulk] and a quantum mechanical energy dissipation term, the stopping power, as determined from the method of Echenique, Nieminen, and Ritchie. The code then generates the trajectory of the ionic projectile for a given incident position on the unit cell face and an initial velocity. We use CHANNEL to generate an ion (proton) implantation profile for the test case of simple cubic hydrogen with the projectile's initial velocity parallel to the $\langle 100 \rangle$ channel. Further preliminary results for ion implantation profiles of protons in diamond structured Si, with initial velocity along the $\langle 100 \rangle$ and $\langle 110 \rangle$ channels, are given. © 1994 John Wiley & Sons, Inc.

Introduction

The CHANNEL code (a detailed treatment will be presented in Ref. [1]) calculates trajectories for low energy ions, $E \approx 1 - 25$ keV, impinging on bulk solids. The method uses realistic, quantum mechanically derived charge densities, potentials, and forces in describing the interaction of the projectile (thus far restricted to protons) with the bulk solid target. This type of simulation enables prediction of the penetration depths (ion implantation profiles) as well as observation of the channeling behavior of the incident ions.

Successful modeling of ion trajectories in solids is obviously desirable. With a physically realistic simulation, a theoretical study of ion implantation profiles can be made. In turn, this would allow predictive studies of defect growth in micro-electronic devices which are subjected to various environments in which radiation effects are important (solar flux, reactor sensors, radiation therapy). In addition, predictive studies on various potential radiation hard compounds and devices, as well as radiation detectors, can be made. Lastly, the usefulness of such a simulation in the doping of semiconductor chips can not be overlooked.

This method is intended to yield better (in the sense of including more basic physics) results than previous codes such as the Monte Carlo codes, MARLOWE [2-5], TRIM [6-8], BCCRY [9], PEPPER [10], BABOUM [11], and LAROSE [12]. In particular these tend to treat the scattering of the incident ions by the crystal

lattice as binary collisions using screened atomic-like potentials. The dissipation force used includes, in an approximate way, both electronic and nuclear energy dissipation terms. Some programs, like TRIM and BABOUM, treat the target as an amorphous or random solid. However, TRIM can do calculations of various compounds which have up to three layers of differing materials. CHANNEL, on the other hand, appears to be the first code which uses a potential and charge density generated from a quantum mechanical crystalline calculation. In calculating ion implantation profiles, the ion's incident energy must, by necessity, be low (of the order keV's) in order for the ion to be trapped in the solid in a computationally realistic time. Thus, by the nature of the problem, the ion's trajectory will be influenced strongly by the potential with which it interacts. This means that a method for calculating accurate ion implantation profiles must have a realistic representation of the crystalline potential as well as of the dissipative force. The method of Echenique et al. [13a,13b,14], which we use, is particularly suited for low energy ions. It expresses the energy dissipation term as a function of the local electronic density. This dependence allows an accurate determination of the dissipative force from the solid's electronic charge density. As we use a density functional theory based calculation of the bulk structure, and use the density to determine the energy dissipation (stopping) this method is conceptually consistent, at least in the sense that all essential quantities are obtained from the electron density.

We present our first calculations simulating the interaction of $E \leq 1$ keV protons with extended systems. The first solid target studied was simple cubic hydrogen (scH). The reasons for selecting scH as our test case are: (1) It has a very simple structure which allows us straightforwardly to analyze the results, and (2) the one-electron nature of H makes the calculation of the potential and charge density computationally easy. After analyzing the scH results and determining the success of the method, we present preliminary results for Si with the diamond structure, space group $Fd\bar{3}m-O_h^7$ (diaSi).

Method

In approaching the simulation of ion trajectories in solids, we make the following argument. We want: (1) a realistic representation of the crystalline coulombic potential which the ion will see, (2) a realistic energy dissipation term to represent the stopping power of the solid, and (3) a reasonably quick computation. With these goals in mind, we chose to use a classical equation of motion for which the input potentials are quantum mechanical in origin. Newton's equation of motion for the force \mathbf{F} on a particle at position \mathbf{r} is

$$\mathbf{F}(\mathbf{r}) = m\ddot{\mathbf{r}}, \quad (1)$$

where

$$\mathbf{r} = \mathbf{r}(t) \quad (2)$$

is the particle's (in this case a proton) position as a function of time t . The force, $\mathbf{F}(\mathbf{r})$,

$$\mathbf{F}(\mathbf{r}) = -\nabla U(\mathbf{r}) - \frac{dE}{dx}(\mathbf{r}) \quad (3)$$

consists of two parts: the coulombic potential $U(\mathbf{r})$ and $-(dE/dx)(\mathbf{r})$, the energy loss (stopping power) along the trajectory. Both of these quantities are determined *via* a full potential augmented plane wave (FLAPW) calculation [15]. The stopping power can be written

$$-\frac{dE}{dx}(\mathbf{r}) = Q(r_s(\mathbf{r}))\mathbf{v}, \quad (4)$$

where

$$r_s(\mathbf{r}) = [3/4\pi\rho(\mathbf{r})]^{1/3}. \quad (5)$$

Here $Q(r_s)$ is the energy dissipation term due to interaction of the projectile with the solid as it passes through the system, evaluated here using the method of Eche-nique [13,14], which is consistent with the local density approximation (LDA) used in the FLAPW calculation [15]. Q is dependent on the local electron density, described by the local electron sphere radius r_s . The value for the dissipative force $Q(\mathbf{r})\mathbf{v}$ can be written analytically [13,14] as

$$Q(\mathbf{r})\mathbf{v} = \mathbf{v}v_F\rho(\mathbf{r})\sigma_{tr}(v_F), \quad (6)$$

where v_F is the Fermi velocity of the solid and \mathbf{v} is the ion's velocity. The transport cross section σ_{tr} is given by

$$\sigma_{tr} = \frac{4\pi}{v_F^2} \sum_{\lambda=0}^{\infty} (\lambda + 1) \sin^2[\delta_{\lambda}(E_F) - \delta_{\lambda+1}(E_F)], \quad (7)$$

where δ_{λ} are the scattering phase shifts at the Fermi energy E_F . Throughout the calculation, Hartree atomic units are used.

Channels

Before proceeding to the results, it is useful to consider what is meant by the terminology "channel" in a solid. Qualitatively a channel is an open region characterized by a longitudinal axis aligned parallel with a crystallographic direction. The qualitative aspect is that the channel cross section is determined by the extent to which the atoms adjacent to the channel protrude into it. As the concept of an atomic radius is chemically and physically appealing, but ill-defined, so also are the lateral boundaries of the channel ill-defined. Thus, when one looks along a channel direction or axis in a hard sphere model, gaps or holes in the solid which run the entire extent of the solid (see Figs. 1 and 2) are visible. The center of a channel is defined as the center of the geometric figure defined by the projection of the space group sites onto the path perpendicular to the channel axis. Again see Figures 1 and 2. Note: The channel center need not have the same point group symmetry as that used to find the channel (see Fig. 2, Si $\langle 100 \rangle$ and $\langle 110 \rangle$).

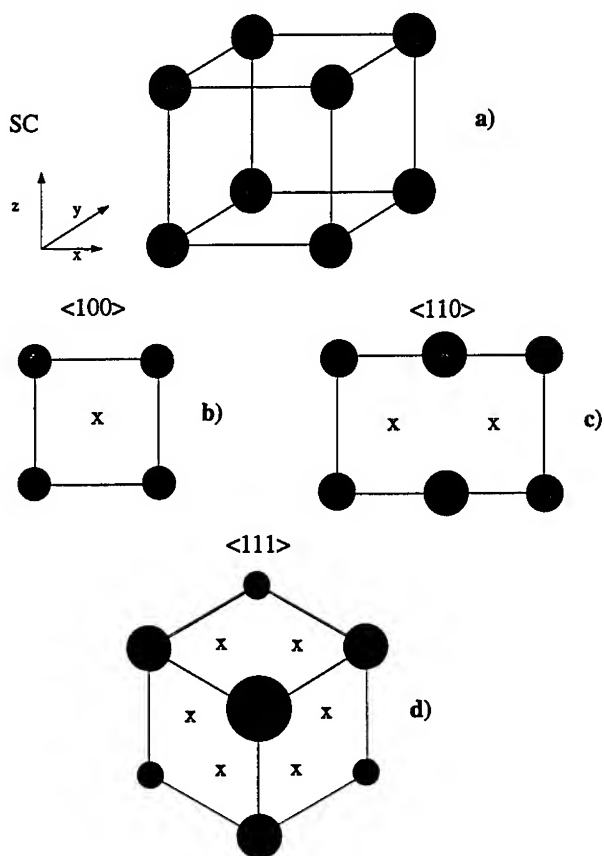


Figure 1. Simple cubic lattice: (a) simple cubic unit cell showing the atomic positions of H; (b) view along the axis of the $\langle 100 \rangle$ channel; (c) a view looking down the $\langle 110 \rangle$ channel; (d) a view looking down the $\langle 111 \rangle$ channel. The X's mark the center of the channels in (b), (c), and (d). The various sizes of spheres indicates that the atoms are at different distances along the channel direction.

Classically, channels represent directions of lowered resistance to the passage of ions. They are regions of relatively low electronic charge density as they are interstitial regions by nature, and as such are regions of low stopping power (regions of low Q and high r_s). Thus a projectile will have a tendency to be deflected from an arbitrary path so that it travels along a channel regardless of its incident velocity, provided that its velocity is not so great that it does not scatter to any appreciable extent as it traverses the solid. What this implies is that an ion will channel axially provided the ion's velocity [$\mathbf{v} = (v_{\perp} v_{\parallel})$, where v_{\perp} is the component of the velocity transverse to the channel direction and v_{\parallel} the component parallel to the channel direction] does not have too large a perpendicular component. This says that v_{\perp} has a maximum value beyond which axial channeling does not occur and that v_{\perp}^{\max} is sample-dependent. Thus there is a maximum impact angle that an ion can

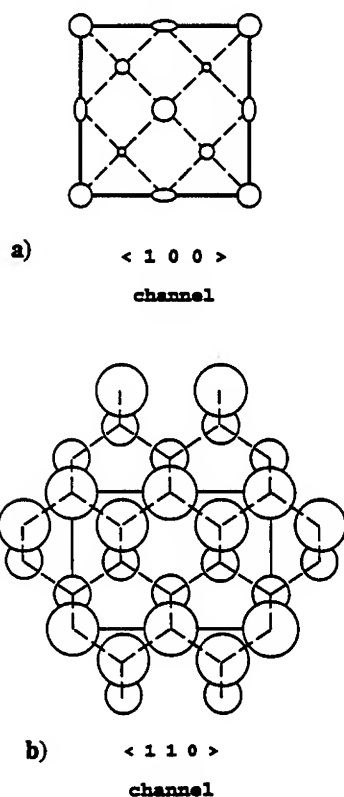
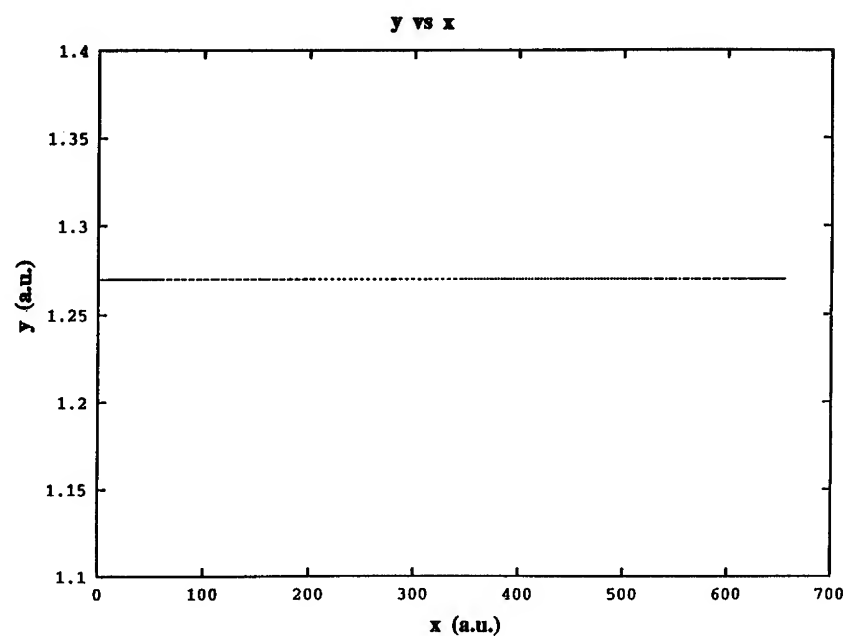


Figure 2. Diamond structure lattice: (a) view looking down the $\langle 100 \rangle$ channel; (b) view looking down the $\langle 110 \rangle$ channel. The various shapes and sizes of spheres indicate that the atoms are actually located at different distances along the channel direction. The dashed lines are used to indicate the channel boundaries.

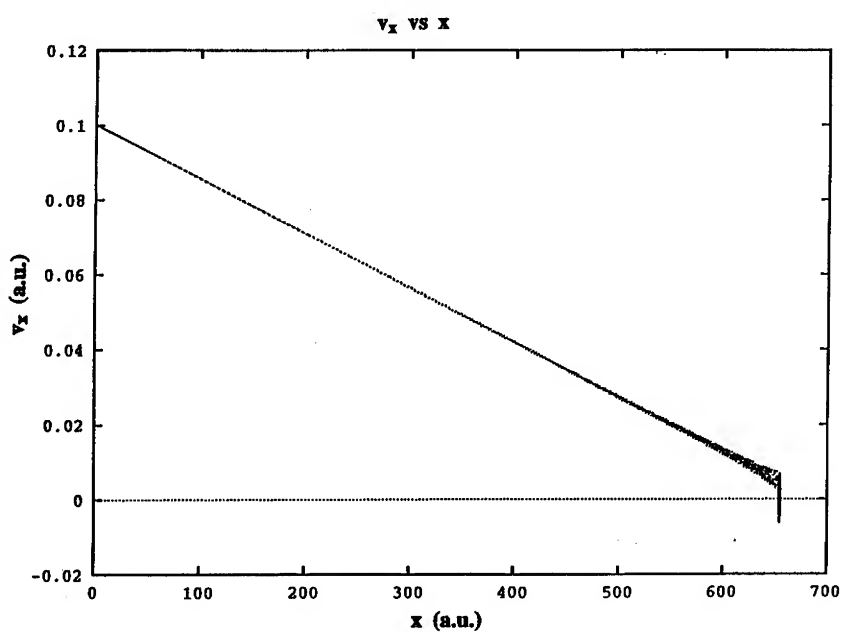
have in order to undergo channeling immediately upon entering the solid. For high energy projectiles ($E > 1$ MeV) this impact angle, given by $\arctan(v_{\perp}/v_{\parallel})$, has a upper limit which can be approximated by

$$\arctan(v_{\perp}/v_{\parallel}) \approx v_{\perp}^{\max}/v, \quad (8)$$

where v_{\perp}^{\max} for scH was found to be less than 0.1 keV. For scH this analysis would lead to a maximum incident angle for channeling of approximately 0.5° . For high energy ions this angle is very important since v_{\perp} may not be dissipated quickly enough to allow the ion to demonstrate any axial channeling before leaving the sample. Low energy projectiles (E in keV range) tend to follow the potential well minima within a relatively short distance after entering the solid so that this maximum impact angle is not very critical, as our trajectories indicate.



(a)



(b)

Figure 3. Case (1) of scH: (a) the projection of the trajectory of the proton on the x - y plane; (b) the v_x component of velocity plotted throughout the proton's trajectory.

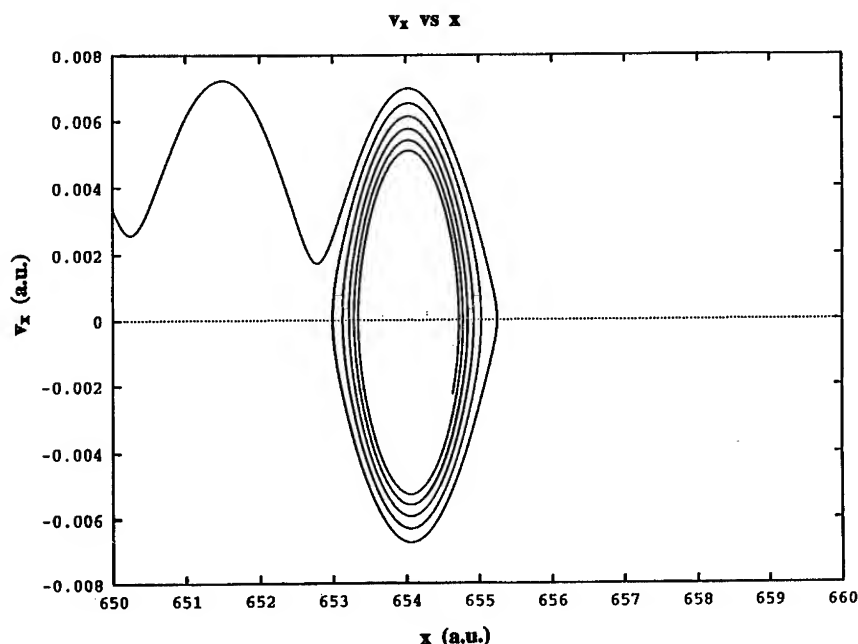


Figure 3. Case (1) of scH: (c) enlargement of the end of the proton's trajectory. The orbiting behavior indicates that the proton is trapped by the crystalline potential.

Results

scH

The first test case was simple cubic atomic hydrogen (scH). We performed an FLAPW calculation using a lattice constant $a_e = 2.54$ a.u. This lattice constant was chosen because it is slightly compressed relative to equilibrium [16], and consequently gives electronic densities in the interstitial region which ensure $r_s \leq 5$ a.u. (upper limit of our analytic fit to $Q(r_s)$; see Ref. [1]). The parameters of interest for the FLAPW calculation are the plane wave expansion cutoff $R_{mt} \cdot K_{\max} = 8$ (R_{mt} is the radius of the atomic sphere and K_{\max} the largest plane wave used), the maximum l value used in the spherical harmonic expansion of the potential and charge density is $l_{\max} = 6$, and the radius of the spherical regions is $R_{mt} = 1.2699$ a.u. (chosen to require touching, nonoverlapping spheres). We chose the $\langle 100 \rangle$ channel and tried various initial conditions. The first case (1) was with the proton's initial velocity parallel to $[100]$ direction and its initial position the center of the channel. The second case (2) had the same initial position as (1) but the proton's initial velocity was tilted relative to the channel direction so that $v_{\perp} > v_{\perp}^{\max}$. The third case (3) had the same initial velocity as (1) but with the initial position displaced from the center of the channel. These three cases demonstrate that CHANNEL has the proper behavior for an accurate simulation of proton trajectories in solids.

Case (1) results are shown in Figure 3. It shows that a proton traveling down the highly symmetric channel center does not deviate from its initial path until it is trapped, and even then the deviation is small (see Fig. 3). The straight line trajectory is what one would expect from symmetry. The absence of apparent deviation from a straight line path demonstrates that numerical errors are not accumulating. If they were, unrealistic trajectories would occur, which is not the case. In examining the numerical values of the ion's position the deviations from a linear trajectory are of the order 10^{-14} a.u. perpendicular to the channel direction until the proton is trapped. Once the proton is trapped within a unit cell, any deviation due to numerical round off has no effect since the proton remains within the same unit cell [see Fig. 3(c)].

Case (2) results are shown in Figure 4. We see that the proton travels several unit cells perpendicular to the channel axis before v_{\perp} is sufficiently dissipated that the proton's average trajectory is along the channel axis. Once the proton starts to channel, the trajectory clearly demonstrates that the proton scatters from the solid's potential energy surface, and an oscillatory path ensues.

Case (3) results are shown in Figure 5. Figure 5(a) shows that, though the proton initially has a velocity with $v_{\perp} = 0$, it is subjected immediately to a force perpendicular to $\langle 100 \rangle$ and v_{\perp} very quickly becomes nonzero. Figure 5(b) displays the trajectory of the proton as it becomes trapped by the solid. The end of the trajectory

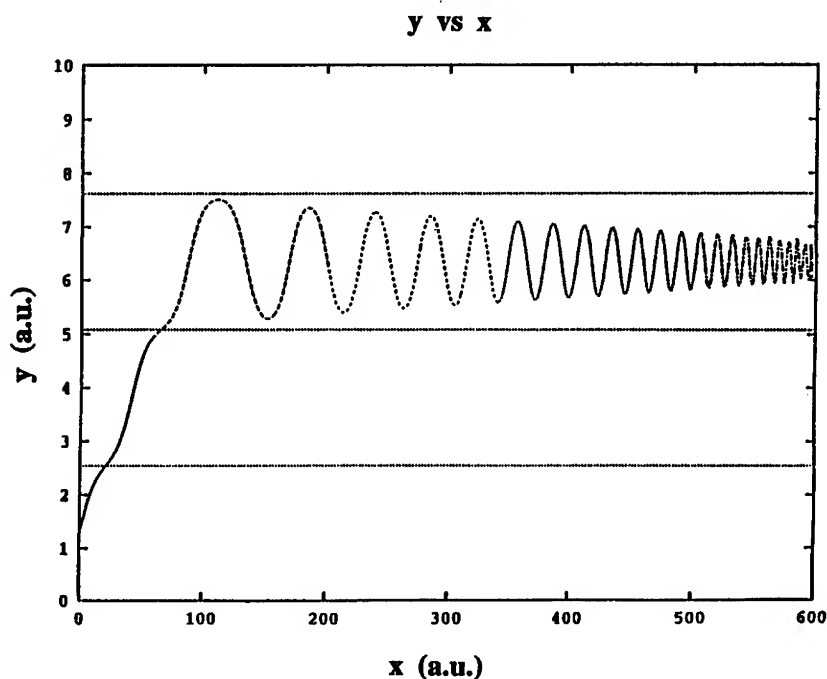


Figure 4. Case (2) of sch. The dotted lines indicate the projection of the atomic positions onto the x - y plane. The x -axis is parallel to the $\langle 100 \rangle$ channel.

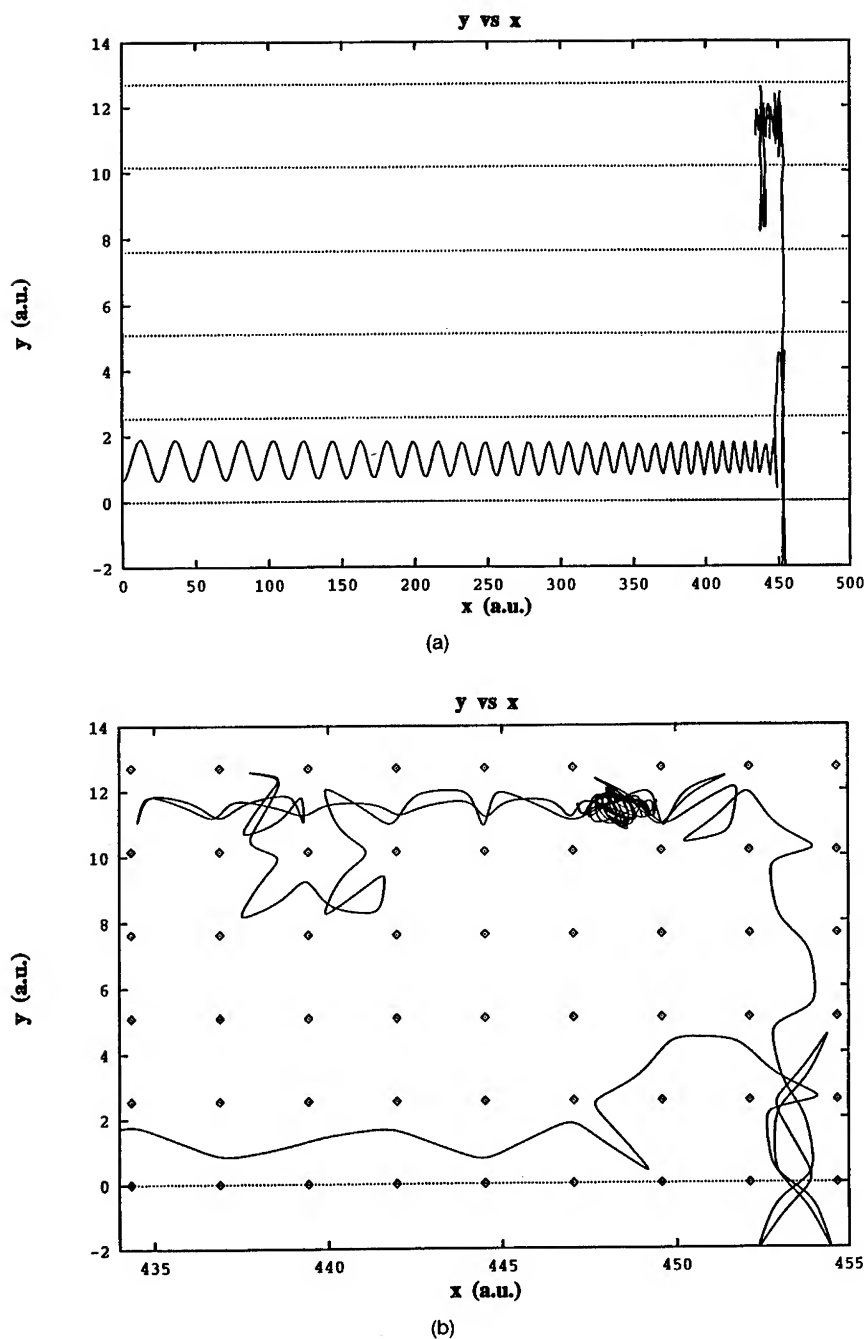


Figure 5. Case (3) of scH. (a) Projection of the proton's trajectory onto the x - y plane. The dotted lines are the projection of the crystalline atomic sites onto the x - y plane. The x -axis is parallel to the $\langle 100 \rangle$ channel. (b) Enlargement of the end of the proton's trajectory. The diamonds indicate the projection of the crystalline atomic sites onto the x - y plane.

shows that the proton "stops" in the crystal with nonzero velocity. It is trapped in a potential well, then comes to rest slowly, much latter. Figure 5(b) clearly shows the proton scatters from the potential maxima which are located at the atomic sites (the projections of the atomic sites are represented by the diamonds). Thus the proton's trajectory becomes quite erratic once its velocity has been dissipated sufficiently to the point where the velocity is of the order of the trapping velocity.

Satisfied that CHANNEL behaves as expected, we calculated the ion implantation profile of scH for the $\langle 100 \rangle$ channel for 0.25 keV protons ($v = 0.1$ a.u.). This study required an entire series of calculations with the same initial velocity but different initial positions throughout a segment of the channel cross-sectional area which is representative, through symmetry operations, of the entire cross section. The representative area is shown in Figure 6, and the ion implantation profile in Figure 7. There were a total of 45 points in the representative area (which corresponds to only 1/8 of the full channel area). This selection represents a total of 289 points over the entire cross-sectional area. From the ion implantation profile we see that an average penetration depth of 625 a.u. can be inferred. In addition to the average penetration depth (usually called range), there are three other distances of interest: the path-length straggling, lateral straggling, and penetration depth straggling or range straggling. Path-length straggling is defined to be the "variation of total path length for monoenergetic identical ions" [17], while range straggling is the variation in total penetration depth and lateral straggling is the variation in total displacement perpendicular to the channel direction. From Figure 7 we cannot determine the path length or lateral straggling but range straggling can be determined. The penetration depth straggling for scH is approximately 550 a.u.

diaSi

In order to examine systems of real scientific interest, we have started calculations of the ion implantation profiles of 0.25 keV protons in diamond structured Si

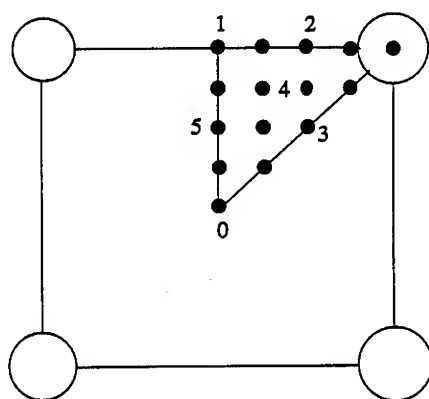


Figure 6. Diagram of the representative area of the $\langle 100 \rangle$ channel cross section for scH. The solid spheres are representative of the computational grid points.

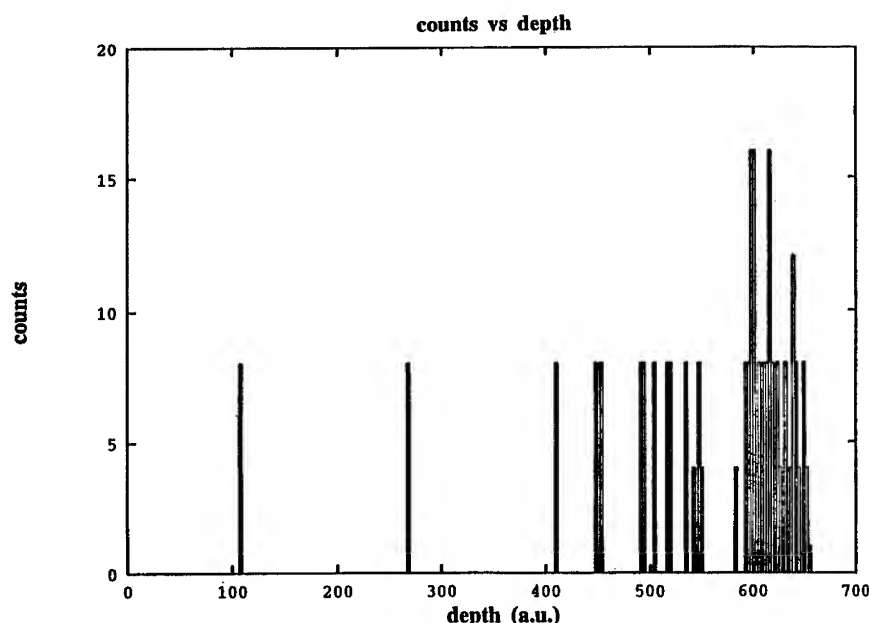


Figure 7. Ion Implantation profile for 0.25 keV protons incident along the $\langle 100 \rangle$ channel of scH. The depth is the distance along the $[100]$ direction where the proton is trapped.

(α -Si) along the $\langle 100 \rangle$ and $\langle 110 \rangle$ channels. The FLAPW parameters of interest are $a_e = 10.26254$ a.u. (chosen because it is approximately the experimental lattice constant for Si [18]), $R_{mt} \cdot K_{\max} = 8$, $l_{\max} = 6$, and an atomic sphere radius $R_{mt} = 2.2216$ a.u. Figure 8 shows the channel cross sections for the $\langle 100 \rangle$ and $\langle 110 \rangle$ channels. The preliminary results are shown in Figures 9(a) and 9(b). Figure 9 demonstrates that a greater number of data points (trajectories) is needed in order for the implantation profiles for diaSi to be of the same quality as that presented for scH $\langle 100 \rangle$. The grid used for the diaSi $\langle 100 \rangle$ channel has 42 points covering the full channel cross-sectional area, while the grid for diaSi $\langle 110 \rangle$ has only 39 points in the full channel area. With so few points, the ion implantation results are incomplete. However, if we ignore backscattered ions (the points with zero penetration depth), we can see that the profile is taking shape. In particular, Figure 9(a) would tend to indicate the average penetration depth to be around 250 a.u. for $\langle 100 \rangle$ with a penetration depth straggling of 570 a.u. Figure 9(b) seems to indicate that the average penetration depth could be approximately 850 a.u. with a straggling of 1250 a.u. Hopefully, we will not have to calculate 289 points, as in scH, in order to get a representative profile. What is definitely observable from these figures is that the proton's penetration depth along the $\langle 110 \rangle$ channel is approximately three times its penetration depth along the $\langle 100 \rangle$ channel. This is expected since from Figures 8(a) and 8(b) one can see that the $\langle 110 \rangle$ channel is much more open than the $\langle 100 \rangle$ channel. Also notice that the center of the $\langle 100 \rangle$ channel has only the

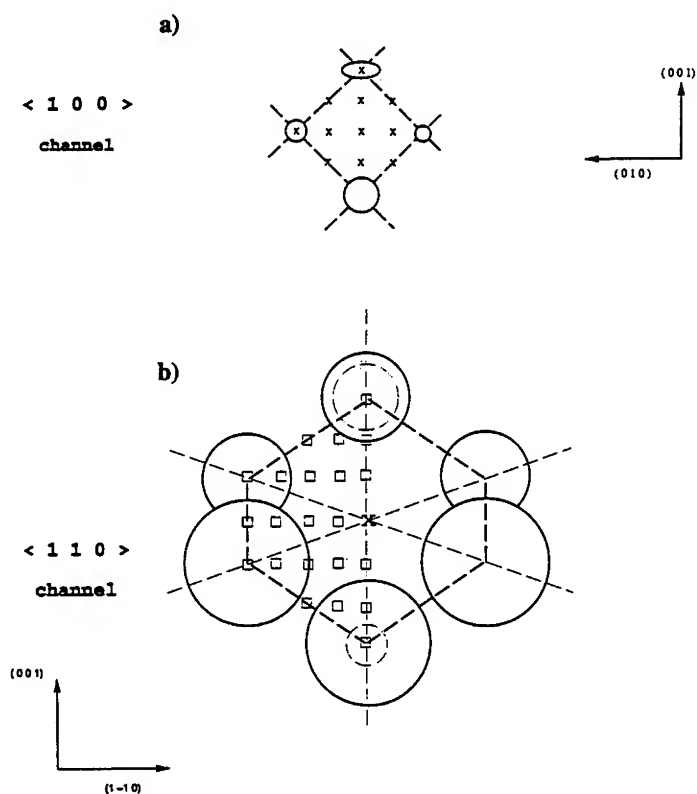
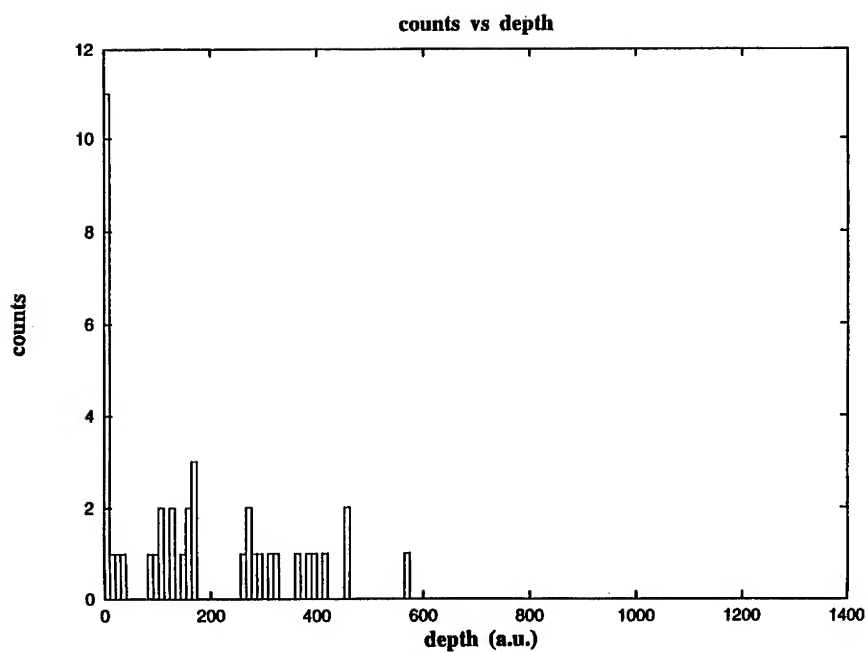


Figure 8. Si diamond structure channel cross sections. (a) The $\langle 100 \rangle$ channel cross section used in the calculation of the implantation profile. The X's are representative of the grid points used in the calculation. (b) The $\langle 110 \rangle$ channel cross section used in the calculation of the ion implantation profile. The squares in the left half of the figure represent the grid of point used in the calculation. The squares are only in the representative area of the cross section.

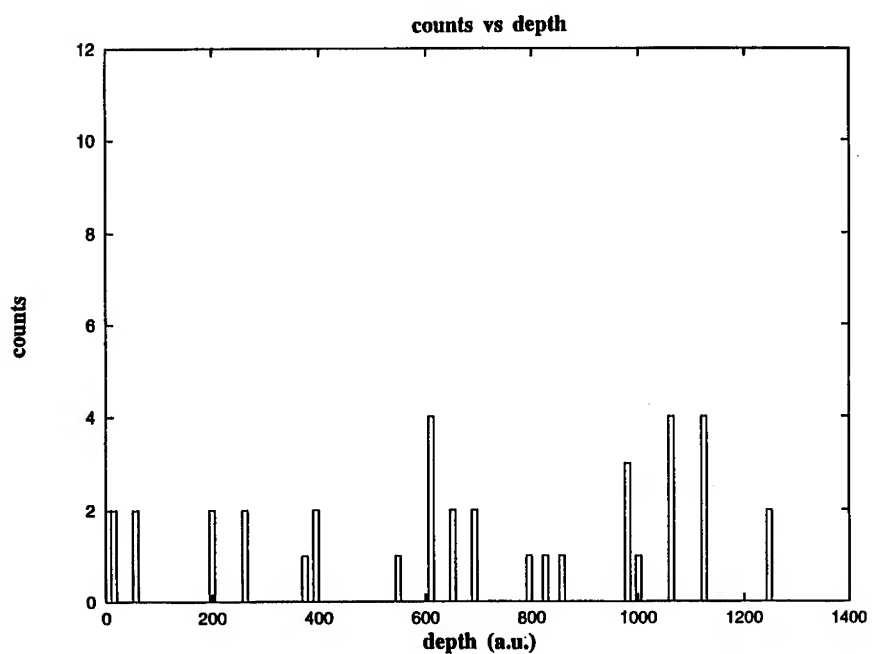
identity as a symmetry operation. This explains why the trajectory of a proton starting out on the channel center initially with $v_{\perp} = 0$ quickly has imparted to it a $v_{\perp} \neq 0$. On observing the $\langle 110 \rangle$ channel, one can see that the channel center has a mirror plane passing through it. As a result of this symmetry, a proton starting out on the $\langle 110 \rangle$ channel center, with \mathbf{v} purely along the $[110]$ direction, has very little

$$v_{\perp} = (v_{[1\bar{1}0]}, v_{[001]})$$

imparted to it in the $[1\bar{1}0]$ direction (the perpendicular to this mirror plane). The value of $v_{[1\bar{1}0]}$ is not precisely zero, as it should be, due to numerical roundoff which exists in specifying the center of the $\langle 110 \rangle$ channel. The only sizable component to v_{\perp} is in the $[001]$ direction (the mirror plane contains this direction).



(a)



(b)

Figure 9. diaSi implantation profiles for 0.25 keV protons. (a) Protons incident along the $\langle 100 \rangle$ channel of Si: The depth is the distance along the $[100]$ direction where the proton is trapped. (b) Protons incident along the $\langle 110 \rangle$ channel of Si: The depth is the distance along the $[110]$ channel where the proton is trapped.

Conclusion

We have demonstrated, using scH, that CHANNEL can be used to simulate realistically the trajectories of charged particles in solids. The choice of scH was one of computational expedience since it is a one-electron atom and the solid has one atom per unit cell. Even so we were able to generate hypothetical ion implantation profiles for protons traveling parallel to the $\langle 100 \rangle$ channel. We are unable to compare our results with experiment, but that was not the purpose of the calculation on scH.

Furthermore, we have presented preliminary results for implantation profiles for diaSi along the $\langle 100 \rangle$ and $\langle 110 \rangle$ channels. There is an insufficient number of trajectories to determine a well-defined average penetration depth. The curves appear to indicate an more trajectories will produce a proper profile. The curves also indicate that the depth of the $\langle 110 \rangle$ channel should be 3 times that of the $\langle 100 \rangle$. Because of the reduced symmetry of the $\langle 100 \rangle$ and $\langle 110 \rangle$ channels compared to the scH $\langle 100 \rangle$ channel, the diaSi system poses a computational challenge. The diaSi $\langle 100 \rangle$ channel has no symmetry operation except for the identity operation which causes the representative area of the channel cross-section to be the entire channel area. diaSi $\langle 110 \rangle$ is only slightly better because it has a reflection symmetry which makes the representative cross-sectional area 1/2 the full cross section. However, this reduction in computational work is more than compensated by the greater penetration depth of the proton along this direction. We shall present these results in a future paper, in which we also will discuss our calculational method in great detail.

From our results we can conclude that the method has promise for describing in a quasiclassical manner the channeling of low energy ions, E in keV range, in extended systems. There have been numerous studies on single crystal Si [4,9,19–29]; however, so far we have not found any low energy channeling results for protons (although low energy B implantation has been studied [9]). This is may be a technical problem with the experiments which we hope can be solved in the future. We have been in contact with an experimental group that believes energies of 1 keV are too low for their present detectors [30].

Acknowledgments

This work was supported by the U.S. Army Research Office through Contract #DAA-L03-91-G-0119. The authors express their appreciation to P. M. Echenique for providing us the numerical data for the $Q(r_s)$ function and for very useful conversations. J. R. Sabin is grateful for support from the Department of Education of the Basque Government for a stay in Donostia, Spain while some of this work was done.

Bibliography

- [1] J. A. Nobel, S. B. Trickey, and J. R. Sabin, to appear.
- [2] M. T. Robinson and I. M. Torrens, Phys. Rev. B9, 5008 (1974).
- [3] T. L. Crandle and B. J. Mulvaney, IEEE Electron Device Lett. 11, 42 (1990).
- [4] K. M. Klein, C. Park, and A. F. Tasch, Nucl. Instrum. Meth. B59, 60 (1991).

- [5] K. M. Klein, C. Park, and A. F. Tasch, *Appl. Phys. Lett.* **57**, 2701 (1990).
- [6] W. Eckstein, *Computer Simulation of Ion-Solid Interactions*, Springer Series in Material Science **10** (Springer-Verlag, New York, 1991), p. 10.
- [7] J. P. Biersack and W. Eckstein, *Appl. Phys.* **34**, 73 (1984).
- [8] J. F. Ziegler, J. P. Biersack, and U. Littmark, *The Stopping and Range of Ions in Solids* (Pergamon, New York, 1985), p. 109.
- [9] K. Gärtner, M. Nitschke, and W. Eckstein, *Nucl. Instrum. Meth.* **B83**, 87 (1993).
- [10] B. J. Mulvaney, W. B. Richardson, and T. L. Crandle, *IEEE Trans. Comput. Aided Des.* **8**, 336 (1989).
- [11] R. Becerra-Acevedo and B. Terreault, *Nucl. Instrum. Meth.* **B28**, 1 (1987).
- [12] J. H. Barrett, *Phys. Rev. B* **3**, 1527 (1971).
- [13] (a) P. M. Echenique, R. M. Nieminen, and R. H. Ritchie, *Solid State Commun.* **37**, 779 (1981).
(b) P. M. Echenique and M. E. Uranga, *Interaction of Charged Particles with Solids and Surfaces* (Plenum, New York, 1991), p. 39.
- [14] M. Peñalba, A. Arnau, and P. M. Echenique, *Nucl. Instrum. Meth.* **B67**, 66 (1992).
- [15] P. Blaha, K. Schwarz, P. Sorantin, and S. B. Trickey, *Comp. Phys. Commun.* **59**, 399 (1990) and references therein.
- [16] J. A. Nobel, G. A. Wilson, and S. B. Trickey, *Int. J. Quantum Chem.* **42**, 1037 (1992).
- [17] D. W. Anderson, *Absorption of Ionizing Radiation* (University Park Press, Baltimore, MD, 1984), p. 72.
- [18] J. Donohue, *The Structures of the Elements*, Krieger Publishing Company (1985), p. 263.
- [19] B. R. Appleton, B. Erginsoy, and W. R. Gibson, *Phys. Rev.* **161**, 330 (1967).
- [20] A. R. Sattler and G. Dearnaley, *Phys. Rev.* **161**, 244 (1967).
- [21] F. H. Eisen and M. H. Robinson, *Phys. Rev.* **B4**, 1457 (1971).
- [22] J. A. Golovchenko, A. N. Boland, F. S. Rosner, C. E. Thorn, H. E. Wegner, H. Knudsen, and C. D. Moak, *Phys. Rev.* **B23**, 957 (1981).
- [23] P. Gehrman, K. Lenkeit and R. Stolle, *Phys. Stat. Sol.* **B13**, 519 (1985).
- [24] H. W. Jin and W. M. Gibson, *Nucl. Instrum. Meth.* **B13**, 76 (1986).
- [25] A. Dygo and A. Turos, *Phys. Lett.* **A127**, 281 (1988).
- [26] K. Lenkeit, Ch. Trikalinos, L. L. Balashova, N. M. Kabachink, and V. I. Shulga, *Phys. Stat. Sol.* **B161**, 513 (1990).
- [27] K. M. Klein, C. Park and A. F. Tasch, *IEEE Trans. Electron Dev.* **39**, 1614 (1992).
- [28] A. LaFerla, G. Galvagno, V. Raineri, R. Setola, E. Rimini, A. Carnera, and A. Gasparotto, *Nucl. Instr. Meth.* **B66**, 339 (1992).
- [29] L. R. Logan, C. S. Murthy and G. R. Srinivasan, *Phys. Rev.* **A46**, 5754 (1992).
- [30] L. E. Seiberling, private communication.

Received April 1, 1994

Energy Depositions of Protons in Allotropic Carbon Ultrathin Films

JIN Z. WU, S. B. TRICKEY, JOHN R. SABIN, and J. NOBEL

Quantum Theory Project, University of Florida, Gainesville, Florida 32611

Abstract

We present the effects of structure, chemical binding, and number of layers on stopping for clean, unreconstructed diamond (100) one- to four-layer films with lattice constants fixed at crystalline values, and for graphite mono- and dilayers at their optimized bond lengths. First Born approximation stopping cross sections for protons incident normally on the films were obtained from orbital versions of the kinetic theory of stopping and of the local plasma approximation. The required electron momentum density was generated from the real space Kohn–Sham orbitals. We find a strong static quantum size effect in the stopping of diamond ultra-thin films as opposed to graphite, for which the stopping is only very weakly dependent on the layer number. © 1994 John Wiley & Sons, Inc.

Introduction

For many years, there has been great interest, both theoretically and technologically, in the allotropic forms of carbon, especially graphite and diamond. Because graphite and diamond are the simplest realistic materials with both a typical covalently bonded structure and with four valence electrons, these forms are ideal targets in which to study structural effects upon stopping. Graphite has a six-membered benzenelike structure with delocalized double bonds. Its interplanar binding is very weak. Diamond has localized single bonds and is isostructural with several important electronic materials such as Ge and Si. A number of diamond-based electronic devices have been proposed [1]. Advances in material science have made possible the deposition of diamond thin films on many other surfaces [2]. Experimentally [3], for example, a 1×1 low energy electron diffraction pattern appears when a polished C(100) surface is heated from 500 to 700 K. Thus we were motivated to study the C(100) diamond film.

The stopping of graphite and diamond was studied experimentally by Softky [4] in 1961 and later on by Grygoriev et al. [5] and by Kulikaukas et al. [6]. Several papers concerning stopping in bulk carbon allotropes have been published [7–15] as well. Experimental determination of stopping properties in these cases generally is by extrapolation to zero sample thickness in order to eliminate multiple scattering effects. So far as we are aware, stopping in ultrathin films (e.g., a few layers) of allotropic carbon has never been published. Experimentally 20–100 Å (100) carbon foils can be produced, but stopping in them is yet to be measured [16].

The lattice structure and electronic structure for energy optimized graphite 1–2 layers and for clean, unreconstructed diamond (100) 1–4 layers (fixed at the bulk crystalline bond length) have been calculated previously by Trickey et al. [17] and Wu et al. [18], respectively. Here we present calculations of the stopping cross section for protons (at normal incidence) on these ultrathin layered structures and on the isolated carbon atom. The next section describes the method that we used. The results and discussion are in the third section, where the effects on stopping of structure, chemical binding, and layer number (i.e., the quantum size effect) are discussed.

Methods

The linear energy loss of a charged particle in matter is given as

$$-\frac{1}{N} \frac{dE}{dx} = S(\vec{v}) = \frac{4\pi Z_1^2 Z_2}{v^2} L(\vec{v}), \quad (1)$$

where N is the number density of scatterers (here the carbon atom), S and L are the stopping cross section and stopping number per scatterer, \vec{v} the velocity of the incident particle (we restrict the discussion to protons in this work), E its energy, x its path length, Z_1 the projectile charge, and Z_2 the number of electrons per target atom. We use Hartree atomic units in Eq. (1) and throughout this paper unless otherwise noted. The effects of channeling and of projectile dynamic charge state are neglected. Following Sabin and Oddershede [19], first Born approximation stopping cross sections for protons incident normally on the films were calculated with an orbital version of the kinetic theory of stopping [20]. Details are found in Ref. [21]. Briefly,

$$L(\vec{v}) = \sum_l L_l(\vec{v}), \quad (2)$$

$$L_l(\vec{v}) = \int_{-\infty}^{\infty} d\vec{v}_{2xy} \int_{-\infty}^{\infty} dv_{2z} \rho_l(\vec{v}_2) L_l^0(|\vec{v} - \vec{v}_2|) \frac{\vec{v} \cdot (\vec{v} - \vec{v}_2)}{|\vec{v} - \vec{v}_2|^3} v. \quad (3)$$

In Eq. (3), $\rho_l(\vec{v}_2)$ is the momentum density of the l th energy sub-band, L_l^0 is of Bethe form with a low energy cutoff

$$L_l^0(v) = \frac{\eta_l}{nZ_2} \ln\left(\frac{2v^2}{I_l}\right) \theta\left(v^2 - \frac{I_l}{2}\right), \quad (4)$$

where n is the number of atoms per unit cell and η_l is the occupation of the l th energy subband (see below).

The orbital mean excitation energy I_l is determined through the orbital local plasma approximation (OLPA) [22]

$$\ln I_l = \frac{1}{\eta_l} \int_{-\infty}^{\infty} dz \int_A d\sigma \rho_l(\vec{r}) \ln[(4\pi\rho(\vec{r}))^{1/2}]. \quad (5)$$

The required momentum density is constructed from the Fourier transform of the real space Kohn–Sham (KS) eigenfunctions

$$\Psi_{j,\vec{k}}(\vec{p}) = \frac{1}{[2\pi N_{\text{cell}}A]^{1/2}} \int_{-\infty}^{\infty} dz \int_{N_{\text{cell}}A} d\sigma e^{i\vec{p}\cdot\vec{r}} \psi_{j,\vec{k}}(\vec{r}),$$

$$\rho_j(\vec{p}) = \sum_{\vec{k} \in \text{BZ}}^{\text{occ.}} n_{j,\vec{k}} |\psi_{j,\vec{k}}(\vec{p})|^2. \quad (6)$$

The KS functions were obtained in the local density approximation to density functional theory (LDA/DFT) utilizing the Hedin–Lundqvist (HL) exchange–correlation functional. This scheme is internally consistent, as ρ plays the pivotal role in both DFT and the OLPA. The atomic calculations used the same OLPA and LDA but were spin polarized in the central field approximation. A is the area per unit cell, N_{cell} is the total number of periodic unit cells, and $\vec{p} = \vec{v}$ in atomic units.

The electronic structure calculations were carried out using the FILMS [23–25] code which solves the KS equations in a Gaussian basis representation. The basis sets are given in Refs. [17] and [18]. The atomic calculation used the 9s4p Hartree–Fock basis of Van Duijneveldt [26].

The graphite dilayer (monolayer) has a simple hexagonal Bravais lattice with four (two) carbon atoms per unit cell [see Fig. 1(a)]. Each lattice plane perpendicular to the c -axis has a honeycomb arrangement. For graphite, the irreducible triangle of the Brillouin zone (BZ) is 1/12 of the zone, with 37 \vec{k} points in that triangle. The diamond films have square lattice symmetry and n atoms in one unit cell of an

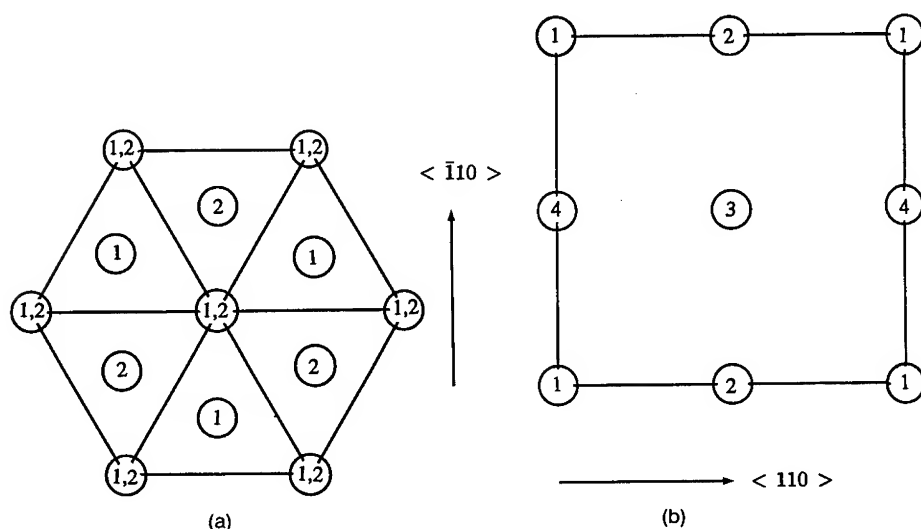


Figure 1. Top views of the lattice structures of allotropic carbon ultra-thin films. The atoms denoted by "1" are in layer 1, and those by "2" are in the second layer, etc. "1,2" means atoms in layer 1 and 2 are in overhead positions, etc.: (a) lattice structure of the graphite 2L; (b) lattice structure of the diamond 4L.

n -layer [see Fig. 1(b)]. The irreducible regions for the diamond 1 and 3 layers are $1/8$ of the BZ with 21 \vec{k} points in the region, and, for the diamond 2 and 4 layers, are $1/4$ of the BZ with 36 \vec{k} points [18] in the region.

The energy sub-bands in equation (3) were chosen as follows. The atomic stopping cross section was used for the 1s bands (in tests with graphite, the difference in stopping between the atom and the monolayer for this band is in the second decimal place at the peak value of the stopping cross-section). For the diamond monolayer, we used one window for the 2s-like band and one window for the 2p-like band, since both the 2s-like band and 2p-like band are narrow and do not overlap. Except in the diamond monolayer, the valence bands of 2s-like and 2p-like character all overlap, so we divided the energy range of those valence bands into four windows for graphite and three windows for diamond 2–4 layers according to

$$E_l = E_{\min}^{2p,2s} + l[(E_{\max}^{2p,2s} - E_{\min}^{2p,2s})/m], \quad l = 0, 1, 2, \dots, m. \quad (7)$$

Here m is the number of windows for 2s-like and 2p-like orbitals. We tested the dependence of the calculated stopping cross section on the number of windows for the graphite 1L at one velocity ($v = 1.75$ a.u.) near the maximum in the stopping cross section and find the discrepancy between the two calculations ($m = 3$ and $m = 4$) to be in the second decimal place (see Table I). As the velocity of the proton is along the z direction (i.e., normal to the film), we have tested whether the p_{xy} - and p_z -like states have the same contributions to the stopping cross section. The stopping cross section obtained using two windows by treating $2p_z$ and $(2s, 2p_{xy})$ separately (i.e., the whole $2p_z$ as one window, the whole $2s$ and $2p_{xy}$ as another window) is 12.451×10^{-15} eV cm²/atom. If we treat the $2s$ and $2p$ together (combine $2p_z$ and $2s, 2p_{xy}$ together in one window), with $m = 2$, the stopping cross section is 12.515×10^{-15} eV cm²/atom. The discrepancy in stopping cross section between these two cases is also in the second decimal place (see Table I). For the diamond 2–4L system, the $2s, 2p_{xy}$ orbitals and $2p_z$ orbital are hybridized and, hence, cannot be separated.

TABLE I. The total stopping cross section S at $v = 1.75$ a.u. as a function of the total number of divisions of the energy subband for graphite-1L in the energetically optimized state with $a = 4.635$ a.u.

Orbitals	No. of windows	I (eV)	S
			(10^{-15} eV cm ² /atom)
Treat 2s and 2p bands together	1	67.033	12.181
	2	67.033	12.515
	3	67.033	12.620
	4	67.033	12.614
Separate $2p_z$ from $2s, 2p_{xy}$ bands	2s, $2p_{xy}$	1	
	$2p_z$	1	12.451

Results

Calculated stopping cross sections for the isolated carbon atom and for graphite 1- and 2-layer system are shown in Figure 2 and Table II. The stopping for protons of bulk graphite at $v = 6.63$ a.u. is also indicated for comparison with the experimental result (see below). We find the stopping to be nearly additive per layer, that is, the difference in stopping per atom between the graphite monolayer and dilayer is rather small, no doubt due to the weak interplanar binding [17] (0.03 eV/atom). The presence of the graphite second layer has no significant influence on the electron density of the first layer and thus neither on the stopping. The present result for the stopping cross section for the graphite-2L at a proton velocity of 6.63 a.u. (or proton energy $E_p = 1.1$ MeV) is $S_{g-2L} = 4.30 \times 10^{-15}$ eV cm²/atom, which is in reasonable agreement with the measurement of $S_{g-bulk} = 4.0 \times 10^{-15}$ eV cm²/atom for carbon obtained by Fuchs et al. [27] and with Softky's estimate [4] for bulk graphite of $S_{g-bulk} = 3.98 \pm 0.2 \times 10^{-15}$ eV cm²/atom at $E_p = 1.1$ MeV. {The uncertainties in the Softky data arise from uncertainties in the scattering cross section (σ) extrapolation and in the value of the incident energy used, which could be in error by as much as 5% according to Ref. [4]}.

Calculated stopping cross sections for the isolated carbon atom and for diamond n -layers ($n = 1-4$) films are shown in Figure 3 and Table III. We find a strong static quantum size effect in the stopping for the ultra-thin diamond films: The stopping cross section decreases significantly as the number of layers increases. This effect arises from the interaction between layers which is much stronger in diamond (e.g., the interplanar binding energy for diamond-2L [18] is 3.93 eV/atom) than in graphite. The total energy per atom decreases and the mean excitation energy increases

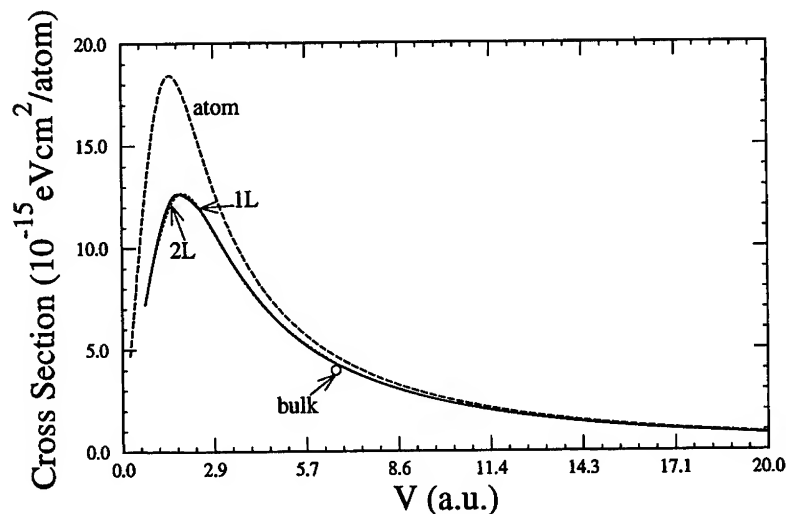


Figure 2. The stopping cross section of isolated carbon atom, graphite-1L and graphite-2L as functions of proton velocity.

TABLE II. The stopping properties at v_{\max} as a function of the total number of layers for the graphite- nL^a

System Lattice constants (a.u.)		Atom	Monolayer $a = 4.635$	Dilayer $a = 4.636,$ $c = 12.988$
v_{\max} (a.u.)		1.52	1.75	1.89
1s orbital	I_{1s} (eV)	240.24	242.81	242.82
	S_{1s}^b	0.34	0.39	0.41
2s and 2p orbitals	$I_{2s}^{(1)}$ (eV)	24.96(2s)	36.31	36.28
	$S_{2s}^{(1)}$	9.87(2s)	3.07	2.95
	$I_{2s}^{(2)}$ (eV)	21.17(2p)	38.42	38.44
	$S_{2s}^{(2)}$	8.29(2p)	2.62	2.57
	$I_{2s}^{(3)}$ (eV)		36.28	36.46
	$S_{2s}^{(3)}$		4.17	4.27
	$I_{2s}^{(4)}$ (eV)		28.81	29.74
	$S_{2s}^{(4)}$		2.38	2.47
I_{tot} (eV)		50.26	67.03	67.27
S_{\max}		18.50	12.63	12.67
S at $v = 6.63$ a.u.		4.68	4.31	4.30

^a The superscripts on I and S are the indices of the windows. The intraplanar unit cell parameter (hexagonal bond length) is denoted as a . The interplanar separations are designated as c . The stopping cross section S is in 10^{-15} eV cm²/atom.

^b From the spin polarized atomic calculation.

as the number of layers increases. Experimental [13] and semi-empirical [9,14,15] results have been given for stopping in bulk diamond. In Figure 3, we present the semi-empirical values of Sabin and Oddershede (SO) [9] and of Elkomoss and Pape (EP) [14], and compare them to stopping for dilute gas and thin films targets as calculated here. The EP values were generated using the Brandt-Reinheimer formalism [14], which is a generalization of the Lindhard and Winther [28] dielectric scheme. The energy gap is obtained by requiring that $\kappa(0, 0, E_g)$ is equal to the static dielectric constant of diamond. Sabin and Oddershede [9] use momentum densities obtained from the valence electron Compton profiles and a mean excitation energy ($I = 96$ eV) derived from experimental stopping cross section. This value is slightly higher than that reported by Tung and Watt (TW) [15] (86 eV) derived from a combined method that treats the core electrons in the local plasma approximation and uses the dielectric response formalism for valence electrons. Lowering of the SO mean excitation energy to that of TW would raise the SO values of the stopping cross section and put them in much better agreement with the results of EP. In any case, it is clear that the stopping cross section becomes lower and broadens with increasing layer number, as seen previously [29], and that the approach to bulk behavior is slow; that is, there is a strong quantum size effect.

The calculated lattice constants for graphite films [17] are shown in Table II. The experimental value of the bond length of bulk diamond is 2.919 a.u. [30],

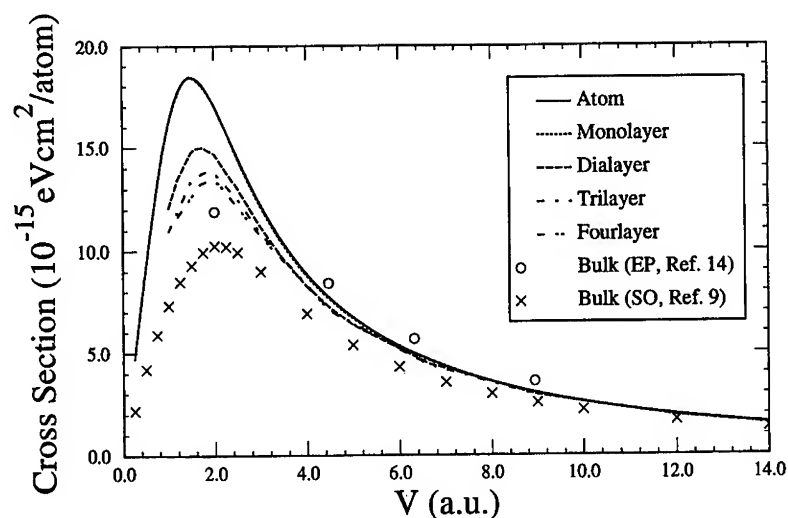


Figure 3. The stopping cross section of an isolated carbon atom, of diamond 1-4 layer films, and of bulk diamond as functions of proton velocity.

which leads to an intraplanar lattice constant of 4.766 a.u. and an interplanar distance of 1.685 a.u. at which the lattice constants of the diamond films were fixed. The graphite monolayer has an areal density of 0.648 electrons/a.u. [2], which

TABLE III. The stopping properties at v_{\max} as the function of the total number of layers for the diamond- nL .^a

System		Monolayer	Dilayer	Trilayer	Fourlayer
v_{\max} (a.u.)		1.48	1.73	1.88	1.91
1 s orbital	I_{1s} (eV)	240.09	241.34	241.70	241.94
	S_{1s}^b	0.33	0.38	0.41	0.42
2s and 2p orbitals	$I_{2s\&2p}^{(1)}$ (eV)	25.76 (2s)	33.22	34.69	34.92
	$S_{2s\&2p}^{(1)}$	9.77	4.01	2.64	3.01
	$I_{2s\&2p}^{(2)}$ (eV)	22.90 (2p)	31.93	34.31	35.05
	$S_{2s\&2p}^{(2)}$	8.36	2.72	4.57	4.11
	$I_{2s\&2p}^{(3)}$ (eV)		27.97	29.84	31.64
	$S_{2s\&2p}^{(3)}$		7.88	6.23	5.88
I_{tot} (eV)		52.117	60.10	62.98	64.54
S_{tot} at v_{\max}		18.46	14.99	13.86	13.42
$S_{\text{graphite}}^{2L}/S_{\text{diamond}}^{nL}$ at $v = 6.63$ a.u.		0.932	0.969	0.982	0.987

^a The superscripts on I and S are the indices of the windows. The stopping cross section S is in 10^{-15} eV cm²/atom.

^b From a spin polarized atomic calculation.

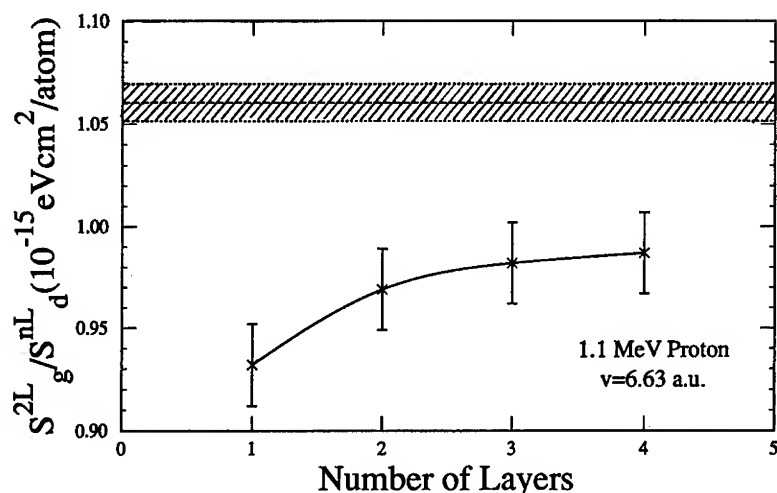


Figure 4. The ratio of the stopping cross section for 1.1 MeV protons in the graphite dilayer to that in the diamond-nL as a function of the number of layers (denoted by solid line). The error bars represent estimated uncertainties in our calculations. The dotted line represents the ratio of the stopping cross section in bulk graphite to that in bulk diamond. The shadowed area represents the reported standard deviation in the bulk value.

is higher than that for the diamond monolayer (0.264 electrons/a.u. [2]). Typically a higher areal electron density causes a lower stopping cross section and a higher value of the velocity at which the stopping cross section achieves its maximum value, since the system with higher areal density has lower total energy and higher mean excitation energy. This binding dependence for graphite and diamond is consistent with that general tendency.

Since the stopping cross sections of 1s-like core bands are less than 5% of the total stopping cross section for both graphite and diamond, the difference between graphite and diamond stopping is clearly due to the valence band electron distribution, just as one would expect on chemical grounds. Graphite films and diamond films have quite different electronic structures, and correspondingly different valence density distributions. Bulk graphite has a small overlap of the valence and conduction bands, whereas bulk diamond is an insulator with a large band gap. Therefore, the contribution to the mean excitation energy, I , from the interband transition is smaller for graphite than for diamond leading to a larger stopping cross section for bulk graphite than for bulk diamond.

In early 1961, Softky [4] experimentally found the stopping power of bulk graphite to be 1.0604 ± 0.0090 times that of bulk diamond for 1.1 MeV protons. (The quoted error refers to the standard deviation in the measurements.) More recently, Kulikauskas et al. [6] gave experimental results at lower proton energies which when extrapolated give good agreement with the value reported by Softky. Grygoriev's calculation [5], based on the dielectric description and average concentrations of electrons in graphite and diamond, gave a similar ratio. The ratio of the

stopping cross section for the graphite-2L to that of the diamond n L as a function of layer number (n) is shown in Table III and plotted in Figure 4. (Because of the weak binding in graphite, it is reasonable to use the 2L result for $1 \leq n \leq 4$.) The numerical uncertainty of our calculation is estimated to be 2%. Thus the present results are consistent with previous findings in the sense that we find thin film stopping is distinct from that of bulk [21,29]. However, the extrapolated value of the ratio is 0.99 at $E_p = 1.1$ MeV. The remaining discrepancy in the extrapolated value from Softky's value may be attributed to the limitations in the OLPA model itself and the unreconstructed (hence metallic [18]) geometry of the calculated diamond films or systematic error in the measurement.

To summarize, the stopping of ultrathin layers of carbon allotropes shows a strong static quantum size effect in the stopping of diamond n -layers. This is in contrast to graphite, where the layers are only weakly interacting, compared to diamond, and the stopping is nearly additive per layer.

Acknowledgments

This work was supported in part by the U.S. Army Research Office under contract DAA L03-91-G-0119.

Bibliography

- [1] A. T. Collins, *Semiconductor Sci. Technol.* **4**, 605 (1989).
- [2] P. K. Bachmann and R. Messler, *C&EN* (May), 24 (1989).
- [3] Y. L. Yang and M. P. D'Evelyn, *J. Vac. Sci. Technol.* **10**, 978 (1992).
- [4] S. D. Softky, *Phys. Rev.* **123**, 1685 (1961).
- [5] V. G. Grygoriev, F. G. Neshov, A. A. Puzanov, and A. R. Urmanov, *Phys. Stat. Sol. (a)* **83**, 573 (1984).
- [6] V. S. Kulikauskas, F. G. Neshov, A. A. Puzanov, A. R. Urmanov, and V. P. Shubin, *Sov. Tech. Phys. Lett.* **10**, 46 (1984).
- [7] H. H. Andersen and J. F. Ziegler, *Hydrogen Stopping Power and Ranges in All Elements* (Pergamon, New York, 1977).
- [8] H. H. Andersen, *Bibliography and Index of Experimental Range and Stopping Power Data* (Pergamon, New York, 1977).
- [9] J. R. Sabin and J. Oddershede, *Nucl. Instr. Meth.* **B24/25**, 339 (1987).
- [10] C. A. Sautter and E. J. Zimmerman, *Phys. Rev.* **140**, A490 (1965).
- [11] F. Schulz and J. Shchuchinsky, *Nucl. Instrum. Meth.* **B12**, 90 (1985).
- [12] S. Matteson, E. K. L. Chau, and D. Powers, *Phys. Rev.* **A14**, 169 (1976).
- [13] R. W. Fearick and J. P. F. Sellschop, *Nucl. Instrum. Meth.* **168**, 51 (1980).
- [14] S. G. Elkomoss and A. Pape, *Phys. Rev.* **B26**, 6739 (1982).
- [15] C. J. Tung and D. E. Watt, *Radiation Effects* **90**, 177 (1985).
- [16] N. Tolk, private communication.
- [17] S. B. Trickey, F. Müller-Plathe, G. H. F. Diercksen, and J. C. Boettger, *Phys. Rev.* **B45**, 4460 (1992).
- [18] J. Z. Wu, S. B. Trickey, and J. R. Sabin, unpublished.
- [19] J. Oddershede and J. R. Sabin, *Phys. Rev.* **A26**, 3209 (1982).
- [20] P. Sigmund, *Phys. Rev.* **A26**, 2497 (1982).
- [21] S. B. Trickey, J. Z. Wu, and J. R. Sabin, *Nucl. Instrum. and Meth.*, to appear.
- [22] D. E. Meltzer, J. R. Sabin, S. B. Trickey, and J. Z. Wu, *Nucl. Instrum. Meth.* **B82**, 493 (1993).
- [23] J. C. Boettger and S. B. Trickey, *J. Phys. Cond. Mat.* **1**, 4323 (1989).

- [24] J. C. Boettger and S. B. Trickey, *J. Phys. F Met. Phys.* **16**, 693 (1986).
- [25] J. W. Mintmire, J. R. Sabin, and S. B. Trickey, *Phys. Rev.* **B26**, 1743 (1982).
- [26] F. B. Van Duijneveldt, IBM Research Report RJ945, San Jose, 1971 (unpublished).
- [27] R. Fuchs and W. Whaling, California Institute of Technology Report, Pasadena (unpublished), as cited in Ref. [4].
- [28] J. Lindhard and A. Winter, *K. Dan. Vidensk. Selsk. Mat. Fys. Medd.* **34**, No. 4 (1964).
- [29] J. Z. Wu, S. B. Trickey, and J. R. Sabin, *Nucl. Instrum. Meth.* **B79**, 206 (1993).
- [30] J. Thewlis and A. R. Davey, *Phil. Mag.* **1**, 409 (1956).

Received April 8, 1994

Examination of the Limits of Accuracy of the Extended Koopmans' Theorem Ionization Potentials into Excited States of Ions of LiH, He₂, and Li₂

ROBERT C. MORRISON, CHRISTOPHER M. DIXON,
and JERRY R. MIZELL, JR.

Department of Chemistry, East Carolina University, Greenville, North Carolina 27858-4353

Abstract

A comparison is made between the ionization potentials (IPs) calculated by the extended Koopmans' theorem (EKT) and by taking energy differences (ΔCI) from configuration interaction calculations in the same basis. Several ionization potentials were calculated for LiH, He₂, and Li₂. The best ΔIP , the difference between the EKT IP and the corresponding ΔCI value, was 0.05 meV for the 2σ orbital for LiH and 83.5 meV for the 3σ orbital. The ΔIP s for He₂ were 0.7 meV for the $1\sigma_u$ orbital, 6 eV for the $2\sigma_u$ orbital, 5 meV for the $2\sigma_g$ orbital, and 3 eV for the $3\sigma_g$ orbital. The ΔIP s for Li₂ are 0.1 meV for $2\sigma_g$, 53 meV for $3\sigma_g$, 0.6 meV for $2\sigma_u$, and 1.73 eV for $3\sigma_u$. © 1994 John Wiley & Sons, Inc.

Introduction

The extended Koopman's theorem (EKT) [1–3] provides a method of calculating ionization potentials (IPs) from certain classes of reference wave functions which go beyond the independent particle model. Such wave functions include multi-configurational-self-consistent field (MCSCF) wave functions, full configuration interaction wave functions, and complete-active-space-self-consistent field wave functions. The EKT can be considered to be a special case of the electron propagator and Green's function methods [4–8].

There has been considerable interest [9–16] in the question of the exactness of the EKT for the lowest ionization potential. It has been demonstrated numerically that the lowest EKT IP is exact [11,13]. There is also numerical evidence the EKT is exact for IPs besides the lowest one [15,16].

The EKT IPs are found by solving the matrix equations

$$(\mathbf{V} - \epsilon\gamma)\mathbf{c} = \mathbf{0}, \quad (1)$$

where

$$V_{ij} = -\langle \Psi^N | \hat{a}_i^\dagger [\hat{H}, \hat{a}_j] | \Psi^N \rangle. \quad (2)$$

We can consider \hat{a}_i to annihilate the i th natural spin orbital (NSO) of $|\Psi^N\rangle$ to form an $(N-1)$ -electron wave function $|\Phi_i^{N-1}\rangle$:

$$|\Phi_i^{N-1}\rangle = \hat{a}_i |\Psi^N\rangle.$$

The $|\Phi_i^{N-1}\rangle$ form the basis for the $(N-1)$ -electron wave function, although the $(N-1)$ -electron wave function is not calculated explicitly. The matrix γ is the overlap matrix of the $|\Phi_i^{N-1}\rangle$ and in the NSO-derived basis is a diagonal matrix of NSO occupation numbers n_i ,

$$n_i = \gamma_{ii} = \langle \Psi^N | \hat{a}_i^\dagger \hat{a}_i | \Psi^N \rangle. \quad (3)$$

It is well known that for the ground states of most atoms and molecules N of the n_i are near 1 and the rest fall off very rapidly toward zero. It is not known whether any are actually zero for ground states of many-electron atoms and molecules. It is believed that none of the n_i are zero for ground states of 2-electron systems [12]. Although it has been assumed that some n_i might be zero for ground states of many-electron systems [17], it is unlikely that any are identically zero [12]. Related questions are whether or not the generalized overlap amplitudes, also called Feynman Dyson amplitudes, are linearly independent [18], whether or not the $|\Phi_i^{N-1}\rangle$ form a complete set, and whether or not the set of eigenfunctions having nonzero eigenvalues of the $(N-1)$ -particle reduced density matrix form a complete set [17]. Although we do not expect the EKT calculations to answer these questions, whether or not all the EKT IPs are exact depends on their answers.

The fact that the smallest n_i rapidly decreases as the size of the basis set is increased causes Eq. (1) to become ill-conditioned. Thus EKT calculations using large basis sets which result in a number of very small n_i become difficult and seemingly impractical. We have used canonical orthonormalization to eliminate $|\Phi_i^{N-1}\rangle$ corresponding to n_i below a certain threshold. However, this discards information which might be critical for obtaining accurate ionization potentials.

In this article we examine several IPs for He_2 , LiH , and Li_2 by carrying out a series of calculations in which basis set sizes are varied. Basis sets are systematically changed from one calculation to the next by including additional SCF virtual orbitals in the set.

Calculations and Results

All calculations were performed using the GAMESS [19] program. The basis sets for He and Li were taken from Rizzo, Clementi, and Sekiya [20]. The basis set for H is the same as that used in a previous calculation on H_2^+ [11]. Self-consistent field calculations were performed on each of the three molecules He_2 , LiH , and Li_2 . The SCF orbitals were systematically included in full CI calculations on the ground state of the neutral molecules He_2 , LiH , and Li_2 , and on several states of the positive ions He_2^+ , LiH^+ , and Li_2^+ .

The number of orbitals included in the calculations ranged from 3–18 for He_2 , 3–23 for LiH , and 4–16 for Li_2 . In order to avoid numerical difficulties the $(N-1)$ -electron basis functions, $|\Phi_i^{N-1}\rangle$, were excluded from the basis set for most of the calculations if the corresponding NSO occupation was smaller than 10^{-8} . This excludes many of the $(N-1)$ -electron basis functions for the larger orbital basis

sets. For comparison several calculations were performed using smaller n_i tolerances for excluding the $|\Phi_i^{N-1}\rangle$.

The ionization energies were calculated using both the EKT method and by taking the energy difference $IP(\Delta CI)$ of full CI calculations on the neutral molecule and on the ion in the same basis set.

In the work of Sundholm and Olsen [13] the best comparison between EKT IPs and ΔCI IPs was obtained using only s orbitals. If the higher EKT IPs involving ionization from σ orbitals LiH, He₂, and Li₂ are exact it should be apparent even when only s orbitals are in the basis set. In order to include as many s orbitals as possible within the constraints of our computer system most of the calculations were performed using only s orbitals. For comparison one calculation which includes p orbitals was performed on LiH.

The results of calculations for LiH, He₂, and Li₂ are given in Tables I, II, and III, respectively. The first column lists the number of SCF orbitals included in the basis set for the full CI calculation. The number of natural orbitals kept in the EKT calculation is given in parentheses. The IPs are labeled by the EKT orbital. For example 2σ for LiH corresponds to ionization into the $^2\Sigma^+(1\sigma^2 2\sigma)$ state of LiH⁺, 3σ corresponds to ionization into the $^2\Sigma^+(1\sigma^2 3\sigma)$ state of LiH⁺, $1\sigma_u$ for He₂ corresponds to ionization into the $^2\Sigma_g^+(1\sigma_g^2 1\sigma_u)$ state of He₂⁺, and $2\sigma_g$ for Li₂ corresponds to ionization into the $^2\Sigma_g^+(1\sigma_g^2 1\sigma_u^2 2\sigma_g)$ state of Li₂, etc.

TABLE I. A comparison of the EKT and ΔCI ionization potentials for LiH for increasingly larger basis sets. The natural orbital occupation tolerance for excluding natural orbitals is 10^{-8} . The internuclear distance is 1.5955 Å.

Orbitals SCF (NOS)	Energy	2σ			3σ		
		ΔCI	EKT	ΔIP	ΔCI	EKT	ΔIP
5σ (3σ)	-7.97210	7.9783	7.9789	0.0006	21.9230	21.9765	0.0535
10σ (6σ)	-7.97814	7.5534	7.5535	0.00006	19.1115	19.2642	0.1528
12σ (8σ)	-7.98916	7.3641	7.3641	0.00004	19.1409	19.1901	0.0492
15σ (11σ)	-8.00022	7.3748	7.3748	0.00003	19.2091	19.2908	0.0816
19σ (15σ)	-8.00734	7.3808	7.3809	0.00004	19.2138	19.2959	0.0822
23σ (17σ)	-8.00788	7.3811	7.3812	0.00005	19.2138	19.2972	0.0835
$15\sigma 6\pi$ ($8\sigma 2\pi$)	-7.99137	7.6553	7.6554	0.00008	19.8188	20.1706	0.3519

Orbitals SCF (NOS)	Energy	4σ			5σ		
		ΔCI	EKT	ΔIP	ΔCI	EKT	ΔIP
5σ (3σ)	-7.97210	26.6495	67.2539	40.6043	—	—	—
10σ (6σ)	-7.97814	22.2983	23.0676	0.7694	24.7488	27.9142	3.1654
12σ (8σ)	-7.98916	22.0029	22.1765	0.1736	24.5706	30.0822	5.5116
15σ (11σ)	-8.00022	22.0496	22.3935	0.3439	24.6318	30.0280	5.3962
19σ (15σ)	-8.00734	22.0565	22.3864	0.3299	24.6385	30.1374	5.4988
23σ (17σ)	-8.00788	22.0568	22.4621	0.4053	24.6388	30.1537	5.5149
$15\sigma 6\pi$ ($8\sigma 2\pi$)	-7.99137	22.7876	23.5631	0.7755	24.4740	27.0050	2.5310

TABLE II. A comparison of EKT and Δ CI ionization potentials for He_2 . The natural orbital threshold for excluding natural orbitals is 10^{-8} , except where noted. The internuclear distance is 1.08 Å.

Orbitals SCF (NO)	Energy	$1\sigma_u$			$2\sigma_u$		
		Δ CI	EKT	Δ IP	Δ CI	EKT	Δ IP
$2\sigma_g 2\sigma_u (1\sigma_g 1\sigma_u)$	-5.60963	19.8741	19.8750	0.0008	—	—	—
$3\sigma_g 3\sigma_u (2\sigma_g 2\sigma_u)$	-5.60964	19.8692	19.8696	0.0003	53.2231	69.4167	16.1937
$4\sigma_g 4\sigma_u (2\sigma_g 2\sigma_u)$	-5.60964	19.8518	19.8525	0.0007	51.9285	66.1611	14.2327
$5\sigma_g 5\sigma_u (2\sigma_g 2\sigma_u)$	-5.60967	19.8026	19.8047	0.0021	50.6575	64.5225	13.8651
$6\sigma_g 6\sigma_u (2\sigma_g 2\sigma_u)$	-5.60986	19.6890	19.6947	0.0057	49.4427	63.6271	14.1843
$7\sigma_g 7\sigma_u (3\sigma_g 2\sigma_u)$	-5.61078	19.4876	19.4892	0.0017	48.3200	51.9340	3.6140
$8\sigma_g 8\sigma_u (3\sigma_g 3\sigma_u)$	-5.61391	19.2335	19.2343	0.0008	44.9955	51.8642	6.8687
$9\sigma_g 8\sigma_u (3\sigma_g 4\sigma_u)$	-5.61713	19.1230	19.1235	0.0005	44.8019	50.1532	5.3513
$9\sigma_g 8\sigma_u (5\sigma_g 6\sigma_u)^a$	-5.61713	19.1230	19.1235	0.0005	44.8019	50.1327	5.3308
$9\sigma_g 9\sigma_u (4\sigma_g 4\sigma_u)$	-5.62075	19.0037	19.0038	0.0001	44.4116	51.5217	7.1101
$9\sigma_g 9\sigma_u (7\sigma_g 6\sigma_u)^b$	-5.62075	19.0037	19.0044	0.0007	44.4116	50.0672	5.6556

Orbitals SCF (NO)	Energy	$2\sigma_g$			$3\sigma_g$		
		Δ CI	EKT	Δ IP	Δ CI	EKT	Δ IP
$2\sigma_g 2\sigma_u (1\sigma_g 1\sigma_u)$	-5.60963	30.0663	30.0671	0.0008	—	—	—
$3\sigma_g 3\sigma_u (2\sigma_g 2\sigma_u)$	-5.60964	30.0612	30.0614	0.0002	51.9024	73.4326	21.5302
$4\sigma_g 4\sigma_u (2\sigma_g 2\sigma_u)$	-5.60964	30.0420	30.0428	0.0007	50.2310	71.3962	21.1651
$5\sigma_g 5\sigma_u (2\sigma_g 2\sigma_u)$	-5.60967	29.9858	29.9882	0.0024	48.6722	69.9379	21.2656
$6\sigma_g 6\sigma_u (2\sigma_g 2\sigma_u)$	-5.60986	29.8520	29.8587	0.0067	47.2402	69.0186	21.7784
$7\sigma_g 7\sigma_u (3\sigma_g 2\sigma_u)$	-5.61078	29.6050	29.6062	0.0012	45.9840	56.9979	11.0139
$8\sigma_g 8\sigma_u (3\sigma_g 3\sigma_u)$	-5.61391	29.2706	29.2734	0.0029	47.3676	58.3577	10.9901
$9\sigma_g 8\sigma_u (3\sigma_g 4\sigma_u)$	-5.61713	29.1061	29.1109	0.0048	47.0126	60.1247	13.1121
$9\sigma_g 8\sigma_u (5\sigma_g 6\sigma_u)^a$	-5.61713	29.1061	29.1086	0.0025	47.0126	57.1854	10.1728
$9\sigma_g 9\sigma_u (4\sigma_g 4\sigma_u)$	-5.62075	28.9410	28.9488	0.0077	46.7567	57.5458	10.7891
$9\sigma_g 9\sigma_u (7\sigma_g 6\sigma_u)^b$	-5.62075	28.9410	28.9461	0.0051	46.7567	50.0604	3.3037

^a Natural orbital occupation threshold is 10^{-12} .^b Natural orbital occupation threshold is 10^{-13} .

LiH

For the case using 23 σ SCF orbitals and 17 σ NO's the Δ IP for the lowest IP, 2σ , is 0.05 meV whereas the Δ IP for the next IP, 3σ , is 83.5 meV. The lowest IP is 1670 times more accurate than the next one. The 4σ EKT IP is about five times less accurate than the 3σ EKT IP and the 5σ IP is an order of magnitude less accurate than the 4σ EKT IP. Adding p orbitals to the basis set does not significantly improve the accuracy of the EKT IPs. Lowering the n_i threshold to 10^{-10} for exclusion of $|\Phi_i^{N-1}\rangle$ gives negative Δ IPs in some cases (not shown in the table). This illustrates the problem of including $|\Phi_i^{N-1}\rangle$ with small n_i in the EKT calculation.

He₂

The results for He_2 are given in Table II. The best Δ IP values for the lowest IP, $1\sigma_u$, are 0.1 meV to 0.7 meV whereas the best Δ IP for the $2\sigma_u$ is 5.6 eV, about 8000

TABLE III. A comparison of EKT and Δ CI ionization potentials for Li_2 . The natural orbital occupation tolerances for excluding natural orbitals are 10^{-8} . The internuclear distance is 2.6731 Å.

Orbital space SCF (NO)	Total energy	$2\sigma_g$			$3\sigma_g$		
		Δ CI	EKT	Δ IP	Δ CI	EKT	Δ IP
$4\sigma_g 4\sigma_u (3\sigma_g 2\sigma_u)$	-14.86434	5.1457	5.1463	0.0006	13.3540	15.8394	2.4854
$5\sigma_g 5\sigma_u (3\sigma_g 3\sigma_u)$	-14.86657	5.1897	5.1901	0.0005	12.5370	13.0719	0.5349
$6\sigma_g 6\sigma_u (4\sigma_g 3\sigma_u)$	-14.87012	5.2358	5.2366	0.0008	11.7940	12.1503	0.3563
$7\sigma_g 7\sigma_u (5\sigma_g 4\sigma_u)$	-14.87419	5.2582	5.2584	0.0002	11.2485	11.3375	0.0890
$8\sigma_g 8\sigma_u (5\sigma_g 5\sigma_u)$	-14.87658	5.2778	5.2779	0.0001	11.1113	11.1643	0.0531
SCF (NO)	Energy	$2\sigma_u$			$3\sigma_u$		
		Δ CI	EKT	Δ IP	Δ CI	EKT	Δ IP
$4\sigma_g 4\sigma_u (3\sigma_g 2\sigma_u)$	-14.86434	9.3520	9.3716	0.0196	13.9851	67.3533	53.3682
$5\sigma_g 5\sigma_u (3\sigma_g 3\sigma_u)$	-14.86657	8.8066	8.8352	0.0286	13.3470	67.4025	54.0554
$6\sigma_g 6\sigma_u (4\sigma_g 3\sigma_u)$	-14.87012	8.3671	8.3807	0.0136	12.7659	28.2091	15.4431
$7\sigma_g 7\sigma_u (5\sigma_g 4\sigma_u)$	-14.87419	8.1080	8.1082	0.0002	12.3718	13.3395	0.9677
$8\sigma_g 8\sigma_u (5\sigma_g 5\sigma_u)$	-14.87658	8.0359	8.0365	0.0006	12.2437	13.9737	1.7300

times greater. The Δ IP for the $2\sigma_g$ IP is about 5 meV, about 10 times greater than for the $1\sigma_u$ IP. Both the $1\sigma_u$ and the $2\sigma_g$ IPs can be calculated very accurately.

Li_2

The $2\sigma_g$ Δ IP of 0.1 meV is 530 times less than the 53 meV Δ IP for the $3\sigma_g$ IP. The $2\sigma_g$ IP is about six times more accurate than the $2\sigma_u$ IP. The $3\sigma_u$ EKT IP is considerably worse. As is the case with He_2 , the lowest EKT IP of each symmetry type, σ_g and σ_u , can be calculated very accurately, with the lowest IP of the two being an order of magnitude more accurate.

Conclusions

In He_2 and Li_2 the next to lowest IP, corresponding to a different symmetry state of the ion than the ground state symmetry, can be calculated very accurately, several orders of magnitude more accurately than the next IP. But it is not quite as accurate as the lowest IP of the molecule. The question arises whether it is not as accurate because it is not exact, or whether the method of calculation has systematically excluded the basis functions needed to obtain more accurate calculations. In a previous calculation on Be [16] the basis set was partially optimized to obtain the best EKT IP into the second ^2P state of Be^+ . This produced an accurate EKT IP into the lowest ^2P state of Be^+ and resulted in the conclusion that this EKT IP was exact. A systematic calculation of the same system resulted in the conclusion that it was not exact [15]. Whether or not these "other symmetry" lowest EKT IPs are exact, it appears that in some cases they can be obtained very accurately.

It is not clear whether the apparent inaccuracy of the EKT IPs is due to a fundamental theoretical limit or whether it is because in practical calculations the ill-conditioned nature of Eq. (1) precludes including natural orbitals with very small occupation numbers. It is likely that none of the natural orbital occupation numbers are identically zero for ground states of atoms and molecules [12]. If this is the case, one would expect that all of the EKT IPs would be exact and that the inaccuracies of the higher EKT IPs is due to omitting orbitals which are needed to obtain accurate ionization energies.

Acknowledgments

The authors are grateful for National Science Foundation support in the form of Grant CHE-9301562 to East Carolina University.

Bibliography

- [1] O. W. Day, D. W. Smith, and C. Garrod, *Int. J. Quantum Chem., Quantum Chem. Symp.* **8**, 501 (1974).
- [2] D. W. Smith and O. W. Day, *J. Chem. Phys.* **62**, 113 (1975).
- [3] M. M. Morrell, R. G. Parr, and M. Levy, *J. Chem. Phys.* **62**, 549 (1975).
- [4] L. S. Cederbaum and W. Domcke, *Advances in Chemical Physics*, I. Prigogine and S. A. Rice, Ed. (Wiley, New York, 1977), Vol. 36, p. 205.
- [5] M. F. Herman, K. F. Freed, and D. L. Yeager, *Advances in Chemical Physics* (Wiley, New York, 1981), Vol. 48, p. 1.
- [6] J. Linderberg, and Y. Öhrn, *Propagators in Quantum Chemistry* (Academic Press, London, 1973).
- [7] Y. Öhrn and G. Born, *Advances in Quantum Chemistry*, P. O. Löwdin, Ed. (Wiley, New York, 1981), Vol. 13, p. 1.
- [8] J. A. Nichols, D. L. Yeager, and P. Jørgensen, *J. Chem. Phys.* **80**, 293 (1984).
- [9] J. Katriel and E. R. Davidson, *Proc. Natl. Acad. Sci. USA* **77**, 4403 (1980).
- [10] B. T. Pickup and J. G. Snijders, *Chem. Phys. Lett.* **153**, 69 (1988).
- [11] R. C. Morrison, *J. Chem. Phys.* **96**, 3718 (1992).
- [12] R. C. Morrison, Z. Zhou, and R. G. Parr, *Theor. Chim. Acta* **86**, 3 (1993).
- [13] D. Sundholm and J. Olsen, *J. Chem. Phys.* **98**, 3999 (1993).
- [14] R. C. Morrison, *J. Chem. Phys.* **99**, 6221 (1993).
- [15] D. Sundholm and J. Olsen, *J. Chem. Phys.* **99**, 6222 (1993).
- [16] R. C. Morrison, *Int. J. Quantum Chem.* **49**, 649 (1994).
- [17] B. C. Carlson and J. M. Keller, *Phys. Rev.* **121**, 659 (1961).
- [18] O. Goscinski and P. Lindner, *J. Math. Phys.* **11**, 1313 (1970).
- [19] M. W. Schmidt, K. K. Baldridge, J. A. Boatz, J. H. Jensen, S. Koseki, M. S. Gordon, K. A. Nguyen, T. L. Windus, and S. T. Elbert, *QCPE Bull.* **10**, 52 (1990).
- [20] A. Rizzo, E. Clementi, and M. Sekiya, *Chem. Phys. Lett.* **177**, 477 (1991).

Received March 1, 1994

Chiroptical Techniques and Their Relationship to Biological Molecules, Big or Small

A. RAUK

Department of Chemistry, University of Calgary, Calgary, Alberta T2N 1N4, Canada

T. B. FREEDMAN

Department of Chemistry, Syracuse University, Syracuse, New York 13244

Abstract

The *ab initio* theories of electronic and vibrational circular dichroism are presented in brief. For electronic circular dichroism, emphasis is placed on the derivation of optical rotatory strengths by the perturbative configuration interaction approach as implemented in the program PCI. An application to the chiroptical properties of the disulfide chromophore is described. In the infrared region, the *ab initio* vibronic coupling theory (VCT) of vibrational circular dichroism (VCD) as implemented in the program VCT90, is presented. The relationship to the *ab initio* magnetic field perturbation (MFP) formalism and an approximate locally distributed origin-gauge (LDO) model is described. The VCT and MFP formulations are compared in large basis set and electron correlated studies of the model system, NHDT, and the experimentally characterized molecule, 2,3-dideuteriooxirane. The LDO model of VCD is applied, together with NMR and molecular mechanics techniques, to the investigation of the conformations of the anticancer drug, taxol. Coupled oscillator models are introduced. Applications both in the area of electronic and vibrational circular dichroism, especially to the determination of secondary structures of proteins and nucleic acids are remarked upon. © 1994 John Wiley & Sons, Inc.

Introduction

Chemical transformations take place in three-dimensional space and often require that the reactants be able to adopt very specific geometric configurations and to orient themselves in a very specific manner relative to each other. For complex molecules, the spatial requirements are especially severe, but tremendous advantages from the point of view of reactivity and selectivity can be gained by shape-selective and shape sensitive catalysis. A billion years of evolution has resulted in very sophisticated (bio)chemical systems, which chemists are vigorously trying to understand and emulate *in vitro*. A proper study of the three-dimensional structures of molecules logically requires techniques that are sensitive to the three-dimensional shapes of molecules, especially the property of handedness. Such techniques are collectively called chiroptical techniques. We will focus here on two of these, electronic circular dichroism (ECD), and its counterpart in the infrared region, vibrational circular dichroism (VCD). A CD spectrometer measures the difference, $\Delta A = A_L - A_R$ or $\Delta \epsilon = \epsilon_L - \epsilon_R$, between absorbance of left and right circularly polarized light

as a function of wave length, λ . The area under the CD absorption band of a given transition, K , is $[R]_K$,

$$[R]_K = 0.229 \times 10^{-38} \int_0^\infty \Delta\epsilon_K(\lambda) \frac{d\lambda}{\lambda} \quad (1)$$

in units of $\text{esu}^2 \text{cm}^2$, where $\Delta\epsilon$ is in units of molar extinction coefficient. An analogous measure of the area under the normal absorption band determines the oscillator strength of the transition. Observation of a nonzero CD spectrum requires that the substance being measured be chiral (not superimposable on its own mirror image), and separated (at least in part) from its antipode. All biological molecules of any complexity satisfy these requirements. A substance that consists of a single antipode is said to be *optically pure*. The *absolute configuration* of a chiral substance distinguishes between the two antipodes. It is a major thrust of synthetic organic chemistry to synthesize substances in optically pure form and of known absolute configuration.

The antipodes (enantiomers) of a substance have rotatory strengths of equal magnitude and opposite in sign for every transition. The CD spectra are mirror images of each other. It is sufficient to predict correctly the sign of the rotatory strength of any single transition in order to assign the absolute configuration of a substance, provided the relative spatial dispositions of the nuclei, i.e., the conformation, is known. Different conformations of the same optically pure substance may have very different CD spectra, with rotatory strengths differing in magnitude and possibly in sign. The principal application of chiroptical techniques to biomolecules is not to determine absolute configurations, since for the most part, these are now known, but rather to determine conformations on which the biological activity usually depends.

The theoretical foundation for all chiroptical techniques was elucidated by Rosenfeld [1], who showed that the rotatory strength of a transition, assumed to be between states 0 and n , is simply the imaginary part of the scalar product of the electric dipole and magnetic dipole transition moments for the transition.

$$[R]_K = [R_{0n}] = \text{Im}(\langle \Psi_0 | \vec{\mu} | \Psi_n \rangle \cdot \langle \Psi_n | \vec{m} | \Psi_0 \rangle) \quad (2)$$

where the electric and magnetic dipole moment operators, $\vec{\mu}$ and \vec{m} , respectively, are the sums of electron and nuclear operators,

$$\vec{\mu} = \vec{\mu}^e + \vec{\mu}^n = -\sum_i e\vec{r}_i + \sum_I Z_I e\vec{R}_I \quad (3)$$

and

$$\vec{m} = \vec{m}^e + \vec{m}^n = -\sum_i \frac{e}{2mc} \vec{r}_i \times \vec{p}_i + \sum_I \frac{Z_I e}{2M_I c} \vec{R}_I \times \vec{P}_I \quad (4)$$

The quantities, e , m , \vec{r}_i , and \vec{p}_i , are the charge, mass, position, and momentum of the i th electron, $Z_I e$, M_I , \vec{R}_I , and \vec{P}_I , are the charge, mass, position, and momentum of the I th nucleus, and c is the speed of light. The deceptively simple Rosenfeld relationship (2) has been difficult to put into practice, and despite a 20

year head start for CD spectroscopists, the *first* reliable determination of the absolute configuration of *any* substance [2] was accomplished by x-ray diffraction in 1951, 100 years after Pasteur showed that optical activity has a molecular origin. The transition may be between electronic states, typically the ground state and an electronically excited state, or it may be between different vibrational levels of the ground state. The theoretical description of ECD and VCD [3,4] therefore reduces to the task of evaluating these transition moments in a computationally viable manner. Because of the inherent complexities involved, reasonably reliable evaluation of transition moments has only been available relatively recently for small molecules. For the foreseeable future, direct application of *ab initio* methods to even the smallest biopolymers must remain out of reach. However, it was realized very early that coupled oscillating electric dipoles separated in space and chirally disposed will have an associated magnetic dipole moment. Coupling of degenerate electric dipole allowed transitions (exciton coupling) of two chromophores, suitably oriented in space, will therefore give rise to a couplet of Cotton Effects (CEs) whose order, positive-negative or negative-positive, is intrinsically related to the handedness of the spatial arrangement of the chromophoric groups. The exciton coupling technique, as elucidated by Harada and Nakanishi [5,6], can be reliably used to determine the absolute configurations of molecules that have degenerate chromophores, and the principles of the approach have been extended to large arrays of quasidegenerate chromophores, as may occur in a polymeric material such as a peptide or a nucleic acid.

We describe here successful *ab initio* approaches to both ECD and VCD which have been implemented as computer programs and which permit the prediction of optical rotatory strengths by Eq. (2), citing several studies on small molecules that have been carried out in our laboratories. The results of the *ab initio* studies can be applied to the much larger molecules of interest to biochemists, as illustrated by the study of the conformations of taxol described below. We conclude by describing several theoretical and experimental approaches to the determination of information about the secondary and tertiary structures of polypeptides and nucleic acids.

Theory of Electronic Circular Dichroism

The usual practice in electronic structure calculations is to invoke the Born-Oppenheimer approximation of fixed nuclei. Electronic transitions are accurately described in the same approximation, i.e., as vertical transitions. This has the consequence that the nuclear part of the electric and magnetic dipole moment operators do not contribute to the transition moments, and one may deal solely with the electronic part of the molecular wave function. The method used to calculate electric dipole and magnetic dipole transition moments is based on a configuration interaction (CI) expansion of the ground and excited states. In order to make this approach viable, the expansions must be truncated severely. Each wave function is considered to consist of a small set of strongly interacting configurations (the "zero-order" set) and a much larger set of weakly interacting configurations (the "first-order" set).

The effects of the zero-order set are accommodated by diagonalization of the Hamiltonian matrix of these configurations. The effects of the first-order set are included by perturbation theory. The ground and excited states are assumed not to mix. In assembling the dipole matrix elements, all terms up to first order are kept. The method, implemented in a computer code we call PCI, has seen extensive use [7–10], and has been described in detail elsewhere [11]. A brief summary here serves to illustrate the main features. Partially correlated wave functions for the ground and excited states are determined to first order in Rayleigh–Schrödinger perturbation theory,

$$\Psi_n = \Psi_n^o - \sum_j a_{nj} \Phi_j^o \quad (5)$$

where

$$a_{nj} = \langle \Psi_n^o | H | \Phi_j^o \rangle / (\langle \Phi_j^o | H | \Phi_j^o \rangle - \langle \Psi_n^o | H | \Psi_n^o \rangle) \quad (6)$$

H is the exact Hamiltonian, Φ_j^o is a singlet singly or more highly excited configuration derived from the Hartree–Fock determinant, Φ_{HF} , and Ψ_n^o is a linear combination of strongly interacting Φ_l^o ($l \neq j$) selected from at most singly excited configurations. Thus, for the ground state, $\Psi_0^o = \Phi_{HF}$. All configurations for which the interaction coefficient a_{nj} [Eq. (6)] is greater than 0.03 are normally included in the zero-order part of the CI wavefunction. Electric dipole transition moments in the length $\langle r \rangle_{on}$ and velocity $\langle v \rangle_{on}$ formalism and magnetic dipole transition moments $\langle m \rangle_{on}$ are explicitly evaluated from

$$\langle r \rangle_{on} = \langle \Psi_0 | \vec{\mu}^e | \Psi_n \rangle \quad (7)$$

$$\langle v \rangle_{on} = \langle \Psi_0 | \vec{\nabla}^e | \Psi_n \rangle / (E_n - E_0) \quad (8)$$

$$\langle m \rangle_{n0} = -i \langle \Psi_n | \vec{m}^e | \Psi_0 \rangle \quad (9)$$

where the dipole, gradient, and magnetic moment operators, $\vec{\mu}^e$, $\vec{\nabla}^e$, and \vec{m}^e , have their usual definitions [see, for example, Eqs. (3) and (4)], and

$$E_n = \langle \Psi_n | H | \Psi_n \rangle \quad (10)$$

Oscillator strengths \tilde{R}_{ab} are calculated by the “mixed” formalism

$$f_{0n} = \frac{2}{3} \langle \Psi_0 | \vec{\nabla} | \Psi_n \rangle \cdot \langle r \rangle_{n0} \quad (11)$$

Optical rotatory strengths are evaluated as

$$[R_{0n}]^r = \langle r \rangle_{0n} \cdot \langle m \rangle_{n0} \quad (12)$$

and in the origin independent form

$$[R_{0n}]^v = \langle v \rangle_{0n} \cdot \langle m \rangle_{n0} \quad (13)$$

The extent of the deviation of the vectors $\langle r \rangle$ and $\langle v \rangle$ from collinearity and in magnitude is a measure of the quality of the wave function for the particular states and of the origin dependence of $[R]^r$.

In practice, configurations are generated from only 10 to 20 of the highest occupied MOs and the lowest 50 to 75 unoccupied MOs. Program PCI is implemented on IBM RS/6000 work stations and acquires molecular orbital coefficients and integrals from the GAUSSIAN 92 [12] read-write file.

There is only one other *ab initio* implementation of the theory of optical activity to calculate optical rotatory strengths, that due to Hansen and Bouman [13], based on the random-phase approximation (RPA) [14] and implemented in the program package, RPAC [15].

We describe below an application of ECD as implemented in the program PCI to the study of the chiroptical properties of the disulfide group [16].

The Chiroptical Properties of the Disulfide Group

The disulfide chromophore, which occurs in proteins as disulfide bridges formed from the oxidative coupling of L-cysteine moieties, may exhibit a non-negligible CD in the region 230–330 nm. The equilibrium geometry about a disulfide bond corresponds to a chiral arrangement of the bonds to sulfur with a dihedral angle in the vicinity of 90°. The essential features of the electronic states may be understood from an analysis of the state correlation diagram for the simplest model,

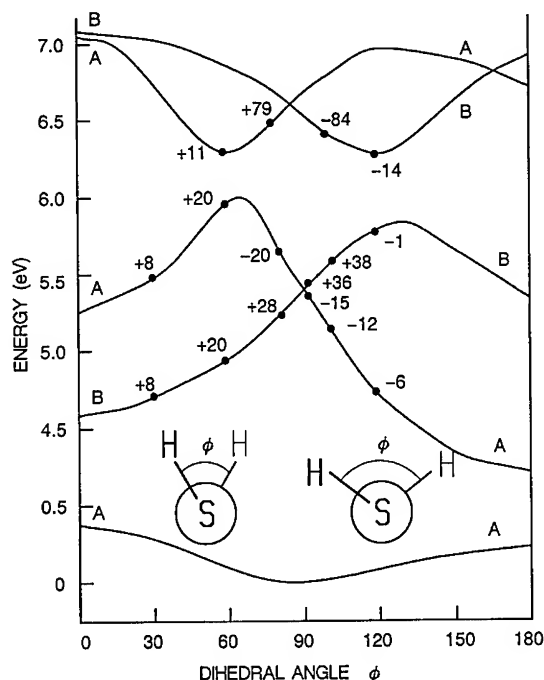


Figure 1. The state correlation diagram for H_2S_2 of *P* chirality. The numbers at the points are the values of the rotatory strengths, $[R]'$ $\times 10^{-40}$ cgs, of the transition to that state at the geometry indicated by the points (see Ref. 16).

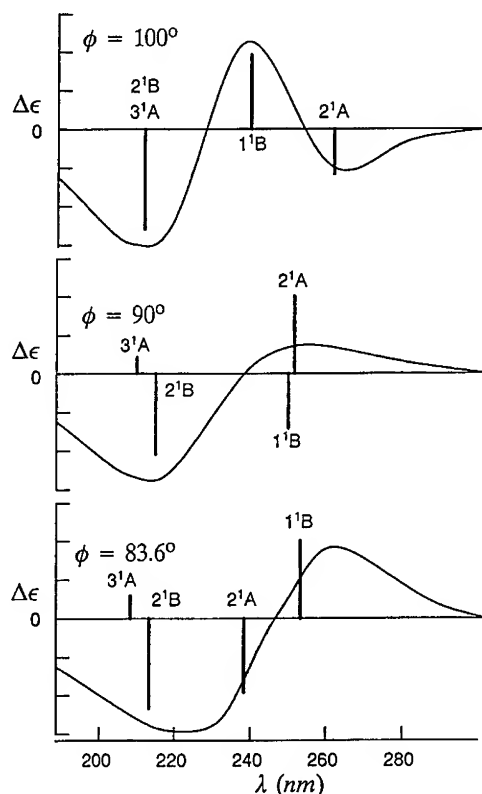


Figure 2. Calculated ECD spectra of *P*-dimethyl disulfide at three values of the dihedral angle. Gaussian line shapes whose areas correspond to the calculated rotatory strengths (width at half height = 0.67 eV) were centered on the transition energies. The vertical bars are proportional to $[R]^*$ (see Ref. 16).

H_2S_2 , shown in Figure 1 [16]. The first two transitions are to valence states, and are designated $n \rightarrow \sigma^*$. Over the range of dihedral angle which corresponds to *P* chirality, the lowest excited state has B symmetry in the range $\phi \leq 90^\circ$ and A symmetry in the range $\phi \geq 90^\circ$. The lowest B state increases in energy with increasing dihedral angle until it has an avoided crossing with a descending state of the same symmetry near $\phi = 120^\circ$. The predicted rotatory strength of the $1^1\text{A} \rightarrow 1^1\text{B}$ transition increases monotonically with dihedral angle, reaching a maximum positive value near 100° and then decreases rapidly to zero. The second excited state, 2^1A , increases with dihedral angle until it suffers an avoided crossing near $\phi = 60^\circ$ and then rapidly descends, crossing the rising 1^1B state to become the lowest excited state at $\phi \geq 90^\circ$. The rotatory strength of the $1^1\text{A} \rightarrow 2^1\text{A}$ transition is positive before the avoided crossing, but changes sign and reaches its largest negative value shortly after. The rotatory strength then decreases monotonically in magnitude with increasing dihedral angle. At the crossing of the two states, a net positive rotatory

strength is predicted. Dimethyl disulfide is a more realistic model for cystine. The state correlation diagram is qualitatively similar. Simulated CD spectra of dimethyl disulfide of *P* chirality at three dihedral angles are shown in Figure 2. At dihedral angles less than or equal to 90°, a positive first Cotton effect (CE) is predicted, whereas for greater than 100°, a first negative CE is expected, followed by a positive CE [16].

Theory of Vibrational Circular Dichroism

For vibrational transitions it is not appropriate to use the Born–Oppenheimer (BO) approximation because the ground and excited states in the context of vibrational transitions have the same electronic wave function and differ only in the nuclear wavefunctions, a consequence of which is that the electronic contribution to the magnetic dipole transition matrix element vanishes in the BO approximation. One must therefore use non-BO wavefunctions [17–20]. The molecular wavefunction of an arbitrary electronic–vibrational state, (e' , ν'), can be expanded in terms of adiabatic BO wavefunctions as

$$\Psi(r, Q)_{e', \nu'} \approx \Psi(r, Q)_{e'} \Phi(Q)_{e', \nu'} - \sum_{e \neq e'} a(Q)_{e', \nu', e} \Psi(r, Q)_e \Phi(Q)_{e, \nu} \quad (14)$$

where the coefficient, $a(Q)_{e', \nu', e}$, is approximated by first order Rayleigh–Schrödinger perturbation theory, using that part of the nuclear kinetic energy operator that acts on the electronic part of the product wavefunction as the perturbation. Thus,

$$a(Q)_{e', \nu', e} = \frac{\langle \Psi(r, Q)_e \Phi(Q)_{e, \nu} | \hat{T} | \Psi(r, Q)_{e'} \Phi(Q)_{e', \nu'} \rangle}{E(Q)_{e, \nu} - E(Q)_{e', \nu'}} \quad (15)$$

where

$$\hat{T} = -\frac{\hbar^2}{2} \left[\left(\frac{\partial^2}{\partial Q^2} \right)_e + 2 \left(\frac{\partial}{\partial Q} \right)_e \left(\frac{\partial}{\partial Q} \right)_n \right] \quad (16)$$

A missing first order term which describes the nuclear (represented by Q) dependence of the electronic part of the wavefunction is introduced by means of a Taylor expansion about the equilibrium geometry of the ground electronic state

$$\Psi(r, Q)_{e'} \approx (\Psi_{e'})_0 + \left(\frac{\partial \Psi_{e'}}{\partial Q} \right)_0 Q \quad (17)$$

Only first order terms are kept in the wavefunction and in the derived matrix elements. Nuclear wavefunctions are assumed to be harmonic oscillator wavefunctions. The harmonic force field and the nuclear displacement dependence of the electronic part of the wave function are readily derived by standard quantum mechanical methods as implemented in computer codes such as GAUSSIAN 92 [12].

Implementations of two *a priori* theoretical models, vibronic coupling theory (VCT) [18] and the magnetic field perturbation (MFP) theory [19,20], and two ap-

proximate but nonempirical models, the localized molecular orbital (LMO) theory [21] model and the locally distributed origins gauge (LDO) model [22], have been developed, and except for the last and most recent, have seen broad application in recent years.

In the VCT method [18], the individual electric and magnetic dipole transition moments are evaluated by Eqs. (18) and (19), respectively,

$$(\vec{\mu})_{(00,01),j}^{\text{VC}} = e \left(\frac{\hbar}{2\omega_j} \right)^{1/2} \left[\sum_I^{\text{atoms}} Z_I \vec{S}_I^j - 2 \sum_I^{\text{atoms}} \sum_i^{\text{electrons}} \left\langle \Psi_0 \left| \vec{r}_i \frac{\partial}{\partial \vec{R}_I} \right| \Psi_0 \right\rangle \vec{S}_I^j \right] \quad (18)$$

$$(\vec{m})_{(01,00),j}^{\text{VC}} = \frac{e}{2c} \left(\frac{\hbar\omega_j}{2} \right)^{1/2} \left[i \sum_I^{\text{atoms}} Z_I (\vec{R}_I^0 \times \vec{S}_I^j) + \frac{2\hbar}{m_e} \sum_I^{\text{atoms}} \sum_i^{\text{electrons}} \sum_e^{\text{ex}} \left\langle \Psi_0 \left| \vec{r}_i \times \vec{p}_i \right| \Psi_e \right\rangle \left\langle \Psi_e \left| \frac{\partial}{\partial \vec{R}_I} \right| \Psi_0 \right\rangle \vec{S}_I^j \frac{1}{E_e - E_0} \right] \quad (19)$$

where Z_I is the bare nuclear charge of atom I with positional vector, \vec{R}_I , and displacement vector $\vec{S}_I^j = (\partial \vec{R}_I / \partial Q_j)$ during a normal vibrational mode Q_j , \vec{r}_i and \vec{p}_i are the position and momentum of the i th electron, ω_j is the frequency of the j th normal mode, and $E_e - E_0$ is the vertical electronic excitation energy. The electronic wavefunctions are denoted as Ψ_0 and Ψ_e for ground and excited states, respectively. The superscript VC indicates that these expressions describe a vibronic coupling mechanism for IR and VCD intensities. The subscripts (00,01) and (01,00) signify that the transition is between the 0 and 1 vibrational levels of the ground electronic state of the molecule.

Since the usual description of the ground electronic wavefunction is the Hartree-Fock determinant (the SCF level), the set of excited states may be restricted to the set of singlet spin adapted singly excited configurations as was the practice in the case of ECD. The VCT rotatory strength is then the imaginary part of the scalar product of $\vec{\mu}_{(00,01),j}^{\text{VC}}$ and $\vec{m}_{(01,00),j}^{\text{VC}}$. The atomic polar tensor (APT), $\mathbf{P}_{\alpha\beta}^I$, and atomic axial tensor (AAT), $\mathbf{M}_{\alpha\beta}^I$, can be extracted from Eqs. (18) and (19) respectively, as:

$$\mathbf{P}_{\alpha\beta}^I = e Z_I \delta_{\alpha\beta} - 2e \sum_i^{\text{electrons}} \left\langle \Psi_0 \left| \vec{r}_i^{\alpha} \frac{\partial}{\partial \vec{R}_I^{\beta}} \right| \Psi_0 \right\rangle \quad (20)$$

and

$$\mathbf{M}_{\alpha\beta}^I = \frac{e}{2c} Z_I \vec{R}_{0,\alpha}^I \epsilon_{\alpha\beta\gamma} - \frac{i\hbar e}{m_e c} \sum_i^{\text{electrons}} \sum_{e \neq 0}^{\text{ex}} \frac{\left\langle \Psi_0 \left| (\vec{r}_i^{\alpha} \times \vec{p}_i^{\beta}) \right| \Psi_e \right\rangle \left\langle \Psi_e \left| \frac{\partial}{\partial \vec{R}_I^{\alpha}} \right| \Psi_0 \right\rangle}{E_e - E_0} \quad (21)$$

The definition for the nuclear and electronic parts of $\mathbf{M}_{\alpha\beta}^I$ differ by a factor of $i/2\hbar$ from the one introduced by Stephens [23]. The AATs are in general origin dependent, and may be calculated either in a common origin (CO) gauge or in a distributed origin (DO) gauge [23,24]. With rare exceptions, the DO results are consistently better than the CO results for each basis set and at both the SCF and MP2 levels. In the latter, the electronic ground state, Ψ_0 , is approximated by the normalized MP2 wavefunction, i.e.,

$$\Psi_0 = N(\Phi_{\text{HF}} + \Phi_{\text{MF2}}) = N \left(\Phi_{\text{HF}} + \sum_{a < b}^{\text{occ spin}} \sum_{r < s}^{\text{vir spin}} C_{ab}^{rs} \Phi_{ab}^{rs} \right) \quad (22)$$

where N is the normalization factor, Φ_{HF} is the HF determinantal wavefunction, Φ_{ab}^{rs} is the doubly excited configuration generated by replacement of the occupied orbitals a and b by the virtual orbitals r and s , and C_{ab}^{rs} is the MP2 coefficient. The APTs at the SCF level or MP2 level may be adopted directly from the GAUSSIAN codes [25]. AATs at both levels are obtained using the locally developed program VCT90 [24,26,27].

The locally distributed origin-gauge (LDO) model is derived from the exact *a priori* VCT formalism by ignoring terms involving local atomic magnetic dipole moment operators and converting the remaining term involving velocity-form atomic APT contributions to position-form in a well-defined manner. The LDO model rotational strength expression

$$(R_r^a)^{\text{LDO}} \approx \frac{\hbar}{4c} \left(\sum_A \sum_B [P_{r,\alpha\beta}^A]^B S_{A\alpha,a} \right) \cdot \left(\sum_{A'} \sum_{B'} \epsilon_{\beta\gamma\delta} R_{\beta'\gamma}^0 [P_{r,\alpha\delta}^{A'}]^{B'} S_{A'\alpha,a} \right) \quad (23)$$

employs a position-form APT broken down into atomic contributions, with the moment arm in the magnetic dipole transition moment term directed to the contributing atomic center. This origin choice, which differs from the DO gauge (wherein the moment arm is to the moving atom) provides a more local description of the contributions to VCD intensity. This method requires only unperturbed, nonlocalized, ground-state electronic wavefunctions, and is thus suitable for calculations on larger molecules than those to which the current *a priori* methods are limited. The LDO model has been implemented as an extension of the VCT90 software. Good agreement in sign and relative magnitude for calculations with the LDO model and the *a priori* methods has been found for small molecules such as (*S,S*)-oxirane-2,3-d₂, (*S,S*)-cyclopropane-1,2-d₂, and for the OH- and NH-stretches in R-methyl lactate and (*S*)-1-amino-2-propanol [22].

The APTs and AATs have been reformulated [28] in terms on nuclear shielding tensors and implemented using the RPA [14] approximation to evaluate the sum over states. The *ab initio* implementation has been incorporated into the RPAC program [15].

In VCT, the first-order-non-BO description of the electronic part of the magnetic dipole transition moment, at the level of first order Rayleigh–Schrödinger perturbation theory, is the same as a magnetic field perturbation of the electronic part of the wavefunction,

$$\left(\frac{\partial \Psi_0}{\partial \vec{B}} \right)_{\vec{B}=0} = - \sum_{e \neq 0} \frac{\langle \Psi_e | \vec{m}^e | \Psi_0 \rangle}{E_e - E_0} \Psi_e \quad (24)$$

The magnetic field dependence of the electronic part of the wavefunction [the left-hand side of Eq. (24)] at the SCF level may be evaluated directly by means of a coupled perturbed Hartree–Fock calculation. This is the basis of the magnetic field

perturbation (MFP) formulation of VCD intensities [19,20]. The MFP approach has been implemented first by Stephens and co-workers [29] and others [30,31], and has been incorporated into the *ab initio* program system, CADPAC [32]. Very recently, the MFP method has been extended to include AATs evaluated over MCSCF wavefunctions expanded in terms of gauge invariant (London) atomic orbitals [33].

Table I compares the results of different VCD models with Hartree-Fock-limit basis sets for NHDT, the largest molecule for which such a limiting comparison may be carried out. The last column and column 9 [VCT/MP2/vd3p(u)] differ by an average of 8% and represent the most accurate values realistically achievable at the post-HF level. A direct comparison with actual experimental results for the 2,3-dideuteriooxirane molecule [34] is shown in Table II. A measure of the average % deviation from experimental results is provided across the bottom of the table. The MFP method, using MP2 APTs and force field, but SCF AATs [35], yields exceedingly good results in all regions of the spectrum except the C—H stretching region. The VCT/MP2 is a little less successful but performs equally well throughout the spectrum [27]. Accumulated experience with VCD calculations suggests that the most critical factor is the quality of the molecular force field, the MP2 *ab initio* force field being significantly superior to an SCF force field. Thus reasonably accurate results are achievable with a much smaller basis set provided an MP2 force field is used. The VCT/MP2/6-31G* results listed in Table II (column 5) are an indication of this. It is particularly noteworthy that comparable results may be obtained at the fully SCF level with the 6-31G*(0.3) (superstar) basis set (Table II, column 9), which was originally designed to mimic a much larger basis set for VCD applications [36], but which fortuitously yields MP2-like force fields and geometries. Experience gained in applications to a series of three-ring heterocycles [24,37–40] for which experimental results are also available suggests that VCT/SCF/6-31G*(0.3) calculations may be applied with confidence to larger systems which begin to have some biological interest.

We describe below an example of the application of an *ab initio* VCD theoretical model, the LDO model, to the resolution of a conformational problem in an intermediate sized molecule, taxol.

Conformational Analysis of Taxol Side-Chains

A combination of molecular modeling and *ab initio* quantum mechanical calculations and VCD and IR measurements have been used to define the conformations of the anticancer chemotherapeutic agent taxol and its side-chain methyl ester [41]. This work was a collaborative project of C. S. Swindell and co-workers L. E. Chirlian, M. M. Francl, J. M. Heering, and N. E. Krauss, of Bryn Mawr College, who provided samples [taxol (1), O-Ac-Baccatin III (2), the taxol side-chain methyl ester (3) and taxols with modified side-chains 4 and 5] and carried out molecular modeling calculations, and T. B. Freedman and co-workers D. M. Gigante and X. Qu, of Syracuse University, who measured the spectra and performed the *ab initio* calculations of geometries, frequencies, and VCD intensities of taxol fragments.

TABLE I. Rotatory strengths^b of (S)-NHDT.^c

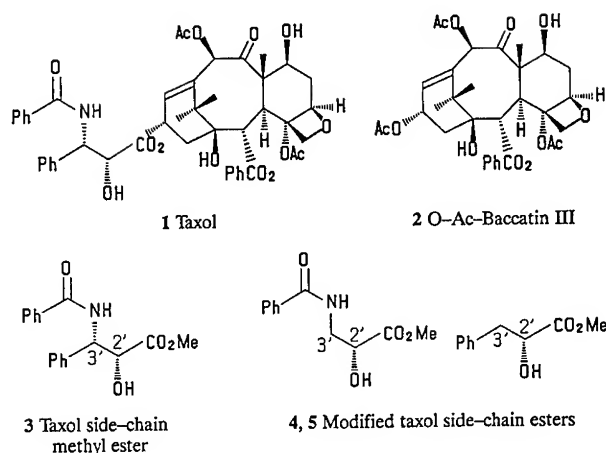
No.	Freq ^d	VCT				MFP			
		6-31g*		6-31g*(0.3)		vd/3p ^e		pVTZ(++) ^f	
		SCF	MP2	SCF	MP2	SCF	MP2	SCF	CAS2
1	846	-3.36	-3.84	-3.67	-4.22	-4.57	-5.14	-6.30	-4.72
2	1192	6.73	7.66	7.30	8.14	9.02	10.72	11.88	9.50
3	1480	-3.50	-3.92	-3.75	-4.07	-4.56	-5.36	-5.71	-4.82
4	2195	0.46	0.51	0.53	0.68	0.64	0.82	0.75	0.61
5	2632	-0.26	-0.35	-0.37	-0.59	-0.58	-0.85	-0.67	-0.64
6	3603	0.02	0.05	0.05	0.11	0.11	0.18	0.13	0.14

^a Ref. 27.^b In units of 10⁻⁴⁴ esu² cm².^c Geometry of NH₃: SCF/vd/3p(u), r_{NH} = 0.998 Å, <_{HNH} = 107.6°; MP2/vd/3p(u), r_{NH} = 1.009 Å, <_{HNH} = 107.0°; Expt (Ref. 82), r_{NH} = 1.012 Å, <_{HNH} = 106.7°.^d MP2/vd/3p(u) force field. Dipole strengths (10⁻⁴⁰ esu² cm²) for modes 1-6 are 467.0, 35.9, 57.3, 6.2, 7.4, 7.4, respectively.^e Ref. 29; Duncan and Mills harmonic force field (Ref. 82); at experimental geometry, in the DO gauge.^f Ref. 33; at experimental geometry, in the common origin gauge, with GIAO orbitals, and *ab initio* force field: CAS1, 924 CSFs; CAS2 71947 CSFs.^g MP2 with all singles CI for the sum over states.

TABLE II. Rotatory strengths^a of (S,S)-2,3-dideuteriooxirane in DO gauge.

No.	Sym.	VCT										MFP ^b		Expt ^c					
		6-31g*					6-31g*(0.3)					vd/3p							
		SCF	Δ	MP2	Δ	MS ^d	Δ	SCF ^e	Δ	MP2	Δ		SCF		Δ	MP2	Δ	MP2 ^f	Δ
1	b	-0.4		-0.1		0.0		0.6		0.2		0.9		0.3		0.0			(673)
2	a	2.1		-4.1		-6		4.7		-3.2		11.1		4.4		11.8			(754)
3	b	-4.6	x	-0.3	x	-0.7	x	-0.7	x	1.2		-0.7	x	2.7		1.7		(+)	(817)
4	a	8.9	78	13.9	178	14.7	193	6.0	20	8.3	66	0.9	82	5.7	13	8.0	60	(+5.0)	(885)
5	b	7.0	x	-2.7	56	-2.0	68	1.8	x	-3.2	48	1.0	x	-6.6	6	-3.7	40	-6.2	914
6	a	-17.6	39	-15.2	48	-19.2	34	-18.9	35	-6.8	77	-27.6	5	-19.9	31	-28.2	3	-29.0	948(961)
7	b	2.0	82	5.2	53	2.9	74	3.6	68	10.7	4	6.7	40	16.8	51	10.1	9	11.1	1102(1106)
8	a	2.8	x	-1.2	76	-1.4	71	0.1	x	-8.8	80	5.9	x	-5.3	9	-6.3	29	-4.9	1109(1112)
9	a	5.4	78	10.1	58	9.1	62	8.1	66	10.1	58	8.0	67	13.3	45	10.9	55	24.1	1226(1235)
10	b	-5.2	108	-2	92	-1.1	56	-1.5	41	-1.6	36	-1.7	31	-1.0	61	-1.3	48	(-2.5)	(1339)
11	a	-4.3	71	-9.0	40	-7.5	50	-4.9	67	-5.4	64	-7.1	53	-11.1	26	-8.3	45	(-15.0)	(1397)
12	b	-15.6	50	-6.6	37	-10.9	5	-8.3	20	-2.3	78	-11.7	12	-4.3	59	-11.2	8	-10.4	2232(2240)
13	a	13.3	10	7.0	42	11.1	9	9.1	25	3.1	74	11.8	3	5.2	57	12.7	5	12.1	2252(2254)
14	a	-22.5	153	-10.7	20	-19.8	122	-16.2	82	-3.9	56	-20.3	128	-5.5	38	-24.4	174	-8.9	3014(3015)
15	b	28.8	153	12.0	5	20.6	81	16.7	46	4.1	64	23.1	102	7.6	34	22.8	100	11.4	3027(3028)
Average Δ ^g		99(89)		1	59(68)		69(62)	58(57)		0	59(58)		72(63)	36(36)		48(30)			
Wrong signs		3				1		3			0	3		0			0		

^a In units of 10⁻⁴⁴ esu² cm².^b Ref. 35.^c Ref. 34; values in parentheses are from the gas-phase spectrum.^d MP2 with all singles CI for the sum over states.^e Values previously reported were obtained at the geometry optimized with five *d* functions rather than the default six, and differ from the present values by a maximum of 0.2 × 10⁻⁴⁴ esu² cm².^f Calculated using MP2 force field, MP2-APTS and SCF-AATS.^g Percentage error. The bands with incorrect signs are taken into account; the values in parentheses are obtained with modes 14 and 15 excluded.



Conformational data on the free taxol ligand in aqueous and nonaqueous solution is a preliminary step to the determination of the bound conformation of taxol to cellular microtubules. Due to the rigidity of the baccatin III nucleus, these studies have focused on the side-chain conformation. In aqueous solution, $^1\text{H-NMR}$ studies reveal a conformation with *anti* 2'-CH and 3'-CH side-chain bonds [42], whereas only *gauche* bonds are detected in chloroform solution [43]. In the crystal structure of the side-chain methyl ester **3**, these bonds are also *gauche* [44]. No crystal structure of taxol itself is available. VCD is a useful additional tool for determining the taxol side-chain conformation, since VCD intensity arising from local OH- and NH-oscillators provides information on the local chiral environments of the oscillators and is particularly sensitive to stabilizing intramolecular hydrogen bonding.

Spectra of **1**, **2**, and **3** were recorded in the OH- and NH-stretching regions ($3800\text{--}3300\text{ cm}^{-1}$) on samples 0.0025 to 0.005 M in chloroform. In Figure 3, the VCD spectrum of the taxol side-chain ester (---) is compared with VCD spectra of taxol from which the VCD features of the baccatin III nucleus have been subtracted (—), or from which the features of both baccatin III and the side-chain methyl ester (\cdots) have been subtracted. For the side-chain of **1**, a single intense positive OH-stretching VCD band is observed at 3525 cm^{-1} , ascribed to a conformer with strong $\text{OH} \cdots \text{O}=\text{C}$ hydrogen bonding by comparison to the VCD spectra of R-methyl lactate and R-methyl mandelate [45], which exhibit similar positive OH-stretching VCD features. This type of conformation is found in the side-chain crystal structure, shown in Figure 4(A). No VCD is observed for the peptide NH-stretch of the side-chain corresponding to the intense sharp absorption feature at 3443 cm^{-1} , assigned to free NH-stretch. The VCD spectrum of the A-ring side-chain in taxol, obtained by subtracting the VCD features arising from the OH-stretches on the baccatin III nucleus from the VCD spectrum of taxol, is dominated by an intense positive feature that coincides with that of the side-chain OH-stretch, but in addition two new positive bands are observed. The band at 3592 cm^{-1} is ascribed to a more weakly bound OH-stretch, and the fairly sharp positive feature at 3430 cm^{-1} , which is shifted to lower frequency by 13 cm^{-1} compared to free NH-stretching absorption,

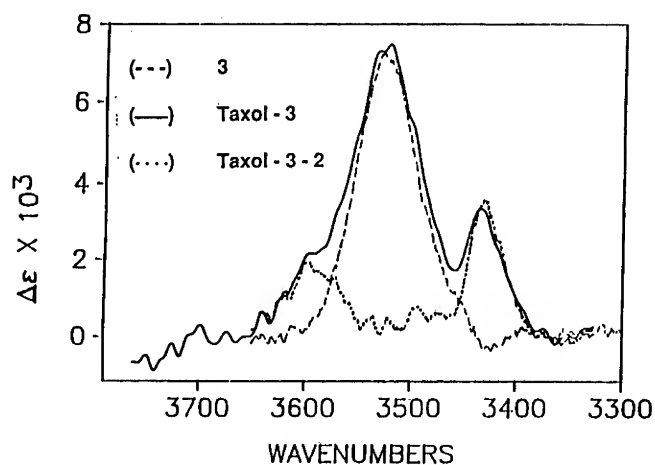


Figure 3. Side-chain OH- and NH-stretching VCD features: (---) side-chain methyl ester [1]; (—) [(taxol)-(13-O-Ac-baccatin III)] VCD difference spectrum [taxol-2]; (····) [(taxol)-(13-O-Ac-baccatin III)-(side chain ester)] VCD difference spectrum [taxol-2-3].

is assigned to a hydrogen-bonded NH-stretch. By contrast, the taxol with modified side-chain **4** or **5** exhibits only a single positive OH-stretching VCD feature that is identical in frequency and intensity with the spectra of the corresponding free side-chain methyl ester. These data are consistent with a dominant side-chain conformation of the native taxol that corresponds to (A), and a minor conformation such

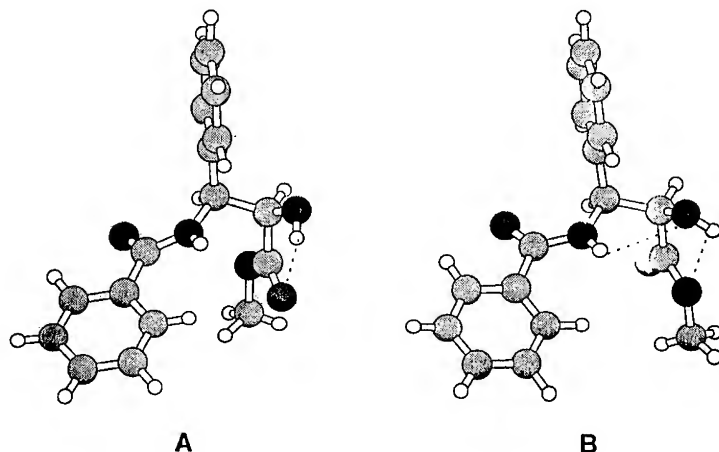


Figure 4. Taxol side-chain methyl ester conformations: (A) crystal structure geometry; (B) structure obtained from (A) by rotation of OH and ester groups for OH···OCH₃ hydrogen bonding with dihedral angles as calculated for corresponding methyl lactate conformer.

as (**B**), in which a $\sim 180^\circ$ rotation of the ester group introduces a weaker $\text{OH} \cdots \text{OCH}_3$ hydrogen bond and a reorientation of the OH that now allows $\text{NH} \cdots \text{OH}$ hydrogen bonding (Fig. 4). We have previously observed that peptide or amino NH bonds adjacent to a chiral center and involved in intramolecular hydrogen bonding exhibit intense monosignate NH-stretching VCD, but similar free NH-stretches do not [46]. A similar minor conformer does not occur for the modified taxols with side-chains **4** or **5**.

Conformational searches of the entire taxol structure using internal coordinate Monte Carlo conformational searches with a molecular mechanics MM2 force field and a chloroform continuum solvation model were carried out at Bryn Mawr College [41]. This study identified four low energy structural types, shown in Figure 5 (**C**)–(**F**), where the A-ring side-chain and any associated atoms of the baccatin III nucleus are highlighted. To further define solution structures consistent with the VCD data, a taxol side chain fragment with the phenyl groups replaced by hydrogen was employed for *ab initio* geometry, frequency and VCD intensity calculations. Geometries and frequencies for six optimized side-chain backbone conformations related to the MM2 structures or the aqueous solution conformation were calculated [Fig. 6(**G**)–(**H**), with positions of the phenyl groups shown in black]. Calculations were performed with Gaussian 90 [25] with a 6-31G* basis set.

The results of the LDO model [22] VCD calculations of the fragment OH- and NH-stretches in the six taxol fragment conformers are shown in Figure 6. The lowest energy conformer (**G**) corresponds to the crystal structure of the side-chain (**A**) and to MM2 structure (**C**). The calculated LDO model VCD intensity for the OH-stretch is large and positive, with only a very small calculated NH-stretching VCD intensity, in agreement with experimental measurements for the side-chain ester and the major taxol conformer. Conformation (**H**) corresponds to the aqueous solution conformation with *trans* methine bonds. Positive OH-stretching VCD, smaller than that for (**G**) is calculated; this structure is ruled out by NMR for the chloroform solution conformation of native taxol, but it may be important for the modified taxols, which exhibit smaller OH-stretching anisotropy ratios. The calculated NH- and OH-stretching VCD intensities for conformation (**I**) are both positive, but small. Although the frequency shift for (**I**) compared to (**G**) for the OH-stretch agrees with that for the minor taxol conformer, the NH-stretching frequency does not decrease, and the transannular $\text{OH} \cdots \text{O}=\text{C}$ hydrogen bonding in the corresponding MM2 structure (**D**) would decrease the OH-stretching frequency for the side chain when attached to baccatin III. In conformation **J**, which corresponds to MM2 structure (**E**), the OH-stretching VCD intensity is calculated to be negative and the OH-stretching frequency to be lower than that for (**G**). The frequency shifts and NH-stretching VCD intensity for (**K**), the $\sim 180^\circ$ ester rotamer of (**I**), do not agree with experiment for the minor conformer. Conformer (**L**), the $\sim 180^\circ$ ester rotamer of (**G**), which corresponds to (**B**) and MM2 structure (**F**), is calculated to have large positive VCD intensities for both the NH- and OH-stretches and a calculated 63 cm^{-1} increase in OH-stretching frequency and 11 cm^{-1} decrease in NH-stretching frequency. These values agree well with the positive VCD intensities and frequency shifts ($+67$ and -13 cm^{-1} , respectively) observed for the minor taxol

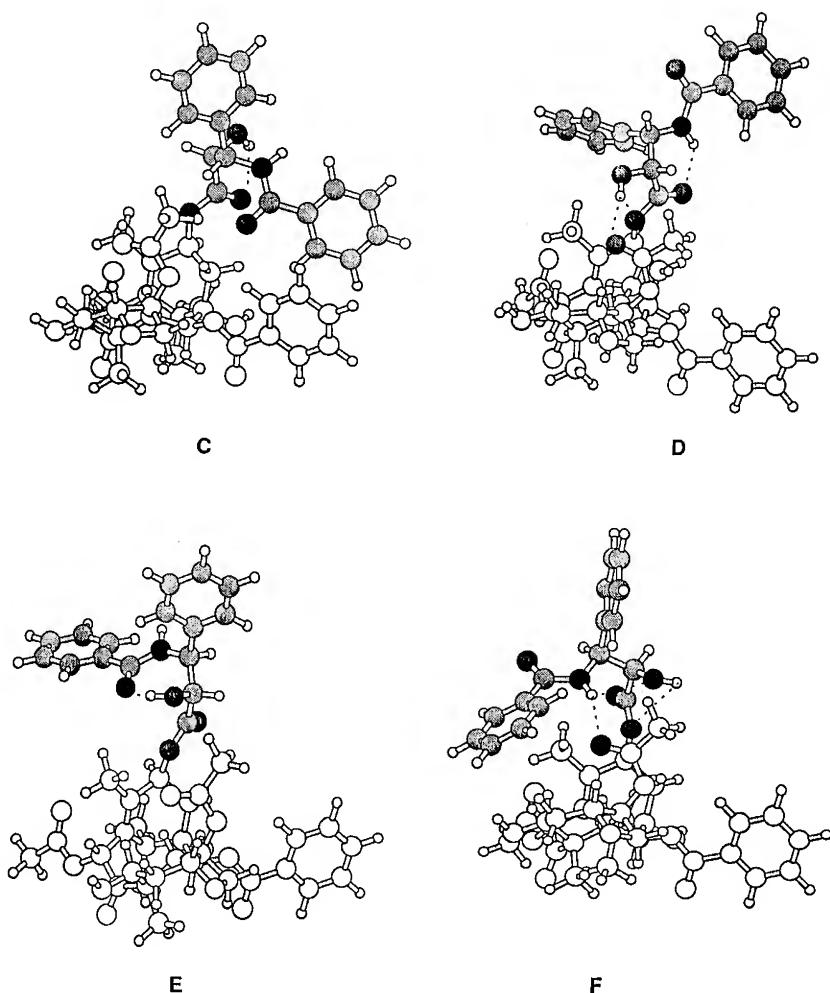


Figure 5. Taxol conformational types (C)–(F) deduced from MM2 Monte Carlo conformational searches.

conformer. The VCD studies and geometry, frequency, and intensity calculations thus support conformational type (A/C/G) for the major conformer in taxol and (B/F/L) for the minor conformer. Further examination of the MM2 structures reveals that although the side-chain $\text{OH} \cdots \text{O}$ hydrogen bonding for (F) is weaker than that for (C), steric interaction between side-chain and baccatin III phenyl groups is relieved in (F) and a stabilizing *trans*-annular hydrogen bond can form between the side chain NH and the 4-OAc group on the oxetane ring.

Chiroptical Methods for Large Molecules

Larger systems require the application of approximate theoretical models. We restrict our attention to applications aimed at the determination of secondary and

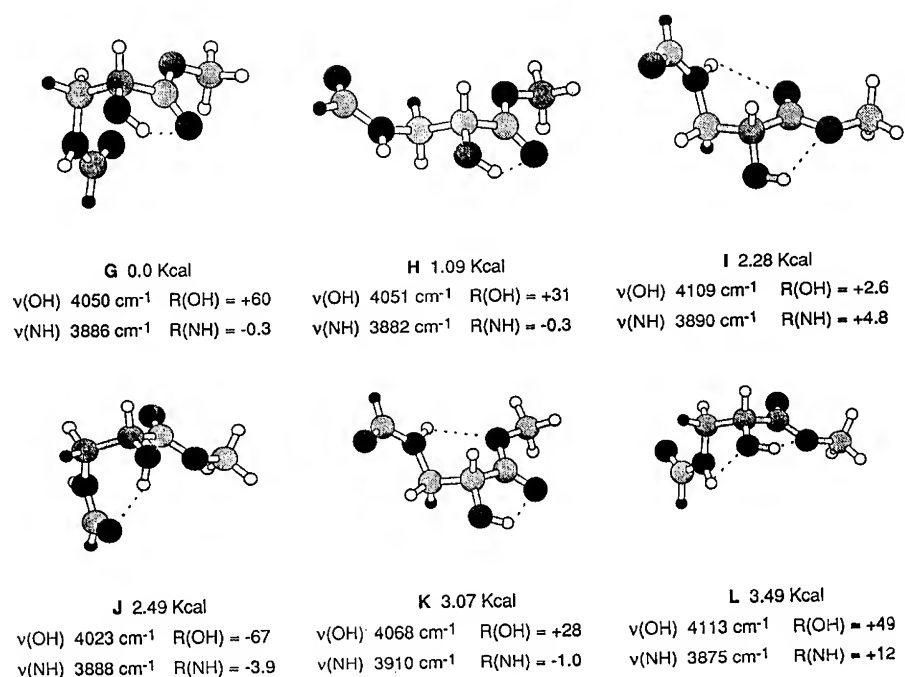


Figure 6. Gaussian 90 optimized geometries (6-31G* basis) calculated for a taxol side chain methyl ester fragment with the phenyl rings replaced by hydrogen atoms. Relative energies, calculated OH- and NH-stretching frequencies and LDO model rotational strengths ($10^{44} \text{esu}^2 \text{cm}^2$) are indicated for each conformer.

tertiary structures of polypeptides and nucleic acids. The intrinsic difficulty with chiroptical methods, as with any spectroscopic methods applied to large complex molecules is that the observed spectrum is the superposition of the spectra of many subunits which differ in their local chirality and which may or not be coupled in some way. ECD and VCD have complementary strengths in that they sample different spatial aspects of the superstructure. Electronic transitions may have rather large dipole moments and couple over large distances. ECD therefore may be expected to be diagnostic of long range order of the superstructure. On the other hand, vibrational transitions are associated with relatively small dipole transition moments, which would be sensitive to local geometry, particularly since mechanical coupling of vibrational modes is also expected to contribute to the chiroptical properties.

ECD has been applied to the analysis of peptide secondary structure for many decades. The basic premise is that biopolymers exhibit a rather limited range of structural features (α -helix, β -sheet, "coil," etc., for polypeptides, A-form, B-form, etc., for polynucleotides). Since compositions in terms of these structural forms may be elicited from x-ray and NMR data, as well as the chiroptical methods, one approach that has seen good success is the deconvolution of a set of experimental spectra to extract spectra of the "pure" forms (Fig. 7) [47-50], which may then be

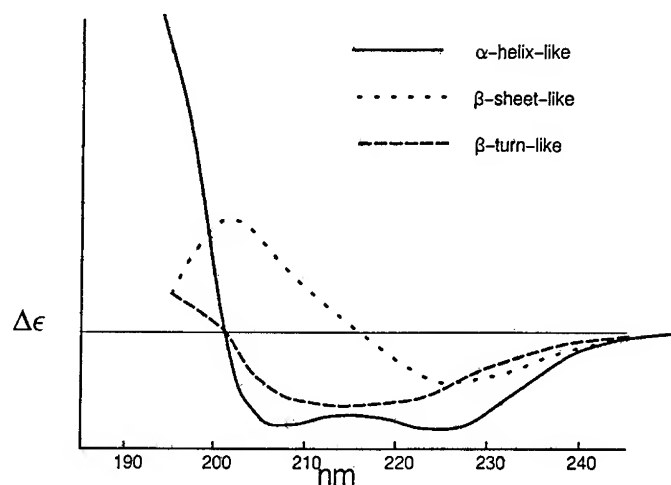


Figure 7. Three "pure" ECD curves extracted by component analysis of the spectra of a set of proteins (see Ref. 58).

fitted to spectra of polymers of unknown make-up to obtain the fractions or weights of the various forms.

Little in the way of "sector" rules has emerged to assist in the interpretation of VCD spectral features [51–54]. However, early VCD measurements of polypeptides, principally by Keiderling's group, have demonstrated that different secondary structural types give rise to characteristic VCD patterns, especially in the amide I (mainly CO stretch, $\sim 1650\text{ cm}^{-1}$) region [55,56]. For instance, α -helical structures yield a bisignate amide I band, the sign of which depends on the handedness of the

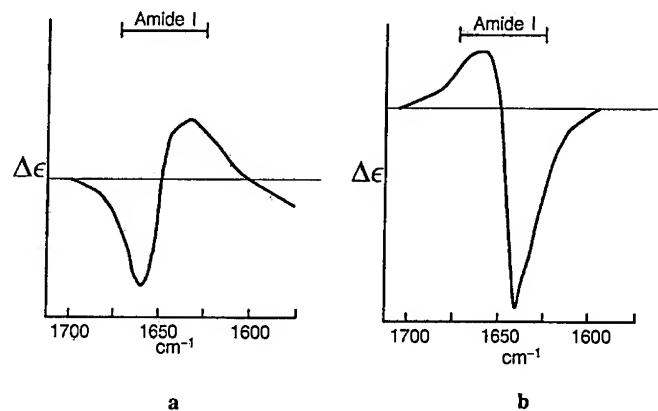


Figure 8. Typical VCD spectra of polypeptides in the Amide I region: (a) α -helix (simulated spectrum of albumin [Ref. 56]); (b) "random coil" (simulated spectrum of poly-L-lysine [Ref. 56]).

helix, positive for a right-handed helix [Fig. 8(a)], and not on the absolute configuration of the α -carbon. The "random coil" form gives rise in many polypeptides and proteins to a large negative couplet, especially in D₂O, indicating residual order in the form of a left-handed helix. Indeed, VCD has been shown to be more robust than ECD in its diagnosis of secondary structure, the latter being more sensitive to the presence of chromophores other than the amide linkage itself [57]. A component deconvolution analogous to that employed for ECD has also met with good success in the case of VCD [57–59].

The Empirical Coupled Oscillator Models

The coupled oscillator models of chiroptical properties [60–63] are based on molecular exciton coupling theory [64–66]. The electronic or vibronic transitions of two identical chromophoric groups, with frequency, ν_0 , separated in space by a displacement vector, \vec{R}_{ab} , will couple to give two absorption bands at frequencies,

$$\nu_{\pm} = \nu_0 \pm V_{ab} \quad (25)$$

with associated rotational strengths,

$$R^{\pm} = \mp \frac{\pi \nu_0}{2c} \vec{R}_{ab} \cdot (\vec{\mu}_a \times \vec{\mu}_b) \quad (26)$$

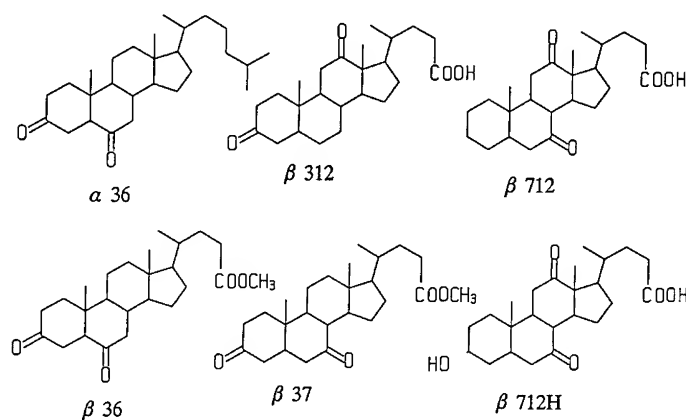
The coupling energy is assumed to be primarily due to dipolar coupling,

$$V_{ab} = \frac{\vec{\mu}_a \cdot \vec{\mu}_b}{|\vec{R}_{ab}|^3} - \frac{3(\vec{\mu}_a \cdot \vec{R}_{ab})(\vec{\mu}_b \cdot \vec{R}_{ab})}{|\vec{R}_{ab}|^5} \quad (27)$$

where $\vec{\mu}_a$ and $\vec{\mu}_b$ are electric dipole transition moment vectors associated with the two chromophores. The approach may be extended to more than two coupled oscillators, and to coupling of nearly degenerate oscillators [67]. The transitions should be strongly electric dipole allowed. Therefore, π – π^* transitions are desirable for ECD, while localized excitations such as carbonyl, NH, or OH stretching vibrations are desirable for VCD. One needs to know the direction and magnitude of the transition dipole vectors. The magnitude may be measured from the normal absorption spectrum. The direction relative to the chromophore skeleton can be inferred from the electronic structure of the chromophore if the nature of the electronic transition can be identified, or from the direction of the bond moment in the case of VCD. Positioning of the chromophores in space corresponds to assignment of different configurations or conformations of the molecule. Coupled oscillator models have seen wide application to ECD. They form the basis of the exciton chirality method for the determination of absolute configurations of organic compounds as developed by Harada and Nakanishi [5]. The recent report by Lightner and co-workers on the conformational analysis of bilirubin illustrates the combined power of ECD spectroscopy, the exciton coupling approach, and molecular modelling techniques [68]. Coupled oscillator methods were first applied to VCD by Holzwarth and Chabay [69], who applied the method to diketopiperazines (formed by cyclic dimerization of amino acids).

In polypeptides, the obvious chromophoric transition which should display an intimate connection to the secondary structure is the π - π^* transition of the amide backbone, which is responsible for the CD bands in the range 200–220 nm. However, coupling of the transitions of other chromophores, such as π - π^* transitions of tyrosines and histidines, or n - σ^* transitions of disulfide links, which occur at longer wavelengths (240–280 nm) may also be used to advantage. A matrix formulation of the theory of optical activity has been developed by Bayley, Nielsen, and Schellmann [70], based on a coupling of the excited states of the various chromophores in a manner analogous to configuration interaction. Chromophores may be coupled if their relative coordinates are known. The method has been applied to ribonuclease S to show that the solution phase CD spectral features may be predicted from the x-ray coordinates, thereby suggesting similarity of the solution conformation to that in the solid state [71].

The limits of the degenerate coupled oscillator (DCO) model (with dipolar coupling) for VCD applications have been evaluated against the *a priori* magnetic field perturbation (MFP) model [72]. It was found that for two formaldehyde molecules at reasonably large separations, the DCO and MFP models agreed well, but severe and unpredictable deviations may occur at short distances or when the coupling is between adjacent oscillators in the same molecule. In the latter case, the frequency order and phasing of coupled oscillators is best obtained from an *ab initio* normal coordinate analysis, rather than dipolar coupling. The DCO model has been applied to predict the VCD spectra of a series of dicarbonyl-containing steroids with substantial success [73].



In this series of compounds, which satisfy the “remoteness” criterion, only the steroid, β 37, showed only a monosignate VCD curve rather than the bisignate signal expected on the basis of the coupled oscillator model and the model calculations.

The spectral features of several polypeptides in the amide I (and amide II) region were well reproduced by MFP calculations on a simple alanine-like model dipeptide that was conformationally constrained to mimic the local geometry of not only α -helix and β -sheet, but also 3_{10} -helix and left-handed poly-L-proline (as a model for

random coil) [74]. The DCO model failed to reproduce these features of the dipeptides in the amide I region and fared little better in the Amide II [74]. However, the group of Diem has had some success in the application of an extended coupled oscillator model to the conformations of a prototypical peptide, poly-L-tyrosine [75], and have used the method to detect a VCD feature in the amide I region associated with a β -turn in a model cyclic peptide [76].

Extensive use has been made of ECD to interpret nucleic acid base stacking, conformational change, and double helix formation [77]. If the nucleic acids are in a highly condensed form (due to changes in the tertiary structure from extended to, e.g., coiled), additional sources of rotatory strength are observed and the sign of the CD may depend on the degree of aggregation. This psi-type CD [78] has been explained by invoking intermediate and radiation coupling effects as well as dipole-dipole coupling [79]. Similar effects have been observed in complexes between DNA and polypeptides [80]. We will not discuss these mechanisms further.

Polyribonucleic acids display well-defined couplets in their VCD spectra, in the 1600 cm^{-1} to 1700 cm^{-1} region (Fig. 9) [81], indicating the possible applicability of coupled oscillator models [67,81]. The separation of the nucleic acid bases in the usual helical structures ensures independence of mechanical coupling of chromophores situated on them. Three of the nucleic acid bases have carbonyl groups, but since the molecules also have conjugated $\text{C}=\text{C}$ and $\text{C}=\text{N}$ double bonds, it

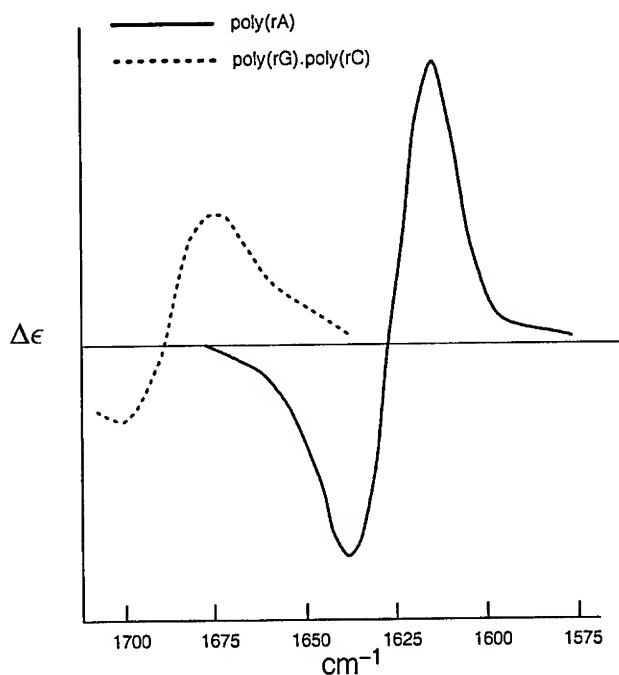


Figure 9. VCD spectra of poly(riboseadenine) (—, adapted from Ref. 81) and poly(riboseguanine).poly(ribosecytosine) (-----, adapted from Ref. 67).

is not clear that the carbonyls are sufficiently isolated to utilize in the same sense as the work described above for the steroid-based models. Adenine has no carbonyl groups at all. Diem and co-workers have applied the degenerate extended coupled oscillator (DECO) model to the problem of the helicity of nucleic acids carrying out DECO calculations for up to three separate modes using moment directions deduced from semiempirical force field calculations [67].

Acknowledgments

T. B. F. acknowledges support from the National Institutes of Health (GM-23567 to L. A. Nafie and T. B. F.). A. R. is grateful for research support from the Natural Sciences and Engineering Council of Canada.

Bibliography

- [1] L. Z. Rosenfeld, *Physik* **52**, 161 (1928).
- [2] J. M. Bijvoet, A. F. Peerdeman, and A. J. van Bommel, *Nature* **168**, 271 (1951).
- [3] T. B. Freedman and L. A. Nafie, in *Non-Linear Optics, Part 3*, M. Evans and S. Kielich, Eds., Advances in Chemical Physics Series, Vol LXXXV (J Wiley, New York, 1994), pp. 207–263, and references therein.
- [4] A. Rauk, in *New Developments in Molecular Chirality*, P. G. Mezey, Ed. (Kluwer Academic Publishers, Amsterdam, The Netherlands, 1991), pp. 57–92.
- [5] N. Harada and K. Nakanishi, *Acc. Chem. Res.* **5**, 257 (1972).
- [6] N. Harada and K. Nakanishi, *Circular Dichroism-Exciton Coupling in Organic Stereochemistry* (University Science Books, Mill Valley, CA, 1983).
- [7] G. V. Shustov, G. K. Kadorkina, S. V. Varlamov, A. V. Kachanov, R. G. Kostyanovsky, and A. Rauk, *J. Am. Chem. Soc.* (in press).
- [8] G. V. Shustov, G. K. Kadorkina, R. G. Kostyanovsky, and A. Rauk, *J. Am. Chem. Soc.* **110**, 1719 (1988).
- [9] G. V. Shustov, S. V. Varlamov, I. I. Chervin, A. E. Aliev, R. G. Kostyanovsky, D. Kim, and A. Rauk, *J. Am. Chem. Soc.* **111**, 4210 (1989).
- [10] G. V. Shustov, S. V. Varlamov, A. Rauk, and R. G. Kostyanovsky, *J. Am. Chem. Soc.* **112**, 3403 (1990).
- [11] A. Rauk and J. M. Barriol, *Chem. Phys.* **25**, 409 (1977).
- [12] M. J. Frisch, G. W. Trucks, M. Head-Gordon, P. M. W. Gill, M. W. Wong, J. B. Foresman, B. G. Johnson, H. B. Schlegel, M. A. Robb, E. S. Replogle, R. Gomperts, J. L. Andres, K. Raghavachari, J. S. Binkley, C. Gonzalez, R. L. Martin, D. J. Fox, D. J. Defrees, J. Baker, J. J. P. Stewart, and J. A. Pople, *Gaussian 92, Revision B* (Gaussian, Inc., Pittsburgh, PA, 1992).
- [13] Aa. E. Hansen and T. D. Bouman, *J. Am. Chem. Soc.* **107**, 4828 and references therein (1985).
- [14] C. W. McCurdy, Jr., T. N. Rescigno, D. L. Yeager, and V. McKoy, in *Methods of Electronic Structure Theory*, H. F. Schaefer III, Ed. (Plenum, New York, 1977), p. 339.
- [15] T. D. Bouman and Aa. E. Hansen, *RPAC Molecular Properties Package*, Version 9.0, University of Copenhagen, 1991.
- [16] A. Rauk, *J. Am. Chem. Soc.* **106**, 6517 (1984).
- [17] (a) D. P. Craig and T. Thirunamachandran, *Mol. Phys.* **35**, 825 (1978). (b) D. P. Craig and T. Thirunamachandran, *Can. J. Chem.* **63**, 1773 (1985).
- [18] L. A. Nafie and T. B. Freedman, *J. Chem. Phys.* **78**, 7108 (1983).
- [19] P. J. Stephens, *J. Phys. Chem.* **89**, 748 (1985).
- [20] A. D. Buckingham, P. W. Fowler, and P. A. Galwas, *Chem. Phys.* **112**, 1 (1987).
- [21] (a) L. A. Nafie and T. H. Walnut, *Chem. Phys. Lett.* **49**, 441 (1977). (b) T. H. Walnut and L. A. Nafie, *J. Chem. Phys.* **67**, 1501 (1977). (c) L. A. Nafie and P. L. Polavarapu, *J. Chem. Phys.* **75**, 2935 (1981).

- [22] T. B. Freedman, L. A. Nafie, and D. Yang, *Chem. Phys. Lett.* (submitted).
- [23] P. J. Stephens, *J. Phys. Chem.* **91**, 1712 (1987).
- [24] D. Yang and A. Rauk, *J. Chem. Phys.* **97**, 6517 (1992).
- [25] M. J. Frisch, M. Head-Gordon, G. W. Trucks, J. B. Foresman, H. B. Schlegel, K. Raghavachari, M. A. Robb, J. S. Binkley, C. Gonzalez, D. J. Defrees, D. J. Fox, R. A. Whiteside, R. Seeger, C. C. F. Melius, J. Baker, R. L. Martin, L. R. Kahn, J. J. P. Stewart, S. Topiol, and J. A. Pople, *Gaussian 90*, Gaussian, Inc., Pittsburgh, PA, 1990. The version at the University of Calgary was modified to write extra information to the Read-Write file for VCD calculations.
- [26] D. Yang, Ph. D. dissertation, The University of Calgary, Calgary, Canada, 1992.
- [27] D. Yang and A. Rauk, *J. Chem. Phys.* (in press).
- [28] Aa. E. Hansen, P. J. Stephens, and T. D. Bouman, *J. Phys. Chem.* **95**, 4255 (1991).
- [29] K. J. Jalkanen, P. J. Stephens, R. D. Amos, and N. C. Handy, *J. Phys. Chem.* **92**, 1781 (1988).
- [30] (a) R. D. Amos, N. C. Handy, and P. Palmieri, *J. Chem. Phys.* **93**, 5796 (1990). (b) R. D. Amos, N. C. Handy, A. F. Drake, and P. Palmieri, *J. Chem. Phys.* **89**, 7287 (1988).
- [31] K. Morokuma and H. Sugeta, *Chem. Phys. Lett.* **134**, 23 (1987).
- [32] R. D. Amos, *The Cambridge Analytic Derivatives Package*, Publication CCP 1/84/4, SERC, Daresbury Laboratory, Daresbury, Warrington, U. K., 1984.
- [33] K. L. Bak, P. Jorgensen, T. Helgaker, K. Ruud, and H. J. Aa. Jensen, *J. Chem. Phys.* **98**, 8873 (1993).
- [34] T. B. Freedman, K. M. Spencer, N. Ragunathan, L. A. Nafie, J. A. Moore, and H. M. Schwab, *Can. J. Chem.* **69**, 1619 (1991).
- [35] P. J. Stephens, K. J. Jalkanen, F. J. Devlin, and C. F. Chabalowski, *J. Phys. Chem.* **97**, 6107 (1993).
- [36] A. Rauk and D. Yang, *J. Phys. Chem.* **96**, 437 (1992).
- [37] S. T. Pickard, H. E. Smith, T. M. Black, P. L. Polavarapu, T. M. Black, A. Rauk, and D. Yang, *J. Am. Chem. Soc.* **114**, 6850 (1992).
- [38] P. L. Polavarapu, S. T. Pickard, H. E. Smith, T. M. Black, A. Rauk, and D. Yang, *J. Am. Chem. Soc.* **113**, 9748 (1991).
- [39] A. Rauk, T. Eggimann, H. Wieser, G. V. Shustov, and D. Yang, *Can. J. Chem.* (in press).
- [40] D. Yang, G. V. Shustov, R. G. Kostyanovski, T. Eggimann, H. Wieser, and A. Rauk, *Can. J. Chem.* **71**, 2028 (1993).
- [41] G. M. Gigante, X. Qu, T. B. Freedman, C. S. Swindell, L. E. Chirlian, M. M. Francl, J. M. Heerding, and N. E. Krauss (submitted).
- [42] H. J. Williams, A. I. Scott, R. A. Dieden, C. S. Swindell, L. E. Chirlian, M. M. Francl, J. M. Heerding, and N. E. Krauss, *Tetrahedron* **55**, 6545 (1993).
- [43] (a) G. N. Chmurny, B. D. Hilton, S. Brobst, S. A. Look, K. M. Witherup, and J. A. Beutler, *J. Nat. Prod.* **55**, 414 (1992). (b) J. K. Baker, *Spectrosc. Lett.* **25**, 31 (1992). (c) C. J. Falzone, A. J. Benesi, and J. T. J. Lecomte, *Tetrahedron Lett.* **33**, 1169 (1992). (d) B. D. Hilton, G. N. Chmurny, and G. M. Musckik, *J. Nat. Prod.* **55**, 1157 (1992).
- [44] J. R. Peterson, H. D. Do, and R. D. Rogers, *Pharm. Res.* **8**, 908 (1991).
- [45] (a) Y. Nakao, H. Sugeta, and Y. Kyogoku, *Chem. Lett.* 623 (1984). (b) T. B. Freedman, G. A. Balukjian, and L. A. Nafie, *J. Am. Chem. Soc.* **107**, 6213 (1985).
- [46] (a) M. G. Paterlini, T. B. Freedman, L. A. Nafie, Y. Tor, and A. Shanzer, *Biopolymers* **32**, 765 (1992). (b) M. G. Paterlini, Ph.D. dissertation, Syracuse University, New York, 1990. (c) D. A. Young, E. D. Lipp, and L. A. Nafie, *J. Am. Chem. Soc.* **107**, 6205 (1985).
- [47] A. Perczel, K. Park, and G. D. Fasman, *Anal. Biochem.* **203**, 83 (1992).
- [48] A. Perczel, Zs. Majer, S. Holly, D. Macintka, G. D. Fasman, and M. Hollósi, *Tetrahedron Asymm.* **4**, 591 (1993).
- [49] R. W. Server, Jr. and W. C. Krueger, *Anal. Biochem.* **199**, 61 (1991).
- [50] I. H. M. van Stokkum, H. J. W. Spoelder, M. Bloemendal, R. van Grondelle, and F. C. A. Groen, *Anal. Biochem.* **191**, 110 (1990).
- [51] D. Yang, G. V. Shustov, T. Eggimann, H. Wieser, and A. Rauk, *Can. J. Chem.* **71**, 2028 (1993).
- [52] L. A. Nafie, M. R. Oboddi, and T. B. Freedman, *J. Am. Chem. Soc.* **105**, 7449 (1983).
- [53] T. B. Freedman, A. C. Chernovitz, W. M. Zuk, G. M. Paterlini, and L. A. Nafie, *J. Am. Chem. Soc.* **110**, 6970 (1988).

- [54] T. B. Freedman and L. A. Nafie, in *Topics in Stereochemistry*, E. Eliel and S. Wilen, Eds. (Wiley, New York, 1987), Vol. 17, pp. 113–206.
- [55] S. C. Yasui and T. A. Keiderling, *J. Am. Chem. Soc.* **108**, 5576 and references therein (1986).
- [56] V. Baumruk and T. A. Keiderling, *J. Am. Chem. Soc.* **115**, 6939 (1993).
- [57] P. Pancoska, S. C. Yasui, and T. A. Keiderling, *Biochemistry* **28**, 5917 (1989).
- [58] P. Pancoska, S. C. Yasui, and T. A. Keiderling, *Biochemistry*, **30**, 5089 (1991).
- [59] V. P. Gupta and T. A. Keiderling, *Biopolymers* **32**, 239 (1992).
- [60] W. Kuhn, *Ann. Rev. Phys. Chem.* **9**, 417 (1958).
- [61] W. Moffit, *J. Chem. Phys.* **25**, 467 (1956).
- [62] I. Tinoco, Jr., *Radiat. Res.* **20**, 133 (1963).
- [63] I. Tinoco, Jr., R. W. Woody, and D. F. Bradley, *J. Chem. Phys.* **38**, 1317 (1963).
- [64] A. S. Davydov, *Theory of Molecular Excitons*, M. Kasha and M. Oppenheimer, Jr., Transl. (McGraw-Hill, New York, 1962).
- [65] J. A. Schellman, *Acc. Chem. Res.* **1**, 144 and references therein (1968).
- [66] B. Bosnich, *Acc. Chem. Res.* **2**, 266 and references therein (1969).
- [67] T. Xiang, D. J. Goss, and M. Diem, *Biophys. J.* **65**, 1255 (1993).
- [68] R. V. Person, B. R. Peterson, and D. A. Lightner, *J. Am. Chem. Soc.* **116**, 42 (1994).
- [69] G. Holzwarth and I. Chabay, *J. Chem. Phys.* **57**, 1632 (1972).
- [70] P. M. Bayley, E. B. Nielsen, and J. A. Schellmann, *J. Phys. Chem.* **73**, 228 (1969).
- [71] W. J. Goux and T. M. Hooker, Jr., *J. Am. Chem. Soc.* **102**, 7080 (1980).
- [72] P. Bour and T. A. Keiderling, *J. Am. Chem. Soc.* **114**, 9100 (1992).
- [73] U. Narayanan and T. A. Keiderling, *J. Am. Chem. Soc.* **105**, 6406 (1983).
- [74] P. Bour and T. A. Keiderling, *J. Am. Chem. Soc.* **115**, 9602 (1993).
- [75] S. S. Birke, I. AgBaje, and M. Diem, *Biochemistry* **31**, 450 (1992).
- [76] H. Wyssbrod and M. Diem, *Biopolymers* **32**, 1237 (1992).
- [77] C. A. Bush and J. Brahms, in *Physico-Chemical Properties of Nucleic Acids*, J. Duchesne, Ed. (Academic Press, New York, 1973), Vol. 2, pp. 147–186. C. A. Bush, in *Basic Principles of Nucleic Acid Chemistry*, P. O. P. Ts'o, Ed. (Academic Press, New York, 1974), Vol. II, pp. 92–172.
- [78] C. F. Jordan, L. S. Lerman, and J. H. Venable, Jr., *Nature* **236**, 67 (1972).
- [79] (a) D. Keller and C. Bustamente, *J. Chem. Phys.* **84**, 2961 (1986). (b) D. Keller and C. Bustamente, *J. Chem. Phys.* **84**, 2972 (1986).
- [80] S. Weinberger, C. Berman, and A. Minsky, *J. Am. Chem. Soc.* **110**, 8231 (1988).
- [81] A. Annamalai and T. A. Keiderling, *J. Am. Chem. Soc.* **109**, 3125 (1987).
- [82] J. L. Duncan and I. M. Mills, *Spectrochim. Acta* **20**, 523 (1964).

Received March 3, 1994

Multicavity SCRF Calculation of Ion Hydration Energies

GEERD H. F. DIERCKSEN

*Max-Planck-Institut für Astrophysik, Karl-Schwarzschild-Strasse 1,
Garching bei, München, Deutschland*

MATI KARELSON

Department of Chemistry, University of Tartu, Tartu, EE 2400, Estonia

TOOMAS TAMM* and MICHAEL C. ZERNER†

Department of Chemistry, University of Florida, Gainesville, Florida 32611

Abstract

The hydration energies of the proton, hydroxyl ion, and several inorganic ions were calculated using the multicavity self-consistent reaction field (Mca SCRF) method developed for the quantum-mechanical modeling of rotationally or flexible systems in dielectric media. The ionic complexes $\text{H}_3\text{O}^+(\text{H}_2\text{O})_4$, $\text{OH}^-(\text{H}_2\text{O})_4$, $\text{NH}_4^+(\text{H}_2\text{O})_4$, and $\text{Hal}^-(\text{H}_2\text{O})_4$, where $\text{Hal} = \text{F}, \text{Cl}, \text{or Br}$, have been studied. Each complex was divided between five spheres, corresponding to the central ion and four water molecules in their first coordination sphere, respectively. Each cavity was surrounded by a polarizable medium with the dielectric permittivity of water at room temperature (80). The ionic hydration energies of ions were divided into specific and nonspecific parts. After accounting for the cavity-formation energy using scaled particle theory, good agreement between the total calculated and experimental hydration energies was obtained for all ions studied. © 1994 John Wiley & Sons, Inc.

Introduction

Ad hoc calculation of ion solvation energies has been a target for many generations of physical and theoretical chemists [1–7]. The classical Born model [1] of the electrostatic solvation of spherical ions had been thoroughly tested in the landmark work by Latimer, Pitzer, and Slansky [2], and by others [3–7]. The more recent developments of this model include semiempirical approaches for the definition of ionic radii in solution and its application for the multiaatomic ions of more complex shape and charge distribution (e.g., zwitterions) [8–14]. Another classical approach to ion solvation has been based on various approximations of rigorous statistical mechanical theory of fluids, which include the mean, spherical approximation (MSA) in hypernetted chain (HNC) or Percus–Yevick (PY) expansion or extended reference interaction site (RISM) methods [15–19]. The Monte Carlo and molecular dynamic

* Permanent address: Department of Chemistry, University of Tartu, Tartu, EE 2400, Estonia.

† To whom correspondence should be addressed.

simulations of ion solvation and the related free-energy perturbation calculations [20–30] can conventionally be classified also as classical methods, even if quantum-mechanical intermolecular interaction potentials are applied in these simulations.

A common shortcoming of all the above-listed methods is the neglect of the influence of intermolecular interactions to the electronic structure, and thus to the charge distribution of the solute (ion) and solvent molecules in the vicinity of the solute. Therefore, different variations of the quantum-mechanical approach, based on the Born [1] and Kirkwood-Onsager [31–33] reaction field theories of the dielectric continuum have been developed by a number of groups at different level of quantum theory for equilibrium [34–59] and nonequilibrium [60–63] systems. Some of these theories have been subsequently applied to the calculation of the solvation energies of molecules and ions [64–70].

In parallel to the development of the quantum-mechanical continuum solvation models, the *ab initio* calculations of ion-solvent clusters have added valuable information about the structure of the closest solvation shell [71–82]. While in most cases correctly calculating the ion solvation energies in different gaseous clusters [83,84], these supermolecule calculations neglect, in principle, a substantial amount of the bulk solvation energy due to the solvent orientational, electronic, and nuclear polarization in the field of the solute (ion). Consequently, the most feasible way to approach these calculations would seem to us to treat the closest solvation shell using quantum mechanics and then include the dielectric polarization of the bulk solvent [64,85–87]. A recent development of an *ab initio* pseudopotential free energy approach, an interesting unification of the quantum theory and statistical mechanics, looks very promising, from this viewpoint [88,89].

In this work, we present the application of the combined supermolecule-continuum approach to ion solvation using a recently developed multicavity self-consistent reaction field (MCA SCRF) method [90]. In this method, the (super)molecule under the study is divided into rotationally inversionally flexible fragments, each of which is embedded into a spherical cavity, surrounded by the bulk dielectric continuum. Each fragment generates its own reaction field, respectively, which are interacting with each other and with the charge distribution in other fragments. For the present application, a separate cavity has been ascribed to the central ion and each of the water molecules in the first coordination sphere.

Theory

The MCA SCRF method has been described in detail elsewhere [90] and thus we present only the essentials here. We notice that the interaction of charge and higher electrical moments of a charge distribution in a spherical cavity with the corresponding reaction fields localized in the center of cavity, does not depend on the position of charge or (point) multipole centers in this cavity [33]. It is therefore possible to divide a molecule between two or more spherical cavities which border each other along the rotating bond or the bond to be cleaved in the process of a chemical reaction. Correspondingly each molecular fragment has its own reaction field, which interacts with the charge density, and reaction fields of other fragments.

We proceed by the partitioning the solute molecule into M fragments, indexed as A, B, \dots , which are embedded into M spherical cavities with radii a_{oi} ($i = A, B, \dots$). Assuming the classical Born-Kirkwood-Onsager expansion [33] for each of these fragments one obtains an expansion for the total energy of the solute in a dielectric medium.

$$E = E_o + E(\text{intrafragment}) + E(\text{interfragment}) \quad (1)$$

The terms in Eq. (1) correspond to the energies arising from the interaction of the partial charge and the moments of a molecular fragment with the reaction field (drf) of its own and other fragments as well from the interaction between the reaction fields of different fragments. Terms in these expansions proportional to the reaction field tensors Γ_i ,

$$\Gamma_{io} = \frac{\epsilon - 1}{2\epsilon a_{oi}}; \Gamma_i = \frac{(\epsilon - 1)}{(2\epsilon + 1)a_{oi}^3} F_i \quad (2)$$

can be referred to as the first-order reaction field energies, terms proportional to the square of Γ as the second-order energies. We also notice that the use of the dielectric permittivity ϵ in Γ assumes full orientational and electronic relaxation of the solvent in the field of solute fragment and therefore corresponds to the full coupling between rotational-inversional movements of the solute fragment and the solvent molecules. In formula (2), a_{oi} denotes the cavity radius for a given fragment i , and F_i the factor accounting for a net charge on fragment i [90].

In the framework of the one-electron approximation, the quantum-mechanical extension of Eq. (1) now has the following form, up to the dipole term, of

$$\begin{aligned} E_{\text{tot}} = \langle \phi | \mathbf{H} | \phi \rangle = \langle \phi | \mathbf{H}_o | \phi \rangle + \sum_A \Gamma_A \langle \phi | \mu_A | \phi \rangle \langle \phi | \mu_A | \phi \rangle \\ + \sum_A \Gamma_A \langle \phi | \mathbf{P}_A | \phi \rangle \langle \phi | \mathbf{P}_A | \phi \rangle + \sum_{A \neq B} \Gamma_A \langle \phi | \mu_A | \phi \rangle \langle \phi | \mu_B | \phi \rangle / R_{AB}^2 \\ + \sum_{A \neq B} \Gamma_A \langle \phi | \mathbf{P}_A | \phi \rangle \langle \phi | \mathbf{P}_B | \phi \rangle / R_{AB} \\ + \sum_{A \neq B} \Gamma_A \langle \phi | \mu_A | \phi \rangle \langle \phi | \mathbf{P}_B | \phi \rangle / R_{AB}^2 + \sum_{A \neq B} \Gamma_B \langle \phi | \mu_B | \phi \rangle \langle \phi | \mathbf{P}_A | \phi \rangle / R_{AB}^2 \\ + \sum_{A \neq B} \Gamma_A \Gamma_B \langle \phi | \mu_A | \phi \rangle \langle \phi | \mu_B | \phi \rangle / R_{AB}^3 \\ + \sum_{A \neq B} \Gamma_A \Gamma_B \langle \phi | \mathbf{P}_A | \phi \rangle \langle \phi | \mathbf{P}_B | \phi \rangle / R_{AB} \\ + \sum_{A \neq B} \Gamma_A \Gamma_B \langle \phi | \mu_A | \phi \rangle \langle \phi | \mathbf{P}_B | \phi \rangle / R_{AB}^2 \quad (3) \end{aligned}$$

where \mathbf{H}_o is the solvent-unperturbed Hamiltonian of the solute molecule, R_{AB} —the distance between the centers of adjacent cavities, μ_A and μ_B represent the dipole moment operators of the respective molecular fragments, and \mathbf{P}_A and \mathbf{P}_B are the projection operators of the partial charge on fragments A and B to the total molecular wavefunction ϕ , respectively. The \mathbf{P}_A and \mathbf{P}_B operators can be defined following one of the possible LCAO MO charge partitioning schemes in the molecule. Mulliken

charges have been used in the present application. It is possible now to build a variational functional for the total energy E and derive the corresponding Hartree-Fock-type equations which can be again to be solved iteratively (SCRF) [90].

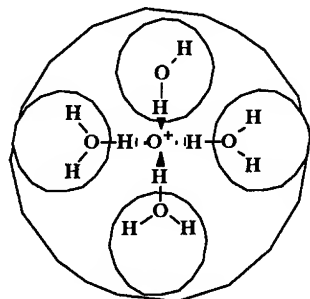
The cavity radius for the water molecule was calculated on the basis of the number density ρ at the room temperature as follows [91]:

$$a_o(\text{H}_2\text{O}) = (3\rho/4\pi)^{1/3} = 1.922 \text{ \AA}. \quad (4)$$

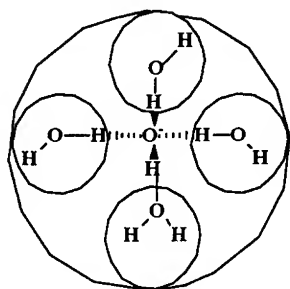
The same radius was used for the cavities for hydroxonium and hydroxyl ions, by the assumption that the addition or the removal of a proton from the water molecule leads to a small change in its internal volume. For the central ion, the cavity radius was calculated as the sum of the corresponding crystallographic radius of the ion and the diameter of the water molecule (3.844 Å). The following crystallographic radii were used [92]: $r(\text{NH}_4^+) = 1.49 \text{ \AA}$; $r(\text{F}^-) = 1.33 \text{ \AA}$; $r(\text{Cl}^-) = 1.81 \text{ \AA}$; $r(\text{Br}^-) = 1.96 \text{ \AA}$; $r(\text{I}^-) = 2.20 \text{ \AA}$.

Results and Discussion

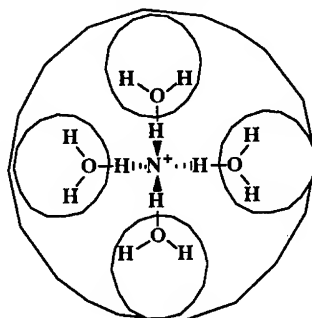
The ionic hydration of the proton, hydroxyl ion, and 5 simple inorganic ions (NH_4^+ , F^- , Cl^- , Br^- , and I^-) was studied by using the semiempirical AM1 theory [93,94] with the inclusion of the MCa SCRF model. Thus we have studied the ionic complexes $\text{H}_3\text{O}^+(\text{H}_2\text{O})_4$, $\text{OH}^-(\text{H}_2\text{O})_4$, $\text{NH}_4^+(\text{H}_2\text{O})_4$, and $\text{Hal}^-(\text{H}_2\text{O})_4$, where $\text{Hal} = \text{F}, \text{Cl}, \text{or Br}$. With the full protonation of one water molecule (formation of the H_3O^+ ion), the first hydration shell of the proton was assumed to have the following structure



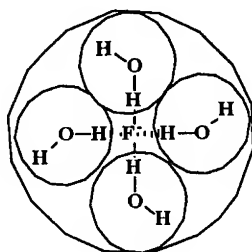
In the case of hydroxyl ion, the complex initial structure was as follows



whereas the following structure of the first coordination shell of the NH_4^+



and halide ions



was used.

In Table I, the AM1 calculated heats of formation for the isolated ions and water molecule, and ion-water complexes in the gas phase ($\epsilon = 1$) and the high dielectric constant medium ($\epsilon = 80$), are given. The total ion hydration energies were obtained according to the following procedure:

$$\Delta H_i = \Delta H_f^\circ[\text{I}^\pm(\text{H}_2\text{O})_4]_w - \Delta H_f^\circ[\text{I}^\pm(\text{H}_2\text{O})_4]_g + \{ \Delta H_f^\circ[\text{I}^\pm(\text{H}_2\text{O})_4]_g - \Delta H_f^\circ[\text{I}^\pm]_g - 4\Delta H_f^\circ[\text{H}_2\text{O}]_g \} \quad (5)$$

where $\Delta H_f^\circ[X]_w$ and $\Delta H_f^\circ[X]_g$ denote the calculated heats of formation for the

TABLE I. The AM1 calculated heats of formation (kcal/mol) for the isolated ions ($\Delta H_f^\circ[\text{I}^\pm]_g$) and ion-water complexes in the gas phase ($\Delta H_f^\circ[\text{I}^\pm(\text{H}_2\text{O})_4]_g$) and in the medium with the dielectric constant $\epsilon = 80$ ($\Delta H_f^\circ[\text{I}^\pm(\text{H}_2\text{O})_4]_w$).

Ion	$\Delta H_f^\circ[\text{I}^\pm]_g$	$\Delta H_f^\circ[\text{I}^\pm(\text{H}_2\text{O})_4]_g$	$\Delta H_f^\circ[\text{I}^\pm(\text{H}_2\text{O})_4]_w$
H^+	362.68	-163.51 ^a	-207.70 ^a
H_3O^+	143.48	-163.51	-208.81
OH^-	-14.12	-327.43	-371.58
NH_4^+	150.58	-136.08	-178.28
F^-	3.44	-311.08	-355.42
Cl^-	-37.66	-321.20	-364.85
Br^-	-20.41	-296.70	-338.60
I^-	-2.22	-274.66	-316.88

^a $\Delta H_f^\circ[\text{H}^+(\text{H}_2\text{O})_5]$.

TABLE II. AM1 MCA SCRF calculated specific (ΔH_i^s), nonspecific (ΔH_i^{ns}) and total electrostatic (ΔH_i) ion solvation energies in aqueous solution (kcal/mol), and experimental heats of solvation ($\Delta H_i(\text{exp})$) [98].

Ion	ΔH_i^s	ΔH_i^{ns}	ΔH_i	$\Delta H_i(\text{exp})$
H ⁺	-229.89	-45.30	-275.29	-261.7
H ₃ O ⁺	-69.93	-45.30	-115.33	—
OH ⁻	-76.35	-44.15	-120.50	-126.6
NH ₄ ⁺	-49.70	-42.20	-91.90	-76.6
F ⁻	-77.56	-44.34	-121.90	-124.1
Cl ⁻	-46.58	-43.65	-90.23	-90.0
Br ⁻	-39.33	-41.90	-81.23	-82.5
I ⁻	-35.48	-42.22	-77.70	-71.8

species X (ion–water complex $\text{I}^\pm(\text{H}_2\text{O})_4$, ion I^\pm and the water molecule) in the dielectric medium or in the gas phase, respectively. The difference in curly brackets corresponds conventionally to the specific solvation energy of the ion (ΔH_i^s) whereas the difference between the heats of formation of the ionic complex in two phases gives the nonspecific (dielectric) solvation energy of the ion (ΔH_i^{ns}). The respective total hydration energies and its components are given in Table II. It is most interesting to note that the variance in the total hydration energies of different ions is caused by the difference in the specific ion–water interactions in the first coordination sphere whereas the nonspecific long-range electrostatic solvation energies are remarkably constant (44 ± 2 kcal/mol). A good correlation between the calculated

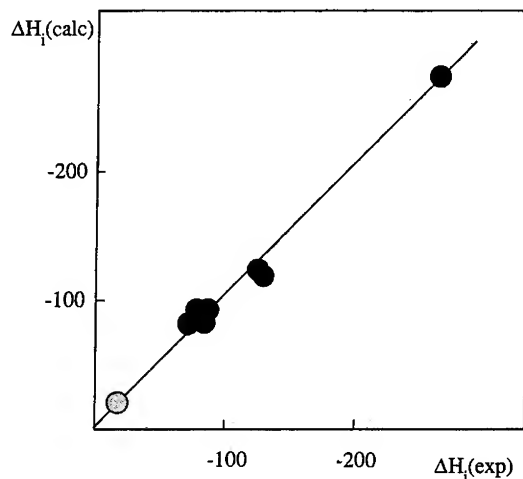


Figure 1. The linear relationship between the AM1 MCA SCRF calculated total electrostatic ion hydration energies ΔH_i and experimental ion hydration energies [98]. Filled point corresponds to the water molecule (electroneutral compound).

and experimental total hydration energies was obtained for all ions studied (cf. Fig. 1) with the following regression coefficients:

$$\Delta H_i = (0.8 \pm 7.0) + (1.03 \pm 0.05)\Delta H_i(\text{exp}) \quad (6)$$

(correlation coefficient $R = 0.994$; standard deviation $s = 8.6$ kcal/mol). The slope of this linear relationship is close to unity (as expected) and the intercept close to zero. However, the data in Table II indicate some overestimate of the ion hydration energies by AM1 MCa SCRF results. One should keep in mind that in this level the theory accounts only for the electrostatic and short-term quantum effects of intermolecular ion-solvent interaction. One should also consider the term for the cavity-formation in the medium, which has always a positive contribution to the solvation energy. Considering the similarity of the volume of the ionic complexes studied in this work, these contributions should be close for different ions. A quantitative estimate of the cavity-formation energy may be calculated using the scaled particle theory (SPT) [95-97]. We have proceeded from the following formula for the reversible work $W(\mathbf{r}, \rho)$ required to produce a cavity of radius r in a fluid with the number density ρ [97]:

$$W(\mathbf{r}, \rho) = kT\{-\ln(1-y) + [3y/(1-y)]\mathbf{R} + [3y/(1-y)]\mathbf{R}^2 + 4.5[y/(1-y)]^2\mathbf{R}^2 + yP\mathbf{R}^3/\rho kT\} \quad (7)$$

where $y = \pi\rho\sigma_1^3/6$ is the reduced number density of the solvent, $\mathbf{R} = \sigma_2/\sigma_1$, and σ_2 is the diameter of the hard-sphere solute molecule such that the cavity radius is $r = (\sigma_1 + \sigma_2)/2$. The term proportional to the internal pressure of solution, P , is considered negligible (cf. [95,96]) and thus neglected in our calculation. The calculated cavity-formation energy for one water molecule is 1.25 kcal/mol ($y = 0.2055$, using additive bond refractions calculated internal volume of the water molecule [98]).

TABLE III. AM1 MCa SCRF (ΔH_i) and SPT (W) calculated neutral electrolyte solvation energies, the total calculated neutral electrolyte solvation energies (ΔH_s), and the respective experimental heats of solvation ($\Delta H_s(\text{exp})$ [98]) in aqueous solution (kcal/mol).

Electrolyte	ΔH_i	W	ΔH_s	$\Delta H_s(\text{exp})$	δ^a
HF	-397.19	12.12	-385.07	-385.8	0.7
HCl	-365.52	12.43	-353.09	-351.7	-1.4
HBr	-356.52	12.52	-344.00	-344.2	0.2
HI	-352.99	12.67	-340.32	-333.5	-6.8
NH ₄ OH	-212.40	12.20	-200.20	-203.2	3.0
NH ₄ F	-213.80	11.82	-201.98	-200.7	-1.3
NH ₄ Cl	-182.13	12.15	-169.98	-166.6	-3.4
NH ₄ Br	-173.13	12.22	-160.91	-159.1	-1.8
NH ₄ I	-169.48	12.37	-157.11	-148.4	-8.7

^a $\delta = \Delta H_s - \Delta H_s(\text{exp})$.

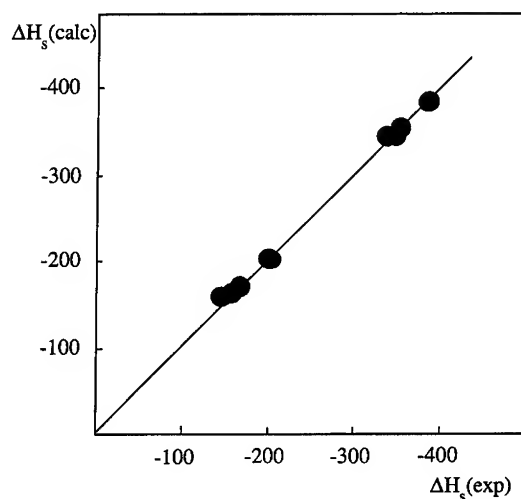


Figure 2. The linear relationship between the AM1 MCA SCRF and SPT calculated total hydration energies ΔH_s and experimental hydration energies of neutral electrolytes.

The ionic solvation energies are obtained by the separation of the total hydration energy of a neutral electrolyte in ionic parts using various empirical schemes. Therefore it is more correct to compare the calculated total hydration energies of neutral electrolytes $\Delta H_s(\text{calc})$, which include both the quantum-chemical and cavity formation contributions, with the corresponding experimental numbers, $\Delta H_s(\text{exp})$. In Table III, we have given the respective data for nine strong electrolytes, obtained by the combination of seven ions used in this study. An excellent agreement between the theoretical and experimental results is obvious (cf. also Fig. 2). The results correspond to the following linear regression:

$$\Delta H_s(\text{calc}) = (-4.7 \pm 3.8) + (0.99 \pm 0.01)\Delta H_s(\text{exp}) \quad (7)$$

(Correlation coefficient $R = 0.999$; standard deviation $s = 3.8$ kcal/mol). The slope of this relationship is again unity and the intercept zero within the limits of error. The standard deviation of the correlation is somewhat larger than the estimate of the respective experimental error (± 2 kcal/mol) and thus the model is not overfitted. Therefore, by using only the dielectric constant of the medium and the crystallographic radii of ions as the external information, we have been able to correctly describe most of the ion solvation in water.

Acknowledgments

M. Karelson is grateful for the European Commission support and M. C. Zerner for the continuing support of the Humboldt Foundation which allowed them to visit the Max Planck Institute of Astrophysics where most of the work was done. This work was also supported by grants from the US Office of Naval Research, and the Estonian Science Foundation.

Bibliography

- [1] M. Born, *Physik. Z.* **1**, 45 (1920).
- [2] W. M. Latimer, K. S. Pitzer, and C. M. Slansky, *J. Chem. Phys.* **7**, 108 (1939).
- [3] R. W. Gurney, *Ions in Solution* (Dover Press, New York, 1962).
- [4] Y. Marcus, *Ion Solvation* (Wiley Interscience, Chichester, 1986).
- [5] A. Ben-Naim, *Solvation Thermodynamics* (Plenum, New York, 1987).
- [6] Y. Marcus, *Chem. Rev.* **88**, 1475 (1988).
- [7] G. A. Krestov, *Thermodynamics of Ion Solvation* (Ellis Horwood, New York, 1991).
- [8] A. A. Rashin and B. Honig, *J. Phys. Chem.* **89**, 5588 (1985).
- [9] A. A. Rashin, *J. Phys. Chem.* **94**, 1725 (1990).
- [10] J. G. Gersten and A. M. Sapse, *J. Am. Chem. Soc.* **107**, 3786 (1985).
- [11] W. C. Still, A. Tempczyk, R. C. Hawley, and T. Hendrickson, *J. Am. Chem. Soc.* **112**, 6127 (1990).
- [12] J. R. Bontha and P. N. Pintauro, *J. Phys. Chem.* **96**, 7778 (1992).
- [13] B. Honig, K. Sharp, and A-S. Yang, *J. Phys. Chem.* **97**, 1101 (1993).
- [14] D. Sitkoff, K. Sharp, and B. Honig, *J. Phys. Chem.* **98**, 1978 (1994).
- [15] M. S. Wertheim, *J. Chem. Phys.* **55**, 4291 (1971).
- [16] D. Y. Chan, D. J. Mitchell, and B. W. Ninham, *J. Chem. Phys.* **70**, 2946 (1979).
- [17] P. G. Wolynes, *J. Chem. Phys.* **86**, 5133 (1987).
- [18] I. Rips, J. Klaftar, and J. Jortner, *J. Chem. Phys.* **89**, 3246 (1988).
- [19] B. Roux, H.-A. Yu, and M. Karplus, *J. Phys. Chem.* **94**, 4683 (1990).
- [20] Gy. I. Szász, K. Heinzinger, and W. O. Riede, *Z. f. Naturforsch.* **36a**, 1067 (1981).
- [21] K. Heinzinger, *Physica B&C* **131**, 196 (1985).
- [22] J. P. Valteau and K. L. Cohen, *J. Chem. Phys.* **72**, 5935 (1980).
- [23] J. P. Valteau, K. L. Cohen, and D. N. Card, *J. Chem. Phys.* **72**, 5942 (1980).
- [24] W. L. Jorgensen and J. M. Briggs, *J. Am. Chem. Soc.* **111**, 4190 (1989).
- [25] J. Tirado-Rives and W. L. Jorgensen, *J. Am. Chem. Soc.* **112**, 2773 (1990).
- [26] J. Pranata, S. G. Wierschke, and W. L. Jorgensen, *J. Am. Chem. Soc.* **113**, 2810 (1991).
- [27] J. M. Briggs, T. B. Nguyen, and W. L. Jorgensen, *J. Phys. Chem.* **95**, 3315 (1991).
- [28] E. N. Brodskaya and A. I. Rusanov, *Mol. Phys.* **71**, 567 (1990).
- [29] L. Perera and M. L. Berkowitz, *J. Chem. Phys.* **95**, 1954 (1991).
- [30] R. Barrett, U. Landman, C. L. Cleveland, and J. Jortner, *J. Chem. Phys.* **88**, 4429 (1988).
- [31] J. G. Kirkwood, *J. Chem. Phys.* **2**, 351 (1934).
- [32] L. Onsager, *J. Am. Chem. Soc.* **58**, 1486 (1936).
- [33] C. J. F. Böttcher and P. Bordewijk, *Theory of Electric Polarization*, 2nd ed. (Elsevier Co, Amsterdam, 1978), Vol. II.
- [34] G. Klopman, *Chem. Phys. Lett.* **1**, 200 (1967).
- [35] H. A. Germer, Jr., *Theoret. Chim. Acta* **34**, 145 (1974).
- [36] H. A. Germer, Jr., *Theoret. Chim. Acta* **35**, 273 (1974).
- [37] J. Hylton, R. E. Christoffersen, and G. G. Hall, *Chem. Phys. Lett.* **26**, 501 (1974).
- [38] O. Tapia and O. Goscinski, *Mol. Phys.* **29**, 1653 (1975).
- [39] R. Constanciel and O. Tapia, *Theoret. Chim. Acta* **55**, 177 (1980).
- [40] O. Tapia, in *Molecular Interactions*, H. Ratajczak and W. J. Orville-Thomas, Eds. (Wiley, Chichester, 1983), Vol. 3, p. 183.
- [41] B. T. Thole and P. Th. van Duijnen, *Theoret. Chim. Acta* **55**, 307 (1980).
- [42] M. M. Karelson, *Organic Reactivity (Tartu)* **17**, 357 (1980).
- [43] S. Miertus, E. Scrocco, and J. Tomasi, *Chem. Phys.* **55**, 17 (1981).
- [44] B. Bonaccorsi, R. Cimiraglia, and J. Tomasi, *J. Comput. Chem.* **4**, 467 (1983).
- [45] J.-L. Rivail and B. Terryn, *J. Chim. Phys.* **79**, 1 (1982).
- [46] J. L. Rivail, B. Terryn, D. Rinaldi, and M. F. Ruiz-Lopez, *J. Mol. Struct. (THEOCHEM)* **120**, 387 (1985).
- [47] H. Hoshi, M. Sakurai, Y. Yoshio, and R. Chujo, *J. Chem. Phys.* **87**, 1107 (1987).
- [48] M. L. Drummond, *J. Chem. Phys.* **88**, 5014 (1987).

- [49] H. Ågren, C. Medina-Llanos, and K. V. Mikkelsen, *Chem. Phys.* **115**, 43 (1987).
- [50] K. V. Mikkelsen, H. Ågren, H. J. Aa. Jensen, and T. Helgaker, *J. Chem. Phys.* **89**, 3086 (1988).
- [51] G. Karlström, *J. Phys. Chem.* **92**, 1315 (1988).
- [52] G. Karlström and B. Halle, *J. Chem. Phys.* **99**, 8056 (1993).
- [53] C. J. Cramer and D. G. Truhlar, *J. Am. Chem. Soc.* **113**, 8305, 8552 (1991).
- [54] C. J. Cramer and D. G. Truhlar, *Science* **256**, 213 (1992).
- [55] M. W. Wong, K. B. Wiberg, and M. J. Frisch, *J. Am. Chem. Soc.* **114**, 1645 (1992).
- [56] B. Wang and G. P. Ford, *J. Chem. Phys.* **97**, 4162 (1992).
- [57] G. P. Ford and B. Wang, *J. Comput. Chem.* **13**, 229 (1992).
- [58] T. Fox and N. Rösch, *Chem. Phys. Lett.* **191**, 33 (1992).
- [59] J. G. Ángyán, *J. Math. Chem.* **10**, 93 (1992).
- [60] H. J. Kim and J. T. Hynes, *J. Chem. Phys.* **93**, 5194, 5211 (1990).
- [61] M. V. Basilevsky and G. E. Chudinov, *Chem. Phys.* **157**, 327 (1991).
- [62] D. G. Truhlar, G. K. Schenter, and B. G. Garrett, *J. Chem. Phys.* **98**, 5756 (1993).
- [63] M. A. Aguilar, F. J. Olivares del Valle, and J. Tomasi, *J. Chem. Phys.* **98**, 7375 (1993).
- [64] M. M. Karelson, *Organic Reactivity (Tartu)* **20**, 127 (1983).
- [65] F. J. Olivares del Valle and J. Tomasi, *Chem. Phys.* **150**, 139 (1991).
- [66] R. R. Contreras and A. J. Aizman, *Int. J. Quantum Chem.* **S25**, 281 (1991).
- [67] G. P. Ford and B. Wang, *J. Am. Chem. Soc.* **114**, 10563 (1992).
- [68] G. E. Chudinov, D. V. Napolov, and M. V. Basilevsky, *Chem. Phys.* **160**, 41 (1992).
- [69] T. Furuki, M. Sakurai, Y. Inoue, R. Chujo, and K. Harata, *Chem. Phys. Lett.* **188**, 84 (1992).
- [70] M. Krauss and W. J. Stevens, *J. Am. Chem. Soc.* **112**, 1462 (1990).
- [71] G. H. F. Diercksen and W. P. Kraemer, *Chem. Phys. Lett.* **4**, 373 (1970).
- [72] G. H. F. Diercksen and W. P. Kraemer, *Chem. Phys. Lett.* **5**, 570 (1970).
- [73] G. H. F. Diercksen and W. P. Kraemer, *Theor. Chim. Acta* **23**, 161 (1973).
- [74] G. H. F. Diercksen, W. P. Kraemer, and B. O. Roos, *Theor. Chim. Acta* **36**, 249 (1974).
- [75] M. D. Newton and S. Ehrenson, *J. Am. Chem. Soc.* **93**, 4971 (1973).
- [76] P. A. Kollman and I. R. Kuntz, *J. Am. Chem. Soc.* **94**, 9236 (1972).
- [77] H. Kistenmacher, H. Popkie, and E. Clementi, *J. Chem. Phys.* **59**, 5842 (1973).
- [78] E. Clementi, *Theoretical Treatment of Large Systems* (Springer-Verlag, Berlin, 1980).
- [79] H. Lischka, *Theor. Chim. Acta* **31**, 39 (1973).
- [80] K. Hashimoto, N. Yoda, and S. Iwata, *Chem. Phys.* **116**, 193 (1987).
- [81] R. E. Cachau, H. D. Villar, and E. A. Castro, *Theor. Chim. Acta* **75**, 299 (1989).
- [82] D. Stromberg, M. Sandström, and U. Wahlgren, *Chem. Phys. Lett.* **172**, 49 (1990).
- [83] P. Kebarle, *Annu. Rev. Chem.* **28**, 445 (1977).
- [84] Y. K. Lau, S. Ikuta, and P. Kebarle, *J. Am. Chem. Soc.* **104**, 1462 (1982).
- [85] M. Karelson and M. C. Zerner, *J. Am. Chem. Soc.* **112**, 9405 (1990).
- [86] E. Sanchez Marcos, R. R. Pappalardo, and D. Rinaldi, *J. Phys. Chem.* **95**, 8928 (1991).
- [87] N. Vaidehi, T. Wesolowski, and A. Warshel, *J. Chem. Phys.* **97**, 4264 (1992).
- [88] F. R. Tortonda, J.-L. Pascual-Ahuir, E. Silla, and I. Tuñón, *J. Phys. Chem.* **97**, 11087 (1993).
- [89] A. Warshel, *Computer Modelling of Chemical Reactions in Enzymes and Solutions* (Wiley, New York, 1991).
- [90] M. Karelson, T. Tamm, and M. C. Zerner, *J. Phys. Chem.* **97**, 11901 (1993).
- [91] M. Karelson and M. C. Zerner, *J. Phys. Chem.* **96**, 6949 (1992).
- [92] *CRC Handbook of Chemistry and Physics*, 57th ed. (CRC Press, Cleveland, 1976).
- [93] M. J. S. Dewar, E. G. Zoebisch, E. F. Healy, and J. J. P. Stewart, *J. Am. Chem. Soc.* **117**, 3902 (1985).
- [94] J. J. P. Stewart, *MOPAC Program Package*, QCPE, No 455.
- [95] H. L. Frisch, *Adv. Chem. Phys.* **6**, 229 (1963).
- [96] H. Reiss, *Adv. Chem. Phys.* **9**, 1 (1966).
- [97] R. A. Pierotti, *Chem. Rev.* **76**, 717 (1976).
- [98] S. Trasatti, *Pure Appl. Chem.* **58**, 955 (1986).

Quantum-Mechanical Investigation of Large Water Clusters

KARL N. KIRSCHNER and GEORGE C. SHIELDS

Department of Chemistry, Lake Forest College, Lake Forest, Illinois 60045

Abstract

The PM3 quantum-mechanical method has been used to study large water clusters ranging from 8 to 42 water molecules. These large clusters are built from smaller building blocks. The building blocks include cyclic tetramers, pentamers, octamers, and a pentagonal dodecahedron cage. The correlations between the strain energy resulting from bending of the hydrogen bonds formed by different cluster motifs and the number of waters involved in the cluster are discussed. The PM3 results are compared with TIP4P potential and *ab initio* results. The number of net hydrogen bonds per water increases with the cluster size. This places a limit on the size of clusters that would fit the Benson model of liquid water. Many of the 20-mer clusters fit the Benson model well. Calculations of the ion cluster $(\text{H}_2\text{O})_{40}(\text{H}_3\text{O}^+)_2$ reveal that the m/e ratio obtainable by mass spectrometry experiments can uniquely indicate the conformation of the 20 water pentagonal dodecahedron cage present in the larger clusters. © 1994 John Wiley & Sons, Inc.

Introduction

In this paper we discuss large water clusters modeled by the PM3 method and by model building. Gas phase ionic water clusters are experimentally observable and their structures can be determined by experimental and theoretical means [1–9]. The $(\text{H}_2\text{O})_{21}\text{H}^+$ cluster ion is a prominent “magic number entity” as detected with numerous experimental conditions [1–3]. Definitive experimental evidence of the pentagonal dodecahedron structure was provided by Wei et al., who used trimethylamine (TMA) molecules as tags to identify dangling hydrogens on water clusters [6]. They made mixed neutral clusters by expanding vapor containing water and TMA through a pulsed nozzle, ionizing the clusters by multiphoton ionization, and separating the product ions by time-of-flight mass spectrometry. The results of this experiment revealed that the $(\text{H}_2\text{O})_{21}(\text{TMA})_m\text{H}^+$ ion distribution was a maximum when $m = 10$ with an abrupt drop in intensity when $m = 11$. This experiment proved that the $(\text{H}_2\text{O})_{21}\text{H}^+$ ion has a total number of 10 hydrogen bonding sites available for TMA to bind. The deformed pentagonal dodecahedron is the only possible structure for the $(\text{H}_2\text{O})_{21}\text{H}^+$ ion that provides a total of 10 dangling hydrogen atoms [2].

Aside from this one peak, there are many more peaks in the mass spectrum obtained by Castleman's group. Higher-order clusters such as $(\text{H}_2\text{O})_{40}(\text{H}_3\text{O}^+)_2$ will have unique mass/charge (m/e) ratios depending on the unique hydrogen bonding

pattern of each particular cluster. The TMA tag experiment, in conjunction with theoretical predictions, can be used to determine the structures of the individual $(\text{H}_2\text{O})_{20}$ clathrate cage structures that compose the higher order cluster. There have already been reported in the literature three isomers of the $(\text{H}_2\text{O})_{20}$ clathrate cage structure [7,8]. In this paper we present results of PM3 calculations and model building studies that show that the m/e ratio of higher order water cluster ions, tagged with TMA, should allow for the identification of the clathrate cage isomers used as building blocks in forming the higher order clusters.

Benson and Siebert have proposed that liquid water is composed of polycyclic octamers and tetramers [10]. This model has been introduced in order to explain the anomalous heat capacity of liquid water, which requires more than two hydrogen bonds per water molecule to model the heat capacity of liquid water from 0 to 100°C. Tsai and Jordan have studied water clusters $(\text{H}_2\text{O})_n$ from $n = 8$ to $n = 20$ by *ab initio* and TIP4P force field calculations [9]. They show that the stability of water clusters is driven by the number of hydrogen bonds; the driving force to maximize the number of hydrogen bonds more than compensates for the ring strain present in some of their clusters. We have extended their work, and present the results of PM3 calculations of large water clusters and their building blocks. We also discuss the implications of the clusters described here with the model of Benson and Siebert for liquid water.

The semiempirical quantum-mechanical methods developed by Dewar and co-workers [11–14] have been successful at reproducing molecular energies, molecular structures, and modeling chemical reactions. Of these methods, only the PM3 method [14] has successfully described intermolecular hydrogen bonding of neutral molecules [14–18]. PM3 correctly models the hydrogen bonding of small water clusters ($n = 2$ –5) [14–16] and the $(\text{H}_2\text{O})_{21}\text{H}^+$ ion [8], whereas the AM1 method is not able to correctly model the geometries of either the water dimer or small water clusters [15–24].

The ability of the PM3 Hamiltonian to model intermolecular hydrogen bonding between neutral molecules has been attributed to the reduction of two-center repulsive forces brought about by the parameterization of the Gaussian core-core interactions [16]. We have used PM3 to study higher order clusters of the $(\text{H}_2\text{O})_{21}\text{H}^+$ system as well as larger neutral clusters of water ($n = 20$ –40) based on octamer and pentamer building blocks.

Methods

All water clusters were built using Chem 3D Plus software (Cambridge Scientific Computing, Inc., Cambridge, MA) on a Macintosh II computer (Apple Computer, Inc., Cupertino, CA). Clusters were designed with hydrogen bond lengths of 1.7 Å and with the lone pairs of each oxygen oriented towards the hydrogens of the neighboring donor molecules. The small building blocks were fully geometry-optimized with the PM3 method [10] using MOPAC 6.0 software [25]. The keyword PRECISE was used to increase the criterion for terminating all optimizations 100-fold over normal MOPAC limits and the keyword XYZ was used to run these

calculations in cartesian coordinates. The larger clusters (greater than 20 waters) were run with the SPARTAN software package (Wavefunction, Irvine, CA) on a Silicon Graphics Indy workstation (Mountain View, CA). The converge option was used with the default gradient tolerance values. All PM3 calculated structures were characterized as stationary points and true minima by calculating the vibrational frequencies.

In addition to the optimization calculations, single point calculations (SPC) were performed with SPARTAN to determine the contribution of hydrogen bond energy of the H_3O^+ ions in the $(\text{H}_2\text{O})_{40}(\text{H}_3\text{O}^+)_2$ cluster. Single point calculations in SPARTAN are equivalent to 1SCF calculations within MOPAC. In these calculations, the individual H_3O^+ and $(\text{H}_2\text{O})_{40}$ subunits of the $(\text{H}_2\text{O})_{40}(\text{H}_3\text{O}^+)_2$ ion are "frozen" to determine the heats of formation for these species in the 42 mer. This is done by isolating both H_3O^+ and the $(\text{H}_2\text{O})_{40}$ subunits in the exact conformation of the $(\text{H}_2\text{O})_{40}(\text{H}_3\text{O}^+)_2$ ion, followed by a single self-consistent-field (1SCF in MOPAC or SPC in SPARTAN) calculation to determine the heats of formation of each subunit. A thermodynamic cycle was used to contrast hydrogen bonding with ring strain for the $(\text{H}_2\text{O})_{40}(\text{H}_3\text{O}^+)_2$ ion.

Results and Discussion

The PM3 geometrical results for an $(\text{H}_2\text{O})_{40}(\text{H}_3\text{O}^+)_2$ ion cluster are presented in Figures 1 and 2. Figure 1 displays only the oxygen atoms of the geometry-optimized structure in the top of the figure, with the hydronium ions shaded and with oxygens involved in hydrogen bonding with the hydronium ions blackened. In the bottom of the figure the two ionic subunits $(\text{H}_2\text{O})_{20}(\text{H}_3\text{O}^+)$ have been separated at the interface and rotated 90° . The hydronium ion is bound to the furthestmost pentagonal face from the interface in each case. Figure 2 illustrates the hydrogen bonding interface on the top half of the figure, and the hydrogen bonding interactions of the hydronium ion on the bottom half. In Figure 2 the perspectives of the top and bottom views are identical to those in Figure 1, with the exception of a slight rotation of the interface. Only the oxygens and hydrogens involved in hydrogen bonding of the interface and hydrogen bonding of the hydronium ions are displayed. Figure 3 contains the PM3 energetic results for the 42-mer cluster and the thermodynamic cycle used to obtain ΔH_1 , ΔH_2 , and ΔH . In Table I the structures of the three unique $(\text{H}_2\text{O})_{40}(\text{H}_3\text{O}^+)_2$ ions composed from three different $(\text{H}_2\text{O})_{20}$ building blocks [7,8] are compared to predict the expected m/e ratio for these different doubly-charged ions in a mass spectrometry experiment.

Figure 4 contains the two octamer building blocks used to build many of the larger clusters displayed in Figures 5 and 6. We have built on the previous work of Tsai and Jordan and have retained their nomenclature [9]. Figure 5 contains PM3 optimized 20-mers, and Figure 6 contains three PM3 optimized 40-mers. Only the oxygen atoms are shown in Figure 6 for clarity. Table II contains the PM3 heats of formation, association energies, and hydrogen bonding information for the clusters depicted in Figures 4–6, as well as the previously reported pentagonal dodecahedral cage structure for $(\text{H}_2\text{O})_{20}$ [8].

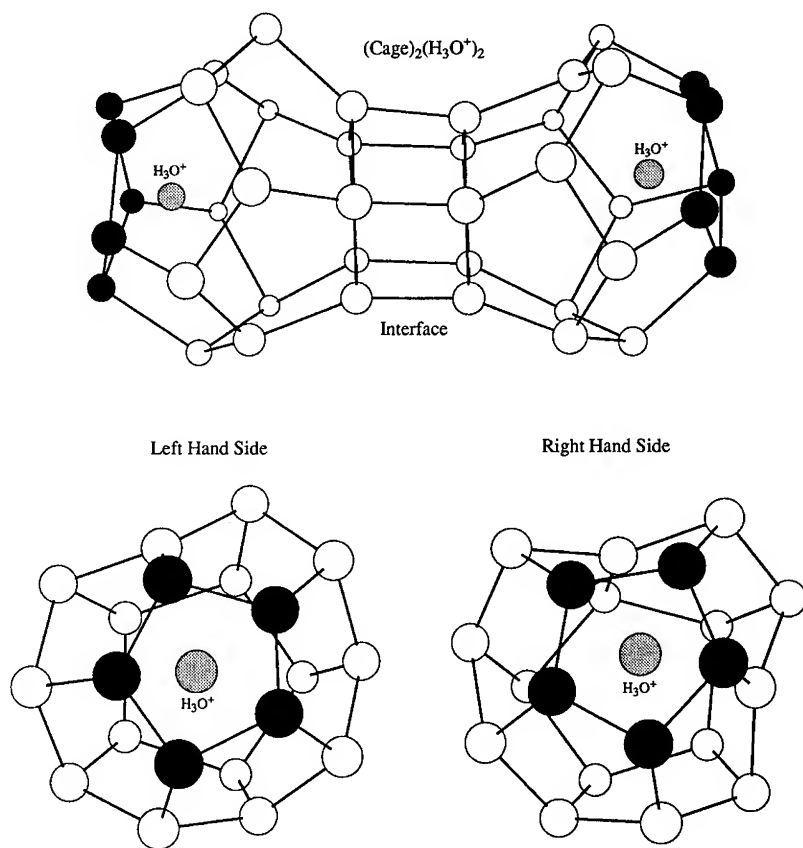


Figure 1. The PM3 optimized structure for the ion cluster $(\text{H}_2\text{O})_{40}(\text{H}_3\text{O}^+)_2$ illustrating the oxygen atoms and the interface of the two pentagonal dodecahedrons. Only oxygens are displayed, and the blackened oxygens represent oxygens that serve as hydrogen bond acceptors for the shaded hydronium ion. The bottom figure shows the two pentagonal faces that bind to the hydronium ion. To obtain the bottom view the interface was broken and the two cages were rotated approximately 90° .

The $(\text{H}_2\text{O})_{40}(\text{H}_3\text{O}^+)_2$ Ion Cluster

This structure was made from two Cage structures (Fig. 6) joined together by matching a pentagonal ring on one 20-mer with its complement on the second 20-mer. In this cluster there are four hydrogen bond donors on a pentagonal face on the right-hand side matching the complement of one hydrogen bond donor on the left-hand side (Fig. 2). Then two hydronium ions were placed in the center of each cage. The ion structure would not optimize until both hydronium ions were displaced slightly from the centers of the cages. Figure 1 reveals that the two hydronium ions migrated to the pentagonal faces furthest from the interface. The detailed hydrogen bonding interactions of the hydronium ions with its cage is displayed at the bottom of Figure 2. These two patterns are different from the six seen previously for the $(\text{H}_2\text{O})_{21}\text{H}^+$ cluster [8]. Using the nomenclature of Jeffrey and Saenger [26],

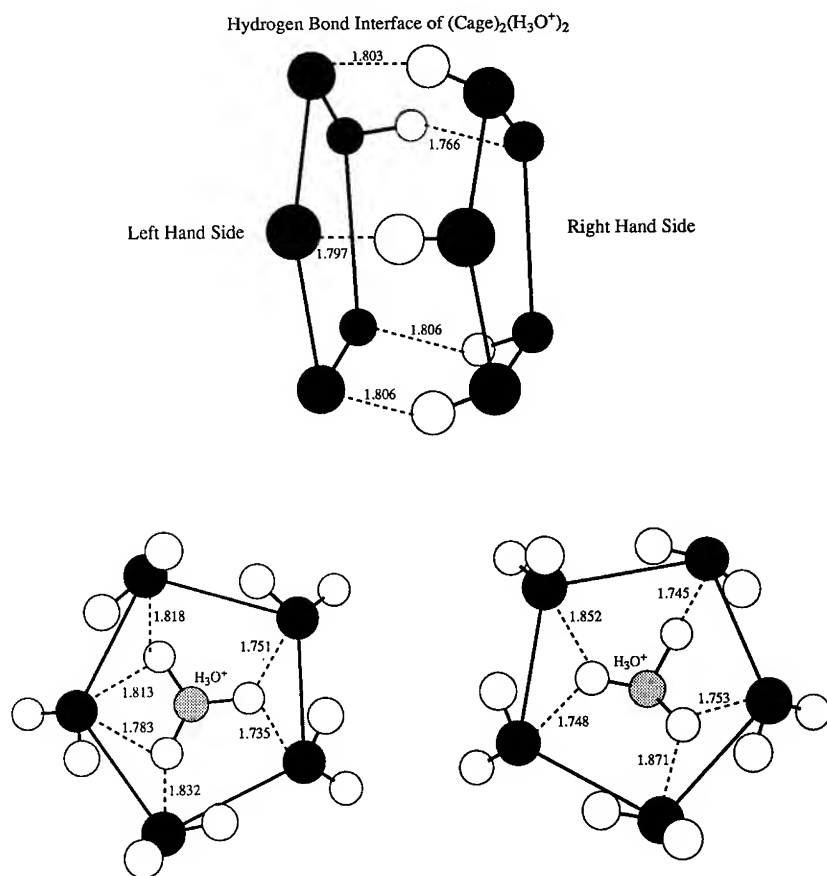


Figure 2. Top: the hydrogen bond interface between the two cage structures, showing all oxygens and hydrogens involved in hydrogen bonds that make the interface. Bottom: the detailed hydrogen bonding interactions of the hydronium ions. The view is the same as in Figure 1 (bottom).

the hydronium ion on the left-hand side of the figure has three three-center bifurcated donor hydrogen bonds and one three-centered bifurcated acceptor. The first three-center hydrogen bond, with hydrogen bond lengths of 1.818 and 1.813 Å, is known as a bifurcated donor since one hydrogen donates to two acceptors. The hydronium ion also forms two more three-center bifurcated donor hydrogen bonds (1.783 and 1.832 Å, 1.751 and 1.735 Å). The one three-center bifurcated acceptor has hydrogen bonds of 1.813 and 1.783 Å. As noted by Jeffrey and Saenger [26], three-center bifurcated acceptors only occur in conjunction with three-center bifurcated donors. The three-center bifurcated acceptors seen here, as in the $(\text{H}_2\text{O})_{21}\text{H}^+$ system [8], appear to be an accidental occurrence necessitated by the hydrogen rich environment of the hydronium ion. The hydronium hydrogen bond distances and angles range from 1.735 to 1.832 Å and 98° to 152° , consistent with the kinds of geometries observed in the $(\text{H}_2\text{O})_{21}\text{H}^+$ system [8]. The three-center bifurcated-acceptor hydro-

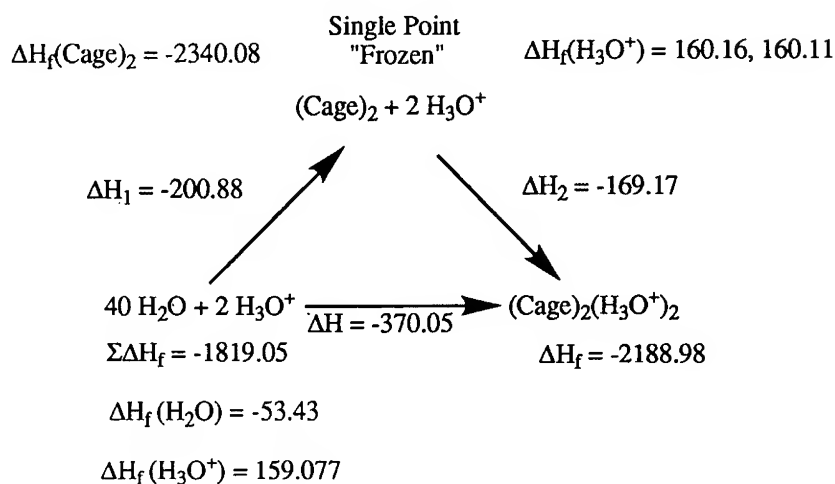


Figure 3. Thermodynamic cycle and energetic information for the formation of the $(\text{Cage})_2(\text{H}_3\text{O}^+)_2$ ion.

gen bond is rarely observed in the crystalline state and is not found in any of the ice structures [26]. When the bifurcated-acceptor hydrogen bond is found, as in some nucleoside crystal structures, it is always in conjunction with three-center bonds [26]. The hydronium ion on the right-hand side of Figure 2 has two three-center bifurcated donor and one two-center hydrogen bond. Bond distances and angles range from 1.745 to 1.871 Å and 128° to 157°.

The hydrogen bond interface that joins two 20-mer cages together to make the 40-mer is depicted in the top half of Figure 2. The bond lengths and bond angles for the interface range from 1.766 to 1.806 Å and 146° to 155°. An important feature of this interface is that while the $(\text{H}_2\text{O})_{21}\text{H}^+$ cage has 10 dangling hydrogens [8], the $(\text{H}_2\text{O})_{40}(\text{H}_3\text{O}^+)_2$ cluster has 20 minus 5, or 15 dangling hydrogen bonds as five are lost in the interface of the two cages. The mass spectrometric experiments performed by Castleman's group showed that the $(\text{H}_2\text{O})_{21}\text{H}^+$ cage had 10 dangling hydrogens because of the large peak observed at the m/e ratio corresponding to 10 trimethylamine (TMA) molecules bound to the 21-mer [6]. Since the pentagonal dodecahedron cage is the only possible structure for the $(\text{H}_2\text{O})_{21}\text{H}^+$ ion that provides a total of 10 dangling hydrogen atoms, the mass spectrometric experiments identified

TABLE I. Comparison of three different $(\text{H}_2\text{O})_{40}(\text{H}_3\text{O}^+)_2$ structures, built from the building blocks described in references seven and eight.

	(Isomer I) $_2(\text{H}_3\text{O}^+)_2$	(Isomer II) $_2(\text{H}_3\text{O}^+)_2$	$(\text{Cage})_2(\text{H}_3\text{O}^+)_2$
Number of hydrogen bonds per interface	2	3	5
Dangling hydrogens available for TMA sites	18	17	15
Mass/charge ratio	910.3	881.8	822.7

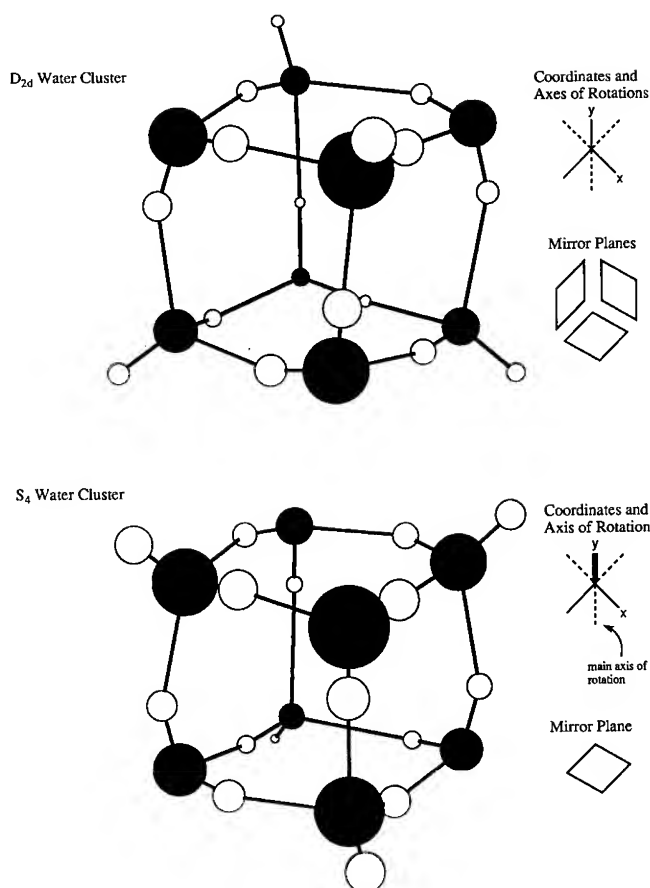


Figure 4. The D_{2d} and S_4 octamer structures. Coordinates, axes of rotation, and mirror planes are shown.

a pentagonal dodecahedron composed of 20 waters with a hydronium ion in the middle as the species formed in their apparatus [6]. We note that the $(H_2O)_{40}(H_3O^+)_2$ doubly-charged ion with 15 dangling hydrogen tags for TMA will have a unique m/e ratio, as would the $(H_2O)_{60}(H_3O^+)_3$ triply-charged ion with 20 available tags. The number of available tags is dependent on the dodecahedral clathrate isomer used as a building block for larger clusters.

Cioslowski and Nanayakkarc performed the first calculations on the $(H_2O)_{20}$ system [7]. They used the HF/6-311G** level of *ab initio* theory within the C_5 symmetry point group to calculate two quite different arrangements of dangling hydrogens for the pentagonal dodecahedral cage. The two isomers are separated by only $0.4 \text{ kcal mol}^{-1}$, and consist of structures composed of two regular pentagons and 10 pentagons with three short and two long edges each [7]. Our model building studies reveal that using isomer I or isomer II as building blocks to form the $(H_2O)_{40}(H_3O^+)_2$ ion will have different numbers of hydrogen bonds involved in the

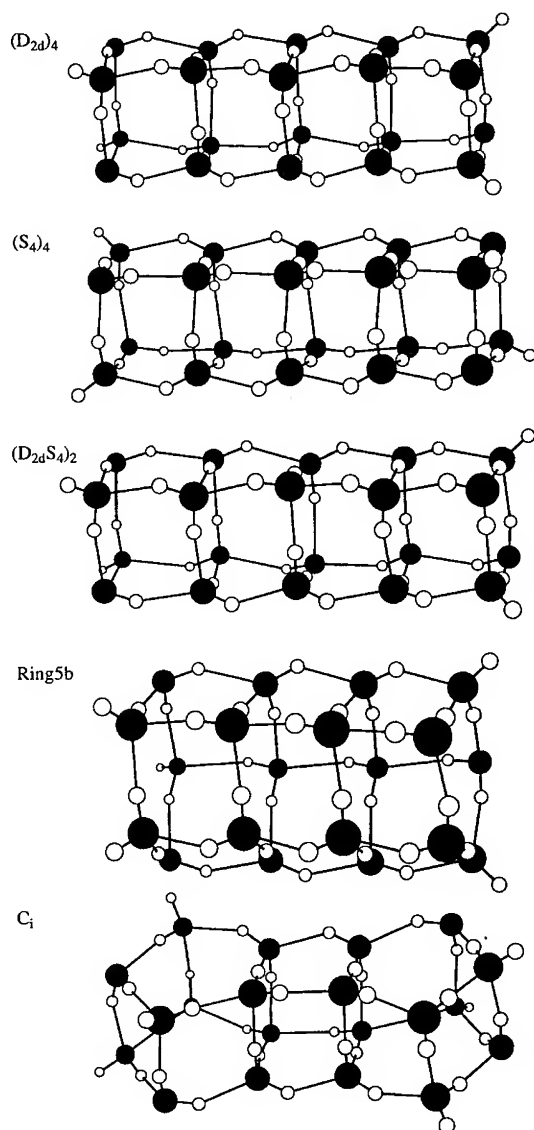


Figure 5. PM3 optimized structures (MOPAC) of neutral water clusters composed of 20 water molecules.

interface, thus changing the number of sites available for TMA tags. Dimers of isomer I will have an interface of two hydrogen bonds and dimers of isomer II will have an interface of three hydrogen bonds. Hence, as shown in Table I, dimers of isomer I will have 18 dangling hydrogen atoms available for TMA labeling, while dimers of isomer II will have 17 TMA tag sites. The m/e ratio of the three $(\text{H}_2\text{O})_{40}(\text{H}_3\text{O}^+)_2(\text{TMA})_n$ ions will be unique (Table I), allowing a study of larger, multiply charged water clusters. Observation of any of the three m/e ratios in the

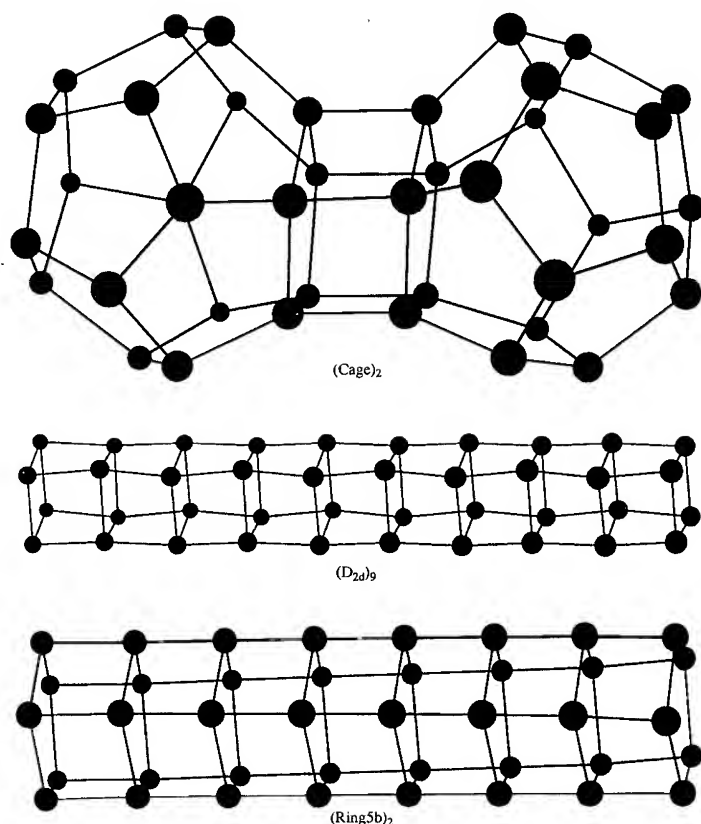


Figure 6. PM3 optimized structures (SPARTAN) of neutral water clusters composed of 40 water molecules.

mass spectrum would be evidence that doubly charged clusters exist and would allow for the identification of the $(\text{H}_2\text{O})_{20}$ building blocks used to form the larger cluster.

A thermodynamic cycle has been used to examine the hydrogen bond energetics of the $(\text{H}_2\text{O})_{40}(\text{H}_3\text{O}^+)_2$ ion. Figure 3 illustrates the cycle where the overall reaction of 40 waters and two hydronium ions reacting to make the 42-mer can be calculated in two steps. Step 1 is the conversion of the 40 water molecules and the hydronium ions into the $(\text{H}_2\text{O})_{40}$ cluster and the two H_3O^+ ions, all "frozen" in the conformation of the final 42-mer structure. Step 2 is the formation of the 42-mer from these two "frozen" structures. The heats of formation of the "frozen" structures were calculated by SPC on the geometries of the separated species from the geometry optimized $(\text{H}_2\text{O})_{40}(\text{H}_3\text{O}^+)_2$ ion. The sum of these three heats of formation yields the single-point "frozen" energies in Figure 3. Figure 3 contains all energetic information obtained from geometry optimization and from the SPC. Also shown are the ΔH s for each step.

TABLE II. Comparison of different water cluster geometries displayed in Figures 1, 4–6. Energies in kcal mol⁻¹.

Structure	PM3 ΔH_f	Total H bonds	No. of H bonds per water molecule	Dangling H	Association energy	H-bond energy
(H ₂ O) ₈						
D _{2d}	-475.96	12	3.00	4	-48.52	-4.04
S ₄	-475.75	12	3.00	4	-48.31	-4.03
(H ₂ O) ₂₀						
(D _{2d}) ₄	-1206.99	36	3.60	4	-138.39	-3.84
(D _{2d} S ₄) ₂	-1206.64	36	3.60	4	-138.04	-3.83
(S ₄) ₄	-1205.96	36	3.60	4	-137.36	-3.82
Ring5b	-1205.33	35	3.50	5	-136.79	-3.91
C _i	-1206.66	34	3.40	6	-138.12	-4.06
Cage	-1185.41	30	3.00	10	-116.99	-3.90
(H ₂ O) ₄₀						
[Cage] ₂	-2399.61	65	3.25	15	-262.53	-4.04
(D _{2d}) ₉	-2427.09	76	3.80	4	-290.01	-3.82
(Ring5b) ₂	-2426.90	75	3.75	5	-289.82	-3.86
(H ₂ O) _n where <i>n</i> > 40						
(Cage) ₂ (H ₃ O ⁺) ₂	-2188.98					

The enthalpy of reaction for step 1 (ΔH_1) is the sum of the SPC "frozen" heats minus the sum of the 40 waters and hydronium ion heats, or $\Delta H_1 = -200.88$ kcal mol⁻¹. The enthalpy of reaction for step 2 (ΔH_2) is found from the SPC heats and the (H₂O)₄₀(H₃O⁺)₂ heat of formation. Formation of the (H₂O)₄₀(H₃O⁺)₂ cluster from 40 separated waters and two hydronium ions releases 370.05 kcal mol⁻¹. The values for ΔH_1 and ΔH_2 reveal that 200.88 kcal mol⁻¹ are released in making the (Cage)₂ structure and straining the hydronium ions and that 169.17 kcal mol⁻¹ are released when the hydronium ions are bound to the 40-mer. Compared to the previously reported system [7,8], there is less strain in the (Cage)₂ structure and less energy is released upon binding hydronium ions.

Neutral Water Clusters

The (H₂O)₈ cluster in its most stable form has a cubic structure which maximizes the number of hydrogen bonds [9]. The two most stable forms have D_{2d} and S₄ symmetry, and they are depicted in Figure 4. The PM3 optimized D_{2d} structure is 0.21 kcal mol⁻¹ more stable than S₄ (Table II), in agreement with MP2/aug-ccp vDZ* *ab initio* calculations [9] that place the D_{2d} structure 0.2 kcal mol⁻¹ more stable than S₄. We have used the D_{2d} and S₄ octamers as building blocks for many of the larger neutral water clusters reported in this paper. The 20-mers displayed in Figure 5 are very similar in energy (Table II). Our results are in general agreement with the TIP4P force field calculations, which predict stabilities of the 20-mers of (D_{2d})₄ > (D_{2d}S₄)₂ > (S₄)₄ > Ring5b > C_i > Cage. The exception is that PM3 predicts that the C_i structure is more stable [(D_{2d})₄ > C_i > (D_{2d}S₄)₂ > (S₄)₄ > Ring5b >

Cage], perhaps because the TIP4P potential exaggerates the stability of the fused cubic species relative to structures containing five- and six-membered rings [9]. The 40-mers displayed in Figure 6 include the (Cage)₂ parent cluster for the (H₂O)₄₀(H₃O⁺)₂ cluster discussed above, and two long repeating cubes and pentagons. The (D_{2d})₉ structure has one more hydrogen bond and is 0.192 kcal mol⁻¹ more stable than the (Ring5b)₂ structure. The (Ring5b)₂ cluster has the interesting feature that it is starting to twist around the long axis of the cluster.

Benson's Two-Structure Model for Liquid Water

In their recent paper, Benson and Siebert argue that the heat capacity data for liquid water can only be modeled if fluid water is composed of discrete units, (H₂O)_n, which can move independently of each other [10]. They argue that to account for the energy of vaporization of water (9.9 kcal mol⁻¹) requires breaking 1.7 hydrogen bonds per water molecule at 300 K. Each water molecule in a cubic octamer (Fig. 4) shares three hydrogen bonds with other waters, for a net of 1.5 hydrogen bonds per water molecule at 300 K. Our results show that larger clusters have higher net hydrogen bonds per water molecule. For the different water clusters displayed in Figure 5, Table II tabulates the number of hydrogen bonds per water molecule. Dividing this number by 2 yields the net number of hydrogen bonds. The (D_{2d})₄, (D_{2d}S₄)₂, and (S₄)₄ clusters (made from octamers) all have a net of 1.8 hydrogen bonds, Ring5b (pentamers) has 1.75, C_i (pentamers and an octamer) has 1.7, and the cage has 1.5 net hydrogen bonds. These values for net hydrogen bonds fit nicely into the Benson/Siebert model, which requires breaking 1.7 hydrogen bonds to vaporize water.

Clusters based on 40 waters have higher net hydrogen bonds than smaller clusters. The (Cage)₂, (D_{2d})₉, and (Ring5b)₂ clusters have net hydrogen bonds of 1.625, 1.9, and 1.875, respectively. An 80 water cluster made of pentamers (Ring5b)₄ would have 3.875 hydrogen bonds per water and a net of 1.94. This increase in net hydrogen bonds with increases in cluster size is because there are four shared hydrogen bonds for each water molecule in the inside region of water clusters made from pentamers and tetramers, but at the ends there are only three. Increasing the cluster size will always increase the number of hydrogen bonds per water and thus the net hydrogen bonds. These results suggest that if the Benson/Siebert model is applicable, water clusters will be limited in size as the vaporization of water requires the breaking of 1.7 hydrogen bonds per water molecule.

Conclusions

The PM3 quantum-mechanical method is a low-cost yet reasonably accurate method for modeling water clusters. The two main results of our research are: First, PM3 results on the (H₂O)₄₀(H₃O⁺)₂ ion indicate that mass spectrometry combined with trimethylamine tags can be used to uniquely indicate the conformation of the 20 water pentagonal dodecahedron cage present in this ion and for other multiply charged, larger clusters. Second, the number of net hydrogen bonds per water increase with the cluster size. This places a limit on the size of clusters that would

fit the Benson model of liquid water. Many clusters of 20 waters fit the Benson model well.

Bibliography

- [1] S. S. Linn, *Rev. Sci. Instrum.* **44**, 516 (1973); J. Q. Searcy and J. B. Finn, *J. Chem. Phys.* **61**, 5282 (1974); G. M. Lancaster, F. Honda, Y. Fukuda, and J. W. Rabalais, *Int. J. Mass Spectrom. Ion Phys.* **29**, 199 (1979); *J. Am. Chem. Soc.* **101**, 1951 (1979); H. R. Carlon and C. S. Harden, *Appl. Opt.* **19**, 1776 (1980); R. J. Beuhler and L. Friedman, *ibid.* **77**, 2549 (1982); D. Dreyfus and H. Y. Wachman, *ibid.* **76**, 2031 (1982); V. Hermann, B. D. Kay, and A. W. Castleman, Jr., *Chem. Phys.* **72**, 2031 (1982); H. Udseth, H. Zmora, R. J. Beuhler, and C. Friedman, *J. Phys. Chem.* **86**, 612 (1982); A. J. Stace and C. Moore, *Chem. Phys. Lett.* **96**, 80 (1983); O. Echt, D. Kreisle, M. Knapp, and E. Recknagel, *ibid.* **108**, 401 (1984).
- [2] H. Shinohara, U. Nagashima, H. Tanaka, and N. Nishi, *J. Chem. Phys.* **83**, 4183 (1985); U. Nagashima, H. Shinohara, N. Nishi, and H. Tanaka, *ibid.* **84**, 209 (1986).
- [3] X. Yang and A. W. Castleman, Jr., *J. Am. Chem. Soc.* **11**, 6845 (1989).
- [4] J. L. Kassner, Jr. and D. E. Hasen, *J. Chem. Phys.* **64**, 1860 (1976).
- [5] P. M. Holland and A. W. Castleman, Jr., *J. Chem. Phys.* **72**, 5984 (1980).
- [6] S. Wei, Z. Shi, and A. W. Castleman, Jr., *J. Chem. Phys.* **94**, 3268 (1991).
- [7] J. Cioslowski and A. Nanayakkarc, *Int. J. Mod. Phys. B* **6**, 3687 (1992).
- [8] M. W. Jurema, K. N. Kirschner, and G. C. Shields, *J. Comp. Chem.* **14**, 1326 (1993).
- [9] C. J. Tsai and K. D. Jordan, *J. Phys. Chem.* **97**, 5208 (1993).
- [10] S. W. Benson and E. D. Siebert, *J. Am. Chem. Soc.* **114**, 4269 (1992).
- [11] R. C. Bingham, M. J. S. Dewar, and D. H. Low, *J. Am. Chem. Soc.* **97**, 1285, 1294, 1302, 1307 (1975).
- [12] M. J. S. Dewar and W. Thiel, *J. Am. Chem. Soc.* **99**, 4899, 4907 (1977).
- [13] M. J. S. Dewar, E. G. Zoebisch, E. F. Healy, and J. J. P. Stewart, *J. Am. Chem. Soc.* **107**, 3902 (1985).
- [14] J. J. P. Stewart, *J. Comp. Chem.* **10**, 209, 221 (1989).
- [15] H. S. Rzepa and M. Yi, *J. Chem. Soc. Perkins Trans. 2*, 943 (1990); I. Juranic, H. S. Rzepa, and M. Yi, *ibid.*, 877 (1990).
- [16] M. W. Jurema and G. C. Shields, *J. Comp. Chem.* **14**, 89 (1993).
- [17] O. N. Ventura, E. L. Coitiño, A. Lledós, and J. Bertrán, *J. Mol. Struct. (Theochem)* **187**, 55 (1989).
- [18] Y.-J. Zheng and K. M. Merz, Jr., *J. Comp. Chem.* **13**, 1151 (1992).
- [19] I. H. Williams, *J. Am. Chem. Soc.* **109**, 6299 (1987).
- [20] A. A. Bliznyuk and A. A. Voityuk, *J. Mol. Struct. (Theochem)* **164**, 343 (1988).
- [21] W. C. Herndon and T. P. Radhakrishnan, *Chem. Phys. Lett.* **148**, 492 (1988).
- [22] J. J. Dannenberg, *J. Phys. Chem.* **92**, 6869 (1988).
- [23] J. Y. Choi, E. R. Davidson, and I. Lee, *J. Comp. Chem.* **10**, 163 (1989).
- [24] B. J. Smith, D. J. Swanton, J. A. Pople, H. F. Schaefer, and L. Radom, *J. Chem. Phys.* **92**, 1240 (1990).
- [25] J. J. P. Stewart, QCPE 455, available from Indiana University, Creative Arts Building 181, Bloomington, IN 47405.
- [26] G. A. Jeffrey and W. Saenger, *Hydrogen Bonding in Biological Structures*, (Springer-Verlag, New York, 1991), pp. 20–24.

Solvent Effects on the Electronic Spectrum of Reichardt's Dye

RICARDO BICCA DE ALENCASTRO

Physical Organic Chemistry Group, Lab. A622, Departamento de Química Orgânica, Instituto de Química da UFRJ, Cidade Universitária, CT, Bloco A, Rio de Janeiro, RJ 21949-900, Brazil

JOAQUIM D. DA MOTTA NETO and MICHAEL C. ZERNER

Quantum Theory Project, PO Box 1184-35, Williamson Hall, University of Florida, Gainesville, Florida 32611

Abstract

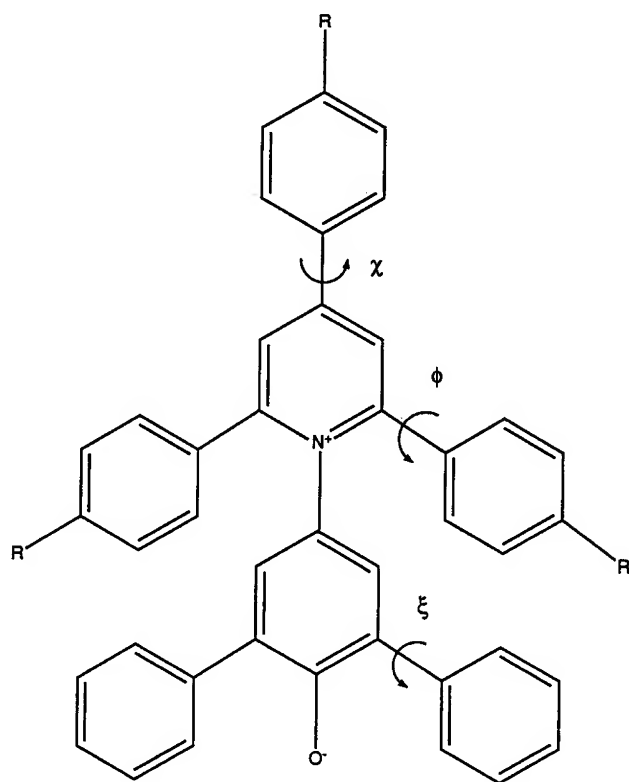
The extreme sensitivity of the absorption spectrum to small changes in the medium polarity has made Reichardt's dyes useful molecular probes in the study of micelle/solution interfaces and phospholipid bilayers. This work reports preliminary results of semiempirical quantum chemical calculations on some conformations of 2,6-diphenyl-(2,4,6-triphenyl-1-pyridinium)-*N*-phenoxide betaine (Reichardt's betaine, RB), which exhibits negative solvatochromic effects. We have used the AM1 Hamiltonian of Dewar in the geometry optimizations, and the Intermediate Neglect of Differential Overlap method parameterized for spectroscopy (INDO/S). For RB, two low-lying conformations have been found. The small difference in energy between them suggests that both forms may be present in solution, an observation confirmed by calculations on the spectra using the SCRF model: the superposition of the calculated spectra for these two forms matches the experimental spectra very well. For nonpolar solvents, the general pattern consists of variation of $\text{Et}(30)$ concurrent with variation of the dielectric constant. We have also carried out calculations for solvents which form specific (e.g., H-bond) binding to the solute, namely methanol and water, using a supermolecule approach. Our results are in excellent agreement with the experiment and present an accurate description of the spectra. © 1994 John Wiley & Sons, Inc.

Introduction

The absorption and emission spectra of a substance change characteristics (positions and intensities) on going from the gas phase to solution. These differences largely depend on the solvent and, although they are generally small, they can be very large in some cases [1–3]. This phenomenon is widely known as *solvatochromism* and was first recognized more than 100 years ago by Kundt [1]. It occurs because dissolved molecules interact differently with the environment in their ground and several excited states. These interactions are not always easily described and this subject has been intensely pursued in the last 40 years: dozens of books and accounts, and innumerable reports have been devoted to it. For empirical approaches, the interested reader will find useful material in Refs. [3–5], and for a thorough description of theoretical and computational aspects, in Refs. [6–7], among many others. From the empirical point of view, solvatochromism has been

used to construct linear solvation free energy relationships (LSER) that give access to solvent properties important to explain several important physicochemical phenomena as, for example, chemical kinetics, conformation or tautomeric equilibria, and even partition coefficients [3,4].

The problem of theoretically predicting the electronic properties of organic substances and their observed spectra in solution has interested and challenged theoretical chemists for more than four decades. This field has been very active especially in the last few years and Rauhut, Clark, and Steinke [8] have recently given a summary of recent literature. Following recent work in this lab on solvent effects [9] we decided to examine the electronic spectrum of one of the most widely used solvatochromic dyes, 2,6-diphenyl-(2,4,6-triphenyl-1-pyridinium)-*N*-phenoxide (Reichardt's betaine #1, a.k.a. Reichardt's dye #1, RB, Fig. 1) [10–18]. The lowest energy band of RB undergoes a negative solvatochromism (hipsochromic shift) of about 360 nm (approximately $10,000\text{ cm}^{-1}$) in going from diethyl ether to water. This is the basis of the very popular $E_T(30)$ scale (or its equivalent E_T^N scale) [3–5,10–16].



dye #1, $R = H$

dye #2, $R = \text{SO}_2\text{CH}_3$

Figure 1. Reichardt's dye #1 (RB).

Method

We initially performed a search of low-lying conformations of RB with geometry optimizations at the SCF level using the AM1 [19–21] model Hamiltonian, within the AMPAC package [22]. Keywords PRECISE and GNORM = 0.05 were used in order to obtain the smallest residual gradient possible. Solvent effects were included in our study at two levels: in a first approximation, the bulk was simulated by a self-consistent reaction field (SCRF) within the continuum model [23–28]. We use in this work the SCRF formulation as given by Karelson and Zerner [9]: in model A of this reference, we write the energy of the universe (molecule + environment) as

$$E_u = E^0 - \frac{1}{2} \cdot \left(1 - \frac{1}{\epsilon}\right) \frac{Q^2}{a_0} - \frac{1}{2} \cdot \vec{g}(\epsilon, a_0) \langle \psi | \vec{\mu} | \psi \rangle \langle \psi | \vec{\mu} | \psi \rangle \quad (1)$$

with Q the net charge of the solute and \vec{g} the reaction field tensor. We now form the functional

$$L = E^0 - \frac{1}{2} \cdot \left(1 - \frac{1}{\epsilon}\right) \frac{Q^2}{a_0} - \frac{1}{2} \cdot \vec{g}(\epsilon, a_0) \times \langle \psi | \vec{\mu} | \psi \rangle \langle \psi | \vec{\mu} | \psi \rangle - W \cdot (\langle \psi | \psi \rangle - 1) \quad (2)$$

with W the Lagrange multiplier ensuring normalization and E^0 the gas phase energy

$$E^0 = \langle \psi | H_0 | \psi \rangle \quad (3)$$

where H_0 is the Hamiltonian for the isolated solute molecule. Applying the variational theorem to Eq. (2) leads to the Schrödinger equation for the state $|\psi\rangle$

$$(H_0 - \vec{g} \langle \psi | \vec{\mu} | \psi \rangle \langle \vec{\mu} \rangle) |\psi\rangle = W \cdot |\psi\rangle \quad (4)$$

with the Fock operator for the electron k given by

$$f(k) = f_0(k) - \vec{g} \cdot \langle \psi | \vec{\mu} | \psi \rangle \cdot \mu(k) \quad (5)$$

and the energy of the universe is then

$$E_u = W + E_{c,c} = W + \frac{1}{2} \vec{g} \cdot |\langle \psi | \vec{\mu} | \psi \rangle|^2 \quad (6)$$

where the "solvent cost" $E_{c,c}$ is a correction that express the energy lost by the solvent in dissolving the solute. Note that the nuclear repulsion energy and the Born term,

$$\sum_A \sum_{B>A} \frac{Z_A Z_B}{R_{AB}} - \frac{1}{2} \cdot \left(1 - \frac{1}{\epsilon}\right) \frac{Q^2}{a_0}, \quad (7)$$

must be added. In this work we use an alternative procedure that includes the solvent relaxation, model B of Ref. [9]: we put a *second* Lagrange constraint in Eq. (2) such that

$$\left(H_0 - \frac{1}{2} \cdot \vec{g} \cdot \langle \psi | \vec{\mu} | \psi \rangle \langle \vec{\mu} \rangle \right) | \psi \rangle = W \cdot | \psi \rangle \quad (8)$$

and the Fock operator for electron k turns out to be

$$f(k) = f_0(k) - \frac{1}{2} \cdot \vec{g} \cdot \langle \psi | \vec{\mu} | \psi \rangle \vec{\mu}(k) \quad (9)$$

an operator that yields Eq. (1) directly (since the interaction term includes the $1/2$). The cavity radius a_0 (6.02 Å for isolated RB) was determined from mass density. In addition, when necessary, we have also used the supermolecule approach [29–31] by including at least two solvent molecules around the solute (RB).

The absorption spectra were obtained (at the AM1 and AM1-SCRF geometries) by the spectroscopic version of the Intermediate Neglect of Differential Overlap (INDO/S) method [32–37]. The two center, two electron integrals are obtained from the modified Mataga–Nishimoto formula [38]

$$\gamma_{AB} = \frac{f_\gamma}{2f_\gamma/(\gamma_{AA} + \gamma_{BB}) + R_{AB}} \quad (10)$$

in which the Weiss parameter f_γ was chosen equal to 1.2 in order to reproduce the spectrum of aromatic compounds [32]. The configuration interaction (CI) calculations included all single excitations from the 19 highest occupied MO's to the 12 lowest unoccupied MO's, plus the ground state, a total of 229 configurations.

Results and Discussion

Results in Gas Phase (AM1)

Table I presents a summary of our AM1 results for RB. Conformers A (Fig. 2) and A' differ only by a rotation of one of the phenyl rings by about 180° , and have virtually the same energy. Conformer B (Fig. 3) was calculated to be 0.1 kcal/mol more stable in gas phase, and this suggests that these conformers coexist in gas phase. In solution (under the SCRF approximation [23–28]), differences between A, A', and B conformers are less than 1 kcal/mol on going from ethanol to water. This suggests that these conformers likely also coexist in solution. If this is the case, then the observed spectral properties must arise from a combination of the spectral properties of all conformers. We assumed that the contributions of both forms should be approximately the same (regardless of the existence of other conformations), so the observed spectra are compared in this article with the average of the spectra of the two forms, A and B.

The INDO/S-CIS calculated spectrum of RB in gas phase is shown in Tables II (Conformer A, Fig. 2) and III (Conformer B, Fig. 3). There is no gas phase spectrum available in the literature (there is little vapor pressure), so we compare our gas phase calculations to the results obtained for a nonpolar solvent, namely, 1,4-dioxane [3], and recognize the limitations of this comparison. In gas phase, the lowest excited singlet state is mostly HOMO \rightarrow LUMO and was calculated at $11,480 \text{ cm}^{-1}$

TABLE I. Summary of AM1-SCRF results for Reichardt's dye #1 (RB).

Medium	ϵ	Dihedral angles ($^{\circ}$)			ΔH_f (kcal/mol)	μ (D)	IP (eV)
		ξ 33-32-9-8	ϕ 15-14-2-1	χ 21-20-4-3			
Vacuum							
A	1.000	-39.0	128.4	-37.9	202.8	13.005	6.938
A'	1.000	-39.1	-55.2	-37.8	202.8	12.979	6.939
B	1.000	-140.8	-54.1	-37.9	202.9	13.094	6.923
A Conformation							
dioxane	2.209	-38.4	131.2	-36.9	200.2	15.883	6.950
ethanol	24.30	-38.1	130.0	-34.4	195.4	19.064	7.046
CH ₃ OH	32.63	-38.1	130.0	-34.4	195.3	19.121	7.052
CH ₃ CN	35.94	-38.0	130.0	-34.4	195.2	19.134	7.054
H ₂ O	78.54	-38.1	129.9	-34.4	195.0	19.225	7.062
A' Conformation							
CH ₃ OH	32.63	-38.1	-52.9	-34.5	195.3	19.116	7.053
CH ₃ CN	35.94	-38.1	-52.9	-34.5	195.2	19.129	7.054
H ₂ O	78.54	-38.1	-54.3	-34.4	195.1	19.191	7.062
B Conformation							
dioxane	2.209	-140.8	-53.9	-37.9	200.0	14.905	6.963
CH ₃ OH	32.63	-141.7	-52.7	-34.6	195.1	19.131	7.043
CH ₃ CN	35.94	-141.7	-52.7	-34.6	195.1	19.146	7.044
H ₂ O	78.54	-141.7	-52.9	-34.4	194.8	19.267	7.052

(Conformer A) and 11,220 cm^{-1} (Conformer B), to be compared to the experimental value of 12,580 cm^{-1} in 1,4-dioxane [3,10-18].

A broad shoulder is observed between about 20,000-22,200 cm^{-1} . We assign it to our next two calculated transitions: HOMO \rightarrow LUMO + 1, calculated at 17,140 cm^{-1} (conformer A) and 16,920 cm^{-1} (conformer B), and HOMO-1 \rightarrow LUMO, calculated at 24,180 cm^{-1} (conformer A) and 24,690 cm^{-1} (conformer B). Both of these excitations are of medium strength. Their oscillator strength average is at about 19,400 cm^{-1} , to be compared to the observed maximum of the shoulder at about 21,000 cm^{-1} in 1,4-dioxane [3,10-18]. The next observed peak is at 25,000 cm^{-1} and is strong. This compares very well with calculated values of 25,560 cm^{-1} (conformer A) and 25,190 cm^{-1} (conformer B).

Finally, we consider a broad, intense band, observed with maximum at 32,260 cm^{-1} with a slight shoulder at 30,300 cm^{-1} . Both conformers are calculated to have a great many transitions in this region. At about 31,500 cm^{-1} (317 nm), both have strong transitions and both have strong transitions at about 34,500 cm^{-1} . Experimentally this band shows little solvent shift [3].

We conclude that the absorption spectrum as a whole is well described, as one can see by comparing Tables II and III with the observed spectrum of RB in 1,4-dioxane [3]. The most important peak for our purposes is the first, observed at 10,500 cm^{-1} [3]. We calculate 11,480 cm^{-1} for conformer A and 11,220 cm^{-1} for conformer B.

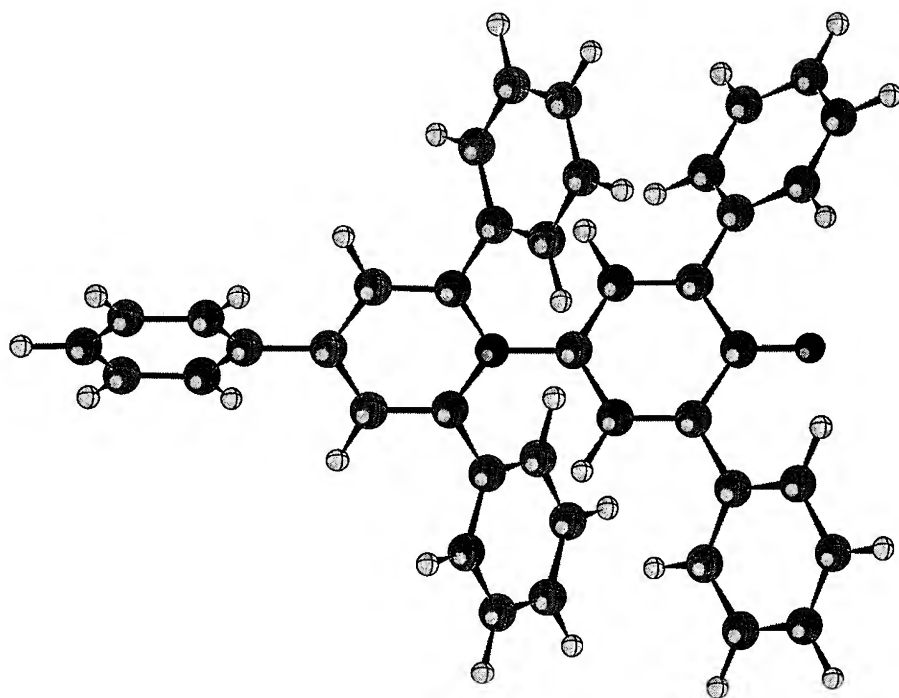


Figure 2. Reichardt's dye #1, conformer A, in gas phase. AM1 optimized geometry.

Solvent Effects: 1,4-Dioxane

Our next step was the consideration of solvent effects. One of our immediate goals was to establish the procedure that could be applied to a large number of solvents, in order to reproduce Reichardt's $E_T(30)$ scale [3–5,10–16] and to check our understanding of this scale. For the nonpolar solvents, that have no specific bonding with the solute (RB), the continuum approximation [23–28] should be enough to reach agreement with the observed spectra. However, we have to apply some caution, because even for the nonpolar solvents the dielectric constant variation does *not* concur with the polarity of the solvent that is expressed by the $E_T(30)$ parameter. For example, 1,4-dioxane ($\epsilon = 2.209$) is more polar than benzene ($\epsilon = 2.284$) and acetonitrile ($\epsilon = 35.94$) is more polar than DMSO ($\epsilon = 46.45$) on the $E_T(30)$ scale.

The INDO/S-CIS calculated spectra of RB (conformations A and B) in 1,4-dioxane treated by the SCRF approach [9] are shown in Tables IV and V. The first band is calculated at $10,591\text{ cm}^{-1}$ (for A) and $11,871\text{ cm}^{-1}$ (for B). If we take the result for B (based on the fact that the intensity is twice as large), the agreement with the experiment ($12,600\text{ cm}^{-1}$ [3,10–16]) is very good.

A second band was calculated at $567\text{ nm} = 17,640\text{ cm}^{-1}$ (conformer A) and $550\text{ nm} = 18,193\text{ cm}^{-1}$ (conformer B), and accounts for a shift of about $600\text{--}900\text{ cm}^{-1}$

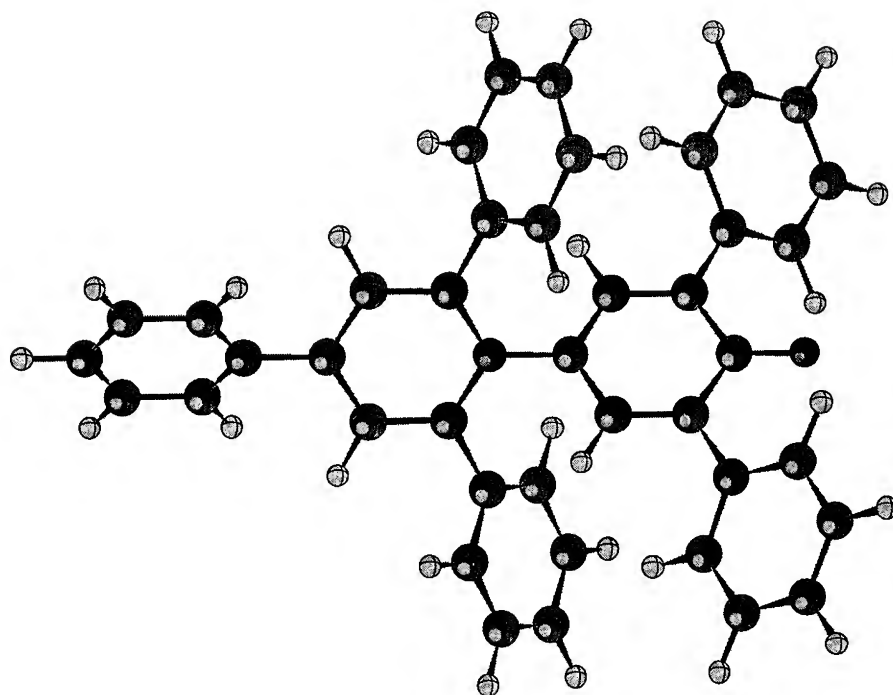


Figure 3. Reichardt's dye #1, conformer B, in gas phase. AM1 optimized geometry.

from the gas phase result (see above). Again, the relation between oscillator strengths enables us to assign this band to the shoulder with maximum at about $21,000\text{ cm}^{-1}$.

Comparison of Tables II-V show that the third and fourth transitions undergo an inversion from gas phase to solution. A third transition ($\text{HOMO} \rightarrow \text{LUMO} + 4$, $\text{HOMO} \rightarrow \text{LUMO} + 8$) is now calculated at $25,220\text{ cm}^{-1}$ (conformer A) and $24,925\text{ cm}^{-1}$ (conformer B). Both numbers match very well the sharp peak observed at approximately $25,000\text{ cm}^{-1} = 400\text{ nm}$.

Again we found a series of five very weak transitions beginning at 370 nm (including a $n \rightarrow \pi^*$ transition from the lone pair of oxygen). This system is not observed in 1,4-dioxane, but the band appears in acetonitrile, and helps demonstrate the consistency of our assignments. Finally, the large, broad band calculated to begin at 330 nm is nearly unshifted with respect to the gas phase spectrum (compare Table II with IV, and Table III with V).

Other Nonpolar Solvents: The Special Case of Chloroform

Other solvents in this range of $E_T(30)$ follow the same pattern: in general, increase of the dielectric constant is followed by an increase in the transition energy of the first band. Therefore, we simply give the calculated values in Table VI, in order to avoid repetition. It is observed that the value of $E_T(30)$ for benzene is underestimated

TABLE II. Calculated (gas phase) absorption spectrum of Reichardt's dye #1, conformer A.

ΔE^a (cm ⁻¹)	f_{osc}^b	Main CI contributions and single excitations
11483 ^c	0.405	+0.96901 (102 → 103) (HOMO → LUMO)
17138 ^d	0.045	-0.97468 (102 → 104) HOMO → LUMO + 1)
24180	0.027	-0.89879 (101 → 103) (HOMO-1 → LUMO)
25556 ^e	0.478	-0.69212 (102 → 107), -0.59668 (102 → 111)
26418	0.054	+0.61817 (102 → 105), +0.51282 (102 → 108)
26951	0.022	+0.75531 (102 → 110), +0.49626 (102 → 109)
27550	0.016	-0.74336 (102 → 108), -0.41459 (102 → 109)
27784	0.038	+0.63383 (102 → 111), -0.54800 (102 → 107)
27900	0.058	+0.83022 (100 → 103), -0.35859 (102 → 111)
30085 ^f	0.049	+0.53846 (102 → 105), +0.52160 (99 → 103)
31572 ^f	0.305	-0.73333 (96 → 103), +0.41061 (94 → 103)
31719 ^f	0.084	-0.53730 (99 → 103), +0.46658 (102 → 105)
31901	0.006	+0.95613 (102 → 106)
33515 ^g	0.012	+0.67122 (101 → 104), +0.48958 (102 → 113)
33603 ^g	0.047	-0.58691 (102 → 113), +0.43957 (102 → 112)
33871 ^g	0.015	+0.86539 (102 → 114)
34264 ^g	0.464	+0.83022 (100 → 103), -0.35859 (102 → 111)

^a Transition energies.^b Oscillator strengths: $f_{ij} = 4.7092 \times \Delta E_{ij} \langle i | \mu | j \rangle^2$.

Experimental values in 1,4-dioxane [1], (c)–(g).

^c 12,600 cm⁻¹ = 795 nm.^d 21,500 cm⁻¹ = 465 nm.^e 25,000 cm⁻¹ = 400 nm.^f A shoulder at 31,000 cm⁻¹ = 322 nm.^g A broad band centered at approximately 33,330 cm⁻¹ = 300 nm.

by ca. 2.0 kcal/mol (700 cm⁻¹). The solvents 1,4-dioxane and chloroform present us with a larger error (4.0–5.0 kcal/mole) in $E_T(30)$. Since this error is not systematic with that of benzene, we might speculate that very weak specific interactions begin to affect the pattern of the nonpolar solvents. To check this hypothesis, we carried out an additional SM calculation on RB (conformer B) surrounded by four chloroform molecules (Fig. 4) (we have chosen chloroform because the specific interactions—H-bond involving the CHCl₃ proton—were easier to figure out than for the case of 1,4-dioxane). The resulting spectrum is depicted in Table VII. Clearly the H-bond affects the $n \rightarrow \pi^*$ CT transition, and the corrected value of $E_T(30) = 38.8$ kcal/mol (see Table VII) closely matches the experiment. The sharp peak observed at 25,000 cm⁻¹ for 1,4-dioxane is now blue shifted by 1,000 cm⁻¹. Thus, we conclude that results from the SCRF are indeed perturbed for CHCl₃ (and probably also for 1,4-dioxane) due to specific binding, even though the H-bonding is quite weak.

TABLE III. Calculated (gas phase) absorption spectrum of Reichardt's dye #1, conformer B.

ΔE^a (cm ⁻¹)	f_{osc}^b	Main CI contributions and single excitations
11218 ^c	0.392	+0.96687 (102 → 103) (HOMO → LUMO)
16917 ^d	0.045	-0.97398 (102 → 104) (HOMO → LUMO + 1)
24688	0.016	+0.85674 (101 → 103) (HOMO-1 → LUMO)
25187 ^e	0.500	+0.57067 (102 → 111), +0.59781 (102 → 107)
26220	0.056	-0.62569 (102 → 105), +0.52804 (102 → 108)
26797	0.016	+0.76846 (102 → 110), -0.45084 (102 → 109)
27364	0.011	-0.75341 (102 → 108), -0.44406 (102 → 109)
27498	0.001	-0.91681 (100 → 103)
27558	0.052	+0.74652 (102 → 111), -0.61248 (102 → 107)
29895 ^f	0.047	+0.54909 (102 → 105), +0.50071 (99 → 103)
31434 ^f	0.291	-0.79422 (96 → 103), -0.32512 (94 → 103)
31567 ^f	0.125	+0.60065 (99 → 103), -0.43290 (102 → 105)
31699	0.005	+0.96039 (102 → 106) (HOMO → LUMO + 3)
33140 ^g	0.052	-0.87124 (102 → 112)
33592 ^g	0.002	+0.77394 (102 → 114)
33592 ^g	0.002	+0.87672 (101 → 104) (HOMO-1 → LUMO + 1)
33887 ^g	0.012	-0.74600 (102 → 113), -0.41668 (102 → 114)
34658 ^g	0.529	-0.31631 (95 → 107)

^a Transition energies.^b Oscillator strengths: $f_{ij} = 4.7092 \times \Delta E_{ij} \langle i | \mu | j \rangle^2$.

Experimental values in 1,4-dioxane [1], (c)-(g).

^c 12,600 cm⁻¹ = 795 nm.^d 21,500 cm⁻¹ = 465 nm.^e 25,000 cm⁻¹ = 400 nm.^f A shoulder at 31,000 cm⁻¹ = 322 nm.^g A broad band centered at approximately 33,330 cm⁻¹ = 300 nm.

H-Bonding Solvents: Methanol

Inspecting the case of methanol (Fig. 5) is interesting because its dielectric constant ($\epsilon = 32.63$) is very close to that of acetonitrile ($\epsilon = 35.94$). Thus, at the SCRF approximation [23-28], the INDO/S-CIS calculations should yield almost the same spectra. This is, indeed, the case as one can see from inspection of Table VI. The calculated (SCRF only) transition energy of acetonitrile (12,830 cm⁻¹) is slightly larger than that of methanol (12,250 cm⁻¹), while experimentally the first $n \rightarrow \pi^*$ band is observed at 19,420 cm⁻¹ = 515 nm (the solution is red) for methanol and 16,080 cm⁻¹ = 622 nm (green-blue) for acetonitrile [3]. These calculations illustrate the well-known phenomenon of the saturation in the SCRF model as $\bar{\epsilon}(\epsilon)$ approach 1/2 as ϵ increases. Clearly the continuum model [23-28] alone is not satisfactory. To correct this we decided to include two methanol molecules near the oxide terminæ of RB, and two molecules near the positively charged nitrogen. This simple

TABLE IV. Calculated absorption spectrum of Reichardt's dye #1, conformer A in 1,4-dioxane.

ΔE^a (cm ⁻¹)	f_{osc}^b	Main CI contributions and single excitations
10591 ^c	0.153	-0.97127 (102 → 103) (HOMO → LUMO)
17640 ^d	0.030	-0.98076 (102 → 104) (HOMO → LUMO + 1)
25217 ^e	0.414	-0.75027 (102 → 111), -0.43925 (102 → 107)
25611 ^e	0.151	+0.82156 (101 → 103), +0.37918 (100 → 103)
27069	0.040	+0.73119 (102 → 105), +0.48779 (102 → 110)
27772	0.001	-0.72349 (102 → 109), -0.59091 (102 → 107)
27536	0.057	-0.50022 (102 → 108), -0.49728 (102 → 109)
27339	0.030	+0.71390 (102 → 108), +0.34673 (102 → 111)
28305	0.058	-0.82669 (100 → 103), +0.45851 (101 → 103)
31307 ^f	0.342	+0.75436 (96 → 103), -0.35847 (93 → 103)
31842 ^f	0.065	+0.64745 (99 → 103), -0.35764 (95 → 103)
31941	0.069	+0.72591 (102 → 112), +0.47590 (102 → 113)
32186	0.037	+0.86755 (102 → 114) (HOMO → LUMO + 11)
32815 ^g	0.429	+0.65087 (102 → 113), -0.39108 (102 → 112)
32655 ^g	0.062	-0.61304 (102 → 110), +0.47997 (102 → 105)
33945 ^g	0.057	-0.74460 (101 → 104), -0.34662 (99 → 103)
33290 ^g	0.003	-0.81896 (102 → 106), (HOMO → LUMO + 3)
34740 ^g	0.319	+0.56390 (95 → 103), -0.52880 (94 → 103)

^a Transition energies.^b Oscillator strengths: $f_{ij} = 4.7092 \times \Delta E_{ij} \langle i | \mu | j \rangle^2$.

Experimental values in 1,4-dioxane [1], (c)-(g).

^c 12,600 cm⁻¹ = 795 nm.^d 21,500 cm⁻¹ = 465 nm.^e A sharp peak at 25,000 cm⁻¹ = 400 nm.^f A slight shoulder at 31,000 cm⁻¹ = 322 nm.^g A broad band centered at approximately 33,330 cm⁻¹ = 300 nm.

arrangement "fixes" the calculated spectrum for methanol, as shown in Tables VIII and IX. At the SCRF-SM level of approximation, the $n \rightarrow \pi^*$, CT band is located at 15,070 cm⁻¹ for conformer A and 14,140 cm⁻¹ for conformer B. We further observe that the oscillator strength for this transition is drastically reduced (compared to the gas phase calculation). Also, the now stronger HOMO-1 → LUMO transition was calculated at 19,220 cm⁻¹ for conformer A and 19,320 cm⁻¹ for conformer B. This accounts for a blue shift of 7,000 cm⁻¹ with respect to the SCRF result. The agreement with the experimental value of 19,420 cm⁻¹ is very good.

Water

The absorption spectrum of RB in water (Fig. 6) should be the most difficult to reproduce, due to the special properties of the solvent. The INDO/S-CIS calculated spectra of RB surrounded by four water molecules are shown in Tables X (conformer

TABLE V. Calculated absorption spectrum of Reichardt's dye #1, conformer B in 1,4-dioxane.

ΔE^a (cm ⁻¹)	f_{osc}^b	Main CI contributions and single excitations
11871 ^c	0.304	-0.96922 (102 → 103) (HOMO → LUMO)
18193 ^d	0.041	+0.97441 (102 → 104) (HOMO → LUMO + 1)
24925 ^e	0.401	+0.65478 (102 → 111), -0.63700 (102 → 106)
26027 ^e	0.162	-0.91968 (101 → 103)
27469	0.049	-0.71689 (102 → 105), -0.53121 (102 → 110)
27917	0.013	+0.90477 (102 → 109) (HOMO → LUMO + 6)
27495	0.027	-0.55251 (102 → 108), -0.53296 (102 → 111)
27523	0.021	+0.66714 (102 → 108), +0.45593 (102 → 111)
27856	0.003	-0.96844 (100 → 103) (HOMO-2 → LUMO)
31562 ^f	0.145	+0.68260 (99 → 103), -0.40201 (95 → 103)
31938 ^f	0.281	-0.78945 (96 → 103) (HOMO-6 → LUMO)
32015	0.066	-0.87926 (102 → 112) (HOMO → LUMO + 9)
32602	0.050	+0.78754 (102 → 113) (HOMO → LUMO + 10)
33428 ^g	0.195	-0.57387 (102 → 114), +0.49714 (102 → 110)
33474 ^g	0.002	+0.82964 (102 → 107) (HOMO → LUMO + 4)
34215 ^g	0.238	-0.67225 (102 → 107), -0.40388 (102 → 110)
34863 ^g	0.018	+0.85915 (101 → 104) (HOMO-1 → LUMO + 1)
35599 ^g	0.201	-0.46040 (94 → 103), -0.39471 (95 → 103)

^a Transition energies.^b Oscillator strengths: $f_{ij} = 4.7092 \times \Delta E_{ij} \langle i | \mu | j \rangle^2$.

Experimental values in 1,4-dioxane [1], (c)-(g).

^c 12,600 cm⁻¹ = 795 nm.^d 21,500 cm⁻¹ = 465 nm.^e A sharp peak at 25,000 cm⁻¹ = 400 nm.^f A slight shoulder at 31,000 cm⁻¹ = 322 nm.^g A broad band centered at approximately 33,330 cm⁻¹ = 300 nm.TABLE VI. First CT band in the UV-visible absorption spectrum of pyridinium-*N*-phenoxide betaines.

Solvent	ϵ	n_D	$\nu_{calcd.}$ (cm ⁻¹)		$\nu_{exptl.}$ (cm ⁻¹) [3]	E_T (30) (kcal)	
			SCRF	SCRF-SM		Calcd.	Exptl. [3]
hexane	1.890	1.3751	11,050	—	10,850	31.6	31.0
CCl ₄	2.238	1.460	11,260	—	11,338	32.2	32.4
benzene	2.284	1.501	11,297	—	11,990	32.3	34.3
1,4-dioxane	2.209	1.4224	11,231	—	12,600	32.1	36.0
CHCl ₃	4.806	1.446	12,008	13,555	13,680	38.8	39.1
CH ₃ CN	35.94	1.3442	12,831	—	16,077	—	45.6
methanol	32.63	1.3288	12,246	19,272	19,420	55.1	55.4
water	78.54	1.3328	12,370	21,790	22,075	62.3	63.0

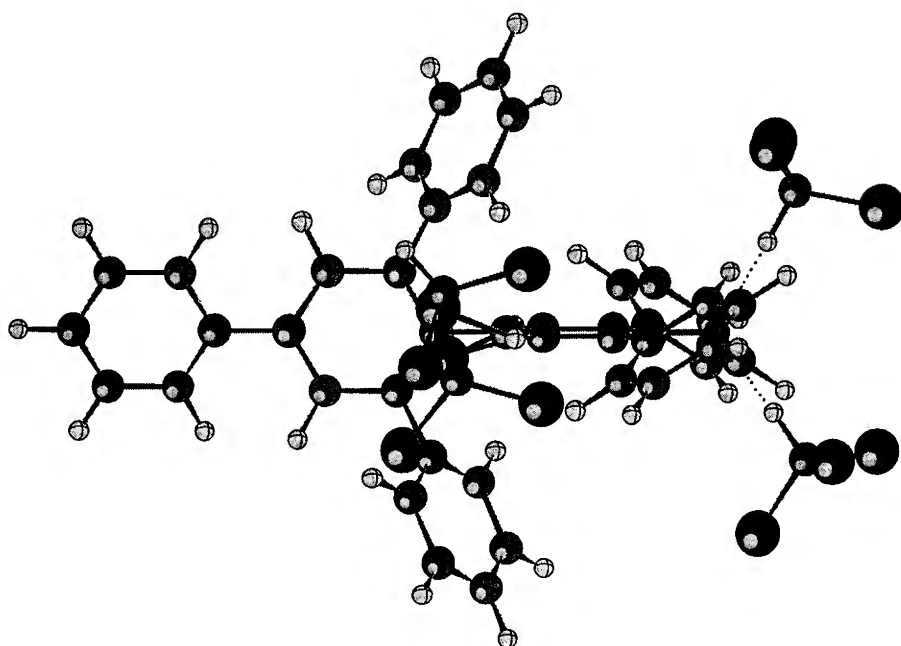


Figure 4. Reichardt's dye #1 (conformer B), in chloroform. AM1-SCRF-SM geometry.

A) and XI (conformer B). The $n \rightarrow \pi^*$, CT band was calculated at $14,060 \text{ cm}^{-1}$ for conformer A and $13,980 \text{ cm}^{-1}$ for conformer B. As previously observed for methanol, this band loses its oscillator strength by at least one order of magnitude (compared to the gas phase result). The experimental spectrum shows a peak at 453 nm, and this peak should be the one related to the $E_t(30)$ scale. However,

TABLE VII. Calculated absorption spectrum of Reichardt's dye #1, conformer B in chloroform, SM approximation.

$\Delta E^a \text{ (cm}^{-1}\text{)}$	f_{osc}^b	Main CI contributions and single excitations
13555 ^c	0.013	$-0.95917 (154 \rightarrow 155) (\text{HOMO} \rightarrow \text{LUMO})$
16260	0.074	$+0.98861 (154 \rightarrow 158) (\text{HOMO} \rightarrow \text{LUMO} + 3)$
16451	0.101	$+0.98535 (154 \rightarrow 159) (\text{HOMO} \rightarrow \text{LUMO} + 4)$
17943	0.009	$+0.98031 (154 \rightarrow 156) (\text{HOMO} \rightarrow \text{LUMO} + 1)$
19979	0.002	$-0.96406 (154 \rightarrow 157) (\text{HOMO} \rightarrow \text{LUMO} + 2)$
22236	0.019	$+0.97694 (154 \rightarrow 160) (\text{HOMO} \rightarrow \text{LUMO} + 5)$
26355	0.484	$-0.79421 (154 \rightarrow 165) (\text{HOMO} \rightarrow \text{LUMO} + 10)$
26465	0.013	$-0.71339 (153 \rightarrow 155) (\text{HOMO-1} \rightarrow \text{LUMO})$

^a Transition energies.

^b Oscillator strengths: $f_{ij} = 4.7092 \times \Delta E_{ij} \langle i | \mu | j \rangle^2$.

^c Exptl. value $13,680 \text{ cm}^{-1} = 833 \text{ nm}$.

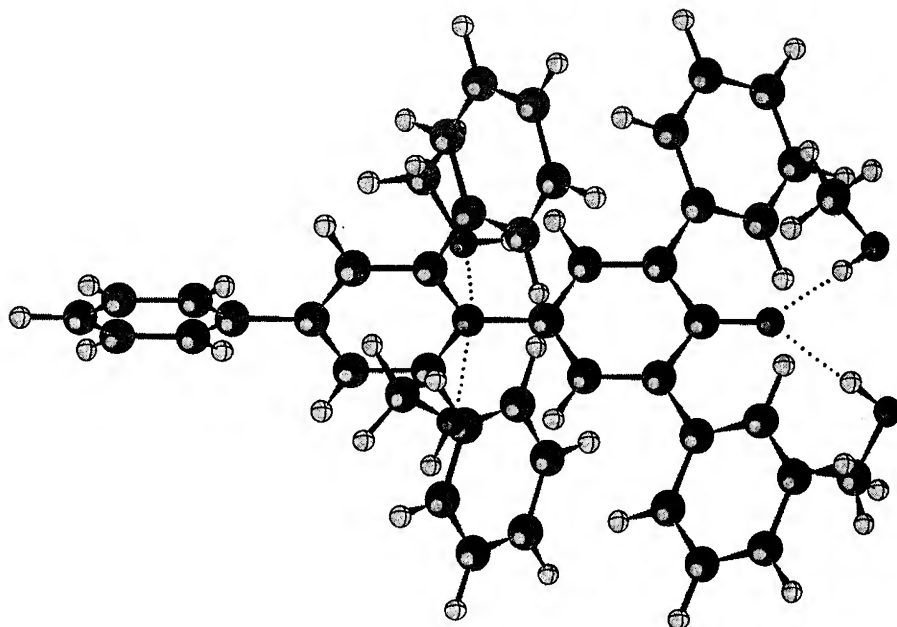


Figure 5. Reichardt's dye #1 (conformer B), in methanol. AM1-SCRF-SM geometry.

based on the results of this article, we now conclude that the observed peak (for methanol and water, and probably also for ethanol) rather corresponds to the second $n \rightarrow \pi^*$ transitions, HOMO-1 \rightarrow LUMO for methanol (see Tables VIII and IX) and HOMO \rightarrow LUMO + 1 for water (see Tables X and XI). We also observe that for both solvents the sharp peak (observed close to 25,000 cm^{-1} for 1,4-dioxane) is red shifted by about 1,000 cm^{-1} .

TABLE VIII. Calculated absorption spectrum of RB, conformer A in methanol, SM approximation.

ΔE^a (cm^{-1})	f_{osc}^b	Main CI contributions and single excitations
15071	0.038	+0.96651 (130 \rightarrow 131) (HOMO \rightarrow LUMO)
19224 ^c	0.103	+0.88285 (129 \rightarrow 131) (HOMO-1 \rightarrow LUMO)
20815	0.077	-0.89996 (130 \rightarrow 132) (HOMO \rightarrow LUMO + 1)
23335	0.037	+0.83438 (129 \rightarrow 132) (HOMO-1 \rightarrow LUMO + 1)
24431	0.442	-0.76913 (130 \rightarrow 136) (HOMO \rightarrow LUMO + 5)
27449	0.032	-0.92785 (130 \rightarrow 134) (HOMO \rightarrow LUMO + 3)

^a Transition energies.

^b Oscillator strengths.

^c Exptl. 19,420 cm^{-1} = 515 nm.

TABLE IX. Calculated absorption spectrum of RB, conformer B in methanol, SM approximation.

ΔE^a (cm ⁻¹)	f_{osc}^b	Main CI contributions and single excitations
14138	0.020	-0.96546 (130 → 131) (HOMO → LUMO)
19320 ^c	0.164	+0.94352 (129 → 131) (HOMO-1 → LUMO)
21343	0.044	-0.96346 (130 → 132) (HOMO → LUMO + 1)
24052	0.442	-0.76055 (130 → 136) (HOMO → LUMO + 5)
24929	0.031	+0.81435 (129 → 132) (HOMO-1 → LUMO + 1)
28427	0.040	+0.69131 (130 → 133) (HOMO → LUMO + 2)

^a Transition energies.^b Oscillator strengths.^c Exptl. 19,420 cm⁻¹ = 515 nm.

Concluding Remarks

In this work we have examined the absorption spectra of a compound which presents negative solvatochromism, Reichardt's dye #1 (RB). The challenge was to obtain a correct description of the negative solvatochromism exhibited by RB. For nonpolar solvents, which make no specific binding to the solute, the continuum model [23–28] was enough to reproduce the experimental spectra. For solvents which form specific binding (e.g., H-bond) with RB, we had to apply the super-

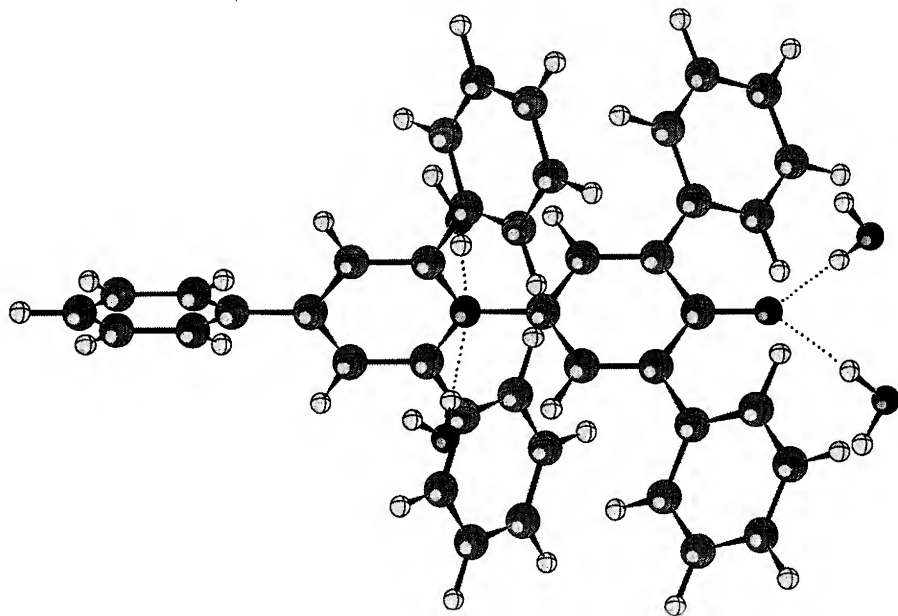


Figure 6. Reichardt's dye #1 (conformer B), in water. AM1-SCRF-SM geometry.

TABLE X. Calculated absorption spectrum of RB, conformer A in water, SM approximation.

ΔE^a (cm ⁻¹)	f_{osc}^b	Main CI contributions and single excitations
14061	0.017	+0.97387 (118 \rightarrow 119) (HOMO \rightarrow LUMO)
21851 ^c	0.035	-0.97906 (118 \rightarrow 120) (HOMO \rightarrow LUMO + 1)
23000	0.168	+0.89137 (115 \rightarrow 119) (HOMO-3 \rightarrow LUMO)
24377	0.470	-0.83016 (118 \rightarrow 124) (HOMO \rightarrow LUMO + 5)
26658	0.003	+0.76182 (115 \rightarrow 120) (HOMO-3 \rightarrow LUMO + 1)
28836	0.070	+0.74919 (118 \rightarrow 122) (HOMO \rightarrow LUMO + 3)
29450	0.016	-0.66650 (118 \rightarrow 121) (HOMO \rightarrow LUMO + 2)

^a Transition energies.^b Oscillator strengths.^c Exptl. 22,075 cm⁻¹ = 543 nm.

molecule approach [29–31]. This work provided basis from drawing some conclusions, that we now present.

(i) AM1 calculations have provided two low-lying conformers very close in heats of formation, which suggests that they coexist, both in gas phase and in solution. (ii) We have confirmed that the first CT band in the spectrum of RB has $n \rightarrow \pi^*$ character and arises from an excitation from the lone pair of the phenoxide oxygen. (iii) For nonpolar solvents increase of the dielectric constant gives rise to increase of $E_t(30)$. (iv) For some nonpolar solvents such as chloroform and 1,4-dioxane, specific binding, although quite weak, is enough to disturb the mentioned pattern and the CT band is further blue shifted. (v) One of the effects of the SCRF on the CI calculations is that the lowest energy $n \rightarrow \pi^*$, CT band loses its intensity as the dielectric constant increases. (vi) We observe that this effect holds even for SM calculations, so the bands used in the $E_t(30)$ scale for methanol and water are

TABLE XI. Calculated absorption spectrum of RB, conformer B in water, SM approximation.

ΔE^a (cm ⁻¹)	f_{osc}^b	Main CI contributions and single excitations
13978	0.018	+0.97253 (118 \rightarrow 119) (HOMO \rightarrow LUMO)
21728 ^c	0.037	-0.97587 (118 \rightarrow 120) (HOMO \rightarrow LUMO + 1)
23029	0.172	+0.91992 (115 \rightarrow 119) (HOMO-3 \rightarrow LUMO)
24056	0.450	+0.87774 (118 \rightarrow 124) (HOMO \rightarrow LUMO + 5)
26674	0.003	+0.78160 (115 \rightarrow 120) (HOMO-3 \rightarrow LUMO + 1)
28325	0.072	+0.87366 (118 \rightarrow 122) (HOMO \rightarrow LUMO + 3)
29288	0.009	-0.83416 (118 \rightarrow 121) (HOMO \rightarrow LUMO + 2)

^a Transition energies.^b Oscillator strengths.^c Exptl. 22,075 cm⁻¹ = 543 nm.

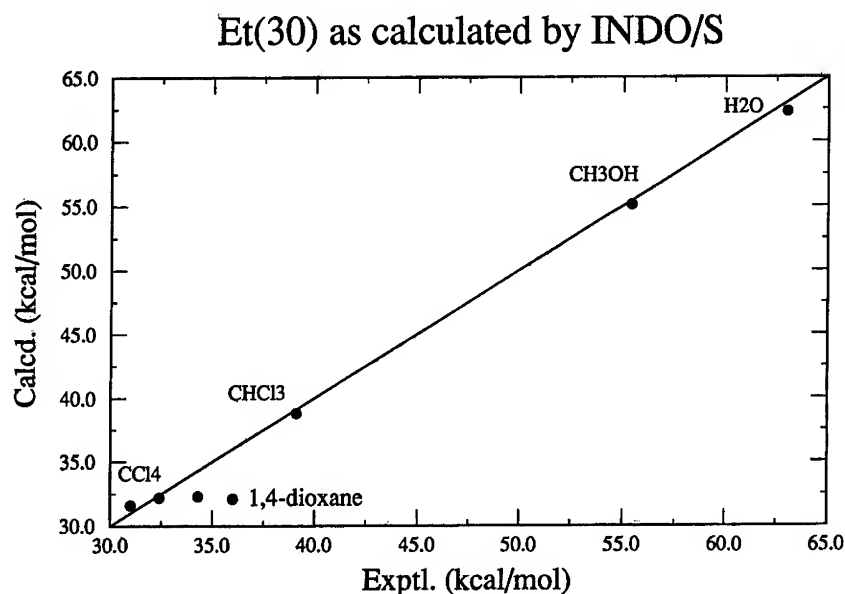


Figure 7. Plot of theoretical versus experimental results for the $E_T(30)$ parameter.

actually due to the second $n \rightarrow \pi^*$ transition. Finally, (vii) the INDO/S-CIS technique proved a successful tool in reproducing the empirical $E_T(30)$ scale. We summarize these results in Table VI and Figure 7. Perhaps slight discrepancies could be removed by increasing the number of solvent molecules, but we are more likely at the limit of the model we use for structure and spectroscopy.

Acknowledgments

The authors are much indebted to Dr. Marshall G. Cory and Mr. Xuehe Zheng (Florida) for many valuable discussions and suggestions. This research has received partial financial support from a grant from CNPq (Conselho Nacional de Desenvolvimento Científico e Tecnológico—Brazil), and the Office of Naval Research (U.S.).

Bibliography

- [1] W. Liptay, *Angew. Chem.* **8**(3), 177–188 (1969).
- [2] N. Mataga and T. Kubota, *Molecular Interactions and Electronic Spectra* (M. Dekker Inc., New York, 1970).
- [3] C. Reichardt, *Solvents and Solvent Effects in Organic Chemistry*, 2nd ed. (VCH Publishers, Weinheim, 1988).
- [4] O. Pytela, *Coll. Czech. Chem. Commun.* **53**, 1333–1400 (1988).
- [5] E. M. Kosower, *An Introduction to Physical Organic Chemistry* (Wiley, New York, 1968).
- [6] I. G. Kaplan, *Theory of Molecular Interactions: Studies in Phys. Theor. Chem.* **42** (Elsevier, Amsterdam, 1986).

- [7] M. P. Allen and D. J. Tildesley, *Computer Simulation of Liquids* (Oxford Univ. Press, Oxford, 1989).
- [8] G. Rauhut, T. Clark, and T. Steinke, *J. Am. Chem. Soc.* **115**(20), 9174-9181 (1993).
- [9] M. M. Karelson and M. C. Zerner, *J. Phys. Chem.* **96**(17), 6949-6957 (1992).
- [10] K. Dimroth, C. Reichardt, T. Siepmann, and F. Bohlmann, *Liebigs Ann. Chem.* **661**, 1 (1963).
- [11] K. Dimroth and C. Reichardt, *Liebigs Ann. Chem.* **727**, 93 (1969).
- [12] C. Reichardt, *Liebigs Ann. Chem.* **752**, 64 (1971).
- [13] C. Reichardt and E. Harbusch-Görnert, *Liebigs Ann. Chem.* **1983**, 721 (1983).
- [14] C. Laurence, P. Nicolet, M. Lucon, and C. Reichardt, *Bull. Soc. Chim. Fr.* **1987**(1), 125-130.
- [15] C. Laurence, P. Nicolet, M. Lucon, and C. Reichardt, *Bull. Soc. Chim. Fr.* **1987**, 1001.
- [16] C. Reichardt, G. Schäfer, and P. Milart, *Collect. Czech. Chem. Commun.* **55**, 97-107 (1990).
- [17] W. Linert and R. F. Jameson, *J. Chem. Soc., Perkin Trans. 2*(8), 1415-1421 (1993).
- [18] W. Linert, B. Strauss, E. Herlinger, and C. Reichardt, *J. Phys. Org. Chem.* **5**, 275-284 (1992).
- [19] M. J. S. Dewar, E. G. Zoebisch, E. F. Healy, and J. J. P. Stewart, *J. Am. Chem. Soc.* **107**(13), 3902-3909 (1985).
- [20] M. J. S. Dewar and E. G. Zoebisch, *J. Mol. Struct. (Theochem)* **180**, 1 (1988).
- [21] A. A. Voityuk, *J. Struct. Chem.* **29**(1), 120 (1988).
- [22] AMPAC 2.1, D. A. Liotard, E. F. Healy, J. M. Ruiz, and M. J. S. Dewar, authors. Austin, 1989.
- [23] O. Tapia and O. Goscinski, *Mol. Phys.* **29**(6), 1653-1661 (1975).
- [24] S. Miertuš, E. Scrocco, and J. Tomasi, *Chem. Phys.* **55**, 117 (1981).
- [25] M. M. Karelson, T. Tamm, A. R. Katritzky, S. J. Cato, and M. C. Zerner, *Int. J. Quantum Chem.* **37**, 1-13 (1990).
- [26] M. M. Karelson, T. Tamm, A. R. Katritzky, M. Szafran, and M. C. Zerner, *Tetrahedron Comp. Meth.* **2**(5), 295-304 (1989).
- [27] D. Rinaldi, J.-L. Rivail, and N. Rguini, *J. Comp. Chem.* **13**(6), 675-680 (1992).
- [28] O. Tapia, *J. Math. Chem.* **10**, 139-181 (1992).
- [29] D. L. Beveridge and G. W. Schnuelle, *J. Phys. Chem.* **78**(20), 2064-2069 (1974).
- [30] P. Claverie, J. P. Daudey, J. Langlet, B. Pullman, D. Piazzola, and M. J. Huron, *J. Phys. Chem.* **82**(4), 405-418 (1978).
- [31] L. C. G. Freitas, R. L. Longo, and A. M. Simas, *J. Chem. Soc., Faraday Trans* **88**(2), 189-193 (1992).
- [32] J. Ridley and M. C. Zerner, *Theor. Chim. Acta* **32**, 111-134 (1973).
- [33] M. C. Zerner, G. H. Loew, R. F. Kirchner, and U. T. Mueller-Westerhoff, *J. Am. Chem. Soc.* **102**(2), 589 (1980).
- [34] J. D. Head and M. C. Zerner, *Chem. Phys. Lett.* **131**, 359 (1986).
- [35] W. P. Anderson, W. D. Edwards, and M. C. Zerner, *Inorg. Chem.* **25**(16), 2728-2732 (1986).
- [36] W. D. Edwards and M. C. Zerner, *Theor. Chim. Acta* **72**, 347 (1987).
- [37] W. P. Anderson, T. R. Cundari, R. S. Drago, and M. C. Zerner, *Inorg. Chem.* **29**(1), 1-3 (1990).
- [38] N. Mataga and K. Nishimoto, *Z. Phys. Chem. (Frankfurt)* **13**, 140 (1957).

Received May 10, 1994

Determination of Higher Electric Polarizability Tensors from Unrelaxed Coupled Cluster Density Matrix Calculations of Electric Multipole Moments

TADEUSZ PLUTA,* JOZEF NOGA,[†] and RODNEY J. BARTLETT[‡]

Quantum Theory Project, University of Florida, Gainesville, Florida 32611-2085

Abstract

The CCSDT-1 method is used to calculate electric dipole, quadrupole, and octopole moments for the HF and H₂O molecule and the F⁻ anion, together with the associated higher-order polarizabilities. All multipole moments are computed as expectation values. Externally perturbed moments are used to determine the components of the electric tensors of second and higher order. It is shown that the correlated electric moments are in good agreement with experiment and that they may be used to obtain the electric polarizability and hyperpolarizability tensors in an effective way. © 1994 John Wiley & Sons, Inc.

Introduction

Electric multipole moments are of major importance in many areas of physical chemistry, including the evaluation of intermolecular interactions [1–3]. The interaction among permanent multipoles represents the coulombic part of the interaction energy, while the induction contribution can be represented as an interaction of permanent moments of a molecule A with the distorted charge density of B. The ability of molecule B to be distorted by the permanent moments of A is measured by the polarizability tensors of B. Unlike the multipole moments, polarizabilities are of second- or higher-order in the perturbation and demand much more computational effort to calculate than first-order electric properties. In principle, one can use analytical differentiation methods [2], but in practice the absence of analytical, mixed higher derivatives at the correlated level dictates the use of more straightforward finite-field techniques.

In this article we present the results of our calculations of electric moments and polarizabilities for model systems: HF, H₂O, and the F⁻ anion. We have chosen to employ the charge perturbation variant of the finite-field method together with direct expectation value calculations of electric first-order moments. Electron correlation effects have been accounted for using the coupled cluster method (CCM) [4–7] with the inclusion of single, double, and triple excitation operators, namely,

* Department of Chemistry, Silesian University, PL-40-006 Katowice, Poland.

[†] Institute of Inorganic Chemistry, Slovak Academy of Sciences, SK-842 36 Bratislava, Slovakia.

[‡] To whom correspondence should be addressed at the University of Florida.

CCSDT-1 [8]. The choice of our systems follows from the fact that there are many calculations of higher-order properties available at the SCF level to compare. However, at the correlated level some components of the polarizability tensors have, to our knowledge, never been obtained before. In particular, F^- is an extremely difficult case for electric properties evaluation, due to the diffuse character of the charge density and the need to account for a substantial part of the electron correlation effects.

We would also like to emphasize that the high quality CCSDT-1 approach satisfies the Hellmann–Feynman theorem to a great accuracy [9,10] and in conjunction with the charge perturbation method provides an effective and accurate tool for calculating electric tensors of small molecules. At the same time, the ability of medium size polarized basis sets suited for calculations of electric properties, as suggested by Sadlej [11], has been tested.

Method

The finite-field technique consists of placing a molecule (atom) in a weak external electric field and then calculating the total energy of the system. In principle, the first-, second-, and higher-order electric properties of the system can be calculated by numerical differentiation of the total perturbed energy [e.g., 12]. Since the only property used in these calculations to determine polarizabilities is the total energy, there is no fundamental difficulty in using correlated methods like MBPT or CCM. The charge perturbation method [13,14] is a variant of the conventional finite-field technique. The external electric field is generated by a charge Q (or charges) placed at a distance R from the molecule and hence do not provide a homogeneous field, but instead a presence of field gradients. Hence, the method can be used to determine higher moment polarizabilities. The Hamiltonian of such a system can be written as

$$H(Q, R) = H^{(0)} + H^{(1)} \quad (1)$$

with the perturbation $H^{(1)}$ given by

$$H^{(1)} = -\sum_{i=1}^{n_{el}} \frac{Q}{|r_i - R|} + \sum_{J=1}^{N_{nucl}} \frac{Z_J Q}{|r_J - R|}, \quad (2)$$

where the symbols have their usual meaning.

Expanding the Hamiltonian about the unperturbed $H^{(0)}$ in terms of the molecular multipole moments, one obtains the following expression:

$$H = H^{(0)} - \mu_\alpha F_\alpha - \frac{1}{3}\Theta_{\alpha\beta} F_{\alpha\beta} - \frac{1}{15}\Omega_{\alpha\beta\gamma} F_{\alpha\beta\gamma} - \dots \quad (3)$$

while the corresponding total perturbed energy E reads

$$\begin{aligned} E = E^{(0)} &- \mu_\alpha F_\alpha - \frac{1}{3}\Theta_{\alpha\beta} F_{\alpha\beta} - \frac{1}{15}\Omega_{\alpha\beta\gamma} F_{\alpha\beta\gamma} - \dots \\ &- \frac{1}{2}\alpha_{\alpha\beta} F_\alpha F_\beta - \frac{1}{6}\beta_{\alpha\beta\gamma} F_\alpha F_\beta F_\gamma - \frac{1}{24}\gamma_{\alpha\beta\gamma\delta} F_\alpha F_\beta F_\gamma F_\delta - \dots \\ &- \frac{1}{3}A_{\alpha\beta\gamma} F_\alpha F_\beta F_\gamma - \frac{1}{6}B_{\alpha\beta\gamma\delta} F_\alpha F_\beta F_\gamma F_\delta - \frac{1}{6}C_{\alpha\beta\gamma\delta} F_{\alpha\beta} F_{\gamma\delta} - \frac{1}{15}E_{\alpha\beta\delta\gamma} F_\alpha F_\beta F_\gamma - \dots \end{aligned} \quad (4)$$

Cartesian coordinates are denoted as α , β , and γ suffixes and the repeated index summation convention is employed throughout the paper. Electric field F_α and the field gradient $F_{\alpha\beta}$ are defined as the derivatives of the electrostatic potential ϕ at the origin of the multipole moments, here taken to be at the center of mass:

$$F_\alpha = -\frac{\partial\phi}{\partial r_\alpha}, \quad (5a)$$

$$F_{\alpha\beta} = -\frac{\partial^2\phi}{\partial r_\alpha\partial r_\beta}. \quad (5b)$$

μ , Θ , and Ω denote the dipole, quadrupole, and octopole moments of the unperturbed molecule. α , β , and γ are the dipole polarizability, hyperpolarizability, and second dipole hyperpolarizability, respectively. Dipole-quadrupole, quadrupole, dipole-octopole, and mixed dipole-dipole-quadrupole hyperpolarizability tensors are denoted by the symbols A , C , E , and B , respectively. Analogous relations like Eq. (4) hold for multipole moments:

$$\mu_\alpha(Q, R) = \mu_\alpha + \alpha_{\alpha\beta}F_\beta + \frac{1}{3}A_{\alpha\beta\gamma} + \frac{1}{3}B_{\alpha\beta\gamma\delta}F_\beta F_{\gamma\delta}, \quad (6a)$$

$$\Theta_{\alpha\beta}(Q, R) = \Theta_{\alpha\beta} + A_{\gamma\alpha\beta}F_\gamma + C_{\alpha\beta\gamma\delta}F_{\gamma\delta} + \frac{1}{2}B_{\gamma\delta\alpha\beta}F_\gamma F_\delta, \quad (6b)$$

$$\Omega_{\alpha\beta\gamma}(Q, R) = \Omega_{\alpha\beta\gamma} + E_{\delta\alpha\beta\gamma}F_\delta. \quad (6c)$$

The above relations along with the energy expansion provide enough information to completely determine the components of the electric tensors and form the basis of the charge perturbation method. For a given system of atoms and external charges, one can get a system of equations relating the known quantities, like the perturbed moments to the unknown tensors α , β , A , B , etc. The presence of a small external charge Q does not change the electron distribution dramatically and, with the proper choice of its magnitude, is sufficient to produce a field that can generate the induced multipoles. Bishop and his coworkers systematically employed this method to study atoms [15], diatomics [16], and small polyatomic systems [17]. The working equations relating the components of the second- and higher-order tensors were derived in [16,17] and need not be repeated here. Bishop performed his calculations mostly at the SCF level using extended, carefully prepared basis sets. For systems like H_2O [17], he also included electron correlation by performing limited MCSCF calculations. Both the SCF and MCSCF methods obey the Hellmann-Feynman theorem and consequently all first-order moments are rigorously given as expectation values. Others [18] have used the charge perturbation method with MBPT and limited coupled cluster applications using the approximate variant, CCD + ST(CCD) [19]. Since neither MBPT nor CC wavefunctions satisfy the Hellmann-Feynman theorem, polarizability tensors must be determined directly from perturbed energies. In this case the charge perturbation method becomes a rather minor modification of the traditional finite field technique and many potential advantages are lost. Alternatively, calculations can be based on the multipole moments calculated as expectation values from CC/MBPT wavefunctions at various electric fields. Such an approach proved to be efficient for the calculation of dipole polarizability of Be [10]. This

follows from the fact that the expectation value error at higher CC levels (like CCSDT) can be expected to be quite small [9,10]. This may be explained as follows:

Let us have a system under the influence of an external one-electron perturbation λO (with the operator O and its strength λ) described by the Hamiltonian (in normal ordered form)

$$H_N(\lambda) = H_N^{(0)} + \lambda O_N. \quad (7)$$

Then the first derivative of the expectation value (correlation) energy

$$\Delta E(\lambda) = \frac{\langle \Psi(\lambda) | H_N(\lambda) | \Psi(\lambda) \rangle}{\langle \Psi | \Psi \rangle} \quad (8)$$

with respect to λ at $\lambda = 0$, defining the correlation contribution to the one-electron property, is given as

$$\left(\frac{\partial \Delta E}{\partial \lambda} \right)_{\lambda=0} = \Delta E^\lambda = \frac{\langle \Psi | O | \Psi \rangle}{\langle \Psi | \Psi \rangle} + \frac{2 \langle \Psi | H_N - \Delta E | \Psi^\lambda \rangle}{\langle \Psi | \Psi \rangle}, \quad (9a)$$

$$\begin{aligned} \langle \Psi | H_N - \Delta E | \Psi^\lambda \rangle &= \langle 0 | e^{T^\dagger} (H_N - \Delta E) (U + T(1)) e^T | 0 \rangle \\ &= \langle 0 | (U^\dagger + T^\dagger(1)) e^{T^\dagger} (H_N - \Delta E) e^T | 0 \rangle. \end{aligned} \quad (9b)$$

For simplicity from this point we have omitted superscript (0) connected with unperturbed quantities. Operator

$$U = \sum u_{ia} a^\dagger i \quad (10)$$

follows from the CPHF theory [20], and $T(1)$ is the first-order change to the excitation operator $T(\lambda)$ expanded in powers of λ

$$T(\lambda) = T + \lambda T(1) + \frac{\lambda^2}{2} T(2) + \dots \quad (11)$$

Finally inserting $1 = e^T \sum |\phi_m\rangle \langle \phi_m| e^{-T}$ to (9b) yields

$$\begin{aligned} &\langle 0 | (U^\dagger + T^\dagger(1)) e^{T^\dagger} e^T \sum_m |\phi_m\rangle \langle \phi_m| e^{-T} (H_N - \Delta E) e^T | 0 \rangle \\ &= \langle 0 | (U^\dagger + T^\dagger(1)) e^{T^\dagger} e^T | 0 \rangle \langle 0 | e^{-T} (H_N - \Delta E) e^T | 0 \rangle \end{aligned} \quad (12a)$$

$$+ \sum_{m \neq 0} \langle 0 | (U^\dagger + T^\dagger(1)) e^{T^\dagger} e^T | \phi_m \rangle \langle \phi_m | (H_N e^T)_C | 0 \rangle. \quad (12b)$$

Now one immediately sees that the last term (12b) vanishes for those excited configurations $|\phi_m\rangle$ which are generated by the action of the actually chosen T on $|0\rangle$, since within the conventional CCM

$$\langle \phi_m | (H_N e^T)_C | 0 \rangle = 0 \quad (13)$$

are the defining equations to determine T_m . The energy dependent term (12a) would only vanish if one assumes the full CC method with all possible excitation operators included in T . For a truncated T operator the expectation value (8) is

no longer equal to the usual CC energy calculated from the asymmetric formula [21], i.e.,

$$\Delta E(\lambda) \neq \langle 0 | (H_N(\lambda) e^{T(\lambda)})_C | 0 \rangle. \quad (14)$$

Nevertheless, the difference between the latter two values is again due to contributions from those excited configurations that are not included in the CC method actually used [21]. The similar conclusion for non-Hellmann-Feynman terms can be drawn for the truncated CI [22]. Hence for $T = T_2$ the error due to the "non-Hellmann-Feynman" or "relaxation" correction [Eq. (12)] is of second order (in T), for CCSD [23] of third order, while for CCSDT [24] with $T = T_1 + T_2 + T_3$ only of fifth order in a generalized sense [25]. As the error of the energy is for CCSDT of the same order, it is quite appropriate to assume the validity of the Hellmann-Feynman theorem and to calculate one electron properties as expectation values. Let us stress that the difference between the conventional CCSDT energy and the expectation value actually defines its error. Therefore, within the limits of this error, starting our analysis from the expectation value was appropriate, too. Finally, if the difference between the full CCSDT and its less accurate variants CCSDT- n [26] is expected to be small, one can safely use the above conclusions. For alternative CC ansatz like UCC(n) [27] even the term with $T(1)$ in Eq. (12) disappear, since the method satisfies the generalized Hellmann-Feynman theorem [27,28].

Čížek has shown [4] that the expectation value of an arbitrary operator in CC theory is

$$\langle O \rangle = \langle \Psi | O | \Psi \rangle_C, \quad (15)$$

which is, however, infinite. Considering only terms, which contribute to lower order than is the actual error inherent to the method, this expansion can be truncated after a few terms. In [9] it was suggested to truncate the wave function in Eq. (15) after the second-order terms, since the wave function is anyway only accurate to this order. One can, of course, formulate Eq. (15) in terms of the density matrix

$$\rho_{pq} = \langle \Psi | p^\dagger q | \Psi \rangle_C, \quad (16)$$

which is independent of O , and, then, as usual, contract this density matrix with integrals of the operator O . Instead of truncating the wave function, one can insist on the accuracy of the density matrix and terminate the expansion of the latter after fourth-order terms [10], which is more precise. We denote in this paper the former approach as approach A and the latter as B. Let us recall that in approach A we have in Eq. (16)

$$e^T \approx 1 + T_1 + T_2 + T_3 + \frac{1}{2} T_2 T_2 \quad (17)$$

and this differs from B by a fourth order term ($\langle 0 | T_2^\dagger a^\dagger i T_1 T_2 | 0 \rangle_C + \text{h.c.}$).

The alternative "response" density approach avoids truncation and has been extensively applied to properties [29], but requires determination of the N operator as well as T .

Results and Discussion

As mentioned, we have selected rather well-known systems to test the approach described in the previous sections: HF, H₂O molecules, and the F⁻ anion. Electric multipoles were calculated at the CCSDT-1 level of theory as expectation values at various charges, and from the perturbed moments higher polarizabilities have then been evaluated. Since the charge perturbation method requires many repetitions of time-consuming calculations, we have decided to use relatively modest basis sets still expected to work well for such calculations. Such basis sets, in particular designed for electric properties calculations (POL bases) have been recently proposed by Sadlej [11]. The POL basis which consists of the contracted set [5s3p2d] for O and F and [3s2p] for H has been used in our calculations. We have partially lifted the contraction of the d shell on O and F and p shell on H to obtain, finally, a [5s3p3d] set for O, F, and [3s3p] for the hydrogen atom. The small differences between our SCF results and the results of the recent study by Sekino and Bartlett (SB) [29] reflects the fact that the latter study employed the original POL basis: [5s3p2d/3s2p]. Our calculations for HF have been performed for the bond length of 1.7330 a.u. and at the experimental geometry for the H₂O molecule as in [29]. The charges and distances have been selected to produce the field strength of near 0.005 a.u. and gradients 0.001 to 0.002 a.u.. The *T*-amplitudes have been converged to at least 10⁻⁷, which means that the accuracy of density matrices was the same or higher.

HF: The results for the dipole, quadrupole, and octopole moments are given in Table I. Numerical Hartree-Fock (NHF) results for the dipole and quadrupole moments [30,31] are 0.756 and 1.733 a.u., respectively, and are in very good agreement with our SCF values. Other comparisons can be made with Bishop and Maroulis (BM) [16], who systematically constructed and employed eight basis sets up to a set of 96 contracted Gaussian functions denoted as B8 [9s6p5d1f/5s4p2d]. Their B8 SCF dipole, quadrupole, and octopole moments are: 0.757133, 1.74071, and 2.62645 a.u., respectively. The overall agreement of these near HF limit values with our results is very good, too, and confirms the reliability of the basis set used for the pertinent properties (Table II). At the correlated CCSDT-1 level the results agree very well with experimental values (where available). The octopole moment has not been determined experimentally so we compare our results with the CISD calculations performed with a [6s5p3d/4s3p] basis: 2.4466 a.u. [32].

TABLE I. Electric moments of the HF molecule (in a.u.).

Moment	SCF	CCSDT-1 (A)	CCSDT-1 (B)	Experiment
μ	0.757	0.700	0.700	0.707 ^a
Θ	1.754	1.727	1.727	1.72 ± 0.0 ^b
Ω	2.593	2.461	2.460	

^a Experimental estimate taken from [37].

^b Experimental estimate taken from [32].

TABLE II. Electric tensors for the HF molecule (in a.u.)

Tensor	SCF	CCSDT-1	CCSDT-1	Other SCF	Exp. or Correlated
α_{zz}	5.72	6.40	6.40	5.75 ^a	6.428 ^b , 6.438 ^f
α_{xx}	4.49	5.33	5.32	4.481 ^c	5.253 ^b , 5.340 ^f
$\bar{\alpha}$	4.90	5.69	5.68		
$\Delta\alpha$	1.23	1.07	1.08		
β_{zzz}	-8.94	-10.26	-10.36	-8.3 ^a	-9.838 ^b , -9.62 ^f
β_{zzx}	0.005	-0.54	-0.64	-0.4 ^c	-0.802 ^b , -1.27 ^f
β	-5.36	-6.80	-6.94		-7.30 ^f
A_{zzz}	3.98	4.56	4.56	3.986 ^c	4.508 ^d
A_{xxz}	0.76	1.07	1.07	0.928 ^c	0.688 ^d
C_{zzz}	6.96	8.16	8.15	7.36 ^c	8.63 ^e
C_{xxz}	3.15	3.71	3.71	4.34 ^c	5.15 ^e
C_{xxx}	3.87	4.70	4.70	5.43 ^c	6.53 ^e
B_{zzz}	-52.6	-64.5	-64.5	-56 ^c	
B_{zzx}	-28.2	-40.6	-40.5	-35 ^c	
B_{xxz}	26.3	41.9	41.6	26 ^c	
B_{xxx}	-39.6	-62.4	-62.1	-45 ^c	
E_{zzz}	6.84	13.30	13.33	6.68 ^c	
E_{xxx}	-0.49	-0.11	-0.19	-0.76 ^c	
γ_{zzzz}	279	411	413	294 ^c	400 ^b , 390 ^f
γ_{xxxx}	299	599	597	340 ^c	540 ^b , 650 ^f
γ_{xxzz}	120	177	178	117 ^c	150 ^b , 180 ^f

^a NHF [30].^b CCSD+T (4) [33].^c SCF [16].^d MCSCF [36].^e MBPT (4) [37].^f CCSD(T) [29].

The dipole polarizability α has been calculated many times at different levels of sophistication. The BM paper [16], the review [3], and a recent study [29] can serve as sources of references. Our SCF result for the parallel component agrees very well with the NHF value [31] while the perpendicular component is very close to the B8 value of BM: 4.481 a.u. The CCSDT-1 results compare very well to the values obtained by Sekino and Bartlett [33] with the CCSD+T(4) method and the extended basis set [5s3p4d2f/5s3p]. Electron correlation contributes 11% to the total value of the parallel component and 8% for the perpendicular case. The average value of α is close to the experimental value of 5.52 a.u. [34] or 5.60 a.u. [35]. The correlated anisotropy $\Delta\alpha$ of 1.07 or 1.08 a.u. does not agree that well with experiment 1.32 a.u. [34] and like recent results by SB [29]: 1.10 a.u. is slightly different from some previous correlated calculations, e.g., the CEPA value of 1.27 a.u. obtained, however, with a larger basis set [35]. The error in the anisotropy of α indicates a delicate imbalance in treating z and x components by the POL basis set. The diagonal hyperpolarizability β_{zzz} is below the NHF value of -8.3 a.u. and recent CCSD(T) results [29] obtained with the original and augmented POL basis set: -8.14 to 8.40 a.u., but very close to -9.1 a.u. B8 basis results [16]. The correlated results are in good

agreement with previous CC calculations -9.838 (CCSD + T(4)) [33] and -9.62 a.u. for the more accurate CCSD(T) method [29] with an extended POL basis set. The zxx component is more difficult to be determined. SCF calculations yielded 0.005 a.u. while SB reported the range from -0.02 to -0.28 a.u. Among eight results of BM, the range is very broad from -1.4 to $+0.2$ a.u.

The basis sets effects are manifested even more at the CC level. Our CCSDT-1 values agree well with the older CCSD + T(4) results of -0.802 a.u., while the most recent study [29] reported -1.27 a.u., i.e., almost twice our value. One should notice the difference in handling triple excitations in the CCSD(T) model (noniteratively) and in CCSDT-1, fully iterative but in an approximate way. These differences and usage of slightly different basis sets lead to differences in the final value of this component reported in the present study and in [29]. The values of $\bar{\beta}$ defined for a linear molecule as

$$\bar{\beta} = \frac{3}{5}(\beta_{zzz} + 2\beta_{zxx}) \quad (18)$$

is fortuitously close to the SCF value of SB [29] obtained with an extended POL basis and higher than any of the eight values reported in [16]. The correlated $\bar{\beta}$ value is close to CCSD(T): -7.30 [29], again obtained with a larger basis set. The dipole-quadrupole polarizability A , quadrupole polarizability C , and dipole-octopole polarizability tensor E are all second-order electric tensors. The knowledge of these tensors can become important in considering ion-molecule interactions where the electric field created by an ion is not homogeneous. The dipole-quadrupole tensor A was determined from the perturbed quadrupole moments. The z,zz component, 3.98 a.u., is very close to the best BM value of 3.986 a.u. While the CCSDT-1 values can be compared to the MCSCF result [36]: 4.508 a.u. The permanent Θ_{xz} moment is zero so the $A_{x,zx}$ must be obtained from a rather weak induced quadrupole moment. Clearly, higher angular momentum and diffuse functions are needed to describe situations like this. Therefore, there is almost a 20% discrepancy between our SCF value and the B8 result from [16]. The correlation contribution amounts to $\sim 30\%$ for this component, and its value is almost two times larger than MCSCF value [36]. For the quadrupole polarizability C , the zz,zz component is in good agreement with the BM value. Electron correlation adds about 15% raising this value to 8.15 a.u., in reasonably good agreement with the MBPT(4) result of Diercksen et al. [37]: 8.63 a.u.. The perpendicular component differs more from the BM value while CCSDT-1 disagree with the MBPT(4) value.

For the "mixed" xz,xz component the pertinent quadrupole moment is zero; therefore again our results disagree with the B8 BM value, but is surprisingly close to the rather extended B7 basis set result of 3.29 a.u. (80 contracted GTOS). The f functions are necessary to describe properly the xz components. A similar situation occurs for the dipole-octopole polarizability tensor E . The diagonal $E_{z,zzz}$ agrees well with the SCF results of BM while the difference for the x,xxx component is larger. The situation can be attributed to the POL basis deficiency. Electron correlation contributes about 50% to the total value of the $E_{z,zzz}$ tensor. CCSDT-1 results for $E_{x,xxx}$ show also a significant role of electron correlation, but the basis set lim-

itations make our values rather approximate. The dipole-dipole-quadrupole hyperpolarizability B is a third-order property that can be formally defined as

$$B_{\alpha\beta,\gamma\delta} = \left(\frac{\partial^3 E}{\partial F_\alpha \partial F_\beta \partial F_{\gamma\delta}} \right)_{F_\alpha, F_\beta, F_{\gamma\delta}=0} \quad (19)$$

Our SCF results are in general agreement with the BM SCF values. Electron correlation contributes: 18%, 30%, 37%, and 36% for zz, zz , xz, zz , xx, zz , and xx, xx components, respectively. Unlike the previous four tensors, γ has attracted a lot of attention. A recent study [29] contains a discussion of the relation of γ to frequency-dependent experiments. The SCF result for the $zzzz$ component is close to the B8 basis BM value. The $xxxx$ component is affected more by the quality of the basis set and the difference between our value and the BM and SB (with expanded POL basis) is 40 and 50 a.u., respectively. The correlated results for $zzzz$ and $xxzz$ are close to the CCSD + T(4) results of Sekino and Bartlett [33] obtained with a larger basis set. The largest discrepancy occurs for the $xxxx$ component; 597 versus 650 a.u. by SB [29] and can be attributed to the basis set deficiency in the x direction. Despite the modest basis set employed in our calculations the CCSDT-1 density matrix results based on perturbed correlated moments compare very well with all the standard finite field highly correlated calculations available.

H₂O: Complete SCF calculations of the electric polarizability tensors were performed by Bishop and Pipin (BP) [17]. We have used the POL basis set with uncontracted d functions on O and p on the H atom; the contracted set [5s3p3d/3s3d] of 56 functions. The C_2 axis coincides with the z axis and the molecule lies in the xz plane. The multipole moments are presented in Table III and compared to experimental values. Electron correlation calculated by the CCSDT-1 method changes the value of μ by about 9% in perfect agreement with experiment, while the correlation contribution to the quadrupole moment is small except for the zz component where it amounts to -19%. Second- and third-order electric properties are displayed in Table IV.

The values of the dipole polarizability tensor α agree very well with the SCF results of Werner and Meyer [35] who employed an extended, uncontracted (11s6p3d/5s2p) carefully optimized basis set: 9.04, 7.93, and 8.47 a.u. for the xx , yy , and zz . Electron correlation improves the results: The CCSDT-1 average polarizability $\bar{\alpha}$ perfectly matches experimental values 9.82 [35] and 9.81 [38]. As for the HF

TABLE III. Electric moments of the H₂O molecule (in a.u.).

Moment	SCF	CCSDT-1	CCSDT-1	Experiment
μ	0.793	0.725	0.725	0.7268 ^a
Θ_{xx}	1.921	1.919	1.918	1.96 ± 0.02 ^b
Θ_{yy}	-1.823	-1.837	-1.835	-1.86 ± 0.02 ^b
Θ_{zz}	-0.099	-0.083	-0.083	-0.10 ± 0.02 ^b

^a Taken from [46].

^b Taken from [47].

TABLE IV. Electric tensors for the H₂O molecule.

Tensor	SCF	CCSDT-1 (A)	CCSDT-1 (B)	Other SCF	Exp. or correlated
α_{xx}	9.10	10.05	10.06	9.24 ^a	9.81 ^b , 9.87 ^c , 9.64 ^e
α_{yy}	7.91	9.71	9.70	7.91 ^a	9.59 ^b , 9.30 ^c , 10.02 ^e
α_{zz}	8.42	9.71	9.71	8.55 ^a	9.64 ^b , 9.54 ^c , 9.73 ^e
$\bar{\alpha}$	8.48	9.82	9.82	8.57	9.68 ^b , 9.79 ^e
$\Delta\alpha$	1.03	0.34	0.35	1.15 ^a	0.34 ^e
β_{xxx}	-9.45	-11.2	-11.3	-7.87 ^a	-10.0 ^c , -6.2 ^e
β_{xyy}	-0.39	-4.13	-4.41	1.41 ^a	-3.7 ^c , -10.2 ^e
β_{zzz}	-6.03	-11.2	-11.4	-4.68 ^a	-9.2 ^c , -13.7 ^e
$\bar{\beta}$	-9.52	-15.9	-16.3	-6.68 ^a	-18.0 ^e
$A_{x,xx}$	3.21	3.55	3.55	6.27 ^a	6.742 ^d
$A_{y,yy}$	0.10	0.44	0.44	1.40 ^a	1.786 ^d
$A_{z,zz}$	2.30	2.31	2.30	1.62 ^a	2.54 ^f
$A_{z,zz}$	2.29	2.28	2.29	1.68 ^a	2.194 ^d , 2.44 ^f
$C_{xx,xx}$	11.6	13.4	13.4	11.78 ^a	11.65 ^f
$C_{yy,yy}$	11.5	14.0	14.0	12.02 ^a	12.58 ^f
$C_{zz,zz}$	9.10	10.6	10.6	10.10 ^a	8.76 ^f
$C_{xy,xy}$	5.45	6.91	6.90	8.48 ^a	8.48 ^f
$C_{xz,xz}$	7.07	8.28	8.29	11.06 ^a	11.33 ^f
$C_{yz,yz}$	4.47	6.02	5.96	4.72 ^a	4.41 ^f
$B_{xx,xx}$	-81.5	-94.9	-94.5	-76.61 ^a	
$B_{xx,zz}$	36.9	50.2	49.5	39.14 ^a	
$B_{yy,xx}$	90.3	144.7	144.3	234.06 ^a	
$B_{yy,zz}$	66.7	109.8	109.1	67.99 ^a	
$B_{zz,zz}$	54.9	82.8	82.3	55.78 ^a	
$B_{zz,zz}$	-94.8	-133	-132	-90.91 ^a	
$B_{xy,xy}$	-57.1	-91.6	-91.1	-83.61 ^a	
$B_{xz,xz}$	-65.0	-88.4	-88.2	-87.11 ^a	
$B_{yz,yz}$	-54.8	-86.5	-86.0	-80.54 ^a	

^a SCF [17].^b Taken from [35].^c MBPT-SDQ (4) [45].^d CISD [48].^e CCSD(T) [29].^f MCSCF [17].

molecule the difference between CCSDT-1 results correct through the second-order in the wave function and correct through the full fourth-order in the corresponding density matrix are negligible. The recent CCSD(T) calculations employing an augmented POL basis yielded 9.79 a.u. for the average value of α [29]. The anisotropy of α defined as:

$$\Delta\alpha = \frac{1}{\sqrt{2}} [(\alpha_{xx} - \alpha_{yy})^2 + (\alpha_{yy} - \alpha_{zz})^2 + (\alpha_{zz} - \alpha_{xx})^2]^{1/2} \quad (20)$$

and reflecting the balanced description of all components is very sensitive to basis set effects. Our correlated $\Delta\alpha$ agree with the SB [29] value of 0.34 a.u. and MBPT

(4) 0.32 a.u. [39] and are off the experimental estimate by a factor of 2. Lazzeretti and Zanasi [40] reported a broad range of β_{zyy} tensor values from -0.299 to 1.098 a.u. and Maroulis [39] constructed five optimized basis sets and obtained values from -1.46 to -1.31 a.u. so that it may be concluded that our SCF value is most probably off the HF limit by a factor of about 3. Our SCF value for the xxz component fits well into the range of previously obtained results: -7.87 [17], -9.5 to -10.6 [40], and -9.53 to -9.35 a.u. [39]. The zzz component is also consistent with previous results, and, again, the range of results is rather broad: -3.574 a.u. [38], -4.68 [17], -8.11 to -7.44 a.u. [39].

To conclude the discussion of the SCF results, it may be interesting to compare Derivative HF (DHF [3]) calculations with the contracted ELP (electric properties) basis set [3,36]. The β components read: -0.5445 , -10.029 , and -5.4715 a.u. for the zyy , zxx , and zzz , respectively, all in a good agreement with our results. $\bar{\beta}$ is not as sensitive to the choice of basis set as some of its components. Our $\bar{\beta}$ equals -9.52 a.u. and agrees very well with DHF ELP calculations, -9.63 a.u., and Maroulis [39] reported -11.15 to -10.86 a.u. and BP obtained -6.68 a.u.. The CCSDT-1 calculations give results fairly close to the previous MBPT-SDQ(4) [45] with [6s5p4d/4s2p]: -13.7 a.u. [12] and CCSDT + T(4) [33] values. The recent accurate CCSD(T) calculations [29] were performed with the POL basis augmented with lone-pair functions. Our CCSDT-1 $\bar{\beta}$ agree well with -18.0 a.u. of SB [29] and lies within rather broad experimental limits quoted in [29], -22 ± 6 a.u. The difference between the CCSDT-1 results is not negligible reflecting the importance of the fourth order component $\langle 0 | T^\dagger T_2^\dagger a^\dagger i T_2 | 0 \rangle$ for the hyperpolarizability β . The A tensor was previously obtained using the DHF method with the ELP basis [3], and BP, who also performed limited MCSCF calculations. The value of our x,zx component is in fair agreement with the DHF result (4.0176 a.u.), but almost half of the corresponding value reported by BP (6.27 a.u.). This difference can be attributed to basis set limitations. The POL basis set is simply not flexible enough to describe properly the very small induced component of the quadrupole Θ_{xz} , which is zero by symmetry for the unperturbed H_2O molecule.

The same effect manifests itself even more for the y,yz component for which both the SCF and the CCSDT-1 results are by an order of magnitude smaller than the SCF results of BP. The z,xx component is on the contrary larger than the values of BP. Our SCF value for the z,zz component lies between the BP (1.68) and the DHF result (2.7406 a.u.). The electron contribution as given by the CCSDT-1 computations is negligible for the z,xx and z,zz components, and it is a moderate $\sim 10\%$ for the $A_{x,zx}$. For the small $A_{y,yz}$ component correlation changes the value by a factor of 4. One can notice that, although our z,xx and z,zz results are different from the corresponding results of BP, we observe the same approximate equality of these two components. This internal consistency shows that the discrepancy for the y,yz as well as other smaller differences are indeed due to basis set limitations. The few existing SCF results suggest that only the z,xx and z,zz components are probably fairly well predicted. Electron correlation seems to be less important than the use of good quality basis sets. There are six independent components of the second-order quadrupole polarizability tensor C . For all "pure" components, our SCF results are in very good agreement with the results of BP but DHF values

are systematically higher: 12.8394, 13.5368, and 11.766 a.u. for xx,yy and zz,zz , respectively. The correlation amounts to $\sim 13\%$, 18% , and 14% for the xx,xx , yy,yy , and zz,zz components. The "mixed" components are all smaller than the corresponding results of BP. The inflexibility of the basis set can be blamed for these differences. The inclusion of electron correlation improves our results, but they are still probably too small. The DHF calculations yield 4.010 a.u. for the yz,yz 4.776 a.u. for the $C_{xy,xy}$ and 7.014 a.u. for the xz,xz component. All results are smaller than our SCF.

To the best of the author's knowledge, the dipole-dipole-quadrupole hyperpolarizability B tensor has not been calculated at any correlated level. Only BP SCF results can be compared to our results. Dykstra uses a different sign convention in his calculations, thus obscuring the comparison. There are nine independent components of the B tensor (Dykstra reports 12 values). Our SCF results are consistent with the Bishop and Pipin results. The xx,xx , zz,zz , xx,zz , zz,xx , and yy,zz components agree very well with the Bishop and Pipin values. Again, the negative "mixed" components are more difficult to determine. Our SCF values are higher than Bishop and Pipin by approximately 30%. The correlation always lowers the results beyond the Bishop and Pipin SCF results. In conclusion we may say that five "pure" components are probably accurately predicted and that the three "mixed" components of the B tensor are fairly well described. The yy,xx component is an exception. It depends critically on the basis set quality and our SCF results amount to only $\sim 40\%$ of the previously reported value. The electron contribution is also substantial so that making any predictions about this component is not reliable at this point.

F⁻: Despite the apparent simplicity of the closed-shell 10-electron system, electric properties of this anion are extremely difficult to calculate correctly. The reason is the diffuse electronic charge distribution requiring extended basis sets and a large portion of the electron correlation energy. For any spherical system in its ground state all permanent multipoles are zero and calculations of the nonzero even polarizabilities α , γ , C , and B must rely on a proper description of small induced moments. Requirements for a basis set led us to the ELP basis set of Dykstra [3,41] which consists of the contracted [6s5p3d] set, denoted as basis II. I is the POL basis. We have also employed a version of the ELP augmented by one f function with the exponent taken from [42], basis III. Table V summarizes our results and shows some literature values. The SCF calculations of Maroulis and Bishop [42] were performed with two extended, optimized sets of 67 contracted or 87 [17s10p5d1f] uncontracted functions. CISD calculations of Diercksen and Sadlej [43] used a contracted [12s8p5d] set derived from a set used by Werner and Meyer [35] in their fluoride atom calculations. All these bases are much larger, and what is more important, are individually optimized for the fluoride anion. Nevertheless, as can be seen from Table V our SCF results for α and γ compare well with the contracted set results of [42].

However, tensors C and B proved rather sensitive to the quality of basis set, and our SCF results differ from the uncontracted Maroulis and Bishop values by 40% and 15%, respectively. Electron correlation is very important for all tensors. For

TABLE V. Electric polarizabilities of the fluoride anion (a.u.).

Tensor	Basis	SCF	CCSDT-1 (A)	CCSDT-1 (B)	Other SCF	Exp. or correlated
α	I	10.21	16.27	16.26	10.66 ^a	18.99 ^c
α	II	10.39	18.82	18.82		
α	III	10.40	18.84	18.84		
C	I	10.29	15.09	15.04	17.35 ^b	
C	II	12.91	32.23	32.05	23.46 ^b	
C	III	16.82	36.22	36.05		
B	I	-275.3	-643.8	-638.2	-471 ^b	
B	II	-422.5	-2,157	-2,140	-552 ^b	
B	III	-441.2	-2,124	-2,108		
γ	I	2,638	9,063	9,110		23,100 ^d
γ	II	10,030	103,000	102,700	10,900 ^b	79,500 ^e
γ	III	10,120	99,700	99,450	12,900 ^b	

^a NHF [49].^b SCF [42].^c CCSD + T (4) [50].^d CISD [43].^e MBPT (4) [44].

the augmented ELP basis set (basis III) it amounts to $\sim 45\%$ for the dipole polarizability, 53% for the quadrupole polarizability, and almost 80% for the dipole-dipole-quadrupole hyperpolarizability B . The second dipole hyperpolarizability γ is known to be difficult to determine by numerical differentiation. The charge perturbation method allows using the perturbed dipole moment and thus may be numerically more stable. Basis ELP and III yield results which are reasonably close to the estimated HF limit of 13,000 a.u. The correlation contribution is enormous even by anionic standards. The CCSDT-1 values are about nine times larger than the corresponding SCF values. The MBPT(4) results with a larger basis set [44] yielded 79,500 a.u., in fair agreement with our results.

Conclusions

We have combined the coupled cluster method (the CCSDT-1 model) to calculate electric multipole moments as expectation values, with the charge perturbation version of the finite field method to calculate electric response properties. This approach has been applied to determine the electric properties of the small systems: HF, H₂O, and F⁻. The approach has been shown to provide values of the higher-order static polarizabilities associated with the higher multipole moments: the quadrupole polarizability C , dipole-quadrupole polarizability A , dipole-octopole polarizability E , and hyperpolarizabilities β , B , γ in an effective way. The relatively modest basis sets, not flexible enough to yield accurate results for hyperpolarizabilities, has nevertheless given accurate results for the multipoles and the dipole polarizability α , while providing good estimates for other tensors. The fluoride anion requires an extended basis set to obtain accurate electric properties, especially

since our results point to very significant electron correlation effects in the hyperpolarizabilities B and γ .

Acknowledgments

This work has been partially supported by the U.S. Air Force Office of Scientific Research under grant No. F-49620-93-I-0118 and by grant No. 2-501/93 of the Slovak Grant Agency for Science.

Bibliography

- [1] A. D. Buckingham, *Adv. Chem. Phys.* **12**, 107 (1967).
- [2] R. D. Amos, *Adv. Chem. Phys.* **67**, 99 (1987).
- [3] C. F. Dykstra, S. Y. Liu, and D. J. Malik, *Adv. Chem. Phys.* **75**, 37 (1989).
- [4] J. Čížek, *Adv. Chem. Phys.* **14**, 35 (1969); *J. Chem. Phys.* **45**, 4256 (1966); J. Paldus, J. Čížek, and I. Shavitt, *Phys. Rev. A* **5**, 50 (1972).
- [5] R. J. Bartlett, *Ann. Rev. Phys. Chem.* **32**, 359 (1981); *J. Phys. Chem.* **93**, 1697 (1989).
- [6] M. Urban, I. Černušák, V. Kellö, J. Noga, in *Methods in Computational Chemistry*, S. Wilson, Ed. (Plenum, New York, 1987), Vol. I, p. 117.
- [7] V. Kvasnička, V. Laurinc, and S. Biskupič, *Phys. Rep.* **90**, 159 (1982).
- [8] Y. S. Lee, S. A. Kucharski, and R. J. Bartlett, *J. Chem. Phys.* **81**, 281 (1984).
- [9] J. Noga and M. Urban, *Theor. Chim. Acta* **73**, 291 (1988).
- [10] M. Urban, G. H. F. Diercksen, A. J. Sadlej, and J. Noga, *Theor. Chim. Acta* **77**, 29 (1990).
- [11] A. J. Sadlej, *Coll. Czech. Chem. Comm.* **53**, 1995 (1988).
- [12] R. J. Bartlett and G. D. Purvis III, *Phys. Rev. A* **20**, 1313 (1979).
- [13] A. D. McLean and M. Yoshimine, *J. Chem. Phys.* **46**, 3682 (1967).
- [14] D. G. Truhlar, D. A. Dixon, and R. A. Eades, *J. Phys. B* **12**, 1913 (1979), D. A. Dixon, R. A. Eades, and D. G. Truhlar, *ibid.* **B12**, 2741 (1979).
- [15] G. Maroulis and D. M. Bishop, *Chem. Phys. Lett.* **114**, 182 (1985).
- [16] D. M. Bishop and G. Maroulis, *J. Chem. Phys.* **82**, 2380 (1985).
- [17] D. M. Bishop and J. Pipin, *Theor. Chim. Acta* **71**, 247 (1987).
- [18] A. Thakkar, *Phys. Rev. A* **40**, 1130 (1989); G. Maroulis and A. Thakkar, *J. Chem. Phys.* **90**, 366 (1989); *J. Chem. Phys.* **92**, 812 (1990).
- [19] K. Raghavachari, *J. Chem. Phys.* **82**, 4142 (1985).
- [20] J. Gerratt and I. M. Mills, *J. Chem. Phys.* **49**, 1719 (1968).
- [21] H. J. Monkhorst, *Int. J. Quantum Chem. Quantum Chem. Symp.* **S11**, 421 (1977).
- [22] P.-O. Nerbrant, B. Roos, and A. J. Sadlej, *Int. J. Quant. Chem.* **15**, 135 (1979).
- [23] G. D. Purvis III and R. J. Bartlett, *J. Chem. Phys.* **76**, 1910 (1982).
- [24] J. Noga and R. J. Bartlett, *J. Chem. Phys.* **86**, 7041 (1987); **89**, 3041 (1989) (E).
- [25] R. J. Bartlett, S. A. Kucharski, J. Noga, J. D. Watts, G. W. Trucks, *Lecture Notes in Chemistry* **52**, U. Kaldor, Ed. (Springer-Verlag, New York, 1988), p. 125.
- [26] M. Urban, J. Noga, S. J. Cole, and R. J. Bartlett, *J. Chem. Phys.* **83**, 4041 (1985); **85**, 5383 (1986) (E); J. Noga, R. J. Bartlett, and M. Urban, *Chem. Phys. Lett.* **134**, 126 (1987).
- [27] R. J. Bartlett, S. A. Kucharski, and J. Noga, *Chem. Phys. Lett.* **155**, 133 (1989).
- [28] R. J. Bartlett and J. Noga, *Chem. Phys. Lett.* **150**, 29 (1988).
- [29] H. Sekino and R. J. Bartlett, *J. Chem. Phys.* **98**, 3022 (1993).
- [30] P. Å. Christiansen and E. A. McCullough, *Chem. Phys. Lett.* **55**, 439 (1978).
- [31] P. Å. Christiansen and E. A. McCullough, *Chem. Phys. Lett.* **53**, 570 (1979).
- [32] R. D. Amos, *Chem. Phys. Lett.* **88**, 89 (1982).
- [33] H. Sekino and R. J. Bartlett, *J. Chem. Phys.* **84**, 2726 (1986).
- [34] G. H. F. Diercksen and A. J. Sadlej, *J. Chem. Phys.* **75**, 1253 (1981).
- [35] H.-J. Werner and W. Meyer, *Mol. Phys.* **31**, 855 (1976).

- [36] R. D. Amos, *Mol. Phys.* **35**, 1765 (1978).
- [37] G. H. F. Diercksen, V. Kellö, and A. J. Sadlej, *Mol. Phys.* **49**, 711 (1983).
- [38] M. A. Spackman, *J. Phys. Chem.* **93**, 7594 (1989).
- [39] G. Maroulis, *J. Chem. Phys.* **94**, 1182 (1991).
- [40] P. Lazzeretti and R. Zanasi, *J. Chem. Phys.* **74**, 5216 (1981).
- [41] S.-Y. Liu and C. E. Dykstra, *J. Phys. Chem.* **91**, 1743 (1987).
- [42] G. Maroulis and D. M. Bishop, *Mol. Phys.* **57**, 359 (1986).
- [43] G. H. F. Diercksen and A. J. Sadlej, *J. Chem. Phys.* **76**, 4239 (1982).
- [44] G. H. F. Diercksen and A. J. Sadlej, *Chem. Phys.* **131**, 215 (1989).
- [45] G. D. Purvis III and R. J. Bartlett, *Phys. Rev. A* **23**, 1594 (1981).
- [46] S. A. Clough, Y. Beers, G. P. Klein, and L. S. Rothman, *J. Chem. Phys.* **59**, 2254 (1973).
- [47] J. Verhoeven and A. J. Dymanus, *J. Chem. Phys.* **52**, 3222 (1970).
- [48] I. G. John, G. B. Bacskay, and N. S. Hush, *Chem. Phys.* **51**, 49 (1978).
- [49] P. C. Schmidt, A. Weiss, and T. P. Das, *Phys. Rev. A* **19**, 5525 (1979).
- [50] S. A. Kucharski, Y. S. Lee, G. D. Purvis III, and R. J. Bartlett, *Phys. Rev. A* **29**, 1619 (1984).

Received May 13, 1994

Nonlinear Optical Effects in Molecules and Polymers: Issues and Opportunities

PARAS N. PRASAD and SHASHI P. KARNA

*Photonics Research Laboratory, Department of Chemistry,
State University of New York, Buffalo, New York 14214*

Abstract

The field of nonlinear optics in molecules and polymers offers challenging opportunities for theorists on both molecular modeling of new structures with enhanced microscopic response and manifestations of bulk effect in nonlinearity. This article presents an experimental point of view in assessing the current status of various theoretical approaches. Experimental results are presented for two model compounds together with predictions by various theoretical models to discuss issues and future opportunities. Three different types of nonlinear optical processes are discussed: (i) second order, (ii) third order, and (iii) photorefractivity. © 1994 John Wiley & Sons, Inc.

Introduction

Nonlinear optical (NLO) effects form the backbone of photonics, a rapidly growing technology that utilizes photons to transmit, process, and store information [1]. The largest immediate application of photonics is in the telecommunication industry for fiber-optic communication. Here, NLO effects will be used to perform the functions of optical switching, optical data storage and processing of information by wavelength multiplexing, and modulating the phase as well as frequencies of the optical signal. The real challenge facing the industrial application of photonic technology is the search for appropriate materials, which, in addition to being highly NLO active, must be easily processible, mechanically and thermally stable, and most importantly, economically viable to compete with the commonly used electronic materials. One such class of materials which fulfill, to a large extent, these requirements is formed by organic molecules and polymers and constitute the topic of this article.

In the past several years, extensive experimental as well as theoretical investigations have been performed at the Photonics Research Laboratory [2–12] and by other groups* to establish structure-NLO property relationship and to identify technologically important organic and polymeric materials. Such investigations have tremendously improved our understanding of the mechanism and origin of optical

* A recent issue (February 1994) of the Chem. Rev. contains several excellent reviews of the experimental and theoretical investigations of NLO properties of organic molecules and polymers.

nonlinearity in organics and helped identify crucial structural factors to control and optimize material NLO response. However, there still remain a number of outstanding issues, particularly of correlation between experiment and theory and that among various theoretical methods, understanding and establishing a definite relationship between the microscopic (molecular) and the macroscopic (bulk) NLO response, and finally applying the available knowledge of structure-property relationship to model new materials that invite further investigation. In order to highlight some of these issues, we report here the results of the experimental characterization and quantum chemical calculations performed in our laboratory on the second- and third-order NLO properties of two potentially important organic molecules. We also briefly describe the structural requirements and our investigation of organic photorefractive materials. The photorefractivity in molecular system is a new field and offers challenging opportunities as the effect is produced by the combined action of both electrical and nonlinear optical properties of a material.

In what follows, a brief account of the underlying theory of NLO processes in molecular systems is presented. The various experimental and theoretical approaches for the study of nonlinear optical response of molecules are then summarized, and the results of our experimental and theoretical studies of second- and third-order NLO properties of 2-nitro-1-(2-thienyl)ethene (NTE) and 4-nitro-1-(2-thienyl)-1,3-butadiene (NTB) (Fig. 1) are presented with a view to compare different theoretical techniques. An attempt is made to identify the issues and opportunities for theoretical modeling of second- and third-order nonlinearities. The final section discusses the photorefractive effect in polymeric composite systems, again identifying some of the relevant issues and opportunities in this field.

Theory of the NLO Processes in Molecular Systems

The NLO effects are best described as a manifestation of the response of materials electron cloud to an external electric field, $E(r,t)$. This electric field, $E(r,t)$, can be taken in a general sense so that it can be a low-frequency ($h\nu \rightarrow 0$) field, such as that of a conventional dc-electric field, or a very high-frequency oscillating field derived from a short laser pulse. The material response to the external electric field can be described in terms of a generalized polarization $P(E)$, which is proportional to the strength of the electric field if the disturbance caused by it in the material electronic environment is small and can be written as

$$P(E) = \chi \cdot E(r,t) \quad (1)$$

Here χ is the linear susceptibility of the system. If, however, the materials electronic environment experiences appreciable changes, the linear dependence of $P(E)$ on $E(r,t)$ [Eq. (1)] is no longer valid. In such cases, assuming that the force on an N -particle system exerted by the external electric field is still smaller than the inter-particle forces, the generalized polarization, $P(E)$, can be expressed as a power series of $E(r,t)$ as,

$$P(E) = \chi^{(1)} \cdot E(r,t) + \chi^{(2)} : E(r,t)E(r,t) + \chi^{(3)} : E(r,t)E(r,t)E(r,t) + \dots \quad (2)$$

where now, $P(E)$ does not only depend on $E(r,t)$ but also on its higher powers. The quantities $\chi^{(n)}$ in Eq. (2) represent the n th order susceptibility and are tensor quantities of rank $(n + 1)$. It is the nonlinear susceptibility terms $\chi^{(2)}$, $\chi^{(3)}$, ... which constitute the topic of interest in this article. It is trivial to show that for systems possessing a center of inversion, the even order susceptibility tensors ($\chi^{(2)}$, $\chi^{(4)}$, etc.) vanish and though the $\chi^{(n)}$ has 3^n elements, not all of them are nonzero and independent, i.e., in practice, only a few elements need to be evaluated independently to get the pertinent information.

A similar expression as Eq. (2) can be used to describe the polarization of an atom or a molecule, written as,

$$p(E) = \alpha \cdot E(r,t) + \beta : E(r,t)E(r,t) + \gamma \vdots E(r,t)E(r,t)E(r,t) + \dots \quad (3)$$

where α , β , γ , ... are now the first-order, second-order, third-order, etc. polarizabilities and are tensor quantities of ranks 2, 3, 4, ..., respectively. The higher-order polarizabilities are also called hyperpolarizabilities, for example, β is known as the first-hyperpolarizability, γ is known as the second-hyperpolarizability, and so on. Of course, for atoms and centrosymmetric molecules, the even-order polarizabilities (for example, β) vanish.

If the physical state of a material is such that the interparticle interaction is insignificant, as is the case, for example, for gases under extremely low pressure, the macroscopic susceptibilities ($\chi^{(n)}$) and the microscopic polarizabilities (α , β , γ) are equal. However, in other phases, e.g., solids or liquids, where the electronic environment is substantially different from that of the isolated systems (atoms/molecules), there is no comfortable way to relate the microscopic and macroscopic NLO properties. An intermediate case is those of the "molecular materials," which include most organic compounds and where, due to weak intermolecular interaction, the bulk properties can be considered as the geometrical superposition of the corresponding microscopic properties. This very property of the organic materials constitutes the motivation for the experimental as well as theoretical investigation of their molecular NLO property and gives hope that by understanding and modifying the microscopic nonlinearity, it would be possible to ultimately control and tailor the macroscopic NLO behavior as required for a particular technological application.

Let N represent the number per unit volume of an organic molecule in a dilute solution or a molecular crystal, then its bulk susceptibilities (assuming an unoriented system) can be approximated as:

$$\chi^{(1)} = f^{(1)}N\alpha \quad (3a)$$

$$\chi^{(2)} = f^{(2)}N\beta \quad (3b)$$

$$\chi^{(3)} = f^{(3)}N\gamma \quad (3c)$$

where $f^{(n)}$, popularly known as the "local field factor," accounts for the overall effect of the intermolecular interaction in the presence of the external electric field. Although the set of Eqs. (3) provide a convenient means to obtain the values of microscopic NLO properties from experimental measurement of $\chi^{(n)}$ or vice versa, in practice it is a nontrivial task due to the complicated nature and often a complete

lack of the accurate knowledge of $f^{(n)}$. The $f^{(n)}$ in Eqs. (3) depend, in addition to the strength and the frequencies of the input and output signals, on the nature and magnitude of the intermolecular interaction, which in turn depends on the overall charge distribution, that is itself a function of the spatial and electronic structure of the system. Unfortunately, there is no rigorous theory to describe the local field effect in NLO materials and generally an approximate estimate of the f^n terms is used to extract the microscopic NLO coefficients, α , β , γ , from the experimentally measured $\chi^{(n)}$ values. Usually, the estimates of the $f^{(n)}$ values are made either by Onsager formula,

$$f_o^{(n)} = \frac{\epsilon_o(\epsilon_\omega + 2)}{(2\epsilon_o + \epsilon_\omega)} \quad (4)$$

or by the Lorentz formula,

$$f_{m\omega}^{(n)} = \frac{\epsilon_{m\omega} + 2}{3} \quad (5)$$

In the above equations, the ϵ_o and $\epsilon_{m\omega}$ terms represent the dielectric constant of the medium at frequencies o and $m\omega$. Eq. (4), that also accounts for the reorientation of the molecules in the presence of dc -electric field ($h\nu = 0$), is used for low-frequency electric fields (or dc field), whereas Eq. (5) is used for an optical field with the angular frequency $m\omega$.

Experimental Measurements

The two important manifestations of second-order nonlinearities are: (a) the second harmonic generation (SHG), whereby from the two input waves of angular frequency ω , the system generates a third wave at the frequency 2ω . The associated second-order NLO coefficients for SHG are designated as $\chi(-2\omega; \omega, \omega)$ for macroscopic nonlinearity and $\beta(-2\omega; \omega, \omega)$ for microscopic nonlinearity. (b) The linear electrooptic effect, (EOE) also known as the Pockels effect, which is described by the phase shift of an optical wave with angular frequency ω by a low frequency or dc -electric field ($\omega = 0$). The output optical wave has the same frequency (ω) as the input wave. The associated macroscopic and the microscopic NLO coefficients for linear EOE are designated by $\chi(-\omega; \omega, o)$ and $\beta(-\omega; \omega, o)$, respectively. (The convention for using the frequency arguments is such that the quantity to the left of the semicolon represents the frequency of the "output" beam, while those at the right are the frequencies of the "input" beams and the sum of the frequencies of the input and output beams is zero.)

The experimental measurements of the molecular second-order NLO coefficients for organic materials are conventionally made by the dc -electric field induced second harmonic (EFISH) generation in solution. This technique utilizes the orientation of the nonlinear molecules by dc -electric field in solution, and therefore, one obtains $\mu \cdot \beta(-2\omega; \omega, \omega)$, which, together with the knowledge of the dipole moment, μ , of the system yields a vector quantity, β_{vec} , i.e., the component of β tensor along the dipole axis.

It is important to note here that in an EFISH measurement (in solution) the actual quantity measured is the intensity, $I_{2\omega}$, of the second harmonic wave normalized with respect to a certain reference (often quartz). Therefore, the accuracy of the subsequent results in these experiments is subject to the accuracy of the reference value. The intensity, $I_{2\omega}$, which is related to the third-order NLO coefficients, finally yields $\chi^{(3)}$ for EFISH process, from which a combination of the relations similar to (3b) and

$$\gamma(\text{EFISH}) = \langle \gamma_e(-2\omega; 0, \omega, \omega) \rangle + \frac{\mu \cdot \beta(-2\omega; \omega, \omega)}{5kT} \quad (6)$$

yields the $\mu \cdot \beta$ vector. In the above equation, $\gamma_e(-2\omega; 0, \omega, \omega)$ represents the electronic part of the γ value for EFISH process, k is the Boltzman constant and T is the temperature. It is clear then that the two important factors influencing the experimental β values obtained by EFISH technique are the (a) local field factors and (b) reference value of $\chi^{(3)}$ (EFISH).

For materials having small dipole moment or where μ makes large angle with β , a more suitable method to obtain β is hyper-Rayleigh scattering (HRS). Often it is useful to measure β by both the EFISH and HRS techniques, which provides a means to obtain the various tensorial components of β .

For the second-order NLO characterization of the bulk materials such as solids or thin films, one often uses either (a) the second harmonic generation (SHG) technique, in which the SH efficiency of the material is obtained relative to a reference and, therefore, the resultant $\chi^{(2)}(-2\omega; \omega, \omega)$ is subject to the assumption of the reference data, or (b) electrooptic modulation, whereby the shift in the phase of an optical wave produced by a dc field is measured, yielding $\chi^{(2)}(-\omega; \omega, 0)$. Unlike the SHG measurement, the electrooptic measurement yields an absolute value of $\chi^{(2)}$. In the low frequency limit of the optical wave, $\chi^{(2)}(-2\omega; \omega, \omega)$ and $\chi^{(2)}(-\omega; \omega, 0)$ are not much different from each other and one can use the electrooptic modulation to complement the SHG measurements. However, when the material displays strong dispersion, as happens, for example, close to a resonance in the system, the two $\chi^{(2)}$ values [$\chi^{(2)}(-2\omega; \omega, \omega)$ and $\chi^{(2)}(-\omega; \omega, 0)$] will be substantially different from each other.

The microscopic third-order nonlinearity of organic materials is also characterized through the measurement of the macroscopic NLO coefficients, $\chi^{(3)}$, in solution. One method, as described above, is the EFISH technique, which yields $\gamma(-2\omega; 0, \omega, \omega)$. The other methods which involve technologically important NLO effects allow one to measure optically induced phase shift or changes in the refractive index. Two such methods generally used to characterize γ values are: (a) Degenerate four-wave mixing (DFWM), which allows one to measure $\gamma(-\omega; \omega, \omega, -\omega)$ by monitoring the interaction of three input beams whereby a resulting output beam of same frequency is produced. (b) Optical Kerr gate (OKG) technique, which allows one to measure the changes in the refractive index of the material by monitoring the phase shift of an optical probe pulse in the presence of a strong pump pulse.

Once again, the local field factor plays a crucial role in yielding the values of γ from measured $\chi^{(3)}$. The refractive index change measurements yield the value of $\chi^{(3)}$ which, in addition to the true third-order NLO contribution $\chi_e^{(3)}$ that has electronic origin, may also include contributions $\chi_i^{(3)}$ which we call "incoherent" contribution. The incoherent contribution arises from a change in the linear susceptibility, $\chi^{(1)}$, by populating the excited states which in turn changes the refractive index of the system. Thus, it is important to separate the $\chi_e^{(3)}$ and $\chi_i^{(3)}$ terms in a measurement based on optically induced refractive index change.

Theoretical Calculations

Quantum chemical calculations of molecular NLO properties are conveniently performed by the use of the perturbation theory [13]. The two commonly used methods are (a) the uncoupled perturbation method and (b) the coupled perturbation method. For the organic systems, both the uncoupled and the coupled methods have been used with varying degrees of success. The uncoupled method leading to the popularly known sum-over-states (SOS) method [14] has been extensively used with semi-empirical Hamiltonian of the complete neglect of the diatomic differential overlap (CNDO) type or one of its variations, such as the intermediate neglect of the diatomic differential overlap (INDO) type and with π -electron Hamiltonian.[†] The need to obtain the dipole transition moment integrals, $\langle \psi_I | \mu | \psi_J \rangle$ between various electronic states ψ_I and ψ_J and the energy spectrum E_I up to the continuum in the SOS method prohibits its application to organic systems in the framework of the nonempirical techniques.

A popular form of the coupled method, known as the time-dependent coupled perturbed Hartree-Fock (TDCPHF) method [15-18], has also been used extensively to investigate molecular nonlinearity of organic molecules. The fact that the perturbed quantities in this method are derived from the ground state wave function alone, makes it ideally suited for nonempirical as well as semi-empirical type Hamiltonians. Indeed, TDCPHF method has been used with the *ab initio* [6-9,11,12,17] INDO, [10] and MINDO [19] type Hamiltonians for the calculation of NLO properties of organic molecules.

The single most important factor to be considered in the theoretical investigation of molecular NLO properties is the selection of the basis function. Since NLO effects arise from the perturbation of the electronic charge density by an external electric field, the region of space most influenced is the outer valence part or the region with loosely bound electron charges. Physical intuition then suggests that it is extremely important that the wave function should be able to provide a good description of the outer valence or the most easily polarizable regions of space. Of course, the ability of a molecular wave function generated by the linear combination of atomic functions to describe a particular region of space will depend on the involved atomic functions or the basis set themselves. It is well known in quantum chemistry

[†] A thorough review of the application of the SOS method with semi-empirical Hamiltonian has been given by Kanis et al., Chem. Rev. **94**, 195 (1994).

that the atomic functions, whether the Slater type or the Gaussian type, used in molecular calculations that are obtained from the self-consistent-field solution of the Schrödinger equation for the atomic ground state, are unsuitable to describe the extra valence region of space.

In molecular calculations, often this discrepancy in the atomic functions is compensated by including additional functions with appropriately optimized radial part. For calculations involving Gaussian functions, a variety of such functions with "diffuse" and/or "semi diffuse" radial part and appropriate angular momentum have been optimized for calculating molecular wave function, energy, and electronic and optical properties [20]. However, such functions are not readily available for molecular calculations involving Slater type orbitals (STO). Thus, almost all the SOS calculations of molecular NLO properties, which employ STO, are performed without auxiliary functions that may be essential to describe the "semi-diffuse" and "diffuse" states involved in the perturbation expression.

The next important factor in the theoretical calculation of molecular NLO properties is the treatment of electron correlation. The TDCPHF methods developed for the closed shell system [16-18] do not adequately account for the correlation between electrons of anti-parallel spins, though some electron correlation is included via mixing of the *occupied* and *unoccupied* molecular orbitals (MO) in the perturbation expression.

The SOS method does include some correlation effect via configuration interaction (CI). However, since calculations performed by SOS method essentially employ a "valence only" one-electron basis set, it is difficult to understand the impact of such CI calculations. It is well documented in quantum chemistry literature [21,22] that a poor one-electron basis may lead to unpredictable and often erroneous many-electron wave functions.

Linear and Nonlinear Optical Properties of NTE and NTB

To illustrate the relative merits of different theoretical techniques in terms of the ease in their application and accuracy of the calculated results with respect to the experimental measurements, we have selected two model compounds NTE and NTB whose structures are shown in Figure 1. We present in Table 1 the dipole moment,

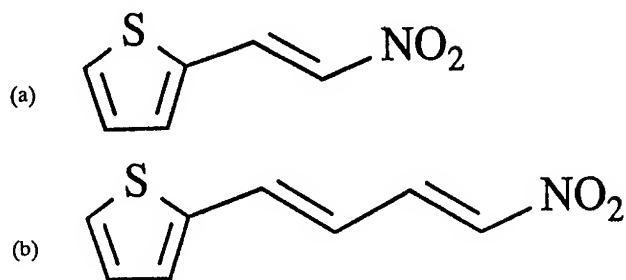


Figure 1. (a) NTE, (b) NTB.

TABLE I. Dipole moment, $\mu(D)$, and linear polarizability, $\alpha(10^{-24}$ esu), of NTE and NTB obtained by different methods.

Method	μ		$\langle\alpha(\omega)\rangle^a$	
	NTE	NTB	NTE	NTB
CNDO-SOS:				
SCI	7.69	8.23	11.31	15.96
SDCI	6.87	7.46	6.37	9.00
INDO-SOS:				
SCI	8.36	8.89	12.20	17.33
SDCI	7.34	8.71	6.66	11.84
INDO-TDHF:				
SZ	7.21	7.92	10.85	16.30
DZ	7.44	8.11	12.20	19.32
<i>Ab initio</i> -TDHF:				
SV + s.d.	7.54	8.28	15.52	23.03
Exp.	5.17	5.44	13.2	25.5

^a All calculations of $\alpha(\omega)$ performed at a fundamental optical wavelength of 1064 nm.

μ , and linear polarizability, $\alpha(\omega)$; and in Table II, the first hyperpolarizability, $\beta(-2\omega; \omega, \omega)$, calculated by the SOS and the TDCPHF methods, along with the corresponding experimental results also obtained in our laboratory.

All theoretical calculations were performed at the *ab initio* self-consistent-field (SCF) optimized geometry reported earlier [12]. The SOS calculations were performed by suitably modifying the ZINDO (Zerner INDO) semi-empirical programs.[‡] Two sets of calculations were performed: One with the CNDO Hamiltonian and the other with the INDO Hamiltonian. In both sets the excited states were generated from a single reference ground state Hartree-Fock configuration by two different CI treatments: (1) A singles only CI, in which all electrons from the highest ten doubly occupied molecular orbitals (MO) were allowed to be singly excited into the lowest ten unoccupied molecular orbitals. This resulted in 101 singly excited configurations and 35 electronic states, which were all included in the SOS expressions. The results obtained from this calculation are listed as SCI. (2) Next, in addition to the above SCI, double excitations were allowed from the three highest occupied MO to the lowest three unoccupied MO. This resulted in a total of 155 singly and doubly excited configurations and 23 electronic states, which were all included in the SOS expressions.

The TDCPHF calculations were performed using the multiple-zeta INDO (MZINDO) [10,23] program developed at the Photonics Research Laboratory. The INDO-TDHF calculations were performed using a single zeta (SZ) as well as a double zeta (DZ) basis set taken from the work of Clementi and Roetti [24]. The *ab initio* results

[‡] ZINDO program system has been developed by Professor M. C. Zerner at the University of Florida.

TABLE II. First-hyperpolarizability, $\beta(-2\omega; \omega, \omega)$, (10^{-30} esu) and second-hyperpolarizability $\gamma(-\omega; \omega, \omega, -\omega)$ (10^{-36} esu) of NTE and NTB obtained by different methods.^a

Method	$ \beta $		$\langle\gamma\rangle^c$	
	NTE	NTB	NTE	NTB
CNDO-SOS:				
SCI	19.43	36.21	88.45	199.34
SDCI	12.36	23.11	73.93	208.21
INDO-SOS:				
SCI	49.23	90.54	365.55	859.37
SDCI	24.31	65.91	178.12	762.01
INDO-TDHF:				
SZ	11.95	23.31		
DZ	7.21	15.26		
<i>Ab initio</i> -TDHF				
SV + s.d.	7.82	18.30	2.66	5.47
Exp.	20.2	66.2	24	84

^a All calculations performed at a fundamental optical wavelength of 1064 nm.

^b $|\beta| = \left(\sum_i \beta_i^2 \right)^{1/2}$; $\beta_i = \frac{1}{3} \sum_j (\beta_{ijj} + \beta_{jij} + \beta_{jji})$; $i, j = x, y, z$.

^c $\langle\gamma\rangle = 1/15 \sum_{ij} (\gamma_{ijj} + \gamma_{jji} + \gamma_{jij})$; $i, j = x, y, z$.

^d Experimental β values measured at a fundamental wavelength of 1064 nm and the γ values measured at a fundamental wavelength of 602 nm.

were obtained from TDCPHF calculations using the HONDO suite of programs [25]. In the *ab initio* calculations, a 4-31G split valence (SV) set augmented by semi-diffuse functions on the heavy atoms was employed. This basis set, called SV + s.d., is listed as basis D in Ref. [12].

The experimental measurements have been described in detail in Ref. [12]. In brief, the experimental measurements were performed in solution with xylene, chloroform, or tetrahydrofuran (THF) as solvent. The linear polarizability was obtained from the refractive index measurement by Abbe refractometer at the wavelength of sodium D-line. The results for $\beta(-2\omega; \omega, \omega)$ were obtained from the EFISH measurement at the fundamental wavelength of a Nd-YAG laser ($\lambda = 1064$ nm) in chloroform ($\chi^{(3)}(\text{EFISH}) = 0.88 \times 10^{-13}$ esu) solution which was also used as reference. The $\gamma(-\omega; \omega, \omega, \omega)$ values were obtained from DFWM measurements at a fundamental wavelength λ of 602 nm and THF ($\chi^{(3)} = 0.37 \times 10^{-13}$ esu) was used as the reference.

An examination of Table I reveals that all theoretical calculations yield larger values of the dipole moment compared to the experiment. The SDCI results of μ show a better accord with the experiment than do the SCI results. In the INDO-TDHF method, improving the basis function seems to worsen the agreement with experiment, though the results get closer to the *ab initio* values.

For the linear polarizability, $\alpha(\omega)$, the SOS method worsens the agreement with the experiment in going from the SCI to SDCI, by reducing the value of $\alpha(\omega)$ by as much as 50%. Both the CNDO and the INDO methods yield comparable results of $\alpha(\omega)$ in the framework of the SOS technique. The INDO-TDHF results in the SZ basis, which are comparable to the SCI (CNDO + INDO) results, show less spectacular changes due to basis set. Similar to the dipole moment results, the value of $\langle\alpha(\omega)\rangle$ increases upon improving the basis set, but now getting closer to the experiment and also to the *ab initio* results. The *ab initio* results for $\langle\alpha\rangle$ show the best agreement with the experiment.

In contrast to the linear polarizability, the nonlinear coefficients, β and γ show a large variation in different theoretical treatment. For example, including the doubles CI reduces the calculated values of β of NTE by about a factor of half and that of NTB by a factor of 1/3 or more in the SOS calculations. Further, the difference between the CNDO and INDO results range from a factor of 2 in the case of NTE and SDCI treatment to almost a factor of 3 for NTB, with the INDO results being larger. In comparison to the experiment, the INDO-SDCI results seem to have the best values for both NTE and NTB followed by the CNDO-SCI results.

In the TDHF calculations, both the *ab initio* and the INDO results of β , which are not too different from each other, are too small by a factor of 3 or more compared to the experimental values. Once again, improving the basis set in INDO-TDHF calculations brings the results closer to the *ab initio* values, though the agreement with the experimental values worsens.

The calculated values of $\langle\gamma\rangle$ show a poor agreement with the experiment. The SOS results of the CNDO and INDO calculations are larger than the experimental values by a factor of 4 to almost an order of magnitude. On the other hand, the TDHF results obtained from the *ab initio* calculations are too small by an order of magnitude or more compared to the experiment. In the SOS calculations of γ , the inclusion of doubles CI has less spectacular effect in CNDO method, where the values between the SCI and SDCI treatments differ from each other by less than 10%. Though a similar difference in the SCI and SDCI results of INDO-SOS calculations of γ for NTB is noted, that for NTE is more than a factor of 2, with the values in SDCI always being smaller than in the SCI treatment.

Issues and Opportunities for Theoretical Modeling of Second- and Third-Order Nonlinearities

Although far from exhaustive, the results discussed in the previous section provide some insight into the problems associated with the theoretical characterization of the linear and NLO properties of organic systems. It is clear that all the available theoretical methods can provide reasonably accurate values of the linear polarizability, α , though two important points can be noted from Table I: (a) The TDHF method (*ab initio* as well as semi-empirical) gives a better agreement with experiment than does SOS. (b) The singles only treatment in the SOS method consistently gives better result than the singles and doubles treatment.

For β , there is no consistency among the results obtained by different theoretical methods, though the INDO-SDCI values are closest to their experimental counter-

parts. The β value in donor-acceptor systems, such as NTE and NTB (Table II), is dominated by the contribution from the lowest-lying charge transfer state, in which case even a two-level model often gives a reasonable description of second-order effects [1]. Therefore, the SOS method within the CNDO and INDO approximations are expected to provide reasonably accurate value of β . This is found to be true in the present study for INDO-SDCI. The SOS semi-empirical methods, (CNDO as well as INDO), however, do not seem to provide reliable values of the third-order non-linear optical properties.

Our studies on other organic molecules [6-9,11-12] have revealed that the *ab initio*-TDHF results of β and γ are consistently too small compared to experiment, as can also be seen from Table II. Furthermore, we have demonstrated [5] that once the basis set has been sufficiently saturated by including a relatively small number of semidiffuse and diffuse p and d functions, rather small changes occur in the calculated results due to further extension of the basis set. This leads us to recognize the absence of the treatment of the electron-correlation effect (EC) as a major shortcoming of the TDHF approach. There has already been some effort to correct the TDHF results either indirectly [26] or directly [27] via perturbative treatment of EC effect. While such treatments have established the importance of EC effect in NLO processes and have provided the first step toward improving the *ab initio* based calculations, their applicability seems to be limited to atoms and small molecules. Further development in the treatment of the EC effect in the *ab initio* method and improvement in the applicability and the efficiency of computer algorithm are required for accurate prediction of NLO effects in organic systems. A similar development for the treatment of EC effect and inclusion of polarization and diffuse functions in the INDO method may perhaps be more fruitful, since such a method will be considerably economical compared to the *ab initio* method.

With regard to the SOS method, there are a number of factors that need to be addressed. Since it is clear that the application of the SOS method to organic molecules is practical only with the semi-empirical Hamiltonians, it would be useful to examine and hopefully improve the factors affecting the accuracy of the calculated results in these methods. It should be recognized that even the most versatile suite of semi-empirical programs, e.g., ZINDO have been parameterized for properties other than the linear and NLO properties. Since ZINDO is the most widely used semi-empirical program for studying structure-property relationship in organics, it would be useful to obtain a new set of parameters to be used with ZINDO for the calculation of NLO properties. At the same time, it is also necessary that extended set of basis functions capable of describing the valence and diffuse states in the CNDO and INDO formalism be optimized. Since the core of the SOS formalism involves the expectation values $\langle \psi_I / \mu / \psi_J \rangle$ between electronic states ψ_I, ψ_J of molecules, where I and J could easily run, even in the limited CI scheme, into the diffuse manifold of the spectrum, a basis set consisting of valence only functions would not provide correct description of the excited state wave functions and transition dipole moments.

Development of auxiliary basis sets of polarization and diffuse type functions would also be beneficial for semi-empirical TDHF calculations. As noted in the

previous section, using a double zeta basis set in INDO-TDHF calculations substantially improves the calculated results of linear and NLO properties. Extending these basis sets with diffuse type functions would hopefully further improve the performance of this method.

Another problem in the application of the semi-empirical SOS methods never discussed in the literature is more of computational nature and involves the program limitation for handling the excited state configurations. The excited states in the SOS methods are obtained from a CI space generated from the single and sometimes also double excitation of a limited set of electrons (except in a few π -electron calculations where it is possible to perform full CI) from the occupied MO to the unoccupied MO of the ground state configuration. The physical question involved in such a scheme is: How many electrons must be correlated to get an accurate description of the many-electron wave function from which the excited states and transition moments are derived? Unlike the spectroscopic studies where a limited number of states of a given symmetry are required and the CI diagonalization on a maximum of ten low-lying states often suffices the computation, the SOS expressions for calculating linear and NLO properties require the entire manifold of the excited state spectrum and, therefore, ideally, one would need to correlate all electrons. However, assuming that the core-core and core-valence correlations have only minor influence on NLO effects (which may not be true for molecules containing first row atoms), one is at least required to correlate *all* valence electrons of the molecule. Although, in small molecules containing less than 10 first-row atoms, such a calculation is not prohibitive, the program limitations to handle large CI space at the present time forbids such calculations on organic molecules. For example, the ZINDO program permits a maximum of 250 singly and doubly excited configurations and 200 excited states. For the two examples given in the previous section, we extended the maximum configuration limitation (NBMAX) to 350 and yet the number of such configurations generated by including any additional electron pair over the 10 electrons already included for single excitation and six electrons for double excitation would easily go beyond 400 to cause the program to stop.

In a preliminary SOS study on *para*-nitroaniline and other related molecules [23] we have found that the calculated values of β and γ are strongly dependent on the (1) number of electrons to be included in CI, (2) the type of excitation (singles/doubles) for generating the CI space, and (3) the number of excited states included in the SOS expressions. Our study indicates that with the increasing CI space and the number of excited states, the calculated results tend to saturate. Therefore, in order to include a large enough CI space in the SOS calculation, further extension of the capability of popular semi-empirical programs such as ZINDO will be valuable in the theoretical modeling of NLO materials.

Apart from the limitation of the presently available theoretical methods, there is also the question of the comparison between the results of the molecular calculations and those obtained from the bulk, generally solution, measurements. It is important to recognize that the molecular calculations are performed on "gas-like" isolated structures that (1) have no contribution from the intermolecular interaction, (2) often ignore contributions from vibrational effect in molecule, and (3) assume

an idealized geometry to remain fixed during the entire interaction time. The experimental measurements, however, are performed in environments where one or more of these effects may be present to complicate the observed values. The effect of molecular interaction, for example, as discussed in the previous section is included in the experimental measurements through the Onsager or the Lorentz "local field factor". Experimental studies performed on the "concentration dependence" of the measured γ values in dilute solution indicate, through a linear behavior of the concentration vs. $\chi^{(3)}$ curve, that the present models of local field adequately account for molecular interaction for "nonpolar" or low dipole moment organic materials. The situation is not so simple in highly polar materials with large β values which exhibit strong solvatochromic effects [1]. Therefore, a reliable theory of the "local field effect" would be extremely useful both for correctly deriving β values from measured $\chi^{(2)}$ and also for theoretically predicting the optical nonlinearity of molecular materials in the bulk form. Studies directed at understanding the local field effects and the validity of the Onsager model are being pursued in several laboratories [28,29] including ours at the present time.

The vibrational optical nonlinearity though important within its own right in processes such as hyper-Raman and antistokes-Raman effects, also becomes significant in the low-frequency limit. Recent studies by Bishop and Kirtman [30] and Bishop et al. [31], on FH, H₂O, CO₂, and NH₃ indicate that the vibrational contribution to the static hyperpolarizabilities may vary from 620% in the case of NH₃ to -37% in the case of H₂O of their electronic counterparts for $\beta(o; o, o)$ and from 15% in the case of H₂O to 84% in the case of NH₃ of their electronic counterparts for $\gamma(o; o, o)$. At optical frequencies, the calculated vibrational contributions to electronic nonlinearity in these molecules are much smaller. Further studies and theoretical analysis of this effect are, however, needed to establish its relative contribution as well as to understanding the mechanism of some nuclear level NLO effects in organic molecules.

Another nuclear effect which makes significant contribution to the measured γ values, especially those obtained from the DFWM and Kerr gate experiments, arises from the reorientation of molecules by the optical field. These experiments show both the electronic as well as the "reorientation" contributions. If sufficient care has not been taken in the experimental measurement to separate the reorientation contribution from the electronic part, γ_e : the quantity obtainable from the theoretical calculations, a comparison between the two sets of result may not be meaningful.

It should be also noted that the idealized geometry of a molecule assumed in theoretical calculations may not represent the true geometry of the molecule in bulk. The true geometry in a bulk form may be different due to several reasons. For example, a conformational chemical defect present in the molecule, as in the case of extended conjugated systems, may substantially alter the effective π -electron conjugation, and consequently, the NLO response. This may further complicate the comparison between theory and experiment.

Another factor often responsible for discrepancy between theory and experiment is the dispersion effect. Theoretical calculations of NLO effects are often performed

assuming a nonresonant optical frequency. The experimental measurements, where the optical frequency is close to one- or two-photon absorption in the molecule, may contain substantial resonant contributions due to dispersion of NLO coefficients.

Finally, the measurements are susceptible to variations of experimental conditions, references, and the method used. Often, experimental results performed on the same molecule by different groups greatly vary from each other. One such example is the frequently referenced system, *para*-nitroaniline, whose reported β value varies over a range of a factor of two [6]. Such discrepancies in the experimental results only add to the already complicated situation facing theoretical characterization of NLO properties.

Photorefractive Materials

Photorefractivity is produced by a combined action of electrical properties and the electrooptic properties. The photorefractive phenomenon can be described in terms of the following steps [32]. The light is absorbed by a photosensitizing group whereby electron-hole pairs are created. One of the carriers, which has the higher mobility, moves from the original site, gets trapped in the dark region and creates a space-charge field due to separation of charges. This resulting space-charge electric field then produces a refractive index change due to the electrooptic activity of the material. The result is a light-induced refractive index change in the material, so the overall manifestation is similar to $\chi^{(3)}$ except that it is not purely an electronic effect at the molecular level. This is an effect which is a bulk manifestation because the charges have to move spatially on macroscopic distances in order for them to set up a space-charge field that is sufficiently large to produce refractive index change by electrooptic effect. In understanding the photorefractive behavior, therefore, one has to consider at molecular level the efficiency of the charge carrier generation by the action of light, the mobilities of the carriers in bulk and formation of the resulting space-charge field.

The organic photorefractive system would be different from widely investigated inorganic ferroelectrics and semiconductors in the sense that both the quantum efficiency for charge carrier generation and the mobilities of the carriers are strongly dependent on the electric field [33]. The efficiency of photogenerated charge carriers is often described by the Onsager model. The dependence of mobility on the field is in turn dependent on the model used for the transport of charge carriers. In a dispersive model, where the mobilities are dominated by the multiple trapping dynamics, one can describe the dependence and mobility of the field by some power law for a limited range of electric field applied. In our laboratory, we have considered the field dependence of the photogeneration efficiency by using the Onsager model and the dependence of mobility on the electric field by power dependence such as E^p , where p is determined by experimental measurements [34,35]. With numerical simulation of the space charge field using this model, we have calculated the diffraction efficiency. The agreement between the experimentally observed field applied dependence of diffraction efficiency and that calculated is satisfactory [34,35].

This new field of photorefractive polymers offers opportunities for theoretical modeling at the bulk level. A more complete modeling of space-charge field and trapping dynamics to understand the time response is very much needed.

Acknowledgment

We thank Professor Mike Zerner for making a copy of his ZINDO program available to us. We also thank Bruce Reinhardt of Polymer Branch, Wright Laboratory, for providing us with the two model compounds reported in this article. This research was supported by the Air Force Office of Scientific Research, the Directorate of Chemistry and Materials Sciences, and Wright Laboratory, Polymer Branch through Contract No. F49620-93-C-0017. Partial support from NSF-Solid State Chemistry Program Grant No. DMR-90-22017 is also acknowledged.

Bibliography

- [1] P. N. Prasad and D. J. Williams, *Introduction to Nonlinear Optical Effects in Organic Molecules and Polymers* (Wiley, New York, 1991).
- [2] P. N. Prasad and B. A. Reinhardt, *Chem. Mater.* **2**, 660 (1990).
- [3] P. Chopra, L. Carlucci, H. F. King, and P. N. Prasad, *J. Phys. Chem.* **93**, 7120 (1989).
- [4] E. Perrin, P. N. Prasad, P. Mougnot, and M. Dupuis, *J. Chem. Phys.* **91**, 4728 (1989).
- [5] S. P. Karna, M. Dupuis, E. Perrin, and P. N. Prasad, *J. Chem. Phys.* **92**, 7418 (1990).
- [6] S. P. Karna, P. N. Prasad, and M. Dupuis, *J. Chem. Phys.* **94**, 1171 (1991).
- [7] S. P. Karna, Z. Laskowski, G. B. Talapatra, and P. N. Prasad, *J. Phys. Chem.* **95**, 6508 (1991).
- [8] S. P. Karna, G. B. Talapatra, and P. N. Prasad, *J. Chem. Phys.* **95**, 5873 (1991).
- [9] S. P. Karna, G. B. Talapatra, W. M. K. P. Wijekoon, and P. N. Prasad, *Phys. Rev. A* **45**, 2763 (1992).
- [10] G. B. Talapatra, N. Manickam, M. Samoc, M. E. Orczyk, S. P. Karna, and P. N. Prasad, *J. Phys. Chem.* **96**, 5206 (1992).
- [11] V. Keshari, S. P. Karna, and P. N. Prasad, *J. Phys. Chem.* **97**, 23 (1993).
- [12] S. P. Karna, Y. Zhang, M. Samoc, P. N. Prasad, B. A. Reinhardt, and A. G. Dillard, *J. Chem. Phys.* **99**, 9984 (1993).
- [13] P. W. Langhoff, S. T. Epstein, and M. Karplus, *Rev. Mod. Phys.* **44**, 602 (1972).
- [14] J. F. Ward, *Rev. Mod. Phys.* **37**, 1 (1965); B. J. Orr and J. F. Ward, *Mol. Phys.* **20**, 513 (1971).
- [15] A. Dalgarno, in *Perturbation Theory and its Applications in Quantum Mechanics*, C. H. Wilcox, Ed. (Wiley, New York, 1966).
- [16] D. P. Santry and T. E. Raidy, *Chem. Phys. Lett.* **61**, 473 (1979).
- [17] H. Sekino and R. J. Bartlett, *J. Chem. Phys.* **85**, 975 (1986).
- [18] S. P. Karna and M. Dupuis, *J. Comp. Chem.* **12**, 487 (1991).
- [19] P. Korambath and H. Kurtz, MOPAC-93.
- [20] T. H. Dunning, Jr. and P. J. Hay, in *Modern Theoretical Chemistry*, Vol. I, H. F. Schaefer, Ed. (Plenum, New York, 1977).
- [21] (a) I. Shavitt, in *Modern Theoretical Chemistry*, Vol. II, H. F. Schaefer, Ed., **111**, (Plenum, New York, 1977). (b) R. J. Buenker, *Int. J. Quantum Chem.* **29**, 435 (1986).
- [22] P. J. Bruna and S. D. Peyerimhoff, *Adv. Chem. Phys.* **67**, 1 (1987).
- [23] G. B. Talapatra, S. P. Karna, and P. N. Prasad, unpublished.
- [24] E. Clementi and C. Roetti, *At. Data Nucl. Data Tables* **14**, 177 (1974).
- [25] M. Dupuis, A. Farazdel, S. P. Karna, and S. Maluendes, in *Modern Techniques in Computational Chemistry*, E. Clementi, Ed. (ESCOM, Leiden, 1990), p. 277.
- [26] H. Sekino and R. J. Bartlett, *Int. J. Quantum Chem.* **43**, 119 (1992), *J. Chem. Phys.* **94**, 3665 (1991).

- [27] J. E. Rice and N. C. Handy, J. Chem. Phys. **94**, 4959 (1991).
- [28] M. Zerner, unpublished results.
- [29] H. Kurtz, unpublished results.
- [30] D. M. Bishop and B. Kirtman, J. Phys. Chem. **95**, 2646 (1991).
- [31] D. M. Bishop, B. Kirtman, H. A. Kurtz, and J. E. Rice, J. Chem. Phys. **98**, 8024 (1993).
- [32] P. Yeh, *Introduction to Photorefractive Nonlinear Optics* (Wiley, New York, 1993).
- [33] S. Ducharme, J. C. Scott, R. J. Twieg, and W. E. Moerner, Phys. Rev. Lett. **66**, 1846 (1991).
- [34] Y. Zhang, Y. Cui, and P. N. Prasad, Phys. Rev. **B46**, 9900 (1992).
- [35] M. E. Orczyk, J. Zieba, and P. N. Prasad, Proc. Soc. Photo-Opt. Instrum. **2025**, 298 (1993).

Received May 25, 1994

Calculation of Optical Second-Harmonic Susceptibilities and Optical Activity for Crystals

ZACHARY H. LEVINE

Department of Physics, The Ohio State University, Columbus, Ohio 43210-1106

Abstract

A new generation of nearly first-principles calculations predicts both the linear and second-harmonic susceptibilities for a variety of insulating crystals, including GaAs, GaP, AlAs, AlP, Se, α -quartz, and *c*-urea. The results are typically in agreement with experimental measurements. The calculations have been extended to optical activity, with somewhat less success to date. The theory, based on a simple self-energy correction to the local density approximation, and results are reviewed herein. © 1994 John Wiley & Sons, Inc.

Introduction

The optical properties of solids have both scientific and technological interest. For solid-state physics, the response of matter to an electric field is one of its most fundamental properties. This interaction has helped to elucidate the nature of light itself. Historically, crystalline quartz has been the key material, including the discovery of birefringence in 1690, optical activity in 1811, and optical second-harmonic generation in 1961. The present scientific interest is centered on the calculation of the tensors in the constitutive equations of macroscopic electromagnetism rather than the electrodynamics.

Technologically, one need only look to laser technology and telecommunications to see applications of second-harmonic generation and related phenomena such as optical parametric oscillation and electro-optic modulators. The scientific motivation is to understand what is required to model these phenomena; if the understanding is sufficiently robust, the hope is the predictions may help select materials that are technologically superior.

Because of its relative simplicity and accuracy, the local density approximation (LDA) is the most widely used computational method for determining the structural and electronic structure properties of solids using little or no experimental input [1]. Nevertheless, its application to the optical response of solids has been limited largely to linear optical response. The present work reviews an attempt to extend the predictive powers of the LDA (with its leading error corrected, as explained in the next section) to higher optical response tensors. To date, the second-harmonic susceptibility and the optical activity tensor have been considered. Although not discussed here, it would be natural to ultimately extend the present work to yet

higher tensors, specifically those governing third-harmonic generation, second-harmonic generation in centrosymmetric systems, and the anisotropy of the dielectric constant in cubic materials. The intent of this paper is to present a readable overview; the reader is referred to the original papers for technical details.

A Self-Energy Correction to LDA

By 1980, it became apparent that the local density approximation systematically underestimated band gaps in essentially all semiconductors. In the case of germanium, metallic rather than semiconducting behavior is predicted. This systematic failure led solid-state theorists to consider more sophisticated alternatives to LDA. After a few years, it became evident that the GW theory of Hedin [2] did correctly predict the band gaps of semiconductors to within perhaps 100 meV [3,4]. Remarkably, although the GW eigenvalues differ from LDA eigenvalues by about 1 eV the GW quasiparticle wave functions are little different than the LDA wave functions [3].

In the mid-1980s, it also became apparent that the LDA was overestimating the calculated dielectric constants of semiconductors [5,6]. This is a natural consequence of the underestimate of the band gap: The simplest model for dielectric response that is consistent with causality, and the f -sum rule is the single-pole model. The static dielectric constant is given in this model by

$$\epsilon = 1 + \omega_p^2 / \omega_0^2,$$

where ω_p is the plasma frequency and ω_0 is position of the pole. An underestimate of the gap is analogous to setting ω_0 too small, which leads to an unwanted increase in ϵ .

It was natural to suppose that, by correcting the band gap with the GW values, a more accurate dielectric constant could be found for semiconductors. Consider the formula the static dielectric constant for insulators

$$\epsilon = 1 - 8\pi e^2 \bar{\Omega}_0 \int_{\text{BZ}} d\vec{k} \sum_n^{\text{occ}} \langle n\vec{k} | \vec{p} G_{n\vec{k}}^3 \vec{p} | n\vec{k} \rangle, \quad (1)$$

where $-e$ is the charge on an electron, \vec{k} is the crystal momentum whose domain of integration is the Brillouin zone (BZ), $\bar{\Omega}_0$ is the unit cell volume divided by $(2\pi)^3$, \vec{p} is the momentum operator, and

$$G_{n\vec{k}} = \sum_{m \neq n} \frac{|m\vec{k}\rangle \langle m\vec{k}|}{\epsilon_{n\vec{k}} - \epsilon_{m\vec{k}}},$$

where $\epsilon_{n\vec{k}}$ the energy eigenvalue associated with the state $|n\vec{k}\rangle$. As first suggested [6] and later shown numerically [7,8], using the GW eigenvalues in Eq. (1) leads to a substantial overcorrection (i.e., underestimate) of the static dielectric constant for Si, Ge, and other semiconductors.

The intuitive notion that improved band structure should lead to an improved calculation of the dielectric constants of semiconductors proved to be correct, but

a deeper analysis was required. Levine and Allan [8,9] summarized the GW results in the effective crystal Hamiltonian

$$H_{\vec{k}}^{\text{eff}} = H_{\vec{k}}^{\text{LDA}} + \Delta P_{c\vec{k}}, \quad (2)$$

where Δ is the difference between the GW eigenvalues and the LDA eigenvalues in the notation of Sham and Schlüter [10] and $P_{c\vec{k}}$ is the projection operator acting on the conduction bands. The term $\Delta P_{c\vec{k}}$ along with the usual exchange-correlation term of the LDA, approximates the self-energy suggested by GW calculations.

It had been pointed out in the context of the calculation of the dielectric constants of solids that a nonlocal potential required a correction to the momentum matrix elements [5]. In Ref. [5] the nonlocal potential was a nonlocal pseudopotential. This term may be thought of as arising either from the commutator of \vec{r} and H (Ref. [5]) or from $\nabla_{\vec{k}} H_{\vec{k}}$ [8,9]. These forms are equivalent [11]. Matrix elements of \vec{p} are not fundamental, but depend upon a particular form of the Hamiltonian. Matrix elements of $\nabla_{\vec{k}} H_{\vec{k}}$ are more general for crystalline solids.

In the calculation of Refs. [8] and [9], the nonlocal pseudopotential appears as well as an additional nonlocality in the term $\Delta P_{c\vec{k}}$. Even though Δ need not carry \vec{k} -dependence, because the conduction bands are different from \vec{k} -point to \vec{k} -point in the Brillouin zone, the projection operator has \vec{k} dependence, i.e., there is a nonzero gradient with respect to \vec{k} . The detailed mathematical consequences are given elsewhere [7,8]. Only one example is given here. The static dielectric constant with this effective Hamiltonian is given by

$$\epsilon = 1 - 8\pi e^2 \bar{\Omega}_0 \int_{\text{BZ}} d\vec{k} \sum_n^{\text{occ}} \langle n\vec{k} | \vec{p} G_{n\vec{k}}^{\text{LDA}} G_{n\vec{k}}^{\text{LDA}} \vec{p} | n\vec{k} \rangle. \quad (3)$$

Thus, when the self-energy correction $\Delta P_{c\vec{k}}$ is added to the LDA Hamiltonian, only one of three energy denominators participates in the energy shift. The resulting predictions are extremely accurate by the standards of solid-state physics.

The calculation proceeds as follows: Well-converged self-consistent LDA ground state potentials are found within the pseudopotential/plane wave method using the Corning code [12]. We retain about 600 plane waves for a small system such as GaAs, and about 6000 plane waves for *c*-urea, the largest system calculated to date (with 16 atoms in the unit cell). Virtual orbitals are found in the (fixed) ground state potential. These are used in a "sums over states" implementation of perturbation theory.

The calculated dielectric constants are given for a number of materials in Table I, and their size derivatives are given for a few materials in this table. An excellent account of the experimental values, including the birefringence; only *c*-urea is exceptional in that there is an underestimate of the static dielectric constant, in contrast to the usual LDA overestimate. The size derivatives for Si and Ge differ by an order of magnitude (in both theory and experiment), yet these materials are chemically and structurally very similar. The difference is largely due states near the Γ -point in the Brillouin zone. In Ge, the direct gap is much smaller than the average gap, and this region dominates the optical response. In Si, the bands are flat throughout

TABLE I. The static dielectric constants and their size derivatives for a variety of materials.

Material	Δ (eV)	ϵ_∞			$d \ln \epsilon_\infty / d \ln a$			Ref.
		LDA	Present	Expt.	LDA	Present	Expt.	
Si	0.9	13.5	11.2	11.4	1.21	0.77	0.68, 0.83	[8]
Ge	0.8	21.3	16.0	15.3	10.8	7.2	5.3, 7.8	[8]
AlP	0.9	8.3	7.2	7.4	0.7	0.4		[7]
AlAs	0.9	9.5	8.1	8.2	2.0	1.4		[7]
GaP	0.9	10.4	8.8	9.0	2.7	1.9	1.6, 1.9	[7]
GaAs	0.8	13.7	11.2	10.8	5.9	4.2	2.2, 3.1	[7]
Se (o)	1.1	10.3	7.9	6.2–8.4				[22]
Se (e)	1.1	15.2	11.5	10.2–13.7				[22]
α -Quartz (o)	1.8	2.48	2.30	2.35				[22]
α -Quartz (e)	1.8	2.51	2.33	2.38				[22]
c-Urea (o)		2.03		2.17				[23]
c-Urea (e)		2.14		2.49				[23]

The experimental data are cited in the references. For the uniaxial crystals, “o” refers to the ordinary ray, and “e” refers to the extraordinary ray.

the Brillouin zone, so that no single region dominates the optical response to this extent. A two-band model fails to obtain this order of magnitude difference [13].

Second-Harmonic Generation

The discovery of second-harmonic generation in 1961 [14] led to a great deal of theoretical development in the field. Both the electrodynamics and the band theoretical description were elucidated shortly thereafter [15,16]. Local-field corrections were first given in this period as well [17]. Unfortunately, the formalism was far too complicated for a realistic implementation at that time.

Perhaps the first attempt at a realistic band structure calculation came in 1975, from Fong and Shen [18], who used the empirical pseudopotential method—already known to give reasonable results for linear dielectric response [19]—to calculate $\chi^{(2)}$ for GaAs and other III–V semiconductors. Unfortunately, their results were below the experimental values by at least an order of magnitude. They speculated that local-field effects were responsible, but did not attempt to include these explicitly. The field lay fallow for over a decade, when it was suggested by Sipe and co-workers that perhaps it was the matrix elements of Fong and Shen [18], rather than the local-field corrections, which were principally in error [20]. The relevant matrix elements were estimated using a semiempirical method, leading to much improved values for $\chi^{(2)}$ compared to experiment. Further work in the area has been pursued by Sipe and co-workers [21], ourselves [7,22–24], and Huang and Ching [25,26]. The work of the present group has featured great attention to the issue of numerical convergence, local-field corrections, and the self-energy correction discussed in the previous section for linear response.

TABLE II. The second-harmonic susceptibility in the static limit for a variety of materials.

Material	Δ (eV)	$d = \frac{1}{2}\chi^{(2)}$ (pm/V)			$d \ln \chi^{(2)}/d \ln a$			Ref.
		LDA	Present	Expt.	LDA	Present	Expt.	
AlP	0.9	23	15		11	10		[7]
AlAs	0.9	39	24		15	13		[7]
GaP	0.9	60	35	37	20	18		[7,24]
GaAs	0.8	174	86	83	30	23		[7,24]
Se (d_{11})	1.1	220	97	100				[22]
α -Quartz (d_{11})	1.8	0.48	0.33	0.30				[22]
c-Urea (d_{36})		1.1		1.2				[23]

When more than one tensor component exists only the Kleinman-allowed component [35] is reported. The experimental data are cited in the references. For GaP and GaAs, the experimental values given are from the review and reanalysis of Roberts [36].

Results for the second-harmonic susceptibility for the static limit $\lim_{\omega \rightarrow 0} \chi^{(2)}(-2\omega; \omega, \omega)$ are given in Table II. Frequency-dependent results for GaP are shown in Figure 1; the frequency dependence of GaAs has also been studied [24]. The results are seen to be in excellent agreement with experiment for those cases for which experimental results exist. The LDA calculation has a larger second-

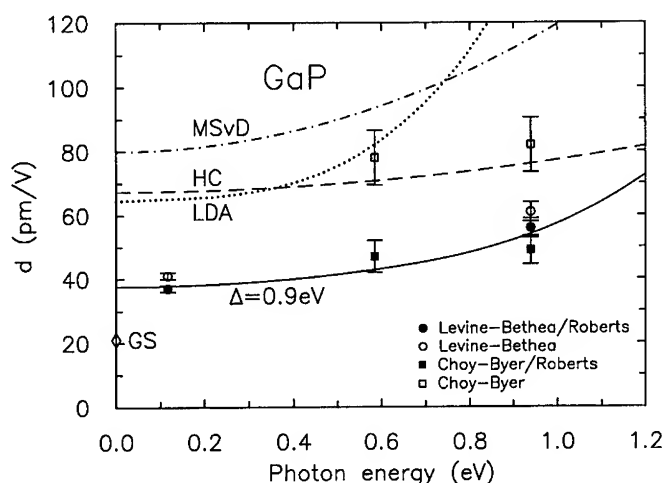


Figure 1. Frequency dependence of the second-harmonic susceptibility as a function of frequency. The open symbols are original data from Refs. [37] and [38]; the solid symbols are from the reanalysis of Roberts [36]. The present self-energy-corrected calculation is given by the solid line, and the present LDA calculation is represented by the dotted line. The dash dot line is from the calculation of Moss, Sipe, and van Driel [20]; the diamond is from the calculation of Ghahramani and Sipe [21]. The dashed line is due to the calculation of Huang and Ching [25].

harmonic susceptibility than the self-energy corrected value, and also has a larger dispersion. In contrast, the results of Huang and Ching [25] have a larger second-harmonic susceptibility, but a smaller dispersion. So the differences between the present calculation and those of Huang and Ching cannot be summarized by a simple shift of oscillator strength.

Local-field corrections are given in Table III. For the semiconductors, these are modest. However, for urea, the results are quite large. Urea, $(\text{NH}_2)_2\text{CO}$ with two molecules per unit cell, is a hydrogen bonded crystal; the intercell charge transfer is therefore much lower than the covalently bonded semiconductors. The CO group is a tiny conjugated π system and is therefore a good candidate for having a large nonlinear optical response. Our calculations suggest that urea is in a "crossover" regime in which both molecular (i.e., local-field) and solid-state effects are important.

Optical Activity

When linearly polarized light propagates along the optic axis of certain uniaxial crystals, the plane of polarization is rotated by a certain angle per unit length of the material. Specifically, when the eigenmodes of propagation in the crystal are left and right circularly polarized light waves, the optical rotatory power ρ is related to the indices of refraction n_L and n_R by

$$\rho = \frac{\omega}{2c} (n_L - n_R).$$

Optical rotatory power is the best-known manifestation of optical activity [27], which encompasses all optical phenomena which depend upon both the direction of the electric field and the direction of propagation.

As discussed in Ref. [22], the linear interaction of a monochromatic electromagnetic wave (with wave vector \vec{q}) traveling through a medium may be described through the joint solution of the wave equations for the vector potential \vec{A}

TABLE III. Local field corrections for a variety of materials for the linear dielectric response and second-harmonic susceptibility.

Material	Δ (eV)	Local field/total (%)		Ref.
		ϵ_∞	$\chi^{(2)}$	
AlP	0.9	-8	-12	[7]
AlAs	0.9	-7	-8	[7]
GaP	0.9	-6	-13	[7,24]
GaAs	0.8	-5	-8	[7,24]
Se	1.1	-15, -14	+22	[22]
α -Quartz	1.8	-5, -4	-6	[22]
c-Urea	0	-17, -12	-89	[23]

If two values are given, these are for the ordinary and extraordinary rays, respectively.

$$\nabla^2 \vec{A} - \frac{1}{c^2} \frac{\partial^2 \vec{A}}{\partial t^2} - \nabla(\nabla \cdot \vec{A}) = -\frac{4\pi}{c} \vec{J} \quad (4)$$

and a constitutive relation

$$J_i = \frac{\omega^2}{4\pi c} (\epsilon_{ij} - \delta_{ij}) A_j + \frac{i\omega^2}{4\pi c} \eta_{ijl} q_j A_l + O(q^2), \quad (5)$$

where \vec{J} is the current, i, j , and l are Cartesian indices, and δ is the Kronecker δ . Given a knowledge of ϵ and η , the relationship between the wave vector and the frequency can be determined, and from this any optical constant may be extracted. Band theory can supply the equations for the dielectric function [8,28] and the optical activity tensor [22]. The formulas are quite complicated, so will not be repeated here. Suffice it to say that they are given in terms of matrix elements of direct transitions and an integral over the Brillouin zone.

We have completed calculations of the optical rotatory power for selenium [22,29] and α -quartz [22]. We restrict our presentation to Figure 2, the case of α -quartz, for which the experimental data are more reliable than selenium. We plot the optical rotatory power ρ in the combination $\omega/\rho^{1/2}$ because this brings both the experiment and the calculation into a straight line form, as suggested by the single-oscillator model [30]. The deviation of the experimental data at the lowest frequency

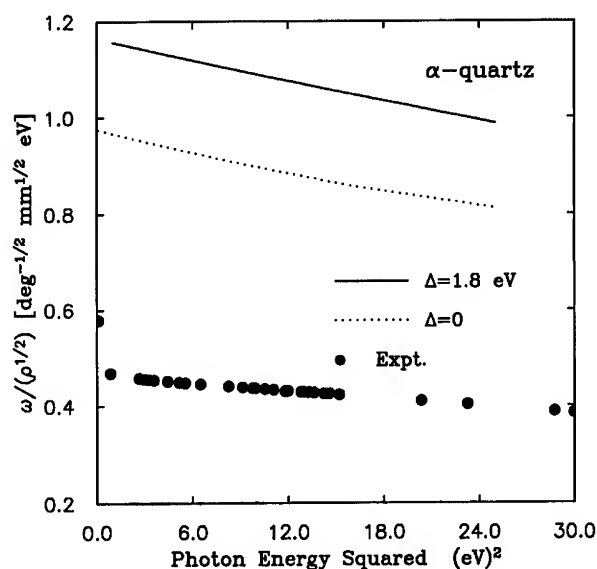


Figure 2. Frequency dependence of the optical rotatory power ρ of α -quartz. The combination $\omega/\rho^{1/2}$ is chosen so that the data and predictions will be approximately straight lines. The LDA prediction is given by the dotted line, and the self-energy corrected curve by the solid line. Local fields are neglected from this calculation. The calculation underestimates ρ by about a factor of 5.

plotted is almost certainly due to phonons. It is troubling that the predicted optical rotatory power is too small by a factor of 5. For selenium, the calculation is too small by a factor of about 1.5. To date, local-field corrections have not been included in the calculation. However, preliminary results indicate these will represent order 1 corrections to the values reported here [31].

Concluding Remarks

The local density approximation modified by a simple self-energy correction has successfully predicted the linear and second-harmonic susceptibilities for crystalline solids in the insulating regime in a series of calculations. Systems as diverse as simple and compound semiconductors, α -quartz and *c*-urea have been investigated. The strain derivatives have been considered as well [32]. In many cases these are in good agreement with experiments; in some cases, the predictions are made in advance of experiments. Optical rotatory power has been calculated as well, although with less quantitative success to date. Local-field corrections may play a larger role in optical rotatory power than they did in linear optical response or second-harmonic generation.

While the ability to predict optical constants of solids has progressed quite a bit recently, it is worth considering some of the principal obstacles to further progress. One concerns the simple approximation of the GW solutions. Obviously, including more of energy dependence and genuine GW quasiparticle wave functions rather than LDA wave functions should improve matters. However, the GW quasiparticle peak strengths are only about 0.8 [3,4]. This means that 20% of the total oscillator strength is of unknown form and at unknown energies. The present theory simply places the "missing" oscillator strength at the quasiparticle energies. A better scheme would require a considerable advance in the theory [33]. The GW itself is in principle a theory of the one-electron Green's function. Particle-hole interactions are known to be important in the optical response of semiconductors [34]. Yet their realistic treatment is a post-state-of-the-art task in 1994. Despite these difficulties in the theory, personally I find it remarkable just how well a simple one-electron *ansatz*, implemented with sufficient variational freedom, works in comparison to the experiments.

Acknowledgments

I thank Professors D. C. Allan and M. P. Teter for providing and supporting the ground-state local-density code used in this study as well as the pseudopotentials. This work was supported by the National Science Foundation (DMR-9306318), the Department of Energy—Division of Materials Sciences, the Ohio Supercomputer Center, and the Cornell Theory Center.

Bibliography

- [1] R. O. Jones and O. Gunnarsson, Rev. Mod. Phys. **61**, 689 (1989).
- [2] L. Hedin, Phys. Rev. **139**, A796 (1965); L. Hedin and S. Lundqvist, Solid State Physics **23**, 1 (1969).

- [3] M. S. Hybertsen and S. G. Louie, Phys. Rev. B **34**, 5390 (1986).
- [4] R. W. Godby, M. Schlüter, and L. J. Sham, Phys. Rev. B **37**, 10159 (1988).
- [5] S. Baroni and R. Resta, Phys. Rev. B **33**, 7017 (1986).
- [6] M. S. Hybertsen and S. G. Louie, Phys. Rev. B **35**, 5585 (1987).
- [7] Z. H. Levine and D. C. Allan, Phys. Rev. B **44**, 12781 (1991); Erratum **48**, 14768 (1993).
- [8] Z. H. Levine and D. C. Allan, Phys. Rev. B **43**, 4187 (1991).
- [9] Z. H. Levine and D. C. Allan, Phys. Rev. Lett. **63**, 1719 (1989).
- [10] L. J. Sham and M. Schlüter, Phys. Rev. Lett. **51**, 1888 (1983).
- [11] W. E. Lawrence, private communication.
- [12] M. P. Teter, M. C. Payne, and D. C. Allan, Phys. Rev. B **40**, 12255 (1989).
- [13] W. A. Harrison, *Electronic Structure and the Properties of Solids* (Freeman, San Francisco, 1980), p. 115.
- [14] P. A. Franken, A. E. Hill, C. W. Peters, and G. Weinreich, Phys. Rev. Lett. **7**, 118 (1961).
- [15] D. A. Kleinman, Phys. Rev. **128**, 1761 (1962).
- [16] J. A. Armstrong, N. Bloembergen, J. Ducuing, and P. S. Pershan, Phys. Rev. **127**, 1918 (1962).
- [17] A. S. Pine, Phys. Rev. **139**, A901 (1965).
- [18] C. Y. Fong and Y. R. Shen, Phys. Rev. B **12**, 2325 (1975).
- [19] J. P. Walter and M. L. Cohen, Phys. Rev. B **2**, 1821 (1970).
- [20] D. J. Moss, J. E. Sipe, and H. M. van Driel, Phys. Rev. B **36**, 9708 (1987).
- [21] E. Ghahramani and J. E. Sipe, Phys. Rev. B **46**, 1831 (1992).
- [22] H. Zhong, Z. H. Levine, D. C. Allan, and J. W. Wilkins, Phys. Rev. B **48**, 1384 (1993).
- [23] Z. H. Levine and D. C. Allan, Phys. Rev. B **48**, 7783 (1993).
- [24] Z. H. Levine, Phys. Rev. B **49**, 4532 (1994).
- [25] M.-Z. Huang and W. Y. Ching, Phys. Rev. B **45**, 8738 (1992).
- [26] M.-Z. Huang and W. Y. Ching, Phys. Rev. B **47**, 9464 (1993).
- [27] J. Jerphagnon and D. S. Chemla, J. Chem. Phys. **65**, 1522 (1976).
- [28] H. Ehrenreich and M. H. Cohen, Phys. Rev. **115**, 786 (1959).
- [29] H. Zhong, Z. H. Levine, D. C. Allan, and J. W. Wilkins, Phys. Rev. Lett. **69**, 379 (1992); Erratum **70**, 1032 (1993).
- [30] T. M. Lowry, *Optical Rotatory Power* (Dover, New York, 1964), p. 392.
- [31] L. Jönsson, Z. H. Levine, and J. W. Wilkins, Bull. Am. Phys. Soc. **39**, 615 (1994).
- [32] Z. H. Levine, H. Zhong, S. Wei, D. C. Allan, and J. W. Wilkins, Phys. Rev. B **45**, 4131 (1992).
- [33] B. I. Lundqvist, private communication.
- [34] W. Hanke and L. J. Sham, Phys. Rev. B **21**, 4656 (1980).
- [35] D. A. Kleinman, Phys. Rev. **126**, 1777 (1962).
- [36] D. A. Roberts, IEEE J. Quant. Electron. **QE-28**, 2057 (1992).
- [37] B. F. Levine and C. G. Bethea, Appl. Phys. Lett. **20**, 272 (1972).
- [38] M. M. Choy and R. L. Byer, Phys. Rev. B **14**, 1693 (1976).

Received May 16, 1994

The Relation between Magnetism and Electronic Transport Properties in Strongly Correlated Electron Liquids, Including High T_c Materials

N. H. MARCH

*Department of Theoretical Chemistry, University of Oxford, 5 South Parks Road,
Oxford, OX1 3UB, United Kingdom*

Abstract

Liquid metallic caesium, taken up the liquid–vapor coexistence curve towards the critical point, exhibits a crossover from Pauli spin paramagnetism near freezing to Curie-like behavior near criticality. This transition is discussed in terms of conventional Fermi liquid theory at low temperatures and heavy Fermion behavior on approaching the critical region. The maximum in the magnetic susceptibility permits an estimate of the discontinuity q in the momentum distribution at the corresponding density, and this has recently been checked independently using NMR data. An argument is presented, via q , which links a nonequilibrium transport property, namely, electronic conductivity, to a thermodynamic quantity, the magnetic susceptibility. With the above as background, a search has been made for related correlations in the normal state of the high T_c superconducting copper oxides. Using again Fermi liquid theory (now two-dimensional), it is first argued that there should be an intimate correlation between nuclear spin–lattice relaxation time T_1 and electrical resistivity R . This is borne out, at least partially, by available experiments. In the same context, the antiferromagnetic susceptibility $\chi(Q)$, with Q the antiferromagnetic wave number, is linked with T_1 and R . Finally some brief comments are made on the interpretation of Hall and thermopower measurements. © 1994 John Wiley & Sons, Inc.

Introduction

In earlier work on strongly correlated liquid metals, taken along the liquid–vapor coexistence curve towards the critical point, a relation between a transport property, electrical resistivity, and a thermodynamic quantity, magnetic susceptibility, has been demonstrated. The basic arguments underlying this relation are first summarized in the next section.

This same type of correlation is then pressed here for electron or hole liquids flowing through antiferromagnetic assemblies in the normal state of some high T_c copper oxide materials. Elimination of magnetic susceptibility in a Fermi liquid framework leads to the prediction that electrical resistivity is intimately linked with nuclear spin–lattice relaxation time and empirical data is employed to test this relation.

Experiments on Hall constant and thermopower are also briefly referred to. The possible role of interlayer coupling at the lowest temperatures encountered in the normal state is considered, as is a crossover from a two-dimensional Fermi liquid

behavior at the higher temperatures to a phase with quite different behavior at lower temperatures. Properties near the crossover may perhaps be influenced by the strength of the interlayer coupling, and some experiments are proposed to examine this.

Summary of Properties of Expanded Alkali Metals

When heated from the melting point to the liquid–gas critical point, Cs undergoes a roughly fivefold volume expansion. Freyland has measured the total magnetic susceptibility along the liquid–vapor coexistence curve from the melting point up to the critical region [1]. It is clear from these experiments that the magnetic properties of the dilute metal exhibit new features. Figure 1 already shows the density dependence of the volume spin susceptibility $\chi'(0, 0)$ extracted from the measured total susceptibility [1] by correcting for the ionic and electronic diamagnetism [2,3]. These data show an initial decrease of the susceptibility with decreasing density, followed by increasing enhancement at lower densities until $\chi'(0, 0)$ reaches a limit imposed by the Curie susceptibility evaluated for one electron per atom. ^{133}Cs Knight shift data shown later will be seen to exhibit a similar enhancement effect.

Turning next to structure, neutron experiments of Jüngst et al. [4] have recently yielded the liquid structure factors of Cs at various thermodynamic states along the liquid–vapor coexistence curve. Motivated by this data and its interpretation, theory and results will be summarized on electrical resistivity, in relation to the magnetic susceptibility already discussed, over a substantial density range. A key quantity in the interpretation will be the magnitude q of the discontinuity in the electronic momentum distribution at the Fermi surface, q being unity in a non-interacting Fermi gas (cf. Fig. 2). Especially from the magnetic susceptibility, when used in conjunction with either (i) phenomenology or (ii) elevated temperature heavy Fermion theory, q can be estimated at a characteristic density, and can be compared with its calculated value in the jellium model. This demonstrates the

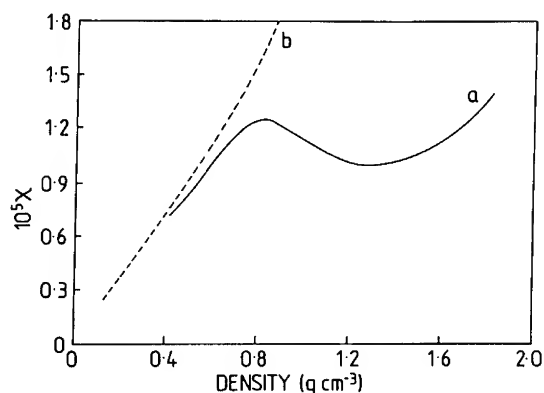


Figure 1. Magnetic susceptibility of expanded Cs along liquid–vapor coexistence curve. Dashed curve depicts Curie limiting law (after Warren [2]).

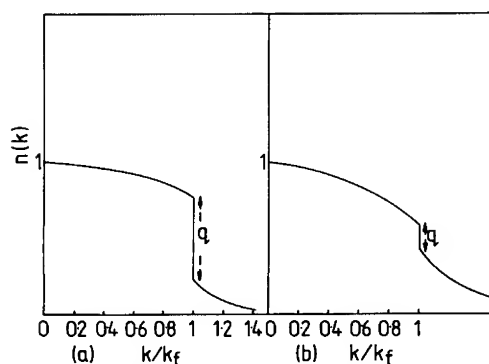


Figure 2. Schematic representation of electronic momentum distribution $n(k)$ as a function of k/k_f , where k_f is the Fermi wave number. (a) Depicts schematically reduction from unity (for Fermi gas) of Fermi surface discontinuity q due to electron-electron interactions. (b) Shows further reduction in q , at same density as in (a), when jellium background is replaced by granular ions.

importance of electron-ion interaction, as well as electron-electron correlation, as the critical point of Cs is approached. It is then shown that q can be used to forge a somewhat surprising link between a transport property, electrical resistivity, and a static property, magnetic susceptibility. Experimental data are employed to confirm this link directly.

Theory of Magnetic Susceptibility

A brief outline will first be given of an extension of the phenomenological theory of March et al. [5], which was posed for metal-insulator transitions occurring at absolute zero, to elevated temperatures (see also Chapman and March [6], where a microscopic theory based on heavy Fermion ideas at $T \neq 0$ was developed).

One writes, phenomenologically, the free energy per atom as an expansion in the magnetization per atom, m , and the discontinuity (quasiparticle renormalization factor) q in the electronic momentum distribution $n(k)$. Thus

$$F(m, q, T) = E_0 + a(T)m^2 + b(T)q + c(T)q^2 + \dots + e(T)qm^2 + \dots \quad (1)$$

Here, the interpretation of q in terms of the average number of doubly occupied sites (see March et al. [5] at $T = 0$) is more appropriate, since the discontinuity in the single-particle occupation number will not be such a well-defined quantity when $T \neq 0$. Furthermore, as $T \rightarrow \infty$, one expects (Warren [2]) a reversion to Curie-like behavior in the (paramagnetic contribution to) magnetic susceptibility, as the degeneracy temperature of the Fermi liquid is exceeded. This is achieved if $a(T)$ in Eq. (1) is proportional to T , with the coefficient $e(T)$ much less strongly dependent on T , and remaining finite as $T \rightarrow 0$. Thus, if $a = \alpha T$, then as $T \rightarrow \infty$, $\chi \rightarrow n_0 \mu_0 \mu_B^2 / 2\alpha T$, and for lower temperatures χ is always less than this limiting value,

for all densities. If α is chosen as $(\frac{1}{2})k_B$ this is simply the Curie law for the electrons. In the opposite $T \rightarrow 0$ limit, one has $\chi \rightarrow n_0\mu_0\mu_B^2/2eq$ and one requires $1/2e \rightarrow N(E_F)$, the density of states at the Fermi level in the limit of high density ($q \rightarrow 1$), to regain the Pauli susceptibility. A crossover between Curie- and Pauli-type susceptibility will therefore correspond to the condition where $a \sim eq$, i.e., $2eq \simeq k_B T$.

Chapman and March have used heavy Fermion theory to estimate q at the maximum in χ shown in Figure 1 (see Warren [2], Freyland [1], and Bottyan et al. [7]). They find $q \sim 0.18$, a result which has subsequently been confirmed by Warren [3] using NMR data (see also the subsection after next).

It is important to contrast the above with the result of the jellium model at the same density: here, from the work of Lantto [8], q is 0.53. The conclusion is clearly that at the density of 0.8 g cm^{-3} corresponding to the maximum in χ in Figure 1, both electron-electron interactions (reducing q in jellium from 1 in the noninteracting case to 0.53 at 0.8 g cm^{-3}) and electron-ion interactions ($q \sim 0.18$ at same density) are important in determining the properties of expanded fluid Cs.

Magnetic Susceptibility of Strongly Correlated Expanded Cs Related to Electrical Resistivity near Criticality

Having discussed theories of χ in the previous subsection, the purpose of this section is to expose an intimate link between χ and electrical resistivity R , which is forged via the discontinuity q . In Figure 2(a), a schematic representation is shown of the electronic momentum distribution $n(k)$ as a function of k/k_F in the jellium model. Figure 2(b) depicts schematically the reduction in q , at the same density as in Figure 2(a), due to the introduction of granular ions. While in (a), it is evident that electron-electron correlation is already strong, (b) shows that this is also the case for the electron-ion interaction (at a density $\sim 0.8 \text{ g cm}^{-3}$ in expanded Cs; see Figure 2).

To relate χ and R , let us note first from the discussion of the previous subsection that if the Curie limiting susceptibility is denoted by χ_c , then

$$\frac{1}{\chi} - \frac{1}{\chi_c} \propto q, \quad (2)$$

leading to χ tending to the dashed curve in Figure 1 as q is reduced on approaching the critical point.

Turning to the electrical resistivity R , it has to be said that there is presently no fully satisfactory electronic transport theory for strongly correlated electrons. Therefore, to gain orientation, as well as to provide motivation for a particular presentation of experimental data on R and χ below, let us employ the independent electron force-force correlation function formula of Rousseau, Stoddart, and March (RSM) [9]. The one-body nature of this equation is reflected in:

- (i) The appearance of a one-body scattering potential $V(r)$.
- (ii) The use of the Dirac density matrix ρ , which satisfies the idempotency condition $\rho^2 = \rho$.

As to (i), it is to be noted that one has the equation of motion for the Dirac density matrix as

$$\nabla_{\mathbf{r}_1}^2 \rho - \nabla_{\mathbf{r}_2}^2 \rho = \frac{2m}{\hbar^2} [V(\mathbf{r}_1) - V(\mathbf{r}_2)] \rho. \quad (3)$$

Dividing both sides by ρ , one can then form both the forces $\partial V(\mathbf{r}_1)/\partial \mathbf{r}_1$ and $\partial V(\mathbf{r}_2)/\partial \mathbf{r}_2$ solely in terms of the Dirac density matrix ρ , and hence these forces can be eliminated from the RSM formula. This leads to a formula for the electrical resistivity R , which is solely a functional of the Dirac density matrix.

However, for orientation, let us now assume that R can be characterized in the many-electron case by replacing the Dirac density matrix ρ above by the first-order density matrix γ , which satisfies $\gamma^2 < \gamma$, essentially because of the Pauli exclusion principle. With jellium as an example, one has

$$\rho_0 \propto \sum_{|\mathbf{k}| \leq k_F} \exp(i\mathbf{k} \cdot \mathbf{r}_1 - \mathbf{r}_2), \quad (4)$$

whereas

$$\gamma_0 \propto \sum_{\text{all } k} n(k) \exp(i\mathbf{k} \cdot \mathbf{r}_1 - \mathbf{r}_2). \quad (5)$$

The final step then is to expand $R \equiv R[\gamma(\mathbf{r}_1, \mathbf{r}_2)]$ when q is small as

$$R = R_0 + qR_1 + \dots \quad (6)$$

Since, as noted in Eq. (2), $(1/\chi - 1/\chi_c)$ provides an empirical measure of the discontinuity q , substitution in the (assumed) expansion (6) motivates the final plot, using experimental data, of R vs. $(1/\chi - 1/\chi_c)$. There is a striking correlation, as shown in Figure 3.

Knight Shift and Mass Enhancement

Independent support for the use of elevated temperature heavy Fermion theory (Chapman and March [6]) for expanded Cs comes from work reported very recently by Warren [3], who analyzed Knight shift data on this system. The summary below is based on his work, and strongly supports the conclusions of Chapman and March.

Brinkman and Rice [10] predicted an enhancement of the effective mass (m^*) as a consequence of the reduced instantaneous fraction of doubly occupied sites. The susceptibility and Knight shift data shown in Figures 1 and 4 thus immediately raise the question: Given the conventional description of the magnetic properties of the dense metal, is the enhancement of $\chi'(0, 0)$ observed in the dilute metal a result of increase of the interaction parameter α or an enhancement of the effective mass?

The apparent limitation of the susceptibility by the Curie value suggests the answer. Because the Stoner parameter can, in principle, approach arbitrarily close to unity, there is no reason for the Stoner-enhanced susceptibility to be limited at the Curie value. A mass-enhanced susceptibility, on the other hand, cannot exceed

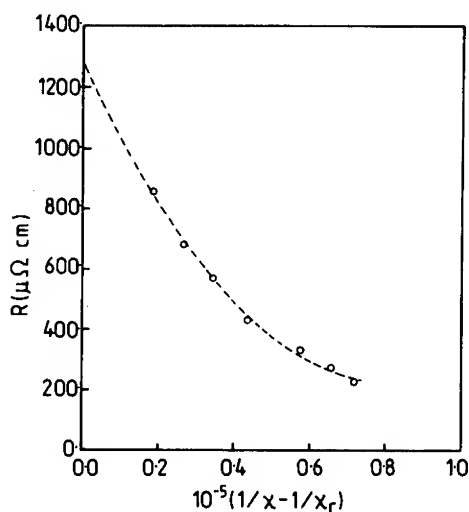


Figure 3. Shows relation between measured electrical resistivity R and deviation from Curie law $(1/X - 1/X_c)$. Plot is motivated by elimination of Fermi surface discontinuity q between Eqs. (2) and (6).

the Curie value. Increase of m^* is necessarily accompanied by a decrease in the Fermi energy as the bands narrow, and, when E_F approaches $k_B T$, a Curie susceptibility is to be expected.

The enhancement of the effective mass can be estimated using a free electron form of the electronic density of states with the mass ratio m^* as a parameter. Results of this simple model plotted in Figure 5 show a striking increase from $m^* \simeq 1$ at a mass density $\rho = 1.3 \text{ g cm}^{-3}$ to $m^* \simeq 5$ at $\rho = 0.8 \text{ g cm}^{-3}$. As discussed

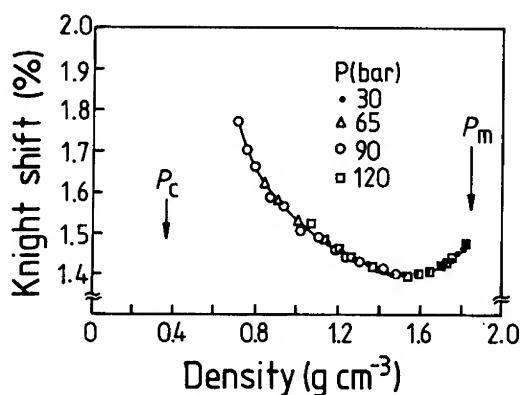


Figure 4. Knight shift data on expanded liquid Cs vs density. Data obtained at different pressures exhibited on plot. (After Warren [3].)

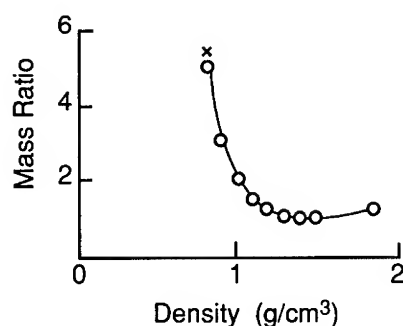


Figure 5. Enhancement of effective electron mass estimated using a free electron form of the electronic density of states. Circles are from work of Warren [3]. Cross obtained earlier by Chapman and March [6] at density of 0.8 g cm^{-3} .

above, Chapman and March [6] earlier obtained a similar mass enhancement at 0.8 g cm^{-3} using a finite-temperature extension of the Brinkman-Rice theory.

Recent measurements [11] of the optical reflectivity of expanded Cs provide an independent confirmation of the onset of mass enhancement. The plasma frequency $\omega_p = 4\pi n_e^2/m_{\text{eff}}$ is determined by the electron density n_e and the effective mass and can be extracted from the Drude contribution of the optical response. "Optical" values of m^* have been derived from the reflectivity data and can be compared with the "magnetic" masses in the same density range. While there is a systematic difference of roughly 20% between the magnetic and optical masses, the latter show a clear onset of enhancement at the same density as the susceptibility enhancement onset. From two distinctly different experiments, therefore, one now has clear evidence for the enhancement of the electron effective mass in the dilute metal (see also Warren [3]).

A second predicted feature of the highly correlated metal is the development of antiferromagnetism [3]. This behavior is quite different from the dense metal where, as discussed in the previous section, electron interactions push the system in the direction of ferromagnetism. Korringa ratios $\eta < 1$ provide clear experimental signatures of ferromagnetic correlation effects in the alkali metals at normal densities. Figure 6, following Warren [3], shows the behavior of the Korringa ratio in expanded Cs as a function of density. Below a mass density of about 1.4 g cm^{-3} , η begins to increase, and values exceeding unity are observed at the lowest densities. This result is clearly inconsistent with the generalized Stoner picture, for which increasing interaction effects would lower the Korringa ratio (cf. Warren [3]).

The increase in Korringa ratio at low density reveals a change in the character of spin correlations from the ferromagnetic tendency in the dense metal to antiferromagnetic-like correlation in the dilute conducting phase. Values of $\eta > 1$ require an increase in $\chi''(Q, \omega_0)$ at nonzero Q relative to the $Q = 0$ value. This implies an antiferromagnetic fluctuation peak at some value of Q which, if the peak were to diverge, would correspond to the antiferromagnetic Q vector. It is not possible to determine the detailed Q dependence of $\chi''(Q, \omega_0)$ from the NMR data

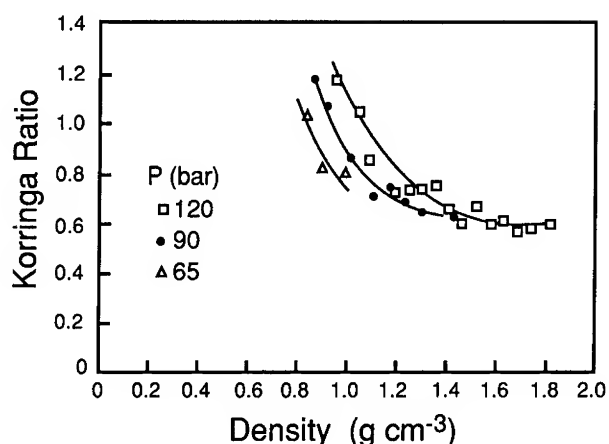


Figure 6. Behavior of Korrington ratio in expanded liquid metal Cs as a function of density. Increase at low density heralds change in nature of spin correlations from “ferromagnetic-like” in dense metal to “antiferromagnetic-like” behavior in dilute Cs. (Redrawn from Warren [3].)

alone, but Warren has suggested a model dependence that is consistent with the observed η values (see Fig. 6). It seems from Warren’s work likely that the system is far from an antiferromagnetically ordered state.

High Temperature Superconductors: Relation between Transport and Magnetism

Concerning high T_c copper oxides, the author [12] has recently emphasized, in a related context, the importance for the properties of the electron or hole liquids in the normal state that these are flowing through antiferromagnetic assemblies of copper spins. To press in this case the correlation referred to above between electrical resistivity and magnetic susceptibility, a useful starting point is afforded by the two-dimensional Fermi liquid study of Kohno and Yamada [13]. These workers link the electrical resistivity R with the magnetic susceptibility $\chi(\mathbf{Q})$, where \mathbf{Q} is the antiferromagnetic wave vector. In particular, the analysis of Kohno and Yamada leads to the proportionality

$$R \propto T^2 \chi(\mathbf{Q}). \quad (7)$$

They note then that if the further assumption is made of Curie–Weiss form $C/(T + \theta)$ for $\chi(\mathbf{Q})$ with $\theta > 0$, then one has for $T \gg \theta$ that $R \propto T$, which is an experimental finding over a substantial range of temperature in the normal state of high T_c superconductors (see, for example, Fig. 3 of Ref. [12]).

Following Egorov and March [14], one can test the form (7) of Kohno and Yamada [13] by linking it with a quite different property, namely, the nuclear spin-lattice relaxation time T_1 at copper sites. The above workers use their same Fermi liquid analysis to link T_1 with $\chi(\mathbf{Q})$ via

$$(T_1 T)^{-1} \propto \chi(Q). \quad (8)$$

Substituting the form $\chi(Q)$ in Eq. (8) into Eq. (7), one is led to the further prediction

$$RT_1 \propto T, \quad (9)$$

and experimental values of R and T_1 have been used to construct Figure 7. The prediction (9) is well borne out at the higher temperatures in the plot of Figure 7, but there is a marked deviation from the two-dimensional Fermi liquid prediction (9) at the lowest temperatures shown.

This behavior will now be shown to have parallels in the forms of Hall coefficient and thermopower over a similar temperature range.

Hall Coefficient and Thermopower

Returning to the introductory points made on strongly correlated electrons in the liquid alkalis approaching criticality, the author [15] has argued elsewhere, again from Fermi liquid theory, that the Hall coefficient R_H is itself closely connected with electrical resistivity R . However, though Kohno and Yamada [16] have given a general expression for the Hall coefficient based on Fermi liquid theory, the situation is not, it would appear, sufficiently well understood to lead to an immediate relation to $\chi(Q)$ appearing in Eqs. (7) and (8). Therefore, we shall here content ourselves with noting that the various curves of R_H can be scaled approximately. If, as noted in [12], for example, one considers R_H^{-1} instead of R_H then the slope of R_H^{-1} correlates with the superconducting transition temperature T_c .

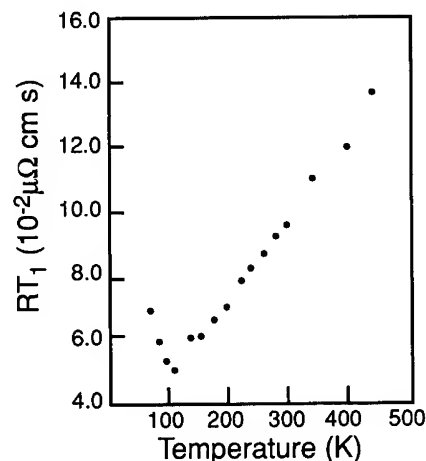


Figure 7. Experimental data for electrical resistivity R and nuclear spin-lattice relaxation time T_1 at copper sites for normal state of high T_c $\text{YBa}_2\text{Cu}_4\text{O}_8$. Plot shown is motivated by two-dimensional Fermi liquid prediction in Eq. (9). Departure from Fermi liquid is evident below 100 K (see Egorov and March [14]).

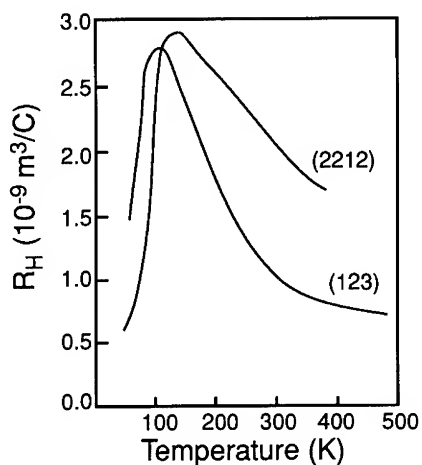


Figure 8. Behavior of Hall coefficient R_H for high T_c copper oxides (compare Egorov and March [14]) vs. temperature.

The turning points of the Hall coefficient and the thermopower, plotted in Figures 8 and 9, respectively, are in the same temperature regime as the minimum in Figure 7. It is tempting then to ascribe all the turning points to a common feature. While various possible explanations come to mind, e.g., the transition from Fermi liquid to Luttinger liquid behavior, evidence will be presented below that is consistent with the assumption that one is observing, in Figure 7 and possibly also in Figures 8 and 9, “crossover” behavior from a strongly correlated two-dimensional Fermi liquid behavior at the higher temperatures to a new phase, with quite different

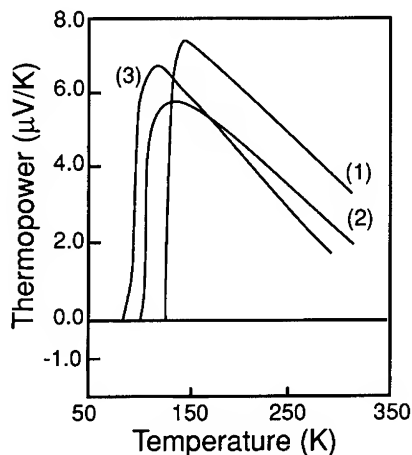


Figure 9. Similar to Figure 8 but now for thermopower.

behavior at the lower values of T in Figure 7. It is natural then to look for evidence for the importance of interlayer coupling.

Crossover Behavior and Interlayer Coupling

While Harshman and Mills [17] have given arguments for the relevance of interlayer coupling in high T_c materials, the work of a Japanese group [18] has demonstrated more recently a correlation between T_c itself and the strength of the interlayer coupling. It seems clear, therefore, that it will be interesting for the future if measurements can be made to reproduce Figures 7–9 for high T_c materials with different interlayer coupling strengths. The test of the “crossover” behavior above is whether then the “turning point” temperatures T_t prove to move in a way correlated with the strength of the interlayer coupling.

Discussion and Summary

It seems remarkable that, at least in the expanded alkalis and in high T_c materials in the normal state, there is an intimate relation between nonequilibrium transport properties and a thermodynamic quantity, the magnetic susceptibility. The origin in each case can be traced directly to Fermi liquid behavior: In high T_c to two-dimensional behavior and its antiferromagnetic consequences.

But it is important to understand the “crossover” behavior in Figures 7–9 from a fundamental point of view. This behavior may perhaps be explained in terms of interlayer coupling, and the consequent change from two-dimensional Fermi liquid behavior to a new phase with quite different behavior as the temperature is lowered.

Acknowledgment

The author thanks Mr. S. A. Egorov for stimulating correspondence and much help with parts of the work reported here.

Bibliography

- [1] W. Freyland, *Phys. Rev.* **B20**, 5104 (1979).
- [2] W. W. Warren, *Phys. Rev.* **B29**, 7012 (1984); see also N. H. March, in *Recent Developments in the Physics of Fluids, Int. Symposium*, Oxford, UK, IOP, Section 3, 1991, p. F189.
- [3] W. W. Warren, *J. Phys. Condensed Matter Suppl* **34B 5**, B211 (1993).
- [4] S. Jüngst, B. Knuth, and F. Hensel, *Phys. Rev. Lett.* **55**, 2160 (1989); see also R. Winter and F. Hensel, *Phys. Chem. Liq.* **20**, 1 (1989).
- [5] N. H. March, M. Suzuki, and M. Parrinello, *Phys. Rev.* **B19**, 2027 (1979).
- [6] R. G. Chapman and N. H. March, *Phys. Rev.* **B38**, 792 (1988); see also D. E. Logan, *J. Chem. Phys.* **94**, 628 (1991).
- [7] L. Bottyan, R. Dupree, and W. Freyland, *J. Phys.* **F13**, L173 (1983).
- [8] L. J. Lantto, *Phys. Rev.* **B22**, 1380 (1980).
- [9] J. S. Rousseau, J. C. Stoddart, and N. H. March, *J. Phys.* **C4**, L59 (1971).
- [10] W. F. Brinkman and T. M. Rice, *Phys. Rev.* **B2**, 4302 (1970).
- [11] B. Knuth, Thesis, Universität Marburg, unpublished; see also W. W. Warren, *J. Phys. Condensed Matter Suppl.* **34B 5**, B211 (1993).
- [12] N. H. March, *Phys. Chem. Liq.* **25**, 65 (1993).

- [13] H. Kohno and K. Yamada, Prog. Theor. Phys. **83**, 13 (1991).
- [14] S. A. Egorov and N. H. March, to appear.
- [15] N. H. March, Phys. Chem. Liq. **19**, 59 (1989).
- [16] H. Kohno and K. Yamada, Prog. Theor. Phys. **80**, 623 (1988).
- [17] D. R. Harshman and A. P. Mills, Phys. Rev. **B45**, 10684 (1992).
- [18] A. Maeda and K. Uchinokura, Annual Report, Engineering Research Institute, University of Toyko, 1991, Vol. 50, p. 101.

Received February 15, 1994

Complexity of Entanglements and Degree of Folding in Branched Polymers with Excluded-Volume Interaction

GUSTAVO A. ARTECA

*Département de Chimie et Biochimie, Laurentian University—Université Laurentienne,
Ramsey Lake Road, Sudbury, Ontario, Canada P3E 2C6*

Abstract

A methodology to characterize large-scale shape of macromolecular conformations is generalized and applied to a simple model of branched polymers. The standard global analysis of polymer configurations uses geometric shape descriptors, such as the mean radius of gyration. However, geometric descriptors alone do not depict well the intricate folding features found in many macromolecules. For a more complete characterization, we employ here a new class of shape descriptors which convey the degree and complexity of the "entanglements" in a branched chain. Recently, the methodology has been applied to study statistical properties of linear polymer chains. In the present work, we extend the technique to branched polymers and analyze the configurational and long-chain behavior of their entanglement descriptors. A family of "stars" (polymers with a single branchpoint) with excluded volume interaction is studied, and the results are contrasted with those for linear chains. The relation between changes in geometric and shape descriptors within the polymer conformational space is presented. The complexity of entanglements for large chains and large stars are compared. The results suggest a similar scaling behavior of the entanglement descriptors for the two polymer architectures. © 1994 John Wiley & Sons, Inc.

Introduction

Assessing global features of three-dimensional (3D) macromolecular shape is essential for an understanding of polymer structure and function. Physical properties such as elasticity, viscosity, and melting points can be related, to some extent, to the nature of large-scale entanglements of single polymer configurations, in addition to local and intermolecular interactions [1,2]. Molecular recognition and catalytic functions of enzymes are also strongly related to the global folding features of the macromolecular backbone [3,4].

Standard tools for the global analysis of polymer configurations include geometry-derived parameters, such as the mean radius of gyration and the mean end-to-end distance in the chain [1,2]. These *geometric descriptors* convey mostly size and, to some degree, the compactness of the chain's configuration. Most of these descriptors can be measured experimentally, and they allow one to follow the polymer's response to exterior variables. For instance, several *phase transitions* in polymers (e.g., swelling) involve *configurational transitions* in single molecules [5,6]. These transitions

are marked by a rapid change in geometric descriptors as a function of an external parameter, such as the temperature of a thermostat exchanging heat with the molecule.

A more informative analysis of polymer shape is achieved by monitoring both geometric and topological properties. Topological properties include features such as knotting and entanglements in closed-loop polymers [6–8]. Recently, a characterization of global folding features of macromolecules has been proposed, based on the occurrence of crossings in the two-dimensional (2D) projections of a rigid backbone [9]. From this information, one derives the *probability of overcrossings of a rigid polymer configuration* [10], which provides a description of the *complexity of self-entanglements* (or *degree of folding*) in molecular chains. A related approach has been presented for self-avoiding walks [11]. This methodology presents some advantages over purely topological approaches: the analysis uses (and preserves) the geometry of a rigid configuration, whereas the features described go beyond size and compactness. The term *geometric descriptor* will be reserved to parameters which depend only on the polymer geometry. The term *shape descriptor* will be used for the parameters which depend on both molecular geometry *and* backbone connectivity. The descriptors of entanglement complexity we study in this work belong to the latter class and therefore combine aspects of the geometry and the topology of the polymer chain.

In Ref. [12], we have shown evidence that a marked change in entanglement descriptors also accompanies a configurational transition in a linear polymer, caused by either a temperature change or a change in excluded volume. For this reason, the fluctuations in the shape descriptors along dynamic trajectories have been used to monitor molecular flexibility and detect configurational transitions [12,13].

Similarly, averaging shape descriptors over molecular conformations provides insights on the configurational state of the polymer [12,14]. The change in configurational averages over various parameters (e.g., temperature, chain length) is a valuable piece of information. The configurationally averaged geometric descriptors, such as the radius of gyration, satisfy simple power laws in terms of the number of monomers [5,15]. Similar scaling behavior has been found for shape descriptors of linear chains, although with different exponents and small dependence on excluded volume [14,16].

Statistical properties of geometric descriptors of polymer architectures other than the linear one have been studied in the past few years [17–19, and refs. therein]. Special attention has been given to branched structures because these are often found experimentally in liquid crystal polymers. These polymer architectures (also referred to as “topologies”) include [17]: *stars* (polymers with several branches stemming from a single branchpoint), *combs* (two or more single-branch branchpoints, with either regular or random positions for branches of various lengths), and *brushes* (several multibranch branchpoints, with either free branches or branches grafted onto a surface). In cases, the scaling behavior of geometric descriptors is the same as for linear polymers [18,19]. Differences are found for some polymer architectures with special constraints in the number and length of the branches [17]. No information is available so far for descriptors other than geometric ones.

In this work, we begin the study of branched polymers from the viewpoint of entanglement descriptors. In the next section we discuss the extension of the methodology to the analysis of nonlinear polymers and test the accuracy of the configurational averages of their geometric and shape descriptors. Another section compares the conformations of linear polymers and "regular" stars with excluded-volume interaction. The relation between geometric and shape descriptors of these configurations is discussed and some approximate scaling is established. A further section compares shape descriptors of stars and chains with the same (large) number of monomers and discusses their scaling behavior. Conclusions and aspects for further research are found in the closing section.

Global Descriptors of Entanglements in Linear and Branched Polymers

In this work, *degree and complexity of entanglements* in a single polymer is used as equivalent to a "degree of folding" of a rigid configuration. Here, a molecular backbone is more "entangled" the more complex and numerous are the turns, twists, or folds in the chain. In this context, we describe the macromolecular shape by using an intuitive notion. The more entangled a rigid backbone, the larger the *mean number of "bond-bond crossings"* that it would exhibit when projected onto two dimensions. This mean number can be derived from the probability of observing a given number of branches crossing over each other when the rigid polymer chain is "photographed" from an arbitrary viewing direction [10,12].

The quantitative evaluation of the probabilities of observing projected crossings has been discussed in detail elsewhere for linear polymers [10,13]. The extension for branched polymers is straightforward. When projected onto a plane, a polymer with an arbitrary monomer connectivity will exhibit a number of "double points" [7] produced by two or more bonds *crossing over* each other. For this reason, these double points are here referred to as *overcrossings*. Overcrossings can be due to two bonds belonging to the same branch of the polymer or to two different branches.

From our viewpoint, the number of observed overcrossings characterizes a given 2D projection. The average of this number over *all possible projections* characterizes the polymer at the given configuration. Finally, the average of the mean number of overcrossings over all possible polymer configurations is a characteristic of the topology, number of monomers, and physical parameters defining the macromolecule.

The actual descriptors of entanglement complexity are as follows. Let n be the number of monomers (or main chain "atoms") for a generic polymer. The probability of observing N overcrossings ($N \geq 0$) at a given polymer configuration K_i will be indicated as $A_N(n)$. [If required, the dependence with the configuration will be denoted by $A_N(n,i)$.] The distribution of overcrossing probabilities satisfies:

$$\sum_{N=0}^{\max N} A_N(n) = 1, \quad \forall n \geq 3, \quad (1)$$

where $\max N$ depends on the polymer architecture (i.e., monomer connectivity). For linear chains, $\max N = (n-2)(n-3)/2$. As discussed elsewhere, the distribution

$\{A_N(n)\}$ is a *global shape descriptor* [10], which conveys aspects of the polymer's folding. A configuration exhibiting little degree of entanglement is characterized by high $A_N(n)$ values for low N (i.e., it will appear usually in placements with few overcrossings). In this work, we shall use only two shape descriptors derived from $\{A_N(n)\}$, namely, the probability (A^*) of the most probable number of overcrossings (N^*):

$$A^* = A_{N^*}(n) = \max_{\{N\}} A_N(n) \quad (2)$$

and the *mean number of overcrossings* \bar{N} :

$$\bar{N} = \sum_{N=0}^{\max N} N A_N(n) \quad (3)$$

The conformational dependence of these two shape descriptors will be indicated by $(A^*)_i$ and $(\bar{N})_i$ for a generic configuration K_i , whenever needed.

The actual computation of overcrossing probabilities for branched polymer configurations can be carried out as discussed in Refs. [9] and [10], with only minor changes to the algorithm. For each polymer configuration, the probabilities $\{A_N(n)\}$ and the mean number \bar{N} are evaluated in this work up to three significant figures.

We have computed the shape descriptors A^* and \bar{N} for a series of branched polymer configurations. Architectures for branched polymers up to six monomers

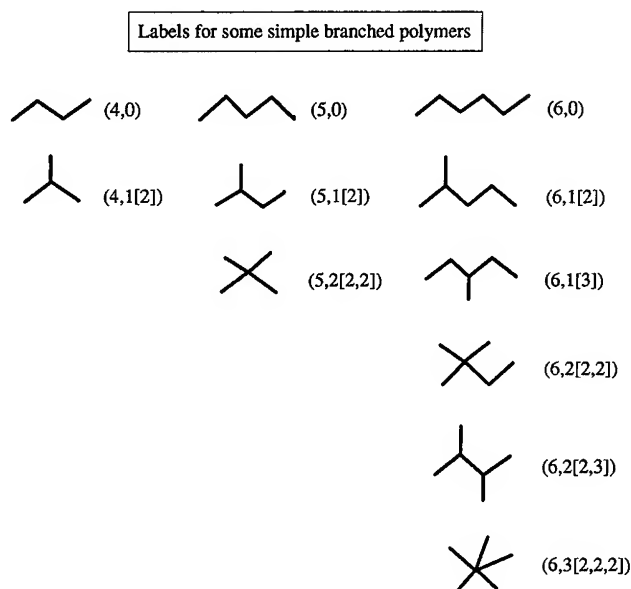


Figure 1. List of polymer architectures with number of main chain atoms $n < 7$. [See text for the labels $(n, b[z_1, z_2, \dots])$. These simple branched polymers are used to test the accuracy of the conformational searches.]

are listed in Figure 1. For simplicity, we shall identify these polymer "topologies" with the label $(n, b[z_1, z_2, \dots])$, where n is total number of monomers, b is the number of branches attached to the main chain, and z_1, z_2, \dots label the location of the main chain atoms where the branches occur. This simple nomenclature is enough for the present purposes. In Figure 1, the polymers $(4, 1[2])$, $(5, 2[2,2])$, $(6, 3[2,2,2])$ identify stars, since they have a single branchpoint ("atom" 2). Moreover, these are *regular stars* [16], because the length of each branch is identical. In later sections, we shall use the term "star" with the restricted meaning of a *regular 3-star*, a branched polymer with three segments of the same length stemming from the single branchpoint. [Note that $b = 1$ for 3-stars.]

For a given polymer architecture, the actual configurations are generated by constrained random walks, with a purely repulsive interaction between monomers due to excluded volume. When generating these configurations, the constraints are as follows: (1) The distance between any two *bonded* atoms is a constant ℓ (i.e., a constant Kuhn's length [5]); (2) The distance between any two *nonbonded* atoms must be larger than or equal to a constant r_{ex} , the *radius of the excluded volume*. Otherwise, the positions of the atoms are arbitrary. The actual algorithm is discussed in more detail in Refs. [12] and [14].

Due to the simple form of the potential energy for the monomer interaction, all configurations which satisfy the above two constraints have the same statistical weight. Therefore, the configurational averages correspond to the microcanonical ensemble, and the averaged shape descriptors can be expressed as follows:

$$\langle A^* \rangle \approx \frac{1}{M} \sum_{i=1}^M (A^*)_i \quad (4a)$$

$$\langle \bar{N} \rangle \approx \frac{1}{M} \sum_{i=1}^M (\bar{N})_i \quad (4b)$$

where M ($M \gg 1$) is the number of (random) polymer configurations generated. [In practice, we have added configurations until reaching a desired stability in the averages $\langle A^* \rangle$ and $\langle \bar{N} \rangle$.] The fluctuations in the molecular shape can be represented by standard deviations in the shape descriptors, such as $\sigma_{A^*} = (\langle A^{*2} \rangle - \langle A^* \rangle^2)^{1/2}$.

The instantaneous and configurationally averaged values of the geometric descriptors are evaluated in the same manner. In what follows, we shall compare the behavior of $\langle A^* \rangle$ and $\langle \bar{N} \rangle$ with that of the radius of gyration. The instantaneous value of the radius of gyration for a given configuration is indicated as R_G , and its configurational average as $\langle R_G \rangle$. Another useful geometric descriptor is R , the radius of the smallest sphere (centered at the center of mass of the chain) that encloses the polymer completely [12]. Its corresponding average will be indicated by $\langle R \rangle$.

Each averaged geometric and shape descriptor is obtained for a given topology, number of monomers n , and given values for the parameters ℓ and r_{ex} . [Note that the actual results depend only on the ratio r_{ex}/ℓ .] A useful parameter combining the latter is $y = r_{ex}/r_c$, where r_c is the *critical (or maximum possible) radius of excluded volume*. For radius of excluded volume $r_{ex} > r_c$, no polymer configuration can be found where all atoms satisfy the constraints mentioned above. This critical

TABLE I. Convergence of configurational averages of the radius of gyration ($\langle R_G \rangle$), its fluctuation (σ_{RG}), and the minimum spherical radius ($\langle R \rangle$) for the branched "polymer" (4,1[2]) ($n = 4$ with one branch, $b = 1$). (All data are given in Å. A constant interatomic distance $\ell = 1.53$ Å is used. The exact limit corresponds to the single plane-trigonal configuration found for maximum excluded volume.)

r_{ex}	$\langle R_G \rangle$	σ_{RG}	$\langle R \rangle$
0.001	1.14	0.14	1.48
0.500	1.16	0.12	1.51
1.500	1.226	0.069	1.55
2.300	1.301	0.021	1.567
2.500	1.315	0.009	1.548
2.65004	1.3250	0.0000	1.530 (Exact values)

value r_c depends on the chosen architecture. A simple analysis gives the following values in some particular cases: $r_c = 2\ell \sin(\phi_1/2)$ for linear chains, $r_c = 2\ell \sin(\phi_2/2)$ for 3-stars, $r_c = 2\ell \sin(\phi_3/2)$ for 4-stars, where $\phi_i = \arccos(-1/i)$, for $i = 1, 2, 3$. With this notation, the completely random chains (no excluded volume) correspond to $y = 0$; in this case, the whole configurational space is accessible. On the other hand, the polymer spans the smallest possible configurational space at $y = 1$.

Note that $y = 1$ in a linear chain corresponds to precisely *one* configuration, the rod-like chain. For branched polymers this may not need the case, and one can find infinitely many configurations at the critical limit $y \rightarrow 1$. In some special cases, the values of the geometric and shape descriptors can be known exactly at this limit, thus providing a test for the accuracy of their averages and the configurational search.

Consider the simplest regular 3-star, corresponding to (4, 1[2]) in Figure 1. In this case, no bond can overcross another since any two bonds lie always on one plane. Therefore, the probability of overcrossings will be $A_N = \delta_{0N}$, where δ_{0N} is the Kronecker delta, for any configuration and any r_{ex} value. The shape descriptors in this case will be:

$$\langle A^* \rangle = 1, \quad \langle \bar{N} \rangle = 0, \quad \text{for the 3-star with } n = 4, \text{ all } y \quad (5)$$

with the configurational fluctuations in the descriptors (standard deviations) exactly zero. In contrast, the value of the radius of gyration depends on y . In the limit $y \rightarrow 1$, this particular 3-star is forced to adopt a single plane-trigonal configuration with bond angles of exactly 120° . In this case, the two geometric descriptors $\langle R_G \rangle$ and $\langle R \rangle$ are:

$$\lim_{y \uparrow 1} \langle R_G \rangle = 3^{1/2} \ell / 2, \quad \lim_{y \uparrow 1} \langle R \rangle = \ell, \quad \text{for a 3-star with } n = 4 \quad (6)$$

We have verified how the averages reach these limit values with our algorithm of configurational search. For actual calculations, we use the value $\ell = 1.53$ Å

throughout, which corresponds to a typical carbon-carbon single-bond distance in polymers. The results for $\langle R_G \rangle$, $\langle R \rangle$, and the fluctuation σ_{RG} for the $n = 4$ star are given in Table I. The averages have been computed by including enough configurations to make stable the number of significant figures shown in Table I. This typically involves some 1000 configurations. Even for this very small system, the calculations become computer-intensive near the critical r_c value, and the limit itself cannot be reached numerically. For instance, the computation of averages for $r_{ex} = 2.3 \text{ \AA}$ requires ca. 2 h CPU on a VAX-4000 computer. The numerical results in Table I tend to the limit (6). [They also verify the behavior (5) for all configurations.] It is noted that $\langle R_G \rangle$ and $\langle R \rangle$ do not behave equally in terms of the excluded volume, *contrary* to what is found in linear polymers [12,14]. The behavior of $\langle R \rangle$ is remarkable: it exhibits a *maximum* as a function of r_{ex} .

A similar analysis can be made for the special class of $(n - 1)$ -stars with only n atoms (i.e., $b = n - 3$). For these branched polymers, the results (5) hold for all configurations. Similarly, one can compute the exact limits of the geometric descriptors at the critical radius of excluded volume, since a single conformation is found. For the polymer (5, 2[2,2]) (see Fig. 1) this configuration is a tetrahedron, and one finds:

$$\lim_{y \uparrow 1} \langle R_G \rangle = 2\ell/5^{1/2}, \quad \lim_{y \uparrow 1} \langle R \rangle = \ell, \quad \text{for a 4-star with } n = 5 \quad (7)$$

The results for this polymer are found in Table II, with $\ell = 1.53 \text{ \AA}$. The numerical averages slowly reach the limit (7). The behaviors of $\langle R_G \rangle$ and $\langle R \rangle$ are similar to those in Table I.

For all other polymer architectures in Figure 1, the chains give rise to configurations which do exhibit overcrossings. In this case, one finds $\langle A^* \rangle < 1$ and $\langle \bar{N} \rangle > 0$. As an illustration, Figure 2 shows the results for the configurational average

TABLE II. Convergence of configurational averages of the radius of gyration ($\langle R_G \rangle$), its fluctuation (σ_{RG}), and the minimum spherical radius ($\langle R \rangle$) for the branched "polymer" (5,2[2,2]) ($n = 5$ with two branches, $b = 2$). (All data are given in \AA . A constant interatomic distance $\ell = 1.53 \text{ \AA}$ is used. The exact limit corresponds to the single tetrahedral configuration found for maximum excluded volume.)

r_{ex}	$\langle R_G \rangle$	σ_{RG}	$\langle R \rangle$
0.001	1.230	0.108	1.647
0.500	1.241	0.104	1.647
1.000	1.271	0.076	1.648
1.500	1.311	0.045	1.652
2.000	1.349	0.016	1.632
2.300	1.364	0.0034	1.593
2.400	1.3672	0.0010	1.566
2.450	1.3682	0.0003	1.549
2.4985	1.3685	0.0000	1.530 (Exact values)

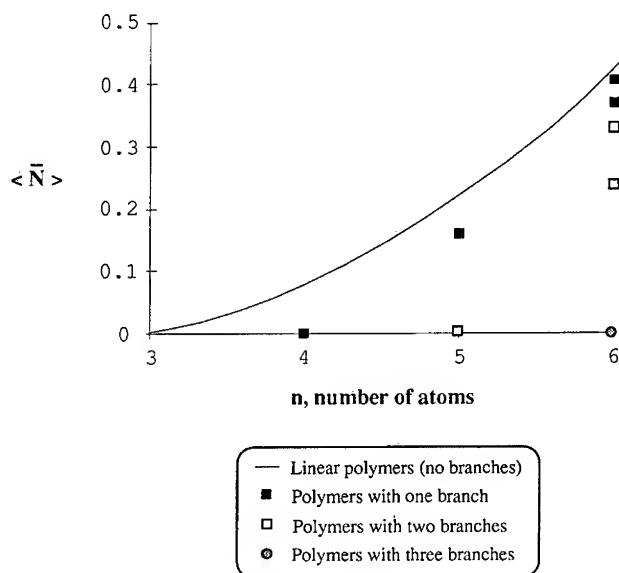


Figure 2. Configurational average of the mean number of overcrossings ($\langle \bar{N} \rangle$) for simple branched polymers. [The full line joins the results for the linear polymers and provides an upper bound for the branched polymers, which are therefore less entangled.]

of the mean number of overcrossings for all polymers in Figure 1, calculated with $r_{ex} = 0.001 \text{ \AA}$ (virtually no-excluded volume interaction). The continuous line in Figure 2 joins the results for linear chains (nonbranched random polymers). This line provides an upper bound to the $\langle \bar{N} \rangle$ values of all branched polymers with the same number n of monomers. The results indicate that the larger the number of branches for a given n , the smaller the number of overcrossings. In other words, for n fixed and small excluded volume, an increase in the number of atoms forming part of the branches reduces the complexity of the entanglements which can be formed by the polymer. This is reasonable since in this case the main chain is shortened, thereby restricting the possibilities of foldings which can give rise to complex entanglements.

The above results illustrate the computation and some elementary properties of the averaged shape descriptors of short branched polymers. In the next sections we deal with a more detailed analysis for a family of branched polymers with larger n .

Behavior of Geometric and Shape Descriptors in the Configurational Spaces of Linear Polymers and Regular Stars

In the limit of large number of atoms, the shape descriptors of branched polymers with few and short chains behave similarly to those found in linear chains. In order to test possible differences in the behaviors of branched and linear polymers, one must choose a family of nontrivial branched polymers. In what follows, we discuss

some properties of the simplest of such polymers. The chosen family are the regular 3-stars (in short, "stars"), which exhibit three single-chains of the same length stemming from a single branchpoint. [Note that the values of n in this class of stars are restricted to $n = 3n' + 1$, where $n' \geq 1$ is the number of atoms in each one of the single-chains.]

The configurationally averaged geometric properties of star polymers have been discussed in the literature as a function of the number of atoms [17,18]. In this section, we analyze the detailed interrelation between geometric descriptors and entanglement descriptors within the configurational space of linear and star polymers with a given n value. The larger- n behavior of averaged descriptors is discussed in another section.

We have surveyed the configurational space of linear and star polymers with various n values and various values of excluded volume. As a representative example, we consider here the case with $n = 16$. This corresponds to a star with three 5-atom single-chains stemming from the central atom. As illustration, the 2D projections of two random configurations are displayed in Figure 3. The left-hand side configuration (I) has been generated with virtually no-excluded volume, whereas the one on the right-hand side (II) corresponds to large excluded volume. The effect of excluded volume is clearly seen in the local geometry about the central atom (atom "6"). In the configuration II, atoms 5, 6, 7, and 12 lie closer to plane-trigonal positions. [Bond angles involving atom 6 are 102° , 112° , and 131° , and the associated dihedral angle is 146° .] The geometric descriptors reflect the general trend whereby, on average, one expects the stars with smaller excluded volume to be smaller in size (more compact). [Configuration I has the instantaneous values $R_G = 2.69 \text{ \AA}$ and $R = 4.41 \text{ \AA}$, whereas configuration II presents $R_G = 4.13 \text{ \AA}$ and $R = 6.62 \text{ \AA}$.] Similarly, the role of excluded volume in modifying the 3D shape of a polymer is well reflected in the distribution of overcrossings. Figures 4 and 5 compare the histograms of overcrossings probabilities (or overcrossing spectra) for the two star configurations. In Figure 4 there is a predominance of no-overcrossings (approximately 30% of the projections will show no overcrossings), but also a significant

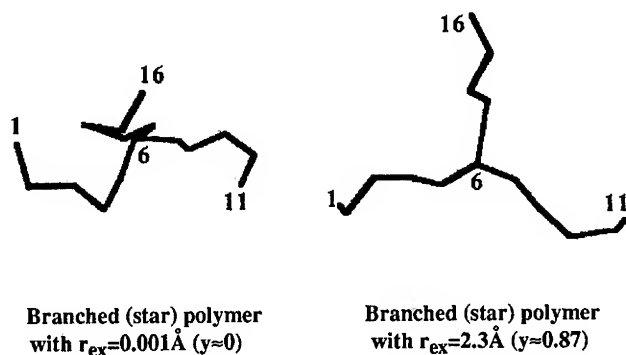


Figure 3. Two configurations for the regular 3-star with $n = 16$ and different excluded-volume parameter $y = r_{ex}/r_c$. [For these stars, $\ell = 1.53 \text{ \AA}$ and $r_c \approx 2.65 \text{ \AA}$.]

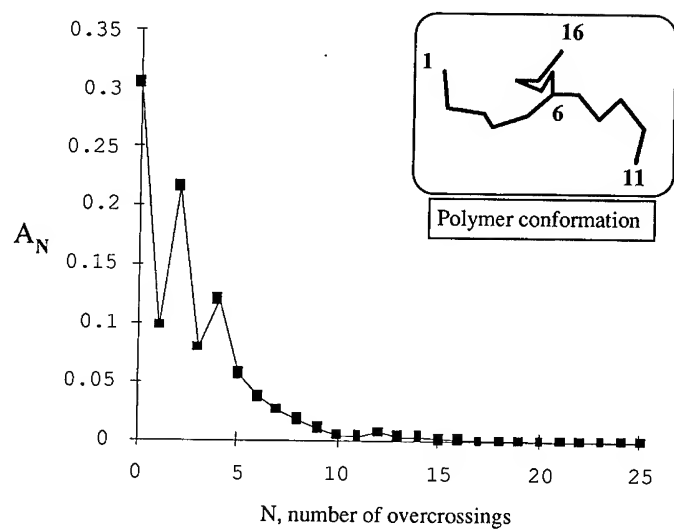


Figure 4. Overcrossing spectrum for one-star polymer configuration with $n = 16$ and small excluded volume (left-hand side in Fig. 3).

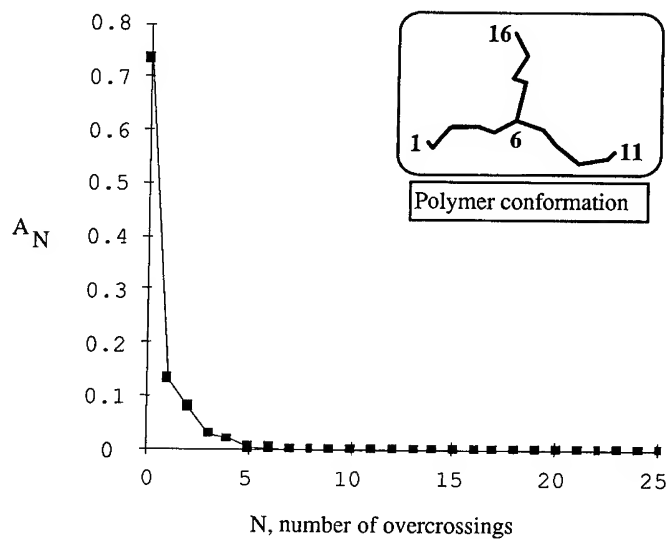


Figure 5. Overcrossing spectrum for one-star polymer configuration with $n = 16$ and large excluded volume (right-hand side in Fig. 3).

frequency of placements where the configuration exhibits 2 and 4 overcrossings. Several other overcrossing numbers have probabilities of 1% or more. Finally, the global shape of this configuration is characterized by $\bar{N} = 2.59$ and $A^* = 0.305$. In contrast, Figure 5 shows the complete predominance of no-overcrossings in the star with large excluded volume. Configuration II is characterized by $\bar{N} = 0.495$ and $A^* = 0.733$. Therefore, it can be classified as not only larger in size than configuration I but also *less entangled* (i.e., with entanglements of less complexity).

A large number of randomly generated configurations for linear and star polymers with $n = 16$ have been analyzed in the same manner. For a given excluded volume radius r_{ex} , the geometric descriptor R_G and the shape descriptors \bar{N} and A^* have been computed and monitored within the configurational space. For a given n , one would expect that the two families of descriptors, though independent from each other, should exhibit some correlation. Intuitively, for n fixed, one would expect that configurations with small size should be more entangled than configurations with large size. This notion can now be put in quantitative terms.

Figures 6 and 7 display the configurations of linear chains and stars, respectively, in 2D diagrams of instantaneous values of R_G and \bar{N} (for $n = 16$). This 2D plot represents the correlations between the size and compactness of the polymer, on the one hand, and the complexity of its entanglements, on the other. [We shall refer to this plot as a *compactness-and-entanglement map*.] Figures 6 and 7 include the first 333 configurations generated for each one of the values of excluded volume, $r_{ex} = 0.001 \text{ \AA}$, 1.5 \AA , and 2.3 \AA , for a total of 999 configurations. The diagrams indicate the most representative regions of compactness-and-entanglement values

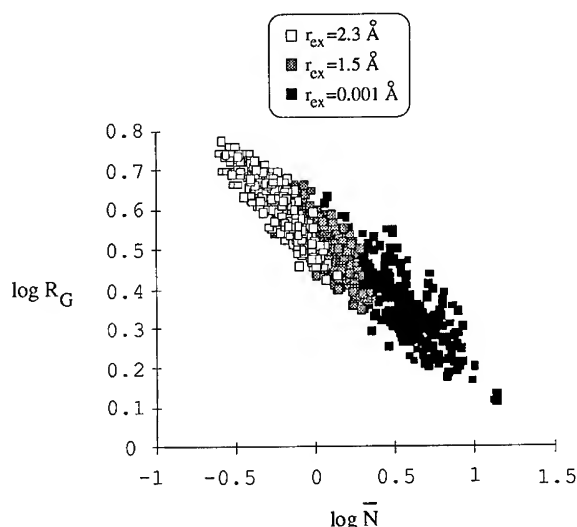


Figure 6. Compactness-and-entanglement map for configurations of linear chains ($n = 16$) with various values of excluded volume. [Each point gives the radius of gyration and mean overcrossing number for one configuration. The same number of configurations (333) are plotted for each r_{ex} value.]

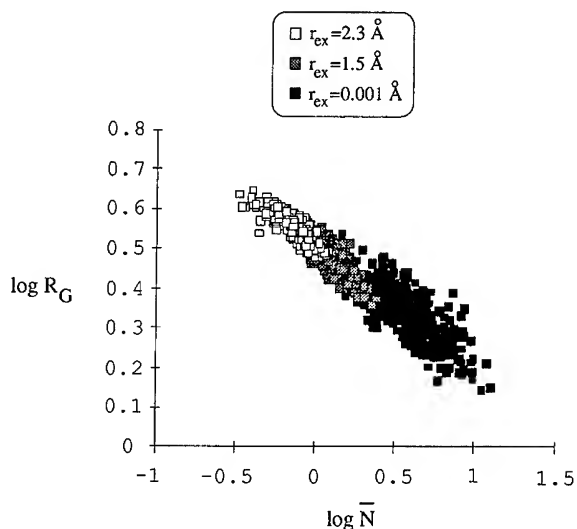


Figure 7. Compactness-and-entanglement map for configurations of regular 3-stars ($n = 16$) with various values of excluded volume. [Each point gives the radius of gyration and mean overcrossing number for one configuration. The same number of configurations (333) are plotted for each r_{ex} value.]

associated with each choice of excluded volume. [Note that the configurations for $r_{ex} = 2.3 \text{ \AA}$ (white squares) lie above some configurations found with $r_{ex} = 1.5 \text{ \AA}$. In turn, some of the latter coincide with configurations found when no-excluded volume is considered.]

The results indicate that, even though linear chains are larger in size than stars, both exhibit the same range of entanglement complexity at small and intermediate values of excluded volume. At larger excluded volume, the stars appear less entangled than chains. The result is reasonable since the critical excluded volume r_c for stars ($r_c \approx 2.65 \text{ \AA}$) is reached before the r_c value for linear chains ($r_c \approx 3.06 \text{ \AA}$), thus reducing the folding possibilities for stars. [Note that the limit $r_c \approx 2.65 \text{ \AA}$ for stars is satisfied by infinitely many configurations with $\bar{N} > 0$.]

Despite the scattering of $R_G - \bar{N}$ data, which suggests the independent nature of the two descriptors, some correlation is evident. A regression over the 999 configurations of various excluded volumes r_{ex} and $n = 16$ displayed in Figures 6 and 7 provides the following results:

$$\log R_G \approx (-0.34 \pm 0.01) \log \bar{N} + (0.539 \pm 0.004), \quad \mathcal{C} = 0.930, \text{ linear chains} \quad (8a)$$

$$\log R_G \approx (-0.31 \pm 0.01) \log \bar{N} + (0.511 \pm 0.002), \quad \mathcal{C} = 0.957, \text{ stars} \quad (8b)$$

where the 95%-confidence errors are given and \mathcal{C} is the correlation coefficient. The results express the qualitative correlation between geometric descriptors of size and compactness and the shape descriptors of entanglements. Equations (8) do not indicate a major difference between the scaling of R_G and \bar{N} in the conformational spaces of stars and linear chains. The results for various n values ($n < 100$) support

by the following qualitative relation between the instantaneous values of descriptors:

$$(\bar{N})_i \sim (R_G)_i^{-\xi}, \quad \text{for stars and linear chains, constant } n \quad (9)$$

where the exponent, rounded-off to the first significant figure, appears to be $\xi \approx 3$. The subindex "i" in Eq. (9) indicates a generic configurations K_i with constant n . The scaling (9) must be interpreted as a relation between the ranges of values of both descriptors. Actual configurations show important fluctuations about Eq. (9). A precise correlation between R_G and \bar{N} does not exist, thus suggesting that the entanglement nature of a polymer fold cannot be established on the sole basis of size and compactness.

The small dependence of Eq. (9) on the polymer architecture is probably not a general feature. If the shape descriptor A^* is chosen to monitor the entanglements, the correlation with the radius of gyration shows some dependence on the connectivity. The results with $n = 16$ and all r_{ex} values give:

$$(R_G)_i \sim (A^*)_i^{\xi}, \quad \text{constant } n \quad (10)$$

with $\xi \approx 0.55 \pm 0.05$ for stars and $\xi \approx 0.63 \pm 0.05$ for linear chains. The difference in ξ exponents appears to be beyond what can be accounted for by the configurational dispersion about the mean.

In summary, the interrelation of geometric and shape descriptors expresses quantitatively the notion that, for a given n , compact polymers are more entangled than swollen polymers. Yet, the relation between descriptors is nonlinear and exhibits large fluctuations. In the case of \bar{N} and R_G , their proportionality [Eq. (9)] depends little on the polymer topology. In the next section, the analysis is extended to the case of variable n .

Configurationally Averaged Shape Descriptors for Longer Regular 3-Stars

The scaling behavior of the configurationally averaged radius of gyration (or other "distance" descriptor such as R) with the number of monomers n is well known for a linear chain [2,5]:

$$\langle R_G \rangle \sim kn^{\nu} \quad (11)$$

in the case of long linear chains. With no excluded-volume interaction, these chains are said to be "ideal" or in their "Θ-conditions". In this case, they can be represented by gaussian statistics with an exponent $\nu = 0.5$ [2,5]. In the asymptotic limit of large excluded volume, the best estimation for the exponent is currently $\nu \approx 0.588$ [15]. In this latter case, corrections to scaling can play an important role for short chains [15]. Equation (11) is known to be valid also for regular stars [18]. Modifications in the scaling exponents appear to be needed for some special topologies [17]. These "exact" results provide a reference to test the completeness of the conformational search in the computation of averaged shape descriptors for longer chains and stars.

Figure 8 shows the present results for $\langle R_G \rangle$ in linear chains and stars with monomer numbers $n \leq 100$. The stars represented correspond to $n = 7, 16, 31, 61$, and 100, in the case of no excluded volume ($r_{ex} = 0.001 \text{ \AA}$). The computations for r_{ex}

$= 1.5 \text{ \AA}$ are much more demanding since fewer conformations pass the excluded-volume criterion. The largest star handled in this case had $n = 40$. Nevertheless, the number of monomers appears to be large enough to reach the correct large- n behavior in the radius of gyration (cf. Fig. 8). A linear regression fitting of the results in Figure 8 for $n \leq 16$ gives the exponents $\nu \approx 0.500 \pm 0.024$ for stars with $r_{ex} = 0.001 \text{ \AA}$ and $\nu \approx 0.59 \pm 0.02$ for stars with $r_{ex} = 1.5 \text{ \AA}$. The good agreement with the exact results indicates a satisfactory sampling of the configurational space. Therefore, the configurational averages $\langle A^* \rangle$ and $\langle \bar{N} \rangle$ should be as reliable as the average $\langle R_G \rangle$.

A previous analysis of shape descriptors for linear chains with excluded-volume interaction and number of monomers $20 \leq n \leq 500$ showed that the averages of $\langle A^* \rangle$ and $\langle \bar{N} \rangle$ follow similar power laws to that for the radius of gyration [14]:

$$\langle A^* \rangle \sim an^\lambda \quad (12a)$$

$$\langle \bar{N} \rangle \sim \alpha n^\beta \quad (12b)$$

The estimated exponents in Ref. [14] are $\lambda \approx -1.00 \pm 0.03$ and $\beta \approx 1.4 \pm 0.1$, for the medium-size polymers. Recent results by Whittington and co-workers [16] with longer polymer chains ($400 \leq n \leq 1500$) indicate a smaller asymptotic exponent, $\beta \approx 1.122 \pm 0.005$. The difference is certainly due to the fact that $\langle \bar{N} \rangle$ reaches the asymptotic limit slowly; the exponent $\beta \approx 1.4$ represents accurately the results in

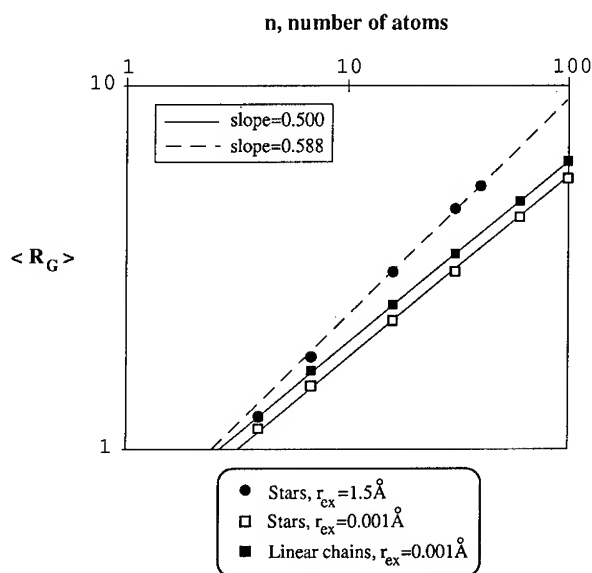


Figure 8. Scaling behavior for the configurational average of the radius of gyration $\langle R_G \rangle$ (in \AA) for linear chains and regular 3-stars with $n \leq 100$. [The slopes marked 0.5 and 0.588 correspond to the expected exact results of polymers with and without excluded-volume interaction, respectively. The agreement with the exact results ensures a thorough conformational search.]

the "cross over" regime of polymer chains of intermediate size ($n < 500$). As we show below, the results in this work support the view that power laws such as (12) also describe the molecular shape of regular 3-star polymers, at least for intermediate values of n . Our findings are summarized in Figures 9 and 10.

Figure 9 shows the results for the shape descriptor $\langle A^* \rangle$ as a function of the number of monomers n for stars with and without excluded volume. The results for the linear chains (full line) are included for comparison. The stars with no-excluded volume follow closely the behavior of linear chains. The estimated exponent in the scaling (12a) for these stars is $\lambda \approx -1.06 \pm 0.12$ ($\mathcal{C} = 0.9993$), which lies within the uncertainty of the exponent for chains [14]. In the case of larger excluded volume ($r_{ex} = 1.5 \text{ \AA}$), the largest stars we can handle are still too short to make an accurate estimation of scaling. Nevertheless, Figure 9 suggests the same qualitative behavior as the stars with no-excluded volume.

Figure 10 compares the averaged mean number of overcrossings $\langle \bar{N} \rangle$ in stars and linear chains. The results indicate a similar behavior to that found in the shape descriptor $\langle A^* \rangle$. The stars with no-excluded volume follow closely the behavior of linear chains, leading to an estimated exponent $\beta \approx 1.4 \pm 0.2$ ($\mathcal{C} = 0.9987$) for a power law as in Eq. (12b). For the regular 3-stars with $r_{ex} = 1.5 \text{ \AA}$, although the values of $\langle \bar{N} \rangle$ are smaller (i.e., lesser degree of folding), the behavior of $\langle \bar{N} \rangle$ as a function of n appears to follow the same trend observed with no-excluded volume. As commented before, this latter shape descriptor reaches its asymptotic behavior

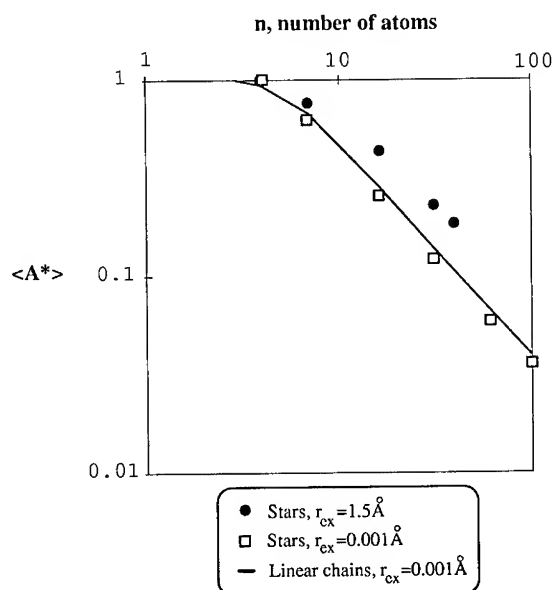


Figure 9. Scaling behavior for the configurational average of the maximum probability of overcrossings $\langle A^* \rangle$ for linear chains and regular 3-stars with $n \leq 100$. [The behavior for the stars with large and small excluded volumes agrees well with the scaling exponent $\lambda \approx -1$ obtained for linear chains [14].]

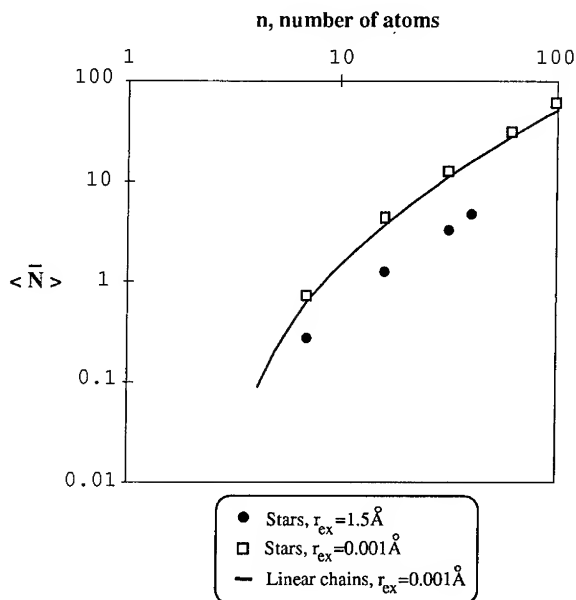


Figure 10. Scaling behavior for the configurational average of the mean number of overcrossings $\langle \bar{N} \rangle$ for linear chains and regular 3-stars with $n \leq 100$. [The behavior for the stars with large and small excluded volumes follows the behavior of linear chains. The results for intermediate values of the number of monomers suggest an effective scaling exponent $\beta \approx 1.4$ [14]. The true exponent in the asymptotic limit must be smaller than 1.4 [16]. Reaching the asymptotic behavior requires probably $n > 500$.]

more slowly, and therefore our results should be considered as corresponding only to a regime of intermediate polymer lengths.

In conclusion, averaged shape descriptors of regular stars follow power laws in terms of n that are similar to those found for linear polymers. As far as the present results indicate, the exponents λ and β appear to depend little on the different polymer topology and the change in excluded volume. Note, however, that the multiplying coefficients a and α in Eqs. (12) do depend on excluded volume. The coefficient a increases with r_{ex} , whereas the α decreases. Both behaviors establish that stars with large r_{ex} exhibit, on average, fewer overcrossings than the stars with smaller excluded volume, i.e., they former are less entangled than the latter.

Further Comments and Conclusions

In this work, we have extended the analysis of entanglement complexity and degree of folding in macromolecules from linear to branched polymers. Approximate relations have been found between geometric descriptors and shape descriptors [cf. Eqs. (9) and (10)] within the configurational space of polymers with a constant number of monomers. Nevertheless, the results show that the two families of prop-

erties are independent: the features conveyed by shape descriptors \bar{N} and A^* cannot be fully retrieved from the geometric ones.

The results contribute to a knowledge of the general properties of regular stars as a subclass of branched polymers. Regarding the geometric characterization of size and compactness, the scaling law (11) is well established for stars [18]. We have shown here how the analysis of these polymers can be enriched by studying features other than size. In our case, we characterize the self-entanglements in the chain by means of shape descriptors which also follow simple scaling laws [14,16]. In a similar fashion to what is known for geometric descriptors, it is found that the descriptors of entanglement complexity scale similarly whether the polymer is a linear chain or a star.

The architectures of regular 3-stars and linear polymers are sufficiently different so as to make not self-evident a coincidence in the behavior of their shape descriptors. This finding will probably not be true for all other topologies. For instance, polymers with large branching and complicated connectivities (e.g., where branches form complex loops with the main chain) may show an averaged mean number of overcrossings growing with n even faster than a power law. It remains to be seen for which families of simpler branched polymers, such as combs and brushes, the behavior of the shape descriptors is similar to the one found here for regular stars.

The present methodology does not describe completely all the essential features of macromolecular shape, but it complements the analyses based on purely geometric properties of polymers. All distinct aspects of polymer shape (e.g., size, compactness, degree of folding, self-entanglements, writhing, etc.) must be taken into account for a full understanding of the relation between 3D molecular structure and various physico-chemical properties. We believe that the use of overcrossing numbers (and their related shape descriptors) can be a valuable tool in the difficult task of characterizing the folding state of a macromolecule with a given architecture.

Acknowledgment

I thank Prof. S. Whittington (Toronto) for sending his manuscript of Ref. [16] prior to publication. This work has been supported by an individual operating grant from the Natural Sciences and Engineering Research Council (NSERC) of Canada.

Bibliography

- [1] M. V. Volkenstein, *Configurational Statistics of Polymeric Chains* (Interscience, New York, 1963).
- [2] P. J. Flory, *Statistical Mechanics of Chain Molecules* (Interscience, New York, 1969).
- [3] C. Brändén and J. Tooze, *Introduction to Protein Structure* (Garland, New York, 1991).
- [4] R. A. Bradshaw and M. Purton, Eds., *Proteins: Form and Function* (Elsevier, Cambridge, 1990).
- [5] P. G. de Gennes, *Scaling Concepts in Polymer Physics* (Cornell University Press, Ithaca, 1985).
- [6] F. W. Wiegel, in *Phase Transitions and Critical Phenomena*, C. Domb and J. L. Lebowitz, Eds., (Academic, London, 1983). Vol. 7, pp. 101–149.
- [7] K. Koniaris and M. Muthukumar, *J. Chem. Phys.* **95**, 2873 (1991).
- [8] E. J. Janse van Rensburg, E. Orlandini, D. W. Sumners, M. C. Tesi, and S. G. Whittington, *J. Phys. A* **26**, L 981 (1993).
- [9] G. A. Arteca and P. G. Mezey, *Biopolymers* **32**, 1609 (1992).

- [10] G. A. Arteca, *Biopolymers* **33**, 1829 (1993).
- [11] E. J. Janse van Rensburg, D. W. Sumners, E. Wasserman, and S. G. Whittington, *J. Phys. A* **25**, 6557 (1992).
- [12] G. A. Arteca, *J. Phys. Chem.* **97**, 13831 (1993).
- [13] G. A. Arteca, *Int. J. Quantum Chem. (QCS)* **27**, 547 (1993).
- [14] G. A. Arteca, *Phys. Rev. E* **49**, 2417 (1994).
- [15] J. C. Le Guillou and J. Zinn-Justin, *Phys. Rev. B* **21**, 3976 (1980).
- [16] E. Orlandini, M. C. Tesi, S. G. Whittington, D. W. Sumners, and E. J. Janse van Rensburg, *J. Phys. A* **27**, L333 (1994).
- [17] J. E. G. Lipson, *Macromolecules* **26**, 203 (1993).
- [18] S. G. Whittington, J. E. G. Lipson, M. K. Wilkinson, and D. S. Gaunt, *Macromolecules* **19**, 1241 (1986).
- [19] J. E. G. Lipson, *Macromolecules* **24**, 1327 (1991).

Received May 12, 1994

***Ab Initio* Investigation of the Static Polarizability of Planar and Twisted Infinite Polythiophene Chains**

DAVID H. MOSLEY, JOSEPH G. FRIPIAT, BENOÎT CHAMPAGNE,*
and JEAN-MARIE ANDRÉ

*Laboratoire de Chimie Théorique Appliquée, Facultés Universitaires Notre-Dame de la Paix,
Rue de Bruxelles 61, B-5000 Namur, Belgium*

Abstract

In this paper we investigate the electronic structure and the static longitudinal polarizability of regular finite and infinite chains of polythiophene at the *ab initio* Hartree-Fock level. The effects of the inclusion of polarization functions in the basis set and the influence of introducing a torsional twist between adjacent rings are considered. © 1994 John Wiley & Sons, Inc.

Introduction

Conjugated polymers have attracted a great deal of theoretical and experimental interest in recent years. These systems possess potential with respect to their interesting conductivity properties and their large nonlinear optical responses [1–3]. In this area, much attention is directed towards polythiophene and its derivatives (for example [4–7]). This is an attractive polymer due to its stability in air and the possibilities of introducing side-chain substituents to enhance its solubility in common organic solvents [8,9]. Materials based upon polythiophene have been synthesized that exhibit high conductivities and large linear and nonlinear responses [10,11].

Large response properties are critically dependent upon the degree of electron delocalization along the polymer backbone [12]. X-ray crystal structures indicate that 2,2'-bithiophene and terthiophene adopt a planar conformation, with the sulfurs in adjacent rings anti to each other [13]. In part of this paper we study the effect of introducing a twist between successive rings in finite and infinite polythiophene chains in order to observe the effect this disruption of conjugation has upon the computed properties. Such distortion from the planar conformation is observed on the introduction of side-chain substituents [14]. Previous studies have studied the variation in the ionization energy, valence band width, and band gap with such twists using parameterized *ab initio* (valence effective Hamiltonian) [15] and MNDO calculations [16].

* Senior Research Assistant of the National Fund For Scientific Research (Belgium).

In this study, in addition to the energies, band energies and band gap, we present *ab initio* uncoupled and coupled Hartree–Fock predictions of the static longitudinal polarizabilities. Both the uncoupled and coupled schemes were applied to the finite chains, while the treatment of the infinite chains was restricted to the uncoupled Hartree–Fock level. Recently, we have published [17] the results of a comprehensive study of the dipole polarizabilities of oligothiophenes using several basis sets (3-21G, 6-31G**, 6-311G**, and the Sadlej medium-sized polarized basis sets [18]) and the extrapolated values of the longitudinal polarizability per unit cell of polythiophene. This paper is a companion to this in studying the effects of changes in the conformation on the electronic properties of polythiophene.

Methodology

The calculations presented in this paper fall into two categories. Initially, geometry optimizations were performed on *ter*-thiophene at various conformations, using the Gaussian-92 package [19]. The geometries of the central rings were then used as the repeating unit in calculations of the polarizabilities of extended thiophene oligomers, again using Gaussian-92, and of infinite stereoregular polythiophene, using a program developed in our laboratory, PLH-93 [20,21].

The polarizabilities of the oligomers were calculated at the uncoupled and coupled Hartree–Fock levels (from hereon referred to as UCHF and CHF, respectively). The UCHF method, sometimes referred to as the sum over states or SOS method [22], is based upon a perturbation treatment of the Hartree–Fock wavefunction, or the corresponding SCF-MOS. The components of the polarizability can be expressed as

$$\alpha_{uv} = 4 \sum_i \sum_a \frac{\langle \phi_i | \mu_u | \phi_a \rangle \langle \phi_a | \mu_v | \phi_i \rangle}{\epsilon_a - \epsilon_i} \quad (1)$$

where ϕ_i and ϕ_a represent doubly occupied and virtual molecular orbitals, in the absence of an electric field, respectively, and ϵ_a and ϵ_i their corresponding orbital energies. The scheme neglects field-induced reorganizational effects, and is thus described as an uncoupled scheme. In the CHF method [23], the field-induced electron reorganization is included in a way which is fully consistent in terms of adjustments in the average two-electron interactions via analytical differentiation of the field dependent Hartree–Fock equation.

The standard quantum chemical treatment of polymers is based on the periodic model of the polymer chain. In restricted Hartree–Fock theory, the many-electron wave functions of the closed shell periodic systems are approximated by Slater determinants constructed from doubly occupied crystalline orbitals. The LCAO form of such a crystalline orbital is given by

$$\phi_n(k, \mathbf{r}) = N_C^{-1/2} \sum_j \exp[ikja] \sum_p c_{pn}(k) \chi_p(\mathbf{r} - \mathbf{P} - jae_z), \quad (2)$$

where n is the band index, k the reciprocal lattice vector in the first Brillouin zone, j represents the cell index, $N_C^{-1/2}$ the normalization factor, $c_{pn}(k)$ the k -dependent

LCAO coefficients, and $\chi_p(\mathbf{r} - \mathbf{P} - ja\mathbf{e}_z)$, the p th atomic orbital centered in the j th cell. The standard theory of band structure is covered in detail in several reviews (for example, see [24,25]).

In methods for the calculation of the polarizability of polymers serious problems have to be overcome. The most serious of these is that the electric field operator acting on a polymer is unbounded and thus results in destruction of the translational symmetry of the system. Means of overcoming this problem have been proposed and discussed in detail in the literature [26,27].

In this paper, we apply a scheme for the computation of the uncoupled Hartree-Fock asymptotic longitudinal static polarizability per unit cell of infinite systems developed recently [28,29] based upon the perturbational approach of Genkin and Mednis [30]. The longitudinal polarizability can be expressed as

$$\alpha_{zz} = 4 \sum_i \sum_a \sum_k \frac{|\Omega_{ia}(k)|^2}{\epsilon_a(k) - \epsilon_i(k)}, \quad (3)$$

where the sums over i and a represent sums over occupied and unoccupied bands respectively, $\Omega_{ia}(k)$ are the dipole transition strengths [28,29,31,32]. In order to calculate the polarizability per unit cell, the sum over k is replaced by an integration over the first Brillouin zone, to give

$$\begin{aligned} \frac{\alpha_{zz}}{N_C} &= \frac{2a}{\pi} \sum_i \sum_a \int \frac{|\Omega_{ia}(k)|^2}{\epsilon_a(k) - \epsilon_i(k)} dk \\ &= \sum_i \int \alpha_{zz}(i, k) dk \\ &= \sum_i \alpha_{zz}(i). \end{aligned} \quad (4)$$

This final result illustrates how the polarizability can be decomposed into the contributions made from each of the occupied bands. This can be used to establish relationships between the topology of the bands and the polarizability to provide insight into the nature of bonding and conjugation in the polymer [17,29,33,34]. Coupled schemes to calculate the polarizability have been developed recently [35-37], but their application has been restricted to model systems due to the substantial computational cost involved.

All calculations were performed on IBM RS6000 Model 560 machines of the Namur Scientific Computing Facility.

Results

Geometry Optimizations

All-Anti, Planar Polythiophene. The geometry of the trimer in the all anti conformation was optimized at the Hartree-Fock level with the 3-21G and 3-21G* basis sets. In these geometry optimizations all atoms in the three rings were constrained to be coplanar. The molecule is represented in Figure 1 and the results

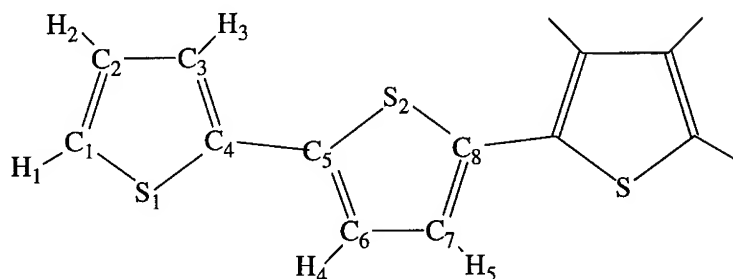


Figure 1. Ter-thiophene with atom labels as referred to in Tables I and II.

listed in Table I. Parameters obtained from an MNDO geometry optimization [4] are also included for comparison. The values of δ given in the final two rows of Table I represent the bond-length alternation, which is the difference between the two adjacent single and double carbon-carbon bond lengths indicated. This alternation gives an indication of the amount electron delocalization along the carbon backbone. The geometrical parameters obtained for the central ring were used in the subsequent polymer calculations. Two such rings constitute the translational unit cell used for the calculations on the infinite chain. It has been noted [7] that using the trimer is sufficient to obtain reliable geometrical parameters for the central ring, with little further change being observed in continuing to higher oligomers.

Twisted Polythiophene. In the idealized conformations considered for twisted polythiophene, equivalence of alternate thiophene rings was imposed. Partial geometry optimizations using the 3-21G basis set were carried out on the three-ring chains for inter-ring twists between 0° and 180° , at 15° intervals. In order to retain the translational periodicity for the polymer calculations, the chains were constrained to be linear (or rodlike) [15], that is, with the interranging carbon-carbon bonds lying along the axis of periodicity. In practice, the carbon-sulfur-carbon angle ($C_5-S_2-C_8$) in the central ring and the sulfur-carbon-carbon angle ($S_2-C_5-C_4$) along the backbone were fixed to be 89.77° (the value obtained in the optimization of the planar, anti conformation) and 134.89° , respectively. Additionally, the central ring carbon-sulfur interatomic distances were fixed at 1.809 \AA . All atoms in individual rings were constrained to be coplanar, but all other bond lengths and bond angles were free to vary. The results of the optimizations for the geometrical parameters of the central ring are presented in Table II. An inter-ring twist angle of 180° corresponds to the all-anti conformation. The carbon-hydrogen bond lengths remained nearly constant for all twist angles ($1.069 \pm 0.001 \text{ \AA}$) and, therefore, are not included in the table. The values of δ given in the fifth and sixth columns of Table II give the degree of alternation between adjacent carbon-carbon single and double bonds.

Energy and Polarizability Calculations

All-Anti, Planar Conformation. Using the geometrical parameters given in Table I, molecular calculations were performed for chains containing from one to six

TABLE I. Optimized geometrical parameters of all-anti, planar *ter*-thiophene.^a

	Polythiophene		
	3-21G	3-21G*	MNDO
S ₁ —C ₁	1.795	1.721	
S ₁ —C ₄	1.810	1.738	
C ₁ —C ₂	1.335	1.347	
C ₂ —C ₃	1.442	1.433	
C ₃ —C ₄	1.343	1.355	
C ₁ —H ₁	1.065	1.067	
C ₂ —H ₂	1.070	1.069	
C ₃ —H ₃	1.069	1.069	
<(S ₁ —C ₁ —C ₂)	111.16	111.97	
<(S ₁ —C ₄ —C ₃)	110.59	110.72	
<(C ₁ —C ₂ —C ₃)	113.91	112.50	
<(C ₄ —C ₃ —C ₂)	114.40	113.16	
<(C ₁ —S ₁ —C ₄)	89.45	91.65	
<(S ₁ —C ₄ —C ₃)	120.54	121.40	
<(S ₁ —C ₁ —H ₁)	120.19	120.76	
<(C ₁ —C ₂ —H ₂)	123.47	124.02	
<(C ₄ —C ₃ —H ₃)	122.84	123.59	
S ₂ —C ₅	1.809	1.737	1.704
C ₅ —C ₆	1.342	1.354	1.380
C ₆ —C ₇	1.435	1.427	1.447
C ₄ —C ₅	1.439	1.454	1.444
C ₆ —H ₄	1.069	1.069	1.085
<(S ₂ —C ₅ —C ₄)	120.45	121.29	119.6
<(C ₅ —S ₂ —C ₈)	89.77	92.01	94.6
<(S ₂ —C ₅ —C ₆)	110.49	110.66	110.2
<(C ₅ —C ₆ —C ₇)	114.62	113.34	112.5
<(C ₅ —C ₆ —H ₄)	122.83	123.63	125.7
$\delta_{C_5-C_6, C_6-C_7}$	0.093	0.073	0.067
$\delta_{C_4-C_5, C_5-C_6}$	0.097	0.100	0.064

^a Geometry of central rings used in calculations on the extended oligomers and infinite chains. The MNDO parameters are listed for comparison. All bond lengths are given in angstroms. The atom labels correspond to Figure 1.

thiophene rings with the 3-21G and 3-21G* basis sets. The larger chains were constructed using the geometries obtained for the terminal rings in the trimer optimizations, and repeating the central unit. The evolution of the UCHF and CHF static longitudinal polarizability per thiophene ring [calculated by $\alpha_{zz}(N) - \alpha_{zz}(N-1)$] with an increasing number of thiophene rings for both basis sets at the two optimized geometries is represented graphically in Figures 2 and 3.

Calculations on infinite chains with two thiophene rings per unit cell were also carried out using the 3-21G and 3-21G* basis sets using the optimized geometries in both cases. The short and intermediate ranges of interaction were set to ± 3 and

TABLE II. 3-21G geometrical parameters of the central ring resulting from the restricted optimization of *ter*-thiophene at various twist angles.

	C ₄ —C ₅	C ₅ —C ₆	C ₆ —C ₇	$\delta_{C_{4-5},C_{5-6}}$	$\delta_{C_{5-6},C_{6-7}}$	$\angle(S_2-C_5-C_6)$	$\angle(C_5-C_6-C_7)$	$\angle(C_5-C_6-H_4)$
180.0	1.454	1.347	1.401	0.107	0.054	109.81	115.31	121.83
165.0	1.455	1.347	1.402	0.108	0.055	109.82	115.30	121.78
150.0	1.458	1.347	1.404	0.111	0.057	109.86	115.26	121.67
135.0	1.463	1.345	1.407	0.118	0.062	109.90	115.22	121.59
120.0	1.467	1.343	1.410	0.124	0.067	109.94	115.18	121.56
105.0	1.471	1.342	1.413	0.129	0.071	109.97	115.14	121.59
90.0	1.472	1.341	1.415	0.131	0.074	110.0	115.12	121.64
75.0	1.463	1.344	1.408	0.119	0.064	109.91	115.21	121.74
60.0	1.464	1.345	1.408	0.119	0.063	109.91	115.21	121.77
45.0	1.467	1.345	1.406	0.122	0.061	109.87	115.25	122.00
30.0	1.474	1.343	1.402	0.131	0.059	109.75	115.36	122.64
15.0	1.482	1.341	1.400	0.141	0.059	109.60	115.51	122.51
0.0	1.487	1.340	1.396	0.147	0.056	109.54	115.57	123.94

± 6 unit cells about the reference cell respectively. The total energies, energy of the highest occupied crystalline orbital (HOCO), valence band-gap (E_{gap}), and UCHF polarizabilities per unit cell and length are presented in Table III.

Twisted Conformations. The 3-21G basis set was used for all oligomeric and polymeric calculations on the twisted conformations of thiophene chains. This choice is justified due to the increased computational cost and relatively small effect of the inclusion polarization functions on the sulfur atom. Using the optimized geometries described in the previous subsection and listed in Table II for each twist angle, the UCHF and CHF static polarizabilities were calculated for the three-, five-, and seven-ring oligomer chains. The evolution of the CHF polarizability per pair of thiophene rings with an increasing number of rings for each twist angle is illustrated in Figure 4.

Polymeric calculations for the infinite chains were performed for each twist angle at the optimized geometry obtained in each case. The short and intermediate ranges of interaction were again set to ± 3 and ± 6 translational cells. The effect of the twist angle on the electronic properties is detailed in Table IV and the behavior of the band gap and UCHF static polarizability per unit cell are illustrated in Figures 5 and 6, respectively.

Discussion

Effect of Polarization Functions on the Sulfur Atom

The inclusion of polarization functions on the sulfur atom in the 3-21G* basis set generally has a more marked effect on the results of the geometry optimizations of the all-anti trimer than on the subsequent energy and polarizability calculations.

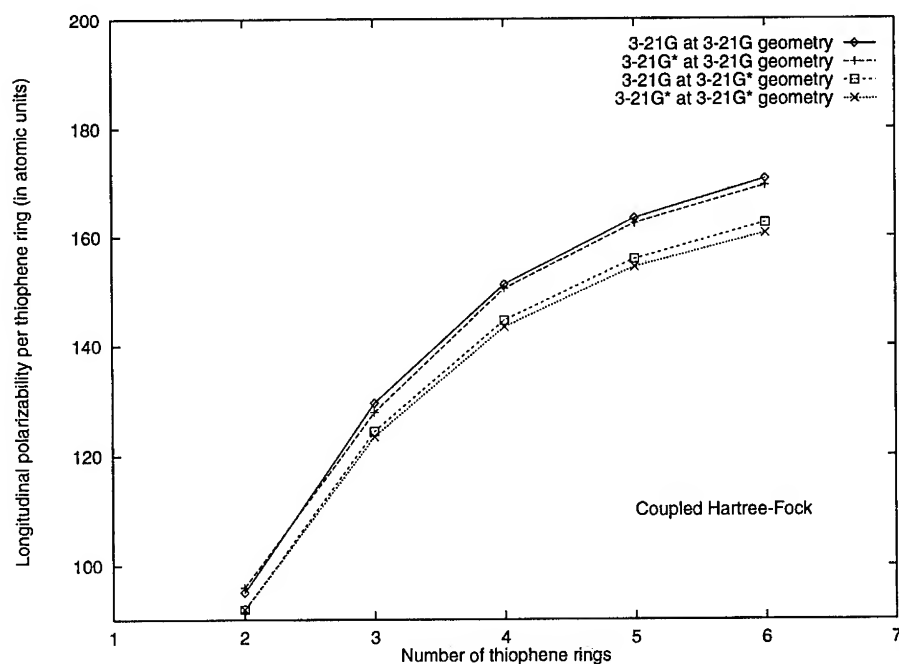


Figure 2. Evolution of the CHF longitudinal polarizability per thiophene ring with an increasing number of thiophene rings with the 3-21G and 3-21G* basis sets at the geometries indicated.

The calculated carbon-sulfur bond length using the 3-21G* basis set is substantially shorter (0.072 Å) compared to that obtained using the basis set without the polarization functions. The carbon-sulfur-carbon angle is correspondingly wider (2.2°) in the former case. Further investigation [38] indicates that any role for the d-orbitals in the bonding orbitals is small, and that this observation can be attributed, at least in part, to the paucity of the 3-21G basis set in the core region.

For the carbon-carbon bonds, the polarized basis set results in a lengthening of the carbon-carbon double bond (0.012 Å) and a lengthening and shortening of the interring and intraring carbon bonds (+0.015 and -0.008 Å) respectively, compared to the 3-21G basis set. Due to these contrary effects, it is difficult to make any overall remarks regarding the bond length alternation with the two basis sets used. The overestimation of bond length alternancy using *ab initio* Hartree-Fock methods is well known and can be attributed largely to the absence of electron correlation effects. The MNDO method is regarded as quite capable of yielding acceptable geometrical parameters for conjugated systems at low computational cost.

Comparison of the electronic properties of the valence region of infinite planar polythiophene obtained using the two basis sets listed in Table III indicate a minor role for the polarization functions located on the sulfur atom. At the two fixed geometries, the difference between the energy gaps obtained using the 3-21G and

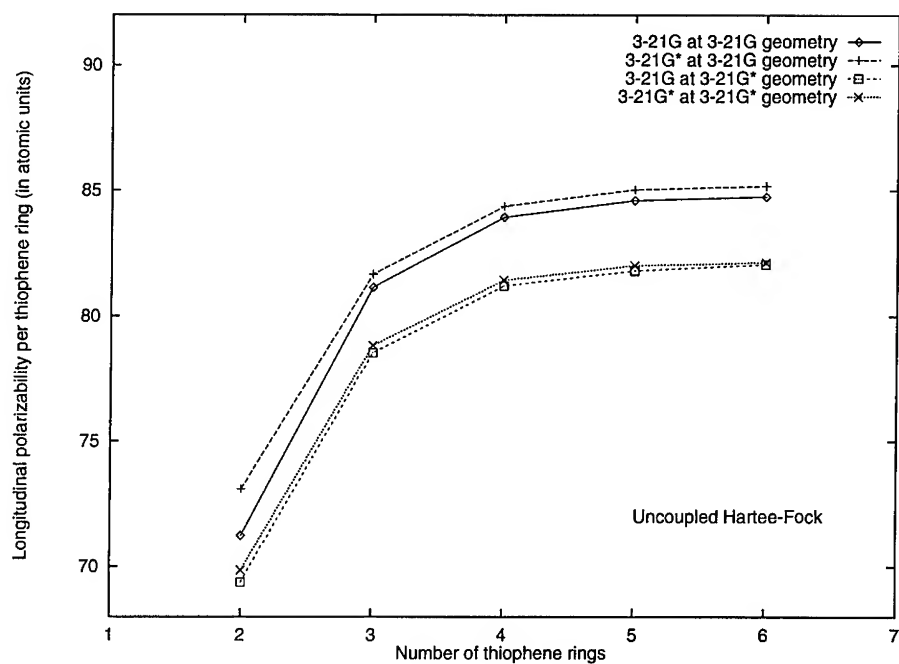


Figure 3. Evolution of the UCHF longitudinal polarizability per thiophene ring with an increasing number of thiophene rings with the 3-21G and 3-21G* basis sets at the geometries indicated.

3-21G* basis sets is small (≤ 0.02 eV). The difference between the gaps predicted at the two optimized geometries is more marked, with the predicted gap being in the region of 0.1 eV larger with the 3-21G* basis set.

The CHF and UCHF polarizabilities per thiophene ring in the extended oligomeric calculations illustrated in Figures 2 and 3 show similar behavior. The difference

TABLE III. Electron properties of infinite polythiophene using 3-21G and 3-21G* basis sets at two different geometries. All values in atomic units (except where marked).

	3-21G optimized geometry		3-21G* optimized geometry	
	3-21G	3-21G*	3-21G	3-21G*
Total energy	-1094.662095	-1094.87989241	-1094.65346482	-1094.88779487
HOCO	-0.254888	-0.251336	-0.250778	-0.247438
E_{gap}	0.2668	0.2660	0.2704	0.2702
	(7.26 eV)	(7.24 eV)	(7.36 eV)	(7.35 eV)
$\alpha_{zz}/\text{unit cell}$	169.58	170.53	163.77	164.16
$\alpha_{zz}/\text{thiophene ring}$	84.79	85.26	81.89	82.08
$\alpha_{zz}/\text{unit length}$	11.369	11.432	11.095	11.121

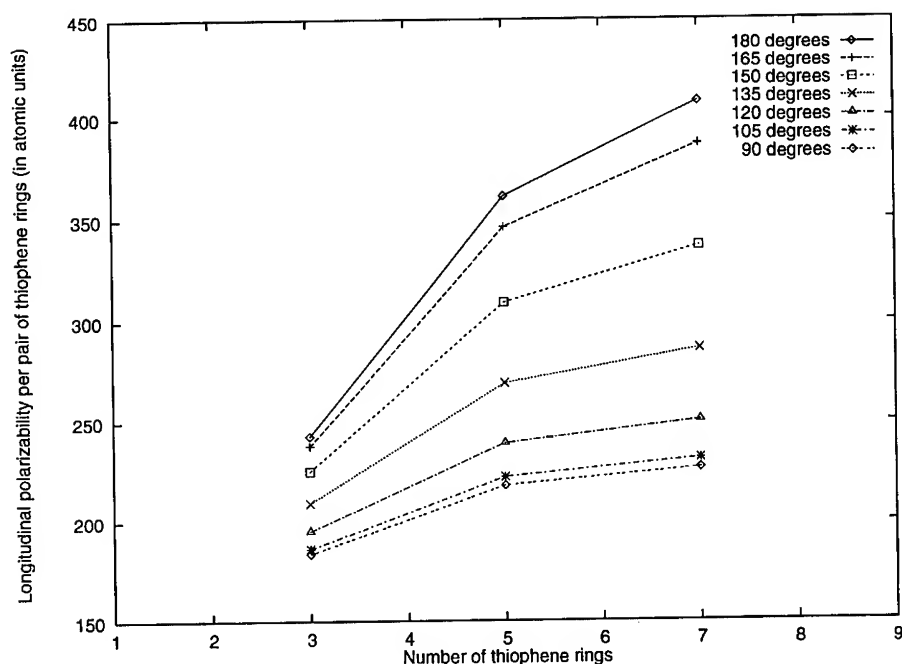


Figure 4. Evolution of the 3-21G Coupled Hartree-Fock longitudinal polarizability per pair of thiophene rings with increasing chain length at different torsion angles between adjacent rings.

between the polarizabilities obtained at the two optimized geometries using the two basis sets is small. Taking the example of the six-ring chain, at the 3-21G optimized geometry, the coupled value per thiophene ring using the 3-21G basis set (170.6 a.u.) slightly exceeds that obtained using the 3-21G* basis (169.4 a.u.). At the same geometry, the ordering of the uncoupled polarizabilities is reversed, with that obtained using the 3-21G* basis (85.18 a.u.) greater than that found with the unpolarized basis (84.75 a.u.). These features are replicated at the 3-21G* optimized geometry. The coupled and uncoupled polarizability per ring for the hexamer obtained, with the 3-21G and 3-21G* basis sets, respectively, are 162.5 and 160.6 a.u. and 82.05 and 82.13 a.u. For chains containing four and more thiophene rings, the uncoupled polarizability per ring is very close to saturation. However, the coupled value has still not reached saturation for the six-ring chain, the longest chain considered in this part of the work.

The uncoupled polarizabilities per thiophene ring obtained on the infinite polythiophene chains are detailed in Table III. At the 3-21G optimized geometry, the computed polarizabilities per thiophene ring are 84.79 and 85.26 a.u. with the 3-21G and 3-21G* basis sets, respectively, while, at the 3-21G* optimized geometry, the values are 81.89 and 82.08 a.u. These are all in very close concordance with the values obtained from the extended oligomer calculations. This confirms that

TABLE IV. 3-21G electronic properties of infinite polythiophene for various twist angles between successive rings.^a

	Total energy	HOCO	E_{gap}	α_{zz}/N	α_{zz}/L
180°	-1094.61007260	-0.2384	0.2508 (6.82 eV)	190.47	12.58
165°	-1094.61001614	-0.2416	0.2578 (7.01 eV)	184.01	12.15
150°	-1094.60995122	-0.2514	0.2780 (7.57 eV)	168.39	11.11
135°	-1094.60999025	-0.2682	0.3109 (8.46 eV)	150.37	9.91
120°	-1094.61039159	-0.2894	0.3504 (9.54 eV)	137.16	9.03
105°	-1094.61170400	-0.3137	0.3933 (10.70 eV)	129.83	8.54
90°	-1094.61397675	-0.3398	0.4171 (11.35 eV)	127.85	8.40
75°	-1094.61647400	-0.3148	0.3764 (10.24 eV)	132.56	8.73
60°	-1094.61803623	-0.2923	0.3393 (9.23 eV)	141.06	9.29
45°	-1094.61559726	-0.2724	0.3061 (8.33 eV)	153.11	10.08
30°	-1094.60669924	-0.2570	0.2803 (7.63 eV)	165.61	10.88
15°	-1094.59456895	-0.2469	0.2642 (7.19 eV)	175.34	11.50
0°	-1094.58876100	-0.2435	0.2591 (7.05 eV)	178.68	11.71

^a All values in atomic units (except where marked).

the uncoupled static polarizability per ring in the larger oligomers is very close to its saturation value, as discussed above. The smaller polarizability at the 3-21G* optimized geometry indicates less delocalization along the polymer backbone at this geometry. This is supported by the slight increase in interranging bond length alternation compared to the 3-21G optimized geometry and the increase in band gap. The HOCO, which makes the largest contribution to the polarizability, is of π -symmetry [17], composed of contributions from the carbon atoms along the backbone, thus resembling segments of all-*trans* and *trans-cisoid* polyacetylene. For this reason, it is not surprising that the addition of d-orbitals on the sulfur atom in the 3-21G* basis set has only a small effect on the computed polarizability. The influence of the bond length alternation on the computed polarizability is critical. Using the less alternating MNDO optimized geometry, the longitudinal polarizability per unit cell of infinite polythiophene has been calculated to be 86.02 a.u. using the 3-21G basis set [17], slightly larger than the values obtained here.

Influence of Torsional Twist between Adjacent Rings

Generally speaking, the effect of introducing a torsional twist between adjacent thiophene rings, thus disrupting the conjugation, is seen to be large. From the values listed in Table II, it can be seen that the intraring bond length alternation is at a minimum at the all-anti conformation, indicating a larger degree of electron delocalization. The alternation then increases to a maximum for the case in which the planes containing adjacent rings are perpendicular to each other, pointing to a reduction in conjugation, before decreasing for twist angles between 90° and 0°. The interranging carbon-carbon bond length alternation shows similar behavior for twist angles between 180° (all anti-) and 60°. For smaller angles, the length of the

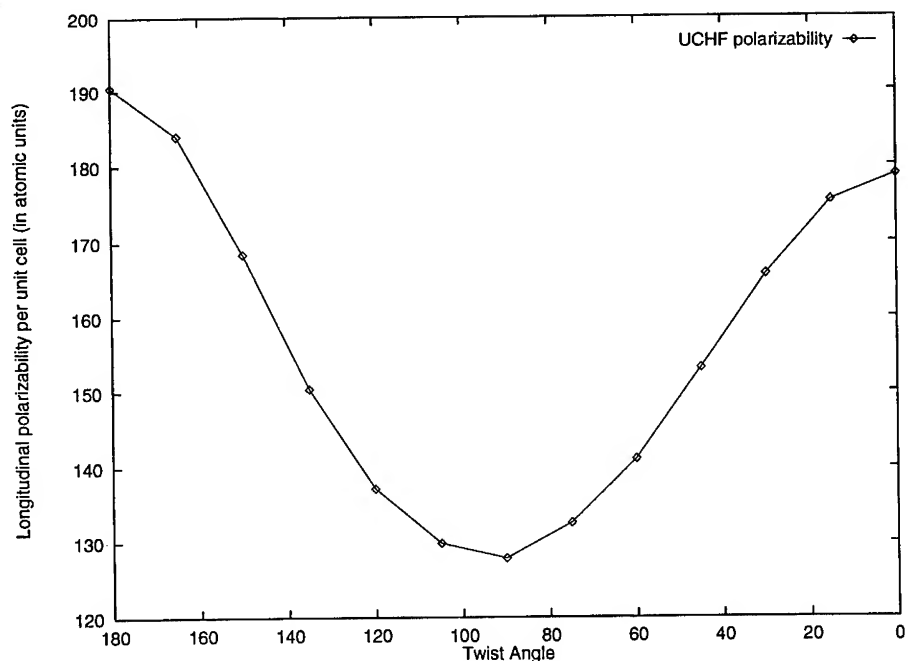


Figure 5. Evolution of the 3-21G uncoupled longitudinal polarizability per unit cell of infinite polythiophene with the torsion angle between adjacent rings.

interring carbon-carbon increases, increasing the bond length alternation. This effect is most likely due to steric effects and inherent strain as a result of the restricted optimization.

For the polymer calculations, the variation in the total energies calculated (see Table IV) are generally small. As the twist angles decrease towards 0° , the increase is notable, but this is primarily a result of the imposed, idealized geometry of the chain.

For the oligomer calculations, the values of the CHF polarizability per pair of thiophene rings for the heptamer in the most conjugated case (all-anti, 180° degree twist between adjacent rings) and the case in which adjacent rings are perpendicular to each other are 407.7 and 226.5 a.u., respectively, representing a decrease of over 40% between the two extremes. The difference is slightly less marked for the UCHF polarizability calculations, with the values at the all-anti and perpendicular conformations 190.3 and 127.9 a.u., respectively. The ratio of the CHF and UCHF polarizabilities for the most conjugated case is 2.12, while for the least conjugated case it is somewhat smaller at 1.79.

Two important features of Figure 4 showing the CHF polarizability per unit cell with increasing chain length for twist angles between 180° and 90° should be emphasized. First, it is evident that, in the less conjugated cases, the saturated value of the polarizability is attained more rapidly than for the more conjugated chains.

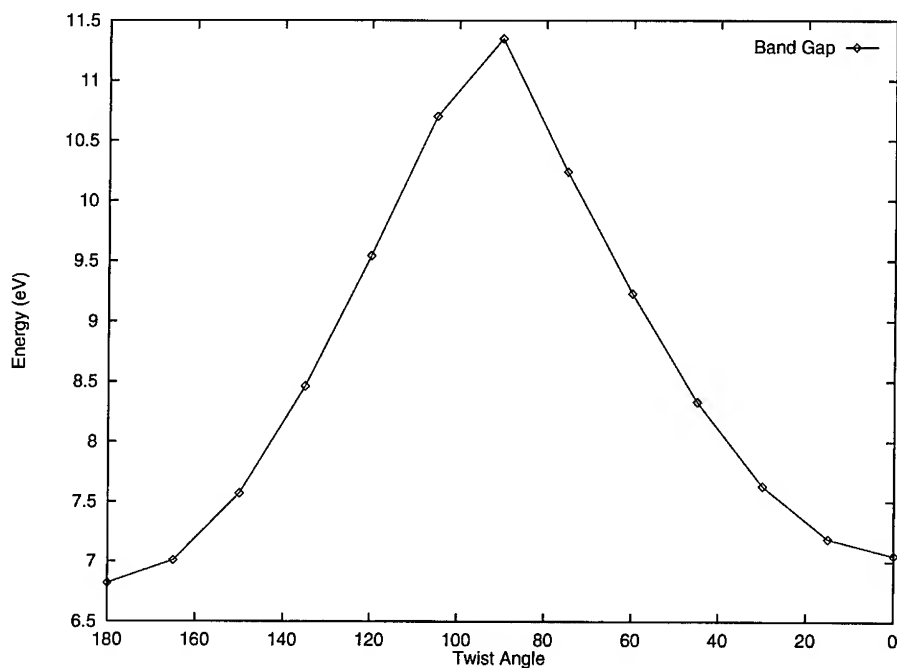


Figure 6. Evolution of the 3-21G band gap of infinite polythiophene with the torsion angle between adjacent rings.

This demonstrates the appeal of polymer calculations able to provide the asymptotic value directly. Second, the evolution of the polarizability per unit cell with twist angle does not evolve linearly. Small deviations in the twist angles, at either the more or less conjugated extremes, provoke only small changes in the computed values. More substantial twists induce more substantial changes.

This behavior is seen again in the smooth cosinelike curve for the variation of the uncoupled polarizability per unit cell with twist angle for infinite polythiophene chains in Figure 5. In Figure 6, in which the variation of the band gap with twist angle is illustrated, the overall form of the curve is repeated (although inverted, as would be expected, with the band gap increasing as the conjugation is reduced), but with a less smooth variation for twist angles around 90° . The ionization energies given in Table IV ($-E_{\text{HOCO}}$) also show this behavior, with the ionization energy being highest when two adjacent rings are perpendicular to each other. The overestimation of the band gap by Hartree-Fock calculations due to the neglect of electron correlation is well known. As can be seen from Eq. (3), the prediction of the UCHF polarizability is critically dependent on the size of the band gap. The excessively large band gap will result in an underestimation of the polarizability. UCHF polarizabilities can only, at best, give a qualitative indication, but are sufficient to reproduce trends. Accurate predictions of polarizabilities require coupled schemes and consideration of electron correlation.

This cosinelike form has been observed previously in studies of the electronic properties of polythiophene using the valence effective Hamiltonian method [15]. However, there the authors suggest torsions of up to 40° fail to induce any significant modifications of the electronic properties. While this may be the case for the computed ionization energies and band gaps, such a twist has substantial impact on the electron delocalization along the chain, evidenced by the substantial reduction of polarizability. Our observation is that small distortions from planarity (0 – 15°) will have only a small detrimental effect on the conjugation and computed properties, while larger twists result in considerable changes.

Figure 7 shows the valence band structures at two adjacent-ring twist angles (180° and 90°). There are strong similarities between the band structures for the anti (180°) and syn (0°) conformations (not shown), while that for the perpendicular case shows some strikingly different features. Perhaps the most obvious is the narrowness of the upper-valence bands. This supports the idea that the π -electronic distribution is significantly more localized in this case.

The bands making significant contributions to the UCHF longitudinal polarizability per unit cell for adjacent ring twist angles of 180° , 90° , and 0° are given in Table V. Distinction between bands of π - and σ -symmetry enables some conclusions to be drawn regarding the nature of the conjugation and its disruption as adjacent rings are twisted with respect to each other. For the anti and syn conformers, in which all atoms are coplanar, the π -bands are composed entirely of $2p_y$ (C,S) and $3p_y$ (S only) atomic orbitals perpendicular to the plane of the chain, and the π -electrons are delocalized over the whole system. For the conformer with a 90° torsion angle the situation is different, with the π -structure being defined by p_x and p_y orbitals alternately. This leads to the observed localization of the states (the top four bands, 39–42). However, it is also important to note that there is also a weak interaction of the sulfur $3p_z$ orbital with the π -subsystem on the adjacent ring. The overall picture is more complicated and assignment to π and σ contributions more difficult.

The approximate summed π and σ contributions to the polarizability for each conformer are given at the foot of Table V. A twist of 90° results in a sharp reduction of the π and slight reduction of the σ contributions. Additionally, the different π contributions distinguish between the syn and anti forms. The bands which contribute most to the polarizability of the anti conformer have the same form as the HOCO of alternate all *trans* and *trans-cisoid* segments of polyacetylene, while for the syn conformer, they correspond to the HOCO of *trans-cisoid* polyacetylene. The sulfur p_y orbitals do not contribute in either case. The larger polarizability of the anti conformer can be explained bearing in mind that *trans-transoid* (all *trans*) polyacetylene is more polarizable than the *trans-cisoid* form [34].

Conclusions

In this paper we have shown the attractiveness of polymeric methods to compute the asymptotic polarizability per unit cell directly and their ability to yield useful scientific insight into an interesting problem. Unfortunately, the polymeric calcu-

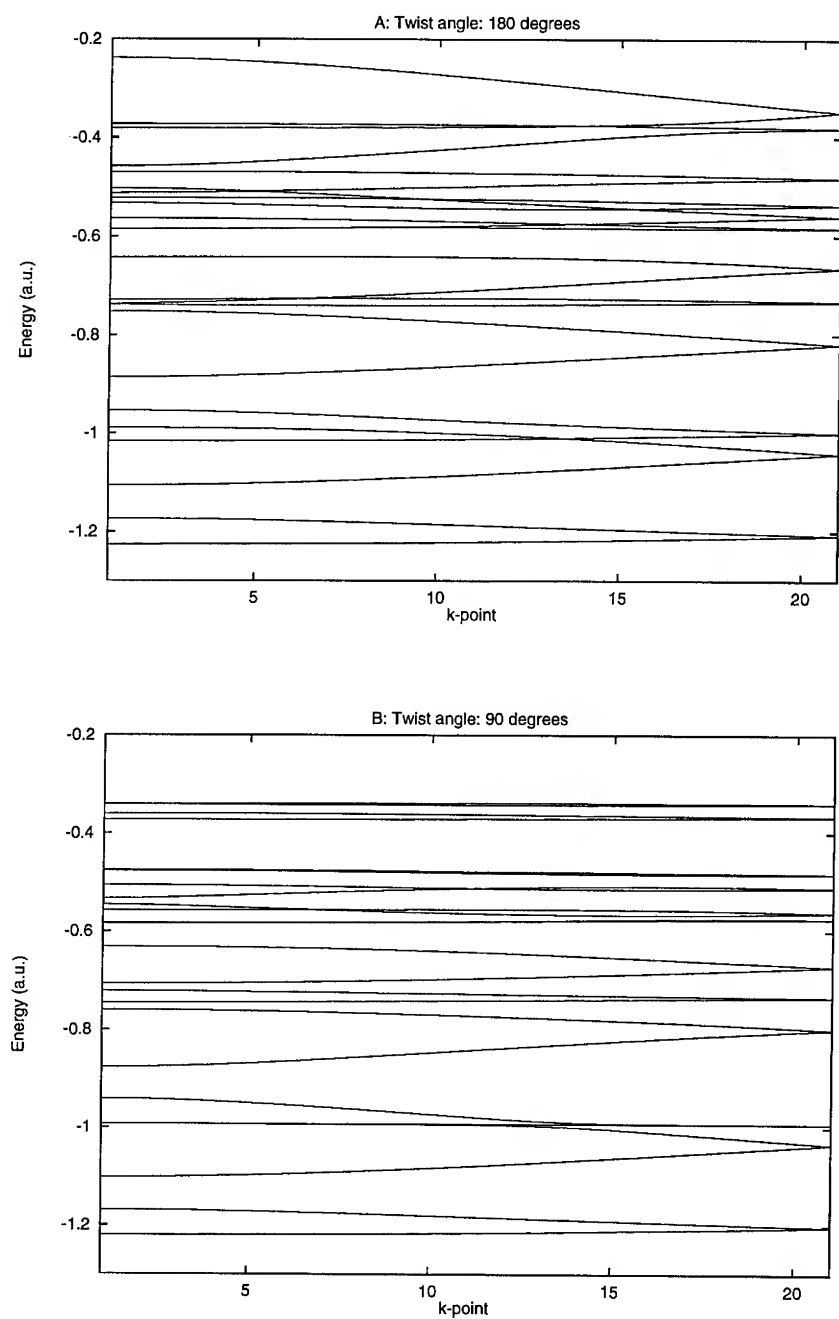


Figure 7. 3-21G valence band structures of polythiophene at two different interring twist angles: A: 180°, and B: 90°.

TABLE V. 3-21G valence band contributions to the longitudinal polarizability per unit cell at inter-ring twist angles of 180°, 90°, and 0°.^a

Band	180°	90°	0°
19	0.07	0.07	0.06
20	0.08	0.08	0.08
21	0.18	0.18	0.16
22	0.12	0.20	0.14
23	0.22	0.17	0.19
24	0.31	0.29	0.31
25	0.57	0.67	0.60
26	0.54	0.69	0.46
27	0.73	0.57	0.70
28	2.64	0.85	0.54
29	1.12	2.61	2.33
30	5.09	4.59	3.30
31	0.03	3.43	5.38
32	10.29	8.00	0.02
33	4.42	5.87	5.54
34	11.08	5.79	16.13
35	8.83	6.28	12.86
36	9.21	3.70	0.08
37	0.09	7.06	8.03
38	14.05	7.74	11.58
39	1.59	3.03	1.68
40	1.82	5.57	3.64
41	5.86	31.60	4.59
42	111.47	28.76	100.24
α_{zz}/N	190.47	127.85	178.68
Approx. total π	120.8	69.0	110.1
Approx. total σ	69.7	58.8	68.6

^a The final four bands are of π -character.

lations of the polarizability are limited to an uncoupled scheme. A coupled scheme for polymers has been developed, but due to the substantial computational cost involved its implementation has been restricted to model cases [35,36]. For accurate polarizabilities, the corrections brought about by including electron correlation, vibrational contributions, and the frequency dependent character of the polarizability should also be considered [37].

There is much scope for further work, considering the effects of ring substituents on the polarizability, and also the *ab initio* study of the electronic properties and polarizabilities of polythiophene chains in helical coil conformations. The energetics of such systems have already been studied at the MNDO level [16].

The potential of polythiophene and its derivatives offers an incentive to understand fully the effect of substituents on the structure, electronic properties and linear and nonlinear response.

Acknowledgments

D. H. M. thanks the Services de Programmation de la Politique Scientifique for their support in the framework of the ELSAM (Electronic Large Scale Computational System for Advanced Materials) project. B. C. thanks the Belgian Fund for Scientific Research (FNRS) for his Senior Research Assistant Position. J. G. F. thanks the organizers of the Sanibel Symposium for inviting him to attend the 1994 meeting. This work has benefited from the financial support of the Belgian National Inter-university Research Program on 'Sciences of Interfacial and Mesoscopic Structures' (PAI/IUAP No. P3-049). All calculations have been performed on the IBM RS6000 Models 730 and 560 of the Namur Scientific Computing Facility (Namur-SCF). The authors gratefully acknowledge the financial support of the FNRS-FRFC, the "Loterie Nationale" for the Convention No. 9.4593.92, and the FNRS within the framework of the "Action d'Impulsion à la Recherche Fondamentale" of the Belgian Ministry of Science under the Convention D.4511.93.

Bibliography

- [1] D. S. Chemla and J. Zyss, Eds., *Nonlinear Optical Properties of Organic Molecules and Crystals*, (Academic, New York, 1987), Vols. I and II.
- [2] P. Prasad and D. J. Williams, *Introduction to Nonlinear Optical Effects in Molecules and Polymers* (Wiley, New York, 1991).
- [3] J. M. André and J. Delhalle, *Chem. Rev.* **91**, 843 (1991).
- [4] H. Eckhardt, L. W. Shacklette, K. Y. Jen, and R. L. Elsenbaumer, *J. Chem. Phys.* **91**, 1303 (1989).
- [5] P. Otto and J. Ladik, *Synth. Met.* **36**, 327 (1990).
- [6] D. Beljonne, Z. Shuai, and J. L. Brédas, *J. Chem. Phys.* **98**, 8819 (1993).
- [7] H. Villar, P. Otto, M. Dupuis, and J. Ladik, *Synth. Met.* **59**, 97 (1993).
- [8] R. J. Waltman, J. Bargon, and A. D. Diaz, *J. Phys. Chem.* **87**, 1459 (1993).
- [9] R. L. Elsenbaumer, K. Y. Jen, and R. Obodoi, *Synth. Met.* **15**, 164 (1986); R. L. Elsenbaumer, K. Y. Jen, G. G. Miller, and L. W. Shacklette, *Synth. Met.* **18**, 277 (1987).
- [10] G. Wegner and J. Rühle, *Faraday Discuss. Chem. Soc.* **88**, 333 (1989).
- [11] M. T. Zhao, B. P. Singh, and P. N. Prasad, *J. Chem. Phys.* **89**, 5535 (1988); H. Thienpoint, G. L. J. A. Rikken, E. W. Meijer, W. ten Hoeve, and H. Wynberg, *Phys. Rev. Lett.* **65**, 2141 (1990).
- [12] C. Flytzanis, in Ref. [1], Chapter III-4, p. 121.
- [13] G. J. Visser, G. J. Heeres, J. Wolters, and A. Vos, *Acta Cryst.* **24**, 464 (1968); F. Van Bolthuis, H. Wynberg, E. E. Havinga, E. W. Meijer, and E. G. J. Staring, *Synth. Met.* **30**, 381 (1989).
- [14] W. R. Salaneck, O. Inganäs, B. Thémans, J. O. Nilsson, B. Sjögreen, J. E. Onsterholm, J. L. Brédas, and S. Svensson, *J. Chem. Phys.* **89**, 4613 (1988).
- [15] J. L. Brédas, G. B. Street, B. Thémans, and J. M. André, *J. Chem. Phys.* **83**, 1323 (1985).
- [16] C. X. Cui and M. Kertesz, *Phys. Rev. B* **40**, 9661 (1989).
- [17] B. Champagne, D. H. Mosley, and J. M. André, *J. Chem. Phys.* **100**, 2034 (1994).
- [18] A. J. Sadlej, *Theor. Chim. Acta* **79**, 123 (1991).
- [19] M. J. Frisch, G. W. Trucks, H. B. Schlegel, P. M. W. Gill, B. G. Johnson, M. W. Wong, J. B. Foresman, M. A. Robb, M. Head-Gordon, E. S. Replogle, R. Gomperts, J. L. Andres, K. Raghavachari, J. S. Binkley, C. Gonzalez, R. L. Martin, D. J. Fox, D. J. Defrees, J. Baker, J. J. P. Stewart, and J. A. Pople, *Gaussian-92/DFT, Revision F.2*, Gaussian, Inc., Pittsburgh, PA, 1993.
- [20] J. G. Fripiat, D. H. Mosley, B. Champagne, and J. M. André, PLH-93 [available from Club Européen-MOTECC, c/o Prof. E. Clementi, CRS4, Cagliari, Italy].
- [21] J. M. André, D. H. Mosley, B. Champagne, J. Delhalle, J. G. Fripiat, J. L. Brédas, D. J. Vanderveken, and D. P. Vercauteren, in *METECC-94: Methods and Techniques in Computational Chemistry*, E. Clementi, Ed. (STEF, Cagliari, 1993), Vol. B, Chap. 10, p. 423.

- [22] A. Szabo and N. S. Ostlund, *Modern Quantum Chemistry: Introduction to Advanced Electronic Structure Theory* (Macmillan, New York, 1982).
- [23] C. E. Dykstra and P. G. Jasien, *Chem. Phys. Lett.* **109**, 388 (1984); S. P. Karna and M. Dupuis, *J. Comput. Chem.* **12**, 487 (1991).
- [24] J. M. André, J. Delhalle, and J. L. Brédas, *Quantum Chemistry Aided Design of Organic Polymers* (World Scientific, London, 1991).
- [25] J. Ladik, *Quantum Theory of Polymers as Solids* (Plenum, New York, 1988).
- [26] J. Ladik, *J. Mol. Struct.* **206**, 39 (1989).
- [27] P. Otto, *Phys. Rev.* **B45**, 10876 (1992).
- [28] C. Barbier, *Chem. Phys. Lett.* **142**, 53 (1987).
- [29] B. Champagne and J. M. André, *Int. J. Quantum Chem.* **42**, 1009 (1992).
- [30] V. M. Genkin and P. M. Mednis, *Sov. Phys. JETP* **54**, 609 (1968).
- [31] C. Barbier, J. Delhalle, and J. M. André, in *Nonlinear Optical Properties of Polymers*, A. J. Heeger, J. Orenstein, and D. R. Ulrich, Eds., (Materials Research Society, Pittsburgh, 1988), Vol. 109, pp. 143ff.
- [32] C. Barbier, J. Delhalle, and J. M. André, *J. Mol. Struct. (Theochem.)* **188**, 299 (1989).
- [33] B. Champagne, J. G. Fripiat, and J. M. André, *Nonlin. Opt.*, to appear.
- [34] B. Champagne, D. H. Mosley, J. G. Fripiat, and J. M. André, *SPIE Proc. Nonlin. Opt. Properties Org. Mater.* **V1775**, 237 (1992).
- [35] B. Champagne, D. H. Mosley, J. G. Fripiat, and J. M. André, *Int. J. Quantum Chem.* **46**, 1 (1993).
- [36] B. Champagne, D. H. Mosley, and J. M. André, *Int. J. Quantum Chem. Quantum Chem. Symp.* **27**, 667 (1993).
- [37] J. Ladik and P. Otto, *Int. J. Quantum Chem. Quantum Chem. Symp.* **27**, 111 (1993).
- [38] D. H. Mosley, unpublished results.

Received March 14, 1994

Dependence of the Electronic Structure on the Chain Geometry in Stereoregular Polypropylene: An Exploratory Theoretical Study

I. FLAMANT, D. H. MOSLEY, M. DELEUZE,
J. M. ANDRE, and J. DELHALLE

*Laboratoire de Chimie Théorique Appliquée, Facultés Universitaires Notre-Dame de la Paix,
61, rue de Bruxelles, B-5000 Namur, Belgium*

Abstract

Ab initio RHF/STO-3G band structure calculations are carried out on extended regular polypropylene chains (isotactic helical, syndiotactic helical, and zigzag planar) to assess qualitatively the dependence of the energy band structure and density of states on the molecular geometry. It is found that discrimination between the two syndiotactic forms should be possible from spectral features in the valence region of corresponding PS spectra. © 1994 John Wiley & Sons, Inc.

Introduction

In spite of the appealing properties of advanced thermoplastics which perform in 175°C plus environments under harsh and corrosive conditions [1], polyolefins like polypropylene still have a bright future. The reasons are not only the low production costs of polyolefins relative to advanced thermoplastics, but also constant progress in olefin polymerisation leading to more versatile polymers of better controlled properties, e.g., the primary structure. Polyolefins are mostly used as bulk materials and free-standing films [2], yet they occur in an increasing number of applications as films deposited or grafted on substrates. In the most advanced applications, information on the chemical composition and molecular structure of the top layers of such films is needed because they determine the nature and strength of the interactions taking place between the polymer surface and the medium brought in contact with it (ambient atmosphere, liquids, deposited metals, other polymer films, cell cultures, etc.). A major problem with probing the surface molecular structure is that it has to be carried out on the films as received, a condition that disqualifies many of existing spectroscopies.

Theoretical predictions [3] first, then experimental studies have pointed out that changes in the secondary structure of polyethylene chains [4] at the sample surface can be followed in the valence region of X-ray photoelectron spectra. Similarly inspired by theoretical predictions [5], very recent experiments [6] carried out in gas phase on normal and cyclic pentane and hexane have further proved that the XPS valence region is very sensitive to the primary and secondary structure and

thus should be another useful source of information of the molecular structure. With these premises and because of the favorable escape depth of the photoelectrons (1–10 nm), X-ray photoelectron spectroscopy (XPS) could then be particularly well suited to obtain information of the molecular structure of polymer chains at the sample surface.

To our knowledge, only three XPS measurements have been reported on the valence region of polypropylene (PP) [7–9], but with very little attempt if any to relate the data to the chain molecular structure of PP chains at the surface. The theoretical situation on polypropylene is not better since reported calculations have only been carried out at the extended Hückel level [7,10,11], which is not really suitable for describing the interactions responsible for the changes in the molecular structure (primary and secondary). The purpose of this work is to carry out exploratory *ab initio* RHF/STO-3G calculations on extended regular polypropylene chains in order to assess qualitatively the dependence of the energy band structure on the primary and secondary structures and its possible future exploitation in more applied situations.

Methodology

In this section we introduce the model structures and provide justification for the level of the theory used in this preliminary contribution.

Work Motivation and Model Structures

Polypropylene, $[-CH_2-CH(CH_3)-]_x$, is polymerized stereoselectively using Ziegler–Natta catalysts. Isotactic PP is obtained by heterogeneous catalysis with $TiCl_3/Al(C_2H_5)_3$ and its chain structure is found to be a (3/1) helix [12], hereafter denoted *it*-(TG)₃. Syndiotactic PP can be prepared by homogeneous catalysis with $VCl_4/Al(C_2H_5)_2Cl$. In the syndiotactic configuration two conformations have been reported: a (4/1) helix [13] and a planar zigzag form [14], respectively denoted *st*-(T₂G₂)₂ and *st*-(PZZ). The *st*-(PZZ) conformation can be prepared by rapid cooling in ice water of the helical form *st*-(T₂G₂)₂ previously melted at 140°C, and subsequently stretching. Infrared and X-ray diffraction (DRX) measurements indicate that under such conditions the *st*-(T₂G₂)₂ sample is completely converted to the zigzag planar *st*-(PZZ) form. The original helical *st*-(T₂G₂)₂ structure can be reversibly recovered by heating the *st*-(PZZ) form at 100°C for a few hours.

When it comes to molecular structure at the surface, however, the situation is not as clearcut as in bulk because infrared, which has a sampling depth of 1 μm and more, and DRX are poor detectors of the surface characteristics. It is known, for example, that in bulk the high molecular weight poly(ethylene oxide) chains, $[-CH_2-CH_2-O-]_x$, adopt a zigzag planar conformation, while those of low molecular weight are (7/2) helices [15]. Thanks to combined theoretical and XPS studies [16], it has been pointed out that poly(ethylene oxide) chains at the surface sample are dominantly in the helical form, irrespective of their molecular weight. Accordingly, it cannot be concluded without a further check that at the surface sample the polypropylene syndiotactic chains undergo similar changes as in the

bulk during the above-mentioned heat treatments. The purpose of the present work is therefore to establish a preliminary theoretical basis for forthcoming XPS measurements on PP samples treated in the way just described.

In this exploratory study we confine our interest to a comparison of the electronic band structure of the regular *it*-(TG)₃, *st*-(T₂G₂)₂, and *st*-(PZZ) extended PP chains. In constructing the model structures shown in Figure 1, standard bond distances have been used (0.154 and 0.108 nm for C—C and C—H, respectively) and tetrahedral valence angles have been assumed for C—C—C, C—C—H, and H—C—H.

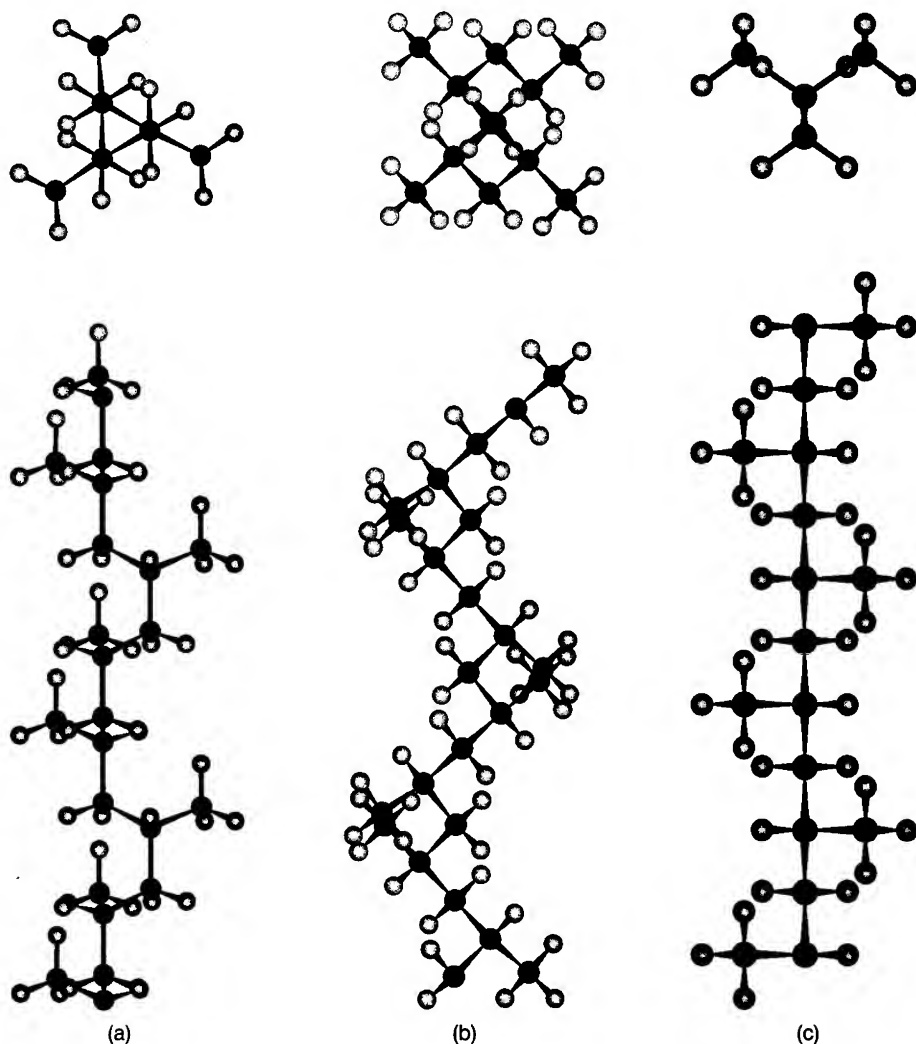


Figure 1. Top and side views of the molecular structure of polypropylene chains in (a) isotactic helical *it*-(TG)₃, (b) syndiotactic helical *st*-(T₂G₂)₂, and (c) syndiotactic planar zigzag *st*-(PZZ) forms.

Calculations

The analysis in this work is based on band structures [17,18] computed at the RHF level with the PLH program [19], using the STO-3G basis set [20]. The PLH program includes long-range coulomb interactions which are accounted for via a multipole expansion technique including all monopole-quadrupole and dipole-dipole interactions. For the three forms, the number of unit cells in the short and intermediate region are 7 (-3 to +3) and 13 (-6 to +6), respectively, which is found sufficient to ensure proper convergence of the results with respect to the lattice summations. The threshold for the two-electron integrals and the criterion for convergence on the density matrix elements are set to 10^{-7} a.u. and 10^{-5} , respectively.

The choice of this theoretical level stems from previously successful comparisons [3-6] of similar calculations with corresponding experimental data on the closely related linear and cyclic alkanes as well as polyethylene. First, they show that the electronic structure signature of polyethylene chain conformations depends on the strength of hyperconjugative interactions between the $\text{—CH}_2\text{—}$ moieties along the polymer spine. Therefore, it is important to rely on SCF approaches to allow the electron charge distribution to relax according to the conformational modifications imposed. Second, the main features of the one-electron picture are conserved in the case of saturated hydrocarbons, except possibly in the high energy region of the inner valence band [3,5,6]. Since most of the conformational changes take place in the outer part of the inner valence band and in the outer valence band, band structure calculations can be fruitfully and safely used for qualitative searches of structural information in the XPS valence band of saturated hydrocarbons. It was stressed, however, that a similar approach would be totally inappropriate in the case of conjugated polymers as recently shown experimentally [21] and theoretically [22]. Finally, in all these studies the STO-3G minimal basis has been found to perform quite satisfactorily compared to the other bases, an observation that has motivated our choice for this basis set in the context of this exploratory contribution.

Results and Discussion

In this section we briefly compare the relative stability of the three PP chain structures as calculated in this work before considering salient differences in their electronic structure.

Relative Stability of the Chains

As intuitively expected, calculations predict very comparable total energies E_T for the three structures. It must be kept in mind that these calculations have been carried out on model structures built with standard bond lengths and angles. Nevertheless, it is interesting to find that the isotactic and syndiotactic helical structures, respectively *it*-(TG)₃ and *st*-(T₂G₂)₂, are very comparable in energy, differing by less than 1.6 kJ mol⁻¹. This difference is nearly five times larger, amounting to 7.3 kJ mol⁻¹ for the two syndiotactic structures, i.e., *st*-(T₂G₂)₂ and *st*-(PZZ). In the

case of the isotactic structure, it is easy to understand that the formation of a helix is favored because it reduces the steric interactions between methyl groups, which would be much too close in a straight zigzag planar form. In the syndiotactic case the situation is less clearcut because, due to their alternate locations with respect to the carbon-carbon backbone, the methyl groups are much further apart than they would be in a hypothetical zigzag planar isotactic form. Thus, it appears that the interactions between the methyl groups and the neighboring hydrogens are still too large and impose to the chain its helical $st-(T_2G_2)_2$ structure. This point, however, would require further work with a more sophisticated theoretical description to be properly analysed.

Despite the present level of the theory and the arbitrariness of geometrical parameters used in this exploratory study to build the chain structures, if 7.3 kJ mol^{-1} is a realistic energy difference, then packing interactions should be the factors ultimately controlling the molecular structure adopted by the syndiotactic form as a function of temperature. This alone is important for the main purpose of this contribution since chain interactions at the surface, and therefore molecular structure, could be somewhat different than in the bulk. It also raises an interesting question as to the long-term stability of the planar zigzag form at low temperatures and ultimately the role of chain interactions in this situation.

Electronic Structure

In this subsection we examine the difference in the shape of band structures and their corresponding density of states and make some comments on the possible observation of these changes by actual XPS experiments. The band structures of the three selected structures, $it-(TG)_3$, $st-(T_2G_2)_2$, and $st-(PZZ)$, shown in Figures 2a, 2b, and 2c, look apparently different, but this is only due to the difference in the number of $-\text{CH}_2-\text{CH}(\text{CH}_3)-$ moieties, respectively three, four, and two, needed to constitute the translational repeat.

Considering first the two helical structures, $it-(TG)_3$ and $st-(T_2G_2)_2$, the overall one-electron energy dispersion curves with respect to k are rather similar and lead to closely related density of states graphs, $D(E)$, in Figures 3a and 3b. This observation fits with the one-electron energies which delineate the inner- and outer-valence regions (Table 1). There are differences, however, in the $D(E)$ graphs that are worth stressing in view of XPS detection. We will limit our attention to three regions, respectively denoted I, II, and III in Figure 3.

Owing to the relatively high photoionization cross sections of C_{2s} atomic functions prevailing in the description of the one-electron states in the inner valence region, the apparently minor inverted relative intensities of the two outermost peaks, I in Figure 3, should be detectable even if it is less marked than in the case of the folds in polyethylene chains [3]. In region II (Fig. 3), characteristic of the methyl groups, two lines are predicted in the case of the syndiotactic helix, $st-(T_2G_2)_2$, while only one peak is obtained in the case of the isotactic case, $it-(TG)_3$. However, it will require high resolution instruments such as the SCIENTA 300 to reveal such a difference which simply could amount to variable peak widths.

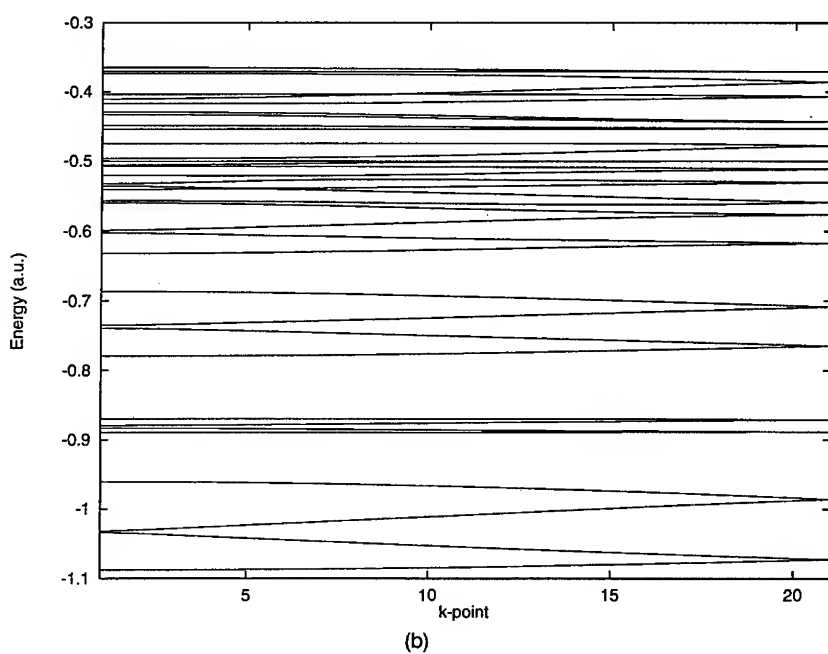
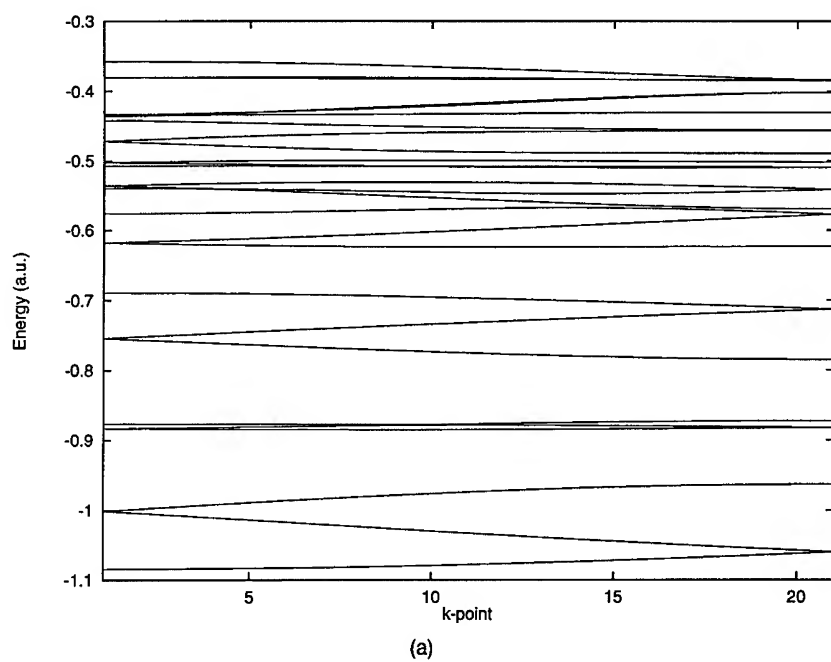


Figure 2. RHF/STO-3G valence electronic band structure of extended chains of polypropylene in (a) isotactic helical it -(TG)₃ and (b) syndiotactic helical st -(T₂G₂)₂ forms.

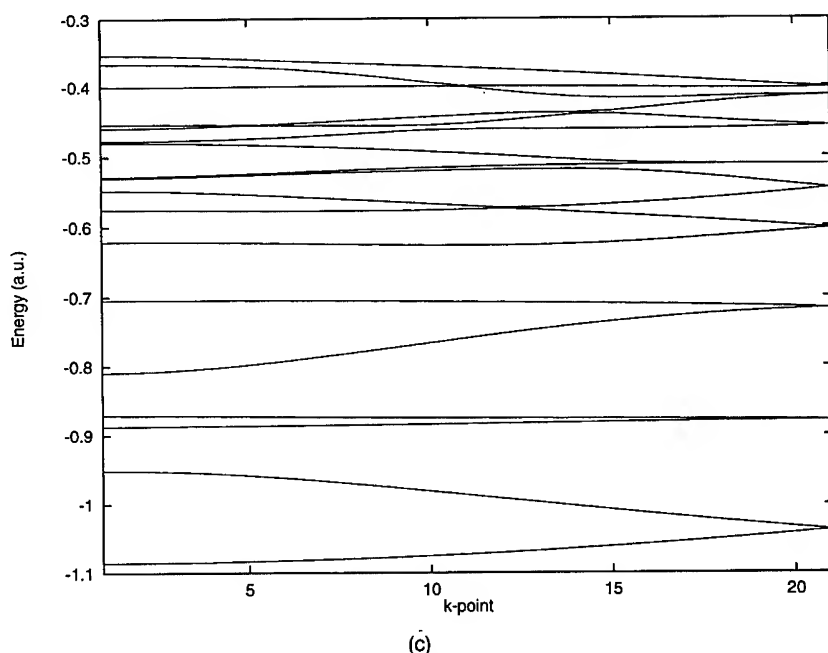


Figure 2. (c) Syndiotactic planar zigzag *st*-(PZZ) form. Energies are expressed in atomic units.

The outer valence region, III in Figure 3, which appears to be quite different for the *it*-(TG)₃ and *st*-(T₂G₂)₂ forms, could in principle be used as a source to discriminate the primary structure of polypropylene chains. Caution should be exercised in this case, however, because in the outer valence region the atomic functions representing the one-electron states are dominantly C_{2p} and their relative photoionisation cross sections are at least 10 times smaller than the C_{2s} ones. In addition to a resulting lower intensity, the individual levels will also be more differently affected by these cross-section effects than the inner valence states [3b-d,5,6]. Despite the neglect of cross-section and many-body effects in the present calculations, we can only acknowledge the fact that this region is potentially rich in information on the molecular structure; but more advanced treatments using a Green's function approach should be considered, e.g., as in Refs. [3b-d,5,6]. For instance, with such a treatment it was theoretically pointed out [5] and experimentally verified [6] that this region contains information that allows the differentiation between two types of folds at the surface of polyethylene lamellae. Thus, with this proviso of cross-section and electron correlation effects, the XPS outer valence region is likely to be different in both isotactic and syndiotactic helices, as suggested by the differences in the shape of region III in Figures 3a and 3b; but, as in the case of the levels signing the methyl groups, high resolution experiments will be needed to assess these predictions.

In our problem, detecting conformations by XPS is a more interesting goal than discriminating the primary structure. Indeed, before deposition as thin films on

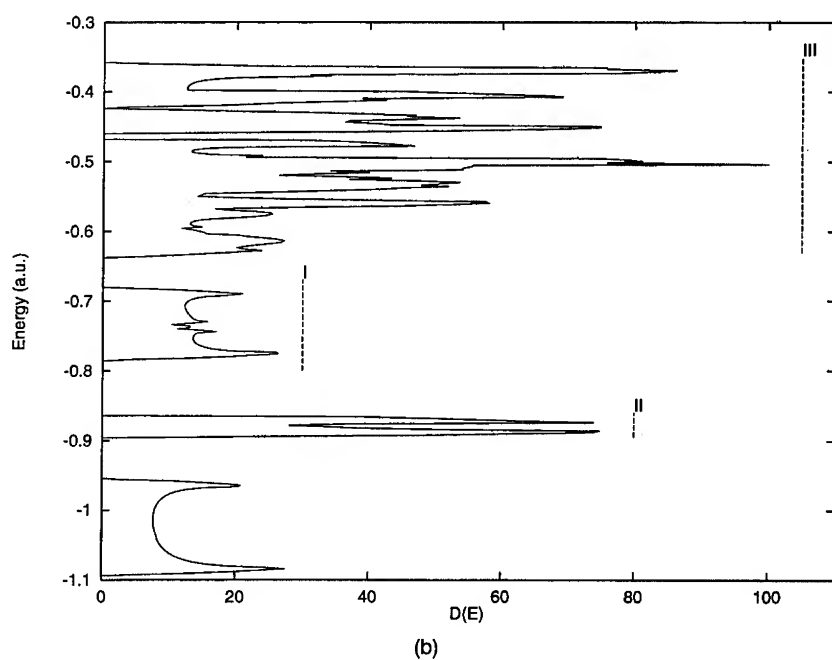
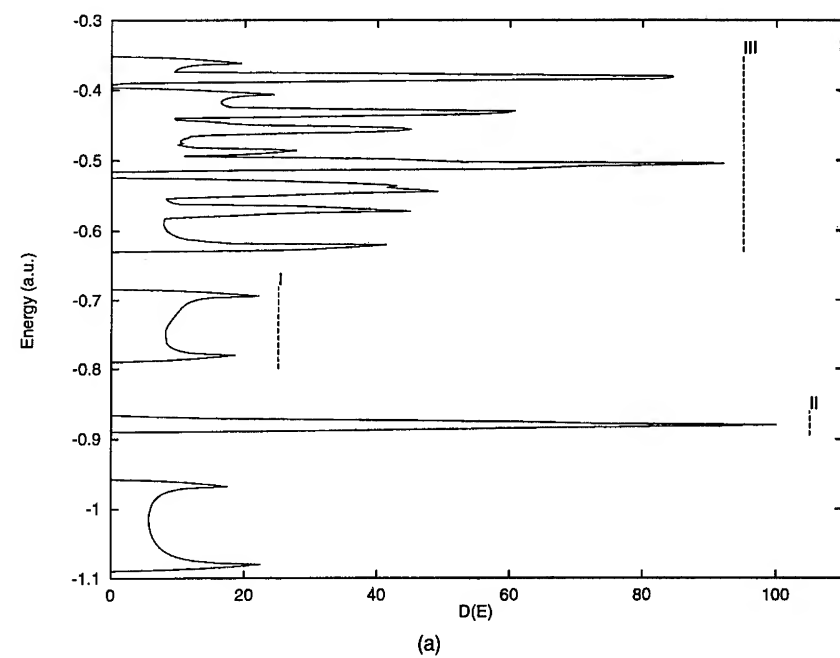


Figure 3. RHF/STO-3G valence electronic band density of states of extended chains of polypropylene in: (a) isotactic helical $it-(TG)_3$ and (b) syndiotactic helical $st-(T_2G_2)_2$ forms.

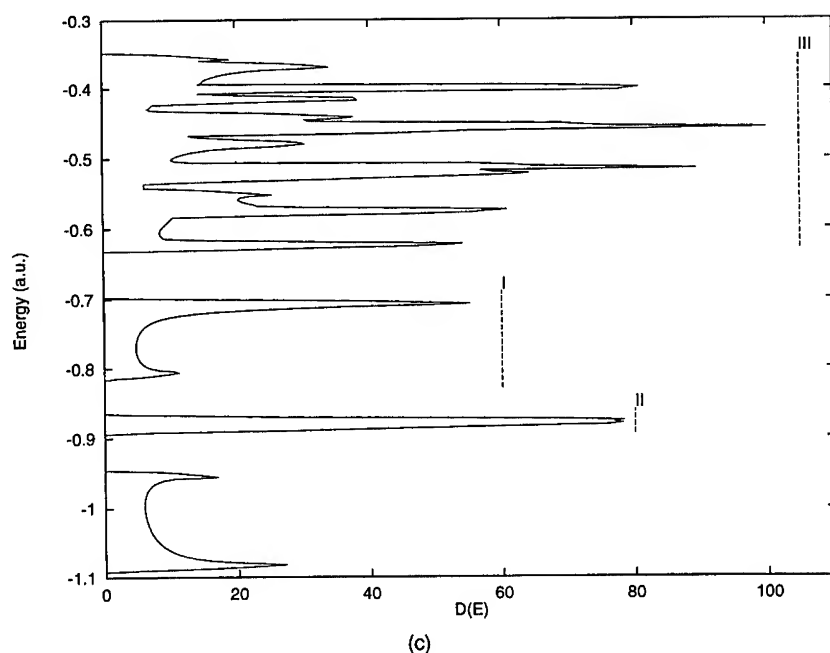


Figure 3. (c) Syndiotactic planar zigzag *st*-(PZZ) form. Energies are expressed in atomic units.

substrates, the primary structure of the polymer chains can easily be assessed by NMR, but it is less obvious to probe the conformation of the chains at the surface of the polymer film once deposited. It is precisely this kind of difference that exist between the syndiotactic *st*-(T₂G₂)₂ and *st*-(PZZ) forms that we are addressing now.

In the case of the *st*-(T₂G₂)₂ and *st*-(PZZ) forms, one notices that the relative intensity ratio of the two peaks in the region I of the density of states is significantly more different than found previously when comparing the two helical structures

TABLE I. Total energy E_T per $-\text{CH}_2-\text{CH}(\text{CH}_3)-$ fragment of the polymer chain and selected one-electron energies $\epsilon_{x,y}$ of the band structure ($x = o$ or i , respectively for outer and inner valence, and $y = h$ or l , respectively for highest or lowest energy).

E_T	<i>it</i> -(TG) ₃ -115.732323	<i>st</i> -(T ₂ G ₂) ₂ -115.732916	<i>st</i> -(PZZ) -115.730098
Inner valence			
$\epsilon_{i,l}$	-1.084	-1.088	-1.086
$\epsilon_{i,h}$	-0.689	-0.687	-0.705
Outer valence			
$\epsilon_{o,l}$	-0.623	-0.632	-0.627
$\epsilon_{o,h}$	-0.357	-0.365	-0.354

it-(TG)₃ and *st*-(T₂G₂)₂. More important from an experimental viewpoint is that the ratio of the low energy peak of region I compared to peak II is also very different in structures *st*-(T₂G₂)₂ and *st*-(PZZ). This behavior has been understood in recent work on polyethylene folds [3a–b]. The intensity rise of the low energy peak in region I is related to the weak dispersion of the topmost band of the inner valence region around -0.70 a.u. as can be seen in Figure 2c (see also Table 1). With respect to the corresponding band in *st*-(T₂G₂)₂, a significant energy stabilisation of the order of 0.5 eV is noted for *st*-(PZZ). This originates in a sizeable through-space interaction of hyperconjugative nature building up in the zigzag planar form between the $\text{—CH}_2\text{—}$ moieties oriented in a parallel direction. This particular orbital mixing, also referred to as sigma conjugation along the polymer backbone, has been previously invoked [23] to explain the extremely weak absorption intensity in the infrared spectra of the $\text{—CH}_2\text{—}$ wagging motions of the all-staggered conformation of polyethylene. The net result of this stabilization and weak energy dispersion with respect to k is a higher density of state at -0.70 a.u. and a higher intensity peak in the region I. As in the case of polyethylene folds, the shift and intensity variation should be detected by XPS provided, of course, that the chains are dominantly in a zigzag planar conformation at the surface of the cooled and stretched syndiotactic polypropylene. These features should be useful signatures of the conformational changes that can take place in the chains at the surface of polymer films.

Regarding the outer valence region III, we will limit our comments to those already made in the case of the two helical structures. They definitely show differences that should be traced in actual spectra provided the intensity is not too low. In any event, more advanced treatments including effects of the photoionization cross section and electron correlation will be needed to provide a better basis for interpretation.

Concluding Remarks

The goal of this work was to assess the dependence of the electronic structure of polypropylene chains on their primary and secondary structures and the extent to which the changes can constitute fingerprints for XPS experiments.

The main result of this exploratory and rather simple study is that the two reported conformations of syndiotactic polypropylene, *st*-(T₂G₂)₂ and *st*-(PZZ), could be detected from features of their XPS valence bands, especially the relative intensities of two main peaks in the low energy regions I and II of the inner valence band. In that respect, it is worth stressing the consistency between vibrational and electronic structure information: They both point to the importance in extended systems of hyperconjugative interaction between the $\text{—CH}_2\text{—}$ moieties of the polymer and their role in “transmitting” the conformational message. It should be added that the majority of vinyl polymers are based on repeat units of the general type, $\text{—CH}_2\text{—CR}_1\text{R}_2\text{—}$, and thus are likely to have such sigma conjugation operating along their backbone depending on the chain structure. More advanced descriptions of the electronic structure of polypropylene are now in progress [24]; they will be paralleled with XPS measurements on carefully designed heat treatments of polypropylene samples [25].

It should be stressed at this point that effects of primary and secondary structures on the electronic structures cannot really be taken into account separately in model calculations. For example and along the same line, theoretical calculations [26] have recently pointed out the danger in relying on straightforward correlations between NMR and infrared results to afterwards assess the isotacticity percentage in polyacrylonitrile from infrared data alone.

Regarding the conformation of polyolefin chains in the bulk, it is interesting to note that the polarizability per $\text{—C}_2\text{H}_4\text{—}$ unit in polyethylene is roughly 2% higher in zigzag planar form than in other conformations [27]. Owing to the role played by the electric polarizability on the strength of intermolecular interactions, this observation might provide another clue as to why alkane chains favor rather systematically the straight zigzag planar form, even when quickly cooled down on cold substrates from the gas to solid phase. In relation with syndiotactic polypropylene, it is conceivable that, when thermal agitation is reduced, the zigzag planar form is actually preferred, most likely because of synergetic interactions between the chains in which polarizability is enhanced by hyperconjugation mechanisms. Polarizability, being an extensive property, has ample opportunity to become decisive with respect to the preferred conformation adopted by polyolefin chains.

Acknowledgments

I. F. and D. H. M. thank the Services de la Programmation Scientifique (SPPS) for the grant received in the framework of the ELSAM project. M. D. thanks the Belgian National Fund for Scientific Research (FNRS) for his Research Assistant position and J. D. acknowledges the financial support of the Communauté Française de Belgique. This contribution has also been supported by the projects FNRS-FRFC Nos. 9.4624.90 and 2.45119.91 and the Belgian National Interuniversity Research Program (PAI/IUAP No. P3-049). The calculations reported have been carried out on the "Namur Scientific Computing Facility", with the financial support of the FNRS-FRFC, the "Loterie Nationale" (9.4553.92), and the FNRS/Belgian Ministry of Science "Action d'Impulsion à la Recherche Fondamentale" (D.4511.93).

Bibliography

- [1] M. S. Reisch, *Chem. Eng. News*, August 30, 24 (1993).
- [2] J. I. Kroschwitz, Exec. Ed., *Concise Encyclopedia of Polymer Science and Engineering*, (Wiley, New York, 1990).
- [3] (a) J. Delhalle, S. Delhalle, and J. Riga, *J. Chem. Soc. Faraday Trans. 2* **83**, 503 (1988). (b) M. Deleuze, J. P. Denis, J. Delhalle, and B. T. Pickup, *J. Phys. Chem.* **97**, 5115 (1993). (c) M. Deleuze, J. Delhalle, and B. T. Pickup, *Chem. Phys.* **175**, 427 (1993). (d) M. Deleuze, Ph.D. thesis, FUNDP, Namur, Belgium (1993).
- [4] (a) J. Delhalle, J. Riga, J. P. Denis, M. Deleuze, and M. Dosière, *Chem. Phys. Lett.* **210**, 21 (1993). (b) J. Riga, J. Delhalle, M. Deleuze, J. J. Pireaux, and J. J. Verbist, *Surf. Interf. Sci. Anal.*, to appear.
- [5] M. Deleuze, J. Delhalle, and B. T. Pickup, *J. Phys. Chem.* **98**, 2382 (1994).
- [6] M. Deleuze, J. Delhalle, and B. T. Pickup, S. Svensson, to appear.
- [7] J. J. Pireaux, J. Riga, R. Caudano, J. J. Verbist, J. Delhalle, S. Delhalle, J. M. André, and Y. Gobillon, *Phys. Scripta* **16**, 329 (1977).

- [8] J. J. Pireaux, J. Riga, R. Caudano, and J. Verbist, *Am. Chem. Soc. Symp. Seri.* **162**, 169 (1981).
- [9] G. Beamson and D. Briggs, *High Resolution XPS of Organic Polymers* (Wiley, Chichester, 1992).
- [10] J. Delhalle, R. Montigny, C. Demanet, and J. M. André, *Theor. Chim. Acta* **50**, 343 (1979).
- [11] V. Van Wonterghem, *Mémoire de Licence, Facultés Universitaires Notre-Dame de la Paix, Namur, Belgium* (1981).
- [12] (a) G. Natta and P. Corradini, *Nuovo Cimento Suppl.* **15**, 40 (1960). (b) E. J. Addink and J. Beintema, *Polymer* **2**, 185 (1961). (c) A. Turner-Jones and A. J. Cobbold, *J. Polym. Sci.* **B6**, 539 (1968). (d) R. J. Samuels and R. Y. Yee, *J. Polym. Sci. A-2* **10**, 358 (1972).
- [13] P. Corradini, G. Natta, P. Ganis, and P. A. Temussi, *J. Polym. Sci.* **C16**, 2477 (1967).
- [14] (a) G. Natta, M. Peraldo, and G. Allegra, *Makromol. Chem.* **75**, 215 (1964). (b) H. Tadokoro, M. Kobayashi, Shodo Kobayashi, K. Yasufuku, and K. Mori, *Rep. Prog. Polym. Phys. Jpn.* **9**, 181 (1966).
- [15] (a) T. Miyazawa, K. Fukushima, and Y. Ideguchi, *J. Chem. Phys.* **37**, 2764 (1962). (b) T. Yoshirara, H. Tadokoro, and S. Murahashi, *J. Chem. Phys.* **41**, 2902 (1964). (c) H. Matsuura, T. Miyazawa, and K. Machida, *Spectrochim. Acta* **29A**, 771 (1973). G. R. Rao, C. Castiglioni, M. Gussoni, and G. Zerbi, *Polymer* **26**, 811 (1985).
- [16] P. Boulanger, J. Riga, J. J. Verbist, and J. Delhalle, in *Polymer-Solid Interfaces*, J. J. Pireaux, P. Bertrand, and J. L. Brédas, Eds. (Adam Hilger, Bristol, 1992), pp. 315-323.
- [17] G. Del Re, J. Ladik, and G. Bicz, *Phys. Rev.* **155**, 977 (1967).
- [18] J. M. André, L. Gouverneur, and G. Leroy, *Int. J. Quantum Chem.* **1**, 427 (1967).
- [19] (a) J. M. André, D. H. Mosley, B. Champagne, J. Delhalle, J. G. Fripiat, J. L. Brédas, D. J. Vanderveken, and D. P. Vercouteren, in *Methods and Techniques in Computational Chemistry (METECC-94)*, E. Clementi, Ed. (Stef, Cagliari, 1993), Vol. B, Chap. 10, pp. 429ff. (b) J. G. Fripiat, D. H. Mosley, B. Champagne, and J. M. André, PLH-93 available from Club Européen-MOTECC, c/o Prof. E. Clementi, CRS4, Cagliari, Italy.
- [20] W. J. Hehre, R. Ditchfield, R. F. Stewart, and J. A. Pople, *J. Chem. Phys.* **52**, 2769 (1970).
- [21] M. P. Keane, A. Naves de Brito, N. Correia, S. Svensson, L. Karlsson, B. Wannberg, U. Gelius, S. Lunell, W. Salaneck, M. Lögdlund, D. Swanson, and A. McDiarmid, *Phys. Rev.* **B45**, 6390 (1992).
- [22] (a) M. Deleuze, P. Horeczky, J. Delhalle, and B. T. Pickup, *Int. J. Quantum Chem. Quantum Chem. Symp.* **26**, 31 (1992). (b) C.-M. Liegener, *Phys. Rev.* **B47**, 1607 (1993).
- [23] C. Castiglioni, M. Gusoni, and G. Zerbi, *J. Chem. Phys.* **95**, 7144 (1991).
- [24] M. Deleuze et al., to appear.
- [25] J. Riga et al., to appear.
- [26] (a) D. Mathieu, M. Defranceschi, G. Lécayon, A. Grand, and J. Delhalle, *Chem. Phys.* **171**, 133 (1993). (b) D. Mathieu, M. Defranceschi, G. Lécayon, and J. Delhalle, *Chem. Phys.*, to appear.
- [27] D. H. Mosley, M. Deleuze, J. G. Fripiat, J. M. André, and J. Delhalle, to appear.

Received March 14, 1994

Semiempirical Studies of the Interaction between Metals and π -Conjugated Polymers: Sodium on Diphenylpolyenes and Aluminum on Poly(*p*-phenylenevinylene) and Derivatives

M. LÖGDLUND and J. L. BRÉDAS

Service de Chimie des Matériaux Nouveaux, Centre de Recherche en Electronique et Photonique Moléculaires, Université de Mons-Hainaut, Place du Parc 20, B-7000 Mons, Belgium

Abstract

We report some of our recent results from theoretical modeling of the interaction between metals and π -conjugated molecules. We apply the semiempirical Austin Model 1 method for the investigation of two fundamentally different systems: sodium interacting with diphenylpolyenes and aluminum interacting with poly(*p*-phenylenevinylene) and derivatives. In the former case, electronic-structure calculations are also performed using the nonempirical pseudopotential Valence Effective Hamiltonian (VEH) technique. For sodium interacting with diphenylpolyenes, we investigate the geometric and electronic structure modifications that are induced upon charge transfer in a series of diphenylpolyenes with an even number of carbons (from stilbene to α,ω -diphenyltetradecaheptaene, i.e., one to seven double bonds in the polyene part of the molecule). Densities of valence states generated from the VEH calculations are directly compared to experimental ultraviolet photoelectron spectroscopy valence band spectra; these are recorded during successive sodium exposure of the molecular solids. The charge-storage states in the series are discussed in terms of soliton-antisoliton-pairs and polaron-like states induced upon doping (reduction). Introducing aluminum atoms onto poly(*p*-phenylenevinylene) systems allows us to study the initial stages of interface formation. We find that aluminum atoms preferentially react with the vinylene linkages in both poly(*p*-phenylenevinylene) and poly(2,5-dimethoxy-*p*-phenylenevinylene). When carbonyl groups appear on the side of the chains, as in poly(2,5-dialdehyde-*p*-phenylenevinylene), new reactive sites are induced, leading to structures with stabilities comparable to those in the most stable configurations involving a single vinylene group. In all three systems investigated, the interaction with aluminum induces major modifications of the polymer chains with interruptions of the π -system caused by formation of sp^3 -like defects. © 1994 John Wiley & Sons, Inc.

Introduction

Conjugated polymers constitute a class of materials that has attracted much attention during the past decade. Initially, studies mainly focused on the ability of doping conjugated polymers to high electrical conductivities; considerable work has been devoted to the understanding of the charge storage mechanisms in these materials [1,2]. Nowadays, it is well established that excess electronic charges, introduced via redox chemistry either by electron acceptors or donors, are accommodated as charged solitons in trans-polyacetylene, due to the degeneracy of the ground state [3–5]. The extension of these soliton wave functions is about 15–20

carbons in long polyene chains [5]. However, theoretical studies have suggested that the width of the solitons shrinks as the length of the polyene chain decreases, down to an extension of about 3–5 carbon sites in tetradecaheptaene [6]. A recent ultraviolet photoelectron spectroscopy study of the sodium doping of α,ω -diphenyltetradecaheptaene supports this prediction; the charge-storage states appear to be in the form of soliton–antisoliton pairs, confined within the 14-carbon long polyene chain [7].

These quasi-one-dimensional systems also possess many other interesting features such as nonlinear excitations, very large nonlinear optical responses, as well as remarkable semiconducting properties. The latter have made it possible to use some of the π -conjugated materials as active components in electronic or optoelectronic devices; in particular devices such as Schottky diodes [8], field-effect transistors [8], and light-emitting diodes (LED's) [9–14] have been demonstrated.

A number of LED's based on different conjugated polymers have been reported. The color of the emitted light can be tuned, from blue [13] to green/yellow [9] or to red [10], by either choosing the appropriate polymer, modifying a specific polymer by means of attaching side groups, or using copolymers. The polymer LED's show promising characteristics and unique properties such as flexibility [12] and the possibility of emission of polarized light (a first step towards polarized light-emitting diodes has been the observation of polarized photoluminescence from highly oriented polymer blends [15]). The most common polymers in LED's nowadays are poly(*p*-phenylenevinylene), PPV, and its derivatives [9–12]. In polymer-based LED's, the polymer is sandwiched between two metal electrodes. Electrons and holes are injected from the metal contacts into the polymer and negatively and positively charged polarons are formed. These charged polarons migrate under the influence of the applied field and when oppositely charged species find each other, they form polaron-excitons which can then undergo radiative recombination.

The interfaces between the electroactive polymer and the metal electrodes thus represent important characteristics of the devices. Low workfunction metals such as aluminum and calcium are used for the electron injecting contact, while the hole injecting contact usually consists of indium–tin–oxide or in some cases, the highly conducting form of polyaniline [12]. X-ray photoelectron spectroscopy (XPS) studies of Al on PPV [16] and Al on poly(*p*-phenylene) [17] have indicated the presence of significant amounts of oxygen at the metal/polymer interface. The exact influence, on the device function, of the oxygen present at the interface is not fully understood at the moment; interfacial oxygen can build up during the metal evaporation [17] or be introduced during film preparation. Examples of the latter case can be found in the literature; results from XPS studies of PPV surfaces show that oxygen is present in significant amounts [18–20], although the precise form of the oxygen in these samples is not clear. In contaminated polyphenylquinoxaline, both C—O and C=O species were identified by XPS measurements [21].

The use of conjugated molecules or oligomers of conjugated polymers as models for the conjugated polymers themselves has been an approach extensively used during the last few years [22–29]. For example, many studies have been devoted to the investigation of the interaction between metals and conjugated molecules,

including oligomers of conjugated polymers [25,30–34]. These studies can be helpful for the understanding of the interface formation between metals and conjugated systems as well as the possible charge-storage configurations induced by charge transfer. In addition, information from this type of model studies can contribute significantly to the understanding of the real conjugated polymer systems; it might be possible to predict, on the basis of the oligomers, the behavior in the polymeric case. The study of oligomers of conjugated polymers and of conjugated molecules is attracting increasing interest also due to the fact that these molecular materials can themselves be exploited in device applications, as for example in the all-organic transistor developed by Garnier et al. where α -sexithienyl has been used as the active component [35].

In this contribution, we review the results of some of our recent theoretical studies on the interaction between metals and conjugated molecules. We have chosen to present two fundamentally different systems; the interaction between sodium and diphenylpolyenes and that between aluminum and poly(*p*-phenylenevinylene) and derivatives; this allows us to study the initial stages of metal/conjugated polymer interface formation.

In the sodium/polyene study, we have considered α,ω -diphenylpolyenes with 1 to 7 double bonds in the polyene part of the molecules. The molecules are hereafter denoted DP x ($x = 1-7$), where DP stands for diphenyl and x is the number of double bonds in the polyene segment. The molecular structures are shown in Figure 1(a). The theoretical results are compared to XPS and ultraviolet photoelectron

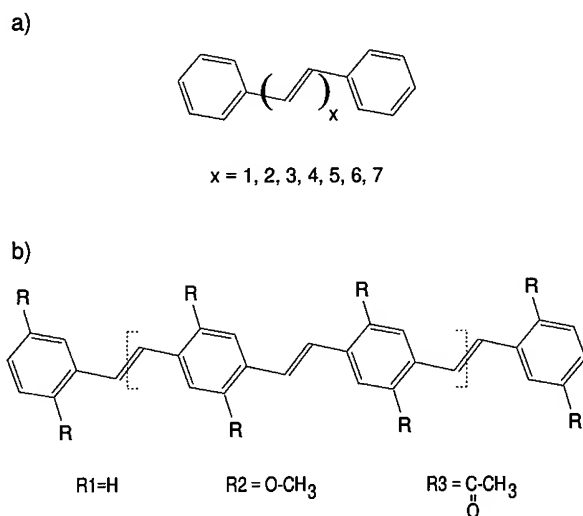


Figure 1. Molecular structures of: (a) the diphenylpolyene series, where x denotes the number of double bonds in the polyene part; and (b) the oligomers of poly(*p*-phenylenevinylene) where the substituents refer to: R1, poly(*p*-phenylenevinylene) itself; R2, poly(2,5-dimethoxy-*p*-phenylenevinylene); and R3, poly(2,5-dialdehyde-*p*-phenylenevinylene).

spectroscopy (UPS) data recorded during successive sodium exposure of the diphenylpolyene molecular solids [36].

We then discuss the results of calculations on aluminum interacting with PPV and poly(2,5-dimethoxy-*p*-phenylenevinylene), DMeOPPV. Due to the lack of current information about the exact configuration of oxygen in contaminated surfaces of PPV, we have also chosen to investigate some possible effects of oxygen by incorporating carbonyl groups on the side of the polymer chains. In this case, we actually replaced the MeO groups along the DMeOPPV chains by carbonyl groups to form poly(2,5-dialdehyde-*p*-phenylenevinylene), DAPPV. The molecular structures are shown in Figure 1(b).

Theoretical Methodology

Geometry optimizations have been performed on the pristine and metal/molecule systems, using the semiempirical Austin Model 1 (AM1) method [37], which is known to yield reliable geometries for large organic molecules. The experimental XPS data on the sodium/diphenylpolyene interaction indicate the appearance of ionic sodium atoms, i.e., there occurs complete charge transfer between the sodiums and the DP x molecules [36]. The interaction can thus be considered as corresponding to a doping (reduction) of the DP x molecules by sodium. The doping is simply simulated in the calculations by adding one or two electrons to the molecules in the case of singly and doubly doped systems (i.e., effectively taking into account one or two sodiums per molecule, respectively). In the case of doubly charged systems, calculations including explicitly the counter-ions have also been carried out.

From experimental data, it is deduced that the diphenylpolyenes are almost totally planar in the molecular solids. The tilt angles of the phenyl groups with respect to the polyene plane have been measured to be on the order of 5.4° in the case of DP4 [38] and about 3–7° for stilbene (DP1) [39–42]. Such small torsion angles have negligible effects on the electronic structure; the molecules have therefore been taken as fully planar in all the calculations. The AM1-optimized geometries of the neutral and doubly charged diphenylpolyenes have served as input for electronic-structure calculations performed using the Valence Effective Hamiltonian (VEH) pseudopotential method [43,44]; the applicability of the VEH approach in interpreting photoelectron valence band spectra of conjugated systems is well established [45–48]. In addition, VEH provides accurate estimates of the location of the gap states in doped conjugated systems [49].

In order to make a direct comparison between the VEH-calculated electronic densities of valence states (DOVS) and the experimental solid-state UPS valence band spectra, a broadening by convolution with a gaussian, whose full width at half maximum is taken to be 0.7 eV, is applied to the calculated electronic levels. This is in order to simulate the experimental resolution as well as peak broadening due to solid-state effects, e.g., intermolecular interactions.

The appearance of charges in conjugated molecules usually leads to strong geometry relaxations [5,50]; a single charge, i.e., a radical-ion, is then referred to as

a polaron in condensed matter physics terminology; two charges on the molecule, i.e., a di-ion, correspond to a so-called bipolaron or confined soliton–antisoliton pair [5,50]. We will be using this terminology throughout this article; also, the lowest electronic transition will be referred to as the bandgap since we are dealing with molecular solids.

In order to model the reaction between aluminum and PPV compounds, we have considered oligomers of PPV, DMeOPPV, and DAPPV as representatives for the polymers. The results of a preliminary study of the interaction between Al and PPV have been reported recently [51]; the PPV chain was in that case simply represented by a *trans*-stilbene molecule; here, we have considered oligomers consisting of three monomer units capped by the appropriate phenyl group for each system investigated. Recently, a systematic study of the interface between Al and *trans*-polyenes indicated that the Modified Neglect of Diatomic Overlap (MNDO) and AM1 methods are able to describe adequately the metal/polymer interactions, in comparison to *ab initio* Hartree–Fock methods including polarization functions [31]. Torsions between different units along the chains can occur in the case of PPV and its derivatives; such torsions are treated more accurately by the AM1 method than the MNDO method, which explains our choice of the former.

Full geometry optimizations for pairs of Al atoms reacting with the three PPV-based polymers have been carried out for a wide number of possible configurations, leading to different local energy minima. The Al atoms have been introduced on the central units of the trimers, i.e., within the region indicated by the dashed parentheses in Figure 1(b). Estimates of the charge distributions have been obtained following a simple Mulliken population analysis; since this approach is strongly method dependent, we are interested only in the qualitative trends in the charge-distribution evolutions.

Sodium Interacting with Diphenylpolyenes

Neutral Systems

The AM1 optimized geometries of the neutral DP7 to DP1 molecules are shown in Table I. The optimizations results in very similar bond-length differences between the central single and double bonds throughout the whole series; the bond-length alternation ranges from 0.097 Å in DP7 to DP4, up to 0.109 Å in DP1. The corresponding value for the central part in an AM1-optimized 30-carbon long *trans*-polyacetylene segment is 0.096 Å (1.347 and 1.443 Å for the double and single bonds, respectively), i.e., very close to what is obtained in the diphenylpolyenes. The experimental values for the carbon–carbon bonds in *trans*-polyacetylene are 1.36 and 1.44 Å, i.e., a bond-length alternation of 0.08 Å [52].

The wave functions of the highest occupied and lowest unoccupied molecular orbitals (HOMO and LUMO, respectively) show dominant contributions from the polyene part of the molecules in the case of neutral DP3–DP7. The polyene-localized nature of these orbitals is the reason why diphenylpolyenes, at least the longer molecules, are suitable as models for *trans*-polyenes [7,53]. However, in DP2 and

TABLE I. AM1 optimized geometries for the neutral DP7-DP1 molecules; the bond lengths are in Å (the labels are those from Fig. 2).

rCx—Cy	DP7	DP6	DP5	DP4	DP3	DP2	DP1
C1—C2	1.396	1.395	1.396	1.396	1.396	1.396	1.396
C2—C3	1.391	1.392	1.391	1.391	1.392	1.392	1.396
C3—C4	1.406	1.406	1.406	1.406	1.406	1.407	1.407
C4—C5	1.451	1.451	1.451	1.451	1.451	1.451	1.452
C5—C6	1.346	1.346	1.346	1.346	1.346	1.345	1.343
C6—C7	1.445	1.445	1.445	1.445	1.445	1.447	
C7—C8	1.347	1.347	1.347	1.347	1.347		
C8—C9	1.444	1.444	1.444	1.444			
C9—C10	1.347	1.347	1.347				
C10—C11	1.444	1.444					
C11—C11'	1.347						

DP1, there occur significant contributions from the phenyl groups to the HOMO and LUMO levels.

Singly Charged Systems

The evolution of the experimental UPS valence band spectra upon sodium exposure of DP5-DP1 are such that at the lowest sodium exposure levels, a single broad feature grows up in the originally forbidden energy gap; upon further doping, i.e., beyond about one sodium atom per molecule, a second feature appears [36,54]. Such an evolution is not observed in DP7 and DP6, where two in-gap features are observed even for the lowest doping levels [7]. These data are interpreted to indicate: (i) the formation of singly doped species at low doping levels in the cases of DP5-DP1, the low doping regime being therefore simulated in the calculations by adding a single electron to the DP5-DP1 molecules; (ii) in DP6 and DP7, even low sodium exposure leads to two alkali atoms per molecule.

In Table II, we display the AM1-optimized structures for the singly charged DP5-DP1 molecules. The polyene part of the molecules evolves towards an almost undimerized situation; the bond-length difference between the central single- and double-bonds is 0.006, 0.008, 0.010, 0.017, 0.029 Å in going from DP5 to DP1. This kind of geometry evolution in the singly charged DP x molecules can be referred to as corresponding to the formation of a polaron; the situation is actually very reminiscent of that occurring in *trans*-polyacetylene [5,50].

The HOMO (singly occupied) and HOMO-1 wave functions in the case of the singly charged DP5-DP1 are mainly localized on the central part of the polyene. Upon charging the molecules with one electron, the LUMO of the neutral molecules becomes singly occupied and moves into the originally forbidden energy gap, forming the singly occupied HOMO of the charged molecules. The former HOMO of the neutral molecules moves upward in energy forming the HOMO-1 level in the charged molecules; this upward motion is small (for instance, 0.29 eV in DP5), which

TABLE II. AM1 optimized geometries for the singly charged DP5–DP1 molecules; the bond lengths are in Å (the labels are those from Fig. 2).

rC _x —C _y	DP5 [−]	DP4 [−]	DP3 [−]	DP2 [−]	DP1 [−]
C1—C2	1.395	1.395	1.396	1.396	1.398
C2—C3	1.390	1.388	1.387	1.386	1.383
C3—C4	1.412	1.413	1.416	1.420	1.424
C4—C5	1.436	1.431	1.424	1.417	1.412
C5—C6	1.362	1.369	1.376	1.382	1.383
C6—C7	1.412	1.405	1.399	1.399	
C7—C8	1.381	1.387	1.389		
C8—C9	1.396	1.395			
C9—C9'	1.390				

explains that in the UPS data, a single in-gap state appears in the polaron-like situations [36,54].

It is important to note at this stage that the UPS data for DP1–DP5 show a continuous motion of the Fermi level away from the valence band edge, until the saturated doping level of about two sodiums per molecule is reached. This is in agreement with a transformation upon doping from polaron-like charged species towards soliton–antisoliton pair defects. In contrast, in the case of DP7 and DP6, the Fermi level shifts only in the very first sodium exposure step and then remains at the same position throughout the whole doping regime.

Doubly Charged Systems

The doping levels in the saturation regime are estimated through the relative intensities between the Na(1s) and C(1s) XPS core-level spectra; they are found to be about two sodiums per molecule throughout the whole series of diphenyl-polyenes included in this study. The experiments also indicate the sodiums to be ionic; this thus corresponds to the formation of doubly charged DP_x molecules (dianions). The AM1 optimizations for the doubly charged molecules are performed with the sodium counter-ions explicitly included. The calculations are restricted to conformations where the DP_x molecules are taken to be planar and the counter-ions are introduced above the molecular plane; these simplifications are consistent with the results of x-ray scattering data [55] and recent high-level *ab initio* calculations including correlation effects [56].

The optimized AM1 geometries are shown in Table III. The sodium atoms are located symmetrically around the center of the molecules, see Figure 2. A total reversal of the bond-length alternation pattern is observed in the middle of the molecules for all of the doubly charged systems; these can therefore be described as containing a confined soliton–antisoliton pair. The sodiums are centered on top of the third carbons from the phenyl groups (i.e., carbons 7 and 7' in Fig. 2) in the cases of DP7 and DP6; for DP5–DP3, the sodiums are above the polyene carbons labeled 5 and 5', which are directly connected to the phenyl groups; finally, for

TABLE III. AM1 optimized geometries (bond lengths in Å) for the doubly charged DPx molecules with counter-ions included. The bonds are labeled following the structures in Fig. 2.

rCx—Cy	Na ₂ DP7	Na ₂ DP6	Na ₂ DP5	Na ₂ DP4	Na ₂ DP3	Na ₂ DP2	Na ₂ DP1
C1—C2	1.396	1.396	1.396	1.396	1.394	1.398	1.404
C2—C3	1.389	1.388	1.387	1.386	1.386	1.380	1.373
C3—C4	1.411	1.413	1.419	1.421	1.424	1.441	1.450
C4—C5	1.435	1.431	1.416	1.412	1.404	1.377	1.369
C5—C6	1.367	1.375	1.402	1.409	1.419	1.430	1.429
C6—C7	1.400	1.390	1.366	1.362	1.357	1.356	
C7—C8	1.412	1.419	1.432	1.435	1.438		
C8—C9	1.360	1.356	1.351	1.351			
C9—C10	1.434	1.438	1.439				
C10—C11	1.350	1.350					
C11—C11'	1.440						
Na—Cx	2.663 (C7)	2.728 (C7)	2.665 (C5)	2.617 (C5)	2.596 (C5)	2.770 (C4)	3.087 (C4)

DP2 and DP1, the sodiums are situated above the phenyl groups (above carbons 4 and 4' and on top of the center of the phenyl groups, respectively). The sodium to molecular plane distances are close to 2.6 Å for DP7 to DP3 and increases somewhat, to about 2.7 Å, when the sodiums are located over the phenyl groups as in DP2 and DP1. *Ab initio* calculations including electron correlation effects result in a sodium to polyene distance of 2.4 Å [56], in agreement with the experimental results [55]; thus, the sodium to polyene distance is somewhat overestimated with the semiempirical AM1 method.

The HOMO and HOMO-1 wave functions (which correspond to the soliton-antisoliton levels in the doubly charged systems) have large contributions from the polyene part of the molecules and are centered at the carbons closest to the sodium atoms in the cases of DP7 to DP3; for these molecules, there are only very small contributions from the phenyl groups. However, as the polyene segment shrinks in size and the defects are forced towards the phenyl groups, the contributions from these groups increase and lead to significant LCAO coefficients on the phenyls for DP1 (although the largest coefficients are still found on the vinylene moiety).

Comparison with Experiment

In the comparison with the UPS experimental data, we focus on the low binding energy part of the spectra, i.e., the region covering the topmost π -levels. These are the π -levels which are mainly involved in the doping process.

In Figure 3, we compare the densities of states (DOS) obtained from VEH calculations with the experimental UPS He I (21.2 eV) valence bands for the neutral DPx molecules. The energy scales are relative to the vacuum level. The energy levels as obtained from VEH are indicated by bars in the figure. The experimental valence bands and the calculated DOS are in excellent agreement. The peaks labeled A, at about -8 eV in the UPS spectra, have their most significant contributions

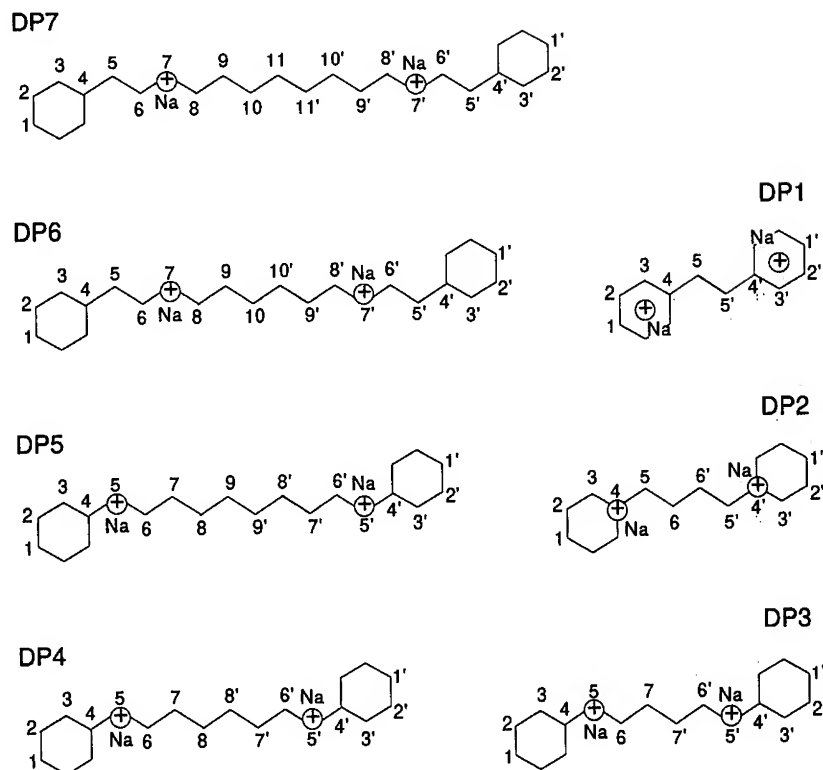


Figure 2. Atom labeling for the diphenylpolyenes and optimized positions of the sodium counter-ions included in the case of doubly charged molecules.

coming from the phenyl groups. We recall that the degenerate HOMO orbitals of benzene split upon connection to the polyene segment. One of these orbitals has a node at the carbon site attached to the polyene, resulting in orbitals localized within the phenyl groups of the diphenylpolyenes. Since peak A is dominated by such contributions, this peak is unaffected by the length of the polyene segment. The peaks at lower binding energies, i.e., the two peaks labeled B and C in the cases of DP7–DP4 and the peak labeled C for DP3–DP1, strongly depend on the polyene length since large coefficients are present on the polyene part of the molecules. To point out the quality of the VEH simulation of the UPS data, it is particularly illustrative to compare the evolutions of the peak originally labeled B in DP7, see Figure 3. As the polyene segment shortens, peak B goes up in binding energy to form a low-energy shoulder to peak A in DP4. In DP3, it appears as a high-energy side shoulder and in DP2, as a separate peak at higher binding energy. The evolutions are identical on both experimental and theoretical spectra.

In Figure 4, we compare the experimental UPS valence bands, as recorded at saturation doping (i.e., at about two sodiums per molecule) with the VEH-calculated DOS. Again, the general features in the experimental and theoretical spectra agree

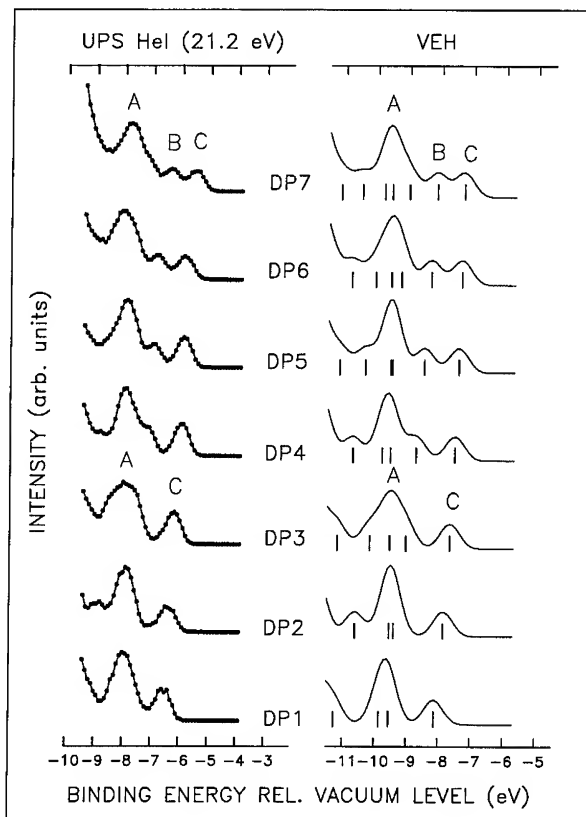


Figure 3. Comparison between the low binding energy part of the VEH-calculated densities of states and the experimental UPS valence band spectra in the cases of the neutral DP7-DP1 molecules.

very well throughout the series. The most important result is the appearance of two new states, labeled D and E, within the originally forbidden bandgap. The splitting between the two gap states depends on the polyene length; as the polyene segment shortens, the splitting increases due to the increased overlap between the soliton-antisoliton wave functions. The theoretical VEH and experimental splittings between the D and E peaks are summarized in Table IV. The experimental data and the results from the VEH calculations agree extremely well (within the experimental error of about 0.1 eV) for DP7 to DP3. In the cases of DP2 and DP1, however, the VEH splitting is overestimated by about 0.3 eV.

We note that the results for the longer diphenylpolyenes are fully consistent with those of a recent study on the *p*-doping of β -carotene, a molecule which contains 11 carbon-carbon double bonds along the conjugated backbone [24]. ESR and optical absorption data indicate the formation of spinless dication, which are described as containing soliton-antisoliton pairs.

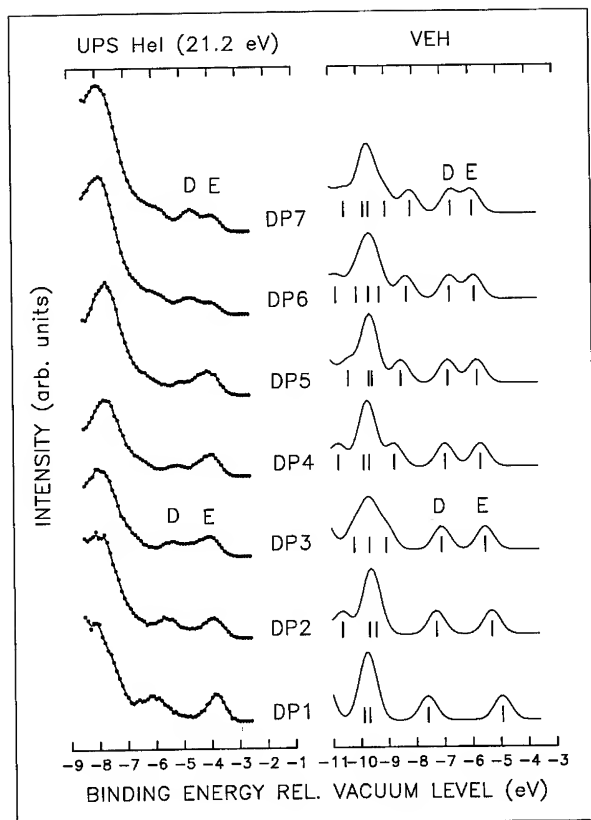


Figure 4. Comparison between the low binding energy part of the VEH-calculated densities of states and the experimental UPS valence band spectra in the cases of the doubly charged DP7-DP1 molecules.

Aluminum Interacting with Poly(*p*-phenylenevinylene) and Derivatives

We are able to find many different stable configurations at the AM1 level for the aluminum/PPV systems investigated, depending on the initial positions of the aluminum atoms. We have considered pairs of aluminum atoms introduced either on the same side or on opposite sides of the molecular plane of the oligomers and

TABLE IV. Experimental UPS and VEH values of the energy difference (in eV) between the two highest occupied levels in doubly charged DP7-DP1.

	DP7	DP6	DP5	DP4	DP3	DP2	DP1
VEH (eV)	0.85	1.00	1.08	1.34	1.66	2.02	2.66
UPS (eV)	0.75	0.8	1.0	1.2	1.5	1.7	2.4

located either on the same unit or on separate units. A general result is that the most energetically stable structures are found when the two aluminum atoms interact with the same chemical moiety, i.e., the same vinylene group or the same phenylene ring. We now discuss the most representative (most stable) configurations for each system.

*The Al₂/poly(*p*-phenylenevinylene) System*

In Figure 5, we display the most energetically favorable structures of the Al₂/poly(*p*-phenylenevinylene) complex in the cases where: (a) two aluminum atoms interact with a vinylene group; and (b) two aluminum atoms interact with a phenylene ring. Only the part mostly affected by the interaction with the aluminum atoms is shown, i.e., the central part of the molecules [as indicated by the dashed parentheses in Fig. 1(b)]. In the same manner as what is found for polyacetylene [31] or polythiophene [57], *each aluminum atom tends to form a covalent bond with a carbon atom*.

The most stable configuration for the Al₂/PPV complex is when the two aluminum atoms are bonded to a single vinylene group. The energy difference between structures (a) and (b) is about 16.4 kcal/mol in favor of structure (a); this can be explained by the loss of aromaticity of the phenylene ring in case (b). This result is in qualitative agreement with a recent *ab initio* modeling of the Al₂/poly(*p*-phenylenevinylene) system, using a stilbene molecule as a model for PPV [51]. In addition, recent XPS and UPS studies of the initial stages of interface formation between aluminum and PPV indicate [through the changes in the UPS valence band

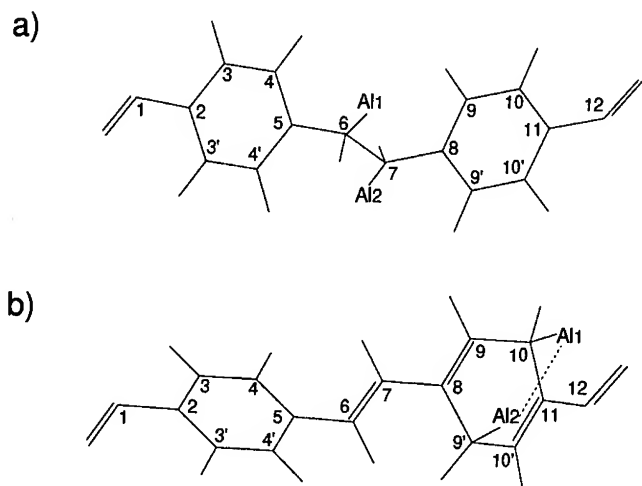


Figure 5. Illustration of two of the most energetically favorable AM1-optimized structures of the Al₂/poly(*p*-phenylenevinylene) complex. Only the central part of the molecule [indicated by the dashed parenthesis in Fig. 1(b)] is shown.

and in the shake-up structure of the XPS C(1s) peak] that the aluminum atoms preferentially interact with the vinylene moieties [58].

The modifications induced by the aluminum atoms are mainly localized to the units to which the aluminum atoms are bonded. When the aluminum atoms are attached to a vinylene group, all the bonds associated with this moiety elongate (the double bond, r6—7, increases from about 1.34 Å to 1.54 Å (pure single bond) and the single-like bonds, r5—6 and r7—8, elongate to about 1.48 Å and 1.49 Å, respectively) and the π -conjugation is interrupted. In the case when the two aluminum atoms interacts with a phenylene ring [structure (b) in Fig. 5], strong modifications occur and the planarity of the ring is lost; torsion angles of about 30° appear around bonds r9—10 and r8—9'. The aromatic character of the phenylene ring disappears and a dienic structure is formed (bonds r8—9 and r10'—11 decreasing down to 1.36 Å from about 1.41 Å while the other bonds in the phenylene ring elongate to 1.48 Å or more).

The changes in Mulliken atomic charges as a result of the interaction with aluminum show a charge transfer of about 0.47 |e| from each aluminum atom to the conjugated molecule in both systems. The additional charge on the molecule is mainly accommodated on the carbons to which the aluminum atoms are attached; the net atomic charge on carbons 6 and 7 in structure (a) increases by about 0.42 |e|, that on carbons 9' and 10 in structure (b) by about 0.35 |e|. The highest occupied molecular orbitals are localized in character; the HOMO and HOMO-1 levels are almost totally confined to the aluminum atoms and the carbons within the moieties the aluminums are attached to.

The Al₂/poly(2,5-dimethoxy-p-phenylenevinylene) System

Some of the stable structures of the Al₂/DMeOPPV complex are shown in Figure 6. When two aluminum atoms are introduced in the vicinity of a phenylene ring, many different stable configurations are obtained, of which several are comparable in stability. We display some of the most stable cases involving: in structure (b), only phenylene ring carbons; in (c), a multiple-bond structure; and in (d), the formation of an Al—O—C complex. The most stable configuration is, as in the case of Al₂/PPV, a situation where the two aluminum atoms interact with a single vinylene group; structure (a) is more stable than systems (b), (c), and (d) by about 21.4, 20.2, and 55.5 kcal/mol, respectively. These results indicate that the interaction with oxygen is *not* favored in this system.

The aluminum atoms induces modifications in structures (a) and (b) that are very similar to those obtained for the corresponding situations for Al₂/PPV. In the case of structure (c), one of the aluminum atoms interacts with both a vinylene and a phenylene moiety; the shortest Al—C distance, about 1.88 Å, is found for the bond to C9 of the phenylene ring. We note that such an AM1-calculated Al—C bond length might be on the short side, since high-level *ab initio* calculations including the effects of electron correlation indicate Al—C bond lengths on the order of 1.95 Å [59,60]. The Al—C distances involving carbons 6, 7, and 8 are in the range 2.32–2.55 Å. The second aluminum atom is positioned above the phenylene

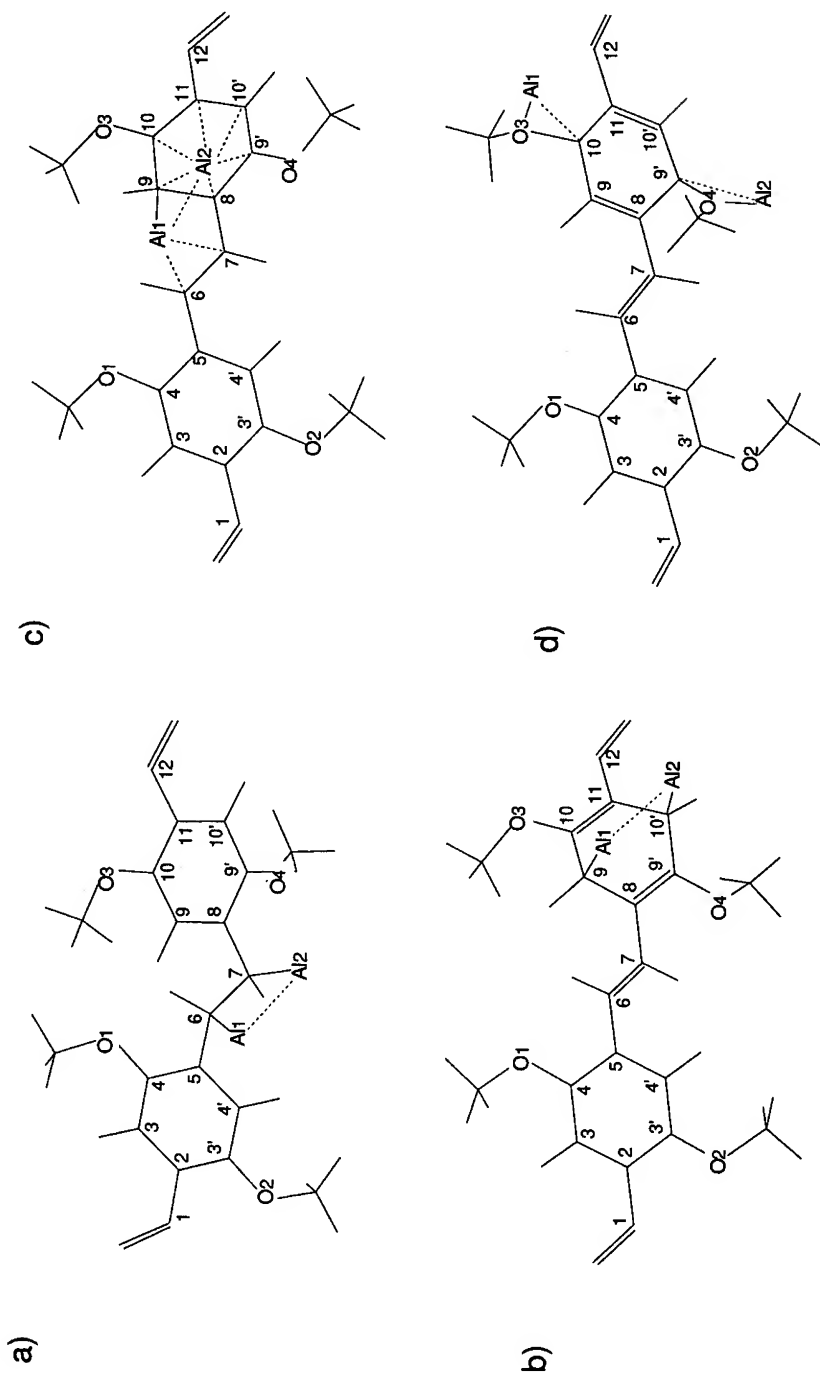


Figure 6. Illustration of four of the most energetically favorable AM1-optimized structures of the $\text{Al}_2/\text{poly}(2,5\text{-dimethoxy-}p\text{-phenylenevinylene})$ complex. Only the central part of the molecule [indicated by the dashed parenthesis in Fig. 1 (b)] is shown.

ring, with Al—C distances ranging between 2.50 Å for Al2—C10' and 2.82 Å for Al2—C9. The planarity of the phenylene ring is lost, with the largest torsion angle, about 19.6°, occurring around bond C8—C9'. Finally, in structure (d), the two aluminum atoms forms Al—O—C complexes. As in structure (b), the phenylene ring acquires a dienic structure, with bonds C8—9 and C10'—11 shortening to 1.36 Å. The planarity of the phenylene ring is also lost with torsion angles around the single bonds of about 16–17°. The Al—O bonds have lengths of about 1.80 Å and the Al—C bonds, about 2.26 Å.

The changes in Mulliken atomic charges indicate a charge transfer from each aluminum atom to the conjugated molecule of about 0.4–0.5 |e| in systems (a), (b), and (d). As in the case of the Al₂/PPV system, the additional charge is mainly accommodated on the carbons to which the aluminum atoms are attached; the net atomic charge on these carbons increases by about 0.3–0.4 |e| for structures (a) and (b) and 0.26 |e| for structure (d). In structure (c), about 0.16 |e| is transferred from Al1, while about 0.54 |e| is transferred from Al2. The multiple-bonding character of structure (c) is reflected in the charge transfer which involves several carbons; the largest increases in net atomic charges are seen on carbons C6, C8, C9, and C11.

The presence of the methoxy substituents in DMeOPPV allows for stable configurations involving Al—O—C complex formation. These structures, however, are less stable than those where aluminums bind to carbons on the phenylene and/or vinylene moieties. As in the case of unsubstituted PPV, the most stable structure is found when the two aluminum atoms are situated on a single vinylene group, i.e., structure (a). This structure is about 20 kcal/mol more stable than any configuration involving the phenylene carbons. We can thus conclude that the aluminum atoms preferentially interact with the vinylene groups in the initial stages of interface formation with DMeOPPV.

The Al₂/poly(2,5-dialdehyde-p-phenylenevinylene) System

Stable configurations for the Al₂/DAPPV complex are illustrated in Figure 7. Structures (a) and (b) are again nearly identical to those found in the Al₂/PPV complexes. The major difference here, however, is that there occur configurations involving interactions between the aluminums and the carbonyl groups which are as stable as structure (a). These are illustrated in Figure 7 as structures (c) and (d), which are 1.4 kcal/mol more stable and 2.0 kcal/mol less stable than structure (a), respectively. Structure (c) is actually similar to structure (a), one aluminum being however linked to both the vinylene moiety and a carbonyl group. Structure (d) is reminiscent of structure (c) in the Al₂/MeOPPV complex; it is a configuration where one aluminum has multiple bonding to a ring, the other being attached to the oxygen of a carbonyl and the nearly vinylene moiety. We note that the high reactivity between aluminum atoms and carbonyl groups indicated here is consistent with the results from both experimental studies (e.g., polycaprolactone [61], polyethyleneterephthalate [62,63], polyacrylic acid [64], or polyimide [65–67]) and theoretical studies (e.g., polyimide [68] and polymethylmethacrylate [69]) of aluminum interacting with C=O containing polymers.

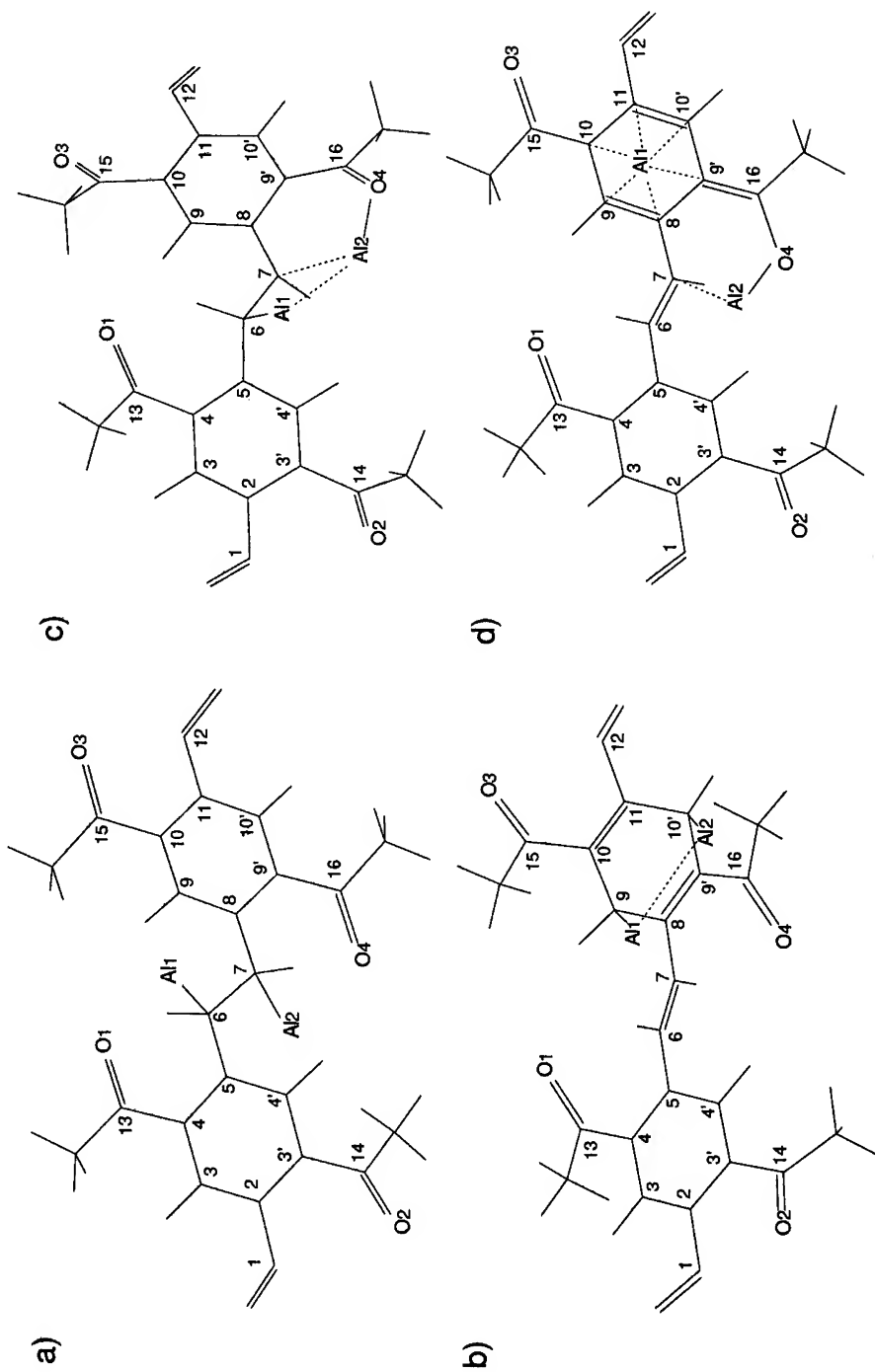


Figure 7. Illustration of four of the most energetically favorable $\Delta M1$ -optimized structures of the Al_2 /poly(2,5-dialdehyde-*p*-phenylenevinylene) complex. Only the central part of the molecule [indicated by the dashed parenthesis in Fig. 1(b)] is shown.

The modifications induced by the aluminum atoms in structures (a) and (b) are very similar to those obtained for the corresponding situations in Al_2/PPV . In the case of structure (c), one $\text{C}=\text{O}$ group is involved in the complex. The shortest bond lengths involving aluminum atoms can be found for $\text{Al1}-\text{C6}$ and $\text{Al2}-\text{O4}$ (about 1.82 and 1.76 Å, respectively); the $\text{Al2}-\text{C7}$ distance is about 2.3 Å. This is reflected in the carbon-carbon backbone around the vinylene group; the double bond character of the $\text{C6}-\text{C7}$ bond is lost (the bond increases from 1.34–1.50 Å); a small decrease is found for the $\text{C7}-\text{C8}$ bond length, from 1.45 to 1.43 Å, while the $\text{C5}-\text{C6}$ bond elongates from 1.45 to 1.48 Å. In structure (d), Al2 forms a complex with C7 and O4 ; the $\text{Al2}-\text{C7}$ distance is long, about 2.5 Å, which leads to only small modifications in the vinylene bridge; the $\text{Al2}-\text{O4}$ distance is ca. 1.72 Å. The $\text{O4}-\text{C16}$ bond elongates, from 1.24 to 1.35 Å, while the $\text{C16}-\text{C9'}$ bond goes from 1.48 Å down to 1.37 Å. Al1 is positioned above the phenylene ring, with the shortest $\text{Al}-\text{C}$ bond, $\text{Al1}-\text{C10}$, about 2.39 Å long; the other $\text{Al1}-\text{C}$ bonds are about 2.5 Å long; the phenylene acquires a quinoid character. The $\text{Al}-\text{O}$ bond lengths in these structures [1.76 Å in structure (c) and 1.72 Å in structure (d)] are close to those obtained in other theoretical studies of the interaction between aluminum and carbonyl containing molecules: the *ab initio* local spin density, LSD, modeling of the Al -polyimide interaction results in an $\text{Al}-\text{O}$ bond length of 1.80 Å [68] and an MNDO study of aluminum interacting with polymethylmethacrylate gives a bond length of about 1.6 Å [69].

The changes in Mulliken atomic charges in the cases where there are bonds only between aluminum and carbons, i.e., structures (a) and (b), show that about 0.4–0.5 | e | is transferred from each aluminum atom. In the structures involving oxygen in the bonding, structures (c) and (d), the charge transfer from the aluminum atom connected to an oxygen atom is, as expected, lower than that for the aluminum atom connected to a carbon atom. The increase in net atomic charge on the oxygen atom closest to an aluminum atom is about 0.034 | e | in structure (c) and about 0.164 | e | in structure (d). Noteworthy is the increase in net atomic charge on the carbonyl carbon C16 in structure (d), by ca. 0.20 | e |.

The replacement of the methoxy groups along the DMeOPPV oligomer by the carbonyl (acceptor) groups allows for the formation of new stable structures, which involve the appearance of $\text{Al}-\text{O}-\text{C}$ bonds and are comparable in stability with the otherwise most stable structure, i.e., that where the two aluminum atoms interact with a single vinylene moiety. The most stable of these new structures is found when the two aluminum atoms forms a complex with a vinylene moiety and an oxygen atom of a carbonyl group, as in structure (c). These results indicate that if oxygen is present in the form of $\text{C}=\text{O}$ groups on the PPV surface, the vinylene unit no longer constitutes the single most favorable site of bonding for aluminum atoms at the initial stage of interface formation. Since the oxygen in the carbonyl groups are directly bonded to an aluminum atom in the $\text{Al}-\text{O}-\text{C}$ complexes, we expect this to be true even for other positions of the carbonyl groups.

Synopsis

We have applied the semiempirical Austin Model 1 method for the investigation of the interaction between metals and conjugated molecules. Two systems repre-

senting two different situations have been presented: (i) the interaction between sodium and a series of diphenylpolyenes where charge transfer doping (reduction) occurs; and (ii) the interaction between aluminum and PPV and derivatives where covalent bonding takes place.

We find that extra electronic charges, induced by doping, are stored in polaron-like charge storage states for DP5 to DP1 at low doping levels, with a transformation to soliton-antisoliton-like charge storage states upon increasing the doping towards saturation, i.e., a doping level of two charges per molecule. The scenario for DP7 and DP6 is such that the doubly charged molecules are formed even at very low doping, and thus the extra charges are accommodated in soliton-antisoliton-like charge storage states throughout the whole doping range.

In the case of the Al_2/PPV system, the most stable structure is found to correspond to a configuration where the two aluminum atoms bind to a single vinylene moiety, in agreement with recent experimental photoelectron spectroscopy studies of the initial stages of interface formation between aluminum and PPV [58]. The presence of methoxy substituents in the $\text{Al}_2/\text{DMeOPPV}$ system allows for stable structures involving $\text{Al}-\text{O}-\text{C}$ bond formation; however, these structures are here much less stable than those involving carbons on the phenylene rings and/or vinylene moieties. As in the case of Al_2/PPV , the most stable structure for the $\text{Al}_2/\text{DMeOPPV}$ system is calculated to be that where the two aluminum atoms interact with a single vinylene unit.

New stable structures, containing $\text{Al}-\text{O}-\text{C}$ complexes, are found when $\text{C}=\text{O}$ groups are present on the side of the PPV chains. Some of these new stable structures are comparable in stability with the case where the two aluminum atoms interact with a single vinylene moiety. The most stable structure calculated for this system involves both a vinylene unit and the adjacent carbonyl group.

Acknowledgments

This work is partly supported by the Belgian Prime Minister Office of Science Policy "Pôle d'Attraction Interuniversitaire en Chimie Supramoléculaire et Catalyse" and "Programme d'Impulsion en Technologie de l'Information (contract IT/SC/22)," the European Commission programme SCIENCE (project 0661 POLY-SURF), and an IBM Academic Joint Study. One of us (ML) is also partly supported by the Swedish Natural Science Research Council (NFR).

Bibliography

- [1] *Handbook of Conducting Polymers*, T. A. Skotheim, Ed. (Markel Dekker, New York, 1986).
- [2] *Conjugated Polymers: The Novel Science and Technology of Highly Conducting and Nonlinear Optically Active Materials*, J. L. Brédas and R. Silbey, Eds. (Kluwer, Dordrecht, 1991).
- [3] W. P. Su, J. R. Schieffer, and A. J. Heeger, *Phys. Rev. Lett.* **42**, 1698 (1979).
- [4] M. J. Rice, *Phys. Rev. Lett.* **71**, 152 (1979).
- [5] A. J. Heeger, S. Kivelson, J. R. Schrieffer, and W.-P. Su, *Rev. Mod. Phys.* **60**, 781 (1988).
- [6] J. L. Brédas and A. J. Heeger, *Chem. Phys. Lett.* **154**, 56 (1989).
- [7] M. Lögdlund, P. Dannetun, S. Stafström, W. R. Salaneck, M. G. Ramsey, C. W. Spangler, C. Fredriksson, and J. L. Brédas, *Phys. Rev. Lett.* **70**, 970 (1993).

- [8] J. H. Burroughes, C. A. Jones, and R. H. Friend, *Nature* **335**, 137 (1988).
- [9] J. H. Burroughes, D. D. C. Bradley, A. R. Brown, R. N. Marks, K. Mackay, R. H. Friend, P. L. Burns, and A. B. Holmes, *Nature* **347**, 539 (1990).
- [10] D. Braun and A. J. Heeger, *Appl. Phys. Lett.* **58**, 1982 (1991).
- [11] P. L. Burn, A. B. Holmes, A. Kraft, D. D. C. Bradley, A. R. Brown, R. H. Friend, and R. W. Gymer, *Nature* **356**, 47 (1992).
- [12] G. Gustafsson, Y. Cao, G. M. Treacy, F. Klavetter, N. Colaneri, and A. J. Heeger, *Nature* **357**, 477 (1992).
- [13] G. Grem, G. Leditzky, B. Ullrich, and G. Leising, *Adv. Mat.* **4**, 36 (1992).
- [14] N. C. Greenham, S. C. Moratti, D. D. C. Bradley, R. H. Friend, and A. B. Holmes, *Nature* **365**, 628 (1993).
- [15] T. W. Hagler, K. Pakbaz, K. F. Voss, and A. J. Heeger, *Phys. Rev.* **B44**, 8652 (1991).
- [16] T. P. Nguyen, V. Massardier, V. H. Tran, and A. Guyot, *Synth. Met.* **55-57**, 235 (1993).
- [17] T. P. Nguyen, H. Ettaik, S. Lefrant, G. Leising, and F. Stelzer, *Synth. Met.* **38**, 69 (1990).
- [18] Y. Gao, K. T. Park, and B. R. Hsieh, *J. Chem. Phys.* **97**, 6991 (1992).
- [19] J. Obrzut, M. J. Obrzut, and F. E. Karasz, *Synth. Met.* **29**, E109 (1989).
- [20] M. Fahlman, M. Lögdlund, S. Stafström, W. R. Salaneck, S. C. Graham, R. H. Friend, P. L. Burn, A. B. Holmes, K. Kaeriyama, Y. Sonoda, O. Lhost, F. Meyers, and J. L. Brédas, submitted for publication.
- [21] J. J. Pireaux, C. Grégoire, R. Giustini, and A. Cros, in *Polymer-Solid Interfaces*, J. J. Pireaux, P. Bertrand, and J. L. Brédas, Eds. (IOP Publishing, Bristol, 1992), p. 237.
- [22] C. B. Duke, A. Paton, W. R. Salaneck, H. R. Thomas, E. W. Plummer, A. J. Heeger, and A. G. MacDiarmid, *Chem. Phys. Lett.* **59**, 146 (1978).
- [23] R. R. Chance, H. Schaffer, K. Knoll, R. Schrock, and R. Silbey, *Synth. Met.* **49-50**, 271 (1992).
- [24] E. Ehrenfreund, D. Moses, A. J. Heeger, J. Cornil, and J. L. Brédas, *Chem. Phys. Lett.* **192**, 84 (1992).
- [25] M. G. Ramsey, D. Steinmüller, and F. P. Netzer, *Phys. Rev.* **B42**, 5902 (1990).
- [26] R. Schenk, H. Gregorius, and K. Müllen, *Adv. Mater.* **3**, 492 (1991).
- [27] D. Fichou, G. Horowitz, and F. Garnier, *Synth. Met.* **39**, 125 (1990).
- [28] B. E. Kohler and J. J. A. Pescatore, in *Conjugated Polymeric Materials: Opportunities in Electronics, Optoelectronics and Molecular Electronics*, J. L. Brédas and R. R. Chance, Eds. (Kluwer, Dordrecht, 1990), p. 353.
- [29] C. W. Spangler, E. G. Nickel, and T. J. Hall, *Polymer Preprints* **28**, 219 (1987).
- [30] P. Dannetun, M. Lögdlund, M. Fahlman, M. Boman, C. Fredriksson, S. Stafström, R. Lazzaroni, J. L. Brédas, S. Graham, R. H. Friend, A. B. Holmes, R. Zamboni, C. Taliani, and W. R. Salaneck, *Synth. Met.* **55-57**, 212 (1993).
- [31] C. Fredriksson and J. L. Brédas, *J. Chem. Phys.* **98**, 4253 (1993).
- [32] P. Dannetun, M. Boman, S. Stafström, W. R. Salaneck, R. Lazzaroni, C. Fredriksson, J. L. Brédas, R. Zamboni, and C. Taliani, *J. Chem. Phys.* **99**, 664 (1993).
- [33] L. M. Tolbert and J. A. Schomaker, *Synth. Met.* **41-43**, 169 (1991).
- [34] C. Tanaka and J. Tanaka, *Bull. Chem. Soc. Jpn.* **66**, 357 (1993).
- [35] F. Garnier, G. Horowitz, X. Peng, and D. Fichou, *Adv. Mater.* **2**, 592 (1990).
- [36] P. Dannetun, M. Lögdlund, C. W. Spangler, J. L. Brédas, and W. R. Salaneck, *J. Phys. Chem.* **98**, 2853 (1994).
- [37] M. J. S. Dewar, E. G. Zoebisch, E. F. Healy, and J. J. P. Stewart, *J. Am. Chem. Soc.* **107**, 3902 (1985).
- [38] W. Drenth and E. H. Wiebenga, *Acta Crystallogr.* **8**, 755 (1955).
- [39] J. A. Bouwstra, A. Schouten, and J. Kroon, *Acta Crystallogr., Sect. C* **40**, 428 (1984).
- [40] J. Bernstein, *Acta Crystallogr., Sect. B* **31**, 1268 (1975).
- [41] C. J. Finder, M. G. Newton, and N. L. Allinger, *Acta Crystallogr., Sect. B* **30**, 411 (1974).
- [42] A. Hoekstra, P. Meertens, and A. Vos, *Acta Crystallogr., Sect. B* **31**, 2813 (1975).
- [43] J. L. Brédas, R. R. Chance, R. Silbey, G. Nicolas, and P. Durand, *J. Chem. Phys.* **75**, 255 (1981).
- [44] J. M. André, J. Delhalle, and J. L. Brédas, *Quantum Chemistry Aided Design of Organic Polymers* (World Scientific, Singapore, 1991).

- [45] J. L. Brédas and W. R. Salaneck, *J. Chem. Phys.* **85**, 2219 (1986).
- [46] E. Orti and J. L. Brédas, *J. Chem. Phys.* **89**, 1009 (1988).
- [47] E. Orti and J. L. Brédas, *J. Am. Chem. Soc.* **114**, 8669 (1992).
- [48] W. R. Salaneck, *CRC Crit. Rev. Solid State Mater. Sci.* **12**, 267 (1985).
- [49] J. L. Brédas, B. Thémans, J. G. Fripiat, J. M. André, and R. R. Chance, *Phys. Rev.* **B29**, 6761 (1984).
- [50] J. L. Brédas and G. B. Street, *Acc. Chem. Res.* **18**, 309 (1985).
- [51] C. Fredriksson, R. Lazzaroni, J. L. Brédas, P. Dannetun, M. Lögdlund, and W. R. Salaneck, *Synth. Met.* **55-57**, 4632 (1993).
- [52] C. S. Yannoni and T. C. Clarke, *Phys. Rev. Lett.* **51**, 1191 (1983).
- [53] P. Dannetun, M. Lögdlund, C. Fredriksson, M. Boman, S. Stafström, W. R. Salaneck, B. E. Kohler, and C. W. Spangler, in *Polymer-Solid Interfaces*, J. J. Pireaux, P. Bertrand, and J. L. Brédas Eds. (IOP Publishing, Bristol, 1992), p. 201.
- [54] M. Lögdlund, P. Dannetun, C. Fredriksson, S. Stafström, C. W. Spangler, J. L. Brédas, and W. R. Salaneck, in *Proceedings of the 2nd International Conference on Frontiers of Polymers and Advanced Materials, Jakarta, Indonesia* (Plenum, New York, in press).
- [55] M. Winokur, Y. B. Moon, A. J. Heeger, J. Baker, D. C. Bott, and H. Shirakawa, *Phys. Rev. Lett.* **58**, 2329 (1987).
- [56] S. Stafström, J. L. Brédas, M. Lögdlund, and W. R. Salaneck, *J. Chem. Phys.* **99**, 7938 (1993).
- [57] M. Boman, S. Stafström, and J. L. Brédas, *J. Chem. Phys.* **97**, 9144 (1992).
- [58] P. Dannetun, M. Lögdlund, W. R. Salaneck, C. Fredriksson, S. Stafström, A. B. Holmes, A. Brown, S. Graham, R. H. Friend, and O. Lhost, *Mol. Cryst. Liq. Cryst.* **228**, 43 (1993).
- [59] S. Q. Jin, Y. Xie, and H. F. Schaefer, *Chem. Phys. Lett.* **170**, 301 (1990).
- [60] S. Q. Jin, Y. Xie, and H. F. Schaefer, *J. Chem. Phys.* **95**, 1834 (1991).
- [61] C. Grégoire, P. Noël, R. Caudano, and J. J. Pireaux, in *Polymer-Solid Interfaces*, J. J. Pireaux, P. Bertrand, and J. L. Brédas, Eds. (IOP Publishing, Bristol, 1992), p. 225.
- [62] Quoc Toan Le, M. Chtaib, J. J. Pireaux, and R. Cuadano, in *Polymer-Solid Interfaces*, J. J. Pireaux, P. Bertrand, and J. L. Brédas, Eds. (IOP Publishing, Bristol, 1992), p. 245.
- [63] M. Bou, J. M. Martin, T. L. Mogne, and L. Vovelle, in *Metallized Plastics 2*, K. L. Mittal, Ed. (Plenum, New York, 1991), p. 219.
- [64] B. M. deKoven and P. L. Hagans, *Appl. Surf. Sci.* **27**, 199 (1986).
- [65] L. Atanasoska, S. G. Anderson, H. M. Meyer III, Z. Lin, and J. H. Weaver, *J. Vac. Sci. Technol.* **A5**, 3325 (1987).
- [66] J. W. Bartha, P. O. Hahn, F. K. Le Goues, and P. S. Ho, *J. Vac. Sci. Technol.* **A3**, 1390 (1985).
- [67] P. S. Ho, P. O. Hahn, J. W. Bartha, G. W. Rubloff, F. K. Le Goues, and B. D. Silverman, *J. Vac. Sci. Technol.* **A3**, 739 (1985).
- [68] A. Selmani, in *Metallization of Polymers*, E. Sacher, J. J. Pireaux, and S. P. Kowalczyk, Eds. (American Chemical Society, Washington D.C., 1990), p. 344.
- [69] A. K. Chakraborty, H. T. Davis, and M. Tirrell, *J. Polym. Sci., Polym. Chem. Ed.* **28**, 3185 (1990).

Received May 11, 1994

Elemental Carbon Isomerism

D. J. KLEIN and X. LIU

Texas A&M University Galveston Campus, Galveston, Texas 77553-1675

Abstract

A systematic mathematically based approach is made to categorize the different stereochemical possibilities for finite carbon clusters comprised of fully bonded smooth nets of carbon atoms all of which are trigonally hybridized. An exceptional richness of ideas and theorems from topology, differential geometry, and graph theory are found to be relevant and to govern not only the conventional chemical graph-theoretic molecular interconnection patterns but also topo-geometric features of the stereochemically conceivable structures and their associated strain. The usually considered fullerenes (with or without isolated pentagonal rings) form but a fraction of the overall possibilities, some of which e.g., do not require pentagonal rings (or other "small" rings). But too there emerges from the theory certain special structures which turn out often to correspond to experimentally observed fullerenes. © 1994 John Wiley & Sons, Inc.

Background

The theory of isomerism has long been an issue of principal interest in chemistry for well over a century. In the last few decades "quantum chemistry" has developed as an important field to compute relative stabilities of different isomeric structures—each treated as an individual (well-pronounced) minimum in a many-dimensional potential-energy hypersurface. But a formalized classical approach remains of crucial value for a unified view—to indicate possibilities and to provide a framework for thought and discussion. The elegant classically based mathematical ideas developed (e.g.) by Polya [1] and now much elaborated [2] focus almost entirely on "substitutional" isomerism. In distinct contrast is isomerism involving a single chemical element. In this regard, because of the recognized singular ability of carbon to form numerous well-characterized structures (and thereby give rise to the field of organic chemistry), the isomerism of elemental carbon clusters should be of key interest. Indeed this is an area where traditional stereochemistry [3] also turns out to focus more on "locally" defined features, e.g., substitutional isomerism or chiral centers.

Here then a mathematically formalized classical approach to *elemental carbon isomers* is indicated, especially for the case where every atom is in the same valence state. In fact (somewhat "brief") suggestions of possibilities for such isomers dates back some time [4,5], though focus was on just a couple possibilities: C_{20} and C_{60} icosahedral-symmetry cages. Further, interest was immensely boosted: first in 1985 with the laser-ablation molecular-beam experimental realization [6] of C_{60} clusters assigned to the "uniquely elegant" truncated-icosahedral structure of Figure 1; and

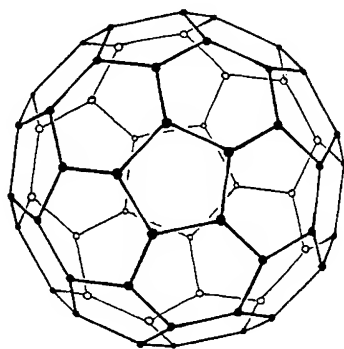


Figure 1. The truncated-icosahedron structure, wherein the double bonds may be distributed in numerous ways (12500 in number), one of which makes double all the bonds not in a pentagon.

second in 1990 with the experimental isolation [7] and characterization of macroscopic quantities of this novel species. Also now experimentally studied are C_{70} , C_{76} , C_{78} , C_{84} species [8–11] (among others), all evidently polyhedral cage structures such as in Figure 2 involving similar local ring structures but exhibiting lower symmetries. On the theoretical side electronic-structure calculations have now been made at widely varying levels of computational sophistication, usually on one or two (repeatedly investigated) structures. Within the realm of purely sp^2 -hybridized classical polyhedral structures focus has been on those involving just 5- and 6-membered rings: all higher-symmetry such C_{60} structures were identified [12]; the class of icosahedral-symmetry such carbon species of any size was studied [13,14]; higher-symmetry such cages of different sizes were systematically considered [15,16]; and finally attempts were made [17,18] (and even realized [19]) to generate all possible such cages of arbitrary symmetries up to a given size.

Besides these polyhedral cages with carbon atoms of a single (sp^2) valence state there remain numerous other classical possibilities. Other ring sizes may be considered [15,20] and also there are toroidal possibilities [15,21,22] for structures. Beyond these possibilities one could consider the general problem of identifying all possible connected (so-called *regular*) graphs where every vertex is of the same appropriate degree. Indeed Balaban and coworkers [23] have repeatedly addressed

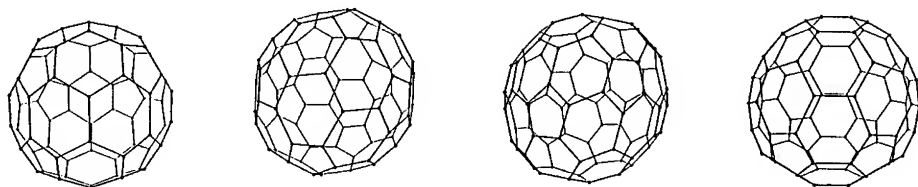


Figure 2. Examples of C_{70} , C_{76} , C_{78} , and C_{84} polyhedral cages, wherein in each case double bonds may be distributed in numerous ways so that no unpaired sites remain.

such a graph-theoretic problem in reference to the valence isomers of the annulenes. But for our present problem this would too easily overlook the preferences dictated by geometric strain, as is known [24] to be important—and further such an approach would miss some interesting stereochemical possibilities. Here we seek a global accounting of both strain effects and novel stereoisomeric possibilities within a classical view by considering embeddings of molecular graphs in various surfaces which in turn are to be embedded in Euclidean 3-space. Such an approach then entails the collection of some graph-theoretic, topological, and differential-geometric ideas and theorematic results so that they can be merged in a way useful for the stereochemical problems at hand. This then sets the bulk of fullerene research in a larger context with many interesting little explored extensions.

Structural Focus

Just what might be the range of conceivable carbon clusters?

First, in flames and molecular beams a number of presumably transient species have been detected and studied, even theoretically. See, e.g., the review by Weltner and Van Zee [25]. Such species of fewer than about 10 carbon atoms are however typically *radicals* or *polyradicals*. Further open chains, as well as fragments cut from the graphite or diamond lattice, should be radicaloid, since classically all entail dangling bonds at the boundary. Here we focus on other possibilities without “dangling bonds.”

Second, there are a great number of possible classical chemical-bonding structures, such as in Figures 3 or 4. The species in Figure 4 are viewed to be based on sets of cages as of Figure 1, but now with pairs or quartets of carbon atoms taken to be tetrahedrally hybridized, each such atom with one bond external to the cage connecting to a similar atom in another cage. But all these species entail atoms of

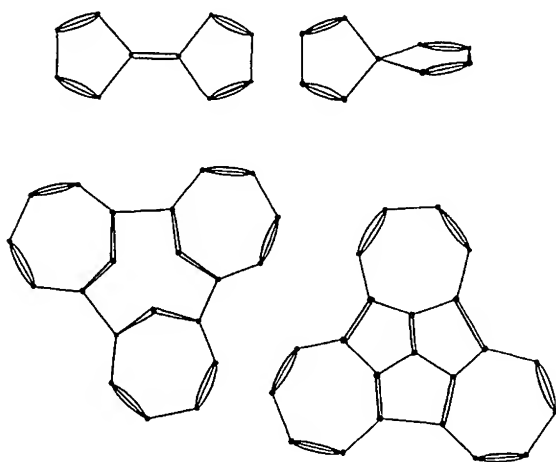


Figure 3. Examples of classically allowed (more-or-less planar) elemental-carbon molecular “clusters” wherein the tetravalence of each carbon atom is satisfied.

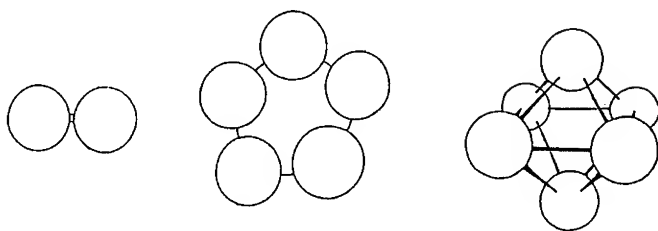


Figure 4. Examples of conceivable "multi-cage" elemental carbon clusters. The structure within the cages is not detailed, and in the second and more so in the third example cage sizes have been artifactually diminished while retaining cage separation so that the inter-cage bonds may be clearly discerned.

different hybridizations (while also there is considerable strain for the species in Fig. 3), and here we choose to focus on species with but a single type of hybridization.

Third, with but a single hybridization there are a variety of possibilities. For exclusive sp -hybridization the situation seems perhaps the most clearly resolved: all classical structures are just cycles, so that there are no *constitutional* isomers among these species, though upon embedding in Euclidean 3-space \mathcal{E}_3 these cycles may be knotted in many conceivable ways. For solely sp^3 -hybridization each site is to be bonded to four others, such as is the case for the graphs of Figure 5—but in *all* known cases there seems to be excessive strain upon embedding in \mathcal{E}_3 , with constraints: that bonds radiating from each atom should be at an angle $\approx 109^\circ$ to the others, that these bonds are not too bent, and that they are of similar lengths. Evidently the remaining case where the sole type of hybridization is sp^2 is the case of primary interest—there being examples of structures without inordinate strain already noted in Figures 1 and 2.

The case of entirely sp^2 -hybridized classically bonded structures then is the area (of natural interest) pursued here. In addition, to the polyhedral and torihedral structures considered earlier (as noted in the introduction) there are many other possibilities even if we avoid overstrained structures (such as indicated in the previous paragraph involving sp^3 carbons). For instance, one may consider the manner of interconnecting three graphitic sheets as indicated in Figure 6(a), then imagine the sheets bent around as indicated in 6(b), or any one of numerous other con-

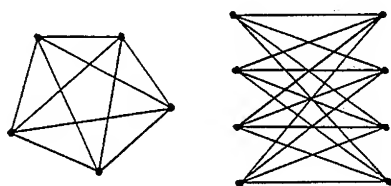


Figure 5. Two (mathematically well-known) graphs with each site connected to four other sites.

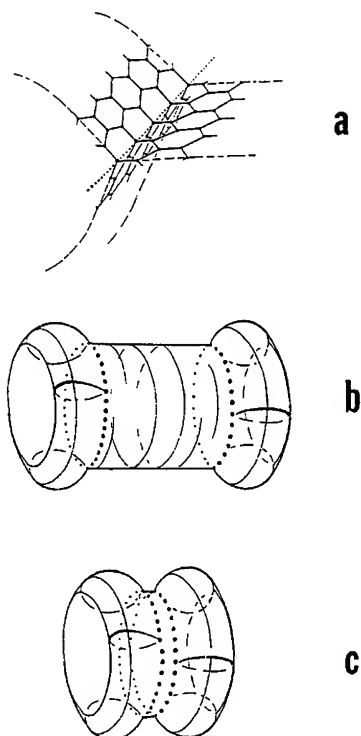


Figure 6. In (a) a local way of interconnecting sp^2 -carbons is indicated so that an overall entirely sp^2 -hybridized structure as in (b) or (c) can be constructed. Note that the atoms along the dotted lines have their trigonal hybridization axes orthogonal to the neighboring atoms to which they are bonded.

ceivable possibilities. Here there are adjacent sp^2 -atoms with dramatically (near orthogonal) different orientations, so that range of conjugation is limited. Indeed these carbons along the dotted lines in 6(a) and (b) tend to leave their π -electrons unpaired, so that such species should have an (unstable) polyradicaloid character. Of course arranging two such dotted-line arrays of carbon atoms to be immediately adjacent as in 6(c), atoms along the two dotted lines may pair to one another, thereby avoiding radicaloid character. Nevertheless here as a beginning we consider situations where not only is there uniformity in hybridization but also in *local* orientation of the hybridization axes (as is equivalent to requiring that there is no boundary for the conjugation). Hopefully some of the ideas elucidated in this case will carry back to more general circumstances such as mentioned in this paragraph.

Closed Surfaces

The formal construction of feasible tri- σ -valent (and uni- π -valent) carbon structures should take into account in some fashion the manner of embedding into

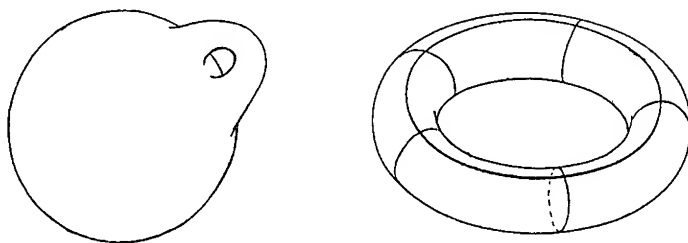


Figure 7. In (a) the result of adding one handle to a sphere—this result being homotopic to the torus of (b).

Euclidean 3-space \mathcal{E}_3 . Since such sp^2 -hybridized carbon atoms generate *locally planar* structures, it is natural to assume a constraint that the molecular graphs are to be drawn in such (usually smooth but always sufficiently well-behaved to at least be compact) 2-manifolds (or surfaces) without intersecting bonds. Since there are to be no dangling bonds and no other (different-valent) atoms, it is natural to constrain the surfaces to be *closed*, i.e., without edges where dangling bonds would occur.

Thence the topology [26,27] and differential geometry [28,29] of closed surfaces should be of relevance. There are two fundamental types of closed surfaces: *orientable* ones with two sides and *nonorientable* ones with a single side. Examples of orientable surfaces S include the sphere and the torus, and they may be characterized in terms of their *genus* $\gamma(S)$, which is the number of “handles” added to a sphere to obtain a surface *homotopic* (i.e., topologically equivalent) to S (see Fig. 7). A common example of a one-sided surface is the Mobius strip, though it has an edge, and so is not closed. A nonorientable closed S may be characterized in terms of its *cross-cap number* $n(S)$, which is the number of cross-caps added to a sphere to obtain a surface homotopic to S (see Fig. 8). The fundamental result governing closed surfaces is:

The Dyck—Dehn—Heegard Theorem—Every closed surface S falls into one of the two categories: either S is orientable with $n(S) = 0$ and $\gamma(S) \geq 0$, or else S is nonorientable with $n(S) > 0$ and $\gamma(S) = 0$.

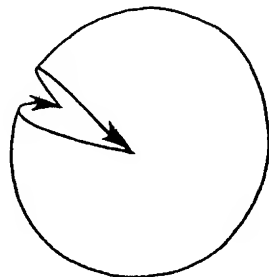


Figure 8. A sphere in which a cut has been made, with “orientations” indicated on the two halves of the cut. Rejoining the two cut edges such that the two arrows match head-to-tail and tail-to-head recovers the sphere; however, rejoining the two edges such that the two arrows match head-to-head and tail-to-tail yields a cross-cap.

The counts $n(S)$ and $\gamma(S)$ so given are homotopic invariants. It is an immediate implication of this theorem that the simultaneous addition of cross-caps and handles to a sphere results in something already identified in the theorem—in fact, when a cross-cap is present any handle also present turns out to be homotopically replaceable by two cross-caps. With only handles or cross-caps, the *Euler characteristic* is often introduced as

$$\chi(S) \equiv \begin{cases} 2 - 2\gamma(S), & n(S) = 0 \\ 2 - n(S), & n(S) \neq 0 \end{cases} \quad (3.1)$$

and turns out to be perhaps the most fundamental topological invariant for a closed surface.

Next the closed surface S is to be embedded in Euclidean 3-space \mathcal{E}_3 . A first fundamental theorem here is:

The Jordan–Alexander Theorem—If a closed surface S is embedded without self-intersection in \mathcal{E}_3 , then S must be orientable, in which case when the points of S are removed from \mathcal{E}_3 the remnant falls into two individually connected regions disconnected from one another.

Henceforth we consider only oriented S as candidates for constructing feasible carbon isomers, though if the assumption of atoms of a single valence-state were dropped the networks on the surface could be “tenuous” enough to allow surface self-intersection [22], and thence (multiply-hybridized) structures on nonorientable surfaces could be realized.

With the presumption of a non-self-intersecting embedding of S in \mathcal{E}_3 , a general characterization of the surface’s shape is of interest. In this regard curvatures along different directions at a point in the surface may be considered, with k_1 and k_2 the minimum and maximum values at that point. (The curvature k at a point on a smooth curve is the inverse of the radius of the circle which “kisses” the curve at that point.) Then the *Gaussian curvature* (at that point of S) is defined as

$$\kappa = \pm |k_1 k_2| \quad (3.2)$$

where the sign is + if the k_1 and k_2 orientations of curvature are toward the same side of S , whereas the sign is – if the k_1 and k_2 orientations of curvature are toward opposite sides of S . A fundamental result involving an area integral over all of S is:

Gauss–Bonnet Theorem—For an orientable closed smooth surface S in \mathcal{E}_3 , the total Gaussian curvature integrated over S is a topological invariant

$$\int_S \kappa \, ds = 2\pi\chi(S).$$

That is, for the surfaces S around the outside of a basketball, or of an (American) football, or of a discus the total Gaussian curvature integrated over all of S has the same value 4π , whereas for the surfaces around a doughnut or a coffee mug the result is another characteristic value 0.

A special natural type of surface [30] embedded in \mathcal{E}_3 is that comprised entirely of planar polygonal *faces*. Indeed a formal study of such so-called *polyhedra* (es-

pecially more "regular" ones with $\chi(S) = 0$) dates back to the Greeks. But we wish to make no constraint on $\chi(S)$ and to emphasize this, we will here refer to these so unconstrained closed orientable surfaces with polygonal faces as *topohedra*. At a vertex i of such a topohedron where several faces meet one may define an angle defect

$$\phi_i = 2\pi - \sum_{\alpha}^i \phi_{\alpha i} \quad (3.3)$$

where the sum is over the face angles $\phi_{\alpha i}$ for the faces α meeting at i . For example, for a cube the 8 angle defects are each $\pi/2$, whereas for a regular tetrahedron each of the 4 angle defects is π . Then a fundamental result for topohedra is:

Descarte's Theorem—If S is a (closed) topohedral surface in \mathcal{C}_3 , then

$$\sum_{i \text{ vertices}} \phi_i = 2\pi\chi(S)$$

where the sum is over all angle defects ϕ_i of the vertices i of S .

In fact, this result may be viewed to be the same as that of the Gauss-Bonnet theorem if we realize the angle defects are essentially the net Gaussian curvatures associated to each vertex—i.e., if small (nonoverlapping) regions around each vertex are smoothed out and κ is integrated over the i th such region, then the result is ϕ_i .

A topohedron S is also characterized by counts v , e , and f of its vertices, edges, and faces. But that S is closed, places an important constraint on these counts:

Euler's Theorem—For a topohedral closed S ,

$$v - e + f = \chi(S).$$

In the present chemical context we associate atoms, bonds and rings to the vertices, edges and faces of such a topohedron.

Embeddings

Beyond the fundamental results of the preceding section characterizing the closed surface S , there is also the mathematical problem [31,32] of characterizing the embedding of the graphical molecular framework G within S . Here an *embedding* of a graph G into a surface S is an (injective) mapping where vertices and edges of G are mapped to points and open line segments such that each such image is entirely disjoint from all others, and each line-segment edge image has (limiting) end points corresponding to the vertices that the edge interconnects. When all these images of vertices and edges of G are removed from S , there results a set of surface fragments, called *faces*. If all these faces are homeomorphic to an (open) disc, then the embedding is said to be *cellular*. Thence we have a more "graphical" version of the last theorem of the previous section:

Euler's Theorem—If a cellular embedding of G with v vertices and e edges in a closed surface S gives f faces, then

$$v - e + f = \chi(S).$$

Clearly vertices and edges of G might be correlated with vertices and edges of polyhedra, as well as with atoms and bonds. The theorem applies to rather general graphs though in the present context we are interested in *3-connected* graphs, being those connected graphs which require the removal of at least 3 edges to separate it into two fragments.

Which of the many embeddings of a graph G into a surface S might be "equivalent" is of chemical relevance, because such equivalences can correspond to chemical (stereo) isomers. Two embeddings ψ and φ are *combinatorially equivalent* if there is a one-to-one correspondence between vertices, edges, and faces of ψ and φ such that incidences between vertices, edges, and faces are preserved. That is, if i , e , and α are vertex, edge and face images under ψ corresponding to i' , e' , and α' under φ , then

$$\begin{aligned} i \sim e &\Leftrightarrow i' \sim e' \\ e \sim \alpha &\Leftrightarrow e' \sim \alpha' \end{aligned} \quad (4.1)$$

where " \sim " indicates "incident to". A key result is:

The Steinitz-Whitney Theorem—If S is homeomorphic to a sphere, then each planar 3-connected graph corresponds to a unique combinatorial equivalence class of polyhedra.

Though a powerful classification result for topologically spherical S , this theorem does not seem to extend (simply) to $\chi(S) \neq 0$. Still for the $\chi(S) = 0$ case this theorem reduces the characterization of these equivalence classes to a standard graph-theoretic problem.

A more refined equivalence is relevant for stereoisomerism. Two cellular embeddings ψ and φ of G into S are *topocombinatorially equivalent* if there exists a continuum of cellular embeddings $\Psi_t : G \rightarrow S$ with $t \in [0,1]$ such that: first, $\Psi_0 = \psi$; second, every point in an image of G in S changes continuously with t ; and third, $\Psi_1 = \varphi$. That is, the atoms and bonds in S are imagined to be able to be moved about (with t the time variable) such that the regions of occupation do not come into coincidence at any time. Presumably then this corresponds more closely to stereoisomer classes in chemistry. Again the case of $\chi(S) = 0$, is better handled:

Whitney-Steinitz Refinement—If S is homeomorphic to a sphere, then each combinatorial equivalence class corresponds either to one or two topocombinatorial equivalence classes depending on whether mirror embeddings are topocombinatorially equivalent or distinct, respectively.

In the case of a single such achiral topocombinatorial equivalence class there often (maybe always) is an achiral embedding within the class. If the condition $\chi(S) = 0$ were removed from the hypothesis in this theorem, the consequent statement would not generally be true. For example, typical topohedral embeddings on a torus may be viewed as a rectangle as in Figure 9 first with top and bottom edges to be joined together and second with left and right edges to be joined together—but typically topocombinatorially inequivalent embeddings result depending on the "order" in which the two joinings are done, at least so long as we also have S

embedded in \mathcal{E}_3 . That is, having joined together the same bonds crossing the edges of the rectangle, the same graph results though we have different consequent stereoisomers. But there are yet more topocombinatorial possibilities [22] if, e.g., on the left in Figure 9 one end of the tube is twisted through a full rotation before making the final joining. (The cyclic arrow on the left in this figure indicates the manner of this twist.) For higher genres beyond the torus surely many more such possibilities arise.

But even with the torus further possibilities arise in connection with the embedding of S into \mathcal{E}_3 . Again with reference to the middle-left side of Figure 9 we can think of the open cylinder as corresponding to the sides of a (somewhat thick) cord, but before forming it into a torus the cord could be knotted. As a consequence knot theory [33] becomes of relevance. But in the present context this issue seems separable [22] from much of the rest of our current interest and will not be considered further here.

Specialization

The theoremtic results of the two preceding sections may be (simply) utilized to establish consequent results. For *trivalent* graphs G (to be embedded in an S) the number of incidences between vertices and edges may be counted in terms either of the number v of vertices or of the number e of edges to yield

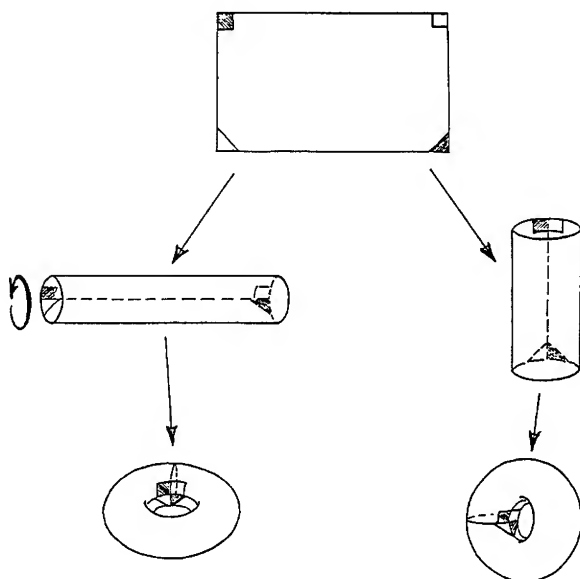


Figure 9. Two manners of forming a rectangle into two different tori, which with a suitable graph embedded on the sheet in a fixed manner can each identify to different stereoisomers.

$$3v = 2e. \quad (5.1)$$

Further if the number of n -sided faces is denoted by f_n , then the number of incidences between vertices and faces can similarly be counted in two ways to yield

$$3v = \sum_n n f_n. \quad (5.2)$$

Thus Euler's theorem of the preceding section leads to:

Euleric Specialization—For trivalent graphs G cellularly embedded in a closed surface S ,

$$3f_3 + 2f_4 + f_5 = 6\chi(S) + f_7 + 2f_8 + 3f_9 + \dots$$

In organic chemistry hexagonal (benzenoid) rings play a special role, so that some sort of constraint to approach this circumstance might be of interest. In fact, rings of size 3 are quite strained, while 4-membered conjugated rings (and to a slightly lesser extent 8-membered conjugated rings) are unstable—this being the content of the standard $4n + 2$ -Hückel rule. Thence it seems plausible to define a cellular embedding of a trivalent G on S to be *benzenoid* if all faces are hexagonal and more generally to be *qua-benzenoid* if it has a minimal number [consistent with $\chi(S)$] of nonhexagonal rings any of which are pentagonal or heptagonal. The preceding theorem readily leads to a characterization of these special embeddings:

Euleric Corollary—For trivalent qua-benzenoid graphs cellularly embedded in a closed surface S , all $f_n = 0$ for $n \neq 6$ except for

$$\begin{array}{lll} f_5 = 12 \text{ and } f_7 = 0 & \text{for} & \chi(S) = 2 \\ f_5 = 6 \text{ and } f_7 = 0 & \text{for} & \chi(S) = 1 \\ f_5 = 0 \text{ and } f_7 = -2\chi(S) & \text{for} & \chi(S) \leq 0. \end{array}$$

Notably benzenoid graphs arise if and only if $\chi(S) = 0$, i.e., if S is a torus or a so-called "Klein bottle" (named after the renowned geometer, Felix Klein). The qua-benzenoids on spherically homeomorphic surfaces are usually termed *fullerenes*, for which a further refinement applies [34]:

Motzkin–Grunbaum Theorem—For every even vertex count $v \geq 24$ there exists at least one fullerene, and the sole smaller fullerene is the dodecahedron with $v = 20$.

In fact, the proof of this is constructive, providing examples of such structures. A further focus notes that the Hückel $4n + 2$ rule is usually extended to a statement concerning cycles around pairs (or even triples) of fused rings—and in particular, the 8-membered cycle around any two fused pentagons should contribute toward instability. Thence fullerenes with no abutting pair of pentagons are defined as *preferable* or *isolated-pentagon-rule* fullerenes. Parallel to the preceding theorem there is another result [35]:

Preferable–Fullerene Theorem—For every even vertex count $v \geq 70$ there exists at least one preferable fullerene, and the sole smaller preferable fullerene is the truncated icosahedron with $v = 60$.

Again, the proof is constructive. Further, all fullerenes so-far experimentally obtained in macroscopic quantities fall into the class of this theorem, with the two

smallest such preferable fullerenes (at $v = 60$ and $v = 70$) corresponding to the two species most readily experimentally obtained.

There are further results which concern structural stability in terms of a classical view of the distribution of double bonds. If one can place double bonds onto the graph embedding with exactly one double bond incident at each site (or alternatively if there exists a spanning subgraph every vertex of which is univalent), then such a placement (or corresponding univalent subgraph) is termed a *Kekule' structure*. Standard classical chemical theory views such structures as a "necessity" (or nearly so) for a stable structure, so that the following is of relevance:

Kekule'-Structure Theorem—Every trivalent graph cellularly embeddable on a sphere admits at least three Kekule' structures.

Amusingly, the proof [35] utilizes the famous "four-color theorem." The present result thence indicates resonance is always conceivable for such carbon cages. Thus a graph-theoretic resonating valence-bond approach seems a possibility as indeed we have pursued [12,13,15,19].

Next slightly less standard but still classical chemical-bonding ideas suggest that [36] conjugated molecular structures are more chemically stable (and more "aromatic") if Kekule' structures are admitted with a larger number of hexagonal rings containing three double bonds, in which case such rings are said to be *conjugated* (at least in the associated Kekule' structures). Thus, it is meaningful [37,38] to define a cellular graph embedding to be a Clar-sextet structure if there exists a Kekule' structure wherein every double bond is a member of two (i.e., the maximum number) conjugated hexagonal faces. On the other hand, Fowler et al. [14,39] have noted that from Hückel calculations there seems to be a stable class of (preferable) fullerenes: the *leap-frog* cages, each such G constructable from another fullerene G_1 (of one third as many vertices) via a two-fold process:

- (a) cap every face of the embedding G_1 on a sphere S to obtain G_2 ; then
- (b) take the dual of G_2 to obtain G .

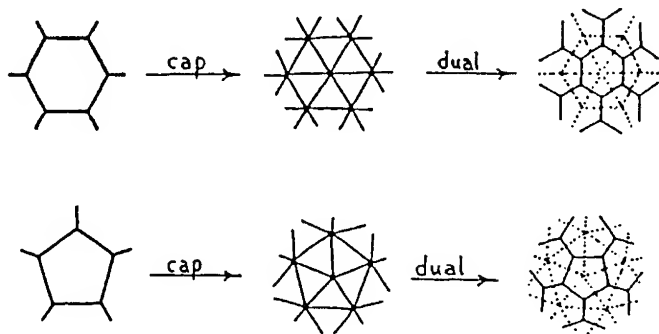


Figure 10. The capping-dualization scheme to generate leap-frog cages.

The process is indicated in Figure 10, but also it can be obtained via an alternative two-step process:

- (a) take the dual of G_1 to obtain G'_1 ; then
- (b) truncate G'_1 to obtain G .

This process is illustrated in Figure 11. The relevant theorem here is [38]:

Leap-Frog-Clar-Sextet Theorem—Clar-sextet fullerenes are exactly the leap-frog fullerenes.

Thence this theorem provides evidence in addition to other evidence for “stable” π -electronic structures for leap-frog cages. Questions concerning σ -strain of the network however require other considerations (as indicated in the up-coming “Cluster Strain” section here). Notably [39] (as is seen from Fowler’s leap-frog transformation, which multiplies the number of vertices in G_1 by 3 in forming G) the truncated icosahedron is the smallest Clar-sextet cage (and the next largest has $v = 72$ vertices as may be seen from the Motzkin-Grünbaum theorem).

Generation and Enumeration

Beyond the theorems of the preceding sections the generation of explicit cage graphs is desired—followed by a characterization of these cages. For the toroidal case an attempt [22] has been made to identify *all* the benzenoid graphs (such as are possible via the “Euleric corollary” of the preceding section)—and even all the possible topocombinatorial equivalence classes of embeddings may have been found. The somewhat related problem of identifying all possible benzenoid graphs for infinite length “buckytubes” (a number of which have been recently experimentally realized [40]) has been simply solved [41]. The case of fullerene graphs embeddable on a spheroidal graph has a simple (one-to-one) correspondence to combinatorial equivalence classes of embeddings, but the generation of all these graphs seems to offer a significant challenge, though the fullerene cages of icosohedral symmetry

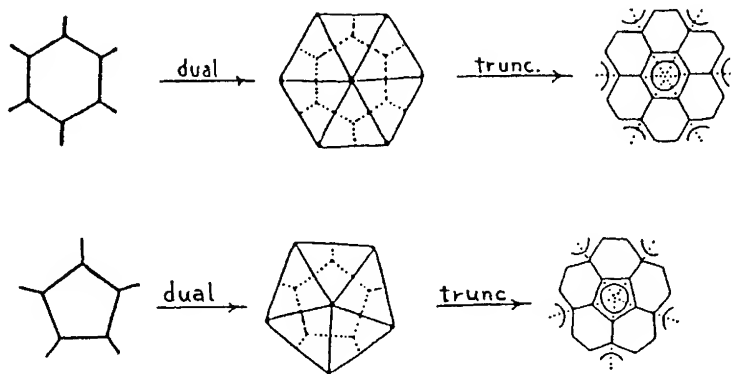


Figure 11. The alternative dualizing-truncation scheme to generate leap-frog cages.

is complete [13,14,42], as well as some aspects [15,16] for other higher symmetry cases.

There is one comprehensive brute-force approach for generation of graph cages embeddable on a spheroidal surfaces, though the computational expense increases rapidly (perhaps exponentially) with vertex number v , though a previous presentation [18] warrants improvement. In this approach Schlegel diagrams are grown, starting from an initial seed (say a pentagonal ring) and adding rings at different locations around the boundary of the current stage of the growing seed.

At any (nonfinal) stage of an acceptable growing seed Γ , there are a number (≥ 1) of pairs of currently divalent sites on the boundary such that no other divalent sites lie between the two on "the" boundary between these two sites, as in the left part of Figure 12. Between *every* such pair a new ring is grown (if possible with the given number of intervening already trivalent sites on the boundary) in two possible ways, as a pentagon or as a hexagon, each result as indicated in the right part of Figure 12. To minimize the length of the rapidly accumulating list L of growing seeds Γ , the seeds are monitored and deleted if they can not yield a desired candidate cage. This is done keeping track of the numbers of different *types* of faces, edges, and vertices generated—where these types are, respectively, defined to be characterized by: the size of a face; the sizes of the two faces on either side of an edge; and the sizes of the three faces incident at a vertex. Hence the admissible (final) types are: 5 or 6 for faces; (5,5), (5,6) or (6,6) for edges; and (5,5,5), (5,5,6), (5,6,6) or (6,6,6) for vertices. We denote the (final) numbers of these various types of graph embedding pieces by a type label appended to every subscript to f , e or v . Then defining p and q as $e_{(5,5)}$ and $v_{(5,5,5)}$ it may be shown that [18]:

Fullerene Cage-Typing Theorem—For a fullerene with $p \equiv e_{(5,5)}$, $q \equiv v_{(5,5,5)}$, and v vertices the numbers of faces, edges, and vertices of the various types are

$$\begin{array}{lll} f_{(5)} = 12 & e_{(5,5)} = p & v_{(5,5,5)} = q \\ f_{(6)} = (v/2) - 10 & e_{(5,6)} = 60 - 2p & v_{(5,5,6)} = 2p - 3q \\ & e_{(6,6)} = v - 60 + p & v_{(5,6,6)} = 60 - 4p + 3q \\ & & v_{(6,6,6)} = v - 60 + 2p - q. \end{array}$$

Thence in growing a seed the current counts of these types of substructures are monitored, discarding a potential growing seed if the number of any one type exceeds the final values as given above for target graphs with chosen fixed values for v , p , q . Thus a list C of candidate cages results.

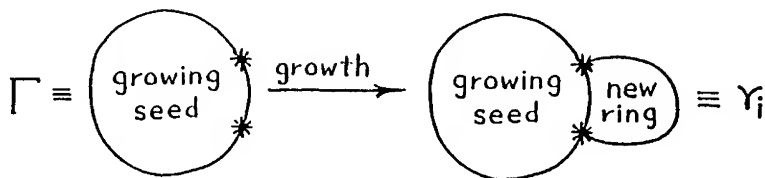


Figure 12. Depiction of the growth step to be independently made at each "subsequent" pair of currently divalent sites such as here indicated by asterisks.

A final matter of concern is the elimination of redundant graphs from the cage list C . This is done by our own effective graph isomorphism testing algorithm [43], though there apparently were algorithms already developed elsewhere [44]. Our scheme scales with time much the same (i.e., $\sim v^3$) as involved in diagonalizing a graph's adjacency (or Hückel) matrix. The algorithm has the broad structure indicated in Figure 13, so that given two graphs G_1 and G_2 the algorithm returns one of three responses:

- (1) G_1 and G_2 not isomorphic.
- (2) G_1 and G_2 isomorphic.
- (3) G_1 and G_2 isomorphism undetermined.

But notably for all (of many thousands) of the cages we have tested only the (favorable) first or second answers have resulted. In fact, such a favorable response has been obtained for all "molecular" graphs we have tested, including those selected because of their presumed difficulty.

For example, we obtain the resultant (combinatorial equivalence classes of) 60-site fullerenes given in Table I. Notably this result (particularly the number in the

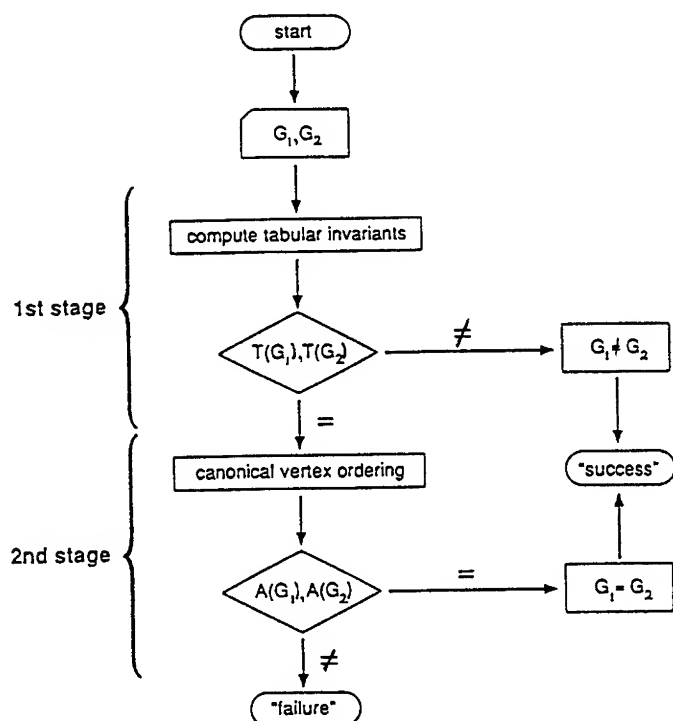


Figure 13. Gross flowchart for graph isomorphism testing. Here $T(G_1)$ and $T(G_2)$ are "tabular invariants" for graphs G_1 and G_2 while $A(G_1)$ and $A(G_2)$ are their adjacency matrices.

TABLE I. Fullerene isomers for $v = 60$ sites.

$p \backslash q$	0	1	2	3	4	5	6	7	8	9	10	q -sum
0	1											1
1	0											0
2	1	0										1
3	3	0	0									3
4	17	0	0									17
5	81	5	0	0								86
6	215	39	0	0	0							254
7	210	147	6	0	0							363
8	145	214	54	0	0	0						413
9	23	132	131	11	0	0	0					297
10	7	28	116	42	4	0	0					197
11	0	1	31	54	10	0	0	0				96
12	1	0	6	16	25	2	0	0	0			50
13	0	0	0	2	10	7	0	0	0			19
14	0	0	0	0	3	5	2	0	0	0		10
15	0	0	0	0	0	0	2	0	0	0	0	2
16			0	0	0	0	1	0	0	0	0	1
17				0	0	0	0	0	0	0	0	0
18					0	0	0	0	1	0	0	1
19						0	0	0	0	0	0	0
20							0	0	0	0	1	1

$q = 3$ column) corrects an earlier table [45] where rather larger but incomplete initiating seeds were used in an attempt to limit the number of members of the list G (before elimination of duplicates). The currently reported generation assumes certainly correct initial seeds as in Figure 14, so that all cages are generated.

Another scheme generates graphs making a "spirality" assumption and the assumption of absence of isospectrality—both assumptions seemingly fairly reliable though there seem [46] to be counter-examples to the first. For the second assumption the results from the application of our algorithm yield:

Empirical Spectrality Theorem—Among the fullerene polyhedra there are no isospectral pairs of fewer than 72 vertices, and among the fullerenes with isolated pentagons there are no isospectral pairs of fewer than 98 vertices.

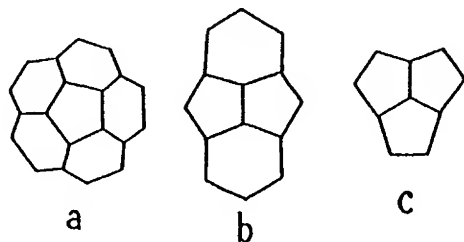


Figure 14. Respective seeds for the three cases: first $p = 0$; second $p \geq 1$ and $q = 0$; and third $q \geq 1$.

There is yet another generation scheme [47] replacing the "spirality" assumption by a weaker one—the approach is much like ours of Figure 12 except that to a growing seed pentagonal and hexagonal faces are added between just one pair of currently divalent vertices selected (in a "desirable" way). This, of course, avoids many cage duplicates, but invokes an assumption (perhaps justified) about the form of the consequent Schlegel diagram.

Curvature for Clusters

Crucial to cluster geometry are the curvature ideas of the "Closed Surfaces" section. But in fact for chemical purposes some extensions of these ideas are relevant. Thus we introduce an *absolute isotropic curvature*

$$|\kappa| \equiv |k_1 k_2| \quad (7.1)$$

and an *absolute anisotropic curvature*

$$\lambda = (|k_1| - |k_2|)^2. \quad (7.2)$$

Of course just as for the Gaussian curvature the corresponding integrated quantities are of interest, and should satisfy inequalities, one of which is:

Absolute-Isotropic-Curvature Theorem—For an orientable closed smooth surface S ,

$$\int_S |\kappa| \, ds \geq 4\pi[1 + \gamma(S)].$$

This in fact "readily" follows from the Gauss-Bonnet theorem, as we now indicate: Associated to S there is a minimum-sized convex surface S^c viewable as being obtained from S by tightly wrapping around it with something like "cellophane," so that all portions of S^c not coincident with S are flat in at least one direction, whence $\kappa = 0$. The portion of S not coincident with S^c is denoted S^i , and one has (from the Gauss-Bonnet theorem)

$$4\pi[1 - \gamma(S)] = \int_{S^c} \kappa \, ds + \int_{S^i} \kappa \, ds. \quad (7.3)$$

Then noting that S^c being convex has $\gamma(S^c) = 0$, we have

$$\int_{S^i} \kappa \, ds = 4\pi[1 - \gamma(S)] - 4\pi[1 - \gamma(S^c)] = -4\pi\gamma(S). \quad (7.4)$$

Thus

$$\int_S |\kappa| \, ds = \int_{S^c} |\kappa| \, ds + \int_{S^i} |\kappa| \, ds = 4\pi + \int_{S^i} |\kappa| \, ds \geq 4\pi + \left| \int_{S^i} \kappa \, ds \right| \quad (7.5)$$

and the theorem is obtained.

General results for the integrated absolute anisotropic curvature seem to be more difficult to obtain. But there is:

Extended Willmore Conjecture—For a closed smooth orientable surface S ,

$$\int_S |k_{\max} - k_{\min}|^2 ds \geq 8(\pi - 2)\pi\gamma(S).$$

In fact the usual Willmore conjecture [48,49] is for $\gamma(S) = 1$ and strictly concerns the integral over $k_1^2 + k_2^2$, but the present conjecture implies the usual one.

In addition to these results belonging to classical differential geometry, there are some further analogous combinatorial results. We define the *combinatorial curvature* at face α of a cellular embedding of G on S to be

$$\Delta_\alpha = 2\pi - \sum_i^\alpha \left(\pi - \frac{2\pi}{|i|} \right) \quad (7.6)$$

where the sum is over vertices around the face and $|i|$ is the degree of vertex i . This definition parallels that of (3.3) where $(\pi - 2\pi/|i|)$ would be the angle turned through at vertex i if the embedded edges incident at i radiated straightly outward at uniformly spaced angles around i . Also in parallel with this and (3.2), one may define a *combinatorial curvature* at each vertex i ,

$$\Delta_i = 2\pi - \sum_\alpha^i \left(\pi - \frac{2\pi}{|\alpha|} \right) \quad (7.7)$$

where the sum is over faces incident at i and $|\alpha|$ is the number of sides to the face α . Then Euler's theorem comes into a close parallel with the differential-geometric curvature theorems of the third section:

Euleric Combinatorial Curvature Theorem—If G is cellularly embedded on a closed orientable surface, then

$$\sum_\alpha \Delta_\alpha = 2\pi\chi(S) = \sum_i \Delta_i.$$

In fact this theorem is just a restatement of the earlier Euler's theorem as may be seen after substitution of the definitions for Δ_α and Δ_i . But in the present version of the theorem the analogy with Descartes' theorem or the Gauss-Bonnet theorem is more closely drawn.

Cluster Strain

These various curvature ideas and results are relevant to the strain arising in realizable cluster geometries. That there are two different curvature measures (geometric and combinatorial) is important. The content of the Gauss-Bonnet theorem and the theorem just finished is that globally these two types of curvatures must match (i.e., be equal). But even local matching is needed if strain is to be avoided. That is if they do not match in some region R containing the ring α , then there arises a consequent strain at ring α involving bond dilatation in order to accommodate the graph-theoretic combinatorial curvature to the geometrically realized

curvature. A strain at α due to the region of rings within a graphical distance n of α then seems to be (proportional to)

$$\varepsilon_n(\alpha) \equiv \left| \sum_{\beta}^{n,\alpha} \left(\Delta_{\beta} - \int_{\beta} \kappa \, ds \right) \right| \quad (8.1)$$

and an overall *curvature mismatch* for face α

$$\varepsilon(\alpha) \equiv \sum_n \varepsilon_n(\alpha). \quad (8.2)$$

In addition there are local isotropic and anisotropic curvature contributions to the strain involving bond-angle bending, as have already been discussed elsewhere [15]. Thus, the total strain energy associated to a molecular graph G cellularly embedded in a surface S which is in turn embedded in \mathcal{E}_3 is

$$E(G, S) = a \int_S |\kappa| \, ds + b \int_S \lambda \, ds + c \sum_{\alpha} \varepsilon(\alpha) \quad (8.3)$$

with a , b , and c parameters (actually with $a \approx 2b$). The first absolute-isotropic-curvature term here is bounded by the first theorem of the preceding section—and in fact this bound evidently is an equality if the surface S (as embedded in \mathcal{E}_3) is “unlumpy.” The second (absolute-anisotropic-curvature) term and the third (curvature-mismatch) term are more problematic and indeed often have opposing tendencies. For example, for a large fullerene graph G say as in Figure 15 it is seen that G is embeddable on the surface of a sphere, whence there is no anisotropic curvature strain, but as a consequence there is curvature mismatch in the regions of hexagonal faces (these having 0 combinatorial curvature), and also there is mismatch at the pentagonal faces, whose combinatorial curvature exceeds the local

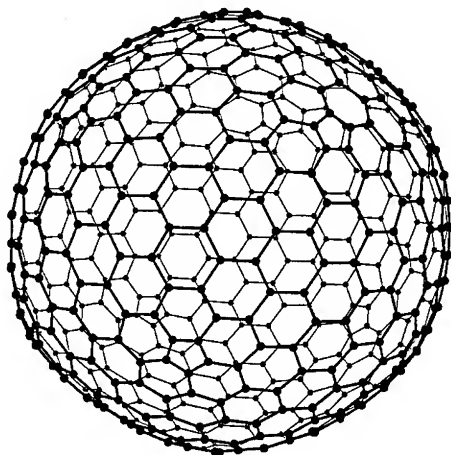


Figure 15. Conceivable spherical structure for C_{540} .

geometric curvature. Alternatively, S may be deformed to the shape of an icosahedron as in Figure 16, whence there is no curvature mismatch, but there is notable anisotropic curvature strain, along the edges of the icosahedron. Evidently a shape between that of an icosahedron and a sphere is preferable, and indeed is just what can be recognized in quantum-chemical computations [50] on such large fullerenes.

As another point of interest one can inquire what might be the conditions that the absolute-anisotropic curvature and curvature mismatch terms both become their minimum value 0. Evidently the extended Willmore conjecture indicates that in order to achieve this we must have $\gamma(S) = 0$, and we might further constrain attention to the fullerenes (i.e., trivalent-graph embeddings in a sphere such that all faces are pentagonal or hexagonal). Then we have:

Fullerenic Conjecture—The only fullerenes such that the curvature mismatch and the absolute-anisotropic curvature both vanish simultaneously are the dodecahedron and the truncated icosahedron.

Of course the dodecahedral structure is unfavorable for other reasons: because it is open shell (at icosahedral symmetry) and because the absolute-isotropic curvature per site is rather high (i.e., $60/20 = 3$ times as high). Thence the truncated icosahedron structure is singled out as exceptional in several ways: first, by the preferable-fullerene theorem of the "Specialization" section; second, by the Clar-sextet leap-frog theorem along with the comment shortly following the theorem) in the same section; and third, by the present fullerenic conjecture. Thus there is a 3-fold justification of Kroto et al.'s original suggestion [6] of the "uniquely elegant" truncated-icosahedron structure for C_{60} .

Further qualitative insight and even quantitative results should we believe be possible utilizing our general strain formulation of Eq. (8.3). This we plan to report on further elsewhere.

Prospects

Here an outline towards a broad extension of current organic stereochemical theory has been attempted. Beyond the matter of structural possibilities, many

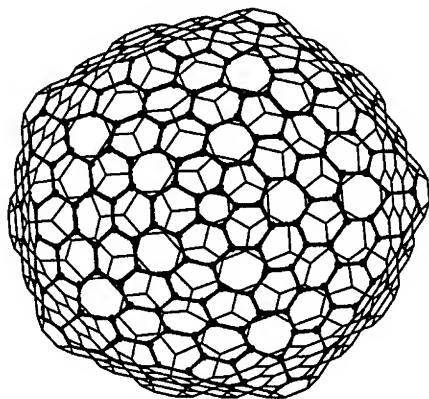


Figure 16. Conceivable more icosahedrally shaped structure for C_{540} .

questions remain unanswered, most prominently: first, as to what sorts of novel "emergent" properties might arise; and second as to what means there might be to synthesize the various conceived possible structures. Of course, current quantum-chemical methods especially of a semiempirical nature may help (and indeed to some extent already have helped) address this first question. But at least to the present authors the second question concerning rational synthesis seems quite opaque. Still the range of possibilities seems intriguing, and might encourage others to address some of the indicated questions.

Here we have looked at the structural possibilities going beyond the simple graph-theoretic cluster structure to embeddings of the graph in appropriate (locally Euclidean) closed surfaces. The consequent features not only of the molecular graph G but also of the surface S and of the embedding of G in S seem to lead far toward a characterization of the conceivable stereoisomers. Thence the presentation here may be viewed as a development of classical stereochemical theory, to be utilized both by experimentalists and quantum chemists. Moreover the curvature ideas marshalled in the section "Curvature for Clusters" are natural in our current stereochemical development and seem in the "Cluster Strain" section to lead to insight concerning strain and its effects. In particular the global shape of large (hypothetic) fullerene shapes is better understood, and the truncated-icosahedral structure of C_{60} is verified to be "uniquely elegant."

Aside from the relevant topological and differential-geometric aspects emphasized here there are a number of more conventional chemical graph-theoretic questions. Here the sections on "Specialization" and "Generation and Enumeration" bear more so on these graphical aspects, as also do most of the theoretical articles we have referenced. The fullerene cage-typing theorem of the "Generation and Enumeration" section distinguishes cages rather poorly (as seen by Table I), and more faithful graphical characterizations would be useful, as is the subject of other work by us [51]. One particular related point concerns IUPAC nomenclature, which for the fullerenes has been recently (correctly) described [52].

Still further developments and work seem likely—and hopefully useful (even at a stage preceding full-blown quantum-chemical computations).

Finally, acknowledgment is made to the Welch Foundation of Houston, Texas and to the donors of the Petroleum Research Fund administered by the American Chemical Society.

Bibliography

- [1] G. Polya, *Zeits. Kristal.* **A93**, 415 (1936).
- [2] (a) G. Polya and R. C. Read, *Combinatorial Enumeration of Groups, Graphs and Chemical Compounds* (Springer-Verlag, Berlin, 1987); (b) S. Fujita, *Symmetry and Combinatorial Enumeration in Chemistry* (Springer-Verlag, Berlin, 1991).
- [3] See, e.g., K. Mislow, *Introduction to Stereochemistry* (W. A. Benjamin, New York, 1965).
- [4] (a) D. E. H. Jones, *New Sci.* **32**, 245 (1966); (b) Z. Yoshida and E. Osawa, in Sec. 5.6.2 of *Aromatic Compounds* (Kagakudojan, Kyoto, 1971); (c) J. Castells and F. Serratosa, *J. Chem. Ed.* **60**, 941 (1983).
- [5] (a) D. A. Bochvar and E. G. Galipern, *Dokl. Akad. Nauk. SSSR* **209**, 610 (1973); (b) R. A. Davidson, *Theor. Chim. Acta* **58**, 193 (1981).

- [6] H. W. Kroto, J. R. Heath, S. C. O'Brien, R. F. Curl, and R. E. Smalley, *Nature* **318**, 162 (1985).
- [7] W. R. Krätschmer, L. D. Lamb, K. Fostiropoulos, and D. R. Huffman, *Nature* **347**, 354 (1990).
- [8] R. Taylor, J. P. Hare, A. K. Abdul-Sada, and H. W. Kroto, *J. Chem. Soc., Chem. Commun.* **20**, 1423 (1990).
- [9] R. Ettl, I. Chao, F. Diederich, and R. L. Whetten, *Nature* **353**, 149 (1991).
- [10] F. Diederich, R. L. Whetten, C. Thilgen, R. Ettl, I. Chao, and M. M. Alvarez, *Science* **254**, 1768 (1991).
- [11] (a) F. Diederich, R. Ettl, Y. Rubin, R. L. Whetten, R. Beck, M. Alvarez, S. Anz, D. Sensharma, F. Wudl, K. Khemani, and A. Koch, *Science* **252**, 548 (1991); (b) D. Ben-Amotz, R. G. Cooks, L. Dejarne, J. C. Gunderson, S. H. Hoke II, B. Kahr, G. L. Payne, and J. M. Wood, *Chem. Phys. Lett.* **183**, 149 (1991); (c) K. Kikuchi, N. Nakahara, T. Wakabayashi, M. Honda, H. Matsumiya, T. Monkawi, S. Suzuki, H. Shiromaru, K. Saito, K. Yamauchi, I. Ikemoto, and Y. Achiba, *Chem. Phys. Lett.* **186**, 177 (1992).
- [12] T. G. Schmalz, W. A. Seitz, D. J. Klein, and G. E. Hite, *Chem. Phys. Lett.* **130**, 203 (1986).
- [13] D. J. Klein, W. A. Seitz, and T. G. Schmalz, *Nature* **323**, 703 (1986).
- [14] P. W. Fowler and J. M. Woolrich, *Chem. Phys. Lett.* **127**, 78 (1986).
- [15] T. G. Schmalz, W. A. Seitz, D. J. Klein, and G. E. Hite, *J. Am. Chem. Soc.* **110**, 1113 (1988).
- [16] P. W. Fowler, J. E. Cremmona, and J. I. Steer, *Theor. Chim. Acta* **73**, 1 (1988).
- [17] D. E. Manolopoulos, J. C. May, and S. E. Down, *Chem. Phys. Lett.* **181**, 105 (1991).
- [18] X. Liu, D. J. Klein, T. G. Schmalz, and W. A. Seitz, *J. Comp. Chem.* **12**, 1265 (1991).
- [19] T. G. Schmalz, X. Liu, and D. J. Klein, *Chem. Phys. Lett.* **192**, 331 (1992).
- [20] Y.-D. Gao and W. C. Herndon, *J. Am. Chem. Soc.* **115**, 8459 (1993).
- [21] (a) R. Tosić and S. J. Cyvin, *Zbornik radova Privodnomatematičkog fakulteta-Univerziteta u Novom Sadu* **22** (1992); (b) S. Itoh, S. Ihara, and J. Kitakami, *Phys. Rev. B* **47**, 1703 (1993); (c) E. C. Kirby, *Croat Chem. Acta* **66**, 13 (1993).
- [22] D. J. Klein, *J. Chem. Inf. & Comp. Sci.* **34**, 453 (1994).
- [23] (a) A. T. Balaban, *Stud. Cercet. Chim. Acad. R. P. Romania* **7**, 257 (1957); (b) A. T. Balaban, M. Banciv, and V. Corba, *Annulenes, Benzo-Hetero-Homo-Derivatives and Their Valence Isomers* (CRC Press, Boca Raton, FL, 1987).
- [24] See, e.g., *Molecular Structure and Energetics* vols. 1 and 2, J. F. Liebman and A. Greenberg, Eds. (Verlag-Chemie, New York, 1986, 1987).
- [25] W. Weltner, Jr. and R. J. Van Zee, *Chem. Rev.* **89**, 1713 (1989).
- [26] D. Hilbert and S. Cohn-Vossen, *Anshauliche Geometrie* published in 1932, and reissued in translation as *Geometry and the Imagination* (Chelsea, New York, 1952).
- [27] J. Stillwell, *Classical Topology & Combinatorial Group Theory* (Springer-Verlag, Berlin, 1980).
- [28] D. J. Struik, *Classical Differential Geometry* published in 1950, and reissued by (Dover Pub., New York, 1988).
- [29] T. Y. Thomas, *Tensor Analysis and Differential Geometry* (Academic Press, New York, 1965).
- [30] B. Grünbaum, *Convex Polytopes* (Interscience Pub., New York, 1967), Chap. 13.
- [31] P. J. Giblin, *Graphs, Surfaces and Homology* (Chapman and Hall, London, 1981).
- [32] J. L. Gross and T. N. Tucker, *Topological Graph Theory* (Wiley, New York, 1987).
- [33] See, e.g., (a) D. Rolfsen, *Knots and Links* (Publish or Perish, Berkeley, 1976); (b) L. H. Kauffman, *Formal Knot Theory* (Princeton University Press, Princeton, 1983).
- [34] B. Grünbaum and T. S. Motzkin, *Can. J. Math.* **15**, 744 (1963).
- [35] D. J. Klein and X. Liu, *J. Math. Chem.* **11**, 199 (1992).
- [36] E. Clar, *The Aromatic Sextet* (Wiley, New York, 1972).
- [37] (a) M. Randić, S. Nikolić, and N. Trinajstić, *Croat. Chem. Acta* **60**, 595 (1987); (b) R. Taylor, *Tetrahedron Lett.* **32**, 3731 (1991).
- [38] X. Liu, D. J. Klein, and T. G. Schmalz, *Full. Sci. & Tech.* (to appear, 1994).
- [39] P. W. Fowler, *Chem. Phys. Lett.* **131**, 444 (1986).
- [40] S. Iijima, *Nature* **354**, 56 (1991).
- [41] D. J. Klein, W. A. Seitz, and T. G. Schmalz, *J. Phys. Chem.* **97**, 1231 (1993).
- [42] M. Goldberg, *Tohoku Math. J.* **43**, 104 (1937).
- [43] X. Liu and D. J. Klein, *J. Comp. Chem.* **12**, 1260 (1991).

- [44] B. Mackay, *Congressus Numerant.* **30**, 45 (1981).
- [45] X. Liu, D. J. Klein, W. A. Seitz, and T. G. Schmalz, *J. Comp. Chem.* **12**, 1265 (1990).
- [46] D. F. Manolopoulos and P. W. Fowler, *Chem. Phys. Lett.* **204**, 1 (1993).
- [47] (a) D. Babić and N. Trinajstić, *Comp. in Chem.* (1993); (b) D. Babić, D. J. Klein, and C. H. Sah, *Chem. Phys. Lett.* **211**, 235 (1993).
- [48] J. Langer and D. A. Singer, *Bull. London Math. Soc.* **16**, 531 (1984).
- [49] R. Osserman, *Am. Math. Mon.* **97**, 731 (1990).
- [50] D. Bakoweis and W. Thiel, *J. Am. Chem. Soc.* **113**, 3704 (1991).
- [51] X. Liu, A. T. Balaban, D. Babić, D. J. Klein, and M. Randic, *J. Chem. Inf. & Comp. Sci.* (submitted).
- [52] (a) C. Ruecker and G. Ruecker, *Chimia* **44**, 116 (1990); (b) A. T. Balaban, D. Babić, and D. J. Klein, *J. Chem. Ed.*, to appear, 1994.

Received June 3, 1994

A Note on the Number of Spanning Trees in Buckminsterfullerene

NENAD TRINAJSTIĆ

The Rugjer Bošković Institute, HR-41001 Zagreb, The Republic of Croatia

ZLATKO MIHALIĆ

Faculty of Science, The University of Zagreb, HR-41001 Zagreb, The Republic of Croatia

FRANK E. HARRIS

Department of Chemistry, The University of Utah, Salt Lake City, Utah 84112

Abstract

A "pedestrian" approach is used to enumerate the spanning trees in buckminsterfullerene. The approach is called "pedestrian" because calculations were carried out by hand and pocket calculator. The number of spanning trees obtained for buckminsterfullerene is 375,291,866,372,898,816,000, a number identical to the value reported by Brown et al. [J. Comput. Chem. 12, 1118 (1991)] who used a computationally more involved approach. © 1994 John Wiley & Sons, Inc.

In this note we present a "pedestrian" approach to the enumeration of spanning trees of buckminsterfullerene (see the soccerball-like model of this molecule in Fig. 1). A spanning tree of a graph G is a spanning acyclic subgraph of G [1].

The number of spanning trees of buckminsterfullerene is already available in the literature. Brown et al. [2] have used the Gutman-Mallion-Essam theorem [3] (derived from the Matrix-Tree theorem [4]) for enumerating the number of spanning trees in a graph corresponding to buckminsterfullerene. The concept of a spanning tree underlies the method of McWeeny [5] for computing π -electron "ring-current" magnetic properties of conjugated molecules [6]. It is also used in attempts to quantify the complexity of a structure [e.g., 7].

Our procedure is based on the spectrum of the Laplacian matrix [8] L of buckminsterfullerene and consists of the following steps:

(1) Setting up the Laplacian matrix L of buckminsterfullerene: The Laplacian matrix is defined as [7]:

$$L = V - A \quad (1)$$

where A is the adjacency matrix [9] of a molecule and V is the degree (valency) matrix which is a diagonal matrix whose entries are graph-theoretical valencies. The easiest way of setting up the Laplacian matrix of buckminsterfullerene is by using the corresponding Schlegel diagram [10]. The Schlegel diagram is the representation of buckminsterfullerene in a plane. It is shown in Figure 2. Note that

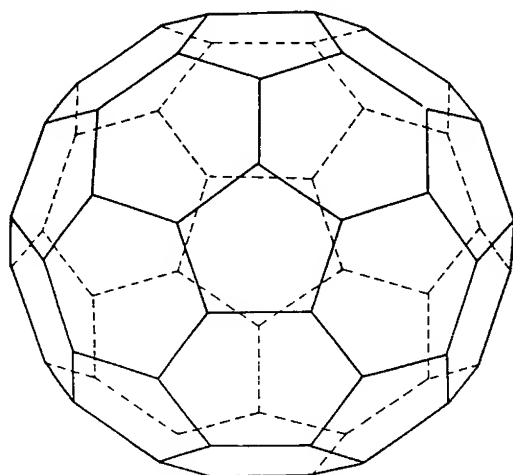


Figure 1. A soccerball-like surface structure of buckminsterfullerene.

the Schlegel diagram of buckminsterfullerene is a regular graph of degree 3, so that all diagonal elements of matrix V are equal to 3.

(2) The diagonalization of the Laplacian matrix: In Table I we give the spectrum of the Laplacian matrix of buckminsterfullerene. It has been obtained by hand computation [11] utilizing the irreducible representations of the I_h symmetry group to which buckminsterfullerene belongs [e.g., 12,13]. Thus, the 60 by 60 matrix was broken into three 1-by-1 matrices (two of which occur 3 times), five 2-by-2 matrices (two of which occur 3 times, two more of which occur 4 times, and the last of which occurs 5 times) and one 3-by-3 matrix (which occurs 5 times).

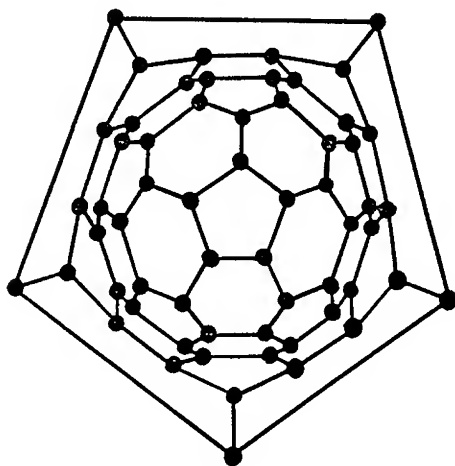


Figure 2. The Schlegel diagram of buckminsterfullerene.

TABLE I. The spectrum of the Laplacian matrix of buckminsterfullerene.

$x_1 = 0$
$x_2 = x_3 = x_4 = [9\sqrt{2} - \sqrt{10} - 2\sqrt{(19 - \sqrt{5})}]/4\sqrt{2}$
$x_5 = x_6 = x_7 = x_8 = x_9 = (5 - \sqrt{13})/2$
$x_{10} = x_{11} = x_{12} = [9\sqrt{2} + \sqrt{10} - 2\sqrt{(19 + \sqrt{5})}]/4\sqrt{2}$
$x_{13} = x_{14} = x_{15} = x_{16} = (7 - \sqrt{17})/2$
$x_{17} = x_{18} = x_{19} = x_{20} = x_{21} = x_{22} = x_{23} = x_{24} = x_{25} = 2$
$x_{26} = x_{27} = x_{28} = x_{29} = x_{30} = (7 - \sqrt{5})/2$
$x_{31} = x_{32} = x_{33} = [9\sqrt{2} - \sqrt{10} + 2\sqrt{(19 - \sqrt{5})}]/4\sqrt{2}$
$x_{34} = x_{35} = x_{36} = (9 - \sqrt{5})/2$
$x_{37} = x_{38} = x_{39} = x_{40} = x_{41} = (5 + \sqrt{13})/2$
$x_{42} = x_{43} = x_{44} = [9\sqrt{2} + \sqrt{10} + 2\sqrt{(19 + \sqrt{5})}]/4\sqrt{2}$
$x_{45} = x_{46} = x_{47} = x_{48} = x_{49} = (7 + \sqrt{5})/2$
$x_{50} = x_{51} = x_{52} = x_{53} = 5$
$x_{54} = x_{55} = x_{56} = x_{57} = (7 + \sqrt{17})/2$
$x_{58} = x_{59} = x_{60} = (9 + \sqrt{5})/2$

Note that the first Laplacian eigenvalue is always zero. The zero value for the first Laplacian eigenvalue is the result of the special structure of the Laplacian matrix [7,14].

(3) The computation of the number of spanning trees: The number $t(G)$ of spanning trees of a graph G is given by [7,15]:

$$t(G) = (1/N) \prod_{i=2}^N x_i(L) \quad (2)$$

where N is the number of vertices in G and the $x_i(L)$ denote the Laplacian spectrum. The multiplication starts with the second Laplacian eigenvalue since the first eigenvalue is always zero and does not, of course, play a part in the formula. The above formula is generally valid for computing the number of spanning trees for any graph [16].

By substituting the values reported in Table I into formula (2) we obtain the number of spanning trees in buckminsterfullerene:

$$\begin{aligned} t(G) &= 2^{27} \times 3^5 \times 5^4 \times 11^5 \times 19^3 / 2^2 \times 3 \times 5 \\ &= 2^{25} \times 3^4 \times 5^3 \times 11^5 \times 19^3 \\ &= 375,291,866,372,898,816,000 \end{aligned} \quad (3)$$

which is identical to the value reported by Brown et al. [2].

Acknowledgments

This work was supported in part by the Ministry of Science and Technology of the Republic of Croatia via grants nos. 1-07-159 and 1-07-185. We also thank referees for useful comments.

Bibliography

- [1] R. J. Wilson, *Introduction to Graph Theory*, 2nd printing (Oliver & Boyd, Edinburgh, 1972), p. 46.
- [2] T. J. N. Brown, R. B. Mallion, P. Pollak, B. R. M. de Castro, and J. A. N. F. Gomes, *J. Comput. Chem.* **12**, 1118 (1991).
- [3] I. Gutman, R. B. Mallion, and J. W. Essam, *Mol. Phys.* **50**, 859 (1983).
- [4] D. M. Cvetković, M. Doob, and H. Sachs, *Spectra of Graphs* (Academic, New York, 1980), p. 38.
- [5] R. McWeeny, *Mol. Phys.* **1**, 311 (1958).
- [6] R. B. Mallion, *Proc. Roy. Soc. (London)* **A341**, 429 (1975).
- [7] B. Mohar, in *MATH/CHEM/COMP 1988*, A. Graovac, Ed. (Elsevier, Amsterdam, 1989), p. 1.
- [8] B. Mohar, in *Graph Theory, Combinatorics and Applications*, Y. Alavi, G. Chartrand, O. R. Ollermann, and A. J. Schwenk, Eds. (Wiley, New York, 1991), p. 871.
- [9] N. Trinajstić, *Chemical Graph Theory*, 2nd revised edition (CRC Press, Boca Raton, FL, 1992), p. 41.
- [10] H. S. M. Coxeter, *Regular Polytopes*, 3rd edition (Dover, New York, 1973).
- [11] W. Byers Brown, *Chem. Phys. Lett.* **136**, 128 (1987).
- [12] R. A. Davidson, *Theoret. Chim. Acta* **58**, 193 (1981).
- [13] E. Brendsdal, S. J. Cyvin, B. N. Cyvin, J. Brunvoll, D. J. Klein, and W. A. Seitz, in *Quasicrystals, Networks and Molecules of Fivefold Symmetry*, I. Hargittai, Ed. (VCH, New York, 1990), p. 157.
- [14] Ref. 4, p. 27.
- [15] Z. Mihalić and N. Trinajstić, *Fullerene Sci. Techn.* **2**, 89 (1994).
- [16] N. Trinajstić, D. Babić, S. Nikolić, D. Plavšić, D. Amić, and Z. Mihalić, *J. Chem. Inf. Comput. Sci.* **34**, 368 (1994).

Received February 14, 1994

Theoretical Study on the Non-Adiabatic Photodissociation Process of Argon Cluster Ions Ar_7^+

TSUTOMU IKEGAMI and SUEHIRO IWATA*

Department of Chemistry, Faculty of Science and Technology, Keio University, Hiyoshi, Kohoku-ku, Yokohama 223, Japan

Abstract

The photodissociation process of argon cluster ion is studied by using the molecular dynamics method with non-adiabatic transitions. The potential energy surfaces and the electronic states are calculated with the diatomics-in-molecules (DIM) hamiltonian. The initial configurations are sampled from the classical trajectory paths on the potential energy surface of the electronic ground state. The non-adiabatic process is treated with the scheme proposed by J. C. Tully [J. Chem. Phys. **93**, 1061 (1990)] with a slight modification. The method is applied to the photodissociation process of Ar_7^+ . The calculated kinetic energy distribution and angular distribution of the photofragment are in good agreement with the experimental results, but the branching ratio between Ar^+ and Ar_2^+ fragment ions is not. © 1994 John Wiley & Sons, Inc.

Introduction

Several experimental and theoretical studies revealed that the argon cluster ion, Ar_n^+ , consists of the trimer ion core, Ar_3^+ , and the surrounding solvent atoms [1–10]. The trimer ion has a strong photoabsorption band in the visible region, and it photodissociates into Ar^+ ion and two Ar atoms on the photoabsorption [11–13]. So do the larger clusters, but the fragment ion is not always Ar^+ , and several small cluster ions are produced as a result of the photodissociation [5,9,10]. All the excited states of these small cluster ions are unstable, so that the fragment ions must be in the electronic ground state. Therefore, the non-adiabatic transitions from the photo-excited state to the ground state are essential in the photodissociation process. In these experimental conditions, no collisions take place during the dissociation processes. Therefore, the transition process to the ground state is a typical example of the intramolecular energy relaxation process.

In this study, the method proposed by J. C. Tully [14], which is referred as CSH (coupled surface hopping trajectory) hereafter, is employed to treat the non-adiabatic transitions. In the CSH method, the nuclear motion is treated classically, and the electronic state that governs the nuclear motion is selected statistically among the

* Present address: Division of Theoretical Studies, Institute for Molecular Science, Myodaiji, Okazaki 444.

adiabatic electronic states. The method is applied to the photodissociation process of Ar_7^+ . The kinetic energy distribution, the angular distribution, and the size distribution of produced photofragments are calculated and compared with the experimental results.

Calculation

Hamiltonian

The adiabatic potential energies and the electronic states are calculated from the DIM hamiltonian, H [1,4,15]. The $3p$ -hole valence extreme structures, in which the positive hole in the cluster is localized on $3p_w$ ($w = x, y, \text{ or } z$) orbital of one of the constituent atoms, are taken as the basis set. The dimension of the basis set is $3n$. The derivatives of the potential energies with respect to the nuclear coordinates can be calculated from the derivatives of each element of H [16]:

$$\nabla \langle \Psi_i | H | \Psi_i \rangle = \langle \Psi_i | \nabla H | \Psi_i \rangle, \quad (1)$$

where Ψ_i is the i th eigen function of H and is normalized. The DIM hamiltonian matrix is explicitly represented as a sum of the dimeric hamiltonian matrix H^{AB} , where A and B are constituent atoms. Because H^{AB} is a function of the internuclear distance R_{AB} , the derivatives of the matrix elements of H^{AB} are readily obtained analytically, as are the derivatives of H . The non-adiabatic coupling vectors are also calculated analytically from the derivatives of H [16]:

$$\langle \Psi_i | \nabla | \Psi_j \rangle = - \frac{\langle \Psi_i | \nabla H | \Psi_j \rangle}{E_i - E_j}, \quad (2)$$

where E_i is the i th eigenvalue of H .

Initial Configuration

The initial configurations and momenta of the nuclei are sampled from the normal molecular dynamics (MD) calculation of the cluster ion in the electronic ground state. The initial internal energies of the trajectories are taken moderately high enough that a few trajectories dissociate through the thermal evaporation of the Ar atoms; the typical microcanonical temperature is 190–200 K. After about 6 ps at high temperature, the cooling down process is started. The clusters are cooled down to 40 K, by removing the kinetic energy gradually. The annealing process takes about 15 ps, followed by the normal trajectory calculation for 1.2 ps. After that, 50 structures are sampled with the time interval of 0.1 ps. The total number of 2500 structures are obtained from 50 trajectories generated independently. The photoexcited state from which the CSH trajectory calculation starts is selected among the adiabatic states. The probability to be selected is proportional to the oscillator strength of the transition from the ground state.

Dynamics

The photodissociation trajectory is calculated by using the CSH method, followed by the normal MD calculation. At first, each trajectory is evolved with the CSH

method for ca. 0.5 ps. Then, the trajectory is examined to determine whether the electronic state drops down to the ground state and whether the ground state is well isolated from all other excited states in energy. If both of the conditions are satisfied, the rest of the trajectory is calculated by using the normal MD calculation, which is much faster than the CSH calculation.

The details of the CSH calculation are described elsewhere [13], and only a brief outline is shown here. At the starting point of the CSH calculation, the electronic wave function, Φ , is taken as one of the adiabatic electronic states, Ψ_ξ . The electronic state is evolved in time according to the Schrödinger equation,

$$i \frac{d\Phi}{dt} = H(R(t))\Phi. \quad (3)$$

Note that the electronic state Φ is no longer the eigen function of H after the time evolution, because H changes in the time through the changes of the nuclear coordinates R . The nuclear motion itself is governed by the adiabatic potential energy surface, $E_\xi(R)$, and it is calculated by using the Newton equation of motion. The population of Ψ_ξ in Φ ,

$$a_\xi = |\langle \Psi_\xi | \Phi \rangle|^2, \quad (4)$$

is monitored, and the non-adiabatic transition is invoked when a_ξ decreases. The timing of the transition is determined according to the *fewest switching* algorithm [13,14]. The destination state, Ψ_η , is selected among the adiabatic states, by examining (a) the increase of a_η and (b) the magnitude of the non-adiabatic coupling between Ψ_ξ and Ψ_η [13].

The fifth-order Adams' formula is employed in the numerical integration. Because the electronic wave function oscillates rapidly, the time step in the CSH calculation is taken as short as 0.05 fs. The time step in the normal MD calculation is 2.4 fs.

Results

One of the photodissociation trajectories of Ar_7^+ is shown in Figure 1. The actual potential energy surface on which the nuclei are moving is plotted in a solid line, while the other adiabatic potential energies are plotted in dashed lines. There are 21 adiabatic states in Ar_7^+ , but only the lowest seven states are shown in the figure for clarity. The trajectory starts from the sixth excited electronic state at $t = 0$. After seven non-adiabatic transitions indicated by vertical arrows at the top of the figure, it finally settles down to the ground electronic state, to produce a dimer ion and five neutral atoms. The potential energy starts to oscillate regularly at 1 ps, which reflects the vibration of the dimer ion.

Several snapshots of the trajectory are shown in Figure 2. The atoms labeled as "1", "2", and "3" form a linear Ar_3^+ ion core before the photoexcitation. Just after the excitation, "1" is ejected along the colinear axis of the ion core ($t = 0.3$ ps), and it flies away. On the other side of the ion core, "3" also tries to escape, but it is blocked by "4" located on the colinear axis, and instead, "4" is slowly ejected along the axis. From 0.3 to 0.9 ps, the rest of the five atoms undergoes several non-

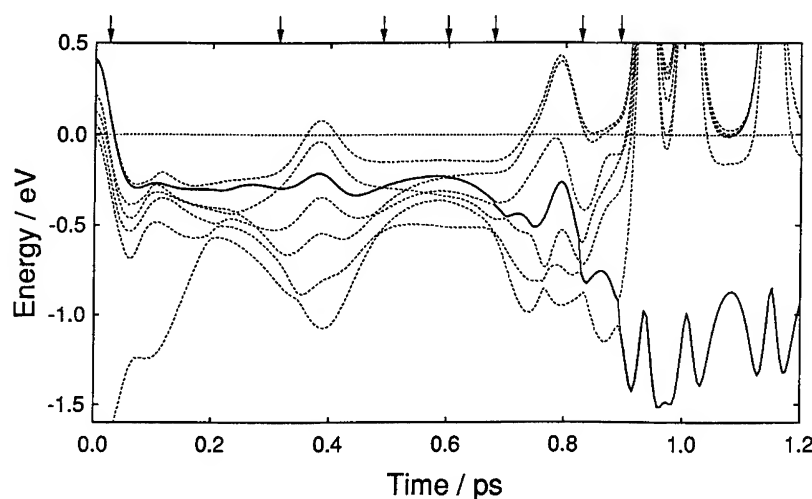


Figure 1. The potential energy curve along the photodissociation trajectory of Ar_7^+ is plotted in a solid line as a function of time. The adiabatic potential energies of the lowest seven states are also plotted in dashed lines. The trajectory starts from the sixth excited state at $t = 0$, commits seven non-adiabatic transitions (as indicated by arrows at the top of the figure), and finally settles down in the ground state.

adiabatic transitions and charge re-distributions, and finally, the charge is localized on the atoms labeled by "3" and "7" to form the dimer ion.

The photoabsorption cross section of Ar_7^+ is calculated at the starting points of 2500 photodissociation trajectories and plotted in Figure 3. The resolution of the spectrum is 20 nm. To make a meaningful comparison with the experimental results [10], we concentrate on those trajectories such that their excitation energies fall within the range between 2.25–2.75 eV (450–550 nm). The region, indicated as a shaded area in the figure, contains 1575 trajectories. Among those trajectories, 13% of them are not completely terminated: 11% still remain in the excited state at 2.7 ps after the photoexcitation, while 2% do drop to the ground state but the internal energy is large enough for further dissociation. The remaining 87% trajectories are terminated normally: 54% produce an Ar^+ fragment ion, while 33% end up with an Ar_2^+ fragment ion.

The kinetic energy distribution of the monomer fragment ion, Ar^+ , and that of the neutral fragments are calculated from those terminated trajectories, and are plotted in Figure 4. The kinetic energy of the neutral fragments shows a bimodal distribution as is seen in Figure 4(b). We refer to the components peaked at 0.4 eV as the fast fragments hereafter. The threshold energy is arbitrarily set to 0.2 eV. As shown in Figure 4(a), the fast fragments dominate the distribution of the monomer fragment ion.

The translational energy (a) and the internal energy (b) distributions of the dimer fragment ion are shown in Figure 5. Unlike the monomer ion and the neutral fragments, the dimer fragments carry little translational energy, and its distribution

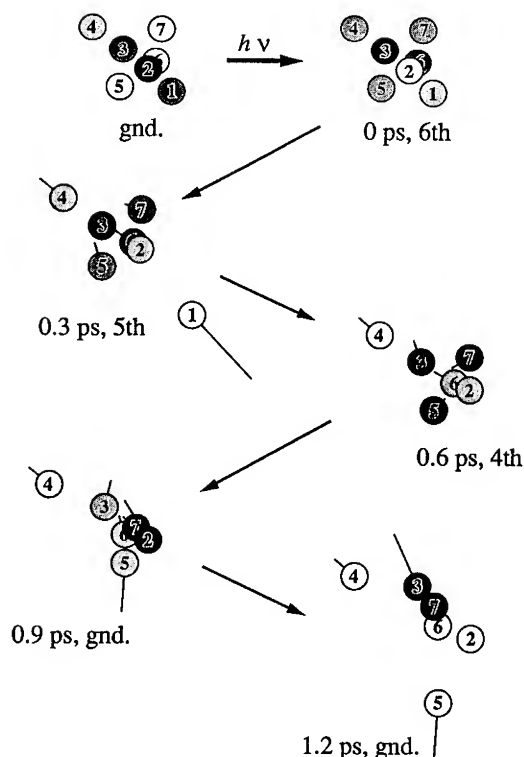


Figure 2. The snapshots on the trajectory shown in Figure 1. The darkness on atoms reflects charge density on them. The lines drawn from atoms indicate the velocity, which correspond to the movements in the next 1 ps.

decreases monotonously. A large amount of energy is stored in the vibrational mode, as is evident in Figure 5(b). As the binding energy of the dimer ion is 1.31 eV, the produced dimer ion is considered to be highly vibrationally excited, and besides, its energy distribution is far from the thermal one. Note that the plotted energy is that of the dimer, so that the average energy per atom becomes as large as the kinetic energy of the monomer fragment ion (ca. 0.4 eV).

The angular distributions of the fast component of the monomer fragment ion and the neutral fragments are plotted in Figure 6, as well as that of the dimer fragment ion. The angle is measured between the transition dipole moment of the photoexcitation and the velocity vector of the photofragment. The distribution of the fast monomer ions and that of the fast neutral fragments are anisotropic: they are mainly ejected along the transition dipole moment. The distribution for the dimer ions is isotropic.

Discussion

Excitation Energy Dependence

In this study, the multi-dimensional and multi-state non-adiabatic dynamics are directly treated. The non-adiabatic transitions are expected to occur more frequently

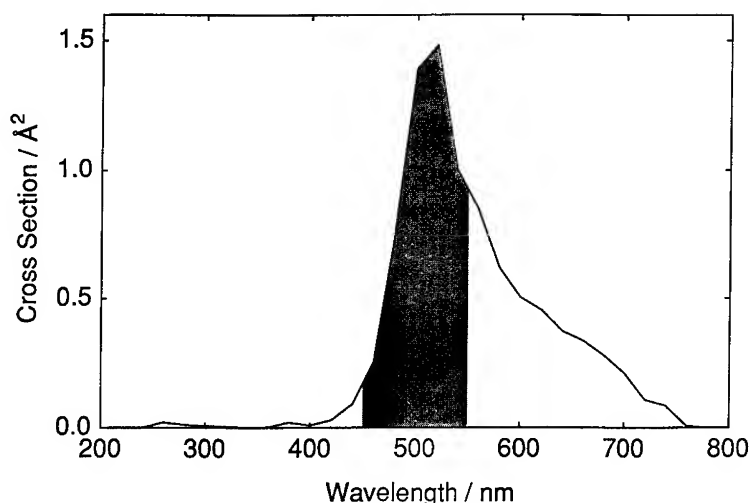


Figure 3. The photoabsorption spectrum of Ar_3^+ calculated from the ensembles of the initial configurations for the photodissociation trajectories. The resolution of the spectrum is 20 nm. The shaded area (2.25–2.75 eV) contains 63% of the 2500 trajectories.

as the nuclear velocity becomes large. In the present case of the photodissociation of Ar_3^+ , the nuclear kinetic energy originates from the initial excitation energy, ΔE . To examine the dependence of the dynamics on ΔE , the 2238 normally terminated trajectories among 2500 samples are grouped into three parts: $\Delta E > 2.75$ eV (the left blank area in Fig. 3), $2.25 \leq \Delta E \leq 2.75$ eV (the shaded area), and $\Delta E < 2.25$ eV (the right blank area). The excitation energy ΔE and frequency of the non-adiabatic jumps are averaged separately in each part, and summarized in Table I with the other statistical values. The number of non-adiabatic jumps does become large with the excitation energy, but it is because more jumps are required to go down to the ground state, if the trajectory starts from higher excited states. The number of jumps *per unit time* is almost independent from ΔE . It is probably because the fast fragments are ejected in the early stage of the photodissociation as typically seen in atom “1” of Figure 2. The fast fragments carry away the excess energy, leaving a much-the-same amount of the internal energy in the residuals. Note that the non-adiabaticity is determined by the relative velocities among atoms located within the interacting part of the cluster.

Origin of the Fast Fragments

The visible photoabsorption band of Ar_3^+ is mainly attributed to the $^2\Sigma_u^+ \rightarrow ^2\Sigma_g^+$ transition [4,11–13,17–20]. The transition dipole moment is parallel to the colinear symmetric axis of Ar_3^+ , and when it is excited, both of the side atoms attached to the center atom of Ar_3^+ are ejected along the colinear axis. Because the charge is located on both of the side atoms in the photoexcited state $^2\Sigma_g^+$, a fast Ar^+ fragment [9,21–23], a fast neutral Ar fragment [10], and a slow Ar

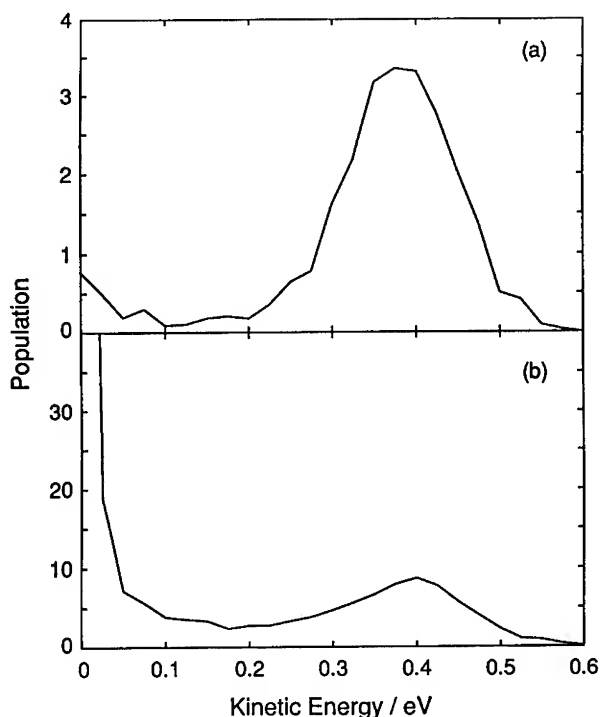


Figure 4. Kinetic energy distributions of monomer ions (a) and neutral fragments (b) produced from the photoexcitation of Ar_7^+ between 2.25–2.75 eV. The distribution of neutral fragments is bimodal, while the distribution of ionic fragments has only the fast component.

fragment are produced on the photoexcitation. These dissociation processes were elucidated in our previous article [13]. Note that a few slow Ar^+ fragments are produced through non-adiabatic transitions during the photodissociation.

As discussed in the previous article [4], the photoexcited state of the larger clusters remembers the $^2\Sigma_g^+$ character of Ar_3^+ . Naturally, the fast Ar^+ fragment is expected to be produced through the photoexcitation of Ar_7^+ and to be ejected along the transition dipole moment. The fast Ar^+ fragment is, however, no longer a major ionic product of the photodissociation. The non-adiabatic transitions now play a more important role in the photodissociation process of Ar_7^+ . Most of the charge carried by the fast escaping atoms as atom "1" in Figure 2 is drawn back to the residual part of the cluster. Fast neutral atoms are thus produced, and the majority of the neutral fragments that constitute the slow component in the velocity distribution are produced from successive evaporation from the residuals. Note that not all the fast neutral fragments originate from either of the two side atoms that initially form an ion core with the center atom. The number of fast neutral fragments, the number of those originating from an ion core, and their kinetic energies are averaged and summarized in Table II, as

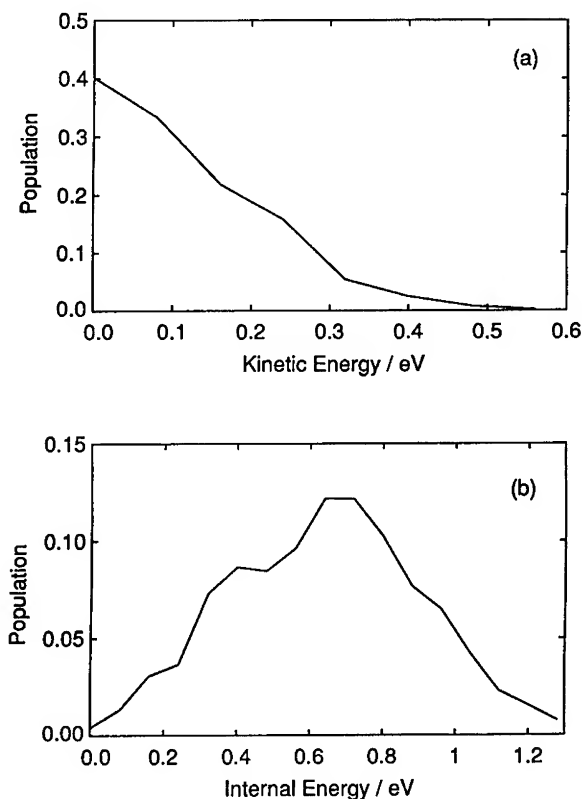


Figure 5. The translational (a) and the internal (b) energy distribution of the dimer fragment ion. The rotational energy is included in the internal energy.

well as the number of fast Ar^+ fragments. For excitation energies between 2.25 to 2.75 eV, about 20% of the fast neutral fragments originate from the solvent atoms. These atoms are likely to be generated from a rear-end collision between the solvent atoms and the atom ejected from an ion core, as atom "4" in Figure 2.

When Ar_2^+ is excited higher than 2.75 eV, 96% of the trajectories produce Ar^+ fragment ions. Nevertheless, only 29% of the trajectories produce fast Ar^+ fragments. It is because when excited higher, ejected atoms from the ion core get much kinetic energy, which makes the non-adiabatic transitions (or the charge draw-back process) easier. Indeed, only 16% of the fast Ar^+ fragment originates from the ion core. On the other hand, when excitation energies are between 2.25 and 2.75 eV, 57% of the trajectories produce fast Ar^+ fragments, and 90% of them originate from the ion core. Since 62% of the trajectories end up with Ar^+ fragments, more than 80% of the Ar^+ fragment ions come from the ion core. When the excitation energy is lower

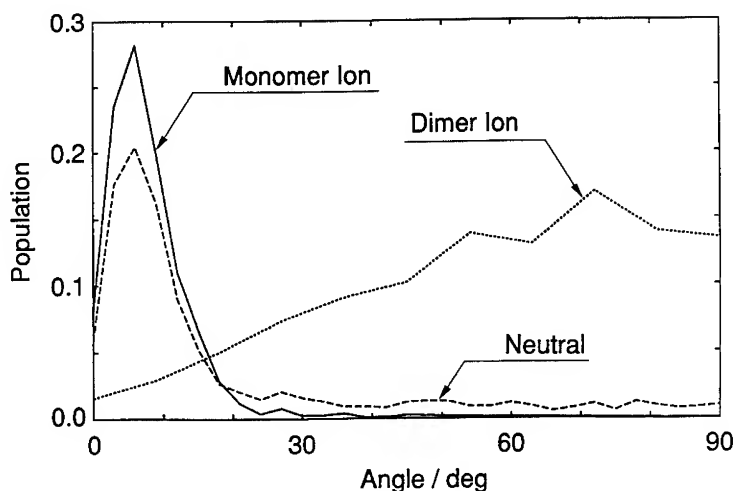


Figure 6. The angular distribution of the photofragments of Ar_7^+ around the transition dipole moment of the photoexcitation. The distributions of fast monomer fragment ions (solid line), fast neutral fragments (dashed line), and dimer fragment ions (dotted line) are plotted.

than 2.25 eV, almost no Ar^+ fragment is produced. Since the binding energy of Ar_7^+ with respect to $\text{Ar}^+ + 6 \text{Ar}$ is -1.79 eV at 0 K [4], it is energetically improbable to produce Ar^+ . Instead, the cluster utilizes the binding energy of Ar_2^+ to evaporate solvent atoms.

Comparison with Experiments

Nagata and Kondow observed the kinetic energy distribution of the neutral fragments from their time-of-flight mass spectra [10]. They found a bimodal distribution in the photodissociation of Ar_7^+ at 532 nm (2.33 eV), with an average kinetic energy

TABLE I. Characteristics of the trajectories for the three regions of the excitation energy, ΔE .

Excitation energy/eV	>2.75	2.25–2.75	<2.25
No. of trajectories ^a	90	1365	783
Averaged ΔE^b /eV	3.58	2.44	2.04
No. of non-adiabatic jumps	12.4	8.2	4.4
Freq. of non-adiabatic jumps/ps ⁻¹	7.6	7.7	7.0
No. of fast fragments ^c	2.25	2.27	2.06
Kinetic energy of fast fragments ^c /eV	0.75	0.38	0.43

^a Number of the trajectories, which start after the excitation with ΔE and terminate normally.

^b Averaged excitation energy ΔE over the trajectories.

^c A fast fragment is defined as the one which has more than 0.2 eV of kinetic energy. Charges on the fragments are not considered here.

TABLE II. Characteristics of the neutral fragments for the three regions of the excitation energy.

Excitation energy/eV	>2.75	2.25–2.75	<2.25
No. of fast neutrals ^a	1.96	1.70	2.05
No. of fast neutrals come from the ion core ^b	1.52	1.35	1.15
Kinetic energy of fast neutrals/eV	0.75	0.39	0.43
No. of fast Ar ⁺ fragments ^c	0.29	0.57	<0.01

^a Total number of fast neutral fragments per one photodissociation event.

^b Number of the fast neutral fragments originating from the side atoms of the ion core.

^c Number of fast Ar⁺ fragments per one photodissociation event.

of the fast components as ca. 0.35 eV. They also estimated the anisotropy parameter β of the fast neutral atoms to be 1.5–2, and the number of the fast neutrals ejected per single photodissociation event to be two. The present calculation reproduces the experimental results very well. The average kinetic energy of fast neutral fragments calculated from Figure 4 is 0.38 eV, the angular distribution shown in Figure 6 indicates the positive anisotropy parameter, and the calculated number of fast neutral fragments per trajectory is 1.7.

There is, however, a discrepancy between the present calculation and the experimental result in the branching ratio between monomer ion productions and dimer ion productions, Ar⁺/Ar₂⁺. The observed branching ratio is almost 0, that is, no Ar⁺ fragment ion is observed experimentally, while the calculated one is 1.6 for $2.25 \leq \Delta E \leq 2.75$. Because the branching ratio calculated for $\Delta E < 2.25$ is 0.01 and the one for $\Delta E > 2.75$ is 21.6, it is a steep function of the excitation energy. So that if the energy range were taken narrower around 2.33 eV (532 nm) in the calculations, the branching ratio might be reduced.

Conclusion

The photodissociation process of the argon cluster ion is studied by using Tully's scheme with a slight modification. The agreements with the experimental observation for the kinetic energy distribution and the angular distribution for the photofragments of Ar₇⁺ are satisfactory. For the branching ratio between Ar⁺ and Ar₂⁺ fragment ion, however, the calculation overestimates the production of Ar⁺. The poor resolution of the excitation energy seems to be responsible for the discrepancy, but the dependency of the ratio on the initial conditions of the trajectories, such as the rotational state or the temperature of the cluster, must be examined.

Acknowledgments

The authors thank Professor T. Nagata and Professor T. Kondow for helpful discussions on the photodissociation experiments. This work was partly supported by a Grant-in-Aid for Scientific Research from the Japanese Ministry of Education, Science and Culture (No. 05453024 and No. 04243104).

Bibliography

- [1] P. J. Kuntz and J. Valldorf, *Z. Phys. D—Atoms, Molecules and Clusters* **8**, 195 (1988).
- [2] I. Last and T. F. George, *J. Chem. Phys.* **93**, 8925 (1990).
- [3] H.-U. Böhmer and S. D. Peyerimhoff, *Z. Phys. D—Atoms, Molecules and Clusters* **11**, 239 (1989).
- [4] T. Ikegami, T. Kondow, and S. Iwata, *J. Chem. Phys.* **98**, 3038 (1993).
- [5] N. E. Levinger, D. Ray, M. L. Alexander, and W. C. Lineberger, *J. Chem. Phys.* **89**, 5654 (1988).
- [6] H. Haberland, B. von Issendorff, T. Kolar, H. Kornmeier, C. Ludewigt, and A. Risch, *Phys. Rev. Lett.* **67**, 3290 (1991).
- [7] W. Kamke, J. de Vries, J. Krauss, E. Kaiser, B. Kamke, and I. V. Hertel, *Z. Phys. D—Atoms, Molecules and Clusters* **14**, 339 (1989).
- [8] G. Ganteför, G. Bröker, E. Holub-Krappe, and A. Ding, *J. Chem. Phys.* **91**, 7972 (1989).
- [9] T. Nagata, J. Hirokawa, and T. Kondow, *Chem. Phys. Lett.* **176**, 526 (1990).
- [10] T. Nagata and T. Kondow, *J. Chem. Phys.* **98**, 290 (1993).
- [11] N. E. Levinger, D. Ray, K. K. Murray, A. S. Mullin, C. P. Schulz, and W. C. Lineberger, *J. Chem. Phys.* **89**, 71 (1988).
- [12] Z. Y. Chen, C. R. Albertoni, M. Hasegawa, R. Kuhn, and A. W. Castleman, Jr., *J. Chem. Phys.* **91**, 4019 (1989).
- [13] T. Ikegami, T. Kondow, and S. Iwata, *J. Chem. Phys.* **99**, 3588 (1993).
- [14] J. C. Tully, *J. Chem. Phys.* **93**, 1061 (1990).
- [15] J. C. Tully, in *Semiempirical Methods of Electronic Structure Calculation* G. A. Segal, Ed. (Plenum, New York, 1977); J. C. Tully, *Adv. Chem. Phys.* **42**, 63 (1980); P. J. Kuntz, in *Atom-Molecule Collision Theory*, R. B. Bernstein, Ed. (Plenum, New York, 1979).
- [16] J. C. Tully, *J. Chem. Phys.* **59**, 5122 (1973).
- [17] T. F. Magnera and J. Michl, *Chem. Phys. Lett.* **192**, 99 (1992).
- [18] W. R. Wadt, *Appl. Phys. Lett.* **38**, 1030 (1981).
- [19] F. X. Gadea and M. Amarouche, *Chem. Phys.* **140**, 385 (1990).
- [20] I. Last and T. F. George, *J. Chem. Phys.* **93**, 8925 (1990).
- [21] T. Nagata, J. Hirokawa, T. Ikegami, and T. Kondow, *Chem. Phys. Lett.* **171**, 433 (1990).
- [22] J. T. Snodgrass, C. M. Roehl, and M. T. Bowers, *Chem. Phys. Lett.* **159**, 10 (1989).
- [23] M. T. Bowers, W. E. Palke, K. Robins, C. Roehl, and S. Walsh, *Chem. Phys. Lett.* **180**, 235 (1991).

Received May 3, 1994

First-Principles Monte Carlo Simulated Annealing Study of the Structures and Properties of Hydrogenated Lithium Clusters

VIJAYA KESHARI and YASUYUKI ISHIKAWA*

Department of Chemistry and the Chemical Physics Program, University of Puerto Rico, P.O. Box
23346, San Juan, Puerto Rico 00931-3346

Abstract

The minimum-energy structures and bonding properties of the hydrogenated lithium clusters, Li_4H_2 and Li_7H , have been investigated by means of an *ab initio* Monte Carlo simulated annealing method. The minimum-energy structures of Li_4H_2 and Li_7H are found to resemble those of the triangular planar (D_{3h}) isomer of Li_6 and T_d isomer of Li_8 clusters, respectively. © 1994 John Wiley & Sons, Inc.

Introduction

Interactions of hydrogen and oxygen with small metal clusters and bulk metal surfaces are of fundamental importance for many chemical processes such as catalysis, corrosion, and materials processing, and play an important role in chemical and electronics industries. Recent advances in experimental techniques have enabled detailed spectroscopic studies on gas-phase clusters and their interaction with small molecules. A number of theoretical studies have been performed to model the electronic structure and reactivity of metal clusters and molecule-metal surface interactions [1].

Kaldor et al. [2] have pointed out that there are important differences between the reactions on metal surfaces and the reactions with bare metal clusters. Clusters of metal atoms react readily with small molecules and their reactivity exhibits very characteristic cluster-size dependency. In small clusters of up to 15 atoms, most of the atoms are surface atoms. Owing to its small dimension, the surface of the clusters are strongly curved with high step densities [2,3]. As the steps and other defects on the surfaces enhance the reactivity, bare metal clusters are usually highly reactive. The capability of small metal clusters to undergo geometric relaxation during the reaction with small molecules is quite unique. Because numerous structural isomers with low energy barrier exist, the clusters can easily undergo structural changes to react with adsorbates [2,3].

* To whom correspondence should be addressed.

Recently, Przybylski et al. [4] have studied the reaction pathways for the interaction of H_2 with Li_4 and Li_6 clusters by means of *ab initio* correlated methods. In that study, they have used a conventional geometry optimization technique at the Hartree-Fock (HF) level and calculated the configuration interaction (CI) energies for the optimal HF geometries using multireference diexcited (MRD)-CI procedure. Kato et al. [5] have studied the electronic structure of Li_nH_m clusters ($m \leq n \leq 4$) using the HF and CI methods with a 5-21G basis set. In a previous study [6], we have investigated the minimum-energy structures of a hydrogenated lithium cluster, Li_3H using the first-principles Monte Carlo (MC) simulated annealing method.

Most *ab initio* studies have employed conventional geometry optimization techniques to determine the structure of small metal and semiconductor clusters. Since the energy-minimization procedures make only downhill movements, the starting structure and the minimized structure are always in the same potential energy well in the conventional energy-minimization algorithm [7]. With such an approach, one may easily fall into one of several local minima if the starting conformation is in the local energy minimum region [7]. In order to find the global minimum, a brute-force strategy has been employed in the past [8]. This approach attempts to locate this global energy minimum by generating all of the possible starting geometries, and minimizing each to the nearest (local or global) minimum. However, as the number of atoms increases in the cluster, the number of local minima increases exponentially. Therefore, it becomes very difficult to enumerate all of the possible geometries to locate the global minimum among the local minima.

Recently, a number of simulation algorithms have been developed and applied to the study of the structure and dynamics of the metal and semiconductor clusters. Among these are the Monte Carlo (MC) [6,9] and molecular dynamics (MD) [10-13] simulated annealing algorithms to locate the global minimum energy structure. The former attempts to locate the global minimum by searching configuration space (i.e., by sampling canonical ensemble) using the MC approach known as simulated annealing [7,14,15]. The latter attempts to locate the global minimum by evolving the system with time. The MC and MD simulated annealing techniques have been successfully applied to a number of systems including rare gas atom clusters using the Lennard-Jones pair potential and embedded-atom potential [15-17]. However, in the case of metal and semiconductor clusters, phenomenological potentials fail dramatically for covalent and metallic systems where many-body interactions play a crucial role.

The major difficulty in computer simulations of metal and semiconductor clusters is the description of the many-body interactions. Several attempts have been made to include *ab initio* the many-body effects through computer simulation. Rothlisberger and Andreoni [13] have reported the simulated annealing MD method of Car and Parrinello [12] for alkali metal clusters using the density-functional approach. The approach attempts to include the many-body interactions in terms of the Local Density Approximation (LDA). Hartke and Carter [10] have implemented an *ab initio* MD simulation by employing the Generalized Valence Bond (GVB) method. The MD simulated annealing is performed with first-principles forces derived from the GVB wave function to locate the global potential minimum. Recently

Hammes-Schiffer and Andersen [11] have reported a simulated annealing MD study of small lithium clusters of up to five atoms by using the general Hartree-Fock (GHF) theory/STO-3G basis set. These methods are designed to solve the many-body simulation by evolving the system with time.

In a recent study [6], we have implemented an algorithm for MC simulated annealing based on an *ab initio* correlated electronic structure theory. In our first-principles MC simulated annealing procedure, we describe the many-body interactions in metal and semiconductor clusters in terms of an *ab initio* correlated method at the level of second-order Moller-Plesset perturbation theory (MP2). We have chosen the MP2 level of theory because, in a number of studies, *ab initio* calculations at the MP2 level have proven to be the most efficient correlated method to obtain correct geometrical structures. The first-principles MC procedure involves performing MC on a system of nuclei without prior knowledge of the quantum mechanical potential energy surface. The MC annealing procedure allows for an efficient sampling of the global minimum, and thus, is ideally suited for locating energy global minimum in metal and semiconductor clusters which possess a large number of local minima separated by tunneling barriers of varying height. In contrast with the MD methods, the interparticle forces are not required in the MC procedure, making the use of the *ab initio* correlated MP2 method more efficient in terms of computer time. In a preliminary study, we have successfully applied our *ab initio* MC simulated annealing method to the geometry optimization of the lithium clusters, Li_n ($n = 4, 6$) and the hydrogenated lithium clusters, Li_4H_2 , Li_5H [6], and Li_7H . This article outlines our first-principles MC simulated annealing algorithm and describes the applications to Li_4H_2 and Li_7H . In the next section, our *ab initio* MC simulated annealing algorithm is outlined. In the third section, the results of the applications to the lithium-hydrogen clusters, Li_4H_2 and Li_7H are presented.

Methods

In our first-principles Monte Carlo simulated annealing procedure [6], we employ the correlated *ab initio* method to approximate the total energy E_{total} of the system as a sum of the HF and MP2 energies; $E_{\text{total}} = E_{\text{HF}} + E_{\text{MP2}}$. This is in contrast with the conventional approach in which one approximates the system energy as a sum of model potentials, e.g., the pair-wise Lennard-Jones potential [16,17]. The MC simulated annealing procedure starts at a given temperature by calculating the HF and MP2 energies for an initial cluster configuration \mathbf{R}_0 . This is followed by making a random move for one of the atoms in the cluster to produce a new configuration \mathbf{R}_{new} with which a new total energy $E_{\text{total}}(\mathbf{R}_{\text{new}})$ is evaluated by computing the HF and MP2 energies. The change in the total energy of the cluster, ΔE , associated with the random move, $\Delta E = E_{\text{total}}(\mathbf{R}_{\text{new}}) - E_{\text{total}}(\mathbf{R}_0)$ is computed. If ΔE is negative, the configuration \mathbf{R}_{new} is accepted as \mathbf{R}_0 for the next random move. If ΔE is positive, the move is accepted with the probability given by the Boltzmann factor, $p = \exp(-\Delta E/kT)$. This is the so-called Metropolis algorithm [18] which makes use of the energy dependency of the Boltzmann distribution at a given temperature. In the Metropolis algorithm, uphill moves are always allowed at nonzero temperature.

Consequently, the MC annealing procedure does not have the problem of becoming trapped in one of the local minima as is found using the conventional optimization techniques. The stepsize $\Delta \mathbf{R}_{\max}$, which restricts the maximum displacement of the atoms, is adjusted in such a way that about 50% of the move is accepted in order to maintain the detailed balance at a given temperature. For a given temperature, a number of Metropolis samplings are performed to simulate the structural equilibrium.

The simulated annealing algorithm pioneered by Kirkpatrick et al. [14] makes use of the temperature dependence of the Boltzmann distribution [7]. The algorithm is based on the "crystal forming" process, i.e., during the simulation, temperature is lowered slowly from a sufficiently high temperature to a "freezing" temperature [7,15]. However, the algorithm is not completely satisfactory in the sense that there is no established protocol for the annealing procedure and a certain number of annealing runs are necessary to evaluate its performance [7,15]. Thus, in practice, the annealing procedure is repeated several times to ensure that the global minimum has been found. The algorithm was successfully used to locate the global minimum energy conformations of polypeptides and proteins where a very large number of local minima exist [7,15]. In our annealing procedure, we adopt the temperature-quenching scheme according to Kirkpatrick et al. [14];

$$T_{\text{new}} = \gamma T_{\text{old}} \quad (1)$$

γ is the quenching factor that determines the rate of temperature drop.

The stepsize $\Delta \mathbf{R}_{\max}$ also is slowly lowered to maintain the detailed balance;

$$\Delta \mathbf{R}_{\max}(\text{new}) = \gamma^{1/2} \Delta \mathbf{R}_{\max}(\text{old}) \quad (2)$$

The value of the quenching factor γ used in our study varies between 0.90 and 0.99. A computer program has been developed for our Monte Carlo simulated annealing procedure which utilizes the HONDO electronic structure program package [19] to compute the HF and MP2 energies. The random number generation routine URAND of Forsythe et al. [20] has been used. In each MC annealing run, we start with a different initial temperature, initial geometry, and random number initialization. In the annealing process, the temperature is lowered to ≈ 1 Kelvin according to Eq. (1).

In order to study the interactions of hydrogen with lithium clusters and the minimum-energy structures of the products, MC simulated annealing run is initiated with a reactant (i.e., H or H₂) separated at least 3 Å apart from the Li_{*n*} cluster (*n* = 4 or 7) at a reasonably high temperature (i.e., 300–500 K). This procedure is repeated several times by varying the initial temperature, quenching factor, and initial configuration. The basis sets employed are double-zeta plus polarization (DZP) basis sets reported by Dunning and Hay [21] for both H and Li. The atomization energy E_A is calculated according to Kato et al. [5];

$$E_A = E^{\text{MP2}}(\text{Li}_n\text{H}_m) - nE^{\text{MP2}}(\text{Li}) - mE(\text{H}) \quad (3)$$

where *n* and *m* are the number of the lithium and hydrogen atoms in the Li_{*n*}H_{*m*} cluster.

Results and Discussion

Figure 1 shows a typical MC simulated annealing run that maps variation of the average total energy of the $\text{H}_2 + \text{Li}_4$ interaction obtained at a given temperature as a function of temperature. Contrary to the conventional energy optimization techniques, the total energy does not decrease monotonically. In the Metropolis algorithm, uphill moves are always allowed at nonzero temperature: In a number of instances, the total energy is seen to rise due to the Metropolis sampling scheme. This particular feature enables the system to overcome the energy barriers of the local minima.

A total of four MC simulated annealing calculations were performed on the $\text{H}_2 + \text{Li}_4$ interaction by varying initial conditions. All the MC annealing runs gave the same global energy minimum structure of the closed-shell singlet ($^1\text{A}_1$, C_{2v}) Li_4H_2 . This planar structure obtained from the $\text{H}_2 + \text{Li}_4$ interaction is identical to that obtained earlier by Kato et al. [5] using a conventional geometry optimization technique. The minimum-energy structure of the planar Li_4H_2 cluster is shown in Figure 2. Since the final energy of the system obtained from a MC simulated annealing is the average total energy obtained by the Metropolis sampling scheme at the final temperature, the system energy may be refined by a standard geometry optimization technique: Thus, the structure and energy obtained in the MC simulations were refined further by a conventional gradient optimization technique employing a larger basis set of Lie and Clementi (i.e., $(13s4p/7s4p)$ for Li and $(8s2p/$

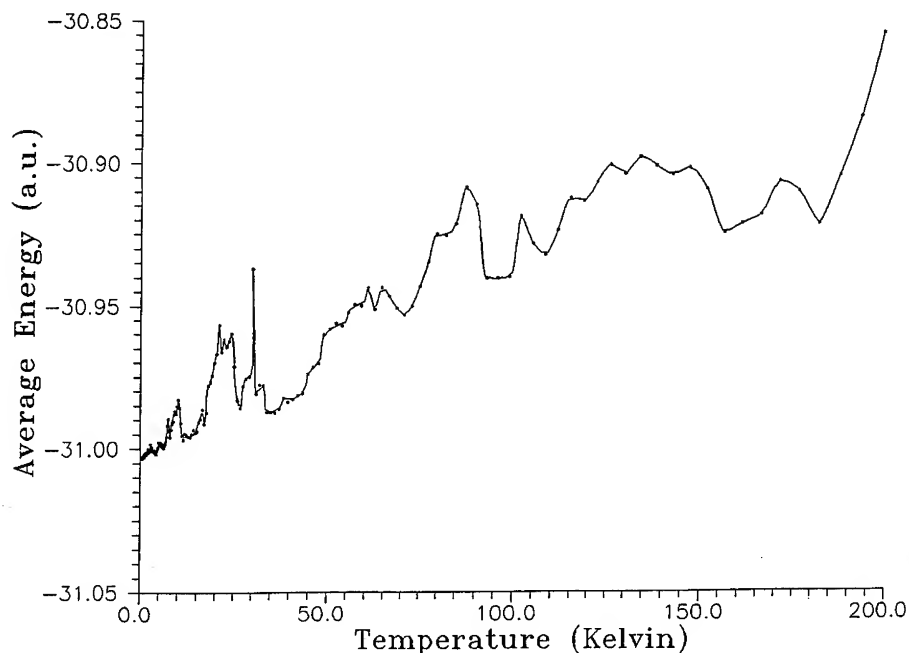


Figure 1. Average energy of Li_4H_2 as a function of temperature.

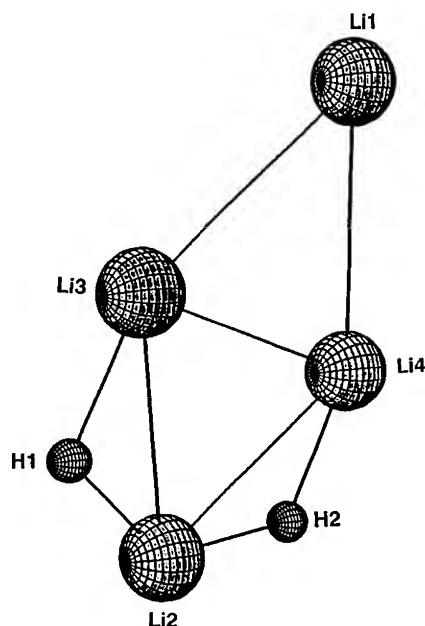


Figure 2. Minimum-energy structure of the planar Li_4H_2 .

$5s2p$) for H) [22]. Table I shows the results of the refinement along with the CI results reported by Kato et al. [5] and Przybylski et al. [4] for comparative purpose. All the Li—Li, Li—H, and H—H bond lengths obtained in our calculations on Li_4H_2 cluster agree to within 0.05 Å with those obtained by Przybylski et al. who employed (13s,3p/6s,3p) basis for Li and (4s,2p/2s,2p) basis for H.

The global energy minimum structure of the planar Li_4H_2 cluster is analogous to a local energy minimum structure of triangular-planar (D_{3h}) Li_6 cluster [23]: The Li_4H_2 structure may be obtained by replacing two of the corner lithium atoms in the triangular Li_6 by two hydrogen atoms. Net charges on the atoms obtained by means of Mulliken population analysis are given in Table II. The analysis reveals that the lithium atom, which is directly bonded to the two hydrogen atoms (labeled Li2 in Fig. 2), possesses a large net positive charge (+0.77) indicating that there is a significant amount of charge transfer between the Li and hydrogen atoms. The hydrogen atoms possess a large net negative charge (−0.72 each) due to their large electronegativity. This difference in the electronegativity between H and Li causes substantial changes in the charge distribution as well as the stability of the cluster isomers. When the hydrogen atoms replace the lithium atoms in the pure lithium cluster, the global energy minimum structure of Li_4H_2 no longer resembles the global minimum structure of Li_6 cluster, but is analogous to one of the local energy minimum structures of Li_6 .

A total of five MC simulated annealing calculations were performed on the H + Li_7 interaction by varying initial conditions. The MC simulated annealing study revealed the existence of two low-lying structural isomers of closed-shell singlet

TABLE I. Structural parameters and energies of Li_4H_2 .

	Present work	Previous work	
		Ref. [4]	Ref. [5]
Bond length (Å)			
R(Li1–Li3)	3.12	3.16	3.14
R(Li2–Li3)	2.87	2.89	2.95
R(Li3–Li4)	3.07	3.12	3.22
R(Li3–H1)	1.72	1.73	1.76
R(Li2–H2)	1.72	1.72	1.76
R(H1–H2)	3.16	—	3.22
Total energy			
$\langle E \rangle$ (a.u.) ^a	−31.00325	—	—
E_{opt} (a.u.) ^b	−31.15790	−31.10060	—
E_{A} (kcal/mol) ^c	147.6	—	115.7

^a Average total energy obtained by MC simulated annealing.^b Total energy obtained after refinement using Lie-Clementi basis set.^c Atomization energy.

Li_7H . Figure 3 displays the structure of the two isomers (labeled A and B). Four out of a total of five MC annealing runs gave the structure A. The fifth run gave the structure B as a local minimum. In the global energy minimum structure (isomer A), the hydrogen atom is directly bonded to three lithium atoms, while in isomer B the hydrogen atom is bonded to two lithium atoms and energetically less stable. The structure and average total energy obtained in the MC simulations were refined further by a conventional gradient optimization technique employing the basis set of Lie and Clementi [22]. Table III shows the results of the refinement. The total energy of the isomer B is only about 12 kcal/mol above that of the isomer A.

The results support the argument [24] that the most stable adsorption position is usually the site with the largest coordination number available on the cluster

TABLE II. Net charges obtained from Mulliken population analysis on Li_4H_2 .

Atom	This work	Kato et al. (Ref. [5])
Li1	-0.19	-0.17
Li2	0.77	0.377
Li3	0.43	0.286
Li4	0.43	0.286
H1	-0.72	-0.389
H2	-0.72	-0.389

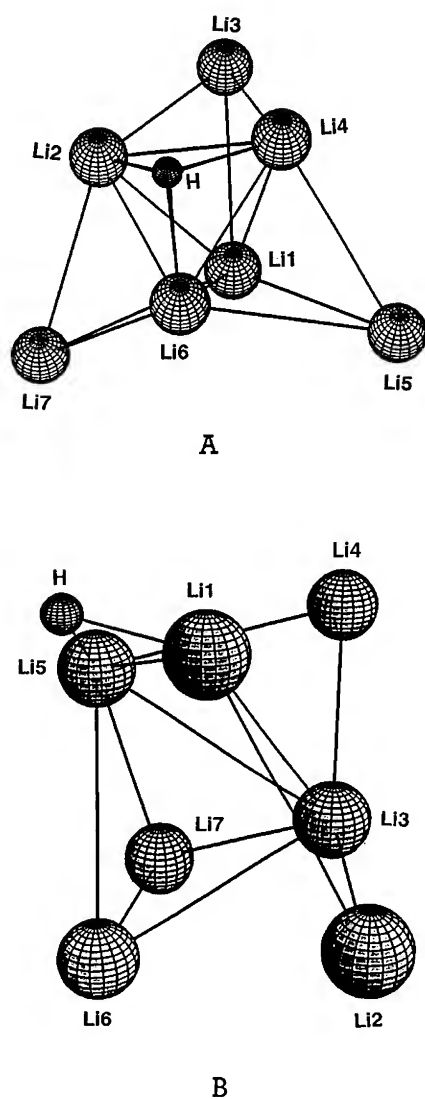


Figure 3. Two structural isomers of Li_7H obtained by MC simulated annealing.

surface. The global energy minimum structure of the hydrogenated Li_7H cluster obtained from the MC annealing of the $\text{Li}_7 + \text{H}$ interaction, has the coordination number of three for the hydrogen atom. There is a topological equivalence between the structure of isomer A and the T_d structure of Li_8 [25]: The Li_7H may be obtained by replacing one of the bridge-capped lithium atoms in Li_8 by a hydrogen atom. This structure of Li_7H also resembles the structure of Li_6H_2 reported by Przybylski et al. [4].

TABLE III. Structural parameters and energies of Li_7H .

Isomer A		Isomer B	
Bond length (Å)			
R(Li1–Li2)	2.94	R(Li1–Li2)	3.13
R(Li1–Li3)	3.18	R(Li1–Li3)	3.01
R(Li1–Li4)	2.93	R(Li1–Li5)	2.73
R(Li1–Li5)	3.18	R(Li1–H)	1.70
R(Li1–Li6)	2.95	R(Li2–Li3)	3.07
R(Li1–Li7)	3.17	R(Li3–Li4)	2.97
R(Li2–Li3)	3.22	R(Li3–Li5)	3.08
R(Li2–Li4)	2.75	R(Li3–Li6)	3.04
R(Li2–Li6)	2.73	R(Li3–Li7)	2.94
R(Li2–Li7)	3.23	R(Li4–Li5)	3.21
R(Li2–H)	1.82	R(Li5–Li6)	3.02
R(Li3–Li4)	3.24	R(Li5–Li7)	3.22
R(Li4–Li5)	3.26	R(Li5–H)	1.71
R(Li4–Li6)	2.74	R(Li6–Li7)	3.08
R(Li4–H)	1.82		
R(Li5–Li6)	3.19		
R(Li6–Li7)	3.21		
R(Li6–H)	1.82		
Total energy			
$\langle E \rangle$ (a.u.) ^a	–52.79072		–52.77513
E_{opt} (a.u.) ^b	–53.03524		–53.01547
E_A (kcal/mol) ^c	106.8		94.4

^a Average total energy obtained by MC simulated annealing.^b Total energy obtained after refinement using Lie-Clementi basis set.^c Atomization energy.TABLE IV. Net charges obtained from Mulliken population analysis on Li_7H .

Atom	Isomer A	Isomer B
Li1	0.22	0.45
Li2	0.34	-0.12
Li3	-0.18	0.17
Li4	0.33	-0.21
Li5	-0.19	0.48
Li6	0.34	-0.06
Li7	-0.19	-0.01
H	-0.68	-0.70

Table IV shows the net charges on the atoms contained in Li_7H , which are obtained by Mulliken population analysis for the two stable isomers. Two sets of equal net charges on three of the lithium atoms, i.e., ($\text{Li}3$, $\text{Li}5$, $\text{Li}7$) and ($\text{Li}2$, $\text{Li}4$, $\text{Li}6$), as well as the bond lengths indicate that the structure of isomer A possesses the C_{3v} symmetry with a C_3 rotation axis along the $\text{H}—\text{Li}1$ bond. In both isomers, the hydrogen atom possesses a large negative charge.

Acknowledgment

This work has been supported by the National Science Foundation through EPSCoR program.

Bibliography

- [1] H. Nakatsuji, H. Nakai, and M. Hada in *Metal-Ligand Interactions: From Atoms, to Clusters, to Surfaces*, Salahub and Russo, Eds. (Kluwer, 1992), pp. 251–285; W. Steele, *Chem. Rev.* **93**, 2355 (1993).
- [2] A. Kaldor, D. M. Cox, and M. R. Zakin, *Adv. Chem. Phys.* **70**, 211 (1988).
- [3] M. F. Jarrold and J. E. Bower, *J. Chem. Phys.* **85**, 5373 (1986); M. F. Jarrold and J. E. Bower, *Z. Phys. D* **12**, 551 (1989); M. D. Morse, J. B. Hopkins, P. R. R. Langridge-Smith, and R. E. Smalley, *J. Chem. Phys.* **79**, 5316 (1983).
- [4] K. Przybylski, J. Koutecky, V. Bonacic-Koutecky, P. von R. Schleyer, and M. F. Guest, *J. Chem. Phys.* **94**, 5533 (1991).
- [5] H. Kato, K. Hirao, I. Nishida, K. Kimoto, and K. Akagi, *J. Phys. Chem.* **85**, 3391 (1981); H. Kato, K. Hirao, and K. Akagi, *Inorg. Chem.* **20**, 3659 (1981).
- [6] V. Keshari and Y. Ishikawa, *Chem. Phys. Lett.* **218**, 406 (1994).
- [7] S. R. Wilson, W. Cui, J. W. Moskowitz, and K. E. Schmidt, *Tetrahedron Lett.* **29**, 4373 (1988); J. Moskowitz, K. E. Schmidt, S. R. Wilson, and W. Cui, *Int. J. Quantum Chem., Quantum Chem. Symp.* **22**, 611 (1988); S. R. Wilson, W. Cui, J. W. Moskowitz, and K. E. Schmidt, *J. Comp. Chem.* **12**, 342 (1991).
- [8] "Calc/Conf" in Chem-X, Chemical Design Ltd., Oxford, England; Macromodel, Copyright 1986, W. C. Still, Columbia Univ.
- [9] U. Nagashima, K. Morokuma, and H. Tanaka, *J. Phys. Chem.* **96**, 4294 (1992).
- [10] B. Hartke and E. A. Carter, *J. Chem. Phys.* **97**, 6569, (1992).
- [11] S. Hammes-Schiffer and H. C. Andersen, *J. Chem. Phys.* **99**, 523 (1993).
- [12] R. Car and M. Parrinello, *Phys. Rev. Lett.* **55**, 2471 (1985); E. S. Fois, A. Selloni, M. Parrinello, and R. Car, *J. Phys. Chem.* **92**, 3268 (1988).
- [13] U. Rothlisberger and W. Andreoni, *J. Chem. Phys.* **94**, 8129 (1991).
- [14] S. Kirkpatrick, C. D. Gelatt, Jr., and M. P. Vecchi, *Science* **220**, 671 (1983).
- [15] H. Kawai, T. Kikuchi, and Y. Okamoto, *Protein Eng.* **3**, 85 (1989); Y. Okamoto, M. Fukugita, T. Nakazawa, and H. Kawai, *Protein Eng.* **4**, 639 (1991); Y. Okamoto, T. Kikuchi, and H. Kawai, *Chem. Lett.* 1275 (1992).
- [16] D. G. Vlachos, L. D. Schmidt, and R. Aris, *J. Chem. Phys.* **96**, 6880 (1992).
- [17] D. D. Frantz, D. L. Freeman, and J. D. Doll, *J. Chem. Phys.* **93**, 2769 (1990).
- [18] N. Metropolis, A. W. Rosenbluth, M. N. Rosenbluth, A. H. Teller, and E. Teller, *J. Chem. Phys.* **21**, 1087 (1953).
- [19] HONDO; QCPE Program #544, Univ. of Indiana, Bloomington, IN.
- [20] G. E. Forsythe, M. A. Malcolm, and C. B. Moler, *Computer Methods for Mathematical Computations* (Prentice-Hall, Englewood Cliffs, NJ, 1977), p. 246.
- [21] T. H. Dunning, Jr. and P. J. Hay in *Modern Theoretical Chemistry*, Vol. 3, H. F. Schaefer III, Ed. (Plenum, New York, 1977).
- [22] G. C. Lie and E. Clementi, *J. Chem. Phys.* **60**, 1275 (1974).

- [23] I. Boustani, W. Pewestorf, P. Fantucci, V. Bonacic-Koutecky, and J. Koutecky, *Phys. Rev. B* **35**, 9437 (1987); J. Koutecky, I. Boustani, and V. Bonacic-Koutecky, *Int. J. Quantum Chem.* **38**, 149 (1991).
- [24] D. Spanjaard and M. C. Desjonqueres, in *Interaction of Atoms and Molecules with Solid Surface, Physics of Solid and Liquid*, V. Bortolani, N. H. March, and M. P. Tosi, Eds. (Plenum Press, New York, 1990).
- [25] V. Bonacic-Koutecky, P. Fantucci, and J. Koutecky, *Chem. Rev.* **91**, 1035 (1991).

Received March 18, 1994

On the Interaction of Cyanate and Thiocyanate Anions with Li^+ and Mg^{2+}

MICHAEL PROBST

*Institute of General, Inorganic and Theoretical Chemistry, Innsbruck University,
6020 Innsbruck, Austria*

Abstract

The energy surfaces of M^n/SCN^- and M^n/OCN^- ($\text{M} = \text{Li}^+$ and Mg^{2+}) ion pairs have been calculated at the Hartree-Fock and MP2 levels of theory. The electrostatic potential and the actual binding energies are compared. Besides linear ion pairs, nonlinear ones are also found and are in some cases the most stable ones. The electrostatic potential and the actual binding to cations are compared. © 1994 John Wiley & Sons, Inc.

Introduction

Cyanate and thiocyanate anions are interesting from the viewpoint of coordination chemistry because they are small, linear molecules and represent most simple types of anions with more than one coordination site. In general it is assumed that each end represents a possible coordination site.

Solutions containing ion pairs of Zn^{2+} , Cd^{2+} , and Hg^{2+} with SCN^- have recently been studied by Ohtaki by means of x-ray diffraction [1] and both S-site and N-site coordination has been found. Also, there is indication that in aqueous solutions of the corresponding salts ion pair formation occurs under various circumstances [2].

Despite SCN^- and OCN^- being quite common anions, they have been subjected to few theoretical investigations so far. After this work was finished an article by Parrini and Morales [3] came to our attention. Those authors studied Li^+/SCN^- with Hartree-Fock calculations and smaller basis sets (up to 4-31G*). Their findings are similar to this article but they do not mention the stable linear complex $\text{Li}^+ \cdots \text{NCS}^-$. A recent study of the cyanate anion [4] discusses geometries in the ground and excited states.

Therefore we have selected Li^+ and Mg^{2+} as examples of mono- and divalent counterions and study the structure of the ion pairs and the influence of ion pair formation on the intramolecular SCN^- and OCN^- geometry.

After mentioning the details of the calculations, we present the results for the systems Li^+/SCN^- and Li^+/OCN^- , and the differences if Li is substituted with Mg^{2+} .

Details of the Calculations

Optimized geometries and binding energies for the various complexes have been calculated. All calculations were performed with the 6-311G(d,p) basis set [5]. With this rather large basis, inadequacies due to the basis set limitations can be assumed to be small for the systems under study here. Therefore, no counterpoise corrections or similar treatment was performed. All complexes were calculated within the MP2 approximation except the ones where we included water molecules to model solvation effects. For those, only Hartree–Fock calculations could be afforded. Several test calculations were performed at the MP4 level and most of the geometry optimizations were performed at the Hartree–Fock level, too.

Interaction Energies in Li^+/SCN^-

The interaction energies of the ion pairs $\text{Li}^+ \cdots \text{SCN}^-$ and $\text{Li}^+ \cdots \text{NCS}^-$ at the optimized geometries are summarized in Table I. The Hartree–Fock binding energies are slightly lower than the corresponding MP2 values. The MP2 values given in Table I correlate only the valence electrons. Test calculations showed that if all electrons are correlated, the corresponding MP2_{all} energies are again slightly lower and are about 8% lower than the Hartree–Fock values. Differences between MP2 and MP4 binding energies were less than 1 kcal/mol for both $\text{Li}^+ \cdots \text{SCN}^-$ and $\text{Li}^+ \cdots \text{NCS}^-$. In the following, only the MP2 energies are discussed unless mentioned otherwise.

Coordination of Li^+ to the N-site is preferred over coordination to the S-site by 22 kcal/mol. However, a calculation of the force constants at the equilibrium ge-

TABLE I. Interaction energies in the various systems.

Anion Cation Method	SCN^-				OCN^-			
	Li^+		Mg^{2+}		Li^+		Mg^{2+}	
	HF	MP2	HF	MP2	HF	MP2	HF	MP2
S- or O-site coordination	-115	-120	-263	-272	-149	-150	-305	-307
N-site coordination	-139	-143	-306	-315 ^a	-161	-162	-337	-339
"T-shaped" coordination		-143		-315				
Complexes with three H_2O molecules. ^b								
S- or O-site coordination	-177		-411		-201		-455	
N-site coordination	-194		-447		-209		-475	
"T-shaped" coordination	-199		-440		-213		-464	

The interaction energies are given in kcal/mol.

^a The optimal nonlinear conformation is 0.1 kcal/mol lower in energy than the linear one (-315.3 vs. -315.2 kcal/mol).

^b The energies include the binding energy of the water molecules to the complexes: $\Delta E = E((\text{H}_2\text{O})_3\text{M}^{n+}\text{XCN}^-) - E(\text{M}^{n+}) - E(\text{XCN}^-) - 3E(\text{H}_2\text{O})$.

ometry showed that the $\text{Li}^+ \cdots \text{SCN}^-$ complex is not a stable local minimum whereas the $\text{Li}^+ \cdots \text{NCS}^-$ complex is. The energy hypersurface of the system shows a second stable minimum at a conformation where Li^+ is coordinated above the carbon forming a T-shaped complex (denoted as $\text{S}-\text{C}(\text{Li})-\text{N}$) which is shown in Figure 1 (top). This complexation changes the $\text{S}-\text{C}-\text{N}$ angle from 180.0° to 162.6° with N and S being bent towards the cation. The $\text{Li}-\text{S}-\text{C}-\text{N}$ dihedral angle is 0° , that is, the complex is planar. The relative stability of this local minimum is -143 kcal/mol, making it practically identical in stability to the linear $\text{Li}^+ \cdots \text{NCS}^-$ conformation. In the ongoing discussion, however, we do not neglect the $\text{Li}^+ \cdots \text{SCN}^-$ configuration because in some environments it might still become a stable complex or at least a real minimum of the potential surface.

In order to be able to draw conclusions more relevant to aqueous salt solutions we performed calculations on the complexes $(\text{H}_2\text{O})_3\text{Li}^+ \cdots \text{SCN}^-$ and $(\text{H}_2\text{O})_3\text{Li}^+ \cdots \text{NCS}^-$ (Fig. 5). The complexes might be used as models of hydrated Li^+ cations with one hydration shell water molecule substituted by the SCN^- anion. It is known from molecular dynamics experiments that in dilute aqueous solutions Li^+ prefers octahedral coordination to water [6] but we are mainly interested in knowing whether the water molecules have any qualitative effect on the order of the binding energies and geometries of the ion pairs and therefore we studied the computationally less demanding "pseudotetrahedral" coordination. The geometries of the complexes with three water molecules were optimized at the Hartree-Fock level. We neglected further hydration at the site of the anion because it is energetically less important than hydration of the cation. The order of stability for the linear molecules stays the same as for the unhydrated cations. $\text{Li}^+ \cdots \text{NCS}^-$ is 17 kcal/mol more stable than $\text{Li}^+ \cdots \text{SCN}^-$. Here, too, the latter is not a stable conformation but a saddle point only. For the T-shaped complex with three molecules of water around the Li^+ , $\text{S}-\text{C}(\text{Li}(\text{H}_2\text{O})_3)-\text{N}$, we could not perform a completely converged geometry optimization due to the very shallow potential surface. Nevertheless, the binding energy after 100 iterations was almost constant and 5 kcal/mol lower than in the linear coordinated $(\text{H}_2\text{O})_3\text{Li}^+ \cdots \text{NCS}^-$. No indication of a change back to a linear coordination was found. Therefore the T-shaped complex could well be present in aqueous solution.

The unexpected T-shaped nonlinear arrangement of Li^+ and SCN^- was investigated further. A map of the electrostatic potential of SCN^- (Fig. 2) shows indeed a local minimum besides the sulfur atom away from the molecular axis. In the optimized nonlinear $\text{S}-\text{C}(\text{Li})-\text{N}$ structure described above, however, Li^+ is closer to the carbon atom than to the sulfur atom (making the complex not L- but T-shaped). The electrostatic potential maps show the MP2 potential. Maps with the Hartree-Fock potential were virtually identical. Since the electrostatic potential measures the interaction of the molecule with a proton in the limit of negligible polarization, we investigated if mainly electronic polarization of the SCN^- anion or the bending of $\text{S}-\text{C}-\text{N}$ (which can be regarded as geometric "polarization") are responsible for the difference between electrostatic potential minima and actual minimum energy structure. A calculation of the T-shaped complex with a rigid linear SCN^- gave nearly the same binding energy (-140 kcal/mol) as the

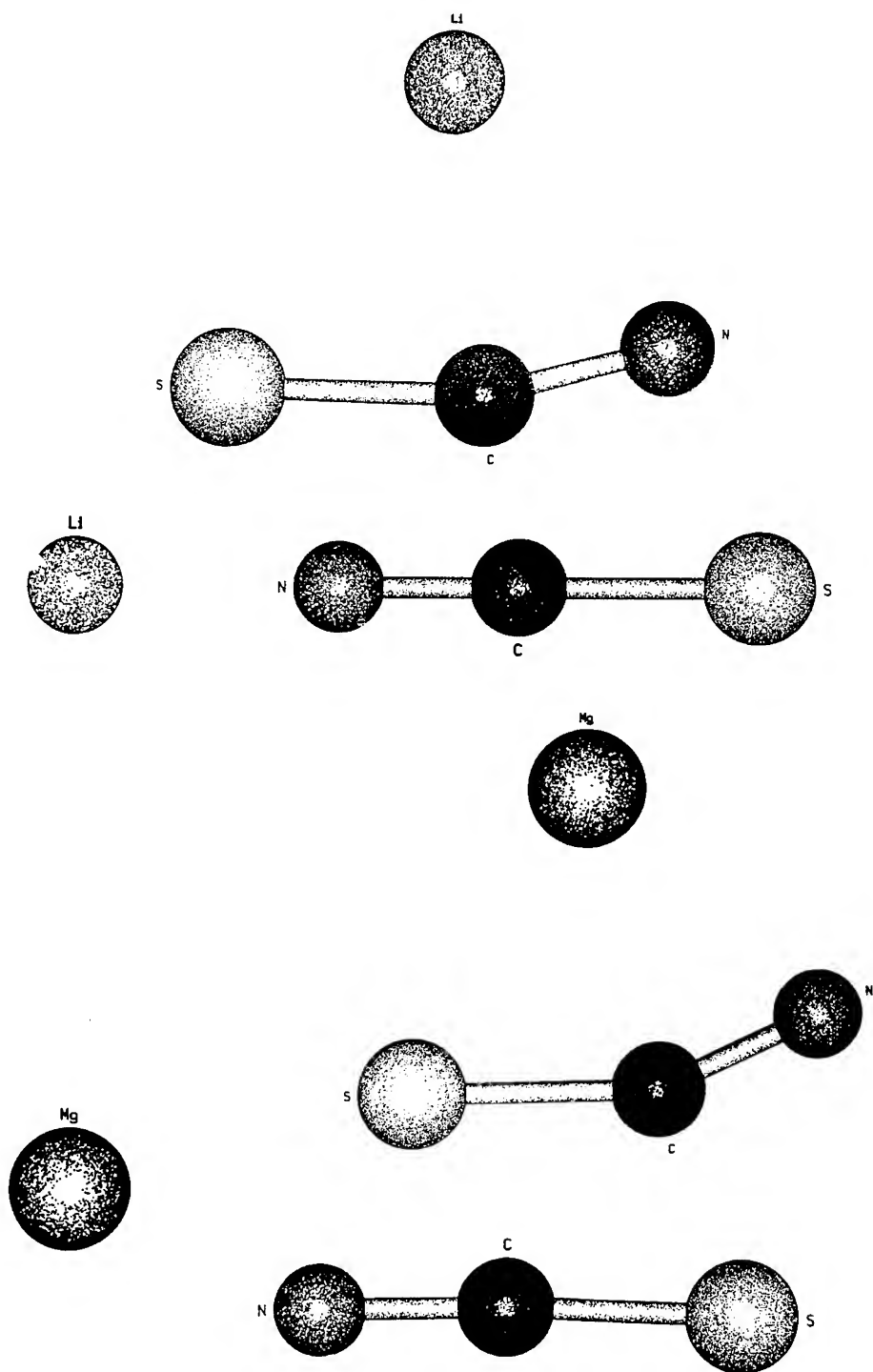


Figure 1. Equilibrium geometries of the ion pairs of SCN^- with Li^+ (upper 2 plots) and Mg^{2+} (lower 2 plots). The figures show the MP2/6-311G(d,p) optimized geometries.

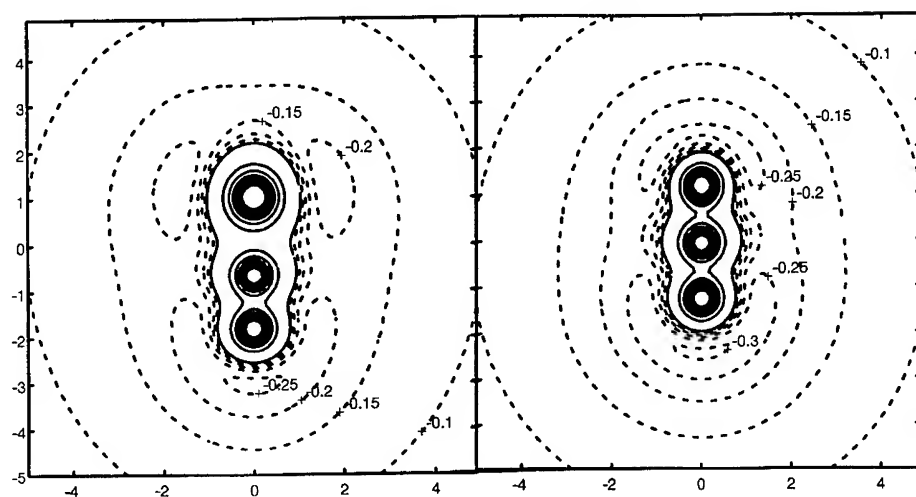


Figure 2. Contour maps of the MP2/6-311G(d,p) electrostatic potential of SCN^- (left) and OCN^- (right) in the molecular plane. Dashed lines denote negative and full lines positive values. The contour lines are labeled in atomic units.

one where all geometric degrees of freedom were relaxed (-142 kcal/mol). If instead of the electrostatic potential the actual interaction between Li^+ and SCN^- as a function of the position of Li^+ is calculated (upper left plot of Fig. 3), the minimum near the carbon atom can be found. Additionally, the contour plot shows that the "valley" with a depth of -130 to -140 kcal/mol reaches around most of the anion except the vicinity of the sulfur atom where there is no indication of a binding site. It should be mentioned that a Mulliken population analysis of SCN^- gives an equal distribution of the electronic excess charge between S and N (S: -0.51 , C: 0.05 , N: -0.54).

Geometrical Changes upon Complex Formation

Complexation at the S-site causes both the S—C and the C—N bond to be shortened by about 0.007 Å, a quite small geometrical change. Complexation at the N-site shortens the S—C bond by 0.064 Å whereas the C—N bond gets longer by 0.011 Å. The same trend is found for the $(\text{H}_2\text{O})_3\text{Li} \cdots \text{SCN}$ and $(\text{H}_2\text{O})_3\text{Li} \cdots \text{NCS}$ complexes with slightly smaller changes in the bond length. In the T-shaped complex the S—C bond gets shorter by 0.014 Å and the C—N bond becomes longer by 0.008 Å. Whereas for the two linear configurations MP2 and MP4 calculations give nearly identical results, a MP4 calculation of the T-shaped complex gives an elongation of 0.005 Å for the S—C distance and no change of the C—N bond, indicating that such small changes are beyond the limits of our method. We can conclude that for $\text{Li}^+ \cdots \text{SCN}^-$ and S—C(Li)—N the internal geometry of SCN^- hardly changes whereas for $\text{Li}^+ \cdots \text{NCS}^-$ it does change significantly. Table II summarizes the geometrical parameters of the complexes.

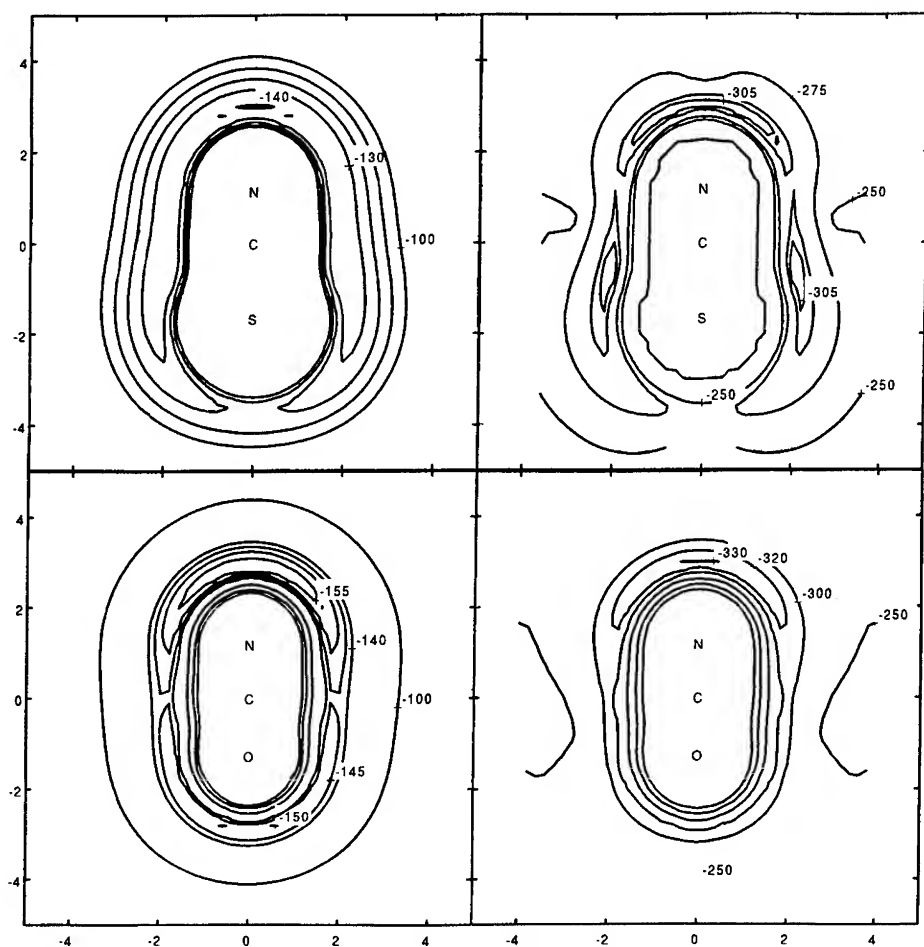


Figure 3. Isoenergy contour maps of the interaction energy between Li^+ (left plots) and Mg^{2+} (right plots) moving in a plane containing SCN^- (upper plots) and OCN^- (lower plots). MP2 energies calculated with the 6-311G(d,p) basis set. The values given are in kcal/mol.

Energies and Geometries in Li^+/OCN^-

The cyanate anion, OCN^- is normally found to behave similarly to SCN^- . We performed the same type of calculations as described above for SCN^- in order to find out which differences can be found in the binding of cations to OCN^- . The energies are summarized in Table I and the structures of $\text{Li}^+ \cdots \text{OCN}^-$ and $\text{Li}^+ \cdots \text{NCO}^-$ are shown in Figure 4.

Again the binding energies on Hartree-Fock and MP2 levels are very close. Binding to the N-site is preferred by 12 kcal/mol. For the complex with three water molecules this value decreases to 8 kcal/mol. In contrast to the thiocyanates, binding to the

TABLE II. Geometric parameters in the complexes. Values calculated with MP2/6-311G(d,p). Distances in Å and angles in degrees.

	$r(\text{S—C})$ or $r(\text{O—C})$	$r(\text{C—N})$	$r(\text{M—S})$ or $r(\text{M—N})$	$\angle(\text{S—C—N})$ or $\angle(\text{O—C—N})$
SCN ⁻	1.6690	1.1913		180
OCN ⁻¹	1.2322	1.2046		180
Li...SCN	1.6625	1.1841	2.0684	180
Li...NCS	1.6050	1.2025	1.7699	180
T-shaped S—C(Li)N	1.6866	1.1970	2.2907	163
Mg...SCN	1.6614	1.1828	2.1346	180
Mg...NCS	1.5575	1.2280	1.8439	177
T-shaped S—C(Mg)N	1.6868	1.2004	2.3959	156
Li...OCN	1.2600	1.1846	1.6476	180
Li...NCO	1.1925	1.2101	1.7403	180
Mg...OCN	1.2864	1.1778	1.7676	180
Mg...NCO	1.1670	1.2220	1.8203	180

O-site results here in a stable minimum as was found by inspecting the eigenvalues of the force constant matrix. A contour map of the interaction energy between Li⁺ and OCN⁻ as a function of the position of Li⁺ (lower left plot of Fig. 3) shows that for this ion pair no T-shaped complex exists as a stable minimum. However, from this figure it appears that a slightly nonlinear Li—O—C angle would be preferred. This is only true, however, for the map of the interaction energies where the equilibrium geometry of OCN⁻ is kept frozen as the cation samples the surface. If the internal OCN⁻ geometry is relaxed, too, the energy minima are found in linear conformations only.

The map of the electrostatic potential of OCN⁻ (right plot of Fig. 2) again shows a minimum near O at angle of about 45° from the C—O axis and the linear configuration is only a saddle point. This minimum, however, is less pronounced than the corresponding one for SCN⁻. The difference between the electrostatic potential and the actual binding energy can be explained by the fact that the energy gain by polarizing the anion is mostly possible in the direction of its molecular axis, therefore changing the kind of "lone pair" orientation predicted by the electrostatic potential.

The geometrical parameters of the cyanates are shown in Table II. Complexation to the oxygen causes an elongation of the O—C bond by 0.028 Å whereas the C—N bond is shortened by 0.020 Å. Complexation of the N-site changes the intramolecular distances in the opposite way: $r_{\text{O—C}}$ gets smaller by 0.040 Å and $r_{\text{C—N}}$ increases by 0.006 Å. The pattern of the bond length changes in Li...NCO is therefore the same as for the corresponding thiocyanate.

The main difference between lithium thiocyanate and lithium cyanate ion pairs is that the first one is able to form a nonlinear complex that equals in stability the linear Li⁺...NCS⁻ complex and that linear Li⁺...SCN⁻ is not a minimum on the potential hypersurface. In case of lithium cyanate the two linear complexes are

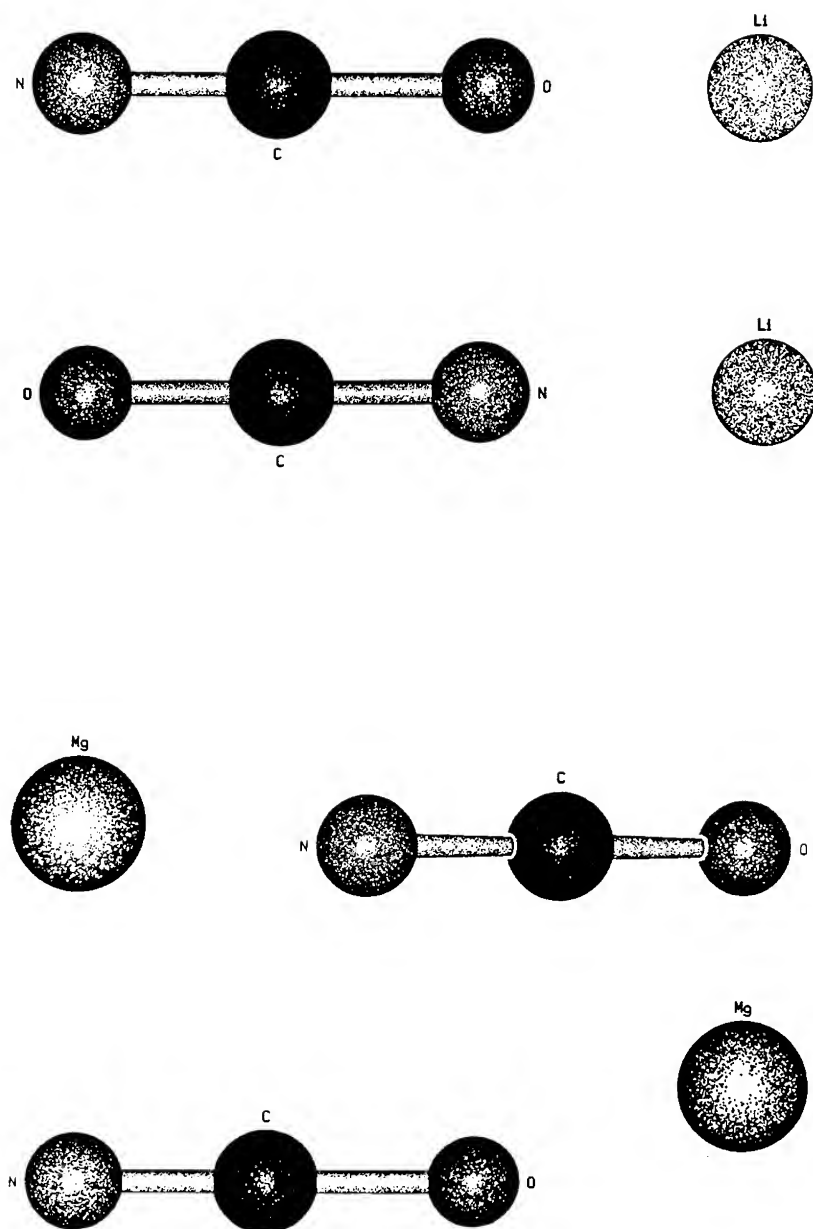


Figure 4. Equilibrium geometries of the ion pairs of OCN^- with Li^+ (upper 2 plots) and Mg^{2+} (lower 2 plots). The figures show the MP2/6-311G(d,p) optimized geometries.

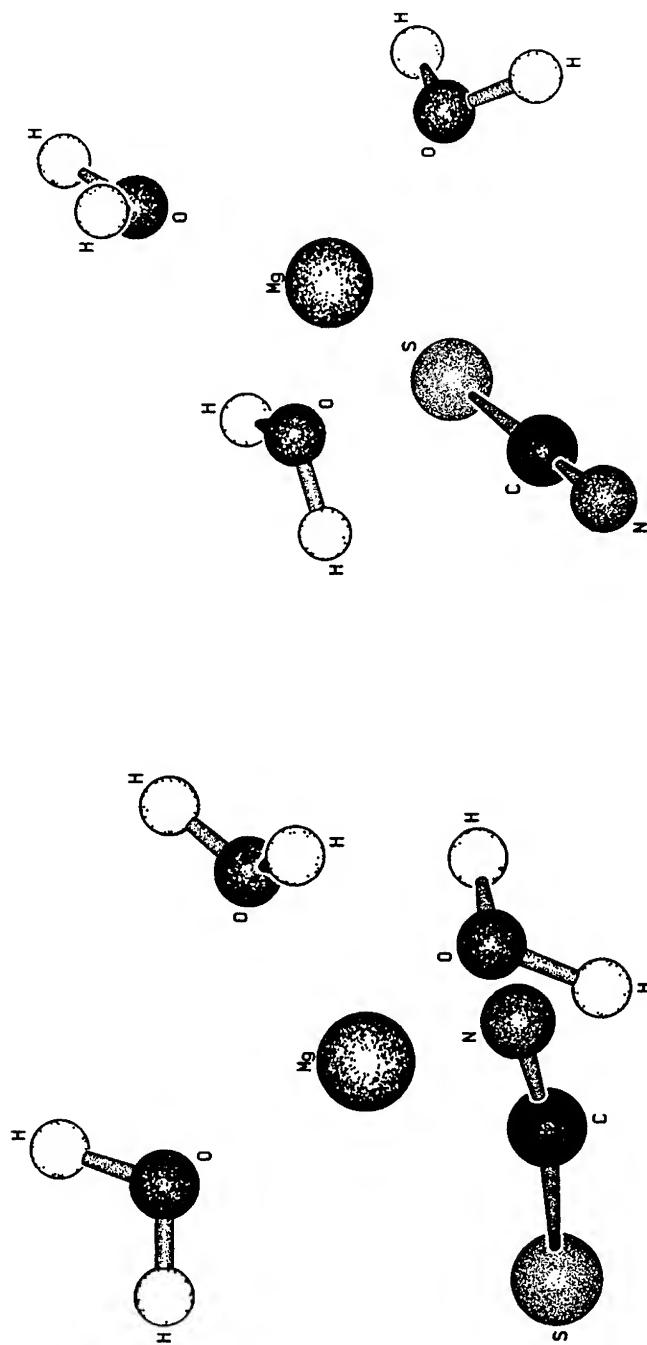


Figure 5. The $[(\text{H}_2\text{O})_3\text{MgSCN}]^+$ complex with the stable T-shaped (left) and the unstable linear coordination (right) of the metal cation. The figures show the HF/6-311G(d,p) optimized geometries.

the only stable minima of the potential surface. The binding of Li^+ cation to OCN^- is about 20 kcal/mol more stable than the binding to SCN^- .

The Complexation of SCN^- with Mg^{2+}

In order to study the interaction of a doubly charged cation with thiocyanate and cyanate anion, we performed calculations on the systems $[\text{Mg}/\text{SCN}]^+$ and $[\text{Mg}/\text{OCN}]^+$.

For $[\text{Mg}/\text{SCN}]^+$, a similar situation as for Li/SCN is found concerning complexation at the S-site and the formation of a T-shaped complex: An approach of the cation at the S-site does not result in a stable linear $\text{Mg}^{2+} \cdots \text{SCN}^-$ cationic complex. In contrast to Li/SCN , however, linear $\text{Mg}^{2+} \cdots \text{NCS}^-$ is only a saddle point too and the energy minimum with Mg^{2+} at the N-site occurs at a nonlinear conformation with a C—N—Mg angle of 154° . Also the optimal S—C—N angle deviates slightly from linearity (177°). The complexes are shown in Figure 1 (lower part). The potential surface is quite flat so that linear $\text{Mg}^{2+} \cdots \text{NCS}^-$ has practically the same energy as the true minimum structure.

Again, both N-site and T-shaped complexes have practically identical binding energies. This can be seen also from the map of the interaction energy (upper right plot of Fig. 5). The same pattern as for the lithium coordination with slightly larger changes of the bond length can be found. Both S—C and C—N bond length are increased by about 0.01 Å for the T-shaped complex whereas complexation on the N-site increases the C—N bond by 0.04 Å and makes the S—C bond shorter by 0.11 Å.

The Complexation of OCN^- with Mg^{2+}

For this ion pair, both O-site and N-site coordinated complexes are the only local minima of the energy hypersurface. $\text{Mg}^{2+} \cdots \text{NCO}^-$ is more stable by about 32 kcal/mol. This is a much bigger difference than for Li^+ . The potential energy surface is extremely shallow with respect to deviations from linearity. The energy minimum at the oxygen site is a bent complex (Fig. 4) with a C—O—Mg angle of 160° whereas linear $\text{Mg}^{2+} \cdots \text{NCO}^-$ is found to be stable by inspection of the force constant matrix.

For changes of the internal geometry of the cation, the same alternating pattern can be found as for the other linear complexes. Coordination of the cation leads to an elongation of the bond at the coordination site by 0.05 Å (O—C) and 0.03 Å (C—N) whereas the other bond in the anion becomes shorter by 0.01 Å and 0.07 Å, respectively.

Summary

It was found that the complexes which can be made up of the four possible combinations of the cations Li^+ and Mg^{2+} and the anions SCN^- and OCN^- show remarkable differences. For Li^+/OCN^- and $\text{Mg}^{2+}/\text{OCN}^-$, linear or slightly bent complexes are stable minima of the energy surface, with N-site coordination sig-

nificantly preferred by 10 (Li^+) and 33 (Mg^{2+}) kcal/mol. For Li^+/SCN^- the linear complex $\text{Li}^+ \cdots \text{NCS}^-$ and a T-shaped complex $\text{S}-\text{C}(\text{li})-\text{N}$ have very similar stability. Linear coordination to the S-site does not result in a minimum. The latter is also true for $[\text{Mg}/\text{SCN}]^+$. For this complex coordination at the N-site results in a nonlinear complex. Hydration of the complexes by three molecules of water decreases the energetic differences and intramolecular geometric changes by 20–50% but did not qualitatively change the above observations. These calculations might therefore be relevant to structural questions in solution chemistry where normally only linear complexes [1] and, for the “hard” cations Li^+ and Mg^{2+} , N-site coordination is considered. Additionally, the results show that pure electrostatic calculations would give wrong geometries of the complexes.

Acknowledgment

Support from the Austrian FWF, project P9010-MOB, is gratefully acknowledged as is computer time from the center for numerically intensive computations of Vienna University (NIC) and support from Innsbruck University computer center.

Bibliography

- [1] K. Ozutsumi, T. Takamuku, S. Ishiguro, and H. Ohtaki, *Bull. Chem. Soc. Jpn.* **65**, 2104 (1992).
- [2] W. Hage, A. Hallbrucker, and E. Mayer, *J. Phys. Chem.* **96**, 6488 (1992).
- [3] F. Parrini and R. Morales, *J. Mol. Struct. (Theochem)*, **101**, 59 (1993).
- [4] Z-L. Cai, *Chem. Phys.* **170**, 33 (1983).
- [5] R. Krishnan, S. Binkley, R. Seeger, and J. Pople, *J. Chem. Phys.* **72**, 650 (1980) and A. McLean and G. Chandler, *J. Chem. Phys.* **72**, 5639 (1980).
- [6] See, for example, K. Heinzinger, *Physica* **131B**, 196 (1985) or K. Heinzinger in *Water-Biomolecule Interactions*, M. Palma, V. Palma-Vittorelli, and F. Parak, Eds. (SIF, Bologna, 1993), p. 23.

Received April 4, 1994

SC-MEH-MO Calculations on Lanthanide Systems. I. $\text{Sm}(\text{Cp}^*)_2$, *bis*(Pentamethyl-Cyclopentadienyl) $\text{Sm}(\text{II})$

EDWARD A. BOUDREAUX and ERIC BAXTER

Department of Chemistry, University of New Orleans, New Orleans, Louisiana 70148

Abstract

SC-MEH-MO calculations with electron repulsion correlation and configuration interaction included, have been carried out on $\text{Sm}(\text{Cp}^*)_2$ in both its *linear* and *bent* geometrical forms. Except for relatively small factors, there are virtually no major differences in the electronic structures of the two conformers. In both cases, the bonding is found to be very close to being nearly totally ionic. An estimation of the ionic bond energy is made and discussed. © 1994 John Wiley & Sons, Inc.

Introduction

A number of *bis*(pentamethylcyclopentadienyl) compounds having the general formula $\text{M}(\text{Cp}^*)_2$, where Cp^* is the pentamethylcyclopentadienyl ligand, usually expressed in its nonradical, anion form, $(\text{Cp}^*)^-$. It is generally accepted that these systems fall into two structural classifications; those that have *linear* (parallel) and *bent* Cp^* dispositions relative to the $\text{Cp}^*-\text{M}-\text{Cp}^*$ centroid angles. If $\text{M} = \text{Ge}(\text{II})$, $\text{Sn}(\text{II})$, or $\text{Ph}(\text{II})$, the *bent* conformation is observed in both the solid and gas phases [1]. This is believed to be a consequence of the nonbonding electron pair on the metal interacting with the electron π -system of the Cp^* rings. However, when $\text{M} = \text{Ca}$, Sr , or Ba , the structures are also bent; but if $\text{M} = \text{Mg}$, it is linear in both solid and gas phases [2]. Since there are no nonbonding electron pairs on these metals to interact with the Cp^* rings, bent structures would not be anticipated in these latter cases. Conversely, if M is a transition metal having d valence electrons, the structures appear to be invariably linear; but large-scale *ab initio* LCAO-SCF calculations have not been able to reproduce accurate $\text{M}-\text{Cp}^*$ equilibrium bond distances, no matter how extensive the basis sets used [3]. This failure is apparently due to the lack of d -electron correlation in these calculations. It is equally interesting that for $\text{M} = \text{Yb}(\text{II})$, the structure is also bent in both solid and gas phases [4]. If $\text{M} = \text{Sm}(\text{II})$ or $\text{Eu}(\text{II})$, the structures are bent in the solid phases [5]. Although the gas phase structures have not been reported, other studies imply that these would be bent also [6].

The only electronic structure calculations reported on $\text{Ln}(\text{Cp}^*)_2$ complex thus far are the Extended Huckel (EH-MO) calculations on $\text{Sm}(\text{Cp}^*)_2$ and $\text{Lu}(\text{Cp}^*)_2$ [7], and the SW- $X\alpha$ computation on $\text{Yb}(\text{Cp}^*)_2$ [8].

The recent work of Hollis, Burdett, and Bosnich suggests that interligand van der Waals contact interactions are largely responsible for the *bent* vs. *linear* geometrical conformations of $M(\text{Cp}^*)_2$ systems [6]. Thus it is presumed that electronic factors play little or no role in determining the equilibrium geometrical disposition of these complexes.

The objective of this study is to examine electronic structures and bonding in the lanthanide $M(\text{Cp}^*)_2$ complexes. The results obtained thus far, specifically for $\text{Sm}(\text{Cp}^*)_2$, is the subject of this report.

Method of Calculation

The approximate quasirelativistic SC-MEH-MO method which has been previously applied with considerable success in a number of other instances, has been utilized in this study as well [9]. The pertinent STO wave functions and orbital energy parameters were computed from a quasirelativistic HF-SCF atomic program [10]. The Sm AO configurations included a frozen core plus $4f^a 5d^b 6s^c 6p^d$ valence states for various q charges of Sm^q , $0 \leq q \leq 4$, $3 \leq a \leq 6$, $0 \leq b \leq 1$, $0 \leq c \leq 2$, $0 \leq d \leq 1$. The Cp^* was calculated as a full $\text{C}_{10}\text{H}_{15}$ molecule in the $-1, 0, +1$ charged states. These results were fitted into the charge-dependent, orbital energy equations required for the calculations.

One of the major difficulties with computations on lanthanides by this technique is that the charge and configuration dependent hamiltonian elements for the 4f and 5d levels generate MOs that are energetically more stable than any other levels. Consequently, the Sm configurations become $4f^{14}$ and $5d^9$ rather than $4f^6 5d^0$ or $4f^5 5d^1$ appropriate for Sm^{2+} in the $\text{Sm}(\text{Cp}^*)_2$. The only way to compensate for this problem is to run the calculation initially with only the Sm valence $6s^2$ level, omitting the 4f, 5d, and 6p orbitals. In this way, reasonable atom charges and populations for the Sm and Cp^* components are obtained. This is followed by a second calculation with atom charges fixed from the initial results, but including the 4f, 5d, and 6p orbitals. The resulting $4f^{14}$ and $5d^9$ configurations are corrected for electron repulsion correlation. This is evaluated as the difference in electron repulsion energies for $4f^{14}$ vs. $4f^6$ and $4f^5 5d^1$ (averaged) and the $5d^9$ vs. $4f^5 5d^1$ configurations. The necessary Slater-Condon parameters obtained from the quasirelativistic HF-SCF atomic program cited above, were used to generate the atomic inputs for this phase of the computation. The repulsive energy corrections are large, amounting to 36.426 and 20.188 eV for the 4f and 5d levels, respectively, at a Sm charge of 1.47 (*bent* Sm— Cp^* bonds).

The final third calculation is done with the electron repulsion correlation for the 4f and 5d levels included. Following this, a one-electron configuration interaction procedure with spin-orbit coupling, is carried out on all MO's. This procedure is hereafter designated SCMEH-RCCI, (self-consistent modified extended Huckel with repulsion correlation and configuration interaction). Or, as in this case, when quasirelativistic AO functions are employed (for Sm anyway), the method is labeled QR-SCMEH-RCCI.

Results and Discussion

The pertinent final data for both the *bent* (C_{2v}) and *linear* (D_{5h}) geometries of $\text{Sm}(\text{Cp}^*)_2$ are presented in Tables I and II. Filled HOMO's for both cases are almost totally Cp^* character, except for the small degree of 5d character, which are only 1.8% and 0.4% for linear and bent forms, respectively. Of course, there is a $4f^6$ sextet manifold (a spin heptet state) of singularly occupied levels lying about 4.4 eV above the filled HOMO, in each case. The LUMO is almost 100% 4f character, but the next to lowest unoccupied MO is about 97% Cp^* character, and lies only 0.22 eV above the LUMO.

Based on the very small degree of direct covalent bonding, it can be deduced that the $\text{Sm}-\text{Cp}^*$ bonding in $\text{Sm}(\text{Cp}^*)_2$ is some 93% vs. 85% ionic, in bent and linear forms, respectively. However, owing to the appreciable charge difference between Sm and Cp^* and the facile polarization of the ligand, secondary polarization interaction may play a significant role in reducing this degree of ionicity.

Not taking into account this latter factor, the energy to break the ionic $\text{Sm}-\text{Cp}^*$ bond will be that required to overcome the total attractive and repulsive interactions involving the $\text{Sm}-\text{Cp}^*$ bond. Using the charges provided in Table II together with the $\text{Sm}-\text{C}(\text{ring})$ distance of 2.79 Å and the closest Cp^*-Cp^* contact

TABLE I. MO parameters for $\text{Sm}(\text{Cp}^*)_2$.

	MO (no.)	E (eV)	Occ	Percent AO Character				Cp^* (total 2's,2p)
				4f	5d	6s	6p	
Bent	33	-4.141	0	1.7	0.8	—	—	97.5
	34	-4.356	0	99.7	—	—	—	0.3
	35	-4.443	1	99.9	—	—	—	0.1
	36	-4.444	1	99.9	—	—	—	0.1
	37	-4.446	1	99.2	—	—	—	0.8
	38	-4.446	1	99.5	—	—	—	0.5
	39	-4.448	1	98.2	—	—	—	0.8
	40	-4.449	1	98.5	—	—	—	0.5
	41	-8.021	2	—	0.4	—	—	99.6
	42	-8.129	2	—	0.5	—	—	99.5
Linear	33	-4.075	0	0.1	3.1	—	—	96.6
	34	-4.287	0	99.2	0.4	—	—	0.4
	35	-4.372	1	100.0	—	—	—	—
	36	-4.373	1	100.0	—	—	—	—
	37	-4.375	1	99.9	—	—	—	0.1
	38	-4.375	1	95.2	4.6	—	—	0.2
	39	-4.377	1	99.3	0.5	—	—	0.2
	40	-4.378	1	99.9	—	—	—	0.1
	41	-8.023	2	—	1.8	—	—	98.2
	42	-8.119	2	—	1.4	—	—	98.6

TABLE II. MO characteristics of $\text{Sm}(\text{Cp}^*)_2$.

Orbital parameters	Bent		Parallel (QR-SCMEH-RCCI)
	(EH MO) ^a	(QR-SCMEH-RCCI)	
% AO character per doubly occupied MO			
4f	—	—	0.4
5d	—	0.2	0.6
6s	—	4.3	11.3
6p	—	2.8	2.7
Total Löwdin population			
4f	—	5.957	5.952
5d	8.20	0.074	0.210
6s	0.49	0.512	0.677
6p	0.41	1.008	1.074
Charges			
Sm	-7.10 ^b	1.47	1.50
Cp*	3.55 ^b	-0.735	-0.750

^a From Ref. [7].^b Derived from data given in Ref. [7].

distance of 3.5 Å [6], the total electrostatic energy for the $\text{Sm}-\text{Cp}^*$ bond is computed to be 80.7 kcal/mol. An experimental value for $\text{Sm}(\text{Cp}^*)_2$ has not been reported, but the values listed for the lanthanide tricyclopentadienides $\text{Ln}(\text{Cp})_3$, range from 78.0 to 82.0 kcal/mol [11]. Since these latter compounds have been characterized to be ionic, the results obtained from the present calculations are clearly reasonable.

It is interesting to compare these results with that reported for $\text{Sm}(\text{Cp}^*)_2$ via the EH-MO method [7]. The AO orbital character, populations, and charges are given in Table II. It can be readily deduced from the data given in Ref. [7] that the total populations for Sm 5d, 6s, and 6p orbitals are 8.20, 0.49, and 0.41, respectively. This results in a net Sm charge of -7.10, which is, of course, totally unrealistic. Hence, these data are of little or no value for determining the bonding in $\text{Sm}(\text{Cp}^*)_2$.

Finally, it may be concluded that electronic bonding factors do not play any meaningful role in determining the preferred equilibrium geometrical conformation of $\text{Sm}(\text{Cp}^*)_2$. Thus the findings of Hollis, Burdett, and Bosnich, which suggest that van der Waals forces play the dominant role in establishing the molecular geometry of this system, appear to be vindicated.

Acknowledgments

We are indebted to the University of New Orleans Chemistry Department and the Computer Research Center, for providing the facilities and resources to do this work.

Bibliography

- [1] P. Jutzi, F. Kohl, P. Hofmann, C. Kruger, and Yi-H. Tsay, *Chem. Ber.* **113**, 757 (1980); J. L. Atwood and W. E. Hunter, *J. Chem. Soc. Chem. Commun.*, 925 (1981); L. Fernholt, A. Haaland, P. Jutzi, F. Kohl, and R. Seip, *Acta Chem. Scand.* **A38**, 211 (1984).
- [2] R. Blum, K. Faegri, Jr., and H. V. Volden, *Organometallics* **9**, 372 (1990); R. A. Williams, T. P. Hanusa, and J. C. Huffman, *Organometallics* **9**, 1128 (1990).
- [3] H. P. Luthi, J. H. Ammeter, J. Almlof, and K. Faegri, Jr., *J. Chem. Phys.* **77**, 2002 (1982).
- [4] R. A. Andersen, J. M. Boncella, C. J. Burns, R. Blom, A. Haaland, and H. V. Volden, *J. Organometall. Chem.* **C49**, 312 (1986); R. A. Andersen, R. Bloom, J. M. Boncella, C. J. Burns, and H. V. Volden, *Acta Chem. Scand.* **A41**, 24 (1987); R. A. Andersen, R. Bloom, C. J. Burns, and H. V. Volden, *J. Chem. Soc. Chem. Commun.*, 768 (1987).
- [5] W. J. Evans, L. A. Hughes, and T. P. Hanusa, *Organometallics* **5**, 1285 (1986).
- [6] T. K. Hollis, J. K. Burdett, and B. Bosnick, *Organometallics* **12**, 3385 (1993).
- [7] J. V. Ortiz and R. Hoffmann, *Inorg. Chem.* **24**, 2095 (1985).
- [8] J. C. Breen, D. Hohl, and N. Rosch, *Organometallics* **6**, 712 (1987).
- [9] E. A. Boudreaux, in *Vibrational Spectra and Structure*, J. R. Durig, Ed. (Elsevier, Amsterdam, 1993), Vol. 20, pp. 189-238.
- [10] E. A. Boudreaux, S. P. Doussa, and M. Klobukowski, *Int. J. Quant. Chem.* **20**, 239 (1986).
- [11] F. R. Hartley and S. Patin, *The Chemistry of the Metal-Carbon Bond* (Wiley, London, 1982), Chap. 2.

Received February 17, 1994

Structural and Electronic Studies of Ga_3As_3 , Ga_4As_3 , and Ga_3As_4

P. PIQUINI, S. CANUTO, and A. FAZZIO

Instituto de Física, Universidade de São Paulo, CxP 20516, 01452-990 São Paulo, SP, Brazil

Abstract

Ab-initio self-consistent-field calculations are performed on Ga_3As_3 , Ga_3As_4 , and Ga_4As_3 clusters. Geometries, electron affinities, ionization potentials, and bondings are analyzed for these clusters. Geometry optimizations using analytic energy gradients followed by single point MP2 calculations are performed to decide for the equilibrium structure. The alternation pattern observed for the ionization potential and electron affinity are verified for these clusters after correlation energy is included. Our results are compared with previous theoretical and experimental calculations. © 1994 John Wiley & Sons, Inc.

Introduction

The understanding of the experimentally observed results regarding geometry and relative stability of covalent clusters is of great interest and challenge. These clusters can be produced by Laser Vaporization and Supersonic Clustering technics [1]. An important point in these studies is the understanding of the relationship between the physical properties of a cluster and its size and composition. Theoretical efforts have concentrated on calculations of the geometric properties of these new species generated by laser vaporization [2–15].

Recently, interesting experimental results on geometric and electronic properties of GaAs clusters have been obtained by different groups [16–20]. In particular, the Rice group [1,16] has observed an alternation pattern in the ionization potential (IP) and electron affinity (EA) for Ga_mAs_n clusters up to $m + n \simeq 20$ atoms. The experimental analysis [1] indicate that for clusters with $m + n$ even the IP is greater than 6.4 eV whereas for $m + n$ odd the IP is lower than this value that corresponds to the energy of the ArF excimer laser. There are still many questions regarding the relative stability and properties of these GaAs clusters.

In this article we report the results of our theoretical studies on the geometries, IP, EA, and bonding of Ga_3As_3 , Ga_3As_4 , and Ga_4As_3 clusters. The Ga_3As_3 cluster has been studied previously by other theoretical groups [8–10]. Lou et al. [9] have determined the geometry and vertical IP and EA within the Local-Density Approximation (LDA). Al-Laham and Raghavachari [11] have determined the geometry and orbital atomic population using an effective-core-potential [21] calculation. Graves and Scuseria [10] have calculated the energetics and geometry of this six-atom cluster within a SCF all-electron calculation. The seven-atom clusters, however,

have been nearly ignored but Lou et al. [9] have estimated the geometries, IP and EA, within the LDA.

Our calculation on these three species is an extension of our previous article [13] where we have studied GaAs clusters up to 5 atoms with an *ab-initio* Hartree-Fock SCF all-electron calculation with a MIDI basis set [22]. The complexity of an all-electron calculation becomes more and more pronounced as we increase the number of Ga and As atoms in the cluster. Thus in this study we have utilized a double-zeta valence basis set which gives a good compromise between accuracy and computational cost.

Methods and Results

The calculations are performed at the Hartree-Fock *ab-initio* self-consistent-field level followed by single point second-order perturbation theory (MP2) [23]. We have utilized the effective-core-potential gaussian basis set proposed by Wadt and Hay [21] which is a double-zeta plus diffuse basis set representation of the outer electrons of each Ga and As atoms. All calculations were made using the GAMESS program [24].

The possible geometrical arrangements increase as the number of atoms in a mixed cluster increase [5]. Hence, we have implemented an experimental- and theoretical-based strategy to guide our search of the minimum energy configuration. In the case of the Ga_3As_3 system, we chose the initial configurations for the geometry optimization as those obtained by edge-capping and face-capping the previous theoretically proposed structures of Ga_3As_2 and Ga_2As_3 clusters [13,9], as shown in Figure 1. This theoretically proposed structure for the Ga_2As_3 is in agreement with a recent ESR study [20] that indicates the two Ga and the three As atoms to be symmetrically equivalent. For the Ga_3As_4 and Ga_4As_3 cases, the initial config-

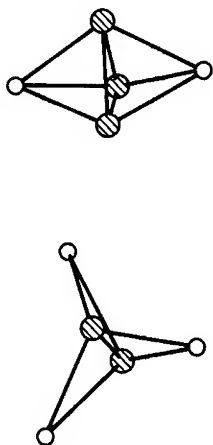


Figure 1. The calculated SCF structures for Ga_2As_3 and Ga_3As_2 . Full circles correspond to As and open circles to Ga atoms.

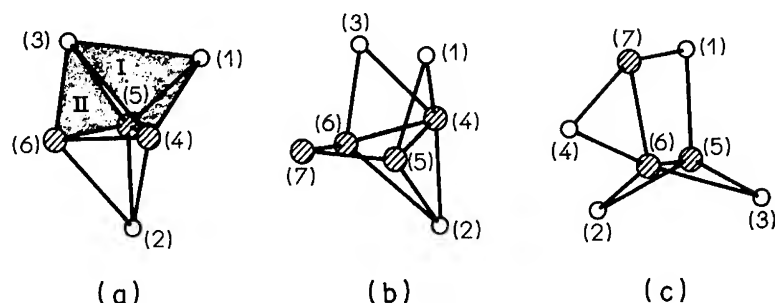


Figure 2. The calculated SCF + single-point MP2 structures for Ga_3As_3 (C_s symmetry), Ga_3As_4 (C_s symmetry) and Ga_4As_3 (near C_s symmetry). The numbers identify the atoms in the Table I.

urations are that obtained by edge and face-capping the determined Ga_3As_3 minimum energy structure. The strategy utilized for the initial configuration is based on the experimental fact that the GaAs clusters are photofragmented atom by atom, without fission of the cluster [1]. We also note that in the case of Ga_nAs_m clusters with $n + m \leq 5$, all proposed structures can be obtained in this way [7-9,13]. Besides these configurations we have also taken as initial configuration those structures proposed in other theoretical studies [9,11].

We optimized these structures without any symmetry constraints. Once satisfied the gradient criterion (0.0003 Hartree/Bohr) we calculated the vibrational frequencies to verify if the optimized structure was a local minimum. Once the SCF local minima were obtained we have performed a single point MP2 calculation.

The more stable structures obtained here are shown in Figure 2. In the case of Ga_3As_3 we have obtained a face-capped trigonal bipyramidal structure [Fig. 2(a)] which is in perfect agreement with previous theoretical calculations [9,11].

The calculated Ga_3As_4 equilibrium structure was obtained when we relaxed a face-capped structure where the As approximates the face labeled I in Figure 2(a). The configuration obtained after relaxing a pentagonal bipyramidal structure, proposed by Lou et al. [9], have led us to the structure shown in Figure 3(b). [Fig.

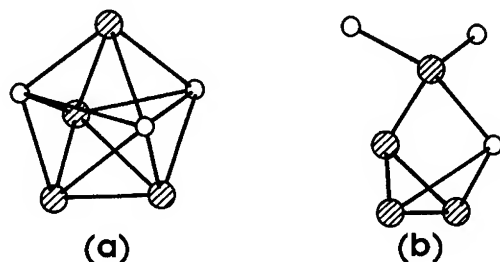


Figure 3. The figure in the left is the initial pentagonal bipyramidal configuration of Ga_3As_4 used for a structure optimization run. The figure in right is the final structure obtained at a SCF level starting from the pentagonal bipyramid.

3(a) shows the initial configuration] which is 3.2 kcal/mol above in energy than the configuration shown in Figure 2(b).

The calculated Ga_4As_3 structure, shown in Figure 2(c), was obtained by approximating one Ga atom to the face labeled II in Figure 2(a). This calculated structure is 6.0 kcal/mol below in energy than that obtained when we start the optimization procedure with the pentagonal bipyramidal structure proposed by Lou et al. [9]. The final calculated geometrical parameters for the three systems studied are shown in Table I.

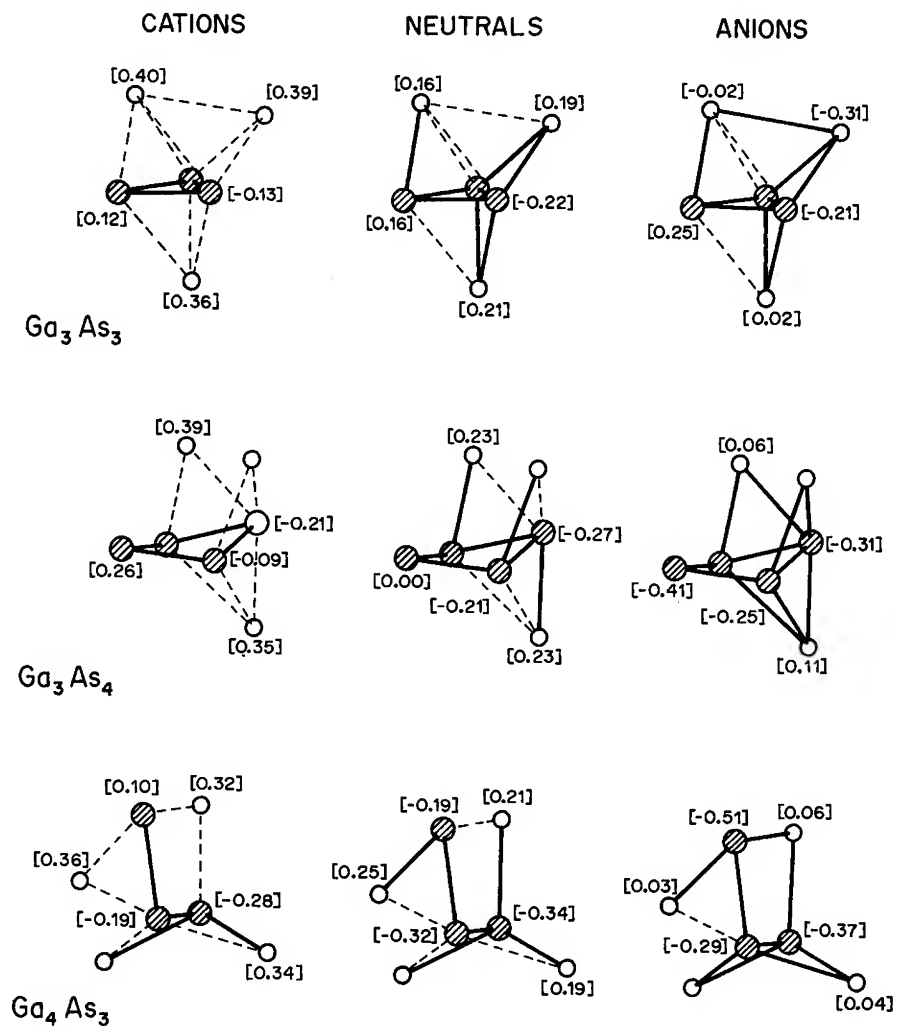


Figure 4. The calculated net charges (in brackets) of the neutral species and the vertical cation and anion. The solid lines represent bond-order values greater than 0.1.

TABLE I. Calculated geometric parameters.

Distances (Å)					
Ga ₃ As ₃		Ga ₃ As ₄		Ga ₄ As ₃	
(1)-(3)	3.59	(1)-(3)	4.66	(1)-(5)	2.78
(1)-(4)	2.91	(1)-(4)	3.18	(1)-(6)	3.91
(1)-(6)	4.45	(1)-(5)	2.71	(1)-(7)	3.17
(2)-(3)	5.34	(1)-(7)	4.20	(2)-(3)	4.59
(2)-(6)	3.22	(2)-(4)	2.75	(2)-(4)	5.09
(3)-(5)	3.35	(2)-(5)	3.28	(2)-(5)	2.69
(3)-(6)	2.64	(2)-(7)	4.30	(4)-(6)	2.95
(4)-(5)	2.69	(4)-(5)	2.66	(4)-(7)	2.75
(4)-(6)	2.60	(4)-(7)	3.72	(5)-(6)	3.56
		(5)-(6)	3.56	(5)-(7)	3.96
		(5)-(7)	2.56	(6)-(7)	2.57

Numbers in the parentheses refer to those in Figure 2.

An interesting result obtained here is the change in bond-order when the neutral cluster accepts or donates an electron. In Figure 4 we show the positively and negatively charged clusters obtained after a SCF calculation of their total energies, bond-order, and charges using the geometry of the neutral species. The solid lines represent bond-order values greater than 0.1. The numbers in brackets are our calculated values for the net charges. We verify that the introduction of one electron in the positively charge and neutral systems increases the Ga—As bond and decreases the As—As bond. We also note that at the SCF level of calculation the Ga atoms have a tendency to bind to a maximum of two As atoms. The introduction (removal) of one electron in the neutral cluster increases (decreases) the *p* contribution and decreases (increases) the *s* contribution in the atomic orbital population on each atom. By these findings we infer that the hybridization of the *s* and *p* orbitals makes an important role in the effective realization of the Ga—As binding.

Another interesting aspect related to these clusters is the experimental suggestion of an alternating pattern regarding the IP and EA with the number of atoms in the cluster [1,16]. Thus, using the optimized geometries obtained at the SCF level we have calculated the IP and EA of the three clusters considered here.

The Table II shows our results for the vertical IP and EA obtained both at the SCF and MP2 levels but using the SCF geometries. Typically the IP of the GaAs clusters lie between 5eV and 7eV with the bulk value of crystalline GaAs being 5.49eV [25]. As to the EA, the cluster values lie between 0.4eV and 1.40eV, with the bulk value of the crystal being 4.07eV [26]. Our results are in fair agreement with these numbers. We also note that partial inclusion of the electron correlation effects, in second-order MP2, decreases the IP of the three clusters. The results obtained for the seven-atom clusters are below 6.4eV after inclusion of this correlation correction. For the EA, the correlation correction introduced by MP2 increases for

TABLE II. Comparison of SCF and second-order Møller–Plesset results for the vertical IP(eV) and EA(eV) of Ga_3As_3 , Ga_4As_3 , and Ga_3As_4 .

	Ga_3As_3	Ga_3As_4	Ga_4As_3
IP(SCF)	6.87	6.46	6.37
IP(MP2)	6.60	5.50	5.77
EA(SCF)	0.40	0.68	0.84
EA(MP2)	0.36	0.82	1.38

the seven-atom clusters and decreases for the six-atom. These numbers are in good agreement with the experimental results but at this level of calculation we do not find the As-rich (Ga_3As_4) EA higher than the Ga-rich (Ga_4As_3), as suggested before. Our calculated values for the EA should be less accurate than those for the IP because of the diffuse character of the anions. In any case, the partial introduction of the electron correlation energy is very important for the quantitative verification of the experimentally observed even/odd alternation pattern in the IP and EA [1,16], the even (odd) clusters having IP greater (lower) than 6.4eV.

Conclusions

We have made *ab-initio* SCF plus single-point MP2 calculations, employing effective-core-potential, to study the electronic and structural properties of Ga_3As_3 , Ga_4As_3 , and Ga_3As_4 clusters. Our calculated structure for the Ga_3As_3 cluster is in perfect agreement with previous theoretical studies using local-density [9] and SCF followed by high-order Møller–Plesset calculations in the effective-core-potential model [11]. For the seven-atom clusters theoretical investigations are more scanty and only a local-density calculation [9] has been performed before. For these systems we have obtained equilibrium configurations that are 6.0 kcal/mol (Ga_4As_3) and 3.2 kcal/mol (Ga_3As_4) below the pentagonal bipyramid structures with C_{2v} symmetry proposed previously. These small energy differences may suggest the existence of several local minima. We also suggest that the alternation pattern observed experimentally for the IP and EA [1,16] demands the inclusion of electron correlation effects for a proper theoretical description.

Acknowledgments

This work was supported by the Brazilian Agencies CNPq and Fapesp.

Bibliography

- [1] S. C. O'Brien, Y. Liu, Q. Zhang, J. R. Heath, F. K. Tittel, R. F. Curl, and R. E. Smalley, *J. Chem. Phys.* **84**, 4074 (1986).
- [2] K. Balasubramanian, *J. Mol. Spectrosc.* **139**, 405 (1990).
- [3] Kalyan K. Das and K. Balasubramanian, *J. Chem. Phys.* **94**, 6620 (1991); D. W. Liao and K. Balasubramanian, *J. Chem. Phys.* **96**, 8938 (1992).

- [4] K. Balasubramanian, Chem. Phys. Lett. **171**, 58 (1990); K. Balasubramanian, Chem. Rev. **90**, 93 (1990).
- [5] K. Balasubramanian, Chem. Phys. Lett. **150**, 71 (1988).
- [6] U. Meier, S. D. Peyerimhoff, P. J. Bruna, and F. Grein, J. Mol. Spectrosc. **134**, 259 (1989).
- [7] U. Meier, S. D. Peyerimhoff, and F. Grein, Chem. Phys. **150**, 331 (1991).
- [8] L. Lou, L. Wang, L. P. Chibante, R. T. Laaksonen, P. Nordlander, and R. E. Smalley, J. Chem. Phys. **94**, 8015 (1991).
- [9] L. Lou, P. Nordlander, and R. E. Smalley, J. Chem. Phys. **97**, 1958 (1992).
- [10] R. M. Graves and G. E. Scuseria, J. Chem. Phys. **95**, 6602 (1991).
- [11] M. A. Al-Laham and K. Raghavachari, Chem. Phys. Lett. **187**, 13 (1991).
- [12] M. A. Al-Laham and K. Raghavachari, J. Chem. Phys. **98**, 8770 (1993).
- [13] P. Piquini, A. Fazzio, and S. Canuto, submitted for publication.
- [14] W. Andreoni, Z. Phys. **D19**, 31 (1991).
- [15] P. Balone, W. Andreoni, R. Car, and M. Parrinello, Phys. Rev. Lett. **60**, 271 (1988); W. Andreoni and G. Pastore, Phys. Rev. **B41**, 1024 (1990).
- [16] Y. Liu, Q. Zhang, F. K. Tittel, R. F. Curl, and R. E. Smalley, J. Chem. Phys. **85**, 7434 (1986).
- [17] G. W. Lemire, G. A. Bishea, S. A. Heidecke, and M. D. Morse, J. Chem. Phys. **92**, 1 (1990).
- [18] L. B. Knight, Jr. and J. T. Petty, J. Chem. Phys. **88**, 481 (1988).
- [19] W. D. Reents Jr., J. Chem. Phys. **90**, 4258 (1989).
- [20] R. J. Van Zee, S. Li, and W. Weltner Jr., J. Chem. Phys. **98**, 4335 (1993).
- [21] W. R. Wadt and P. J. Hay, J. Chem. Phys. **82**, 284 (1985).
- [22] S. Huzinaga, Comp. Phys. Rep. **2**, 279 (1985).
- [23] C. Møller and M. S. Plesset, Phys. Rev. **46**, 618 (1934); R. J. Bartlett, J. Phys. Chem. **93**, 1697 (1989).
- [24] M. Dupuis, D. Spangler, and J. J. Wendolowski: NRCC Software Catalog vol. 1, Prog. GG01 (GAMESS) 1980.
- [25] R. K. Swank, Phys. Rev. **153**, 844 (1967).
- [26] A. G. Milnes and D. L. Feucht *Heterojunctions and Metal-Semiconductor Junctions* (Academic, New York, 1972).

Received May 25, 1994

Diborane, Dialane, and Digallane: Accurate Geometries and Vibrational Frequencies

DAVID H. MAGERS and R. BRYAN HOOD

Department of Chemistry, Mississippi College, Clinton, Mississippi 39058

JERZY LESZCZYŃSKI

Department of Chemistry, Jackson State University, Jackson, Mississippi 39217

Abstract

Optimum equilibrium geometries, harmonic vibrational frequencies, and infrared intensities within the double harmonic approximation are computed for diborane, B_2H_6 , dialane, Al_2H_6 , and digallane, Ga_2H_6 , at both the SCF level of theory and the second-order perturbation theory [E(2)] using three large basis sets: 6-311G(d,p), 6-311G(2d,2p), and 6-311G(2df,2p). In particular, the results obtained with the latter basis set make this present work the first study to include *f*-type polarization functions in a systematic investigation of the molecular structure and properties of all three molecules in the series. Because of the good agreement of the present theoretical results with experimental data and with previous theoretical studies which employed a higher treatment of electron correlation, this study serves to show that large basis sets can in part compensate for the lack of a more advanced treatment of electron correlation in these electron-deficient systems. In addition, this study establishes the level of basis set needed for future work on these systems including a thorough description of the total electronic density at a correlated level. © 1994 John Wiley & Sons, Inc.

Introduction

Diborane is the prototypical molecule for μ -hydrido bridging in electron-deficient compounds. As a result, many experimental [1–10] and theoretical [11–21] studies have been made on this system and its corresponding monomer. In contrast, much less work has been published on dialane and digallane. Experimental results are especially rare for these systems: dialane has still not been isolated and digallane only just synthesized in 1989 by Downs, Goode, and Pulham [22]. However, quite a few theoretical studies have been published recently [23–28]. Among them was a thorough investigation by Shen and Schaefer in which optimum equilibrium geometries, harmonic vibrational frequencies, and infrared intensities were computed for all three systems through the level of configuration interaction limited to single and double excitations (CISD) using a standard double-zeta plus polarization (DZP) basis set [28]. Their study also included optimum geometries, vibrational frequencies, and infrared intensities for diborane and dialane and optimum geometries for digallane at the level of the single and double excitation coupled-cluster method with the same DZP basis set.

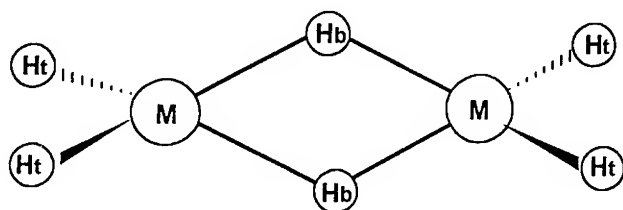
The fact that dialane has not been synthesized yet is somewhat of an enigma. *Ab initio* predictions of its binding energy (ca. 31 kcal/mol) [24,28] indicate its larger stability as compared to digallane (binding energy ca. 22 kcal/mol) [24,28]. Possibly, factors other than simple thermodynamical ones are responsible for such unique properties of this aluminum hydride. Therefore, we have undertaken a systematic study including all three corresponding systems in order to lighten the shadow of this unusual chemistry.

In the present work we report the optimized geometries, harmonic vibrational frequencies, and infrared absorption intensities within the double harmonic approximation for M_2H_6 ($M = B, Al, Ga$) using three relatively large basis sets at both the SCF level of theory and the second-order perturbation theory [MBPT(2) = MP2 = E(2)]. The main reason for introducing more geometries and vibrational frequencies into the literature is to compare our results with previous theoretical values to see what effects extra polarization functions have. In particular, this is the first study to include *f*-type polarization functions in a systematic investigation of all three molecules in the series. Thus, we hope to determine the level of basis set needed for future work on these systems such as a thorough description of the total electronic density at a correlated level. Such a determination may yield new insight into the nature of bridge bonds in these systems and related, more complex species.

Computational Details

In the present study, optimized equilibrium geometries, vibrational frequencies, and infrared intensities are determined for each of the three molecular species at both the SCF level and the second-order perturbation theory level [E(2)] using the GAUSSIAN92 program package [29]. Rotational constants are also determined at each optimum geometry. Each molecule has D_{2h} symmetry (see Fig. 1), and the ground electronic state for each system is 1A_g . Therefore, the SCF calculations all employ a single-configuration RHF wave function.

Three basis sets of valence triple-zeta quality are used for each system. For B_2H_6 and Al_2H_6 , the three basis sets are 6-311G(d,p), 6-311G(2d,2p), and 6-311G(2df,2p). The 6-311G basis is a standard basis set in GAUSSIAN92 and



$M = B, Al, Ga$

Figure 1. General structure for diborane, dialane, and digallane.

indicates a split-valence basis set comprising a single-zeta core description and a triple-zeta description for the valence orbitals [30]. The (d,p), (2d,2p), and (2df,2p) indicate the types and number of polarization functions included on the heavy atoms and on the hydrogens, respectively. Each *d* function represents five energy-equivalent complex *d*-functions, and the *f* function represents seven energy-equivalent complex *f*-functions. Thus, for diborane the 6-311G(d,p) basis set consists of 72 basis functions contracted from 110 primitive gaussian functions; the 6-311G(2d,2p) basis set consists of 100 basis functions contracted from 138 primitive gaussian; and the 6-311G(2df,2p) basis set consists of 114 basis functions contracted from 152 primitive gaussians. For dialane the 6-311G(d,p) basis set consists of 88 basis functions contracted from 138 primitive gaussian functions; the 6-311G(2d,2p) basis set consists of 116 basis functions contracted from 166 primitive gaussians; and the 6-311G(2df,2p) basis set consists of 130 basis functions contracted from 180 primitive gaussians.

Basis sets for gallium similar to those that we used for diborane and dialane are not included as standard basis sets in GAUSSIAN92, so we input similar basis sets [31] via the input decks. Because these basis sets consist of a triple-zeta description for valence orbitals, we refer to them as TZ(d,p), TZ(2d,2p), and TZ(2df,2p). The TZ(d,p) basis set consists of 98 basis functions contracted from 184 primitive gaussian functions; the TZ(2d,2p) basis set consists of 126 basis functions contracted from 212 primitive gaussians; and the TZ(2df,2p) basis set consists of 140 basis functions contracted from 226 primitive gaussians.

Second-order perturbation theory is the least expensive level of correlated calculation with regards to computer cpu time and disk space, and yet it often accounts for >80% of the electron correlation energy [32–33]. At this level, relatively large molecules with heavy atoms may be studied with large basis sets. Such calculations as those reported in this study may be run on workstations with limited amounts of memory and disk space. In contrast, a CISD calculation with a similar sized basis set would be more expensive and require more memory. A CISD calculation requires computational steps that scale in cost according to the sixth power of the size of the basis set.

In the second-order calculations reported in this study, core molecular orbitals (MOs) are frozen. In diborane, this amounts to the freezing of two 1*s*-type MOs. In dialane ten 1*s*-, 2*s*-, and 2*p*-type core MOs are frozen; in digallane a total of 28 1*s*-, 2*s*-, 2*p*-, 3*s*-, 3*p*-, and 3*d*-type MOs are frozen. No virtual orbitals are deleted for any of the correlated calculations. Using the smaller basis set [6-311G(d,p)], optimum geometries, vibrational frequencies, and infrared intensities for diborane and dialane are computed with no frozen core for comparison purposes.

As Shen and Schaefer report, the number of vibrational modes belonging to each symmetry type for these molecules is different depending upon which of the six possible right-handed coordinate systems is chosen [28]. They chose the coordinate system in which the *x*-axis passes through the heavy atom nuclei and the *y*-axis passes through the bridging hydrogen nuclei. We follow the choice of Lammertsma and Leszczyński in which the *x*-axis passes through the heavy atom nuclei and the *z*-axis passes through the bridging hydrogen nuclei [24]. In this orientation there are the following types of normal vibrational modes:

A_g	four
A_u	one
B_{1g}	two
B_{1u}	two
B_{2g}	two
B_{2u}	three
B_{3g}	one
B_{3u}	three.

Because all of the molecules studied here have an inversion center, all vibrational modes of *gerade* symmetry will be IR forbidden within the doubly harmonic approximation in which the vibrational modes are taken to be harmonic and the dipole moment function is assumed to be linear.

Results and Discussion

Results of geometry optimizations for diborane are given in Table I along with the experimental equilibrium geometry of Duncan and Harper [9]. Note the consistency and trends in changes of the theoretical bond distances from one basis set to the next. The SCF level B—B interatomic distance for the smallest basis set differs by only 0.006 Å from the SCF result of the largest basis set. The B—H bond distances are even more invariant. The terminal B—H bond distance differs by only 0.002 Å at this level, and the bridge B—H bond distance differs by 0.005 Å. The changes in these distances from one basis set to the next are slightly larger at the E(2) level: 0.017 Å, 0.004 Å, and 0.007 Å, respectively, but are still quite consistent. The bond angle also varies little for the applied basis sets. This consistency indicates that an even larger basis set would probably have little effect on our best predicted geometry. The agreement between the SCF and E(2) results for diborane's equilibrium geometry is also quite good. The terminal B—H bond distance changes the least with the addition of electron correlation; and, as Shen and Schaefer point out, the B—B interatomic distance is the most sensitive to electron correlation [28]. Interestingly, the two interatomic distances associated with the central ring in the molecule are calculated to be shorter at the E(2) level than at the SCF level. This result is most likely due to the fact that the unusual bonding in hydrogen bridge systems is not completely defined by a single configuration reference function. Specifically, the B—B bonding molecular orbital is unoccupied in the SCF reference state. The correlated calculation incorporates this orbital and other important contributions to the bonding and results in shorter distances.

Not only are these theoretical results for B₂H₆ internally consistent, they also agree quite well with the experimental results of Duncan and Harper [9]. The 6-311G(2df,2p) E(2) distances are all within 0.009 Å of the experimental data, and the bond angle differs by only 0.6°. In fact, two of these three bond distances are within the error bars of the experiment. This agreement is even better than the highly correlated DZP CCSD results of Shen and Schaefer [28]. Their calculated interatomic distances at that level differ from the experimental results by up to 0.042 Å, and the bond angle differs by 1.5°.

TABLE I. B₂H₆ Total energies, optimized equilibrium geometries, and rotational constants.

	6-311G (d,p)			6-311G (2d,2p)			6-311G (2df,2p)		
	SCF	E(2) ^a	SCF	E(2) ^a	SCF	E(2) ^a	SCF	E(2) ^a	Exp. ^b
Total energy (a.u.)	-52.82795	-53.05651	-52.83231	-53.07248	-52.83317	-53.08609	-52.83317	-53.08609	
r _e (BB), Å	1.783	1.769	1.779	1.760	1.777	1.752	1.777	1.752	1.743 ± 0.013 ^c
Terminal r _e (BH), Å	1.185	1.188	1.183	1.183	1.183	1.184	1.183	1.184	1.184 ± 0.003
Bridge r _e (BH), Å	1.323	1.316	1.319	1.309	1.318	1.309	1.318	1.309	1.314 ± 0.003
Terminal ∠(HBH)	122.1°	122.4°	122.1°	122.3°	122.0°	122.1°	122.0°	122.1°	121.5° ± 0.5°
Rotational const. (GHz)	80.75	80.45	81.10	81.20	81.12	81.06	81.12	81.06	
	18.00	18.25	18.08	18.42	18.11	18.54	18.11	18.54	
	16.58	16.77	16.64	16.91	16.67	17.02	16.67	17.02	

^a Two 1s-type core molecular orbitals are frozen; no virtual orbitals are deleted.^b See Ref. [9].^c This distance value and the corresponding error bars are geometrically determined from other experimental values.

In Table II the computed harmonic vibrational frequencies and infrared intensities for diborane are presented along with the experimental vibrational frequencies of Duncan [10]. Once again, the theoretical results are quite consistent from one basis set to the next at both the SCF and E(2) levels. The E(2) frequencies computed with the 6-311G(2d,2p) basis set are all within 18 cm^{-1} from those calculated with the 6-311G(2df,2p) basis set; all but three are within 10 cm^{-1} . The differences between the SCF and correlated results are more pronounced for the harmonic vibrational frequencies and the infrared intensities than the differences between these levels for the geometrical parameters. However, such a result is common. The somewhat unusual result is that four of the vibrational modes have higher frequency values than the corresponding SCF results. Normally one expects to see the opposite trend [34,35]. Shen and Schaefer also point out that some of their correlated frequencies are greater in value than the corresponding SCF results, and they explain that this result is due to the fact that some of the correlated interatomic distances are smaller than the SCF distances [28].

TABLE II. B_2H_6 harmonic vibrational frequencies (cm^{-1}) and IR intensities (km/mol).^a

Sym	6-311G (d,p)		6-311G (2d,2p)		6-311G (2df,2p)		Exp. ^c
	SCF	E(2) ^b	SCF	E(2) ^b	SCF	E(2) ^b	
A_g	819	822	819	823	821	830	788
	1291	1230	1297	1235	1295	1226	1187
	2230	2210	2241	2221	2243	2222	2096
	2694	2660	2703	2662	2702	2670	2526
A_u	888	869	889	870	889	869	833
B_{1g}	990	954	993	954	992	953	918
	2763	2743	2771	2745	2769	2752	2597
B_{1u}	1061 (21)	1010 (19)	1061 (26)	1008 (25)	1061 (26)	1008 (24)	974
	2006 (43)	2031 (10)	2013 (39)	2035 (9)	2018 (39)	2053 (8)	1924
B_{2g}	900	904	900	918	903	916	860
	1886	1926	1897	1936	1902	1944	1756
B_{2u}	404 (14)	359 (15)	409 (15)	380 (16)	408 (15)	372 (17)	367
	1091 (5)	983 (1)	1094 (3)	993 (0.9)	1092 (3)	974 (0.6)	951
	2779 (262)	2756 (174)	2787 (245)	2759 (172)	2785 (246)	2766 (163)	2613
B_{3g}	1160	1085	1160	1082	1158	1066	1023
B_{3u}	1270 (132)	1217 (87)	1276 (128)	1225 (83)	1275 (126)	1215 (76)	1175
	1772 (752)	1764 (523)	1785 (734)	1780 (513)	1789 (728)	1777 (489)	1615
	2674 (185)	2645 (144)	2683 (182)	2646 (146)	2683 (182)	2654 (144)	2518

^a Infrared intensities are shown in parentheses. Blanks indicate identically zero values for modes forbidden in the infrared spectrum.

^b Two 1s-type core molecular orbitals are frozen; no virtual orbitals are deleted.

^c See Ref. [10].

Our computed harmonic vibrational frequencies compare quite well with the experimental anharmonic frequencies reported. As expected, the theoretical results are all too high due to the fact that they are harmonic. The 6-311G(2df,2p) E(2) level results are higher than the experimental frequencies by 5%, 3%, 6%, 6%, 4%, 4%, 6%, 3%, 7%, 7%, 11%, 1%, 2%, 6%, 4%, 3%, 10%, 5%, respectively (in the order given in Table II). These results do not compare quite as well as the DZP CCSD results of Shen and Schaefer; but the difference is slight. The average discrepancy of their results with experiment is just under 4%; our results differ on average by just over 5%.

Table III contains the results of the geometry optimizations for Al_2H_6 . As before, the different basis sets yield interatomic distances and bond angles that vary little at both the SCF and the E(2) levels. In addition, the difference between the SCF and E(2) results are not quite as large as they were for diborane. This trend of vanishing differences with the increase of atomic mass has been noted previously for some molecules containing elements from the IVth and Vth groups of the periodic table [36]. Similar to the B—B distance in B_2H_6 , the Al—Al interatomic distance is the most sensitive to electron correlation, but it is not as sensitive as the corresponding diborane parameter. Also similar to the results of B_2H_6 , we note that the interatomic distances associated with the ring in the molecule are smaller at the correlated level than at the SCF level. Again, this is most likely due to the ring structure being somewhat poorly described by a single configuration reference function.

Perhaps the most interesting observation from the comparison of the optimized equilibrium geometries of diborane and dialane is the fact that the H—Al—H angle in dialane's ring is less than 85° at both levels of theory for all basis sets used. The corresponding angle in diborane is greater than 95° in all cases we considered. A

TABLE III. Al_2H_6 total energies, optimized equilibrium geometries, and rotational constants.

	6-311G (d,p)		6-311G (2d,2p)		6-311G (2df,2p)	
	SCF	E(2) ^a	SCF	E(2) ^a	SCF	E(2) ^a
Total energy (a.u.)	-487.32011	-487.49018	-487.32603	-487.50822	-487.32708	-487.51667
r_e (BB), Å	2.623	2.606	2.616	2.608	2.617	2.607
Terminal r_e (BH), Å	1.571	1.568	1.569	1.569	1.570	1.571
Bridge r_e (BH), Å	1.741	1.730	1.739	1.732	1.740	1.733
Terminal \angle (HBH)	127.1°	128.1°	126.9°	127.6°	126.9°	127.9°
Rotational const. (GHz)	47.57	47.55	47.69	47.60	47.70	47.42
	4.52	4.59	4.54	4.58	4.54	4.58
	4.31	4.37	4.34	4.37	4.33	4.37

^a Ten 1s-, 2s-, and 2p-type core molecular orbitals are frozen; no virtual orbitals are deleted.

recent study of B_2H_6 which appraised the bonding from a valence-bond point of view concluded that the directional B—H interactions were the chief interactions in this species, but that the direct through space B—B interactions were not negligible [21]. If this is true, the bonding between the two borons may pull them closer together than a distance for which the bridge bonds alone could account, thereby accounting for the large H—B—H angle. Similar reasoning from the opposite direction would imply that little or no direct bonding exists between the two aluminum atoms in dialane. Comparison of the largest coefficients from the second-order calculations of diborane and dialane support this conclusion; the coefficients are larger for B_2H_6 . Similarly, the simple fact that the energy for diborane changes more with correlation than does that of dialane indicates that the SCF reference state in which the M—M bonding orbital is unoccupied describes Al_2H_6 better than B_2H_6 .

The theoretical harmonic vibrational frequencies and infrared intensities for dialane are presented in Table IV. As before, the theoretical results are quite consistent from one basis set to the next at both levels of theory. The E(2) frequencies calculated

TABLE IV. Al_2H_6 harmonic vibrational frequencies (cm^{-1}) and IR intensities (km/mol).^a

Sym	6-311G (d,p)		6-311G (2d,2p)		6-311G (2df,2p)	
	SCF	E(2) ^b	SCF	E(2) ^b	SCF	E(2) ^b
A_g	390	396	391	389	389	387
	813	779	814	782	814	775
	1620	1613	1604	1582	1594	1569
	2049	2035	2044	2015	2041	2009
A_u	445	433	442	433	442	431
B_{1g}	497	480	497	479	497	476
	2046	2043	2039	2020	2036	2015
B_{1u}	685 (346)	658 (320)	681 (327)	656 (308)	680 (324)	652 (302)
	1326 (537)	1344 (423)	1315 (475)	1315 (386)	1309 (467)	1312 (367)
B_{2g}	508	502	506	506	506	502
	1451	1473	1440	1453	1435	1452
B_{2u}	241 (18)	227 (16)	242 (21)	227 (18)	242 (20)	224 (17)
	964 (348)	913 (298)	939 (268)	899 (240)	935 (261)	880 (225)
	2054 (536)	2050 (438)	2046 (497)	2027 (414)	2043 (497)	2022 (397)
B_{3g}	824	788	808	787	807	783
B_{3u}	765 (845)	733 (731)	768 (783)	739 (696)	769 (778)	731 (676)
	1559 (1386)	1562 (1221)	1547 (1315)	1540 (1165)	1539 (1316)	1535 (1154)
	2041 (122)	2028 (12)	2036 (133)	2008 (125)	2033 (133)	2002 (123)

^a Infrared intensities are shown in parentheses. Blanks indicate identically zero values for modes forbidden in the infrared spectrum.

^b Ten 1s-, 2s-, and 2p-type core molecular orbitals are frozen; no virtual orbitals are deleted.

with the 6-311G(2d,2p) basis set all differ from those computed with the larger basis set by less than 20 cm^{-1} ; all but two are within 8 cm^{-1} of each other. The differences between the SCF and E(2) results are again more pronounced for the computed frequencies and intensities than for the geometrical parameters.

Absent from both Table III and Table IV is a column for experimental results because dialane has not been observed to date. However, we may compare our results to the DZP CCSD results of Shen and Schaefer [28]. Even though the basis set they used is much smaller than any of those incorporated in the present study, they used a higher level of theory. All of the interatomic distances from our 6-311G(2df,2p) E(2) results are within 0.014 \AA of the DZP CCSD distances, and the angle differs by only 0.5° . Based on this agreement and on the fact that our results for diborane were slightly closer to the experimental values than their DZP CCSD results, we believe that our geometry should give good agreement to experiment if ever dialane is observed experimentally.

To compare the vibrational frequencies, one must remember that the choice of molecular orientation is different in the two theoretical studies. Thus, the B_{1g} and B_{1u} vibrational modes in the present study correspond to the B_{2g} and B_{2u} in the work of Shen and Schaefer and vice versa. Our harmonic vibrational frequencies computed at the E(2) level with the 6-311G(2df,2p) basis set differ from the DZP CCSD results of Shen and Schaefer by 3%, 2%, 4%, 1%, 3%, 3%, 1%, 2%, 4%, 3%, 1%, 5%, 8%, 1%, 5%, 2%, 3%, 2%, respectively (in the order given in Table IV). It is interesting to note that all of our frequencies are lower. This was not the case for diborane, where only five of our 6-311G(2df,2p) E(2) level frequencies were lower than the corresponding DZP CCSD results of Shen and Schaefer, 12 frequencies were higher, and one was the same. Due to the close agreement of these two theoretical sets of frequencies and due to the fact that calculated harmonic vibrational frequencies are usually higher than corresponding anharmonic experimental frequencies, we again believe our results will yield good agreement to experiment.

Table V presents results which compare the effects of frozen core and full electron correlation on E(2) geometries of diborane and dialane computed with the 6-

TABLE V. Effects of frozen core on E(2) geometries using a 6-311G (d,p) basis set

	B_2H_6		Al_2H_6	
	Frozen ^a core	Full electron correlation	Frozen ^b core	Full electron correlation
Total energy (a.u.)	-53.05651	-53.09193	-487.49018	-487.74034
$r_e(\text{MM})^c, \text{\AA}$	1.769	1.765	2.606	2.602
Terminal $r_e(\text{MH}), \text{\AA}$	1.188	1.188	1.568	1.567
Bridge $r_e(\text{MH}), \text{\AA}$	1.316	1.315	1.730	1.728
Terminal $\angle(\text{HMH})$	122.4°	122.3°	128.1°	128.1°

^a Two 1s-type core molecular orbitals are frozen; no virtual orbitals are deleted.

^b Ten 1s-, 2s-, and 2p-type core molecular orbitals are frozen; no virtual orbitals are deleted.

^c M = B or Al.

31G(d,p) basis set. The interatomic distance between the heavy atoms appears to be the geometrical parameter affected the most by frozen core molecular orbitals, but even these differences are small—0.004 Å for both molecules. The other geometrical parameters are affected even less. They vary by either 0.001 Å, 0.1°, or not at all.

The effects of freezing and not freezing core molecular orbitals on harmonic vibrational frequencies and infrared intensities of diborane and dialane computed at the E(2) level with a 6-311G(d,p) basis set are seen in the results listed in Table VI. The differences in wave numbers between the frozen core frequencies and full correlation frequencies for B₂H₆ are 4, 0, 3, 0, 2, 2, 1, 2, 8, 6, 6, 1, 0, 0, 1, 1, 2, 1, respectively. The differences in infrared intensities between these two levels for B₂H₆ are 0, 1, 0, 0, 2, 3, 6, 1, respectively (in the order of nonzero intensities given in Table VI). The differences in wave numbers between the frozen core frequencies

TABLE VI. Effects of frozen core on E(2) harmonic vibrational frequencies (cm⁻¹) and infrared intensities (km/mol)^a using a 6-311G (d,p) basis set.

Sym	B ₂ H ₆		Al ₂ H ₆	
	Frozen ^b core	Full electron correlation	Frozen ^c core	Full electron correlation
A _g	822	826	396	393
	1230	1230	779	779
	2210	2213	1613	1616
	2660	2660	2035	2051
A _u	869	871	433	434
B _{1g}	954	956	480	481
	2743	2742	2043	2042
B _{1u}	1010 (19)	1012 (19)	658 (320)	659 (318)
	2031 (10)	2039 (9)	1344 (423)	1351 (417)
B _{2g}	904	910	502	504
	1926	1932	1473	1482
B _{2u}	359 (15)	360 (15)	227 (16)	226 (16)
	983 (1)	983 (1)	913 (298)	914 (296)
	2756 (174)	2756 (172)	2050 (438)	2057 (435)
B _{3g}	1085	1086	788	791
B _{3u}	1217 (87)	1218 (84)	733 (731)	733 (726)
	1764 (523)	1766 (517)	1562 (1221)	1569 (1215)
	2645 (144)	2644 (143)	2028 (120)	2035 (121)

^a Infrared intensities are shown in parentheses. Blanks indicate identically zero values for modes forbidden in the infrared spectrum.

^b Two 1s-type core molecular orbitals are frozen; no virtual orbitals are deleted.

^c Ten 1s-, 2s-, and 2p-type core molecular orbitals are frozen; no virtual orbitals are deleted.

and full correlation frequencies for Al_2H_6 are 3, 0, 3, 16, 1, 1, 1, 1, 7, 2, 9, 1, 1, 7, 3, 0, 7, 7, respectively. The differences in infrared intensities between these two levels for Al_2H_6 are 2, 6, 0, 2, 3, 5, 6, 1, respectively. The agreement between results computed with frozen core and those with no frozen core presented in Table V and Table VI leads us to believe that freezing core molecular orbitals when the 6-311G(d,p) basis set is used will have little effect on overall theoretical predictions in the series of molecules under present study. For the larger basis sets, the core molecular orbitals should be stabilized more; therefore, freezing core MOs in the larger basis sets is even more justified.

Results of geometry optimizations for digallane are given in Table VII along with the gas-phase electron diffraction structure from Pulham et al. [37]. In contrast to the similar results for the different basis sets at both the SCF and E(2) levels for both diborane and dialane, the theoretical geometries for digallane are much more basis set dependent at both levels of theory. The general trend for the theoretical geometrical parameters to become smaller as the basis set is enlarged is much more pronounced in these results of digallane than it is in the computations of diborane presented in Table I. This trend is actually reversed in dialane, in which most of the calculated geometrical parameters become slightly larger at both levels of theory as the basis set is increased.

Even though the geometry for digallane is more basis set dependent than the geometries of diborane and dialane, the SCF and E(2) results for digallane are quite similar for all three basis sets. In addition, the agreement between the 6-311G(2df,2p) E(2) level results and the experimental data is quite good. The differences between the computed interatomic distances at this level and the experimental results are 0.014 Å, 0.035 Å, and 0.035 Å, respectively. These last two parameters are both Ga—H bond distances, and the theoretical results for both are within the error bars of the experiment [37]. In addition, these 6-311G(2df,2p) E(2) results are on average closer to the experimental values than the DZP CCSD results of Shen and Schaefer [28].

Two further points should be made with regards to the geometry of digallane. First, as with dialane the H—Ga—H ring angle is computed to be less than 85° at both levels of theory for all three basis sets. In addition, the experimental geometry yields this ring angle to be approximately 82° . If we use the same argument discussed earlier, this result would appear to indicate that only very little direct through space Ga—Ga interaction exists. The second point is related, but more obvious. In comparing the interatomic distances reported for dialane and digallane, we note that they are quite similar. This similarity originates from the fact that aluminum and gallium have similar valence radii. Such a result is expected for a pair of third- and fourth-row elements [38]. However, even though similar, our predicted distances associated with the μ -hydrido bridge are actually shorter for digallane. If shorter bonds indicate a greater degree of chemical bonding, then we may assume that digallane is more tightly bound than dialane. This fact may be one of the reasons that dialane has eluded experimental observation thus far. It is interesting to note that the DZP CCSD results of Shen and Schaefer predicted the opposite trend in these interatomic distances of Al_2H_6 and Ga_2H_6 [28].

TABLE VII. Ga₂H₆ total energies, optimized equilibrium geometries, and rotational constants.

	TZ (d,p)		TZ (2d,2p)		TZ (2df,2p)		Exp. ^b
	SCF	E(2) ^a	SCF	E(2) ^a	SCF	E(2) ^a	
Total energy (a.u.)	-3846.36062	-3846.53095	-3846.35483	-3846.53687	-3846.36359	-3846.55412	
<i>r_e</i> (GaGa), Å	2.637	2.630	2.625	2.621	2.602	2.594	2.580 ± 0.002
Terminal <i>r_e</i> (GaH), Å	1.557	1.560	1.556	1.560	1.550	1.554	1.519 ± 0.035
Bridge <i>r_e</i> (GaH), Å	1.766	1.761	1.758	1.754	1.750	1.745	1.710 ± 0.038
Terminal ∠(HGaH)	129.3°	130.4°	129.0°	129.8°	128.5°	129.4°	130°
Rotational const. (GHz)	46.99	46.58	47.19	46.85	47.59	47.2	
	1.96	1.97	1.97	1.98	2.01	2.02	
	1.92	1.93	1.93	1.94	1.97	1.98	

^a Twenty-eight 1s-, 2s-, 2p-, 3s-, 3p-, and 3d-type core molecular orbitals are frozen; no virtual orbitals are deleted.^b See Ref. [37] D_{2h} symmetry was assumed in the least-squares fitting of the electron diffraction data, and the terminal angle (HGaH) was fixed at 130°.

In Table VIII the computed harmonic vibrational frequencies and infrared intensities for digallane are presented along with the experimental vibrational modes reported by Pulham et al. [37]. Once again, the theoretical results are quite consistent from one basis set to the next at both levels of theory. The E(2) vibrational frequencies calculated with the 6-311G(d,p) basis set all differ from those computed with the 6-311G(2d,2p) basis set by less than 30 cm^{-1} ; all but two of the frequencies are within 19 cm^{-1} . The E(2) vibrational frequencies calculated with the 6-311G(2d,2p) basis set are all within 27 cm^{-1} of those computed with the 6-311G(2df,2p) basis set, and all but two are within 15 cm^{-1} of each other. With the exception of the two lower frequency vibrational modes of B_{3u} symmetry, the theoretical infrared intensities also compare quite well between the different basis sets employed. Except for these two B_{3u} modes, the intensities computed at the E(2) level with the larger two basis sets are all within 20 km/mol of each other.

TABLE VIII. Ga_2H_6 harmonic vibrational frequencies (cm^{-1}) and IR intensities (km/mol).^a

Sym	TZ (d,p)		TZ (2d,2p)		TZ (2df,2p)		Exp. ^c
	SCF	E(2) ^b	SCF	E(2) ^b	SCF	E(2) ^b	
A_g	239	239	237	235	242	241	
	789	752	795	755	804	762	
	1584	1570	1572	1553	1600	1580	
	2081	2054	2108	2071	2118	2086	
A_u	479	460	483	470	480	466	
B_{1g}	503	480	509	489	501	481	
	2067	2052	2096	2071	2104	2084	
B_{1u}	700 (198)	666 (176)	704 (196)	672 (183)	694 (198)	660 (179)	~652
	1276 (400)	1292 (309)	1274 (378)	1284 (301)	1285 (366)	1304 (281)	1202
B_{2g}	394	421	406	429	410	429	
	1349	1365	1360	1376	1365	1382	
B_{2u}	242 (9)	221 (7)	252 (10)	235 (9)	253 (11)	236 (9)	
	879 (221)	814 (182)	888 (209)	842 (181)	879 (196)	823 (163)	760
	2074 (493)	2058 (413)	2102 (481)	2077 (419)	2111 (489)	2090 (414)	1993
B_{3g}	834	787	840	809	830	795	
B_{3u}	726 (760)	695 (619)	732 (750)	697 (638)	744 (729)	709 (598)	671
	1423 (1375)	1417 (1226)	1431 (1321)	1426 (1182)	1434 (1302)	1428 (1157)	1273
	2074 (136)	2048 (130)	2100 (143)	2065 (137)	2110 (149)	2079 (141)	1976

^a Infrared intensities are shown in parentheses. Blanks indicate identically zero values for modes forbidden in the infrared spectrum.

^b Twenty-eight $1s$ -, $2s$ -, $2p$ -, $3s$ -, $3p$ -, and $3d$ -type core molecular orbitals are frozen; no virtual orbitals are deleted.

^c See Ref. [37]. Cited here are fundamental vibrational frequencies for digallane in the vapor phase at ca. 270 K. The exception is the approximate value at 652 cm^{-1} , which is an average for values obtained in solid argon and nitrogen matrices at 20 K.

Our computed harmonic vibrational frequencies for digallane also compare quite well to the experimental anharmonic frequencies reported [37]. As with diborane, the theoretical results are all too high due to the fact that they are harmonic. The 6-311G(2df,2p) E(2) level results differ from the experimental frequencies by 1%, 8%, 8%, 5%, 6%, 12%, and 5%, respectively (in the order of observed experimental frequencies reported in Table VIII). The average discrepancy of our theoretical frequencies with the experimental data is just over 6.5%. The corresponding DZP CCSD results of Shen and Schaefer [28] are higher than the experimental frequencies by 5%, 8%, 10%, 5%, 8%, 11%, and 6%, respectively, yielding an average discrepancy of just under 7.5%. This comparison gives more support to our contention that calculations made with the large basis sets employed in this study at the E(2) level can compensate for the lack of a more advanced treatment of electron correlation in these electron deficient systems.

Conclusions

One of the principle objectives of this article was to show that reliable geometries and harmonic vibrational frequencies can be calculated at the second-order perturbation theory level provided that a good basis set is used. For the three molecules considered in this study, experimental data exists for two. For both of these molecules, the 6-311G(2df,2p) E(2) computed geometries are in closer agreement to experiment than the DZP CCSD results of Shen and Schaefer, and the theoretical harmonic vibrational frequencies are almost as good. The larger basis sets used in this study appear to compensate for the lack of extended correlation in these systems. This result implies that a higher level of correlation with these same large basis sets would yield even better results.

Due to a computational bottleneck for larger molecular systems, especially those involving heavy elements such as aluminum and gallium, correlated calculations with such large basis sets are often not feasible. However, our study proved that a TZ basis set augmented by one set of *d* polarization functions on the heavy atoms and one *p*-orbital on the hydrogens gives a good balance between necessary computer resources and reliability of predictions at the E(2) level of theory.

Another objective of this study was to find a level of basis set appropriate for future investigations of correlated densities in series of related molecules. As previously mentioned, a recent study of the bonding in diborane which took a valence-bond point of view concluded that while the directional B—H interactions are the chief interactions in the system, the direct through space B—B interactions are not negligible [21]. Many contour maps of the electronic charge density for this system have been computed at the SCF level. Perhaps a contour map from a correlated wave function determined with a large basis set, such as those used in this study, will provide an interesting comparison for this valence bond interpretation.

Acknowledgments

This work was supported by the National Science Foundation with the Grant RII-8902064 and by the JSU/Earth Observing System Program—NASA Subcontract

No. NCA + TSU-JSU-TASK13-93-001 under Contract No. NAS1-19157. The authors wish to thank the Mississippi Center for Supercomputing for an allotment of computer time to perform some of the calculations presented here. The authors also wish to thank the reviewer for many useful comments and suggestions.

Bibliography

- [1] R. A. Beaudet, in *Advances in Boron and the Boranes*, J. F. Liebman, A. Greenberg, and R. E. Williams, Eds. (VCH, New York, 1984), pp. 417-490.
- [2] K. Kuchitsu and S. J. Cyvin, in *Molecular Structures and Vibrations*, S. J. Cyvin, Ed. (Elsevier, New York, 1972), pp. 183-211.
- [3] W. C. Price, *J. Chem. Phys.* **15**, 614 (1947); **16**, 894 (1948).
- [4] K. Hedberg and V. Schomaker, *J. Am. Chem. Soc.* **73**, 1482 (1951).
- [5] L. S. Bartell and B. L. Carroll, *J. Chem. Soc.* **42**, 1135 (1965).
- [6] K. Kuchitsu, *J. Chem. Phys.* **49**, 4456 (1968).
- [7] D. S. Jones and W. N. Lipscomb, *J. Chem. Phys.* **51**, 3133 (1969).
- [8] D. S. Jones and W. N. Lipscomb, *Acta Crystallogr. A* **26**, 196 (1970).
- [9] J. L. Duncan and J. Harper, *Mol. Phys.* **51**, 371 (1984).
- [10] J. L. Duncan, *J. Mol. Spectrosc.* **113**, 63 (1985).
- [11] E. Switkes, R. M. Stevens, W. N. Lipscomb, and M. D. Newton, *J. Chem. Phys.* **51**, 2085 (1969).
- [12] J. D. Dill, P. von R. Schleyer, and J. A. Pople, *J. Am. Chem. Soc.* **97**, 3402 (1975).
- [13] R. F. Hout, B. A. Levi, and W. H. Hehre, *J. Comput. Chem.* **3**, 234 (1982).
- [14] D. J. DeFrees, R. Krishnan, H. B. Schlegel, and J. A. Pople, *J. Am. Chem. Soc.* **104**, 5576 (1982).
- [15] J. F. Stanton, R. J. Bartlett, and W. N. Lipscomb, *Chem. Phys. Lett.* **138**, 525 (1987).
- [16] H. Horn, R. Ahlrichs, and C. Kölmel, *Chem. Phys. Lett.* **150**, 263 (1988).
- [17] M. Sana, G. Leroy, and C. Henriët, *J. Mol. Struct.* **187**, 233 (1989).
- [18] A. P. Rendell, T. J. Lee, and A. Komornicki, *Chem. Phys. Lett.* **178**, 462 (1991).
- [19] M. Sironi, M. Raimondi, D. L. Cooper, and J. Gerratt, *J. Phys. Chem.* **95**, 10617 (1991).
- [20] J. Cioslowski and M. L. McKee, *J. Phys. Chem.* **96**, 9264 (1992).
- [21] G. Trinquier, J. P. Malrieu, and I. Garcia-Cuesta, *J. Am. Chem. Soc.* **113**, 6465 (1991).
- [22] A. J. Downs, M. J. Goode, and C. R. Pulham, *J. Am. Chem. Soc.* **111**, 1936 (1989).
- [23] C. Liang, R. D. Davy, and H. F. Schaefer, *Chem. Phys. Lett.* **159**, 393 (1989).
- [24] K. Lammertsma and J. Leszczyński, *J. Phys. Chem.* **94**, 2806 (1990).
- [25] M. J. van der Woerd, K. Lammertsma, B. J. Duke, and H. F. Schaefer, *J. Chem. Phys.* **95**, 1160 (1991).
- [26] B. J. Duke, C. Liang, and H. F. Schaefer, *J. Am. Chem. Soc.* **113**, 2884 (1991).
- [27] C. W. Bock, M. Trachtman, C. Murphy, B. Muschert, and G. J. Mains, *J. Phys. Chem.* **95**, 2339 (1991).
- [28] M. Shen and H. F. Schaefer, *J. Chem. Phys.* **96**, 2868 (1992).
- [29] GAUSSIAN 92/DFT, Revision F.3, M. J. Frisch, G. W. Trucks, H. B. Schlegel, P. M. W. Gill, B. G. Johnson, M. W. Wong, J. B. Foresman, M. A. Robb, M. Head-Gordon, E. S. Replogle, R. Gomperts, J. L. Andres, K. Raghavachari, J. S. Binkley, C. Gonzalez, R. L. Martin, D. J. Fox, D. J. DeFrees, J. Baker, J. J. P. Stewart, and J. A. Pople, Gaussian, Inc., Pittsburgh PA, 1993.
- [30] A. D. McLean and G. S. Chandler, *J. Chem. Phys.* **72**, 5639 (1980).
- [31] S. Huzinaga, J. Andzelm, M. Klobukowski, E. Radzio-Andzelm, Y. Sakai, and H. Tatewski, *Gaussian Basis Sets for Molecular Calculations* (Elsevier, New York, 1984).
- [32] R. J. Bartlett, *Ann. Rev. Phys. Chem.* **32**, 359 (1981).
- [33] S. J. Cole and R. J. Bartlett, *J. Chem. Phys.* **86**, 873 (1987).
- [34] B. H. Besler, G. E. Scuseria, A. C. Scheiner, and H. F. Schaefer, *J. Chem. Phys.* **89**, 360 (1988).

- [35] J. F. Stanton, W. N. Lipscomb, D. H. Magers, and R. J. Bartlett, *J. Chem. Phys.* **90**, 3241 (1989).
- [36] J. Leszczyński and J. S. Kwiatkowski, *J. Phys. Chem.* **97**, 12189 (1993).
- [37] C. R. Pulham, A. J. Downs, M. J. Goode, D. W. H. Rankin, and H. E. Robertson, *J. Am. Chem. Soc.* **113**, 5149 (1991).
- [38] N. N. Greenwood and A. Earnshaw, *Chemistry of the Elements* (Pergamon, Oxford, 1985).

Received June 13, 1994

Relativistic Density-Functional Studies of Naked and Ligated Gold Clusters

OLIVER D. HÄBERLEN, SAI-CHEONG CHUNG, and
NOTKER RÖSCH*

Lehrstuhl für Theoretische Chemie, Technische Universität München, D-85747 Garching, Germany

Abstract

Electronic structure investigations on a broad range of gold compounds, including naked and ligated gold clusters, are reviewed. The calculations have been carried out with a recently introduced relativistic variant of the linear combination of Gaussian-type orbitals density-functional (LCGTO-DF) method which affords all-electron investigations for very large systems. The accuracy of the method will be evaluated for the gold dimer. Then the electronic structure of the naked cluster Au_{55} is studied, both in I_h and O_h symmetry. Nonrelativistic and relativistic results obtained by the present method are compared to those of the much simpler jellium model. Since triphenylphosphine is among the most common ligands in gold chemistry a series of mononuclear gold phosphine compounds MeAuPR_3 with increasingly complex ligands PR_3 ($R = \text{H}, \text{CH}_3, \text{C}_6\text{H}_5$) is discussed. The calculations reveal the success and the limitations of simpler phosphines often employed as model ligands in theoretical studies. Some aspects of the phosphine gold interaction in these simpler compounds carry over to the main group element centered gold clusters. Thereby one arrives at a rationalization of the particularly high stability of the carbon-centered octahedral cluster cation $[(\text{R}_3\text{PAu})_6\text{C}]^{2+}$ as compared to the neighboring isoelectronic boron and nitrogen-centered clusters. © 1994 John Wiley & Sons, Inc.

Introduction

Gold is a noble metal, yet it affords a surprisingly rich structural chemistry [1–3]. This is perhaps best exemplified by the discovery of the beautiful octahedral cluster cations $[(\text{Ph}_3\text{PAu})_6\text{C}]^{2+}$ [4] and $[(\text{Ph}_3\text{PAu})_6\text{P}]^{3+}$ [5,6] (with $\text{Ph} = \text{C}_6\text{H}_5$) which boast carbon and phosphorus as central atoms, respectively, in the unusual six-fold coordination. A further example is provided by the unexpected square-pyramidal C_{4v} structure of the four-fold coordinate cluster cation $[(\text{Ph}_3\text{PAu})_4\text{As}]^+$ [7] which is in contrast to that of the tetragonal cluster $[(\text{Ph}_3\text{PAu})_4\text{N}]^+$ [8]. Even some rather large clusters are known with a well-defined stoichiometry and structure, the compound $\text{Au}_{55}(\text{PPh}_3)_{12}\text{Cl}_6$ being arguably the most prominent one [9]. A large variety of physical measurements on this compound is at hand [10] and an accurate electronic calculation is highly desirable to assist in their interpretation, particularly concerning the question to which extent the Au_{55} cluster core exhibits metallic behavior.

* Author to whom correspondence should be addressed.

Gold cluster compounds, with and without ligands, find widespread applications ranging from novel materials for nonlinear optics [11] to labeling agents in biochemistry [12]. On the other hand, more fundamental interests are fueled by the fact that gold compounds feature very prominent relativistic effects as the ratio of nonrelativistically and relativistically calculated atomic radii exhibits a maximum value for gold within the periodic table of elements [13]. Thus gold compounds require a relativistic treatment of the electronic structure. We have recently proposed a scalar-relativistic extension of the linear combination of Gaussian-type orbitals density-functional (LCGTO-DF) method which has been implemented in a self-consistent fashion [14–16]. The method affords a variationally stable and numerically efficient treatment even for larger compounds. In the next section we will briefly describe the salient features of the method and discuss some computational details concerning the applications to be presented in later sections of the article.

To demonstrate the accuracy of the method, we will discuss results for the gold dimer Au_2 , a widely used benchmark system for relativistic electronic structure methods, and compare them to those obtained by other methods. Then we will proceed to a study of the cluster Au_{55} which is presented here for the first time. Differences and common features in the electronic structure of this compound between various symmetries and computational models will be discussed. Particular attention will be paid to the question to which extent the spherical jellium model may serve as a basis for a qualitative description of the valence level spectrum of this metal cluster. One of the most common ligands encountered in gold chemistry is triphenylphosphine, PPh_3 . Electronic structure investigations on PPh_3 ligated gold clusters are commonly carried out with the help of model phosphine ligands. To explore the validity and the limitations of this approach, we will analyze the effects of phosphine substituents for the series of gold(I) compounds MeAuPR_3 (with $\text{R} = \text{H}, \text{Me}, \text{Ph}$).

The carbon-centered octahedral cluster $[(\text{LAu})_6\text{C}]^{2+}$ (with $\text{L} = \text{PPh}_3$) is available in high experimental abundance [4] whereas the clusters $[(\text{LAu})_6\text{B}]^+$ and $[(\text{LAu})_6\text{N}]^{3+}$ have not been observed so far. Therefore, we finally address the problem how the carbon-centered gold cluster cation differs from its isoelectronic boron- and nitrogen-centered analogues. To this end we will analyze the changes in the electronic structure of the octahedral gold phosphine clusters along the series $\text{B} \rightarrow \text{C} \rightarrow \text{N}$.

The Quasirelativistic LCGTO-DF Method

The four-component Dirac-Kohn-Sham equations [17,18],

$$h_{\text{KS}}^{(4)}\psi_i = (c\vec{\alpha} \cdot \vec{\pi} + \beta c^2 + v_n + v_c + v_{xc})\psi_i = \varepsilon_i\psi_i, \quad (1)$$

provide a convenient starting point for a relativistic density-functional method. Here, the effective one-particle "Hamiltonian" $h_{\text{KS}}^{(4)}$ contains the nuclear potential v_n , the classical electronic Coulomb potential v_c , and the exchange-correlation potential v_{xc} . The latter also comprises relativistic contributions, such as radiative corrections [18]. Since chemistry is largely dominated by the electronic solutions

the elimination of the positronic degrees of freedom from Eq. (1) by some transformation is computationally advantageous.

The quasi-relativistic extension [14–16] of the LCGTO-DF method [19,20] is based on the Douglas–Kroll (DK) transformation [21]. This transformation allows for a variationally stable reduction of the four-component Dirac-type to the familiar two-component formalism and permits the self-consistent treatment of relativistic effects. This methodology which employs the no-pair projection operator formalism of quantum electrodynamics has been used previously in the context of wave function-based electronic structure methods [22–24].

Here, we merely report the results of the DK transformation in the framework of the Kohn–Sham theory, correct to the second order in the effective one-particle potential $v (=v_n + v_c + v_{xc})$. One arrives at a set of two-component Kohn–Sham like equations with an effective one-particle “Hamiltonian” [15,16]

$$h_{\text{KS}}^{(2)} = E_p + A_p v A_p + A_p R_p v R_p A_p - \frac{1}{2} (E_p W^2 + W^2 E_p + 2W E_p W). \quad (2)$$

In this equation, the abbreviations

$$E_p = c\sqrt{p^2 + c^2}, \quad A_p = \sqrt{\frac{E_p + c^2}{2E_p}}, \quad R_p = \frac{c(\vec{\sigma} \cdot \vec{p})}{E_p + c^2} \quad (3)$$

have been used where $\vec{\sigma}$ designates the vector of the Pauli spin matrices, and \vec{p} the electronic momentum operator. The integral operator W is given in the momentum representation by

$$W_{p,p'} = A_p \left(\frac{R_p v_{p,p'} - v_{p,p'} R_{p'}}{E_p + E_{p'}} \right) A_{p'}. \quad (4)$$

This DK transformation avoids the generation of highly singular operators that arise when the more familiar Foldy–Wouthuysen transformation is used [25,26]. As a consequence of the DK transformation, matrix techniques [24] may be successfully employed for the evaluation of the various, rather complicated operators. However, only matrix elements of the operators $(\vec{p} \cdot v \vec{p})$ and $(\vec{p} \times v \vec{p})$ have to be evaluated in addition to those already required in the standard nonrelativistic version of the method.

For the investigations to be discussed in this article, a scalar-relativistic variant of the above methodology has been employed which is obtained when one formally replaces the Pauli spin matrices by unit matrices. This procedure is equivalent to the neglect of the spin-orbit interaction. Furthermore, only the dominating nuclear potential has so far been taken into account in the DK transformation, but not the costly electronic contributions to the potential. This level of theory has been termed “vn2” in Ref. [16]. Recent applications, besides the studies of gold compounds, comprise a wide range of other heavy element compounds including Ce@C₂₈ [27,28] and Ni₃₈Pt₆(CO)₄₈ [29].

Before presenting the results for gold compounds, it is appropriate to touch on some computational details. The orbital and fitting basis sets employed for all investigations but in the fourth section as well as the geometries used have been

described previously ([16], [30], and [31]). For a rough orientation, we nevertheless mention the size of the uncontracted and of the contracted basis sets in shorthand notation: Au (21s,17p,11d,7f)/[11s,10p,7d,3f]; B, C, and N as central atoms (9s,6p,1d)/[7s,5p,1d]; C in the CH₃ and P(CH₃)₃ ligands (9s,5p,1d)/[7s,4p,1d]; P (12s,9p,1d)/[8s,6p,1d]; and H (6s,1p)/[4s,1p]. Atomic contractions have been used throughout.

For the naked Au₅₅ clusters a somewhat smaller orbital basis set was designed for gold, since the larger clusters with their increasing average coordination numbers lead to approximate linear dependencies caused by the diffuse exponents. Therefore the original Au (21s,17p,11d,7f) basis set [16] was reduced to (19s,15p,10d,6f) by dropping the most diffuse exponents. The resulting basis set was contracted using atomic orbitals from a spin-restricted calculation. Test calculations on the octahedral cluster Au₆ and the icosahedral cluster Au₁₃ produced changes of less than 1 pm in the bond distances, less than 3 kJ/mol in the binding energy per atom and less than 5% in the frequency of the totally symmetric breathing mode. With this basis set the 4345 electrons of Au₅₅ are described by 3960 contracted Gaussian-type orbitals.

Both Au₅₅ clusters, in I_h and in O_h symmetry, consist of two shells of gold atoms arranged around a central atom (see Fig. 1). In the octahedral cluster all gold-gold distances were constrained to be the same and only the total symmetric breathing mode was optimized. The icosahedral cluster features two different bond lengths, a radial "intershell" distance d_r and a tangential "intrashell" distance d_t . Their ratio $d_r:d_t$ is fixed to 0.95105 [32]. Thus, in the icosahedral case only one degree of freedom has been optimized, too. All LCGTO-DF calculations on the Au₅₅ clusters have been performed with the spin-unrestricted formalism although the energetic

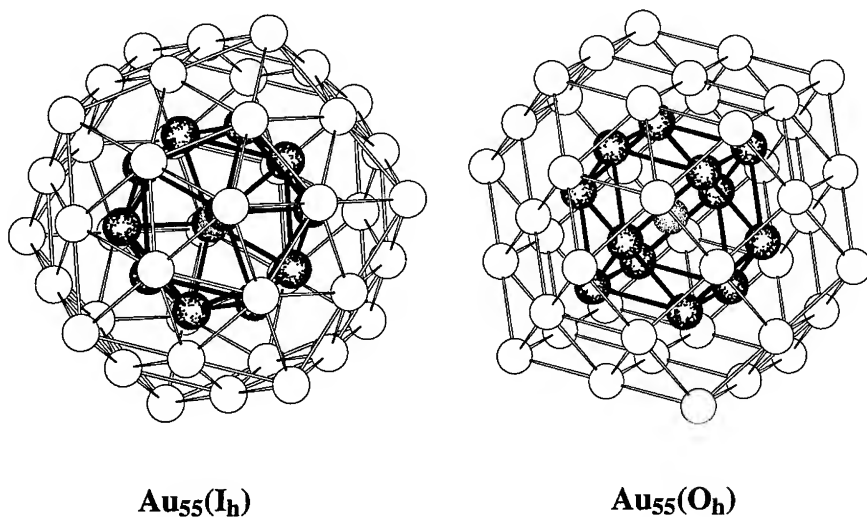


Figure 1. The structures of the icosahedral (I_h) and cuboctahedral (O_h) Au₅₅ clusters. The central atom and the first shell are indicated by shading.

differences between corresponding levels of majority and minority spin were found to be very small (less than 0.1 eV), as is to be expected for a nonmagnetic metal.

The jellium model calculations for Au_{55} were performed with a spherical homogeneous background charge density of radius $R = 629$ pm and with a total of 55 electrons. The radius R corresponds to the average radius of the icosahedral Au_{55} cluster as obtained from the relativistic LCGTO-DF method by averaging over the radial distances of the second shell atomic positions and adding half of the tangential nearest neighbor distance.

The exchange-correlation potential used throughout this work (in LCGTO-DF as well as in jellium calculations) was employed as parameterized by Vosko, Wilk, and Nusair (VWN) [33] based on the essentially exact homogeneous electron gas data of Ceperley and Alder [34].

Benchmark Results on the Gold Dimer Au_2

The gold dimer is a popular benchmark compound for relativistic electronic structure methods since the relativistic effects of its spectroscopic constants are among the largest known. The scalar-relativistic variant of the LCGTO-DF method yields a relativistic bond length contraction of 23 pm, a corresponding increase in the vibrational frequency by 60 cm^{-1} , and a relativistic increase of the binding energy by about 60 kJ/mol. As can be seen from Table I this leads to excellent agreement with the experimental values in case of the bond length and the vibrational frequency whereas the binding energy is too large compared to experiment. Such overbinding is quite frequently encountered in local density-functional calculations [17,35].

The present LCGTO-DF results compare quite well to those of other relativistic density functional methods. Two variants of the Hartree-Fock-Slater method are listed in Table I, one that takes relativistic effects into account by first order perturbation theory (HFS-FOPT) [36] and a fully relativistic four-component method (DFS-DVM) [37]. Proper treatment of electron correlation is essential if one aims for an accurate description of Au_2 in the framework of wave function-based *ab initio* methods. This is clearly demonstrated by the Hartree-Fock (HF) all-electron calculations that treat relativistic effects by first order perturbation theory [38]. Uncorrelated (HF-FOPT) and correlated (HF-FOPT-CPF) calculations yield a relativistic effect on the bond length of about 4 pm, almost no effect on the vibrational frequency, and a strong increase of the binding energy by 92 kJ/mol, but even the correlated values do not match the experimental values very well. The authors attribute this result to the basis set used which was too small to allow for an efficient correlation of the Au 5d electrons. The role of the Au 4f electrons for the electron correlation was pointed out by Schwerdtfeger who found an 3 pm increase of the gold-gold distance by neglecting this effect [39].

The different pseudopotential methods quoted in Table I (REP-CI [40,41], ARPP-CEPA [42], and ARPP-QCI(T) [39]) reproduce the experimental values more or less equally well, the differences being due to varying parameterizations of the pseudopotentials and to the different treatments of the electron correlation. At this

TABLE I. Comparison of the spectroscopic constants of Au₂ (bond length r_e , vibrational frequency ω_e , binding energy D_e) as calculated by various nonrelativistic (nr) and relativistic (rel) electronic structure methods.

Method	r_e		ω_e [cm ⁻¹]		D_e [kJ/mol]	
	nr	rel	nr	rel	nr	rel
HFS-FOPT ^a	290	244	93	201	113	243
HFS/DFS-DVM ^b	272	251	149	191	210	305
HF-FOPT ^c	289	267	108	156	37	80
HF-FOPT-CPF ^d	283	263	105	151	124	172
REP-CI ^e	283	247	105	165	—	218
ARPP-CEPA ^f	293	254	99	170	31	179
ARPP-QCI(T) ^g	279	254	120	178	127	205
LCGTO-DF ^h	270	247	135	195	215	278
Experiment ⁱ		247		191		222

^a Hartree-Fock-Slater method, relativistic effects treated by first-order perturbation theory (FOPT) [36].

^b Nonrelativistic Hartree-Fock-Slater and fully relativistic Dirac-Fock-Slater method [37].

^c Hartree-Fock method with FOPT [38].

^d Same as footnote (c), but electron correlation treated by the coupled pair functional method [38].

^e Relativistic effective-core potential configuration interaction method [40, 41].

^f Spin-orbit averaged relativistic pseudo-potential method with coupled electron pair approximation (CEPA-1), nonrelativistic results without CEPA-1 [42].

^g Same as footnote (f), but with quadratic configuration interaction (single and double substitutions as well as some triple contributions) [39].

^h Scalar-relativistic variant of the LCGTO-DF method [16].

ⁱ Reference [54].

time the ARPP-QCI(T) calculation [39] represents the most complete calculation with respect to the inclusion of correlation effects in a wave function-based *ab initio* method. The experimental values of the vibrational frequency and of the binding energy are reproduced very well, the bond length is calculated too long by 7 pm. The neglect of core-valence correlation yields a further increase of the bond length by 12 pm [39]. It is clearly an advantage of the present LCGTO-DF approach that the correlation of *all* electrons is taken into account in the framework of density-functional theory.

In summary, the presented relativistic LCGTO-DF method performs very advantageously compared to other methods, especially if one takes into account its computational efficiency (50 s of CPU time on one processor of a CRAY-Y/MP computer for the Au₂ molecule).

The Electronic Structure of Au₅₅

The compound Au₅₅(PPh₃)₁₂Cl₆ (**1**) [9] has been well characterized by a large variety of spectroscopic methods [10]. Compound **1** has attracted much interest in the recent years since it is one of the largest stoichiometrically well-characterized

gold cluster compounds. Also, one envisages possible novel applications such as the creation of quantum dot structures [43]. A problem of particular interest is the question whether the Au_{55} core is large enough to exhibit metallic behavior. To supplement the many experimental investigations of compound **1** we present nonrelativistic and relativistic LCGTO-DF calculations on unligated Au_{55} clusters. As compound **1** features a cuboctahedral metal core [9] the calculations for Au_{55} have been performed employing O_h symmetry. We also performed calculations on Au_{55} in I_h symmetry since for unligated pure metal clusters the icosahedral structure often dominates [44].

First, we briefly summarize the structural results of the calculations. The geometry optimization furnished an Au-Au distance of 280 pm for $\text{Au}_{55}(\text{O}_h)$, about 3% less than the bulk gold-gold distance of 288 pm [45]. This result agrees well with an experimental estimate of the average gold-gold distance in the cluster **1** of roughly 4% less than the bulk value [10]. The calculated average Au-Au distance in $\text{Au}_{55}(\text{I}_h)$, 281 pm, is nearly the same as in $\text{Au}_{55}(\text{O}_h)$ although in the icosahedral case two different values for the next-neighbor distance occur, 84 radial distances of 272 pm and 150 tangential distances of 286 pm.

Which of the two isomers was found to be more stable? The calculated average binding energies per atom, 3.59 eV for the icosahedron and 3.55 eV for the cuboctahedron, are very close to each other with a slight preference for the icosahedron. The ligands may very well change this structural advantage so that the present findings in no way exclude a cuboctahedral structure of **1**. Both values for the binding energy seem to be already rather close to the experimental bulk cohesive energy of 3.80 eV [45]. However, if one attempts a proper extrapolation to the bulk based on a series of naked gold clusters [46] one deduces an overestimation of the bulk energy by about 1.0 eV in the local density approximation.

The jellium model works well for alkali clusters [47,48]. Since gold is an also monovalent metal one may expect this model to provide a successful description of gold clusters as well. Obviously the participation of the Au 5d shell in the bonding of gold compounds [31,49,50] will pose restrictions to the applicability of the jellium model but, as we will see in the following, at least some qualitative aspects may be carried over. The results of a spherical jellium model calculation for the 55 s-type valence electrons of Au_{55} (see the second section for details of the model) are presented in Figure 2(a). One obtains the classical ordering of jellium levels (1s, 1p, 1d, 2s, 1f, 2p, 1g, 2d, . . .) with the 1g level as HOMO. This level contains 15 electrons and hence lacks three electrons to the next shell closing which is consistent with the next magic number of 58 electrons.

Relativistic effects lead to a radial contraction and energetic lowering of the Au 6s orbitals while they are destabilizing and spatially extending the Au 5d orbitals [13]. This improves the possibility of hybridization between the two types of orbitals. Thus, one expects a closer match of the jellium electronic structure to that of a full-potential first principles calculation in the nonrelativistic case where the energetic and spatial separation of the Au 6s and 5d orbitals is larger. Furthermore, the icosahedral cluster Au_{55} resembles more the spherical jellium symmetry whence we will start the comparison with the nonrelativistic LCGTO-DF one-particle spec-

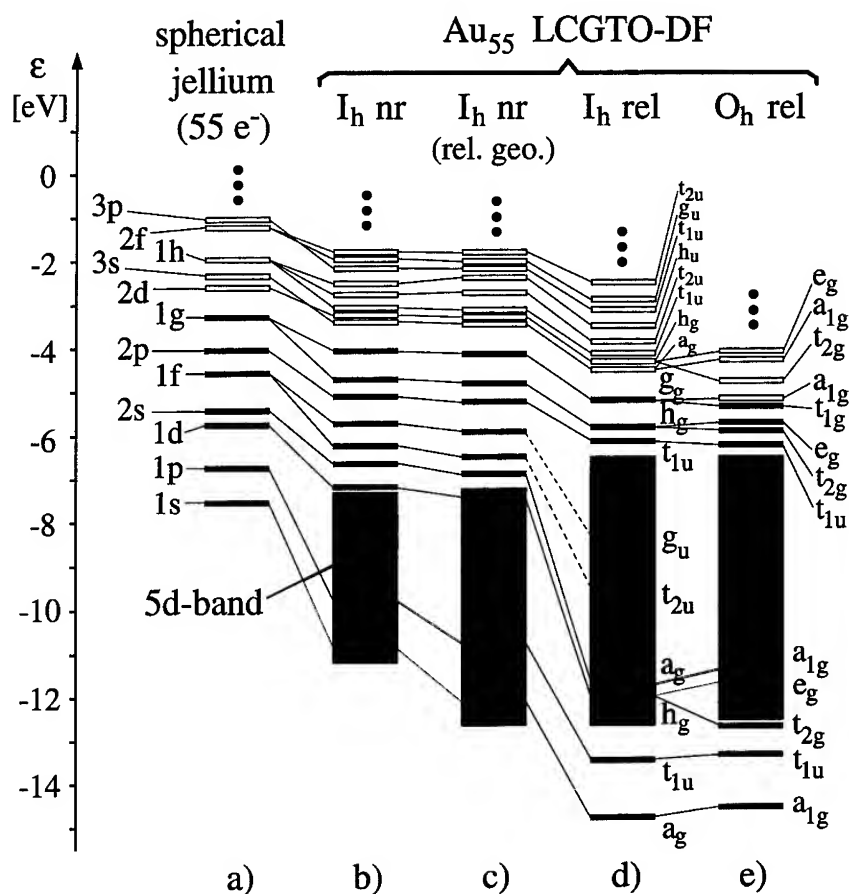


Figure 2. The electronic structure of Au_{55} . Kohn-Sham one-particle energies from relativistic (rel) and nonrelativistic (nr) all-electron LCGTO-DF calculations are compared to results of the spherical jellium model. Filled bars indicate occupied levels, empty bars unoccupied levels. (a) Spherical jellium model calculation with 55 electrons and $R = 629$ pm. (b) Nonrelativistic all-electron LCGTO-DF calculation in icosahedral geometry at equilibrium. (c) Same as (b), but for the geometry obtained from the relativistic calculation. (d) Relativistic LCGTO-DF calculation in icosahedral geometry. (e) Same as (d), but in octahedral symmetry at equilibrium.

trum of $\text{Au}_{55}(\text{I}_h)$ shown in Figure 2(b). All levels with pertinent s-character (more than about 50% s + p character according to a Mulliken population analysis) are drawn as bars, the 5d manifold is indicated by a shaded box.

The first striking feature is the discrete level spectrum around the HOMO (66 g_g occupied by 5 electrons) with an average spacing of about half an eV. In the case of a true metallic behavior, one would expect a much narrower level spacing approaching the continuous level spectrum of the bulk. On the other hand, if the high I_h symmetry were broken, many more levels would result in the energy region

around the HOMO, thus reducing the level spacing significantly. The d-band is quite narrow, 3.9 eV, and located at the lower end of the s-band.

Formal imposition of a lower symmetry constraint on the spherical jellium leads to a splitting of the irreducible representations as shown in Table II for I_h and O_h symmetry. With the help of this correlation table it is possible to establish a one-to-one correspondence between the jellium levels [Fig. 2(a)] and those LCGTO-DF Kohn-Sham levels which exhibit predominantly sp-character [Fig. 2(b)]. If one takes the symmetry reduction into account, one notes that the jellium model correctly predicts the ordering of all the occupied all-electron levels of s-character. The jellium levels whose degeneracy is reduced in I_h symmetry (1f, 1g, 1h, . . .) are split by about 0.5 eV in the all-electron calculation. The two lowest levels of s-character fall within the range of the d-band and are distributed to a certain degree over several levels of d-character, a consequence of the weak but noticeable s-d mixing even in a nonrelativistic description of gold.

As a next step on the way to the one-electron spectrum of a relativistic calculation, the $Au_{55}(I_h)$ cluster is compressed from its nonrelativistic equilibrium structure ($\bar{d}_{AuAu} = 299$ pm) to its calculated relativistic equilibrium geometry ($\bar{d}_{AuAu} = 281$ pm), but still treated nonrelativistically. The results [Fig. 2(c)] may be described mainly as a broadening of the d-band (from 3.9 to 5.4 eV) and a lowering of the s-levels, the latter ones being most distinct in case of the low-lying bonding levels. In the next step the relativistic treatment was switched on. The resulting level spectrum is shown in Figure 2(d). The width of the d-band increases further (from 5.4 to 6.3 eV), mainly due to rearrangements at the upper end of the 5d manifold. The highest lying Au 5d levels now have energies above -7 eV. On the other hand, the Au s-manifold is lowered in energy. As a consequence, the two lowest lying s-type levels now drop out of the range of the d-band whereas some of the higher lying s-levels sink into the upper part of the d-band. Since relativistic effects strongly enhance s-d mixing in gold as explained above some of the s-levels situated within the d-band (e.g., jellium $1f \rightarrow g_u + t_{2u}$ in I_h) can no longer be discriminated as their contribution is spread out over a large number of d-levels.

In the last column of Figure 2, the effect of further reducing the symmetry of the Au_{55} cluster from I_h to O_h is demonstrated. Some of the $Au_{55}(I_h)$ levels split (Table

TABLE II. Correlation table for the irreducible representations of the infinite rotation group $O(3)$ and the I_h and O_h point groups.

Angular momentum	$O(3)$ symmetry	I_h symmetry	O_h symmetry
0	s	a_g	a_{1g}
1	p	t_{1u}	t_{1u}
2	d	h_g	$e_g + t_{2g}$
3	f	$t_{2u} + g_u$	$a_{2u} + t_{1u} + t_{2u}$
4	g	$h_g + g_g$	$a_{1g} + e_g + t_{1g} + t_{2g}$
5	h	$t_{1u} + t_{2u} + h_u$	$e_u + t_{1u} + 2 \times t_{2u}$

II). Particularly noteworthy is the five-fold occupied g_g HOMO in $Au_{55}(I_h)$ which splits into a five-fold occupied t_{1g} HOMO and an empty a_{1g} LUMO in $Au_{55}(O_h)$. However, the splitting is rather small, 0.15 eV. The width of the d-band essentially remains unchanged from I_h (6.3 eV) to O_h (6.1 eV). Both values agree quite well with the experimentally determined width of the d-band in bulk gold, 5.7 ± 0.3 eV [51], indicating near bulk-like behavior for this property. A further point worth noting is the position of the most bonding valence level of s-type which is lower in energy by about 0.3 eV in the icosahedral than in the cuboctahedral Au_{55} cluster. This finding is consistent with the slightly stronger average binding energy of the former cluster.

The Effect of Phosphine Substituents in $MeAuPR_3$

Triphenylphosphine PPh_3 is a very common ligand in gold cluster compounds, in particular due to the extensive steric shielding it affords. On the other hand, this compound causes a heavy burden in any electronic structure calculation. Thus, in electronic structure calculations, triphenylphosphine is most often modeled by simple phosphines PH_3 . However, it is well known that the phosphine substituents are not innocent in any ligand metal bonding. Therefore it seems worthwhile to investigate to which extent it is justified in electronic structure calculations to model the triphenylphosphine ligands PPh_3 of existing compounds by simple phosphines PH_3 . Compounds of the type $MeAuPR_3$ afford the simplest systems for studying this effect as they are tractable by the relativistic LCGTO-DF method up to $MeAuPPh_3$. Furthermore, experimental data are available for the two compounds $MeAuPMe_3$ and $MeAuPPh_3$.

Good agreement is achieved between calculated results and available experimental values of observables (see Table III). Thus, the observed trends should be meaningful. The obvious discrepancy in the gold-carbon bond length of $MeAuPPh_3$ between experiment and calculation has been discussed elsewhere [30]. The Au-P bond distance in $MeAuPR_3$ (see Table III) does not show a monotonic trend along the series $R = H, Me, Ph$: the methyl-substituted compound marks, in a sense, an extremum. As a consequence, the PH_3 ligand may be taken as a satisfactory model ligand for PPh_3 with respect to structural aspects. The values of the dipole moment, the first ionization potential, and the binding energy show a clear convergence along the series of substituents $R = H, Me, Ph$. For these observables, the agreement between PH_3 and the target PPh_3 is rather approximate whereas PMe_3 provides an almost quantitative model for PPh_3 . The monotonic decrease in the ionization potential from 9.10 eV for $MeAuPH_3$ to 8.13 eV for $MeAuPPh_3$ corresponds to an increase in the electron donating capability of the ligands [52] which is also reflected in the increase of the dipole moment.

As an aid in understanding the stabilization of gold cluster compounds by phosphine ligands, it is illuminating to compare the dissociation energies of $AuPR_3$ and $AuPR_3^+$ (see Table III). The binding energy of PR_3 to a gold cation is more than three times larger than to a neutral gold atom. The value of the binding energy increases along the series $R = H, Me, Ph$, in the neutral systems by 60 kJ/mol, in

TABLE III. Comparison of selected properties (bond distances d_{AuC} and d_{AuP} , dipole moment μ , first ionization potential IP, and various binding energies BE) of the compound MeAuPR_3 for the substituents $\text{R} = \text{H, Me, Ph}$. Available experimental values are given in parentheses.

Property	R = H	R = Me	R = Ph
d_{AuC} (MeAuPR_3) [pm]	200	203 (203 ^a)	202 (212 ^b)
d_{AuP} (MeAuPR_3) [pm]	229	225 (228 ^a)	228 (227 ^b)
$\mu(\text{MeAuPR}_3)$ [D]	3.84	5.57 (5.5 ^c)	5.80 (5.6 ^d)
IP(MeAuPR_3) [eV]	9.10	8.34 (8.24 ^e)	8.13
BE(MeAuPR_3) ^f [kJ/mol]	556	610	620
BE(AuPR_3) ^g [kJ/mol]	124	176	184
BE(AuPR_3) ^h [kJ/mol]	401	553	580
BE(HPR_3) ⁱ [kJ/mol]	762 (782 ^k)	906 (935 ^k)	924

^a Reference [55].

^b Reference [56].

^c Reference [57].

^d Reference [58].

^e Reference [59].

^f Reference energy: fragments Me, Au, and PR_3 .

^g Reference energy: fragments Au and PR_3 .

^h Reference energy: fragments Au^+ and PR_3 .

ⁱ Reference energy: fragments H^+ and PR_3 .

^k Reference [60].

the cationic case by 180 kJ/mol. Since no experimental data seem to be available for the "gold ion affinities" of phosphines, these results might be compared to the proton affinities of PR_3 moieties where good agreement between experimental and calculated values is found (Table III). The absolute values of the energy changes are almost by a factor of two larger in the case of a proton as compared to Au^+ , but the change from PH_3 to PPh_3 with about 160 kJ/mol is comparable to that calculated for gold.

Returning to the question raised at the beginning of this section we may summarize this study in the following strategy. Simple phosphine ligands may be used during the geometry optimization of an electronic structure calculation, but, if desirable and feasible, a last calculation at the final geometry should be carried out employing trimethylphosphine ligands to improve the energetic aspects.

The Stability of Element-Centered Octahedral Gold Cluster Cations

Finally, we turn to the recently synthesized octahedral gold cluster cations which feature unusually coordinated main-group elements, namely the carbon centered cluster $[(\text{LAu})_6\text{C}]^{2+}$ [4] where $\text{L} = \text{PPh}_3$. Strong efforts to synthesize its isoelectronic neighbors $[(\text{LAu})_6\text{B}]^+$ and $[(\text{LAu})_6\text{N}]^{3+}$ [3,53] have so far not met with success. It seems as if the carbon-centered octahedral cluster cation exhibits a particular stability. Therefore, we set out to investigate the isoelectronic series of cations $[(\text{LAu})_6\text{X}_m]^{m+}$ with $\text{X}_1 = \text{B}$, $\text{X}_2 = \text{C}$, and $\text{X}_3 = \text{N}$ in a quantum chemical study.

In the following, we present results that point toward an important role of the ligands in stabilizing these cluster cations [31]. Following the computational study established in the preceding section, we optimized the geometry of the clusters using model phosphine ligands ($L = \text{PH}_3$) and employed trimethylphosphine ligands ($L = \text{PMe}_3$) at the obtained equilibrium geometry to improve the values for the binding energies.

The stabilizing effect of the central atom is reflected in the results compiled in the first part of Table IV. In the unligated clusters $[\text{Au}_6\text{X}_m]^{m+}$ the binding energy of the central atom decreases from boron to nitrogen in agreement with orbital overlap arguments advanced earlier [31,50]. Ligands clearly influence the bonding of the central atom to the gold cluster cage; for PMe_3 ligands this binding energy increases by 110 kJ/mol for boron, by 297 kJ/mol for carbon, and by 460 kJ/mol for nitrogen. Thus, carbon acts as the most stabilizing central atom as indicated by underlining in Table IV. On the other hand, it is possible to directly interpret the stabilizing influence of the ligands by means of the ligand shell binding energy (see Table IV, lower part) which rises significantly along the series of central atoms $\text{X}_m = \text{B} \rightarrow \text{C} \rightarrow \text{N}$. Recalling that the binding energy of PR_3 to a gold cation is substantially larger than that to the neutral gold atom (Table III), one discovers a correlation between the cluster stabilization by the ligand shell and the increasing charge of the cluster cations. Furthermore, one notes that the difference in the ligand shell binding energy between PH_3 and PMe_3 increases considerably from boron ($\Delta E = 202$ kJ/mol) to nitrogen ($\Delta E = 560$ kJ/mol), emphasizing once more the necessity of using trimethylphosphine model ligands when studying energetic aspects.

After having established the stabilizing effect of the ligands, we will discuss the stability of the empty cage itself and how it is affected by its net charge. Table V shows the total binding energies of a series of four empty cluster models of increasing complexity for various total charges of the cluster m ; in each row of the table the most stable cluster is indicated by underlining. When proceeding along the first four rows of Table V one notices that in each row the net charge of the most stable

TABLE IV. Binding energy (in kJ/mol) of the central atom ($\text{X}_1 = \text{B}$, $\text{X}_2 = \text{C}$, $\text{X}_3 = \text{N}$) inside the Au_6 cage and of the ligand shell to the gold cage for differently substituted phosphine ligands.

Reaction	X_m		
	B	C	N
$[\text{Au}_6]^{m+} + \text{X}_m \rightarrow [\text{Au}_6\text{X}_m]^{m+}$	-790	-666	-212
$[(\text{H}_3\text{PAu})_6]^{m+} + \text{X}_m \rightarrow [(\text{H}_3\text{PAu})_6\text{X}_m]^{m+}$	-903	-949	-657
$[(\text{Me}_3\text{PAu})_6]^{m+} + \text{X}_m \rightarrow [(\text{Me}_3\text{PAu})_6\text{X}_m]^{m+}$	-900	-963	-672
$[\text{Au}_6\text{X}_m]^{m+} + 6 \text{PH}_3 \rightarrow [(\text{H}_3\text{PAu})_6\text{X}_m]^{m+}$	-1197	-1783	-2482
$[\text{Au}_6\text{X}_m]^{m+} + 6 \text{PMe}_3 \rightarrow [(\text{Me}_3\text{PAu})_6\text{X}_m]^{m+}$	-1399	-2152	-3042

cluster clearly increases. To quantify this effect to a certain degree we also display the (fractional) charge \bar{m} for which the total energy assumes its minimum as determined by interpolating the values along a row.

For an octahedral array of point charges only, the Coulomb repulsion obviously increases when proceeding along the row ($\bar{m} = 0.0$). For the naked gold clusters this electrostatic repulsion is overcompensated by the covalent gold-gold interaction up to cluster charges as high as +3; the singly charged cluster ($\bar{m} = 1.0$) is the most stable one. Attaching phosphine ligands to the cluster further shifts the position of maximum stability toward the dication ($\bar{m} = 2.1$). Here again the ability of the ligands to provide increasing stabilization for clusters with a higher net charge shows up. The trimethylphosphine ligands enhance this effect, furnishing maximum stability for the cluster $[(\text{Me}_3\text{PAu})_6]^{3+}$ ($\bar{m} = 2.7$).

Since the binding energy of the central atom is smallest for nitrogen (see Table IV) the stability maximum of the cluster cations is shifted back to a lower net cluster charge when the central atom is taken into account. In the case of a ligand free cluster model $[\text{Au}_6\text{X}_m]^{m+}$ the boron-centered cluster was found to be most stable ($\bar{m} = 1.0$), whereas the carbon-centered cluster turns out to be the most stable one in the isoelectronic series ($\bar{m} = 1.8$ for $\text{L} = \text{PH}_3$, $\bar{m} = 2.1$ for $\text{L} = \text{PMe}_3$), once the ligands are taken into account.

Thus, three main energy trends may be identified when analyzing the isoelectronic series of cluster cations $[(\text{LAu})_6\text{X}_m]^{m+}$ for the central atoms boron, carbon, and nitrogen: (1) a decreasing affinity of the central atom to the cluster cage, (2) an

TABLE V. Total binding energies^a (in kJ/mol) of various octahedral empty and element-centered model clusters.

Charge	$m =$	0	+1	+2	+3	+4	\bar{m}
Empty cluster models							
$[q_6]^{m+}$ ^b		0	202	802	1818	3232	0.0
$[\text{Au}_6]^{m+}$		-1289	<u>-1504</u>	-1266	-593	523	1.0
$[(\text{H}_3\text{PAu})_6]^{m+}$		-2083	<u>-2588</u>	<u>-2766</u>	-2631	-2143	2.1
$[(\text{Me}_3\text{PAu})_6]^{m+}$		-2159	-2793	-3121	<u>-3176</u>	-2928	2.7
Element-centered clusters							
			X = B	X = C	X = N		
$[\text{Au}_6\text{X}_m]^{m+}$			<u>-2294</u>	-1932	-805		1.0
$[(\text{H}_3\text{PAu})_6\text{X}_m]^{m+}$			-3491	<u>-3715</u>	-3287		1.8
$[(\text{Me}_3\text{PAu})_6\text{X}_m]^{m+}$			-3693	<u>-4084</u>	-3848		2.1

The maximum of the binding energy along each row of varying charge m is indicated by underlining. Also given is the value \bar{m} as determined by a least squares fit to a parabola for which the energy assumes its minimum in a given row of the table.

^a Total binding energy with respect to the constituents X_m , $m \times \text{Au}^+$, $(6 - m) \times \text{Au}$, and $6 \times \text{PR}_3$ ($\text{R} = \text{H}, \text{Me}$).

^b Array of point charges (charge $q = +m/6$) in the geometry of $[\text{Au}_6]^{2+}$ ($d_{\text{AuAu}} = 270$ pm).

increasing electrostatic repulsion due to the rising cluster charge, and (3) a strong counteracting effect brought about by the improved stabilization due to the ligand shell. The net effect of all these trends results in a stability maximum for the carbon-centered cluster although the energy differences to the boron- and nitrogen-centered clusters are small.

Summary and Conclusions

We have presented a broad range of applications of the relativistic LCGTO-DF method to naked and ligated gold clusters. All-electron calculations on icosahedral and cuboctahedral Au_{55} clusters demonstrate the efficiency of the method. They provided new insight into the electronic structure of these systems and showed the spherical jellium model to be adequate for a qualitative analysis of the manifold of s-type one-electron valence levels.

The computational efficiency of the method was also important for allowing an investigation on the series of model compounds MeAuPR_3 with different phosphorus substituents R. The simple phosphine ligands PH_3 , often used in quantum chemical studies instead of the experimental triphenylphosphine ligands, were found to be satisfactory models for structural investigations of gold compounds whereas PMe_3 ligands have to be employed to achieve an accurate description of binding energies. The influence of the phosphine ligands turned out to be essential for rationalizing the high stability of the carbon-centered octahedral gold cluster cation and, in particular, the preferred role of carbon in the isoelectronic series $[(\text{Ph}_3\text{PAu})_6\text{X}_m]^{m+}$ with $\text{X}_m = \text{B}, \text{C}, \text{N}$. The main stabilizing reason was found in the high affinity of the phosphine ligand shell to positively charged clusters that counteract the trend of decreasing stability of the naked cluster core along the series $\text{B} \rightarrow \text{C} \rightarrow \text{N}$.

In summary, the relativistic LCGTO-DF method was shown to be a useful tool for studying the electronic structure of large gold cluster compounds and will allow to tackle many interesting problems of heavy element systems.

Acknowledgments

We thank Prof. H. Schmidbaur for drawing our attention to the fascinating chemistry of gold clusters. This work has been supported by the Deutsche Forschungsgemeinschaft through Sonderforschungsbereich 338, by the Fonds der Chemischen Industrie, and by the European Community Science Program. SCC is grateful to the Deutsche Akademische Austauschdienst for a graduate student scholarship.

Bibliography

- [1] R. J. Puddephatt, *The Chemistry of Gold* (Elsevier, Amsterdam, 1978).
- [2] H. Schmidbaur, in *Gmelin Handbook of Inorganic Chemistry, Organogold Compounds*, A. Slawisch, Ed. (Springer, New York, 1980).
- [3] H. Schmidbaur, *Gold Bull.* **23**, 11 (1990).
- [4] F. Scherbaum, A. Grohmann, B. Huber, C. Krüger, and H. Schmidbaur, *Angew. Chem. Int. Ed. Engl.* **27**, 1544 (1988).

- [5] H. Schmidbaur, *Pure & Appl. Chem.* **65**, 691 (1993).
- [6] E. Zeller and H. Schmidbaur, *J. Chem. Soc. Chem. Commun.* **1993**, 69.
- [7] E. Zeller, H. Beruda, A. Kolb, P. Bissinger, J. Riede, and H. Schmidbaur, *Nature* **352**, 141 (1991).
- [8] Y. L. Slovokhotov and Y. T. Struchkov, *J. Organomet. Chem.* **277**, 143 (1984).
- [9] G. Schmid, R. Pfeil, R. Boese, F. Bandermann, S. Meyer, G. H. M. Calis, and J. W. A. van der Velden, *Chem. Ber.* **114**, 3634 (1981).
- [10] R. C. Thiel, R. E. Benfield, R. Zannoni, H. H. A. Smit, and M. W. Dirken, *Struct. Bond.* **81**, 1 (1993).
- [11] A. W. Olsen and Z. H. Kafafi, *J. Am. Chem. Soc.* **113**, 7758 (1991).
- [12] J. F. Hainfeld and F. R. Furuya, *J. Histochem. Cytochem.* **40**, 177 (1992).
- [13] P. Pyykkö, *Chem. Rev.* **88**, 563 (1988).
- [14] P. Knappe and N. Rösch, *J. Chem. Phys.* **92**, 1153 (1990).
- [15] N. Rösch and O. D. Häberlen, *J. Chem. Phys.* **96**, 6322 (1992).
- [16] O. D. Häberlen and N. Rösch, *Chem. Phys. Lett.* **199**, 491 (1992).
- [17] R. G. Parr and W. Yang, *Density Functional Theory for Atoms and Molecules* (Oxford University Press, New York, 1989).
- [18] M. V. Ramana and A. K. Rajagopal, *Adv. Chem. Phys.* **54**, 231 (1983).
- [19] B. I. Dunlap, J. W. Connolly, and J. R. Sabin, *J. Chem. Phys.* **71**, 3396; 4993 (1979).
- [20] B. I. Dunlap and N. Rösch, *Adv. Quantum Chem.* **21**, 317 (1990).
- [21] M. Douglas and N. M. Kroll, *Ann. Phys.* **82**, 89 (1974).
- [22] J. Sucher, *Phys. Rev. A* **22**, 348 (1980).
- [23] J. Almlöf, K. Fægri, and H. H. Grelland, *Chem. Phys. Lett.* **114**, 53 (1985).
- [24] B. A. Heß, *Phys. Rev. A* **33**, 3742 (1986).
- [25] L. L. Foldy and S. A. Wouthuysen, *Phys. Rev.* **78**, 29 (1950).
- [26] R. E. Moss, *Mol. Phys.* **53**, 269 (1984).
- [27] N. Rösch, O. D. Häberlen, and B. I. Dunlap, *Angew. Chem. Int. Ed. Engl.* **32**, 108 (1993).
- [28] O. D. Häberlen, N. Rösch, and B. I. Dunlap, *Chem. Phys. Lett.* **200**, 418 (1992).
- [29] D. A. van Leeuwen, J. M. van Ruitenbeek, L. J. de Jongh, A. Ceriotti, G. Pacchioni, G. Longoni, O. D. Häberlen, and N. Rösch, *Phys. Rev. Lett.* (in press).
- [30] O. D. Häberlen and N. Rösch, *J. Phys. Chem.* **97**, 4970 (1993).
- [31] O. D. Häberlen, H. Schmidbaur, and N. Rösch, *J. Am. Chem. Soc.* (in press).
- [32] R. Williams, *The Geometrical Foundation of Natural Structure* (Dover Publications, New York, 1979).
- [33] S. H. Vosko, L. Wilk, and M. Nusair, *Can. J. Phys.* **58**, 1200 (1980).
- [34] D. M. Ceperley and B. J. Alder, *Phys. Rev. Lett.* **45**, 566 (1980).
- [35] T. Ziegler, *Chem. Rev.* **91**, 651 (1991).
- [36] T. Ziegler, J. G. Snijders, and E. J. Baerends, *J. Chem. Phys.* **74**, 1271 (1981).
- [37] T. Bastug, D. Heinemann, W.-D. Sepp, D. Kolb, and B. Fricke, *Chem. Phys. Lett.* **211**, 119 (1993).
- [38] D. Strömberg and U. Wahlgren, *Chem. Phys. Lett.* **169**, 109 (1990).
- [39] P. Schwerdtfeger, *Chem. Phys. Lett.* **183**, 457 (1991).
- [40] P. J. Hay, W. R. Wadt, L. R. Kahn, and F. W. Bobrowicz, *J. Chem. Phys.* **69**, 984 (1978).
- [41] Y. S. Lee, W. C. Ermler, K. S. Pitzer, and A. D. McLean, *J. Chem. Phys.* **70**, 293 (1979).
- [42] P. Schwerdtfeger, M. Dolg, W. H. E. Schwarz, G. A. Bowmaker, and P. D. W. Boyd, *J. Chem. Phys.* **91**, 1762 (1989).
- [43] U. Simon, G. Schön, and G. Schmid, *Angew. Chem. Int. Ed. Engl.* **32**, 250 (1993).
- [44] M. Pellarin, B. Bagueard, J. L. Vialle, J. Lermé, M. Broyer, J. Miller, and A. Perez, *Chem. Phys. Lett.* **217**, 349 (1994).
- [45] R. C. Weast, Ed., *CRC Handbook of Chemistry and Physics*, 64th ed. (CRC Press, Florida, 1983).
- [46] O. D. Häberlen, S.-C. Chung, and N. Rösch, (to be published).
- [47] W. Ekardt, *Phys. Rev. B* **29**, 1558 (1984).
- [48] M. Brack, *Rev. Mod. Phys.* **65**, 677 (1993).
- [49] N. Rösch, A. Görling, D. E. Ellis, and H. Schmidbaur, *Angew. Chem. Int. Ed. Engl.* **28**, 1357 (1989).
- [50] A. Görling, N. Rösch, D. E. Ellis, and H. Schmidbaur, *Inorg. Chem.* **30**, 3986 (1991).

- [51] D. E. Eastman and J. K. Cashion, *Phys. Rev. Lett.* **24**, 310 (1970).
- [52] R. L. DeKock, E. J. Baerends, P. M. Boerrigter, and R. Hengelmolen, *J. Am. Chem. Soc.* **106**, 3387 (1984).
- [53] A. Brodbeck and J. Strähle, *Acta Cryst.* **A46**, C-232 (1990).
- [54] K. P. Huber and G. Herzberg, *Molecular Spectra and Molecular Structure Constants of Diatomic Molecules* (Van Nostrand, New York, 1979).
- [55] A. Haaland, J. Hougen, and H. V. Volden, *J. Organomet. Chem.* **325**, 311 (1987).
- [56] P. D. Gavens, J. J. Guy, M. J. Mays, and G. Sheldrick, *Acta Cryst.* **B33**, 137 (1977).
- [57] G. E. Coates and C. Parkin, *J. Chem. Soc.* **1963**, 421.
- [58] G. Calvin, G. E. Coates, and P. S. Dixon, *Chem. Ind. (London)* **1959**, 1628.
- [59] G. M. Bancroft, T. Chan, R. J. Puddephatt, and J. S. Tse, *Inorg. Chem.* **21**, 2946 (1982).
- [60] E. Magnusson, *Austral. J. Chem.* **38**, 23 (1985).

Received June 1, 1994

Dynamics of Metallic and Molecular Hydrogen through Density-Functional Simulations

JOACHIM THEILHABER

Thinking Machines Corporation, 245 First Street, Cambridge, Massachusetts 02142

Abstract

A first-principles quantum molecular dynamics scheme based on density-functional theory is used to investigate the finite-temperature properties of metallic hydrogen at density 2.7 g cm^{-3} ($r_s = 1$), in particular to determine melting temperature, velocity autocorrelation functions below and above melting, and the temperature dependence of proton self-diffusion in the liquid phase. A strong deviation from the prediction of the one-component plasma model is found in the value of the melting temperature. Results of simulations of the molecular phase are also presented and found to be in agreement with previous work on dense molecular hydrogen. The scheme is based, for the modeling of the electrons, on time-dependent Schrödinger equations, coupled to classical equations of motion for the protons. All numerical results were obtained using a parallel computer, and an outline of the computer program implementation is presented. © 1994 John Wiley & Sons, Inc.

Introduction

Recently, a quantum molecular dynamics scheme for condensed-matter systems, based on time-dependent density-functional theory, was implemented by the author [1,2], and principally applied to the simulation of solid and liquid sodium, although preliminary work on hydrogen was also presented in Ref. [1]. In this scheme, the electrons are modeled quantum mechanically by a set of time-dependent wave functions, evolving according to Schrödinger-like equations, whereas the ions obey classical equations of motion. While this approach is similar to the Car-Parrinello scheme [3], the unitarity of the electronic evolution operator automatically insures that orthonormality of the wave functions is maintained at all times. Explicit orthonormality constraints are not required in the electronic equations of motion, resulting in algorithmic simplification.

In the present work, we extend the hydrogen simulations begun in Ref. [1], and explore the properties of metallic hydrogen ($\rho \approx 1.2 \text{ g cm}^{-3}$), especially as regards the determination of the melting temperature and the calculation of proton self-diffusion in the liquid. With this focus, our work is complementary to that reported by Zerah, Cléroutin, and Pollock [4], where a scheme based on the Thomas-Fermi density functional was used to investigate dense plasma physics, and that reported by Hohl et al. [5], which extensively studied the dense molecular phases of hydrogen, using the original Car-Parrinello method. In the present article, we also present

simulation results of the molecular phase, verifying the validity of our scheme in that regime as well.

The present numerical work was entirely achieved on a parallel computer, the Thinking Machines CM-5. Given the growing use of parallel computers for condensed matter physics simulations [6], we sketch here the computer program implementation of our scheme in a high-level language, "High Performance Fortran," and report performance figures for varying machine sizes.

Equations of Motion of the Electron-Ion System

As the theoretical basis and algorithmic implementation of the method used were presented in some detail in Refs. [1] and [2], only a brief outline of the scheme will be given here. In what follows we use atomic units (a.u.), so that with m_e denoting the electron mass and e its charge, length is given in units of the Bohr radius $a_0 = \hbar^2/m_e e^2 = 0.529 \text{ \AA}$, energy in units of 1 hartree $= e^2/a_0 = 27.2 \text{ eV}$ and time in units of $\hbar/1 \text{ hartree} = 2.42 \cdot 10^{-17} \text{ s}$.

We consider a system of N electrons interacting with N classical protons of mass M , the effect of each of which is modeled by a nonsingular, local pseudopotential $v_{ps}(\mathbf{x})$. The ionic positions at time t are given by $\{\mathbf{R}_k(t)\}$, $k = 1, 2, \dots, N$, and, with double occupancy of orbitals, $\psi_j(\mathbf{x})$, $j = 1, 2, \dots, N_o \equiv N/2$ denote the time-dependent electron wave functions. The complete set of equations of motion is given by (keeping the variables $e = m_e = 1$ explicit) [2]

$$i \frac{\partial}{\partial t} \psi_j(\mathbf{x}, t) = -\frac{1}{2m_e} \nabla^2 \psi_j(\mathbf{x}, t) + v_{\text{eff}}(\mathbf{x}, t, [n]) \psi_j(\mathbf{x}, t),$$

$$j = 1, 2, \dots, N_o = N/2, \quad (1)$$

$$M \frac{d^2}{dt^2} \mathbf{R}_k(t) = \mathbf{F}_k(t), \quad k = 1, 2, \dots, N, \quad (2)$$

where \mathbf{F}_k is the total force on the k th proton,

$$\mathbf{F}_k(t) = -\sum_l' \nabla_l \frac{e^2}{|\mathbf{R}_k(t) - \mathbf{R}_l(t)|} - \int d^3x v_{ps}(\mathbf{x} - \mathbf{R}_k(t)) \nabla n(\mathbf{x}, t), \quad (3)$$

and where the electronic number density is given by

$$n(\mathbf{x}, t) = 2 \sum_{j=1}^{N_o} |\psi_j(\mathbf{x}, t)|^2. \quad (4)$$

The effective potential acting on the electrons is

$$v_{\text{eff}}(\mathbf{x}, t, [n]) = \sum_{k=1}^{N_i} v_{ps}(\mathbf{x} - \mathbf{R}_k(t)) + v_H(\mathbf{x}, t) + \mu_{xc}(n(\mathbf{x}, t)) \quad (5)$$

where $v_H(\mathbf{x}, t)$ is the electrostatic, Hartree potential, and where the exchange and correlation term $\mu_{xc}(n)$ is the local derivative

$$\mu_{xc}(n) = \frac{d}{dn} (n\epsilon_{xc}(n)), \quad (6)$$

where $\epsilon_{xc}(n)$ is given by the ground-state local-density approximation (LDA) of density-functional theory [7].

Hydrogen Pseudopotential

The local hydrogen pseudopotential is of the form of Topp and Hopfield [8],

$$v_{ps}(r) = \begin{cases} v_0 \cos(kr) + C, & 0 \leq r \leq r_c, \\ -1/r, & r_c < r, \end{cases} \quad (7)$$

where all four parameters v_0 , k , C , and r_c are adjustable. For given values of r_c and k , v_0 and C are determined by requiring continuity of $v(r)$ and its first derivative across the boundary $r = r_c$. For a given value of r_c , k is then determined by requiring that the energy of the 1s state in the potential of Eq. (7) has the correct value of 1 Ry = $-1/2$ hartree. This is done by repeatedly solving for the energy eigenvalue ϵ of the radial Schrödinger equation for $u(r) = r\psi_{1s}(r)$,

$$-\frac{1}{2} \frac{d^2}{du^2} u(r) + v_{ps}(r)u(r) = \epsilon u(r), \quad (8)$$

successively adjusting the value of k so as to finally obtain $\epsilon = -1/2$.

The choice of the value of r_c is guided by the desire to simultaneously minimize the amplitude of $v(r)$ at the origin, and its extent in Fourier space, while insuring that the electronic charge density is accurately represented for typical nuclear separations. Choosing $r_c = 1.4$ as a reasonable compromise, one finds the remaining parameters

$$k = 2.04137, \quad v_0 = -0.89298, \quad C = -1.57157. \quad (9)$$

While the fitting procedure outlined above is constrained only by the energy of the atomic ground state, it turns out that the energies of the excited states in the potential of Eq. (7) are also accurately represented [8]. Furthermore, the normalized pseudo wave function resulting from Eq. (8) is accurate for $r \gtrsim r_c/2$, so that the potential of Eq. (7) is of the "norm-conserving" variety, insuring transportability into bulk hydrogen [9].

Method of Solution

The equations of motion for the protons, Eqs. (2), are solved using the Verlet (or "leapfrog") algorithm [2]. In the calculation of the effective electron potential, Eq. (5), the Hartree term $v_H(\mathbf{x}, t)$ is found by solving Poisson's equation with periodic boundary conditions, using a three-dimensional fast Fourier transform (FFT). The most demanding part of the computation is, however, in the advancement of the time-dependent Schrödinger equations for the electrons, Eq. (1): for

each wave function, evolution from time-step t^n to $t^{n+1} = t^n + \Delta t$, $n = 0, 1, 2, \dots$, is accomplished by using a "split-step" decomposition of the short-time propagator,

$$\begin{aligned} \psi_j(\mathbf{x}, t^{n+1}) = & \exp\left(-i \frac{\Delta t}{2} v_{\text{eff}}(\mathbf{x}, t^{n+1/2})\right) \cdot \exp(-i\Delta t(-\nabla^2/2m_e)) \\ & \times \exp\left(-i \frac{\Delta t}{2} v_{\text{eff}}(\mathbf{x}, t^{n+1/2})\right) \psi_j(\mathbf{x}, t^n) \quad (10) \end{aligned}$$

where $v_{\text{eff}}(\mathbf{x}, t^{n+1/2})$ is found from a previous half-step extrapolation. The effect of the operator $\exp(-i\Delta t(-\nabla^2/2m_e))$ is computed using three-dimensional FFTs, while the effect of $\exp(-i(\Delta t/2)v_{\text{eff}}(\mathbf{x}, t^{n+1/2}))$ is found from direct multiplication in real space. Because Eq. (10) expresses an explicitly unitary transformation, it conserves to round-off accuracy the norm and orthogonality of all of the wave functions. The scheme is otherwise $O(\Delta t^3)$ accurate.

Parallel Implementation

The algorithm outlined above was implemented on the Thinking Machines CM-5, a distributed-memory, parallel computer of the MIMD type of architecture (MIMD: Multiple Instructions, Multiple Data). The program was written in CM Fortran, a subset of the "High Performance Fortran" (HPF) language [10]. Under HPF, many details of the computer architecture, pertaining to its multiplicity of processors and distributed memory, are largely hidden to the user, who is presented with a single, "global" model of the machine.

For instance, the entire set of three-dimensional electronic wave functions $\psi_j(\mathbf{x}, t)$, $j = 1, 2, \dots, N/2$, is represented by the single Fortran variable PSI, referring to a four-dimensional, complex-valued array: the first index of PSI indicates the orbital j , and the other three indices refer to spatial location on a Cartesian grid. The actual allocation at run time of distributed computer memory for the array, and the division of labor among processors during program execution, when PSI is Fourier transformed, multiplied by other arrays and so forth, is implemented by the HPF compiler without requiring detailed instructions from the programmer. The programmer retains control over data allocation through the use of general compiler directives, which for instance can specify which axes of the array must physically lie in the same processor. The result is a "scalable" code, which can run on any machine size, provided enough memory is available. For the present simulations, the same compiled program has been run on machines with 32, 64 or 128 processors.

Programming a parallel computer with a high-level language such as HPF is to be contrasted with the "message-passing" approach, in which the programmer explicitly implements memory allocation and division of labor among the parallel processors, in effect replacing the compiler in these tasks. The two approaches are largely complementary. The present problem, with its large, homogeneous set of three-dimensional wave functions, appears well suited to an HPF implementation. To give an indication of performance, a Fortran 77 implementation of the algorithm, previously optimized for a Cray architecture [1], requires 4.6 s per time-step on

one processor of a Cray Y-MP computer for a 54-atom system. The corresponding times achieved by the HPF implementation are 3.4, 1.9, 2.0 and 1.1 s per time-step on, respectively, 32 and 64-processor CM-5 computers (Sparc processors), and 32 and 64-processor CM-5E computers (SuperSparc processors).

Simulation Results

Metallic Hydrogen

The simulations were conducted in a fashion similar to those presented in Ref. [2]. We considered a sample of metallic hydrogen, composed of 54 protons and 54 electrons, enclosed in a cubical region of side L with periodic boundary conditions, with the protons initially set at the sites of an atomic *bcc* lattice. The density is defined in terms of the ion-sphere radius,

$$r_s = \left(\frac{3}{4\pi n_p} \right)^{1/3}, \quad (11)$$

where $n_p = N/L^3$ is the average proton number density. The spatial meshes used to define the electronic wave functions are each of extent $n_x \times n_y \times n_z = (32)^3$, with energy cutoff of 136 hartree for $r_s = 1$. Corresponding to the initial proton positions, the electronic ground state was determined by steepest-descent minimization of the electronic energy. Figure 1 is a representation of the initial configuration for $r_s = 1$, in which the protons (small spheres), are encapsulated by the electron density isosurface, calculated for a density half-way between minimum and maximum. The great regularity of the electron distribution can be seen in the left-hand corner of Figure 1, where we show a contour plot of a cross section of the density, taken through the first plane of protons.

The initial ground state energy E_0 as a function of ion-sphere radius r_s is shown in Figure 2(a) for the range of $0.6 \leq r_s \leq 1.8$ ($12.5 \geq \rho \geq 0.46 \text{ g cm}^{-3}$), and the resulting pressure P , as determined by numerical differentiation, is shown in Figure 2(b). The region of existence of metallic hydrogen at zero temperature is estimated to be $r_s \lesssim 1.3$ (Ref. [11]), so that in Figs. 2(a), (b) only the range $r_s \lesssim 1.3$ is physically meaningful. In what follows, we consider dynamical simulations for the specific value $r_s = 1$ ($\rho = 2.7 \text{ g cm}^{-3}$, $P = 5.45 \text{ Mbar}$), well inside the region of existence of the metallic phase.

The dynamical simulations were conducted by initially assigning a Maxwellian distribution of velocities to the protons, and, in the subsequent evolution, by controlling the temperature via a Nosé thermostat [12]. The time-step was $\Delta t = 4.9 \times 10^{-6} \text{ ps}$. For each temperature chosen, an initial equilibration phase of 25,000 time steps was followed by runs of 50,000 to 75,000 time steps (0.24–0.37 ps) during which statistics were gathered.

In Figure 3 a snapshot of the electron-proton configuration is shown for $T = 238 \text{ K}$, after an evolution time of 0.16 ps. There is considerable proton motion, and the resulting electron density is strongly perturbed, as can be directly seen from the isosurface in Figure 3, or from the contour plot displayed in the upper left-hand corner of the figure.

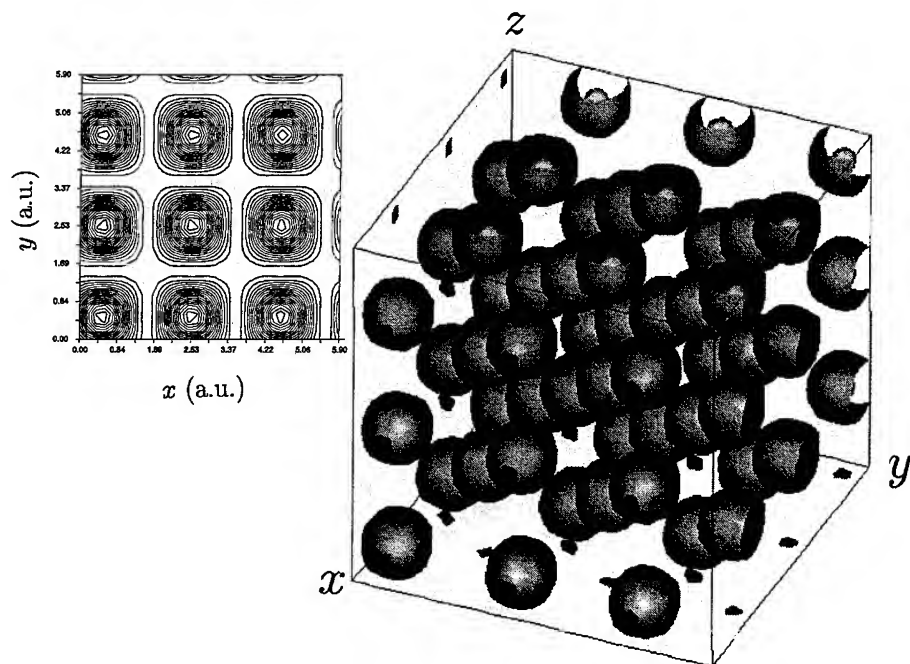


Figure 1. Initial conditions for the dynamical simulations of metallic hydrogen ($\rho = 2.7 \text{ g cm}^{-3}$, $r_s = 1$, 54 protons and 54 electrons, *bcc* atomic crystal lattice). In the three-dimensional figure, the proton positions are labeled by small spheres, encapsulated by the electron density isosurface, plotted for a density half-way between minimum and maximum. The contour plot in the upper left-hand corner refers to a cross section of the electron density taken through the first plane of ions.

The extent of relative proton motion at various temperatures is quantified in Figure 4, which displays the radial distribution functions $g(r)$. Even at the lowest temperature considered, 238 K, the radial distribution function is broad, consistent with the snapshot of Figure 3, which showed large displacements of the protons. As temperature increases, flattening of the distribution functions proceeds until at the largest temperature considered, 5000 K, the first maximum is only a roundish bump.

The solid-liquid transition is not apparent from examining Figure 4. Rather, we determine the melting point of the solid by locating the minimum temperature at which the protons have finite self-diffusion, in other words, the temperature at which the thermally agitated protons wander without returning to the vicinity of their equilibrium lattice sites. For the set of runs presented here, while for $T = 600 \text{ K}$ there is no self-diffusion, finite diffusion does occur at 900 K, indicating that the melting temperature T_m is in the range $600 \text{ K} < T_m < 900 \text{ K}$. It is of some interest to compare this prediction with that of the one-component plasma (OCP) model of the same system, which assumes a completely homogeneous electron background [13]. The OCP melting temperature is given by

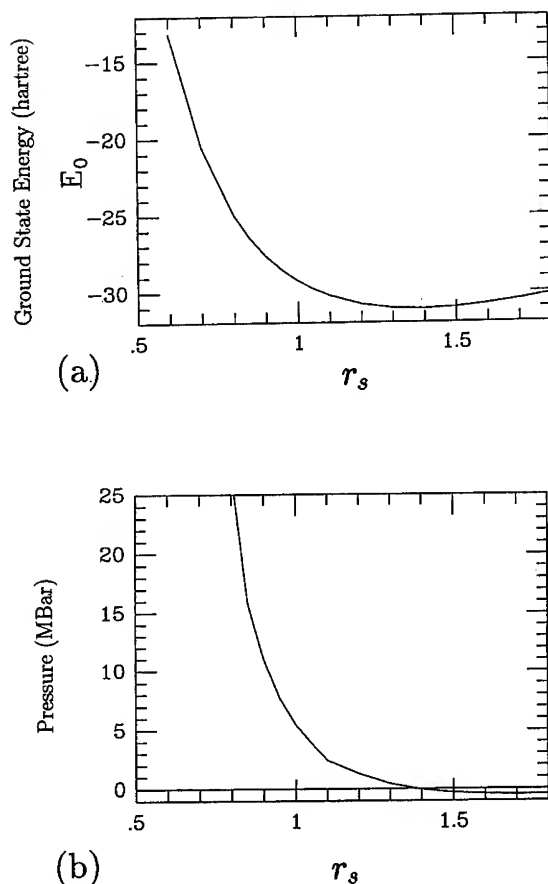


Figure 2. Zero-temperature properties of the atomic crystal (54 protons and 54 electrons), for variable r_s : (a) total ground-state energy, (b) ground-state pressure. The atomic crystal is expected to be stable only for $r_s \lesssim 1.3$, reverting to a molecular phase at larger values of r_s .

$$T_m^{\text{OCP}} = \frac{1}{\Gamma_m r_s}, \quad (12)$$

where, neglecting finite simulation-size effects, $\Gamma_m = 178$ (Ref. [14]). For $r_s = 1$, one obtains $T_m^{\text{OCP}} = 1773$ K, a value much larger than our prediction of $T_m < 900$ K, and this discrepancy shows the importance of the fully quantum-mechanical modeling of the electrons. It is our intention to systematically map the metallic hydrogen melting curve in the near future, so as to determine $T_m = T_m(r_s)$, for a finite range of r_s .

In Figures 5(a) and (b) are shown the velocity autocorrelation functions $Z(t)$, defined by

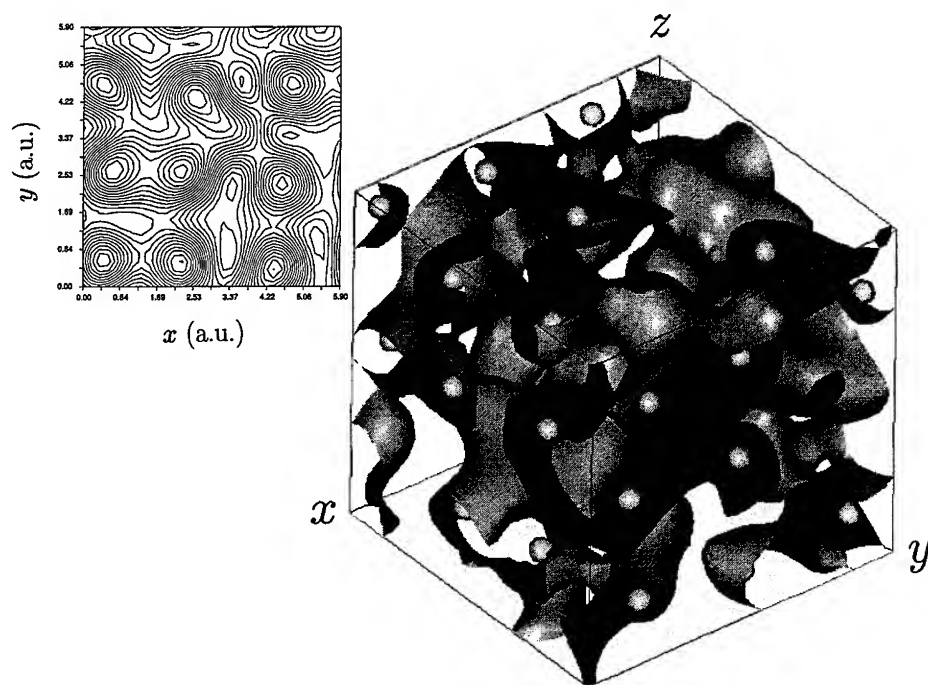


Figure 3. Snapshot of the proton positions (small spheres in the three-dimensional figure) and of the electron density isosurface, for a dynamical simulation at temperature 238 K, after an evolution of 0.16 ps starting from the initial configuration of Figure 1. The contour plot in the upper left-hand corner refers to a cross section of the electron density taken through the same plane as in Figure 1.

$$Z(t) = \frac{1}{3} \langle \mathbf{v}(0) \cdot \mathbf{v}(t) \rangle, \quad (13)$$

for the temperatures of 238 K (solid phase) and 900 K (liquid phase). At the lower temperature, Figure 5(a), the velocity autocorrelation function displays a long-lived oscillatory behavior, extending to about 0.2 ps, with the mix of frequencies that is characteristic of a solid [15]. In the liquid phase, Figure 5(b), the decrease of $Z(t)$ is far more rapid (note the change in horizontal scale as well), indicating a much faster loss of correlation as the protons freely diffuse.

A quantitative measure of the frequency content of the ion motion is given by the power spectrum $\hat{Z}(\omega)$, defined as the Fourier transform of $Z(t)$,

$$\hat{Z}(\omega) = \int_{-\infty}^{\infty} dt e^{i\omega t} Z(t). \quad (14)$$

Graphs of $\hat{Z}(\omega)$ are displayed in Figure 6 for $T = 238, 600, 900$, and 2000 K. For $T = 238$ K, Figure 6(a) (solid phase), the power spectrum displays a set of discrete peaks due to the thermal excitation of the finite number of phonon which exist in

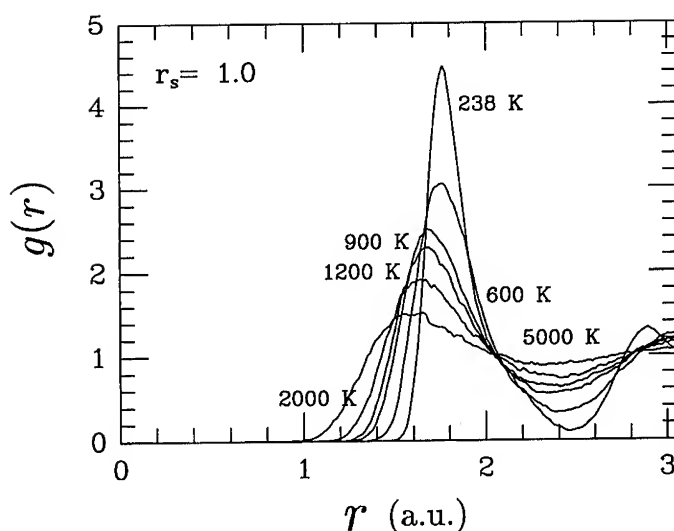


Figure 4. Proton-proton radial distribution functions $g(r)$ for $r_s = 1$, at the temperatures indicated in the plot [the first maximum of $g(r)$ monotonically decreases with increasing temperature].

the crystal lattice. At $T = 600$ K, Figure 6(b) (solid phase), the broadening of the peaks due to inharmonicity and phonon-phonon coupling has largely washed-out the discrete mode structure. For $T = 900$ K, Figure 6(c) (liquid phase), a new feature appears with $\hat{Z}(0) \neq 0$: this is because the proton self-diffusion coefficient D ,

$$D = \int_0^\infty dt Z(t) = \frac{1}{2} \hat{Z}(0), \quad (15)$$

is nonzero. Finally, for $T = 2000$ K, Figure 6(d), the power spectrum has become almost completely diffusive.

In Figure 7 we display the proton self-diffusion coefficient as a function of temperature, as determined by Eq. (15). For the range of temperatures studied, and $r_s = 1$, the diffusion coefficient is approximated by the empirical relation

$$D(T) = l_0 \left(\frac{T - T_0}{M} \right)^{1/2}, \quad (16)$$

where T_0 , a temperature, and l_0 , a length, are adjustable parameters. In Figure 7, $T_0 = 855$ K and $l_0 = 0.18$ a.u.

Molecular Hydrogen

In Ref. [1] results were presented for a simulation under conditions ($r_s = 1.39$, $T = 2000$ K) under which the molecular phase is expected to be stable. Starting

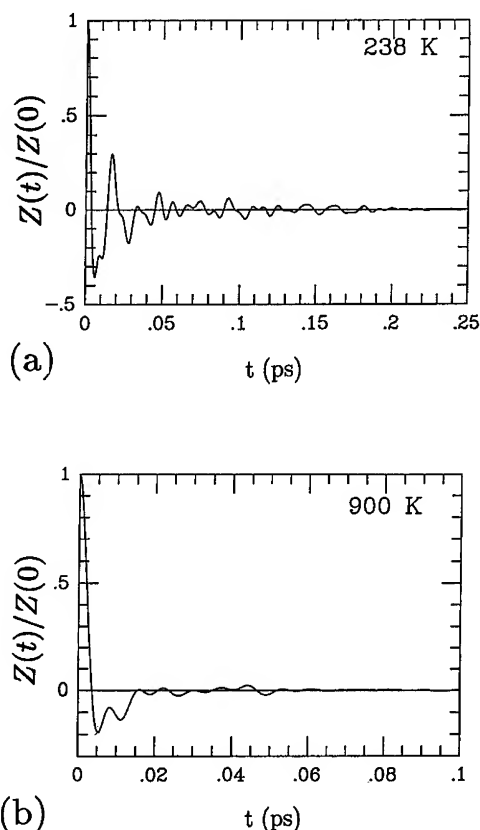


Figure 5. Proton velocity autocorrelation functions, normalized to the value for $t = 0$; (a) $T = 238$ K (solid phase) showing the long-lived oscillatory behavior of the velocity autocorrelation function; (b) $T = 900$ K (liquid phase) showing the much faster loss of correlation (note change in horizontal scale).

from the same atomic *bcc* crystal as considered above, the protons were seen to spontaneously pair into molecules. This behavior has since been confirmed by the extensive simulations of Hohl et al. [5], using the Car-Parrinello method [3].

We report here on a simulation for $v_s = 1.86$ in which the molecular phase is assumed *a priori*. In Figure 8 the radial distribution function is shown for a system of 64 protons and electrons, in which the protons are initially paired with the same separation as occurs in the isolated H_2 molecule. The system is left to self-consistently evolve at temperature 2000 K. The sharp peak in the radial distribution function, which occurs at $r_s = 1.45$, attests to the continued existence of the molecules, while the much broader peak to the right is due to the distance between protons in different molecules. The molecular system is in the liquid state, with unbounded diffusion. Thus, the power spectrum shown in Figure 9 contains both a broad, low frequency peak, due to the diffusive motion of the molecules, and an outlying peak at the

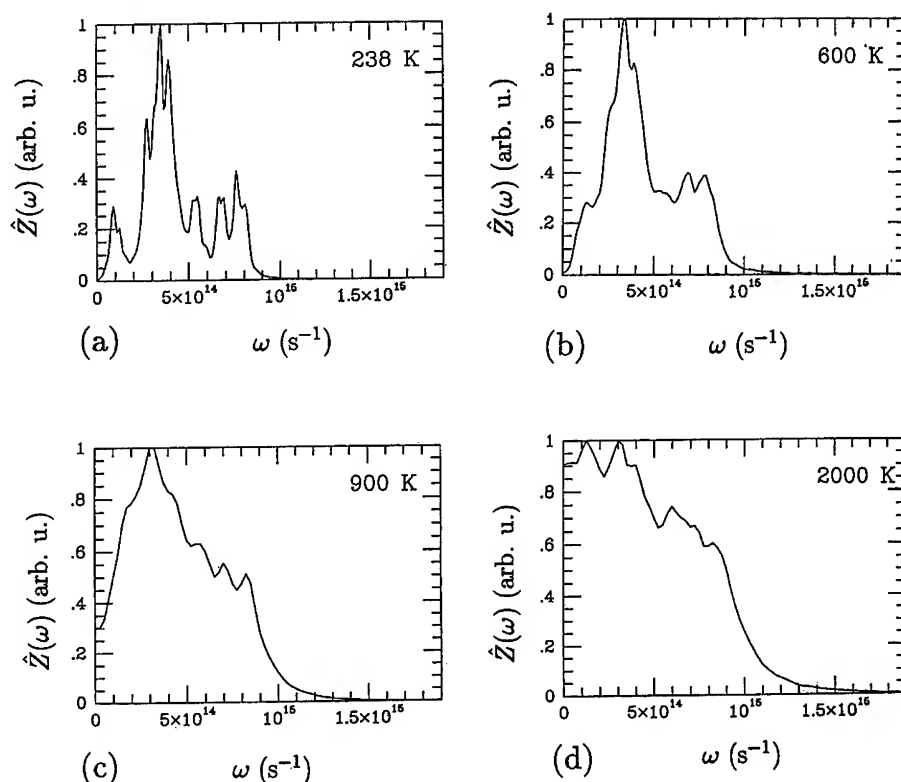


Figure 6. Proton velocity power spectra; (a) $T = 238$ K (solid phase) showing the distinct *bcc* lattice phonon frequencies; (b) $T = 600$ K (solid phase) showing the merging of the phonon peaks due to anharmonicity; (c) $T = 900$ K (liquid phase) showing finite proton self-diffusion, $\hat{Z}(0) \neq 0$; (d) $T = 2000$ K (liquid phase) showing an almost all-diffusive power spectrum.

“vibron” frequency $\omega \approx 7.8 \times 10^{14} \text{ s}^{-1}$. This latter frequency is approximately equal to the vibrational frequency of the isolated hydrogen molecule ($\omega_e = 8.28 \times 10^{14} \text{ s}^{-1}$, Ref. [16]), but also includes numerical errors due to the finite accuracy of the density-functional scheme [1], as well as the physical effects of anharmonicity and many-body interactions.

Conclusions

A first-principles scheme based on a time-dependent, quantum-mechanical modeling of the electrons, coupled to classical equations of motion for the protons, was implemented on a parallel computer, and applied to the study of dense hydrogen. We have estimated the melting temperature of metallic hydrogen at density 2.7 g cm^{-3} ($r_s = 1$) to be approximately 850 K, and we have investigated its dynamical properties both below and above the melting point. A large deviation from the prediction of the one-component plasma model ($T_m^{\text{OCP}} = 1773 \text{ K}$) was thus found

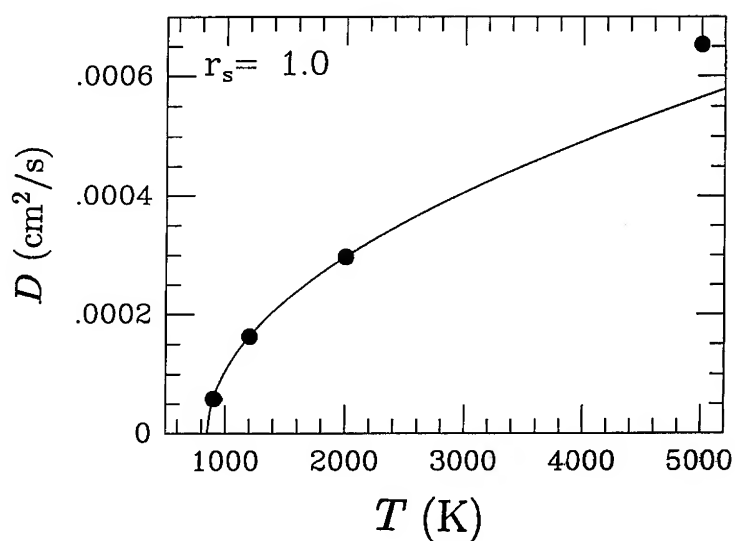


Figure 7. Proton self-diffusion coefficient in metallic hydrogen ($\rho = 2.7 \text{ g cm}^{-3}$, $r_s = 1$), plotted as a function of temperature. The dark line is the empirical fit, Eq. (16).

in the value of the melting temperature. The temperature dependence of the self-diffusion coefficient in the liquid metal was then examined, and in the range studied, found to obey a simple empirical relation.

Following the preliminary work of Ref. [1], a simulation of dense hydrogen in the molecular phase was also conducted, at density 0.16 g cm^{-3} ($r_s = 1.86$) and

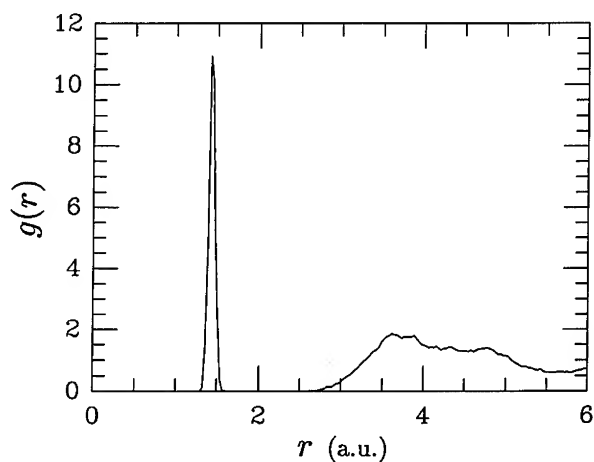


Figure 8. Radial distribution function for the molecular phase at 2000 K ($\rho = 0.16 \text{ g cm}^{-3}$, $r_s = 1.86$), obtained for a system of 64 protons and 64 electrons.

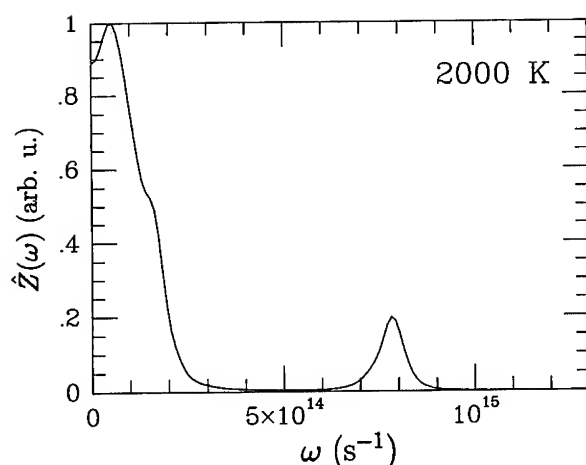


Figure 9. Velocity power spectrum for the molecular phase at 2000 K ($\rho = 0.16 \text{ g cm}^{-3}$, $r_s = 1.86$). The "vibron" peak at the right occurs at $\omega = 7.8 \times 10^{14} \text{ s}^{-1}$.

temperature 2000 K. Results were comparable to those obtained by Hohl et al. [5], with the first principles scheme predicting a molecular liquid, and correct molecular bond lengths and vibrational frequencies.

A systematic investigation of the density dependence of the melting temperature of metallic hydrogen and of its transport properties in the liquid phase is currently under way.

Acknowledgments

The author wishes to thank Drs. Robert Ferrell, Richard Shapiro, and Brond Larson for technical discussions pertaining to this work. The hospitality and support of Samuel B. Trickey and of the organizing committee of the 1994 Sanibel Symposium are also deeply appreciated.

Bibliography

- [1] J. Theilhaber, *Phys. Fluids* **B4**, 2044 (1992).
- [2] J. Theilhaber, *Phys. Rev.* **B46**, 12990 (1992).
- [3] R. Car and M. Parrinello, *Phys. Rev. Lett.* **55**, 2471 (1985).
- [4] G. Zerah, J. Cléroutin, and E. L. Pollock, *Phys. Rev. Lett.* **69**, 446 (1992).
- [5] D. Hohl, V. Natoli, D. M. Ceperley, and R. M. Martin, *Phys. Rev. Lett.* **71**, 541 (1993).
- [6] K. D. Brommer, M. Needels, B. E. Larson, and J. D. Joannopoulos, *Phys. Rev. Lett.* **68**, 1355 (1992).
- [7] J. P. Perdew and A. Zunger, *Phys. Rev.* **B23**, 5048 (1981).
- [8] W. C. Topp and J. J. Hopfield, *Phys. Rev.* **B7**, 1295 (1973).
- [9] G. B. Bachelet, D. R. Hamann, and M. Schlüter, *Phys. Rev.* **B26**, 4199 (1982).
- [10] High Performance Fortran Forum, *Scientific Programming* **2**, No. 1-2, 1 (1993).
- [11] E. Kaxiras and J. Broughton, *Phys. Rev. Lett.* **67**, 1138 (1991).
- [12] S. Nose, *Mol. Phys.* **52**, 255 (1984).

- [13] S. G. Brush, H. L. Sahlén, and E. Teller, *J. Chem. Phys.* **45**, 2102 (1966).
- [14] S. Ichimaru, *Plasma Physics: An Introduction to Statistical Physics of Charged Particles*, (Benjamin, Menlo Park, 1986), p. 184.
- [15] J. M. Dickey and A. Paskin, *Phys. Rev.* **188**, 1407 (1969).
- [16] C. W. Allen, *Astrophysical Quantities*, 3rd ed. (Athlone, London, 1973). p. 48.

Received May 5, 1994

Thermochemical Tests of a Kinetic-Energy Dependent Exchange-Correlation Approximation

AXEL D. BECKE

Department of Chemistry, Queen's University, Kingston, Ontario, Canada K7L 3N6

Abstract

We test an exchange-correlation functional with explicit dependence on kinetic-energy density as well as the density, its gradient, and its Laplacian, on the Gaussian-2 thermochemical data base. With a small degree of exact-exchange mixing, we find average errors with respect to experiment of order 2 kcal/mol, 0.15 eV, and 2 kcal/mol, respectively, for atomization energies, ionization potentials, and proton affinities.
© 1994 John Wiley & Sons, Inc.

Introduction

We are currently engaged in a systematic survey of density-functional exchange-correlation approximations in thermochemical applications [1–3]. Our survey has so far included the local spin-density approximation (LSDA), corrections to the LSDA depending on spin-density gradients (the GGA, or generalized gradient approximation), and mixtures of the latter with exact exchange. These various approximations have been tested on the Gaussian-2 (G2) thermochemical data set of Pople and coworkers [4] containing accurate experimental data on 56 atomization energies, 42 atomic and molecular ionization potentials, and 8 proton affinities of first and second-row systems. Very encouraging results have been obtained. The GGA/exact-exchange mixture of Ref. [3], for example, achieves absolute average errors with respect to experiment of only 2.4 kcal/mol, 0.14 eV, and 1.2 kcal/mol for the G2 atomization energies, ionization potentials, and proton affinities, respectively.

In the present work, we similarly assess an exchange-correlation approximation with explicit dependence on *kinetic-energy* density as well as the density, its gradient, and its Laplacian. The exchange part of the present approximation was introduced several years ago in Ref. [5], and the correlation part in Ref. [6]. Despite the age of these functionals, they have not until now been tested in thermochemical applications due to their complexity in comparison with the GGA. Given the success of the GGA tests of Refs. [1–3], however, exploration of this more complicated class of exchange-correlation approximations is called for. In the following sections, we briefly review the work of Refs. [5] and [6], and then we report the results of the present thermochemical tests.

Exchange

The reader should consult Ref. [5] for a detailed account of the present exchange approximation. Here, we review only the underlying physics.

The exchange energy $E_{X\sigma}$ of electrons of σ spin is given by

$$E_{X\sigma} = -\frac{1}{2} \iint \frac{\rho_{\sigma}(\mathbf{r}_1) \rho_{X\sigma}(\mathbf{r}_1, \mathbf{r}_2)}{r_{12}} d^3\mathbf{r}_1 d^3\mathbf{r}_2 \quad (1)$$

representing the interaction of the spin-density ρ_{σ} with an *exchange* charge (or exchange or Fermi “hole”) $\rho_{X\sigma}$ defined by

$$\rho_{X\sigma}(\mathbf{r}_1, \mathbf{r}_2) = \left| \sum_i \psi_{i\sigma}^*(\mathbf{r}_1) \psi_{i\sigma}(\mathbf{r}_2) \right|^2 / \rho_{\sigma}(\mathbf{r}_1). \quad (2)$$

The following constraints on $\rho_{X\sigma}$ are easily verified:

$$\rho_{X\sigma}(\mathbf{r}_1, \mathbf{r}_1) = \rho_{\sigma}(\mathbf{r}_1) \quad (3)$$

$$\int \rho_{X\sigma}(\mathbf{r}_1, \mathbf{r}_2) d^3\mathbf{r}_2 = 1 \quad (4)$$

and are valid at any reference point \mathbf{r}_1 in any system. Also, note that $\rho_{X\sigma}$ is always *positive*, and that only its *spherical average* around each reference point is required in the energy integral of Eq. (1).

Furthermore, Taylor expansion of the spherically averaged $\rho_{X\sigma}$ around each reference point reveals its quadratic behavior for small values of the interelectronic separation:

$$\rho_{X\sigma}(\mathbf{r}, s) = \rho_{\sigma} + \frac{1}{6} (\nabla^2 \rho_{\sigma} - 2D_{\sigma}) s^2 + \dots \quad (5)$$

$$D_{\sigma} = \tau_{\sigma} - \frac{1}{4} (\nabla \rho_{\sigma})^2 / \rho_{\sigma} \quad (6)$$

with arguments (\mathbf{r}, s) denoting spherical average on a shell of radius s about the reference point \mathbf{r} , and with the positive definite kinetic-energy density τ_{σ} defined by

$$\tau_{\sigma} = \sum_i |\nabla \psi_{i\sigma}|^2. \quad (7)$$

Eq. (5) is *exact* at any reference point in any system with zero current density (see Ref. [7] for the generalization to nonzero currents).

We introduced in Ref. [5] a relatively simple model, inspired by $\rho_{X\sigma}$ in the special case of the hydrogenic atom, able to satisfy the conditions of Eqs. (3)–(5) at all reference points in any system with *no empirical parameters*. The resulting exchange functional is unfortunately not expressible in closed analytical form, and we refer the reader to Ref. [5] for discussion of its evaluation. In atomic tests, our model gives significantly better exchange energies, by about an order of magnitude, than the exchange LSDA [5].

Our model does not, however, exactly treat the uniform electron gas, resulting in systematic underestimation of exchange energies in the heavy-atom limit (see Ref. [5]). We therefore introduced an *ad hoc* parameter γ designed to enforce the uniform gas limit, at the expense of slightly altering the quadratic behavior in Eq. (5). Though this manipulation somewhat improves the exchange energies of heavy atoms, we do *not* employ it here. In the present work, we use the unaltered form (i.e., $\gamma = 1$) of our model.

Correlation

As with exchange, we refer the reader to a previous article (Ref. [6]) for a full account of our correlation approximation.

Our correlation approximation is based on well-known interelectronic cusp conditions on the correlation hole, and the *zero-charge* sum rule as opposed to the *unit-charge* sum rule, Eq. (4), for exchange. Since opposite and parallel-spin electron pairs are governed by *different* cusp conditions, we obtain separate functionals for opposite-spin and parallel-spin correlation energies:

$$E_C^{\text{opp}} = -0.8 \int \rho_{\alpha} \rho_{\beta} z_{\alpha\beta}^2 \left[1 - \frac{\ln(1 + z_{\alpha\beta})}{z_{\alpha\beta}} \right] d^3\mathbf{r} \quad (8)$$

$$E_C^{\sigma\sigma} = -0.01 \int \rho_{\sigma} D_{\sigma} z_{\sigma\sigma}^4 \left[1 - \frac{2}{z_{\sigma\sigma}} \ln \left(1 + \frac{z_{\sigma\sigma}}{2} \right) \right] d^3\mathbf{r} \quad (9)$$

where the parallel-spin functional Eq. (9) again involves the kinetic-energy density τ_{σ} through the function D_{σ} of Eq. (6), and where E_C^{opp} and $E_C^{\sigma\sigma}$, respectively, involve the correlation “lengths” or “ranges” $z_{\alpha\beta}$ and $z_{\sigma\sigma}$. These are defined (see Ref. [6]) as the interelectronic separations at which the opposite and the parallel-spin correlation holes cross zero (as they must, due to the zero-charge sum rule).

For the correlation ranges $z_{\alpha\beta}$ and $z_{\sigma\sigma}$, we apply reasonable physical intuition. Since each electron is screened, in effect, by its *Fermi* hole $\rho_{X\sigma}$, we assume that the correlation range for the $\sigma\sigma'$ pair is related to a sum of the Fermi hole radii R_F^{σ} and $R_F^{\sigma'}$:

$$z_{\sigma\sigma'} = c_{\sigma\sigma'} (R_F^{\sigma} + R_F^{\sigma'}) \quad (10)$$

where $c_{\sigma\sigma'}$ is a constant of proportionality with only two independent values: $c_{\alpha\beta} = c_{\beta\alpha}$ for opposite-spin pairs, and $c_{\alpha\alpha} = c_{\beta\beta}$ for parallel-spin pairs. Moreover, we assume that the Fermi hole “radius” R_F^{σ} is given by the inverse of the coulomb potential $U_{X\sigma}$ arising from $\rho_{X\sigma}$:

$$R_F^{\sigma} = U_{X\sigma}^{-1} \quad \text{and} \quad U_{X\sigma}(\mathbf{r}_1) = \int \frac{\rho_{X\sigma}(\mathbf{r}_1, \mathbf{r}_2)}{r_{12}} d^3\mathbf{r}_2 \quad (11)$$

where $U_{X\sigma}$ is computed from the present τ -dependent exchange functional in the manner of Ref. [5]. Herein lies a minor deviation from our original work of Ref. [6]. In Ref. [6], we used an old and now-outdated exchange GGA [8] to determine

$U_{\chi\sigma}$ at each reference point, whereas we now employ the exchange model of the preceding section.

The correlation range parameters may be determined by fitting to exact correlation energies of atoms, and for this purpose we use the recent compilations of Davidson and coworkers [9]. The value $c_{\alpha\beta} = 0.63$ has been determined by the correlation energy of the helium atom, and a least squares fit to the remaining atoms in the first and second rows (minimizing the *relative* deviation from experiment) gives $c_{\alpha\alpha} = 0.88$. The resulting correlation energies are presented in Table I, and the overall rms relative deviation from experiment is 4.9%.

Thermochemical Tests

The explicitly τ -dependent functionals described above have been tested on the atoms and molecules of the G2 thermochemical data set of Pople and coworkers [4] using the fully numerical NUMOL density-functional program [10]. For now, our computations are post-LSDA: that is, performed using LSDA orbitals and densities. Complete self-consistency will require considerable effort to implement, because τ dependence introduces awkward complications in the orbital equation [11]. These will be discussed elsewhere. Note that the post-LSDA nature of this work precludes the computation of electron affinities, since the LSDA does not bind anions. We therefore restrict our tests to the G2 atomization energies, ionization potentials, and proton affinities only.

TABLE I. Atomic correlation energies (a.u.).

	Exact ^a	PW ^b
H	0.000	0.000
He	-0.042	-0.042
Li	-0.045	-0.053
Be	-0.094	-0.090
B	-0.125	-0.126
C	-0.156	-0.160
N	-0.188	-0.192
O	-0.258	-0.259
F	-0.325	-0.315
Ne	-0.390	-0.365
Na	-0.396	-0.389
Mg	-0.438	-0.431
Al	-0.470	-0.470
Si	-0.505	-0.508
P	-0.540	-0.543
S	-0.605	-0.615
Cl	-0.666	-0.675
Ar	-0.722	-0.730

^a Exact: Ref. [9].

^b PW: present work, using Hartree-Fock orbitals and densities [12].

TABLE II. Atomization energies D_0 (kcal/mol).

	Expt. ^a	PW ^b	Eq. (12) ^c		Expt. ^a	PW ^b	Eq. (12) ^c
H ₂	103.5	101.5	104.3	O ₂	118.0	128.7	121.5
LiH	56.0	55.8	57.1	H ₂ O ₂	252.3	251.0	248.7
BeH	46.9	53.7	54.5	F ₂	36.9	43.3	35.4
CH	79.9	77.5	79.2	CO ₂	381.9	391.9	384.1
CH ₂ (³ B ₁)	179.6	178.6	181.4	SiH ₂ (¹ A ₁)	144.4	140.5	145.3
CH ₂ (¹ A ₁)	170.6	165.1	168.9	SiH ₂ (³ B ₁)	123.4	119.5	123.5
CH ₃	289.2	286.0	291.7	SiH ₃	214.0	205.8	212.8
CH ₄	392.5	386.6	394.6	SiH ₄	302.8	292.2	302.2
NH	79.0	77.8	79.0	PH ₂	144.7	141.7	146.8
NH ₂	170.0	167.9	170.8	PH ₃	227.4	219.3	226.8
NH ₃	276.7	271.4	276.3	H ₂ S	173.2	168.5	173.0
OH	101.3	101.6	102.1	HCl	102.2	100.2	102.1
H ₂ O	219.3	217.5	218.9	Na ₂	16.6	16.4	16.1
HF	135.2	136.6	135.9	Si ₂	74.0	74.5	75.0
Li ₂	24.0	19.4	20.4	P ₂	116.1	113.3	114.2
LiF	137.6	143.6	140.2	S ₂	100.7	106.3	105.2
C ₂ H ₂	388.9	388.2	389.9	Cl ₂	57.2	57.2	56.3
C ₂ H ₄	531.9	526.6	534.0	NaCl	97.5	93.1	94.1
C ₂ H ₆	666.3	653.2	666.6	SiO	190.5	193.0	188.9
CN	176.6	181.6	175.2	CS	169.5	169.9	167.3
HCN	301.8	303.2	301.7	SO	123.5	131.5	126.7
CO	256.2	258.3	254.5	ClO	63.3	70.3	65.1
HCO	270.3	276.0	273.2	ClF	60.3	65.0	60.7
H ₂ CO	357.2	357.5	357.8	Si ₂ H ₆	500.1	478.8	495.6
CH ₃ OH	480.8	473.0	479.4	CH ₃ Cl	371.0	364.3	371.0
N ₂	225.1	223.7	219.9	CH ₃ SH	445.1	435.6	445.0
N ₂ H ₄	405.4	393.6	400.4	HOCl	156.3	156.6	154.9
NO	150.1	153.5	148.1	SO ₂	254.0	259.8	251.1

^a Expt: from Refs. [4] and [13].^b PW: present work with $c_{\alpha\beta} = 0.63$ and $c_{\alpha\alpha} = 0.88$.^c Eq. (12): with $c_X = 0.154$, $c_{\alpha\beta} = 0.66$ and $c_{\alpha\alpha} = 0.88$.

In Tables II, III, and IV, we list atomization energies, ionization potentials, and proton affinities, respectively, of the G2 data set. Column "PW" of each table contains data for the exchange-correlation approximation of the present work. The average absolute deviations from experiment are 4.6 kcal/mol for the atomization energies, 0.15 eV for the ionization potentials, and 2.8 kcal/mol for the proton affinities. These errors are similar to those of the generalized gradient approximation (GGA) reported in Ref. [2] (i.e., 5.7 kcal/mol, 0.15 eV, and 1.5 kcal/mol).

The data in the third columns of Tables II, III, and IV are obtained by replacing a small fraction of the present exchange approximation with *exact* (essentially Hartree-Fock) exchange as follows:

$$E_{XC} = E_X^{\text{model}} + c_X(E_X^{\text{exact}} - E_X^{\text{model}}) + E_C^{\text{opp}} + E_C^{\alpha\alpha} + E_C^{\beta\beta}. \quad (12)$$

TABLE III. Ionization potentials (eV).

	Expt. ^a	PW ^b	Eq. (12) ^c
H	13.60	13.62	13.61
He	24.59	24.97	25.05
Li	5.39	5.42	5.42
Be	9.32	8.96	9.03
B	8.30	8.62	8.63
C	11.26	11.58	11.57
N	14.54	14.89	14.86
O	13.61	13.94	13.91
F	17.42	17.77	17.71
Ne	21.56	21.97	21.88
Na	5.14	5.36	5.31
Mg	7.65	7.59	7.61
Al	5.98	5.80	5.84
Si	8.15	8.01	8.05
P	10.49	10.40	10.44
S	10.36	10.33	10.43
Cl	12.97	12.97	13.05
Ar	15.76	15.80	15.86
CH ₄	12.62	12.56	12.62
NH ₃	10.18	10.25	10.23
OH	13.01	13.18	13.16
H ₂ O	12.62	12.71	12.68
HF	16.04	16.23	16.17
SiH ₄	11.00	10.77	10.90
PH	10.15	10.12	10.15
PH ₂	9.82	9.80	9.84
PH ₃	9.87	9.79	9.83
SH	10.37	10.33	10.41
SH ₂ (² B ₁)	10.47	10.36	10.42
SH ₂ (² A ₁)	12.78	12.59	12.66
HCl	12.75	12.71	12.77
C ₂ H ₂	11.40	11.34	11.34
C ₂ H ₄	10.51	10.48	10.46
CO	14.01	14.02	14.18
N ₂ (² Σ _g)	15.58	15.55	15.81
N ₂ (² Π _u)	16.70	16.73	16.77
O ₂	12.07	12.46	12.55
P ₂	10.53	10.63	10.83
S ₂	9.36	9.38	9.49
Cl ₂	11.50	11.17	11.32
ClF	12.66	12.45	12.58
CS	11.33	11.26	11.36

^a Expt: from Refs. [4] and [13].^b PW: present work with $c_{\alpha\beta} = 0.63$ and $c_{\alpha\alpha} = 0.88$.^c Eq. (12): with $c_X = 0.154$, $c_{\alpha\beta} = 0.66$ and $c_{\alpha\alpha} = 0.88$.

TABLE IV. Proton affinities (kcal/mol).

	Expt. ^a	PW ^b	Eq. (12) ^c
H ₂	100.8	97.0	97.8
C ₂ H ₂	152.3	151.0	153.0
NH ₃	202.5	199.4	201.6
H ₂ O	165.1	160.2	162.3
SiH ₄	154.0	152.6	152.6
PH ₃	187.1	183.5	185.5
H ₂ S	168.8	166.8	167.6
HCl	133.6	131.5	132.1

^a Expt: from Refs. [4] and [13].^b PW: present work with $c_{\alpha\beta} = 0.63$ and $c_{\alpha\alpha} = 0.88$.^c Eq. (12): with $c_X = 0.154$, $c_{\alpha\beta} = 0.66$ and $c_{\alpha\alpha} = 0.88$.

Small admixture of exact exchange is motivated by the coupling-strength integration formula of Kohn–Sham theory, and was proposed in Ref. [3] to which we refer the reader for further discussion. For the present τ -dependent exchange-correlation model, Eq. (12) is the analog of Eq. (2) in Ref. [3] for the GGA. We find that exact-exchange mixing improves thermochemical results insignificantly unless the correlation range parameter $c_{\alpha\beta}$ has slightly larger value than its atomic helium value. The outcome of a two-parameter fit to the G2 data, with $c_{\alpha\beta} = 0.66$ and an exact-exchange mixing fraction of $c_X = 0.154$, is recorded in Tables II, III, and IV. Average error in the atomization energies is reduced to a remarkably small 1.8 kcal/mol, with errors in the ionization potentials and proton affinities of 0.14 eV and 1.6 kcal/mol, respectively. The average errors of the analogous GGA plus exact-exchange theory of Ref. [3] are 2.4 kcal/mol, 0.14 eV, and 1.2 kcal/mol.

Conclusions

The functionals of this work give slightly better atomization energies than their GGA counterparts. They are based, however, on a totally different philosophy. The GGA relies on the uniform electron gas as starting point, and adds gradient-dependent corrections to account for local inhomogeneities. As such the GGA does not treat the simplest conceivable chemical system, the hydrogenic atom, exactly. Conversely, the functionals of the present work are inspired by the hydrogenic atom as a prototypical system, but do not exactly treat the uniform electron gas. Interestingly, these two rather different approaches give results of comparable quality in these molecular tests. We are now investigating their relative merits in transition-metal chemistry.

In summary, contemporary exchange-correlation approximations, whether of the GGA variety or the present τ -dependent variety, typically yield average errors with respect to experiment of 5 kcal/mol, 0.15 eV, and 2 kcal/mol, respectively, for the atomization energies, ionization potentials, and proton affinities of the G2

data base [4]. With exact-exchange mixing of order 15–20%, as espoused in Ref. [3] the average error of the atomization energies may be reduced to order 2 kcal/mol.

Acknowledgments

This work is supported by the Natural Sciences and Engineering Research Council of Canada.

Bibliography

- [1] A. D. Becke, *J. Chem. Phys.* **96**, 2155 (1992).
- [2] A. D. Becke, *J. Chem. Phys.* **97**, 9173 (1992).
- [3] A. D. Becke, *J. Chem. Phys.* **98**, 5648 (1993).
- [4] J. A. Pople, M. Head-Gordon, D. J. Fox, K. Raghavachari, and L. A. Curtiss, *J. Chem. Phys.* **90**, 5622 (1989); L. A. Curtiss, C. Jones, G. W. Trucks, K. Raghavachari, and J. A. Pople, *J. Chem. Phys.* **93**, 2537 (1990); L. A. Curtiss, K. Raghavachari, G. W. Trucks, and J. A. Pople, *J. Chem. Phys.* **94**, 7221 (1991).
- [5] A. D. Becke and M. R. Roussel, *Phys. Rev. A* **39**, 3761 (1989).
- [6] A. D. Becke, *J. Chem. Phys.* **88**, 1053 (1988).
- [7] J. F. Dobson, *J. Chem. Phys.* **98**, 8870 (1993).
- [8] A. D. Becke, *J. Chem. Phys.* **85**, 7184 (1986).
- [9] S. J. Chakravorty, S. R. Gwaltney, E. R. Davidson, F. A. Parpia, and C. Froese Fischer, *Phys. Rev. A* **47**, 3649 (1993).
- [10] A. D. Becke, *Int. J. Quantum Chem., Quantum Chem. Symp.* **23**, 599 (1989).
- [11] J. F. Dobson, *J. Phys. Condens. Matt.* **4**, 7877 (1992).
- [12] E. Clementi and C. Roetti, *At. Data Nucl. Data Tables* **14**, 177 (1974).
- [13] P. M. W. Gill, B. G. Johnson, J. A. Pople, and M. J. Frisch, *Int. J. Quantum Chem., Quantum Chem. Symp.* **26**, 319 (1992).

Received May 13, 1994

Density-Functional LCAO Calculations for Solids: Comparison between Hartree-Fock and Kohn-Sham Structural Properties

MAURO CAUSÁ

*Department of Inorganic, Physical, and Materials Chemistry, University of Torino,
Via P. Giuria 5, 10125 Torino, Italy*

ALEŠ ZUPAN

*Department of Physical and Environmental Chemistry, "Jožef Stefan" Institute,
Jamova 39, 61111 Ljubljana, Slovenia*

Abstract

The Density-Functional method, with Linear Combination of Atomic Orbitals, has been applied to eight crystals: the lattice equilibrium parameters, and the lattice formation energies have been calculated at the Hartree-Fock level (HF), at the hybrid Hartree-Fock Density-Functional level (DFT/HF), and at the Kohn-Sham Density-Functional level (DFT). The band structures and the electronic charge distributions calculated at the DFT and HF levels are compared. © 1994 John Wiley & Sons, Inc.

Introduction

Computational methods connected with the Density-Functional Theory have for many years been applied to crystalline solids, using various basis sets to expand the one-electron Bloch orbitals, such as plane waves [1], muffin-tin orbitals [2], and augmented plane waves [3]. Recently DFT methods have been applied extensively to molecular systems [4–12]. With the use of the Linear Combination of Atomic Orbitals (LCAO) method, the DFT has been successfully compared with the Hartree-Fock method and with the standard molecular correlation methods, like Configurations Interaction, the perturbative and the Coupled Cluster methods. Only a few examples of the periodic LCAO DFT method exist in the literature [13]. In the present work, the Hartree-Fock LCAO method for periodic systems [14] has been modified to deal with DFT methods. The comparison is now possible between DFT and HF related methods for condensed systems, in a way strictly analogous to molecular systems. The CRYSTAL [15] suite of programs has therefore been generalized in order to apply DFT LCAO methods as well as the HF LCAO technique to bulk crystals, slabs, as models of surfaces, polymers, and molecules.

At a first stage [16,17] the correlation energy functionals have been taken into consideration: the Colle-Salvetti [18] and Perdew [19] correlation functionals have been applied to the Hartree-Fock electronic density, in the so called *a posteriori*

DFT correlation method. Then the exchange-correlation energy functionals have been applied *a posteriori* to the HF density [20]: this method has been defined as the hybrid DFT-HF method. The hybrid method has been applied to a set of 20 covalent and ionic crystals. In the present work the Density-Functional Theory, in the Local-Density Approximation (LDA), has been introduced to the Self-Consistent Field (SCF) process, resolving at each stage the Kohn-Sham (KS) equations, instead of the Hartree-Fock equations. It is thus possible to compare not only the HF and DFT energies (and the structural related quantities), but also the eigenvalue spectra and the observables related with the first order density matrix, such as the electronic charge distribution in the direct or in the momentum space.

With the computer program developed in the present work it is therefore possible to study the electronic structure at the Hartree-Fock or Kohn-Sham level, by using the same computational conditions, like the basis set or the limits and approximation of the infinite sums of interactions. With the use of gaussian basis sets, obtained by a few modifications of the molecular basis sets, the periodic and the molecular systems can be treated in the same way, and the genuine solid state effects, that arise from the application of the DFT and the HF methods, can be explored.

Methods and Computational Details

In this work the Hartree-Fock electron density ρ_{HF} and the Kohn-Sham density ρ_{KS} have been calculated. In the following, $\rho_{\text{HF/KS}}$ indicates both HF and KS densities:

$$\rho_{\text{HF/KS}}(\vec{r}) = \int_{\text{Brill. Zone}} d\vec{k} \sum_i^{\text{occ. bands}[\vec{k}]} |\varphi_{i,\text{HF/KS}}^{\vec{k}}(\vec{r})|^2.$$

The crystalline orbitals $\varphi_{i,\text{HF/KS}}^{\vec{k}}(\vec{r})$ are a solution of the one-particle equations:

$$\hat{h}_{\text{HF/KS}} \varphi_{i,\text{HF/KS}}^{\vec{k}}(\vec{r}) = \epsilon_i^{\vec{k}} \varphi_{i,\text{HF/KS}}^{\vec{k}}(\vec{r}).$$

The Hartree-Fock mono-electronic operator is defined as follows:

$$\hat{h}_{\text{HF}} = \hat{t} + \hat{v} + \hat{J}[\rho(\vec{r})] + \hat{K}_{\text{HF}}[\rho(\vec{r}, \vec{r}')],$$

where \hat{t} , \hat{v} , \hat{J} , and \hat{K} are, respectively, the kinetic, the external-potential, the Coulomb, and the exchange operators. The infinite lattice sums, that are implicit in the direct lattice implementation of the LCAO periodic HF method are limited and approximated as described in Ref. [14].

The Kohn-Sham mono-electronic operator is defined as follows:

$$\hat{h}_{\text{KS}} = \hat{t} + \hat{v} + \hat{J}[\rho(\vec{r})] + \hat{v}^{X-C}(\vec{r}).$$

The exchange-correlation potential v^{X-C} is the functional derivative of the exchange-correlation Density-Functional Energy:

$$v^{X-C}(\vec{r}) = \frac{\delta E^{X-C}[\rho]}{\delta \rho(\vec{r})}; \quad E^{X-C} = \int_{\text{UNIT CELL}} d\vec{r} \epsilon^{X-C}[\rho](\vec{r}).$$

Only few examples of application of DFT correlation and Hartree-Fock exchange can be found in the literature [21]. The main reason is that the HF density of molecules is affected by the lack of static correlation, while the local (or gradient) DFT exchange densities are less affected by this problem [22]: on the other hand, correlation DFT takes only dynamical effects into account. For covalent and ionic solids the static correlation is probably less important: * so the HF electronic density could be a good basis for the application of correlation DFT. In the present work both the approaches have been followed: exchange and correlation have been treated by DFT (using \hat{v}^{XC} potential) and also calculations with HF "exact" exchange and DFT correlation have been performed. In this way the effects of the DFT exchange and correlation on the electronic density and on the band structure (better defined as the one-particle eigenvalue spectrum) have been separately studied. Thus, a correlation-only Kohn-Sham operator $\hat{h}_{\text{HF-KS correl}}$ has been defined:

$$\hat{h}_{\text{HF-KS correl}} = \hat{t} + \hat{v} + \hat{J}[\rho(\vec{r})] + \hat{K}_{\text{HF}}[\rho(\vec{r}, \vec{r}')] + \hat{v}^C(\vec{r}).$$

This method will be defined in the following as HF-LDA.

In DFT LCAO methods, the ν^{X-C} potential is represented in a basis set of gaussian atomic orbitals $\chi_\mu(\vec{r} - \vec{g})$, where \vec{g} labels the unit where the μ th orbital is located. The integrals:

$$\nu_{\mu;v,\vec{g}}^{X-C} = \int_{\text{SPACE}} d\vec{r} \chi_\mu(\vec{r}) \nu^{X-C}(\vec{r}) \chi_v(\vec{r} - \vec{g}).$$

must be calculated numerically, owing to the complex analytical expression of the exchange-correlation potentials ν^{X-C} , even at a local level. The analytical method for calculating DFT matrix elements, recently proposed by Almlöf [23], is computationally too expensive to be used in LCAO calculations of periodic systems. Instead of performing the numerical integration directly over each pair of atomic orbitals (for each unit cell \vec{g}), in the present work the exchange-correlation potential has been expanded in the following way:

$$\nu^{X-C}(\vec{r}) \cong \sum_j^N c_j G_j(\vec{r}).$$

The fitting functions G_j are linear combinations of gaussian-type functions, total symmetric with respect to translations and rotations: the exchange-correlation potential $\nu^{X-C}(\vec{r})$ is a basis of the total symmetric irreducible representation of the space group. The DFT potential integrals are consequently:

$$\nu_{\mu;v,\vec{g}}^{X-C} = \sum_i^N c_i g_{\mu;v,\vec{g}}^i,$$

$$g_{\mu;v,\vec{g}}^j = \int_{\text{SPACE}} d\vec{r} \chi_\mu(\vec{r}) G_j(\vec{r}) \chi_v(\vec{r} - \vec{g}).$$

* Work is in progress in our laboratory to analyze the correlation of ionic solids with the usual "chemical" concepts of static and dynamic correlations.

The integrals $g_{\mu;p,\vec{g}}^j$ are calculated only once analytically, and stored. At each SCF iteration the best fitting coefficients are evaluated, c_j , by solving a linear least square equation:

$$\mathbf{A}\bar{c} = \bar{b}.$$

\mathbf{A} is the overlap matrix between the fitting functions:

$$A_{i,j} = \int_{\substack{\text{UNIT} \\ \text{CELL}}} d\vec{r} G_i(\vec{r}) G_j(\vec{r}).$$

\bar{c} is the vector of the unknown coefficients c_j ; \bar{b} is the vector of the constant coefficients b_j , that depend on the density, and are calculated numerically:

$$b_j = \int_{\substack{\text{UNIT} \\ \text{CELL}}} d\vec{r} G_j(\vec{r}) \nu^{X-C}(\vec{r}).$$

The last numerical integration has great advantages with respect to the direct numerical evaluation of the integrals $\nu_{\mu;p,\vec{g}}^{X-C}$: it is restricted to the unit cell, and the integrand is total symmetric. In this way the numerical integration can be limited to the irreducible set of points.

The fitting functions do not introduce any inaccuracy in the evaluation of the DFT matrix elements: in the present work a set of eight even-tempered gaussian functions for each atom have been employed: the exponential coefficients belong to an interval that goes from twice the highest exponent to the lower exponent of the Atomic Orbital basis set. Further fitting functions have been added in the bond regions. Only fitting functions with angular s symmetry have been adopted: p , d , and f functions do not give any contribution to the fitting, due to the cubic symmetry: g functions give unimportant contributions. The $\nu_{\mu;p,\vec{g}}^{X-C}$ integrals have been calculated numerically for silicon to test the effect of the fitting technique, with a high computational time (10 times the CPU time of the fitting method): the equilibrium lattice parameters change only by less than 0.001 Å, and total energy changes by 0.1 kcal/mol.

The numerical integration over the unit cell is performed by an extension to the periodic systems of the atomic partition method, introduced by Becke [24]. The fitting parameters b_j are calculated at each cycle of the SCF process with a moderate numerical accuracy (about 1000 points per atom), while the DFT energy is calculated at the end of the SCF process with high accuracy (about 10,000 points per atom). During the SCF process exponential weights are used [25], while the energy is calculated by means of a partition in overlapping Voronoi polyhedra [26]. The numerical integration technique, as well as the numerical accuracy, will be object of a separate analysis [26]. The limits of the lattice sums ensure an accuracy of 0.1 kcal/mol in the total energy.

In the present work eight cubic crystals have been considered, ranging from perfect covalency (Diamond, Si, Ge) to perfect ionicity (MgO, NaCl), including

partially ionic bond situations (BN, AlP, GaAs). For covalent and partially covalent systems, the 6-21G* basis set has been adopted [27]; the basis sets of the ionic systems have been optimized with periodic Hartree-Fock calculations [28].

The LDA energy correlation functional used in this work is the Perdew-Zunger [29] parametrization of the numerical results obtained by Ceperley and Alder for the electron gas [30]; the new parametrization proposed by Perdew and Wang [31] gives equivalent results for equilibrium lattice parameters and lattice formation energies. Gradient dependent functionals are defined by the Generalized Gradient Approximation (GGA), formulated by Becke for exchange energy (BEC) [32] and by Perdew for correlation energy (P91) [31].

Results and Discussion

In Tables I and II the lattice parameters, calculated by the different approximations, are compared. Table I contains results obtained with exchange-correlation energy functionals, while the data of Table II are calculated by a Hartree-Fock "exact exchange" energy functional plus correlation-only density functional. In each table the experimental and the HF data are reported for comparison.

HF systematically overestimates the lattice parameters. For first and second row covalent crystals (C, Si, Ge, BN, AlP, and GaAs) the error is about +0.05 angstroms (\AA), that corresponds to an error of +0.02 \AA in the bond lengths. The error increases to +0.12 \AA for GaAs, that belongs to the fourth row of the periodic table.

MgO and NaCl are almost totally ionic; the Mulliken charges of the cations are 1.95 and 0.99 at the HF level, respectively. At LDA level they appear slightly less ionic: the charges are 1.85 and 0.95, respectively. MgO is an example of ionic crystals that have a correct lattice parameter at HF level. On the other hand HF gives an error of +0.22 \AA for the lattice parameter of NaCl. The very different

TABLE I. Lattice parameters of crystals (in angstroms), calculated using exchange and correlation energy Density Functionals.

	Expt. [36]	HF	<i>a posteriori</i>	Kohn-Sham	<i>a posteriori</i>	Kohn-Sham
			LDA-LDA/HF	LDA-LDA/LDA-LDA	BEC-P91/HF	BEC-P91/LDA-LDA
Diamond	3.57	3.58	3.55	3.56	3.6	3.61
Si	5.43	5.49	5.43	5.42	5.48	5.49
Ge	5.66	5.81	5.85	5.85	5.86	5.87
BN	3.62	3.62	3.6	3.6	3.64	3.65
AlP	5.45	5.55	5.45	5.48	5.53	5.56
GaAs	5.65	5.77	5.77	5.78	5.78	5.79
MgO	4.20	4.21	4.18	4.19	4.27	4.27
NaCl	5.57	5.79	5.49	5.41	5.83	5.78

The electronic density is calculated by Hartree-Fock method (*a posteriori* columns) or by Kohn-Sham LDA, using exchange-correlation DFT potential (Kohn-Sham columns). The local (LDA) energy functional and the gradient corrected Perdew GGA (P91) are utilized.

TABLE II. Lattice parameters of crystals (in angstroms), calculated using Hartree-Fock "exact exchange" energy and correlation energy Density-Functional (HF-DFT method).

	Expt.	HF	<i>a posteriori</i>	Kohn-Sham	<i>a posteriori</i>	Kohn-Sham
			HF-LDA/HF	HF-LDA/HF-LDA	HF-P91/HF	HF-P91/HF-LDA
Diamond	3.57	3.58	3.53	3.53	3.51	3.51
Si	5.43	5.49	5.42	5.41	5.38	5.37
Ge	5.66	5.81	5.74	5.74	5.71	5.71
BN	3.62	3.62	3.57	3.57	3.55	3.55
AlP	5.45	5.55	5.47	5.47	5.42	5.42
GaAs	5.65	5.77	5.69	5.70	5.67	5.67
MgO	4.20	4.21	4.16	4.16	4.11	4.11
NaCl	5.57	5.79	5.68	5.67	5.47	5.47

The electronic density is calculated by HF method (*a posteriori* columns) or by Kohn-Sham LDA, using HF exchange potential and correlation DFT potential (Kohn-Sham columns). The local (LDA) energy functional and the gradient corrected Perdew GGA (P91) are utilized.

behavior of the two ionic crystals is due to the different importance of the electron correlation in the anions: the electronic structure of the Cl^- ion is highly influenced by the electronic correlation, while the O^{2-} ion is acceptably described at SCF level. All the DFT models give a parallel effect on the lattice parameters of MgO and NaCl. The local correlation-only DFT (HF-LDA) decreases the lattice parameters, giving errors of -0.04 and $+0.11$ Å, respectively. The gradient corrected correlation DFT (HF-P91) reduces the lattice parameters, giving errors of -0.10 and -0.20 Å. The local exchange (LDA-LDA) increases the lattice parameters, with respect to HF exchange, with errors of -0.02 and -0.08 Å. The gradient exchange (BEC-P91) expands the lattices, giving errors of $+0.07$ and $+0.25$ Å. Ionic crystals, for which electronic correlation is very important, confirm being the most difficult to treat by DFT and HF methods. Work is in progress to estimate the effect of other correlation techniques (such as Configurations Interaction, Perturbation Theory, and Coupled Cluster Method) on equilibrium parameter of NaCl.

As it is clear from the data in Tables I and II, the geometries of the crystals do not depend on the electronic density: on the other hand the geometries are strongly dependent on the method used to calculate the energy. This confirms the results of the application of DFT to molecular systems: the quality of the hybrid models [11] and Kohn-Sham methods [4,12] show that the HF density, when used to calculate the DFT energy, performs equally or even better than the KS density.

The difference between HF and KS density, even not detectable in the calculation of energy and of energy-related quantities, can be analyzed, for more deeply understanding the physical consequences of the two methods.

Figure 1(b) shows the difference between the Kohn-Sham density, in the Local-Density approximation, and the Hartree-Fock density, for silicon. LDA gives less electron density close to the core region ($r < 0.5$ Å) and in the bond region: this is due to the less effective Fermi hole that the LDA method builds around each

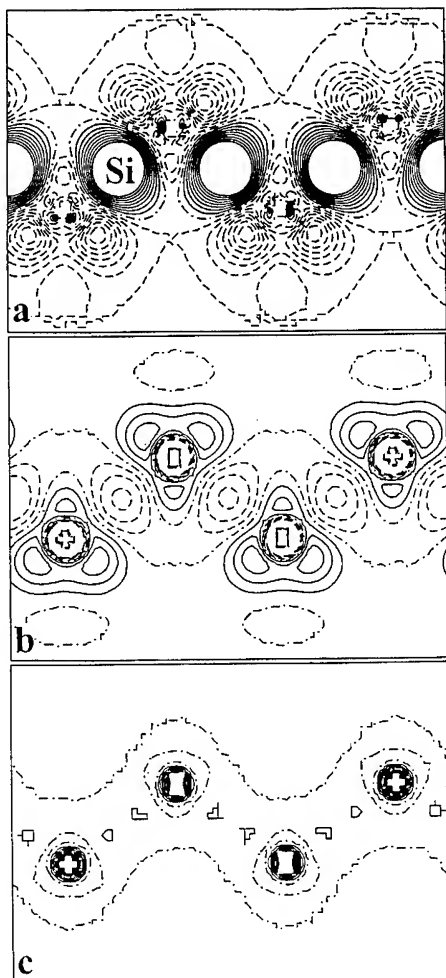


Figure 1. Comparison between LDA and HF electronic charge distribution (electron density) of silicon. Continuous lines correspond to positive values, dotted lines correspond to negative values, dot-dashed lines correspond to zero value. (a) Difference between HF density the crystal and overlapping free atom densities. Two contiguous lines correspond to a difference of 0.002 atomic units (electrons per cubic bohrs), (b) difference between LDA density and HF density. Two contiguous lines correspond to a difference of 0.002 a.u.; (c) difference between HF-LDA (Hartree-Fock exchange and LDA correlation) and HF density. Two contiguous lines correspond to a difference of 0.001 a.u.

electron in the high-density regions, with respect to the HF method. The electrons are then pushed out into regions away from the cores, in opposition to the Si—Si bonds, where the density is lower. Figure 2(a) (for MgO) confirms these features: in the regions where electronic density is higher, that is the core of the Mg^{2+} cation and the valence of the O^{2-} anion, the LDA concentrates fewer electrons on average

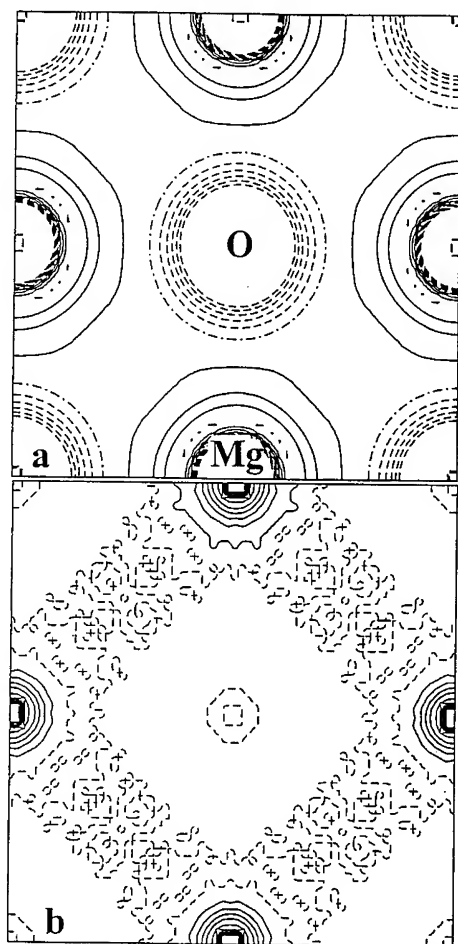


Figure 2. Comparison between LDA and HF electron densities of magnesium oxide. The symbols are as in Figure 1. The O^{2-} anion is in the center of the figure. (a) difference between LDA density and HF density. Two contiguous lines correspond to a difference of 0.001 a.u.; (b) difference between HF-LDA (Hartree-Fock exchange and LDA correlation) and HF density. Two contiguous lines correspond to a difference of 0.0005 a.u.

than the HF method: the electrons are then pushed to the regions where the density is lower, that is, the valence region of the cation. The difference between the HF density of silicon and the overlapping densities of silicon-free atoms is reported in Figure 1(a), for better understanding the scale of the differences between HF and KS densities. The chemical effects of Si—Si bond formation are more than one order of magnitude higher than the differences between the LDA and the KS density.

The LDA correlation effects are separately analyzed in Figures 1(c) and 2(b), in which the HF density is subtracted from the density obtained by an SCF process with the HF "exact exchange" potential and the LDA correlation potential. The

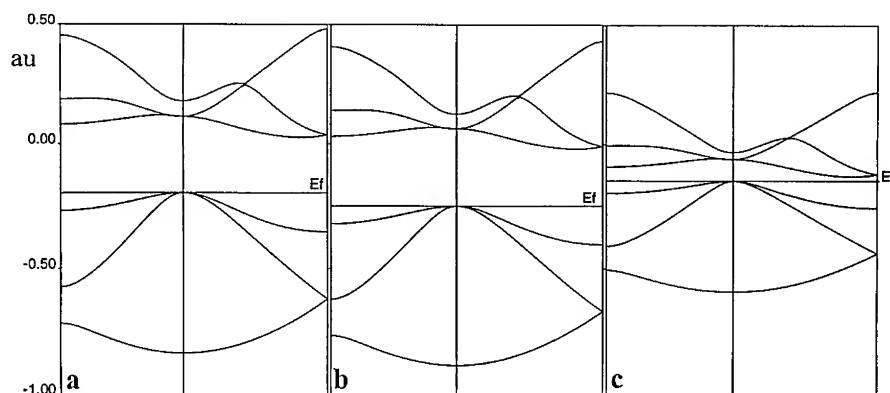


Figure 3. Band structure of silicon. The energy scale is in Hartree. The orbital zero energy is arbitrary, but common to the three models. (a) HF band structure; (b) HF-LDA band structure (HF exchange and LDA correlation). (c) LDA band structure (LDA exchange-correlation).

effects of correlation are one order of magnitude weaker than the exchange-correlation effects, and are confined in the cores of the heavier atoms, like silicon [Fig. 1(c)] and Mg [Fig. 2(b)]. The correlation effects in the core of the oxygen are not detectable on the same scale, confirming that the O^{2-} anion is well described at the HF level.

The band structures of Silicon and MgO are reported in Figures 3 and 4, following a path that connects the higher symmetry points of the First Brillouin zone of the reciprocal space. Figures 3(a) and 4(a) contain the HF band structures; 3(b) and 4(b) the HF-LDA bands; 3(c) and 4(c) the LDA bands. The LDA correlation stabilizes the one-particle orbitals by 1.1

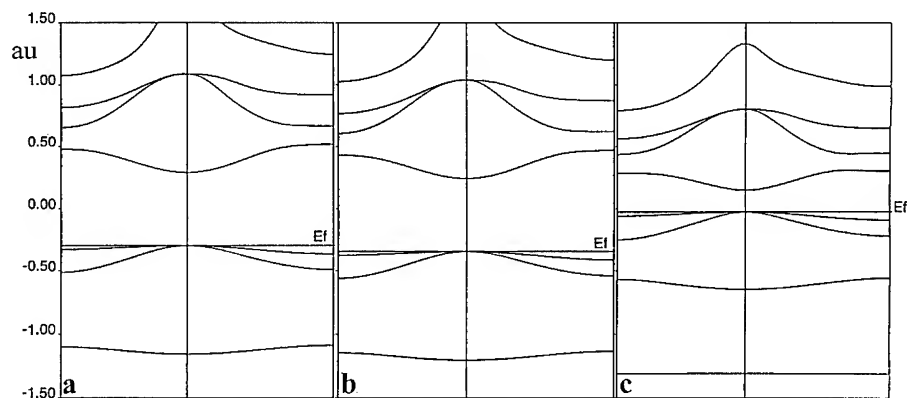


Figure 4. Band structure of Magnesium Oxide. Energy scale is in Hartree. (a) HF band structure, (b) HF-LDA band structure (HF exchange and LDA correlation), (c) LDA band structure (LDA exchange-correlation).

TABLE III. Formation energies of crystals (in Kcal/mol), calculated using exchange and correlation energy Density Functionals.

	Expt. [37]	HF	<i>a posteriori</i>	Kohn-Sham	<i>a posteriori</i>	Kohn-Sham
			LDA-LDA/HF	LDA-LDA/LDA-LDA	BEC-P91/HF	BEC-P91/LDA-LDA
Diamond	-339.	-249.	-409.	-420.	-344.	-351.
Si	-216.	-141.	-235.	-248.	-195.	-203.
Ge	-180.	-105.	-197.	-205.	-164.	-171.
BN	-314.	-222.	-367.	-380.	-308.	-316.
AlP	-192.	-125.	-222.	-231.	-186.	-192.
GaAs	-155.	-82.	-172.	-178.	-140.	-146.
MgO	-726.	-673.	-745.	-765.	-705.	-716.
NaCl	-189.	-182.	-196.	-212.	-179.	-185.

The electronic density is calculated by HF method (*a posteriori* columns) or by Kohn-Sham LDA, using exchange-correlation DFT potential (Kohn-Sham columns). The local (LDA) energy functional and the gradient corrected Perdew GGA (P91) are utilized.

eV for Si and by 1.5 eV for MgO, with respect to HF, while the gaps remain unchanged at values 7.0 and 16.1 eV, respectively. The LDA exchange-correlation, that does not contain the Exchange Self-Energy singularity [33], decreases the gaps to 0.5 and 3.2 eV. The band structures calculated in the present work are in agreement with the LDA band structures reported in the literature [34,35].

Tables III and IV report lattice formation energies. As for the geometries (Tables I and II) there are no great difference between the data calculated by the *a posteriori* and the Kohn-Sham method.

TABLE IV. Formation energies of crystals (in Kcal/mol), calculated using Hartree-Fock "exact exchange" energy and correlation energy Density Functional.

	Expt.	HF	<i>a posteriori</i>	Kohn-Sham	<i>a posteriori</i>	Kohn-Sham
			HF-LDA/HF	HF-LDA/HF-LDA	HF-P91/HF	HF-P91/HF-LDA
Diamond	-339.	-249.	-307.	-306.	-348.	-348.
Si	-216.	-141.	-190.	-186.	-221.	-218.
Ge	-180.	-105.	-152.	-151.	-177.	-176.
BN	-314.	-222.	-282.	-282.	-312.	-312.
AlP	-192.	-125.	-175.	-174.	-200.	-199.
GaAs	-155.	-82.	-130.	-130.	-150.	-150.
MgO	-726.	-673.	-721.	-721.	-727.	-726.
NaCl	-189.	-182.	-186.	-186.	-191.	-190.

The electronic density is calculated by HF method (*a posteriori* columns) or by Kohn-Sham LDA, using HF exchange potential and correlation DFT potential (Kohn-Sham columns). The local energy (LDA) functional and the gradient corrected Perdew GGA (P91) are utilized.

The HF method underestimates the lattice formation energies, by about 30%, while the LDA method overestimates the binding energies in all cases. The gradient corrected DFT, both at the correlation only and at the exchange-correlation level, gives accurate thermo-chemical data, compatibly with the quality of the basis set, that is double zeta plus polarization.

Conclusions

The Kohn-Sham Density-Functional structural results (equilibrium lattice parameters, and formation energies) confirm the trend observed for the corresponding data calculated by the hybrid DFT/HF method. The method used to compute total energy is much more relevant than the method used to calculate electronic density. Differences between the equilibrium geometries calculated using the HF or the KS electronic densities are only detectable for ionic crystals like NaCl, where the correlation effects are very important.

Bibliography

- [1] M. L. Cohen, *Structure and Bonding in Crystals*, M. O'Keeffe and A. Navrotsky, Eds. (New York, 1981), p. 25; A. Zunger, *ibid.*, p. 73.
- [2] O. K. Andersen, *Phys. Rev. B* **12**, 3060 (1975).
- [3] P. Blaha, K. Swarz, and P. Herzig, *Phys. Rev. Lett.* **54**, 1192 (1985).
- [4] A. D. Becke, *J. Chem. Phys.* **96**, 2155 (1992); *ibid.* **97**, 9173 (1992); *ibid.* **98**, 5648 (1993).
- [5] L. Fan and T. Ziegler, *J. Chem. Phys.* **94**, 6057 (1991).
- [6] A. Savin, H. Stoll, and H. Preuss, *Theor. Chim. Acta* **70**, 407 (1986); R. Merkle, A. Savin, and H. Preuss, *Chem. Phys. Lett.* **194**, 32 (1992).
- [7] A. Peluso, D. R. Salhaub, and A. Goursot, *Inorg. Chem.* **29**, 1544 (1990).
- [8] P. M. Boerrigter, G. te Velde, and E. J. Baerends, *Int. J. Quantum Chem.* **33**, 87 (1988).
- [9] C. W. Murray, G. J. Laming, N. C. Handy, and R. D. Amos, *Chem. Phys. Lett.* **199**, 551 (1992).
- [10] M. W. Gill, B. G. Johnson, J. A. Pople, and M. J. Frisch, *Chem. Phys. Lett.* **197**, 499 (1992).
- [11] B. G. Johnson, P. M. W. Gill, and J. A. Pople, *J. Chem. Phys.* **98**, 5612 (1993).
- [12] J. Andzeilm and E. Wimmer, *J. Chem. Phys.* **96**, 1280 (1992).
- [13] J. R. Chelcowsly and S. G. Louie, *Phys. Rev. B* **29**, 3470 (1984). G. te Velde and E. J. Baerends, *Phys. Rev. B* **44**, 7888 (1991).
- [14] R. Dovesi, C. Pisani, and C. Roetti, *Int. J. Quantum Chem.* **17**, 517; C. Pisani, R. Dovesi, and C. Roetti, *Hartree-Fock Ab Initio Treatment of Crystalline Systems*, Lecture Notes in Chemistry, vol. 48 (Springer-Verlag, Heidelberg, 1988).
- [15] R. Dovesi, C. Pisani, C. Roetti, M. Causá, and V. R. Saunders, *CRYSTAL 88. An Ab-initio all-electron LCAO-Hartree-Fock program for periodic systems*. QCPE Pgm N. 577, Quantum Chemistry Program exchange, Indiana University, Bloomington, IN 1989; R. Dovesi, V. R. Saunders, and C. Roetti, *CRYSTAL92 User's Manual*, Gruppo di Chimica Teorica, Univ. Torino, and Daresbury SERC Lab.
- [16] M. Causá, R. Dovesi, C. Pisani, R. Colle, and A. Fortunelli, *Phys. Rev. B* **36**, 891 (1987); M. Causá, R. Colle, A. Fortunelli, R. Dovesi, C. Pisani, *Phys. Scripta* **38**, 194 (1988).
- [17] M. Causá, R. Dovesi, and C. Roetti, *Phys. Rev. B* **43**, 11937 (1991).
- [18] R. Colle and O. Salvetti, *Theor. Chim. Acta* **37**, 329 (1975); *ibid.* **53**, 55 (1979).
- [19] J. P. Perdew, *Phys. Rev. B* **33**, 8822 (1986).
- [20] M. Causá and A. Zupan, *Chem. Phys. Lett.* **220**, 145 (1994).
- [21] E. Clementi, S. J. Chakravorty, G. Corongiu, and V. Carravetta, *In Modern Techniques in Computational Chemistry*, E. Clementi, Ed. (Escom, Leiden, 1989).
- [22] T. Ziegler, *Chem. Review.* **91**, 651 (1991).

- [23] J. Almlof, Conference in Electronic Structure (Girona, Spain, 1993).
- [24] A. D. Becke, J. Chem. Phys. **88**, 2547 (1988).
- [25] A. Savin, J. Jour. Quant. Chem. **S22**, 457 (1988).
- [26] M. Causá et al., J. Comp. Phys., to be submitted.
- [27] M. S. Gordon, J. S. Binkley, J. A. Pople, and W. J. Hehre, J. Am. Chem. Soc. **104**, 2797 (1982).
- [28] M. Causá, R. Dovesi, C. Pisani, and C. Roetti, Phys. Rev. **B33**, 1308 (1986).
- [29] J. P. Perdew and A. Zunger, Phys. Rev. **B23**, 5048 (1981).
- [30] D. M. Ceperley and B. J. Alder, Phys. Rev. Lett. **45**, 566 (1980).
- [31] J. P. Perdew and Y. Wang, Phys. Rev. **B45**, 13244 (1991); J. P. Perdew, J. A. Chevary, S. H. Vosko, M. R. Pederson, D. J. Singh, and C. Fiolhais, Phys. Rev. **B46**, 6671 (1992).
- [32] A. Becke, Phys. Rev. **A33**, 2786 (1986).
- [33] G. Assing and H. J. Monkhorst, Int. J. Quantum Chem Symp. **27**, 81 (1993).
- [34] A. Swane and O. K. Andersen, Phys. Rev. **B34**, 5512 (1986).
- [35] S. Froyen and M. L. Cohen, Phys. Rev. **B29**, 3770 (1984); S. Froyen and M. L. Cohen, J. Phys. **C19**, 2623 (1986).
- [36] R. W. G. Wyckoff, *Crystal Structures*, 2nd ed. (Interscience, New York, 1963).
- [37] The experimental atomization energies and lattice energies are calculated by standard heat of formation at 0 K, ionization potential, and electronic affinity reported in: *Handbook of Chemistry and Physics*, 72nd ed., (CRC, Boca Raton, 1990).

Received May 31, 1994

A Density Functional Study of the Interaction of CO₂ with a Pd Atom

SUZANNE SIROIS, MIGUEL CASTRO, and DENNIS R. SALAHUB

Département de Chimie, Université de Montréal, C.P. 6128 Succursale A, Montréal, Québec, H3X 2H9, Canada and Centre de Recherche en Calcul Appliqué, 5160, Boul. Décarie, Bureau 400, Montréal, Québec, H3X 2H9, Canada

Abstract

The interaction of the CO₂ molecule with a single palladium atom has been studied by means of a linear combination of Gaussian type orbitals–density functional (LCGTO–DF) method, as implemented in the code **deMon**. Local and nonlocal functionals were used. The core electrons of the palladium atom were represented by a model core potential, which includes relativistic effects. Several coordination modes of the CO₂ moiety to the Pd atom were studied. They were fully optimized by allowing both electronic and structural relaxation. The calculations indicate a dihapto CO (η^2 -CO) coordination mode (or mixed Pd–C/Pd–O bonding), of C_s symmetry, as the one of lowest energy. There is a strong charge transfer from Pd to CO₂, which produces a large structural change in CO₂: It goes from a linear to a bent geometry. The calculated frequencies of CO₂ in Pd–CO₂ are 689, 1212, and 2018 cm^{–1} for the bending, symmetric, and asymmetric vibrational modes, respectively. These results agree reasonably with the observed frequencies of CO₂ adsorbed on H₂O/Pd(110) and Pd(111)/Na surfaces. The η^2 -CO structure is a likely candidate for the adsorption of CO₂ on palladium surfaces, since the asymmetric mode is observed. This mode is dipole allowed in C_s symmetry but dipole forbidden in C_{2v}. The monohapto C (η^1 -C) coordination mode, of C_{2v} symmetry, was found to be a transition state, 2.2 and 8.4 kcal/mol, for the local and nonlocal levels, respectively, above the (η^2 -CO) minimum. The η^2 -O–O mode is not attainable for Pd–CO₂; calculations started with this configuration converge to the η^2 -CO mode, the ground state. This is a quite different picture to that found for Ni–CO₂, where the moiety is chemisorbed in the dihapto η^2 -O–O coordination mode. © 1994 John Wiley & Sons, Inc.

Introduction

The experimental and theoretical study of transition metal–ligand (TM–L) interactions has been of high interest during the last years [1,2]. In particular, the study of the adsorption of CO₂ on TM surfaces is potentially important, since CO₂ is a reaction product in the oxidation of CO, the catalytic hydrogenation of CO₂ is quite important in organic chemistry, and CO₂ can serve as an unexpensive reagent in some reduction processes [3]. Although there are many experimental studies of the adsorption of the carbon monoxide, CO, on metal surfaces [4,5,6] the adsorption of CO₂ has received less attention. Recently, experimental and theoretical chemists have been interested in the study of the bonding of CO₂ to TM clusters and surfaces. They have tried to determine its coordination behavior, so as to be able to consider the bonding and the reaction pathways [7] (ground and transition states).

Even though that CO_2 is highly unreactive, it is immediately activated in the presence of a TM surface. There have been proposed two ways for the fixation of CO_2 by a metal surface: physisorbed linear CO_2 species and chemisorbed (negatively charged) bent CO_2^- species. The latter form was predicted theoretically [8], and it has been observed on clean surfaces of $\text{Ni}(110)$ [9,10] as well as on surfaces which have been modified via alkali adsorption [11,12,13].

There is IR spectroscopic evidence which supports the existence of several $\text{M}-\text{CO}_2$ complexes. For instance, 1-to-1 $\text{M}-\text{CO}_2$ complexes have been made with the following metals [14]: Ni, Li, Na, K, and Cs. Also, some research has been done for Ti, V, Fe, Co, Ni, and Cu [15,16]. In the case of Pd, some complexes have been identified in which the Pd atom is coordinated to CO_2 and to other ligands [17]. But the 1-to-1 $\text{Pd}-\text{CO}_2$ complex has not been reported. Recently, Brosseau et al. [18], by means of HREELS spectroscopy, have shown conclusively that the CO_2 molecule is chemisorbed (in the presence of H_2O) onto the $\text{Pd}(110)$ surface as a negative moiety CO_2^- . A bent C_{2v} geometry was suggested for the chemisorbed CO_2^- , the bending and the stretching vibrational modes were assigned at 770 and 1200 cm^{-1} , respectively. Later on, the same authors [19] redid the experiments and found another peak, at 1631 cm^{-1} ; the previous observations were moved, from 770 and 1200 cm^{-1} , to 786 and 1199 cm^{-1} . The bending mode at 786 cm^{-1} and the symmetric stretch at 1199 cm^{-1} are allowed for the C_s and the C_{2v} symmetry, while the asymmetric mode at 1631 cm^{-1} is dipole forbidden for C_{2v} . This suggests C_s symmetry for CO_2^- chemisorbed on $\text{Pd}(110)/\text{H}_2\text{O}$.

Clearly, theoretical calculations would be of interest to confirm or deny, and further describe the mode of bonding of CO_2 to Pd, and to other TM systems [1]. There is a theoretical study of CO_2 on Ni surfaces which addresses the bonding of the moiety [8], but there have, to our knowledge, been no calculations for CO_2 bonded to Pd atoms or surfaces. In this contribution we present a theoretical analysis for $\text{Pd}-\text{CO}_2$, which has been performed by means of a density functional method. Our goal is a determination of the preferred coordination modes, as well as the estimation of chemisorption energies, bond lengths, and vibrational frequencies. Although $\text{Pd}-\text{CO}_2$ is a minimal model, it will be shown that some of our theoretical estimates correlate with the experimental results obtained for the adsorption of CO_2 on infinite palladium surfaces. Our results provide insight into the $\text{Pd}-\text{CO}_2$ bonding and provide support to some previous assignments of the vibrational modes, which have been made on experimental grounds. As we shall see, a quite different picture is emerged from our calculations for $\text{Pd}-\text{CO}_2$ vs. $\text{Ni}-\text{CO}_2$.

Computational Details

We have used the code **deMon** [20,21,22], which implements a *linear combination of Gaussian-type orbitals-density functional* method. Calculations were done at the local spin density approximation (LSDA) level, using the Vosko, Wilk, and Nusair (VWN) [23] functional. Nonlocal density gradient-type corrections were included self-consistently, using the functional of Perdew and Wang (1986) for exchange [24], and Perdew (1986) for correlation [25,26]. These calculations will be labeled

simply as NL (for nonlocal). The (5211/411/1) orbital basis sets for carbon and oxygen, optimized for DFT calculations [28] were used. These bases are of 6-31G** quality. The core electrons of the Pd atom were approximated by a model core potential (MCP). The scalar relativistic effects are incorporated into the MCP [29]. The 4p⁶4d⁹5s¹ electrons were included explicitly in the calculation, for which a palladium(+16)(2211/2111/21) orbital basis set was constructed. The auxiliary basis sets, used in the fitting of the charge density (CD) and the exchange-correlation (XC) potential have the pattern (5,2;5,2) for both carbon and oxygen, and palladium(+16)(3,4;3,4) for the Pd atom. In this notation ($k_1, k_2; l_1, l_2$), $k_1(l_1)$ is the number of s-type gaussians in the CD (XC) basis and $k_2(l_2)$ is the number of s-, p-, and d-type gaussians constrained to have the same exponent in the CD (XC) basis. The charge density was fitted analytically, while the XC potential was fitted numerically on a FINE grid [27] comprised of 32 radial shells and 26 angular points per shell, giving rise to a total of 832 points per atom [30].¹ At the end of each SCF procedure, the exchange-correlation contribution to the energy gradients were calculated by numerical integration on an augmented set of grid points consisting of the same 32 radial shells with either 50, 110, or 194 angular grid points [27].

Without imposed symmetry constraints, and by means of the Broyden-Fletcher-Goldfarb-Shanno (BFGS) algorithm [31], the geometries were optimized by minimizing the norm of the gradient with a threshold of 10⁻⁶ a.u. The BFGS algorithm searches the PES through its first derivatives, evaluated analytically, and through approximate second derivatives (the Hessian matrix) updated numerically. All R_e 's and bond angles were simultaneously refined. A vibrational analysis was done for the lowest energy structures. Here, the harmonic approximation was used with two-point numerical differentiation of gradients [27]. Additionally, the infrared intensities were calculated by two-point differencing of the dipole moments. In our model core potential spin-polarized calculations, the standard Mulliken population analyses were done to obtain the atomic charges.

Results: Coordination Modes of Pd—CO₂

We have done an exhaustive search for the possible coordination modes of CO₂ to a single palladium atom. In Figure 1 are shown the four possibilities. They are: (a) carbon-oxygen (η^2 -CO), with C_s symmetry, (b) carbon (η^1 -C), with C_{2v} symmetry, (c) oxygen (η^1 -O), and (d) oxygen-oxygen (η^2 -OO), with C_{2v} symmetry. The first and the last are dihapto modes, that is, the metal atom is bonded to two *ligand* atoms, whereas b) and c) are monohapto coordination modes. To determine which one is the most stable, we have done a full optimization for each of the corresponding geometries. Afterwards, a vibrational analysis was made for the converged structures. The results are shown in Table I. We discuss the main findings below.

The η^2 -CO Coordination Mode

The dihapto η^2 -CO coordination mode was found as the one of lowest energy. Here, there is a strong charge transfer from Pd to CO₂ (about 0.7 electrons; see

¹ The radial grid used in deMon was inspired by [30] and differing only in the fact that it uses the Gaussian-Legendre quadrature scheme instead of Gauss-Chebyshev.

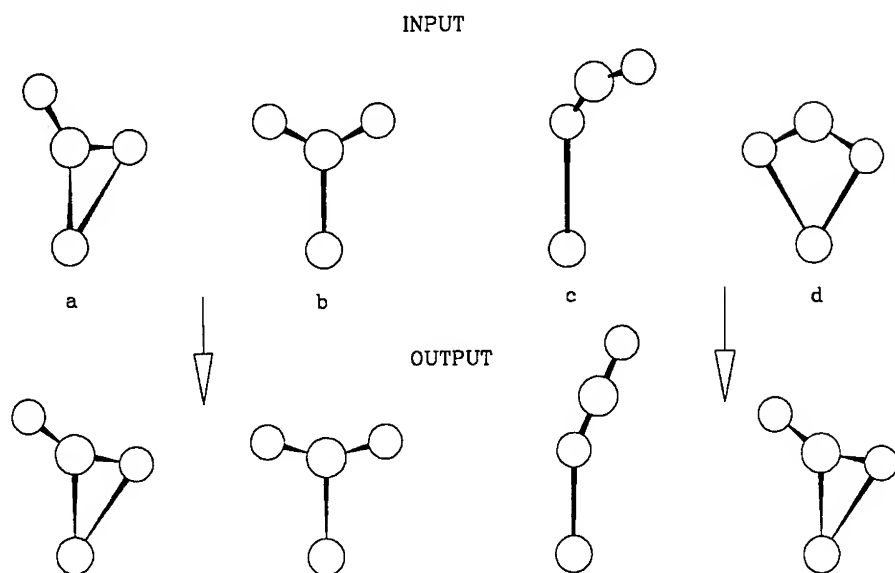


Figure 1. The four possible coordination modes of CO₂ to Pd: (a) the η^2 -CO mode, (b) the η^1 -C mode, (c) the η^1 -O, and (d) the η^2 -O—O mode. The input and the converged structures are indicated.

Table II), which produces a large structural change in CO₂: It goes from a linear to a bent geometry (our vibrational analysis, see below, is consistent with this feature). In this η^2 -CO mode (or mixed Pd—C/Pd—O bond), of C_s symmetry, there is an elongation (with respect to free CO₂) of the C=O bond involving the oxygen atom nearest to the metal center (see Fig. 1). The two C=O bond lengths, in Pd—CO₂, are no longer equal; they are 1.20 and 1.24 Å. The Mulliken population analysis (see Table 2) shows that the metal atom is positive (+0.7), the carbon atom is positive (+0.1), the oxygen atom nearest to the Pd center is negative (−0.5), and the other oxygen atom is also negative, but to a lesser extent (−0.3 electrons). Hence, there are two types of electrostatic interactions in the η^2 -CO mode, repulsive between the metal center and the carbon atom, and attractive between the oxygen and the palladium atoms, the latter contributing to the total energy lowering of the η^2 -CO mode. These two types of electrostatic interaction are shown in Figure 2.

The vibrational analysis for the η^2 -CO geometry yields no imaginary frequency, (see Table I) showing that this structure is a local minimum. The calculated frequencies associated with metal—carbon and metal—oxygen modes are 203, 373, and 561 cm^{−1}. In particular, 373 cm^{−1} corresponds to the symmetric elongation of the Pd—C and Pd—O bonds. This mode favors the occurrence of a *mixed* carbon—oxygen bond in Pd—CO₂. The bending, symmetric, and asymmetric vibrational modes of CO₂ in Pd—CO₂ have calculated frequencies of 689, 1212, and 2018 cm^{−1}, respectively.

The experimental frequencies of CO₂ on a H₂O/Pd(110) surface [19] are 786, 1199, and 1631 cm^{−1}, respectively. This suggests a C_s symmetry because the asym-

TABLE I. Bond lengths R_e , bond angles, relative energies, ΔE , and vibrational frequencies, for the CO₂ to Pd coordination modes.

	η^2 (Pd—CO)	η^1 (Pd—C)	η^1 (Pd—O)
R_e (Å)			
Pd—C	1.99	1.96	
C—O ₁	1.24	1.22	1.18
C—O ₂	1.20	1.22	1.17
Pd—O ₁			2.07
Bond angle			
O ₁ —C—Pd	79.7	104.6	
O ₂ —C—Pd	129.9	104.6	
O ₁ —C—O ₂	150.4	150.8	179.0
Pd—O ₁ —C			146.0
ΔE (kcal/mol)			
0.0 (0.0) ^a	+2.2 (+8.4) ^a	+13.8	
	$\nu(\text{cm}^{-1})^d$		Exp. ^c
203	-112	97	
373	311	333	
561	586	538	
689 δ^b	707 δ^b	543	786
1212 ν_s^c	1245 ν_s^c	1321	1199
2012 ν_{as}^d	1974 ν_{as}^d	2398	1631

^a Nonlocal results.^b Bending, ^c symmetric, and ^d asymmetric stretch of CO₂.^c CO₂ on Pd(110)/H₂O, from Ref. [19].

metric mode (1631 cm⁻¹) is dipole-forbidden in C_{2v} symmetry but dipole-allowed in C_s. Two of the observed bands agree quite well with our calculations for the minimal Pd—CO₂ model, but there is a large discrepancy for the asymmetric mode (calculated: 2018 cm⁻¹, experimental: 1631 cm⁻¹). However, this mode is quite sensitive to the *details* of the surface. For example, Wohlrab et al. [11] have determined the frequencies of CO₂ on a Pd(111)/Na surface; the observed values, 744,

TABLE II. Electron populations on each atom (a 16-valence electron MCP is used).

Mode	PdCO ₂			
	Pd ₁	C	O ₁	O ₂
Pd ₁ — η^2 (C—O)	15.3	5.9	8.5	8.3
Pd ₁ — η^1 (C)	15.5	5.9	8.3	8.3
Pd ₁ — η_1 (O)	15.7	5.4	8.6	8.3

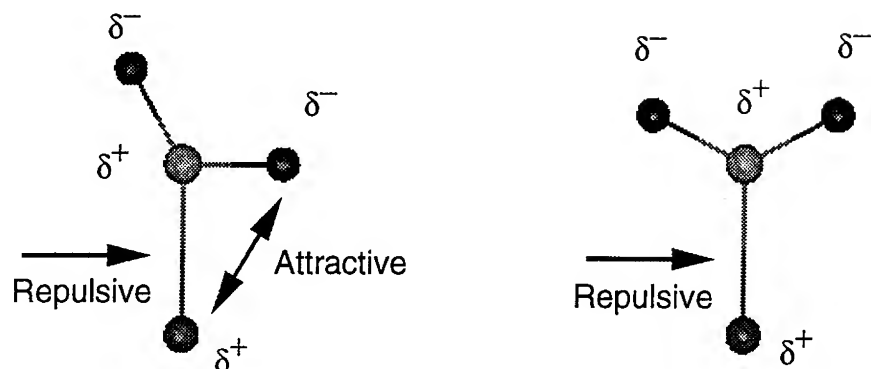


Figure 2. The attractive and repulsive electrostatic interactions for the η^2 -CO and the η^1 -C coordination modes.

1210, and 1530 cm^{-1} , show a close correspondence to those of Brosseau et al. and also indicate C_s symmetry as the likely coordination mode of $\text{Pd}-\text{CO}_2$. However, the asymmetric mode is the most sensitive, showing a large difference (about 100 cm^{-1}) between the two surfaces. We have also found such a sensitivity in calculations involving larger clusters (to be published elsewhere). The asymmetric mode is shifted to lower values as the size of the cluster is increased. For example, in Pd_4-CO_2 that frequency is equal to 1843 cm^{-1} , which is closer to the experimental findings than the calculated value, 2018 cm^{-1} , for $\text{Pd}-\text{CO}_2$. Calculations for an infinite $\text{CO}_2/\text{Pd}(110)$ surface, using periodic boundary conditions [32] in the code **deMon**, are in progress in our laboratory; this will complement our studies using small Pd_n clusters.

The calculated chemisorption energy of CO_2 is 1.10 eV for the LSDA, and 0.88 eV at the NL level. As is well known, the LSDA substantially overestimates the binding energies in TM-L systems [33], the introduction of NL corrections improves dramatically the calculations of the binding properties. However, an accurate estimation of the binding energy of CO_2 on palladium surfaces would require (in addition to NL corrections) the use of larger Pd_n clusters or an infinite Pd surface. Both approaches are in progress in our laboratory. (For a Pd_4-CO_2 system, the chemisorption energies are 2.67 eV for LSDA and 2.36 eV at the NL level).

The η^1 -C Coordination Mode

The η^1 -C mode (monocoordinated CO_2 through the carbon atom) was located 2.2 kcal/mol, for the LSDA, and 8.4 kcal/mol, at the NL level, above the η^2 -CO minimum. (The NL approach, a higher level of theory, enhances the stability of the η^2 -CO structure). Since there is C_{2v} symmetry in the η^1 -C mode, the two C—O bonds have the same bond length, equal to 1.22 Å; it is interesting to observe that this value is the average of the two unequal C—O bond lengths in the η^2 -CO structure (1.20 and 1.24 Å). Here, there is also a charge transfer from Pd to CO_2 , about 0.5

electrons (see Table II). This charge transfer is smaller than that found in η^2 -CO. From the total charge distribution it is observed that the Pd and C centers are positive, whereas the oxygen atom is negative (see Table II). Hence, there is a repulsive electrostatic interaction between the metal center and the carbon atom which contributes to the reduced stability.

Our vibrational analysis shows that the η^1 -C structure is not a minimum but rather a transition state, since there is an imaginary frequency (associated with the Pd—C and Pd—O vibrational modes; see Table I). In this structure, values of 707, 1245, and 1974 cm⁻¹ are assigned to the bending, symmetric, and asymmetric stretching vibrations of CO₂ in Pd—CO₂. There is an increase in the frequencies for the bending and symmetric modes, and a decrease in the asymmetric mode with respect to our calculated values for the η^2 -CO structure.

The η^1 -O Mode

The oxygen, η^1 -O, coordination mode was located much higher in energy, 13.8 kcal/mol for the LSDA. It is interesting to observe that, in this structure, the CO₂ molecule remains almost linear, slightly perturbed by the Pd atom and there is only a small charge transfer from the metal center to the CO₂ moiety, about 0.3 electrons. The bonds lengths are almost the same as in the free linear CO₂ molecule: 1.18 and 1.17 Å.

Our vibrational analysis for the η^1 -O mode is consistent with the occurrence of a linear CO₂ molecule in this coordination mode (though there should be some differences due to the elongation of one C=O bond). The experimental frequencies for free CO₂ are: 667, 1340, and 2349 cm⁻¹; our calculated frequencies are: 543, 1321 and 2398 cm⁻¹ for CO₂ in Pd—CO₂ in this coordination mode. Note that the 1321 and 2398 cm⁻¹ theoretical estimates are quite close to their experimental counterparts, 1340 and 2349 cm⁻¹ for the bare CO₂ molecule but the bending mode is put about 100 cm⁻¹ below the bare CO₂ value.

The η^2 -O—O Mode

It was not possible to converge the η^2 -O—O coordination mode for Pd—CO₂, where the moiety should be coordinated by the two oxygen centers. The two oxygen atoms in η^2 -O—O starting geometries always moved away from the Pd center, the result converging to the η^2 (C—O) mode, which is the one of lowest energy, as shown above. This implies that in the η^2 (O—O) structure there is a repulsive interaction between the Pd and the two oxygen atoms. We have examined this mode of binding, more closely, through the following theoretical experiment. Since the formate ion HCOO^{-δ} and CO₂^{-δ} have similar effects and are often compared [9], we have modeled the transition of the formate ion into the CO₂^{-δ} moiety by gradually taking away the hydrogen atom. We have applied this process to both NiHCO₂ and PdHCO₂. For NiHCO₂, our calculations agree with experimental results for bulk surfaces in that the two oxygen atoms are down [8] (see Fig. 3); that is, in NiCO₂ the preferred coordination mode is η^2 (O—O) [8]. In contrast, we have found that while pulling away the hydrogen atom of the formate moiety, the oxygen atoms

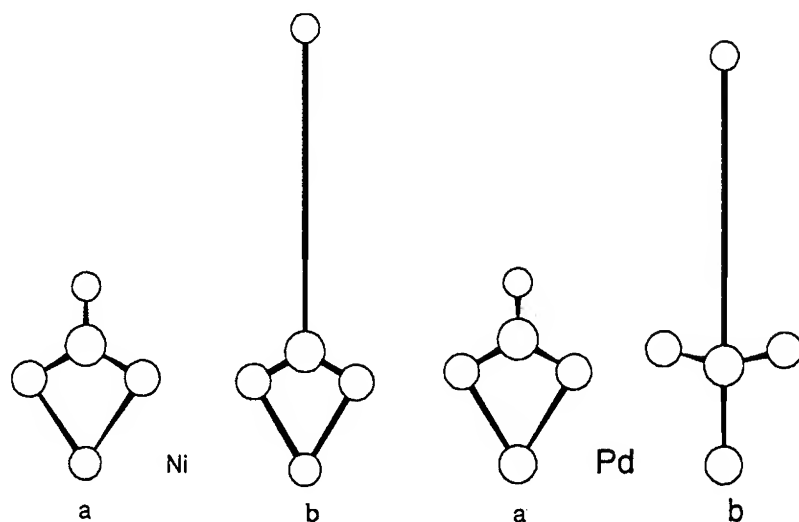


Figure 3. Evolution, through a geometry optimization, of the η^2 -O—O coordination mode for NiHCO_2 and PdHCO_2 . The input and the converged structures are indicated.

are displaced upward in the case of palladium (see Fig. 3). This leads us to exclude the possibility of adsorption of CO_2 by the coordination of the two oxygens, the η^2 -O—O mode, for Pd. The η^2 (O—O) structure is still a possible mode of coordination of CO_2 to an Ni(110) surface, since it is close in energy to the ground state η^2 (C—O) mode.

Conclusions

The preferred coordination modes of the CO_2 molecule to a single palladium atom have been determined by means of the Gaussian DFT code **deMon**. The lowest energy coordination mode is η^2 -CO, where there is a mixed Pd—C/Pd—O bonding. A strong charge transfer from the metal to the CO_2 moiety was found, which produces a strong structural change in CO_2 : It goes from a linear to a bent geometry. This picture and the results of our vibrational analysis for the η^2 -CO mode are in agreement with the experimental results for the adsorption of CO_2 on the $\text{H}_2\text{O}/\text{Pd}(110)$ and $\text{Pd}(110)/\text{Na}$ surfaces. Theory and experiment agree in that the η^2 -CO mode, of C_s symmetry, is the most likely for the chemisorption of CO_2 on palladium surfaces, since the asymmetric mode (observed at 1530 or 1631 cm^{-1} , calculated at 2018 cm^{-1}) is dipole-allowed for C_s symmetry and dipole-forbidden for C_{2v} . In fact, the η^1 -C mode, of C_{2v} symmetry, was found to be a transition state, 2.2 kcal/mol (LSDA) or 8.4 kcal/mol (NL), above the minimum. The asymmetric mode for chemisorbed CO_2 is quite sensitive to the details of the surface. [In further calculations, to be published elsewhere, this is directly related to the size of the cluster. Using a Pd_4 — CO_2 system, we have calculated 1843 cm^{-1} for the asymmetric mode, which is closer to the experimental observations. Calculations for bigger Pd_n — CO_2

systems and for an infinite CO₂/Pd(110) surface are in progress in our laboratory. These will give more insight and will complement the present study of the minimal Pd—CO₂ model.] The η^2 -O—O mode is not attainable in Pd—CO₂, it converges to the η^2 -CO mode, the ground state. This is a quite different picture to that found for Ni—CO₂, where the dihapto η^2 -O—O coordination mode is nearly degenerate with the η^2 -CO structure.

Acknowledgments

Support from NSERC (Canada), FCAR (Québec), and the Canadian Network of Centres of Excellence in Molecular and Interfacial Dynamics is gratefully acknowledged, as is the provision of computing resources by the Services Informatiques de l'Université de Montréal. We are grateful to Tom Ellis and Robert Brosseau for stimulating discussions.

Bibliography

- [1] D. R. Salahub and N. Russo, Eds., *Metal-Ligand Interactions: From Atoms, to Clusters, to Surfaces*, NATO-ASI (Kluwer Academic, Dordrecht, 1992).
- [2] D. R. Salahub and M. C. Zerner, Eds., *The Challenge of d and f Electrons* ACS Symp. Ser. 394 (American Chemical Society, Washington, DC, 1989).
- [3] J. Haggin, *Chem. Eng. News* **8**, 13 (1982).
- [4] E. W. Plummer, Ed., *Topics in Applied Physics* (Springer-Verlag, New York, 1975), Vol. 4.
- [5] T. N. Rhodin and G. Ertl, Eds. *The Nature of the Surface Chemical Bond* (North-Holland, Amsterdam, 1978).
- [6] E. W. Plummer, C. T. Chen, W. K. Ford, W. Eberhardt, R. P. Messmer, and H. J. Freund, *Surf. Sci.* **158**, 58 (1985).
- [7] S. Sakaki and A. Dedieu, *Inorg. Chem.* **26**, 3278 (1987).
- [8] H. J. Freund and R. P. Messmer, *Surf. Sci.* **172**, 1–30 (1986).
- [9] B.artos, H. Kuhlenbeck, H. J. Freund, M. Neumann, T. Linder, and K. Müller, *Surf. Sci.* **179**, 59 (1989).
- [10] H. J. Freund, H. Behner, B.artos, G. Wedler, H. Kuhlenbeck, and M. Neumann, *Surf. Sci.* **180**, 550 (1987).
- [11] S. Wohlrab, D. Ehrlich, J. Wambach, H. Kuhlenbeck, and H. J. Freund, *Surf. Sci.* **220**, 243 (1989).
- [12] F. Solymosi and A. Berkó, *J. Catal.* **101**, 458 (1986).
- [13] A. Berkó and F. Solymosi, *Surf. Sci.* **171**, 498 (1986).
- [14] J. L. Kafafi, P. H. Hauge, W. E. Billups, and J. L. Margrove, *Inorg. Chem.* **23**, 177 (1984).
- [15] J. Mascetti and M. Tranquille, *J. Phys. Chem.* **92**, 2177 (1988).
- [16] J. Mascetti and M. Tranquille, *Surf. Sci.* **156**, 201 (1985).
- [17] T. Herskovitz, *Inorg. Synth.* **21**, 99 (1982).
- [18] R. Brosseau, T. H. Ellis, and Wang, *Chem. Phys. Lett.* **117**, 118 (1991).
- [19] R. Brosseau, Ph.D. thesis, Université de Montréal, March 1993.
- [20] A. St-Amant and D. R. Salahub, *Chem. Phys. Lett.* **169**, 387 (1990).
- [21] D. R. Salahub, R. Fournier, P. Mlynarski, I. Papai, A. St-Amant, and Jiro Ushio, in *Density Functional Methods in Chemistry*, J. Labanowski and J. Andzelm, Eds. (Springer-Verlag, Berlin, 1991).
- [22] A. St-Amant, Ph.D. thesis, Université de Montréal, 1992.
- [23] S. H. Vosko, L. Wilk, and M. Nusair, *Can. J. Phys.* **58**, 1200 (1980).
- [24] J. P. Perdew and Y. Wang, *Phys. Rev. B* **33**, 8800 (1986).
- [25] J. P. Perdew, *Phys. Rev. B* **33**, 8822 (1986).
- [26] J. P. Perdew, *Phys. Rev. B* **34**, 7406E (1986).

- [27] Biosym Technologies, *deMon User's Guide and Version 1.0 Beta* (San Diego, 1992).
- [28] N. Godbout, D. R. Salahub, J. Andzelm, and E. Wimmer, *Can. J. Chem.* **70**, 560 (1992).
- [29] J. Andzelm, E. Radzio, and D. R. Salahub, *J. Chem. Phys.* **83**, 4573 (1985).
- [30] A. D. Becke, *J. Chem. Phys.* **88**, 2547 (1988).
- [31] H. B. Schlegel, *Ab Initio Methods in Quantum Chemistry—I* (Wiley, New York, 1987).
- [32] H. Kobayashi, A. St-Amant, D. R. Salahub, and T. Ito, in *New Frontiers in Catalysis*, L. Guzzi et al., Eds. (Elsevier, Lausanne, 1993); H. Kobayashi, D. R. Salahub, and T. Ito, *J. Phys. Chem.* (1993), to appear.
- [33] M. Castro, D. R. Salahub, and R. Fournier, *J. Chem. Phys.*, to appear.

Received February 16, 1994

A Study of Small Systems Containing H and O Atoms Using Nonlocal Functionals: Comparisons with *Ab Initio* and Experiment

JORGE M. SEMINARIO

Department of Chemistry, University of New Orleans, New Orleans, Louisiana 70148

Abstract

Structures and energies have been calculated for HO, H₂O, O₂, HO₂, H₂O₂, and O₃ molecules using the nonlocal functionals PW86, PW91, B-P86, and B-LYP with the goal of obtaining their atomization energies. Results were compared with those from highly correlated methods and experiment. It was found that all nonlocal functionals perform similarly to or better than correlated methods MP4 and QCI (using relatively equivalent basis sets). All nonlocal energies were self-consistently calculated using the optimized geometries for each functional. None of the results contain any empirical correction except those inherent to some of the functionals. Increasing the size of the basis set when using the nonlocal functionals does not lead to any significant improvement of the energies and surprisingly it worsens the results for one of the functionals. © 1994 John Wiley & Sons, Inc.

Introduction

We are interested in improving the accuracy of energies calculated using nonlocal functionals. The main goal is to determine what corrections, if any, are needed to compensate for the errors due to the approximate nature of the exchange-correlation functionals, and for the errors due to the finite character of the basis sets used. Previous works on this matter [1,2] have shown that corrections were possible in some cases, especially when using local functionals. In the present work, we have focused specifically upon the smallest neutral molecular systems containing only hydrogen and oxygen atoms. We have computed geometries and atomization energies using state of the art nonlocal functionals and compared them with sophisticated *ab initio* results and with precise experimental data. The evaluation of the atomization energies is one of the most challenging tasks for *ab initio* methods. Modern experimental techniques are able to yield atomization energies within 1 kcal/mol of error (chemical accuracy).

In an effort to develop methods able to yield atomization energies of chemical accuracy, many schemes have been proposed to correct *ab initio* energies, including those that were obtained using highly correlated methods. Two of these successful schemes are the Gaussian 1 (G1) [3] and the Gaussian 2 (G2) [4] procedures. The G1 procedure adds to the molecular atomization energy a correction of -3.85 kcal/mol times the difference of the number of paired electron shells between the molecule

and the constituent atoms, and an additional 0.12 kcal/mol per each singly occupied-shell difference. Given the importance of the above two differences, we define, for any molecule: the Double Occupied Difference (DOD) as the difference of the number of doubly occupied MO's (Molecular Orbitals) in the molecule minus the number of doubly occupied AO's (Atomic Orbitals) in the constituent atoms, and the Single Occupied Difference (SOD) as the difference between the number of singly occupied AO's in the constituent atoms minus the number of singly occupied MO's in the molecule. For a small molecule like water, the corrections due to the DOD and SOD yield -7.2 kcal/mol, which is many times bigger than the chemical accuracy. The errors in the atomization energies are mostly due to the bonds of the molecular systems. The bonds have a complicated character that always require the use of basis sets with atomic functions of high angular momentum number. Normally, high angular momentum numbers cannot be used in atomic basis sets because of technical limitations in computational resources.

Methodology

Density functional theory (DFT), as it has been applied in this work, is based on the Hohenberg-Kohn theorem [5] and the Kohn-Sham [6] procedure. DFT is strictly speaking a first principles formalism, and it can be developed from the nonrelativistic Schrödinger equation:

$$\hat{H}\Psi = E\Psi \quad (1)$$

where Ψ is the electronic wave function (i.e., within the Born-Oppenheimer approximation) and \hat{H} is the Hamiltonian operator:

$$\hat{H} = v_{\text{ext}} + \hat{T} + V_{ee} \quad (2)$$

where v_{ext} is the external potential due to the nuclei, \hat{T} is the kinetic energy operator, and V_{ee} is the electron-electron energy operator. Because of the Hohenberg-Kohn theorem, the energy of the system can be written as a functional of the electron density ρ which can be defined as

$$\rho(\vec{r}) = N \langle \Psi | \delta(\vec{r} - \vec{r}_i) | \Psi \rangle \quad (3)$$

where δ is the Dirac delta function and N is the total number of electrons. Because of the antisymmetric character of the wave function, \vec{r}_i can be any of the N spatial variables of Ψ . To express the total energy as a functional of ρ , the electron-electron operator in Eq. (2) is multiplied by a parameter λ ($0 \leq \lambda \leq 1$); as a result, a new Hamiltonian [7] is implemented:

$$\hat{H}_\lambda = \hat{T} + \hat{v}_\lambda + \lambda \hat{V}_{ee} \quad (4)$$

whose eigenfunction and eigenvalue are Ψ_λ and E_λ , respectively, and they are related by

$$\hat{H}_\lambda \Psi_\lambda = E_\lambda \Psi_\lambda. \quad (5)$$

v_λ in Eq. (4) is chosen such that the density for any λ is always constraint to be the same as the density for $\lambda = 1$ [8,9]. Therefore, for $\lambda = 0$ we have a system of noninteracting electrons with density identical to the density of the real system. The total energy for this new Hamiltonian is

$$E_\lambda = \langle \Psi_\lambda | \hat{H}_\lambda | \Psi_\lambda \rangle = \int v_\lambda(\vec{r}) \rho(\vec{r}) d\vec{r} + \langle \Psi_\lambda | \hat{T} + \lambda \hat{V}_{ee} | \Psi_\lambda \rangle. \quad (6)$$

By taking partial derivative with respect to λ , invoking the Hellmann-Feynman theorem and integrating between 0 and 1, we obtain

$$E(\rho) = \int v_{\text{ext}}(\vec{r}) \rho(\vec{r}) d\vec{r} + T_s + \int_0^1 \langle \Psi_\lambda | V_{ee} | \Psi_\lambda \rangle d\lambda \quad (7)$$

where T_s is the kinetic energy of the noninteractive system of electrons ($\lambda = 0$). From the above expression the exchange-correlation functional, E_{xc} , is defined

$$\int_0^1 \langle \Psi_\lambda | V_{ee} | \Psi_\lambda \rangle d\lambda = \frac{1}{2} \iint d\vec{r}_1 d\vec{r}_2 \frac{\rho(\vec{r}_1) \rho(\vec{r}_2)}{|\vec{r}_1 - \vec{r}_2|} + E_{xc}(\rho) \quad (8)$$

where the double integral is the classical electron-electron energy interaction V_{class} . Finally, the total energy of the interactive or real system ($\lambda = 1$) is exactly

$$E[\rho] = \int v_{\text{ext}}(r) \rho(r) dr + T_s[\rho] + V_{\text{class}}[\rho] + E_{xc}[\rho] \quad (9)$$

where the $E_{xc}[\rho]$ will have to be approximated because it can only be evaluated in special cases like the uniform electron gas (jellium). Once an exchange-correlation functional has been chosen, the variational principle [1] of DFT is invoked; Consequently, the minimization of the total energy functional, Eq. (9), with respect to the density is straightforward. In this work we are using a group of nonlocal functionals referred to as generalized gradient approximations (GGA).

We have used the programs deMon [10,11] and Gaussian 92/DFT [12]. The calculations with the functionals Perdew-Wang 86 (PW86) [13,14] and Perdew-Wang 91 (PW91) [15-17] were done using the program deMon, and the calculations with the combination of functionals Becke exchange [18] and correlation PW86 (B-PW86) as well as the combination Becke exchange and Lee-Yang-Parr correlation (B-LYP) [19] were done using the program Gaussian 92/DFT. Two basis sets were used [20] with the program deMon: Double- ζ valence plus polarization on all atoms (DZVP2) and its extension to a triple- ζ (TZVP2). Two basis sets were used [12] with the program Gaussian 92/DFT: the standard 6-31G** and the largest built-in 6-311++G(3df,3pd). The DZVP2 and the 6-31G** are of equal size and almost equivalent, and they will also be designated as (D). The TZVP2 and the full 6-311++G(3df,3pd) will be designated as (T) and (F), respectively. DFT results were compared with those obtained using the *ab initio* method Møller-Plesset (MP4) that includes single, double, triple, and quadruple substitutions; and with those obtained using the quadratic configuration interaction (QCI) method that includes single, double, and perturbative triple substitutions. The MP4 calculations were done using the 6-311G**, 6-311+G**, and 6-311G(2df,p) basis sets.

The QCI calculations were performed using the 6-311G** basis set. All the above *ab initio* procedures are part of the Gaussian 1 (G1) procedure [3].

Results

Table I shows the atomic energies of hydrogen and oxygen atoms together with their errors with respect to exact values. Both PW functionals give results for hydrogen in excellent agreement with the exact values, with the old PW86 results being slightly better. The results from the combination B-P86 and B-LYP improve when a full basis set is used. For oxygen, the old PW86 does not perform so accurately; however, the new PW91 gives a large improvement in the total energy. The combinations B-P86 and B-LYP perform similarly for oxygen but their errors increase in the opposite direction when using a larger basis set. This suggests that with some intermediate size basis set, the error for the oxygen atom can be made zero; however, this is not necessarily going to improve the study of the chemistry of oxygen-containing molecules, yet it is going to make the selection of basis sets for DFT difficult. In this respect, it can also be observed in Table I that some of the DFT energies for hydrogen are lower than the exact energy of -0.5 hartrees. This pseudo violation of the variational principle is because all functionals are approximations; therefore, the calculated energies are not upper bounds to the exact energies. Another related problem that can also be observed for the hydrogen atom, and it will also appear on some molecules containing hydrogen atoms is that the energies calculated with the TZVP2 are bigger than the energies obtained with the smaller DZVP2 basis set. The reason for this anomalous behavior is the auxiliary hydrogen basis set that is

TABLE I. Calculated energies of H and O atoms and errors with respect to the exact values.

	Hydrogen (hartrees)	H error (kcal/mol)	Oxygen (hartrees)	O error (kcal/mol)
PW86/DZVPP	-0.50004 ^a	-0.03	-75.14784 ^a	-53.43
PW86/TZVPP	-0.50001	-0.01	-75.15608	-58.60
PW91/DZVPP	-0.49927	0.46	-75.05879	2.45
PW91/TZVPP	-0.49927	0.46	-75.05980	1.82
B-P86/6-31G**	-0.49810	1.19	-75.05028	7.80
B-LYP/6-31G**	-0.49545	2.86	-75.04696	9.88
B-P86/6-311++G(3df,3pd)	-0.50014	-0.09	-75.08096	-11.46
B-LYP/6-311++G(3df,3pd)	-0.49772	1.43	-75.08025	-11.01
MP4/6-311G**	-0.49981 ^b	0.12	-74.93333 ^b	81.18
MP4/6-311+G**	-0.49981 ^b	0.12	-74.93724 ^b	78.73
MP4/6-311G(2df,p)	-0.49981 ^b	0.12	-74.96478 ^b	61.45
QCISD(T)/6-311G**	-0.49981 ^b	0.12	-74.93402 ^b	80.75
Exact	-0.5		-74.9820 ^c	

^a Reference [2].

^b Reference [3].

^c Estimated in Ref. [3].

unsuitable to be used in conjunction with the TZVP2 orbital basis set and the PW functionals. The hydrogen energy obtained from the *ab initio* methods is the same as the one obtained with the Hartree-Fock procedure because no correlation is involved and all basis sets used are equivalent for the hydrogen atom. The error of 0.12 kcal/mol corresponds to the correction of -0.12 kcal/mol used in the G1 procedure. This is an error G1 procedure corrects whenever a single electron occupies a molecular orbital.

For oxygen, the *ab initio* errors are relatively large, but this is not of major concern because the core electrons are not correlated on either the MP4 or QCI calculations; therefore, when calculating atomization or any other energy difference, most of these errors will be canceled with an analogous error from the core electrons in the molecule. This is not the case for the DFT energies.

Table II shows the total energies for the molecules using various levels of theory. Each energy corresponds to a local minimum geometry for all the DFT procedures and to a geometry optimized at the MP2 level for all the *ab initio* procedures. The calculations using the PW 86/DZVP2 were done using an earlier version of the program deMon with slightly different functions for the fitting of the electronic density.

The parameters of the optimized structures for various nonlocal functionals and basis sets are shown in Table III. Each structure corresponds to a local minima self-consistently evaluated. We have also tabulated MP2/6-31G* and experimental geometries for comparison purposes. Although the energies are the best indicators of the quality of the model used, the geometries furnish additional insight on the performance of the various functionals and basis sets. As a rule, all GGA functionals overestimate bond lengths. The increase in size of the basis set using the PW 86 functional does not lead to any improvement of the geometries; the bond lengths become slightly worse, angles hardly change, and the dihedral on H₂O₂ gets 0.7 degrees worse. The PW 91 geometries are slightly better when increasing the basis set size. In addition, the bond lengths are improved when going from PW 86 to PW 91, but the bond angles get worse. There is a perceptible improvement in the dihedral angle of H₂O₂ when the new PW 91 functional is used. Comparing only the cases where a double- ζ valence basis set is used, the best bond lengths are calculated by the MP2 method followed by those calculated using the PW 91 and PW 86 functionals, the worst bond lengths are obtained with the B-LYP functional. The best bond angles are obtained with the PW 86 functional followed by those obtained with the B-P86, MP2, and B-LYP methods; the worst bond angles are calculated with the PW 91 functional. The dihedral of H₂O₂ is almost perfectly reproduced with PW 91, and with slightly less quality with the PW 86 and B-P86 functionals. The worst dihedral is calculated with the MP2 procedure. We conclude that no definite favored method can be advocated from analyzing the optimized geometries. The use of the large basis set 6-311++G(3df,3pd), with B-P86 and B-LYP functionals, reduces the errors in bond lengths and angles by a factor of two, but the dihedral of H₂O₂ is spoiled yielding the largest errors. Presently, due to its high demand on computational resources, the full basis set does not have practical interest for larger systems.

TABLE II. Total energies (in hartrees).

	H ₂	HO	H ₂ O	O ₂	HO ₂	HOOH	O ₃
PW86/DZVPP	-1.18334 ^a	-75.82589 ^a	-76.52487 ^a	-150.51130 ^a	-151.09406 ^a	-151.74700 ^a	-225.71944
PW86/TZVPP	-1.17986	-75.83326	-76.53202	-150.52624	-151.11724	-151.76137	-225.74197
PW91/DZVPP	-1.17429	-75.73349	-76.43292	-150.33762	-150.92669	-151.56912	-225.46010
PW91/TZVPP	-1.17416	-75.73335	-76.43132	-150.34148	-150.92676	-151.56789	-225.46369
B-P86/6-31G**	-1.17647	-75.72371	-76.41957	-150.33033	-150.91279	-151.55080	-225.44495
B-LYP/6-31G**	-1.16791	-75.71224	-76.39887	-150.31543	-150.89116	-151.52215	-225.41883
B-P86/6-311++G(3df,3df)	-1.17791	-75.76182	-76.46463	-150.38877	-150.97696	-151.62112	-225.53472
B-LYP/6-311++G(3df,3df)	-1.16962	-75.75356	-76.44770	-150.37740	-150.95968	-151.59743	-225.51334
MP4/6-311G**	-1.16772 ^b	-75.58825 ^b	-76.27607 ^b	-150.04161 ^b	-150.61219 ^b	-151.25522 ^b	-225.00462
MP4/6-311+G**	-1.16772 ^b	-75.59594 ^b	-76.28690 ^b	-150.04860 ^b	-150.62100 ^b	-151.26716 ^b	-225.01948
MP4/6-311G(2df,p)	-1.16772 ^b	-75.62361 ^b	-76.31346 ^b	-150.11869 ^b	-150.69088 ^b	-151.33467 ^b	-225.12771
QCISD(T)/6-311G**	-1.16832 ^b	-75.58921 ^b	-76.27607 ^b	-150.03681 ^b	-150.61489 ^b	-151.25470 ^b	-224.99051

^a Reference [2].^b Reference [3].

TABLE III. Geometries (distances d in Angstroms, angles α , and dihedrals w in degrees).

	PW86/D ^a	PW86/T	PW91/D	PW91/T	BP86/D	BLYP/D	BP86/F	BLYP/F	MP2/D ^a	EXP ^b
H ₂										
d	0.749	0.749	0.743	0.749	0.751	0.747	0.750	0.746	0.738	0.742
HO										
d	0.990	0.990	0.984	0.986	0.989	0.991	0.984	0.985	0.979	0.970
H ₂ O										
d	0.974	0.974	0.969	0.965	0.974	0.976	0.971	0.971	0.969	0.958
α	105.0	105.1	101.7	102.1	102.9	102.7	104.1	104.4	104.0	104.5
O ₂										
d	1.242	1.242	1.246	1.240	1.232	1.240	1.220	1.228	1.242	1.208
HO ₂										
d_1	1.357	1.365	1.363	1.355	1.345	1.359	1.338	1.353	1.325	1.331
d_2	1.006	0.991	0.985	0.981	0.993	0.994	0.988	0.988	0.983	0.971
α	105.4	104.7	102.1	102.5	104.9	104.9	105.0	104.9	104.5	104.3
HOOH										
d_1	1.490	1.500	1.467	1.467	1.476	1.494	1.468	1.487	1.468	1.452
d_2	0.981	0.981	0.977	0.973	0.981	0.982	0.976	0.977	0.976	0.965
α	99.7	99.2	98.8	99.0	98.9	98.5	99.9	99.6	98.7	100.0
w	118.8	118.1	119.2	119.1	118.7	119.8	124.4	114.1	121.1	119.1
O ₃										
d	1.298	1.390	1.299	1.294	1.287	1.298	1.274	1.285	1.299	1.272 ^c
α	118.1	117.9	116.8	116.9	117.9	117.8	118.2	118.1	116.3	117.8 ^c
Errors										
d	0.022	0.025	0.018	0.016	0.018	0.024	0.011	0.017	0.014	
α	0.5	0.5	1.8	1.5	0.9	1.0	0.4	0.4	0.9	

^a Reference [2], except O₃ (this work).^b Experimental references are given in Ref. [1], except O₃.^c Reference [21].

TABLE IV. Atomization energies including zero point energies (in kcal/mol).

	H ₂	HO	H ₂ O	O ₂	HO ₂	HOOH	O ₃
PW86/DZVP2 ^a	109.1	106.6	223.6	132.8	178.3	266.8	168.2
PW86/TZVP2	106.9	106.1	223.0	131.8	182.5	265.5	166.9
PW91/DZVP2	104.4	105.0	222.8	135.6	185.5	267.9	173.1
PW91/TZVP2	104.3	104.3	221.2	136.7	184.3	265.8	173.5
B-P86/6-31G**	107.2	104.9	221.2	141.7	188.2	268.5	179.7
B-LYP/6-31G**	105.2	101.5	213.6	136.5	180.5	258.0	169.5
B-P86/6-311++G(3df,3pd)	105.6	108.3	227.7	139.9	188.7	271.6	178.2
B-LYP/6-311++G(3df,3pd)	103.4	105.1	220.5	133.6	180.3	260.6	166.2
MP4/6-311G**b	99.6	92.2	202.4	107.3	145.3	227.7	123.5
MP4/6-311+G**b	99.6	94.6	206.8	106.8	145.9	230.2	125.5
MP4/6-311G(2df,p) ^b	99.6	94.7	206.1	116.2	155.2	238.0	141.5
QCISD(T)/6-311G**b	100.0	92.4	202.0	103.4	146.1	226.5	113.4
ZPE ^b	5.9	5.1	12.9	2.5	8.9	16.4	4.9
Experiment ^c	103.5	101.3	219.3	118.0	161.1	252.3	142.2

^a Reference [2], except O₃ (this work).^b Taken or calculated from Ref. [3], except O₃ (this work).^c Experimental references are given in Refs. [3] and [4].

The atomization energies are shown in Table IV. For purposes of comparing with experiment, the zero point energies (ZPE) from the G1 procedure have been added in all cases. We also include in Table IV the energies from the MP4 and QCI models used in the G1 procedure. The errors in the atomization energies with respect to experiment are shown in Table V. We have added a column with the average of the absolute errors. The average errors for all procedures, DFT and *ab initio*, are very far from the chemical accuracy. This is very unfortunate because they are the most sophisticated purely *ab initio* (i.e., with no empirical corrections) methods existing today. The *ab initio* procedures shown here, MP4 and QCI using large basis sets, are hardly applicable to systems containing more than four or five heavy atoms because of their immense requirement of computational resources.

The best functional using a double- ζ basis set for this small set of molecules is the B-LYP combination, followed by the PW86 and PW91 functionals. These three functionals yield atomization energies that are comparable to or better than those calculated with the MP4 and QCI procedures that do not use f-functions but larger basis sets. The worst atomization energies are those from the B-P86 combination; even though, the separated exchange and correlation parts work as expected in the other two cases (B-LYP and PW86). The fact that the energies from the DFT calculations are at least comparable with those from the MP4 and QCI procedures that use larger basis sets is very promising for the analysis of large molecular systems. The DZVP2 or the 6-31G** basis set requires of only 15 basis functions per heavy atom; while the 6-311G**, which is the minimal basis set recommended for MP4 or QCI calculations, uses 18 functions. The 6-311+G** uses 22 and the 6-311G(2df,p) uses 30 basis functions per oxygen atom. On the other hand, the MP4 and QCI methods scale like N^7 while the DFT methods scale like N^3 with respect to the size (N in this particular case) of the basis set or the system.

The increase of basis set size directly improves the atomization energies obtained from the MP4 calculations. The inclusion of f-functions yields a marked decrease of errors. This is not the case with the DFT results. The upgrade from double- ζ to triple- ζ on both PW cases decreases the average errors by about 0.5 kcal/mol. In the case of the B-LYP combination the improvement is only 0.9 kcal/mol; however, the size of the basis set grows from 15 to 39 basis functions per heavy atom. In the case of the B-P86 combination the errors increase by 1.3 kcal/mol becoming the case with the worst atomization energies in this study. It is recommended that the Perdew correlation functional be used with the akin Perdew exchange functional to take advantage of inherent error cancellations [15–17] between them. The present results show that a basis set of double- ζ valence with a simple polarization function on all atoms is enough to obtain the best energies that can be achieved with this group of nonlocal functionals. DFT methods do not require the basis sets to be as large as the *ab initio* methods require. Given a basis set, then it is much easier to assemble the electronic density than the N -electron wave function. The complicated character of the correlation portion of the energy is handled by the correlation functional in DFT; the more sophisticated this functional the more precise the calculation will be. Whereas, in an *ab initio* calculation, this complicated character of the correlation portion of the energy is handled entirely by the wave function

TABLE V. Errors in the atomization energies (kcal/mol).

	H ₂	HO	H ₂ O	O ₂	HO ₂	HOOH	O ₃	Average error
PW86/DZVP2 ^a	5.6	5.3	4.3	14.8	17.2	14.5	26.0	12.5
PW86/TZVP2	3.4	4.8	3.7	13.8	21.4	13.2	24.7	12.1
PW91/DZVP2	0.9	3.7	3.5	17.6	24.4	15.6	30.9	13.8
PW91/TZVP2	0.8	3.0	1.9	18.7	23.2	13.5	31.3	13.2
B-P86/6-31G**	3.7	3.6	1.9	23.7	27.1	16.2	37.5	16.2
B-LYP/6-31G**	1.7	0.2	-5.7	18.5	19.4	5.7	27.3	11.2
B-P86/6-311++G(3df,3pd)	2.1	7.0	8.4	21.9	27.6	19.3	36.0	17.5
B-LYP/6-311++G(3df,3pd)	-0.1	3.8	1.2	15.6	19.2	8.3	24.0	10.3
MP4/6-311G** ^b	-3.9	-9.1	-16.9	-10.7	-15.8	-24.6	-18.7	14.2
MP4/6-311+G** ^b	-3.9	-6.7	-12.5	-11.2	-15.2	-22.1	-16.7	12.6
MP4/6-311G(2df,p) ^b	-3.9	-6.6	-13.2	-1.8	-5.9	-14.3	-0.7	6.6
QCISD(T)/6-311G** ^b	-3.5	-8.9	-17.3	-14.6	-15.0	-25.8	-28.8	16.3

^a Reference [2], except O₃ (this work).^b Estimated from the data in Ref. [3], except O₃ (this work).

requiring a large basis set with high angular momentum functions. However, it is important to understand that the definitions of correlation energies in DFT and *ab initio* are not entirely equivalent.

The DFT methods used in the present work overestimate atomization energies while *ab initio* correlated methods underestimate them. In both cases, the errors can be reduced by using the error average as a correction to the energies. Although the *ab initio* MP4 and QCI errors are relatively large, straightforward corrections can be made to these values because the errors are roughly proportional to the number of electrons. For instance, the average error per molecule could be reduced from 16.3 kcal/mol to 3.2 kcal/mol if the atomization QCI energies were corrected by a 1.1875 kcal/mol per each electron in the molecule. These kinds of corrections are possible with high-level *ab initio* energies [3,4] as well as with local DFT energies [1,2]. Besides the basis set additivity, the most important correction in the G1 procedure is the high level correction (HLC). This can be predicted by noticing that the errors in the atomization energies are proportional to the DOD. Table V shows that the errors increase in the following order: first HO and O₂ that have a DOD of one, followed by H₂O and HO₂ that have DOD of two, and finally O₂H₂ and O₃ that have DOD of three. The 3.9 kcal/mol (more exactly 3.85) error in the hydrogen molecule is the correction used in the G1 per each fully occupied MO. This explains why when using *ab initio* methods, the error for the atomization energy of the water molecule is bigger than the error for the oxygen molecule. The DFT nonlocal energies do not show the trend in errors observed in the *ab initio* results. Although other kinds of corrections have been successfully done to DFT energies using local functionals [1,2], the nonlocal results are not suitable for such corrections. However, it can be observed that the nonlocal energy errors are strongly correlated to the number of heavy atoms in the molecule as it happens with two local functionals [2]. With the exception of the B-LYP functional, all the other nonlocal functionals show a large and systematic increase in errors when the number of oxygens increases from one to three. Therefore, if we correct the PW 86 atomization energies by 7.46 kcal/mol per oxygen atom present in the molecule, the average absolute error is reduced to just 2.0 kcal/mol from the original 12.5 kcal/mol. In both cases, DFT and *ab initio*, the errors of dissociation energies or bond energies (when the fragments are not individual atoms) are not too severe because the errors in the fragments will cancel the error in the molecule. The errors are proportional to the number of electrons (*ab initio*) or to the number of atoms (DFT); therefore, tolerances from 1 to 3 kcal/mol in bond energies are always anticipated with the above DFT methods using modest basis sets. This dependence of the error on the number of heavy atoms for the nonlocal functionals suggests that a correction of nonuniversal (depending on the external potential) character is required in most of the functionals. This would be the case if the complicated effects of atoms making bonds can not be properly accounted for in the already complicated functionals used in this work. The PW91 functional is the only free-parameter functional (i.e., deduced purely from first principles arguments). However, the accuracy of results without corrections, although better than expensive *ab initio* methods, is not yet of the chemical

accuracy available to the best experiments; therefore, work is still required to develop better functionals.

Acknowledgments

The author would like to thank Prof. J. P. Perdew for a critical reading of the manuscript, and Dr. Perla B. Balbuena and Pat Lane for help in preparing this manuscript.

Bibliography

- [1] J. M. Seminario, M. C. Concha, and P. Politzer, *Int. J. Quantum Chem.* **S25**, 249 (1991).
- [2] J. M. Seminario, *Chem. Phys. Lett.* **206**, 547 (1993).
- [3] J. A. Pople, M. Head-Gordon, D. J. Fox, K. Raghavachari, and L. A. Curtiss, *J. Chem. Phys.* **90**, 5622 (1989).
- [4] L. A. Curtiss, K. Raghavachari, G. W. Trucks, and J. A. Pople, *J. Chem. Phys.* **94**, 7221 (1991).
- [5] P. Hohenberg and W. Kohn, *Phys. Rev.* **136**, B864 (1964).
- [6] W. Kohn and L. J. Sham, *Phys. Rev.* **140**, A1133 (1965).
- [7] J. Harris and R. O. Jones, *J. Phys.* **F4**, 1170 (1974).
- [8] D. C. Langreth and J. P. Perdew, *Solid State Commun.* **17**, 425 (1975).
- [9] O. Gunnarsson and B. I. Lundqvist, *Phys. Rev.* **B13**, 4274 (1976).
- [10] A. St-Amant, Ph.D. thesis, Université de Montréal (1992).
- [11] A. St-Amant and D. R. Salahub, *Chem. Phys. Lett.* **169**, 387 (1990).
- [12] Gaussian 92/DFT, Revision F.2, M. J. Frisch, G. W. Trucks, H. B. Schlegel, P. M. W. Gill, B. G. Johnson, M. W. Wong, J. B. Foresman, M. A. Robb, M. Head-Gordon, E. S. Replogle, R. Gomperts, J. L. Andres, K. Raghavachari, J. S. Binkley, C. Gonzalez, R. L. Martin, D. J. Fox, D. J. Defrees, J. Baker, J. J. P. Stewart, and J. A. Pople, Gaussian, Inc., Pittsburgh PA, 1993.
- [13] J. P. Perdew, *Phys. Rev.* **B33**, 8822 (1986); **34**, 7406(E) (1986).
- [14] J. P. Perdew and Y. Wang, *Phys. Rev.* **B33**, 8800 (1986).
- [15] J. P. Perdew and Y. Wang, *Phys. Rev.* **B45**, 13244 (1992).
- [16] J. P. Perdew, in *Electronic Structure of Solids*, P. Ziesche and H. Eschrig, Eds. (Akademie Verlag, Berlin, 1991).
- [17] J. P. Perdew, J. A. Chevary, S. H. Vosko, K. A. Jackson, M. R. Pederson, D. J. Singh, and C. Fiolhais, *Phys. Rev.* **B46**, 6671 (1992).
- [18] A. D. Becke, *Phys. Rev.* **A33**, 3098 (1988).
- [19] C. Lee, W. Yang, and R. G. Parr, *Phys. Rev.* **B37**, 785 (1988).
- [20] N. Godbout, D. R. Salahub, J. Andzelm, and E. Wimmer, *Can. J. Chem.* **70**, 560 (1992).
- [21] J. C. Depannemaecker and J. Bellet, *J. Mol. Spectrosc.* **60**, 106 (1977).

Received June 6, 1994

Electronic Properties of Multiple Delta-Doped Layers in Silicon and GaAs

L. M. R. SCOLFARO, D. BELIAEV, and J. R. LEITE

Instituto de Física da Universidade de São Paulo, C. P. 20516, São Paulo, 01498-970, Brazil

A. T. LINO and E. K. TAKAHASHI

Departamento de Ciências Físicas da Universidade Federal de Uberlândia, C. P. 593, Uberlândia, 38400-902, MG, Brazil

Abstract

Self-consistent electronic subband structure calculations of periodic n -type delta(δ)-doped layers in Si and GaAs are performed within the local density-functional approximation. The behavior of the energy levels, potential profiles, miniband occupancies, and Fermi level position with the variation of the dopant concentration N_D and the spacing between the δ -layers d_s is examined for Si δ -doping in GaAs and Sb δ -doping in Si. The physical properties of these δ -doping structures show a strong dependence on d_s , reflecting a transition from isolated delta-wells to superlattices as d_s decreases. The crossover involving the change from a two-dimensional to three-dimensional behavior is discussed for both kinds of systems. © 1994 John Wiley & Sons, Inc.

Introduction

Improvements in epitaxial growth of materials have allowed for a better control of impurity incorporation in semiconductors. Nowadays, there has been an increasing interest in the delta(δ)-doped systems, thus called because of the final target of achieving impurities distributed in one atomic layer. In these planar doping structures, the carriers released by the ionized dopants are confined in the V-shaped potential-well induced by a δ -function-like doped sheet. Such two-dimensional (2D) doping sheets have been used as parts of many semiconductor devices and will certainly play an important role in the development of future quantum electronic devices [1–4].

While isolated and multiple δ -doped layers in GaAs have been the subject of intense investigations [5–10], the study of δ -doping in Si is more recent due mainly to the difficulties in achieving well-controlled impurity incorporation during epitaxial growth of silicon [11,12].

The purpose of this work is to present results of self-consistent (SCF) one-electron state calculations of periodic n -type δ -doped layers in GaAs and Si, for different doping concentrations N_D and sheet periods d_s . Many-body effects such as exchange and correlation are taken into account within the local density-functional approximation (LDA). It is shown that the electronic properties produced by multiple Si-

δ -doping in GaAs and Sb- δ -doping in Si change considerably with the variation of N_D and d_s and a transition from independent isolated δ -wells to a superlattice is found to take place.

Theoretical Model and Calculations

We consider an infinite sequence of equally spaced n - δ -doping layers perpendicular to the [001] direction of a GaAs (or Si) host crystal. All donors are assumed to be ionized and uniformly distributed within a range of 10 Å. Since low temperature is usually employed to reduce diffusion of Si and Sb out of the doped planes, no significant spread of the donors is expected. The electrons released by the donors form a quasi 2D-electron gas which screens the potential of the positive charges. The subband structure of the systems is calculated on the basis of the effective mass approximation. Using the local-density approximation (LDA), the electrons will be described by the wave function $e^{ik_x x} e^{ik_y y} F_{k_z}(z)$ where x and y are the directions parallel to the δ -layers and $F_{k_z}(z)$ is the solution of the one-dimensional Schrödinger equation

$$\left[\frac{-\hbar^2}{2m^*} \frac{d^2}{dz^2} + V(z) \right] F_{k_z}(z) = E_n(k_z) F_{k_z}(z) \quad (1)$$

Here $V(z)$ is the effective potential given by a sum of the Coulombic potential $V_C(z)$ and the local exchange-correlation potential $V_{XC}(z)$, n is the subband index, k_z is the electron wave vector along the z -direction, and m^* is the electron effective mass in GaAs. In the case of silicon, due to the many-valley structure of the Si conduction band and the anisotropy of the electron effective mass in a single valley, the 2D electron gas within the δ -region is described by two kinds of free electron states with different effective masses m_l^* and m_t^* , corresponding, respectively, to the longitudinal and transverse axis of the Si constant-energy ellipsoidal surfaces [13]. Two types of minibands are to be distinguished in this case: one arising from conduction band valleys with m_l^* parallel to the z -axis, and one due to valleys with m_t^* perpendicular to the z -axis. Details of the model can be found elsewhere [9,13].

Equation (1) has to be solved self-consistently for the electrons in connection with the Poisson equation which determines $V_C(z)$. Eq. (1) is numerically integrated by adopting the Wigner-Seitz-Slater version of the cellular method with space filling one-dimensional cells and the exact point-match approach [14] with the boundary conditions

$$F_{nk_z}\left(\frac{d_s}{2}\right) = e^{ik_z d_s} F_{nk_z}\left(-\frac{d_s}{2}\right), \quad (2a)$$

$$F'_{nk_z}\left(\frac{d_s}{2}\right) = -e^{ik_z d_s} F'_{nk_z}\left(-\frac{d_s}{2}\right). \quad (2b)$$

The Eqs. (2a) and (2b) assure the continuities of the envelope functions and their normal derivatives at the cell boundaries, respectively.

The Coulombic potential $V_C(z)$, due to the electrostatic electron-electron, and electron-ionized donors interactions, is obtained from the Poisson equation

$$\frac{d^2 V_C(z)}{dz^2} = -\frac{e^2}{\epsilon} [n(z) - N_D(z)], \quad (3)$$

with $n(z)$ being the electron density which is given by

$$n(z) = \sum_{n,k_z} N_{nk_z}(z) |F_{nk_z}(z)|^2 \quad (4)$$

Assuming zero temperature, the distribution function becomes $\theta[E_F - E_n(k_z)]$, where E_F is the Fermi energy and θ is the Heaviside step function. Then, one gets

$$N_{nk_z} = \frac{m^*}{\pi h^2} [E_F - E_n(k_z)] \theta[E_F - E_n(k_z)]. \quad (5)$$

For the exchange-correlation potential $V_{XC}(z)$ we have assumed the well-known analytic expression suggested by Hedin and Lundqvist [15]. The values used for the effective masses m^* , m_l^* and m_t^* are $0.068m_0$, $0.1905m_0$, and $0.9163m_0$, respectively, where m_0 is the electron mass. For the dielectric constants of GaAs and Si we adopted the values $12.5\epsilon_0$ and $12.1\epsilon_0$, respectively [16].

Results

Figure 1 shows typical results for Si δ -doped GaAs layers, for $N_D = 3 \times 10^{12} \text{ cm}^{-2}$ and three different values of d_s . For the larger value of $d_s = 800 \text{ \AA}$ four discrete subband levels are found occupied. The general aspect of the potential and charge density profiles does not change in a significant manner with the decrease in d_s . It is more interesting to look at the variations of the potential depth (V_0), the Fermi level position (E_F), and miniband widths, which contain the information physically more significant in practice. As can be seen in Figure 1, the potential depth V_0 decreases as d_s decreases. The general trend of the Fermi level E_F shows that it remains practically constant, suffering only a slight increase for $d_s < 70 \text{ \AA}$. When the δ -wells are wide apart and their potentials have negligible overlap, the system behaves as a set of independent isolated wells; as d_s decreases, their coupling is increased, and minibands start to appear characteristic of superlattice behavior. Similar results are obtained for Sb δ -doping in Si.

In Table I are depicted the values of V_0 , E_F , E_i , ΔE_i , and n_i , corresponding, respectively, to the potential depth, Fermi level position, energy of the bottom of the subbands, their energy dispersion (obtained as $\Delta E = |E_i(k_z = 0) - E_i(k_z = \pi/d_s)|$), and the subband occupancy, for Si δ -doping in GaAs with $N_D = 3 \times 10^{12} \text{ cm}^{-2}$ and for d_s varying between 800 and 40 \AA . As expected, higher subbands start to be populated as d_s increases. This behavior is accompanied by a narrowing of the minibands, indicating that confinement is enhanced in this case.

Table II shows the results obtained for V_0 , E_F , E_i , ΔE_i , and n_i for Sb δ -doped layers in Si for a typical donor concentration of $N_D = 1.3 \times 10^{13} \text{ cm}^{-2}$, and for d_s

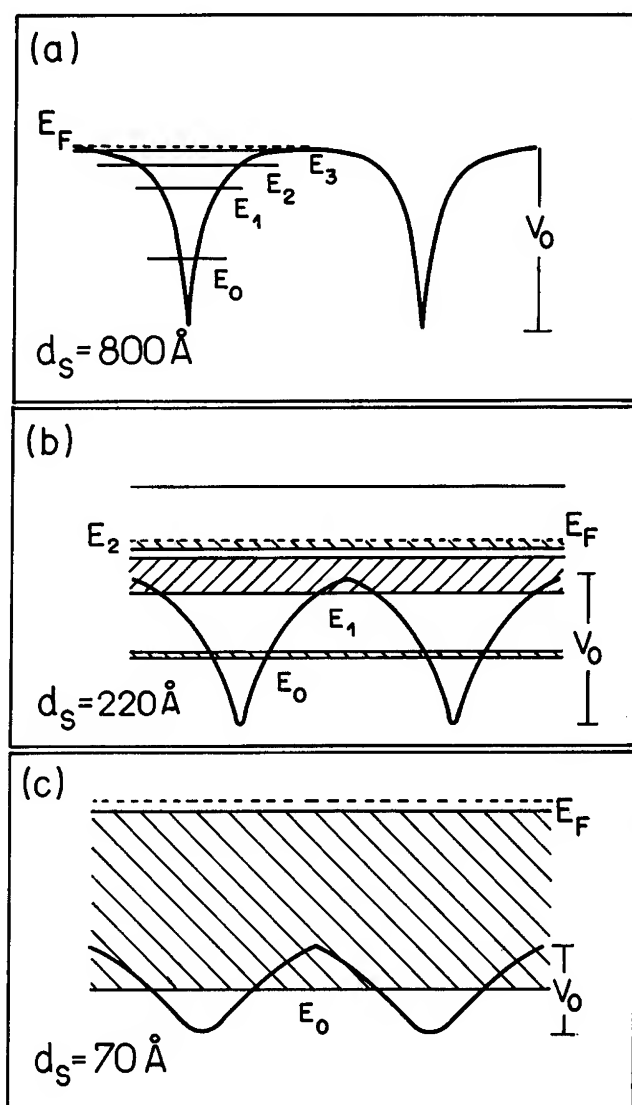


Figure 1. Band diagram scheme for periodic Si δ -doped layers in GaAs for $N_D = 3 \times 10^{12} \text{ cm}^{-2}$ and a spread of 10 Å. In (a) $d_s = 800 \text{ Å}$, in (b) $d_s = 220 \text{ Å}$, and in (c) $d_s = 70 \text{ Å}$. Potential profiles and subband energies are drawn to scale as obtained from SCF calculations. E_i indicates the bottom of the electron energy subbands. The Fermi level E_F is indicated by a dashed line.

varying between 300 and 50 Å which covers the entire range of periods in which the transition from isolated wells to a superlattice of δ -wells is observed. It is worth noting that since the effective masses in silicon are larger than in GaAs, for the former we expect the electrons will be less delocalized. This is indeed seen in the results shown in Tables I and II. Whereas for δ -doping in Si the system already

TABLE I. Characteristics of the periodic Si δ -doped GaAs systems, extracted from the SCF calculations for $N_D = 3 \times 10^{12} \text{ cm}^{-2}$. V_0 is the potential depth, E_F is the Fermi energy, E_i is the energy of the bottom of the subbands, ΔE_i is the energy dispersion (see text) and n_i is the subband occupancy. The values of V_0 , E_F , E_i , and ΔE_i are in meV. The occupancies n_i are given in units of 10^{12} cm^{-2} .

d_s (Å)	800	400	220	100	40
V_0	119.7	113.8	98.9	65.4	29.3
E_F	119.6	119.6	119.9	122.7	125.1
E_0	48.1	48.2	47.5	34.3	19.5
ΔE_0	—	—	1.6	42.3	336.4
n_0	2.03	2.03	2.06	2.51	3.00
E_1	96.0	96.0	91.0	105.0	—
ΔE_1	—	1.2	20.1	153.3	—
n_1	0.67	0.68	0.82	0.49	—
E_2	111.1	109.5	115.7	—	—
ΔE_2	0.1	7.9	50.2	—	—
n_2	0.25	0.29	0.12	—	—
E_3	117.9	—	—	—	—
ΔE_3	1.8	—	—	—	—
n_3	0.05	—	—	—	—

behaves as a set of independent wells for $d_s \geq 150 \text{ Å}$, in the case of GaAs the separate well behavior is observed only for $d_s \approx 800 \text{ Å}$. We should mention that the values of d_s , for which the transition from isolated to superlattice behavior takes place, are practically independent of the donor concentration N_D .

In the range of donor concentrations investigated for δ -doping in Si ($8 \times 10^{12} \text{ cm}^{-2} \leq N_D \leq 3 \times 10^{14} \text{ cm}^{-2}$), the transition from 2D to 3D behavior is observed only for high doping densities, i.e., $N_D \geq 2 \times 10^{13} \text{ cm}^{-2}$, and short periods $d_s \approx 50 \text{ Å}$, when the Fermi level is found to lie above the potential barrier between the δ -layers. We note, however, that although part of the electron gas exhibits a 3D character, the percentage of 3D electrons is very low (≈ 1 –2% of the total electron concentration). Shown in Figure 2 is a plot of the Fermi level position E_F , relative to the bottom of the δ -well, as a function of N_D for $d_s = 50 \text{ Å}$. We observe that E_F is linear for $N_D \leq 10^{14} \text{ cm}^{-2}$, reflecting the 2D character, while for larger values of N_D the behavior is typically 3D. These results could be an indication that even for electron densities as high as $\approx 10^{14} \text{ cm}^{-2}$, the real behavior is still not actually free-electron like. We mention, however, that these “delocalized” electrons could cause a remarkable increase of the mobility along the [001] direction. Further experiments would be required in order to confirm these predictions.

Conclusions

In conclusion, we have presented theoretical results of the electronic subband structure of periodic n -type δ -doped layers in GaAs and Si, within the local-density

TABLE II. Characteristics of the periodic Sb δ -doped Si systems, extracted from the SCF calculations for $N_D = 1.3 \times 10^{13} \text{ cm}^{-2}$. The quantities V_0 , E_F , E_i , and ΔE_i are the same as in Table I and are given in meV. The subband occupancies n_i are in units of 10^{13} cm^{-2} . Transverse levels are primed while the longitudinal ones are unprimed (see text).

$d_s (\text{\AA})$	300	200	150	100	50
V_0	99.1	99.2	99.2	99.0	92.4
E_F	98.8	98.8	98.7	97.7	91.2
E_0	39.6	39.6	39.6	39.7	39.1
ΔE_0	—	—	—	—	4.0
n_0	0.51	0.51	0.51	0.5	0.45
E'_0	62.9	62.8	62.5	60.4	48.6
$\Delta E'_0$	—	0.10	0.8	6.3	60.2
n'_0	0.68	0.68	0.68	0.71	0.81
E_1	86.9	87.0	87.0	86.5	85.9
ΔE_1	—	—	0.2	2.5	32.1
n_1	0.10	0.10	0.10	0.09	0.05
E_2	98.0	97.9	97.8	—	—
ΔE_2	0.3	1.3	3.6	—	—
n_2	0.01	3.6	0.01	—	—

approximation, for different doping periods and donor concentrations. The physical properties of these systems are strongly dependent on period and donor concentration, showing a transition from isolated wells to superlattices. We expect that, particularly in the case of δ -doping in silicon for which less experimental work is available, magnetotransport measurements can verify the validity of our calculation. Also, experimental results are needed to provide a guide for further theoretical efforts.

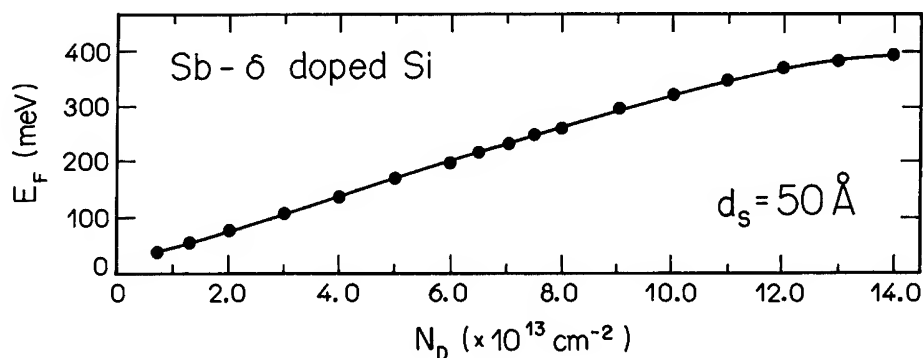


Figure 2. Dependence of the Fermi level position E_F , relative to the bottom of the wells placed at the zero of the energy, on the donor sheet concentration N_D for periodic Sb δ -doped layers in Si with $d_s = 50 \text{ \AA}$.

Acknowledgments

We would like to acknowledge CAPES, CNPq, and FAPEMIG (Brazilian funding agencies) for partial support.

Bibliography

- [1] J. Ploog, *J. Cryst. Growth* **81**, 304 (1987).
- [2] E. F. Schubert, *J. Vac. Sci. Technol.* **A8**, 2980 (1990).
- [3] H. P. Zeindl, T. Wegehaupt, I. Eisele, H. Oppolzer, H. Reisinger, G. Tempel, and F. Koch, *Appl. Phys. Lett.* **50**, 1164 (1987).
- [4] N. L. Matthey, M. G. Dowsett, E. H. C. Parker, T. E. Whall, S. Taylor, and J. F. Zhang, *Appl. Phys. Lett.* **57**, 1648 (1990).
- [5] A. Zrenner, F. Koch, and K. Ploog, *Surf. Sci.* **196**, 671 (1988).
- [6] M. Santos, T. Sajoto, A. Zrenner, and M. Shayegan, *Appl. Phys.* **53**, 2504 (1988).
- [7] M. H. Degani, *J. Appl. Phys.* **70**, 4362 (1991).
- [8] S. M. Shibli, L. M. R. Scolfaro, J. R. Leite, C. A. C. Mendonça, F. Plentz, and E. A. Meneses, *Appl. Phys. Lett.* **60**, 2895 (1992).
- [9] C. A. C. Mendonça, F. Plentz, J. B. B. Oliveira, E. A. Meneses, L. M. R. Scolfaro, D. Beliaev, S. M. Shibli, and J. R. Leite, *Phys. Rev. B* **48**, 12316 (1993).
- [10] L. Chico, F. Garcia-Moliner, and V. R. Velasco, *Phys. Rev. B* **48**, 11427 (1993).
- [11] H. J. Gossmann and F. C. Unterwald, *Phys. Rev. B* **47**, 12618 (1993).
- [12] I. Eisele, *Superlattices and Microstructures* **6**, 123 (1989).
- [13] L. M. R. Scolfaro, D. Beliaev, R. Enderlein, and J. R. Leite, to be published.
- [14] J. R. Leite, B. I. Bennett, and F. Herman, *Phys. Rev. B* **12**, 1466 (1975).
- [15] L. Hedin and B. I. Lundqvist, *J. Phys. C* **4**, 2064 (1971).
- [16] Landolt-Börnstein, *Numerical Data and Functional Relationships in Science and Technology*, Vol. 17 O. Madelung, Ed. (Springer-Verlag, Berlin, 1982).

Received March 31, 1994

Quantum Size Effects in Hexagonal Aluminum Films

J. C. BOETTGER

Theoretical Division, Los Alamos National Laboratory, Los Alamos, New Mexico 87545

U. BIRKENHEUER and N. RÖSCH

Lehrstuhl Für Theoretische Chemie, Technische Universität München, 85747 Garching, Germany

S. B. TRICKEY

Departments of Physics and Chemistry, University of Florida, Gainesville, Florida 32611

Abstract

The work functions and surface energies of Al(111) films ranging from one to seven layers thick have been calculated using the linear combinations of Gaussian type orbitals-fitting function (LCGTO-FF) technique, as implemented in the program package FILMS, an all-electron full-potential electronic structure method. Both quantities exhibit significant quantum size effect (QSE), in basic agreement with three previous investigations using more approximate techniques. However, there are significant quantitative differences among the four sets of results. © 1994 John Wiley & Sons, Inc.*

Introduction

It has been nearly two decades since it was first demonstrated that the work function of a jellium ultra-thin film (UTF) exhibits quantum oscillations as a function of film thickness [1,2]. That discovery stimulated a number of theoretical studies directed toward determining the size and extent of this so-called quantum size effect (QSE) in the work functions of real systems. Between 1983 and 1986, a series of three systematic investigations of thickness dependencies in the work function and surface energy of an fcc Al(111) film made it clear that a free standing (unsupported) metallic UTF composed of discrete atoms also could exhibit a significant QSE [3–5]. Unfortunately, it was soon demonstrated that there is little hope of actually observing a work function QSE because of the need to grow a metallic film on an electronically inert substrate in a controlled layer-by-layer fashion [4].

Although it seems unlikely that the work function QSE will ever be observed experimentally, there has been a continuing interest in studying the QSE in various properties of free standing films for both fundamental and pragmatic reasons. Fundamentally, one may hope to uncover an observable static QSE in other properties. Practically, perhaps the most important theoretical tool used to study surfaces is

* This article was work performed under the auspices of the US Department of Energy. This article is a US Government work and, as such, is in the public domain in the United States of America.

the UTF approximation. If a surface can be modelled adequately by a reasonably thin film, the properties of that surface can be calculated using modern high-precision UTF electronic structure techniques. Obviously, the adequacy of the UTF approximation will depend on the extent of the QSE in the relevant properties of the film. Thus, it is imperative to determine carefully the magnitude of any QSE in a given UTF prior to using that UTF as a model for a surface.

During the past decade, the linear combinations of Gaussian type orbitals-fitting function (LCGTO-FF) technique, as embodied in the computer code FILMS [6], has been used extensively to study QSE in the electronic and structural properties of numerous UTF systems; see Ref. [7] for a review. Most of the work done to date with FILMS has focussed either on very thin films (1 or 2 layers thick) or very small atoms (H, Li, Be, C) because of the large demands FILMS makes on computer resources, particularly CPU time. Recently, two of us (UB and NR) have implemented a number of improvements in the algorithms used in FILMS, thereby achieving a significant reduction in the needed CPU time [8]. This improved version of FILMS was then used to calculate the properties of MgO films up to 5 layers thick [9]. Adsorption systems, such as hydrogen on Li(001) and ethylene on Ni(110), also have been investigated recently [10].

In the present investigation, FILMS has been used to study the work function and surface energy QSE of unrelaxed Al(111) films ranging from one to seven layers thick. Although the Al(111) film was the first atomic UTF to be systematically examined for QSE [3-5], none of those early studies employed all-electron full-potential band structure techniques comparable to the current state-of-the-art. Furthermore, there are significant differences among the three existing sets of results which remain to be resolved. Finally, the present work is intended as a precursor to a more demanding investigation of alkali-metal adsorption on the Al(111) surface; providing the requisite study of convergence with respect to thickness mentioned earlier. Thus, considerable effort has been devoted here to developing compact orbital and fitting function basis sets to be used in future calculations involving Al.

The organization of the remainder of this article is as follows. First, the early work on QSE in Al(111) films is reviewed. The LCGTO-FF technique and the basis sets used then are discussed. The current results are presented in the penultimate section. A few concluding remarks are given in the final section.

Background

In 1983, Feibelman [3] conducted the first systematic investigation of QSE in the work function and surface energy of a real metal film. That work studied 1, 2, 3, 4, and 6 layer thick Al(111) films using a linear combinations of atomic orbitals (LCAO) electronic structure method. The work functions were calculated both for ideal (bulk) geometries and for partially relaxed geometries, while the surface energies only were obtained at the relaxed geometries. Those LCAO calculations employed the Wigner interpolation form of the local density approximation (LDA) to exchange-correlation (XC) [11], used a frozen-core approximation, and fitted the charge density and the XC integral kernels with *s*-type GTOs. The irreducible part of the Brillouin zone (BZ) was sampled at only 10 points.

The work functions calculated by Feibelman [3] for the ideal Al(111) films began with a maximum value of 4.2 eV for the monolayer, dropped steadily to a minimum of 3.7 eV for the 3-layer, and then rose steadily to 4.0 eV in the 6-layer. For the relaxed films, which exhibit slightly expanded outer-layer spacings, the work functions again began at a monolayer value of 4.2 eV, dropped to 3.8 eV for the 3-layer, and then remained nearly constant for the 4- and 6-layer films. The surface energies of the relaxed films began with a monolayer value of 0.40 eV/atom, dropped to an exceptionally small value (0.18 eV/atom) for the 2-layer, jumped back up to 0.39 eV/atom for the 3-layer, and then steadily rose to 0.52 eV/atom in the 6-layer. To this date, the prediction [3] of a significant QSE in Al(111) films has never been challenged. However, there was considerable concern at the time that the quantitative results might have been affected seriously by the various approximations made in the LCAO code, especially the use of GTO fitting functions [3,4].

To check and improve on the results of Ref. [3], Feibelman and Hamann [4] repeated the calculations on the ideal Al(111) films (adding the 5-layer film) using a surface linearized augmented-plane-wave (SLAPW) method. Like the LCAO results, the SLAPW Al(111) work function begins with its maximum value for the monolayer (4.74 eV) and drops to its minimum at the 3-layer (4.10 eV). However, the SLAPW work function then jumps up to 4.43 eV for the 4-layer followed by a steady decline to 4.31 eV in the 6-layer. For all of the films studied, the SLAPW work functions were larger than the corresponding LCAO results by 0.3 to 0.6 eV. This rather large quantitative difference was attributed to errors in the LCAO results due to the charge fitting procedure. The basic problem was that the charge fitting produced a spurious negative electron density in the far vacuum region, thereby reducing the dipole barrier and the work function. Such an error in the charge density clearly would also affect the surface energies of the films. Unfortunately, the SLAPW code did not calculate the total energies of the films and thus could not be used to study the surface energy QSE.

The third systematic investigation of the Al(111) films was conducted by Batra et al. [5] using norm conserving pseudopotentials and the XC model of Perdew and Zunger [12]. Batra et al. calculated the work functions and surface energies for 1-, 3-, 5-, and 7-layer Al(111) films using the repeated slab approximation. As in the previous studies [3,4], a relatively sparse BZ mesh was used; only 49 points in the entire BZ. For a uniformly distributed mesh, this would correspond to only 8 points in the irreducible part of the BZ. Batra et al. concluded on the basis of analytical force calculations that, contrary to the earlier results [3], geometry relaxation effects should be small. For this reason, the work functions and surface energies were only calculated for the ideal geometries.

The Al(111) work function calculated by Batra et al. [5] ranges from a maximum of 4.1 eV for the monolayer to a minimum of 3.2 eV for the 3-layer, and then steadily rises to 3.7 eV for the 7-layer. Although this behavior appears to be in better qualitative agreement with the results of Ref. [3] than with those of Ref. [4], there is no fundamental disagreement between Refs. [4] and [5], since the SLAPW calculations did not consider the 7-layer film while the pseudopotential calculations did not include the 4- or 6-layer films. In addition, the surface energies found in

the pseudopotential calculations [5] only vary between 0.44 and 0.50 eV/atom; a considerably smaller range than was found with the LCAO method [3], even if one ignores the exceptionally small surface energy predicted for the 2-layer in the latter study.

Methodology

The LCGTO-FF Technique

The LCGTO-FF technique is an all-electron, full-potential, electronic structure method which is characterized by its use of three independent GTO basis sets to expand the orbitals, charge density, and LDA XC integral kernels (here Hedin-Lundqvist [13]). The purpose of the charge fit is to reduce the total number of integrals by ensuring that only 3-center integrals appear in the total energy and one-electron equations, instead of the usual 4-center integrals. The XC fit acts as a sophisticated numerical quadrature scheme capable of producing accurate results on a rather coarse numerical integration mesh.

The current implementation of the LCGTO-FF method in the program FILMS was discussed recently in detail [6]. Since that time, there have been a number of important algorithmic improvements [8]. First, the multiple expansions used in the past to speed up the evaluation of the orbital-fitting function-orbital integrals have been replaced by a generalized Ewald procedure utilizing mixed real and reciprocal space integration. Thus, convergence of the lattice sums is achieved by splitting the Coulomb integrals into long-range and short-range parts. A further speedup is attained by performing the Coulomb integrals for all needed l and m values simultaneously for each combination of GTO exponents. In addition to these major algorithmic modifications, numerous changes have been made throughout FILMS to allow vectorization.

For all of these calculations, the BZ integrals are performed via the linear triangle integration scheme, using 19, 37, or 61 points in the irreducible triangle of the BZ. Those points were distributed and grouped in a manner that ensures a more rapid convergence of the BZ integrals than is usually achieved by linear triangle integration; see the Appendix of Ref. [14]. The SCF cycle was iterated until the total energy changed by less than 1 μ H per atom.

The GTO Basis Sets

As was noted above, considerable effort was devoted to developing compact orbital and fitting function basis sets for Al. To this end, we began by performing reference calculations on the 1-, 2-, and 3-layer films using very rich basis sets and the 37 point BZ scan. As discussed elsewhere [15], different basis sets must be used for atoms in the interior and exterior layers of a UTF due to differences in their environments.

For the exterior layers, the rich orbital basis set was constructed from Huzinaga's [16] 11s7p atomic basis set as follows. First, the exponent of the most diffuse p -type GTO was shifted to 0.12. The basis set was then augmented by a single p_z -type

GTO with an exponent of 0.05. Finally, a d -type polarization function with an exponent of 0.30 was added. To reduce the size of the calculations slightly, the four tightest s -type and three tightest p -type GTOs were contracted using the coefficients of the $1s$ and $2p$ LDA atomic orbitals. The orbital basis for the interior layers was obtained from the exterior layer basis by shifting the exponent of the most diffuse s -type GTO to 0.10 and eliminating the most diffuse p_z -type GTO.

For the reference calculations, the same $10s3d2p_z$ GTO basis set was used for both the charge and XC fit functions in the exterior layers. For the interior layers, the exponent of the most diffuse s -type function was increased slightly and the p_z -type functions were removed [17]. Overall, these large orbital and fitting function basis sets should provide high quality reference results.

To develop compact orbital basis sets for Al from these rich basis sets, the primitive GTOs were contracted into a $6s3p1d$ plus $1p_z$ basis set for the exterior layers and a $6s3p1d$ basis for the interior layers. These compact orbital basis sets are given in Table I. The sizes of the charge and XC basis sets were reduced by eliminating a number of the largest exponents, and adjusting the remaining exponents. Ultimately,

TABLE I. Gaussian exponents (α) and contraction coefficients (C) of the compact orbital basis sets for the exterior and interior layers of the Al(111) films. Horizontal lines separate the contractions.

Type	Exterior		Interior	
	α	C	α	C
s	0.23491082e + 05	0.0010120	0.23491082e + 05	0.0010120
	0.35475323e + 04	0.0076655	0.35476323e + 04	0.0076655
	0.82347199e + 03	0.0375355	0.82347199e + 03	0.0375355
	0.23767938e + 03	0.1355686	0.23767938e + 03	0.1355686
	<u>0.78602059e + 02</u>	<u>0.2614458</u>	<u>0.78602059e + 02</u>	<u>0.2614458</u>
	0.78602059e + 02	0.0717569	0.78602059e + 02	0.0717569
	0.29049906e + 02	0.4328815	0.29049906e + 02	0.4328815
	<u>0.11623812e + 02</u>	<u>0.1973914</u>	<u>0.11623812e + 02</u>	<u>0.1973914</u>
	<u>0.34653431e + 01</u>	<u>1.0000000</u>	<u>0.34653431e + 01</u>	<u>1.0000000</u>
	<u>0.12331429e + 01</u>	<u>1.0000000</u>	<u>0.12331429e + 01</u>	<u>1.0000000</u>
	<u>0.20181005e + 00</u>	<u>1.0000000</u>	<u>0.20181005e + 00</u>	<u>1.0000000</u>
	0.07804797e + 00	1.0000000	0.10000000e + 00	1.0000000
p	0.14151036e + 03	0.0112485	0.14151036e + 03	0.0112485
	0.33217629e + 02	0.0759425	0.33217629e + 02	0.0759425
	0.10393014e + 02	0.2569316	0.10393014e + 02	0.2569316
	0.35925839e + 01	0.4541624	0.35925839e + 01	0.4541624
	<u>0.12421020e + 01</u>	<u>0.3852556</u>	<u>0.12421020e + 01</u>	<u>0.3852556</u>
	<u>0.30402357e + 00</u>	<u>1.0000000</u>	<u>0.30402357e + 00</u>	<u>1.0000000</u>
	0.12000000e + 00	1.0000000	0.12000000e + 00	1.0000000
p_z	0.05000000e + 00	1.0000000		
d	0.30000000e + 00	1.0000000	0.30000000e + 00	1.0000000

TABLE II. Gaussian exponents of the compact charge and XC basis sets for the exterior and interior layers of the Al(111) films.

Type	Charge		XC	
	Exterior	Interior	Exterior	Interior
<i>s</i>	900.00	900.00	80.00	80.00
	240.00	240.00	16.00	16.00
	80.00	80.00	3.80	3.80
	27.00	27.00	1.00	1.00
	9.00	9.00	0.27	0.27
	3.00	3.00	0.08	0.10
	0.90	0.90		
	0.27	0.27		
	0.08	0.10		
<i>d</i>	0.90	0.90	0.90	0.90
	0.30	0.30	0.30	0.30
<i>p_z</i>	1.00		0.90	
	0.30		0.30	

the charge fit basis sets were reduced to a $9s2d2p_z$ basis for the exterior layers and a $9s2d$ basis for the interior layers. The XC basis set was reduced in a similar fashion to a $6s2d2p_z$ basis for the exterior layers and a $6s2d$ basis set for the interior layers. These compact fitting function basis sets are given in Table II.

Table III compares cohesive energies per atom (E_c) and work functions (ϕ) obtained for the 1-, 2-, and 3-layer Al(111) films with both the rich and compact basis sets, using the 37 point BZ mesh. The systematic relative error (relative with respect to variations of the film thickness) in both quantities should be much larger for these three films than for all subsequent films because they encompass two important thickness-dependent changes in the basis sets: 1) the inclusion of p_z -type fitting functions for $n \geq 2$, and 2) the use of interior basis sets for $n \geq 3$. For films with $n \geq 3$, the basis set induced errors in E_c and ϕ will both converge rapidly to constant

TABLE III. Comparison of cohesive energies (E_c) and work functions (ϕ) obtained with the rich and compact basis sets (using the 37 point BZ mesh) for the 1-layer, 2-layer, and 3-layer Al(111) films; in eV.

	E_c		ϕ	
	Rich	Compact	Rich	Compact
1-layer	3.100	3.078	4.908	4.873
2-layer	3.626	3.605	4.685	4.636
3-layer	3.816	3.787	4.386	4.372

offsets and should have virtually no influence on the layer-dependent oscillations which are the focus of the present study. The cumulative effect of all of the basis set reductions is a lowering of E_c by 21 to 29 meV and of ϕ by 14 to 50 meV. Since these shifts all have the same sign, the relative imprecisions are only 8 meV for E_c and 35 meV for ϕ . For films with $n \geq 3$, these relative imprecisions in E_c and ϕ should be no more than 5 meV and 20 meV, respectively.

For all of the calculations presented in the next section, an additional size reduction was achieved by constraining each of the six most local charge fitting functions to have the same coefficient on all sites. This intersite core contraction scheme forces that portion of the density nearest to the nucleus to be identical for all of the Al atoms in the film. Similarly, the three most local XC fitting functions were also site contracted. In test calculations on the Al(111) 4-layer film, this intersite core contraction scheme changed the total energy per atom and the work function by much less than 1 meV.

The calculations reported here were carried out on a SUN SPARC ELC workstation with only 250 Mbytes of swap space, and required less than 500 Mbytes of disk file space. Thus, the present work provides a demonstration of the type of calculations of which FILMS is capable in a small scale computing environment.

Results

The total energies and work functions for ideal fcc Al(111) films ranging from one to seven layers thick were calculated using the 19 point BZ mesh. Those calculations were repeated for the one to six layer films using the 37 point BZ mesh. (The 7-layer calculation with the 37 point mesh required more memory than was available). The cohesive energies per atom were then determined relative to a spin-polarized LDA atomic energy (-482.596608 Ry) calculated without the use of fitting functions. The cohesive energies, work functions, and widths (W) of the occupied bands found here for the Al(111) films are listed in Table IV.

Comparing the results in Table IV obtained with the two BZ meshes reveals several interesting trends. First, the mesh induced shifts in E_c all have the same

TABLE IV. Comparison of cohesive energies (E_c), work functions (ϕ), and widths (W) of the occupied bands obtained with the 19 and 37 point BZ scans for the 1 \rightarrow 7 layer thick Al(111) films; in eV.

	E_c		ϕ		W	
	19 pt.	37 pt.	19 pt.	37 pt.	19 pt.	37 pt.
1-layer	3.021	3.078	4.847	4.873	8.09	8.10
2-layer	3.580	3.605	4.700	4.636	10.14	10.09
3-layer	3.778	3.787	4.498	4.372	10.65	10.76
4-layer	3.818	3.831	4.265	4.323	10.97	10.94
5-layer	3.870	3.880	4.583	4.553	11.07	11.05
6-layer	3.905	3.915	4.483	4.482	11.08	11.08
7-layer	3.926		4.487		11.14	

sign with the largest change being 57 meV for the 1-layer. Second, for the films with $n \geq 3$, the change in E_c is nearly constant and is less than 15 meV. These results suggest that for the 37 point mesh, the relative imprecision in E_c due to the BZ integration should be no more than 5 meV for n -layers with $n \geq 3$, and no more than 50 meV for all of the films. Combining this result with the basis set error suggests a total relative error in E_c of no more than 10 meV for $n \geq 3$. Again, the absolute error should approach a constant offset for large n .

The work function is more strongly influenced by the BZ mesh density, with the largest shift being 126 meV for the 3-layer. Furthermore, the sign of the shift in ϕ is not the same for all of the films. Thus, the relative error in ϕ is greater than the absolute error. To better assess the influence of the BZ mesh on the workfunction, the 3-layer calculation (the worst case) was repeated using a 61 point BZ mesh. That calculation produced $E_c = 3.790$ eV, $\phi = 4.393$ eV, and $W = 10.69$ eV. These results indicate that ϕ is converged to within 30 meV for the 37 point mesh. Assuming that the sign of the error in ϕ still varies and that the error is greatest for the 3-layer, the relative error in ϕ due to the BZ mesh should be no more than about 50 meV. Combining this result with the basis set error implies a total relative imprecision of no more than 75 meV over the full range of film thicknesses considered here, with most of that imprecision being due to the BZ mesh. Given the fact that even the 19 point mesh used here is denser than those used in the previous studies, the present results should be more reliable than the earlier results.

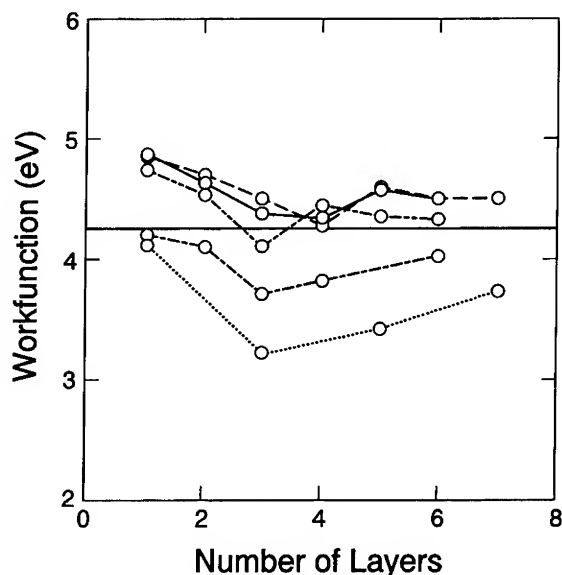


Figure 1. Calculated work functions vs. the number of layers (n) for the LCGTO-FF calculations with 37 BZ points (solid line) and 19 BZ points (dashed line). Also shown are the results from Ref. [3] (dash-dot line), Ref. [4] (dash-triple dot line), and Ref. [5] (dotted line). The experimental result from Ref. [18] is indicated by a horizontal line.

Figure 1 compares the work functions listed in Table IV with those found in the previous studies [3–5]. The experimental work function for the Al(111) surface (4.24 eV) [18] is indicated by a horizontal line. The five curves in Figure 1 can be divided into two groups; three curves tightly clustered above the measured surface value and two located well below. The latter two curves (from Refs. [3] and [5]) give no indication that ϕ is converging with increasing n . In contrast, the current results for both BZ meshes and the SLAPW results from Ref. [4] are all clearly converging as n increases.

The present calculations predict that ϕ steadily decreases for $n = 1 \rightarrow 4$, jumps up between $n = 4$ and 5, and then steadily decreases for $n = 5 \rightarrow 7$. The SLAPW calculations [4] predict a similar behavior, but locate the jump in ϕ between $n = 3$ and 4. There are at least two methodological differences between the SLAPW calculations and the present LCGTO-FF calculations that could be responsible for this rather minor disagreement. First, different XC models were used in the two calculations (HL here and Wigner in Ref. [4]). Alternatively, the results in Table IV indicate that the values of ϕ at $n = 3$ and 4 are particularly sensitive to the BZ mesh density. Since Ref. [4] only used a 10 point mesh vs. the 19 and 37 point meshes used here, it may be that the order of the two points was reversed in that study.

The surface energies for the Al(111) films were determined here using an approach suggested in Ref. [19]. First, define the incremental energy for an N -layer film as

$$\Delta E(N) = E_N - E_{N-1}, \quad (1)$$

where E_N is the total energy per cell of the N -layer. Then, assuming there is only one atom per layer in the film unit cell, the surface energy per atom of any n -layer with $n \leq N$ can be approximated as,

$$E_s(n) = \frac{1}{2} \times [E_n - n \times \Delta E(N)]. \quad (2)$$

In the limit of large N , $\Delta E(N)$ will converge to a value for the bulk energy per atom that is consistent with the film calculation and $E_s(N)$ will converge to the semi-infinite surface energy. Any attempt to replace ΔE in Eq. (2) with an independently calculated bulk energy (E_b) will introduce an error in E_s that increases linearly with n [19].

Table V shows the incremental energies obtained for the Al(111) films using both BZ meshes, relative to the free atom energy. The bulk binding energy of Al reported by Moruzzi, Janak, and Williams [20] is also given. By the 7-layer, the incremental energy has converged to about -4.05 ± 0.05 eV. This result is in reasonable agreement with the bulk binding energy of -3.88 eV, given the significantly different computational method used in Ref. [20]. The minimum at $n = 4$ is again striking.

Table VI compares the surface energies obtained for the 37 point BZ mesh using $N = 6$ in Eq. (2) with those obtained for the 19 point mesh using $N = 6$ and 7 in Eq. (2). Also shown in Table VI is a value of E_s (0.51 eV/atom) deduced from the surface tension of the liquid metal [21]. Two features are immediately apparent in Table VI. First, the change in the BZ scan density has only a minor effect on E_s .

TABLE V. The incremental energies (ΔE) obtained with the 19 and 37 point BZ scans, relative to the atomic energy; in eV. The bulk binding energy of Al from Ref. [20] is also listed.

	ΔE	
	19 pt.	37 pt.
1-layer	-3.021	-3.078
2-layer	-4.138	-4.131
3-layer	-4.174	-4.153
4-layer	-3.937	-3.962
5-layer	-4.079	-4.076
6-layer	-4.080	-4.090
7-layer	-4.055	
Bulk	-3.878	

Second, the relatively small difference between $\Delta E(6)$ and $\Delta E(7)$ produces a substantial change in E_s vs. n . This sensitivity to small changes in ΔE is due to the linear increase of the error in E_s as a function of n [19]. For the remainder of this discussion only the 19 point results will be considered.

Figure 2 compares E_s values obtained here using $N = 6$ and 7 with the results from Refs. [3] and [5]; recall that no values of E_s were given in Ref. [4]. Again, the curves from Refs. [3] and [5] show no sign of converging as n increases. This lack of convergence may be due to the fact that Refs. [3] and [5] both relied on inde-

TABLE VI. Surface energies (E_s) obtained with the 19 point BZ scan for $N = 6$ and 7 compared to values obtained with the 37 point BZ scan for $N = 6$; in eV/surface-atom. Also shown is the experimental value deduced by Ref. [21].

	19 pt.		37 pt.
	$N = 7$	$N = 6$	$N = 6$
1-layer	0.517	0.529	0.506
2-layer	0.475	0.501	0.486
3-layer	0.415	0.454	0.454
4-layer	0.474	0.525	0.519
5-layer	0.462	0.526	0.526
6-layer	0.449	0.526	0.526
7-layer	0.449		
Expt.	0.51		

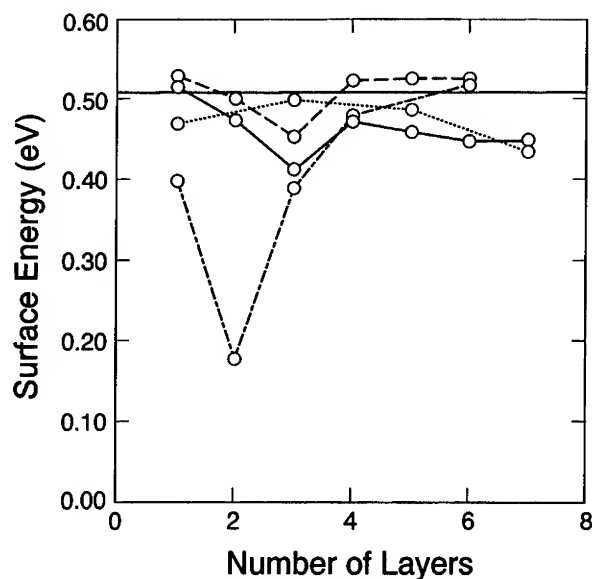


Figure 2. Calculated surface energies vs. the number of layers n are shown for the 19 k-point LCGTO-FF calculations using $N = 7$ (solid line) and $N = 6$ (dashed line). Also shown are the results from Ref. [3] (dash-dot line) and Ref. [5] (dotted line). The experimental result from Ref. [21] is indicated by a horizontal line.

pendently calculated bulk energies to find E_s . In contrast, the present results for E_s are based on incremental energies and both curves show a clear convergence with increasing n , although not to the same value.

Comparison of the two curves in Figure 2 obtained here using $N = 6$ and 7 clearly illustrates the linear divergence caused by shifts in ΔE [19]. However, this divergence does not alter the qualitative behavior of E_s . There is an initial decrease in E_s for $n = 1 \rightarrow 3$, followed by an abrupt increase between $n = 3$ and 4, and then a very slow decrease for $n = 4 \rightarrow 7$. Although it is not entirely clear what the converged value of E_s would be for very large N since ΔE has not yet stabilized, it is reassuring that the "experimental" surface energy lies between the two results calculated here.

Conclusions

A significant QSE has been found in both ϕ and E_s for Al(111) films ranging from one to seven layers thick. The present results for ϕ vs. n are in excellent qualitative agreement with the previous SLAPW calculations [4]. The only noteworthy difference between the LCGTO-FF and SLAPW results is the location of the abrupt increase in ϕ predicted in both calculations. On the other hand, the present results for the QSE in both ϕ and E_s differ significantly from the LCAO results of Ref. [3] and the pseudopotential results of Ref. [5]. The current results should be more reliable than all previous results.

In spite of the QSE in ϕ and E_s , both quantities are clearly converging as n increases. However, it is not clear that the region of significant QSE has been passed even for $n = 7$. The overall impact of the QSE on the work function should be no more than 0.3 eV for $n \geq 7$. The QSE in E_s should be even smaller, no more than 0.05 eV for $n \geq 7$. However, even for the 7-layer film, the calculated surface energy is still being affected by small fluctuations in the incremental energy, $\Delta E(N)$. If solid surface modelling is desired, elimination of that particular variation in E_s might require the use of much thicker films.

Acknowledgments

The work of JCB was supported by the US Department of Energy. The work of the Munich group was supported by the Deutsche Forschungsgemeinschaft via SFB 338 and by the Fonds der Chemischen Industrie. SBT was supported in part by the US Army Research Office.

Bibliography

- [1] F. K. Schulte, *Surf. Sci.* **55**, 427 (1976).
- [2] E. E. Mola and J. L. Vicente, *J. Chem. Phys.* **84**, 2876 (1986).
- [3] P. Feibelman, *Phys. Rev. B* **27**, 1991 (1983).
- [4] P. Feibelman and D. R. Hamann, *Phys. Rev. B* **29**, 6463 (1984).
- [5] I. P. Batra, S. Ciraci, G. P. Srivastava, J. S. Nelson, and C. Y. Feng, *Phys. Rev. B* **34**, 8246 (1986).
- [6] J. C. Boettger, *Int. J. Quantum Chem. Quantum Chem. Symp.* **27**, 147 (1993); see also J. C. Boettger and S. B. Trickey, *Phys. Rev. B* **32**, 1356 (1985); and J. W. Mintmire, J. R. Sabin, and S. B. Trickey, *Phys. Rev. B* **26**, 1743 (1982).
- [7] J. C. Boettger, *Int. J. Quantum Chem. Quantum Chem. Symp.* **26**, 633 (1992).
- [8] U. Birkenheuer and N. Rösch, unpublished (1992).
- [9] U. Birkenheuer, J. C. Boettger, and N. Rösch, *J. Chem. Phys.* (submitted).
- [10] U. Birkenheuer, P. Ulbricht, N. Rösch, and J. C. Boettger, unpublished.
- [11] E. Wigner, *Phys. Rev.* **46**, 1002 (1934).
- [12] J. P. Perdew and A. Zunger, *Phys. Rev. B* **23**, 5048 (1981).
- [13] L. Hedin and B. I. Lundqvist, *J. Phys. C* **4**, 2064 (1971).
- [14] J. C. Boettger and S. B. Trickey, *J. Phys.: Condens. Matter* **2**, 9589 (1990).
- [15] J. C. Boettger and S. B. Trickey, *Phys. Rev. B* **45**, 1363 (1992).
- [16] S. Huzinaga, *Approximate Atomic Functions II*, Report from Department of Chemistry, University of Alberta (1971).
- [17] The exponents for the rich fitting function basis sets can be obtained from the authors.
- [18] H. B. Michaelson, *J. Appl. Phys.* **48**, 4729 (1977).
- [19] J. C. Boettger, manuscript in preparation.
- [20] V. L. Moruzzi, J. F. Janak, and A. R. Williams, *Calculated Electronic Properties of Elemental Solids* (Pergamon, New York, 1978).
- [21] F. R. de Boer, R. Boom, W. C. M. Mattens, A. R. Miedema, and A. K. Niessen, *Cohesion in Metals* (North-Holland, Amsterdam, The Netherlands, 1988).

On the Role of Doping in High- T_c Superconductors*

CHANGJIANG MEI

Quantum Theory Project, 362 Williamson Hall, University of Florida, Gainesville, FL 32611

VEDENE H. SMITH, JR.

Department of Chemistry, Queen's University, Kingston, Ontario, Canada, K7L 3N6

Abstract

High- T_c superconductors (HTSCs) are usually obtained by doping electron donors or acceptors into parent materials. The actual role played by doping is still uncertain with various interpretations. The present electronic structure study provides some hints which may help to solve the mystery. © 1994 John Wiley & Sons, Inc.

Introduction

Müller and Bednorz [1] synthesized the first HTSC by doping some Ba^{+2} to replace some of the La^{+3} in the parent material La_2CuO_4 . This process is considered to dope holes into the half-filled band structure of the parent material. The analogous electron doping can also lead to HTSC [2], but for simplicity, hereafter only hole doping will be considered.

The synthesis of the known HTSCs, especially the simplest $SrCuO_2$ based HTSC [2], reveal that the CuO_2 layer(s) must be the responsible component. Indeed, electronic structure studies showed that the active band, i.e., the half-filled band, is just the in-plane $Cu-d$ $O-p$ antibonding band [3]. However, it is still not very clear what rôle doping really plays.

There have been many interpretations and speculations about the effect(s) that doping causes. A typical theory [4] starts from the Mott insulating state [5] of the parent material with a half-filled electronic band. Due to the strong electronic correlations in the half-filled band, electrons become very localized with one electron per site and with only magnetic coupling between them. The parent material is a poor conductor, although it should not be so with a partially occupied valence band, according to traditional band theory. As holes are doped in, the valence band is brought away from half-filling, and the material becomes conducting. It is believed [4] that high- T_c superconductivity arises from the Bose condensation of the holes.

Such theories may be internally consistent within a model itself, but they cannot explain a large number of experimental facts. However, they bring out very inter-

* This work was partly supported by the US Office of Naval Research, and partly by the Natural Science and Engineering Research Council of Canada.

esting ideas, which has resulted in many studies on the Hubbard model [6], and variants thereof.

In the next section, the method and the system studied are first briefly introduced, and the results are presented. Discussion on the obtained results and their validity are given in the third section. Finally, in the last section, concluding remarks are made.

Method and Results

In order to find out what the effect the doped holes have in the material, a Hartree-Fock (HF) electronic structure study with CRYSTAL-88 [7] was carried out for a two-sided symmetric slab, which mimics the CuO_2 layer of the La_2CuO_4 crystal. It has [8] the space group D_{4h}^1 (P_4/mmm), No. 123, lattice constants $a = 3.787 \text{ \AA}$ and $c = 13.288 \text{ \AA}$, and atom positions $\text{Cu}(0.0, 0.0, 0.0)$, $\text{O}_p(0.0, 1.894, 0.0)$, $\text{La}_1(1.894, 1.894, 1.852)$, $\text{O}_o(0.0, 0.0, 2.428)$, $\text{La}_2(0.0, 0.0, 4.792)$, where O_p and O_o designate in-plane and out-of-plane oxygens, respectively.

The slab under investigation has the unit cell configuration $\text{CuO}_2[\text{Na}^{+1}]_2$. Here $[\text{Na}^{+1}]$ is the +1 sodium pseudopotential. Each is placed at the position corresponding to La_1 in the La_2CuO_4 crystal as the electron donor, and each contributes one electron to the CuO_2 unit cell so that the formal electronic configuration is $\text{Cu-}3d^9 \text{ O-}2p^6$, in which the highest occupied band is the half-filled Cu-d O-p σ -antibonding band, i.e., E_g band, corresponding to the previously mentioned one for the parent material in the nonsuperconducting phase.

For the present study, a He-core pseudopotential for O [9], an Ar-core pseudopotential for Cu [10], and the Na^{+1} pseudopotential [9], are used. For Cu-3d valence orbitals, *triple* ζ Gaussian Orbitals (*TZ* GTOs) are used with *double* ζ (*DZ*) 4s 4p basis [11] also included. For O, a *DZ* GTO basis for the 2p valence orbitals are employed including a polarization d-function basis with an exponent equal to that of the outer p function [9].

To simulate the doping, the hole concentration can be modulated by taking electrons out of the CuO_2 plane and putting them on the out-of-plane Na^{+1} centers. In this way, *ab initio* self-consistent computations for an arbitrary in-plane hole concentration can be made without employing super-cells or the Rigid-Band Approximation [12]. The reason the La_1 position was considered instead of the out-of-plane O_o position was that the O_o positions are further away from the CuO_2 plane and known to be far less important for the in-plane electronic structures [13]. Moreover, the Na^{+1} centers will be used as hole modulators as described below, which is the function of the La atoms.

The electronic structure computation was carried out for a number of hole concentrations. In Figure 1, the total density of states (DOSS) for hole concentrations 0.0, 0.352, 0.425, 0.505, and 0.745 holes-per- CuO_2 -unit-cell are given, respectively. It can be seen clearly that there is a bump in the total DOS in the neighborhood of the Fermi energy (e_f), which is of an amplitude twice as large as that in its vicinity. It moves from below e_f to above e_f with increasing hole concentration.

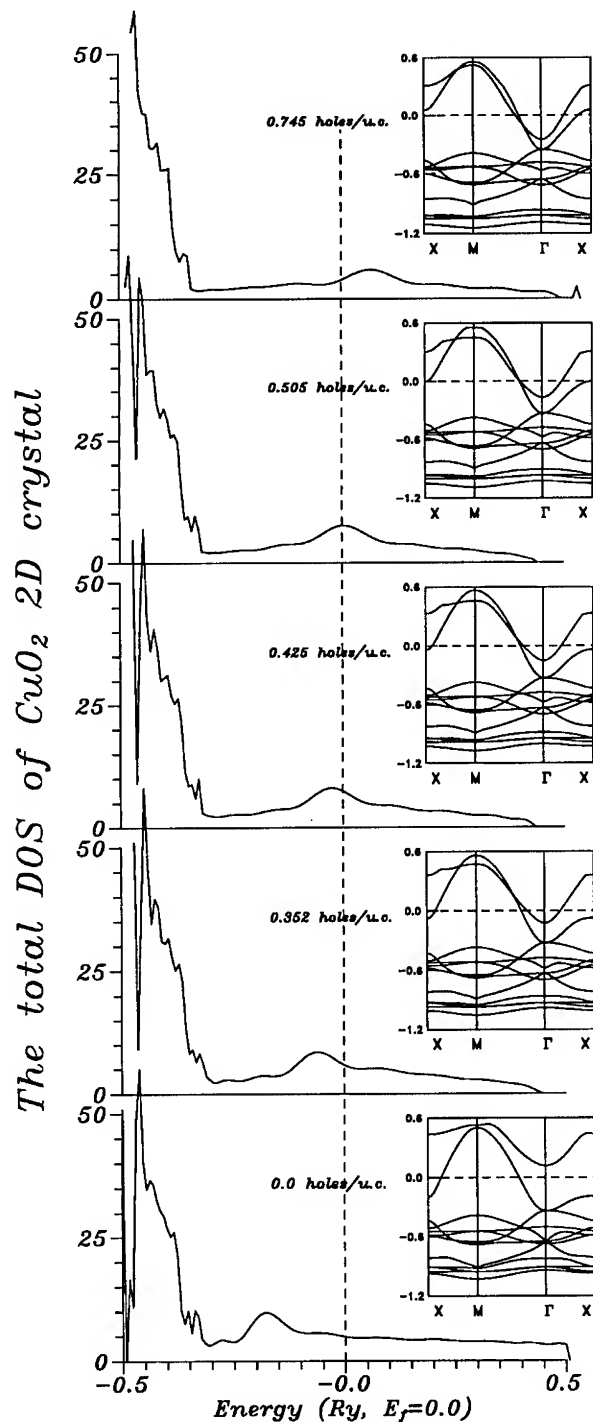


Figure 1. The total DOS for the CuO_2 plane with hole dopings, 0.0, 0.352, 0.425, 0.505, and 0.745 holes/(unit cell), respectively. The DOS of the localized nonbonding Cu- d states have not been included because they change little with the different dopings and are also too far below ϵ_F and less important for the properties considered here. However, it is such states that differentiate the HF computations from the corresponding LDA ones.

Discussion

According to the BCS theory [14], once there is an attractive potential between two electrons (in BCS it was due to phonons) around ϵ_f electrons may pair together, and the superconducting state occurs. The superconducting temperature, T_c , can be expressed as

$$T_c = a * e^{-b/n(\epsilon_f)}, \quad (1)$$

where $a = 1.14\Theta_D$, in which $\Theta_D = (\hbar\omega)/k_B$ is the average phonon energy scaled in temperature units, $n(\epsilon_f)$ is the average total DOS around the Fermi energy (ϵ_f), and b is proportional to the inverse of V , the average energy of the electron-quasiparticle interaction, which resulted in the pairing of electrons that in turn led to the superconductivity. T_c therefore increases with increasing $n(\epsilon_f)$. A schematic representation of changes of T_c with varying $n(\epsilon_f)$ is given in Figure 2. It is obvious that the $n(\epsilon_f)$ changes with hole doping obtained in the present study can result in large changes in T_c .

The BCS theory may not fully explain high- T_c superconductivity. However, the magnetic flux quantum experiment [15] showed that electrons in the new HTSCs are still paired, so that if Θ_D is simply considered as an average energy scaled in temperature units, and V is of the corresponding origin, Eq. (1) should still indicate the right trends.

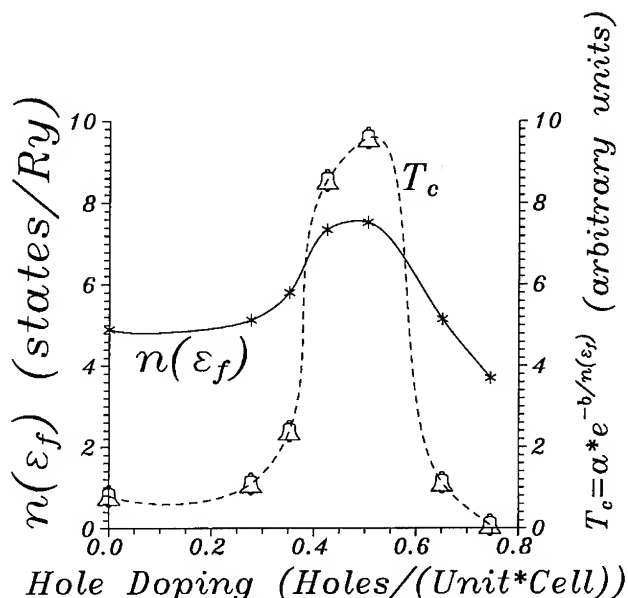


Figure 2. The schematic representation of $T_c = a * e^{-b/n(\epsilon_f)}$ changes with varying $n(\epsilon_f)$. The parameters are chosen to be within the range of the realistic values of conventional superconductors ($a = 1000$, $b = 35$), and to give conventional T_c 's.

The quantities in Eq. (1) are of the orders of magnitude $T_c \sim 10^1$, $\Theta_D \sim 10^3$, and $e^{[-b/n(\epsilon_f)]} \sim 10^{-2}$, so that a doubled magnitude of the DOS in the neighborhood of ϵ_f will result in a T_c roughly one order of magnitude larger, according to the BCS theory, which means that a low T_c superconductor will be turned into a HTSC!

If the present result is compared with experiment, the consistency becomes more obvious. Recall Figure 1. of Ref. [3], i.e., the phase diagram of the HTSCs under different dopings. Beyond a threshold doping level, T_c increases with increasing hole concentration until a maximum is reached, and then decreases as the hole concentration continuously increases until T_c drops to zero.

These experimental results can be understood from the point of view of the present computations: the high bump in the total DOS shifts with the hole concentration x . As x increases, the bump moves towards ϵ_f from below. At a value of x such that the bump is sufficiently close to ϵ_f , there is the onset of superconductivity. As x continues to increase, the bump moves further until it is right at the ϵ_f , which corresponds to the maximum T_c in Figure 1. of Ref. [3]. As x changes further from that point, the bump begins to move away from ϵ_f , which corresponds to the drop of T_c after the maximum. After the DOS bump moves sufficiently beyond ϵ_f , the superconductivity fades out again.

From the band structure, it is easily seen that the DOS bump near ϵ_f is mainly from the weakly dispersed portion of the partially filled band(s) around X/Y points. So when the bump is right at ϵ_f , the Fermi surface becomes nesting in the X-Y plane. The band, which is completely empty in the zero hole case, and becomes increasingly occupied with increasing hole concentration is the hole modulator band.

It should be mentioned that a peak in the computed DOS of La_2CuO_4 was noticed earlier, and an estimate about the shift of the peak with the hole concentration change was made under the Rigid-Band Approximation [16]. However, the continuous movement of the peak driven by the changing hole concentration shown above suggests that the doping induced DOS enhancement at the Fermi energy is possibly responsible for the high- T_c superconductivity.

Some comments should be made regarding the use of the HF method [17]. Unlike the local density approximated density functional method (LDA) [18,19], it does not use local approximations on the exchange(-correlation) potential. The corresponding single determinantal wavefunction is a clearly defined quantity which takes account of the different nodal structures of the different orbitals via its nonlocal, exact exchange term. In principle, it is known what is missing from the HF state and how it can be improved by introducing correlations either through perturbative or variational procedures [20]. As a result, HF calculations can be used as a good reference for other computations. In fact, in the original Kohn-Sham paper [18], a variant of the LDA scheme was proposed with the HF state as the reference. It is also known that the HF density is accurate up to the second order [21].

However, it is well-known that due to the uncompensated nonlocal exchange term under the HF approximation (or to say the unscreened long range Coulomb interaction) calculated HF band structures for metals are about twice as wide as those from experiment, as are band gaps for insulators and semiconductors. What

is more alarming is that for a metallic system with partly filled band at ε_f the derivative of the band, $\partial\varepsilon/\partial k$, becomes logarithmically infinite. This divergence will affect the DOS through

$$n(\varepsilon) \propto \int_{S(\varepsilon)} \frac{dS}{\left| \frac{\partial\varepsilon}{\partial k} \right|}, \quad (2)$$

and result in a vanishing $n(\varepsilon_f)$ [22]. However, all this is due to the divergence at $k = 0$ of $4\pi e^2/k^2$, which is the Fourier transform of the Coulomb potential e^2/r . It is just a reflection of the unscreened long range Coulomb interaction in the HF scheme. The part of the interaction integrals/lattice summations which result in the so called HF pathology were identified in the works given in Ref. [23].

Nevertheless, the interaction in reality is screened, and with the form

$$V(r) \propto e^2 \left(\frac{e^{-k_0 r}}{r} \right), \quad (3)$$

according to the Random Phase Approximation (RPA) [24], which takes care of the *zero point plasmon fluctuations*, or the *long-range* correlations. (This form of potential is often called the Yukawa potential.)

From the form of the screened potential, it is clear that it results in a rapid decrease of the interaction beyond a distance $1/k_0$ in metallic systems, i.e., the interaction becomes short range, instead of long range.

In the numerical scheme [17] of solid state HF computations, the interaction integral and lattice summation are carried out only up to a cut-off distance, not to infinity. This is a numerical approximation, but it has partially compensated the error from the HF approximation, eliminated the unphysical divergence, and thus removed the vanishing at ε_f from the computed DOS. Essentially, the cut-off of the interaction integral/lattice summation can be considered as equivalent to replacing the RPA screening factor $e^{-k_0 r}$ by a step function $1 - \Theta(r - 1/k_0)$. With this comparison, the nonvanishing DOS at ε_f becomes straightforward to understand, and the reliability of HF calculations is increased, too.

Nevertheless, another important fact is that in the presence of strong correlations, as in transition metal oxides with quite localized d electrons, which includes the parent materials of HTSCs, the lack of correlation in the HF scheme will lead to complete failure in explaining Mott insulating [5] behavior. Fortunately, the systems under investigation here are the normal state of the HTSC phase which is already out of the Mott insulating range. So except for the band width and band gap overestimation, the result should be generally correct and give qualitatively right predictions.

Conclusions

From the results shown above, it seems that the initial doping causes the parent material to become metallic. Then increased doping moves ε_f towards the DOS

maximum and the onset of high- T_c superconductivity. Then further dopings eventually destroy HTSC again and return the normal state.

Acknowledgments

One of the authors, C.-J. Mei, would like to thank Dr. R. Bartlett for his hospitality during completion of this work. The authors would like to thank Dr. J.-L. Calais for fruitful correspondence, and Dr. H. J. Monkhorst for stimulating discussions.

References

- [1] K. A. Müller and J. G. Bednorz, *Z. Phys.* **B64**, 189 (1986).
- [2] M. G. Smith, A. Manthiran, J. Zhou, and J. B. Goodenough, *Nature* **351**, 549 (1991).
- [3] W. E. Pickett, *Rev. Mod. Phys.* **61**, 433, 749 E (1989).
- [4] V. J. Emery, *Phys. Rev. Lett.* **58**, 2794 (1987); P. W. Anderson, G. Baskaran, Z. Zou, and T. Hsu, *Phys. Rev. Lett.* **58**, 2790 (1987).
- [5] N. F. Mott, *Nature* **327**, 185 (1987).
- [6] J. E. Hubbard, *Proc. Roy. Soc. (London)*, *Serv. A* **276**, 238 (1963), *A* **277**, 237 (1964).
- [7] C. Pisani, R. Dovesi, C. Roetti, and M. Causa, *CRYSTAL 88*, QCPE program No. 577.
- [8] J. D. Jorgensen, H. B. Schüttler, D. G. Hinks, D. W. Capone II, K. Zhang, M. B. Brodsky, and D. J. Scalapino, *Phys. Rev. Lett.* **58**, 1024 (1987).
- [9] H. Preuss, H. Stoll, U. Wedig, and Th. Krüger, *Int. J. Quantum Chem.* **19**, 113 (1981).
- [10] P. J. Hay and W. R. Wadt, *J. Chem. Phys.* **82**, 270 (1985).
- [11] M. Dolg, U. Wedig, H. Stoll, and H. Preuss, *J. Chem. Phys.* **86**, 866 (1987).
- [12] W. Jones and N. H. March, *Theoretical Solid State Physics, Vol. 2: Non-equilibrium and Disorder* (Wiley, Chichester, England, 1973).
- [13] G. Bubeck, Doctoral Thesis, Max Planck Institut für Festkörperforschung, Stuttgart, Germany (1988).
- [14] L. N. Cooper, *Phys. Rev.* **104**, 1189 (1956), J. Bardeen, L. N. Cooper, and J. R. Schrieffer, *Phys. Rev.* **108**, 1175 (1957).
- [15] C. E. Gough, M. S. Colclough, E. M. Forgan, R. G. Jordan, M. Keene, C. M. Muirhead, A. I. M. Rae, N. Thomas, J. S. Abell, and S. Sutton, *Nature* **326**, 855 (1987).
- [16] W. E. Pickett and H. Krakauer, *Phys. Rev.* **B35**, 7252 (1987); J. C. Phillips, *Physics of High- T_c Superconductors* (Academic, New York, 1989).
- [17] C. Pisani, R. Dovesi, and C. Roetti, *Hartree-Fock ab initio Treatment of Crystalline Systems*, Lecture Notes in Chemistry 48 (Springer-Verlag, Berlin, 1988).
- [19] O. K. Andersen, O. Jepsen, and D. Glötzl, in *Highlights of Condensed Matter Theory*, Proceedings of the International School of Physics, Enrico Fermi, Varenna, Italy, July 1983, F. Bassani et al., Eds., (Elsevier, Amsterdam, The Netherlands, 1985); and refs. therein.
- [20] Correlation can be added to the HF state by using, for example, the Local Ansatz, see, e.g.: B. Kiel, G. Stollhoff, C. Weigel, P. Fulde, and H. Stoll, *Z. Phys.* **B46**, 1 (1982).
- [21] C. Möller and M. S. Plesset, *Phys. Rev.* **46**, 618 (1934); W. Kutzelnigg and V. H. Smith, Jr., *J. Chem. Phys.* **42**, 2791 (1965).
- [22] H. J. Monkhorst, *Phys. Rev. B* **20**, 1504 (1979).
- [23] J. Delhalle and J.-L. Calais, *Int. J. Quantum Chem.* **21**, 115 (1987); J. Delhalle, M. H. Delvaux, J. G. Fripiat, J. M. André, and J.-L. Calais, *J. Chem. Phys.* **88**, 3141 (1988), J.-L. Calais and J. Delhalle, *Int. J. Quantum Chem.* **42**, 35 (1992).
- [24] D. Bohm and D. Pines, *Phys. Rev.* **92**, 609 (1953).

1994 Sanibel Symposia List of Participants

IOURI ABACHKINE
Program Resources, Inc. National Cancer
Institute
Frederick Cancer Research & Development
Center, P.O. Box B
Frederick, MD 21702

GUSTAVO ARTECA
Laurentian University
Chemistry & Biochemistry Depts
Ramsey Lake Road
Sudbury, Ontario P3E 2C6
Canada

OSMAN ATABEK
CNRS, Universite de Paris Laboratoire de
Photophysique Moleculaire
Bat. 213, Campus D'Orsay
Orsay 91405
France

RICHARD BADER
McMaster University
Chemistry Department
1280 Main St. W.
Hamilton, Ontario L8S 4M1
Canada

KYOUNG BAECK
University of Florida
Quantum Theory Project
377 WM Hall
Gainesville, FL 32611

JON BAKER
BIOSYM Technologies, Inc.
9685 Scranton Road
San Diego, CA 92121-2777

ANNA BALKOVA
University of Florida
Quantum Theory Project
370 WM Hall
Gainesville, FL 32611

RODNEY BARTLETT
University of Florida
Quantum Theory Project
381 WM Hall
Gainesville, FL 32611

INDER BATRA
IBM Almaden Research Center
K44/802 650 Harry Road
San Jose, CA 95120-6099

SULLIVAN BECK
University of Florida
Quantum Theory Project
345 WM Hall
Gainesville, FL 32611

AXEL BECKE
Queen's University
Department of Chemistry
Kingston, Ontario K7L 3N6
Canada

DARIO BEKSIC
University of Florida
Quantum Theory Project
348 WM Hall
Gainesville, FL 32611

MICHAEL BENSON
Memphis State University
Department of Chemistry
Memphis, TN 38152

MARK BERGER
Silicon Graphics
1100 Abernathy Rd NE STE.1120
Atlanta, GA 30328

GORAN BERGSON
Uppsala University
Department of Chemistry
P.O. Box 531
Uppsala S-751 21
Sweden

MICHAEL BERMAN
Scientific Research Air Force Office of
AFOSR/NC Suite B115
110 Duncan Ave.
Bolling AFB, DC 20332-0001

MARGARITA BERNAL-URUCHURTU
Universidad Autonoma del Estado de Morelos
Av. Universidad 1001
Col. Chamilpa
Cuernavaca, Morelos
Mexico

DAVID BERNHOLDT
Pacific Northwest Laboratory
Molecular Science Research Ctr
P.O. Box 999
Richland, WA 99352-0999

MANUEL BERRONDO
Brigham Young University
Physics Department
296-ESC
Provo, UT 84602-1022

DAVID BEVERIDGE
Wesleyan University
Chemistry Department
Hall-Atwater Laboratories
Middletown, CT 06457

RICARDO BICCA DE ALENCASTRO
Rio de Janeiro Universidade Federal de
Instituto de Quimica
Cidade Universitaria, CT, BL A
Rio de Janeiro, RJ 21941
Brazil

DAVID BISHOP
University of Ottawa
Chemistry Department
Ottawa K1N6N5
Canada

RAYMOND BISHOP
University of Manchester Institute of Science
& Tech.
Department of Mathematics
P.O. Box 88
Manchester M60 1QD
United Kingdom

RUUD BLOCK
University of Amsterdam
Physics Chemistry Department
Nieuwe Achtergracht 126
Amsterdam 1018 WS
The Netherlands

JONATHAN BOETTGER
Los Alamos National Laboratory
Group T-1, MS B221
Los Alamos, NM 87545-0000

EDWARD BOUDREAUX
University of New Orleans
Chemistry Department
Lakefront
New Orleans, LA 70148-2820

J. L. BREDAS
University of Mons
Chimie des Materiaux Nouveaux
Place du Parc 20
Mons B-7000
Belgium

MARCUS BREWSTER
University of Florida
Pharmos Corporation
Two Innovation Drive, Suite A
Alachua, FL 32615

ANDERS BROO
University of Florida
Quantum Theory Project
380 WM Hall
Gainesville, FL 32611

PAUL BRUMER
University of Toronto
Department of Chemistry
80 St. George Street
Toronto, Ontario M5S 1A1
Canada

JEAN-LOUIS CALAIS
University of Uppsala
Quantum Chemistry Group
Box 518
Uppsala S-75120
Sweden

SYLVIO CANUTO
Universidade de Sao Paulo
Instituto de Fisica
Cxp 20516
Sao Paulo, Sao Paulo 01452-990
Brazil

CRISTIAN CARDENAS
University of Florida
Quantum Theory Project
P.O. Box 118435
345 WM Hall
Gainesville, FL 32611-8435

MIGUEL CASTRO
University of Montreal
Department of Chemistry
CP 6128, Succursale A
Montreal, Quebec H3C 3J7
Canada

LIST OF PARTICIPANTS

697

MAURO CAUSA
University of Torino
Dept. of Inorganic Chemistry
Via P. Giuria 5
Torino 10125
Italy

ANDRES CEDILLO
Universidad Autonoma Metropolitana
Depto. de Quimica
Apartado Postal 86-219
Villa Coapa, DF 14391
Mexico

CARY CHABALOWSKI
US Army Research Lab
AMSRL-WT-PC
Aberdeen Proving Ground, MD 21005-5066

PIERRE CHABRIER
University of Florida
Quantum Theory Project
Gainesville, FL 32611

ANNE CHAKA
The Lubrizol Corporation
29400 Lakeland Blvd.
Research Division
Wickliffe, OH 44092-2298

GRZEGORZ CHALASINSKI
University of Warsaw
Chemistry Department
ul. Pasteura 1
Warsaw 02-093
Poland

MATT CHALLACOMBE
Florida State University
Chemistry Department
Tallahassee, FL 32306-3006

DAVID CHANDLER
University of California
Department of Chemistry
Berkeley, CA 94720

DANIEL CHIPMAN
University of Notre Dame
Radiation Laboratory
Notre Dame, IN 46556-0579

SAN-YAN CHU
National Tsing Hua University
Department of Chemistry
Hsinchu, Taiwan 30043
China

PAUL CHUN
University of Florida J. Hillis Miller Health Ctr.
Biochem. & Mol. Biology Dept.
Box 100245
Gainesville, FL 32610-0245

JERZY CIOSLOWSKI
The Florida State University
Department of Chemistry, B-164
Tallahassee, FL 32306-3006

OAKLEY CRAWFORD
Oak Ridge National Laboratory
Health Sciences Research Div.
P.O. Box 2008, NS 6123
Oak Ridge, TN 37831-6123

PETER CSAVINSZKY
University of Maine
Physics and Astronomy Dept.
Orono, ME 04469-0108

CHRISTINE CULOT
University of Namur
Department of Chemistry
61 Rue de Bruxelles
Namur
Belgium

TOM CUNDARI
Memphis State University
Department of Chemistry
3744 Walker
Memphis, TN 38152

JOAQUIM DA MOTTA NETO
University of Florida
Quantum Theory Project
348 WM Hall
Gainesville, FL 32611

HERBERT DACOSTA
University of Florida
Quantum Theory Project
372 WM Hall
Gainesville, FL 32611

- ROBERT DAMBURG
Latvian Academy of Sciences
Institute of Physics
Salaspils, Riga 229021
Latvia
- ROBIN DAVIES
University of Wales College of Cardiff
Welsh School of Pharmacy
King Edward VII Avenue
Cardiff, Wales CF1 3XF
United Kingdom
- MURRAY DAW
Sandia National Laboratory
MS9161, Sandia Labs
Livermore, CA 94551
- ALEX DE VRIES
Rijksuniversiteit Groningen
Department of Chemistry
Nijenborgh 4
Groningen, AG 9747
The Netherlands
- ALAIN DEDIEU
Universite Louis Pasteur CNRS
Lab. de Chimie Quantique
4 rue Blaise Pascal
Strasbourg F-67000
France
- GERARDO DELGADO-BARRIO
CSIC Instituto de Matematicas y Fisica
Fundamental
Calle Serrano, 113-123
Madrid 28006
Spain
- JOSEPH DELHALLE
Universitaires Notre-Dame de la Paix
Departement de Chimie
Rue de Bruxelles 61
Namur B-5000
Belgium
- BRUCE DERBY
Sun Microsystems Marketing Soni Strang
500 Cypress Creek Rd. W. #250
Ft. Lauderdale, FL 33309
- ERIK DEUMENS
University of Florida
Quantum Theory Project
359 Wm Hall
Gainesville, FL 32611
- KEN DILL
University of California
Pharmaceutical Chemistry, S926
San Francisco, CA 94143-1204
- AGUSTIN DIZ
University of Florida
Quantum Theory Project
372 WM Hall
Gainesville, FL 32611
- ANTHONY DRIBBEN
University of Florida
Department of Chemistry
305 CRB
Gainesville, FL 32611
- CLIFFORD DYKSTRA
Indiana University
Department of Chemistry
402 N. Blackford Street
Indianapolis, IN 46202-3274
- RON ELBER
University of Illinois
Chemistry M/C 111
829 W. Taylor
Chicago, IL 60680
- EPHRAIM ELIAV
Tel Aviv University
School of Chemistry
Tel Aviv 69978
Israel
- THOMAS ENEVOLDSEN
Odense University
Dept. of Chemistry
Campusvej 55
Odense M DK-5230
Denmark
- GUILLERMINA ESTIU
Universidad Nacional de La Plata
Programma Quinor
47 y 115, CC 962
La Plata 1900
Argentina

JACK FAJER
Brookhaven National Laboratory
Department of Applied Science
Upton, NY 11973-5000

ADELBERTO FAZZIO
Universidade de Sao Paulo Instituto de Fisica
CxP 20516
Sao Paulo, SP 01452-990
Brasil

FRANCISCO FERNANDEZ
La Plata Universidad Nacional de
Departamento de Quimica
Calle 47 esquina 115, C.C. 962
La Plata 1900
Argentina

BERND FEYEN
University of Antwerp
Dep. WIS-INF
Groenenborgerlaan 171
Antwerpen 2020
Belgium

SIGHART FISCHER
Technische Universitat Munchen
Physik Department T38
Boltzmannstrasse
Garching 8046
Germany

JOSEPH FRIPIAT
Universitaires Notre-Dame de la Paix
Departement de Chimie
Rue de Bruxelles, 61
Namur B-5000
Belgium

ED GAINES
Silicon Graphics
100 Abernathy Rd.
N.E. Ste. 1120
Atlanta, GA 30328

VLADIMIR GALKIN
Ukrainian Academy of Science
Inst. for Low Temperature Phys & Engineering
47 Lenin pr.
Kharkov 310164
Ukraine

JURGEN GAUSS
Universitat Karlsruhe
Lehrstuhl fur Theoretische y Physikalische
Chemie
Karlsruhe D-76128
Germany

DENNIS GERSON
IBM
2511 N.W. 41st Street
Gainesville, FL 32606

LIONEL GOODMAN
Rutgers University
Chemistry Department
New Brunswick, NJ 08903

MARK GORDON
Iowa State University
Department of Chemistry
Wilhelm 304
Ames, IA 50011-3111

JURGEN GRAFENSTEIN
Max Planck Institute
Physik Komplexes Systeme
Postfach 80 06 65
Stuttgart D-70506
Germany

FRITZ GREIN
University of New Brunswick
Chemistry Department
Fredericton, NB E3B 6E2
Canada

J. GRIGERA
Universidad Nacional de La Plata
CONICET, IFLYSIB
C.C. 67
La Plata 1900
Argentina

STEVEN GWALTNEY
University of Florida
Quantum Theory Project
345 WM Hall
Gainesville, FL 32611

MARK HAGMANN
Florida International University
Department of Electrical and Computer
Engineering
Miami, FL 33199

MICHAEL HALL
Texas A&M University
Department of Chemistry
College Station, TX 77843-3255

NICHOLAS HANDY
University of Cambridge
Department of Chemistry
Lensfield Road
Cambridge CB2 1EW
United Kingdom

AAGE HANSEN
University of Copenhagen
Department of Chemistry
Universitetsparken 5
Copenhagen Ø DK-2100
Denmark

DAN HARRIS
Molecular Research Institute
845 Page Mill Road
Palo Alto, CA 94304

FRANK HARRIS
University of Utah
Department of Chemistry
Salt Lake City, UT 84112

MARTIN HEAD-GORDON
University of California
Department of Chemistry
Berkeley, CA 94720-9989

KAI-MING HO
Iowa State University
Department of Physics
Ames Laboratory
Ames, IA 50011-3020

GERMUND HOJER
de Mexico Universidad Nacional Autónoma
Facultad de Química
Ciudad Universitaria
Mexico, D.F. 04510
Mexico

YA-WEN HSIAO
University of Florida
Quantum Theory Project
348 WM Hall
Gainesville, FL 32611-8435

CHING HAN HU
The University of Georgia CCQC
1001 Cedar Street
Athens, GA 30602-2556

MING-JU HUANG
University of Florida Center for Drug Discovery
College of Pharmacy
Box 100497
Gainesville, FL 32610

KONCAY HUSEYIN
University of Waterloo Systems Designs Eng.
Waterloo, Ontario N2L 3G1
Canada

TSUTOMU IKEGAMI
Keio University
Science & Technology Dept.
3-14-1 Hiyoshi
Kohoku-ku, Yokohama 223
Japan

I. A. IL'ICHEVA
Russian Academy of Sciences
Institute of Molecular Biology
Vavilov Str. 32
Moscow B-334 117984
Russia

YASUYUKI ISHIKAWA
University of Puerto Rico
Department of Chemistry
P.O. Box 23346
San Juan 00931-3346
Puerto Rico

SAUL JACCHIERI
Universidade Federal de Minas Gerais
Depto. de Bioquímica
Laboratório de Biologia Computacional
Belo Horizonte, MG 31270
Brazil

MEHRAN JALAE
Purdue University
Department of Chemistry
402 North Blackford Street
Indianapolis, IN 46202

JAN JENSEN
Iowa State University
Chemistry Department
Gilman Hall
Ames, IA 50011-3111

BOGUMIL JEZIORSKI
University of Warsaw
Chemistry Department
Pasteura 1
Warsaw 02-093
Poland

BENNY JOHNSON
Q-Chem, Inc.
7520 Graymore Road
Pittsburgh, PA 15221

LIST OF PARTICIPANTS

701

HERBERT JONES
Florida A&M University
Physics Department
Tallahassee, FL 32307

POUL JORGENSEN
Aarhus University
Department of Chemistry
Langelandsgade 140
Aarhus C DK-8000
Denmark

UZI KALDOR
Tel Aviv University
School of Chemistry
Tel Aviv 69978
Israel

MICHAEL KASHA
Florida State University
Institute of Molecular
Biophysics
Tallahassee, FL 32306-3015

PATRICK KELLY
John Wiley and Sons, Inc.
605 Third Ave.
New York, NY 10158

JAMES KING
U.S. Army Edgewood RD&E Center
SCBRD-RTC
Aberdeen Proving Ground, MD 21010-5423

KARL KIRSCHNER
Lake Forest College
Chemistry Department
555 N. Sheridan
Lake Forest, IL 60045

BERNARD KIRTMAN
University of California
Department of Chemistry
Santa Barbara, CA 93106-9510

DOUGLAS KLEIN
Texas A&M University
Marine Science Department
Galveston, TX 77553-1675

ANTONIOS KOURES
Allied Signal
50 E. Algonquin Rd.
Des Plaines, IL 60017-5016

MORRIS KRAUSS
NIST Center for Advanced
Research Biotechnology
9600 Gudelsky Drive
Rockville, MD 20850

CARLOS KUBLI-GARFIAS
University of Mexico
Biomedical Institute
Apartado Postal 70-469
Mexico, DF
Mexico

HENRY KURTZ
Memphis State University
Department of Chemistry
Memphis, TN 38152

JANOS LADIK
Erlangen-Nuremberg University
Institut fur Theoretische Chem
Egerlandstrasse 3
Erlangen D-91058
Germany

ANTONIO LAGANA
Universita di Perugia
Dipartimento di Chimica
Perugia 06100
Italy

WILLIAM LAIDIG
Proctor & Gamble Company
Miami Valley Laboratories
P.O. Box 398707
Cincinnati, OH 45239-8707

UZI LANDMAN
Georgia Institute of Technology
School of Physics
Atlanta, GA 30332

GUY LARSON
Brigham Young University Physics &
Astronomy
296 ESC
Provo, UT 84602

WALTER LAUDERDALE
Laboratory Frank J. Seiler Research
2354 Vandenberg Drive
Suite 2A35
USAF Academy, CO 80840-6272

PIERRE LEBRETON
The University of Illinois
Chemistry Department
845 W. Taylor St., M/C 111
Chicago, IL 60607

KEE LEE
WonKwang University
Department of Chemistry
344-2 ShinYong-Dong
Iri 570-749
Korea

THERESA LEE
U.S. Army Corps of Engineers WES
IM-MI-C, Bldg. 112, Rm. 113
3909 Halls Ferry Road
Vicksburg, MS 39180-6199

YOON LEE
KAIST
Department of Chemistry
Taejon 305-701
Korea

WILLIAM LESTER
University of California
Department of Chemistry
Berkeley, CA 94720

JERZY LESZCZYNSKI
Jackson State University
Chemistry Department
1400 Lynch Street
Jackson, MS 39217

ZACHARY LEVINE
Ohio State University
Department of Physics
174 W. 18th Avenue
Columbus, OH 43210-1106

ZE-SHENG LI
Jilin University Inst. of Theoretical Chemistry
Changchun 130021
China

QUN LIN
Florida State University
Chemistry Department
Tallahassee, FL 32306-3006

JAN LINDERBERG
Aarhus University
Chemistry Department
Langelandsgade 140
Aarhus C DK-8000
Denmark

ANTONIO LINO
de Uberlandia Universidade Federal
Depto. de Ciencias Fisicas
Campus Santa Monica
Uberlandia, MG 38400-902
Brazil

RICARDO LONGO
University of Florida
Quantum Theory Project
372 WM Hall
Gainesville, FL 32611

PER-OLOV LOWDIN
University of Florida Quantum Theory Project
P.O. Box 118435
362 Williamson Hall
Gainesville, FL 32611-8435

CHI-HAO LUAN
Birmingham University of Alabama
Laboratory of Molecular
Biophysics, VH 300
Birmingham, AL 35294-0019

STACY LUCAS
University of North Florida
Natural Sciences
4567 St. Johns Bluff Rd. S.
Jacksonville, FL 32224-2645

DAVID MAGERS
Mississippi College
Chemistry Department
Box 4065
Clinton, MS 39058

PER-AKE MALMQUIST
University of Lund Chemical Center
Theoretical Chemistry Dept.
P.O. Box 124
Lund S-22100
Sweden

LIST OF PARTICIPANTS

703

NORMAN MARCH
Oxford University
Theoretical Chemistry Dept.
5 South Parks Road
Oxford, England OX1 3UB
United Kingdom

MARTIN MARTINOV
Florida State University
Chemistry Department
Tallahassee, FL 32306-3006

RENEE MATTIE
University of Florida

CHANGJIANG MEI
University of Florida
Quantum Theory Project
362 WM Hall
Gainesville, FL 32611

HORIA METIU
University of California
Department of Chemistry
Santa Barbara, CA 93106-9510

SARA MEZA-HOJER
de Mexico Universidad Nacional Autonoma
Facultad de Quimica
Cuidad Universitaria
Mexico, D.F. 04510
Mexico

DAVID MICHA
University of Florida
Quantum Theory Project
356 WM Hall
Gainesville, FL 32611

FREDERICK MIES
N.I.S.T.
Physics Bldg., Rm. B268
Gaithersburg, MD 20899

MANOJ MISHRA
Indian Institute of Technology
Department of Chemistry
Powai, Bombay 400076
India

STACEY MIXON
Florida State University
Chemistry Department
Tallahassee, FL 32306-3006

BENNY MOGENSEN
University of Florida
Quantum Theory Project
372 WM Hall
Gainesville, FL 32611

HENDRIK MONKHORST
University of Florida
Quantum Theory Project
361 WM Hall, Box 8435
Gainesville, FL 32611-8435

MARK MONTTOYA
University of Florida
Dept. of Chem. Engineering
Gainesville, FL 32611

JORGE MORALES
University of Florida
Quantum Theory Project
362 WM Hall, P.O. Box 118435
Gainesville, FL 32611-8435

JOHN MORGAN III
Institute for Advanced Study
School of Historical Studies
Princeton, NJ 08540

ROBERT MORRISON
East Carolina University
Chemistry Department
Greenville, NC 27858-4353

BENGT NAGEL
Royal Institute of Technology
Theoretical Physics Department
Stockholm S-100 44
Sweden

GABOR NARAY-SZABO
Eotvos University
Theoretical Chemistry Dept.
P.O. Box 32
Budapest H-1518
Hungary

ROBERT NESBET
IBM Almaden Research Center
K43/802, 650 Harry Road
San Jose, CA 95120-6099

MARSHALL NEWTON
Brookhaven National Lab.
Department of Chemistry
555A, PO Box 5000
Upton, NY 11973

JAN NOBEL
University of Florida
Quantum Theory Project
375 WM Hall
Gainesville, FL 32611

MARCEL NOOIJEN
University of Florida
Quantum Theory Project
371 WM Hall
Gainesville, FL 32611

JAMES NORRIS
Argonne National Lab.
Chemistry Department
9700 Cass Avenue
Argonne, IL 60439

MARCO NUNEZ
Metropolitana Iztapalapa Universidad
Autonoma
Depto. de Fisica
Apartado Postal 55-534
Mexico, DF 09340
Mexico

N. YNGVE OHRN
University of Florida
Quantum Theory Project
363 Williamson Hall
Gainesville, FL 32611-2085

NEVIN OLIPHANT
University of Florida
Quantum Theory Project
377 WM Hall
Gainesville, FL 32611

JUAN ORIERO
University of Florida
Quantum Theory Project
348 WM Hall
Gainesville, FL 32611

VINCENT ORTIZ
University of New Mexico
Chemistry Department
Albuquerque, NM 87131

RADOVAN PADJEN
CNET—France Telecom
Laboratoire de Bagneux
196 Ave. Henri Ravers, BP 107
Bagneux, Cedex 92225
France

ALEJANDRO PALMA
Universidad Autonoma de Puebla
Instituto de Fisicas
y Astrofisica
Tonantzintla, Puebla 72000
Mexico

CAROL PARISH
Indiana University
Department of Chemistry
402 N. Blackford Street
Indianapolis, IN 46202

WILLIAM PARKINSON
Southeastern Louisiana University
Department of Chemistry
Hammond, LA 70402

AJITH PERERA
University of Florida
Quantum Theory Project
345 WM Hall
Gainesville, FL 32611

JORGE PEREZ
de Rio Cuarto Universidad Nacional
Chemistry & Physics Department
Estafeta Postal No. 9
Rio Cuarto 5800
Argentina

GEORGE PERKINS
Sun Microsystems Marketing Soni Strang
500 Cypress Creek Rd. W. #250
Ft. Lauderdale, FL 33309

JOAKIM PERSSON
University of Lund Chemical Center
Theoretical Chemistry Dept.
P.O. Box 124
Lund S-22100
Sweden

EMIL POP
Pharmos Corporation
2 Innovation Drive
Alachua, FL 32615

LIST OF PARTICIPANTS

705

JOHN POPLÉ
Northwestern University
Chemistry Department
2145 Sheridan Road
Wilmette, IL 60208

PARAS PRASAD
State University of New York
Department of Chemistry
113 Acheson Hall
Buffalo, NY 14214

MICHAEL PROBST
Innsbruck University
Institut für Allgemeine, Anorganische und
Theor. Chemie
Innsbruck, Innsbruck
Austria

GEORGE PURVIS III
CACHÉ Scientific, Inc.
P.O. Box 5000, MS 13-400
Beaverton, OR 97077

JAMES RABINOWITZ
Agency U.S. Environmental Protection
GTD/HERL, MD-68
Research Triangle Park, NC 27711

HERSCHEL RABITZ
Princeton University
Department of Chemistry
Frick Laboratory
Princeton, NJ 08544-1009

MICHAEL RAMEK
Technische Universität Graz
Physikal. Chem.
Graz A-8010
Austria

MILAN RANDIC
Drake University
Mathematics & Computer Science
Des Moines, IA 50311

ARVI RAUK
The University of Calgary
Department of Chemistry
2500 University Drive, N.W.
Calgary, Alberta T2N 1N4
Canada

JOSE RECAMIER
de México Universidad de Autónoma
Instituto de Física
Lab. de Cuernavaca, AP 139-13
Cuernavaca, Morelos 62191
Mexico

ALISTAIR RENDELL
SERC Daresbury Laboratory
Theory & Computational
Science Division
Daresbury, Warrington WA44AD
United Kingdom

PETER REYNOLDS
Office of Naval Research
Physics Division, Code 3121
800 N. Quincy Street
Arlington, VA 22217

WILLIAM RHODES
Florida State University
Chemistry Department
Tallahassee, FL 32306-3006

ANN RICHARD
Agency U.S. Environmental Protection
Maildrop-68
Research Triangle Park, NC 27711

NIGEL RICHARDS
University of Florida
Department of Chemistry
301 CRB
Gainesville, FL 32611

BJORN ROOS
University of Lund
Theoretical Chemistry Dept.
Chemical Centre, POB 124
Lund S-221 00
Sweden

NOTKER ROSCH
Technische Universität München
Chemistry, Dept of Theor.
Lichtenbergstrasse 4
Garching D8046
Germany

JOHN ROSENBERG
University of Pittsburgh
Dept. of Biological Sciences
Pittsburgh, PA 15260

PIOTR ROZYCZKO
University of Florida
Quantum Theory Project
345 WM Hall
Gainesville, FL 32611

JURI RUBIN
Ukrainian Academy of Sciences
Inst. of Low Temperature Phys.
& Engineering, 47, Lenin Ave.
Khazkov 310164
Ukraine

KEITH RUNGE
University of Florida
Quantum Theory Project
376 WM Hall
Gainesville, FL 32611

JOHN SABIN
University of Florida
Quantum Theory Project
355 Williamson Hall
Gainesville, FL 32611-8435

LYNN SALEMI
University of Florida
Quantum Theory Project
345 WM Hall
Gainesville, FL 32611

MALUISA SAN ROMAN Z
Edo. Morelos Universidad Autonoma del Lab.
Ingenieria Molecular
Av. Universidad S/N
Cuernavaca, Morelos
Mexico

RUBEN SANTIAGO ACOSTA
de Mexico Universidad Nacional Autonoma
Instituto de Ciencias Nucleare
Circuito Exterior, AP 70-543
Mexico, DF 04510
Mexico

HAROLD SCHERAGA
Cornell University
Baker Lab of Chemistry
Ithaca, NY 14853-1301

MICHAEL SCHMIDT
Iowa State University
Chemistry Department
311 Wilhelm Hall
Ames, IA 50011-3111

PETER SCHMIDT
Office of Naval Research Chemistry Division
800 N. Quincy Street
Arlington, VA 22217-5000

DIETER SCHUCH
J.W. Goethe-Universitat
Inst. fur Theoretische Physik
Robert-Mayer Str. 8-10
Frankfurt am Main 60054
Germany

GUSTAVO SCUSERIA
Rice University
Chemistry Department
P.O. Box 1892
Houston, TX 77251-1892

MAX SEEL
University of Michigan Technological College of
Sciences & Arts
1400 Townsend Drive
Houghton, MI 49931-1295

ELIZABETH SEIBERLING
University of Florida
Department of Physics
528 NSC
Gainesville, FL 32611

HIDEO SEKINO
University of Florida
Quantum Theory Project
370 WM Hall
Gainesville, FL 32611

JORGE SEMINARIO
University of New Orleans
Chemistry Department
New Orleans, LA 70148

ISAIAH SHAVITT
Ohio State University
Department of Chemistry
120 W. 18th Avenue
Columbus, OH 43210-1173

GEORGE SHIELDS
Lake Forest College
Chemistry Department
555 N. Sheridan
Lake Forest, IL 60045

HARRIS SILVERSTONE
Johns Hopkins University
Department of Chemistry
3400 N. Charles Street
Baltimore, MD 21218-2685

CARLOS SIMMERLING
University of Illinois
Chemistry Department, M/C 111
845 W. Taylor
Chicago, IL 60607-7061

OKTAY SINANOGLU
Yale University
Chemistry Department, SCL
P.O. Box 6666
New Haven, CT 06511-8118

VEDENE SMITH, JR.
Queen's University
Department of Chemistry
Kingston, Ontario K7L 3N6
Canada

RICHARD SQUIRE
Marshall University
Department of Chemistry
901 W. DuPont Avenue
Belle, WV 25015

CHRISTOPHER STANTON
University of Florida
Department of Physics
Gainesville, FL 32611

JOHN STANTON
University of Texas at Austin
Department of Chemistry and Biochemistry
Austin, TX 78712-1167

KRASSIMIR STAVREV
University of Florida
Quantum Theory Project
380 WM Hall
Gainesville, FL 32611

BORIS STEFANOV
Florida State University
Department of Chemistry
Tallahassee, FL 32306-3006

WALTER STEVENS
Standards & Technology National Institute of
CARB
9600 Gudelsky Drive
Rockville, MD 20850

MALCOLM STOCKS
Oak Ridge National Laboratory Materials
Science Section
Metals and Ceramics Division
P.O. Box 2008
Oak Ridge, TN 37831-6114

JOYCE STOUT
Indianapolis Indiana-Purdue University
Chemistry Department
402 N. Blackford Street
Indianapolis, IN 46202

ALAN STRATTON
CACHe Scientific
P.O. Box 349
Chilhowie, VA 24319

SPERANTA SVIRSCHEVSKY
Florida State University Inst. of Molecular
Biophysics
Tallahassee, FL 32306-3015

PETER SZALAY
University of Florida
Quantum Theory Project
362 WM Hall, P.O. Box 118435
Gainesville, FL 32611-8435

KRZYSZTOF SZALEWICZ
University of Delaware
Department of Physics
Newark, DE 19716

LASZLO SZENTPALY
University of the West Indies
Chemistry Department
Mona Campus
Kingston 7
Jamaica

JAMES TALMAN
University of Western Ontario
Applied Mathematics Department
London, Ontario N6A 5B7
Canada

TOOMAS TAMM
University of Florida
Quantum Theory Project
380 WM Hall
Gainesville, FL 32611

UFUK TANERI
University of Waterloo Quantum Theory Group
Department of Chemistry
T.R.N.C.
Gazi Magosa, Mersin 10
Turkey

JOACHIM THEILHABER
Thinking Machines Corporation
245 First Street
Cambridge, MA 02142

WALTER THIEL
Universitat Zurich
Organisch-Chemisches Institut
Winterthurerstr. 190
Zurich CH-8057
Switzerland

COLIN THOMSON
University of St. Andrews
Department of Chemistry
North Haugh
St. Andrews KY16 9ST
Scotland

ERIK THULSTRUP
Roskilde University
Institute of Life Sciences
P.O. Box 260
Roskilde DK-4000
Denmark

IGOR TOPOL
Program Resources, Inc. National Cancer
Institute
Frederick Cancer Research & Development
Center, P.O. Box B
Frederick, MD 21702

SAMUEL B. TRICKEY
University of Florida
Quantum Theory Project
364 WM Hall
Gainesville, FL 32611-2085

NENAD TRINAJSTIC
The Rugjer Boskovic Institute
Physical Chemistry Dept.
Bijenicka 54
Zagreb, HR 41001
Croatia

CARL TRINDLE
University of Virginia
Department of Chemistry
NCB 242, UVA
Charlottesville, VA 22903

DAN URRY
Birmingham University of Alabama
Lab. of Molecular Biophysics
525 Volker Hall, VH 300
Birmingham, AL 35294-0019

CARMELA VALDEMORO
Investigaciones Cientificas Consejo Superior de
Instituto de Ciencias Material
Serrano 123
Madrid 28006
Spain

PIET VAN DUIJNEN
University of Groningen
Chemistry Department
Nyenborgh 4
Groningen, AG 9747
The Netherlands

MATESH VARMA
Department of Energy
ER-73
Washington, DC 20585

DAN VASILESCU
Universite de Nice
Laboratoire de Biophysique
Parc Valrose
Nice, Cedex 2 06108
France

DANIEL VERCAUTEREN
de la Paix Universite Notre Dame
Lab. Physico Chimie Info.
Rue de Bruxelles, 61
Namur B-5000
Belgium

ROBERT VERGENZ
University of North Florida
Department of Natural Sciences
Jacksonville, FL 32225-2645

SHAWN WALLACE
University of North Florida
12426 Valpariss Tr.
Jacksonville, FL 32223

JIAN WANG
Dalhousie University
Department of Chemistry
Halifax, Nova Scotia B3H 4J3
Canada

ARIEH WARSHEL
University of Southern California
Chemistry Department
Los Angeles, CA 90089

DAVID WATT
University of St. Andrews
Physics & Astronomy Department
Bute Medical Bldgs.
St. Andrews, Fife KY16 9TS
Scotland

JOHN WATTS
University of Florida
Quantum Theory Project
367 WM Hall
Gainesville, FL 32611

BRIAN WEINER
Penn State University
Physics Department
College Place
Dubois, PA 15801

CARTER WHITE
Naval Research Laboratory
Supervisory Research Physicist
Head Theor. Chem. Section
Washington, DC 20375

CHRISTOPHER WHITE
University of California at Berkeley
Department of Chemistry
Berkeley, CA 94720

ANGELA WILSON
University of Minnesota Department of
Chemistry
139 Smith Hall
207 Pleasant St., S.E.
Minneapolis, MN 55455-0431

PETER WINKLER
University of Nevada
Department of Physics, 220
Reno, NV 89557-0058

BRIAN WLADKOWSKI
Biotechnology Center for Advanced Research
9600 Gudelsky Dr.
Rockville, MD 20850

PETER WOLYNES
University of Illinois
Department of Chemistry
505 South Mathews Avenue
Urbana, IL 61801

JIN ZHONG WU
University of Florida
Quantum Theory Project
368 WM Hall
Gainesville, FL 32611

SATOSHI YABUSHITA
Chiba University
Chemistry Department
1-33, Yayoi-cho
Inage-ku, Chiba 263
Japan

JIAN-MIN YUAN
Drexel University
Physics Department
32nd & Chestnut Street
Philadelphia, PA 19104

MICHAEL ZERNER
University of Florida
Quantum Theory Project
382 WM Hall
Gainesville, FL 32611

CHANG-GUO ZHAN
University Central China Normal
Department of Chemistry
Wuhan 430070
China

HONGXING ZHANG
Jilin University Inst. of Theoretical Chemistry
Changchun 130023
China

ZHONGXIANG ZHOU
Protein Design Labs, Inc.
2375 Garcia Avenue
Mountain View, CA 94043

QINGSHENG ZHAO
University of North Carolina
Department of Chemistry
Chapel Hill, NC 27599

JAMES ZIEGLER
IBM Research
P.O. Box 218
Yorktown Heights, NY 10598

XUEHE ZHENG
University of Florida
Dept. of Chemistry
440 CRB
Gainesville, FL 32611

YU ZUB
Ukrainian Academy of Science
Institute of Surface Chemistry
pr. Nauki, 31
Kiev 252022
Ukraine

Author Index

- André, J.-M., 451, 469
Arteca, G. A., 433
Atabek, O., 113

Baraglia, R., 85
Bartlett, R. J., 3, 195, 379
Baxter, E., 565
Becke, A. D., 625
Beliaev, D., 667
Benson, M. T., 181
Bicca de Alencastro, R., 361
Birkenheuer, U., 675
Bishop, R. F., 155
Boettger, J. C., 675
Boudreaux, E. A., 565
Brédas, J. L., 481
Brenner, D. W., 129
Broeckhove, J., 173

Canuto, S., 265, 571
Castro, M., 645
Causá, M., 633
Cedillo, A., 231
Champagne, B., 451
Chung, S.-C., 595
Contreras, R. H., 39
Csavinsky, P., 227
Cuenya, H. H., 39
Cundari, T. R., 181

da Costa, H. F. M., 49
da Motta Neto, J. D., 361
Deleuze, M., 469
Delhalle, J., 469
Deumens, E., 3
Diercks, G. H. F., 339
Dixon, C. M., 309
Diz, A., 11

Edgecombe, K. E., 215
Eliav, E., 205

Fazzio, A., 571
Feyn, B., 173
Flamant, I., 469
Freedman, T. B., 315
Fripiat, J. G., 451

Gervasi, O., 85
Giribet, C. G., 39
Grinberg, H., 39

Häberlen, O. D., 595
Hagmann, M. J., 271
Harris, F. E., 525
Hô, M., 215
Hood, R. B., 579

Ikegami, T., 529
Ishikawa, Y., 205, 541
Iwata, S., 529
Izquierdo B., G., 241

Jiang, T.-F., 65

Kaldor, U., 205
Karelson, M., 339
Karna, S. P., 395
Keshari, V., 541
Kirschner, K. N., 349
Klein, D. J., 501

Laforenza, D., 85
Laganà, A., 85
Leite, J. R., 667
Leszczyński, J., 579
Levine, Z. H., 411
Li, Y., 181
Linderberg, J., 7
Lino, A. T., 667
Liu, X., 501
Lögdin, M., 481
Löwdin, P.-O., 3

Magers, D. H., 579
March, N. H., 421
Martín, M., 261
Medikeri, M. N., 29
Mei, C., 687
Micha, D. A., 3, 49
Mihalić, Z., 525
Mintmire, J. W., 129
Mishra, M. K., 29
Mizell, J. R., 309
Monkhorst, H. J., 3

- Morrison, R. C., 309
Mosley, D. H., 451, 469
Nesbet, R. K., 77
Nobel, J. A., 283, 299
Noga, J., 379
Núñez, M. A., 241
Öhrn, N. Y., 1
Öhrn, Y., 11
Ortiz, F. S., 39
Ortiz, J. V., 23
Paldus, J., 139
Palma, A., 261
Pérez, J. E., 39
Piquini, P., 571
Pluta, T., 379
Prasad, P. N., 395
Probst, M., 553
Rauk, A., 315
Robertson, D. H., 129
Rösch, N., 595, 675
Ruiz de Azúa, M. C., 39
Sabin, J. R., 1, 3, 283, 299
Salahub, D. R., 645
Sandoval, L., 261
Schmider, H., 215
Schuch, D., 251
Scolfaro, L. M. R., 667
Seminario, J. M., 655
Shields, G. C., 349
Sinnott, S. B., 129
Sirois, S., 645
Smith, V. H., Jr., 215, 687
Strohecker, L. A., 181
Takahashi, E. K., 667
Tamm, T., 339
Taneri, U., 139
Theilhaber, J., 611
Trickey, S. B., 3, 283, 299, 675
Trinajstić, N., 525
van Leuven, P., 173
Watts, J. D., 195
White, C. T., 129
Winkler, P., 103
Wu, J. Z., 299
Xian, Y., 155
Yuan, J.-M., 65
Zakrzewski, V. G., 23
Zerner, M. C., 1, 3, 339, 361
Zhan, H., 103
Zhang, Y., 103
Zupan, A., 633

**Published Symposia of the
*International Journal of Quantum Chemistry***

- 1967** QUANTUM CHEMISTRY SYMPOSIUM NO. 1
(Proceedings of the International Symposium on Atomic, Molecular, and Solid-State Theory)
- 1968** QUANTUM CHEMISTRY SYMPOSIUM NO. 2
(Proceedings of the International Symposium on Atomic, Molecular, and Solid-State Theory and Quantum Biology)
- 1969** QUANTUM CHEMISTRY SYMPOSIUM NO. 3 PART 1
(Proceedings of the International Symposium on Atomic, Molecular, and Solid-State Theory and Quantum Biology)
- 1970** QUANTUM CHEMISTRY SYMPOSIUM NO. 3 PART 2
(Proceedings of the International Symposium on Atomic, Molecular, and Solid-State Theory and Quantum Biology)
- 1971** QUANTUM CHEMISTRY SYMPOSIUM NO. 4
(Proceedings of the International Symposium on Atomic, Molecular, and Solid-State Theory and Quantum Biology)
- 1971** QUANTUM CHEMISTRY SYMPOSIUM NO. 5
(Proceedings of the International Symposium on Atomic, Molecular, and Solid-State Theory and Quantum Biology)
- 1972** QUANTUM CHEMISTRY SYMPOSIUM NO. 6
(Proceedings of the International Symposium on Atomic, Molecular, and Solid-State Theory and Quantum Biology)
- 1973** QUANTUM CHEMISTRY SYMPOSIUM NO. 7
(Proceedings of the International Symposium on Atomic, Molecular, and Solid-State Theory and Quantum Biology)
- 1974** QUANTUM CHEMISTRY SYMPOSIUM NO. 8
(Proceedings of the International Symposium on Atomic, Molecular, and Solid-State Theory and Quantum Statistics)
QUANTUM BIOLOGY SYMPOSIUM NO. 1
(Proceedings of the International Symposium on Quantum Biology and Quantum Pharmacology)
- 1975** QUANTUM CHEMISTRY SYMPOSIUM NO. 9
(Proceedings of the International Symposium on Atomic, Molecular, and Solid-State Theory and Quantum Statistics)
QUANTUM BIOLOGY SYMPOSIUM NO. 2
(Proceedings of the International Symposium on Quantum Biology and Quantum Pharmacology)

- 1976** QUANTUM CHEMISTRY SYMPOSIUM NO. 10
(Proceedings of the International Symposium on Atomic, Molecular, and Solid-State Theory and Quantum Statistics)
QUANTUM BIOLOGY SYMPOSIUM NO. 3
(Proceedings of the International Symposium on Quantum Biology and Quantum Pharmacology)
- 1977** QUANTUM CHEMISTRY SYMPOSIUM NO. 11
(Proceedings of the International Symposium on Atomic, Molecular, and Solid-State Theory, Collision Phenomena, and Computational Methods)
QUANTUM BIOLOGY SYMPOSIUM NO. 4
(Proceedings of the International Symposium on Quantum Biology and Quantum Pharmacology)
- 1978** QUANTUM CHEMISTRY SYMPOSIUM NO. 12
(Proceedings of the International Symposium on Atomic, Molecular, and Solid-State Theory, Collision Phenomena, and Computational Methods)
QUANTUM BIOLOGY SYMPOSIUM NO. 5
(Proceedings of the International Symposium on Quantum Biology and Quantum Pharmacology)
- 1979** QUANTUM CHEMISTRY SYMPOSIUM NO. 13
(Proceedings of the International Symposium on Atomic, Molecular, and Solid-State Theory, Collision Phenomena, Quantum Statistics, and Computational Methods)
QUANTUM BIOLOGY SYMPOSIUM NO. 6
(Proceedings of the International Symposium on Quantum Biology and Quantum Pharmacology)
- 1980** QUANTUM CHEMISTRY SYMPOSIUM NO. 14
(Proceedings of the International Symposium on Atomic, Molecular, and Solid-State Theory, Collision Phenomena, Quantum Statistics, and Computational Methods)
QUANTUM BIOLOGY SYMPOSIUM NO. 7
(Proceedings of the International Symposium on Quantum Biology and Quantum Pharmacology)
- 1981** QUANTUM CHEMISTRY SYMPOSIUM NO. 15
(Proceedings of the International Symposium on Atomic, Molecular, and Solid-State Theory, Collision Phenomena, and Computational Quantum Chemistry)
QUANTUM BIOLOGY SYMPOSIUM NO. 8
(Proceedings of the International Symposium on Quantum Biology and Quantum Pharmacology)
- 1982** QUANTUM CHEMISTRY SYMPOSIUM NO. 16
(Proceedings of the International Symposium on Quantum Chemistry, Theory of Condensed Matter, and Propagator Methods in the Quantum Theory of Matter)
QUANTUM BIOLOGY SYMPOSIUM NO. 9
(Proceedings of the International Symposium on Quantum Biology and Quantum Pharmacology)
- 1983** QUANTUM CHEMISTRY SYMPOSIUM NO. 17
(Proceedings of the International Symposium on Atomic, Molecular, and Solid-State Theory, Collision Phenomena, and Computational Quantum Chemistry)

QUANTUM BIOLOGY SYMPOSIUM NO. 10
(Proceedings of the International Symposium on Quantum Biology and Quantum Pharmacology)

1984 QUANTUM CHEMISTRY SYMPOSIUM NO. 18
(Proceedings of the International Symposium on Atomic, Molecular, and Solid-State Theory, and Computational Quantum Chemistry)
QUANTUM BIOLOGY SYMPOSIUM NO. 11
(Proceedings of the International Symposium on Quantum Biology and Quantum Pharmacology)

1985 QUANTUM CHEMISTRY SYMPOSIUM NO. 19
(Proceedings of the International Symposium on Atomic, Molecular, and Solid-State Theory, Scattering Problems, Many Body Phenomena, and Computational Quantum Chemistry)
QUANTUM BIOLOGY SYMPOSIUM NO. 12
(Proceedings of the International Symposium on Quantum Biology and Quantum Pharmacology)

1986 QUANTUM CHEMISTRY SYMPOSIUM NO. 20
(Proceedings of the International Symposium on Atomic, Molecular, and Solid-State Theory, Scattering Problems, Many Body Phenomena, and Computational Quantum Chemistry)
QUANTUM BIOLOGY SYMPOSIUM NO. 13
(Proceedings of the International Symposium on Quantum Biology and Quantum Pharmacology)

1987 QUANTUM CHEMISTRY SYMPOSIUM NO. 21
(Proceedings of the International Symposium on Quantum Chemistry, Solid-State Theory, and Computational Methods)
QUANTUM BIOLOGY SYMPOSIUM NO. 14
(Proceedings of the International Symposium on Quantum Biology and Quantum Pharmacology)

1988 QUANTUM CHEMISTRY SYMPOSIUM NO. 22
(Proceedings of the International Symposium on Quantum Chemistry, Solid-State Theory, and Computational Methods)
QUANTUM BIOLOGY SYMPOSIUM NO. 15
(Proceedings of the International Symposium on Quantum Biology and Quantum Pharmacology)

1989 QUANTUM CHEMISTRY SYMPOSIUM NO. 23
(Proceedings of the International Symposium on Quantum Chemistry, Solid-State Theory, and Molecular Dynamics)
QUANTUM BIOLOGY SYMPOSIUM NO. 16
(Proceedings of the International Symposium on Quantum Biology and Quantum Pharmacology)

1990 QUANTUM CHEMISTRY SYMPOSIUM NO. 24
(Proceedings of the International Symposium on Quantum Chemistry, Solid State Physics, and Computational Methods)
QUANTUM BIOLOGY SYMPOSIUM NO. 17
(Proceedings of the International Symposium on Quantum Biology and Quantum Pharmacology)

-
- 1991** QUANTUM CHEMISTRY SYMPOSIUM NO. 25
(Proceedings of the International Symposium on Quantum Chemistry, Solid State Physics, and Computational Methods)
QUANTUM BIOLOGY SYMPOSIUM NO. 18
(Proceedings of the International Symposium on Quantum Biology and Quantum Pharmacology)
- 1992** QUANTUM CHEMISTRY SYMPOSIUM NO. 26
(Proceedings of the International Symposium on Atomic, Molecular, and Condensed Matter Theory and Computational Methods)
QUANTUM BIOLOGY SYMPOSIUM NO. 19
(Proceedings of the International Symposium on the Application of Fundamental Theory to Problems of Biology and Pharmacology)
- 1993** QUANTUM CHEMISTRY SYMPOSIUM NO. 27
(Proceedings of the International Symposium on Atomic, Molecular, and Condensed Matter Theory and Computational Methods)
QUANTUM BIOLOGY SYMPOSIUM NO. 20
(Proceedings of the International Symposium on the Application of Fundamental Theory to Problems of Biology and Pharmacology)
- 1994** QUANTUM CHEMISTRY SYMPOSIUM NO. 28
(Proceedings of the International Symposium on Atomic, Molecular, and Condensed Matter Theory and Computational Methods)
QUANTUM BIOLOGY SYMPOSIUM NO. 21
(Proceedings of the International Symposium on the Application of Fundamental Theory to Problems of Biology and Pharmacology)

All of the above symposia can be individually purchased from the Subscription Department, John Wiley & Sons.